

Piet Christof Wölcken
Michael Papadopoulos *Editors*

Smart Intelligent Aircraft Structures (SARISTU)

Proceedings of the Final Project Conference



 Springer

The Springer logo, featuring a stylized white chess knight on a red background, followed by the word "Springer" in a white serif font.

Smart Intelligent Aircraft Structures (SARISTU)

Piet Christof Wölcken · Michael Papadopoulos
Editors

Smart Intelligent Aircraft Structures (SARISTU)

Proceedings of the Final Project Conference



Editors

Piet Christof Wölcken
AIRBUS Operations GmbH
Bremen
Germany

Michael Papadopoulos
EASN Technology Innovation Services
Budingem
Belgium

ISBN 978-3-319-22412-1 ISBN 978-3-319-22413-8 (eBook)
DOI 10.1007/978-3-319-22413-8

Library of Congress Control Number: 2015945325

Springer Cham Heidelberg New York Dordrecht London
© Springer International Publishing Switzerland 2016

This work is subject to copyright. All rights are reserved by the Publisher, whether the whole or part of the material is concerned, specifically the rights of translation, reprinting, reuse of illustrations, recitation, broadcasting, reproduction on microfilms or in any other physical way, and transmission or information storage and retrieval, electronic adaptation, computer software, or by similar or dissimilar methodology now known or hereafter developed.

The use of general descriptive names, registered names, trademarks, service marks, etc. in this publication does not imply, even in the absence of a specific statement, that such names are exempt from the relevant protective laws and regulations and therefore free for general use.

The publisher, the authors and the editors are safe to assume that the advice and information in this book are believed to be true and accurate at the date of publication. Neither the publisher nor the authors or the editors give a warranty, express or implied, with respect to the material contained herein or for any errors or omissions that may have been made.

Printed on acid-free paper

Springer International Publishing AG Switzerland is part of Springer Science+Business Media
(www.springer.com)

In memory of Kristina Ditzel

Foreword

About 3 billion people every year use air transport to realize their business and leisure needs, whereas about 5 trillion Euros worth of goods are transported by air. And these figures are on the rise: Annual passengers are expected to reach over 6 billion by 2030, according to current projections.

As the number of flights increases, pollution and noise from air travel impose significant challenges on the industry. This is why airlines, aircraft manufacturers, and researchers are constantly searching for new ways to make their planes lighter, with increased aerodynamic performance, achieving at the same time greater fuel efficiency and thereby reduce the environmental footprint of air travel.

Coordinated by Airbus, the Smart Intelligent Aircraft Structures (SARISTU) project brought together 64 partners from 16 countries with a common goal: to demonstrate the feasibility of reducing aircraft weight and operational costs, as well as improving the flight profile-specific aerodynamic performance.

During the four years of project implementation (September 2011–August 2015), the synergy of leading entities participating in this ambitious venture has succeeded to achieve some major breakthroughs in a number of technological fields.

Firstly, developments with respect to conformal morphing, in other words the gap- and kink-less change of the shape of aerodynamic surfaces, validated not only a suitable skin material, but even the ability to integrate additional functionalities such as heating and environmental protection. Furthermore, the technical feasibility of trailing edge morphing and the ability to consider active winglet control were investigated.

Secondly, developments in the wide area of structural health monitoring covered analysis methods, physical system integration at part manufacturing level, the combination of different measurement and analysis techniques on single areas of the aircraft, and a screening program for fundamental approaches to passive damage indicating surfaces.

Thirdly, multi-functional structure developments highlighted the ability to upscale nanocomposite improvements from the basic resin all the way up to industrially relevant laminates of complex and large geometries, as well as opening development

routes to further improvement. This also includes electrically conductive nanocomposites and the investigation of possibilities for metallic co-bonding.

Finally, these technologies have been verified at assembly level on major demonstrators. All in all, SARISTU represents a major step forward in successfully integrating smart intelligent structural concepts into traditional aircraft design and reflects the potential of nanotechnology in aircraft manufacturing applications. Furthermore, the project has shown that incremental improvements taken together can lead to significant weight and operational cost reductions and lead to improved aerodynamic performance.

This book includes the research papers presented in the project's Final Conference held at Moscow, Russia, between 19 and 21 of May 2015. It provides to the reader a selection of the most significant developments, achievements, and key technological steps achieved through the four-year long cooperation of the SARISTU partners with the financial support of the European Commission.

Acknowledgments

The editors wish to acknowledge the involvement of all Work Area Leaders in the selection of the papers included in this volume, as well as their contribution in ensuring the high scientific and technical merit of the manuscripts.

Our special thanks and sincere gratitude for their constant support and commitment throughout the realization of this book go to:

- Markus Kintscher for papers relating to the Enhanced Adaptive Droop Nose
- Antonio Concilio and Ignacio Dimino for papers relating to the Kinematic Rib based SStructural systems for INnovative Adaptive trailing edges also referred to as Advanced Trailing Edge Device
- Andreas Wildschek for papers relating to the Winglet Active Trailing Edge
- Christos Koimtzoglou for papers relating to Fiber Optic Monitoring Systems
- Ernesto Monaco for papers relating to Acoustic Structural Health Monitoring using Guided Waves
- Martin Bach for papers relating to Acoustic Structural Health Monitoring for fuselage applications
- Domenico Furfari for papers relating to Multi-Site Damage Detection and Assessment
- Silvere Barut for papers relating to Damage Indicating Surfaces
- Sonia Fernandez Florez for papers relating to Nanocomposites for improved damage tolerance and composites with electrical properties
- Alfonso Apicella for papers relating to the major Wing Integration and Demonstration exercises
- Ben Newman for papers relating to the major Fuselage Integration and Demonstration exercises
- Natalia Miroshnichenko, Rebecca Wadleigh, and Georgia Protogerou for their outstanding efforts in the organization of SARISTU's End of Project Conference and the preparation of this book.

Additionally, the editors would like to express their gratitude to the companies contributing to the work presented in this book: TsAGI, Tsentralniy

Aerogidrodinamicheskiy Institut, for hosting the SARISTU End of Project conference, AIRBUS Operations GmbH, Altran GmbH & Co. KG and EASN-Technology Innovation Services for its co-organization and the European Commission without which these developments would have been impossible.

SARISTU received funding from the European Union's Seventh Framework Programme for research, technological development, and demonstration under grant agreement no 284562.

Contents

SARISTU: Six Years of Project Management	1
Piet Christof Wölcken, Andreas Kötter, Ben Newman, Rebecca Wadleigh and Katrin Genzel	
 Part I Technology Stream: Morphing. Enhanced Adaptive Droop Nose for a Morphing Wing	
Morphing Wing Integrated Safety Approach and Results	43
Maurizio Verrastro and Sylvain Metge	
Development and Validation of a Bird Strike Protection System for an Enhanced Adaptive Droop Nose	71
Charles Chary	
Testing Overview of the EADN Samples	85
Vladimir Snop and Vaclav Horak	
Enhanced Adaptive Droop Nose—from Computer Model to Multi-functional Integrated Part.	97
Olaf Heintze, Stefan Steeger, Alexander Falken and Jürgen Heckmann	
Assessment of the SARISTU Enhanced Adaptive Droop Nose	113
Markus Kintscher, Johannes Kirn, Stefan Storm and Fabian Peter	

Part II Technology Stream: Morphing. The Adaptive Trailing Edge Device (ATED)

Adaptive Trailing Edge: Specifications, Aerodynamics, and Exploitation 143
Giovanni Marco Carossa, Sergio Ricci, Alessandro De Gaspari, Cedric Liauzun, Antoine Dumont and Moshe Steinbuch

Structural Design of an Adaptive Wing Trailing Edge for Large Aeroplanes. 159
Rosario Pecora, Marco Magnifico, Francesco Amoroso, Leonardo Lecce, Marco Bellucci, Ignazio Dimino, Antonio Concilio and Monica Ciminello

Distributed Actuation and Control of a Morphing Wing Trailing Edge 171
Ignazio Dimino, Monica Ciminello, Antonio Concilio, Rosario Pecora, Francesco Amoroso, Marco Magnifico, Martin Schueller, Andre Gratias, Avner Volovick and Lior Zivan

Elastomer-Based Skin for Seamless Morphing of Adaptive Wings . . . 187
Oliver Schorsch, Andreas Lühring and Christof Nagel

Manufacturing and Testing of Smart Morphing SARISTU Trailing Edge 199
Yasser Essa, Federico Martin de la Escalera Cutillas, Ignazio Dimino, Monica Ciminello and Antonio Concilio

Part III Technology Stream: Morphing. Wingtip Morphing Trailing Edge

Design, Optimization, Testing, Verification, and Validation of the Wingtip Active Trailing Edge 219
Andreas Wildschek, Stefan Storm, Martin Herring, Danijel Drezga, Viken Korian and Olaf Roock

Winglet Design, Manufacturing, and Testing. 257
Danijel Drezga, Viken Korian, Olaf Roock, Bernardo Lopez, Arne Fiedler, Stefan Storm and Vladimir Snop

Seamless Morphing Concepts for Smart Aircraft Wing Tip 275
 Christof Nagel, Arne Fiedler, Oliver Schorsch and Andreas Lühring

Dynamic Aircraft Model with Active Winglet, Effects of Flight Mechanics and Loads Analysis 293
 Toni Kanakis, Bimo Prananta, Hans van Tongeren and Rob Huls

Influence of H_2 and \mathcal{L}_∞ Criteria on Feed-Forward Gust Loads Control Optimized for the Minimization of Wing Box Structural Mass on an Aircraft with Active Winglets 319
 Andreas Wildschek

Evaluation of the Performance Benefits of the Winglet Active Trailing Edge in AS03 333
 Martin Herring

Part IV Technology Stream: Integrated Sensing. Fiber Optic-Based Monitoring System

Ribbon Tapes, Shape Sensors, and Hardware 349
 Matthijs Bosboom, Martijn van Wijngaarden, Rolf Evenblij, Paolo Bettini, Theodoros Loutas, Vassilis Kostopoulos, Dimitrios Habas, Moshe Tur, Nahum Gorbato, Arik Bergman, Uri Ben Simon, Iddo Kressel, Christos Koimtzoglou, Monica Ciminello, Alexander Weisser and Christophe Paget

Methodologies for the Damage Detection Based on Fiber-Optic Sensors. Applications to the Fuselage Panel and Lower Wing Panel 407
 Alfredo Güemes, Julian Sierra, Frank Grooteman, Toni Kanakis, Pavlos Michaelides, Dimitrios Habas, Moshe Tur, Nahum Gorbato, Christos Koimtzoglou and Nikolaos Kontis

Load Monitoring by Means of Optical Fibres and Strain Gages 433
 Alessandro Airoldi, Giuseppe Sala, Rolf Evenblij, Christos Koimtzoglou, Theodoros Loutas, Giovanni Marco Carossa, Pasquale Mastromauro and Toni Kanakis

Shape Sensing for Morphing Structures Using Fiber Bragg Grating Technology 471
 Rolf Evenblij, Frank Kong, Christos Koimtzoglou, Monica Ciminello, Ignazio Dimino and Antonio Concilio

Part V Technology Stream: Integrated Sensing. Wing Damage Detection Employing Guided Waves Techniques

Methodologies for Guided Wave-Based SHM System Implementation on Composite Wing Panels: Results and Perspectives from SARISTU Scenario 5 495
Ernesto Monaco, Natalino Daniele Boffa, Vittorio Memmolo, Fabrizio Ricci, Nicola Testoni, Luca De Marchi, Alessandro Marzani, Jan Hettler, Morteza Tabatabaeipour, Steven Delrue and Van Den Abeele Koen

An Electromechanical Impedance-Based Mobile System for Structural Health Monitoring and Reliability Check of Bonded Piezoelectric Sensors 529
Mihail Lilov and Thomas Siebel

PAMELA SHM System Implementation on Composite Wing Panels 545
Angel Alcaide, Federico Martin, Eduardo Barrera and Mariano Ruiz

Toward the Upscaling of Guided Waves-Based NDE and SHM in Aeronautics 557
Nicola Testoni, Luca De Marchi and Alessandro Marzani

Part VI Technology Stream: Integrated Sensing. Impact Damage Assessment Using Integrated Ultrasonic Sensors

Damage Identification in Composite Panels—Methodologies and Visualisation 579
Richard Loendersloot, Inka Buethe, Pavlos Michaelides, Maria Moix-Bonet and George Lampeas

Manufacturing of CFRP Panels with Integrated Sensor Network and Contacting of the Network. 605
Dimitrios Habas, Daniel Schmidt and Nicolas Dobmann

Damage Assessment in Composite Structures Based on Acousto-Ultrasonics—Evaluation of Performance 617
Maria Moix-Bonet, Peter Wierach, Richard Loendersloot and Martin Bach

Path-Based MAPOD Using Numerical Simulations 631
 Inka Bueche, Nicolas Dominguez, Henning Jung, Claus-Peter Fritzen,
 Damien Ségur and Frédéric Reverdy

**Part VII Technology Stream: Integrated Sensing. Multi-site
 Damage Assessment of CFRP Structures**

Flat and Curved Panel Manufacturing 645
 Martijn van Wijngaarden

**Compression After Multiple Impacts: Modelling and Experimental
 Validation on Composite Coupon Specimens.** 667
 Spyridon Psarras, Raul Muñoz, Mazdak Ghajari, Paul Robinson
 and Domenico Furfari

**Compression After Multiple Impacts: Modelling and Experimental
 Validation on Composite Curved Stiffened Panels.** 681
 Spyridon Psarras, Raul Muñoz, Mazdak Ghajari, Paul Robinson,
 Domenico Furfari, Arne Hartwig and Ben Newman

Multisite Damage Assessment Tool. 691
 Tulug Pince

**Part VIII Technology Stream: Integrated Sensing. Sensitive
 Coating for Impact Detection**

**Piezochromic Compounds Able to be Used in Shock
 Detecting Paints.** 713
 Manuel Gaudon, Alain Demourgues, Veronica Blanco-Gutierrez
 and Silvere Barut

Brittle Coating Layers for Impact Detection in CFRP. 725
 Frederico Maia, Kiryl Yasakau, Joao Tedim
 and Mikhail L. Zheludkevich

Coating for Detecting Damage with a Manifest Color Change 735
 Laura Monier, Karel Le Jeune, Isabelle Kondolff and Gil Vilaça

**Sensitive Coating Solutions to Lower BVID Threshold
 on Composite Structure** 745
 Silvere Barut

Part IX Technology Stream: Multifunction Materials.	
Enhancement of Primary Structure Robustness	
by Improved Damage Tolerance	
Use of Carbon Nanotubes in Structural Composites	755
Daniel Bonduel, Nadir Kchit and Michael Claes	
Enhancement of Primary Structure Robustness	
by Improved Damage Tolerance.	763
Sonia Flórez and Jorge Gayoso	
Enhancement of Infused CFRP Primary Structure Mechanical	
Properties Using Interleaving Thermoplastic Veils.	777
Daniel Breen	
Multi-scale-Reinforced Prepregs for the Improvement of Damage	
Tolerance and Electrical Properties of Aeronautical Structures	791
A. Vavouliotis, G. Sotiriadis and V. Kostopoulos	
Part X Technology Stream: Multifunction Materials. Improvement	
of the Electrical Isotropy of Composite Structures	
Improvement of the Electrical Isotropy of Composite	
Structures—Overview	805
Sonia Flórez, Idoia Gaztelumendi and Jorge Gayoso	
Fabrication of Carbon Nanotubes-Doped Veils	815
Paulina Latko and Anna Boczkowska	
Finite Element Modelling of CNT-Doped CFRP Plates	
for Lightning Strike Damage	825
Omer Soykasap, Sukru Karakaya, Yelda Akcin and Mehmet Colakoglu	
Metallic Strip Details for Validation of ESN Technologies	839
Richard Perraud, Olivier Urrea, Thierry Pelegrin, Michel Bermudez, Michel Fouquembergh, Stephane Guinard and Christoph Breu	

**Part XI Technology Stream: Integration and Validation.
Implementation of Morphing, Structural Health
Monitoring and Nanomaterials on an Outer Wing Box**

Morphing Value Assessment on Overall Aircraft Level 859
Fabian Peter, Eike Stumpf, Giovanni Marco Carossa,
Markus Kintscher, Ignazio Dimino, Antonio Concilio,
Rosario Pecora and Andreas Wildschek

**Implementation of Morphing, Structural Health
Monitoring and Nanomaterials on an Outer Wing Box** 873
Giovanni Marco Carossa, Michelangelo Giuliani, Alan Johnston,
Christina Altkvist, Alessandro Airoidi, Zahra Sharif Khodaei
and M.H. Aliabadi

**Implementation of a Structural Health Monitoring System
for a Composite Wing Box Skin** 883
Alessandro Marzani, Nicola Testoni, Luca De Marchi,
Ernesto Monaco, Zahra Sharif Khodaei, M.H. Aliabadi and Julio Viana

**Value at Risk for a Guided Waves-Based System Devoted
to Damage Detection in Composite Aerostructures** 909
Luca De Marchi, Alessandro Marzani, Nicola Testoni,
Ulrike Heckenberger and Alfonso Apicella

**Part XII Technology Stream: Integration and Validation.
Fuselage Assembly, Integration and Testing**

**Fuselage Demonstrators: An Overview of the Development
Approach** 921
Ben Newman

**Development of a Door Surround Structure with Integrated
Structural Health Monitoring System** 935
Daniel Schmidt, Andreas Kolbe, Robert Kaps, Peter Wierach,
Stefan Linke, Stefan Steeger, Friedrich von Dungern,
Juergen Tauchner, Christoph Breu and Ben Newman

**Damage Introduction, Detection, and Assessment at CFRP
Door Surrounding Panel** 947
Martin Bach, Nicolas Dobmann and Maria Moix-Bonet

**Installation of Metallic Strip on CRFP Frames:
Assessment of IS13 Mechanical and Electrical Performance.** 959
Richard Perraud, Olivier Urrea, Thierry Pelegrin, Michel Bermudez,
Stephane Guinard and Christoph Breu

**Benefit Analysis Value and Risk Assessment of New
SARISTU-Technologies** 969
Sevgi Batal and Stephne du Rand

**Manufacturing of Nano-treated Lower Panel Demonstrators
for Aircraft Fuselage** 999
Feride Nur Sasal, Aysun Dogangun Akin, Ayhan Kılıc, Guray Erteği,
Caglayan Duygu, Emre İşler, Ben Newman, Christos Koimtzoglou,
Panagiotis Maroulas, Patrick Bara, Antonios Vavouliotis,
George Sotiriadis and Vassilis Kostopoulos

**Design and Manufacturing of WP135 Side Panel for Validation
of Electrical Structure Network (ESN) Technologies** 1021
Christina Altkvist, Jonas Wahlbäck,
Juergen Tauchner and Christoph Breu

Contributors

Alessandro Airoidi Department of Aerospace Science and Technology, Politecnico di Milano, Milan, Italy

Yelda Akcin Department of Metallurgical and Materials Science, Afyon Kocatepe University, A.N.S. Campus, Afyonkarahisar, Turkey

Angel Alcaide Structural Integrity Department, Aernnova Engineering Division, Madrid, Spain

M.H. Aliabadi Department of Aeronautics, Imperial College London, London, UK

Christina Altkvist Saab AB, Linköping, Sweden

Francesco Amoroso Aerospace Division, Department of Industrial Engineering, University of Naples, “Federico II”, Naples, Italy

Alfonso Apicella Ingegneria di Progettazione, Airframe, Alenia Aermacchi S.p.A., Pomigliano d’Arco, Naples, NA, Italy

Martin Bach Structures Engineering, Production and Aeromechanics, Airbus Group Innovations, Bremen, Germany

Patrick Bara New Structural Developments, Société Anonyme Belge de Constructions Aéronautiques, Brussels, Belgium

Eduardo Barrera Instrumentation and Applied Acoustic Research Group, Technical University of Madrid (UPM), Madrid, Spain

Silvere Barut Airbus Group Innovations, Toulouse, France

Sevgi Batal Aerospace, Defence and Rail—Airframe Structure, ALTRAN GmbH & Co. KG, Hamburg, Germany

Marco Bellucci Mare Engineering, Naples, Italy

Uri Ben Simon Department of Mechanical Engineering, Israel Aerospace Industries, Tel Aviv, Israel

Arik Bergman School of Electrical Engineering, Tel-Aviv University, Tel-Aviv, Israel

Michel Bermudez Mechanical System Design, Airbus Group Innovations, Suresnes Cedex, France

Paolo Bettini Department of Aerospace Science and Technology, Politecnico di Milano, Milan, Italy

Veronica Blanco-Gutierrez CNRS, ICMCB, Université de Bordeaux, Pessac, France

Anna Boczkowska Department of Materials Science and Engineering, Warsaw University of Technology, Warsaw, Poland

Natalino Daniele Boffa Department of Industrial Engineering—Aerospace section, University of Naples “Federico II”, Naples, Italy

Daniel Bonduel Research and Development, Nanocyl S.A, Sambreville, Belgium

Matthijs Bosboom KVE Composite Structures BV, GB, The Hague, The Netherlands; R&D, GB, The Hague, The Netherlands

Daniel Breen Strategic Technology Composites Department, Bombardier, Belfast, Northern Ireland

Christoph Breu Prefforming and Textile Technology, Airbus Group Innovations, Munich, Germany

Inka Buethe Institute of Mechanics and Control Engineering—Mechatronics, University of Siegen, Siegen, Germany

Giovanni Marco Carossa Air Vehicle Technology, Alenia Aermacchi S.p.A., Turin, Italy

Charles Chary SONACA SA, Gosselies, Belgium

Monica Ciminello Adaptive Structures Department, CIRA, The Italian Aerospace Research Centre, Capua, CE, Italy; C.I.R.A. S.p.A. Centro Italiano Ricerche Aerospaziali, Italian Aerospace Research Center, Capua, CE, Italy

Michael Claes Research and Development, Nanocyl S.A, Sambreville, Belgium

Mehmet Colakoglu Department of Mechanical Engineering, Adnan Menderes University, Main Campus, Aydın, Turkey

Antonio Concilio Smart Structures Department, CIRA, The Italian Aerospace Research Centre, Capua, CE, Italy

Alessandro De Gaspari Department of Aerospace Science and Technology, Politecnico di Milano, Milan, Italy

Luca De Marchi Department of Electrical, Electronic and Information Engineering—DEI, University of Bologna, Bologna, Italy; Department of Civil, Chemical, Environmental and Materials Engineering—DICAM, University of Bologna, Bologna, Italy

Steven Delrue Department of Physics, KU Leuven, Kulak, Kortrijk, Belgium

Alain Demourgues CNRS, ICMCB, Université de Bordeaux, Pessac, France

Ignazio Dimino Smart Structures Technologies Laboratory, CIRA, The Italian Aerospace Research Centre, Capua, CE, Italy

Nicolas Dobmann Structures Engineering, Production and Aeromechanics, Airbus Group Innovations, Bremen, Germany

Akın Aysun Dogangun Material and Process Technologies, Turkish Aerospace Industries Inc, Ankara, Turkey

Nicolas Dominguez Structure Health Engineering Department, AIRBUS Group Innovations, Toulouse, France

Danijel Drezga FACC Operations GmbH, Ried im Innkreis, Austria

Antoine Dumont Applied Aerodynamics Department, ONERA, 92320 Châtillon, France

Friedrich von Dungern INVENT GmbH, Braunschweig, Germany

Caglayan Duygu Manufacturing Engineering Department, Turkish Aerospace Industries Inc, Ankara, Turkey

Federico Martín de la Escalera Cutillas Aernnova Engineering Division S.A., Madrid, Spain

Guray Erteği Forming Tools Design Engineering, Turkish Aerospace Industries Inc, Ankara, Turkey

Yasser Essa Aernnova Engineering Division S.A., Madrid, Spain

Rolf Evenblij Aeronautics/Space and Automotive Testing, Technobis Fibre Technology, Alkmaar, The Netherlands

Alexander Falken INVENT GmbH, Braunschweig, Germany

Arne Fiedler Materials Science and Engineering, Fraunhofer Institute for Manufacturing Technology and Advanced Materials (IFAM), Adhesive Bonding Technology and Surfaces, Bremen, Germany

Sonia Flórez Aerospace Department, Tecnalia, San Sebastian, Spain

Michel Fouquembergh Heat Transfer Science, Airbus Group Innovations, Suresnes, France

Claus-Peter Fritzen Institute of Mechanics and Control Engineering—Mechatronics, University of Siegen, Siegen, Germany

Domenico Furfari Stress NSDW R&T—ESCRNS, Airbus Operations GmbH, Hamburg, Germany

Manuel Gaudon CNRS, ICMCB, Université de Bordeaux, Pessac, France

Jorge Gayoso Aerospace Department, Tecnia, San Sebastian, Spain

Idoia Gaztelumendi Aerospace Department, Tecnia, San Sebastián, Spain

Katrin Genzel Airbus Operations GmbH, Hamburg, Germany

Mazdak Ghajari The Composites Centre, Department of Aeronautics, Imperial College London, London, UK

Michelangelo Giuliani REDAM—Research and Development in Applied Mechanics, Avellino, Italy

Nahum Gorbatov School of Electrical Engineering, Tel-Aviv University, Tel-Aviv, Israel

Andre Gratias Department of Multi Device Integration, Fraunhofer ENAS, Chemnitz, Germany

Frank Grooteman National Aerospace Laboratory NLR, Amsterdam, The Netherlands

Alfredo Güemes Department of Aeronautics, UPM, Madrid, Spain

Stephane Guinard Computational Structural Mechanics, Airbus Group Innovations, Toulouse, France

Dimitrios Habas Research and Product Design Department, Hellenic Aerospace Industry S.A, Schimatari, Greece; Engineering, Research, Design and Development Directorate, Hellenic Aerospace Industry, Schimatari, Greece

Arne Hartwig Structural Analysis Process and M&T, Airbus Operations GmbH, Hamburg, Germany

Ulrike Heckenberger Technical Material Physics, TX2B—Metallic Technologies and Surface Engineering, Airbus Group Innovations, Munich, Germany

Jürgen Heckmann INVENT GmbH, Braunschweig, Germany

Olaf Heintze INVENT GmbH, Braunschweig, Germany

Martin Herring Airbus Group Innovations, TX3 Aeromechanics, Filton, Bristol, UK

- Jan Hettler** Department of Physics, KU Leuven, Kulak, Kortrijk, Belgium
- Vaclav Horak** Aerospace Research and Test Establishment (VZLU), Prague, Czech Republic
- Rob Huls** Gas Turbines and Structural Integrity Department, National Aerospace Laboratory—NLR, Marknesse, The Netherlands
- Emre İşler** Manufacturing Engineering Department, Turkish Aerospace Industries Inc, Ankara, Turkey
- Alan Johnston** Bombardier Aerostructures and Services, Belfast, Northern Ireland, UK
- Henning Jung** Institute of Mechanics and Control Engineering—Mechatronics, University of Siegen, Siegen, Germany
- Toni Kanakis** Department of Collaborative Engineering Systems, National Aerospace Laboratory (NLR), Amsterdam, The Netherlands
- Robert Kaps** Composite Technology, Institute of Composite Structures and Adaptive Systems, German Aerospace Center, Braunschweig, Germany
- Sukru Karakaya** Department of Mechanical Engineering, Afyon Kocatepe University, A.N.S. Campus, Afyonkarahisar, Turkey
- Nadir Kchit** Research and Development, Nanocyl S.A, Sambreville, Belgium
- Ayhan Kılıc** Material and Process Technologies, Turkish Aerospace Industries Inc, Ankara, Turkey
- Markus Kintscher** German Aerospace Center, DLR Institute of Composite Structures and Adaptive Systems, Braunschweig, Germany
- Johannes Kirn** Airbus Group Innovations, Munich, Germany
- Christos Koimtzoglou** INASCO, Integrated Aerospace Sciences Corporation, Glyfada, Athens, Greece
- Andreas Kolbe** Composite Process Technology, Institute of Composite Structures and Adaptive Systems, German Aerospace Center, Braunschweig, Germany
- Isabelle Kondolff** CATALYSE Company, Marseille, France
- Frank Kong** Technobis Fibre Technologie, Alkmaar, The Netherlands
- Nikolaos Kontis** Integrated Aerospace Sciences Corporation—INASCO, Glyfada, Greece
- Viken Korian** FACC Operations GmbH, Ried im Innkreis, Austria
- Vassilis Kostopoulos** Applied Mechanics Laboratory, Mechanical Engineering and Aeronautics Department, University of Patras, Rion, Achaia, Greece

Andreas Kötter Altran GmbH & Co. KG, Hamburg, Germany

Iddo Kressel Department of Mechanical Engineering, Israel Aerospace Industries, Tel Aviv, Israel

George Lampeas University of Patras, Laboratory of Technology and Strength of Materials, Department of Mechanical Engineering and Aeronautics, Rion, Patras, Greece

Paulina Latko Technology Partners Foundation, Warsaw, Poland

Karel Le Jeune CATALYSE Company, Marseille, France

Leonardo Lecce Industrial Engineering Department, University of Naples “Federico II”, Naples, Italy

Cedric Liauzun Aeroelasticity Department, ONERA, 92320 Châtillon, France

Mihail Lilov Division Smart Structures, Fraunhofer Institute for Structural Durability and System Reliability LBF, Darmstadt, Germany

Stefan Linke INVENT GmbH, Braunschweig, Germany

Richard Loendersloot Engineering Technology, Dynamics Based Maintenance, University of Twente, Enschede, The Netherlands

Bernardo Lopez Foundation for the Research, Advanced Materials, Development and Application of Composite Materials (FIDAMC), Getafe, Spain

Theodoros Loutas Department of Mechanical Engineering and Aeronautics, University of Patras, Panepistimioupoli Patron, Greece

Andreas Lühring Fraunhofer Institute for Manufacturing Technology and Advanced Materials (IFAM), Adhesive Bonding Technology and Surfaces, Bremen, Germany

Marco Magnifico Aerospace Division, Department of Industrial Engineering, University of Naples, “Federico II”, Naples, Italy

Frederico Maia Department of Materials and Ceramic Engineering, CICECO-Aveiro Institute of Materials, University of Aveiro, Aveiro, Portugal

Panagiotis Maroulas Integrated Aerospace Sciences Corporation, Glyfada, Greece

Federico Martin Structural Integrity Department, Aernnova Engineering Division, Madrid, Spain

Alessandro Marzani Department of Civil, Chemical, Environmental and Materials Engineering—DICAM, University of Bologna, Bologna, Italy

Pasquale Mastromauro Alenia Aermacchi, Turin, Italy

Vittorio Memmolo Department of Industrial Engineering—Aerospace section, University of Naples “Federico II”, Naples, Italy

Sylvain Metge Airbus Operations S.A.S., Toulouse, France

Pavlos Michaelides NASTECH—Novel Aerospace Technologies, Ancarano, Italy

Maria Moix-Bonet Multifunctional Materials, Institute of Composite Structures and Adaptive Systems, German Aerospace Center, Braunschweig, Germany

Ernesto Monaco Department of Industrial Engineering—Aerospace section, University of Naples “Federico II”, Naples, Italy

Laura Monier CATALYSE Company, Marseille, France

Raul Muñoz The Composites Centre, Department of Aeronautics, Imperial College London, London, UK

Christof Nagel Fraunhofer Institute for Manufacturing Technology and Advanced Materials (IFAM), Adhesive Bonding Technology and Surfaces, Bremen, Germany

Ben Newman Aerospace and Defence—Flight Physics and Innovation, Altran GmbH & Co KG, Hamburg, Germany

Christophe Paget Materials and Processes Department, Airbus Operations Ltd, Bristol, UK

Rosario Pecora Aerospace Division, Department of Industrial Engineering, University of Naples, “Federico II”, Naples, Italy

Thierry Pelegryn Mechanical System Design, Airbus Group Innovations, Suresnes Cedex, France

Richard Perraud EMC and Propagation, Airbus Group Innovations, Suresnes Cedex, France

Fabian Peter Institute of Aerospace Systems, RWTH Aachen University, Aachen, Germany

Tulug Pince Altran GmbH & Ko KG, Hamburg, Germany

Bimo Prananta Flight Physics and Loads Department, National Aerospace Laboratory—NLR, Amsterdam, The Netherlands

Spyridon Psarras The Composites Centre, Department of Aeronautics, Imperial College London, London, UK

Stephne du Rand Aerospace, Defence and Rail—Flight Physics and Innovation, ALTRAN GmbH & Co. KG, Hamburg, Germany

Frédéric Reverdy NDE for Aeronautics Application Laboratory, CEA List, Toulouse, France

Fabrizio Ricci Department of Industrial Engineering—Aerospace section, University of Naples “Federico II”, Naples, Italy

Sergio Ricci Department of Aerospace Science and Technology, Politecnico di Milano, Milan, Italy

Paul Robinson The Composites Centre, Department of Aeronautics, Imperial College London, London, UK

Olaf Roock FACC Operations GmbH, Ried im Innkreis, Austria

Mariano Ruiz Instrumentation and Applied Acoustic Research Group, Technical University of Madrid (UPM), Madrid, Spain

Giuseppe Sala Department of Aerospace Science and Technology, Milan, Italy

Feride Nur Sasal Material and Process Technologies, Turkish Aerospace Industries Inc, Ankara, Turkey

Daniel Schmidt German Aerospace Center, Institute of Composite Structures and Adaptive Systems, Multifunctional Materials, Braunschweig, Germany

Oliver Schorsch Fraunhofer Institute for Manufacturing Technology and Advanced Materials (IFAM), Adhesive Bonding Technology and Surfaces, Bremen, Germany

Martin Schueller Department of Multi Device Integration, Fraunhofer ENAS, Chemnitz, Germany

Damien Ségur NDE for Aeronautics Application Laboratory, CEA List, Toulouse, France

Zahra Sharif Khodaei Imperial College London, London SW7 2AZ, UK

Thomas Siebel Division Smart Structures, Fraunhofer Institute for Structural Durability and System Reliability LBF, Darmstadt, Germany

Julian Sierra Department of Aeronautics, UPM, Madrid, Spain

Vladimir Snop Aerospace Research and Test Establishment (VZLU), Prague, Czech Republic

George Sotiriadis Applied Mechanics Laboratory, Mechanical Engineering and Aeronautics Department, University of Patras, Rion, Achaia, Greece

Omer Soykasap Department of Material Science and Engineering, Afyon Kocatepe University, A.N.S. Campus, Afyonkarahisar, Turkey

Stefan Steeger INVENT GmbH, Braunschweig, Germany

Moshe Steinbuch Engineering, Israel Aerospace Industries, 70100 Ben-Gurion Airport, Israel

Stefan Storm Airbus Group Innovations, Munich, Germany

Eike Stumpf Institute of Aerospace Systems, RWTH Aachen University, Aachen, Germany

Morteza Tabatabaeipour Department of Physics, KU Leuven, Kulak, Kortrijk, Belgium

Juergen Tauchner FACC Operations GmbH, Sankt Martin im Innkreis, Austria

Joao Tedim Department of Materials and Ceramic Engineering, CICECO-Aveiro Institute of Materials, University of Aveiro, Aveiro, Portugal

Nicola Testoni Department of Electrical, Electronic and Information Engineering—DEI, University of Bologna, Bologna, Italy; Department of Civil, Chemical, Environmental and Materials Engineering—DICAM, University of Bologna, Bologna, Italy

Hans van Tongeren Collaborative Engineering Systems Department, National Aerospace Laboratory—NLR, Marknesse, The Netherlands

Moshe Tur School of Electrical Engineering, Tel-Aviv University (TAU), Tel-Aviv, Israel

O. Urrea EMC and Propagation, Airbus Group Innovations, Suresnes Cedex, France

Koen Van Den Abele Department of Physics, KU Leuven, Kulak, Kortrijk, Belgium

Antonios Vavouliotis Applied Mechanics Laboratory, Mechanical Engineering and Aeronautics Department, University of Patras, Rion, Achaia, Greece

Maurizio Verrastro Alenia Aermacchi S.p.A. Military Aircraft Safety, Caselle, Italy

Julio Viana Critical Materials, Science and Technology Park, Guimares, Portugal

Gil Vilaça CATALYSE Company, Marseille, France

Avner Volovick Engineering Division, Israel Aerospace Industries Flight Control Systems Department, Ben Gurion International Airport, Tel Aviv, Israel

Martijn van Wijngaarden KVE Composite Structures BV, GB, The Hague, The Netherlands; R&D, GB, The Hague, The Netherlands

Rebecca Wadleigh Altran GmbH & Co. KG, Hamburg, Germany

Jonas Wahlbäck Saab AB, Linköping, Sweden

Alexander Weisser Materials, Processes and Tests, AIRBUS Deutschland GmbH, Bremen, Germany

Peter Wierach Multifunctional Materials, Institute of Composite Structures and Adaptive Systems, German Aerospace Center, Braunschweig, Germany

Andreas Wildschek Airbus Group Innovations, Munich, Germany

Piet Christof Wölcken Airbus Operations GmbH, Bremen, Germany

Kiryl Yasakau Department of Materials and Ceramic Engineering, CICECO-Aveiro Institute of Materials, University of Aveiro, Aveiro, Portugal

Mikhail L. Zheludkevich Department of Materials and Ceramic Engineering, CICECO-Aveiro Institute of Materials, University of Aveiro, Aveiro, Portugal; Helmholtz-Zentrum Geesthacht Centre for Materials and Coastal Research, GmbH Institute of Materials Research, MagIC, Geesthacht, Germany

Lior Zivan Engineering Division, Israel Aerospace Industries Flight Control Systems Department, Ben Gurion International Airport, Tel Aviv, Israel

SARISTU: Six Years of Project Management

**Piet Christof Wölcken, Andreas Kötter, Ben Newman,
Rebecca Wadleigh and Katrin Genzel**

Abstract SARISTU—Smart Intelligent Aircraft Structures—is a large, integrated research and technology project funded by the European Union as part of its 7th Framework Programme. This paper investigates some of the key project management decisions taken in the initiation, preparation and conduct of the project in order to assess the effectiveness of individual management principles, measures and activities. In particular, it investigates the effectiveness of lean project planning when coupled with a bottom-up change process, the impact of structured quality gates in the form of both regular peer reviews as well as progress-driven design reviews. In order to do so, it exploits the one-dimensional nature of “Quality, Time, Cost” and investigates the impact of this principal project management philosophy on a project. Supporting this, the paper outlines the specific deliverable dashboard methodology followed and gives an insight into practical research and development management within a Technology Readiness Level framework. Including a short analysis of financial considerations, the paper concludes by providing some key lessons learned for prospective future managers of large, integrated and hardware-based research and technology projects.

P.C. Wölcken (✉)

Airbus Operations GmbH, Airbusallee 1, 28119 Bremen, Germany
e-mail: piet-christof.woelcken@airbus.com

A. Kötter · B. Newman · R. Wadleigh
Altran GmbH & Co. KG, Karnapp 25, 21079 Hamburg, Germany
e-mail: andreas.koetter@altran.com

B. Newman
e-mail: ben.newman@altran.com

R. Wadleigh
e-mail: rebecca.wadleigh@altran.com

K. Genzel
Airbus Operations GmbH, Kreetslag 10, 21129 Hamburg, Germany
e-mail: katrin.genzel@airbus.com

Nomenclature

CA	Consortium Agreement
CCR	Critical Concept Review
CDR	Critical Design Review
DoW	Description of Work
EC	European Commission
GA	Grant Agreement
PDR	Preliminary Design Review
PMO	Project Management Office
PP	Project Plan
PPCR	Project Plan Change Request
Prodaxs	PROject DATA eXchange System
QTC	Quality, Time, Cost
RPR	Regular Progress Review
R&T	Research and Technology
SARISTU	Smart Intelligent Aircraft Structures (project)
SL	Scenario Leader
TRL	Technology Readiness Level
WBS	Work Breakdown Structure
WP	Work Package

1 Introduction

The Smart Intelligent Aircraft Structures—SARISTU—project was launched with a classical Kick-off Meeting at Airbus Operations GmbH Headquarters on 06.09.2011. However, when considering the overall management of this research and technology project, it is important to understand the previous project phases of negotiation, preparation and initiation and to analyse the consequences of assumptions made during these early phases which are of fundamental importance to project success. Most importantly, it is necessary to remember the competitive nature of publicly funded research, in particular ahead of the negotiation phase.

SARISTU was conceived in the early 2000s when a number of aerospace companies and institutions identified a need for major R&T effort to bring together different developments related to the overall concept of a “smart” aircraft. At a later stage, the European Union formulated this broad concept more specifically in the 4th call of its 7th Framework Programme by focusing the project scope on the still large area of morphing structures, structural health monitoring and multifunctional materials, specifically nanocomposites. Henceforward, it was clear that the SARISTU project had to be run more like a program rather than a project as with such a wide variety of fields of technologies no single individual would be able to

identify all potential show-stoppers. Furthermore, the call for proposals established a few important boundary conditions, the most important being the requirement to demonstrate the technological capabilities in significant physical test exercises. Finally, the documents associated to the call [4–9] would prove to have a direct effect on the work breakdown structure beyond the actual work objectives.

Prior to launching the proposal generation, the overall consortium management work was broken down into the usual project phases of initiation, preparation and negotiation, conduct and closure as per [1–3] with key objectives for each phase. During project initiation, the main SARISTU consortium was built with the project partners expressing key expectations and making broad commitments. During this phase, the overall demonstration activities also began to take shape. The project initiation phase was completed by the establishment of the WBS and individual team leader nominations. The subsequent project preparation phase centred around the generation of two key documents: first of all, the written proposal itself. Based on this document, the call for proposals would be won or lost. The second key document was the initial project plan which would drive project conduct and likewise determine project success, failure and its measure of efficiency. Upon selection as one of three projects to be funded in the overall call, the negotiation phase was launched with the aim of generating the two governing contracts: first of all, the Grant Agreement containing, for example, the description of work, financial data, deliverables and milestones, between the consortium and the European Commission; secondly, the Consortium Agreement laying down the consortium internal project governance rules or the handling of potential Intellectual Property issues. The prime objectives of the main project conduct are both the easiest and hardest of all. Simply put, the conduct phase has to deliver the contractual deliverables and overall project objectives as laid out in the GA. In practice, this is much more difficult. In particular in research, it becomes necessary to change project plans as new developments arise, and in consequence, the respective contracts must be amended while still maintaining both project objectives and deliverables. Finally, the project must of course be closed with all deliverables delivered, data secured and archived, final payments organized, knowledge transferred towards product development and possible follow-on work identified and initiated. Ideally, from an R&T point of view, follow-on activities have also been launched or at least initiated where considered beneficial at this point.

Throughout this time, the *Project management office team*, consisting of the authors of this paper in their roles as project coordinator, deputy project manager, administrative and financial focal point and the project office team, endeavours to avoid the key mistakes when managing projects.

As projects may only be tracked, controlled and administered, the PMO team works on the principle that, while projects bring deliverables, is actually people who deliver projects. This management philosophy was summarized as “for people, with people, by people” during SARISTU’s Kick-off Meeting.

2 Fundamental Rules Applied to Project Initiation, Preparation, Negotiation and Conduct

Once company internal approval was obtained by the initiating PMO, which outlined this company’s specific expectations in terms of technical outcomes and implemented specific boundary conditions such as overall timeline and an upper bound for the internal work scope, the project consortium began to assemble through a process of one- to two-pager *letters of intent* collected by the PMO from interested companies, institutes and organizations. In this manner, it was ensured that the upper management of individuals interested in participating in the project was not only informed about this interest, but also able to likewise outline their organizations’ more specific interests, while at the same time ensuring that allocated resources take the form of a reliable commitment without which a robust project cannot be built.

This facilitated the broad *topic mapping* exercise which was launched approximately eight months prior to the deadline for proposal submission expected at the time. Supported by two dedicated workshops with interested parties, well over 100 one pagers were submitted to the PMO (Fig. 1). These were specified to be in either of two forms. A dedicated problem description was mainly, but not only, requested from industrial partners with established aircraft production lines. Other organizations, such as universities, research institutes or small and medium enterprises, were requested to focus on capability and solution one pagers highlighting key aspects of their past and present research as well as equipment and capabilities which would

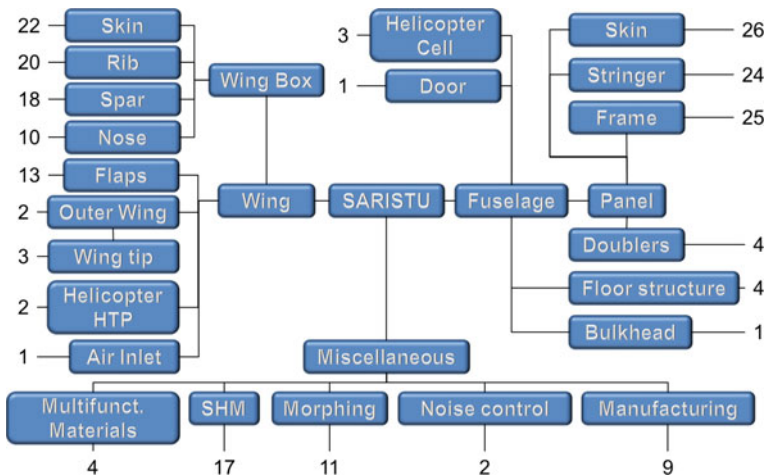


Fig. 1 SARISTU’s initial topic mapping. The important consortium-wide “brainstorming” led to a large number of possible investigation routes. The most promising were subsequently chosen in a dedicated workshop after partners who had by then not submitted a Letter of Intent were given a final chance to do so

be of benefit to the project. The capability and solution one pagers were then mapped to the problem descriptions in a small series of mind mapping exercises and workshops. This problem-solution/capability mapping resulted in the basic application and integration scenarios which represented a first WBS (Fig. 2).

At this point, it also became clear that due to the large variety of technical skills required for the “first time right” decision making, the PMO would have to ensure strong processes for bottom-up risk identification and mitigation rather than actually taking the majority of these decisions itself during the active project phase. Counterbalancing this point was the basic rule to *avoid an under- or over-determined project matrix*. As a result, the SARISTU project organization reflects a strongly hierarchical pyramid which is supported by a clear awareness of *decision points* and *decision levels* (Figs. 2 and 3).

Three months ahead of the by now known proposal submission date and time, the detailed **project preparation phase** was launched. The companies and institutions which had submitted the key problem description one pagers were tasked with formally nominating employees responsible for the leadership of their individual application or integration scenario.

In parallel with these nominations, it became clear that the original WBS resulting from the mind mapping exercise would have to be modified. The templates specified a maximum of two pages per work package. This would have limited the main part of the proposal to just 30 pages. This may be beneficial from a contractors point of view but would be unacceptable to a tax payer being asked to commit to this, at the time, 55 M€ endeavour. Therefore, the individual work streams were broken down into the specific *work phases*. In the case of the

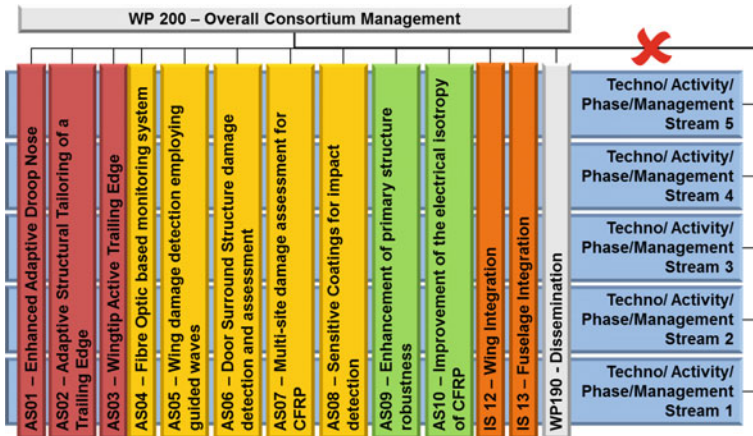


Fig. 2 The SARISTU WBS shown as an overdetermined project. In order to eliminate the risk of overdetermination, the individual WP leaders are identical to the scenario leaders. This enables a WBS by technical project phase and activity while at the same time allowing a straightforward, undetermined management. For management purposes, the “stream” management is conducted at scenario level only



Fig. 3 SARISTU's decision pyramid. With clear roles and responsibilities described in the various contractual document, a simply determined “decision highway” could be formulated. The *dashed decision lines* are not actually contractually foreseen. However, due to the nature of collaborative projects, it would be dangerous for the PMO to overlook their impact

application scenarios, dealing with individual aircraft subassemblies, this was straightforward by differentiating between overall scenario activities: specification, design and methodologies and physical integration/test. In the case of the integration scenarios, dealing with individual aircraft components, this was more diverse. While the fuselage-related scenario could best be broken down into the individual tests, the wing-related scenario was broken down similarly to the application scenarios by work step, i.e. specification, design and methodologies, demonstrator, manufacture and test.

With only a maximum project scope given through both the consortium intentions, as outlined in the letters of intent, as well as the funding boundary conditions set within the call for proposal, the work stream leaders were requested to specify the work scope required to realize the previously determined overall technical project vision. When this task proved to be too unspecific, the PMO formulated *specific budget constraints by scenario* based on past experience and customer expressed expectations. This rapidly enabled the launch of detailed planning actions.

During this time, the PMO was aware that the call contained requests for proposals for six very different topic areas of which only three would be eligible for funding if approved. With one project preparation underway per call topic area, the chance of success therefore stood at 50 %. The PMO sought to improve this likelihood of proposal success by strongly focusing on proposal quality at the time of submission where quality was defined to constitute not only challenging objectives and a readable and understandable project description but also a

high-quality project plan which would greatly facilitate project success. In order to obtain a high-quality project description, a challenging *tact* was implemented for the writing process. Based on the assumption that the quality of a proposal improves with each iteration, the PMO strove to maximize the number of iterations ahead of proposal submission. A weekly tact would in practice have led to a turn around cycle of two weeks. Therefore, this part of PMO activities was mainly performed anticyclically by feeding back to Friday's revision submissions at the beginning of the following week. In this manner, the number of iterations ahead of submission was doubled. In addition, a tacted process enables a risk reduction arising from individual working styles within a team by providing set synchronization points as can be derived from [14]. A further key feature of this tacted writing process was that the principal *ownership of each scenario work description* rested with the scenario leaders.

In order to obtain a *high-quality project plan*, several simple rules were strictly followed. Most importantly, only one plan exists for any project. This is "owned" by a single individual in the PMO. Secondly, all content, responsibility, requested funding ratio, budget and timeline information must be contained within this single database. Thirdly, the DoW's WBS must be reflected in the project plan exactly. Fourthly, each line shall be the responsibility of one partner only. And finally, only the lowest level of the project plan, where clear and specific responsibilities exist, shall contain budget relevant information. From this single database, it is then possible to derive important data such as task, work package or scenario-specific information, deliverable timelines and, most importantly, the company-specific financial project planning information required for submission of the proposal.

Following timely submission and the first evaluation of the project proposal, SARISTU was invited to respond to a number of written questions formulated by an evaluation panel of experts. In preparation of this project presentation, a weekly tact was again established between the PMO and the individual scenario leaders with each SL preparing one presentation slide per evaluator question to their parts of the project. In addition, the PMO prepared introductory and concluding slides as well as responding to cross-scenario-related questions and of course project management questions. Following the SARISTU hearing in defence of the project, the European Commission invited the consortium to enter into contract negotiations with a moderately reduced total project budget of 51 M€ and the request to reduce the number of contractual deliverables by half and the number of milestones by three-quarters.

This resulted in the launch of six dedicated PMO activities. Still directly related to the project planning phase were the implementation of the reduced total project scope, the requested deliverable and milestone reduction, the formulation of the associated Description of Work for the Grant Agreement and the drafting, negotiation, finalization and signature of the Consortium Agreement. The fifth activity launched in this time, the preparation of the Kick-off Meeting, should be regarded as the first part of the project's active conduct phase. As should be the key activity to set-up a project specific data storage and exchange platform.

The moderate *budget reduction* was partially foreseen due to past experiences and as such implemented by first of all a strict adherence to evaluators' comments such as a reduction of the budget dedicated to dissemination activities and the elimination of small, high-risk research areas such as self-healing bulk composite materials. The remaining required reduction unfortunately had to follow the rule "organizations are slow and dumb, people are quick and smart". As such, a weighted target was given to each scenario leader who were able to quickly make reduction proposals. The *deliverable number reduction* was more complex though, as the consortium had originally identified the technically required documentation from the description of work and project plan. As a result, deliverables that were quite different contentwise had to be combined by the scenario leaders.

With these tasks completed, the *preparation of the Grant Agreement* took the form of extensive but uncomplicated copying and pasting into the EC's negotiation tool. Being free of significant added value, it is not surprising that this activity has reportedly been streamlined by the EC. On the administrative side, a direct working relationship between the customer and the PMO was established to good effect. A systematic method applicable to other projects cannot however be established as it is fully based on the quality of the working relationship between key individuals. The important signature loop between the EC and the coordinator could be conducted rapidly, but the signature loop between the coordinator and the project partners was a lengthy process due to the consortium size. In the end, the clear statement by the coordinator that non-signatories of the Grant Agreement meant that partners would be considered to have left the project (based on EC regulations) and would not be granted access to the Kick-off Meeting finally ensured that all signatures were in place on the first day of the Kick-off Meeting.

The preparation of the *Consortium Agreement* was launched in parallel by first modifying a tried and tested model document with the coordinators legal department before requesting comments from the full consortium for the first time. This included key features regarding the handling of Intellectual Property generated within the project which would favour a technological implementation and make it fairly difficult for potential project partners wishing to delay or prohibit an implementation of Intellectual Property generated. Furthermore, it included a clause regarding the terms of payment provisions which split the European Commission's instalments into two tranches each with the second one to be forwarded to participants by the coordinator at the six-month point of each reporting period. This was supported by a clause enabling the coordinator to temporarily withhold this second tranche to individual project partners if deliverables were outstanding or key actions were not completed at this point. The Consortium Agreement also consists of several standard attachments such as "background" (Intellectual Property which has to be made available by the owning party to the other participants when needed for the fulfilment of their project tasks) or the list of Steering Committee Members (one nominated representative of each of the 64 consortium partners). Both of these are fed by partner inputs which are essential for project execution and are subject for modifications during the project lifetime. The Consortium Agreement required only four iterations between the extensive consortium and the coordinator up to

completion. With 64 partners, this may appear surprising. However, with such a large consortium, it is clear that a coordinator cannot allow significant discussions and must either implement change requests, evaluate and argue all comments made and changes proposed, quickly propose alternative compromises or may ask partners not wishing to sign the present draft, in case that no compromise could be agreed on, if they wish to leave the project. Coupled with the division of the forwarding of the first tranche of prepayment on the condition that the Consortium Agreement was signed, the fourth and final version of this important contract was signed by all partners in project month four (after approximately eight months of negotiations) and as such significantly earlier than comparable previous projects known to the PMO.

A key activity launched during the final stages of the project preparation phase was the conceptualization, specification and implementation of the *PROject Data eXchange System, Prodaxs*. As a fully consortium internal online tool, several key functions were specified to be served by this tool. First and foremost, this tool was intended to contain the one and only project plan information for easy access by the entire consortium. It was expected that, in this manner, full internal transparency existed as to resources, commitments and deliverables for each project partner, while at the same time ensuring direct control by the PMO. Secondly, the registration requirement was intended to enable the fulfilment of the coordinator's contractual duty to maintain a database of contact information. Finally, Prodaxs was intended as a secured document exchange platform for ready use by the consortium. Further functionalities such as project plan analysis visualizations (GANTT), database exports, calendar functions, and the integration of an open-source internet-conferencing system were added at a later date. Administrator rights to add or update the interface, project plan or contact details were strictly limited to PMO core team members in order to guarantee the correctness of information available.

Both the last part of the preparation phase and the first activity of the *active project conduct phase* were the *Kick-off Meeting* held at the coordinators headquarters with approximately 140 participants from the 64 strong consortium as well as the project and legal officer from the European Commission. The KoM took the form of an initial two-day project overview primarily by the scenario leaders before parallel sessions enabled the individual scenario leaders to conduct dedicated work launch workshops with their teams. This format was repeated at the *Mid-Term Review meeting* with a stronger focus on the large integration scenarios.

The KoM also marked the first overview of the *Management Handbook* [12], the first version which was made available for download to the consortium shortly afterwards on Prodaxs. While the Grant Agreement specifies the content and scope of the work (including its Annexes and referenced Guidance Notes) between the consortium and the European Commission, the Consortium Agreement covers the way of working within the consortium such as the handling of Intellectual Property. The Management Handbook provides information on more basic codes of conduct such as meeting behaviour, communication channels and means and may be used to look up more easily digestible information also from the legal documents.

However, the main achievement was a clear definition of roles and processes within the project. Other definitions and explanations, such as the roles of focal points, further information on the different review processes, the use of Prodaxs, document naming rules, the method used for public dissemination approval and indications of conflicts and initial resolution actions were integrated in an understandable manner. The contractual documents already specify regular reporting [10, 11] and hence a **controlling tact**. At the level of the EC, this is an annual tact with independent project assessors reviewing the consortium annual reports (which consists of a financial and technical report) and deliverables of the reporting period. At a technical level, this is specified through a project internal, biannual review tact described in more detail further on in this section. At an operational level, a monthly scenario leader assembly is conducted as laid out in the Consortium Agreement. However, due to the project's size, scope and both technical and managerial complexity, an additional weekly tact has been implemented between the scenario leaders and the PMO. This weekly Internet conference is used for the main operational management of SARISTU and results in a weekly report for the inner management circle and key project stakeholders outlining achievements, progress, risks and mitigation action status and provides a view on important upcoming meetings. With the launch of demonstrator manufacturing activities, it also started to include weekly hardware pictures. The monthly tact fulfils the same purpose with the extension to contractual deliverable status assessment, dissemination activity update and, although rarely required, the scenario leader assembly vote on project plan changes necessitating this decision-making body's approval. The monthly project status report is compiled from the weekly report and is used to not only inform the key stakeholders but also the project's Steering Committee. The annual meeting and report are used to inform the European Commission and its appointed independent assessors. While the first annual meeting between the coordinator and the assessment body took the form of a small meeting and Internet conference tying in the individual scenario leaders ahead of report completion, further meetings were conducted inversely, enabling reviewers to read the report ahead of the meeting.

A key aspect of the annual report and meetings is of course **deliverable tracking and control**. The PMO follows a strict red-lighting policy in order to eliminate the risk of water-melon reporting (green on the outside, bright red on the inside). As a result, the project's internal dashboard lists all deliverables and milestones as specified in the Grant Agreement. While this is fairly straightforward for normal deliverables, some specific ones are more complex. The EC requires **subcontracting** in excess of €10.000 to be tracked as individual **deliverables**. In order to avoid subcontracting splits, the PMO sharpened this rule by specifying this limit to be applicable per partner per scenario. In addition, the PMO specified that subcontracting deliverable due dates to be set at the start date of the subcontract rather than its completion date. Otherwise, flags would be raised far too late for effective control and mitigation. In order to facilitate scenario leaders' and partners' tracking of their commitments, the PMO sends out individual **reminders on a monthly basis**

for deliverables which are overdue or due within the coming quarter. Besides the *systematic red-lighting* of subcontracting deliverables, an “overdue” assessment can of course arise from work not completed for a variety of reasons. For example, the teams wishing to keep deliverables open in order to enable an update of a design-related deliverable in the light of possible changes during manufacturing or quite simply time intensive signature loops. In specific cases, the PMO launches *dedicated initiatives to foster deliverable completion* by approaching scenario leaders and deliverable responsible project members outside the respective tact. The biannual review tact was already specified at the proposal stage. Biannual *regular progress reviews or critical concept reviews* to be carried out at scenario level are based on criteria derived from the coordinators Technology Readiness Level assessment. It must be noted, at this point, that there are two distinctly different points of view when considering TRL’s. A technology developers’ view shows many different technical application opportunities in an expanding cone as emerging show-stoppers, for example from test results not meeting specifications, necessitate new technology variations (Fig. 4). A technology integrator, such as an airframer, however, needs to streamline this exponentially increasing range of possibilities to only the ones required for the final product. Remembering that some of history’s more prominent engineering failure arose from “defeat-in-detail”, it is clear that expert knowledge from a wide range of technical competences is required during these reviews. As a result, the SARISTU review process was established as a tacted peer-reviewed process with overall management involved only as meeting chair with the objective of ensuring adherence to technical discussions and agenda. Decisions were taken by the panel members drafted from the consortium based on technical expertise. Budget relevant decisions were implemented in subsequent meetings or exchanges as a technical review shall under no circumstances be sidetracked by time-consuming budget discussions of little benefit. The CCR/RPR process is also considered as a suitable tool for assessing work progress in the consortium as, with 64 partner companies, the Go-Look-See approach is not feasibly implementable in a meaningful tact. As the individual criteria were taken from the coordinator’s TRL process definition, reinterpreted and rearranged to better fulfil their objectives in this project environment, a major *lessons learned* was run as a brainstorming session with all scenario leaders to bring down and adapt the number of criteria and to ensure continuity throughout the project in line with [16]. Defined as important project milestones within the Grant Agreement, these tacted peer reviews may also be used to instil *Project Discipline* at an early stage if contractual provisions are made during the negotiation phase. With a large consortium, it is considered important to ensure that not only all partners fulfil their obligations, but also this is performed while maximizing overall project success and hence supporting each other effectively. The ability to temporarily postpone forwarding of the EC’s payment was used in consequence to partially incomplete initial CCRs at project month six.

A further key aspect of all tacted management methods is the crucial *project risk management*. While the classical risk mapping is used at scenario level within

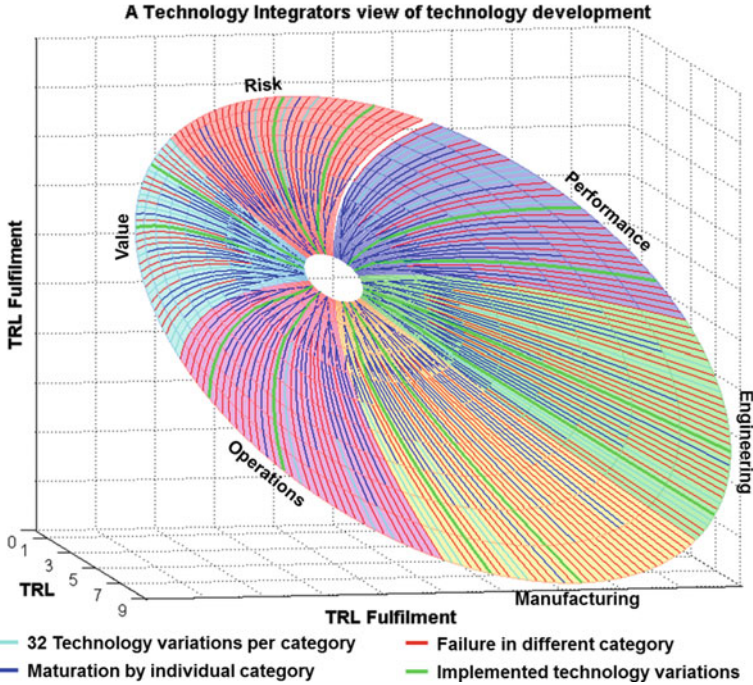


Fig. 4 Technology progress through quality gates. In a simplified graph, this figure assumes a low number of 32 possible technology variations which branch off during the individual quality gate reviews. With six categories, the majority of the 192 combinations could be driven to conclusion (red). However, failure in one category of one variation eliminates the full variant in all categories (blue). Only two variations can actually be implemented by the technology integrator (green). As the remainder can be classified as “waste”, it is an integrators desire to streamline the variation investigation through a holistic quality peer-reviewed process

SARISTU and reviewed during the principal quality gates, it was not considered the most useful approach from a project management background. Much more important than likelihood and impact are, from a time-limited project background, the questions as to when it could be determined if a particular risk would materialize, how this would be determined, what mitigation actions are under consideration, what lead time they have and if mitigation actions need to be launched before it would be known if a particular risk would occur. As a result, this way of questioning was used, but not visualized, during the quality gate reviews as well as any time new risks were raised to the PMO through, for example, the weekly scenario leader updates.

This view on project risk management is a reflection of the *One-Dimensional nature of Quality, Time and Cost*. While frequently highlighted as independent variables to be balanced, SARISTU’s PMO considers planning to be an integral part of the project cycle. As a result, an active balancing of the three variables must be considered to indicate a low quality of project planning. A high-quality project plan on the other hand will deliver its cost through control of the timeline. If

however project changes are required due, for example, to project partners' internal change needs or outcomes of the test program, the project plan must be changed accordingly through a **change management** process. Such partner induced changes must be considered normal in a large consortium and can result from a large variety of reasons. These can be as trivial, but contractually important, such as a change of a partner's task-specific internal budget allocation, or as complex as a partner's identification of major project risks and significant replanning across the consortium to enable required mitigation actions. With the first change requests arriving already before project launch, in this case due to the change of key project personnel from one partner to an outside entity, necessitating the introduction of a new project partner at the expense of an old partner, SARISTU's PMO started to draft a simple yet effective change management process. This involved the generation of a one-pager template with which partners could raise their change requests to the project management office by picking out individual lines of the project plan and then entering changed or new lines with their required changes. All change requests then entered an approval loop with the affected parties and the respective scenario leader or leaders to ensure project objective adherence. In the cases where approved change requests were deemed to impact the project's Description of Work, this was identified in the project change tracker and implemented in the next Grant Agreement Amendment loop, which in turn required the approval from the project Steering Committee. Due to initial issues faced during major change requests, the simple rule of first capturing resource in bulk and then redistributing it to new activities was implemented and communicated.

During the later stages of the project, the main demonstrations increased in importance. During this phase of the project, the tacted quality review process was first complemented and later replaced by **preliminary and critical design reviews**. Again taking the form of peer-reviewed meetings, they centred around the definition and manufacturing status of the project-specific demonstration exercises in order to enable the early identification of critical actions which, if monitored insufficiently, could jeopardize the timely completion of the project. While no dedicated criteria were specified ahead of the project, key aspects were a detailed Digital Mock-Up review, stress reports, manufacturing plan confirmations by partners responsible for manufacturing and purchasing of parts, manufacturing status review, test definition review and of course the obligatory review of contractual and non-contractual deliverables.

As an example, one particular physical demonstrator was already identified during the earliest CCRs to determine the project's critical path. During the preliminary design review, it was confirmed that individual part manufacture was a particular driver for its manufacturing timeline and established the need for high-level parts control. For this reason, the PMO established a weekly tact for **part manufacturing monitoring and control** with key partners involved in the activity.

A major undertaking such as SARISTU cannot of course be performed without adequate funding. Fortunately, the **rules for administration, funding and associated reporting and payment** are described in the Grant Agreement, its Annexes and

the Rules for (Financial) Reporting by the European Commission. These regulations define, for example, that the consortium shall be in a positive cash flow in terms of receiving funding on an annual basis from the European Commission compared to individual occurring project-related costs during the majority of the project duration. That is why the prefinancing (35 % of contractual total funding in this case) was distributed immediately after the signing of the Grant Agreement. Also defined within the rules is annual reporting, consisting of a financial part (the “financial statement”: a completed company-specific form accompanied by a certification of the financial statement in certain cases) and a technical part. The submission of all documents is done electronically only (including signatures) via the European Commission’s online tool whereby the coordinator has the obligation to review and approve all reports prior to submission. This also means that he has the right to reject documents for revision in case that the inserted information has not been provided completely and sufficiently in order to minimize the risk of non-acceptance of cost claims and/or additional inquiries raised by the European Commission. Any delay of submission of the reporting documents and contractual deliverables (exceeding 2 months after the period to be reported) and/or insufficient reporting will automatically lead to a delayed and/or reduced payment.

However, it should be mentioned that several *new reporting demands* in terms of claiming costs accompanied by the corresponding explanations have been raised by the project’s principal customer which are neither part of the guidelines nor have they been communicated by the European Commission in advance. While the first periodic reporting was accepted without any single additional requirement or rejection of costs, the second and the third reportings, executed identically, unfortunately received a high amount of refused financial statements (period 2) or withholding of payment because of non-submitted deliverables which were due at this point of time (period 3). This in turn negated the positive cash flow described above and as such became a severe project risk by jeopardizing work progress in particular at small and medium enterprises and universities.

Finally, two *limits for the total contractual contribution* until the successful termination of project exist. First of all, the contribution to the guarantee fund (5 % of the total EC contribution to the project) is directly transferred from the European Commission to the fund at the time of the payment of the prefinancing and returned to the beneficiaries via the coordinator at the moment of the final payment. Secondly, a 10 % retention of the total contractual contribution will be kept by the European Commission until the date of the last payment.

Ahead of project completion, the PMO must undertake a number of dedicated *closure activities*. While, for obvious reasons, it is too early to assess their effectiveness, some key aspects can already be outlined here.

The PMO has key responsibilities towards its primary and secondary customers, stakeholders and sponsors. With the vast majority of the financial resources for the conduct of this project gratefully received from the European Commission,

acceptance of all contractual deliverables by this funding body is of prime importance. Secondly, the key stakeholders, as represented by the 64 partner entities and their nominated Steering Committee Members, must be enabled to secure the information generated within SARISTU. This is not only limited to enabling their access to the contractual deliverables, which in any case is secured through the European Commission's reporting site, but furthermore includes all information stored on Prodax at project closure. Finally, the PMO must store and disseminate in particular the technical information within their own entities to satisfy individual sponsor and customer needs.

Further actions of importance, but not actual obligations, concern development continuity. With such a diverse field of technologies as progressed within SARISTU, many developments have and will reach respective maturities either within SARISTU or shortly afterwards by the addition of in-house work or the use of other funding and collaboration instruments. Individual technological developments will not be further pursued within the aeronautical area. Some individual remaining technological aspects, variants, and opportunities will however require further development work but without the framework programme to be continued. These aspects should be taken up in future proposals.

The previous pages have heavily centred around the "hard" project management and as such may give the impression that *Human Factors* are of little consequence to project success. As outlined in the introduction, all "hard" management tools and methods are merely a means to an end. This end is, however, not delivered by tools and methods, and it is delivered by people working in different countries and organizations, under different contracts with different internal customers, sponsors and, of course, individual objectives [15].

This mindset must be present from the earliest activities within the initiation phase as it sets the atmosphere in which a project is created and hence conducted. It can be facilitated by aligning the project objectives between the principal sponsor, its project manager and the stakeholders through a series of alignment meetings or exercises such as the topic mapping described above. Furthermore, a human-centric management necessitates frequent human interaction. Where this is not possible, for example where a large team is not colocated, different tacts can be established to ensure frequent interaction. This tact will give ample opportunity to consciously or subconsciously use techniques such as the "Hamburger" approach to passing criticism or to build *positive feedback experiences* in case it would become necessary to provide major negative feedback or circumstances placing exceedingly high demands. Of particular importance is each individual participant's *feeling of responsibility* which can be fostered by topic or activity ownership. This necessitates the creation of an environment where *self-determination* of project participants is fostered at an early stage, i.e. at the latest during project preparation, in order to ensure that the project plan is commonly owned rather than participants being forced to implement other people's visions. Again, the aforementioned topic mapping and collaborative writing processes are important methods to foster individual people's vision and hence engagement. Finally, PMO members must

always understand that *management* is always *by example*. A progressive PMO's behaviour and conduct will more likely inspire a progressive and collaborative project team than a restricting behaviour. As such, a PMO member may be demanding of its project members but must above all strive to *serve the project members* by implementing quick and easy processes which limit the administrative burden on the project participants.

A key feature of team building is typically ensured in these types of call-based publicly funded R&T projects by placing a large burden in terms of both uncertainty and workload on the proposing teams. If conducted well, the process of proposal building will force the team to *overcome significant personal obstacles*, laying a strong foundation for future collaboration. In order to enable all team members, including the PMO staff, to reach the best possible quality at the deadline, key process facts and personal recuperation times were planned nine months ahead of proposal submission. In the case of SARISTU, an additional "obstacle" was inadvertently implemented by the aforementioned extensive quality gates.

During the course of a project, it will be subject to a variety of different *conflicts* requiring *management*. A large variety of methods exist and were already employed within SARISTU. Most commonly, *mediation* was employed where the PMO typically took the role of classical mediator hosting and chairing sessions between conflict parties. These sessions were usually kept as small as possible to reduce the risk of inadvertent escalation. In some cases, the PMO took the role of demanding customer, reminding participants of the plans formulated by themselves and *appealing* to meeting participants to adhere to their self-formulated planning.

On extremely rare occasions, however, the PMO felt forced to revert to *brute force* by withdrawing associated budget from parties repeatedly failing to submit draft deliverables of acceptable quality. On each of these very rare occasions, multiple deadlines for task conduct were requested by the PMO in an escalation ladder starting with verbal requests and culminating in written demands to the partner's focal point. On one occasion each, the PMO reverted to two distinct brute force methods. When the person acting as the PMO's own internal customer changed, the newly emplaced person temporarily withdrew support for the project during its initiation phase. The internal customer peers were enlisted to enforce an alignment meeting between the PMO and the internal customer through essentially *public opinion*. On a different occasion, and in a very different context, a project partner having repeatedly shifted manufacturing schedules was approached bilateral in a *feedback* session involving the participant's superior and Steering Committee Member with the PMO appealing to the respective Steering Committee Member to again become a reliable project partner. Key to the management of these conflicts is always a cause assumption and analysis which involves an understanding of the different motivations present in a conflict, as well as the participant's capabilities important for concrete conflict resolution actions. This usually leads to a "pull"-approach in conflict resolution through mediation or appeal. Where conflicts are effectively ended by one party's written rejection of agreed tasks or repeated task failure, "brute force" methods remain the only viable solution to progressively resolve a conflict. If these methods fail as well, the PMO's prime duty is to *protect*

the project, its customer and remaining stakeholders by arranging mitigation actions with the remaining consortium. The failing parties concerns are of little to no consequence in this case as it has already expressed its unwillingness for progressive conflict resolution.

Thoroughly more enjoyable than the resolution of conflicts is the preparation and conduct of the *Major Meetings*. While the Kick-off Meeting was conducted at the coordinator's headquarters, and organization as such fairly straightforwardly performed by the PMO itself, the Mid-Term Review and End of Project meetings were held at the premises of major project partners. In a transnational project such as SARISTU, it was considered wise to place key local responsibilities and of course budgetary resources for the preparation with the responsible partners. Following the establishment of a weekly preparation tact, brainstorming sessions quickly resulted in an agenda for a *Scouting Mission* by the PMO. Typically, venues and program became clear already during the conduct of these missions. The detailed preparation was then performed locally by the partner organization, while the PMO steered this and took care of the agenda and associated presentations. Again, a weekly tact was implemented for this purpose. Due to the different character of the End of Project Meeting and Conference, this also involved the leadership of the "dissemination" work package.

3 Effects of Fundamental Rules Applied

When attempting to assess the effects of the project management rules and methods introduced above, it is convenient to again group these by the project phase during which they are applied. Of particular importance are the rules and methods used during the *Initiation Phase* as these can be expected to have major impacts on the complete project.

Within the subgroup of the consortium and team building methods, the chronologically first rule to be applied was the use of *letters of intent*. In this manner, the initiating organization ensured that the management of all parties wishing to join the project were adequately informed and able to provide their own expectations and broad commitments, typically in the form of budgetary boundaries on their own organizations involvement. It provided a very early test case for partner commitment, and indeed, a small number of companies were no longer considered as wishing to take part in the project when their respective focal points were unable to submit such committing letters of intent. As such, upon completion of the project preparation phase, the PMO did not expect major changes in the project consortium. Indeed, during the course of the project, only two out of 64 partner organizations withdrew all or part of their commitments. In one case, this was a result of key personnel movement to another organization which then took up the leaving company's responsibilities. Therefore, the Letter of Intent approach can be considered to have served its purpose very well indeed.

The *Topic Mapping* exercise served several purposes. Considering the task of consortium building, it enabled the PMO to identify prospective partners with only vague objectives for the project. This in itself should not actually be considered a problem as for example universities, research centres or small and medium enterprises cannot be expected to be aware of all constraints and requirements modern aircraft products are subject to. Therefore, the industrial use cases were used as a first tier map to which the capability-based proposals were allocated, thereby enabling the suitable integration of small and medium enterprises, universities and research centres. In addition, the resulting workshop on this mapping enabled a large feedback round which can be considered to be of particular importance for the few rejected proposals. With the final topic mapping activity decisions made, the basic demonstration activities quickly became clearer, and in consequence, a first WBS emerged. Furthermore, the one-pager submission process ensured that reliable contact details were available to the PMO team which greatly facilitated the administrative and financial aspects of the project preparation phase. As such, the topic mapping exercise exceeded the PMO's initial expectations.

Due to the basic rules to be adhered to when participating in the European Commission's 7th Framework Programme, it was clear from the start that annual *decision points* would require implementation. Due to the size and complexity of the project, it was already highlighted during the initiation phase that project internally, a biannual tact would be used. However, at this early stage, response from the consortium was weak and a simple statement of the key tacts to be used in the project can be considered sufficient ahead of the actual preparation phase.

More important at this early stage was a *singly determined project matrix* for clear decision-making processes. This was achieved by a clearly hierarchical project structure. Although a matrix style WBS was implemented, all work packages within a scenario were led by the respective scenario leader. In this manner, decisions arising from demonstration requirements were certain to be implemented in the earliest work phases, while at the same time ensuring that information requests had to pass a minimum number of handover points. This greatly increased the speed of information flow and the efficient implementation of decisions. Due to the later development of the project, the SARISTU coordinator considers this single advice received from two consortium partners to be one of, if not the most important recommendation.

The combination of the singly determined decision-making process with clear *decision levels* which maximize participant empowerment ensured an early identification and avoidance or resolution of technical show-stoppers. However, not all project participants were always aware of this bottom-up approach. In particular, members who joined the activity during the projects' active phase occasionally approached the PMO and demanded technical decisions for which the required expertise was not present in the PMO. In these cases, the PMO set-up dedicated rounds of problem analysis meetings involving the key project experts and responsible which usually led to timely, yet technically highly competent, solution plans and hence decisions. As such, the success of SARISTU clearly justifies the bottom-up decision-making process if the PMO can indeed take a step back and

prioritize the definition, organization and conduct of the process. A clearer communication during project launch and conduct would have helped team members joining after project launch though. As such, decision levels and associated processes should be defined in the Management Handbook and reminded of during the major consortium meetings.

A key aspect concluding the initiation phase is the *nomination of work package leaders* (in SARISTU: scenario leaders). By requesting written nominations from the companies whose use cases were mapped to the first tier and selected during the topic mapping exercise, several functions are served. First of all, it again necessitates the key companies' reconfirmation of their commitment. Secondly, it thereby ensures that the respective scenario leaders have their individual internal customer's full support and empowerment. Thirdly, it eliminates potential scenario leaders who, for whatever reason, cannot award the task at hand their fullest attention. And most importantly, it helps to ensure that these key positions are filled by people who are competent in the required technical fields, have a strong vision for the technological goals set out and feel a sense of "ownership" of the project. As shown by SARISTU, this approach can even be used when tier one use cases are all mapped to far too few organizations. In this case, the key institutions may nominate other establishments which they, through their participation and engagement in the topic mapping exercise as well as own experience, have come to consider to be up to the task. These organizations can then lead the respective use cases. Although the nomination of work package leaders was not a time-consuming task, it is certainly one of the key foundations for the current success of SARISTU.

Although the project *Preparation Phase* began with the nomination of scenario leaders, the actual *Work Breakdown Structure* was only finalized afterwards with the visible implementation of project phase and activity-based work packages. This was at first considered a significant risk due to the multiplication of information handover points if separate WP Leaders had been nominated. As described above, this was avoided in SARISTU. For larger undertakings, where individual workload prohibits parallel leadership, either colocation of scenario-specific WP Leaders in one office or a daily tact would be required by the PMO to overcome this threat. The original intention of the PMO was to request fleshed out work descriptions from the nominated scenario leaders in order to arrive at a bottom-up budget requirement. This would have enabled a good achievement of ambitious, yet realistic objectives. Unfortunately, this bottom-up approach was considered unsuccessful as all scenario leaders requested to be given top-down budget targets due to the large variability feared by them. While the PMO would have liked to implement technical workshops to scope out the maximum level of work towards technology maturation within the individual scenarios and driven by the demonstration exercises, this would have required several more months of preparation. These months were unfortunately no longer available ahead of the proposal submission deadline. Therefore, based on own experience as well as expectations as to the approximate work content received from the customer during an earlier public information session, the PMO formulated *individual scenario budget targets*.

This was indeed successful as all but one scenario were able to provide a concise work description and detailed planning within the first month of the writing process. Still, in future proposals, coordinators should reserve significant time for a bottom-up work scope definition following technology maturation requirements. The aforementioned twice-weekly *tact* used for proposal writing is a personally very demanding exercise. However, it is indeed able to double the iterations during the writing of the proposal. In particular for non-native English speakers, and when a proposal is taking shape in a step-wise fashion, it is highly recommended to attempt to maximize the review tact. This is particularly effective when combined with project external proof reading with feedback and recommendations provided on a chapter by chapter basis rather than arbitrary criteria. A further important feature of a demanding collaborative writing process involving several teams is the high level of involvement of individual people. The high empowerment, demanding exercise and regular constructive disputes not only serve to improve the work content planning and description, but are equally important to instil both a sense of empowerment and ownership. The latter proved to be of particular importance during the project's active phase.

An extremely high importance was placed on the generation of the *detailed project plan*. As many partners are involved in SARISTU, unitary project plan ownership was repeatedly emphasized and enforced. This enforcement must be considered highly effective as even during the later stages of the project only a single instance became known to the PMO where a project partner used their own planning information. In this case, a single re-emphasis of the unitary project plan was sufficient to clarify the situation. Similarly, the implementation of all relevant scenario, work package, technical task, subtask, deliverables, milestones and administrative activities down to individual financial certificates within a single spreadsheet allowed rapid time and cost clarifications. Coupled with an interlinked contacts spreadsheet and dedicated financial analysis sheets, it enabled the PMO to form a clear and strong link between technical and financial information. As a result, the PMO was not only able to rapidly implement changes in this period, but also to provide partners not just with the financial information they would need to enter into the proposal submission tool of the European Commission but to even generate this information themselves. This was so effective and efficient that the majority of partners supplied the PMO with financial breakdown information and then asked the PMO what they needed to enter into which cells of the EC's online submission tool. For the later project phases, the golden rule that at its lowest planning level the project plan shall not contain information for more than a single entity proved to be extremely effective for a variety of reasons. First of all, each partner was always aware of their expected work scope by individual technical task. Secondly, in the very rare cases where partners failed to deliver, the PMO was rapidly able to identify exactly which budgetary amount was affected. Finally, this greatly facilitated the change process by eliminating any cross-task, cross-WP or even cross-scenario argumentations. Without this key rule, the PMO would not have been able to recover "lost" resources and reinvest these in the necessary risk

mitigation activities. A typical feature of project plans however was not implemented. Interdependencies between individual budget lines were considered potentially counterproductive, in particular at the preparation stage. Due to the very large number of individual project plan entries, changes to individual timelines were expected. This does not consider human-centric project management and would have quickly led to project time overrun estimates with potentially disastrous effects on morale, and hence project progress.

It also reflects the approach to *Quality, Time and Cost management* taken by the PMO. A high-quality project plan, coupled with an effective and efficient change management process should deliver the expected QTC targets. With technical quality ensured through both through the signature loop of deliverables and the bottom-up peer-reviewed processes, the key controlling item for the PMO is time. Cost then becomes the relevant performance measure for the project plan itself. Although this performance cannot be assessed ahead of the closure of the final financial reporting loop, it can already be stated that this philosophy was highly successful with respect to the expected work completion date, which even for such a large and complex project and consortium remain stable after 90 % of the project's duration. This was facilitated by the PMO's clear communication on individual occasions of its expectation that one of the key project failure scenarios was the need for a project extension. While many partners do not see a problem with cost neutral project extensions, it is clear to the PMO that cost neutral extensions are not actually possible. This is due to continuing running cost (for example extending PMO activities over a longer duration or extending resource availability at partners) as well as significant efforts involved for additional contract amendments, reporting and associated reviews.

The *budget reduction exercise* conducted as a result of proposal evaluators can be considered fairly successful. While initially considered very difficult, due to the detailed and streamlined project plan, the specific comments provided by evaluators could be implemented within a very short duration and without a significant effect on the actual project progress. The remaining budget reduction was then responded to differently by the scenario leaders. Some eliminated individual testing and prerequisites such as the manufacture of associated specimen, being given no other chance but to increase the overall scenario and project risk. Most scenario leaders were able to replace individual testing with increased test simulation. More difficult for the PMO were unilateral changes to the annual budget of key partners as the PMO's authority was limited to the full project's budgetary commitments through the contractual details rather than the actual spend profile. Fortunately, the large consortium enabled the coordinator to shift work between proactive partners. In this manner, the project content remained unaffected by such events. It must be noted that such localized budget reductions placed an undue, but fortunately temporary, burden on individual project members.

The similar bottom-up approach taken by the PMO to *reduce the number of deliverables* to a level in line with customer expectations must be considered less successful. With scenario leaders having initially specified their needs from partners

through contractual deliverables, the grouping of previous deliverables reduced their visibility and control during project conduct. An additional complication was the strict timeline of the negotiation phase. Events in the personal environment of the coordinator required remaining PMO team members to take up key parts of this activity which resulted in a lack of deliverable title and description clarity. This caused understanding issues later on in the project. Furthermore, deliverable due dates were maintained from the original project plan which caused confusion during project tracking and reporting. Fortunately however, this was in line with the PMO's red-lighting philosophy. In future undertakings, this particular PMO would attempt to group deliverables by WP, type of deliverable and project phase. Furthermore, clearer distinctions, guidelines and examples for the different types of deliverable documents would be generated at a much earlier stage than the project active phase.

The *Grant Agreement* was fully signed shortly before the Kick-off Meeting, and thus, all partners were allowed to participate as well as to receive the first tranche of prefinancing as defined in the Consortium Agreement. As both agreements have to be considered as "living documents", especially Annex I to the Grant Agreement, which covers budget- and work scope-related issues, several modifications which resulted in official amendments became and continuously become necessary. These are bundled as far as possible with the fifth and last loop to be started in such a way as to allow submission of the amendment request three months ahead of project completion. While the principal customer's regulations allow flexibility in terms of budget, all re-allocations of individual funding (between partners and/or between cost categories) combined with an update of the description of work content (including deliverable/milestone delivery dates) as well as other contractual changes, for example the cost model application, company names or mergers with other companies, have to be reported to the European Commission by officially requesting an amendment to the Grant Agreement according to the corresponding guideline. Special attention must be given to all changes and additions which refer to "subcontracting", as this is considered as a very sensitive matter by the funding body. This means that each subcontract must be included within the DoW and assigned to the respective beneficiary accompanied by a short description of performed activities and the corresponding costs before the work is going to be subcontracted. These figures must be in strict compliance with the budget-related information as given in Part A of Annex I. Similarly, the lack of a clear rule and definition about the maximum value which is allowed to be subcontracted leads to a very detailed and careful review by the EC. Any non-reported or non-solved issues might interrupt the whole administrative process with respect to payments. Therefore, having a detailed project plan and change management process in place is considered indispensable by this PMO!

One of the first key activities for the project's *Active Conduct Phase* was the generation and implementation of Prodaxs. The relevant project plan data were entered in the final month ahead of project launch. As a human-centric activity, this introduced some smaller errors visible when exporting the data out again. Future

tools may benefit from automatic import functions for this initial one-off activity. Once these very few errors had been identified by automated comparison of export data with the original input file, this functionality of the data exchange platform proved to be extremely useful not only to the PMO, but also for project partners needing to obtain quick financial and timeline information in an easy to search, analyse and digest format unavailable through the contract’s raw data. During the course of the project, additional analysis functionalities were added such as plan visualization using Gantt, exporting of the contacts databases for both project members and organizations legal addresses, exporting and visualization of monthly budget and manmonth data (Fig. 5). The straight spreadsheet exports of the project plan and contacts are considered to be the most used ones and are widely appreciated.

Similarly, the information from the two contractual documents was used to create initial users and passwords for this restricted, consortium internal online space and as such greatly helped to fulfil the coordinator’s duty to maintain a database of contacts. The calendar function, on the other hand, was not extensively used by the consortium as participants typically preferred to use their office calendars for meeting scheduling. It can therefore be recommended to implement functions directly tying into common office scheduling software tools if and where possible as the calendar functionality will otherwise not be in frequent, and certainly not universal, use.

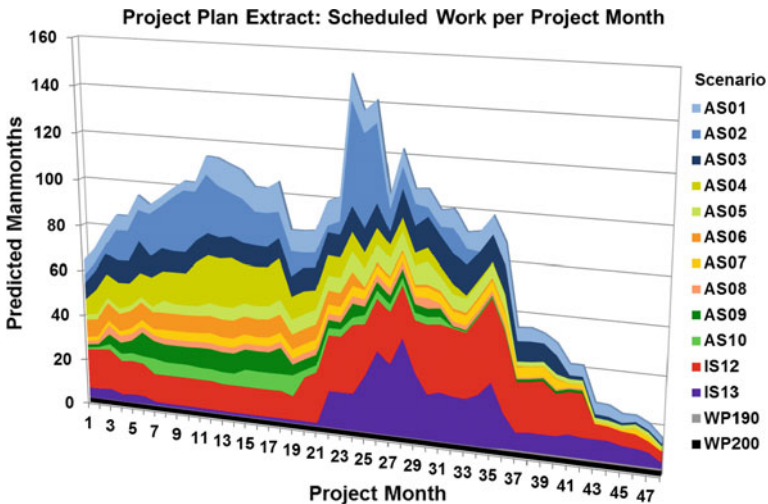


Fig. 5 Scheduled work by project month. This project plan extract may be used for participants workload planning. Due to the PMO’s red-lighting philosophy and direct link to the Grant Agreement, the peak around month 24 did not materialize as extremely. Work shifts to subcontracting had not been implemented contractually at the time of the data export and individual time delays shifted work from the peak period over to the final reporting period

The BigBlueButton internet-conferencing integration was temporarily quite widely used within the consortium. However, data restrictions in some of the major partners' information technology structures prohibited its widespread implementation. Similar systems, which were implemented within these companies and had proven to work for all partners, could not be implemented in the Feng Office environment at this stage. However, due to the strong reliance on internet conferencing within transnational projects, the integration of corresponding tools in a project management and data exchange system is highly desirable and recommended.

The most important functionality of Prodaxs has always been considered to be the ability to exchange large quantities of data across the consortium. Having implemented effective work area and subfolder structures fully based on scenario leaders requests, the use of the data exchange platform was first mandated for the submission of presentations and proof files for the first Critical Concept Review to increase consortium awareness. With, at the time of writing, 3607 documents and 431 users, this functionality can indeed be said to have been implemented highly successfully. Most impressively, its use for the collation of Digital Mock-Up data for the wing integration demonstrator design was a task fulfilled by, but not initially foreseen for, Prodaxs.

The *Management Handbook* can be considered the fourth most important document within SARISTU, after the Grant Agreement, the associated Project Plan and the Consortium Agreement. As such, the first version was completed within one month of project launch with rapid update loops to include major lessons learned, newly implemented methods such as the formalized change management or rules on the use of customer visuals. Sadly, it was rarely used outside the PMO. Nevertheless, the collection of important rules and methods in SARISTU in a single document is an important exercise to ensure consistency throughout the project and to maintain clarity at least within the PMO. The handbook was viewed and downloaded approximately 420 times, but including a multitude of downloads per PMO member. In future undertakings, this PMO may wish to rethink the method of referencing to this document as well as its dissemination.

As with the preparation phase, the project's active phase is characterized by different *tacts*. In particular, the *weekly tact* is a very important operational management tool fulfilling the key functions of information flow assurance, risk monitoring and control, deliverable monitoring, action anticipation and preparation and, through its reporting, customer and sponsor information. Unlike a biweekly or monthly tact, it also allows a high degree of flexibility as individual participants may not always be able to attend. In a weekly tact, individual absences can rapidly be recovered which is not the case for biweekly or even monthly tacts. Due to its identical participants, mission and being scheduled to replace that individual weeks weekly tact, the *monthly tact* was initially confusing to scenario leaders. However, due to the high level of integration, the PMO requires in particular the integration scenario leaders attendance to enable a strong and guaranteed interaction with technology supplying application scenarios. While in many cases this was already but coincidentally enabled by the weekly tact, the PMO should not eliminate the

monthly tact. While most important decisions are in fact prepared and, as such taken, during the weekly tact, the monthly tact fulfils a requirement from the Consortium Agreement on its conduct. Furthermore, the PMO has a strong desire for inter-scenario interaction, and each team member should have the chance to be informed of progress in other scenarios. It is therefore recommended for comparable future endeavours to implement a weekly tact where each session contains weekly topics such as round table reporting, risk monitoring and control and the identification of emerging cross-scenario questions. A second part of each weekly would benefit from cyclically changing topics such as task and deliverable monitoring (biweekly) and project internal cross-scenario exchange (biweekly). Additional temporarily hot topics such as simulation and design harmonization, design progress monitoring, subcontracting status, tool manufacturing, part manufacturing tracking, ongoing project plan changes and current outside influences would round off these weeklies.

A key task in any project, but in particular in projects with a public–private partnership character, is evidently *deliverable tracking and control*. An integral part of the tacted meetings and reporting, visual management is used to provide both overview and detailed information at any time. While the general overview helps to quickly explain the overall deliverable situation, for example in reporting to customers and sponsors, an individual scenario status could immediately be assessed and highlighted in the weeklies. An additional dashboard feature introduced following the first external assessments is used to visualize the review status of all deliverables both at total project and at scenario level. Finally, the different tacts coincided with peaking deliverable due dates, and it is as such important to have visual clarity over the length of time deliverables are overdue as well as being able to provide a quick reference guide for workload anticipation. The latter is particularly useful for the PMO as it uses this information during weeklies and monthlies to pre-empt delayed deliverables. The tracker is designed to always reflect either the state of actual deliverable submissions to the customer or a worse state. In particular during the fourth reporting period, SARISTU had reached a stage where deliverables had been reviewed and accepted by the customer although the consortium itself will implement further updates and additions to these already accepted documents.

For the daily management and in particular during the weekly conferences, a different view of the deliverable tracking was also used to good effect. The deliverable indicator shows the identical information as the dashboard but for each deliverable, milestone and subcontracting deliverable. Filtering of the underlying data allows a less cluttered view for detailed discussions with scenario leaders. Most importantly, the resulting discussions at individual deliverable level are tracked together with the underlying data so that response time to questions raised by the independent assessors and the customer can be measured in seconds.

The use of this deliverable tracking method is therefore of fundamental importance to SARISTU (Figs. 6, 7).

Some of the *rules applied to contractual deliverable planning and controlling* as well as the *red-lighting philosophy* had important consequences for project

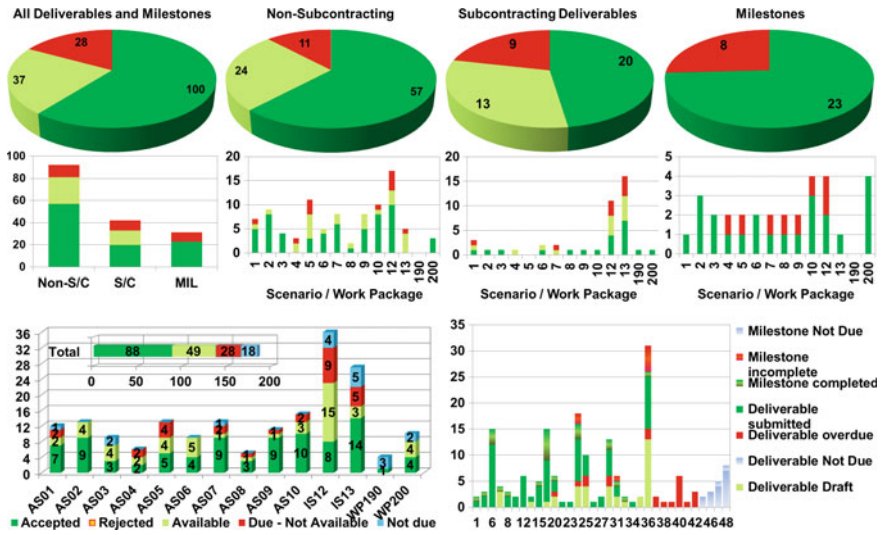


Fig. 6 Deliverable status dashboard on 24 March 2015. The overview dashboard is used by the PMO as a quick reference and reporting tool. As such, it reflects the consortium’s view of deliveries rather than the actual submissions. Due to the PMO’s *red-lighting* philosophy, the dashboard always gives a worse view when compared to the customer information as there the yellow parts are also tracked as green

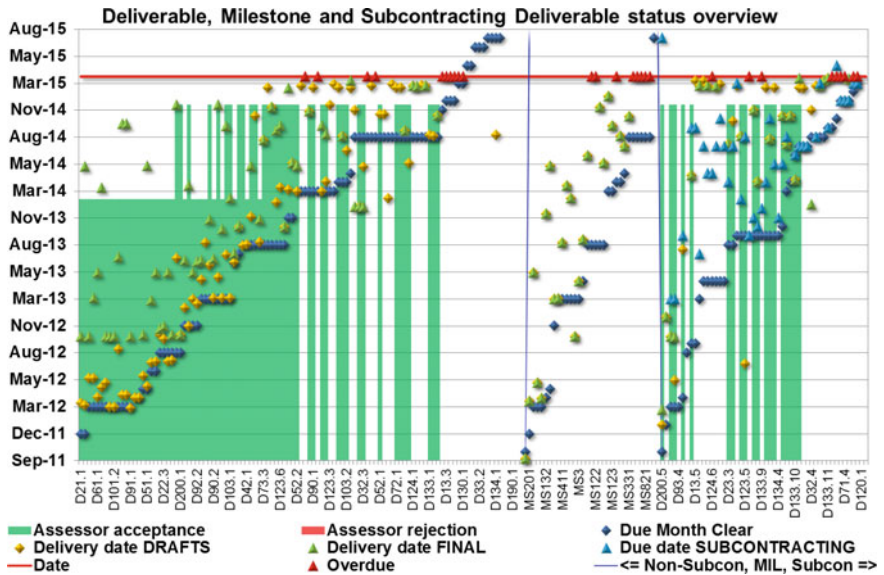


Fig. 7 Deliverable indicator on 24 March 2015. Visual management can be used for all deliverables to very good effect both during operational management and the major reviews

reporting and assessment. The requirement, for *dedicated deliverables for subcontracting* exceeding €10.000, was well understood, but the required content of such explanatory and monitoring deliverables was not specified by any rule or guideline from the customer side. Through several iterations, the consortium arrived at a format for such dedicated reporting. While effective as a quick reference to the efficiency of subcontracting, customer demanded specific deliverables should have templates provided either by the customer or developed early on by the PMO much earlier in a project in future undertakings. Furthermore, the rules as to the content of these deliverables were not specified by the customer and as a result were developed by the PMO based on verbal instructions. Inclusion of these requirements and instructions in the guidelines for reporting would be helpful for other consortia in other projects where such deliverables are requested.

The *systematic red-lighting* by the PMO implemented to counter “water-melon” reporting ensured a good awareness of the main issues not only by the PMO, but by the full consortium, customers and sponsors. It does, however, have some negative effects. While red-lighting ensures that for example subcontracting deliverables are highlighted at their start date rather than their end date—when all mitigation actions would come far too late—and certainly helps to ensure adherence to the project timeline—it can cause delays in the receipt of the annual payments to the consortium. A change of payment rules by the customer in one case led to the full payment tranche being delayed until all deliverables for the period had been formally submitted. In consequence, the PMO rapidly submitted these documents in the knowledge that further work beyond the original work scope will still need to be integrated. Therefore, additional deliverable rejection loops will need to be launched at the consortium’s wish in order to enable highest quality final deliverable submission. Despite this added administrative burden, this new rule on payments certainly helps to obtain a large number of finalized documents. This is even visible in the deliverable indicator.

Finally, the *signature rules* employed are considered a good compromise between the administrative burden, and hence time taken and the assurance of quality. While the superior of the principal author guarantees technical quality, signature by one or more of the scenario leaders guarantees that its content is in-line with project requirements. While this deliverable quality assurance could be further improved by increasing the range of signatories, this was only performed where absolutely necessary due to the increased complexity in obtaining document approval. With the biannual, peer-based reviews functioning as additional quality control gates, the applied signature rules can be considered an effective means of ensuring quality in a publicly funded R&T environment.

The implementation of *regular progress reviews and critical concept reviews* in a biannual tact is considered a very demanding but highly successful method. First of all, it ensured that all project members were tied into the technical work from a very early point. From the technology developers of the consortium, the preparation of these extensive and detailed reviews ensured a high amount of interaction and knowledge collation and creation. From the technology integrators, this required a high level of responsiveness and very early detailed specification work. The latter is

considered particularly important for a streamlined development and was ensured by drafting the review panel predominantly from SARISTU's integration scenarios. Secondly, the holistic nature of the predefined questions to be addressed in these reviews enabled a very important understanding of the involved specialists of the full scope and complexity of technology development for civilian airliners. This was particularly evident where specialists from one discipline learned to appreciate the consequences of requirements in seemingly unrelated categories for their own work. As an easy example, we can highlight operational maintenance requirements resulting in specific performance criteria such as material ageing and reparability. Furthermore, the consideration of manufacturing defects during demonstrator production within SARISTU necessitated the early consideration of repair processes to be available towards the final stages of the project. Finally, the definition of these reviews as contractual deliverables enabled the PMO to send a message of strong deliverable focus into the consortium by postponing prefinancing to individual partners. Directly affected parties subsequently and consistently exceeded initial expectations and became by far the most engaged team members. The latter was only possible as the coordinator chose to merely implement a mild penalty as more drastic measures could have resulted in the complete loss of this part of the consortium. In this manner, *overall project discipline* was markedly improved.

The tacted meetings and in particular the first CCR/RPRs also highlighted the issues with classical risk mapping when used to *assess project risks* as already described above. Indeed, many individual and mainly technical risks could be identified and addressed in a manner which maintained the overall projects QTC targets. Individual risks did however materialize despite this overall effective approach. The manufacturing chains of the main demonstrators, for example, were identified as high-risk work streams in particular when considering the projects timeline and hence cost target. In one case, this resulted in the decision to manufacture an additional major demonstrator in order to allow parallel rather than sequential testing. During the resulting replanning exercise, a small enterprise requested to perform the manufacturing of few but complex key parts. Due to the small company size and local resources, these parts later proved to have the most unpredictable timeline and immense work peaks had to be endured by the company to allow the overall project to maintain its timeline. In another case, where the employed risk reduction methods did not prevent a partial defeat-in-detail, a delay resulted from the lack of availability of specific fastening elements for demonstrator assembly. While a PMO mandated availability check 12 months ahead of assembly had returned a confirmation that said fastening elements were indeed in store, this positive response was a result of mis-labelling. In fact, only the associated nutcaps rather than the fastening elements were available at the time they were required. This resulted in a key activity delay which had fortunately been removed from the projects critical path. As a result, it must be said that the overall project risk management focus on the timeline was largely successful but would have been even more efficient with a clear Go-Look-See component during the biannual reviews and would have benefitted from visual tracking rather than only the list-based tracking used during biannual, monthly and weekly reviews.

The introduction of a formalized *Change Management* process and in particular its one-pager template was not initially well received by the consortium. With this reaction to formalized processes and additional forms anticipated by the PMO, the process was repeatedly explained both at major meetings and on individual occasions. Supported by ad hoc assistance of participants by the PMO up to the point of preparing entire change requests with information supplied by the party wishing to raise changes the consortium’s learning must however be considered very quick. By the second half of the project, the simple process had become very much appreciated by the majority of the consortium and in particular by the scenario leaders due to its transparency and clarity. It should be noted here that an important feature in enabling such an efficient way of working was implemented in the Grant Agreement and associated project plan by specifying a risk reduction and mitigation fund. This was extensively used to first secure resources from subtasks that were identified during the project as having required less resource than initially expected or were not after all required as foreseen risks were mitigated, eliminated or no longer identified as risks. Following the second Grant Agreement Amendment loop, a special flag was introduced into the change request form to facilitate tracking of project plan change request implementation, which can cover a large number of individual changes, into the Description of Work of the Grant Agreement. As such, change management based on the master project plan, a simple template, the risk reduction and innovation fund and a partner supporting PMO mindset must be considered a key contributor to the current success of SARISTU (Fig. 8).

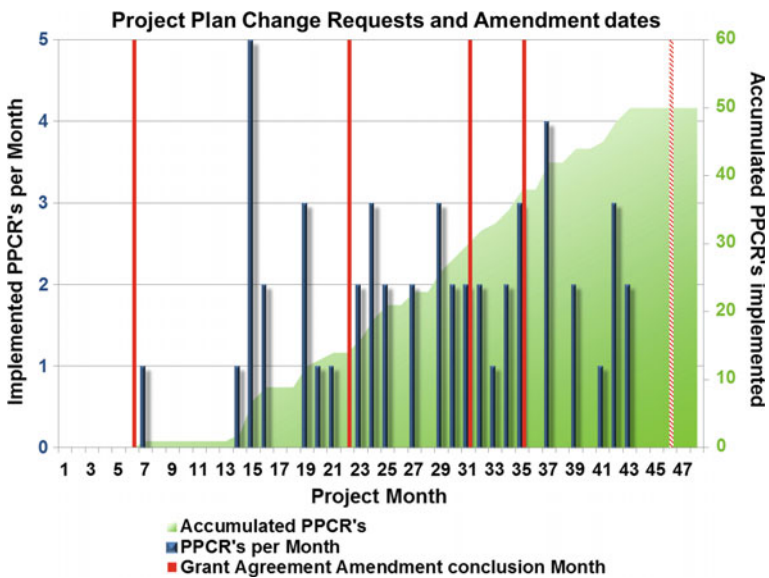


Fig. 8 Project plan change requests by project month and formal implementation date by Grant Agreement by month 44. Fifty individual project plan change requests of differing complexity and background had been implemented in the project plan

The *preliminary and critical design reviews* (Fig. 9) took the place of the critical concept and regular progress reviews during the final 18 months of the project due to the ramp-down of individual technology development activities and the rapid ramp-up of demonstrator manufacturing. Enabling a detailed insight into the status of the detailed design, stress analysis, manufacturing planning and preparation, as well as initial test scheduling and preparation, these reviews are considered extremely important by the PMO to ensure project success. However, unlike for the CCRP/RPR process, no detailed criteria and questions were specified during the project preparation phase which concluded 30 months before the first of these reviews. From the experiences gained during SARISTU, this PMO would however endeavour to provide a more detailed insight into the specific questions to be addressed to facilitate their conduct. Despite this low level of initial specification, the PDR and CDRs must be considered successful key milestones as they allowed key timeline risks to be addressed well before they would have emerged naturally.

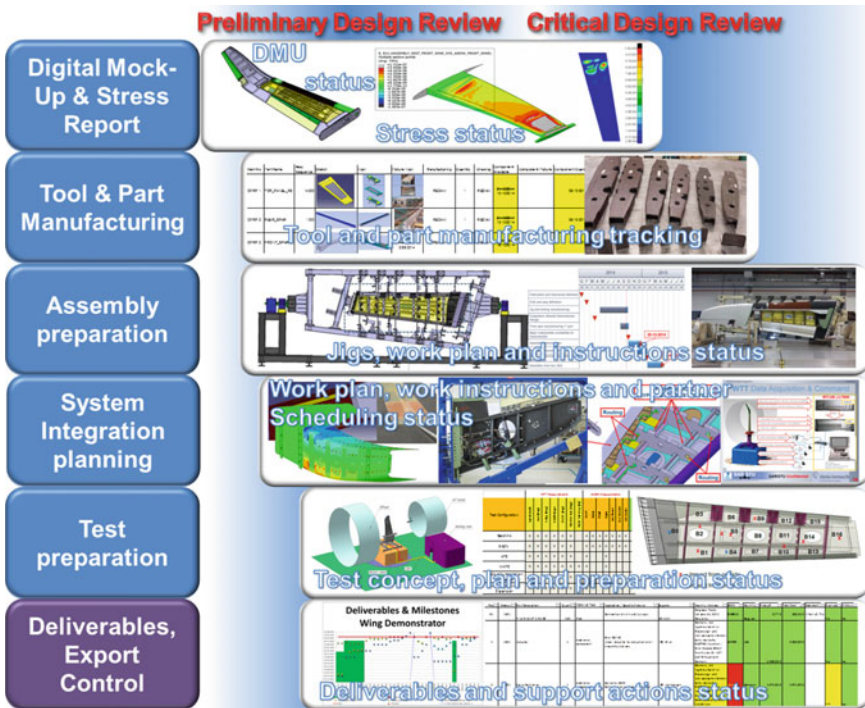


Fig. 9 Illustration of the scope of the preliminary and critical design reviews. Focussed entirely on demonstration success, the PDRs and CDRs are designed to give a full view of the current status of preparatory activities such as the specific design status, preparation for manufacturing and its specification as well as the preparatory status of the final testing itself. As such, they represent a deep dive into each specific area of a demonstrator exercise. Notable is the low focus on aerodynamic performance as these topics were already covered through early SARISTU deliverables

Of course, this was only possible due to their placement well in advance of manufacturing and assembly steps.

The PDR in particular also highlighted one of SARISTU’s weaknesses caused during the preparation phase. With the project being dedicated to further maturing technologies and their integration primarily through physical integration, and hence testing, the harmonization and coordination of required simulation activities were not planned. It is the recommendation of the authors to perform this harmonization already during the project preparation phase in order to ensure a corresponding team set-up and interaction. The latest possible point would be the first three to six months of project conduct. Fortunately, the project objectives were not affected by this lack of initial harmonization.

With one particularly complex demonstration exercise fully defining the projects critical path, the PMO implemented a weekly *part manufacturing monitoring and control* loop with partners supplying critical parts to the demonstrators’ final assembly. It was quickly determined that each partner should be tracked individually to avoid the risk of launching a rescheduling avalanche during these meetings (Fig. 10). While this latter part was effective, it did not prevent individual parts shifting their delivery date. In particular, a salami slicing approach, with part delivery shifted repeatedly by small amounts, is considered a major threat by the PMO. Not only does it pass an increasing burden to the final assembly line to deliver in time, but it also requires the continued availability of resources at the line, increasing project cost beyond those of a single major time shift. Furthermore, a major time shift can be more effectively used than many smaller shifts for other activities such as major work on available components or even further design tuning. Worst of all, confidence in the suppliers is lost in this manner. Unfortunately, the contractual documents in place did not allow hard measures to be taken either in pull through, for example, incentive payments where part delivery

Item No/Part Name	Assy Sequence/Sketch	Tool	Picture Tool	Manufacturing/Quantity	Drawing/Component Available	Comment	Component Picture
CFRP 1 TOP_PANEL_R5	14200			REDAM 1	REDAM 01/10/2014 10/10/2014 10/10/2014 24/10/2014 31/10/2014	19/11/2014 At ALA	
CFRP 8 Rib 12	3300		15/09 In progress 23/09 Near expected 01/10 10/10 available	INASCO 1	ALA "In progress" 23/09/2014 01/10/2014 10/10/2014	23/09/2014: Crisan can not be fully performed 10/10/2014: Mold and Ply patterns completed 01/10/2014: Dimensioned for 23/11/2014: Lamination and Bagging 23/09/2014: First panel has been used 10/10/2014: Panel to be shipped on 13/10/2014 24/10/2014: Confirmed to be in Promobase by Lozano.	
CFRP 1 Lower Panel	2000			BAB 1	BAB 03/10/2014 24/10/2014 24/11/25/11	19/11/2014 At ALA	
SASSY Trailing Edge	22300			AERRINOVA 1	CIRA 15/10/2014	19/11/2014 At ALA	
Met 1 ROOT RB NEW CONCEPT W	11800		29/08/2014	REDAM 1	REDAM "In progress" 01/10/2014 31/10/2014		

Fig. 10 Extract of the wing parts tracker. The tracker attempts to visualize the actual manufacturing and verification status of the main parts required for the assembly of the demonstrators and helping to predict dates for the final assembly line. As such, it captures the readiness of part definition, tool manufacture, part manufacture and quality assurance and tracks repeated delivery forecasts. This parts tracker is fed from more detailed, manufacturer provided documents discussed during the same tacted weekly

QTC is exceeded, or penalties where QTC is not met at part level. In addition, the resources available to the PMO to perform Go-Look-See-Assist actions at a meaningful technical level were at this point extremely limited and would have required significant preparation time. This exceeded the individual projected delay, but not the final total delay. In such circumstances, the coordinator had to rely on the abilities of individual experts in particular at the final assembly line to recuperate these delays. It is, however, recommended for a project customer to enable coordinators to extend their arsenal of incentives and penalties to allow more effective control of such occurrences. Furthermore, a temporary means to rapidly draft in a quick reaction fire fighting force is recommended but is likely only feasible for even larger undertakings. So while individual part manufacturing monitoring and control actions implemented in SARISTU may be improved in future undertakings, this PMO nevertheless has to assume that without the actions taken a time delay would have been incurred to the entire project and that the actions taken were therefore effective. If they are sufficient will be seen in project month 48 when SARISTU has either completed its activities and achieved its objectives or it has incurred a time delay.

Considering the high variation in technologies in SARISTU, the basic separation of both the *Kick-off Meeting* and the *Mid-Term Review* into a two-day overall project review followed by a single day focused on active workshops at scenario level was in retrospect a very successful idea. While the overview part allowed a detailed insight into each work area for all participants including the external assessors and the Steering Committee Members, the individual workshop sessions were highly effective at raising and addressing critical technical questions and invigorating the respective teams. With respect to the organization of the meeting, going through local project partners rather than performing all preparatory actions centrally is also considered an important aspect by the PMO, although the effectiveness in terms of financial efficiency cannot be quantified without a fully centrally organized meeting serving as a benchmark. Nevertheless, the conduct of a PMO scouting mission followed by the implementation of preparation tact must be considered extremely effective.

Acting as a coordinator, special attention refers also to the observance of the given rules and guidelines with respect to financial issues which cover *costs and payments*. As observed above, the binding of individual payments to the fulfilment of contractual requirements by the consortium allows good project control. Therefore, the periodic reporting is useful for obtaining a solid spend overview at WP level, by cost category and by partner. Even more importantly, it imparts both the right and the obligation to review each individual cost claim in comparison with the originally planned activities and associated budgets. The precise check of the financial reporting, which is mainly focused on the “use of resource” report but also includes the correct application of assigning costs to the appropriate category and the rejection for revision whenever anything is missing or incorrect, is of overriding importance. It minimizes refusal of claims and delays in terms of payment. In the particular case that subcontracting has been claimed by a partner which was not included in the DoW, such positions have been either excluded from the current

reporting and postponed to the following reporting period or were subject to an official request for approval accompanied by the commitment to adjust the Grant Agreement, including DoW, through an amendment.

A detailed description of exact reporting needs was always provided as part of the written reminder sent by the PMO to the consortium as the reporting period closed. To ensure that all kind of notifications sent to the consortium partners are received by the correct people, it is important to maintain a dedicated financial and administrative focal point contact list. As this is an obligation defined in the Consortium Agreement to the coordinator, the responsibility of keeping and updating all contacts has been carried out by the PMO via Prodaxs. However, contact details can only be as complete and current as reported to the PMO. It is important to bear in mind that the project status in terms of contractual aspects is up to date in the reporting system and in the Grant Agreement by amendments when a reporting period becomes due. Otherwise, there is also the risk that the process will be interrupted and delayed.

After approval of all reporting documents by the European Commission, which on average requires 6–9 months after submission, the equivalent periodic instalment is transferred to the coordinator. The amount of each payment is calculated by taking into account the payments already given, the total actual funding as accepted and the total contractual contribution but limited to 85 % because of the 5 % distribution to the guarantee fund and the 10 % retention kept by the EC. More or less the same principle could be always applied by the coordinator when distributing the received funding among the partners. However, as soon as the payment was ready for transfer, the consortium has been informed in detail how the calculation and distribution has been done accompanied by the corresponding official documents as provided by the EC (Fig. 11).

Although self-evident, it is still beneficial to highlight that the PMO requires correct banking details for each partner at this time. Between several reporting periods, individual partners' banking details changed but were not communicated to the PMO, leading to additional administrative efforts.

Because of the aforementioned period of time necessary for the approval of documents, including the time needed for the fulfilment of additional requirements, the clause for forwarding the instalments to the partners by splitting them into two tranches as defined within the Consortium Agreement could not be applied for all periodic payments. Instead, payments had to be made in a single transaction.

Although the PMO plan for *Project Closure* exceeds contractual commitments, it is too early at the time of writing this paper to assess its effectiveness.

With respect to *Human Factors* (Fig. 12), relevant metrics are not available to this PMO. For this reason, subjective, qualitative effectiveness assumptions must be sufficient at this stage. Key to overall project success is considered to be the very high personal engagement of project participants. Such high engagement is usually expected to deteriorate over time and negative experiences. As a result, *positive feedback experiences* are very important to maintain and further increase overall project morale. A high inquisitiveness by the PMO in the weekly tact coupled with

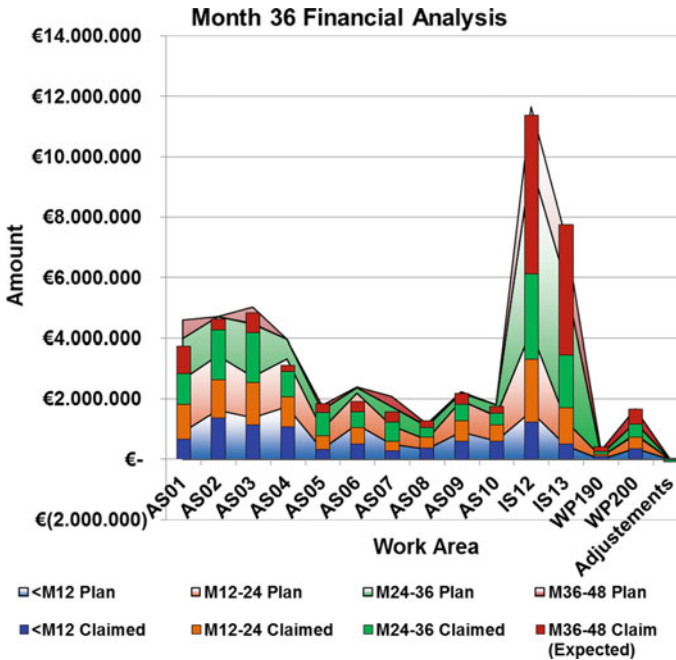


Fig. 11 Summary of financial reporting after $\frac{3}{4}$ of the projects duration including financial prediction to project end, detailed financial analysis is performed on an annual basis from the cost claim information submitted to the principal customer. While at month 36 a drastic underspending was reported, the PMO determined this to be primarily a result of “red lighting”, with cost in particular for subcontracting showing up much earlier in the project plan than they actually occur. Based on these “overdue” cost claims, an extrapolation can be performed, showing in this case and at the time of writing an expected underspending of 2.82 %

reporting cycles that forward information from project members to the project’s customers and sponsors is helpful, but its effectiveness must also be considered to deteriorate over time. Fortunately, numerous further activities provide opportunities for a personal interaction and feedback such as the biannual reviews, the annual reporting loop and, most importantly, the main project meetings. In particularly tough episodes, the PMO also approached individual participants who were at the time expecting negative feedback due to critical time delays. Providing a positive feedback related to the handling of this time delay greatly boosted morale, thereby invigorating the local team and in consequence facilitating delay mitigation. The strong *feeling of responsibility* can be expected to be present in any contractually secured undertaking, and especially those which result from a call-based competition. Nevertheless, the consortium should be repeatedly reminded of this by the PMO during the tacted review opportunities. Appealing to the common vision of project success is usually sufficient for this, although in particular circumstances the PMO decided to also remind participants of contractual features which enable other project partners to claim damages which may arise, for example, from project plan

non-adherence. Due to the change management process described above, these rules did not have to be used by the time of writing of this article. Supporting *self-determination* in an undertaking such as SARISTU must be considered a very difficult balancing act. Although the foundations can be laid during the project preparation phase by driving a bottom-up proposal writing process, the required criticism of individual project constituents to foster the proposals maturation can have a negative effect. Similarly, while a bottom-up change management process serves to foster a feeling of self-determination by project participants, top-down changes, which are necessary due to for example deliverable non-adherence, will have a detrimental effect. Considering the very good present status of the project, the PMO assumes that the balancing act performed in SARISTU was successful, but final judgement on this topic should remain with the actual project participants outside the PMO. Similarly, the perception of *management by example* cannot be judged by the active PMO members but rather the remaining consortium. While the demanding project provided ample opportunity to exceed reasonable expectations by the PMO, and such exceedance was frequently observed within the main project, the PMO is also aware of its failures on individual activities. The authors hope that their handling of individual activity failures supports the perception that they measure project participants with no harsher measures than they apply to themselves. The PMO's self-imposed demand on conduct may also have helped the full SARISTU team to occasionally overcome *significant personal obstacles*. Although the focus is usually to prevent instances of undue personal burden, the six-month project point is a needed reminder to the consortium that all activities should be under way by this point. Considering the performance of the project subsequently, this must be considered a successful venture. Naturally, further instances of emerging team overload occurred within individual scenarios and partner organizations subsequently when, for example, quality control at part level highlighted issues or design iterations are unilaterally introduced by individual project participants. In these events, the affected teams were able to look back upon significant common trust-building experiences and were aware of the individual strengths and weaknesses. This all enables in particular work area leaders to rapidly clarify and implement mitigation actions. From a PMO's perspective, it is considered important that the PMO is inquisitive and supportive during these times by, for example, offering help in terms of meeting scheduling, organization and the set-up or even the implementation of PMO-driven tracking and control at scenario level. The PMO's mindset to *serve the project members* is a fundamental factor in this. This can be observed most visibly in the conduct of activities not usually associated with overall consortium management, such as demonstrator part tracking, but also in the manner in which bottom-up lessons learned are conducted, for example after the first round of Critical Concept Reviews, or the change management process designed to minimize participants' administrative burden. In addition, the preferred method of *mediation* employed by the PMO for *conflict management* can be considered to fall within this category, especially when inter-scenario conflicts transpire. Perhaps even more interestingly, the *brute force* methods of *public opinion, feedback* and win-lose negotiations for *project protection* all served their

purposes when employed during SARISTU. However, a quantitative assessment cannot be made due to the rarity of such methods needing to be employed. Despite the clarity provided by such methods, this PMO remains convinced that the best conflict management is conflict prediction with the objective of collaboratively addressing the possible causes of conflicts early.



Fig. 12 *Human Factors* The main project meetings are a rare opportunity to engage with project members face to face. *Top* Participants to the Kick-off Meeting, 06 September 2011 at Airbus Operations in Hamburg, Germany. *Centre* Workshop impressions during the Mid-Term Review, 26 September 2013 at the University of Napoli, Italy. *Bottom* Participants to the End of Project Meeting, 19 May 2015 at TsAGI in Zhukovsky, Russia

With SARISTU rapidly approaching its targeted end date, an outlook on *future, related activities* and according preparation is required. The technologies matured within the project come from a large variety of very different fields and as such can be expected to move in different directions after the project. In many

cases, the advancement of technological know-how enabled funding bodies and project participants to propose further development work to be conducted in future undertakings such as Clean Sky 2 and the German 5th “Luftfahrtforschungsprogramm”, although specific target applications will change. In other cases, the step from non-specific to specific design work shall be taken, and corresponding functionalities may be offered to prospective commercial customers within a comparatively short time frame. Due to lessons learned in SARISTU, further opportunities for research targeting aircraft and air travel cost reduction have been identified and may be proposed for Horizon 2020. And finally, there are indeed individual technology streams where SARISTU has highlighted that the performance targets can be met, but at currently prohibitive cost, making a near-term implementation in commercial products rather unlikely. This assessment of the less than 8 % of the total projects scope is certainly not the final word in the individual technology’s future developments however. The respective parameter spaces are very large and only a fraction of the full technology streams variations could be investigated in SARISTU.

4 Major Lessons Learned in Project Management

Besides the aforementioned rules and methods, a number of lessons learned can be derived from the SARISTU project. Evidently, an overall mindset which attempts to understand and predict the principal customer’s expectations is beneficial to a project’s smooth conduct. With respect to publicly funded projects, this in turn is facilitated by the coordinator’s clear understanding that the public funds she or he is entrusted with are also a direct result of taxes paid by this particular individual. She or he should therefore conduct the project with a *tax payer’s mindset*.

With respect to hardware-related projects, a *continuous, strong focus on the demonstration exercises* is considered helpful. It is all very well if an individual project partner works diligently through his parts of the DoW, but if knowledge generated during the project necessitates changes to these plans, partners must be able to align their work to these changes to continue to be of relevance to the final objectives. This may be reflected in the WBS by placing the demonstration activities firmly above the feeding work areas and must be driven through the review processes.

While the top-down budget allocation helps for initial planning purposes, future undertakings could benefit from additional time spent in the preparation phase for a more thorough *bottom-up definition of the demonstration activities*. This would, however, come at the cost of subsequent project flexibility.

During the early active phase of a project, several harmonization loops could further improve on a project’s efficiency over SARISTU. Due to this projects strong focus on physical integration, the design process itself was not standardized. This could however have further improved later demonstration activities by better aligning, coordinating and *integrating the different simulation activities*, for

example during the course of the full aircraft aeroelastic model generation. Furthermore, additional design loops are considered to be helpful. In particular, a *design-to-cost loop* is considered fundamental in order to reduce a demonstrator design's complexity and thereby reducing the project risk. A particular harmonization loop, consisting of *part standardisation*, should be conducted during the specification phase in order to minimize the number of different standard parts. Within SARISTU, the design focus at the time when this exercise would have been beneficial was fully focused on design-to-performance.

An aspect significantly underrated by the PMO during the first half of the project was *dissemination* (Fig. 13). With little to publish during the early phases of a project, this activity area received little attention at that time. Furthermore, as it only indirectly, and as such not measurably, contributes to overall project success, it was frequently considered a low-priority, high-effort activity. However, during the second part of the project, with publication requests increasing and visuals becoming more widely available to the PMO, this perception changed as the feedback received from project participants and customers improved further. It is therefore recommended by this PMO to formulate a dissemination strategy early on in the project which exceeds the basic collection of planned dissemination actions.

This topic is also linked to the increased use of *visual management* within SARISTU. Although the work effort in setting-up effective visual management is non-trivial, it can henceforth be used to allow rapid insights into project progress and achievements as well as being used in the different tactics employed for reporting. Complementing this is the very good experiences provided by the visual reporting introduced in SARISTU's third year. Besides the visual dashboard, the launch of major manufacturing provided ample opportunity to showcase visuals



Fig. 13 Geographical view of dissemination actions performed by SARISTU (from [13], M. Papadopoulos) With the vast majority of dissemination actions unsurprisingly located within the European Union, SARISTU did manage to obtain a global reach through repeated contributions to key intercontinental conferences. A wider geographical distribution of dissemination activities is pre-empted by both funding rules and project efficiency considerations

from different work areas as part of the regular reporting. This boosted customer and sponsor awareness significantly better than text alone. Perhaps even more importantly, it provided a clear visual appreciation of the achievements of individuals and teams. This PMO therefore recommends to introduce visuals as early as possible as the first design iterations take place or first test and simulation results become available.

5 Conclusions

The SARISTU—Smart Intelligent Aircraft Structures—project did not invent radical new tools and methods for project management. Instead, it relied on a disciplined and straightforward implementation of a large range of tried and tested management tools tailored to the conduct of this particular undertaking. While the size of the project allowed a large range of these methods to be applied, the technical and contractual complexity as well as the large size of the consortium necessitated this large range to be applied. SARISTU avoided the temptation to use shortcuts from the best practice of project management and instead took up emerging challenges in order to pre-empt future complications which unavoidably result from a strong deviation from this best practice. A few key points, which to SARISTU's project management office are evident, do however merit particular recapitulation as they provide multiple failure opportunities if not followed. Most importantly, a coordinator should have a very strong feeling of responsibility for both the resources, in particular financial, and people entrusted to her or his care. With this fundamental mindset, a significant foundation is already laid. The PMO must then consider project planning an integral part not only of the preparatory phase but equally, if not more importantly, of the projects conduct phase in order to avoid the trap of only partially meeting Quality, Time, Cost targets. Similarly, the basic ways of working in the project benefit from a strong focus on the people working within the project. If this is reflected by providing clarity on decision-making levels, fostered by imparting feelings of self-determination and responsibility within the projects participants and remove blocking points and minimizing disruptions, then the project members will be able to turn a detailed project plan into project success.

Acknowledgments The research leading to these results has received funding from the European Union's Seventh Framework Programme for research, technological development and demonstration under Grant Agreement No 284562.

Most of all, the PMO would like to thank the 431 project members who have turned the vague vision that existed in the earliest parts of the initiation phase into the robust hardware, test and simulation results which are at the core of SARISTU. Particular thanks are directed to Kristina Ditzel and her family in her memory.

Furthermore, the PMO would like to thank its sponsors, its internal customers and its supervisors for their support and continued trust, even when discussions became heated.

Our particular thanks are directed to the PMO's principal customer: the European Commission as represented by our Project Officer Michael Kyriakopoulos, Legal Officers Ulrich Schmid and

Mindaugas Laurinavicius and Financial Officer Guido Sacchetto. Without your extremely rapid and competent support we would find it much more difficult, if not impossible, to meet and exceed expectations.

References

Books

1. Airbus SAS (2011) Project management at Airbus
2. Project Management Institute (2013) A guide to the project management body of knowledge, 5th edn. ISBN 1935589814
3. Schulz-Wimmer H (2007) Projekte managen. Haufe Verlag. ISBN 3448047864

Other: Call Documentation & Guidelines for Reporting

4. Official Journal of the European Union (2006) L 391/1, Regulation (EC) No 1906/2006 of the European Parliament and of the Council of 18 December 2006
5. European Commission (July 2010) Work Programme 2011, cooperation, theme 7, transport (including aeronautics)
6. European Commission (August 2008) Rules for submission of proposals, and the related evaluation, selection and award procedures, Version 3, 21
7. European Commission (2009) Guide for applicants, transport (including aeronautics), collaborative project, FP7-AAT-2010-RTD-1, Version 4
8. European Commission (July 2010) Guide for applicants, common part, coordination and support actions (coordinating)
9. European Commission (July 2010) Guide for applicants, common part, coordination and support actions (Coordinating), Annexes, specific to call: FP7-AAT-2011-RTD-1
10. European Commission, Guidance notes on project reporting, Version 10 Nov 2008 and Version 2012
11. European Commission, Guide to financial issues relating to FP7 indirect actions, Version 28, Feb 2011 and Version 18 Mar 2013

Other: Project documents and Training documentation

12. Koetter A, Ditzel K, Wadleigh R, Genzel K, Woelcken P (2014) SARISTU management handbook, Version 10
13. Woelcken P (ed) (2013) Project period report—period 3
14. Ansoor Creative Communication and Management (4 February 2009) Manage structure and system integration teams course documentation and exercises
15. Airbus Group Learning Services (2014) Leadership at Airbus course documentation and exercises
16. Hobday J, Parfitt R, Patterson C, Saunders G, Airbus Group Learning Services (2010) Lean engineering course documentation and exercises

Part I

Technology Stream: Morphing. Enhanced Adaptive Droop Nose for a Morphing Wing

Introduction and Overview

In the application scenario one (AS01), the enhanced adaptive droop nose (EADN) is developed. The EADN is a morphing leading edge which can adapt its shape to the aircraft configuration needed, namely for low-speed conditions as there are takeoff and landing. In SARISTU, the concept of this smart leading edge device is developed to meet the objective of functional integration into the leading edge as there are functionalities such as de-/anti-icing, bird strike protection, erosion protection, and lightning strike protection. Furthermore, the structure-kinematics system is enhanced by a low-complexity, lightweight kinematic mechanism as well as at damage tolerance and fatigue performance. The integration of the various functionalities into the leading edge leads to a multi-functional composite structure with integrated functional layers. The performance and the effect of these layers on the leading edge design and an assessment on the overall aircraft level are given in the following paper ‘Assessment of the SARISTU Enhanced Adaptive Droop Nose.’ Since the bird strike protection functionality could not be realized by integrating an additional layer but to develop a stand-alone bird strike protection structure, this development is described in the second paper ‘Development and validation of a Bird Strike Protection System for an Enhanced Adaptive Droop Nose.’ An overview on the integration of the functionalities in the manufacturing and tooling design is given in the third paper ‘Enhanced Adaptive Droop Nose—From Computer Model to Multi-functional Integrated Part.’ Finally, an overview of the various tests of the EADN performed in SARISTU is given in the paper ‘Testing Overview of the EADN Samples.’

Morphing Wing Integrated Safety Approach and Results

Maurizio Verrastro and Sylvain Metge

Abstract SARISTU morphing wing is mainly based on three devices: enhanced adaptive droop nose (EADN), adaptive trailing edge device (ATED) and winglet active trailing edge (WATE). All these devices are used together to improve the overall wing efficiency and to reduce the aerodynamic noise. The safety activities described in this paper were performed to verify whether this concept can comply with the standard civil flight safety regulations and airworthiness requirements. The safety analysis was performed in two steps: a functional hazard assessment (FHA) and a system safety assessment (SSA). Both analyses were performed at wing integration level (IS12) and at single morphing wing devices level. A complete mapping between these two levels of analysis was structured from the beginning of the process, starting from the aircraft functional definition, to integrate and harmonize both FHA and fault trees results. FHA was used to assess the severity of the identified Failure Conditions and then allocate safety requirements. Fault tree modelling technique was used to verify the compliance of the system architectures to the quantitative safety requirements resulting from the FHAs. The paper sets out the hypotheses and common data used by the fault trees. A complete but simple example illustrates the safety approach all through the different steps of the safety methodology. Other safety activities commonly performed in the aeronautical field such as the particular risk analysis (PRA), common mode analysis (CMA) and zonal safety analysis (ZSA) were identified in the frame of SARISTU project. This paper concludes with a summary highlighting the main results of these safety activities with some lessons learned from the safety approach adapted to SARISTU context.

M. Verrastro (✉)

Alenia Aermacchi S.p.A. Military Aircraft Safety, 10072 Caselle, Italy
e-mail: maurizio.verrastro@alenia.it

S. Metge

Airbus Operations S.A.S., Toulouse, France
e-mail: sylvain.metge@airbus.com

Nomenclature

A/C	Aircraft
AOA	Angle of attack
ATE(D)	Adaptive trailing edge (device)
AS0x	Application Scenario x
CAT	CATASTROPHIC
CCA	Common cause analyses
CMA	Common mode analyses
DAL	Design assurance level
EADN	Enhanced adaptive droop nose
EASA	European aviation safety agency
EMC	Electro magnetic compatibility
EMI	Electro magnetic interference
FC	Failure Condition
FCS	Flight control system
FDAL	Functional development assurance level
FH	Flight hour(s)
FHA	Functional hazard analysis/assessment
FOD	Foreign object damage
FT	Fault tree
FTA	Fault tree analysis
HAZ	HAZARDOUS
HIRF	High-intensity radiated fields
HW	Hardware
IS12	Integration Scenario 12
LND	Landing
MAJ	MAJOR
MCS	Minimal cut set
MIN	MINOR
MoC	Means of compliance
MT	Maintenance time
NSE	No safety effects
PFHA	Preliminary FHA
PRA	Particular risk analysis
PSSA	Preliminary system safety assessment
REQ	Requirement
SSA	System safety assessment
SW	Software
T/O	Take-off
WATE	Winglet active trailing edge
ZSA	Zonal safety analysis

1 Introduction

The goal of SARISTU project is to design a smart wing with morphing devices aimed to improve the overall aircraft (A/C) aerodynamic efficiency and to reduce the aerodynamic noise. A wing model will be realized to perform wind tunnel testing activity. This activity is required to validate theoretical calculation performed to evaluate the morphing wing advantages. A safety analysis following standard civil flight safety regulations is not required to validate the wind tunnel model and results. Nevertheless, the safety analysis was performed to verify whether SARISTU concept can comply with the applicable airworthiness code requirements, in particular with EASA CS-25 Ref. [1].

SARISTU morphing wing concept is mainly based on three devices working together. Every device is associated with an “Application Scenario” (AS0x) and the integration is provided as separate work package:

AS01—Enhanced Adaptive Droop Nose (EADN): It is a movable leading edge with a morphing skin. The aim of this device is to reduce drag and noise by optimizing the laminar flow in a range of angle of attack (AOAs). In the wing tunnel test model, the EADN will be used only as “high-lift device”. However in the following functional hazard analysis (FHA), the drag optimization function during climb/descent/cruise phases has also been taken into account (Fig. 1).

AS02—Adaptive Trailing Edge Device (ATED): It is a morphing skin trailing edge device, with the aim to optimize the wing shape in order to reduce drag. This device has the capability to be also used for the wing load alleviation/control function (not implemented in SARISTU). This device will be used during cruise and landing flight phases, only (Fig. 2).

AS03—Winglet Active Trailing Edge (WATE): It is a winglet movable trailing edge with a morphing skin part. Its aim is to optimize/reduce wing drag and structural loads (fatigue and vibrations loads control, turbulence, gusts and manoeuvre load alleviation, and wing load protection) (Fig. 3).

IS12—Wing Integration Verification and Validation: this work package consists in integrating the complete morphing wing. The three previously mentioned devices will be integrated in a dedicated wing box, with a proper interface necessary to perform the wing tunnel measurements.

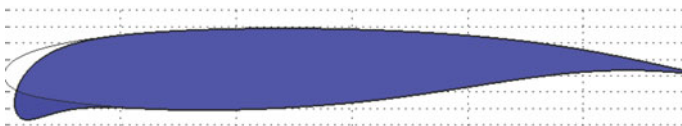


Fig. 1 Wing profile with lowered EADN

Fig. 2 ATED 3D view

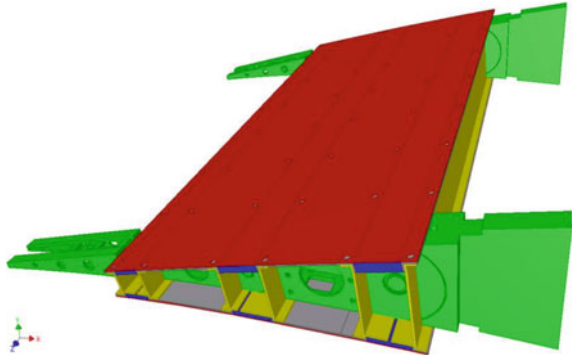
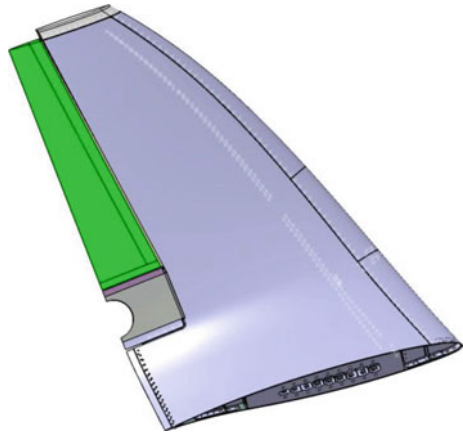


Fig. 3 WATE 3D view



2 Safety Analysis Approach Overview

This section shows the approach used to achieve a SARISTU system safety assessment. Main drivers are the already-mentioned CS-25 regulations as well as the Aerospace Recommended Practices SAE ARP 4754a Ref. [3] and SAE ARP 4761 Ref. [4]. In fact, the SARISTU morphing wing concept can be analysed following the currently available rules and practices. Figure 4 shows a general safety assessment process overview as required by the CS-25 safety regulation. The dotted rectangle highlights the boundary of the process used for SARISTU project.

Activities included in the SARISTU safety assessment boundaries are “*System FHAs*”, “*Analyses*” and “*System Safety Assessment*”. The system level is identified in the complete morphing wing, and therefore it is under IS12 work package responsibility. A preliminary functional hazard assessment (PFHA) at SARISTU level is then the starting point for this process. “*Analyses*” boxes are the functional hazard assessment (FHA) and the fault tree analyses (FTAs) performed by the three Application Scenarios (AS01, AS02 and AS03) leaders. The system safety

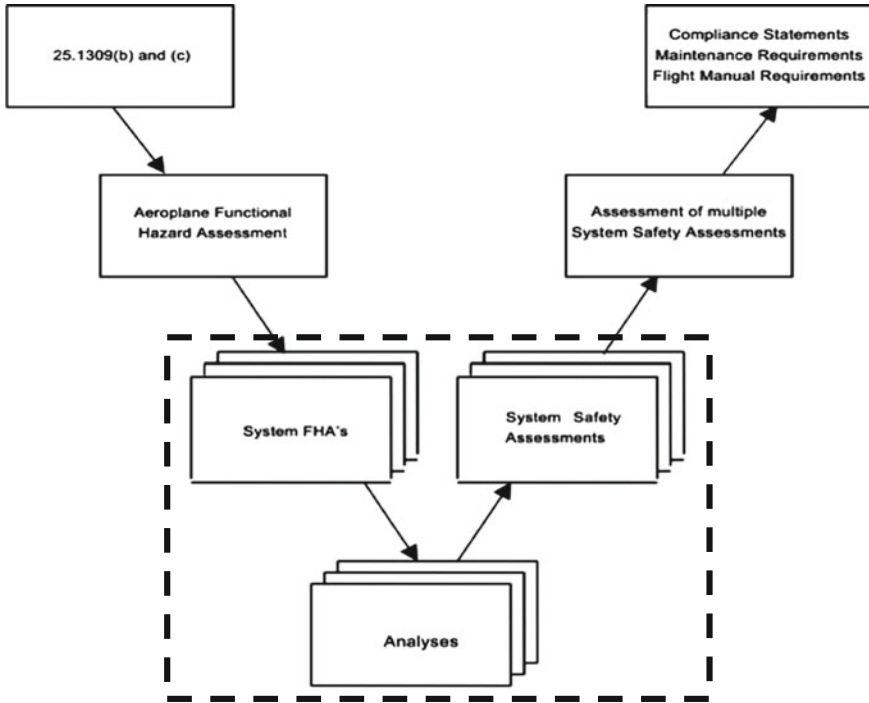


Fig. 4 CS-25 safety assessment process overview

assessment (SSA) is mainly composed of a consolidated FHA and the fault tree analysis at morphing wing level (IS12).

3 Functional Approach Definition

Generic aircraft safety analyses are based on a functional approach. Aircraft and system-level functions are first identified, and then, their failure modes are analysed to identify the end effects (i.e. safety consequences on the aircraft and its occupants). A complete aircraft-level analysis is not the target of this project, but it is clear that SARISTU functional failure repercussions are expected at aircraft level. It is evident from Fig. 4 that System FHAs are connected to the complete airplane functional hazard assessment. In particular for SARISTU project, a reference aircraft has been defined as reported in the deliverable number A_DEU_121_1_R2 Ref. [6] and depicted in Fig. 5. The reference aircraft is a twin-fuselage-mounted engine medium-range type. In the previously mentioned SARISTU deliverable, a morphing wing functional description has been reported, but from the aircraft-level point of view, only major geometrical and system design information have been provided (the goal of this document is an aeromechanical and performance

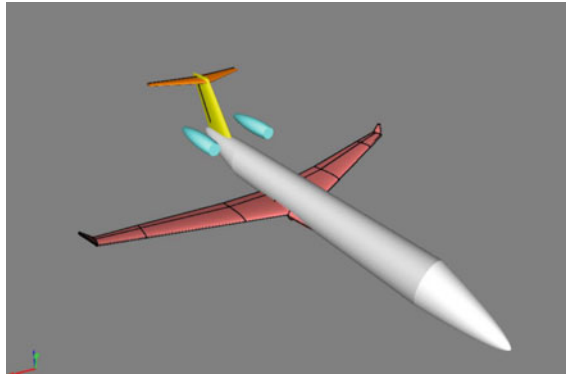


Fig. 5 Reference aircraft overview

assessment). A very generic A/C functional overview is listed in a paper titled “Framework for the Application of System Engineering in the Commercial Aircraft Domain” Ref. [9]. This document collects the results of a working group with people affiliated with several organizations as AIAA, SAE, IEEE, and specialists of many manufacturer’s companies in the aerospace (e.g. Boeing, Rockwell, Honeywell, Airbus-Aeromatra). For SARISTU project, a subset of aircraft-level functions was selected to evaluate high-level SARISTU functional failure effects. A very high-level generic aircraft functional overview is depicted in Fig. 6. The high-level functions potentially impacted by SARISTU are circled. The selected functions are mainly related to the A/C aerodynamic configuration control and forces generation. The structural behaviour has also been considered for the load alleviation/control functions.

SARISTU functions extracted from project deliverable Ref. [6] are the following: drag minimization, lift adaptation, turbulence/gust load alleviation, manoeuvres load alleviation, vibration and fatigue control, and A/C load protection. Following the morphing wing-level functional definition, the detailed selected aircraft functions are reported in Table 1.

SARISTU and relevant aircraft-level functions need to be linked in order to make easier the assessment of the functional failure end effect. This connection is reported in Table 2. This information is also useful to make clear the link between

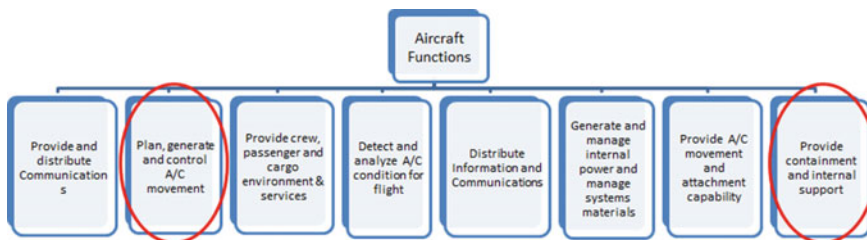


Fig. 6 High-level generic aircraft functional overview

Table 1 Aircraft-level functions selected for SARISTU

Aircraft functions	
2. Plan, generate and control A/C movement	
2.2 Generate and control aircraft movement	
2.2.5 Control A/C aerodynamics configuration	
2.2.5.1 Control lift and drag	
2.2.6 Protect aerodynamic control	
2.2.6.1 To provide protection against turbulence effects	
2.2.6.2 To provide protection against stall load	
2.2.7 Provide aerodynamic control forces	
2.2.8 Support supplemental flight control	
2.2.8.1 To provide overload protection and A/C load protection	
2.2.8.2 To provide protection against manoeuvres effects	
2.2.13 Generate lift	
2.2.14 Provide aerodynamic stability	
8. Provide containment and internal support	
8.1 Provide containment	
8.1.2 Provide structural integrity and load distribution	
8.1.2.1 To provide fatigue protection	

the SARISTU (and IS12)-level FHA and the Application Scenario detailed analyses. Application Scenarios can be easily linked with SARISTU functions. In this way, a complete mapping between Application Scenarios and SARISTU (IS12) aircraft-level functions is traced. This latest connection is reported in Table 3. Drag minimization and lift adaptation cannot be considered as fully independent functions. In fact a modification of the wing profile/shape leads to a wing pressure

Table 2 Link between aircraft and morphing wing functions

Morphing system functions	Aircraft-level functions	
Drag minimization function	2. Plan, generate and control A/C movement	2.2.5.1 Control lift and drag 2.2.7 Provide aerodynamic control forces
Lift adaptation function	2. Plan, generate and control A/C movement	2.2.5.1 Control lift and drag 2.2.7 Provide aerodynamic control forces 2.2.13 Generate lift 2.2.14 Provide aerodynamic stability
Turbulence/gust load alleviation	2. Plan, generate and control A/C movement	2.2.6.1 To provide protection against turbulence effects
Manoeuvres load alleviation	2. Plan, generate and control A/C movement	2.2.8.2 To provide protection against manoeuvres effects
Vibration and fatigue control	8. Provide containment and internal support	8.1.2.1 To provide fatigue protection
A/C load protection	2. Plan, generate and control A/C movement	2.2.6.2 To provide protection against stall load 2.2.8.1 To provide overload protection and A/C load protection

Table 3 Link between morphing wing functions and SARISTU subsystems (Application Scenarios)

Morphing system functions	Involved subsystem	Way to operate	SARISTU FHA Function
Drag minimization function	EADN	Continuous/quasi-static operation	Wing shape optimization control function “Drag minimization” and “lift adaptation” cannot be modified independently (i.e. a modification of the aerodynamic profile in order to increase lift also cause a drag coefficient change). The EADN will be used also as “high-lift device”, during take-off and landing phases
	ATED	Continuous/quasi-static operation	
	WATE	Continuous/quasi-static operation	
Lift adaptation function	EADN	Continuous/quasi-static operation	The EADN will be used also as “high-lift device”, during take-off and landing phases
	ATED	Continuous/quasi-static operation	
	WATE	Continuous/quasi-static operation	
Turbulence/gust load alleviation	WATE	Occasional/dynamic operation	Turbulence/gust load alleviation function
Manoeuvres load alleviation	WATE	Occasional/dynamic operation	Manoeuvres load alleviation function
Vibration and fatigue control	WATE	Continuous/fast-dynamic operation	Wing vibration and fatigue control function
A/C load protection	WATE	Occasional/dynamic operation	Wing loads protection function

distribution change, which simultaneously affects both lift and drag levels. Due to this consideration, at IS12 FHA level, these two functions will be merged in a single function called “wing shape optimization control”. The EADN works in conjunction with ATED and WATE to optimize the wing shape, but during take-off and landing phase, it acts as a “high-lift” device. In this case, the EADN contribution to the A/C flight safety is heavier with respect to the other devices. This is why it can be traced as “stand-alone” effect on lift adaptation function.

Load alleviation/protection/control functions, and vibrations/fatigue loads control will be implemented using the WATE device only, at least for this testing phase and for this SARISTU concept. The ATED has also the capability to perform this task thanks to its fast actuation speed, but in the frame of SARISTU, it will be used for the wing shape optimization only. As a general consideration, the WATE alone cannot perform all the possible wing load alleviation/protection and control functions. For example, to perform stall load protection, aerodynamic surfaces, which greatly modify the lift generation in a more direct way, are required (e.g. ATED, aileron, and spoilers). In the SARISTU project FHA, only the WATE device will be considered for wing loads alleviation/protection/control functions (including vibrations control).

4 Dual-Level Safety Assessment: IS12 and AS0x FHAs and FTAs

4.1 Functional Hazard Assessment General Overview

Functional hazard assessment is a safety analysis focused at system/aircraft functional level. As reported on the already-mentioned SAE ARP 4754a, the FHA “examines aircraft and system functions to identify potential functional failures and classifies the hazards associated with specific Failure Conditions. The FHA is developed early in the development process and is updated as new functions or Failure Conditions are identified. Thus, the FHA is a living document throughout the design development cycle”.

Functional failures are identified with the associated severity. Then, qualitative requirements are set in this analysis (redundancy, functional design assurance level (FDAL), specific monitoring, etc.). In the IS12 FHA, SARISTU-level functional failures are considered. The following failure scenarios are analysed for every morphing system function:

- Total loss of function,
- Partial loss of function,
- Erroneous provision of function, and
- Inadvertent provision of function

Failure Condition’s classification is provided in accordance with CS-25 regulations based on the severity of their effect:

NO SAFETY EFFECT (NSE) “Failure Conditions that would have no effect on safety; for example, Failure Conditions that would not affect the operational capability of the aeroplane or increase crew workload”.

MINOR (MIN) “Failure Conditions which would not significantly reduce aeroplane safety, and which involve crew actions that are well within their capabilities. Minor Failure Conditions may include, for example, a slight reduction in safety margins or functional capabilities, a slight increase in crew workload, such as routine flight plan changes, or some physical discomfort to passengers or cabin crew”.

MAJOR (MAJ) “Failure Conditions which would reduce the capability of the aeroplane or the ability of the crew to cope with adverse operating conditions to the extent that there would be, for example, a significant reduction in safety margins or functional capabilities, a significant increase in crew workload or in conditions impairing crew efficiency, or discomfort to the flight crew, or physical distress to passengers or cabin crew, possibly including injuries”.

HAZARDOUS (HAZ) “Failure Conditions, which would reduce the capability of the aeroplane or the ability of the crew to cope with adverse operating, conditions to the extent that there would be: (i) A large reduction in safety margins or functional capabilities; (ii) Physical distress or excessive workload such that the

Effect on Aeroplane	No effect on operational capabilities or safety	Slight reduction in functional capabilities or safety margins	Significant reduction in functional capabilities or safety margins	Large reduction in functional capabilities or safety margins	Normally with hull loss
Effect on Occupants excluding Flight Crew	Inconvenience	Physical discomfort	Physical distress, possibly including injuries	Serious or fatal injury to a small number of passengers or cabin crew	Multiple fatalities
Effect on Flight Crew	No effect on flight crew	Slight increase in workload	Physical discomfort or a significant increase in workload	Physical distress or excessive workload impairs ability to perform tasks	Fatalities or incapacitation
Allowable Qualitative Probability	No Probability Requirement	<---Probable--->	<---Remote--->	Extremely <-----> Remote	Extremely Improbable
Allowable Quantitative Probability: Average Probability per Flight Hour on the Order of:	No Probability Requirement	<-----> <10 ⁻³ Note 1	<-----> <10 ⁻⁵	<-----> <10 ⁻⁷	<10 ⁻⁹
Classification of Failure Conditions	No Safety Effect	<---Minor--->	<---Major--->	<---Hazardous--->	Catastrophic
<p>Note 1: A numerical probability range is provided here as a reference. The applicant is not required to perform a quantitative analysis, nor substantiate by such an analysis, that this numerical criteria has been met for Minor Failure Conditions. Current transport category aeroplane products are regarded as meeting this standard simply by using current commonly-accepted industry practice.</p>					

Fig. 7 Required probability figures versus safety classification

flight crew cannot be relied upon to perform their tasks accurately or completely; or (iii) Serious or fatal injury to a relatively small number of the occupants other than the flight crew”.

CATASTROPHIC (CAT) *“Failure Conditions, which would result in multiple fatalities, usually with the loss of the aeroplane. (Note: A “Catastrophic” Failure Condition was defined in previous versions of the rule and the advisory material as a Failure Condition which would prevent continued safe flight and landing.)”.*

Figure 7 shows these requirements and the expected effects on flight crew, passengers, and on the aeroplane for every identified severity.

4.2 SARISTU Functional Hazard Assessment Peculiarity

SARISTU-level FHA table provides the following information: (1) a failure mode identification number, (2) failure mode brief description, (3) flight phase during which the failure mode can occur, (4) severity classification according to CS-25

MoC, (5) average failure probability per flight hour according to safety objectives expressed in the CS-25 MoC, (6) Failure Condition identification with reference to involved subsystems and relevant failure modes, (7) detailed description of the A/C-level effects, (8) detection means (if detection is possible), (9) flight crew reaction after failure detection (if detection is possible) and (10) possible requirements coming from safety considerations (e.g. redundancy requirements and inspections), (11) external events involved in the hazard (if applicable) and (12) justification for safety categorization following CS-25 regulations.

In SARISTU project, the Application Scenarios FHA's format was not imposed, but the technical information to be provided was agreed with IS12 leader. In the Scenarios Application FHAs, the following data are reported: (1) A failure mode identification, (2) failure mode title, (3) failure mode description, (4) aircraft-level effects, (5) Failure Condition identification/title, (6) safety classification, (7) justification for safety classification, (8) flight phase during which the failure mode can occur, (9) detection means, (10) flight crew action, (11) associated requirements and (12) link with the impacted IS12 functions (optional).

The morphing wing FHAs are performed following a standard approach. The peculiarity of SARISTU safety analysis is the work packages assignment. In fact, every Application Scenario is a single morphing wing device that shall be integrated in the complete wing. This picture is very close to a "real-life" application: an aircraft manufacturer (in SARISTU, it is represented by IS12 work package) will assemble devices from different suppliers (in this case represented by Application Scenarios AS01, AS02 and AS03). So every SARISTU Application Scenario is analysed as a "stand-alone" device, but the failure mode effects are evaluated at A/C level, merged and properly combined at IS12 (wing integration) level.

Since the above-mentioned safety analyses are performed at different levels, two different approaches have been used to achieve the FHAs:

- **IS12 FHA:** it is a high-level functional safety assessment. A/C-level functions impacted by wing morphing system (see Sect. 3) with the relevant functional failures is the starting point of this analysis.
- **AS0x FHAs:** these analyses are low-level functional hazard assessments. The starting points are the device function failure modes, with the target at IS12-level Failure Conditions (FCs).

The most demanding aspect of this "dual-level approach" is to guarantee consistency between the previously mentioned analyses. The Failure Conditions identified at AS0x level should always be linked with a higher level entry found in the IS12 scenario analysis. For example, the criticality of a FC identified at AS0x level shall be lower or equal to the safety classification of the target FC at IS12 level. A complete mapping between the two levels is required to guarantee that every possible failure is taken into account. The main driver of this mapping activity is provided by the functional approach definition described in the previous section.

Only after the FHA's mapping phase conclusion, the SSAs can be performed starting from devices level. The IS12 FTA is obtained by the proper combination of

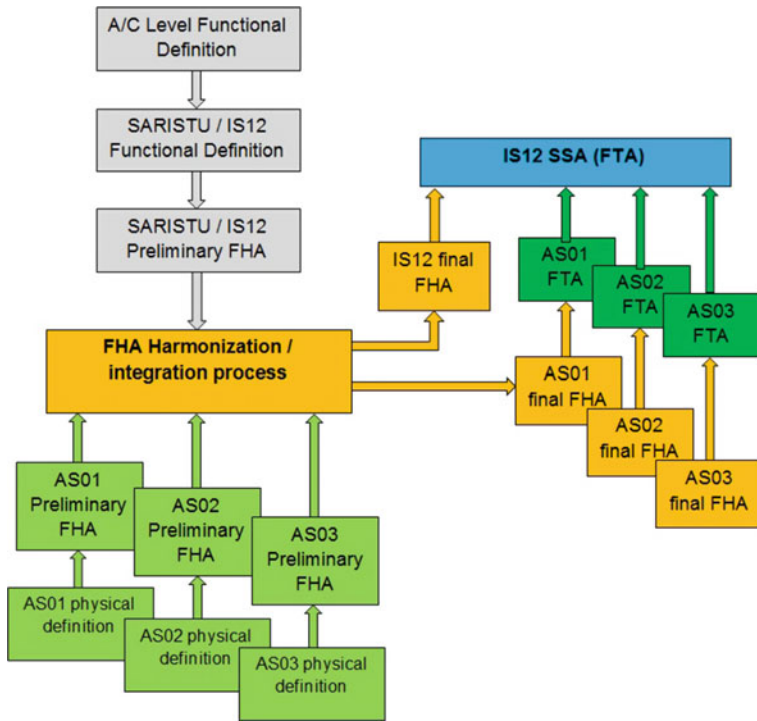


Fig. 8 “Dual-level” approach for SARISTU safety activities

the AS0x fault trees (FTs). This combination is based on the previously mentioned mapping. A flow diagram of the SARISTU safety process is shown in Fig. 8.

Failure scenario classification is always associated with the aircraft-level consequences in terms of pilot workload, safety margin, occupant comfort and health status. In addition, failure scenarios and conditions are associated with the proper flight phases. In the SARISTU safety analyses, only take-off, cruise (including climb and initial descent) and landing were considered. Ground flight phases are out of SARISTU scope.

There are some differences between Scenarios Application and wing integration-level FHAs. For each Scenario Application, a “total loss of function” can be easily identified (i.e. jamming, loss of actuator). At IS12 level, the same Failure Condition is a combination of AS0x-identified failures.

The wing shape optimization (mainly associated to drag minimization) is obtained by the simultaneous actuation of all SARISU devices. The total loss of this IS12 function (i.e. Failure Condition FC 2.2.5.1-01) was classified as MAJOR. The linked system Failure Conditions are as follows: AS01 FC5 “Reduced performances”—MAJ and AS03—FC2 “Jam of both tabs/*electromechanic actuators*”—MAJ. Both FCs are classified with the same severity and their safety classification is in accordance with the concerned IS12 FC. So the “Total loss of wing shape

optimization” is considered as the WATE (AS03) *OR* EADN (AS01) loss of function *OR* the loss of ATED (AS02) in conjunction with WATE or EADN (the ATED FC is AS02—FC01 “Loss of ATED control”—MIN). FC01 from ATED is combined with the other previously mentioned Application Scenario FCs because it has been estimated having a very minor impact on the drag and lift generation as an isolated failure.

Partial loss scenario can be split in two main cases at both safety analysis levels: symmetric partial loss (e.g. loss of performance) or asymmetric partial loss (in this case, “partial” is referring to the loss of wing shape optimization on one wing only). At IS12 level, asymmetric Failure Conditions are combined with proper external events or other system failures (single engine loss, strong crosswind at take-off or landing) to consider worst-case scenarios. Similar considerations are applicable in case of erroneous or inadvertent provision of SARISTU function.

The EADN is designed to be mainly used as “high-lift device” during take-off and landing. For this reason, at IS12 level, some Failure Conditions are also caused by this device only, associated with lift adaptation function. A clear example is the IS12 FC 2.2.13-01, which takes only into account the contribution of AS01 FC 2.1 “Inability to control aircraft during take-off (T/O) and the Landing phase (LND)”.

For structural load-related functions, the CS-25 regulations impose to consider by design the additional stresses caused by the failure of a load control device. In particular, CS-25.301 paragraph states “*For aeroplanes equipped with systems that affect structural performance, either directly or as a result of a failure or malfunction, the influence of these systems and their Failure Conditions must be taken into account*”. The consequence is that the structure will be able to withstand the additional load caused by a failed device without safety relevant damages by design. A physical discomfort for the passengers can be experienced at worst; this is why the safety classification of these events is always MINOR.

The main criticalities emerged from the Application Scenarios FHAs are mainly due to EADN and WATE devices. EADN will be used as a “high-lift” device during take-off and landing. During these flight phases, an erroneous position of morphing droop nose (due to the “loss” or “erroneous” EADN function provision) could cause an aircraft stall (symmetric or asymmetric) which can be unrecoverable if the flight level is too low (see AS01—FC 2.1 “Inability to control aircraft during T/O/LND” classified as CAT). In fact, in such a case, the pilots have a very short lapse of time to start a recovery action. The consequence is that a high functional integrity level is necessary to make this device airworthy. A FDAL A is then required for EADN (or a dual independent DAL B design is also accepted). No single failure shall lead to this Failure Condition.

For the WATE device, a CATASTROPHIC Failure Condition is identified in case of winglet trailing edge-forced oscillations or free float causing a possible flutter, identified as AS03—FC1 “destruction of whole wing”. The higher level consequence can be the aircraft loss. In addition, for this scenario, no single failure shall cause such a Failure Condition. A fail safe design is a requirement for this device. For example, to prevent surface free float, a dual load path is necessary for

the actuator connection, and an independent control/monitor architecture shall be implemented (dual-duplex actuator control unit).

The IS12 Analysis highlighted that SARISTU Failure Conditions can mainly cause passenger discomfort and an increase of pilot workload (conservatively classified as MAJOR assuming a significant increase of workload at worst). The main criticality emerged from this safety analysis is related to possible asymmetric configuration due to SARISTU failures in conjunction with external additional asymmetry effects (flight control system failures are excluded due to the low probability level expected considering the combination of SARISTU failures with flight control system failures). Two additional asymmetry circumstances have been considered: a single engine loss and strong crosswind at take-off or landing.

Asymmetric SARISTU configuration combined with a single engine loss (IS12 FC 2.2.7-02) has been classified HAZARDOUS (HAZ) since the reference A/C is designed with fuselage-mounted engines. This configuration causes a limited thrust asymmetry since both engines are very close to the A/C longitudinal centreline.

Asymmetric SARISTU configuration combined with strong crosswind at T/O or landing (IS12 FC 2.2.7-03, see Sect. 5 for details) has been classified CATASTROPHIC (CAT). Since it is not possible to evaluate the asymmetry level caused by this FC, a conservative approach has been used for the previously mentioned classification.

4.3 SARISTU Functional Hazard Assessment Harmonization and FTA Basis

As already stated, the peculiarity of the SARISTU approach is that A/C-level functions and safety impact have been included in the IS12 Integration-level analysis, performed in parallel with AS0x devices level analyses. These latest analyses are linked with the Integration Scenario according to an iterative harmonization process, in order to achieve a consolidated FHA at both levels. Taking into account the multi-level functional link explained in Sect. 3, the main problem was how to highlight it in the FHA tables. A traceability table was built starting from IS12 FHA (see Tables 4 and 5).

Each row is a failure scenario identified at IS12 level, and three columns are dedicated to each device to identify the associated lower-level Failure Condition, with its reference and severity. In this way, it is possible to easily check the coherence of the safety classification and the completeness of the analysis. In addition, this table provides a basic structure for the IS12-level fault trees (see Sect. 4.3 for details). Safety requirements and means of compliance have been added into this table, as well.

Table 5 Traceability table between IS12 and ASoX FHAs—part 2/2

ID Failure Mode	Title	A/C Flight phases (s)	Severity	Safety Requirement		FT req (Y/N/D)	Failure Cause / Involved Subsys		TRACEABILITY			REQUIREMENTS / COMMENTS	REQUIREMENTS IMPLEMENTATION / DEMONSTRATION
				Rationale	Obligator		WATE	ATE	EADN	External event or condition			
2.2.13.01 ULS:ASX:002	Loss of A/C control due to symmetrical or asymmetrical engine thrust or engine EADN emergence as high lift device	Take-off and Landing phases	CAT	Multiple crew or passenger deaths. Possible A/C loss.	E-3/FPH	Y	FC-22.01 (Loss of SBARSTU wing phase control) high lift device function) -loss DR emergence EADN control as high lift device		FC-21 (low 4, 6, 7, 3, 20%) CAT	Take-off and Landing phases	ASX. A pre-flight functional check can reduce the risk. FDM. As assigned to EADN section, no flight safety check start the test of EADN	FT, design evidences	
2.2.13.02 ULS:ASX:003	Indefinite position of control as high lift device	Cruise	NSE	No effect on flight safety	N/A	N	- EADN high lift function activated during cruise (pushback activation) Totally null loss, enhanced or inadvertent provision of SBARSTU wing phase control. - VATE present when take-off - EADN present (after low excursion only).		FC (low 8) NSE				
2.2.14.01 ULS:ASX:004	Loss (complete or partial, enhanced or reduced) of control as high lift device	All High phases	NSE	No effect on flight safety since A/C control is maintained during margin.	N/A	N	- EADN present (after low excursion only) Totally null loss, enhanced or inadvertent provision of SBARSTU wing phase control. - VATE present when take-off - EADN present (after low excursion only).	MA	FC08 NSE		FC based on the assumption that the A/C stability is not compromised by SBARSTU (UL, drag, A/C controllability)		
2.2.14.02 ULS:ASX:005	Loss of Turbine/er/Gust load alleviation function	All High phases	NSE	No effect on flight safety	N/A	N	Loss of SBARSTU Turbine/er/Gust load alleviation. -Loss of VATE (dynamic/loss of gust load alleviation function	MA			This failure can be hidden without a BFT or a scheduled maintenance task.		
2.2.14.03 ULS:ASX:006	Loss, emergence or reduced capability in case of performance decrease	All High phases	MM	Slight reduction in physical performance or passenger or cabin crew.	E-3/FPH	N	Loss of SBARSTU Turbine/er/Gust load alleviation combined with loss of VATE (dynamic/loss of gust load alleviation function) and Turbine/er/gusts	FC3/FC3 MM		Turbulences / gusts	This failure can be hidden without a BFT or a scheduled maintenance task.		
2.2.14.04 ULS:ASX:007	Loss, emergence or reduced capability in case of performance decrease	All High phases	MM	Slight reduction in physical performance or passenger or cabin crew.	E-3/FPH	N	Loss of SBARSTU manoeuvre load alleviation. -loss of VATE (dynamic/loss of functional function) in case of A/C manoeuvres	FC3/FC3 MM		High load manoeuvre			
2.2.14.05 ULS:ASX:008	Total loss of wing function	All High phases	NSE	No effect on flight safety	N/A	N	Loss of SBARSTU wing overloads stall load protection. -loss of VATE (dynamic/loss of stall load protection	MA			A delay and BFT or a scheduled maintenance can be assigned to detect the failure		
2.2.14.06 ULS:ASX:009	Loss (emergence or reduction) of stall load protection	All High phases	MM	Slight reduction in physical performance or passenger or cabin crew.	E-3/FPH	N	Loss of SBARSTU (wing overloads stall load protection) in combination with overloads on cabin crew.	FC3/FC3 MM		Wing overloads stall load	Delayed BFT or scheduled maintenance task to reduce the risk		
2.2.14.07 ULS:ASX:010	Loss, emergence or reduced capability in case of performance decrease	All High phases	MM	Slight reduction in physical performance or passenger or cabin crew.	E-3/FPH	N	Loss of SBARSTU (wing overloads stall load protection) in combination with overloads on cabin crew.	FC3/FC3 MM			Possible vibration monitoring installation to detect the failure		
2.2.14.08 ULS:ASX:011	Loss of structural integrity due to SBARSTU manoeuvre	All High phases	CAT	Multiple crew or passenger deaths. Possible A/C loss.	E-3/FPH	Y	Loss of SBARSTU (wing overloads stall load protection) in combination with overloads on cabin crew. FC 14.01 (High lift device) references for the functional decomposition, total loss of system damage) in forced conditions - VATE device	FC1			ASX. A flight failure due to high lift device manoeuvre functions, evaluating on position condition (if a independent control is required for the take-off approach on VATE design is required).	FT, design evidences	

4.4 System Safety Assessment—Fault Tree Analysis

This section reminds the basic principle of the fault tree technique used by SARISTU partners in their preliminary system safety assessment activity (PSSA). Fault tree analysis (FTA) was used to check that the qualitative and quantitative requirements associated to each Failure Condition and expressed in the FHAs have been met. FCs classified as NSE (NO SAFETY EFFECT) and MIN (MINOR) do no need to be modelled by a fault tree (FT), according to the CS25 book 2 (Means Of Compliance—Ref. [2]).

A detailed description of the FTA technique can be found in the appendix D of the “*Guidelines and methods for conducting the safety assessment process on civil airborne system and equipment*”—ARP 4761 (see Ref. [4]). A fault tree analysis (FTA) is a deductive failure analysis, which focuses on one particular undesired event (Failure Condition). A FTA is a top-down safety analysis technique that is applied as part of the PSSA to determine what single failures or combinations of failures at the lower levels (basic events) may cause or contribute to each Failure Condition. A fault tree analysis uses Boolean logic gates to show the relationship of failure effects to failure modes. A basic event is defined as an event which for one reason or another has not been further developed (the event does not need to be broken down to a finer level of detail in order to show that the system under analysis complies with applicable safety requirements). A basic event may be internal (system failure) or external (e.g. icing condition, fire) to the system under analysis and can be attributed to hardware failures/errors or software errors. Probability of individual failures is only assigned to the hardware (HW). The occurrence of software (SW) errors are probabilistic but not in the same sense as hardware failures. Unlike hardware failures, these probabilities cannot be qualified. No SW failures were thus considered in the FT built by the SARISTU scenario leaders.

The FT calculation produces the minimal cut sets (MCS), i.e. the shortest *logic And* combination of independent basic failures that lead to the Failure Condition. The *order* of the MCS is the number of elements found in the MCS. Failure Conditions that have been classified as CAT shall comply with the fail safe criteria. This means that no single failure shall lead to the occurrence of a CAT Failure Condition. Therefore, MCS of order equal to 1 are not acceptable for CAT Failure Conditions.

The hypotheses and common data used by the fault trees by the SARISTU partners are briefly described in this section.

One individual FT was built for each Failure Condition coming from the FHAs whose safety classification is equal or more than MAJOR. The FC is the top event of the fault tree as shown in the example depicted in Fig. 9. Its average probability of occurrence per flight hour (FH) is deduced from the quantification of all MCS generated by the calculation of the fault tree.

If a system FC is classified as MINOR at AS0x level, but contributes to a MAJOR or worst safety severity FC at IS12 level, then the FT was built at AS0x

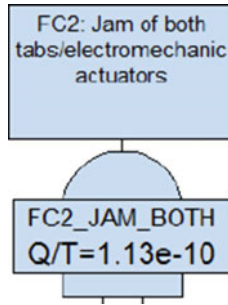


Fig. 9 Top event of a fault showing the title of the FC and its estimated probability

level in order to evaluate its contribution to the IS12 fault trees. An illustration of this specific case is given below. Figure 10 depicts a simplified FT at IS12 level. The top event is the IS12 Failure Condition FC 2.2.5.1-02 “Erroneous provision of wing shape optimization”, which was classified MAJ.

The FT from Fig. 10 shows that one contributor to the top event (IS12 Failure Condition ref. 2.2.5.1-02) is the Failure Conditions ref. FC08 from WATE system. FC08 has a MINOR effect, only. But since this system Failure Condition contributes to the occurrence of the IS12 Failure Condition at wing integration level, the AS03 scenario leader had to build a FT dedicated to FC08 despite the low level of safety. Notations used in the SARISTU fault trees are explained in Sect. 5.

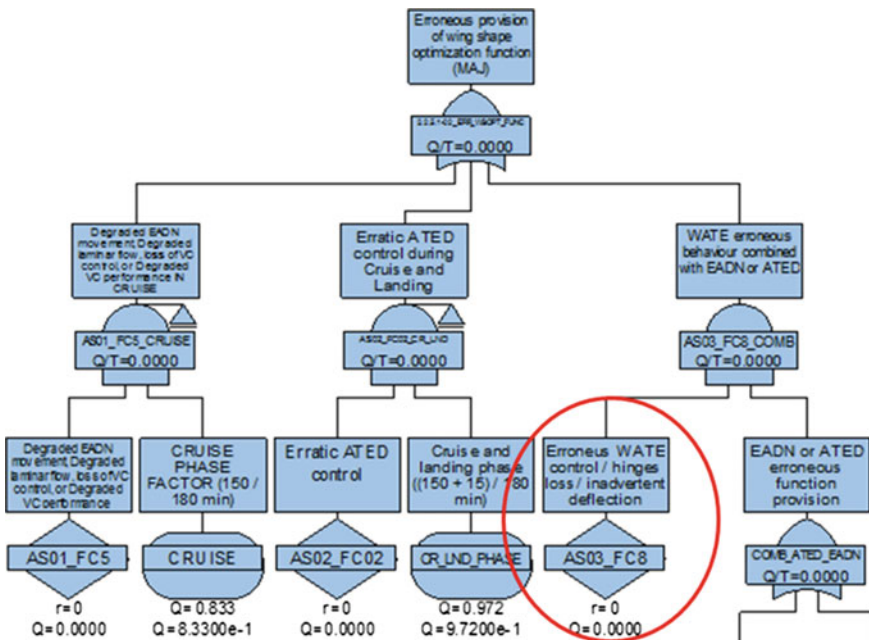


Fig. 10 System-level FC08 from WATE is classified as MIN but contributes to a MAJ IS12 FC

The traceability table reported in Sect. 4.3 provides the guidance for the FT’s integration at IS12 level. The FCs at Application Scenario level are based on component-level failure modes. This level of detail is typical for a “bottom-up” approach. On the contrary, as per FHA case, The FTs at IS12 level are obtained with a “top-down” approach. At IS12 level, every FCs at AS0x is traced as “undeveloped” event. In this way, the higher level FTs can be easily obtained by a proper combination of lower level FCs, with the introduction of the required “exposure factors” or external events where necessary. A concrete example of this dual-level approach for the FTA is described in Sect. 5.

4.4.1 Assumptions—Principles

The following assumptions and principles were followed and applied by SARISTU partners in charge of the FTA.

External events in the FTA: The fault trees must consider the combination of system failures with external events (e.g. wind or icing condition) whenever relevant. The following table shows an example of probabilities for external events that are commonly used in FTA. These figures were used by the SARISTU scenario leaders (see Fig. 11).

4.4.2 Active Versus Hidden Failures—Time Parameters

Both active and hidden failures have been considered in the SARISTU fault trees. Active failures are failures that can be detected by the flight crew when they occur during the current flight. For active failures, a mean flight time, T_0 , must be used in the calculation of the FC. SARISTU partners agreed to use a mean flight time equal to 3 h (mission time used for an A330 aircraft) that has been considered as an appropriate value for SARISTU. However, for some specific scenarios, a proper “exposure” time can be used in case a Failure Condition is expected to occur only in a specific flight phase.

Hidden failures (named also latent/passive/dormant failures) are failures not detected by the flight crew or detected but not reported. Such failures shall be checked at a certain moment of the aircraft life, according to airworthiness

Fig. 11 Environmental conditions events and associated probabilities

ENVIRONMENTAL CONDITIONS EVENTS & ASSOCIATED PROBABILITIES

ENVIRONMENTAL CONDITION EVENT	PROBABILITY
Strong Head wind (> 25 kts)	8×10^{-3} (per cycle)
Strong Tail wind (> 10 kts)	8×10^{-3} (per cycle)
Strong Cross wind (> 18 kts)	1×10^{-2} (per cycle)
Icing conditions	1

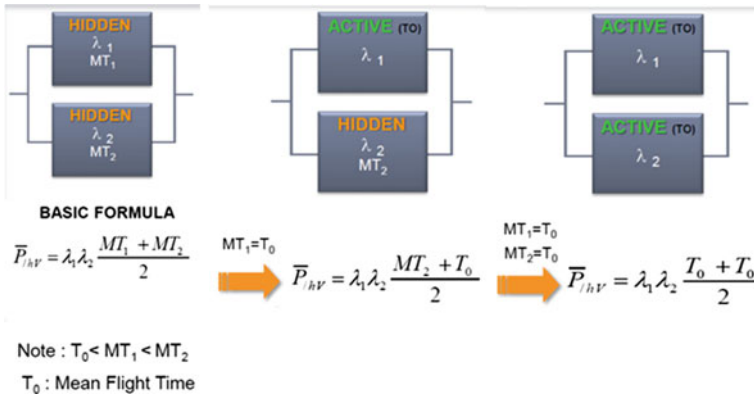


Fig. 12 Example of calculation of a dual system involving active and hidden failures

requirement during periodic inspections for maintenance purpose. Safety check intervals or maintenance time (MT) must be considered in the calculation of the FC involving hidden failures. The MT value is set based on the usual checks (periodic inspections) of the aircraft. The standard safety check intervals (A checks, B checks ...) have been considered in the quantification of the FTs.

In Scenario Application AS03 on WATE system, an interval of 8000 flight hours was considered between maintenance checks, i.e. disassembly and inspection of all hinges for detection and elimination of all dormant failures. For equipments that are never inspected, we use the aircraft lifetime. This value comes from “Fatigue Loads design criteria”. SARISTU partners agreed on a MT of “60,000 h” as a standard value but a calculation with a more conservative value of 87,600 h. This maintenance interval was used by the AS03 scenario leader for disassembly and inspection of WATE device that are only required every D-check.

The figure below shows a simple example of calculation for a simple redundant system highlighting the difference of formulae depending on the type of failures: two active failures, one active failure and hidden failure, and two hidden failures (Fig. 12).

4.4.3 On Safety Factor

The structural damage tolerance and loads are out of the PSSA scope. Such specific safety issues are addressed by structure specialists in separated documents. However what is requested is to identify the systems that may exert loads on structural parts when failures occur as explained in the CS25.303 section “Factor of safety”: “...Unless otherwise specified, a factor of safety of 1.5 must be applied to the prescribed limit load which are considered external loads on the structure” (Fig. 13).

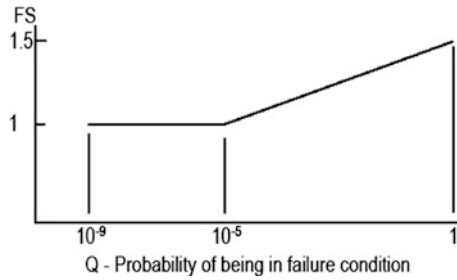


Fig. 13 Computation of the safety factor (FS)

AS03 scenario leader used this principle to quantify the structural damage of the WATE system. The Failure Condition FC5 “Degraded WATE performance” was classified MIN considering the safety repercussions on the occupants of the aircraft. However, the aircraft structure must be seized for jam in worst-case load position, in compliance to CS25.303. This is why, as a result of the FHA made on the WATE system required, the following safety requirement ref. REQ5 asked “*To check ultimate loads and safety factors of the whole aircraft structure for occurrence of failure and continuation of flight loads*”. A fault tree was thus generated and calculated to compute the ultimate loads for degraded WATE performance (see details in paper Ref. [7] titled “*Design, Manufacturing, and Testing of the Wingtip Active Trailing Edge*” from Wildschenk and Storm).

5 Catastrophic Failure Condition: Example of Integrated Safety Analysis

A CATASTROPHIC Failure Condition at IS12 has been identified considering an asymmetric SARISTU devices configuration in combination with strong crosswind at T/O or landing.

This FC is labelled “*FC 2.2.7-03—Partial loss of wing shape control capability (Asymmetric) combined with strong crosswind at take-off or landing*”. This FC is summarized in Fig. 14. This figure allows the identification of the main “actors” of

ID Failure Mode	Title	AC Flight phase(s)	Safety requirement			FT req FT/N/CE	Failure Causes / Involved Subsys	TRACEABILITY			External event or condition	REQUIREMENTS / COMMENTS	REQUIREMENTS SUPPORT/PROOF / DEMONSTRATION
			Severity	Priority	Objective			WATE	AIE	SADN			
2.2.7-03 IS12 CATASTROPHIC CS 25.303	Partial loss of wing shape control capability (Asymmetric) combined with strong cross wind at take off or landing	Take-off and landing	CAT	Multiple axes or percentage of deflection Possible AC loss	RE-PROP	Y	FC 2.2.7-03 Loss of SARISTU wing shape control on one wing only (due to asymmetric failure) combined with strong cross wind at take-off or landing. External event: strong crosswind at take-off or landing. - Bad weather conditions - Bad weather conditions	FC5 WATE	FC5 AIE	FC5 SADN	Strong crosswind at take-off or landing	AIE51: control capability only SARISTU being FC5 and LND is considered as “high life duration” and is not LND as a different failure condition. REQ5: A SARISTU wing shape optimization (due to high structural loads) may generate control law errors. Lightning control system is required to be implemented and validated. AIE51: control capability only SARISTU being FC5 and LND is automatically compared for the experiment.	FC5: design evidence

Fig. 14 FC 2.2.7-03 extracted from traceability table

this Failure Condition: The AS02 FC labelled “*FC07—Partial loss of ATED (Asymmetric) combined with strong crosswind at landing*”, the AS03 FC labelled “*FC4—controllability degradation, asymmetric configuration due to one jammed WATE*”, and the external event “Strong Crosswind”. In addition, also the exposure factor is presented in this table: take-off and landing.

The system FCs (from WATE and ATED Application Scenarios) are reported as “undeveloped events” on the IS12 fault tree. These undeveloped events are depicted as diamonds by the FT tool. The details of these Failure Conditions are reported in the Application Scenario analyses. The undeveloped events probability have been extracted from Application Scenarios FTs.

Flight phases (e.g. landing) and external events (e.g. strong crosswind) are depicted by an elliptical shape in the FTA tool. In the FT reported in Fig. 15, the following “conditional events”¹ have been used:

- I. Landing-phase exposure time, labelled “*LND_PHASE*”. This phase is estimated to be about 15 min long over 180 min (the 3 flight hours used as reference flight time). The exposure factor is then $15/180 = 0.08333$. This exposure factor is applied on the ATED Failure Condition.
- II. Take-off- plus landing-phase exposure times, labelled “*TO_LND_PHASE*”. This exposure factor is based on the take-off duration estimation (2.5 min) plus the landing duration (15 min as before). The exposure factor is then $(2.5 + 15)/180 = 0.09722$.
- III. Strong crosswind external event, labelled “*WIND_TO_LND*”. The probability value is $1e-02$ per cycle as already reported in Fig. 11 depicted on previous section.

The two Application Scenario undeveloped FCs and the external event are connected by a logic *AND* gate, which means that both FCs and the strong crosswind shall simultaneously occur to cause the identified hazard. The main requirement coming from this hazard is that a symmetry check of SARISTU devices is required to reduce the probability of occurrence of this failure scenario. This requirement is comparable with classic aircraft secondary flight controls (e.g. FLAPS). This hazard does not necessitate demanding architectures to comply with required safety figure. In fact, the exposure factors and the FC’s combinations allow SARISTU system to comply with the top event requirement of $1e-9$ /FH also with Application Scenario figures with an order of magnitude of $1e-3$ /FH.

¹Conditional event is a wording used with fault tree + tool.

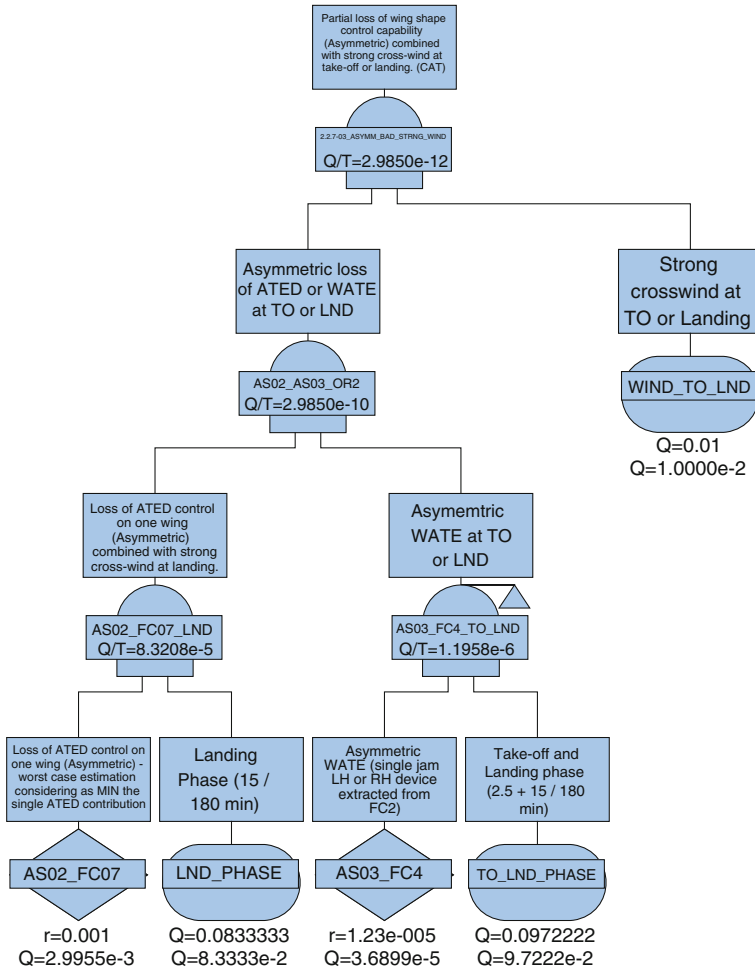


Fig. 15 IS12 fault tree for FC 2.2.7-03

6 Common Cause Analyses (PRA, ZSA, CMA)

In addition to the FHA and PSSA, other safety activities commonly performed in the aeronautical field like common causes analyses (CCA) were identified during the safety assessment of SARISTU. CCA consist of three different but complementary activities:

- A zonal safety analysis (ZSA) to ensure that equipment installation in the aircraft meets the safety requirements and minimize the potential common modes due to this installation. It contributes to the verification of the segregation requirement application from the FHA and PSSA.

- A particular risk analysis (PRA), consisting of systematic studies of all the external and intrinsic hazards such as fire, burst, lightning strike, bird strike and leaking fluids. whose repercussions largely exceed system design perimeter, having effects on structures, system installation, impacting multiple system at the same time and/or affecting different sections of the aircraft.
- A common mode analysis (CMA), which is a qualitative analytical assessment of all potential common causes that can affect a number of elements otherwise considered to be independent and which can lead to CATASTROPHIC Failure Conditions. The CMA contributes to the verification of independence criteria (fail safe criteria) used in the fault trees. In the frame of SARISTU safety assessment, a complete CMA activity was not performed. For the wind tunnel demonstration, there was no real need to do it but absolutely required for a real implementation. However, CATASTROPHIC Failure Conditions expressed in the FHAs were assigned a fail safe requirement (“*no single failure shall lead to a CAT FC*” as stated in the CS25 book 2—Means Of Compliance, Ref. [2]).

At this stage of SARISTU R&T project, the CCA activity has mainly consisted in providing a list of PRA requirements. Alenia Aermacchi as safety leader at system integration level (IS12) involved specialists on PRA to produce a first list of applicable PRA requirements relevant for SARISTU with the support of Airbus based on the several standard documents (e.g. EASA Regulation Ref. [1], in particular CS25.581 on lightning Protection, CS25.631 on Bird strike damage, CS25.867 on Fire protection and CS25.899 on Electric bonding and protection against static electricity, DO-160 for EMI, HIRF applicable requirements Ref. [5]).

Most of the particular risk analyses (PRAs) are strictly related to the whole aircraft design. For a demonstrator, it has no sense to perform such type of analysis. Nevertheless, it is important to consider, for example, that the leading edge design has implemented in SARISTU should be able to withstand a bird impact. Moreover, all the subsystems shall be designed considering the currently available norms regarding the electromagnetic compatibility (EMC), lightning strike. PRAs that are of interest for SARISTU are the following ones:

- Lighting strike protection
- Bird strike/FOD behaviour due to leading edge requirements
- Electromagnetic hazards (lightning strike, EMI, HIRF)
- Flailing shaft (slats and flaps)
- Wiring hazard (failure in wire bundle).

The following picture shows foreseen protections against PRA risks coming from AS01 concept. Particular risks were considered in the SARISTU design (AS01) as depicted in Fig. 16.

Design requirements to protect against aforementioned particular risks were expressed in Sect. 5.3 related to design constraints of SARISTU D123.1 deliverable titled “Wing Demonstrator design principles” Ref. [8].

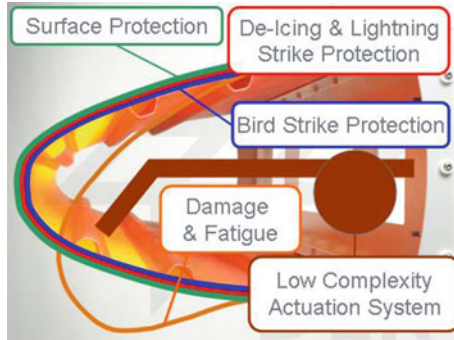


Fig. 16 Protections against PRA risks

ZSA is not required for the SARISTU demonstrator. This is why in the frame of SARISTU project there is no need to verify whether the installed equipment is subjected to these particular risks. This will be done in a real implementation.

7 Conclusion

Even if SARISTU project does not require a safety analysis to perform wind tunnel model validation, this activity was performed in order to provide a clear status on the maturity of the concept regarding safety considerations. Both wing integration- and Application Scenario-level FHAs were performed using standard techniques. However, the approach was tailored for SARISTU project: the morphing wing system analysis was performed starting from a generic aircraft-level functional breakdown and then becoming the target for the Application Scenario safety analyses.

Several lessons have been learnt from the safety activity performed on SARISTU all along the duration of the project. First of all, it is worth reminding that an appropriate methodology was elaborated at the beginning of the project to address the safety of SARISTU concept in an original and very efficient way. Alenia Aermacchi as leading the wing integration activity focused on the A/C-level safety assessment. Each scenario leader concentrated his effort on assessing the safety of their own systems. An iterative harmonization process with a simple but effective traceability form was used to make the safety analyses (both FHAs and FTAs) coherent.

The safety methodology applied in the frame of SARISTU can be easily used in a “real-life” application, making easy to exchange information between the “integration-level” industry and the subsystems suppliers. This methodology shows some advantages also for the detailed quantitative analysis: the lower level FTs can be developed by the subsystem owner, while the Integration Scenario leader can develop high-level FTs, verifying in a very fast and effective way the compliance

with the safety requirements. The safety approach applied in the frame of SARISTU can also be followed for a deeper analysis level, not accounted in SARISTU project.

The support of Airbus in all safety activities, as a major civil aircraft manufacturer, provided a real added-value to the project. Thanks to the organization of safety and airworthiness sessions the first year of the project, Airbus made sure that all contributors had the same level of knowledge on safety; this support from Airbus enabled them to perform the expected safety activity in a well-matched way. Several workshops were managed by Airbus in order to coordinate the safety activities and assure that the SARISTU partners progressed well on their own safety tasks while exchanging their results with the other partners, especially Alenia Aermacchi having the wing integration leadership. Regular technical and progress meetings were organized between Airbus and Alenia Aermacchi in order to reinforce the effectiveness of the safety management of SARISTU. Even if SARISTU is an R&T project that does not require the same level of rigor as an industrial product, all the safety activities were performed in compliance with the airworthiness regulations.

The results of the wind tunnel tests will probably impact some safety feedback like, for example, the pilot workload assumptions made during the FHAs. Lastly, the safety methodology has shown that a limited and optimized effort put on the safety assessment all along the life of the project permitted to provide good, trusted and reusable results. In the near future if such a new wing integration concept is implemented on a new generation of aircraft or on existing aircraft, the safety results from SARISTU can be partly reused.

Acknowledgments The research leading to these results has received funding from the European Union's Seventh Framework Programme for research, technological development and demonstration under Grant Agreement No 284562.

References

Standard regulations and practices

1. EASA CS-25 (2014) Book 1, European Aviation Safety Agency—Certification specifications for large aeroplanes CS-25 amendment 15, 21 July 2014
2. EASA CS-25 (2014) Book 2, European Aviation Safety Agency—Acceptable means of compliance for large aeroplanes CS-25 amendment 15, 21 July 2014
3. SAE ARP 4754a (2010) US SAE international, guidelines for development of civil aircraft and systems, Revised Dec 2010
4. SAE ARP 4761 (1996) US SAE international, guidelines and methods for conducting the safety assessment process on civil airborne systems and equipment, Dec 1996
5. RTCA DO-160, Environmental conditions and test procedures for airborne electronic/electrical equipment and instruments from EUROCAE

SARISTU project documents

6. Baldassin E, Di Gifico M, Gemma R, Carossa GM, Russo S, Ricci S, De Gaspari A, Peter F. Deliverable A_DEU_121_1_R2, Reference baseline wing and morphing wing aeromechanical requirements
7. Wildschek A, Storm S. SARISTU AS03 Final Paper, Design, manufacturing, and testing of the wingtip active trailing edge
8. Apicella A, Russo S, Ricciardelli C. Deliverable A_DEU_ D123_1_R1, Wing demonstrator design principles

Other documents/papers

9. Working group document, Framework for the application of system engineering in the commercial aircraft domain

Development and Validation of a Bird Strike Protection System for an Enhanced Adaptive Droop Nose

Charles Chary

Abstract In the frame of IS12 wing integration scenario of the SARISTU project, SONACA was incharge of the development and the validation of bird strike protection systems integrated into an enhanced adaptive droop nose. Numerical simulations were used to elaborate solutions insuring both the downstream actuation (actuator tube) and the spar integrity adding a constraint on system space allocation and converge towards two relevant “iso-mass” concepts: a bird splitter concept and a bird absorber concept. Nonlinear finite elements analyses (NLFEA) using ABAQUS/Explicit were also performed prior the bird strike physical testings to support the test definition and to predict the impact scenario on the structures. With the principal objective to evaluate the efficiency of the bird strike protection systems (BSPS), the bird impact test campaign took place in VZLU test facilities on 21 and 22 April 2015. Three specimens were assembled and subjected to bird impact tests. Two of those specimens were used to compare the behaviour and the efficiency of the splitter and the absorber at “iso-mass” solutions. The third and fourth tests were performed on a representative EADN leading edge structure connected to actuation systems and containing a morphing outer skin in front of a bird strike splitter protection system. Amongst the two investigated BSPS, the bird splitter concept has demonstrated a better efficiency than the bird absorber concept for the assessment of the spar integrity requirement. In a global point of view, except for the bird absorber concept, the test results are in very good agreement with the predicted numerical simulation results. Moreover, all the shots were performed in very good tolerances with no deviations from requirements.

Nomenclature

BSPS	Bird strike protection system
BST	Bird strike test
EADN	Enhanced adaptive droop nose
ETS	Engineering test specification

C. Chary (✉)
SONACA SA, Gosselies, Belgium
e-mail: charles.chary@sonaca.com

GFRP Glass fibre-reinforced plastics
NLFEA Nonlinear finite elements analyses

1 Introduction

The bird strike problematic on EADN was addressed in the scope of the SARISTU project. Contrary to conventional slats structures, EADN does not offer existing barriers to stop the bird before reaching the front spar. In addition to that, out of kinematics area, the morphing skin, principally made of GFRP, become very thin in the most forward point of the nose and a high level of energy must be absorbed or deviated before reaching the spar. Taking into account all these points, BSPS must handle a big part of the impact energy while insuring the spar and actuation integrities and offering the maximal system space allocation.

2 Frame of the Study, Impact Parameters

The impact parameters are characterised by a 4 lbs bird and an impact speed equals to **180 m/s** corresponding to an envelope value coming from SONACA experience and database. The resulting impact energy is **29.4 kJ**.

Moreover, as explained in Fig. 1, a preliminary study had shown that the morphing skin, principally made of GFRP, does not contribute significantly in the energy absorption as the estimated level of absorbed energy was around 5 % of the

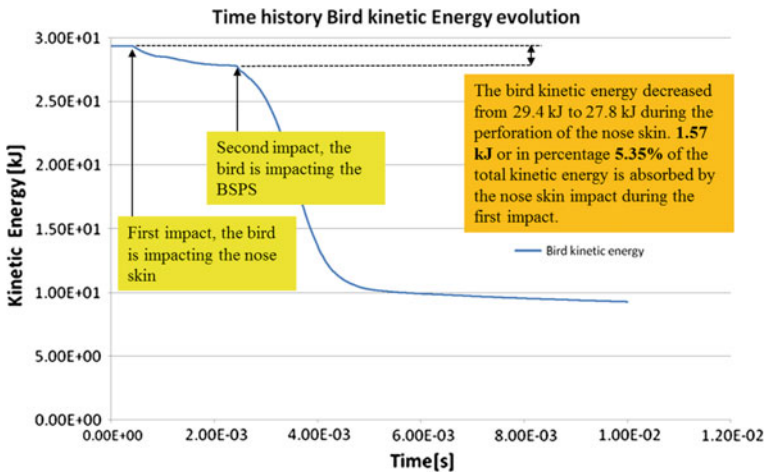


Fig. 1 Preliminary estimation of the energy absorption of the morphing skin

total bird impact energy. That is the reason why the BSPS must be designed to protect the wing front spar against residual kinetic of bird debris representing at least 95 % (100 % to be safe) of the bird impact energy to protect the spar and the actuator tube system considering in addition to a constraint of maximisation of the systems space allocation.

3 Design Loop for Determination of BSPS Concepts

As shown in Fig. 2, several concepts were preliminary numerically studied in order to find the best compromise in terms of protection of the spar and maximisation of the system space allocation. The first one was thought to act as a bird splitter, and the second one was thought as an inner Dnose skin designed to maximise the system space allocation, and the third one was an honeycomb panel directly attached on the spar, and the fourth one was a combination of the second and the third concepts, an honeycomb panel was glued in front of an inner Dnose skin. These preliminary analyses have led to the conclusions that concepts one and four were the most relevant in terms of protection of the spar; nevertheless, the system space allocation was judged too small for the concept one and the mass of the concept four was higher than the concept one and seems to be less efficient.

Finally, two relevant concepts have emerged: a splitter concept which will split the bird and an absorber concept also called hybrid solution as combining aluminium








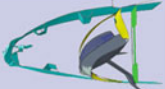
	 <p>Concept 1 Bird Splitter with a circular edge in the nose</p>	 <p>Concept 2 Inner Dnose skin, designed to maximize the space allocation</p>	 <p>Concept 3 Honeycomb panel attached to the subspar.</p>	 <p>Concept 4 Combination of the inner Dnose and the honeycomb panel concept.</p>
Final BSPS Damage				
BSPS masses	2.18 Kg	2.63Kg	3.19Kg	3.43 Kg
Spar protection	Not impacted	impacted	plastified	Not impacted
System Space allocation	Probably not sufficient	Better than concept 1	No space allocation	Better than concept 1
Scenario Description	<ul style="list-style-type: none"> • Nose skin perforated . • Acting as a bird splitter. • BSPS is highly deformed and locally torn. • bird is split and is flowing along the slopes of the BSPS, it leads to the bottom and top failure of the nose skin but the spar is protected. 	<ul style="list-style-type: none"> • Nose skin perforated . • Bird is dragging away the BSPS toward the subspar, the spar is finally impacted. • The BSPS is highly deformed and locally torn. • A part of the bird is flowing along the BSPS and perforate the nose skin. 	<ul style="list-style-type: none"> • Bird stopped • Spar plastified 	<ul style="list-style-type: none"> •Nose skin perforated • BSPS is highly deformed and plastified. • the majority of the bird kinetic energy is absorbed . •A part of the bird is flowing along the BSPS and perforate the nose skin but the spar is protected.

Fig. 2 Preliminary concepts analysis

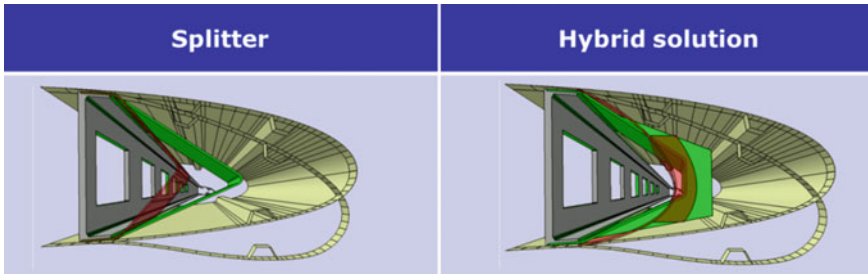


Fig. 3 Relevant concepts resulting from preliminary analysis (is in red, is in green)

sheet and honeycomb core material. Figure 3 illustrates the deformed shape of the morphing skin in fully deployed configuration, and the aluminium BSPS splitter has been extended in the nose to maximise the available space system allocation. The hybrid solution (absorber) BSPS made of aluminium sheet and stuck pieces of honeycomb core material has been extended in the nose to maximise the available space; the honeycomb core depth and attachment surface have been increased, and thicknesses has been optimised in order to work with iso-mass solutions.

4 BST Specimens

As specified in Table 1, two of the specimens were assembled to compare the two concepts of protection by verifying the efficiencies of the BSPS. BSPS 1 and 2, illustrated in Fig. 4, are characterised by a length of 500.7 mm and a height of 273.15 mm.

The first specimen BSPS 1 acts as a bird splitter. The second specimen, BSPS 2, acts as a bird absorber. The location on the wing of specimens 1 and 2 is at midboard section of the wing as illustrated in Fig. 5.

An overall view of the final test rig assembly of the specimens 1 and 2 is shown in Fig. 6.

Table 1 Tests matrix—objectives

Test specimen	Description	Test objective	Location
Specimens 1 and 2	BSPS 1/splitter	Assessment of the efficiency of BSPS	Midboard section
	BSPS 2/absorber		Midboard section
Specimen 3	Leading edge including morphing and BSPS 3 splitter solution	Assessment of the morphing behaviour (damage and failure) and efficiency of BSPS	Outboard section / splitter
Specimen 3	Leading edge including morphing and BSPS 3 splitter solution	Assessment of the morphing behaviour (damage and failure) and kinematic behaviour when directly impacted	Outboard section / kinematic station

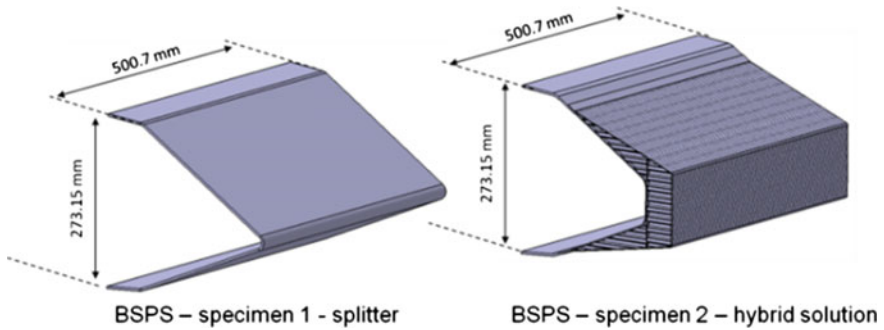
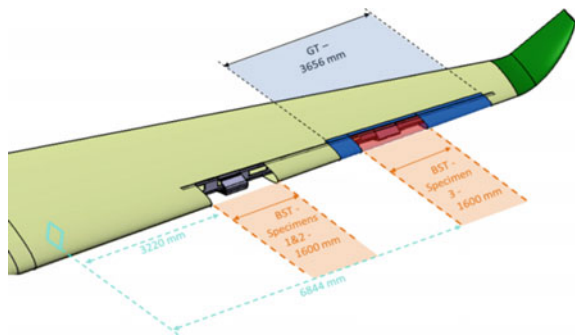


Fig. 4 Views of BSPS 1 and 2

Fig. 5 Specimens location on the wing



The third specimen, illustrated in Fig. 7, was a representative morphing leading edge structure containing a morphing outer skin in front of a bird strike splitter protection system and the actuation systems. As illustrated in Fig. 5, the specimen 3 is located at the outboard section of the wing and corresponds to a leading edge having a 1600 mm spanwise length, a maximum height of 230 mm. The specimen 3 contains the followings:

- A morphing nose connected to a dummy subspar (in green on Fig. 8);
- Two actuators at kinematics stations 11 and 12 (in yellow on Fig. 8);
- The actuation systems (in yellow on Fig. 8); and
- The BSPS 3 splitter made of aluminium located in the impact area (in cyan on Fig. 8)

5 BST Virtual and Experimental Results

In accordance with engineering test specification Ref. [1], bird impact test campaign was conducted at VZLU test facilities on 21 and 22 April 2015. Four shots were defined, and tolerances on impact speed and bird mass are mentioned in Table 2.

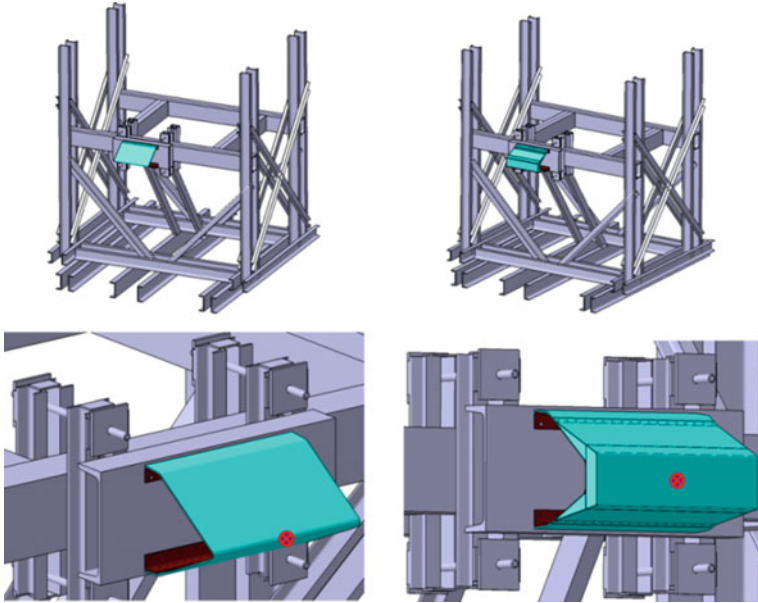


Fig. 6 Views of the test rig assembly of specimens 1 and 2

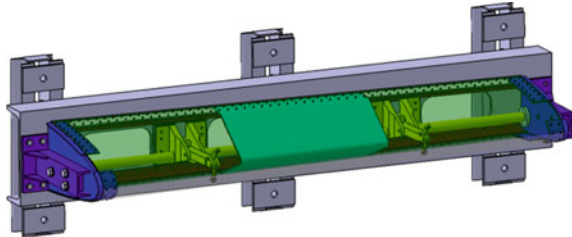


Fig. 7 Illustration of the test specimen 3

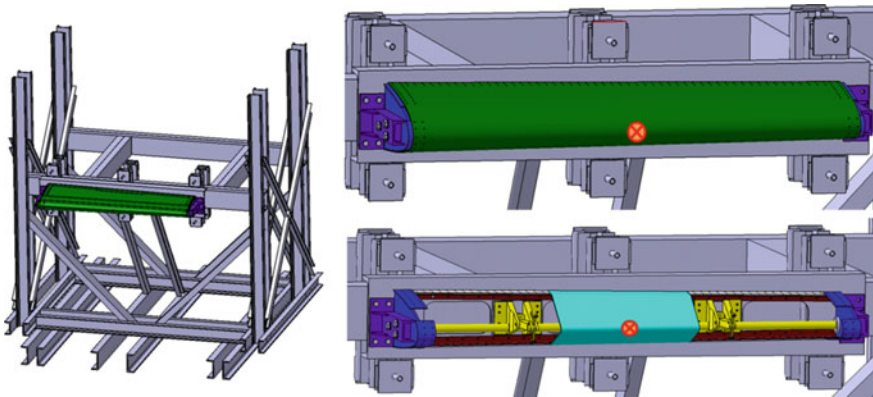


Fig. 8 Views of the test rig assembly of specimen 3

Table 2 Tests matrix—shots requirements

Shot	Specimens	Impact speed (m s ⁻¹)	Projectile	Shot angle	Instrumentation
			Real bird		
1	Splitter bird strike protection system 1 (BSPS 1)	180 ± 5	1.814 ± 0.057	Angle of attack: 0° Sweep back angle: 18°	3 gages + 3 high-speed cameras
2	Absorber bird strike protection system 2 (BSPS 2-hybrid solution)				3 gages + 3 high-speed cameras
3	Leading edge including morphing and splitter bird strike protection system (BSPS 3)				4 gages + 3 high-speed cameras
4	Leading edge including morphing and splitter bird strike protection system (kinematic)				4 gages + 3 high-speed cameras

Freshly killed chicken prior testings were used with a mass of 1814 kg ± 0.057 g. The impact speed was 180 ± 5 m/s; the angle of attack was 0°; and the sweep back angle was 18°. These projectiles were launched by means of an airgun (illustrated in Fig. 9), characterised by a 25 m length and barrel with diameter of muzzle 125 mm. Three high-speed cameras were used to record the impact scenario. Strain gages were installed on splitters, skin, and kinematic parts to measure the time history of strains during the impact event.

On 22 April 2015, one by one, the bird strike specimens were mounted on the test rig as illustrated in Fig. 10 and the four BST of the test matrix were performed.

All the tests were performed in very good tolerances with requirements.

Fig. 9 View of the airgun





Fig. 10 From *left to right*, views of the specimens 1, 2 and 3 mounted on the test rig before testings

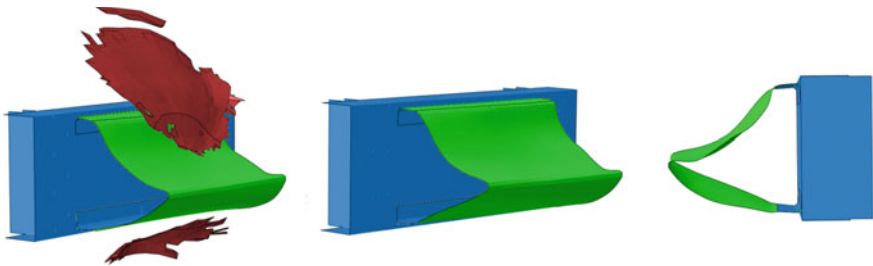


Fig. 11 Predicted numerical simulation results on BSPS 1

5.1 Shot 1 Results

For the shot on the splitter, as shown in Fig. 11, bird flowing along top and bottom inclined panels of the BSPS splitter was predicted by simulation.

Experimental results illustrated in Fig. 12 are in very good agreement with predicted numerical simulation results. The bird body is flowing along the top and bottom inclined panels of the splitter.

5.2 Shot 2 Results

For the shot on the absorber/hybrid, the complete bird absorption by the BSPS was predicted without penetration. No impact of bird debris on the spar was predicted as illustrated in Fig. 13.

Experimental results illustrated in Fig. 14 are not fully in agreement with predicted numerical simulation results due to the fact that test results have highlighted a partial penetration of the bird through the bird absorber. This test has demonstrated that the absorber concept was not so efficient than the splitter concept.



Fig. 12 Experimental test results on BSPPS 1

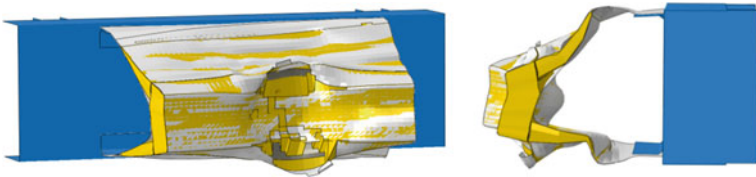


Fig. 13 Predicted numerical simulation results on BSPPS 2

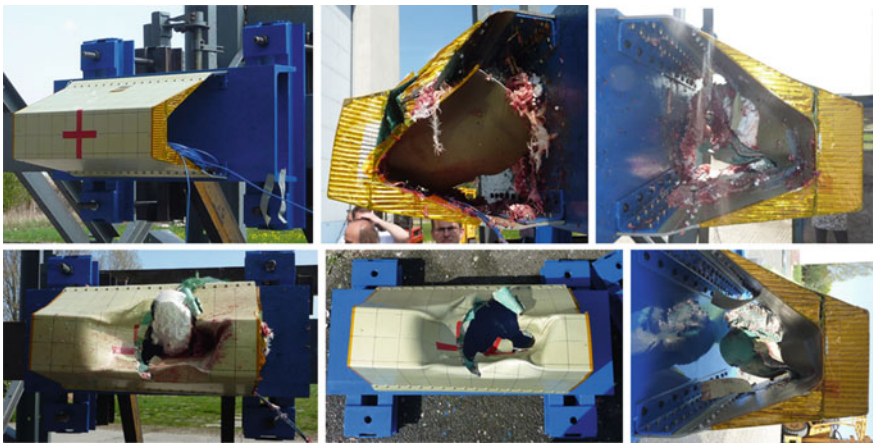


Fig. 14 Experimental test results on BSPPS 2

Post-tests numerical simulations were performed to improve the quality of numerical predictions regarding the impact scenario. In this context, as illustrated in Fig. 15, sensitivity analyses on the damage model of the honeycomb core provide a

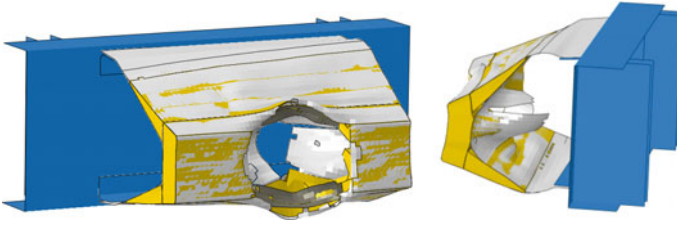


Fig. 15 Numerical investigation on BPS 2

calibrated set of parameters giving a better correlation with the experimental tests. Based on experimental and numerical results, the cause of the absorber perforation seems to be the following: The Aluminium outer sheet in front of the honeycomb core is very thin; as a result, the outer sheet is quickly torn and perforated by the bird which enters the honeycomb cells and destroys them faster than expected. A solution could be to increase the thickness of the outer sheet to slow down the tearing phenomena and allow the honeycomb to work correctly in crushing.

5.3 Shot 3 Results

For the shot on the representative morphing structure, as illustrated on the Fig. 16, the numerical simulations predict a perforation in the nose morphing skin followed by the bird flowing inside the leading edge along the top and bottom inclined panels of the splitter BPS 3 resulting in composite failure at upper and lower connections with the angles of attachment to the rigid wall.

As shown in Fig. 17, Even if the extent of the damage predicted on the morphing skin was larger than the damage observed in the test, the experimental global scenario was in good agreement with the numerical simulations results: firstly, the bird is perforating the morphing skin and is secondly flowing along the top and bottom panels of the splitter BPS 3. As predicted in the simulation, the damage is also localised at the upper and lower connections of the splitter and is characterised by pull through failure of the connections on a 650 mm length in the top and the bottom area.

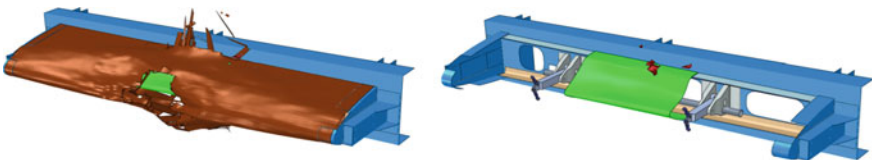


Fig. 16 Predicted numerical simulation results on specimen 3/BSPS splitter 3



Fig. 17 Experimental test results on specimen 3/BSPS splitter 3 installed in a representative morphing leading edge

Spanwise dimension of the opening in the nose is about 150 mm length and the visible spanwise length of the delaminated area is about 250 mm. Chordwise dimension of the damage in the nose is around 150 mm depth at the top and the bottom. Another crucial information to mention is the debonding of the stringers of actuation (omegas) on a large distance (up to the closing ribs of the test rig assembly) resulting in the impossibility to perform a functional testing after bird strike; nevertheless, the protection of the downstream actuation (actuator tube) by the splitter is verified. Locally, the morphing actuation is not possible but remains possible at other kinematic stations on the wing.

5.4 Shot 4 Results

As illustrated in Fig. 18, the experimental scenario when shooting in the vicinity of the kinematic components gives a large hole in the morphing skin. After this second bird strike on the specimen 3, the omegas connecting the actuation components were definitively broken and completely debonded from the morphing skin. Spanwise dimension of the opening in the nose is about 180 mm length and the visible spanwise length of the delaminated area is about 360 mm. Chordwise dimension of the damage in the nose is about 150 mm depth at the top and the bottom.

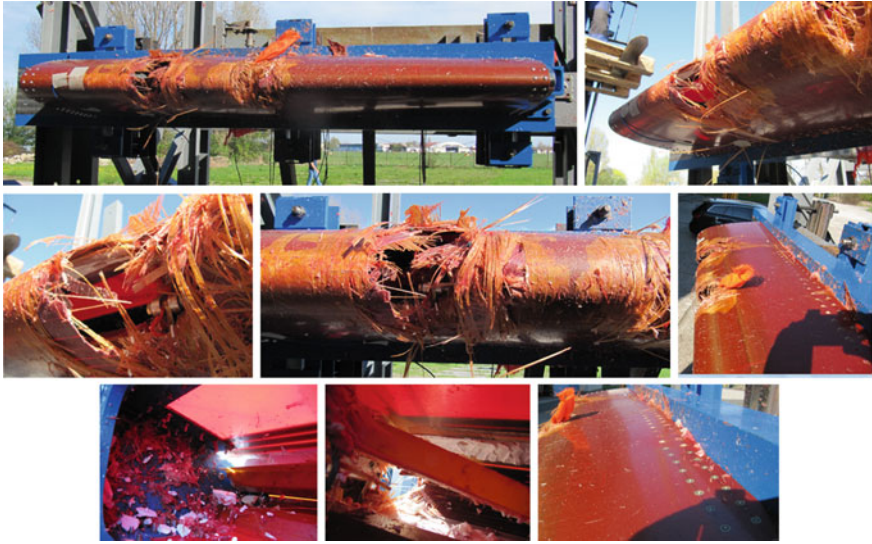


Fig. 18 Experimental test results on specimen 3/kinematics components

6 Conclusion

Bird strike protection systems for an EADN were developed thanks to numerical simulations and validated during a bird strike test campaign. From the splitter and absorber concepts tested, only the splitter concept gives full satisfaction in terms of protection of the spar and the downstream actuation (actuator tube) integrity. Nevertheless, no functional tests were possible on the EADN as complete debonding of the stringers of actuations was observed.

In an overall point of view, except for the absorber BSPS 2 concept, global impact scenarios were in very good agreement with what was predicted and the test campaign was performed in very good tolerances with requirements.

The absorber concept undergoes some investigations to understand the difference between numerical simulation and experimental test results and it seems that some evolutions are possible to optimise and improve the splitter and the absorber concepts.

Another improvement could be trying to improve the balance between the energy absorption capability of the morphing skin and of the BSPS while maintaining the main functionalities of the EADN.

Acknowledgments The research leading to these results has received funding from the European Union's Seventh Framework Programme for research, technological development and demonstration under grant agreement no. 284562.

Sincere thanks go to all the project partners Airbus Group Innovations, DLR, GKN Aerospace, INVENT and VZLU.

Reference

1. Chary C (2014) ETS: bird impact test specification on morphing leading edge. / 0/1754/12-902-3 issue 1, SONACA s.a.

Testing Overview of the EADN Samples

Vladimir Snop and Vaclav Horak

Abstract The several EADN leading edges were developed and assembled in the application scenario AS01 in the European SARISTU project. VZLU manufactured kinematic parts for wind tunnel model including auxiliary spar and assembled this test article. The functional test was performed for verification of the droop nose components. The second one, longer EADN was assembled for ground testing. All kinematic parts including auxiliary spar were also manufactured at VZLU. The functional test, static test of bending and cyclic test were performed on developed, manufactured and assembled test stand. All tests proved high-quality manufactured parts including the whole assembly and well-satisfied functionality of EADN. The third leading edge with manufactured kinematic parts was assembled for bird strike test. The bird strike tests of leading edge and two splitters were performed at VZLU too. This contribution is the description of assemblies of leading edges and overview of performed testing including results evaluation.

Nomenclature

EADN Enhanced adaptive droop nose

1 Introduction

The EADN project is based on physical integration of intelligent sections of wing for commercial aircraft [7]. It is controlled morphing leading edge, which has to serve exact requirements for surface protection and covers de-icing, bird strike and lightning protection systems. These are necessary to locate the complicated

V. Snop (✉) · V. Horak
Aerospace Research and Test Establishment (VZLU), Prague, Czech Republic
e-mail: snop@vzlu.cz

V. Horak
e-mail: horak@vzlu.cz

kinematic mechanism into the above-mentioned structure for morphing part control. VZLU have provided in this section the manufacturing of kinematics parts and auxiliary spars, assembly of kinematics, assembly of complete leading edges, functional tests and ground strength tests.

2 Test Articles of Leading Edges

2.1 *Leading Edge for Wind Tunnel Tests*

The goal was to assembly of leading edge sample including kinematics functional testing and sending complete leading edge to Alenia for integration to the wing part, which was tested in wind tunnel at TsAGI (see Fig. 1).

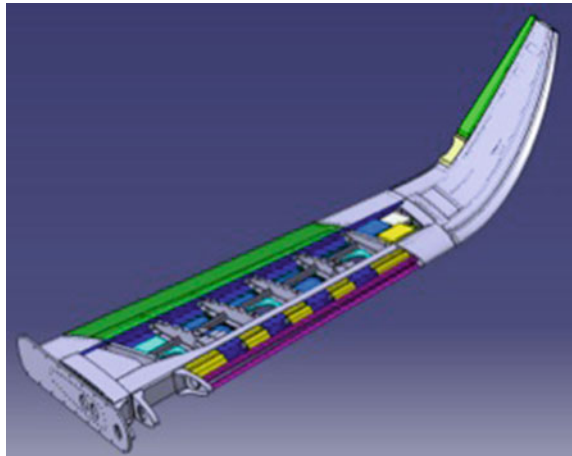
The project partners DLR, AGI, Sonaca, Invent and GKN deal with development of leading edge and have solved following requirements for morphing structure:

- Surface protection
- De-icing;
- Lightning protection;
- Bird strike protection; and
- Simple kinematics for change of shape.

The leading edge was manufactured by Invent. Four semiproducts of approximately 4 m long leading edges were produced, from which cut out samples were prepared for:

- Wind tunnel model;
- Ground test model;
- Bird strike test model; and
- 2 small models with Titanium foil.

Fig. 1 Test sample of wing section



The leading edge for wind tunnel testing consisted of skin, auxiliary spar, kinematic parts and driving motor (see Fig. 2). The kinematics which operates drooping of leading edge has 4 stations which are closely attached to auxiliary spar with using flanged brackets (see Fig. 3). The main levers attached to brackets droop leading edge with using two levers connected to integrated hinges inside of front part of leading edge. The sliding driving shafts pass through flanged brackets and control tilting of main levers with using short connecting levers (see Fig. 4). Whole kinematic system is driven by straight-lined movable electrically powered actuator.

The auxiliary spar was made of aluminium 7050 (see Fig. 5).

The kinematic parts were made of aluminium 7050 or 7075 (see Fig. 6). The steel levers are made of 42CrMo4 + QT steel material (see Fig. 4).

Fig. 2 CAD model of EADN

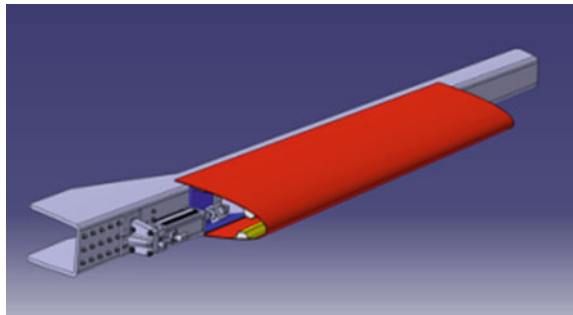


Fig. 3 Detail of kinematics

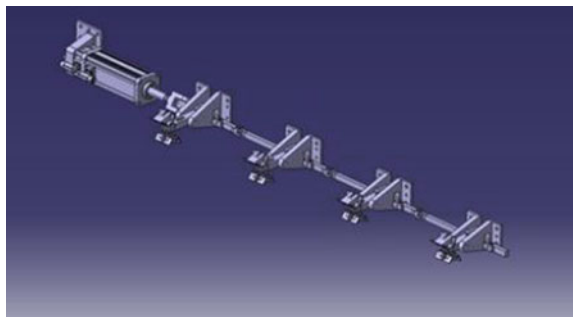


Fig. 4 Detail of kinematic station

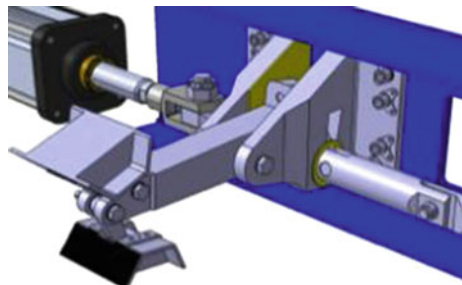


Fig. 5 The auxiliary spar

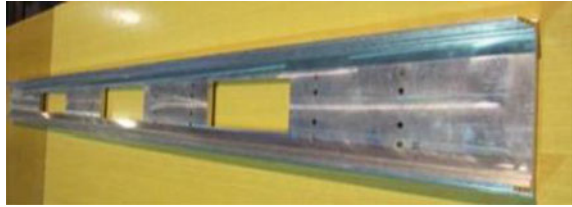


Fig. 6 Kinematic parts



Fig. 7 Assembly of leading edge in rig



The assembly of leading edge was performed in assembly rig according to agreed procedure in September 2014 at VZLU (see Fig. 7). At first, the short levers were installed to the integrated hinges and checked their free moving. After that the main levers with connecting crossbars were connected. Next the flanged brackets

with slipped driving shafts were installed and all were linked. The auxiliary spar was installed after checking all the assembled parts, and flanged brackets were bolted. At the end, the spar was riveted with skin.

The functional test of kinematics was performed on September 2014 at VZLU [2]. The leading edge was equipped by angular sensor for measuring of main lever drooping and two accelerometer sensors before testing. Completed leading edge was installed to the test rig and actuator for driving was connected (see Fig. 8). The deformation of skin and the stress through strain gauges installed on inner side of skin were measured during the functional test (see Fig. 9).

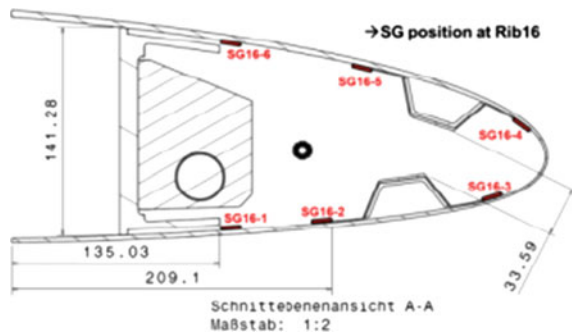
The functional test was successfully completed [4]. It was performed several measurements up to maximum deflection of leading edge drooping, which was approx. 32 mm on the root rib (see Figs. 11 and 12). Measured data in strain gauges corresponded to supposed values obtained from computing model (see Fig. 10).

The completed leading edge was sent after functional test to Alenia in October 2014 for integration to the wing section (see Fig. 13).

Fig. 8 Functional test rig



Fig. 9 The scheme of strain gauge installation (DLR)



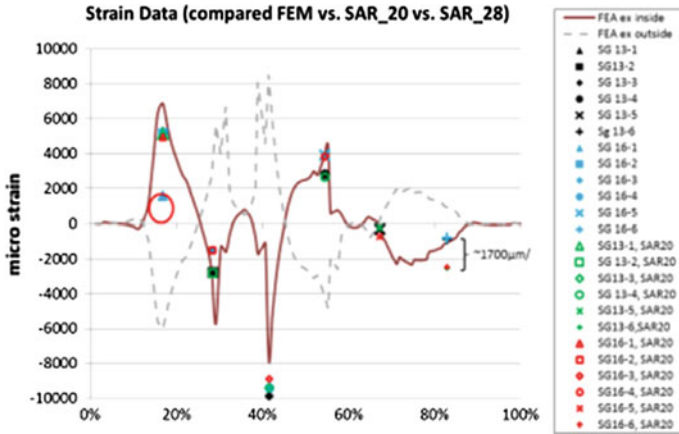


Fig. 10 Comparison of strain gauge measuring with calculation (DLR)

Fig. 11 Detail of drooped leading edge

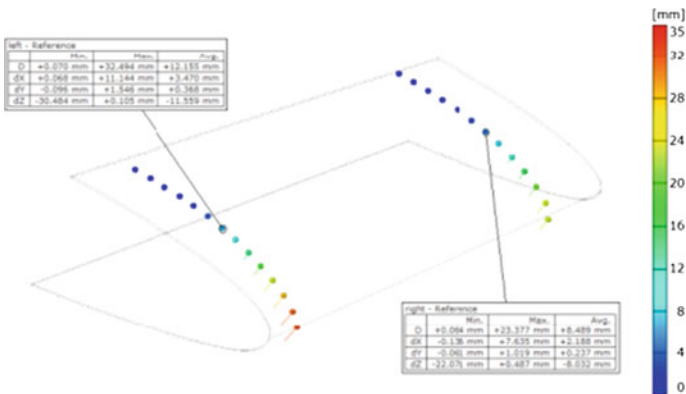
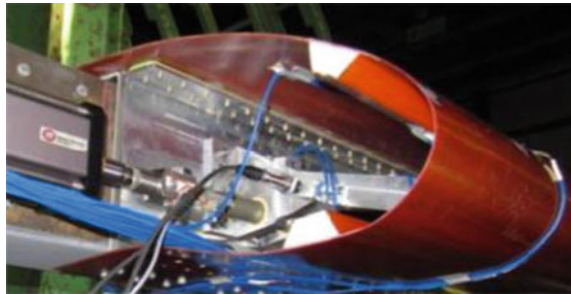


Fig. 12 Results from measuring of deformations

Fig. 13 Assembly of leading edge to the wing section



2.2 Ground Tests

The goal was to assemble the sample of leading edge with 7 kinematic stations 3650 mm long. The functional tests were performed without and with adjusted expected wing deflection and cyclic test with combined loading by deflection and drooping of leading edge. The leading edge was assembled in the same way as the previous shorter model. The assembled leading edge was attached to test rig beam [3] where 3 hydraulic actuators were placed (see Fig. 14). They have provided appropriate deflection of beam using position control (see Fig. 15).

The functional test of kinematics was performed in March 2015 at VZLU (see Fig. 16). The leading edge was equipped by 2 angular sensors for angle of main levers drooping measurement. The deformation of skin, the stress by strain gauges installed on skin and kinematic parts and actuation force were measured during the functional test. The functional test was successfully completed. It was performed several measurement up to maximum deflection of leading edge drooping which

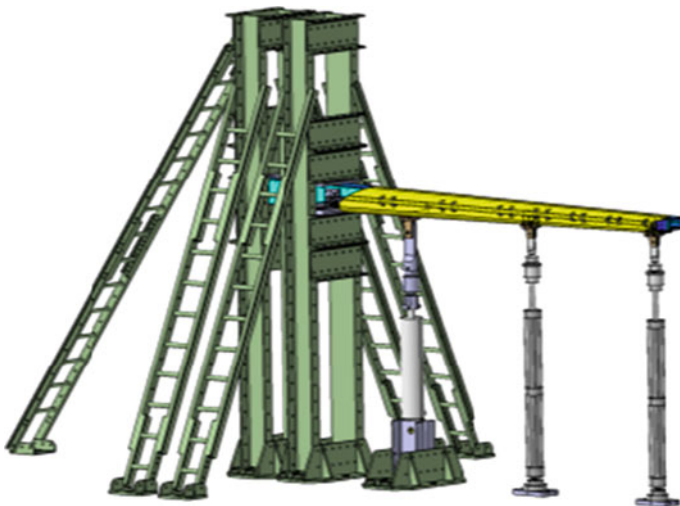


Fig. 14 CAD model of ground test rig

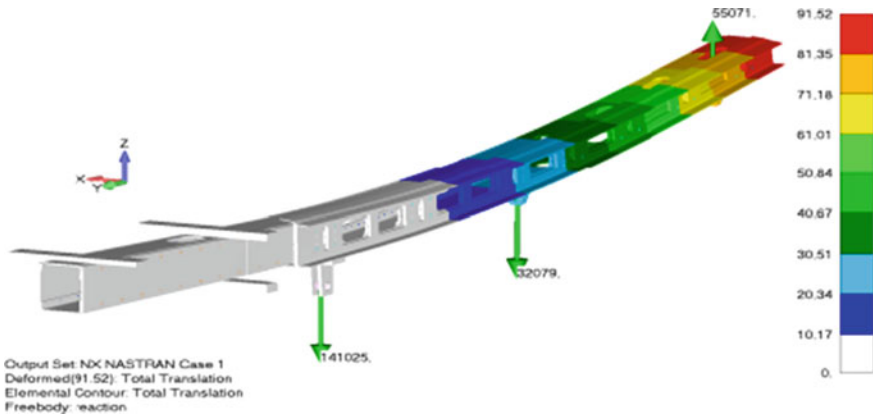
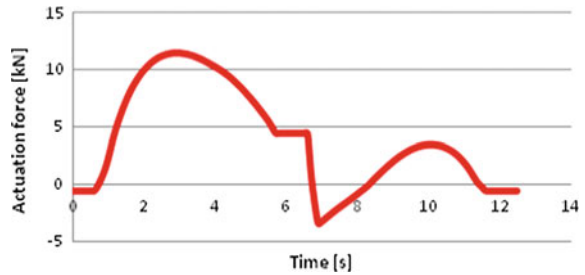


Fig. 15 Computing model of test rig beam

Fig. 16 The setup of functional and cyclic test



Fig. 17 Actuation force (1 droop cycle)



was approx. 40 mm on the root rib. Measured data in strain gauges corresponded to supposed values obtained from computing model (see Fig. 17).

Currently, the cyclic test is in progress. The loading spectrum is compiled from changing blocks with cycling of bending and cycling of drooping. The bending is

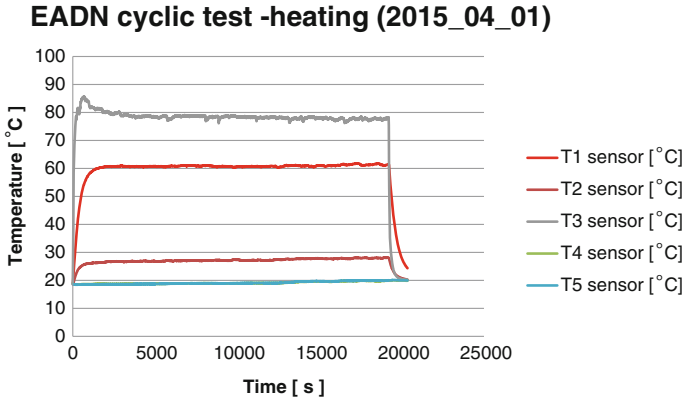
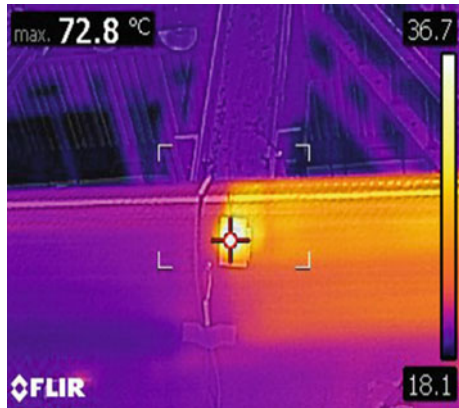


Fig. 18 Record of thermo-sensors

Fig. 19 Critical place monitored by thermo-camera



set by periodic cycle: 0 ... 50 % ... 0 ... -20 % ... 0 % of maximum deflection (rate is 1 cycle = 27 s). The cycle of drooping is simple: 0 ... max 0° angle of drooping (rate is 1 cycle = 10.9 s). During the drooping, the heating of leading edge is applied. Three heating circuits integrated to the skin are monitored by 5 thermo-sensors (see Figs. 18 and 19). Currently, the number of completed cycles is 15,000 of drooping and 19,000 of bending.

Fig. 20 Splitter 1 after test**Fig. 21** Splitter 2 after test

2.3 *Bird Strike Test*

The goal was to assembly of leading edge test sample with 2 kinematic stations and splitter and to perform 2 shots-one to the centre between kinematic stations and second to the area of kinematic station (see Figs. 22 and 23). Further two shots directly to two splitters without leading edge were planned. The first splitter is made of aluminium plate and the second one is hybrid made of aluminium plate and composite sandwich with aluminium honeycomb core (see Figs. 20 and 21).

The bird strike tests were performed in test rig [6] by airgun, 25 m long of barrel with diameter of muzzle 125 mm according to Sonaca specifications [1]. We used real fresh killed birds with mass 1814 kg. The impact speed was 180 m/s, angle of attack was 0° , sweep back angle was 18° . Three high-speed cameras were used for record of impacts. The stress thorough strain gauges installed on splitters, skin and kinematic parts as well as actuation force was measured during the tests. All 4 shots were successfully completed. The achieved strike speeds were in range 167.7–181.7 m/s [5].



Fig. 22 The first shot to the leading edge



Fig. 23 The second shot to the leading edge

3 Conclusion

The function verification of EADN samples for wind tunnel tests and ground tests was performed. The second longer EADN was experimentally analysed during the static, damage and fatigue tests. The third sample of EADN was tested for bird strike protection.

All tests proved high-quality manufactured parts including the whole assembly. The functional tests verified exact functionality of EADN. The proper function of bird strike protection system was verified during bird impact tests.

Acknowledgments The research leading to these results has received funding from the European Union's Seventh Framework Programme for research; technological development and demonstration under grant agreement no. 284562.

References

1. Chary C (2014) Engineering test specification, report ETS SARISTU/TP02/BE/S/D1, SONACA
2. Javurek M (2014) Functional test, set of test rig design documentation SARISTU-PK-225, VZLU
3. Javurek M (2014) Ground test, set of test rig design documentation SARISTU-PK-230, VZLU
4. Snop V (2015) Subcontracting: manufacturing consumables and support, SARISTU deliverable D124.14, VZLU
5. Snop V (2015) Bird strike test of morphing leading edge, report R-6271, VZLU
6. Strnad V (2014) Birdstrike test, set of test rig design documentation SARISTU-PK-210, VZLU
7. Woelcken P-Ch (2014) SARISTU leaflet. <http://www.saristu.eu>. Accessed 26 May 2014

Enhanced Adaptive Droop Nose—from Computer Model to Multi-functional Integrated Part

**Olaf Heintze, Stefan Steeger, Alexander Falken
and Jürgen Heckmann**

Abstract The INVENT GmbH rises in the EU project SARISTU under the lead of Airbus and in cooperation with project partners to the challenge to manufacture a composite gapless and flexible droop nose (enhanced adaptive droop nose, EADN) on the basis of computer models and in compliance with standards and requirements of industrial integration. Therefore, various individual disciplines are integrated into one single manufacturing process and, thus, into one multi-functional part. This is an iterative process which develops along the entire range of structural engineering from material and substructure specimen and tests to the design of tooling and processes. Regarding the industrial integration of the morphing wing leading edge, the individual technical disciplines such as protection against erosion, lightning strike and bird strike as well as deicing were selected for SARISTU. Based on the overall design activities of the DLR, INVENT integrates the surface protection of Airbus Group Innovations, deicing of GKN and lightning strike protection into a flexible composite structure.

Nomenclature

EADN Enhanced adaptive droop nose
LSP Lightning strike protection
SP Surface protection
DI Deicing

O. Heintze (✉) · S. Steeger · A. Falken · J. Heckmann
INVENT GmbH, Christian-Pommer-Straße 34, 38112 Braunschweig, Germany
e-mail: olaf.heintze@invent-gmbh.de

S. Steeger
e-mail: stefan.steeger@invent-gmbh.de

A. Falken
e-mail: Alexander.Falken@invent-gmbh.de

J. Heckmann
e-mail: Juergen.Heckmann@invent-gmbh.de

1 Introduction

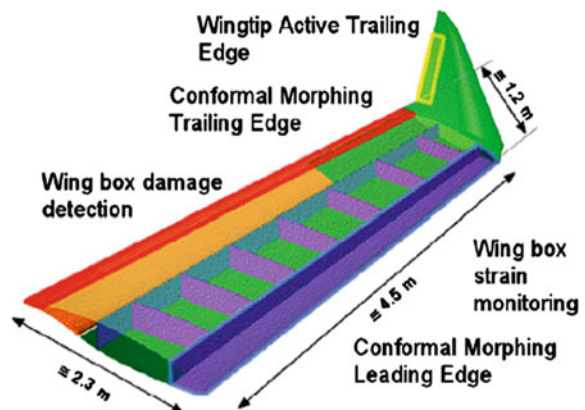
The need for airliners to become more efficient with the focus on the reduction of costs for the air travel is growing. Thus, new technologies have to be designed to allow for a low-drag aircraft. The project target of SARISTU is to reduce the drag by 6 % and to reduce the noise created by the airframe to allow for the minimization of sound pollution [1]. The wing and especially its leading edge inherit an outstanding role in the fulfilment of this requirement.

One requirement for a low-drag wing is a laminar flow of air over the surface of the wing. Modern airliners use high-lift systems which create gaps when moving from high-lift to cruise flight position or vice versa. Gaps and herms create a discontinuous surface which interrupts the laminar flow and causes the laminar flow to detach from the surface. The thickness of the boundary layer increases and becomes a turbulent flow. In order to maintain a great region of laminar flow on the wing, the surface must be as continuous as possible in the desired aerodynamic shape with tight geometrical tolerances. The purpose of the enhanced adaptive droop nose developed in SARISTU is to eliminate gaps and minimize the wing drag for future aircrafts while additionally being a high-lift device. Less drag directly reduces the fuel consumption and affects the aircrafts weight by up to 3 % (Fig. 1).

2 Investigation of Multi-material and Functionally Integrated Material

The development of the morphing leading edge for the SARISTU EADN demands not only a well-founded knowledge of the properties of composite materials but also an understanding of the behaviour of a combination of functional and structural layers. The geometrical constrictions, which are necessary to allow the aerodynamic

Fig. 1 Concepts integrated into the SARISTU-Wing [2]



surface to morph from a high-lift to a low-drag cruise configuration and back, result in thin laminates in areas with high local strain. However, usually functional layers need to be integrated into these regions nevertheless. Both, the structural and the functional layers of the skin ply book have to be matched to suit the other boundary conditions. Overall, the DLR and Airbus’ experience from the former projects SmartLED (German R&D project) and SADE (EU project) proves the structural feasibility of the base concept with plain glass fibre reinforced plastics (GFRP) HexPly 913 prepreg.

To determine the properties of the HexPly 913 prepreg with respect to the structural performance and industrial integration, a specimen program was manufactured by INVENT. More than 350 specimens for more than 30 different test categories with standard and adapted specimen structures are used to provide sufficient information about the structural behaviour for different load cases and in variable environmental conditions.

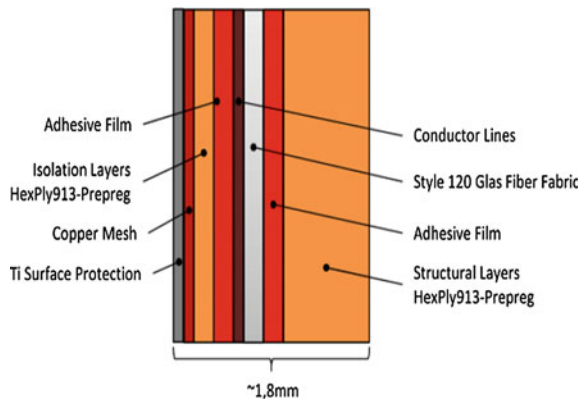
The design of the EADN (Fig. 2) on an industrial level requires the integration of systems needed to allow a safe operation in the anticipated flight conditions. For the skin, these most important and chosen systems include:

- Surface protection from sand and rain erosion
- Deicing system
- Integration of connections for kinematics
- Span-wise stiffening through integrated stringers and tapered skins
- Lightning strike protection

Not only a concept for the combination has to be found but also an economically feasible way to produce the parts in large numbers.

In general, the project partners DLR (design), Airbus Group Innovations (kinematics and erosion protection), SONACA (bird strike protection) and GKN Aerospace (deicing and lightning strike protection) provided their respective technologies to be integrated in a single droop nose part. These inputs were taken into account when designing the tooling and manufacturing concept.

Fig. 2 The layup of the skin in a critical area of the leading edge. The thickness is only approx. 1.8 mm and includes SP, DI and LSP (INVENT)



2.1 *Material Specimen*

Values for engineering constants given by the manufacturer of the material had to be validated by data gained through the testing of samples. The relevant information can be narrowed down to tensile, compressive and shear tests. The specimen was manufactured by INVENT in standard procedures; however, the tests were performed by the DLR-Institute of Composite Structures and Adaptive Systems. The specimens listed below were produced for the SARISTU project with the high requirements stated in the applied standards. No special ply books are considered, but only pure HexPly 913 prepreg with tabs made from GFRP.

DIN-EN 527-5

- 0°- and 90°-tensile, static
- 0°- and 90°-tensile, cyclic @ 5 load levels
- 0°- and 90°-static, tensile, hot, @ +70 °C
- 0°- and 90°-static, tensile, cold, @ -50 °C
- 0°- and 90°-static, tensile, cold, aged @ -50 °C

ISO 14126

- 0°-compression, static (ISO 14126)
- 90°-compression, static (ISO 14126)

DIN EN ISO 14129

- ±45°-tension shear tests

DIN EN ISO 14125

- Cyclic, 4-Pt., pure 0° @ 5 load levels
- Cyclic, 4-Pt., pure 90° @ 5 load levels
- Cyclic, 4-Pt., pure ±45° @ 5 load levels

Additional samples, derived from standardized test methods, were designed to answer leading questions concerning multi-material ply books at a very early stage.

3 *Integration Specimen*

3.1 *Surface Protection Integration*

Combining fibre composite materials with other materials such as metals and polymers eventually leads to the necessity of a bonding process. Several erosion mechanisms are evaluated by Airbus Group Innovations. First tests show that the cured HexPly 913 prepreg has very little erosion resistance when opposed to rain and sand. Different types of material are therefore considered to find a suitable surface protection solution.

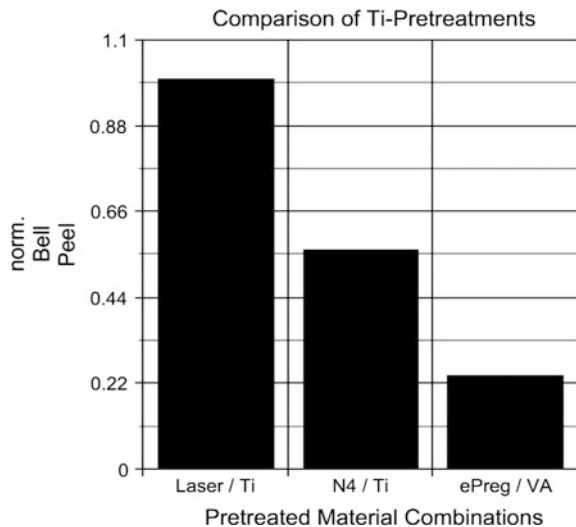
Next to different grade and thickness, Ti-foils, stainless steel foil, PU-foil and a thermally sprayed PA-coating are tested for their erosion properties. Based on the performance of the titanium surface protection in tests with a pulse jet rain system and solid particle erosion, it was chosen for further tests.

The PU-foil erosion resistance is especially against solid particles not the material of choice. However, the advantage of the PU-foil is the exchangeability when worn down. The thermally sprayed polyamide (PA) partially burns the surface and shows an insufficient surface quality. Thus, creating the need to post-process the aerodynamic surfaces of the leading edge skin to an unacceptable extend.

For metallic coatings, roller peel tests according to DIN EN 1464 were carried out by INVENT to assess the strength of different pre-treatments. A normalized comparison of N4-electrolyte anodized and a laser pre-treated titanium foil is shown in Fig. 3. For both laser and N4-pre-treatment, the failure of the samples can be characterized as cohesive. The crack initiated between Ti-foil and GFRP quickly runs into the prepreg layer closest to the Ti-foil leaving resin and fibre residues on the Ti-foil. This leads to a pulling out of fibres, thus proving the bonding concept.

The investigation of a suitable surface coating is still ongoing. However, the availability of 0.1-mm-thick Ti-foil in an adequate size for the leading edge is an issue. A solution still has to be found, leaving the very efficient Ti-coating for future work. The part size is kept to a sample size and the PU-foil is part of a mitigation plan for this specific application in SARISTU.

Fig. 3 Comparison of pre-treated material combinations for an integrated metallic surface protection (Ti pre-treatments were realized by Airbus Group Innovations) (INVENT)



3.2 *Deicing Integration*

The project partner GKN Aerospace provides a heater mat system for the integration into fibre composite structures. The system is made of a dry glass cloth with sprayed on metal structures. By changing the geometry and the material sprayed onto the carrier material, the electrical resistance of the conductor can be adjusted locally and thus the temperature.

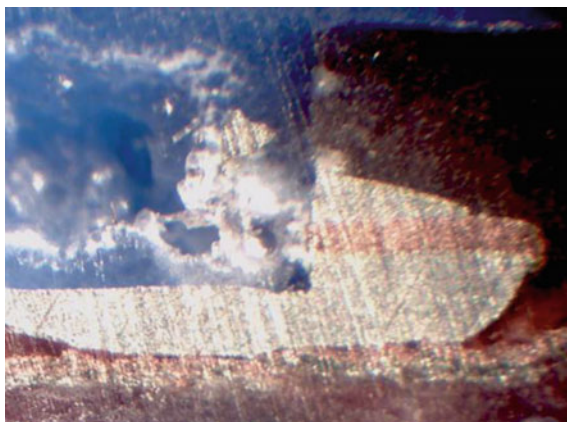
The integration of a dry heater mat contains two very challenging aspects which must be considered. The dry, “Style 120” glass cloth is not impregnated like the HexPly 913 prepreg. It must be soaked with a resin in order to keep a constant fibre volume fraction throughout the laminate. Since a resin film is not available from the manufacturer of the prepreg, using a compatible adhesive was the only option. Different adhesive films are investigated regarding their flow behaviour and the capability to fully surround the dry fibres of the heater mat carrier material.

The pattern sprayed onto the carrier material is a metal substrate. It creates a closed surface which does not allow for the prepreg resin to pass through a widespread area.

Only the clearances between the conductors allow for the cloth to be soaked from this side. Therefore, major amount of resin must be donated by the adhesive film(s) on the glass cloth side. Most adhesive films are designed to produce a constant thickness in the cured part. A thin, knitted, or woven layer of glass filaments is used to secure the position of the adhesive and to protect the bond line from being deformed by the process pressure. This however does only allow small portions of the film to enter the carrier material.

An upfront analysis of the expected impregnation behaviour was performed to identify the most suitable options. Sample plates that reflect different typical areas in the skin were produced with a layup which is representative for the thinnest area in the skin layup. Afterwards, the sample plates were cut at critical positions to

Fig. 4 A cross section of an integrated and soldered copper contact point for the electrification of the heater mat (INVENT)



prepare micro-sections (Fig. 4) and investigate the interaction through microscopy and the determination of the fibre volume fraction in accordance with DIN EN ISO 1172.

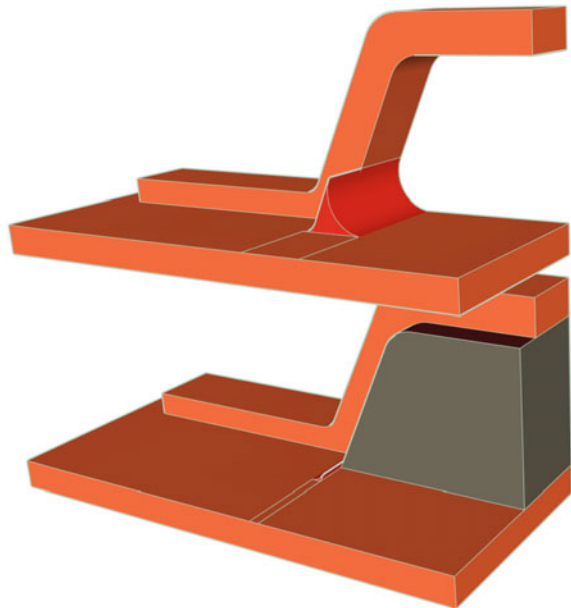
In order to contact the conductors, the prepreg plies had to be removed locally after the curing process. Since the sprayed heater mat material has a thickness of only approx. 0.05 mm, a sacrificial material needed to be placed at the contacting terminals primary to the integration. After the autoclave curing process, the excess material was removed considering the limited workspace of the outboard leading edge section with the choice of tools to be applicable for the final production of parts. Conventional soldering of cables to the contact points was possible without damaging the laminate and allowing for standardized connectors (Fig. 5).

The characteristics of the heater mat and surrounding functional layers lead to the employment of one adhesive film layer on each side of the carrier material and the contact points of pre-soldered copper plates as sacrificial layers and conductive points.

3.3 *Stringer Integration*

The skin has to be actuated by kinematic stations to change its shape. Next to this, its span-wise stiffness has to be increased using stringers. These stringers serve as reinforced load introduction for the thin skin. As a first approach based on the experience from previous programs, a hollow stringer with a removable silicone

Fig. 5 Schematic comparison of omega stringer with a pendentive (*top*) and a solid foam core (*bottom*) which almost thoroughly eliminates undulations in the skin laminate (INVENT)



core was used. This however leads to skin areas with insufficient impregnation and does not allow an exact positioning of the stringer.

Inserting a solid foam core to create an inner shape allows for a nearly constant pressure distribution and a higher process security; the risk of damaging the part during demoulding is furthermore minimized (Fig. 5).

In addition to simplifying the handling and integration when using a foam core to manufacture the omega stringer, the employment of pendentives at the stringer–skin junction is not necessary and, therefore, only a negligible undulation of the skin plies in this area occurs. A very small amount of resin is needed to bond the prepreg and the foam. In this way, the fibre volume fraction complies with the valid range.

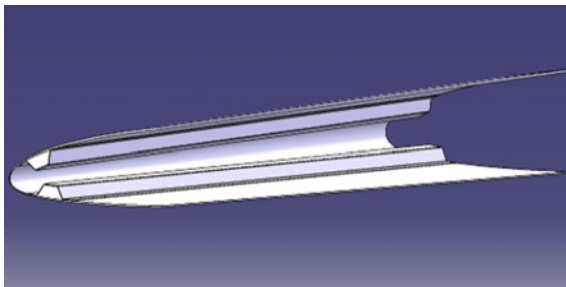
3.4 *Lightning Strike Protection*

Commercial airliners are subjected to lightning strike. A strike can not only cause severe damage to the structure but also influence electrical components. Metallic structures are usually less affected than composite structures. The faraday cage effect channels the strike along the outside.

Composite structures need to be equipped with a conductive layer of some sort to create such an effect. This can, for example, be realized by covering the fibres with a metallic layer or the integration of a copper mesh. Due to the uncovered fibres in the HexPly 913 prepreg, a copper mesh was integrated on the outside. Metallic parts such as the kinematic brackets, which are integrated in the stringer and are positioned very close to the skin, were represented by simple aluminium blocks which are bonded into the stringer core. These were then connected to a ground cable at the test facility (Fig. 6).

The integration was realized with a combination of excess adhesive film and resin from the prepreg. Lightning strike sample tests with four different ply books and four surface coatings, including a heater mat, a stringer and bracket mock-up, were conducted to identify a suitable protection. In the trials, only two of the sixteen combinations tested showed satisfying results due to short circuits and burning. Since these results are not satisfying, further tests will be conducted by GKN and

Fig. 6 CAD model of the final wind tunnel test section (INVENT)



INVENT to allow for well-founded predictions and realization regarding the lightning strike protection.

4 Development of a New Tooling Concept

Goal of SARISTU is to deliver a three-dimensional, large-scale and enhanced morphing wing leading edge that allows for integration in a morphing wing for validation and verification based on structural and wind tunnel testing (Figs. 6 and 7).

Resulting from the requirements of a highly integrated leading edge, the conventional concept of manufacturing has to be analysed and rethought.

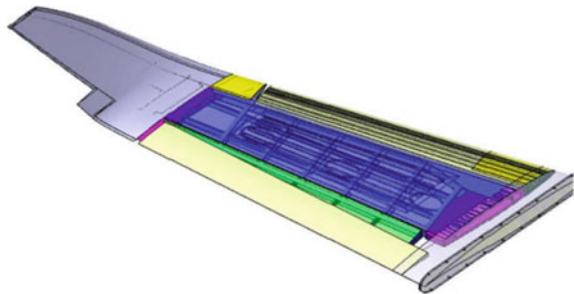
As a result of this process, a tooling concept was developed in which an aluminium multi-part inner core and a composite outer tooling are used to provide the necessary tolerances in positioning and shape (Fig. 8).

4.1 Detailed Morphing Skin Design

Basis for all further steps was a FEM model delivered by the German Aerospace Centre (DLR). Based on this model, a detailed three-dimensional design of leading edge was required to develop the inner shape of the tooling. In order to provide the capability to consider design and layup developments in an iterative loop together with DLR, a parametric wing skin and tooling design were required. Such parametric design approach allows for considering changes in layer thickness and ply order. The necessity arose from the parallel work for optimizing the layup design at DLR and the tool design at INVENT.

In most cases, it is not necessary to have a highly detailed 3D model. A model that shows the different composite layers is typically sufficient since a non-flexible negative mould was used in previous projects to produce the target shape. In the SARISTU project scenario, it is required to estimate the actual inner shape of the leading edge in addition to the outer aerodynamic shape. The CAD model contains

Fig. 7 Wind tunnel section of morphing wing structure with 4.8 m length [1]



smoothed layer transition zones so that a proper aerodynamic shape is guaranteed by a flexible composite outer mould.

The resulting model formed the base for all project partners involved in the subsequent detailed design of test stands (VZLU), kinematics (Airbus Group Innovations, DLR), heater mats (GKN) and bird strike protection (SONACA).

4.2 Bracket Design

One of the major tasks during the detailed design was to develop a kinematic bracket which can be integrated into the manufacturing process of the skin and stringer to avoid further more complicated integration steps.

During the design loop with Airbus Group Innovations and DLR, it turned out that the application of force onto the stringer head was not possible and also not desired. Maintaining the stringer cross section was the preferred option. Airbus Group Innovations developed a kinematics design that would require a joint of kinematics and structure inside of the omega stringer. This kinematic design and in detail the minimally possible lever lengths for the connection of the kinematics to the wing were required to move the junction of kinematic and composite skin/stringer into the centre of the stringer. Therefore, Airbus Group Innovations developed a first concept as the basis for the subsequent design work as shown in Figs. 9 and 10.

Fig. 8 CAD model of the tooling concept. The *blue parts* represent the solid inner core. The *yellow part* shows the outer mould (INVENT)

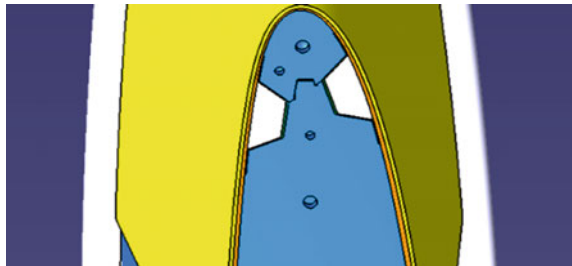


Fig. 9 First concept drawing of bracket design (Airbus Group Innovations)

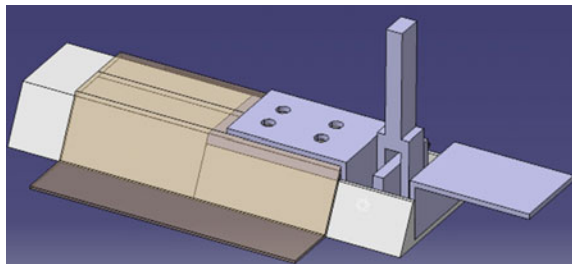
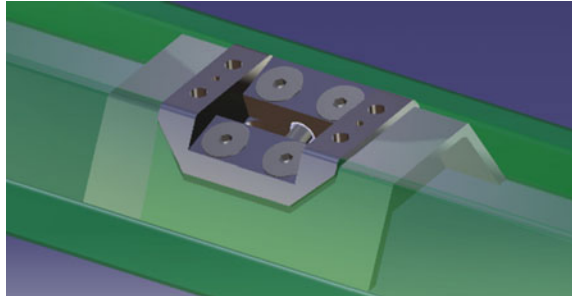


Fig. 10 Final bracket design (INVENT)



In the ongoing kinematic design, it proved to be that the tolerance adjustment is only possible in the bracket and the lever. Therefore, the lever was designed to compensate the tolerances in wingspan direction and the bracket allows the adjustment in chord direction.

The final bracket was designed so that the stringer is notched as little as possible. The adapted bracket allows for almost half of the stringer flank to stay intact and to cause as little interruptions as possible.

Simultaneous to the tooling design, a bracket was developed, which not only provides the necessary loads, maintenance and disassemble possibilities but is also integrated into the stringer during the same curing cycle as skin and stringers despite being a highly complex part (Fig. 11).

5 Tool Design

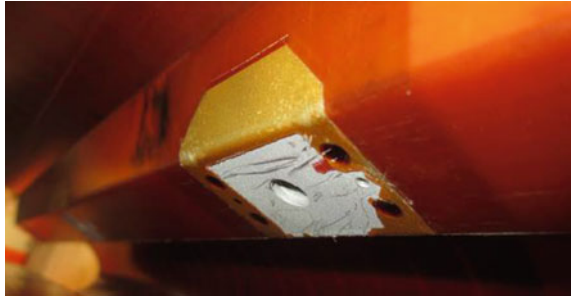
After finalizing skin and stringer, the tool design is started in parallel to the bracket design. For the goal of manufacturing a whole leading edge with integrated kinematic interfaces, a solid inner mould is required. Herewith, the ability to position the brackets with a high precision not only in chord direction but also in wing span direction is assured.

As a result of the tooling concept, the layup procedure starts with the inner most layers. The first manufacturing step is the stringer layup which is followed by the bracket integration. The foam cores then fill the space between each bracket. At last, the GFRP and functional layers of the skin are applied.

The employment of a solid inner structure for the tooling meant to execute the design in a multi-part manner in order to avoid undercuts. A complex factor in the tool design is the accumulation of the influence of thermal expansion of the aluminium tool and the resin shrinking.

To analyse the resulting thermal expansion and to verify the whole newly developed tooling concept, either a complex simulation has to be performed or manufacturing trials with detailed analysis. The latter procedure was chosen here (Fig. 12).

Fig. 11 No gaps were found between integrated test bracket and the stringer after curing (INVENT)



5.1 Test Tool and Results of Trial Runs

For verification purposes of the concept, it was decided to manufacture a small but representative section of the tool. In order to maintain reasonable manufacturing costs for these trials, a section length of 500 mm was chosen. Furthermore, handling efforts are moderate at this size.

The first manufacturing test part was produced to verify the manufacturing process by itself without brackets build in.

The results of this test were very promising. It was found that the geometrical shape and also the layup quality were of the desired high quality. Minor to no marcols were found in critical sections like the transition zone between stringer and skin.

After analysing these results, another test run with brackets was started to test the positioning and the actual thermal expansion factor. The results were planned to provide the final tool with the proper details or adjustments to ensure a high precision of positioning in wingspan direction.

As a result of this test, a section with three brackets on each stringer was manufactured and verified the possibility for a correct bracket positioning with the developed method. Subsequent to the final evaluation of these trials, the trial tooling is employed to manufacture test sections for pull-off tests in order to validate the requirements of load introduction by the DLR.

Based on the experience gained, the manufacturing of the final tool with about 4.5 m length is concluded and the detailed implementation of the final brackets is verified.

6 Prototype Manufacturing

With the experience from the conducted tests on specimen and sectional level, the manufacturing of three full-scale leading edges is started on a secure basis.

Fig. 12 Positioning of brackets and sparing out of the bracket heads with special cutting stamps (*top*); first skin layer applied on full span (*bottom*) (INVENT)



Using the tooling shown in Fig. 12, the first full-scale and full-span prototype is manufactured also verifying the assumptions made for the brackets and their change in position due to the thermal expansion of the tooling.

Since the complex behaviour of the part during the curing cycle can only be estimated, a mitigation plan is used to meet the connection points of the kinematics for this first part. The deviation of approx. 1.5 mm is therefore easily compensated in the assembly. The first manufactured leading edge is used for wind tunnel tests.

The empirically gained knowledge from the first part is then used for an adaption and recalculation of the bracket position, resulting in a deviation of only approx. 0.5 mm for the 4.5 m span of the 2nd and 3rd leading edge prototypes.

The second prototype is used for cyclic ground tests which are still ongoing. Since the dimensions of the leading edge exceed the CNC-milling capability of the machines which are frequently used at INVENT, a concept for edge trimming and bolt drilling is developed, in order to find a faster and easier way to post-process the raw skin elements with a satisfying result regarding accuracy and quality.

By applying the knowledge acquired on bracket positioning and post-processing, the third full-scale leading edge prototype is manufactured successfully and thus reconfirming the envisaged industrial process. The third prototype is used for bird strike tests. First results show satisfactory results in the combination with an aluminium splitter for the protection of the front spar (Fig. 13).

Fig. 13 Bird strike test at VZLU with EADN and conventional aluminium splitter (INVENT)



Fig. 14 Additionally fitted access holes for fast kinematics repair in the test setup (INVENT)



Due to the failure of several friction bearings in the cyclic testing, a mitigation plan for the accessibility of the defect kinematic stations is found. The use of hand holes in the skin is being evaluated in the ongoing ground test; however, negative yet not major impacts are awaited to result from the weakening of the structure (Fig. 13).

By making the kinematic stations accessible on-site, a minimum of ground test time is lost, and thus, it is ensured that the testing complies with the project time plan (Fig. 14).

7 Conclusion and Further Procedure

A wide range of implementation specimens were defined, manufactured and tested with satisfying results. As such, the implementation of features such as erosion protection, deicing, lightning strike protection and bird strike protection into a morphing leading edge appears to be feasible even considering industrial manufacturing requirements.

Furthermore, a detailed part and tooling design were performed employing a parametric CAD model to allow for an iterative approach together with the project partners DLR and Airbus Group Innovations. In addition, a load introduction bracket for the junction of actuation kinematics and composite morphing skin was designed featuring the option to compensate for manufacturing and assembly tolerances.

As a final verification of the manufacturing and tooling concept, a trial tooling was derived, produced and successfully tested. The test results provided relevant insight in effects of thermal expansion for precise bracket positioning and overall geometrical shape. The resulting shape matched very well the allowances without undesired fibre undulations at load critical regimes of the part. The final tooling design was achieved and the tooling manufactured in full scale.

The first full size leading edge will be manufactured with the large-scale tooling in the near future, so that all previously mentioned factors and processes can be evaluated on the final tool. Furthermore, several morphing leading edges for subsequent large-scale experimental analysis in wind tunnel, bird strike and ground based tests will be manufactured.

Through the achievement of the industrial integration of multi-functional hybrid materials in a large-scale gapless droop nose, another milestone towards the application of this technology appears to be reached.

In the next steps, the integration of a titanium foil is evaluated in a sectional demonstrator since the material for the integration on a full-span demonstrator is not available at the moment. Into this demonstrator, all functional layers are to be integrated and tested.

Acknowledgments This project has received funding from the European Union's Seventh Framework Programme for research, technological development and demonstration under Grant Agreement No 284562.

A special thanks is expressed to the involved project partners DLR, Airbus Group Innovations, SONACA, VZLU and GKN Aerospace.

References

1. Wölcken P-C et al SARISTU newsletter-issue 2 (19.12.2012). <http://www.saristu.eu/wp-content/uploads/2012/Newsletter/02/book.swf>. Accessed 26 May 2014
2. Wölcken P-C et al SARISTU leaflet. http://www.saristu.eu/wp-content/uploads/2012/04/SARISTU_LEAFLET.pdf . Accessed 26 May 2014

Assessment of the SARISTU Enhanced Adaptive Droop Nose

Markus Kintscher, Johannes Kirn, Stefan Storm and Fabian Peter

Abstract For the application of laminar flow on commercial aircraft wings, the high-lift devices at the leading edge play a major role. Since conventional leading edge devices like slats do not comply with the high surface quality requirements needed for laminar flow, alternative concepts must be developed. Besides the conventional Krueger device that enables laminar flow on the upper side of the airfoil and additionally implicates an insect shielding functionality, smart droop nose devices are currently being investigated. However, the research on such morphing devices that can deform to a given target shape and provide a smooth, high-quality surface has to give answers to questions of fundamental industrial requirements like erosion protection, anti-/de-icing, lightning strike protection, and bird strike protection. The integration of these functionalities into a given baseline design of a morphing structure is a key challenge for the realization of such devices in the future. This paper focuses on the design drivers, system interdependencies, and effects of the integration of the mentioned functionalities into a smart droop nose device.

Nomenclature

EADN	Enhance adaptive droop nose
GT	Ground test
WTT	Wind tunnel test
BST	Bird strike test

M. Kintscher (✉)

DLR Institute of Composite Structures and Adaptive Systems, Braunschweig, Germany
e-mail: markus.kintscher@dlr.de

J. Kirn · S. Storm

Airbus Group Innovations, TX3, Munich, Germany
e-mail: johannes.kirn@airbus.com

S. Storm

e-mail: stefan.storm@airbus.com

F. Peter

Institute of Aerospace Systems, RWTH Aachen University, Aachen, Germany
e-mail: peter@ilr.rwth-aachen.de

GFRP	Glass fiber-reinforced plastic
ε	Bending strain
$\Delta\kappa$	Distribution of difference in curvature
t	Skin thickness distribution
LSP	Lightning strike protection
AS	Application scenarios
A/C	Aircraft
LoD	Lift over drag
MICADO	Multidisciplinary Integrated Conceptual Aircraft Design and Optimization
SADE	Smart High-Lift Devices for Next Generation Wings
LIP/KAP	Load introduction points
DC	Drive chain
M	Axis of rotation
r_i	Interconnected levers \rightarrow main lever
l_i	Struts to skin/drive chain
K_i	Kinematic point between main lever r and strut l
q	Offset
p	Motion direction
α_i	Rotational angle
x_c	Cruise position
x_d	Droop position

1 Introduction

Because of the large potential of drag reduction, natural laminar flow is one of the challenging aims of the current international aerospace research [1, 2]. For the achievement of the absolutely essential high surface quality, new concepts for the high-lift system at the leading edge are required. Besides the well-known Krueger device, smart droop nose devices are investigated by various research facilities in Europe [3–5]. However, smart droop nose devices at the leading edge are not only advantageous for laminar flow wings. Applied at turbulent wings smart step- and gapless leading edge devices reduce the noise exposure in approach and landing and the drag during takeoff [6]. In 2009, the Institute of Composite Structures and Adaptive Systems at the German Aerospace Center (DLR) in cooperation with Airbus started a new morphing activity aiming at smart leading edge devices. In national and European projects, the concept was consequently advanced. It was tested in structural ground tests [7] as well as in a full-scale low-speed wind tunnel test [8]. In the ground test and in the wind tunnel test, the feasibility of a load-carrying smart droop nose device for a predefined aerodynamically optimized shape was successfully demonstrated. Since the work in the recent project was focused on the demonstration of the feasibility of this technology, based on the results of the ground and wind tunnel tests,

the integration of required technologies for the application at an aircraft's wing is investigated in the follow-up European project SARISTU (smart intelligent aircraft structures) [9]. This includes the integration of

- Anti-/de-icing functionality
- Erosion protection
- Impact protection
- Bird strike protection and
- Lightning strike protection.

The participating project partners are all well known for their expertise on the specific tasks. There are the Airbus Group Innovations for the design of the aero-mechanical kinematics and the erosion protection concept, Invent GmbH for manufacturing of extreme lightweight fiber-reinforced structures and prototypes, GKN Aerospace for the de-/anti-icing technology, SONACA as specialist for bird strike protection design, VZLU for manufacturing of the kinematic mechanism and bird strike tests (BST) as well as a ground test of a full-scale leading edge section and finally the RWTH Aachen for the technology assessment on overall aircraft level.

Particularly, the effect of the developed design procedure on the design and sizing of smart leading edge devices developed in the previous projects is of interest. Furthermore, the design of a smart droop nose device in SARISTU is focused the first time on the outboard wing due to demonstration and testing activities of a full-scale outboard wing section in a wind tunnel test. The small design space and the large curvature at the leading edge tip of airfoils with small chord length are additional challenges for the design.

2 Design Concept and Integration

For the development of the smart droop nose device, a structural concept and idea for the realization of the device and a design and sizing procedure are needed. The design procedure must be adapted to the special characteristics of morphing structures for the sizing and optimization of the smart leading structures. A starting point for the structural concept for the realization of the smart leading edge is the patent DE 2907912-A1 [10]. It features a completely closed skin without any steps and slots and a comparably simple inner mechanism for actuation of the device. However, the design of the flexible skin is not defined in detail. For the design and sizing, the applied design procedure has to comply with the adverse requirements of morphing structures, which are as follows:

- Large deformation but at minimum strain
- Stiff enough for high surface quality under aerodynamic loading but low actuator forces for the shape changing
- Load-carrying inner kinematic mechanism for high surface quality under aerodynamic loading but low complexity.

The targeted wing section is the outer wing of a business jet reference aircraft. The overall main characteristic geometry relevant for the leading edge design is given below (Fig. 1). In order to demonstrate the technology readiness level of the integration of the various functionalities, several demonstrators have been realized within SARISTU (Fig. 2). The objective of the ground test demonstrator (GT) is the investigation of the combination of wing bending and deployment of the leading edge.

Of special interest are the effects on stress/strain and the stability of the structure due to the state of double-curved structure when loaded. Moreover, a cyclic test is performed to identify components or locations which are prone to fatigue. The wind tunnel demonstrator (WTT) is tested in the T-104 wind tunnel at TsAGI Moscow up to a flow speed of about 120 m/s. The objective here is to investigate the structural deformation under relevant aerodynamic loading. In the BST, two different kinds of bird splitters are tested. Since the morphing skin is relatively thin to allow for large deformations, bird strike protection is integrated by a stand-alone bird splitter structure. Besides a standard solid aluminum splitter, a hybrid splitter made of aluminum sheets and an aluminum honeycomb core is tested. There will be two shots on the splitter structures: one without skin and one with a complete assembly including skin and kinematics to check the effectiveness of the bird strike protection.

Since a sufficient technology readiness of some functionalities to be integrated, i.e., especially the erosion protection layer, could not be achieved before the design freeze for the wind tunnel and ground test models, there are two additional demonstrators (Ti1 & Ti2). These demonstrators are equipped with a titanium erosion shield and demonstrate one approach for erosion protection of shape adaptable structures.

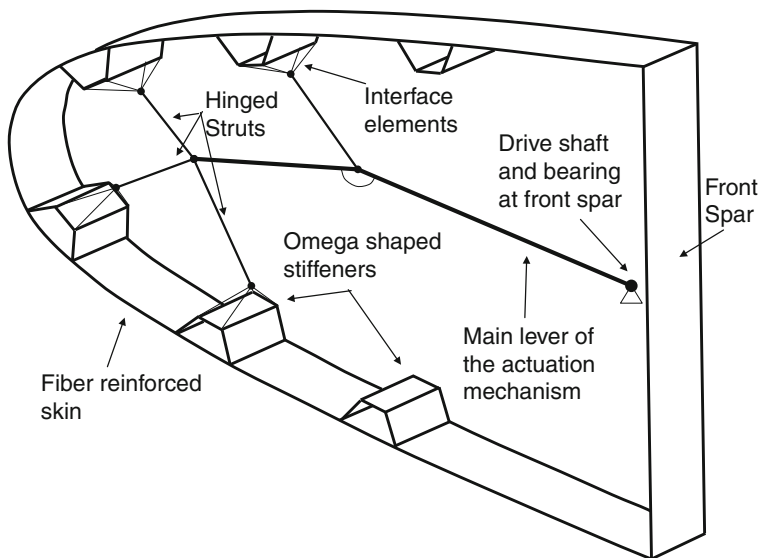
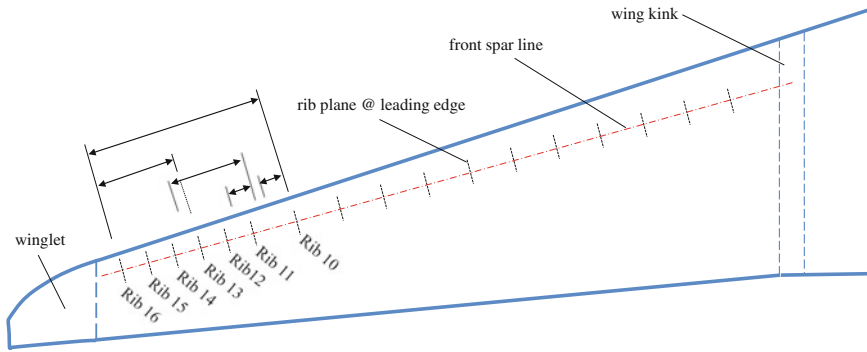


Fig. 1 Design concept for a monolithic morphing leading edge for a conventional skin material



Acr.	Rib Station	Length	Test/Demonstrator	Topic
GT	Rib 10 – Rib 16	3656mm	Large scale test: wing bending, cyclic, heater-mat	Shape, Strain, Strength
WTT	Rib 13 – Rib 16	1760mm	Test under aerodynamic loads	Shape, Strain
BST	Rib 11 – Rib 12	1600mm	Bird Strike Tests, 3 configs: 2x splitter, 1 hybrid	Bird Strike Performance
Ti1	Rib 10	300mm	Demonstrator with Ti-foil (full-chord) & heater-mat	Shape
Ti2	Rib 11	300mm	Small scale test with Ti-Foil (Patch)	Shape, Strain, Strength

Fig. 2 Overview of leading edge sections and test manufactured/performed in SARISTU

3 Morphing Skin

Based on the patent [10], the developed structural concept (see Fig. 1) features a flexible glass fiber structure of the leading edge skin which is actuated by conventional actuators and kinematic mechanisms with several stations in span direction. The glass fiber structure is especially tailored to achieve a desired aerodynamic target shape. The structure is fully closed in chord direction so that there are no steps and gaps and a high-quality surface is guaranteed. The actuator forces are introduced into the skin structure by an inner kinematic mechanism which is attached to the skin using spanwise-oriented omega stringers as load introduction structure. The objective of the design procedure is a GFRP skin which is tailored for achieving a predefined target shape when actuated at a minimum of load introduction points. To reduce the strain in the GFRP skin when actuated, the design process is based on a certain design philosophy. This philosophy allows only bending of the structure when actuated without considering aerodynamic forces, so that membrane stresses and strains are avoided. This enlarges the allowable deformation, since the bending strain when deformation is not superimposed by membrane strain. By tailoring the skin thickness, the stiffness distribution, and especially bending stiffness, is adapted in a way that

- A minimum of load introduction points is needed for actuation of the airfoil.
- The stiffness is sufficient to carry the loads in cruise flight and provide a high-quality surface.

- The target shape when deployed can be provided considering the aerodynamic loads in takeoff and landing.

However, for the leading edge, this design philosophy allows for large deformation of the airfoil since the leading edge represents a continuous geometry. The critical strains are observed at positions of large difference in curvature between undeformed and deformed shapes of the leading edge since the bending strain ε depends directly on the difference in curvature $\Delta\kappa$ and the thickness t of the skin

$$\varepsilon = \frac{1}{2}\Delta\kappa t. \quad (1)$$

Therefore, flexibility at locations of large difference in curvature between undeformed and deformed shapes of the structure is provided by tapering the skin to a minimum skin thickness. However, the integrated functional layers in the stacking sequence lead to an unsymmetric laminate (see sketch in Fig. 3). Therefore, the neutral fiber of the laminate is shifted out of the symmetry plane of the laminate thickness. This effect is especially important to take into account in the design process, especially if an erosion protection shield of a relatively high stiffness compared to GFRP like titanium is selected. The additional functional layers lead not only to an increased stiffness compared to the basic GFRP design but also to a limitation of the maximum achievable difference in curvature between undeformed and deformed shapes of the structure. The main reasons are the increasing thickness of the laminate and the shifting of the neutral fiber.

In Fig. 4, the position of strain gauges and the result from finite element analysis are given. The maximum strain considering wing bending and deployment of the leading edge is located at the lower side of the leading edge tip near the position of the integrated brackets for the attachment of the kinematics.

For a two-dimensional consideration, titanium leads to a decrease of strain in most outside layers and to an increase of strain in most inside layers (GFRP). The maximum strain on the inside layers is dominated by the riveting line at the

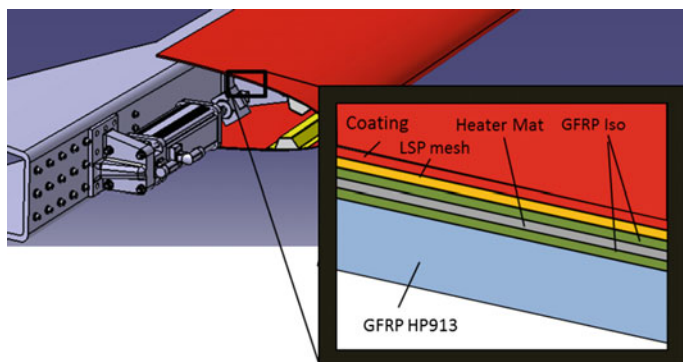


Fig. 3 Schematic of skin stacking sequence with integrated functional layers

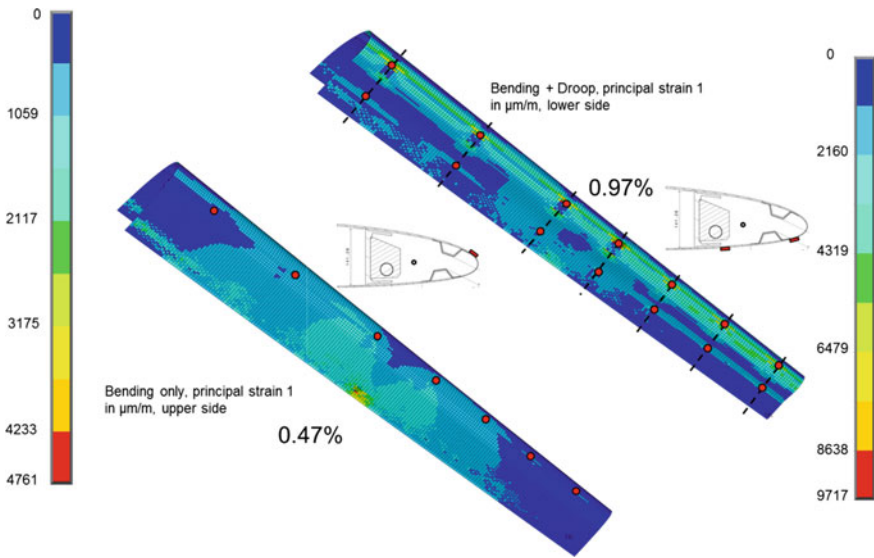


Fig. 4 Position of strain gauges and FE analysis of combined leading edge deployment and wing bending

attachment to the spar. The maximum strain on the outside layers is dominated by the change in stiffness from stringer to skin as presented in Fig. 5.

In the experimental measurements, the maximum strain at the critical locations (SG xx-2, see Fig. 4 and 6) is in good agreement with the calculated strain values. A comparison with values from FEA for pure droop of the EADN is given in Table 1.

With the integration of additional layers (especially the comparably stiff erosion shield), the degree of freedom for the control of the cross-sectional shape is decreasing. Since the adaptation of the cross-sectional shape mainly depends on the difference in bending stiffness which can be realized by tapering the laminate layers, the more functional layers are integrated over the full leading edge chord length and the more stiff the integrated layers are, the less the shape can be adapted to a given aerodynamic shape by tapering the basic GFRP laminate. Furthermore, the achievable shape strongly depends on the maximum strain. As the difference in curvature is increasing in span direction for a shape adaptation with constant parameters,¹ the maximum strain during droop increases as well (Table 1) and the realization of aerodynamically optimized shapes is therefore limited in the outboard sections of the wing. For large changes in curvature as needed on outboard wing sections, new material combination like hybrid GFRP-elastomeric skins as presented in [12] must be applied.

¹Shapes are generated with the droop nose-shaped generator of Kühn and Wild from [11]. Constant parameter is, for example, the droop in percentage of the local chord length.

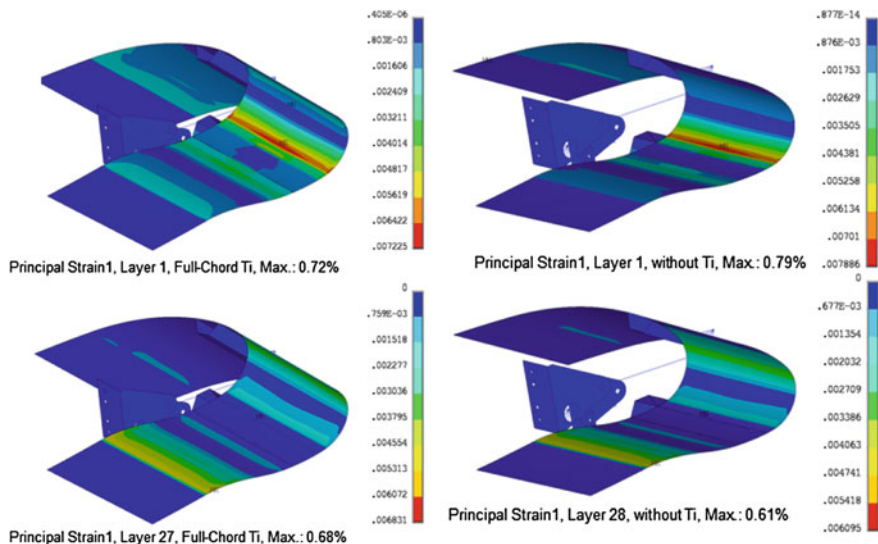


Fig. 5 Comparison of the effect of a titanium erosion shield on the limit strain level (droop only)

Table 1 Experimental strain measurements

SG name	Calculated value of principle strain at max. deflection (FEA, ϵ_1) in $\mu\text{m}/\text{m}$	Measured value in chord direction at max. deflection in $\mu\text{m}/\text{m}$	Difference (%)
SG 10-2	6400	6759	+5.6
SG 11-2	6500	5771	-11.2
SG 12-2	6800	7122	+4.7
SG 13-2	7400	7723	+4.4
SG 14-2	7150	8191	+15
SG 15-2	8400	8792	+4.6
SG 16-2	8577	8886	+3.6

Additionally, the available space is limited significantly by the concept for the attachment of the leading edge. Since an auxiliary spar concept is used for reasons of feasibility, the attachment to the auxiliary spar and to the main spar needs a space of $60\text{ mm} + 70\text{ mm} = 130\text{ mm}$ for riveting the skin to both spars. At the outboard section, this leads to a loss of about 9 % of local chord length which cannot be used for realization of specific shapes from aerodynamic optimization.

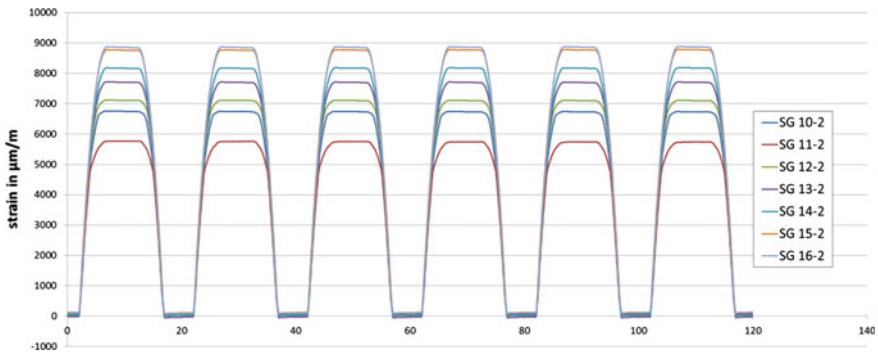


Fig. 6 Experimental results from six deployment cycles in the static ground test. Strain in chord direction at critical locations (SG xx-2) at rib stations 10–16

4 Kinematic Concept

4.1 Introduction

Work on an adaptive droop nose kinematic actuation system started in the previous projects InHiD (LuVo IV) and SADE (EU-FP7) where the feasibility of such a system was demonstrated. In the project SADE (FP7), studies with a different kind of actuation mechanism for smart leading edges were conducted such as eccentric beam mechanism, horn concept, fluidic actuator concept, and kinematic chain [13, 14]. Electromechanical or hydraulic devices are feasible actuator solutions, whereas the utilization of piezoelectric or magneto-resistive material integrated into the structure of the flexible leading edge was ruled out due to unsolved manufacturing, maintenance issues, and power requirement [15].

As the enhanced adaptive droop nose (EADN) in SADE was simply an extruded 2D wing section, within the SARISTU project, it represents a 3D free-formed surface, which has to be smoothly modified between the shape for high-lift and cruise flight [16, 17]. The objective is to develop a mechanical kinematic system with minimal deviation from optimal kinematic path in consideration of limited available design space, aerodynamic loads, and manufacturing constrains. Taking into account the need of simultaneous and uniform deformation of all differently sized kinematic stations implies great effort in the design phase [18].

A separation of actuation and skin is mandatory to meet the joint aviation requirements [19]. The loads introduced by the skin are distributed at discrete support points along the span and in chordwise direction of the wing. As the rotatory movement has to be synchronous for each spanwise kinematic station, consequently, all main levers show the same axis of rotation and uniform kinematic connection to the drive actuator. Hence, the overall system fulfills the requirement of a least complex actuation system by firstly creating and secondly exploiting the advantage of synergies.

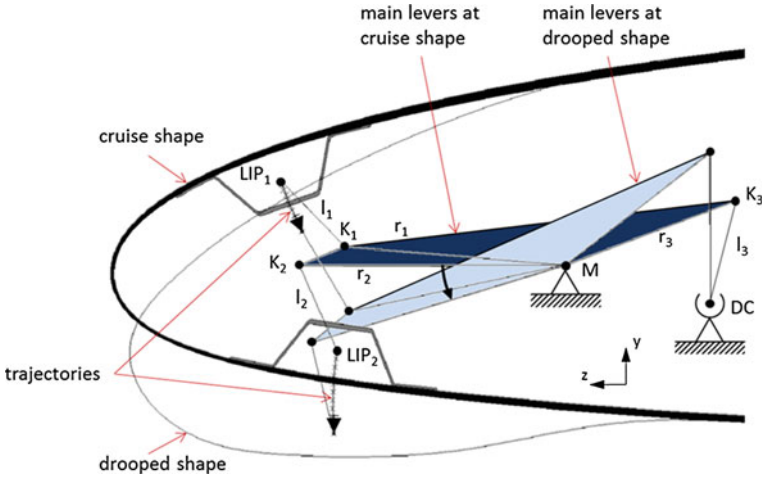


Fig. 7 Cross section of an enhanced adaptive droop nose with an integrated kinematic system for a morphing wing at cruise and (graying out) at droop position

Regarding a single spanwise kinematic station, the main lever is in fact an interconnection of various individual lever (see Fig. 7). The main lever is linked on one side to the overall drive chain DC by using the strut l_3 , whereas the spherical bearings of this strut allow an out-of-plane rotational movement. One huge benefit of this drive mechanism is that the actuator forces are remarkably minimized by supporting the introduced loads by means of the inner structure. This is the result of the varying gearing factor, which is determined by the angle between the cross-link and the drive chain. At droop position, a right angle between the cross-link and the drive chain is designed, which reduces the actuator forces theoretically to zero. On the other side, the main lever is linked to the skin by using the struts l_1 and l_2 , which are attached inside of the stringers at the skin brackets. The measure of locating the load introduction points LIP_1 and LIP_2 inside of the stringers increases the limited design space and, therefore, enables a better kinematic design.

4.2 Numerical Optimization

For optimization purposes, the kinematic system is simplified to a reduced subsystem that consists of a single load introduction point K linked by a lever kinematics l and r with the actuation system DC (further details on this work can be found in [20]). A crucial factor is the main lever, which ensures same rotational angle for all kinematic subsystems. Independent of its actuation, the rotatory movement of the main lever is responsible for simultaneous and uniform deformation of the skin, which is predefined by the trajectories of the load introduction point (provided by project partner DLR). The mathematical formulation of the

optimization problem uses the discrete time positions of LIP trajectories as input parameter, the kinematic points K and M as independent variable, and the rotational angle α as dependent output variable. As the structural conditions limit the position of the axis of rotation M to a small area and a large rotational angle α is desirable to achieve low bending moment, the position M and the angle α are given manually a priori. By this means, the inner optimization loop is considered to apply the quadratic deviation of the calculated rotational angle from the target rotational angle $(\alpha_{\text{calculated}} - \alpha_{\text{target}})^2$ as the optimization function is merely dependent on the position of the kinematic point K . A helpful secondary condition, to fulfill the requirement of simultaneous and uniform deformation of the skin, is given by the variances of all rotational angles at the same time step. The sum of the variances is added to the optimization function by a weighting factor. Depending on the weighting factor, the result of the optimization can be focused on achieving small deviations between the different lever kinematics either at a special droop angle or at a certain range of droop angles. If the result of the inner optimization loop leads to undesirable results like length of struts too short, and crossing struts or angle between skin and struts out of range (70° – 110°), then the target rotational angle has to be adapted or even the axis of rotation M has to be changed.

In the literature, this kind of lever kinematics is described as a crank mechanism with an eccentrically mounted shaft [21]. The different to the presented problem is that the offset q between the rotational axis M and motion direction p is so great that no complete rotation of the lever r is possible, as shown in Fig. 7. Actually, only a pivoting motion is necessary to move the load introduction point from cruise position x_c to droop position x_d . The distance from the top dead center O_B to a random load introduction point B is described by the equation:

$$x = \sqrt{(l+r)^2 - q^2} - l \cdot \cos \beta + r \cdot \cos \varphi. \tag{2}$$

Although the notation of this Eq. (2) is fairly simple, it is hardly possible to transform it in an appropriate form to solve the optimization problem. Another approach has to be taken for the numerical optimization.

The newly selected approach for the equation for the numerical optimization is established based on the law of cosines for arbitrary triangles. The equation calculates the rotational angle α by using the distance formula in the Cartesian coordinate system, which is described as follows:

$$\begin{aligned} \alpha &= \delta - \varepsilon, \quad \text{or} \\ \alpha &= \arccos\left(\frac{r^2 + b^2 - l^2}{2 \cdot r \cdot b}\right) - \arccos\left(\frac{r^2 + b^2 - w^2}{2 \cdot r \cdot b}\right), \quad \text{with} \\ r &= \overline{K_c M} = r', \quad l = \overline{K_c x_c} = l', \quad b = \overline{x_d M} \quad \text{and} \quad w = \overline{K_c x_d}. \end{aligned} \tag{3}$$

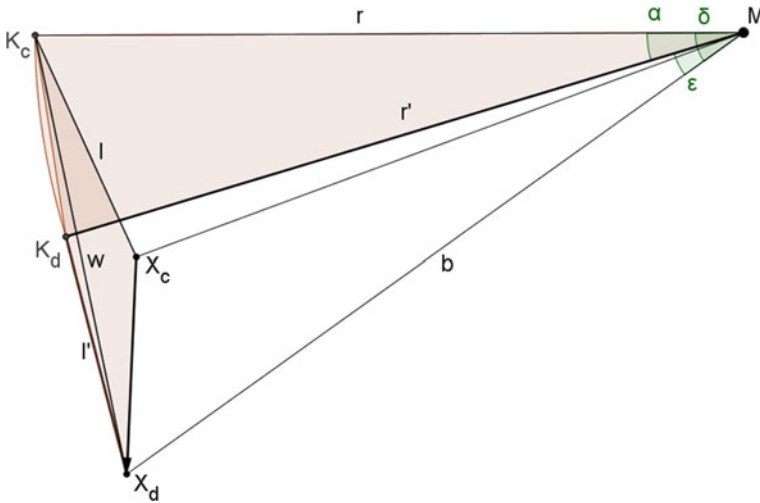


Fig. 8 Geometrical description to the equation applied for the numerical optimization

The improvement of this approach is that the rotational angle α is directly derived by the kinematic points K_c and M for the given load introduction points at cruise position x_c and droop position x_d , as illustrated in Fig. 8.

The drawback of the presented numerical approaches is that the kinematic point K_c could not be derived for a given rotational angle α and axis M . Particularly, the dependency of the rotational angle α would be very helpful, because in most cases, the uniformity of motion can be verified by selecting three different points of the trajectories, e.g., cruise, droop position, and another position in between. Furthermore, the information of possible kinematic points K_c can immediately show whether generally a solution is possible and which measures are necessary to achieve a good solution.

4.3 Geometrical Construction Method

In contrast to the numerical approach, the geometrical construction method allows to visualize all valid kinematic points K_c , which are obtained from inputs given by two load introduction points (e.g., at cruise position x_c and at droop position x_d), rotational angle α and rotational axis M . This methodology (patent pending) enables not only to find a very precise kinematic solution in a convenient way, but also the impact of variation on each parameter becomes obvious and which measures for improvement can be taken. Likewise here, a reduced subsystem consisting of a single lever kinematics is used, which will be assembled to an overall system at the final stage. Geometrically, the possible kinematic points K_c lie along a straight line. If the rotational axis M is fixed, which is usually the case, this line is exclusively

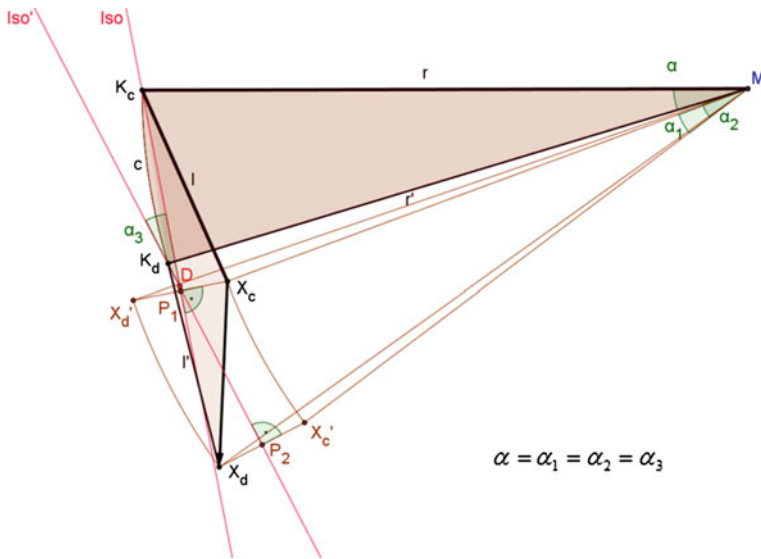


Fig. 9 Graphical illustration of the design procedure for the isogonic lines in case of 2D movement

dependent on the rotational angle α . As curves with equal angle dependency are also described as isogonic lines, this naming will be utilized for the line of possible kinematic points K_c .

One simple method to generate the isogonic line is illustrated in Fig. 9 for the case that the movement of all kinematic points is in-plane. The procedure is as follows: The end point (the load introduction point x_d) is rotated around the rotational axis M by the rotational angle— α to create the new point x_d' . The line segment bisector generated from the two points, the starting point (the load introduction point x_c) and the newly defined point x_d' , characterizes the isogonic line Iso for the start position of all possible kinematic points K_c . The rotation of the line Iso around the rotational axis M by the rotational angle α leads to the isogonic line Iso' characterizing the end position of all possible kinematic points K_d . The idea behind this construction method is that the line segment bisector represents the set of all possible points between two reference points with the same distance to the reference points. This line segment bisector represents therefore the set of points, which have the same distance to the starting points and also to the by— α rotated end points. Points with the same distance to the start points and the by— α rotated end points represent instantaneously the possible kinematic points for this lever kinematics.

The isogonic line provides the information that inaccuracies in production along the isogonic line have no effect on reaching the end position by a given rotational angle α , but could lead to unequal deformation of the skin. On the other hand, orthographic deviations from the isogonic line have huge impact on reaching the

end position, depending on how close together the isogonic lines of different rotational angles α are lying.

Even though the isogonic line represents all valid kinematic points K_c to move the load introduction point from start position x_c to end position x_d of the trajectory, the way of movement between these positions is not constantly progressing and, in fact, is dependent on the location of kinematic point K_c on the isogonic line. That is why, for synchronization of all different lever kinematics, it is favorable not to generate only a single isogonic line but also to take at least another position of the trajectory in between. At a defined time step, the corresponding positions on the trajectory can be taken as an intermediate end position together with an adapted target rotational angle to generate the associated isogonic line. Crossing these isogonic lines indicates the optimum for the kinematic point K_c .

For deformation of the flexible skin of the SARISTU project, there are 14 differently sized lever kinematics required, seven kinematic stations with two lever kinematics each. Its interconnection is achieved by same rotational angle of each main lever. In Fig. 10, the cross section of SARISTU airfoil with all lever kinematics is shown. The characteristic of nearly same slopes of isogonic lines is a sign for an overall good solution, regarding the upper and lower kinematic stations separately. The selected hinge points (K_c) are the result of crossing the isogonic lines with intersection lines. These intersectional lines are selected due to the fact that they represent on average the best solution for simultaneous and uniform

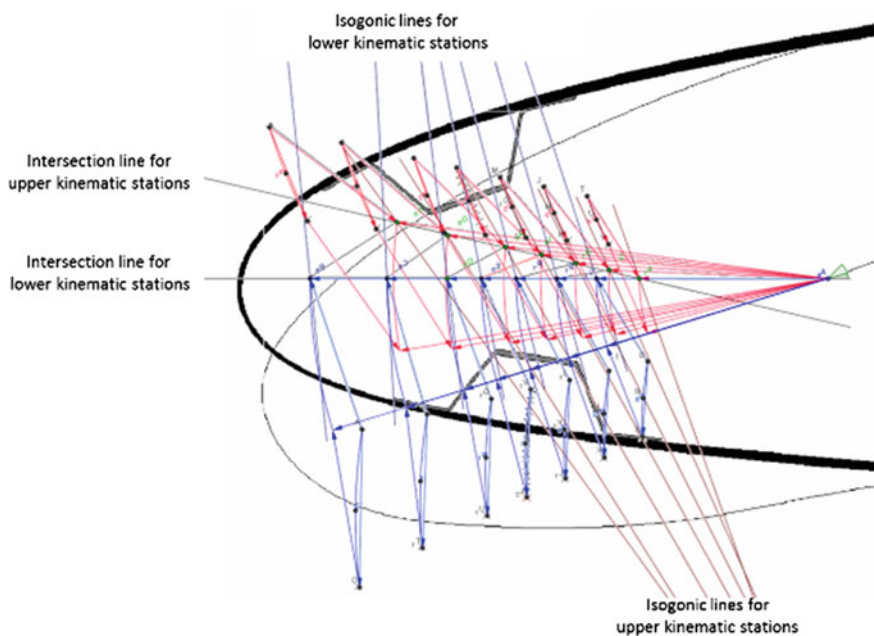


Fig. 10 Cross section of SARISTU airfoil with all lever kinematics together with the overlay of isogonic and intersection lines

deformation. In addition, it simplifies the construction of the kinematics. A further numerical optimization process was deliberately not performed, because the resulting tolerances in manufacturing and assembly are larger than the optimization potential.

Finally, the main levers are linked to the overall drive chain *DC* using a similar lever kinematics, consisting of a main lever *r* and a strut *l* as described above. But the crucial difference is that the movement of the strut connected to the drive chain goes out of plane. Due to the fact that all main levers are synchronized by means of the same rotational axis and rotational angle, only one single design of cross-link is required.

For an arbitrary arrangement of rotational movement and linked trajectories in a three-dimensional space, it is still possible to construct an isogonic line. As shown in Fig. 10, the linear motion of the drive chain (form x_c-x_d) is parallel to the rotational axis of the main lever. For simplification purposes, a coordinate transformation is carried out, whereby the rotational axis through *M* is equivalent to the *z*-coordinate axis. The methodology to generate the isogonic line is similar to the previous description for the two-dimensional case (Fig. 11). Instead of the line segment bisector, the bisecting plane is utilized. Afterward, the intersection of the rotational plane (*xy* plane) with the bisecting plane results in the depicted isogonic line. Particularly for the design of this lever kinematics, connecting the main lever with the drive chain, the isogonic line is helpful. Appropriate kinematic points can be found, which are located within the limited design space and require only low actuator forces.

The presented geometrical construction method can also be easily transferred to other application scenarios. The usage of this geometrical construction method is considerable not only for the development of actuation kinematics of a droop nose in future aircraft, but also for automotive, for watercraft, or even for wind power plants, whenever flexible, fluid dynamic acting surfaces are employed [22].

4.4 Mechanical Design

Some of the information in this chapter can also be found in [23]. In SADE, an individual actuation of each station was deemed important. As such, each station was equipped with a gearbox and a rotary electrical actuator. Assessment of this design philosophy showed an unnecessary complexity and weight (50 % of the weight of each station came from the gearbox and the actuator). As a first change to the SADE concept, a reduction of weight was anticipated by only using one actuator for multiple stations. For simplicity reasons, the first concept to be developed looked at a single rotary actuator for the four WT section stations. The stations were connected with a torque shaft without any sort of gears in between (see Fig. 12).

All four stations are connected via a torque shaft and driven by a single rotary actuator. After a load and precision assessment of this design was performed, it

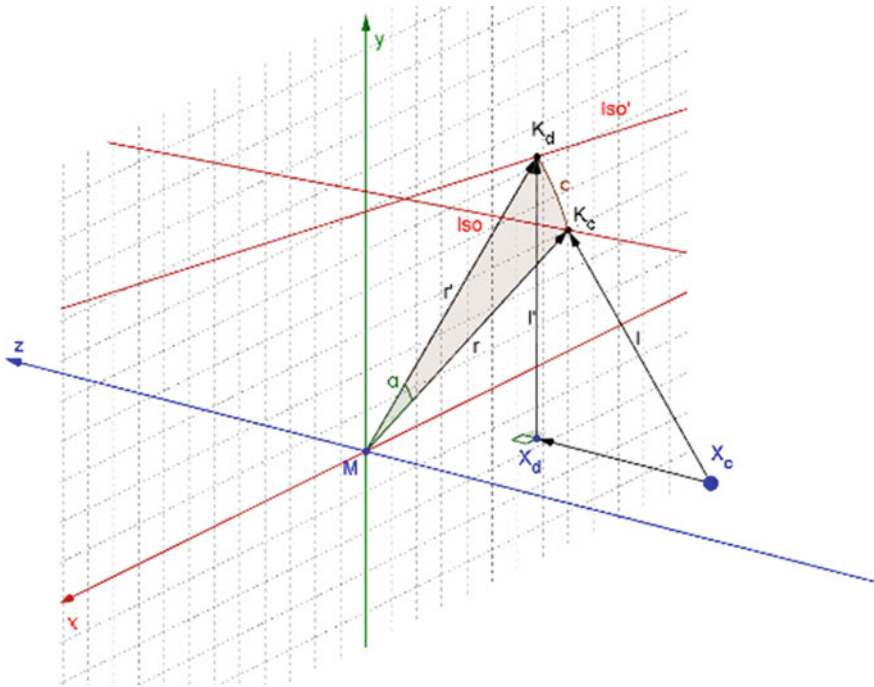


Fig. 11 Graphical illustration for the usage of the isogonic lines to design a drive chain, general 3D construction method

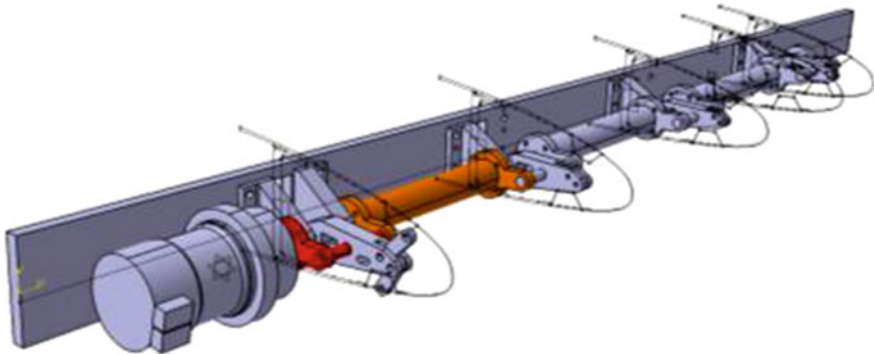


Fig. 12 First design loop with rotary actuation and torque shaft

became clear that this was not feasible. The deformation of the torque shaft grows with each following station, making the deformation less and less precise (the further away from the actuator). To reduce this deformation to an acceptable level would have meant a large increase in weight and in size of the torque shaft.

This design was also too heavy, as the actuator alone weighs roughly 30 kg and is barely able to deliver sufficient torque to all load cases.

Besides the large difference in design space, the design loads in the SARISTU project are much higher than those in SADE. This is in part due to the smaller size of the nose, as the shape of the nose acts as an automatic stiffener; additionally, this (decrease in size) also reduces the torque level of the load introduction points. The other reason for the load increase is that the SADE project only worked with wind tunnel loads [7], whereas SARISTU project works with aircraft sizing load cases. The higher loads coupled with the smaller available space made it impossible to simply scale the SADE system; therefore, a different solution had to be found. As a rotary system was not able to meet the requirements, a linear kinematic system was the next logical step. For this, the forward part of the design was kept as it is; the major change occurred for the drive chain (force transmission).

In this new kinematic drive chain, the linear motion of the actuator is translated via two hinges and one lever into a rotary motion. Figure 13 shows the functionality of the finalized design in detail. The drive chain is a segmented round bar. Each segment is connected to the next via a spherical bearing to counter wing bending and tolerance issues. The drive chain is round for easier friction bearing design and easier assembly. The main lever is connected to the drive chain via the cross-link. The cross-link has a spherical bearing on each end to allow for an out-of-plane rotational movement. The main lever is connected to the skin with two KAP levers (see Fig. 14). The KAP levers are mounted inside the skin brackets. The skin brackets are positioned inside the stringers of the skin. This was done with regard to the limited design space. By moving the force introduction points into the “skin structure,” design space was created which was previously unusable. This enabled a better kinematic design but made the manufacturing more challenging. The brackets

Fig. 13 Linear kinematic concept: functionality

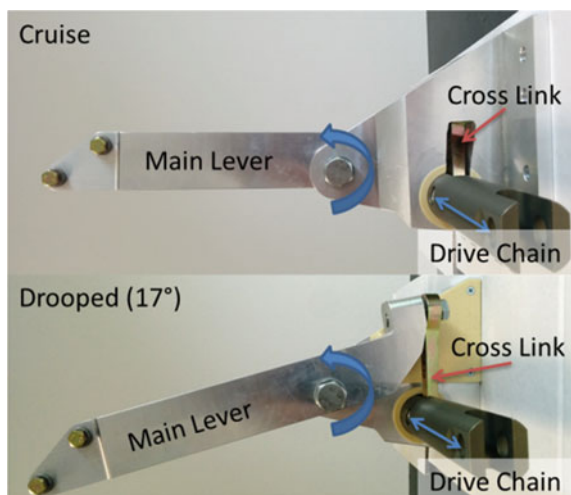


Fig. 14 Finalized kinematic station, detailed view of KAP levers mounted in brackets

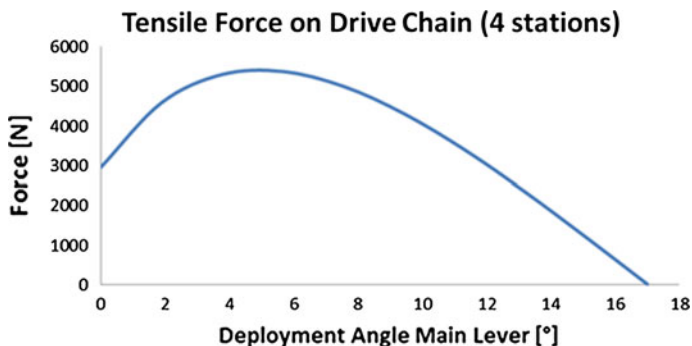
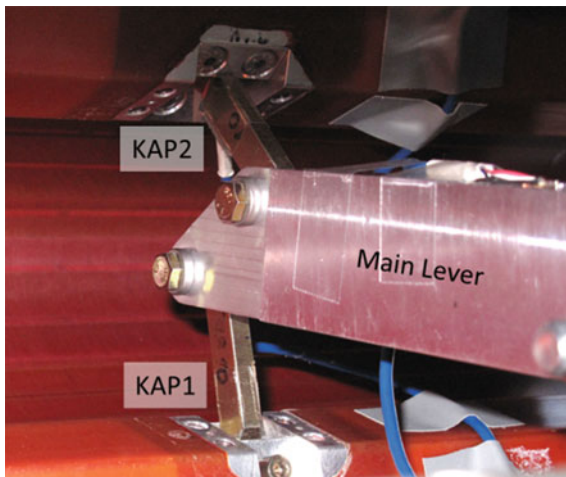


Fig. 15 Force on drive chain versus deployment angle (simulation)

are integrated into the stringers during the manufacturing of the skin at Invent GmbH.

One huge benefit of this design is that the actuator forces are considerably reduced and at maximum deployment angle theoretically vanish completely (Fig. 15). This is the result of the cross-link position and angle to the drive chain. At a 90° angle between cross-link and drive chain, the forces acting along the drive chain are zero. Therefore, the actuator only draws power during movement of the skin, thereby reducing the power requirements for the system dramatically. In undeployed position, a mechanical break keeps the kinematics in place. As is shown in Fig. 15, the force to start the motion is relatively high, quickly reaches its maximum, and declines then until at maximum deployment angle, the force acting along the drive chain (and the actuator) is zero. During various tests, this behavior could be verified.

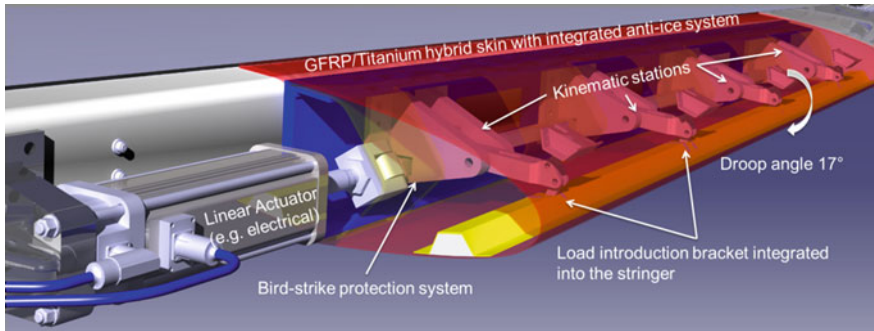


Fig. 16 Full DMU of the AS01 WT-Droop Nose (several details/parts are hidden)

However, the tests indicated a higher force than expected which is most likely due to the application of friction bearings and a supposed stick-slip behavior.

The design is modular, making it easy to add or remove stations. Additionally, the segment rearward the main hinge is identical on all stations. Figure 16 shows a WT-DMU of the complete EADN with all relevant systems included.

In Fig. 17, the finalized demonstrator for the life cycle test of the kinematics, heater mat, and skin is presented. Missing in this model is the bird strike protection structure as it has no impact on this test and the integration is shown at the bird strike test. Also missing is the titanium skin due to manufacturing issues of the titanium foil. The ground test is performed at VZLU and is still running at the time this paper is written, and therefore, no test data is included herein.



Fig. 17 Fully integrated droop nose at VZLU during life cycle ground test

4.5 Weight Estimation and Comparison with Previous Design

For the EADN, an integrated kinematic system is developed based on the aerodynamic requirements and thereof derived load cases. Based on these load cases, all parts were sized (nonstandard parts) and/or selected (standard parts). Either all nonstandard parts of the kinematic system were analyzed using analytical methods (e.g., HSB) or a finite element model was created. With the sizing completed, a weight assessment could be performed.

To be able to compare the weight of two separately developed concepts (SADE vs. SARISTU), at least a similarity in size had to be created. It was stated repeatedly that the SARISTU concept operates inside a much smaller space, and therefore, the system (shown above) is much smaller than that used in the SADE concept. To equalize this difference, the weight of each station (RIB10–16) in the SARISTU concept was measured and then used to extrapolate the larger stations (RIB1–9). As the underlying airfoil is different, the most reliable factor for comparison is the chordwise “length” of each station. This length is measured from the tip of the main lever to the front of the front spar. The weight of each station is given in Table 2. The weight herein contains only the structural mass of each station, and the weight of the skin or the actuator is not considered. Figure 18 shows the position of the kinematic stations along the leading edge of the wing (outboard of the kink).

In Table 2, the RIB3 is emphasized in bold as this station is comparable in size to the in SADE-developed station. Based on this, a weight estimation of a complete station was performed.

Weight estimation of SARISTU kinematic station at RIB3 is as follows:

$$\approx \underline{3.6 \text{ kg (structure)} + 1/8 \text{ of } 24 \text{ kg (motor)} + 2.5 \text{ kg (drive chain)}} \\ = \mathbf{9.1 \text{ kg}} \text{ (} \rightarrow \text{ sized for “real” loads!)}$$

The motor assumed in this calculation is a 24 kg electrical motor with a maximum continuous force of 31kN. It was further assumed that this motor would be used to drive stations on RIB1-8. As such, only two motors would be necessary for the complete section RIB1-16.

A schematic of the SADE kinematic is shown in Fig. 19. Fasteners are not shown, but included in the weight estimate.

Table 2 Weight comparison of the different stations (weight estimated for RIB1–RIB9)

Position	RIB1	RIB2	RIB3	RIB4	RIB5	RIB6	RIB7	RIB8	RIB9
Weight (kg)	4.000	3.816	3.629	3.442	3.255	3.068	2.881	2.694	2.507
Length (m)	0.635	0.577	0.525	0.477	0.434	0.394	0.358	0.326	0.296
Position	RIB10	RIB11	RIB12	RIB13	RIB14	RIB15	RIB16		
Weight (kg)	2.320	2.147	2.053	1.963	1.847	1.716	1.620		
Length (m)	0.267	0.239	0.217	0.205	0.192	0.177	0.163		

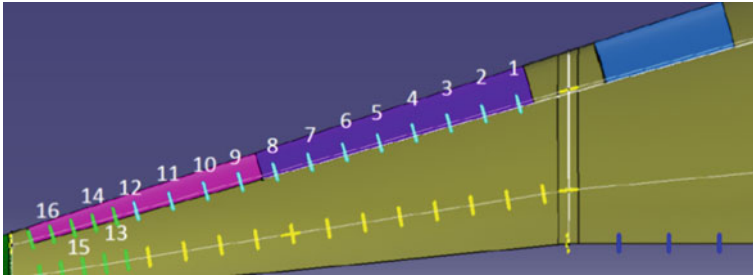


Fig. 18 Kinematic stations on the wing (outboard of the kink)

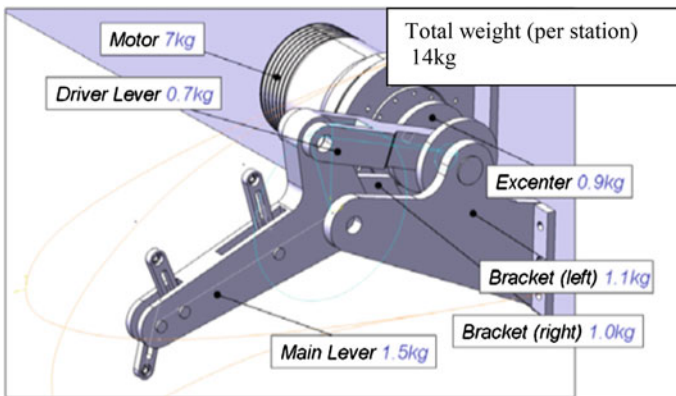


Fig. 19 SADE kinematic station weight estimate

The SARISTU kinematics achieves a weight reduction of about 35 % in comparison with the SADE kinematics. Additionally, it has to be mentioned that the SADE kinematics was designed only for wind tunnel loads, whereas the SARISTU kinematics is designed with regard to sizing loads of a wing (gust and maneuver loads). Figure 20 shows a SADE kinematic station at full deployment during initial functionality testing. As shown in Fig. 19, a SADE kinematic station weighs about 7 kg without the motor and 14 kg with the motor. Both designs are still not fully optimized, for example, in both cases, the selected motors run faster than required for the chosen tasks. Also, a system assessment with regard to failure and hazard analyses should be performed, before a finalized weight assessment can be made. Nonetheless, the SARISTU design shows an improvement in terms of weight, scalability and power consumption.

Fig. 20 SADE kinematic station in WT demonstrator (deployed position)



5 Technology Assessment

5.1 Introduction

Highly matured conventional aircraft systems and designs make it necessary to closely evaluate the potential benefit of new technologies before detailed and expensive effort is put into product development. Comparison on system level often lacks the ability to capture the full potential of technologies due to the restriction that not the entire aircraft model is fully sized with respect to the changes inflicted by the system. Conceptual aircraft design is well suited for this application as its main goal is to assess the performance on overall aircraft level while being able to implement changes to its specifics detailed enough to capture the necessary sensitivities.

The morphing technologies developed in the SARISTU project are aimed to increase the aircraft performance mainly in economical regard while increasing the weight of specific subsystems. For this purpose, an assessment on overall aircraft level is unavoidable in order to give a true evaluation of the performance impact. The application scenario findings have therefore been incorporated in several conceptual aircraft design models and their performance is evaluated.

5.2 *Assessment Platform*

During recent years, a software environment has been developed at the RWTH Aachen University Institute of Aerospace Systems (ILR). The software is named Multidisciplinary Integrated Conceptual Aircraft Design and Optimization (MICADO) [24] and fulfills the above-mentioned requirements necessary for the evaluation of the morphing technologies of SARISTU and has been used for the assessment of morphing devices in previous publications [25].

5.3 *Integration of the EADN*

The EADN developed by application scenario 1 (AS01) is a leading edge device which significantly reduces or eliminates the gap between the leading edge device and the wing box. At a conventional slat, this gap leads to transition from laminar to turbulent flow. For this reason, the main aspect that has to be integrated in MICADO is the increased area of laminar flow. MICADO has a tool chain implemented which includes the MSES [26] flow solver and tools for transition point determination. This tool change is described in dedicated publications [27].

For the weight implementation, the weight of the wind tunnel demonstrator EADN is scaled to the full span of the leading edge devices. This weight is distributed not only to the structural mass of the leading edge devices, but also the motor weight of the EADN is incorporated in the flight control system mass according to the ATA chapter definition. The design of the wind tunnel demonstrator has the potential of weight optimization and can be expected to be lighter if a detailed design is applied. On the other hand, additional weight for controlling and redundancy-driven weight increases are also likely.

Furthermore, an electrical anti-icing system has been implemented in MICADO as has been in the EADN wind tunnel demonstrator. This leads to a decrease of bleed air offtakes and an increase in electrical power demand which in consequence impacts the weight of the electrical generators.

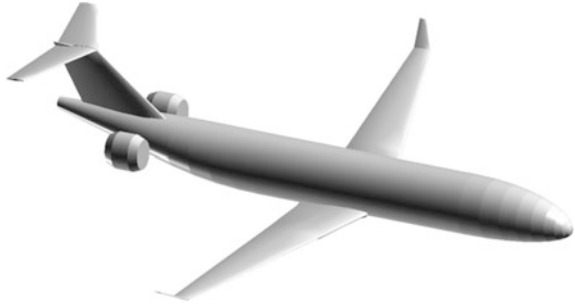
5.4 *Aircraft Models for Comparison*

In order to assess the benefit of the EADN, several aircraft models are designed and assessed. Furthermore, the integration of the EADN is introduced stepwise to analyze the impact of the specific implementation aspect.

5.4.1 **Fully Turbulent Baseline Model**

The first model represents the configuration chosen for SARISTU, which is shown in Fig. 21. This configuration has fuselage-mounted engines in order to avoid flow

Fig. 21 SARISTU aircraft configuration



disturbing influences of wing-mounted engines. The plan form of the wing features a wing with high aspect ratio with small leading edge wing sweep in order to support a large surface fraction with laminar flow. The control device setup is conventional with slats along the entire leading edge of the wing and single slotted flaps on the trailing edge. In this first model, the flow over the airfoils is calculated fully turbulent in order to quantify the benefit of the laminar flow areas introduced in the next aircraft models. This aircraft model will be the baseline and reference for all aircraft models.

5.4.2 Non-Morphing Reference Model

The second model introduces areas of laminar flow. These areas, however, are restricted by the gap between slat and wing box to 20 % of the chord. This leads to a reduction in viscous drag and thereby to a reduced fuel burn and consequently lighter overall aircraft weight compared to the baseline model.

5.4.3 Transition Determined Model

For the third aircraft model, the transition from laminar to turbulent flow is determined for the SARISTU wing geometry. This transition location lies well beyond the slat gap, which justifies the assumption of the second model that laminar flow can be expected until the slat gap. The larger areas of laminar flow lead to a further reduction of block fuel. The assumption of laminar flow beyond the slat gap requires gap less leading edge devices as the EADN. The necessary system impacts of the EADN are incorporated in the next aircraft model.

5.4.4 EADN Model

The EADN model incorporates the aforementioned aspects. The present weight estimations lead to a small weight reduction for the EADN system compared to slat

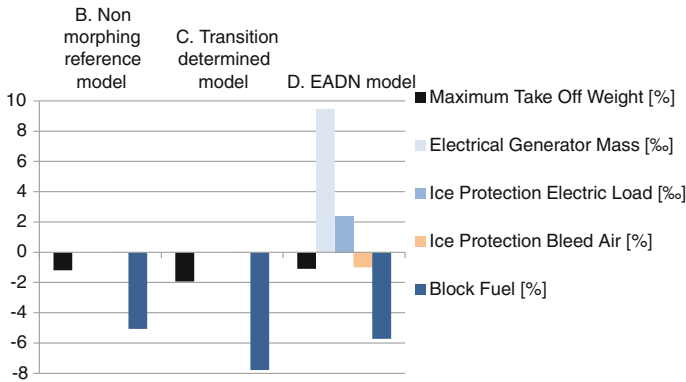


Fig. 22 Changes of assessment parameters toward the baseline model (A)

leading edge devices if the kinematic chain and hydraulic components as the power control unit are considered. This reduction is more than compensated by the increase of generator weight due to the electrical anti-icing systems. The overall increased weight reduces the block fuel reduction gained by the laminar flow.

5.5 Comparison Results

The results of the comparison are shown in Fig 22. As described before, the values are percentage values relating to the fully turbulent baseline model (A). For the non-morphing reference model (C), MTOW and block fuel are reduced as was expected.

This reduction is even stronger for the transition determined model, as was expected. For the EADN model (D), the strong increase of the electrical generator mass is visible. Thereby, the MTOW reduction is smaller compared to the model C. Consequently, the block fuel reduction is smaller as well. However, the block fuel reduction is still bigger than that in model B.

6 Conclusion

In this paper, the design challenges and the assessment for the SARISTU enhanced adaptive leading edge device for a single aisle passenger aircraft is presented. With this study, a big step is taken toward industrial application of morphing wings, considering the fulfillment of industrial requirements. The major design drivers for the skin performance (shape, i.e., maximum deformation and waviness) are as

follows: available space, material stiffness of the erosion protection layer, and dielectric properties of the basic material.

1. Due to small available space for the kinematic design especially at outboard sections of the wing, special brackets had to be integrated into the stringer head for attachment of the kinematics to the structure. This leads to stress/strain peaks near the load introduction points and to inflexibility at these locations which lead for their part to undesired local changes in curvature (waviness).
2. Since the target shape is achieved by tapering the basic GFRP material to a desired bending stiffness distribution, the full-chord material used for the erosion protection (here titanium) jeopardizes this principle if the material is much stiffer than the basic material. In consequence, desired target shapes cannot be obtained anymore. Titanium is selected because of its excellent erosion protection performance on the one hand, and on the other hand, a material for high strain application is needed. However, cyclic bending tests show that even the application of titanium as erosion shield on morphing structures is not able to withstand more than a few thousand cycles of loading before delamination or cracking.
3. For electric isolation of the heater mat for de-icing, certain dielectric properties of the basic material are mandatory. If not sufficient, additional isolation layers must be used. This approach, however, leads to thickening of the skin in regions where a thin skin for maximum flexibility is absolutely essential and additionally an ineffective heating due to increased thermal isolation.

Concluding the skin design, the next generation solution for such kind of design may be the application of nonmetallic erosion protection layers, a basic material with improved dielectric properties and compliant mechanisms for regions with less available space to avoid the integration of brackets and to preserve the stringers as a compliant mechanism in chord direction for a smooth shape.

Over the course of the paper, the challenges related to the development of a highly integrated adaptive droop nose kinematics are explained. The various design requirements and an optimization concept is presented. The design tool enables to optimize the kinematics to follow the specified trajectories by taking into consideration the length of levers and the angle between skin and lever. Likewise, an emphasis can be placed on a selected range of the trajectories to increase the level of accuracy there. In order to simplify the actuation system, the kinematics can be designed for identical droop angle and rotational axis for all kinematic stations. Based on the optimal solution, a detailed mechanical design is performed and compared to a previous development. It is noted that the design still is not completely optimized in terms of weight and that for an assessment on aircraft level, a safety hazard analysis of the complete EADN should be performed. Additionally, a fully developed maintenance concept is also missing. However, the comparison showed that significant progress in terms of weight reduction is made. Also, the scalability of the concepts was demonstrated. The complexity in terms of number of parts is reduced as much as possible.

From overall aircraft view, the enabling large areas of laminar flow on the wing by natural laminar flow showed an improvement of LoD of over seven percent compared to the fully turbulent wing. The necessary system architecture changes (i.e., the application of an electrical anti-icing system) reduce this fuel burn saving. The slightly lighter weight of the EADN, compared to a slat with its kinematic chain, has a positive impact. Taking these aspects into account, a fuel burn saving of over five percent has been estimated.

Information about the performed BST and simulations of the EADN can be found in a corresponding SARISTU conference paper by C. Chary (SONACA). Additional information about the performed cyclic testing can be found in a corresponding paper of V. Snop (VZLU), and information about the tooling design and manufacturing can be found in a corresponding paper by O. Heintze and S. Steeger (Invent).

Acknowledgments We would like to thank all participating partners from the FP7 project consortium SARISTU for the good teamwork and the support during the development of the enhanced adaptive leading edge. We especially enjoyed working together in the AS01 team with Invent, VZLU, SONACA, and GKN. The research leading to these results has received funding from the European Union's Seventh Framework Programme for research, technological development, and demonstration under grant agreement No. 284562.

References

1. ACARE, Vision 2020, European Commission
2. ACARE, Flightpath 2050, European Commission
3. De Gaspari A, Ricci S (2013) Active camber morphing wings based on compliant structures. In: Proceedings of the 2013 AIDAA conference of the Italian association of aeronautics XXI conference, Naples, Italy, 9–12 Sept 2013
4. Weber D, Mueller-Roemer J, Simpson J, Adachi S, Herget W, Landersheim V, Laveuve D (2014) Smart droop nose for application to laminar wing of future green regional A/C. Greener Aviation 2014, 12.03.-14.03.2014, Brussels
5. Thuwis GAA, Abdalla MM, Gürdal Z, Optimization of a variable-stiffness skin for morphing high-lift devices. Smart Mater Struct 19:124010
6. Wild J, Pott-Pollenske M, Nagel B (2006) An integrated design approach for low noise exposing high-lift devices. 3rd AIAA flow control conference, San Francisco, CA (USA), 5 Jun 2006–8 Jun 2006
7. Monner HP, Riemenschneider J, Kintscher M (2012) Groundtest of a composite smart droop nose. AIAA/ASMR/ASCE/AHS/ASC 2012, Honolulu, Hawaii, 23–26 Apr 2012. ISBN 10.2514/6.2012-1580
8. Kintscher M, Monner HP, Kühn T, Wild J, Wiedemann M (2013) Low speed wind tunnel test of a morphing leading edge. In: Proceedings of the 2013 AIDAA conference of the Italian association of aeronautics XXI conference, 9–12 Sept 2013, Naples, Italy
9. SARISTU, FP7 project-consortium. <http://www.saristu.eu>
10. Zimmer H (1979) Quertriebskörper mit veränderbarer Profilierung, insbesondere Flugzeugflügel. German Patent No. DE 2907912-A1
11. Kühn T, Wild J (2010) Aerodynamic optimization of a two-dimensional two-element high lift airfoil with a smart droop nose device. 1st EASN association workshop on aerostructures, 7 Oct 2010–8 Oct 2010, Paris, France

12. Schmitz A, Horst P, Rudenko A, Monner HP (2013) Design of a contourvariable droop nose. In: Forschungsbericht 2013-03, TU Braunschweig Braunschweig: Techn. Univ., Campus Forschungsflughafen. Seiten 110-121. ISBN 978-3-928628-63-1
13. SARISTU 1st Periodic Report Publishable Summary, SARISTU Consortium
14. Monner HP, Kintscher M, Lorkowski T, Storm S (2009) Design of a smart droop nose as leading edge high lift system for transportation aircraft, AIAA
15. SADE Newsletter (2012) SADE Consortium. www.sade-project.eu/publications.html
16. Lorkowski T (2010) Aktuatorssystem für "Morphing Devices". In: Hochauftriebskonfigurationen, Invited Lecture, DLR Wissenschaftstag, Braunschweig, 30 Sept 2010
17. Kintscher M, Wiedemann M, Monner HP, Heintze O, Kuehn T (2011) Design of a smart leading edge device for low speed wind tunnel tests in the European project SADE. *Int J Struct Integr* 2(4). ISSN: 1757-9864, 2011
18. Monner HP, Riemenschneider J, Kintscher M (2012) Groundtest of a composite smart droop nose. AIAA/ASMR/ASCE/AHS/ASC 2012, Honolulu, Hawaii, 23–26 Apr 2012. ISBN 10.2514/6.2012-1580
19. Patent (1979) Lift generating body for example an airfoil of adjustable variable cross-sectional shape, DE19792907912, Dornier Werke
20. Storm S, Kim J (2015) Towards the industrial application of morphing aircraft wings—development of the actuation kinematics of a droop nose, SMART 2015—7th ECCOMAS thematic conference, S. Miguel, Azores, Portugal, 3–6 June 2015
21. Grote KH, Feldhusen J (2011) *Dubbel, Taschenbuch für den Maschinenbau*, 23 Auflage. Springer, Berlin
22. Wolfgang Kempkens. <http://www.ingenieur.de/Fachbereiche/Windenergie/Rotoren-Windraedern-passen-Form-blitzschnell-Wind-an>
23. Kim J, Storm S (2014) Kinematic solution for a highly adaptive droop nose, ICAST2014: 25th international conference on adaptive structures and technologies, 6–8 Oct 2014, The Hague, The Netherlands
24. Risse K, Lammering T, Anton E, Franz K, Hoernschemeyer R (2012) An integrated environment for preliminary aircraft design and optimization. Paper presented at the 8th AIAA multidisciplinary design optimization specialist conference, AIAA, Honolulu, HI, submitted for publication
25. Peter F, Lammering T, Risse K, Franz K, Stumpf E (2013) Economic assessment of morphing leading edge systems in conceptual aircraft design. Paper presented at the AIAA 51st aerospace sciences meeting (ASM), AIAA, Fort Worth
26. Drela C, A users guide to MSES 3.05. Technical report, MIT Department of Aeronautics and Astronautics
27. Risse K, Stumpf E (2014) Conceptual aircraft design with hybrid laminar flow control. *CEAS Aeronaut J* 5:333–343

Part II

Technology Stream: Morphing. The Adaptive Trailing Edge Device (ATED)

Introduction and Overview

The adaptive trailing edge device (ATED) is aimed at developing technologies for realizing a morphing wing extremity for the improvement of general aircraft performance. Civil aircraft flight profiles are quite standard, but different missions may be flown (fast or slow, at low or high altitude). Lift coefficient can span over tenth to unit, while weight reduces by around a quarter as the fuel burns. The best aerodynamic configuration then changes, having to match new conditions. The project addresses medium-range aircraft (around 3h cruise flight). Chord-wise camber variations are implemented through trailing edge (TE) adaptations to get the optimal geometry for different flight conditions. Upgrades are herein estimated in terms of reduction of needed fuel or range increase, expected to amount to 3 % or more. Lift-over-drag (L/D) ratio is the referenced parameter to catch those performance improvements, kept to its optimal value while weight and angle of attack change. Because span-wise action variability could lead to design weight decrease through root bending moment (RBM) reduction, this potentiality can be further exploited.

The study involved 13 companies (large, medium, and small industries, research centers, and universities) from 7 different countries (France, Germany, Greece, Israel, Italy, the Netherlands, and Spain). The wide competences allowed arriving at the important result of actually manufacturing a smart TE, ready for wind tunnel tests and dimensioned to actual operative loads (V dive). Particular technologies (including numerical simulation techniques) were specifically carried out to solve the problems related to this specific engineering challenge: lightness, robustness, compactness, sensitiveness (literally!), and so on, along with the most important—the morphing ability. In detail, morphing is enabled by a multi-finger architecture driven by load-bearing actuator systems. To provide camber variation, devices are designed to work synchronously (2D-type) but can be activated differentially (twist). After information is gained by a widely distributed strain sensor network, the control system drives the actuators actions. An adaptive, highly deformable skin absorbs part of the external loads and insures a smooth profile. The system keeps its

structural properties while actuated, then allowing the preservation of a specific target shape regardless of the action of the operational loads. Static and dynamic responses under external excitation are considered.

The following papers summarize the main achievements which took place in each of the aforementioned steps, giving a focus on the many specialisations herein involved. Namely, the origin of the specifications is tracked, so as to establish the target and the engineering domain boundaries. Next, the structural problem is approached, as a novel fully deformable structure is designed, able to bear the external loads (!). The structure is then completed with the actuation system, something in between the architecture and the morphing control line, providing the ATED with deformation capabilities. To properly accomplish its targets, the device shall be finally integrated with a skin that allows attaining the whole shape envelope, absorbing smoothly the extreme deformations required. Once the design is completed, manufacturing takes place, which is different from the usual processes because it has to integrate active and structural parts; functionality and verification tests are also specific, dealing with an envelope of shapes instead of a defined one.

Adaptive Trailing Edge: Specifications, Aerodynamics, and Exploitation

Giovanni Marco Carossa, Sergio Ricci, Alessandro De Gaspari,
Cedric Liauzun, Antoine Dumont and Moshe Steinbuch

Abstract ATE functional aim is to modify the wing TE shape at high speed in order to obtain an improvement in lift over drag (LoD) ratio in the whole flight envelope, virtually obtaining a wing working always at its actual LoD optimum level. This allows to compensate the weight reduction following the fuel burning and to increase climb and descent A/C performance levels. Initial morphed shapes specification has been obtained by a multidisciplinary optimization process matching the aerodynamic performances and structural loads on wing with a defined level of structural strain for an acceptable duration of skin material life cycle. The so obtained different wing seamless shapes have been further parametrically investigated from aerodynamic point of view so to obtain the most profitable device span and chord extension. Based on these requirements, a full-scale ATE functional concept demonstrator has been designed, sized, and realized, based on reference wing geometry of a 130 Pax jet engines regional A/C

G.M. Carossa (✉)

Air Vehicle Technology, Alenia Aermacchi S.p.A., 10146 Turin, Italy
e-mail: giovanni.carossa@alenia.it

S. Ricci · A. De Gaspari

Department of Aerospace Science and Technology, Politecnico di Milano, via La Masa 34,
20156 Milan, Italy
e-mail: sergio.ricci@polimi.it

A. De Gaspari

e-mail: alessandro.degaspari@polimi.it

C. Liauzun

Aeroelasticity Department, ONERA, 29 av de la Division Leclerc, 92320 Châtillon, France
e-mail: Cedric.Liauzun@onera.fr

A. Dumont

Applied Aerodynamics Department, ONERA, 29 av de la Division Leclerc, 92320 Châtillon,
France
e-mail: Antoine.Dumont@onera.fr

M. Steinbuch

Engineering, Israel Aerospace Industries, 70100 Ben-Gurion Airport, Israel
e-mail: msteinbuch@iai.co.il

with a range of 3000 nautical miles, cruise Mach 0.75, and flight level 35,000 ft. Reference wing aerodynamic studies show the best ATE performances in a relatively high CL range (above 0.5) and for Mach below 0.6. Additional exploitation of ATE has been performed on a light business jet, designed to carry 4 passengers at a speed of Mach 0.65, or fly 1200 nm with 2 passengers. CL range of this A/C is relatively small (below 0.6). In this wing working range, the ATE application seems not to be effective.

Nomenclature

A	Amplitude of oscillation
A/C	Aircraft
ATE	Adaptive trailing edge
CD	Drag coefficient
CL	Lift coefficient
CFD	Computational fluid dynamic
K	Trailing edge (TE) nondimensional angular deflection rate
LoD	Lift over drag
MAC	Mean aerodynamic chord
MTOW	Max. takeoff weight
OEW	Operating empty weight
Pax	Passengers
TE	Trailing edge

1 Introduction

Among mainstream technologies considered in the frame of last years' research projects performed to reduce the environmental impact of next-generation air transport, one is of paramount importance for application to future regional aircraft: to enhance lift over drag ratio in all high-speed flight conditions, thus reducing fuel consumption/air pollutants emission. The basic idea of present concept is to actuate simultaneously some parts of the high-lift devices (HLD) at high speed to modify the wing TE shape in order to obtain an improvement in lift over drag ratio in the whole flight envelope. Key concepts for this technology, treated in SARISTU, are morphing structures relying upon compliant structures and mechanisms applied to the wing trailing edge sections.

2 Specification

Fundamental initial step for morphing concept realization is to supply a suitable set of preliminary requirements able to allow the initial sizing of adaptive TE device. Three different detailed levels of data have been envisaged: aircraft, wing, and TE device. These requirements concern aeromechanic, systems, and structural disciplines and have to be specially tailored to the reference A/C and wing. In particular,

- (a) Top-level requirements of the reference aircraft, as well as of systems architecture;
- (b) Requirements for aerodynamic and structural wing reference configuration such as baseline wing layout and shape (CAD), aerodynamic, and aeroelastic performances;
- (c) Preliminary aerostructural requirements for morphing wing configuration such as aerodynamic loads, needed wing sections' shape changes at defined flight points and relevant resulting preliminary CL over CD.

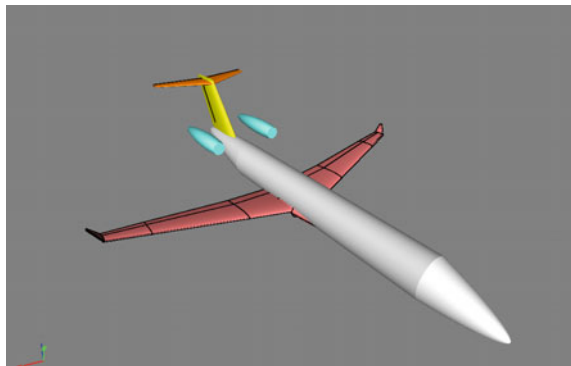
2.1 A/C and Wing Reference Configurations

The general layout and systems architectures of a conventional regional A/C reference aircraft (Fig. 1) have been fixed by means of an aircraft design suite for preliminary design purposes. Resultant reference A/C masses are as follows: MTOW = 60 Tons, OEW = 33 Tons, 130 Pax.

The reference wing is a supercritical wing with blended winglets at the tips with design speed $M = 0.78$, wing reference area 111 m^2 , span 34.14 m, and swept angle leading edge $\Lambda = 18^\circ$ (Fig. 2).

Wing aerodynamic loft lines have been completed with a preliminary linear aeroelastic model (Fig. 3) that represents the stiffness and the inertial characteristics of the SARISTU A/C wing box. Structural stiffness has been sized so to have

Fig. 1 A/C reference configuration



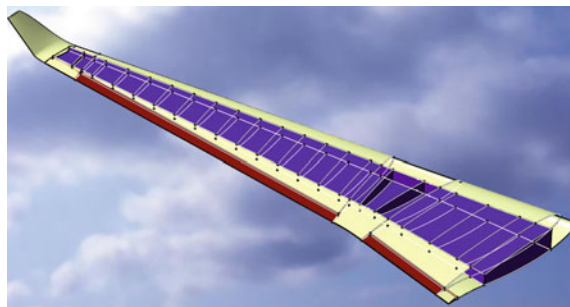


Fig. 2 Reference exposed wing

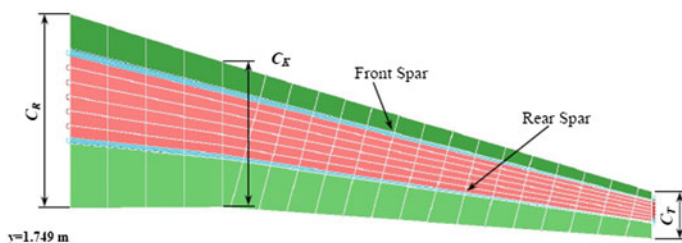


Fig. 3 Aeroelastic wing model

absence of static and dynamic aeroelastic instabilities in the whole A/C flight envelope. Wing surface manufacturing requirements (steps and gaps) for aerodynamic aspects have been defined also by means of semiempirical evaluation and cross-check with existing results for both laminar and turbulent flow regimes.

2.2 *Aerodynamic Shapes Design of Morphing Devices*

The implementation of active camber concept, based on the use of conformable morphing control surfaces, into the SARISTU wing started with the optimal shape design of the morphing wing. Both the performance evaluation in terms of aerodynamic benefits and the computation of the design loads in different morphing configurations have been the targets during this stage of the project. Aiming at the optimal shape design of the morphing devices, a dedicated procedure, based on the combination of a parametric framework called Parametrical sHapes for aerodynamic and structural Modelling of Aircrafts (PHORMA) and a specific optimization, has been used, taking into account both aerodynamic and structural skin requirements. In this paper, only the shape design of the morphing trailing edge for cruise condition is described.

PHORMA is an object-oriented code composed by a suite of tools that allow to exchange and handle different shapes in order to generate corresponding 3D geometries. It can be used for the design of variable camber morphing wings from scratch or can be applied to an already available 3D CAD representation of a reference wing in order to investigate the effect of conformal leading and trailing edge devices. Starting from the CAD model, the shapes, corresponding to a set of the most important sections of the wing model, are locally identified in a parametric way and associated with a set of attributes including the position and the orientation of each section. The core of PHORMA is the CSTv3 tool, based on the CST parameterization technique, originally proposed by Kulfan [1] and extended by PoliMi to morphing airfoils [2]. The 3D parameterized geometry can be directly rebuilt and used to produce the CFD mesh of corresponding models, to provide a fast interface to commercial softwares and to call the commonly used solvers.

The wing was parameterized by combining different parametric airfoils spread along the wing span via particular interpolation surfaces able to reproduce the correct wing thickness distribution in spanwise direction and to accurately describe the original reference wing. The implemented procedure allows to impose different transition laws of the geometry properties among the different airfoils, as well as to modify their global properties such as angle of attack, dihedral, or tow angles. The geometry of the reference wing was rebuilt in a parametrical way in order to have a wing mathematical model suitable to be used to introduce the shape changes into the trailing edge. In this way, PHORMA simultaneously allows to mathematically define the wing shape, run the aerodynamic analysis, and estimate the stress distribution along the skins. This aerostructural scheme allows to combine the estimation of the aerodynamic performances and the skin structural behavior using a small number of design variables.

A total of 13 flight conditions have been analyzed from specification load cases set. The first seven are the same adopted for the structural design of the wing box. The other six are related to the operational conditions of the investigated morphing devices. For each flight condition and morphing configuration, an analysis loop was used to calculate the angle of attack able to guarantee the lift coefficient CL corresponding to the requested load factor.

Finally, the target shapes of the morphing wing have been obtained by an aerostructural shape optimization problem able to define the best shape change to satisfy specifically imposed requirements.

2.3 Aerostructural Shape Optimization

One of the most important obstacles in the wing morphing is due to the structural contribution of the skin. Indeed, even if almost all the proposed approaches for morphing wings are based on a different structural configuration of the ribs, the structural contribution of the skin still remains. In the approach here used, a dedicated optimization procedure is able to determine the best morphing shape able to

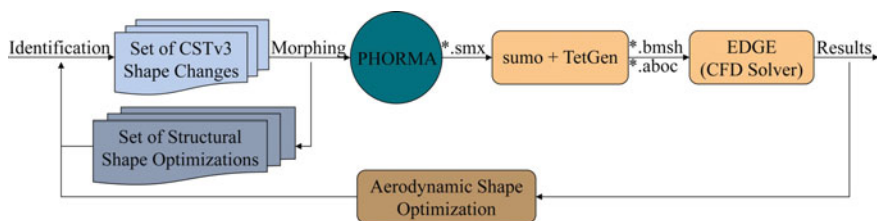


Fig. 4 Scheme of the aerostructural optimization based on the 3D parametric mesh interface

control the deformation of the skin and, at the same time, to limit the power of actuator necessary to control the shape change.

The morphing shape optimization used to introduce shape changes in the SARISTU reference wing model is based on two nested optimization loops (Fig. 4). The outer loop is an aerodynamic optimization able to evaluate the aerodynamic performances directly in 3D space. The 3D geometry is generated combining the set of parameterized airfoils previously subjected to the skin structural constraints via a number of structural shape optimizations, equal to the number of identified sections, which represent the inner optimization loops. In this way, the aerodynamic analyses on the 3D wing shape are performed only starting from feasible morphing shapes. Unstructured surface meshes are generated completely without user intervention. Heuristics parameters can be also tuned to obtain satisfactory mesh. Geometric refinement criteria produce a finer mesh in regions of strong curvature, such as morphing leading edge region, while a limit on the minimum element size can be imposed to correctly resolve the shock wave at the top of the wing. Corresponding unstructured volume meshes can be generated from the surface mesh, provided that Hang Si's tetrahedral mesh generator TetGen is available.

The optimization problem formulation is implemented using the CST representation method both to compute axial and bending stresses along the skins and to generate the wing geometry for the aerodynamic analyses based on EDGE solver, which is a CFD code developed by the Sweden Research Center FOI. The objective function consists of minimizing the aerodynamic efficiency L/D over one or more flight conditions, under the skin structural constraints.

Since different design requirements have been defined for each morphing device, different aerostructural shape optimization problems have been tuned for the different morphing devices.

2.4 Morphing Trailing Edge

The morphing trailing edge has been designed considering the following three different configurations [3]:

1. Morphing TE along 83 % of span and along 10 % of MAC;

2. Morphing TE along 65 % of span (conventional aileron) and along 10 % of MAC;
3. Morphing TE along 65 % of span and along 20 % of MAC in the inboard region.

A subset of the flight conditions was extracted for the evaluation of high-speed morphing device performances. The main design rule from a structural point of view is keeping the strain along the skin less than 2 %. According to the skin material, the following requirements were considered:

- Load condition: cruise;
- Chord: 10 or 20 % (of the CMA);
- Span: 2 morphing areas in spanwise direction (not tapered segment);
- ATE deflection range: $\pm 5^\circ$;
- Max. skin epsilon (strain): 2 %.

The morphing region is divided into two parts along the span by the kink, and each trailing edge device must be a not tapered segment. The shape changes have been introduced into 8 sections so that the morphing shape can be interpolated via piecewise cubic surfaces within each region.

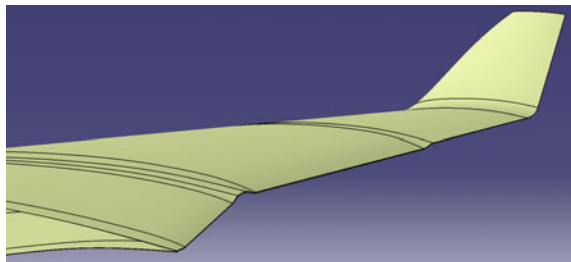
After setting up the optimization problem able to meet the design requirements for the morphing trailing edge device, the 3D morphing shape (Fig. 5), in terms of CAD model, has been obtained from the optimization process.

Aerodynamic performances are initially evaluated by means of CFD Euler computations, and the results reported (Fig. 6) show how the trailing edge shape changes are able to adapt the aerodynamic field over the wing in order to increase the wing efficiency. The results show that in the transonic condition (Mach = 0.74), the morphing trailing edge is able to change the chordwise C_p distribution inside the shock wave.

Figure 7 shows the morphing deformations of the two airfoils placed at the tips of the outboard morphing region.

After generating the Euler mesh, the device performances were evaluated by comparing the polar curves of the 3 previously defined morphing configurations for ATE chord = 10, 20 % local wing chord and for 63 and 85 % of wingspan ATE extensions.

Fig. 5 CAD model of the optimal wing shape with morphing trailing edge device



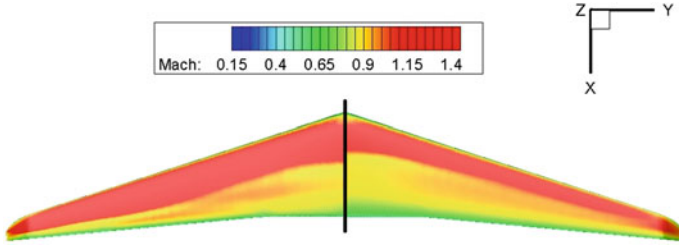


Fig. 6 Comparison between the C_p at cruise Mach (0.74) reference wing (*right*) and the wing equipped with morphing trailing edge (*left*)

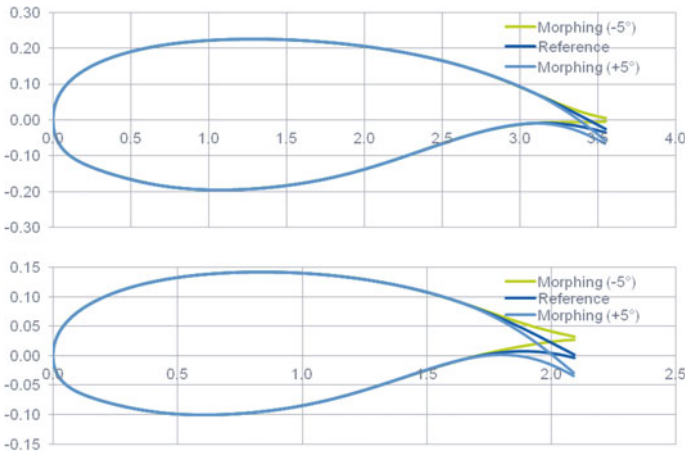


Fig. 7 Morphing airfoils placed at the tips of the outboard morphing region corresponding to the morphing configuration numbers 2 (*top*) and 3 (*bottom*)

Results are reported in Fig. 8a. In cruise conditions, the second configuration (10 % chord, 65 % span extension) gives the greatest drag save for “cruise” speed (Mach 0.74). In “off-design” conditions (i.e., Mach = 0.6), as shown in Fig. 8b, the beneficial range is extended to higher C_L values. It should be pointed out that these

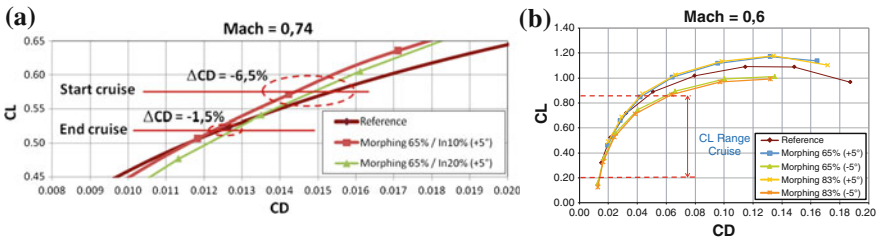


Fig. 8 **a** Polar curves’ comparisons “cruise” $M = 0.74$ performance evaluation and **b** polar curves’ comparisons “off-design” $M = 0.6$ performance evaluation

results are related to the wing and that the benefits would be lower if the contribution of the fuselage was taken into account. In all cases, the ATE deflection reporting the best performances is downward $+5^\circ$. Based on previous requirements, ATE mechanism has been sized and realized.

3 Aerodynamic Final Performance Analysis and Results of ATE

Morphing ATE has been developed and designed aiming at the aircraft weight and fuel consumption decrease by optimizing the lift over drag ratio (LoD) for several flight conditions and thus improving the aerodynamic performance of the aircraft. Therefore, the aerodynamic performance has to be assessed accurately, with respect to the specification requirements, taking into account a wide range of physical phenomena. Morphing indeed implies local shape modifications and seamless hinges, what act finely on the flow field but have a great influence on the overall performance in particular on the drag. Viscous CFD is then well suited for the aerodynamic performance evaluation. Furthermore, since structures become lighter, they are also more and more flexible. Their deformation must then be taken into account in the aerodynamic performance computation process. That is why the aerodynamic performance is assessed using high-fidelity fluid structure coupling simulations with the aeroelastic CFD code *elsA* for which the structure modeling is based on finite element techniques.

In the first step, aerodynamic analyses have been conducted to investigate the effect of different ATE parameters on the performance: deflection angle, chordwise size of the ATE, flight conditions, and shape of the device.

Those analyses have shown that the deflection angle of the morphing trailing edge has a stronger impact on off-design conditions and in particular on high-lift conditions and high incidences (Fig. 9). For these conditions, a downward

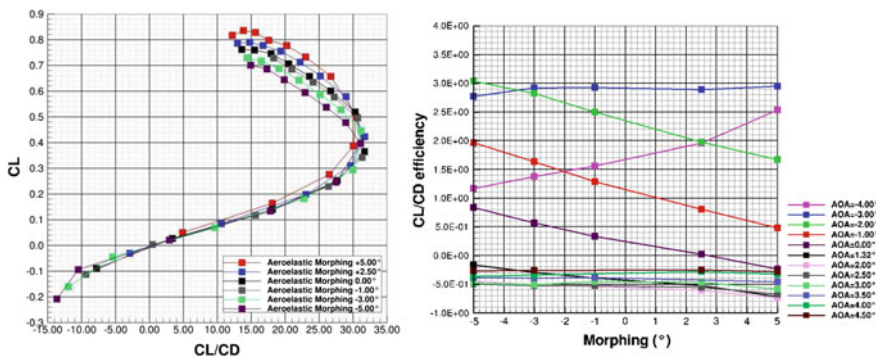


Fig. 9 LoD for different ATE deflection angles

deflection of the ATE induces a significant improvement in the aerodynamic performance.

On the other hand, the influence of the ATE size is rather small on the aerodynamic performance, in particular on high-lift conditions (Fig. 10), but this parameter has a strong impact on the aeroelastic deformation (vertical displacement and wing twist variation) and on the hinge moment. This may be due to stronger local aerodynamic nonlinear phenomena for large ATE (20 % of the mean chord).

And the last investigated parameter is the shape of the ATE and more precisely the camber of the trailing edge (Fig. 11). It has a small impact on the *overall aerodynamic performance* though a larger camber improves slightly LoD for high-lift conditions. But it has a significant influence on the hinge moment.

In the second step, once the predesign of the ATE has been completed, an aerodynamic database has been built from aerodynamic loads computed for a wide

Fig. 10 LoD for different ATE size

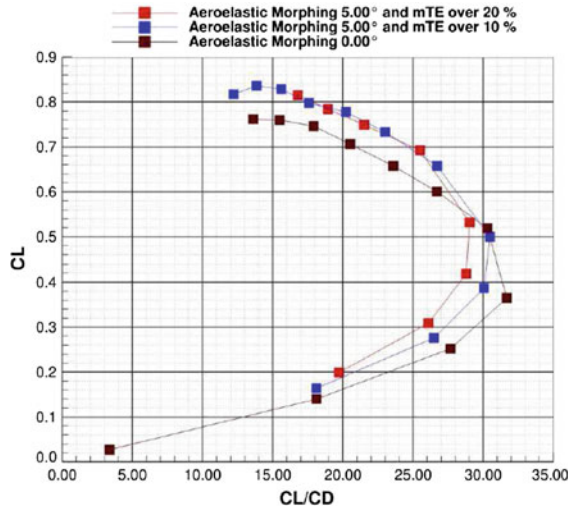
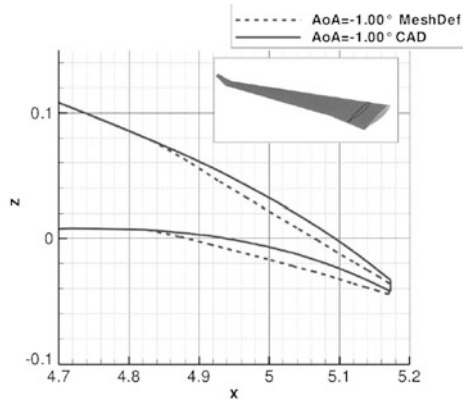


Fig. 11 Camber of ATE



range of flight conditions and of ATE deflections, in order to help the structural design and the sizing of the ATE. In particular, severe flight conditions have been studied for a 5° downward-deflected ATE. Those ones have been defined for the MTOW configuration at sea level and for load factors ranging from 1 to 3.2. Large aeroelastic deformations occur at such conditions which match high-lift conditions close to stall (Fig. 12).

The aerodynamic loads have then been deduced from aeroelastic simulations, taking into account gravity forces.

In the third and last step, once the ATE design has been almost completed, it has been refined by optimizations of the shape for different flight conditions, taking into account technological constraints and degrees of freedom. The parameters of such optimizations were the rotations of the three hinges of the ATE’s mechanism at several span locations. The optimization has been performed using a gradient-based method and the *elsA* CFD adjoint gradient solver associated with the far-field post-treatment code FFD72. The latter is indeed able to compute accurately drag and LoD and to perform drag breakdown from CFD simulations. The objective function has been defined from LoD with lift constraints.

Two flight conditions at Mach 0.75 have been considered: The first one is the cruise and the second matches the highest LoD condition. For the first condition, the optimal ATE deflection (Fig. 13) yields a 2.6 % LoD increase and a 4.3 drag count decrease. For the second flight condition, a gain of 1.3 % on the LoD and 1.2

Fig. 12 Aeroelastic deformations occurring at 3.2 g flight conditions

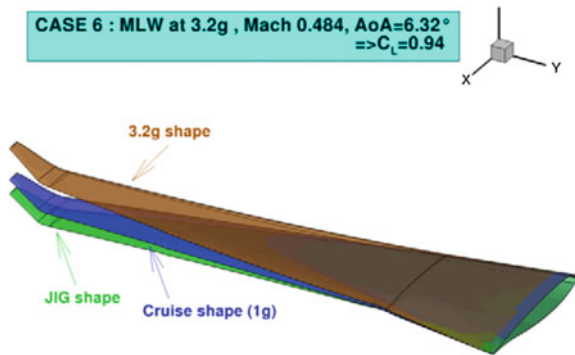


Fig. 13 Optimal ATE deflection for cruise condition

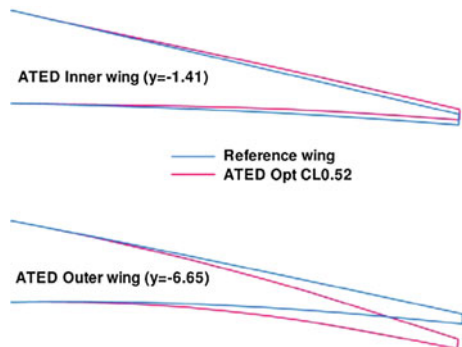
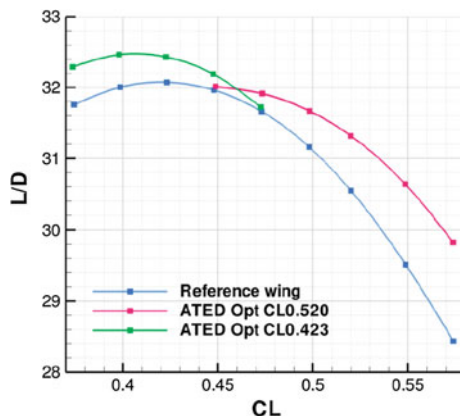


Fig. 14 LoD polar curves for wings without and with optimal ATE deflection



drag count decrease have been obtained. Nevertheless, the LoD polar curves with respect to lift for the wings with no morphing and for the wings with a frozen ATE deflection equal to the optimal deflections (Fig. 14) show that the gain in the aerodynamic performance is visible locally: The higher the lift, the higher the gain for the first optimized wing unlike the second optimized wing for which the gain increases with decreasing lift. It shows the great potential of the morphing ATE with the capability of adaptation to flight conditions, to enhance significantly the aerodynamic performance of an aircraft all along its mission.

4 Exploitation to Business Jet A/C Configuration

One of the final tasks of SARISTU AS02 was to perform an exploitation exercise of morphing trailing edge into a different A/C configuration with respect to the reference A/C. The business jet IAI “Projet” aircraft was selected as a small aeroplane (Fig. 15) designed to carry 4–5 passengers with OEW = 2300 kg, MTOW = 3700 kg, range = 1200 nm, and MMO = 0.66.

The span of the flap is 47 % of semispan of the wing, and it smoothly connects to the wing in spanwise and chordwise directions (Fig. 16).

The chord of the ATE was 160 mm = 10 % of the MAC. The deflections were imposed by the SARISTU ATE design mechanism: -5° , 0° , $+5^\circ$ (Fig. 17).

IAI performed a CFD analysis using in-house CFD Navier–Stokes code NES. Three ATE deflections were computed: 0° , -2.5° , -5° applied to wing body configuration. The delta drag relatively to deflection 0° (reference one) is shown on the left (Fig. 18). The result is that the configuration with deflection -2.5° has the smallest drag for entire operational lift coefficients in both cruise conditions—long range and fast cruise. Therefore, the ATE is pointless; a constant change in OML is the solution. To check better whether ATE is not needed for such A/C, IAI

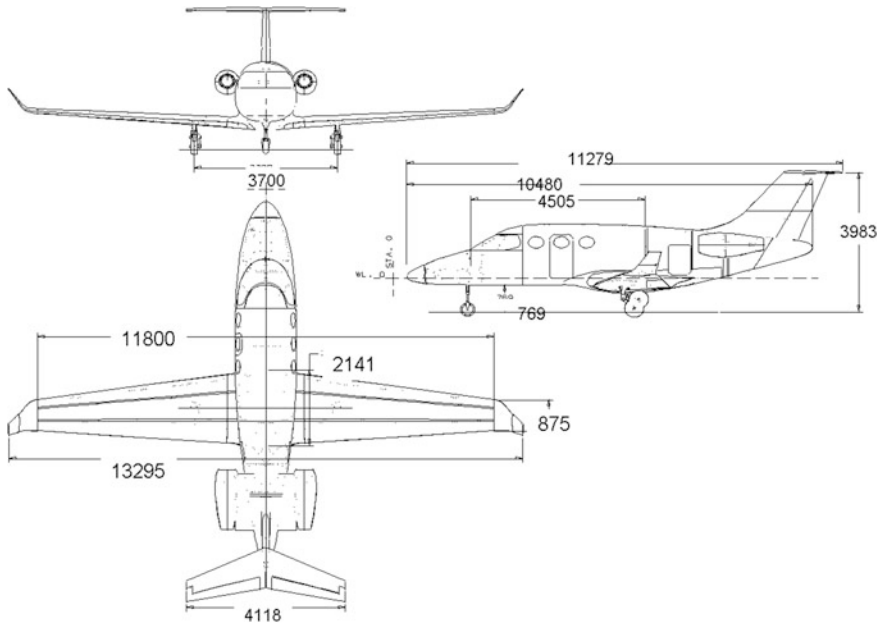


Fig. 15 IAI “Projet” aircraft—three views aircraft selected to implement the advanced trailing edge device (ATE) concept

performed redesign of wing for single lift coefficient using in-house-developed optimization code OPTIMAS that uses genetic algorithm and NES as solver.

The result of wing optimization (Fig. 19) was an improvement in the drag for entire lift range at fast cruise Mach number, 7 counts at $CL = 0.2$, 15 counts at $CL = 0.4$, and this without losing pitching moment.

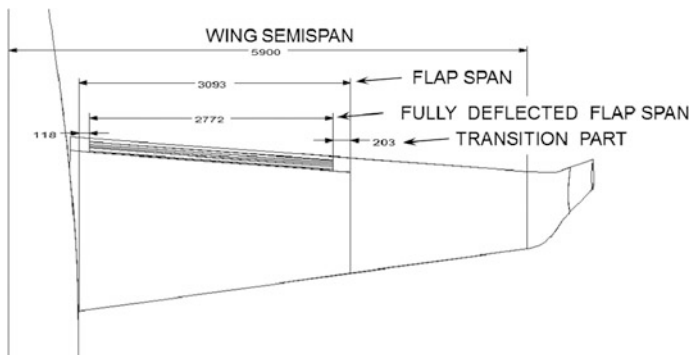


Fig. 16 The ATE size relative to the wing

WING SECTION AT MAC; THREE FLAP DEFLECTIONS

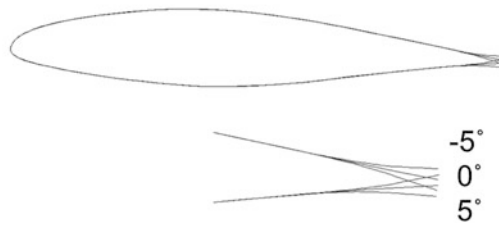


Fig. 17 Wing section at MAC, three ATE deflections

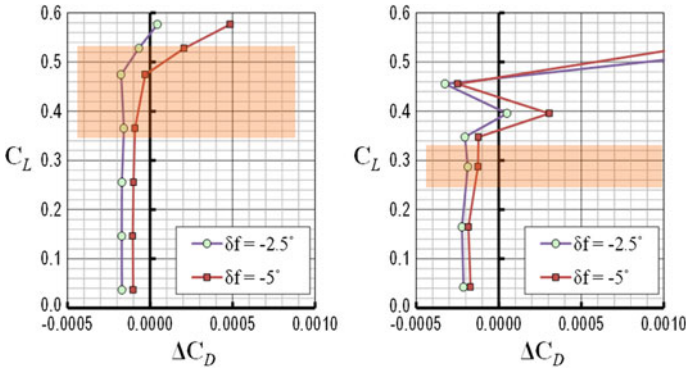


Fig. 18 Drag difference from baseline drag polar due to ATE deflection in “Projet” A/C. Left $M = 0.52, Re = 5 M$; Right $M = 0.65, Re = 6.3 M$

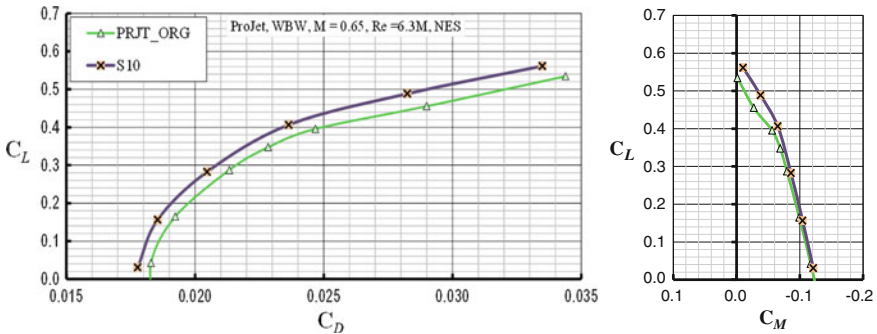
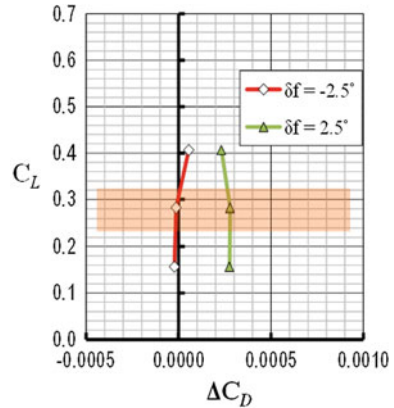


Fig. 19 Original “Projet” wing body versus S10 wing body. $M = 0.65, Re = 6.3 M$; Left drag polars, Right pitching moments

Three ATE deflections ($0^\circ, -2.5^\circ, -5^\circ$) were again applied for the wing body configuration with the new optimized wing S10. The result is that no drag reduction is found for this because of the considered ATE deflections (Fig. 20).

Fig. 20 Drag difference due to ATE deflection “Projet” A/C—S10 wing. $M = 0.65$, $Re = 6.3 M$



5 Conclusion

A preliminary study of the starting ATE concepts has been developed so as to investigate detailed requirements to size and realize the morphing adaptive trailing edge concept. Aerodynamic and structural preliminary optimization studies highlighted the most promising ATE size configuration (63 % extension spanwise, 10 % chordwise) and settings (+5°) of ATE, considering this application a constant spanwise ATE deflection. Structural constrain at this point was the maximum level of strain allowed by device skin (2 %). A preliminary evaluation of the aerodynamic performances was a fallout of this activity, analyzing both wing “cruise” conditions (traditional wing design point) and “off-design” point at lower-speed higher C_L so as to cover all the wing flight regimes for the reference A/C configuration. From optimization, morphed shapes have been defined. These shapes constituted one of the main targets for ATE mechanical and structural design, together with structural design load set.

A specification collected all these requirements, and ATE concept development started. In a most advanced device realization phase, a more detailed and sophisticated aerodynamic performance assessment has been done, considering also aeroelastic wing deflection effects on LoD improvements due to ATE deflections. This investigation basically confirmed the initial requirements’ evaluations, basically confirming the design assumptions. The current reference configuration is based on a MTOW 60 Tons, 130 Pax regional A/C configuration. An exploitation exercise has been performed on a smaller A/C configuration, a business jet, MTOW 3.7 Tons, 3 Pax. The results for this case were not favorable with respect to performance improvement, probably for the different ATE extension (43 % spanwise) and settings (−5°) of the considered devices. Currently, full-scale wind tunnel functional tests of ATE are on course at Tsagi premises gaining an other important goal to the technology readiness level of this morphing concept.

Acknowledgments The authors would like to thank the whole SARISTU consortium for the support and teamwork. In particular, AS02 and IS12 partners involved in morphing ATE specification definition and aerodynamic assessments for the commitment and cooperation spirit in developing such complicate devices.

The research leading to these results has received funding from the European Union's Seventh Framework Programme for research, technological development, and demonstration under grant agreement No. 284562.

References

1. Kulfan BM (2008) Universal parametric geometry representation method. *J Aircr* 45(1):142
2. De Gaspari A, Ricci S (2011) A two-level approach for the optimal design of morphing wings based on compliant structures. *J Intell Mater Syst Struct* 22:1091–1111. doi:[10.1177/1045389X11409081](https://doi.org/10.1177/1045389X11409081)
3. Diodati G et al Estimated performances of an adaptive trailing-edge device aimed at reducing fuel consumption on a medium-size aircraft. In: Farinholt KM (eds) *Industrial and commercial applications of smart structures technologies*. Proceedings of SPIE, vol. 8690, pp. 1–16. SPIE, San Diego, CA, USA, 29 March 2013. doi:[10.1117/12.2013685](https://doi.org/10.1117/12.2013685)

Structural Design of an Adaptive Wing Trailing Edge for Large Aeroplanes

Rosario Pecora, Marco Magnifico, Francesco Amoroso,
Leonardo Lecce, Marco Bellucci, Ignazio Dimino, Antonio Concilio
and Monica Ciminello

Abstract The structural design process of an adaptive wing trailing edge (ATED) was addressed in compliance with the demanding requirements posed by the implementation of the architecture on large aeroplanes. Fast and reliable elementary methods combined with rational design criteria were adopted in order to preliminarily define ATED box geometry, structural properties, and the general configuration of the embedded mechanisms enabling box morphing under the action of aerodynamic loads. Aeroelastic stability issues were duly taken in account in order to safely assess inertial and stiffness distributions of the primary structure as well as to provide requirements for the actuation system harmonics. Results and general guidelines coming from the preliminary design were then converted into detailed drawings of each box component. Implemented solutions were based on designer's industrial experience and were mainly oriented to increase the structural robustness

R. Pecora (✉) · M. Magnifico · F. Amoroso · L. Lecce
Industrial Engineering Department, University of Naples "Federico II",
Via Claudio n. 21, 80125 Naples, Italy
e-mail: rosario.pecora@unina.it

M. Magnifico
e-mail: marco.magnifico@unina.it

F. Amoroso
e-mail: francesco.amoroso@unina.it

L. Lecce
e-mail: leonardo@unina.it

M. Bellucci
Mare Engineering, Via ex aeroporto c/o Consorzio il Sole, 80038 Naples, Italy
e-mail: bellucci@mareengineering.it

I. Dimino · A. Concilio · M. Ciminello
C.I.R.A.—Italian Aerospace Research Centre, Via Maiorise snc, 81043 Capua, CE, Italy
e-mail: i.dimino@cira.it

A. Concilio
e-mail: a.concilio@cira.it

M. Ciminello
e-mail: m.ciminello@cira.it

of the device, to minimize its manufacturing costs, and to simplify assembly and maintenance procedures. The static robustness of the executive layout was verified by means of linear and nonlinear stress analyses based on advanced FE models; dynamic aeroelastic behaviour of the stress-checked structure was finally investigated by means of rational analyses based on theoretical mode association.

Nomenclature

ATE(D)	Adaptive trailing edge (device)
CFD	Computational fluid dynamics
CONM2	Lumped mass element
DMIG	Direct matrix input at grids
FE/FEM	Finite elements/finite element model

1 Introduction: General Requirements and ATE Structural Concept

Aircraft wings are usually optimized for a specific design point. However, since they operate in a wide variety of flight regimes, some of these have conflicting impacts on aircraft design, as an aerodynamically efficient configuration in one instance may perform poorly in others.

Ideally rigid, non-deformable wing structures preclude any adaptation to changing conditions; moreover, conventional devices, such as flaps or slats, lead to limited changes of the overall shape with narrow benefits compared with those that could be obtained from a wing structure that is inherently deformable and adaptable [1]. Several adaptive wing concepts of varying complexity may be found in the literature with regard to specific applications and objectives: from variable camber flaps conceived to optimize take-off and landing performances [2, 3], to wings provided with twist angle variation [4] or overall camber-morphing capabilities [5–9] enabling aerodynamic flow control and drag reduction, and from variable chord wing segments [10], to variable aspect ratio wings [11] for planform control during aircraft mission. Year by year, new aspects are being investigated, thus confirming a positive trend in the exploration of the wing morphing topic. It is therefore not surprising that in the last decades, several research programmes were launched worldwide to exploit the potentials of morphing concepts, especially for what concerns the optimization of aircraft efficiency and the consequent reduction of fuel consumption; among these, SARISTU [12] represents the largest European funded research project which ambitiously addresses the challenges posed by the physical integration of smart concepts in real aircraft structures; for the first time ever, SARISTU experimentally demonstrated the structural feasibility of individual morphing concepts on a full-size outer wing belonging to a CS-25 category aircraft. In the framework of SARISTU project, research was carried out to develop an adaptive trailing edge device aiming at

maximizing wing aerodynamic performance in cruise condition. The shape of wing trailing edge camber is controlled during flight in order to compensate the weight reduction following the fuel burning, by allowing the trimmed configuration to remain optimal in terms of efficiency (lift to drag ratio) or minimal drag. Trailing edge adaptations were investigated to achieve significant benefits in aircraft fuel consumption whose reduction ranges from 3 to 5 % depending on flight mission. Target morphed shapes—to be reproduced in flight—were determined through CFD-based optimization analyses under the following constraints:

- airfoil thickness distribution unaffected by morphing;
- maximum allowed skin deformation equal to 2 %;
- airfoil camber morphing such that the airfoil tip is forced to rotate, by an angle β , around a virtual hinge located on airfoil camber line at the most forward chordwise position (Fig. 1).

Optimal values of β angle were found to be included in the range $[-5^\circ; +5^\circ]$, where negative values indicate upward morphing. In other terms, the aerodynamic efficiency of the wing was proved to be optimized during cruise, if each ATE section changes its shape in compliance with target tip deflections ranging from -5° to $+5^\circ$.

In order to enable the transition of the adaptive trailing edge (ATE) sections from the reference (baseline) shape to the target ones, a morphing structural concept was developed for ATE box ribs. Each rib (Fig. 2) was assumed to be segmented into four consecutive blocks (B0, B1, B2, B3) connected to each other by means of hinges located on the airfoil camber line (A, B, C). Block B0 is rigidly connected to the rest of the wing structure, while all the other blocks are free to rotate around the hinges on the camber line, thus physically turning the camber line into an articulated chain of consecutive segments. Linking rod elements (L1, L2)—hinged on not adjacent blocks—force the camber line segments to rotate according to specific gear ratios.

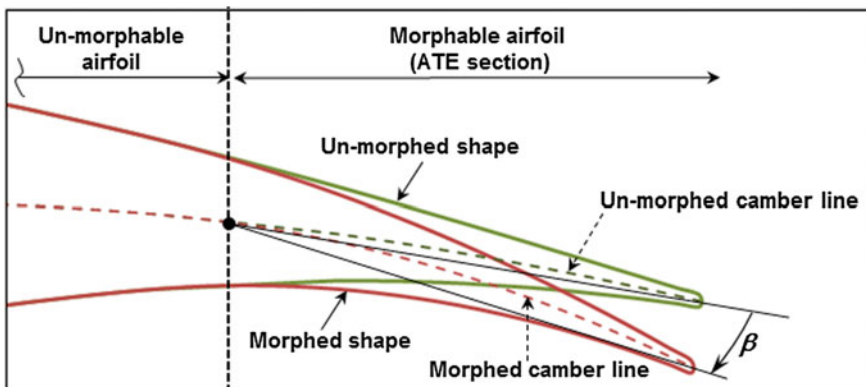


Fig. 1 ATE generic cross section, un-morphed and morphed shapes

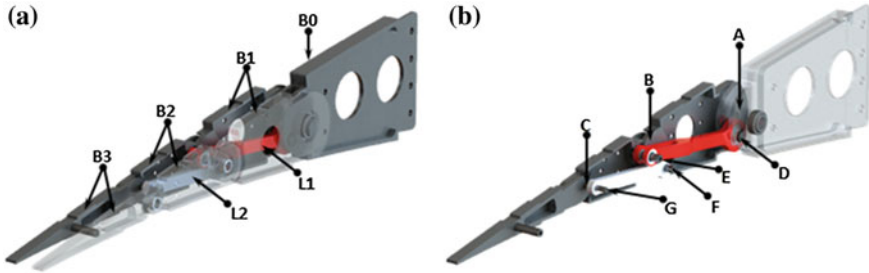


Fig. 2 Morphing rib architecture: **a** blocks and links, **b** hinges

These elements make each rib equivalent to a single-DOF mechanism: if the rotation of any of the blocks is prevented, no change in shape can be obtained; on the other hand, if an actuator moves any of the blocks, all the other blocks follow the movement accordingly. The rib mechanism uses a polygonal line made of three segments to approximate the camber of ATE airfoil and to morph it into the desired configuration while keeping approximately unchanged the airfoil thickness distribution.

The ribs' kinematics was transferred to the overall trailing edge structure by means of a multi-box arrangement (Fig. 3). Each box of the structural arrangement was assumed to be characterized by a single-cell configuration delimited along the span by homologous blocks of consecutive ribs and along the chord by longitudinal stiffening elements (spars and/or stringers).

Upon the actuation of the ribs, all the boxes are put in movement, thus changing the external shape of the trailing edge (Fig. 4); if the shape change of each rib is prevented by locking the actuation chain, the multi-box structure is elastically stable under the action of external aerodynamic loads.

The actuation system was based on servo rotary load-bearing actuators coupled to quick-return mechanisms for the independent control of each rib of the device [13].

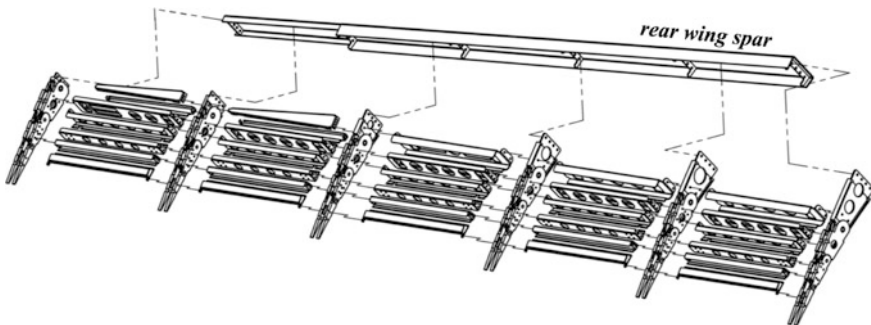


Fig. 3 Morphing box architecture (exploded view)



Fig. 4 ATE configuration: morphed up (*left hand side*), morphed down (*right hand side*)

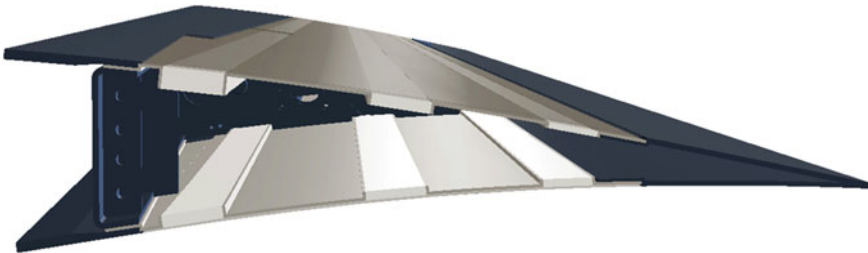


Fig. 5 Multi-material skin arrangement [14]

A multi-material arrangement was assumed for the upper and lower skin panels (Fig. 5, [14]); more in detail, a rational combination of Al alloy panels and soft foam strips was implemented along the chordwise direction. Foam strips were placed in correspondence with camber line hinges, thus adsorbing the tension and compression induced by the camber morphing on the skin; aluminium panels were riveted along rib edge to increase the torsional stiffness of each ATE box. Silicon material—properly designed to withstand temperature excursion typically expected in flight—was introduced as protective layer and glued on the sequence of aluminium panels and foam strips.

The structural concept herein described resulted from an iterative design process consisting of three main loops; (Fig. 6) the executive layout was obtained by progressively updating a preliminary assessed configuration. The updating process followed the design progress of the ATE main equipments (basically actuation/sensing system) and structural interfaces with the rest of the wing (dead box) while duly taking in account recommendations coming from numerical analyses addressing ATE structural behaviour.

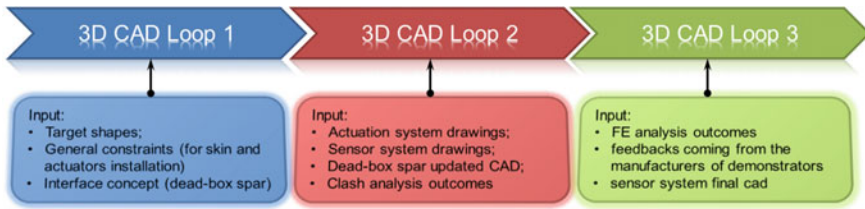


Fig. 6 ATED design loops

2 ATE Stress Analyses

Once the structural layout was sketched and the aerodynamical loads established, the simulation of the ATED behaviour under real flight conditions took place as a critical stage of the design cycle. The detailed modelling of such a complex morphing system involved the proper schematization of a lot of different components and sub-assembly items as the rib chains, connected by spherical and cylindrical joints, and the actuator chains, including motor shaft modelling, the skin, the spars, and some others.

Mesh size and general properties of the finite element (FE) model were rationally defined in order to get detailed and reliable distributions of stress and strains while optimizing the computational time required for each analysis; in the following, some detailed pictures of modelled parts are shown (Fig. 7).

All the constructive details of connection systems (joints, bushing, and fasteners) were accurately taken into account by proper modelling approaches enabling the

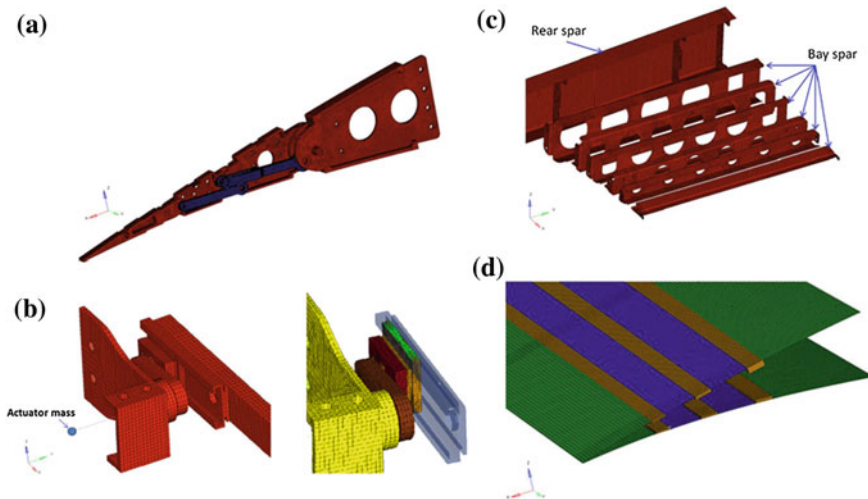


Fig. 7 FE model. **a** rib, **b** actuation chain, **c** spars, **d** skin segments

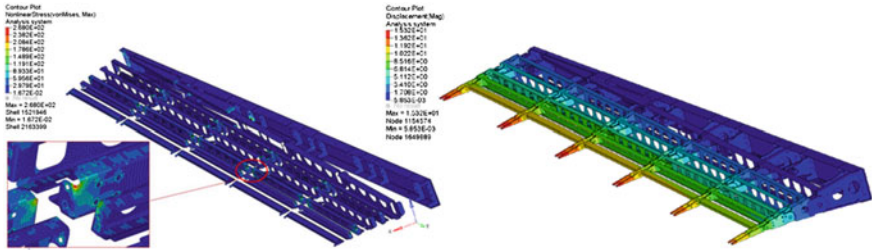


Fig. 8 Limit Von Mises stress contour (left hand side), total displacement contour (right hand side)

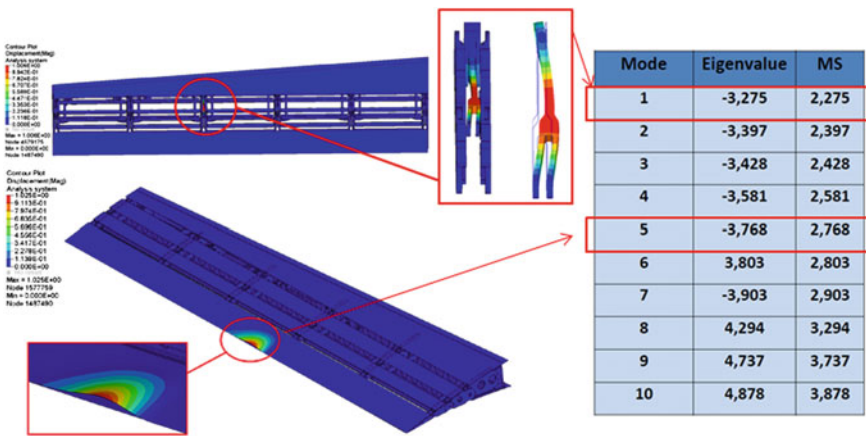


Fig. 9 Buckling eigenvalues and eigenvectors (limit load)

extraction of local forces for separate stress analysis and margin of safety (MOS) evaluations.

These parameters were computed through consolidated sizing formulae, according to standard design manuals. Global and local stress analyses were performed under the actions of distributed pressure fields on the upper and lower skin panels (Fig. 8). Finally, to explore the possible occurrence of buckling and to check the vibration behaviour, dedicated simulations were performed (linear and nonlinear buckling and modal analysis) (Figs. 9 and 10).

3 Aeroelastic Investigations

Due to ATE higher complexity with respect to conventional solutions based on hinged flaps, it was believed necessary to take into account aeroelastic issues since the preliminary design phase of the device. To this aim, trade-off flutter analyses

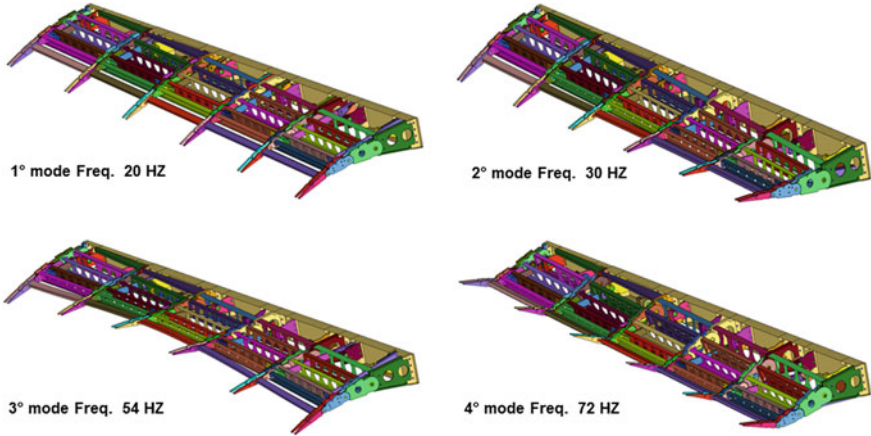


Fig. 10 Modal parameters (shapes and frequencies up to 80 Hz)

[15, 16] were performed in compliance with CS-25 airworthiness requirements in order to define safety ranges for trailing edge inertial and stiffness distributions as well as for the harmonics of trailing edge’s control lines. Rational approaches were therefore implemented in order to simulate the effects induced by variations of trailing edge actuators’ stiffness on the aeroelastic behaviour of the wing also in correspondence with different dynamic properties of the trailing edge component. Reliable aeroelastic models and advanced computational strategies were properly implemented to enable fast flutter analyses covering several configuration cases in terms of structural system parameters. A simplified and fairly representative structural model of the wing system was generated referring to a stick equivalent representation (Fig. 11); stiffness and inertial properties of the model were extracted by two FE models that were elaborated by concurring partners of SARISTU consortium to preliminarily assess the structural layout of the wing. Matrices of

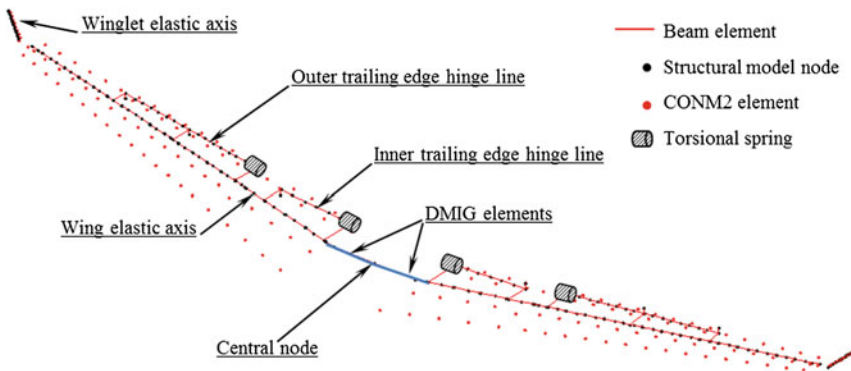


Fig. 11 Trade-off aeroelastic analyses: adopted structural model [15, 16]

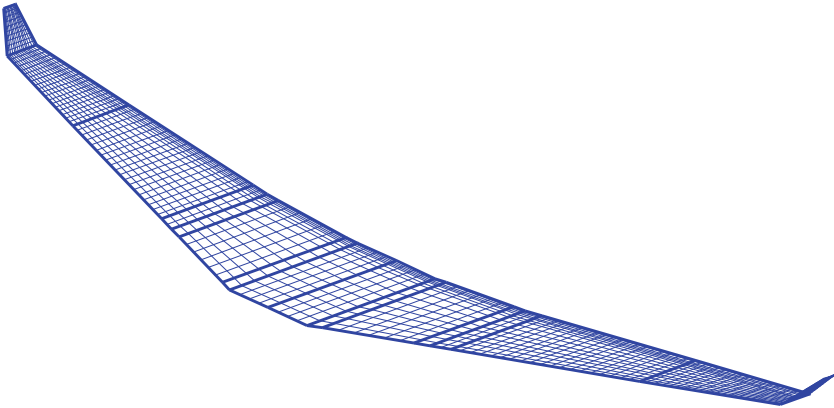


Fig. 12 Trade-off aeroelastic analyses: adopted aerodynamic model [15, 16]

unsteady aerodynamic influence coefficients were evaluated by means of doublet lattice method. The aerodynamic lattice of the wing (Fig. 12) was generated by properly meshing the middle wing plane through eight macro-panels for each side of the wing; macro-panels were further meshed into elementary boxes; higher boxes' density was considered for the movable trailing edge.

Modal displacements at the centre of each aerodynamic box were obtained by means of linear spline functions attached to support nodes of the structural model.

Flutter analyses were carried out under the following assumptions:

- PK continuation method with rationalization of generalized aerodynamic forces for the evaluation of modal frequencies and damping trends versus flight speed;
- theoretical elastic mode association in the frequency range 0–60 Hz (elastic modes being pertinent to free–free aircraft, with only plunge and roll motions allowed);
- modal damping (conservatively) equal to 0.01 for all the elastic modes;
- sea-level altitude and flight speed range 0–300 m/s (≈ 1.5 times the dive speed VD).

Flutter speeds were evaluated in correspondence with different settings for the movable trailing edge, each setting being defined by means of three (trade-off) parameters:

- inertial distribution;
- stiffness distribution;
- harmonic frequency (i.e. frequency of the elastic deflection at locked actuators).

Investigated cases mapped three different inertial distributions in combination with three different stiffness distributions and five harmonic frequencies of the movable surface; the trade-off domain was therefore composed by 45 different configurations of the movable trailing edge.

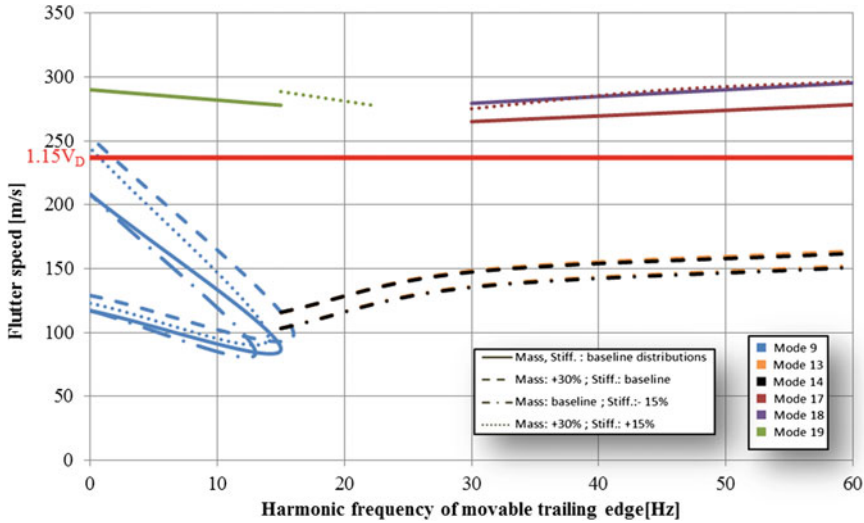


Fig. 13 Carpet plot of flutter speeds [15, 16]

Obtained results (Fig. 13) showed that for the most practical combinations of trailing edge stiffness and inertial distributions, flutter is avoided if sufficient stiffness is provided by the actuation chain. On the other hand, a proper mass balancing of the trailing edge was determined in order to assure the absence of any flutter instability within the certification envelope even in the extremely remote event of simultaneous failure of all the actuators.

Stiffness and inertial distributions of the ATE were duly monitored during the design loops in order to be compliant with the safety levels coming from the trade-off flutter studies, the same applied to actuation system elasticity (intimately related to ATE harmonics) and ATE mass balancing.

At the end of the structural design process, the executive and stressed layout was further investigated from the aeroelastic standpoint in order to check the absence of any instability.

The check was performed with reference to the detailed structural model (described in the previous paragraph) which was duly condensed using a suitable number of super-elements. Analyses did not show any criticality, thus proving the goodness of the adopted *aeroelasticity-in-the-loop* design strategy.

4 Conclusions

The structural design of aircraft components represents a complex process in which several variables are taken into account in order to produce efficient layout compliant with specific requirements.

For conventional items, three primary requirements are commonly referred to:

- the capability of withstanding the most severe loads expected in service without failure or degradation of structural properties during the entire life cycle;
- the avoidance of unnecessary weight;
- the simplicity of the overall layout for what regards the manufacturing and the assembly of the spare parts as well as the installation and maintenance of the assembled component.

When dealing with adaptive structures for lifting surface morphing, the level of complexity of the design process naturally increases as a consequence of the augmented functionality of the system to be assessed; generally speaking, a morphing structure has to assure the controlled and fully reversible transition from a baseline shape to a set of different configurations, each one characterized by specific external loads and transmission paths of the internal stresses; the same design requirements of conventional items have therefore to be fulfilled for each geometrical configuration; moreover, the morphing functionality has to be implemented in order to:

- enable the high-fidelity reproduction of the target shapes under the action of aerodynamic and inertial loads;
- avoid any detrimental impact on flight safety as well as on the overall aircraft maintenance plans.

A brief and general description of the approaches and methodologies followed for the structural assessment of a morphing trailing edge structural layout has been here presented with reference to CS-25 aircraft end applications and the above-recalled requirements. Design strategies and consequent results have been outlined; particular emphasis was given to the procedures implemented for the individuation of the structural arrangements and for the demonstration of their adequacy in a multidisciplinary perspective.

References

1. Barbarino S, Bilgen O, Ajaj RM, Friswell MI, Inman DJ (2011) A review of morphing aircraft. *J Intell Mater Syst Struct* 22:823–877
2. Monner HP, Bein T, Hanselka H, Breitbach E (1998) Design aspects of the adaptive wing—the elastic trailing edge and the local spoiler bump. In: *Proceedings of Royal Aeronautical Society symposium on multidisciplinary design and optimization*. Royal Society Publishing, London, pp 15.1–15.9
3. Pecora R, Barbarino S, Concilio A, Lecce L, Russo S (2011) Design and functional test of a morphing high-lift device for a regional aircraft. *J Intell Mater Syst Struct* 22(10):1005–1023
4. Pecora R, Amoroso F, Lecce L (2012) Effectiveness of wing twist morphing in roll control. *J Aircr* 49(6):1666–1674
5. Barbarino S, Pecora R, Lecce L, Concilio A, Ameduri S, De Rosa L (2011) Airfoil structural morphing based on S.M.A. actuator series: numerical and experimental results. *J Intell Mater Syst Struct* 22:987–1004

6. Stanewsky E (2001) Adaptive wing and flow control technology. *Prog Aerosp Sci* 37 (7):583–667
7. Browman J, Sanders B, Weisshaar T (2002) Evaluating the impact of morphing technologies on aircraft performance. In: *Proceedings of the 43rd AIAA conference on structures, structural dynamics and materials*, AIAA paper 2002-1631, Apr 2002
8. Szodruich J, Hilbig R (1988) Variable wing camber for transport aircraft. *Prog Aerosp Sci* 25 (3):297–328
9. Munday D, Jacob J (2001) Active control of separation on a wing with conformal camber. In: *Proceedings of the 39th AIAA aerospace science meeting and exhibit*, AIAA paper 2001-293, Jan 2001
10. Perkins DA, Reed JL, Havens E (2004) Morphing wing structures for loitering air vehicles. In: *Proceedings of the 45th AIAA conference on structures, structural dynamics and materials*, AIAA paper 2004-1888, Apr 2004
11. Blondeau J, Pines D (2004) Pneumatic morphing aspect ratio wing. In: *Proceedings of the 45th AIAA conference on structures, structural dynamics and materials*, AIAA paper 2004-1808, Apr 2004
12. www.saristu.eu (web site of the SARISTU project)
13. Dimino I, Flauto D, Diodati G, Concilio A, Pecora R (2014) Actuation system design for a morphing wing trailing edge. *Recent Pat Mech Eng* 7(2):138–148
14. Schorsch O, Luhring A, Nagel C, Pecora R, Dimino I (2015) Polymer based morphing skin for adaptive wings. In: *7th ECCOMAS thematic conference on smart structures and materials SMART 2015*, Azores, Portugal, 3–6 June 2015
15. Pecora R, Magnifico M, Amoroso F, Monaco E (2014) Multi-parametric flutter analysis of a morphing wing trailing edge. *Aeronaut J* 118(1207):1063–1078
16. Bisplinghoff RL, Ashley H, Halfman RL (1996) *Aeroelasticity*. Dover Publications Inc., New York

Distributed Actuation and Control of a Morphing Wing Trailing Edge

Ignazio Dimino, Monica Ciminello, Antonio Concilio, Rosario Pecora, Francesco Amoroso, Marco Magnifico, Martin Schueller, Andre Gratias, Avner Volovick and Lior Zivan

Abstract In a morphing wing trailing edge device, the actuated system stiffness, load capacity, and integral volumetric requirements drive flutter, actuation strength, and aerodynamic performance. Design studies concerning aerodynamic loads, structural properties, and actuator response provide sensitivities to aeroelastic performance, actuation authority, and overall weight. Based on these considerations, actuation mechanism constitutes a very crucial aspect for morphing structure design because the main requirement is to accomplish variable shapes for a given trailing edge structural mechanism within the limits of the maximum actuation torque, consumed power, and allowable size and weight. In this work, a lightweight and compact lever driven by electromechanical actuators is investigated to actuate

I. Dimino (✉) · M. Ciminello · A. Concilio
CIRA, The Italian Aerospace Research Centre, Via Maiorise, 81043 Capua, CE, Italy
e-mail: i.dimino@cira.it

M. Ciminello
e-mail: m.ciminello@cira.it

A. Concilio
e-mail: a.concilio@cira.it

R. Pecora · F. Amoroso · M. Magnifico
Aerospace Division, Department of Industrial Engineering, University of Naples,
“Federico II”, Via Claudio, 21, 80125 Naples, Italy
e-mail: rosario.pecora@unina.it

F. Amoroso
e-mail: francesco.amoroso@unina.it

M. Magnifico
e-mail: marco.magnifico@unina.it

M. Schueller · A. Gratias
Department of Multi Device Integration, Fraunhofer ENAS, Technologie-Campus 3,
09126 Chemnitz, Germany
e-mail: martin.schueller@enas.fraunhofer.de

A. Gratias
e-mail: andre.gratias@enas.fraunhofer.de

the morphing trailing edge device. An unshafted distributed servoelectromechanical actuation arrangement driven by a dedicated control system is deployed to realize the transition from the baseline configuration to a set of design target ones and, at the same time, to withstand the external loads. Numerical and experimental investigations are detailed to demonstrate system effectiveness and reliability using a feedback sensing data from integrated FBG sensors.

1 Introduction

Changing the wing shape or geometry for maneuver and general control purposes has its roots at the very early stage of the modern aviation. The Wright Flyer, the first powered aircraft, enabled roll control by changing the twist angle of its wing, by using cables directly actuated by the pilot. The increasing demand for higher cruise speeds and payloads led to more rigid aircraft structures, unable to change their shape to different aerodynamic conditions. The deployment of conventional flaps or slats on a commercial airplane is the common way to modify the wing geometry (other examples are the variable wing plant geometry on the F14 or the Concorde nose): However, they lead to discontinuities, in turn producing geometry sharpening, aerodynamic efficiency worsening, and also noise emission increase. Final wing geometry is generally a compromise allowing the aircraft to fly a range of conditions, at suboptimal performance levels. Benefits could be increased if an inherent deformable wing would be referred to, either globally or locally (see for instance [1], for general aerodynamic performance enhancement or [2] for radiated noise reduction).

Wing shape morphing is a very promising area of research which offers substantial improvements in aircraft aerodynamic performance. It has interested researchers and designers over the years; a quite thorough survey may be found in [3], while early works may be found in the far past. Novel strategies have been considered in the last decade: For example, the idea of producing smooth variations of the geometry even in the presence of large displacements distributed over a wider portion of the wing is well documented [4, 5]. Further works can be found in the literature dealing with original approaches to modify specific wing parameters to achieve better aerodynamic performance as, for instance, the upper skin curvature

A. Volovick · L. Zivan
Engineering Division, Israel Aerospace Industries Flight Control Systems Department, Ben
Gurion International Airport, Tel Aviv, Israel
e-mail: avolovick@iai.co.il

L. Zivan
e-mail: lzivan@iai.co.il

to delay the laminar transition point, [6, 7], the local or global camber, [8–10], the wingspan itself, [11, 12], or the twist angle [13, 14].

Morphing structures require a compromise between high load-carrying capacity and adequate flexibility. This target necessitates innovative structural and actuation solutions. When dealing with adaptive structures for lifting surfaces, the level of complexity naturally increases as a consequence of the augmented functionality. In specific, an adaptive structure ensures a controlled and fully reversible transition from a baseline shape to a set of different configurations, each one capable of withstanding the associated external loads. To this aim, a dedicated actuation system shall be designed. In addition, the adopted morphing structural kinematics shall demonstrate complete functionality under operative loads. Within the frame of SARISTU project (EU-FP7), an innovative structural system incorporating a gap-less adaptive trailing edge device (ATED) has been developed. Such a system is conceived to enhance large commercial aircraft cruise performance by compensating the aircraft weight reduction during a long-range mission due to fuel consumption [15, 16]. Such consistent changes in flight conditions are compensated by varying the wing camber during the mission to obtain a near-optimum geometry in order to preserve aerodynamically efficient flight. As a result, it allows the trimmed configuration to remain optimal in terms of efficiency (L/D ratio) or minimal drag (D). Key benefits have been measured as reduction of fuel consumption or increase of range, expected to amount to 3 % or more. Because span-wise action variability could lead to design weight decrease through root bending moment (RBM) reduction, this potentiality can be further exploited.

1.1 Distributed ServoElectromechanical Actuation

Hydraulic actuators are typically used for primary flight control surfaces due to the high forces required. Whereas electromechanical actuators are considered too slow and bulky to compete with hydraulics on surface actuation, the advent of digital motors has made electromechanical actuators a viable solution for controlling secondary aircraft control surfaces in which jam is not catastrophic. In morphing applications based on rigid-body mechanisms, fewer actuators may be required and the main advantages with respect to conventional arrangements were derived from the reduced mass, volume, force, and consumed power.

In this work, an unshafted distributed servoelectromechanical actuation arrangement is investigated. A major potential advantage of distributed actuation with respect to a shaft mechanism is the ability to move individual ribs either synchronously or independently to different angles (twist), Fig. 1. Varying the angles between inboard and outboard wing as well as between different stations may lead to significant aerodynamic benefits. This architecture uses both inherent rotation sensors on each actuator and a FBG-based distributed sensor system to synchronize the different element action and to monitor localized failures. Each actuator is rated for the torque of a single adaptive rib and is hence smaller than the

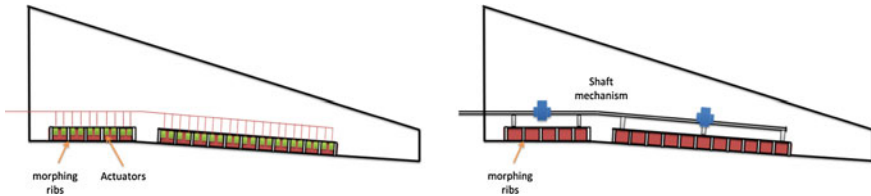


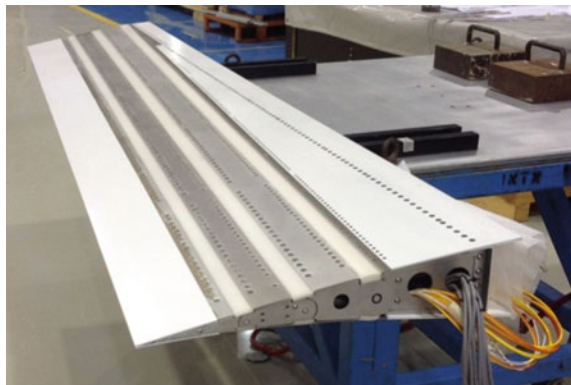
Fig. 1 Unshafted distributed servoelectromechanical actuation arrangement (*left*) and comparison with conventional architectures

equivalent conventional hydraulic actuation of a control surface. As the number of motors increases drastically, such a configuration has potential to fulfill airworthiness requirements for a less safety critical surface such as ATED. On the other hand, however, reliability issues may represent an issue.

2 Morphing Trailing Edge Actuation

A lightweight and compact lever driven by electromechanical actuators is investigated to activate the morphing trailing edge device. Morphing is enabled by a multi-finger architecture driven by load-bearing actuator systems (hidden in Fig. 2). More details on the morphing architecture may be found in [17]. The use of electromechanical actuators is coherent with a “more electric approach” for next-generation aircraft design. Benefits are obvious. No hydraulic supply buses (easier to maintain and store without hydraulics leaks) improved torque control, more efficiency without fluid losses, and elimination of flammable fluids. In addition, it is potentially possible to move individual ribs either synchronously or independently to different angles (twist) in order to enhance aerodynamic benefits during flight. On the other side, actuators susceptibility to jamming may represent the most important drawback.

Fig. 2 The adaptive trailing edge device (ATED)



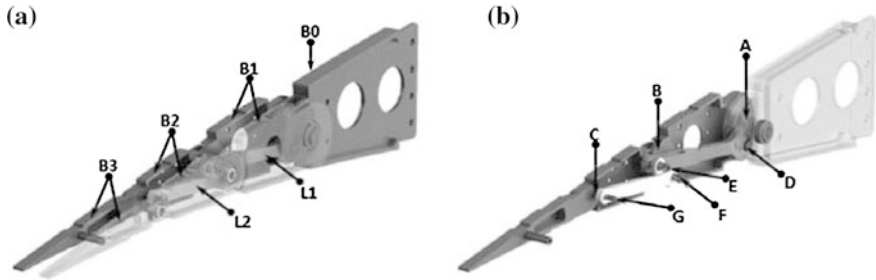


Fig. 3 Morphing rib architecture: **a** blocks and links, **b** Hinges

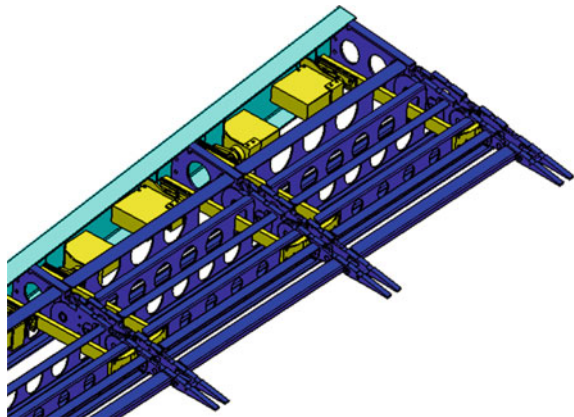
The actuation kinematics of the morphing trailing edge device is based on a “direct-drive” actuation consisting of an arm (actuation beam) that is rigidly connected to the B2 block shown in Fig. 3. This arm rotates the 1-DOF-based mechanical system and transmits the actuation torque from the actuator to the adaptive rib. The control actions aim at producing small camber variation in the adaptive trailing edge corresponding to a rigid rotation of a plain control surface comprised between -5° and $+5^\circ$ during cruise. The closed structure made of the adaptive ribs, the spars, and skin is capable of bearing both the chord-wise and span-wise design loads, being mechanically sustained by the actuator distribution.

Starting from the structural design, the actuator electrical arrangement was defined, as shown in Fig. 4. The main features of the adopted solution are as follows:

- Simplicity: “direct-drive” actuation, without gearboxes;
- Redundancy: duplication of actuation per morphing rib;
- Fault tolerance: continued operation after single-actuator fault.

The connections to the control system hardware, signal conditioning electronics, and routing to each actuator were also defined. After info gained by a widely

Fig. 4 Sketch of the actuation system



distributed strain sensor network, the control system drives actuator action. An adaptive, highly deformable skin absorbs part of the external loads and insures a smooth profile. The system keeps its structural properties while actuated, then allowing the preservation of a specific target shape regardless of the action of the operational loads. Relative actuator movement with regard to transition times and velocity discrepancies between each rib segment was considered to synchronize each actuator.

2.1 Actuator Selection and Layout

In order to reduce the actuation torque necessary to hold and move the ATE device, different kinematic architectures have been considered during the actuation system development. Reducing the actuation torque affects both actuation dimensions and weight. With a suitable actuation kinematics, it is possible to identify a suitable actuator that can be host in the available space of the demonstrator. To actuate the ATE structure, it is necessary to apply a torque on the second rib block. If the force generating this torque was applied parallel to the camber line, then the maximum available arm would be of the order of the wing local thickness. If this force was applied perpendicularly to the camber line, then the maximum available arm would be of the order of the ATE length. These considerations suggested the use of a quick return mechanism.

The actuation kinematics has an arm (actuation beam) that is rigidly connected to the second rib block. This arm rotates as the block itself. Torque is applied to the rib block by means of a force acting perpendicularly to this arm (if the friction can be considered equal to zero). This force is generated by a rotational servoactuator with a crank rotating with the actuator shaft. A simplified scheme of the kinematics is reported in Fig. 5. As shown in Fig. 6, this arm rotates around the “virtual hinge”

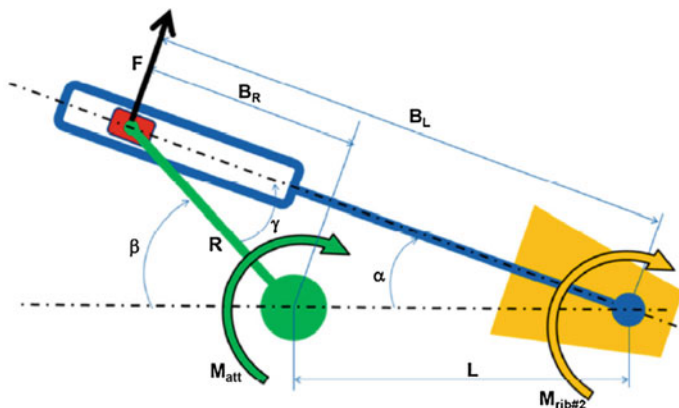


Fig. 5 The actuator layout

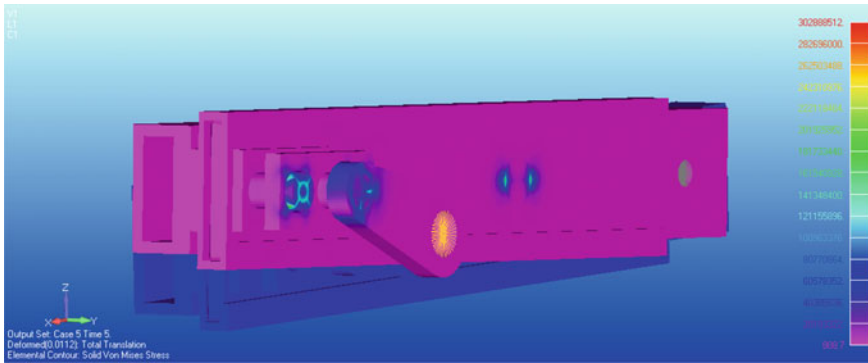


Fig. 6 FE model of the activated rod

(the point around which the second rib block rotates during the movement of the ATE device) and transmits the actuation load (torque) from the actuator to the second rib block.

The mechanical advantage MA of the mechanism (ratio between the loading moment and the driving moment) and the relation between the actuator rotation angle and the rib block rotation may be computed as:

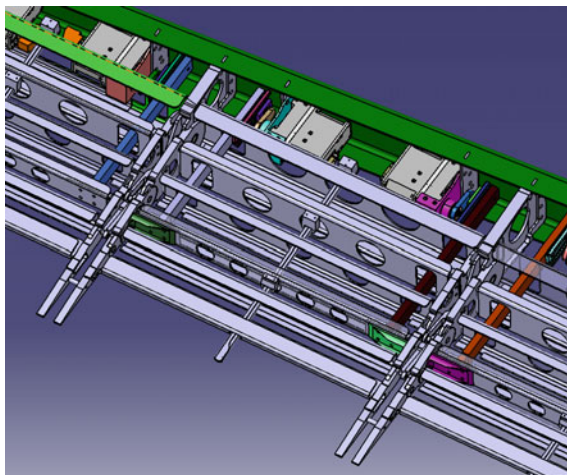
$$\begin{aligned}
 MA &= \frac{B_L}{B_R} \\
 B_R &= R \sin \gamma; \quad B_L = L \cos \alpha - B_R \\
 MA &= \frac{L \cos \alpha}{R \sin \gamma} - 1 \\
 R \cos \gamma &= L \cos \alpha \rightarrow \gamma = \arccos\left(\frac{L}{R} \sin \alpha\right)
 \end{aligned}$$

The mechanical advantage increases as the second rib block angle increases, and this is much more evident as higher is the ratio between the arm length L (distance between the second rib block virtual hinge) and the actuation crank radius R . Similarly, formulas may be derived for the actuator rotation angle versus rib block rotation angle.

Higher is the L/R ratio, higher has to be the actuator rotation angle. This affects the maximum reachable mechanical advantage due to the fact that servoactuators available on the market have a mechanical limit to their rotation. This architecture can reach higher mechanical advantage values, but some limitations can be imposed by the maximum servoactuator rotation angle.

During the design phase, it was chosen to connect this arm to the spar rigidly connected to the second rib block: These spars, together with the rib blocks and the skin, constitute a very rigid closed structure capable of bearing high loads. The chosen arrangement is shown in Fig. 7. FE simulations demonstrated that the

Fig. 7 Actuator system installation detail



actuation beam is capable to bear the load coming from the actuator. Each rib is moved by two actuation systems, each one of them bearing half of the load. The stress on the actuation beam can be then calculated as the ratio between the flexural moment (M_f) and the flexural rigidity (W_f) of the beam M_f/W_f .

The worst-case condition (V_{dive}) is very below the stress limits for both aluminum and steel. The actuation crank dimensions have been chosen in order to have the maximum possible mechanical advantage and to satisfy the $\pm 45^\circ$ of maximum actuator rotation. For each rib, the “virtual hinge” has been identified by considering the second rib block position in three different configurations: morphed up (max top deformation), morphed down (max bottom deformation), and unmorphed. Then, the actuators have been positioned as close as possible to the dead box spar. The distance between the actuator shaft and the virtual hinge has been then measured. The actuation crank dimension has then been fixed, following the previously stated requirements and following a detailed stress analysis.

Starting from the FE model results, the main specifications for the actuators were defined (Table 1):

Available certified servoactuators have been screened on the market in order to derive the best of them suitable for ATE application. Considering actuator speed and individual performances, the Bental RSA-06 actuator has been selected due to its contained weight (less than 0.5 kg) and dimensions respect to the other candidates that satisfy the same specifications.

Table 1 Servoactuators specifications

Parameter	Assumption	Units
Type of actuator	Electromechanical	
Max torque	6 (dynamic) or 15 (static)	Nm
Displacement	±45 (pk to pk)	°
Resolution	0.55–1.1 (max actuator backlash) 0.1–0.05 (ATE device resolution)	°
Dimensions	100 × 50 × 200 (<i>W × H × L</i>)	mm
Weight	<1	kg
Number of actuators	10	–
Actuator speed	>10	°/s
Actuation signal max latency	<10	ms
Nominal voltage	12 or 24	V
Power consumption	<100	W

3 Control Logic

As a last step, the control system architecture was developed and implemented. Resulting scheme is reported in Fig. 8. Depending on the specific flight mission, different ATED shapes are possible. More specifically, the control system aims to drive the structure to reach the specific position of the ATED surface enabling optimal aerodynamic performance.

Two kinds of sensorized systems were used to monitor the ATED shapes: shape beams and ribbon tapes. The shape beam is a sensorized cantilevered beam with integrated fiber optics. The sliding beam is opportunely guided to copy the skin

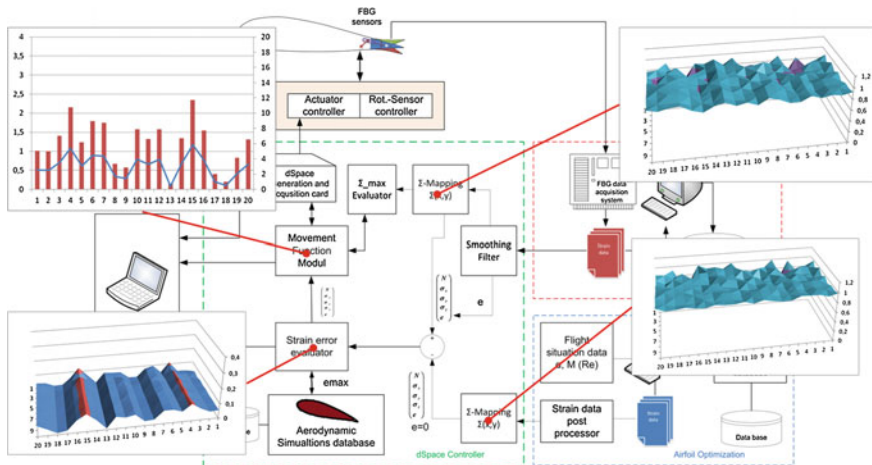


Fig. 8 Control system schematics

profile as an independent structural system able to measure camber variations. The guide itself is opportunely designed to compensate the air gap due to the different thickness of the skin and allowing the skin profile to transfer its curvature to the beam. Basically, at least three points of interest are considered corresponding to the rib hinges. Ribbon tapes are a very thin and flexible glass fiber reinforced patch. The span-wise deformation is expected to be coherent with standard glass FO so that ribbon tapes can be directly bonded in the inner side of the metallic tip cover and then connected to form two measurement lines in order to drastically reduce the number of channels. Structural reshape for a circular recess allows the patch-cord cable to be safely hosted inside the tip without any interference with the skin installation.

After evaluating the actual ATED shape measured by processing sensor system data, the movement function of each actuator is calculated to reach the target position. A synchronization task of the actuation movement signals is also performed to improve the system performance and target shape accuracy during shape movement. The control was created in dSPACE, and the connection between the control board and the actuators was specifically designed to monitor both actuator rotation feedback and the power consumption.

4 Results

The controller was implemented real time in a DSP board. Two architectures were considered: open loop and closed loop. In the former, the controller executed the driving command on the basis of the off-line predictions of the actuator shaft rotations needed to reach specific ATED morphing angles. As a result, the controller gives no feedback on the achieved trailing edge shape. In the latter, the controller monitored either the actual ATED shape information given by the FBG-based sensor system distributed over the structure or the actuator rotation levels given by the servo so that the controller actions could be real-time-adjusted. Then, the control strategy is defined as closed loop (feedback control). Both open- and closed-loop control architectures were developed and tested.

In both experimental campaigns, the actuation mechanism was driven to enforce the structure to the desired shape ($\pm 5^\circ$ of morphing). The experimental results were compared with the CAD model expectations. The actual displacements of ATED structure in morphed conditions were measured and compared with the numerical predictions. The error was evaluated by the sum of square errors between the experimental and simulated data. The position of the ATED device in terms of morphing angle was obtained by minimizing this error function. The results achieved through ground testing performed on the demonstrator are reported in Fig. 9. The range of ATED morphing, assessed by the minimum of the error function, was estimated in the range $[-4.91^\circ, 5.21^\circ]$. The deviations with the respect to the CAD shape are given in Figs. 10, 11, and 12 for the baseline and the

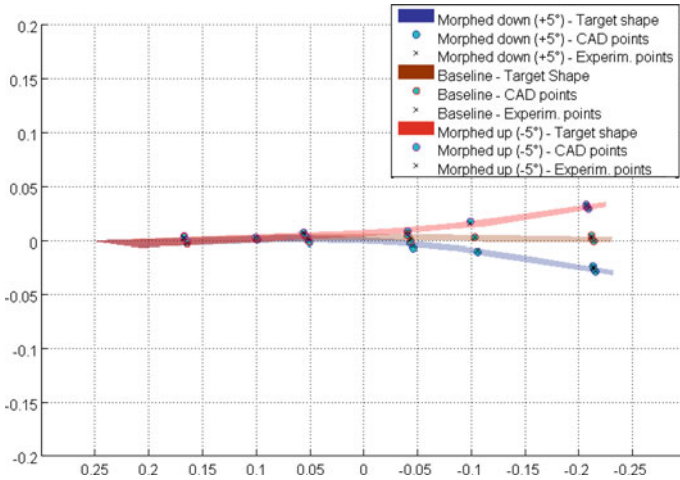


Fig. 9 Comparison between actual and expected shapes

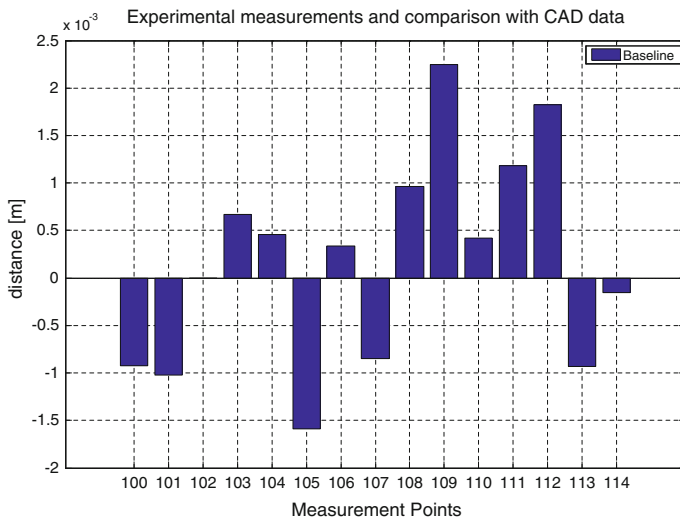


Fig. 10 Shape deviation in baseline configuration

full morphing deployment ($+5^\circ$, -5°), respectively. Control system performance, such as actuation time, slew rate, resolution, and stability, were also assessed.

Shape recovery capability of the feedback control architecture was evaluated along with controller stability and robustness. Such tests were performed by impacting the trailing edge tip with a hammer after commanding the morphing deployment, as shown in Fig. 13.

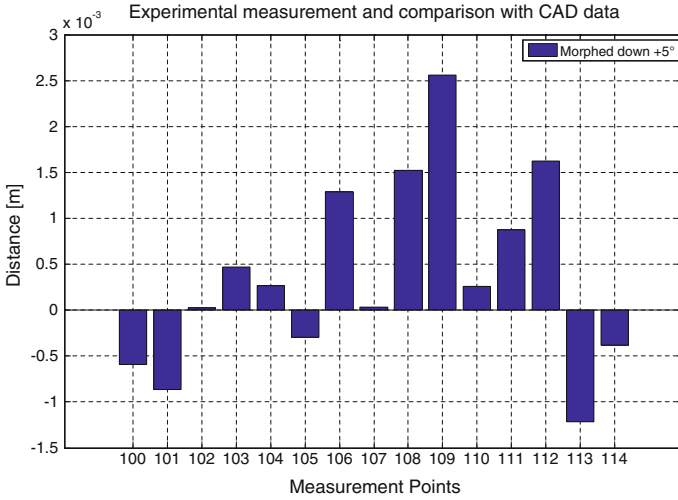


Fig. 11 Shape deviation in morphed down configuration

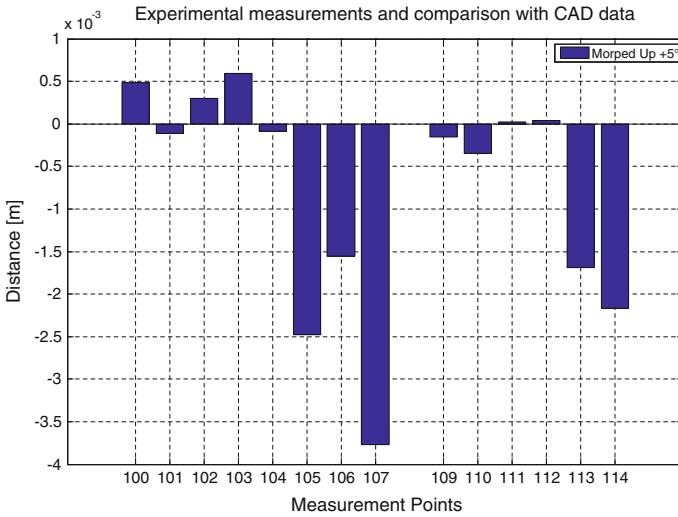
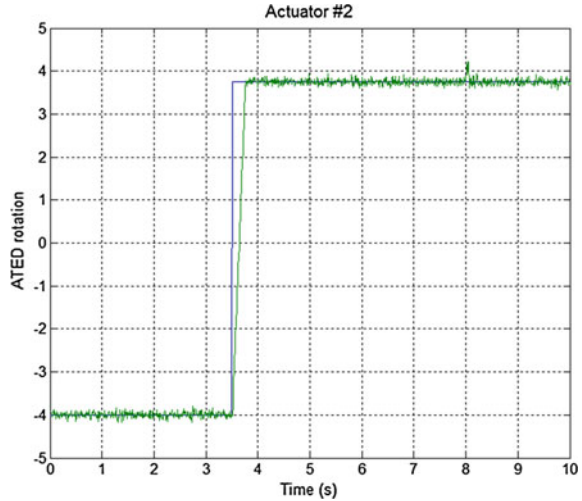


Fig. 12 Shape deviation in morphed up configuration

Strain map distribution sensed by the sensor system was also off-line processed in order to reconstruct ATED shape in morphing conditions. The differences between the actual and target shape was identified by the respective correlations with the strain levels and found satisfactory.

Fig. 13 Controller robustness tests through hammer excitation



5 Conclusions and Future Developments

The technology herein presented has been developed with reference to a real representation of an aircraft. Then, its specifications were derived from realistic load computations and assembly conditions. Its configuration is however defined with respect to a clean wing, i.e., without command and control surfaces. Moreover, in order to properly assess the deriving polar and the consequent L/D estimations, the whole aircraft should be considered, taking into account the presence of the horizontal tail that compensates for the center of gravity excursions and concurs to global produced lift. From the point of view of design, no impressive variations are expected, because what can change is a variation of the absolute value of the load, maybe its distribution, but nothing to drastically change the dimension of the main components. The same applies to the algorithm logic or the sensors installation. Indeed, from the point of view of the real integration in a wing, referring to the investigated layout, an overall simplification should derive, as a consequence of the larger room available, as the device is moved to the wing chord. Some considerations should also be spent regarding the control algorithm. The system is in fact based, as by now, on an adaptive feed-forward slow control logic with a feedback control scheme that compares the measured strain to the target ones, derived from the target shapes. The different forms are established on an off-line computation and refer to the estimated performance of the engines (fuel consumption). This can be improved for at least three steps: referring to the real, reconstructed shape and comparing it to the reference (analytical or numerical) shape; referring to the actual wing performance, by inserting the new morphed geometry into an aerodynamic code, verifying the results and adjusting the control effort, consequently; finally, the assessment of the instant fuel consumption could enable the development of more-accurate control actions aiming at reproducing more fuel-efficient wing

shapes. Then, the passage from a mock-up to a real aircraft should consider at least the following points:

- The installation should be thought with respect to a movable surface (flap), which in turn would mean a different approach and constraints for the installation, including cable routing;
- Finer computation of the achievable L/D and a consequent better prediction of the attainable benefits;
- Modulation of the load, moving from a (virtual) aircraft to another (real);
- Easier overall installation, deriving from a larger available inner space; and
- Integrate real-time controllers, implementing fuel consumption rate as reference variable.

The concept is derived by combining classical and new technologies, all assembled into a new product. In this way, there are well-assessed components (the sensor system, the control system itself, the actuator system, the structural system), combining with other more innovative products, like the morphing skin. While the classical components are not reasonably going to give rise to complex issues on the maintenance and the reliability (classical kinematic, actuator, and sensor chain models may be referred to), the innovative skin should be imagined to undergo a long testing period in order to characterize its behavior outside of the standard design domain above all with respect to fatigue and aging. Following these and the former considerations, it is trivial to consider that a reliable maintenance plan should be designed, in order to properly address the engineering problem concerning the reliability of these devices. An unsolved problem should in the end be cited and concern the use of a multitude or a reduced number of motors. Without going into details of controllability, it is clear that a large number of devices ensure the differential actuation, while a reduced set confines its function to the uniform camber adaptation. Moreover, if a large number of devices are redundant and guarantee the global reliability of the system also in case of failure of some motors, it also needs shorter maintenance periods. This aspect will be investigated in further jobs of the authors concerning the development of the introduced device as generic load modulator. FHA analysis should be also thought as the conclusive part of this path. Summing up all these terms, the actual cost of the device will be derived, that is, a good measure to evaluate its real applicability to real aircraft and, then, to real world. So, in order to increase the proposed technology TRL, the following aspects becomes crucial:

- Maturation of the morphing skin technology;
- Ensure the aging and the fatigue behavior of the overall system;
- Definition of a suitable maintenance plan; and
- Compute costs and benefits, on the basis of the reference architecture.

As a very last point, an expected impact on the general design is expected by the aeroelasticity studies. In fact, because the referred system is a deformable one, it has trivially more degrees of freedom with respect to a standard one. This is why a higher modal density is expected together with a more extensive and complex

coupling of the different modes. Furthermore, because the camber deformation devices are extended, reduction processes should be properly adjusted. This would result in a necessary update in the airworthiness certification regulations and verification procedures to face with this new challenge.

References

1. Botez RM, Molaret P, Laurendeau E (2007) Laminar flow control on a research wing project presentation covering three year period. In: Canadian Aeronautics and Space Institute annual general meeting, Montreal, Canada, Jan 2007
2. Scarselli G, Marulo F, Paonessa A (2010) Sensitivity investigation of aircraft engine noise to operational parameters. In: Proceedings of the 16th AIAA/CEAS aeroacoustics conference (31st AIAA Aeroacoustics Conference), Stockholm, Sweden, June 2010
3. Barbarino S, Bilgen O, Ajaj RM, Friswell MI, Inman D (2011) A review of morphing aircraft. *J Intel Mater Syst Str* 22:823–877
4. Chopra I (2002) Review of state of art of smart structures and integrated systems. *AIAA J* 40(11):2145–2187
5. Vasista S, Tong L, Wong KC (2012) Realization of morphing wings: a multidisciplinary challenge. *J Aircraft* 49:11–28
6. Grigorie LT, Botez RM, Popov AV, Mamou M, Mébarki Y (2012) A hybrid fuzzy logic proportional-integral-derivative and conventional on-off controller for morphing wing actuation using shape memory alloy, Part 1: morphing system mechanisms and controller architecture design. *Aeronaut J* 40(1179):433–449
7. Grigorie LT, Botez RM, Popov AV, Mamou M, Mébarki Y (2012) A hybrid fuzzy logic proportional-integral-derivative and conventional on-off controller for morphing wing actuation using shape memory alloy, Part 2: controller implementation and validation. *Aeronaut J* 116(1179):451–465
8. Spillman J (1992) The use of variable camber to reduce drag, weight and costs of transport aircraft. *Aeronaut J* 96:1–8
9. Wildschek A, Grünwald M, Maier R, Steigenberger J, Judas M, Deligiannidis N, Aversa N (2008) Multi-functional morphing trailing edge device for control of all-composite, all-electric flying wing aircraft. In: Proceedings of the 26th Congress Of International Council of the Aeronautical Science (ICAS), Anchorage, Alaska, US, Sept 2008
10. Ameduri S, Brindisi A, Tiseo B, Concilio A, Pecora R (2012) Optimization and integration of shape memory alloy (SMA)-based elastic actuators within a morphing flap architecture. *J Intel Mat Syst Str* 23(4):381–396
11. Blondeau J, Pines D (2004) Pneumatic morphing aspect ratio wing. In: Proceedings of the 45th AIAA/ASME/ASCE/AHS/ASC structures, structural dynamics and materials conference, Palm Springs, California, Apr 2004
12. Bye DR, McClure PD (2007) Design of a morphing vehicle. In: Proceedings of the 48th AIAA/ASME/ASCE/AHS/ASC structures, structural dynamics and materials conference, Honolulu, Hawaii, US, Apr 2007
13. McGowan AR, Horta LG, Harrison JS, Raney DL (1999) Research activities within NASA's morphing program. In: Proceedings of the RTO AVT specialists' meeting on structural aspects of flexible aircraft control, Ottawa, Canada, Oct 1999
14. Pecora R, Amoroso F, Lecce L (2012) Effectiveness of wing twist morphing in roll control. *J Aircraft* 49(6):1666–1674
15. Dimino I, Flauto D, Diodati G, Concilio A, Pecora R (2014) Actuation system design for a morphing wing trailing edge. *Recent Pat Mech Eng* 7(2):138–148

16. Monner HP, Sachau D, Breitbach E (1999) Design aspects of the elastic trailing edge for an adaptive wing. In: Presented at RTO AVT specialists' meeting on "structural aspects of flexible aircraft control, held in Ottawa, Canada, 18–20 Oct 1999, and published in RTO MP-36
17. Pecora R, Amoroso F, Magnifico M, Dimino I, Ciminello M, Concilio A, Bellucci M (2015) Structural design and aeroelastic analysis of a morphing wing trailing edge. In: SARISTU end of project conference, Moscow, Russia, 19–21 May 2015

Elastomer-Based Skin for Seamless Morphing of Adaptive Wings

Oliver Schorsch, Andreas Lühring and Christof Nagel

Abstract Elastomeric materials are developed for adaptive wings focusing on the elasticity at minus 55 °C to ensure morphing at cruise altitudes. In order to optimize fatigue and ageing properties of this new multi-material device, FEM simulations and mechanical tests are carried out. Two large skin panels are finally manufactured and successfully assembled into a true-scale wind tunnel demonstrator for the experimental validation of adaptive trailing edge device functionality in simulated operative conditions.

Nomenclature

ε_a	Nominal strain amplitude
ε_{a0}	Material-dependent fatigue coefficient
k	Material-dependent fatigue exponent parameter
N	Number of cycles
N_f	Number of cycles to failure or fatigue life
P	Probability
R	Load ratio
n	Statistical sample size

O. Schorsch (✉) · A. Lühring · C. Nagel
Fraunhofer IFAM—Fraunhofer Institute for Manufacturing Technology and Advanced Materials Adhesive Bonding Technology and Surfaces, Wiener Straße, 12, 28359 Bremen, Germany

e-mail: oliver.schorsch@ifam.fraunhofer.de

A. Lühring

e-mail: andreas.luehring@ifam.fraunhofer.de

C. Nagel

e-mail: christof.nagel@ifam.fraunhofer.de

1 Introduction

Aerodynamic morphing for flight profile-specific performance adjustment by changing surface area or camber has been used since the very beginning of aircraft industry. Nowadays, entirely mechanical actuation systems are established, where changes of surface area or angle/shape are obtained by moving solid elements. Well-known examples are swing wing of fighter aircrafts, thrust vectoring of the Harrier or the movable engine of Osprey helicopters as well as slats, flaps and spoilers of every aircraft.

Although widely used, moving solid elements have many disadvantages. Some solutions are quite complex like the trailing edge of the Boeing 747, too heavy or a gapless approach is demanded for reduction of noise and fuel consumption.

On the other hand, seamless or gapless morphing is still a research topic. Gapless morphing combines an appropriate actuation system as well as a skin layer which is able to deform and to carry loads simultaneously. Many actuation systems have been discussed in the past, but there is no single material known yet that solves the mechanical paradox of morphing skins for aviation applications satisfactorily.

Most former morphing wing projects tried to implement large morphing areas, leading to heavy and expensive solutions. In the SARISTU project, funded from the European Union's Seventh Framework Programme, a new morphing approach was investigated focusing on the integration of smaller polymer-based morphing elements to established structures like winglet and trailing edge.

The SARISTU adaptive wing trailing edge device (ATED) was designed with reference to the outer wing of a CS-25 category aircraft. A polymer-based morphing skin was developed by Fraunhofer IFAM to cover seamlessly a multi-finger ribs architecture enabling conformal and differential airfoil camber morphing. Wing shape is controlled during flight (cruise condition) in order to compensate the weight reduction following the fuel burning, by allowing the trimmed configuration to remain optimal in terms of efficiency (L/D ratio) or minimal drag (D). Trailing edge adaptations were investigated to achieve significant benefits in aircraft fuel consumption whose reduction may range from 3 to 5 % due to the improved aerodynamic efficiency.

2 Morphing Skin Design

The primary challenge for adaptive wings is to find a skin design that is able to deform and to carry aerodynamic loads simultaneously. One solution to solve this mechanical paradox is the development of a multi-material skin consisting of hard and soft segments. While soft skin segments release a smooth, gapless transition between movable and fixed parts of the underlying kinematic structure hard skin segments compensate deformations due to air pressure gradients (see Fig. 1).

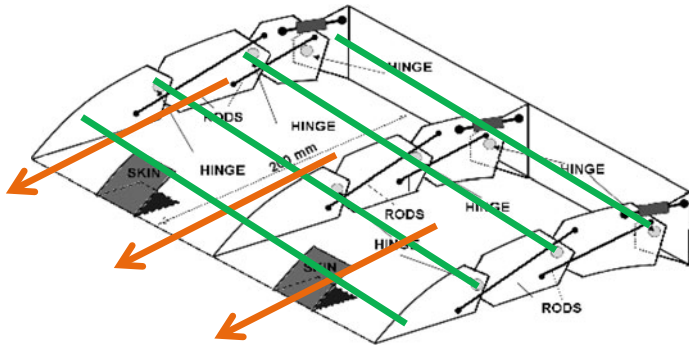


Fig. 1 One solution to solve the mechanical paradox of morphing skins is to transmit loads in spanwise direction and to allow morphing via chordwise movement

The design of such skin is shown in Fig. 2. The soft segments are based on elastomer foam, while the hard segments consist of aluminium profiles. Both segments are covered by a thin layer to ensure a smooth surface. The soft segments are located above and under the rib hinges, while the hard segments are connected to the rib structure.

The morphing skin is able to follow the movement which is prescribed by the active ribs while maintaining the conformity in the deflected configuration for aerodynamic reasons.

The elastomer foam geometry was FEM optimized with respect to the required strain and compression for morphing and to minimize shape deviations due to aerodynamic loads.

Longer foam regions in chordwise direction lead to lower stress and improve fatigue life of the elastomer foam, but buckling caused by aerodynamic suction increases. The foam thickness was calculated to reduce buckling to less than 1 mm height during cruise flight conditions.

Upper and lower skin sides are attached to stringers located between the active ribs (see Fig. 3) to transmit load in spanwise direction and to assure attachment/detachment for ease of maintenance and repair.

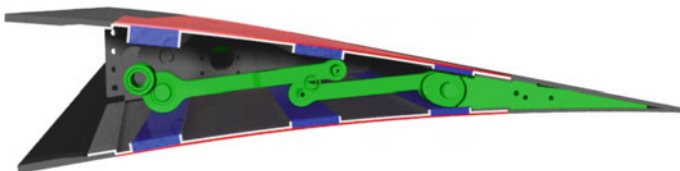


Fig. 2 The morphing skin consists of hard and soft segments. Elastomer foam (blue) is used for soft segments which are located above and under the rib hinges. Hard segments are aluminium profiles (grey). Hard and soft segments are covered with a thin elastomer layer (red). The rib kinematic is shown simplified (green)

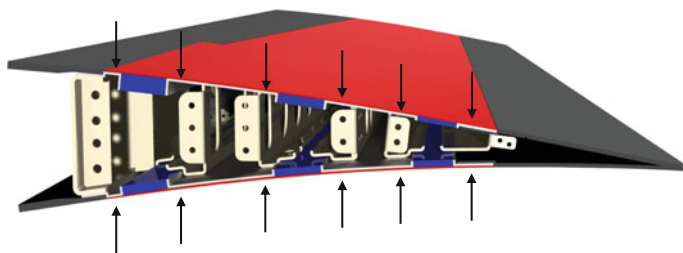


Fig. 3 Upper and lower skin sides are connected to stringers located between the ribs

3 Low-Temperature Elastomers

In order to maximize the durability of an elastomer-based morphing skin, different material properties are required. Most importantly, a material is needed, that show almost constant compression and tension properties as well as storage modulus over the whole temperature range of an aircraft wing surface (-55 to 80 °C) and over a very large number of temperature cycles.

Furthermore, environmental resistances (weather, UV radiation), chemical resistance (Skydrol, deicing agent), as well as resistance to abrasion (sand, small stones on runway), are essential.

The strain within the soft skin segments, given by geometry and deflection angle of the morphing trailing edge, is of great importance for the material selection as well. Maximum strain must not exceed 10 %; otherwise, the elastomer would fail due to fatigue after a number of loading cycles. More than 100,000 cycles is expected to be sufficient for a full service time of a common aircraft.

Finally, high adhesion strength between elastomer skin layer, elastomer foam and aluminium parts is essential for load transmission between hard and soft segments.

Many elastomers are certified for aircraft applications. Examples are silicone, EPDM and polysulfide, which are used as sealants, but not for high strain. One reason is the loss of elasticity as soon as environmental temperature falls below the glass transition temperature of the elastomer (usually between 45 and -10 °C, Fig. 4).

Silicone elastomers are an exception providing excellent elasticity over a wide temperature range. Among the variety of silicone elastomers poly-dimethyl-siloxane (PDMS) is the most used silicone for technical applications. Fluorosilicone is based on polytrifluoropropyl-methyl-siloxane and is used for applications that require fuel or hydrocarbon resistance.

Although glass transition temperature of these silicones is well below -100 °C, common PDMS and fluorinated silicone lose flexibility below 35 °C due to cold crystallization of polymer segments. Crystallization can be reduced or even inhibited by substitution of functional groups at polymer side chains. Polydimethyl-diphenylsiloxane (PDMDPS) is the most important crystallization-hindered

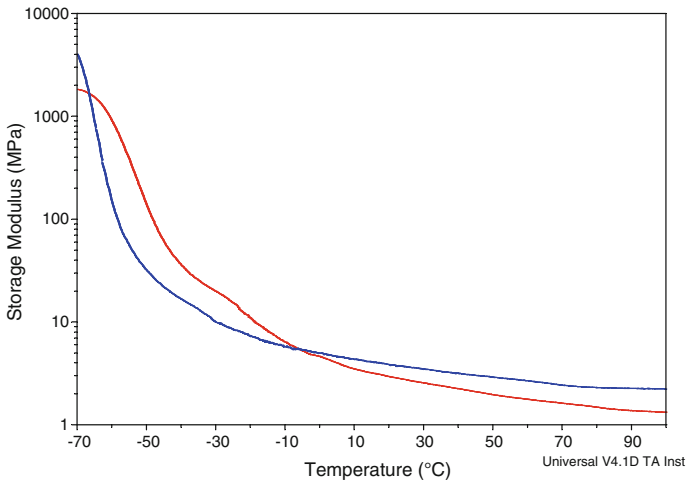


Fig. 4 Dynamic mechanical analysis of low-temperature polyurethane Sikaflex 553 (Sika, *blue*) and EPDM sheeting (Dr. D. Müller, *red*)

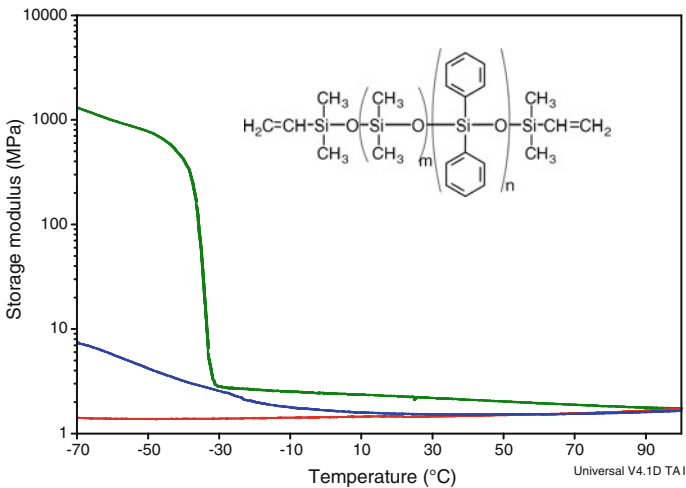


Fig. 5 Dynamic mechanical analysis of common silicone sheeting (MVQ Silicones GmbH, *green*, $n = 0$) and low-temperature silicones with different methyl/phenyl ratio (m/n), Sylgard 184 (Dow Corning, *blue*), Elastosil S690 (Wacker, *red*)

silicone. Because of almost constant elasticity between 100 and -100 °C, phenylated silicone is an important encapsulation material for space applications (Fig. 5).

Several commercial low-temperature silicones are available, mostly for space industry or other low-temperature applications. Most of low-temperature silicones are either platinum-catalysed or peroxidised cured products. Unfortunately, no

commercially available low-temperature silicone sheets and foams meet all the needed material properties for a morphing skin and are known to be very difficult to bond by adhesives.

Hence, in order to adjust the needed material properties and to maximize the adhesion strength between all material interfaces of the morphing skin, it was decided to tailor reactive formulations of platinum-catalysed low-temperature silicones. These tailored reactive formulations can be cured or foamed to obtain the required low-temperature silicone component.

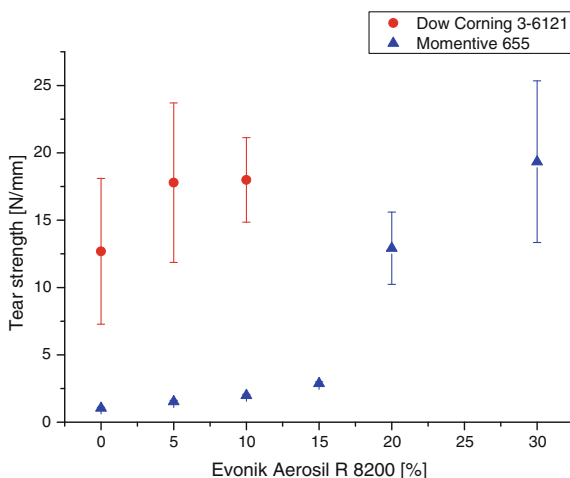
One important example is the addition of fumed silica which improves tensile strength, elongation properties, tear strength and adjusts the viscosity of the formulation at the same time.

The effect of fumed silica on tear strength is shown in Fig. 6. Different levels of Evonik AEROSIL R 8200 were added to the low-temperature silicone encapsulants Momentive 655 and Dow Corning 3-6121. In opposite to the Momentive encapsulant, Dow Corning 3-6121 contains already an unknown amount of fumed silica. All formulations were cured 1 h at 100 °C and the testing was carried out according DIN 53515 using Graves angle test piece.

Fumed silica concentration more than 15 % improves several mechanical properties of the cured silicone elastomers (“locking effect”), but the increased formulation viscosity makes processing more difficult or even impossible.

Liquid formulations of reactive silicone are difficult to foam without special foaming equipment. One possibility is the addition of physical or chemical foaming agents. While chemical foaming agents are thermal reactive components, physical foaming agents consist of encapsulated low-boiling solvents. Both foaming agents release gas after reaching a critical temperature. Since curing reaction and foaming reaction occur at the same time, the formulation must be tailored specifically. The speed of crosslinking reaction can be adjusted by adding inhibitors or crosslinking catalyst.

Fig. 6 Effect of fumed silica on tear strength of different low-temperature silicones



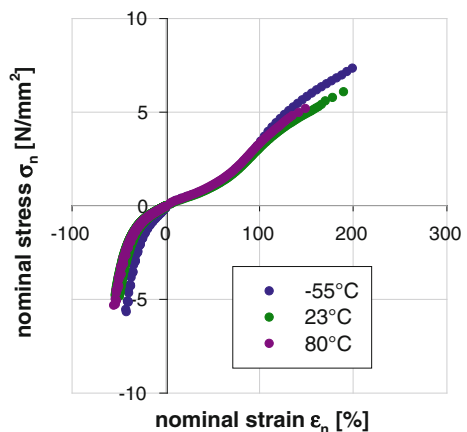
4 Mechanical Properties

Since elasticity and strength properties have to be constant at high and low temperatures, the tailored low-temperature silicones were tested under quasi-static and fatigue loading at -55 , 23 and 80 °C.

Quasi-static tests were performed in uniaxial tension and uniaxial compression at a strain rate of $\sim 0.1/s$. The shape of the tensile test samples was similar to geometry 5A in ISO 527-2. In compression, cylinders with 10 mm height and 20 mm diameter were used. Results are shown in Fig. 7. Considering the slope of the stress–strain curves, it can be confirmed that the stiffness is almost constant over the whole temperature range. A decrease in static tensile strength with increasing temperature can be noticed, but this is not of concern because structures are designed for fatigue loads, which are far below the static limit. Based on the stress–strain curves in Fig. 7, a hyperelastic material model was calibrated, which was later on used to describe the material properties within finite element simulations.

T-joints as depicted in Fig. 8. were used for fatigue tests at test frequencies between $3/s$ and $7/s$ and a load ratio of $R = -1$. The objective of these tests was to set up a strain–life (E–N) curve in order to estimate the fatigue life of the skin module based on finite element modelling with statistical significance. The face-to-face distance of the foam segments between the aluminium parts was ~ 30 mm and the thickness was ~ 10 mm. The sample width was ~ 35 mm and the thickness of the elastomeric top layer was ~ 1 mm. Nominal strain was defined as change in length divided by the initial face-to-face distance of the foam segments. Results are presented in Fig. 8 as nominal strain amplitude versus number of cycles to failure. At lower strain amplitudes, the number of cycles to failure refers to visible crack initiation. No significant crack propagation phase was visible at higher strain amplitudes, so the number of cycles refers to total failure. Visual fracture surface inspection indicated predominantly cohesive failure within the foam segments.

Fig. 7 Stress–strain curves from uniaxial tension and uniaxial compression tests at indicated temperatures and a strain rate of $0.1/s$



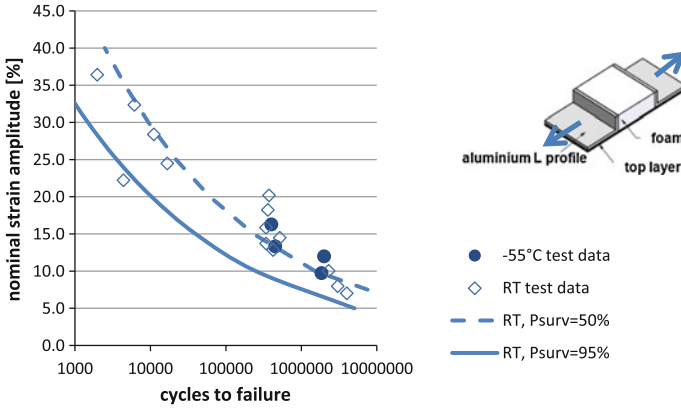


Fig. 8 Strain–life (E–N) curve generated from T-joint fatigue test data at room temperature (RT)

The dashed line in Fig. 8 refers to a power law

$$\varepsilon_a = \varepsilon_{a0} \cdot N_f^{-1/k} \quad (1)$$

as fitted to experimental data, where ε_a denotes nominal strain amplitude, N_f denotes number of cycles to failure, and ε_{a0} and k are material-dependent parameters. Since ε_a acts as controlled variable and N_f as dependent variable, Eq. (1) was resolved for N_f and subsequently least-squares fitted to measured N_f as function of applied ε_{a0} , assuming a lognormal distribution of measured N_f . The values of the corresponding fit parameters are $\log \varepsilon_{a0} = (2.34 \pm 0.12)$ (units of ε in %) and $k = (4.63 \pm 0.47)$.

A lower tolerance limit was calculated based on a t-distribution for $\log N_f$, with a survival probability of $P = 95\%$ and $n = 2$ degrees of freedom. This procedure is similar to the one outlined in ISO 12107. Based on the lower tolerance limit, which is shown as a full line in Fig. 8, it can be stated that the joint can withstand approximately 250,000 cycles at a nominal strain amplitude of 10% until crack initiation. At a nominal strain amplitude of 5%, the joint can withstand approximately 5,000,000 cycles. If a specified number of cycles of $N = 20,000$ is considered, which corresponds to the expected number of the ATED operation cycles, the strain amplitude could be as high as approximately 17%, which is three times as high as the expected strain maximum occurring in operation. It can hence be concluded that, under the current state of knowledge, the skin of the ATED is fail safe.

5 Skin Manufacturing

The morphing skin consists of the three main components. The space between the aluminium profiles is filled with low-temperature foam. Aluminium profiles and foam are covered with a protective layer of low-temperature silicone elastomer (see Fig. 9).

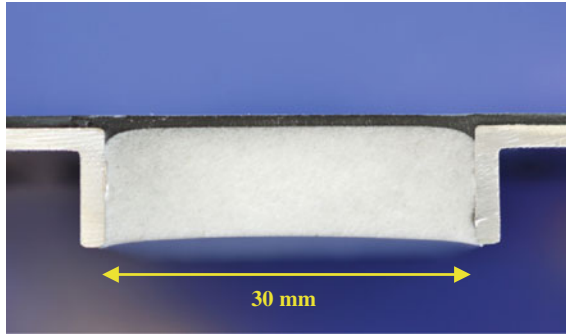


Fig. 9 The morphing skin consists of aluminium profiles, low-temperature silicone foam and a protective layer of low-temperature silicone elastomer

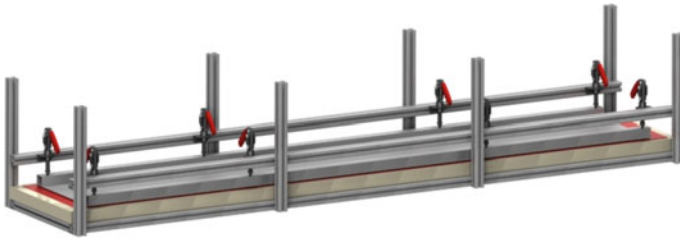


Fig. 10 2.8-m-large heating device to process curing, foaming and adhesive bonding of morphing skin components at the same time

Due to the unavailability of appropriate adhesives to bond those materials for low-temperature purposes, a new manufacturing process was developed. Core feature of this process is to perform the foaming, curing and adhesive bonding of different reactive silicone formulations and aluminium profiles at the same time.

Figure 10 shows a sketch of a heating device to manufacture morphing skins up to 2.3 m length. The heating device consists of several heating pads which are separately controlled to obtain a homogenous temperature distribution and can reach temperatures up to 150 °C.

During the SARISTU project, several large skin panels were manufactured and successfully assembled into a true-scale wind tunnel demonstrator (see Fig. 11).

The experimental validation of adaptive trailing edge device functionality in simulated operative conditions is planned at TsAGI (Moscow) after the integration to the SARISTU morphing wing which consists of an adaptive leading edge, a morphing trailing edge and adaptive wing tip (see Fig. 12) [1].

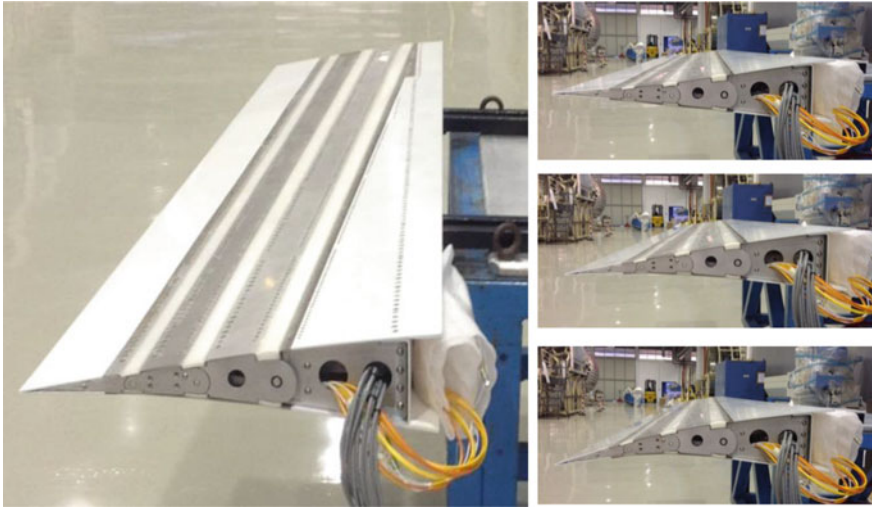


Fig. 11 SARISTU adaptive trailing edge containing morphing skins at upper and lower sides



Fig. 12 SARISTU morphing wing consists of different morphing devices which functionality will be tested in a wind tunnel test at TsAGI, Moscow

6 Conclusions

An elastomer-based skin for seamless morphing of a rib-based adaptive trailing edge was developed. The skin material development focused on low-temperature requirements for cruise flight conditions, resistance to environmental conditions as well as long fatigue life.

Several large skin panels were manufactured in a newly developed moulding process where all skin components are cured, foamed and bonded at the same time to maximize the adhesive bonding between all material interfaces.

Several skins are successfully assembled into a true-scale wind tunnel demonstrator for future functionality tests in simulated operative conditions.

Acknowledgments The research leading to these results has received funding from the European Union's Seventh Framework Programme for research, technological development and demonstration under Grant Agreement No 284562.

Reference

1. <http://www.saristu.eu> (2015). Accessed 01 Apr 2015

Manufacturing and Testing of Smart Morphing SARISTU Trailing Edge

Yasser Essa, Federico Martin de la Escalera Cutillas, Ignazio Dimino,
Monica Ciminello and Antonio Concilio

Abstract Increasing environmental awareness and increasing fuel prices push aircraft industry to enhance aircraft efficiency. Morphing is considered a promising technology for future and next-generation aircrafts. Morphing aircraft changes its external geometry significantly during flight which moderates the design requirements. Adaptive Trailing Edge Device (ATED) is designed and manufactured under SARISTU (Smart Intelligent Aircraft Structures) project. The main challenge is to design and manufacture the smart ATED structure able to support the necessary loads, but it is also capable of changing its geometry. The structure design and actuation system are interrelated. Integration methodology drives multi-disciplinary thinking group from the preliminary design phase. In essence, this considerably amplifies the overall complexity of this work. After manufacturing the ATED, functionality tests have been performed successfully.

Y. Essa (✉) · F.M. de la Escalera Cutillas
Aernnova Engineering Division S.A., 20 Manoteras Avenue, 28050 Madrid, Spain
e-mail: yasser.essa@aernnova.com

F.M. de la Escalera Cutillas
e-mail: federico.martindelaescalera@aernnova.com

I. Dimino · M. Ciminello · A. Concilio
CIRA, the Italian Aerospace Research Centre, Via Maiorise, 81043 Capua, CE, Italy
e-mail: i.dimino@cira.it

M. Ciminello
e-mail: m.ciminello@cira.it

A. Concilio
e-mail: a.concilio@cira.it

Nomenclature

ATED	Adaptive trailing edge device
WT	Wind tunnel
WB	Wing box
FBG	Fiber Bragg grating

1 Introduction

The SARISTU wind tunnel demonstrator (IS12 demonstrator) [1] consists of the following three morphing devices: adaptive droop nose, adaptive trailing edge and adaptive winglet. The main focus of the present paper lays under AS02 and IS12 framework scenarios related to adaptive trailing edge device (ATED). For more information on the morphing box preliminary design, see Ref. [2].

The AS02 demonstrator consists of the first 2 bays of the overall 5 bays ATED implemented in the IS12 demonstrator [3]. The AS02 prototype is shown in Fig. 1 together with the wind tunnel demonstrator (IS12).

The scope of work of the project has been divided into manufacturing, assembly and the latter test campaign system verification plan through a detailed test matrix [4].

2 Manufacturing

The internal structure of the ATED (Fig. 2) can be considered as a skeletal structure composed of ribs and spars. The rear spar is connected directly to the main wing box, carrying the actuators and supporting the whole structure. The ribs divided into various components joined together through pins that enable its rotational

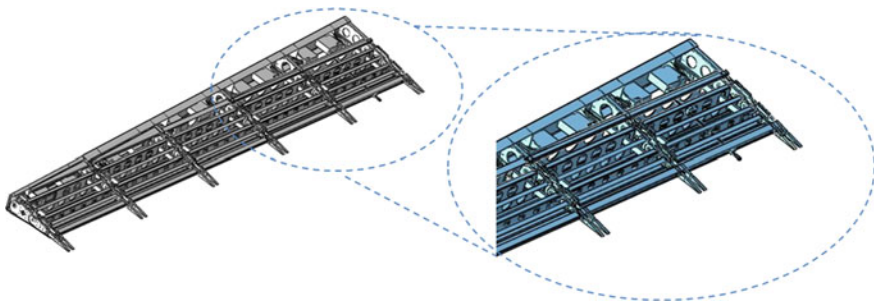


Fig. 1 IS12 five-bay demonstrator (*left*) and AS02 two-bay demonstrator (*right*)

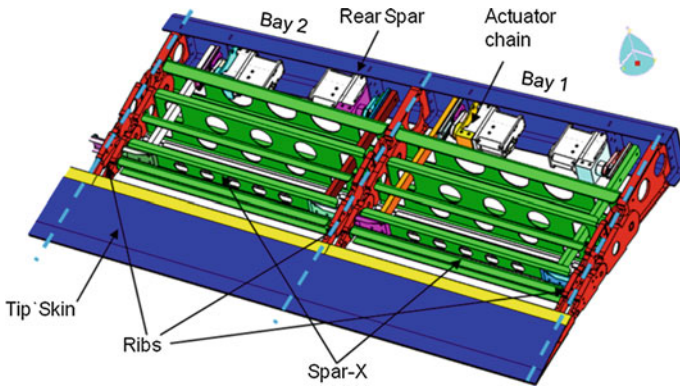


Fig. 2 ATED internal structure, tip skin, rear spar, actuator chain general view

movement as a hinge. The connection mechanism allows the structural morphing of the ATED. At each bay, between two consecutive ribs, the spar-x supports the morphing skin.

The actuator chain carries the morphing movement in the ATED. It transforms the rotational movement of the actuator into displacement of the actuation bar.

The tip skin, as described in Fig. 2, consists of 2 separate aluminium panels of upper and lower skin forming the aerodynamic surface panels.

The dead box skin is an interface between the wing box and the trailing edge. It is made of an upper and lower skin panel as illustrated in Fig. 3. The DB skin is joined to the ATED at the rear spar flange, first spar-x flange and the rib flange (first section only).

The morphing skins are located in the upper and lower surfaces of the trailing edge. The skins are made of aluminium C sections joined through flexible foam and a silicon cover (see Fig. 3). The design and development of the morphing skin has been provided by FhG (Fraunhofer).

Tooling is designed and developed by AERNNOVA to ensure perpendicular drilling between the internal structure and the skins. This is essential for a good load transmission between the components and ensures the quality of the aerodynamic surfaces. The improvement in the assembly phase can be considered unique and only valid for the designed ATED structure assembly.

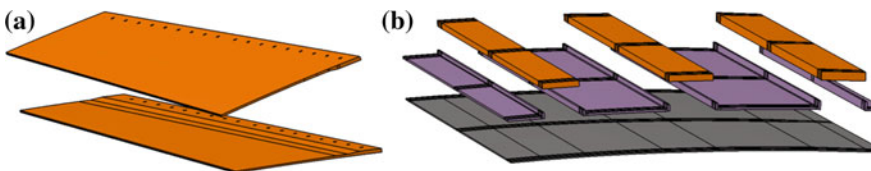


Fig. 3 DB skin and morphing skin view

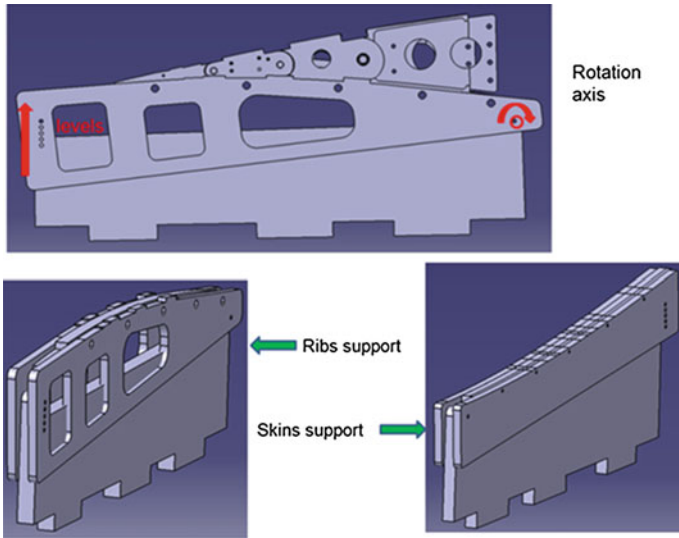


Fig. 4 Tooling design for rib support and skin support

The design of the tooling is developed with a rotational axis in order to allow correct perpendicular positioning of the drill. In addition, the tooling has different setups to enable rib assembly support and skin support. The rib support allows the assembly of the internal structure and upper surface drilling. The skin support allows upper skin support for the lower surface ATED drilling and assembly. Figure 4 describes the rotational behaviour of the tooling and its different setups.

Milling is decided over drilling as tests show unpromising drilling results. The silicone skin is damaged in the drilling process, whereas milling showed much neater holes and higher precision of hole placement (see Fig. 5).

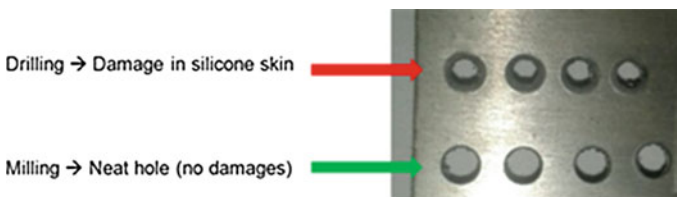


Fig. 5 Drilling versus milling

3 Assembly

3.1 Internal Structure Assembly

The assembly process begins by setting the tooling configuration for rib support. This way rib angles can be modified across the spanwise direction of the 2-bay demonstrator.

Firstly, ribs are positioned on the tooling. Actuators are assembled to the rear spar followed by the rest of the actuator components. After completing this, the rear spar and the actuator are mounted with the ribs on the tooling. The first three spar-x are installed beforehand and the actuator beam is introduced and connected to the actuator chain. The following spar-x FB2 is then installed and connected to the actuator beam and reinforced with brackets. The rest of the spars are installed here in after.

3.2 Milling

Milling is carried out with support of the tooling to ensure perpendicular direction of the holes and fastening positions (Fig. 6).

Firstly, milling in the upper surface is carried out. A drilling mask is positioned on the milling surface and milling is performed through the skin and spar cap. The drilling mask is then removed and a counter sink is placed on each hole of the skin surface (see Fig. 7). Skins are then fastened to the upper surface through blind bolts.

After completing the upper surface, milling is carried out at the lower surface. For this, the tooling configuration for the ribs has to be removed and changed into the skin surface configuration (see Fig. 4).

The upper surface is then placed upside down, on top of the tooling and milling is carried out on the lower surface using the drilling mask. The spar cap is milled to a much larger diameter as shown in Fig. 8 for rivet nut placement. A counter sinks are placed in each hole of the skin surface and spar cap.

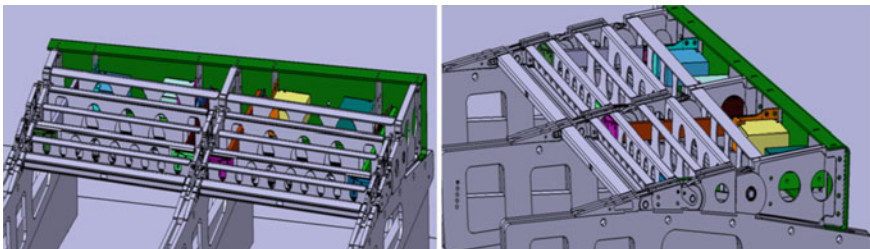


Fig. 6 Tooling support for correct perpendicular milling

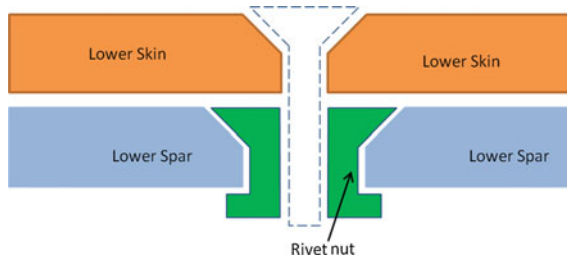


Fig. 7 Milling procedure at lower surface

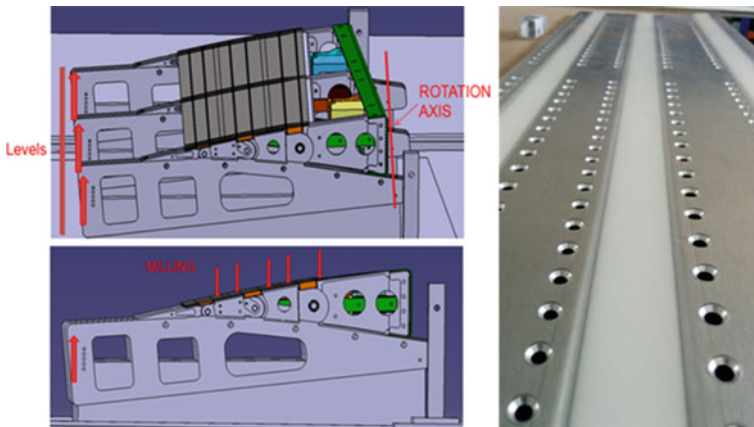


Fig. 8 Milling procedure and final result on morphing skin

3.3 Sensor and Cable Installation

Ribbon tape sensors are installed in the inner section of the upper tip skin. It is arranged in the spanwise direction of the skin in order to measure the spanwise deflection of the ATED. The installation of the sensor is carried out following the steps defined in application scenario AS04. The sensors are joined via epoxy resin and heat treatment.

Shape sensors are installed in the chordwise direction of the ATED to measure displacements produced by movements caused through morphing. The sensor runs in the upper morphing skin to the upper tip skin. For the 2-bay demonstrator, a shape sensor is installed in each bay. The installation procedure of the sensor is done through bonding at the sensor support structure.

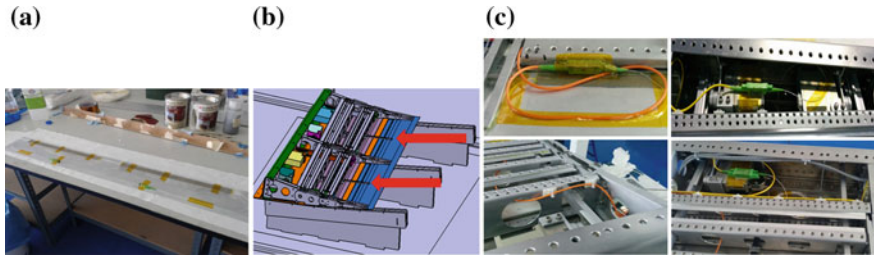


Fig. 9 Sensor and cable installation

Cable routing of the ribbon tape (orange cable) and shape sensors (yellow cable) is done through the spar holes and rib holes in order to ensure minimal interaction with the structure during morphing. Cables are then fixed with supports (white) so that no interference is produced between the internal structure and the cables. Actuator cables are fixed at the rear spar, avoiding the actuator beam (grey) (see Fig. 9).

3.4 Lower Skin Assembly

This is the final step of the assembly of AS02 Demonstrator. The lower tip skin is bonded to the upper tip skin and the rest of the skins are screwed to close the ATED. Extra holes were perforated in the upper and lower skins as a requirement for testing (eyebolts join).

4 Test Campaign

4.1 Test Definition

The following configurations and objectives of the test campaign are defined. See Ref. [5] for more information.

4.2 Test Setup

4.2.1 Boundary Conditions

Two types of boundary conditions are defined for the tests (see Fig. 10).

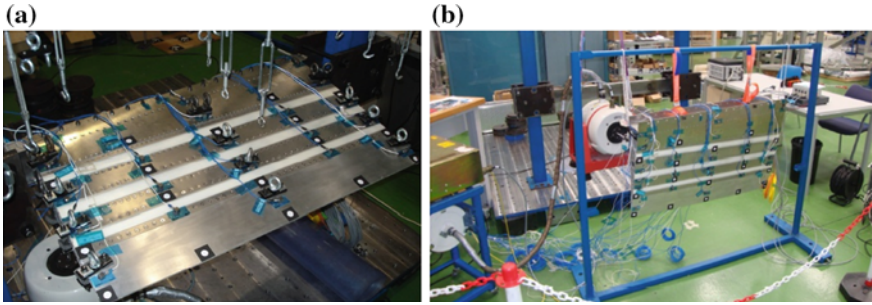


Fig. 10 Specimen clamped and free-free conditions. **a** Clamped, **b** free-free

1. The clamped condition, where the specimen is screwed to a beam.
2. The free-free conditions, where the specimen is hanged through rubber bands.

4.2.2 Control Conditions

Two control conditions are tested:

1. Feed-forward control—Actuator displacement is set in the specimen without actuator displacement correction due to external forces.
2. Feedback control—Actuator displacement is set in the specimen and displacement control correction is enabled due to external forces.

4.2.3 Aerodynamic Load Application

The aerodynamic loads are applied by means of a counterweight lever and using waffle trees at in 4 points for each rib. In order to avoid the tree's influence in the specimen during modal analysis, the connection between the ribs and the load tree is done using a spring (see Fig. 11).

4.2.4 Measuring Results

Displacements are measured through a 3D optical system, where geometry change is determined by a set of reference points called targets. Figure 12 shows the 3D optical system and the targeted points.

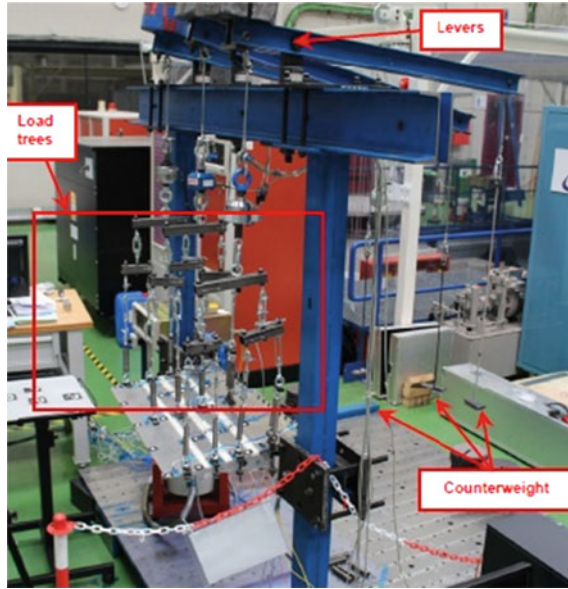


Fig. 11 Aerodynamic load application system

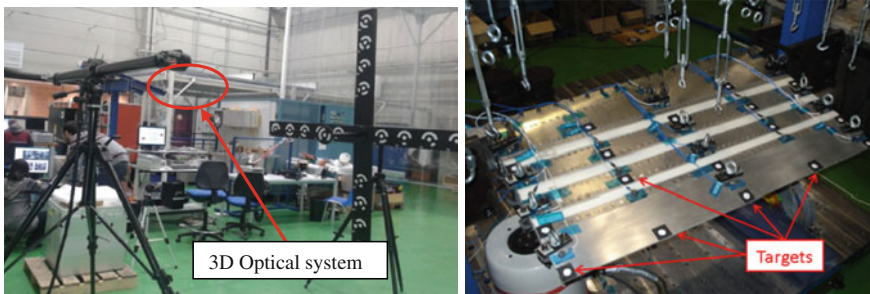


Fig. 12 3D displacement measuring camera and targets

For vibration tests, the system so-called LMS SCADAS III is used. The system produces vibrations through a shaker and measures the movement through accelerometers located at various positions of the specimen (Fig. 13).

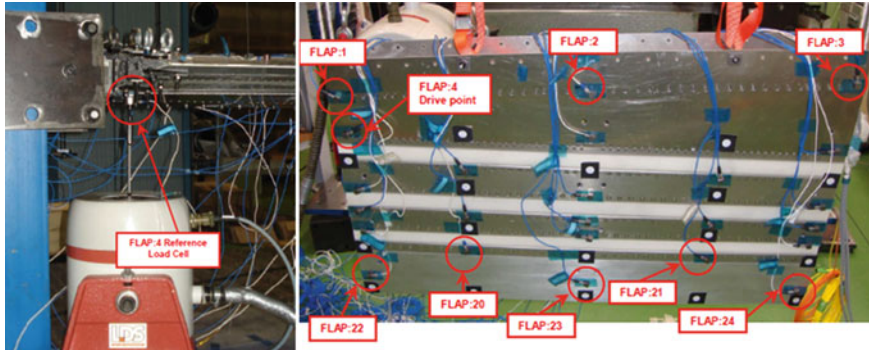


Fig. 13 Vibration and acquisition system characteristics

4.3 Test Results

4.3.1 Modal Analysis—Free–Free Boundary Conditions

Test configuration is described in 8.1 in Table 1. Free–free conditions are applied to detect dynamic properties of the system alone, without any contribution from the test rig and connections (i.e. damping)

Different configurations are tested (-5° , 0° , $+5^\circ$). Control system is offline. Actuators are fed

Results showing the frequency modes of the specimen are displayed in Fig. 14 and Table 2)

4.3.2 Modal Analysis—Clamped Conditions and Feedback Control

Configuration is described in 8.5 in Table 1. Modal analysis is carried out having clamped conditions under aerodynamic loading and unloading. Control system will be offline as the experiment takes place (feed-forward control law). Actuator system will be blocked, following its own internal friction or a safety block.

Results for the various configurations are displayed in Table 3.

From Table 4, results show negligible difference between morphing modes. However, between torsion modes, there is a noticeable difference of 8 Hz.

Table 1 Test campaign definition

Item	Investigated configuration		Declared objectives	Parameter
Modal analysis (free-free system) Range [0–80] Hz ACTUATORS FED	Unloaded structure Control system offline	–5°	Modal parameters • Eigenvectors • Complex eigenvalues	Correlation between numerical and experimental results Previous test campaigns on isolated elements
		0°		
		+5°		
Static analysis (system clamped to a test rig) FF control	Actuated unloaded (V non-applicable)	–5°—VC	Deformed shapes Drive system functionality (FB offline)	Correlation between numerical and experimental results Previous test campaigns on isolated elements
		0°—VD		
	Actuated loaded	+5°—VC		
Static analysis (system clamped to a test rig) FB control (–5°, 0°, +5°)	Actuated unloaded	Non-perturbed	Deformed shapes Control system stability (online)	Correlation between desired and attained shapes Shape recovery capability
		Perturbed		
	Actuated loaded	Non-perturbed		
		Perturbed		
Item	Investigated configuration	Declared objectives	Parameter	
Static analysis Bubbling	Pressurised balloon into the structural body—flexible skin Non-actuated system ACTUATORS FED	Skin deflection	Correlation between numerical and experimental results	
Modal analysis (system clamped to a test rig) Range [0–80] Hz FF control	Unloaded Loaded	–5°	Modal parameters • Eigenvectors • Complex eigenvalues Actuation time measure	Correlation between numerical and experimental results
		0°		
		+5°		Previous test campaigns on isolated elements
Modal analysis (system clamped to a test rig) Range [0–80] Hz FB control	Unloaded	–5°	Modal parameters: • Eigenvectors • Complex eigenvalues Control system stability (online) Actuation time measure	Correlation between numerical and experimental results. Previous test campaigns on isolated elements

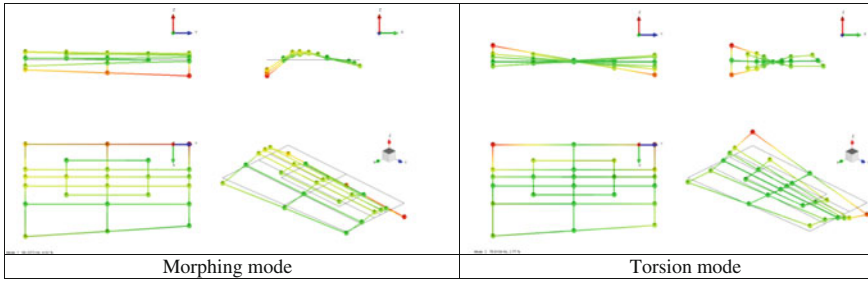


Fig. 14 Modal results for free–free boundary conditions

Table 2 Mode results for free–free boundary conditions

Mode ID	Mode	Frequency (Hz)	Damping (%)	MP (%)
Mode 1	Morphing mode	65.227	4.52	30,634
Mode 2	Torsion	76.610	2.77	69,366

4.3.3 Static Analysis—Feed-Forward Controls

Test configuration is described in Table 1. The test considers both aerodynamic and actuator forces on the specimen and how it behaves to attain the desired deformation. Four cases are studied in this test. Results are displayed below:

- Case 1 Unloaded case. Deformed shapes without external loads, of a smooth transition from morph up to morph down, with a global deflection of 5°. An example result for morphed down configuration is displayed (Fig. 15).
- Case 2 Morphed up at Vc load. Deformed shape with Vc load at -5° (Fig. 16).
- Case 3 Morphed down at Vc load. Deformed shape with Vc load at +5° (Fig. 17).
- Case 4 Loaded at Vd with 0° deflection (Fig. 18).

4.3.4 Static Analysis—Skin Bubbling Effect

Test configuration is described in 8.4 in Table 1. Bubbling effect is simulated by introducing pressurised balloons in the chambers of the 2-bay structure, under the skin. The internal pressure in both chambers is measured with a pressure gauge and skin deformations are measured at three points with dials (Fig. 19).

Results are displayed in Table 5.

Table 3 Modal results for clamped conditions under feed-forward control

Configuration	Deflection degrees	Load type	Case name	Mode	Freq (Hz)	Damping (%)	MP (%)
Unloaded	-5	N/A	Mod_Clamp_FF_1	Morphing	29.810	2.99	53.666
			Torsion	59.597	2.04	46.334	
	0	N/A	Mod_Clamp_FF_2	Morphing	27.779	3.41	52.14
			Torsion	59.009	2.17	47.86	
	+5	N/A	Mod_Clamp_FF_3	Morphing	27.928	3.65	47.998
			Torsion	57.682	3.48	52.002	
Loaded	-5	Vc	Mod_Clamp_FF_4	Morphing	27.255	3.26	59.368
			Torsion	59.140	1.51	40.632	
	0	Vd	Mod_Clamp_FF_5	Morphing	32.923	2.06	73.573
			Torsion	62.815	0.61	26.427	
	+5	Vc	Mod_Clamp_FF_6	Morphing	33.246	1.21	60.04
			Torsion	62.461	1.46	39.96	
	0	N/A	Mod_Clamp_FF_7	Morphing	30.602	2.21	47.719
Torsion			67.629	1.47	52.281		

Extra case unloaded without fixtures

Table 4 Result comparison for test with and without fixture (eyebolt)

Mode ID	Mode	Frequency with fixtures (Hz)	Frequency without fixtures (Hz)
Mode 1	Morphing mode	29.810	30.602
Mode 2	Torsion	59.597	67.629

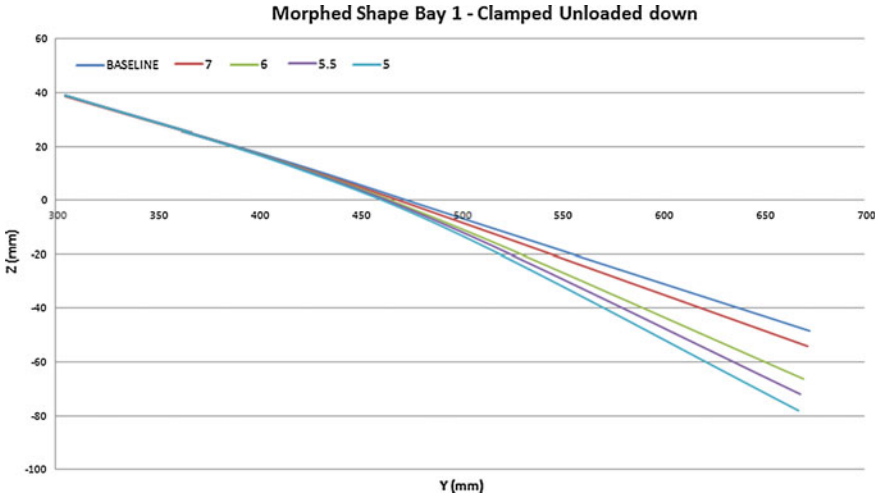


Fig. 15 Deformed shape for bay 1—morphed down

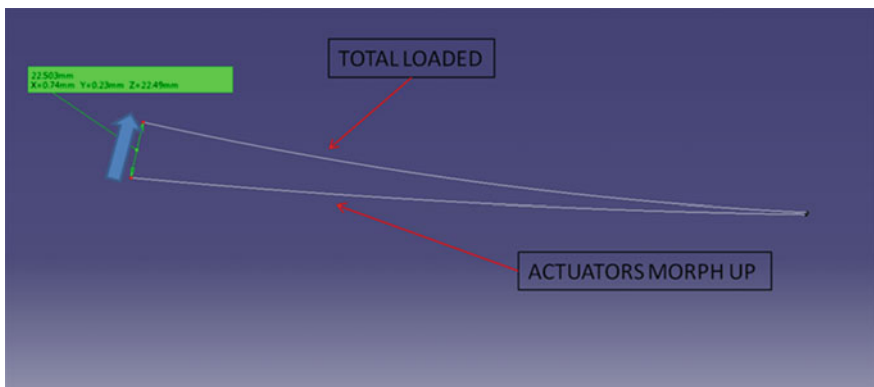


Fig. 16 Deformed shape for bay 1—morphed up under V_c load

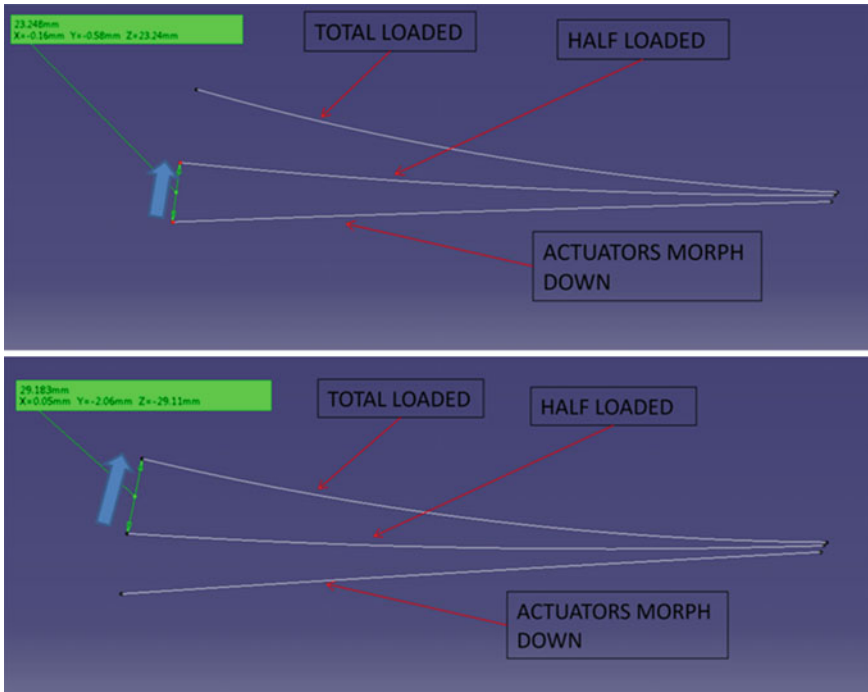


Fig. 17 Deformed shape for bay 1—morphed down under V_c load

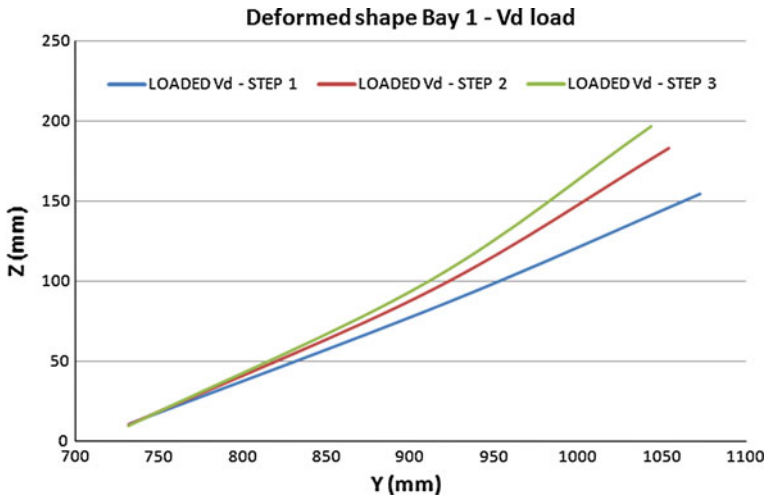


Fig. 18 Deformed shape for bay 1—unmorphed (0°) under V_d load

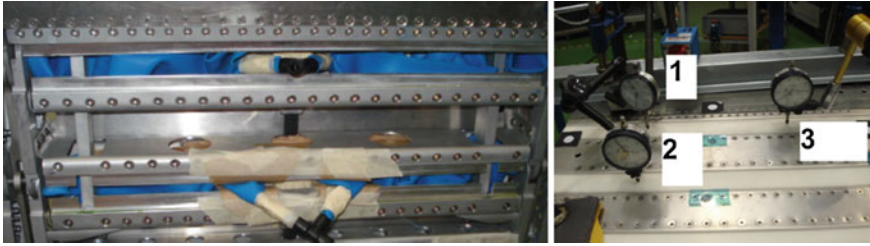


Fig. 19 Test setup and measurement points

Table 5 Bubbling tests results

Pressure (bar)	Displacement (mm)		
	Point ID 1	Point ID 2	Point ID 3
0	0.01	0	0
0.2	0.13	0.28	0.16
0.4	0.4	0.6	0.4
0.4 ^a	N/A	0.72	0.44
0.5	N/A	1.06	0.52
0.5 ^b	N/A	N/A	0.56
0.7 ^c	N/A	N/A	0.62

Notes

Some final values are not consistent with the initial value of the next pressure step due to balloons explosions

^aBalloon located in position 1 explodes

^bBalloon located in position 2 explodes

^cBalloon located in position 3 explodes

5 Conclusion

The main conclusion of this chapter is the accomplishment of ATED manufacturing and especially in the assembly stage, where a brilliant improvement was achieved. It was designed and manufactured as a special tool adapted to ribs' profile and intrados morphing skin profile for the best control of all components and accurate milling of the aluminium and morphing skins.

It is observed that the test campaigns for both static and modal tests implemented are performed successfully. The AS02 demonstrator withstands all loads defined during the test campaign without failure or plastic deformations. The modal results obtained show a good dynamic response of the structure.

AS02 demonstrator was manufactured and assembled successfully with important acquired experience to be implemented during ATED 5-bay demonstrator for wind tunnel test during IS12. In Fig. 20, the final integrated ATED 5-bay demonstrator is shown.

The ATED has been successfully assembled to the torsion box structure in the morphing wing demonstrator as shown in Fig. 21.

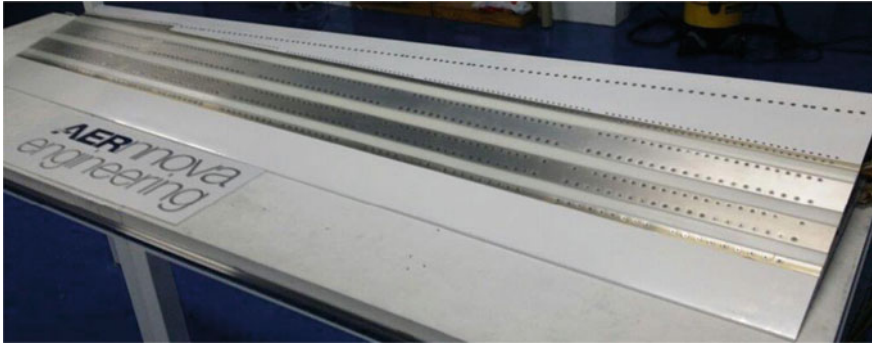
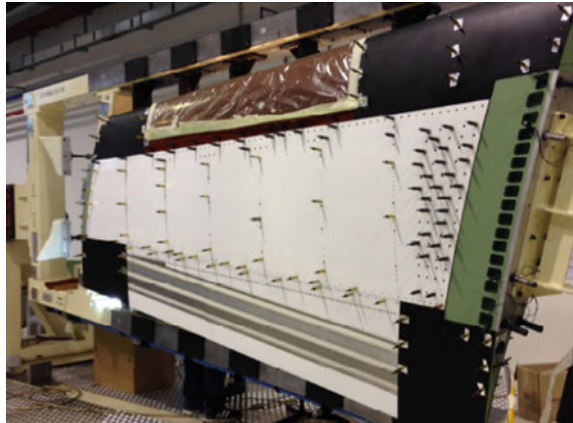


Fig. 20 ATED 5-bay demonstrator

Fig. 21 Morphing wing demonstrator



Acknowledgments The research leading to these results has received funding from the European Union’s Seventh Framework Programme for research, technological development and demonstration under Grant Agreement No 284562. Their financial support is greatly appreciated.

References

1. SARISTU_MTR presentation_Final_Day1 & 2.ppt—www.prodaxs.eu
2. Belluci M MARE—D22.2: SARISTU WP2.2—adaptive trailing edge device (ATE) adaptive trailing edge: WT demonstrator stress report, 14 Mar 2014
3. ONERA—Dumont A, Godard J-L—D22.1: SARISTU WP2.2—Aerodynamic optimization of trailing edge shape (Issue 3), 17 June 2014
4. Airbus—Bauss S; CIRA—Concilio A—D21.2: SARISTU WP2.1—adaptive trailing edge device (ATE) test specifications, 15 Mar 2012
5. AERNN—Muñoz V, Essa Y—D23.2: SARISTU AS02—adaptive trailing edge (ATE) device adaptive structural morphing system, 27 Feb 2015

Part III

Technology Stream: Morphing.

Wingtip Morphing Trailing Edge

Introduction and Overview

The scenario's main targets are to provide an engineering solution for a full-scale active winglet considering certification requirements for large airplanes and to perform a benefit versus risk assessment of this technology. The scenario's main achievements are the close-to-flightworthy design, manufacturing, and testing of such a full-scale active winglet, to provide an estimate of potential mass benefit and drag reduction, as well as to provide an estimate of the potential fuel saving with this technology for an average airline. The results are presented in 6 papers:

1. Design, Optimization, Testing, Verification, and Validation of the Wingtip Active Trailing Edge, Andreas Wildschek et al.
2. Winglet Design, Manufacturing and Testing, Danijel Drezga et al.
3. Seamless Morphing Concepts for Smart Aircraft Wingtip, Christoph Nagel et al.
4. Dynamic Aircraft Model with Active Winglet, Effects of Flight Mechanics and Loads Analysis, Toni Kanakis et al.
5. Influence of H2 and ∞ Criteria on Feed-Forward Gust Loads Control Optimized for the Minimization of Wing Box Structural Mass on an Aircraft with Active Winglets, Andreas Wildschek
6. Evaluation of the Performance Benefits of the Winglet Active Trailing Edge in AS03, Martin Herring.

Design, Optimization, Testing, Verification, and Validation of the Wingtip Active Trailing Edge

Andreas Wildschek, Stefan Storm, Martin Herring, Danijel Drezga,
Viken Korian and Olaf Roock

Abstract Within the scope of the SARISTU project (smart intelligent aircraft structures), a wingtip active trailing edge (WATE) is developed. Winglets are intended to improve the aircraft's efficiency aerodynamically, but simultaneously they introduce important loads into the main wing structure. These additional loads lead to heavier wing structure and can thus diminish the initial benefit. Preliminary investigations have shown that a wingtip active trailing edge can significantly reduce these loads at critical flight points (active load alleviation). Additionally, it can provide adapted winglet geometry in off-design flight conditions to further improve aerodynamic efficiency. The idea of the active winglet has been successfully treated in several theoretical studies and small-scale experiments. However, there is a big step towards bringing this concept to a real flight application. In this project, a full-scale outer wing and winglet are currently being manufactured and will be tested, both structurally and at low speed in a wind tunnel. The scope for eventual EASA CS25 certification of a civil transport aircraft with such a winglet control device will then be assessed. In particular, a

A. Wildschek (✉) · S. Storm
Airbus Group Innovations, 81663 Munich, Germany
e-mail: andreas.wildschek@airbus.com

S. Storm
e-mail: stefan.storm@airbus.com

M. Herring
Airbus Group Innovations, Building 20A1, Filton, Bristol BS34 7QW, UK
e-mail: martin.herring@eads.com

D. Drezga · V. Korian · O. Roock
FACC AG, Fischerstrasse 9, 4910 Ried im Innkreis, Austria
e-mail: d.drezga@facc.com

V. Korian
e-mail: v.korian@facc.com

O. Roock
e-mail: o.roock@facc.com

load alleviation system requires a minimum operational reliability to take effect on the applicable flight load envelope for structural design. Therefore, the potential failure modes are assessed, and a fault tree analysis is performed to draw key requirements for the system architecture design. In order to assess the overall system benefit, manufacturing, operation, and maintenance requirements are taken into account. The confined space inside the winglet loft-line presents a significant challenge for integration of an active control system. It is shown how small changes to the aerodynamic surface have both reduced the aerodynamic hinge moments (leading to lighter actuators) and created additional internal space for systems, whilst maintaining an equivalent overall drag level. The potential for reducing wing and winglet loads with a winglet control device is assessed. The kinematic design challenge of delivering the necessary power in a confined space is described. Actuation is accomplished by a single electromechanical actuator which is housed inside the CFRP winglet.

Nomenclature

ACE	Actuator control electronics
AS	Assumption
CAD	Computer-aided design
CFRP	Carbon fibre reinforced polymer
CG	Centre of gravity
CMM	Coordinate measurement machine
CNC	Computerized numerical control
DAL	Development assurance level
DAQ	Data acquisition
EMA	Electromechanical actuator
FC	Failure condition
FEA	Finite element analysis
FEM	Finite element model
FHA	Failure hazard assessment
FTA	Fault tree analysis
GLAS	Gust load alleviation system
GST	Ground static testing
GVT	Ground vibration testing
IS	Integration scenario
LCM	Liquid composite moulding
L/D	Lift to drag (ratio)
MARI	Membrane-assisted resin infusion
MCU	Motor control unit
MIF	Multivariate mode indicator
NDI	Non-destructive inspection
OOA	Out of autoclave
<i>P</i>	Probability of occurrence of failure
PSSA	Preliminary system safety analysis

Q	Probability of being in failure state
RQ	Requirement
RSDP	Reference structure design principle
RTM	Resin transfer moulding
WATE	Wingtip active trailing edge
WT	Wind tunnel

1 Introduction

Large winglets offer the potential to improve aerodynamic efficiency of an aircraft, but also introduce considerable loads to the main wing structure which leads to an increase of wing weight. This weight increase can jeopardize the aerodynamic performance benefit. Moreover, if large winglets are applied as a retrofit solution for an already operational aircraft type, any requirement to strengthen the primary wing structure would be a very costly drawback. An active trailing edge in the winglet can alleviate these additional loads, and thus, the wing weight can be reduced. Moreover, the winglets' control surfaces can be used to optimize the L/D ratio in off-design flight points offering some additional aircraft efficiency improvement. The idea of active winglets is not completely new with investigations being carried out in various directions.

Bourdin et al. [1] examined in wind tunnel tests a flying wing configuration with winglets having a variable cant angle control. Moving the winglets is used here for primary flight control around all three aircraft axis. A simulated assessment of multiple morphing parameters in the outer wing and winglet is made by Ursache et al. [2]. The outer 25 % of wingspan is divided into several segments, giving more degrees of freedom to adapt the wing. Thus, the wing can be adapted for different flight conditions with regard to an optimized lift distribution. Furthermore, the advantage of a shortened wingspan for ground operation is mentioned. Boeing [3] holds a patent for such a variable winglet cant angle.

A very different application is studied by Breitsamter and Allen [4, 5]. They use a split winglet trailing edge tab actuated dynamically to accelerate trailing vortex breakdown through the creation of instabilities. In their large transport aircraft scaled wind tunnel model, the actuation of the flaps is performed externally due to lack of space with the motor installed in an extra wingtip pod. Static deflections were examined as well and showed higher vorticity. However, big deflections are used (20°), and multiple gaps result from the deflection of the control surfaces. Kauertz et al. [6] investigate similar effects on a simpler airfoil model.

In addition to vortex instability excitation, Park et al. [7] perform computational studies of the influence to the lift-to-drag ratio by the deflection of a winglet flap. With their configuration, the general aerodynamic characteristics were not significantly influenced, but attainable lift-to-drag ratios were reduced with rudder

deflections. Nagel et al. [8] find drag reduction potential for a winglet not optimized purely aerodynamically but with structural targets included in a multiobjective optimization. Moreover, these two designs feature a winglet cant angle around 45° . In order to eliminate the additional wing bending loads introduced at the outer wing by the winglet, Guida [9] has patented an active winglet with rudders for load alleviation. The background is to retrofit small aircraft with winglet without having to modify existing wing structure. Tamarack Aerospace Inc. is building these active winglets; however, the rudder is not implemented into the winglet itself, but into the horizontal wingtip extension (winglet root). The Airbus Group holds patents in this field as well [10, 11], serving as base for this research project.

Aeroelastic control and aerodynamic trimming are also part of the studies and wind tunnel experiments of Buxel and Dafnis [12, 13]. The winglet rudder is able to excite the first bending mode of the wing. They also focus more in detail on the actuator implementation. The piezo-actuator installation fills the whole winglet resulting from an assessment of different actuator candidates.

Research in the field of active winglets has revealed some potential. However, it has to be studied whether such a system is technically realizable in a full-scale application, in compliance with regulations, and whether it proves beneficial at aircraft level. Research work presented in this paper, however, goes one significant step further by providing an engineering solution for a full-scale and close to flight-worthy active winglet for a short-range aircraft taking into account boundary conditions and requirements ranging from safety and reliability considerations, manufacturing, operation, and maintenance standards, to performance and fuel efficiency optimization.

2 Winglet Design Considering Multiobjective Design Criteria

This paragraph mainly summarizes the active winglet design in parts already presented in [14]. The active winglet was designed according to EASA CS-25 design requirements [15]. Figure 1 shows a drawing of the final design. In order to derive design loads for iteration loop zero, necessary tab deflections (the tab is the green part in Fig. 1) are estimated based on CFD computation. Figure 2 illustrates a series of deformed meshes used in the initial investigations, with control surface deflections in the range from -15° to $+15^\circ$. In order to derive realistic mass benefits, it is important to understand the effect a wingtip active trailing edge device will have on the design loads envelope. Exemplarily, the 2.5-g design dive speed manoeuvre loads (bending moment along the span of the wing), are compared for 3 of these deformation states in Fig. 3.

Loads with $\pm 15^\circ$ deflection expressed are illustrated as a ratio of the undeformed condition, i.e. passive winglet. The -15° (up) state shows the potential for alleviating loads, particularly in the outer wing. The $+15^\circ$ (down) state on the other hand

Fig. 1 Final active winglet design

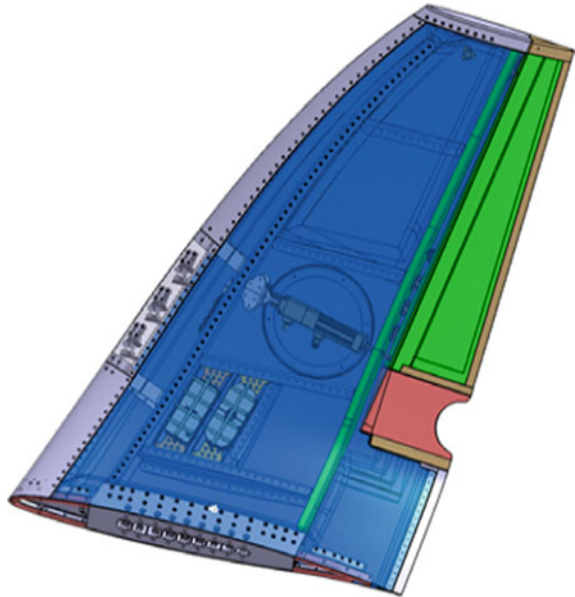
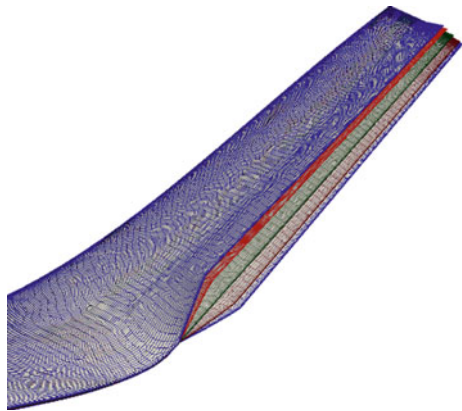


Fig. 2 Deformed CFD meshes (Tau) used to simulate the active winglet [16]



shows the significant load increase in the event of jam of the single electromechanical actuator.

For a reasonable hint on required positive winglet trailing edge deflections, potential drag reduction in off-design points is investigated. Exemplarily, the effect of tab deflection on L/D ratio is given in Fig. 4. It is concluded that positive tab deflections can be mechanically limited to 10° or less without any loss of performance, thus reducing design loads for failure cases such as actuator jam.

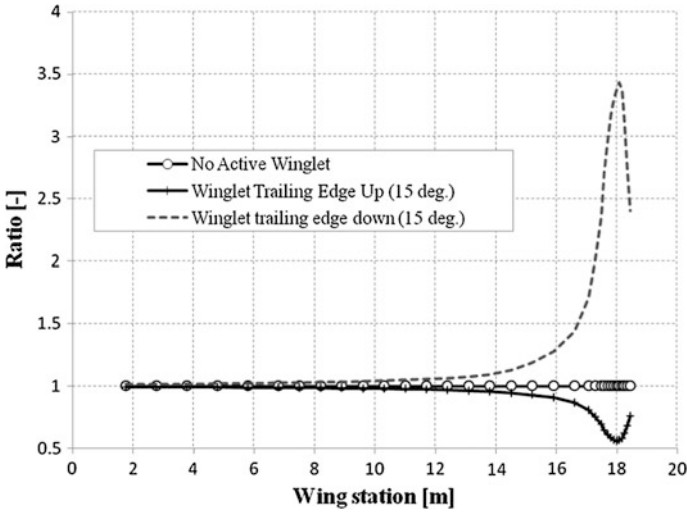


Fig. 3 Comparison of wing bending moments (rigid dive manoeuver) [16]

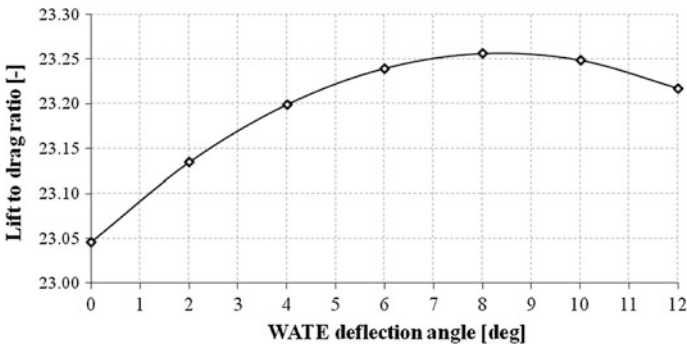


Fig. 4 Effect of WATE deflection on L/D [16]

2.1 Winglet Shape Optimization

Fitting a suitable actuator inside the confined space of a winglet was a challenge encountered very early in the project. In addition, the design of the winglet loft-line has a direct influence on the aerodynamic hinge moments generated by the control surface. The original loft-line (blue sections in Fig. 5) has a lower surface trailing edge cusp, which generates a certain rear loading and leads to aerodynamic hinge moments that are predominantly in one direction over a wide range of control surface deflection angles. This bias leads to large hinge moments, especially when the control surface is deflected downwards, inevitably leading to a larger and heavier actuator.

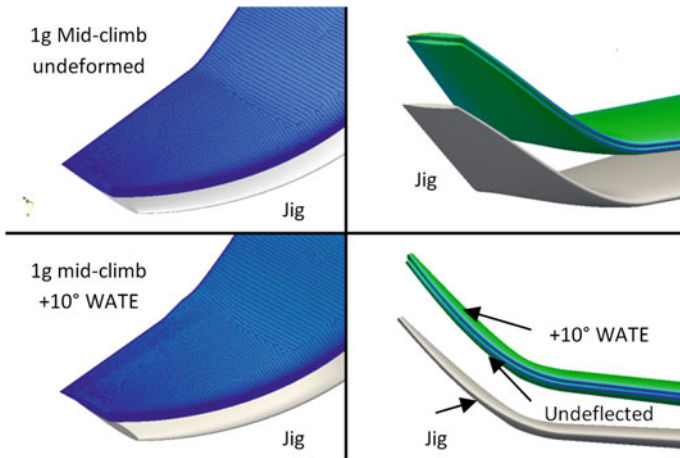


Fig. 5 Wing deformation due to active trailing edge deflection [16]

One method to reduce the hinge moments is to introduce a small trailing edge reflex (upward deformation of the last 3–4 % of chord). This idea was investigated and did achieve a modest reduction in the maximum hinge moment. However, the internal space for accommodating an actuator remained the same and had an associated drag penalty. A more effective method for reducing aerodynamic hinge moments is illustrated in Fig. 6.

The modified section achieves much reduced rear loading, and therefore, the moments about the hinge are lower. At the same time, the additional volume inside the winglet is increased to the point where a suitable electromechanical actuator can be housed inside. An important consideration for the modified loft-line is whether the total drag levels can be maintained relative to the original design. Careful design of pressure gradients is used to maintain levels of viscous drag, and the wave drag

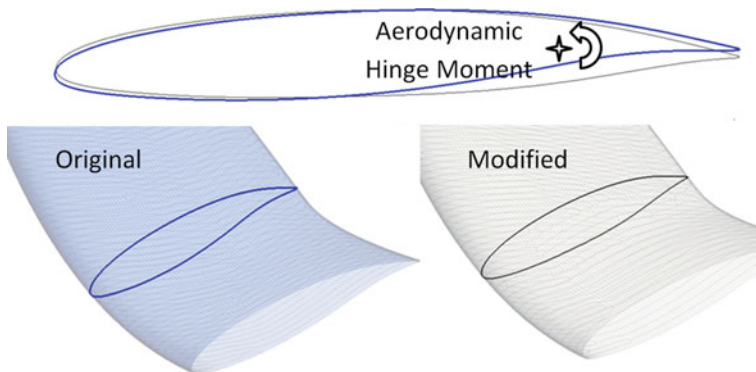


Fig. 6 Section profile modifications made to the inner winglet [16]

(affected by the severity of the shock) is also unchanged. The maximum depth increases are restricted to the span-wise region close to the actuator, with a continuous reduction to the original loft-line at the tip of the wing and the tip of the winglet, as illustrated in Fig. 7. The modified loft-line causes a local reduction in lift, which changes the span loading, moving away from the ideal elliptic distribution and hence leading to an increase in induced drag. In a final modification of the loft-line, the local winglet toe angle is modified, by a maximum of 1.1° at the winglet tip. This is illustrated in Fig. 8.

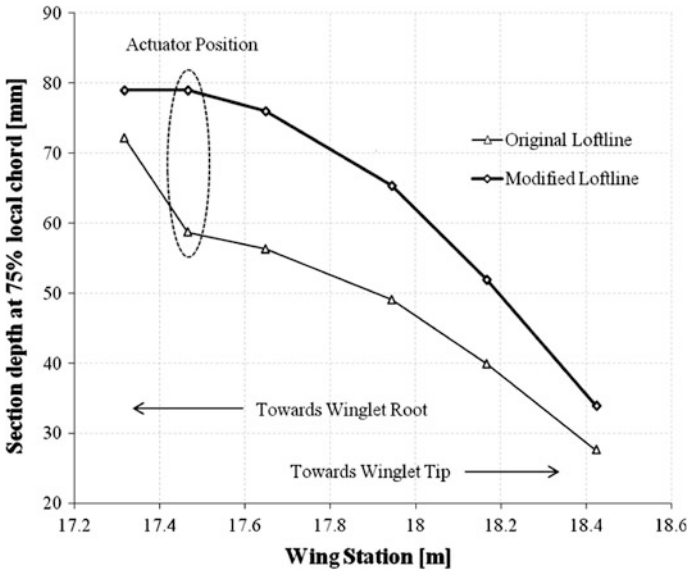


Fig. 7 Changes made to the winglet loft-line's local depth [16]

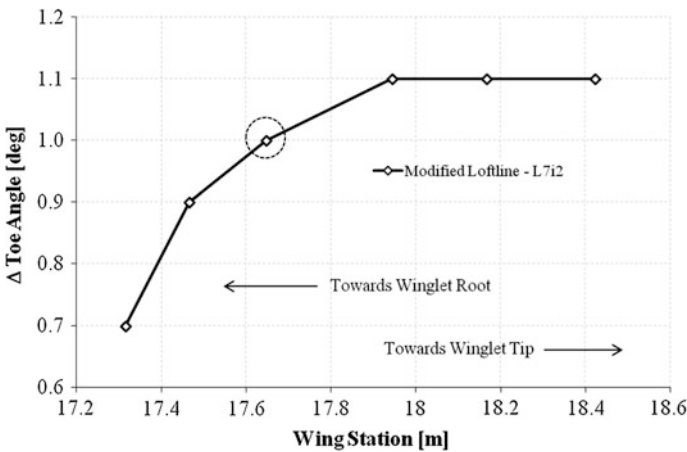
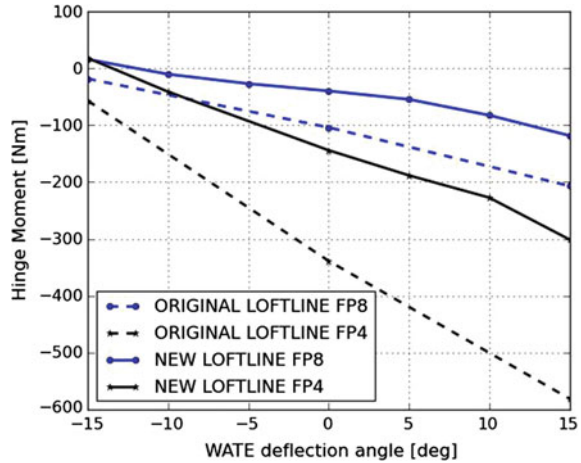


Fig. 8 Changes made to winglet toe angle [16]

Fig. 9 Hinge moment reductions for the modified loft-line [16]



Proof of reduction in aerodynamic hinge moments over a range of winglet tab deflection angles is shown in Fig. 9, for two very different flight points. Flight Point 4 (“FP4”) is the design dive speed case at sea level (highest dynamic pressure) and 2.5 g load factor, and Flight Point 8 (“FP8”) is the cruise design point at 1 g. The dramatic hinge moment reductions between the dashed lines and the solid lines illustrated in Fig. 9 are explained with the help of the section pressure cuts in Figs. 10 and 12. The cuts for both flight points show a reduction in rear loading and an increase in the front loading to compensate. Evolution of the span loading during the shape optimization exercise is shown in Fig. 11. The initial effect of modifying the loft-line was a drop in outer wing and winglet lift (see dashed line), leading to an increase in induced drag. This figure also shows how the change in twist (1.1° retoo) has resulted in a span loading for the modified loft-line, that is very close to

Fig. 10 Winglet pressure coefficient cuts at the position of actuator at design dive speed [16]

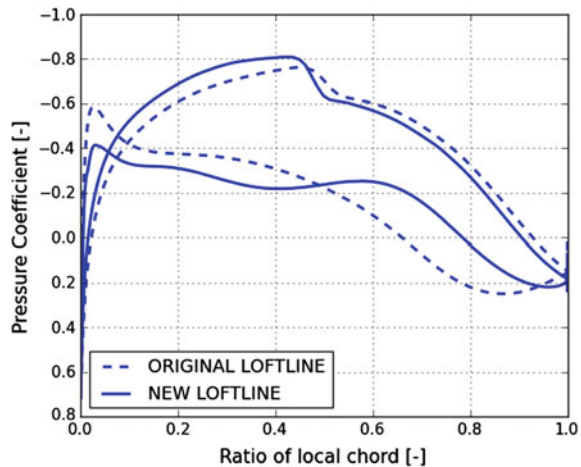


Fig. 11 Control of span loading in the outer wing and winglet [16]

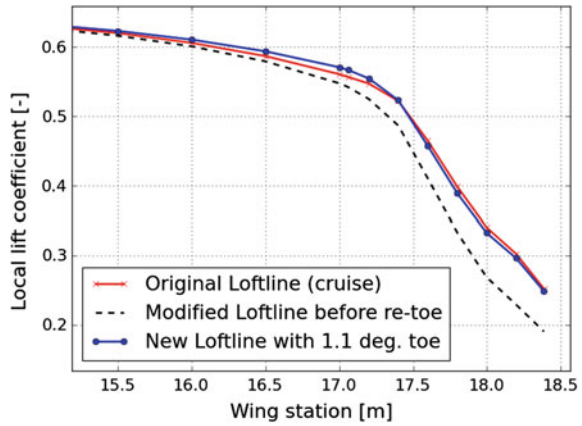
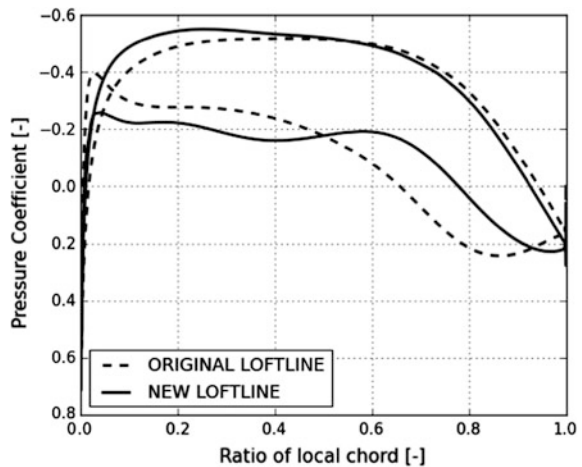


Fig. 12 Winglet pressure coefficient cuts at the position of actuator at design cruise speed [16]



that of the original. A post-processing exercise to compute the detailed drag breakdown for the new winglet shape was performed, and the analysis showed that total (far-field) drag was approximately the same as for the old shape (marginally lower for the new loft-line).

2.2 Actuator and Kinematics Integration

In order to avoid dealing with hydraulics in the winglet, an electromechanical actuator (EMA) is chosen for actuating the WATE. Due to time and budget constraints, no dedicated EMA is designed in the SARISTU project, although an off-the-shelf EMA is selected to power the control surface, assuming that in principle a flight-worthy actuator of similar size, weight, and power can be designed.

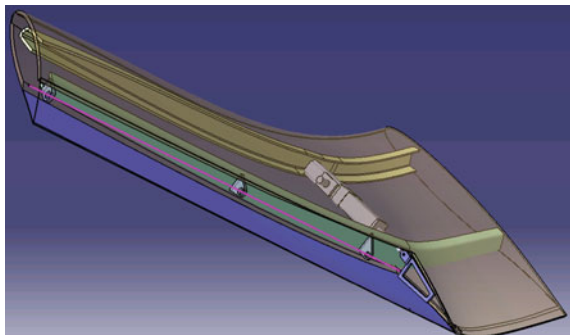


Fig. 13 Effects on the lever for different hinge lines [16]

With the limited space inside of the winglet, the EMA has to be very small, and hence, its available actuation force is limited. Therefore, the achievable lever arm needs to be maximized. The positioning of the hinge line is the main variable of this optimization. The shape of the winglet is bent over the whole span, whereas the hinge line has to be a straight line to allow the rotary movement and has to stay inside of the outer loft. Additionally, all the hinges have to be contained inside of the loft as well, so that no further drag is added. Figure 13 shows two possibilities to place the hinge line, underlining how to take advantage of the given geometry [17]. Other solutions to reduce the necessary actuator forces were examined as well, e.g. through the use of geared levers. However, the resulting forces remain quite high, and a very heavy and complex system of levers is required, making this uninteresting in the global design.

The EMA is finally installed like a standard control surface actuator with spherical bearings at both ends to compensate for movement and installation tolerances. The actuator is supported on the front spar and is located inside the winglet’s main box where there is the biggest available volume, compare Fig. 14. This installation is not ideal however, as the EMA generally is not designed to carry transversal loads. Nevertheless, it was possible to integrate an EMA into the modified loft-line that fulfils force and rate values required for dynamic gust load alleviation. For bigger applications, it can be noticed that the available actuation force of the EMA scales faster than its dimensions and weight making the application more advantageous.

Fig. 14 Hinge line (*magenta line*) [16]



2.3 *Failure Hazard Assessment, System Safety Assessment, and Factors of Safety Used for Structural Sizing*

Safety is the state in which risk is acceptable. It is thus necessary to ensure an “acceptable level of safety” by setting quantitative and qualitative objectives consistent with the failure severity. This is done by identifying failure conditions (FCs) of the system and classifying these according to severity levels, i.e. catastrophic (CAT), hazardous (HAZ), major (MAJ), minor (MIN), and no safety effect (NSE). This process is called failure hazard assessment (FHA). Depending on the severity level of a certain FC, the probability of the occurrence of this FC must be below a certain threshold, i.e. $<10^{-9}$ per flight hour for CAT, $<10^{-7}$ per flight hour for HAZ, $<10^{-5}$ per flight hour for MAJ, and $<10^{-3}$ per flight hour for MIN, compare [15], paragraph CS 25.1309. From these quantitative requirements and using empirical values and experience for subsystem failure rates, an overall system is iteratively designed using fault tree analysis (FTA). Failure hazard assessment (FHA) is performed in order to derive design prerequisites for the control system on the one hand as well as for the structural sizing on the other. With respect to FHA, significant changes were made since design loop zero presented in [14]. The main change is that the tab needed to be connected with 5 single load path hinges to the winglet in order to achieve maintenance intervals being required only every D-check.

Table 1 illustrates the WATE system FHA for the function loads and drag control. The WATE function is later linked to the overall aircraft functions such as:

- Gust load alleviation
- Wing vibration and fatigue control function
- Drag minimization function.

FC1 is classified CAT. Thus, it must be shown that no single failure can lead to FC1. This requirement is fulfilled as the minimum cut set for all related failure scenarios equals 2 (i.e. rupture of primary and secondary EMA load path for failure scenario 1a, and faulty control command by both lanes of the Dual-Duplex ACE for failure scenario 2a, and 2c, compare also Fig. 16). It must be shown that 2 failures which lead to FC1 are independent. This is achieved by segregation, and by choosing appropriate development assurance levels (DALs), see [18]. Failure rates for the EMA components are taken from [19].

For all FCs which are classified more severe than MIN, the probability of occurrence P is proven by FTA. Figure 15 exemplarily shows the fault tree for FC2 (jam of both WATE) resulting from preliminary system safety analysis (PSSA). The computed probability of being in failure state Q equals 3.4×10^{-10} . For the computation of Q , an mean flight time of 3 h was assumed, i.e.:

$$Q = T \cdot P \tag{1}$$

Table 1 WATE system FHA

Failure mode	Failure scenarios	Effects of the failure	Failure conditions	Class	Justification for classification	Crew detection	Recovery action	Parameter ^a
1. Loss of WATE control	(a) Uncontrolled dynamic motion	Tab moving undamped in airflow (control surface flutter)	FC1: significant structural damage of wing	CAT	Hull loss; pilot action (emergency crew action) too slow to safe airplane	Strong vibrations, aircraft uncontrollable	Immediate speed reduction, emergency landing	RQ1: control surface flutter simulation
	(b) Jam of both left and right WATE	Uncontrolled static deflection of both left and right WATE	FC2: Significant drag increase and aircraft performance reduction	MAJ/HAZ	Significant to excessive increase in pilot's workload	Increased fuel consumption and reduced controllability	Diversion	AS1: not further investigated because fault tree shows very low probability, see Fig. 15
	(c1) Jam in worst case drag increasing position	Uncontrolled tab deflection on one side; increased drag reduced controllability	FC3: Drag increase	MAJ	Significant increase in pilot's workload, divert from original flight path	Fuel consumption higher than expected	None	RQ3: adapted range computation based on drag computation with jammed WATE
	(c2) Jam in worst case controllability degrading position	increased loads	FC4: aircraft controllability degradation	MAJ	Significant increase in pilot's workload	Reduced controllability	None	RQ4: check effect of WATE in extreme position on aircraft controllability
	(c3) Jam in worst case loads position		FC5: Degraded WATE performance	MIN	Physical discomfort for passengers; pilot's workload slightly increased; aircraft structure is seized for jam according to CS-25	None	None	RQ5: check ultimate loads and safety factors of the whole aircraft structure for occurrence of failure and continuation of flight loads for jam; AS2: Aircraft structure is seized according to CS25

(continued)

Table 1 (continued)

Failure mode	Failure scenarios	Effects of the failure	Failure conditions	Class	Justification for classification	Crew detection	Recovery action	Parameter ^a
	(d) Detected jam of one WATE (either left or right)	Uncontrolled static tab deflection on one side; increased drag and/or increased loads	FC6: detected drag increase and increased loads	MIN	Physical discomfort for passengers, pilot's workload slightly increased, aircraft structure is seized for jam according to CS-25	Warning and corrective instructions on ECAM	Rely on capability of pilot to reduce speed and avoid severe turbulence in order to prevent ultimate loads, recomputation of block fuel	RQ6: add instructions to pilot manual
	(e) Undetected passive free-floating tab well damped by EMA	Drag increase, only passive load alleviation	FC3	MAJ	Significant increase in pilot's workload, pilot is required to divert from original flight path	Fuel consumption higher than expected	None	RQ5, AS2
2. Inadvertent WATE control	(f) Detected passive free-floating tab well damped by EMA	Drag increase, only passive load alleviation	FC6	MIN	Physical discomfort for passengers, pilot's workload slightly increased, aircraft structure is seized for jam according to CS-25	Warning and corrective instructions on ECAM	Rely on capability of pilot to reduce speed and avoid severe turbulence in order to prevent ultimate loads, recomputation of block fuel	RQ6
	(a) Undetected oscillation	High dynamic loads, aircraft performance, and controllability degradation	FC1	CAT	Hull loss, pilot action (emergency crew action) too slow to safe airplane	Strong vibrations	Immediate speed reduction, emergency landing	AS3: due to dual lane ACE (see Fig. 16) this failure scenario is considered not possible; RQ7: sensitivity analysis of worst case frequency/amplitude of forced oscillation

(continued)

Table 1 (continued)

Failure mode	Failure scenarios	Effects of the failure	Failure conditions	Class	Justification for classification	Crew detection	Recovery action	Parameter ^a
	(b) Detected oscillation	High dynamic loads, system shutdown, drag increase, and/or loads increase	FC7: WATE system shut down	MIN	Pilot's workload slightly increased	Warning and corrective instructions on ECAM	Recomputation of block fuel, reduce speed and/or avoid severe turbulence in order to avoid to come close to ultimate loads	RQ5, RQ8: design, and validate FDI mechanism
	(c) Undetected runaway into dead stop (full tab deflection at maximum rate)	Ultimate loads on outer wing are exceeded due to dynamic excitation	FC1	CAT	Hull loss highly probable due to structural disintegration of outer wing	Aircraft uncontrollable	Immediate speed reduction, emergency landing	AS3
3. Biased WATE control	(d) Detected runaway	High dynamic loads, system shutdown, drag increase, and/or loads increase	FC7	MIN	Pilot's workload slightly increased	Warning and corrective instructions on ECAM	Recomputation of block fuel, reduce speed and/or avoid severe turbulence in order to avoid to come close to ultimate loads	RQ4, RQ8
	(a) Undetected inaccurate deflection of the tab	Inaccurate deflection of the tab, efficiency degradation	FC5	MIN	Physical discomfort for passengers, pilot's workload slightly increased	None	None	RQ9: investigate robustness of drag and loads reduction in order to obtain an estimate for precision tolerance
	(b) Detected inaccurate deflection of the tab	Inaccurate deflection of the tab, efficiency degradation	FC5	MIN	Physical discomfort for passengers, pilot's workload slightly increased	Warning and corrective instructions on ECAM	System deactivation, speed limitation, avoidance of severe turbulence, recalculation of fuel consumption	RQ9, AS5: WATE shutdown gives better drag and loads reduction than biased control

(continued)

Table 1 (continued)

Failure mode	Failure scenarios	Effects of the failure	Failure conditions	Class	Justification for classification	Crew detection	Recovery action	Parameter ^a
	(c) Undetected hinge loss (2 of 5 remaining)	Inaccurate deflection of the tab, efficiency degradation, minor structural damage	FC5	MIN	Physical discomfort for passengers, pilot's workload slightly increased	None	None	RQ9
	(d) Detected hinge loss (2 of 5 remaining)	Inaccurate deflection of the tab, efficiency degradation, minor structural damage	FC5	MIN	Physical discomfort for passengers, pilot's workload slightly increased	Warning and corrective instructions on ECAM	System deactivation, speed limitation, avoidance of severe turbulence, recalculation of fuel consumption	RQ9, AS5

^aIn the context of FHA, the abbreviation *RQ* stands for requirement, and *AS* stands for assumption

The resulting probability Q of being in condition of just one WATE jammed can also be extracted from Fig. 15 and equals 1.84×10^{-5} . This value is used to extract the factor of safety (FS) required for the computation of ultimate loads for structural sizing with respect to a condition with one WATE jammed (see Fig. 17). Despite FC5 being classified as MIN, a fault tree is still generated in order to be able to compute ultimate loads for degraded WATE performance. Note that in above fault trees, failure on the left and right WATE is completely independent from each other.

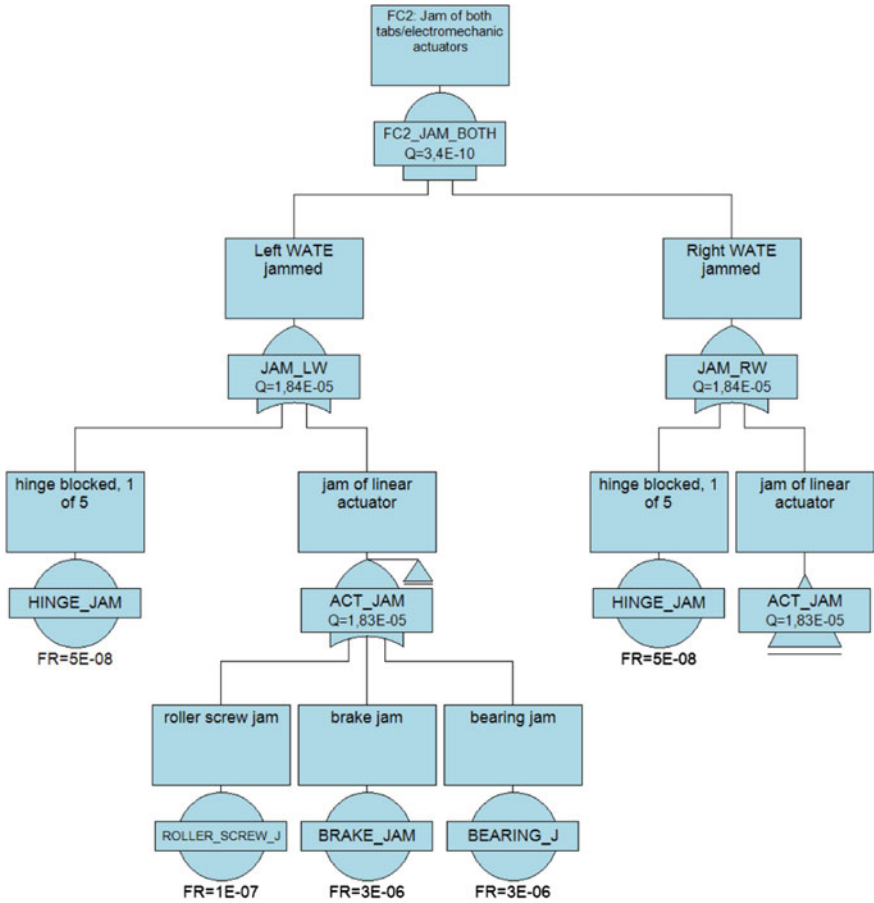


Fig. 15 Fault tree for jam of both WATE

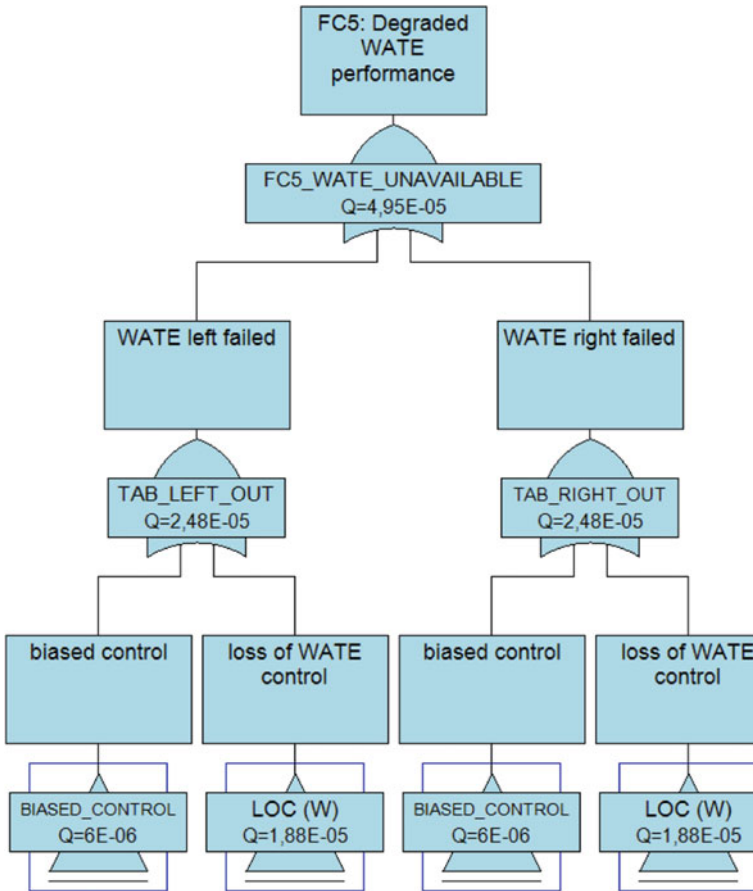
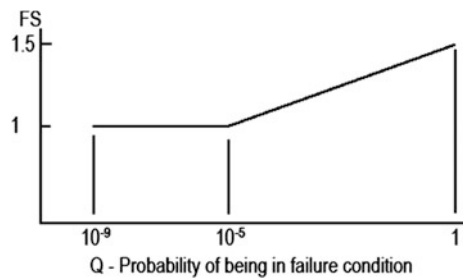


Fig. 16 Fault tree required for computation of factors of safety for structural sizing

Fig. 17 computation of factor of safety [15]



2.4 Overall Control System Layout

The layout of the control system is based on [11]. As defined in the WATE system FHA in Table 1, the most important consequence for the control system is the requirement for Dual-Duplex ACE (see Fig. 18). Each ACE comprises a command lane and a monitoring lane and commands its own motor control unit (MCU) which has its own windings in the motor in order to avoid force fighting. For this purpose, four linear variable displacement transducers (LVDTs) are installed at the ball screw to provide both ACEs with two independent signals each. With the angular position of the rotor, a triplex voting can be conducted [20].

From load alleviation control point of view, two different strategies can be used either separately or in combination [21]:

- Passive load control, e.g. static spoiler deflection for alleviation of wing root bending moment during static g-load such as pull-up manoeuvre [21], i.e. state of the art.
- Active load alleviation, i.e. dynamic symmetric deflection of ailerons in order to compensate wing bending vibrations either with feedback control (active damping) [21, 22], or feed-forward control (active compensation), compare [23, 24].

In principle, the proposed winglet control device can be used for all said strategies. In this document, active load alleviation using feed-forward control will be considered because (assuming that a proper reference signal is available) it is considered to be more efficient in terms of minimizing gust loads than passive load control. A proper reference signal must fulfil the following criteria:

- Sufficient lead time so that the optimal feed-forward controller is causal [23, 25].
- High coherence between the reference signal and the aircraft excitation [23].
- Low parasitic feedback from control surface (WATE) deflection to the reference signal.

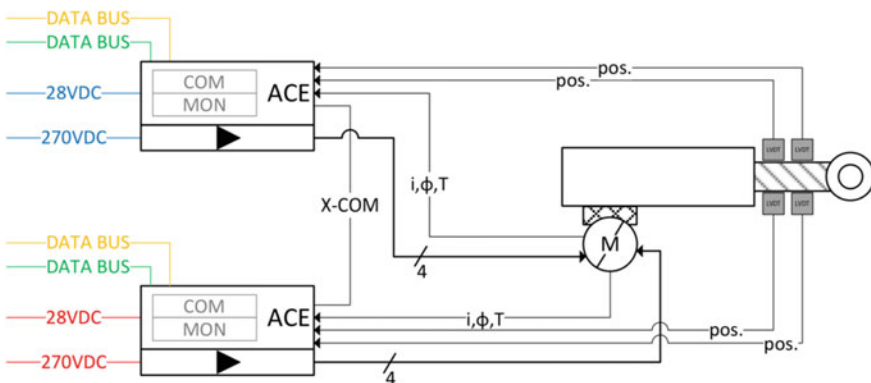


Fig. 18 Dual-Duplex ACE for winglet EMA [20]

From experience, it can be assumed that such a reference signal can be provided by appropriate sensor fusion and filtering [23, 26, 27]. The feed-forward controller can be adapted online in order to compensate plant uncertainties and variations due to fuel filling level in the wings, as it was done on the flight tests presented in [26]. In [28], a universal stability analysis of this adaptation algorithm is presented.

The disadvantage of the adaptation of the feed-forward gust load alleviation controller is that the cost function to be minimized can only contain measurable signals, e.g. modal accelerations. Direct measurement of loads is difficult on an airplane, and thus, loads can only be reduced indirectly. Thus, the adaptive feed-forward gust load alleviation controller is not easily applicable for wing box mass minimization. Therefore, a robust feed-forward controller implementation is chosen in this investigation. Note that such a robust feed-forward controller can also serve as a starting point for the adaptation or controller initialization after longer periods of flight without turbulence excitation, i.e. without online adaptation. Design and optimization of this robust feed-forward controller require an accurate aeroelastic aircraft model.

3 WATE Manufacturing and Assembly

Considering the requirement to be able to integrate the actuation mechanism as well as the electronic equipment for active tab control, a pure laminate skin and stringer grid concept were chosen for the winglet baseline concept. The winglet structure thus consists of a passive, an active, and a morphing structure. The passive structure includes CFRP pure laminate (lower and upper) skin panels and a stringer grid (including front, rear, and middle spars, and four ribs). Root rib, leading edge, trailing edge, and the end cap are conventional aluminium machined parts. The active structure comprises the active tab actuated by the EMA and attached to the winglet's rear spar by 5 single load path hinges, as well as the fail-safe connection of the EMA to the winglet's skins and front spar. The morphing structure (provided by SARISTU partner FRAUNHOFER IFAM) is realized by a solid rubber compound part and represents the function of a flexible gap filler between passive and active winglet structure. For the interface between winglet and wing box, a root rib concept with bolted connection was chosen. An exploded assembly drawing of the active winglet is shown in Fig. 19.

Together with the skins, the front and rear spars constitute a torsion box ranging from the root rib to end tip of the winglet. A centre auxiliary middle spar is incorporated in the lower portion of the winglet in order to transmit bending loads through the curved geometry of the winglet. Four ribs between spars are incorporated for 2 reasons: as closure for the centre rib and to avoid skin warping and buckling. The CFRP upper and lower skin panels are single piece units (including an access door for EMA maintenance and replacement on the lower skin panel) and extend from root to tip and from leading edge to trailing edge. These skins are

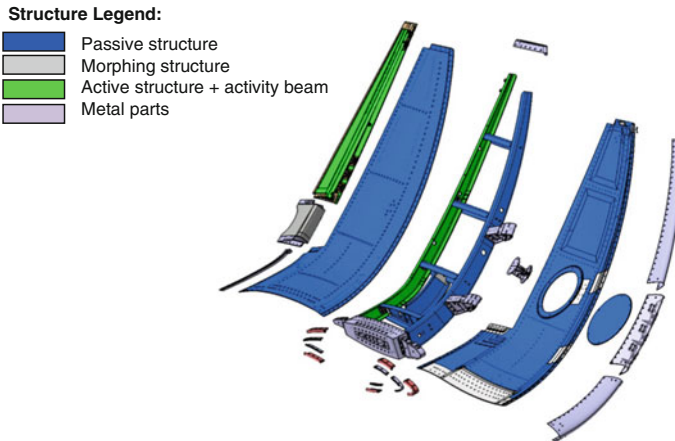


Fig. 19 SARISTU WATE structure overview

realized as pure laminate designs in order to maximize available space for actuation and electronic system integration.

The design rules are specified by AIRBUS by the RSDP A350XWB program (V51RSDP07001.1-1.5). Wherever possible, material specifications were chosen in the following order:

- materials specified and qualified by AIRBUS
- materials qualified for aeronautic applications
- general qualification according to international standards and specifications.

3.1 Composite Structure Components Manufacturing

Winglet passive composite structure components are manufactured using standard aerospace serial manufacturing processes as well as standard aerospace serial materials. Various manufacturing processes were chosen in order to demonstrate the maturity of these manufacturing technologies for the application to manufacturing of different parts of a winglet structure.

Winglet skins are manufactured using serial prepreg materials and prepreg autoclave processing as shown in Fig. 20. For the winglets' skin manufacturing, prepreg material is laid on the tooling surface manually with the support of a laser projection system (ply boundary and lay-up rosette projection).

After completion of this lay-up process, release foil, breather, and vacuum bagging foil are played before lay-up is subjected to the autoclave curing process. When the autoclave curing process is finished, the parts are remoulded and ready for the CNC milling procedure, followed by CMM and NDI quality check procedures.

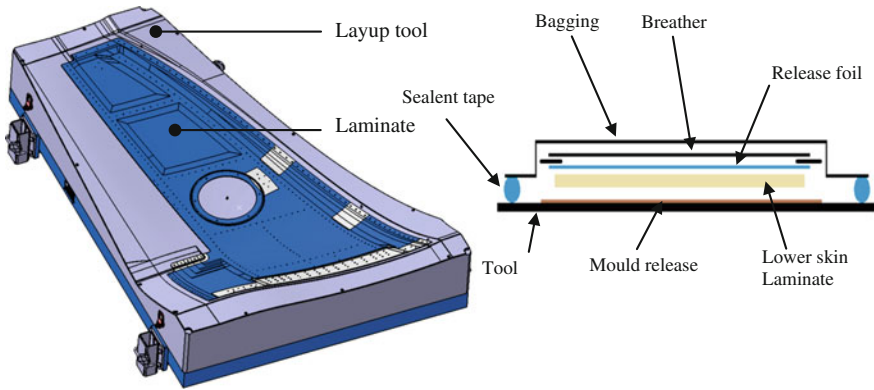


Fig. 20 Winglet skins' manufacturing—prepreg processing

The stringer grid was manufactured by the MARI process [29] (membrane-assisted resin infusion) which is a FACC's patented process based on standard LCM (liquid composite moulding) process. The MARI process used to manufacture the WATE's composite stringer grid (front spar and ribs) consists of a preforming process, where the dry fabrics are preformed in the tool, using a specific temperature profile in an oven. Afterwards, preformed lay-up is infused with the matrix system under the infusion bagging using an OOA curing process in an oven. The process is illustrated in Fig. 21.

The rear spar of the active winglet (to which the tab hinges are connected) is made of CFRP material (carbon fibre/epoxy resin) (see Fig. 22). The manufacturing process carried out by FIDAMC for its production is flat lay-up by means of an automatic fibre placement machine (AFP) with subsequent press forming and autoclave curing cycle in male tool.

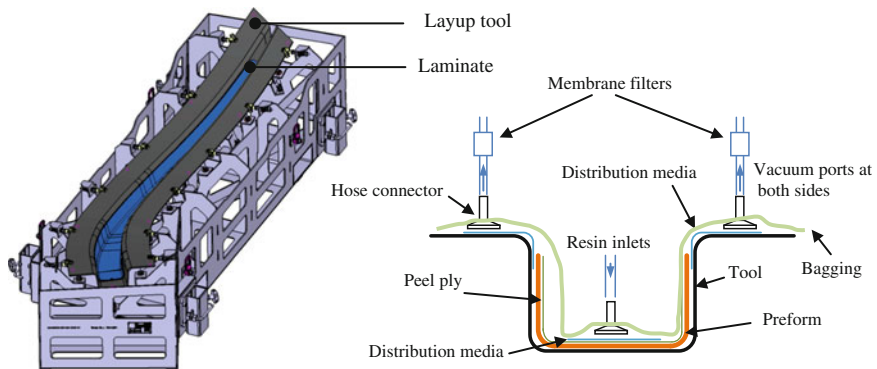


Fig. 21 Winglet stringer grid manufacturing—MARI OOA process

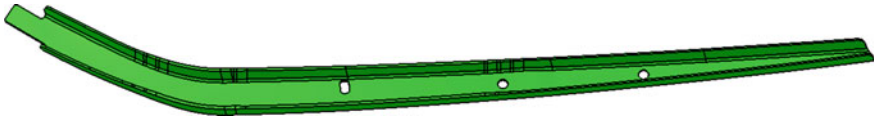


Fig. 22 WATE's activity beam

The active tab was made of CFRP material (carbon fibre/epoxy resin) (see Fig. 23). The manufacturing process selected by FIDAMC for its production was prepreg technology (hand lay-up) and curing in autoclave cycle using a partitioned tool.

The morphing gap filler shown in Fig. 24 is manufactured by Fraunhofer in a casting process. A mould is filled with a reactive mixture of the silicone

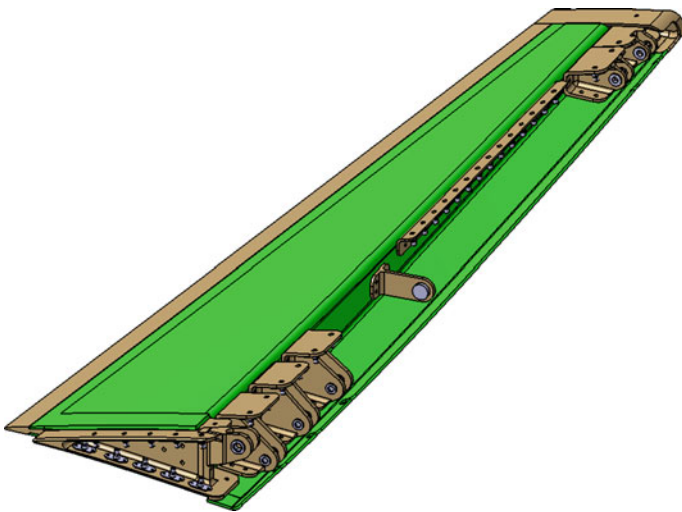


Fig. 23 WATE's active tab

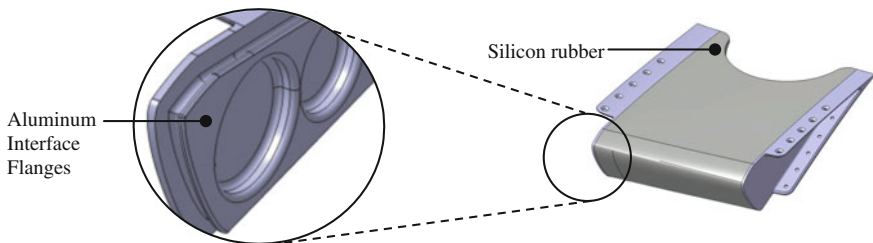


Fig. 24 WATE's morphing structure

components, and the morphing material is cured in the mould. The structural interface with cleaned and activated surfaces acts as a part of the mould. In this way, a morphing structure is obtained which is already equipped with the structural interface for connection with the airframe.

3.2 Winglet Assembly

The overall assembly process is performed according to AIRBUS specifications. The assembly process was divided in several phases. Before the start of the overall assembly process, the assembly jig was positioned in the assembly hall, and its geometry was proven using a CMM measurement system. The calibration of the assembly jig reference coordinate system was done in regard to the CAD model, and this reference was then used during the complete assembly process of the active winglet. Figure 25 illustrates the 8 phases of the WATE assembly process.

All assembly phases are supported by a laser tracking system for positioning of the parts and a “Cleco” fastening system for temporary fixation. Each of the temporary fastening operations uses pilot holes provided in the manufactured parts. Permanent fixation of the parts is done by nominal hole size reaming of pilot holes and parts fastening with bolts. Interfaces between the parts are shimmed when there is a need to meet defined assembly tolerances. Root rib positioning and temporary assembly are done as part of phase 1. This step signifies the reference through the next assembly phases. In phase 2, the front spar and the rear spar are positioned on the lower skin as part of the stringer grid assembly. In phase 3, the middle spar as well as all ribs is positioned. In phases 2 and 3, all parts are temporarily fastened,

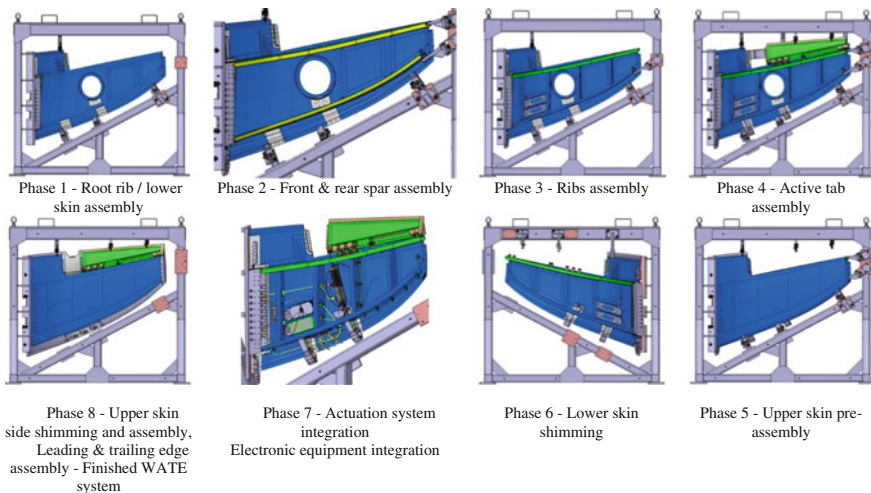


Fig. 25 Assembly concept for the active winglet

and afterwards, their assembled geometry is checked. In order to prove the loft surface after attaching the stringer grid, a laser tracking system is used. Afterwards, when all assembly requirements are met, the complete stringer grid is permanently fastened with bolts. In phase 4, the active tab as well as the hinges is positioned on the rear spar. This assembly phase is supported with a “dummy morphing part” in order to simulate the assembly interface between the morphing structure and active tab, as well as the interface between the morphing structure and the passive structure of the winglet.

Phase 5 comprises upper skin temporary assembly and complete upper and lower surface loft geometry check. In phase 6, in order to meet the assembly tolerances and keep the passive structure in a stress-free state, the stringer grid is partially locally shimmed. The upper skin is kept temporarily assembled in order to ensure stiffness and maintain already achieved assembly tolerances of the stringer grid. Thereafter, the shimmed structure is permanently sealed and fastened with bolts. The complete temporary assembled stringer grid and the lower skin are then ready to enter the next assembly phase where the actuation system and the electronic equipment are integrated to the winglet, namely phase 7. Before the winglet’s passive structure is permanently closed with the assembly of the upper skin, the actuation system and the electronic equipment’s function are tested. In phase 8, the upper skin is fastened with blind fasteners and the complete winglet’s loft geometry is once more completely checked. Before the active winglet is sent for painting and thereafter structurally tested, another functional test of the actuation and electronic system is performed.

Figure 26 shows a close-up of the assembly of morphing part attached to the active tab, EMA, and fail-safe EMA interface to the passive winglet structure, as well as the 5 hinges which connect the active tab with the rear spar. Figure 27 illustrates the location of sensors, as well as the DAQ box, for the recording of measurement data during the WT test. The active tab is actuated by servo controller and Microautobox which are located in the outer wing as described in Sect. 5.

Sensors and data acquisition system allow a detailed monitoring of the adaptive winglet. The WATE’s sensor system consists of differential pressure sensors, an absolute pressure sensor, a three axes acceleration sensor, angular sensors, and strain gages. All data are gathered by a DAQ box, which digitizes the signals and

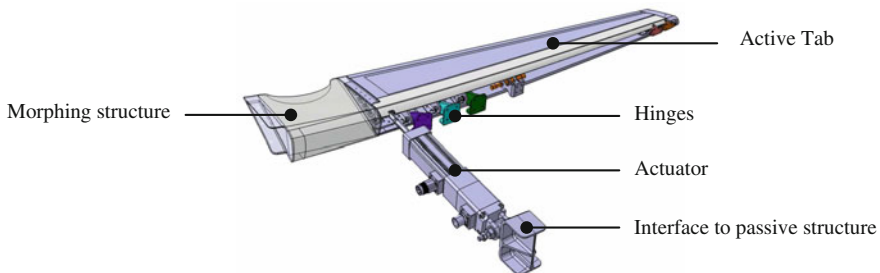


Fig. 26 WATE actuation system with active tab and morphing structure

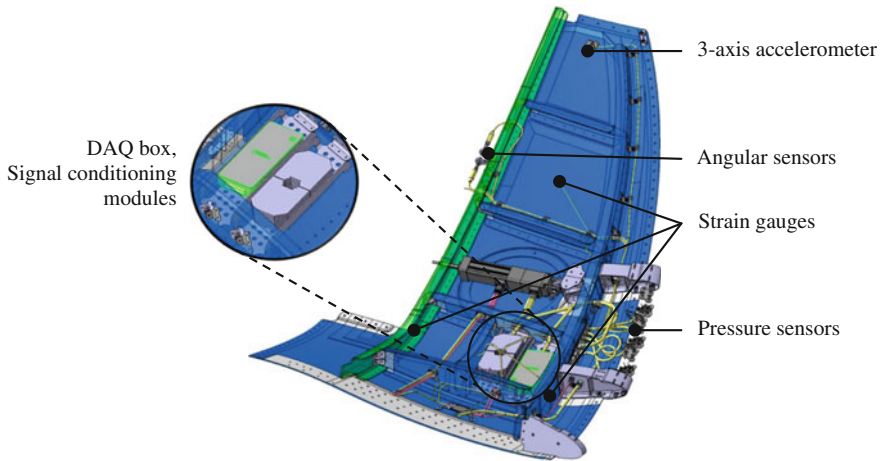


Fig. 27 WATE actuation and electronic system integration concept

sends the data via Ethernet network to the computer for storage and further data analysis. Figure 27 illustrates an overview picture of the integrated actuation and electronic systems of the active winglet. Near the end cap, the acceleration sensor is assembled to the winglet's lower skin. On the rear spar, 2 angular sensors are mounted opposite of each other in order to compensate flexible deformations of the winglet. The access door (service hole) for the EMA can be seen on the lower skin panel. Between the inboard and outboard end ribs of the middle spar, the signal distribution board can be seen. Near this position, the DAQ box and the signal conditioning modules for the strain gages are attached. Pressure sensors are located in the middle part of the leading edge, and their signal distribution board is located close to it on the front spar. Strain gauges are glued on the lower skin and on the spars (front spar, rear spar, and middle spar). For winglet function verification test purposes, strain gauges, accelerometer, and angular sensor data were monitored and used for their assessment.

4 WATE Testing

4.1 Ground Vibration Test

In order to be able to carry out a ground vibration test (GVT) as well as a ground static test (GST), the active winglet was mounted to an interface plate using bolts and barrel nuts. This interface plate was subsequently bolted to a test rig. Different test rigs were used for GVT and GST.

During the GVT, the active tab was blocked in neutral position by the actuator. The actuation system and electronic system were disconnected for the test purposes.

The ambient temperature and relative humidity were maintained (laboratory conditions) in the test area during the testing. The test system consisted of the circuits for excitation, circuits for response measurement, and algorithms for vibration analysis and test control. All response measurement channels were calibrated before the test starts. The vibrations of the specimen and test rig have been measured by 37 uniaxial accelerometers, as illustrated in Fig. 28 (marked in blue). The specimen was excited by electrodynamic shakers at points 1, 2, 16, and 37 (see Fig. 28 (marked in red)).

The distribution overview of modal frequencies of the winglet has been determined by the analysis of response to the swept sine excitation from 10 to 200 Hz. The MIF function (multivariate mode indicator) was used, and excitation was by constant amplitude of force by one exciter during whole sweep.

The individual modes of vibration have been investigated by means of multi-point appropriated excitation method. Modal parameters of each mode were investigated separately. Each mode is determined by its modal parameters: modal frequency, modal mass, damping, and mode shape. The values of modal mass and damping have been obtained by means of complex power method. Logarithmic decrement method for damping measurement was used as well. The amplitude force of excitation by one exciter was set so that the point with maximum acceleration had nearly 1 g. Determined modal frequencies from GVT have been compared with FEM, and some specific cases are represented in Fig. 29.

Legend:

- Accelerometers
- Exciters

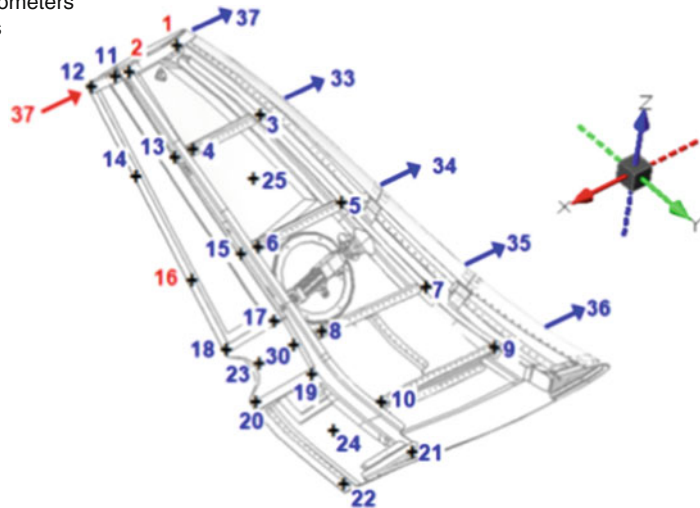
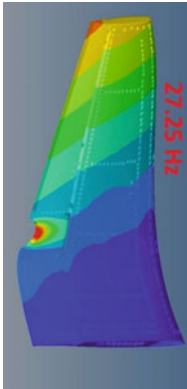
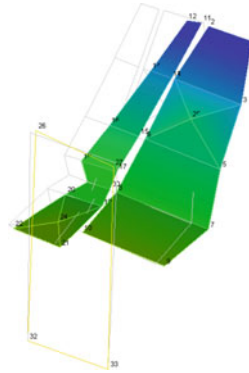


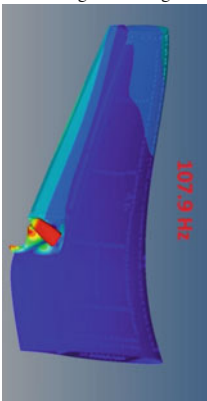
Fig. 28 Accelerometers and exciters position on specimen



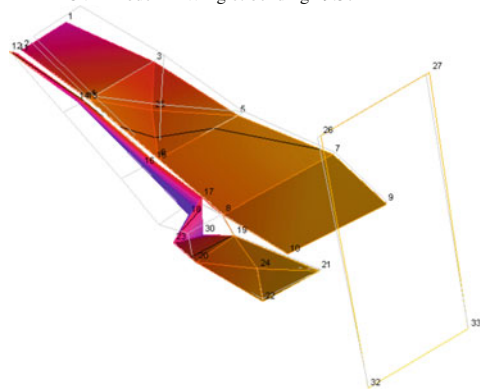
FEA Mode 1 – Winglet bending 27.25 Hz



GVT Mode 1 – Winglet bending 29.57 Hz



FEA Mode 6 - Winglet bending & morphing part vibration 107.9 Hz



GVT Mode 6 - Winglet bending & morphing part vibration 101.40 Hz

Fig. 29 Modal frequencies of the active winglet

4.2 Ground Static Test

For GST purposes, the winglet with interface plate was bolted to a static test rig. The active tab was blocked in requested position by the actuator depending on the simulated load case. The load distribution is defined by 8 points (4 points on the winglet + 4 points on the active tab). Three steel constructed whiffle trees were used for load distribution from load cells to the load distribution pads and simulated the external applied loads. The whiffle trees are connected to 8 loading pads, which are bonded to the lower skin of the winglet and tab. These whiffle trees are able to transmit both, tension or pressure loading, compare Fig. 30. The magnitudes of the forces to be introduced to the winglet were defined such as to represent the stress state anticipated in the WT. The FEA showed that the stress state of 2 selected WT load cases can be accurately reproduced by load introduction using these whiffle

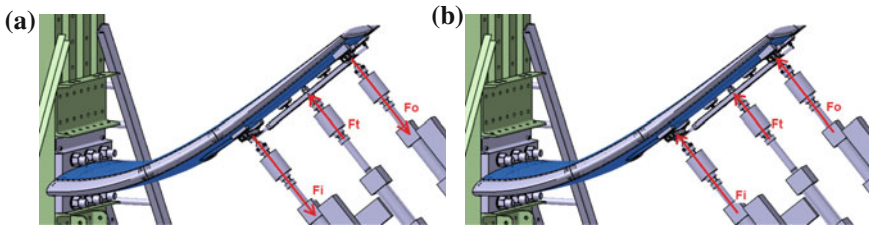


Fig. 30 WATE static load cases. **a** LC1—downward bending ($+10^\circ$ tab deflection). **b** LC2—upward bending (-15° tab deflection)

trees. It was decided to reduce the load level to 25 % of the real WT loads in order to avoid local damage of the winglet structure at the discrete load introduction points of the loading pads. Thus, the following 2 GST load cases were defined:

- Load Case 1—downward bending ($+10^\circ$ tab deflection): $F_i = -1.1$ kN, $F_o = -1.1$ kN, $F_t = 0.3$ kN
- Load Case 2—upward bending (-15° tab deflection): $F_i = 1.3$ kN, $F_o = 1.3$ kN, $F_t = 0.3$ kN

A servo-hydraulic loading system with 20 channels was used for the static test control. Three separate actuators with load cells loaded the whiffle tree system. Strain gauges inside of winglet structure and strain gauges installed on the winglet skins for GST purposes were monitored, and their strain values were recorded with a data acquisition system during both load cases. Displacements of the winglet structure during application of the 2 load cases were measured by the optical system PONTOS. The reference point markers were applied only on the upper surface of the winglet. Afterwards, GVT and GST results were compared with the FEM as shown in Fig. 31.

Comparing the measured deformation to the FEA predicted deformation, it can be concluded that the FEA overestimated deformations by about 20 %.

4.3 Functional Test

In order to implement the functionality of an active load alleviation system in the active winglet, a digital signal processor, namely the Microautobox, is installed in the outer wing. This location is favourable as a short distance between sensor and control system ensures high resistance against electromagnetic and line-associated interferences, since the present electromagnetic actuator is driven by a servo control based on pulsed technology.

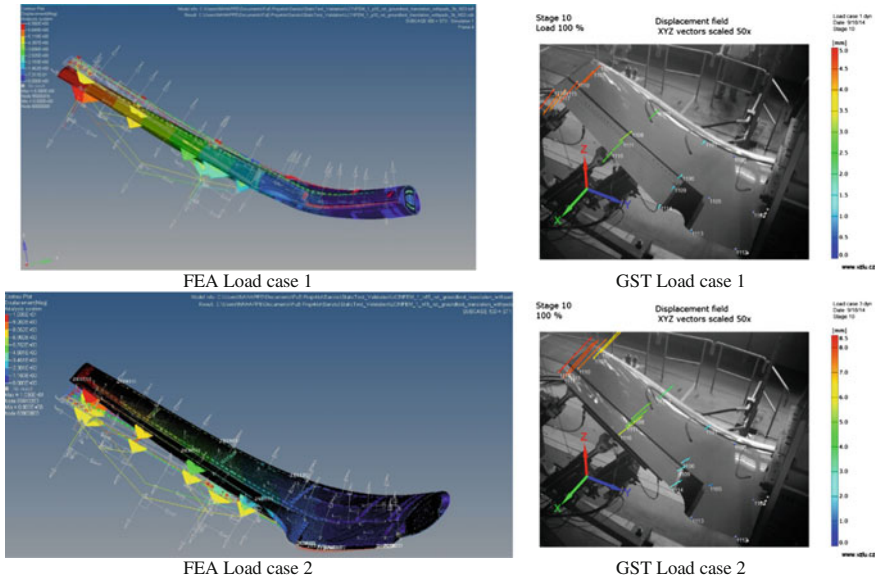


Fig. 31 GST displacements compared with FEM

Due to the absence of gust generators in the wind tunnel, the initially intended closed control loop cannot be tested. Alternatively, the characteristics of the winglet are analysed by a special test sequence in an open-loop control circuit. The new objective of the Microautobox is to provide the actuator system with the analogue tab command signal and to acquire the relevant signals (limited to twelve input signals), which can be used for a subsequent offline controller synthesis.

The control algorithm is developed with the software tool MATLAB/Simulink. The resulting code is compiled to a stand-alone programme and finally transferred to the Microautobox. Besides the test sequence, which commands static as well as dynamic tab deflections and lasts 510 s, the software offers also the possibility to simply generate static tab deflections. As the data acquisition system of National Instruments, which records the complete set of sensor signals of the WATE, has a limited internal buffer memory, it is not possible to record the whole test sequence in one single file using the sample rate of 2.5 kHz. Therefore, the test sequence is divided into 13 individual subsequences of 30 s each.

After each subsequence, the measured data are sent to a personal computer (laptop) via Ethernet for storage and data analysis. In order to simplify synchronous data acquisition of different systems, the control software generates a global trigger signal, which indicates the test start/stop of a subsequence with a rising/falling edge. Both the global trigger signal and the tab command signal are provided to all other data acquisition systems by the Microautobox, as shown in Fig. 32.

Even though the trigger signal is suitable for giving a start impulse for the data acquisition, an unambiguous allocation of data coming from different measurement

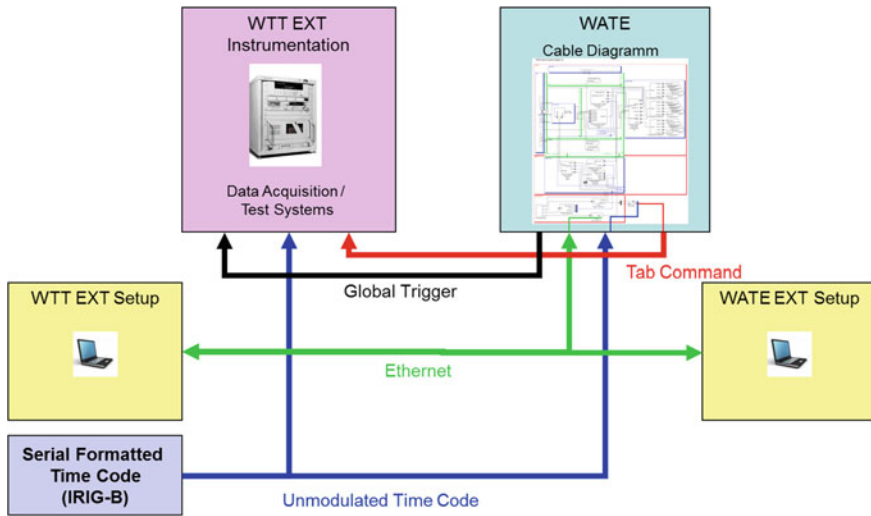


Fig. 32 Synchronization scheme and data exchange of measurement equipment

systems is not precise enough for this application. The utilization of an unique explicit time code (IRIG B, 100 Hz bit rate) allows finding the corresponding point of time when merging together the data of different measurement systems. The only requirement is that the “Binary 0”, which lasts 2 ms, can be resolved. Therefore, the minimum sample rate should be set greater than 1 kHz in order to gain a resolution of at least two samples.

Chosen sample rates are 5 kHz for the Microautobox and 2.5 kHz for the data acquisition system of National Instruments reducing the time misalignment below 0.4 ms. The communication to the Microautobox and the data acquisition is conducted via Ethernet interface in order to avoid long wiring through the demonstrator wing section. The intention is that only power supply and Ethernet cable have to be wired through the wing section. The Ethernet interface is also appropriate to transfer the environment conditions of the wind tunnel (such as angle of attack, side slip angle, flow velocity, humidity, and temperature) via User Datagram Protocol or to exchange measurement data over the connected local data storage.

The aim of the test sequence is to cover different types of actuation modes with which the characteristics of the winglet and the actuation system can be analysed. The test sequence is triggered once by a laptop, and all measurements corresponding to a special WT parameter set (angle of attack, side slip angle, and flow velocity) are performed without interruption during the following 510 s. The control signal has to pause for 10 s after each 30 s of measuring time in order to give the data acquisition system (National Instruments) sufficient time to store the data on the laptop.

Within the test sequence, a ramp procedure is implemented to analyse the effects of static tap deflection (see Fig. 33). In the range from -15° to $+10^\circ$ (tab angle) at

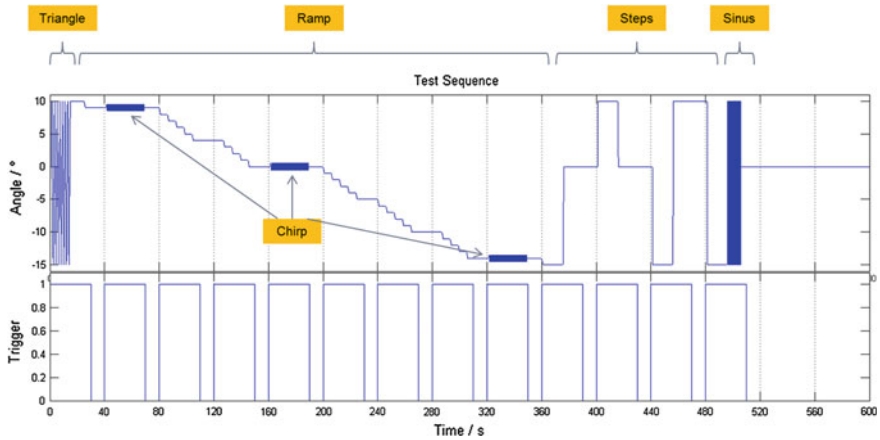


Fig. 33 Test sequence to analyse the effect of the active winglet on the overall winglet-wing system

26 test points, steady-state WT conditions are provided for a duration of 6 s, at each test point. In order to reduce the overall measurement time, the ramp procedure (9° , 0° , -14°) is interrupted at three test points to perform the chirp procedure for harmonic analysis. This excitation signal (frequency range up to 40 Hz, chirp time of 28 s) is utilized to determine transfer functions depending on the tab position.

In order to identify transient responses, the system identification also comprises a step procedure (deflection rate of $260^\circ/\text{s}$, duration of 15 s) which follows after the ramp procedure. The dependency of step height, step direction, and target position of the step (-15° , 0° , 10°) is performed using six individual step functions.

The test sequence is enclosed at the beginning by a triangle procedure and at the end by a sinus procedure. These functions are intentionally designed not to meet an integer multiple of the period length, so that the tab angle can be brought in the correct positions for the ramp procedure at the beginning and also set to zero position at the end of the test sequence.

The purpose of the triangle procedure is to analyse the actuator force in the dependency of the tab position, as the resulting current is proportional to the actuator force at constant actuator velocity (actuator voltage respectively). The sinus procedure allows higher harmonic analysis for a constant large-signal excitation. Hysteresis effects based on friction can be identified by higher harmonic distortion.

The winglet test sequence was investigated for the first time on the assembly rig of FACC in October 2014. As the stiffness of the assembly rig was not foreseen for such a structural test, the available results allow only qualitative and not quantitative conclusions. One result is shown in Fig. 34, where the measured tab angle follows the applied control signal very precisely with a time delay of about 10 ms, which would be sufficient for closed-loop control. The resulting acceleration response (without air flow) shows values of up to 3 g at the winglet tip (see Fig. 35).

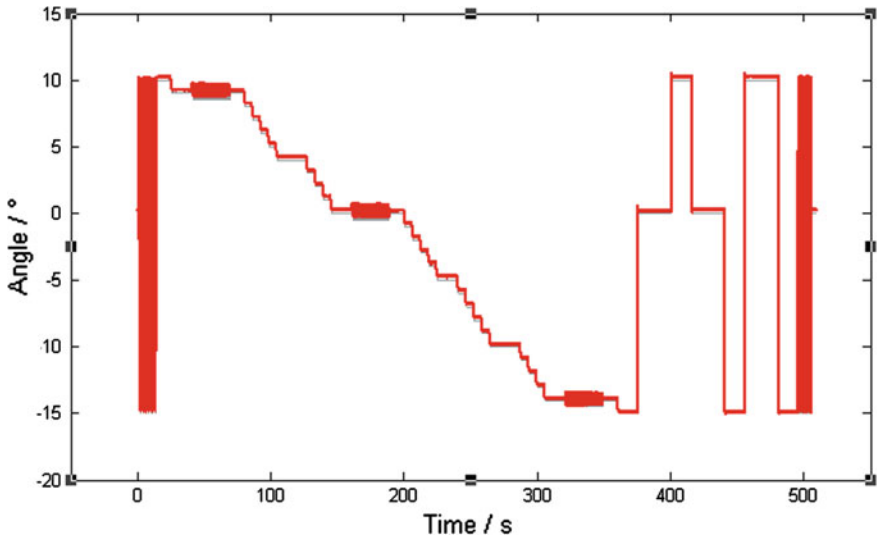


Fig. 34 Measured WATE deflection in comparison with WATE deflection command

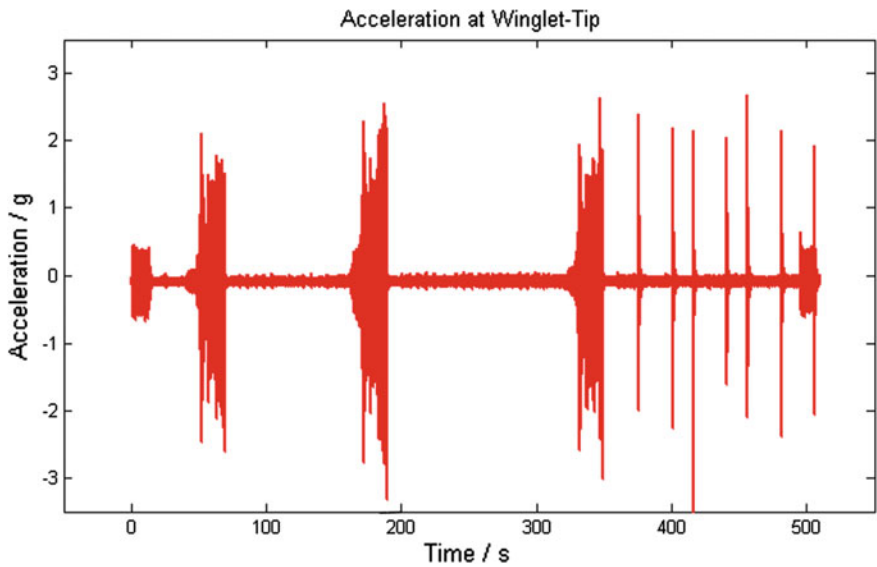


Fig. 35 Accelerations at the winglet tip resulting from applying the test sequence without airflow

5 Winglet Integration in Wing Demonstrator

Due to mentioned space restrictions of the winglet geometry, there was not enough space for integration of selected commercial of-the-shelf control components, servo controller, and Microautobox in the winglet itself. Therefore, an adequate place was

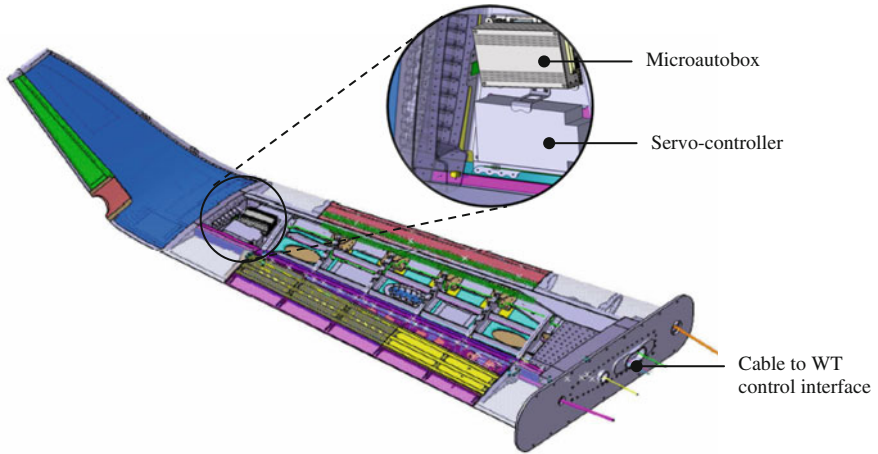


Fig. 36 DMU of WATE integration in wing demonstrator

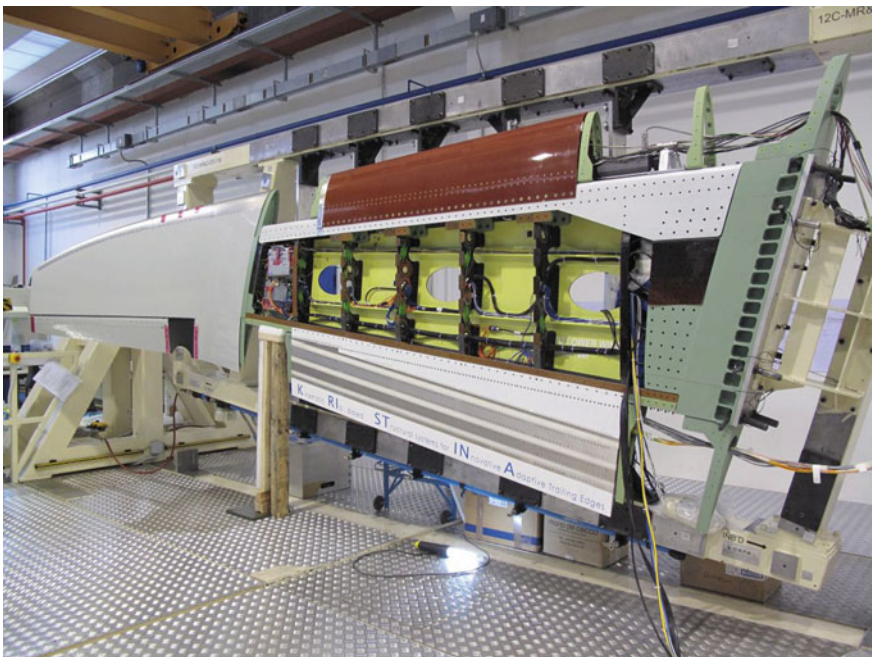


Fig. 37 Active winglet integrated to wing demonstrator

found in the outer section of the wing box, where both components are arranged on a common baseplate or bracket (see Fig. 36). Wiring routing from servo controller and Microautobox to the WT interfaces is provided by a cable bundle going through the wing box stringer grid structure (opening in the ribs). This cable is then connected to the WT control interface.

Figure 37 shows the successful integration of the active winglet to the SARISTU wing demonstrator.

6 Conclusion

The design of a winglet control device for gust and manoeuvre load alleviation and eventually drag minimization in off-design flight cases is presented. The main design challenge encountered is integration of the control and actuation systems inside the winglet surface geometry. This is achieved by adaptation of the aerodynamic shape as well as by optimization of kinematics.

Preliminary FHA results in the requirement for a full secondary load path for the EMA and actuation kinematics in order to reduce probability of catastrophic control surface flutter to a sufficiently small value to be certifiable according to EASA CS-25 criteria. Subsequent work presented in SARISTU IS12 extends the FHA for the winglet device to the complete aircraft, including the control system for load alleviation in order to judge on the impact on aircraft system architecture. It is shown that the probability of the load alleviation system being in a failure condition has a significant impact on the safety factor to be used for computation of ultimate loads in failed condition. Therefore, the availability of the WATE system determines the achievable structural mass saving due to load alleviation, i.e. the achievable benefit. On the other hand, the introduction of the WATE system adds new failure scenarios to an aircraft which have to be handled not only in terms of loads but also in terms of aircraft controllability and performance degradation. Subsequent work presented in SARISTU AS03 presents a complete value versus risk analysis of the proposed device considering the whole aircraft.

Wherever possible, design rules according to the RSDP A350XWB program were used. Applied manufacturing processes range from RTM to MARI depending on the best choice for the respective part. Assembly of the active winglet is performed in 8 phases. Thereby, the most significant difference to the manufacturing of a passive winglet is the actuation system integration and the electronic equipment integration. The eigen modes and frequencies of the assembled winglet are verified in a GVT. The validity of FEA loads prediction is assessed in a static structural test. Functional testing of the active tab is performed before as well as after integration of the active winglet to the SARISTU wing demonstrator, using a dedicated tab deflection command sequency for static, harmonic, and transient response identification. The same test sequency will be applied in the wind tunnel test planned for June 2015.

Acknowledgments The research leading to these results has gratefully received funding from the European Union Seventh Framework Programme (FP7/2007–2013) under Grant Agreement no 284562. Many thanks also go to all SARISTU partners for their invaluable contributions.

References

1. Bourdin P, Gatto A, Friswell M (2006) The application of variable cant angle winglets for morphing aircraft control. In: 24th applied aerodynamics conference, University of Bristol
2. Ursache N et al (2007) Morphing winglets for aircraft multi-phase improvement. In: 7th AIAA aviation technology, integration and operations conference, Bristol University
3. Sankrithi M, Frommer J (2010) Controllable winglets. US Patent 7,744,038 B2, The Boeing Company, June 2010
4. Allen A, Breitsamter C (2006) Investigation on active winglet influencing the wake of a large transport aircraft. In: 25th international congress of the aeronautical sciences, Institute of Aerodynamics, Technische Universität München
5. Breitsamter C, Allen A Aerodynamic body and carrier wing comprising an aerodynamic body, actuating drive control module, computer, computer program and method for influencing post-turbulence. US Patent 2010/0006706 A1, Jan 2010
6. Kauertz S, Neuwert G (2006) Excitation of instabilities in the wake of an airfoil with winglets. In: 24th applied aerodynamics conference, RWTH Aachen, June 2006
7. Park P, Rokhsaz K (2003) Effects of a winglet rudder on lift-to-drag ratio and wake vortex frequency. In 21st applied aerodynamics conference, Department of Aerospace Engineering Wichita State University
8. Nagel B, Kintscher M, Streit T (2008) Active and passive structural measures for aeroelastic winglet design. In: 26th international congress of the aeronautical sciences, DLR
9. Guida N (2011) Active winglet. US Patent 7,900,877 B1, Tamarack Aerospace Group, Inc., March 2011
10. Irving J, Davies R (2007) Wing tip device. European Patent 1531126 (A1), Airbus UK Ltd, Sep 2007
11. Wildschek A, Maier R (2010) Winglet with autonomously actuated tab. European Patent 2233395 (A1), Sep 2010
12. Buxel C, Dafnis A et al (2011) Design and qualification of a winglet with a high speed oscillating active control surface for aeroelastic wind tunnel experiments under cryogenic conditions. In: Deutscher Luft- und Raumfahrtkongress. RWTH Aachen, Institute of Aerospace and Lightweight Structures
13. Dafnis A et al (2010) Stationäre und instationäre Untersuchungen an einem elastischen Flügelmodell mit Winglet im kryogenen Windkanal im Rahmen des ASDMAD-Projektes, Deutscher Luft- und Raumfahrtkongress 2010, RWTH Aachen
14. Heinen C, Wildschek A, Herring M (2013) Design of a Winglet Control Device for Active Load Alleviation. In: International forum on aeroelasticity and structural dynamics, Bristol, UK, 24–26 June 2013
15. EASA CS-25 Amendment 14, dated 19 Dec 2013—“Certification Specification for Large Aeroplanes”
16. Heinen C (2012) Design of a winglet control device for active load alleviation. Diploma thesis, Institute of Lightweight Structures, Technische Universität München, Nov 2012
17. Storm S, Wildschek A (2014) Curved wing profile with a pivotable flap. European Patent 2743177 (A1), June 2014
18. ARP4754 The aerospace recommended practice—guidelines for development of civil aircraft, SAE International, Nov 2011
19. Bennett J (2010) Fault tolerant electromechanical actuators for aircraft. Ph.D. dissertation, Newcastle University, School of Electrical, Electronic and Computer Engineering, Nov 2010

20. Belschner T (2011) System design and preliminary system safety analysis of a blended wing body aircraft. Diploma thesis, Uni Stuttgart
21. Jeanneau M, Aversa N, Delannoy S, Hockenhull M (2004) Awiator's study of a wing load control: design and flight-test results. In: 16th IFAC symposium on automatic control in aerospace, St. Petersburg (RUSSIA), 14–18. June 2004
22. Johnston J et al (1979) Accelerated development and flight evaluation of active controls concepts for subsonic transport aircraft volume 1 load alleviation/extended span development and flight test. NASA CR-159097, pp 2–11
23. Wildschek A (2008) An adaptive feed-forward controller for active wing bending vibration alleviation on large transport aircraft. Ph.D. dissertation, Munich
24. Wildschek A, Maier R, Hoffmann F, Jeanneau M, Aversa N (2009) Minimizing dynamic structural loads of an aircraft. US patent US 2009/0084908, April 2009
25. Elliott S (2001) Signal processing for active control. Academic Press, London, pp 64–69
26. Wildschek A, Maier R, Hahn K-U, Leißling D, Preß M, Zach A (2009) Flight test with an adaptive feed-forward controller for alleviation of turbulence excited wing bending vibrations. In: AIAA guidance, navigation, and control conference and exhibit, Chicago, IL, 10–13 Aug 2009
27. Hecker S, Hahn K-U (2007) Advanced gust load alleviation system for large flexible aircraft. In: 1st CEAS European air & space conference, Berlin, Germany, 10–13 Sept 2007
28. Wildschek A, Bartosiewicz Z, Mozyrska D (2014) A multi-input multi-output adaptive feed-forward controller for vibration alleviation on a large blended wing body airliner. J Sound Vibr
29. Koch O, Schneiderbauer G (2012) Method for producing a fibre composite component, and a tool arrangement for same. Patent CA 2827545 A1, Sept 2012

Winglet Design, Manufacturing, and Testing

Danijel Drezga, Viken Korian, Olaf Roock, Bernardo Lopez, Arne Fiedler, Stefan Storm and Vladimir Snop

Abstract With respect to the SARISTU project (Smart Intelligent Aircraft Structures), a wingtip active trailing edge (WATE) within the application scenario AS03 has been developed. Full-scale demonstrator has been manufactured and successfully tested to prove the maturity of such a device and its technology. This paper contributes to the overview of design, manufacturing, and testing aspects of WATE demonstrator.

Abbreviations

WATE Wingtip active trailing edge
AGI-D Airbus Group Innovations—Germany
FIDAMC The Composites Research, Development and Application Centre

D. Drezga (✉) · V. Korian · O. Roock
FACC Operations GmbH, Fischerstrasse 9, 4910 Ried im Innkreis, Austria
e-mail: d.drezga@facc.com

V. Korian
e-mail: v.korian@facc.com

O. Roock
e-mail: o.roock@facc.com

B. Lopez
Foundation for the Research, Advanced Materials, Development
and Application of Composite Materials (FIDAMC), 28096 Getafe, Spain
e-mail: bernardo.lopez@fidamc.es

A. Fiedler
Materials Science and Engineering, Fraunhofer Institute for Manufacturing Technology
and Advanced Materials (IFAM), Wiener Straße 12, 28359 Bremen, Germany
e-mail: arne.fiedler@ifam.fraunhofer.de

S. Storm
Airbus Group Innovations, 81663 Munich, Germany
e-mail: stefan.storm@airbus.com

V. Snop
Aerospace Research and Test Establishment (VZLU), Prague, Czech Republic
e-mail: snop@vzlu.cz

FH.	FRAUNHOFER Institute for Manufacturing Technology and
IFAM	Advanced Materials
VZLU	Aerospace Research and Test Establishment
TsAGI	Central Aerohydrodynamic Institute
ALA	Alenia Aermacchi
CFRP	Carbon fiber-reinforced polymer
CAD	Computer-aided design
RSDP	Reference structure design principle
OOA	Out of autoclave
MARI	Membrane-assisted resin infusion
LCM	Liquid composite molding
CNC	Computerized numerical control
CMM	Coordinate measurement machine
NDI	Non-destructive inspection
NDT	Non-destructive testing
OML	Outer mold
IML	Inner mold
FEA	Finite element analysis
RTM	Resin transfer molding
GVT	Ground vibration testing
GST	Ground static testing
MMIF	Multivariate mode indicator function
WT	Wind tunnel

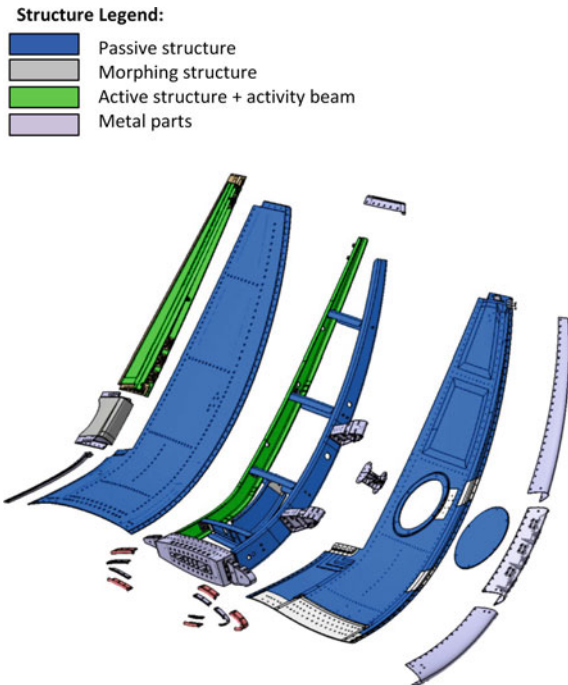
1 Introduction

In the scope of the SARISTU project, which had a goal to reduce the weight and the operating costs of an aircraft and a further optimization of the aerodynamic partners, AGI-D, FACC, FIDAMC, FRAUNHOFER IFAM, and VZLU have been in charge of design, manufacturing, assembly, and testing of a winglet with “wingtip active trailing edge,” called WATE, within the project’s application scenario AS03. Herein, FACC has been responsible for the structural design and analysis of more than 80 % of the passive composite structure as well as the assembly of the WATE demonstrator. AGI-D developed and integrated actuation and control system. FIDAMC contributed with active trailing edge and activity beam manufacturing, as well as FRAUNHOFER IFAM, which has designed and manufactured morphing structure of WATE system. SARISTU WATE demonstrator has been successfully tested by VZLU before its final integration into the wing demonstrator (ALA) and wind tunnel test campaign at TsAGI.

2 WATE Manufacturing and Assembly

In regard to the requirements of integration of actuation and electronic equipment for Active Tab control, pure laminate skin and stringer grid concept have been chosen for the winglet baseline concept. Therefore, WATE system structure consists of passive, active, and morphing structure. Passive structure includes CFRP pure laminate skin panels (lower and upper) and stringer grid (including front, rear, and middle spar, and four ribs). Root rib, leading and trailing edge, and end cap are conventional aluminum machined parts. Active structure is represented by Active Tab (FIDAMC) actuated by electric actuation system mounted on activity beam (FIDAMC) or winglet’s rear spar. Morphing structure (FH.IFAM) is a solid rubber compound part which is used as an aerodynamic gap filler between passive and active winglet structure. As for the interface between winglet and wing box, a root rib concept with a bolted connection has been chosen. The structural configuration of the winglet structure is shown in Fig. 1. The front and rear spars constitute a torsion box from the root rib to end tip of the winglet. A center auxiliary middle spar is incorporated in the lower portion of the winglet to provide additional continuous support through the curved geometry of the winglet in regard to bending loads. Four ribs between spars are incorporated: As closure for the center rib and to avoid skin warping and buckling, the CFRP upper and lower skins’ panels are single piece units (including an access door at the lower skin panel) and extend from root to tip and from leading edge to trailing edge. Skins are pure laminate design to provide as

Fig. 1 SARISTU WATE structure overview



much possible space for actuation and electronic system integration. A machined aluminum, end cap forms the outboard closure on the winglet. Three machined aluminum leading edge ribs support the leading edge structure as well as spar rib and trailing edge rib, which are located at the wing box \leftrightarrow winglet interface. The attachment there is comprised of 18 tension bolts. Actuator fitting, actuation and electronic system, tab hinges, and fastener joints, as well as morphing part aluminum flanges, are interface to the morphing structure of the WATE system.

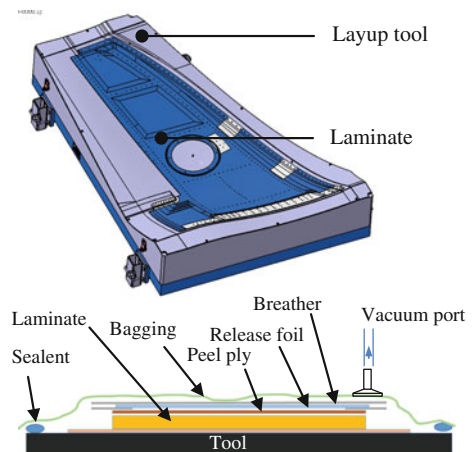
The design rules have been specified by AIRBUS by the RSDP A350XWB program (V51RSDP07001.1-1.5). Wherever possible, materials specifications have been chosen in the following order: Materials specified and qualified by AIRBUS, materials qualified for aeronautic applications, and general qualification has been made according to international standards and specifications.

2.1 Composite Structure Component Manufacturing

Winglet passive composite structure components are manufactured using standard aerospace serial manufacturing processes as well as standard aerospace serial materials. Different manufacturing process has been chosen. Reason was to demonstrate the maturity of several manufacturing technologies which can be applied in manufacturing of deferent parts in a winglet structure.

Winglet skins are manufactured using serial prepreg materials (CYTEC 977-2A-42%-6KHTA-2x2TW-285 and Cytec 977-2-34%-24K-IMS-194) and prepreg autoclave processing. As shown in Fig. 2, prepreg material is laid on the tooling surface manually with support of a laser projection system (ply boundary and layup rosette projection). After completion of layup process, release foil, breather and vacuum bagging material is layed before layup is subjected to autoclave curing process. When autoclave curing process is finished, part was demolded and ready for CNC milling procedure, and then, CMM and NDI quality check procedures were carried out.

Fig. 2 Winglet skins manufacturing—Prepreg processing



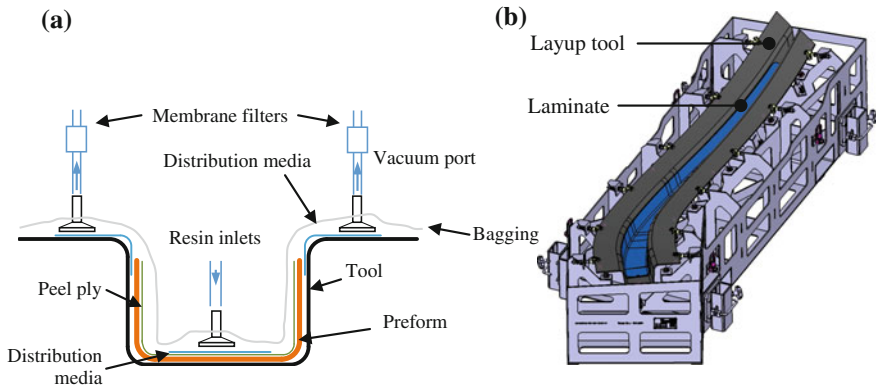


Fig. 3 a MARI process [1]. b Winglet stringer grid manufacturing tool

Stringer grid has been manufactured by MARI process [1] (Membrane Assisted Resin Infusion) which is a FACC's patented process based on standard liquid composite molding (LCM) process. MARI manufacturing process used to manufacture the WATE's composite stringer grid (Front spar and ribs) consists of performing process using Hexcel HexForce G0926 D 1304 TCT INJECTEX E01 2F, where the dry fabrics are preformed in the tool, using a specific temperature profile in oven. Afterward, preformed layup is infused with the Hexcel HexFlow RTM6 matrix system using OOA infusion process. Curing took place in oven at 180 °C. Process is described in Fig. 3.

Activity beam (rear spar of SARISTU winglet) was made of CFRP material (carbon fiber/epoxy resin). The manufacturing process carried out for its production was flat layup by means of Automatic Fiber Placement machine (AFP) with subsequent press forming and autoclave curing cycle in male tool. Materials used for manufacturing were as follows: preimpregnated unidirectional tape ABS5139C-0003 (slit tape for Automatic Fiber Placement, 3.2 mm tow width, 8552 resin/AS4 carbon fiber) as structural material and preimpregnated ultralight glass fiber fabric ABS5009J56EP066 for galvanic protection. The layup of the spar consisted of 36 plies and divided into 7 different zones corresponding to the web (3) and flanges (4). The layup of the spar was done by means of AFP machine. A flat laminate was laid up for being afterward formed in a C shape. Once the flat preform was laid up, it was subsequently transferred from the AFP tool to the press forming machine. The press forming process basically consists of the relative sliding of the prepreg plies, one over each other. A typical press forming tool for C shapes is composed of six metallic modules (four outer modules, upper and lower, and two inner tools). For this work, FIDAMC's press forming machine was designed for sliding downward the inner metallic tools, while the outer ones remain in the starting position (see Figs. 4 and 5). Key parameters of the process such as temperature, forming rate, and gap between metallic modules were investigated and defined concretely for the concerned spar. The as-formed uncured spar was transferred then



Fig. 4 SARISTU WATE rear spar geometry

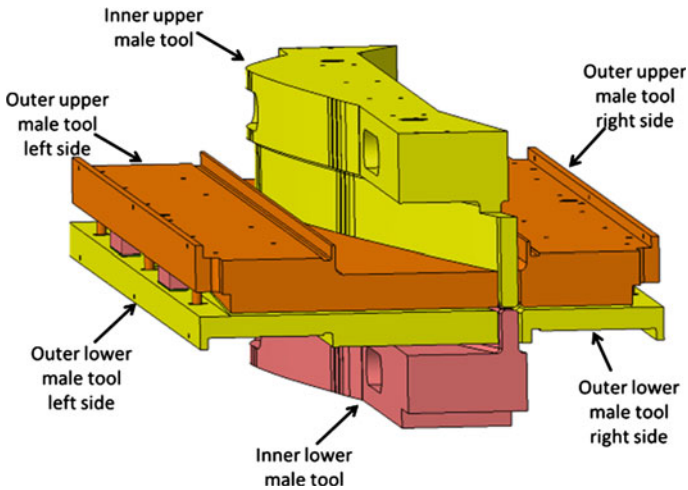


Fig. 5 Press forming tool

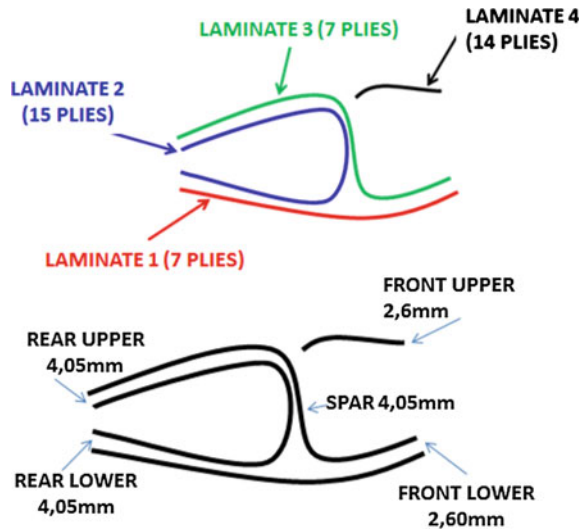


Fig. 6 Finished cured WATE rear spar

to the male curing tool. Caul plates made of CFRP (preimpregnated carbon/epoxy fabric) were placed on the bag face of the flanges in order to improve the surface finish in view of the assembly stage in the whole winglet. Vacuum bag was constructed for curing the element in autoclave at 90 psig and 180 °C. The spar was demolded from the curing male tool and inspected by means of pulse-echo ultrasound technique. Dimensional analysis of the spar was carried out after trimming operation. The specimen was successfully evaluated and was ready for assembly into WATE system. Figure 6 represents finished cured activity beam.

Active Tab (movable part belonging to the active trailing edge of SARISTU winglet) was made of CFRP material (carbon fiber/epoxy resin). The manufacturing process selected for its production was prepreg technology (hand layup) and curing in autoclave cycle. Materials used for manufacturing were preimpregnated unidirectional tape ABS5139C-300 and ABS5139C-150 (8552 resin/AS4 carbon fiber) as structural material and preimpregnated ultralight glass fiber fabric ABS5009J56E

Fig. 7 Layup concept



P066 are used for galvanic protection as well as for avoiding delaminations during trimming/drilling operations. The tab is composed of 4 different laminates. Laminates 1, 2, and 3 are cocured, and they constitute torque box and the lower leading edge of the tab. On the other hand, laminate 4 corresponds to the upper leading edge of the tab and it is cured separately (see Fig. 7 for layup **concept**).

This element is removable, allowing access to the space between rear spar and tab for assembly and maintenance tasks, and it is installed after tab mounted in winglet. The layup was complex due to the difficulty of designing symmetric laminates by means of the combination of sub-laminates which, in turn, are symmetric in themselves as well. This complexity is strengthened by the angle variation in the bending of sub-laminates (laminates 2 and 3), which is fact that had to be taken into account in the design. The tooling for the manufacturing of the TAB consisted of two main tools: the OML and the IML which is divided into three different modules for allowing the demolding phase. Additionally, a tool for the manufacturing of customized caul plates was used. The layup was carried out manually. Laminates 1 and 4 were directly laminated on the OML tool. Laminate 2 were laminated around the IML tool, which subsequently was placed over the OML tool, in contact with Laminate 1. Asymmetric roving was manufactured and placed in the lower radius of the spar of the tab. Then, laminate 3 was laid up over the laminate 2. Caul plates were placed in the bag side in order to obtain a good aerodynamic surface. Afterward, vacuum bag was constructed for curing the element in autoclave at 90 psig and 180 °C. Demolding of the tab was carried out successfully. The tab was inspected by means of manual pulse-echo ultrasounds technique. Subsequently, the tab was trimmed for metallic parts assembly (see Fig. 8). For Active Tab assembly purposes, 10 metallic elements were assembled in the tab previous to its final assembly in WATE system. Five female fittings, an

Fig. 8 Cured Active Tab layup ready for assembly



actuator rib (morphing attachment), end cap, trailing edge, rib to spar connector, and leading edge to spar connector were assembled.

The **morphing structure** is manufactured in a casting process. A mold is filled with a reactive mixture of the silicone components, and the morphing material is cured in the mold. The structural interface with cleaned and activated surfaces acts as a part of the mold. In this way, a morphing structure is obtained which is already equipped with the structural interface for connection with the airframe (see Fig. 9). The manufacturing process of morphing structure comprised the following steps: (a) application of release agent to the mold surface, (b) application of primer to the surfaces of the connecting ribs, (c) insertion of gaskets into the mold, (d) insertion of primed connecting ribs into the mold, (e) fixation of connecting ribs by fixing bolts, (f) closing of mold by attaching upper mold case and tighten fixing bolts, (g) bringing mold into upright position and fill prepared material mixture into feed inlet (Fig. 10) and (h) cure. The dimensional check was performed by measuring the distances between the bolt holes on the connecting ribs and comparing the measured values to the specified values in the CAD drawing. In order to overcome anticipated tolerance issues within winglet assembly process, it was decided to drill the holes on the connection ribs and on the related WATE passive structure counterparts (lower and upper skin).

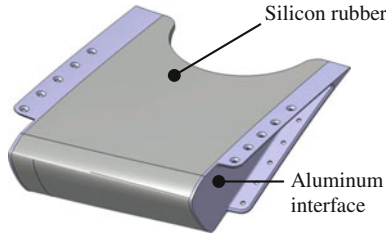
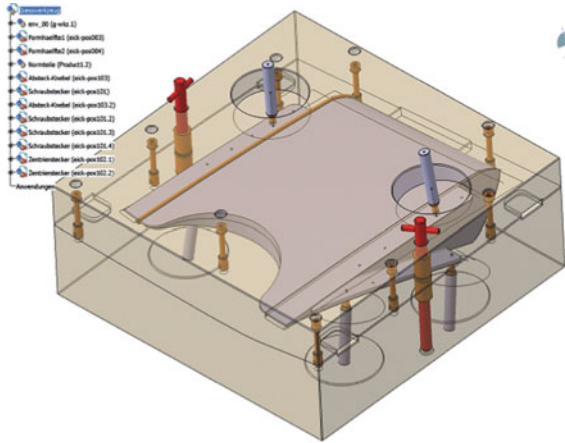


Fig. 9 WATE's morphing structure

Fig. 10 Morphing structure manufacturing tool



2.2 Winglet Assembly

The overall assembly process is done according to AIRBUS specification used in assembly process. Assembly process has been divided into several phases. Before overall assembly process has been started, assembly jig was positioned in assembly hall and its geometry has been proved using CMM measurement system. Calibration of the assembly jig reference coordinate system is done in regard to the CAD model, and such a reference is used during all assembly procedures of WATE system. Assembly process has been divided into several main phases which are shown in Fig. 11.

All assembly phases were supported by laser tracing system for positioning the parts and “Cleco” fastening system for temporary fixation. Each of temporary fastening operations was accompanied by pilot holes provided in manufactured parts. Permanent fixation of the parts has been done by nominal hole size reaming of pilot holes and parts fastening with bolts. Interfaces between the parts were shimmed when there was a need to meet defined assembly tolerances. The fasteners shall be installed. Prior to installation of fasteners, each drill hole must be measured

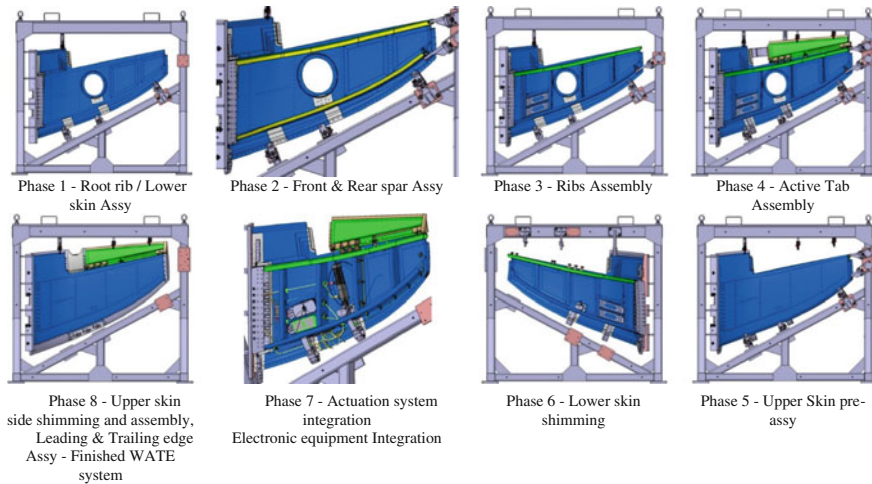
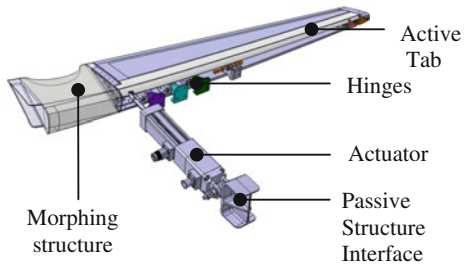


Fig. 11 Assembly concept of WATE system

with a qualified gauge to ensure the right grip length of fastener. It is allowed to vary the grip length ± 2 to nominal. Bolts have been tightened with specified torque in accordance.

Root rib positioning and temporary assembly have been done as part of a Phase 1. This step has been a driving step as well as the reference through next assembly phases. In Phase 2, front spar and rear spar have been positioned on the lower skin as a part of a stringer grid assembly. Further in Phase 3, middle spar, as well as the rest of the stringer grid and the ribs, has been positioned. In Phase 2 and 3, all the parts have been temporarily fastened, and afterward, their assembled geometry has been checked. To prove the loft surface after attaching stringer grid, laser tracking system for this purpose has been used again. Afterward when all of the assembly requirements have been met in Phase 2 and 3, complete stringer grid has been permanently fastened with bolts. Then, in Phase 4, Active Tab together with the hinge line is positioned onto the rear spar. This assembly phase has been supported with the “dummy morphing part” in order to simulate assembly interface morphing structure and Active Tab, as well as interface between morphing structure and passive structure of the winglet. Phase 5 represents upper skin temporary assembly and complete upper and lower surface loft geometry check. In Phase 6, in order to meet the assembly tolerances and keep the passive structure in stress-free state, stringer grid was partially local shimmed. Upper skin has been kept temporary assembled to assure stiffness and maintain already achieved assembly tolerances of stringer grid. Therefore, such a shimmed structure can be permanently sealed and fastened with bolts. Complete temporary assembled stringer grid and lower skin have been ready to enter next assembly phase where actuation system and electronic equipment are integrated into the winglet, Phase 7. Before the winglet passive structure was closed with the permanent assembly of upper skin, actuation and

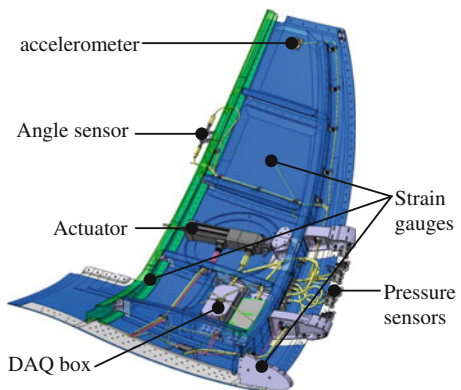
Fig. 12 WATE actuation system with Active Tab and morphing structure



electronic equipment system have been functionally tested. With successful functional test, the winglet structure has been permanently closed with the assembly of upper skin. Skin is fastened with blind fasteners, and complete WATE system’s loft geometry was once more completely checked, Phase 8. Before WATE system was sent for painting work and therefore shipment for static tests, actuation and electronic system have been once more tested.

The full-scale winglet, as mentioned, has been delivered for structural testing with fully equipped Active Tab (actuated trailing edge), as shown in Fig. 12, monitoring sensor system, and a control and communication system, as shown in Fig. 13. The adaptive actuated trailing edge/Active Tab is driven by the controller located in the wing box outer wing bracket (described further in chapter dedicated to winglet integration in wing demonstrator) and was not part of the sensing system. Sensor and data acquisition system allow a detailed monitoring of the adaptive winglet. The WATE’s sensor system consists of differential pressure sensors, absolute pressure sensor, three-axis acceleration sensor, angle sensors, and strain gages. All data are gathered by a DAQ box, which digitizes the signals and sends the data via Ethernet network to the computer for storage and further data analysis. The figure below shows an overview of the integrated actuation and electronic systems of WATE. Inside the WATE system, one may see all the sensors mounted in their positions. Near the end cap, the acceleration sensor package is assembled to the winglet lower skin. At the activity beam, the angle sensor has been mounted.

Fig. 13 WATE actuation and electronic system integration concept



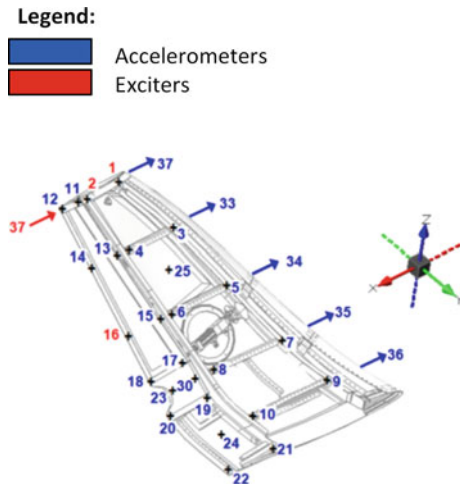
On lower skin, access door can be recognized (service hole) and above mounted actuator. Sideward down between the inboard and outboard end ribs, the signal distribution board can be seen. Near this position, the data acquisition box and the signal conditioning modules for the strain gages are fixed. Pressure sensors are located in the middle part of the leading edge, and their signal distribution board is located on front spar. Strain gauges have been glued on lower skin and spars (front spar, rear spar, and mid spar). For winglet function verification tests purposes, strain gauges, accelerometer sensor, and angle sensor data were monitored and used for their assessment.

2.3 Winglet Testing

For ground vibration test (GVT) and ground static test (GST) purposes, WATE system was needed to be fixed first to the interface plate using bolts and barrel nuts. Such an interface plate was bolted then to one of the test rigs, depending on the GVT or GST setup.

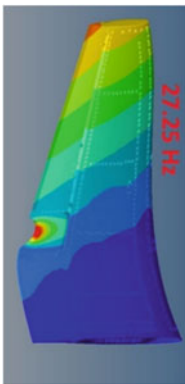
During the **GVT**, the Active Tab was blocked in neutral position by the actuator. The actuation and electronic system were disconnected for the test purposes. The ambient temperature and relative humidity were maintained (laboratory conditions) in the test area during the testing. The test system has been consisted of the circuits for excitation, circuits for response measurement, and algorithms for the analysis of vibration and test control. All response measurement channels were calibrated before the test start. The vibrations of the specimen and test rig have been measured by 37 pieces of uniaxial accelerometers, as shown in Fig. 14 (marked blue). The specimen was excited by electrodynamic shakers at points 1, 2, 16, and 37, which are visible (excited points marked red in Fig. 14.). The distribution overview of

Fig. 14 Accelerometers and exciters position on specimen

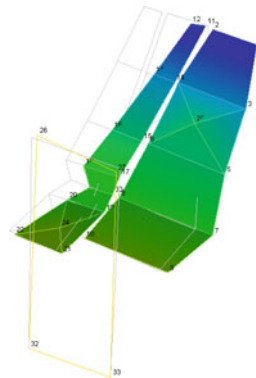


modal frequencies of the winglet has been determined by the analysis of response to the swept sine excitation from 10 to 200 Hz. The MMIF function (multivariate mode indicator function) was used, and excitation was by constant amplitude of force by one exciter during whole sweep.

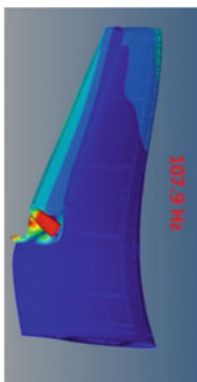
The individual modes of vibration have been investigated by means of multi-point appropriated excitation method. Modal parameters of each mode were investigated separately. Each mode is determined by its modal parameters: modal frequency, modal mass, damping, and mode shape. The values of modal mass and damping have been obtained by means of complex power method. Logarithmic decrement method for damping measurement was used as well. The amplitude force of excitation by one exciter was set so that the point with maximum acceleration had nearly 1 g. Determined modal frequencies from GVT have been compared with FEM, and some specific cases are represented in Fig. 15.



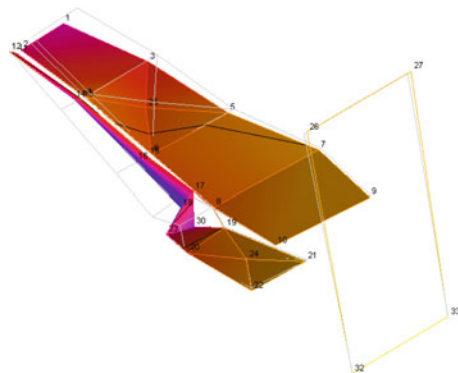
FEA Mode 1 – Winglet bending 27.25 Hz



GVT Mode 1 – Winglet bending 29.57 Hz



FEA Mode 6 - Winglet bending & Morphing part vibration 107.9 Hz



GVT Mode 6 - Winglet bending & Morphing part vibration 101.40 Hz

Fig. 15 Modal frequencies of WATE system

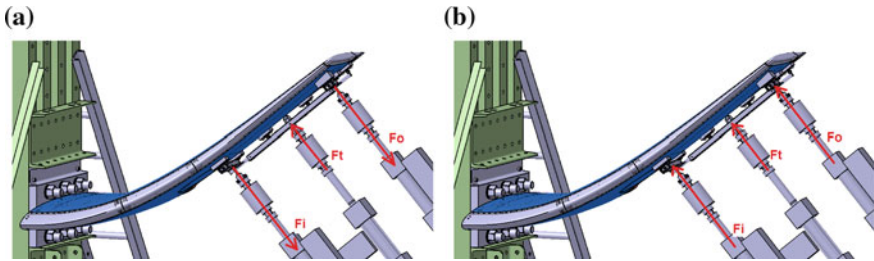


Fig. 16 WATE static load cases. **a** LC1—downward bending ($+10^\circ$ tab deflection). **b** LC2—upward bending (-15° tab deflection)

For **GST** purposes, the winglet with interface plate was bolted to the static test rig. The Active Tab was blocked in requested position by the actuator depending on the load case. The load distribution is defined by 8 points (4 points at the winglet + 4 points at the Active Tab). Three steel constructed whiffle trees have been used for load distribution from load cells to the load distribution pads and have simulated the external applied loads. Whiffle trees were connected to 8 loading pads, which were bonded to the lower skin of the winglet and tab. Whiffle trees were available for tension or pressure loading, as shown in Fig. 16. The magnitudes of the forces to be introduced to the winglet have been defined such as to represent the stress state anticipated in the wind tunnel. The finite element analysis showed that the stress state of wind tunnel load cases can be accurately reproduced by load introduction through the whiffletree with two different load cases and applied approximately 25 % of the loads needed to reproduce the stress state of the wind tunnel load cases. The reduction of the load level to 25 % was in respect to avoid any damage to the winglet structure or its actuation and/or electronics system. Therefore, GST load cases were defined as follows:

Load Case 1—downward bending ($+10^\circ$ tab deflection): $F_i = -1.1$ kN, $F_o = -1.1$ kN, $F_t = 0.3$ kN

Load Case 2—upward bending (-15° tab deflection): $F_i = 1.3$ kN, $F_o = 1.3$ kN, $F_t = 0.3$ kN

Servo-hydraulic loading system with 20 channels was used for the static test control. Three separate actuators with load cells loaded whiffle tree system. Strain gauges inside of winglet structure and strain gauges installed on winglet skins for GST purposes were monitored, and their strain values recorded with data acquisition system during both load cases. Displacements of the winglet structure during

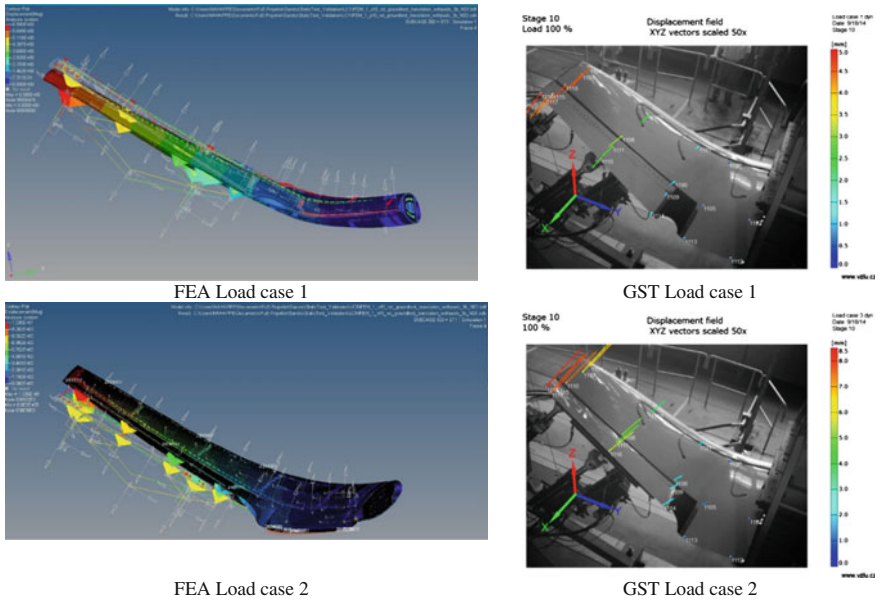


Fig. 17 GST displacements compared with FEM

the load cases have been measured by optical system PONTOS. The reference point markers were applied only on the upper surface of winglet. Afterward, GVT and GST results were compared with FEA model as shown in Fig. 17.

Comparing the measured deformation with the deformation as predicted by the finite element analysis, it can be concluded that the FEA overestimated occurring deformations by about 20 %.

2.4 Winglet Integration in Wing Demonstrator

Due to the mentioned space restrictions of the winglet geometry and not enough space for integration of selected commercial-of-the-shelf control components, servo-controller, and MicroAutoBox, adequate place was found at the outer wing section in the wing box, where both components are arranged on a common baseplate or bracket, as shown in Fig. 18. Wiring routing from servo controller and MicroAutoBox to wind tunnel interfaces has been provided with the cable bundle going through the wing box stringer grid structure (opening in the ribs). This cable is then connected to WT (wind tunnel) control interface.

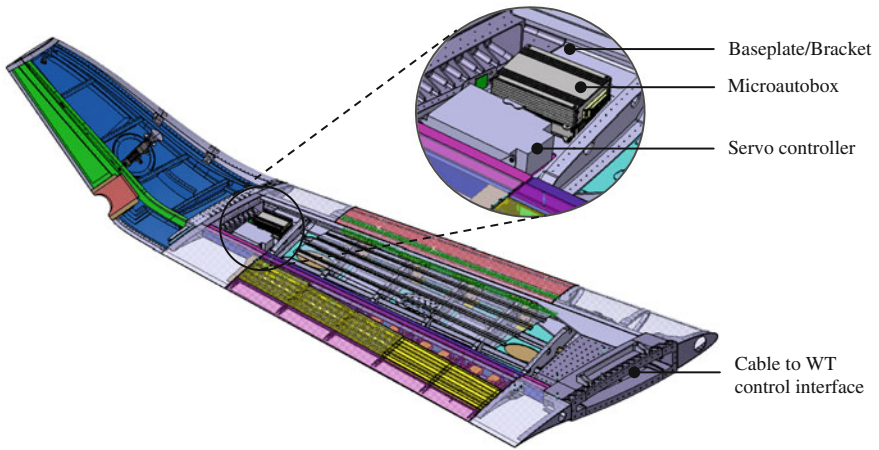


Fig. 18 DMU of WATE integrated servo-controller and MicroAutoBox

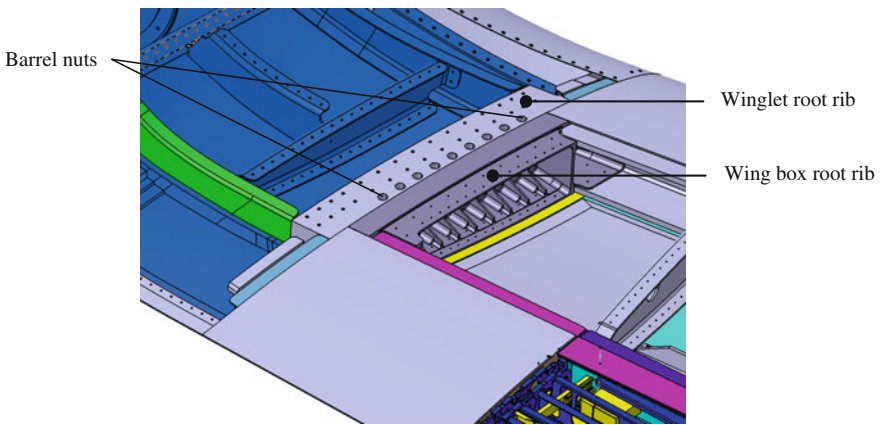


Fig. 19 DMU of WATE integration in wing demonstrator

Assembly interface has been provided both by winglet and by wing box with interface root ribs. The interface zone of both ribs is smooth, and the connection between them is provided by 18 bolts, as shown in Fig. 19. To fix the bolts, barrel nuts have been used in the midsection of the winglet root rib. The bolts have been installed from inner side of the wing and tightened through the wing box root rib.

Figure 20 represents successful integration of WATE system into wing demonstrator.

Fig. 20 WATE integrated into wing demonstrator



3 Conclusion

Reference Structure Design Principle (RSDP) according to A350XWB program was used with respect to passive composite structure design and sizing. Several manufacturing technologies have been applied for manufacturing of passive and active winglet structure. Applying different technologies for different composite structures had an aim to demonstrate the maturity of several manufacturing technologies which could be applied for a such winglet structure. Significant difference in the manufacturing of an active winglet system in comparison with the passive winglet is actuation system integration and the electronic equipment integration for winglet's active control. Assembly of the active winglet has been performed in phases. WATE system has been submitted to ground tests before its integration into the wing demonstrator. Ground test data have been successfully compared with FEA. Functional testing of the Active Tab is performed before, as well as after integration of the active winglet to the SARISTU wing demonstrator. Wind tunnel test campaign is pending mid of 2015 where after all, WATE system maturity and its technology benefits will be investigated.

Acknowledgments The research leading to these results has received funding from the European Union's Seventh Framework Programme for research, technological development, and demonstration under grant agreement no 284562.

Reference

1. Koch O, Schneiderbauer G (2012) Method for producing a fibre composite component, and a tool arrangement for same. Patent CA 2827545 A1, September 2012

Seamless Morphing Concepts for Smart Aircraft Wing Tip

Christof Nagel, Arne Fiedler, Oliver Schorsch
and Andreas Lühring

Abstract Morphing concepts were investigated for a wingtip with active trailing edge (WATE) in an adaptive wing. The basic functionality is to take up geometric gap changes in order to maintain a smooth transition between connected parts. A specific material was tailored in order to meet a set of initially formulated requirements, which involve low modulus, high fatigue life, and stability against physical aging in a temperature range from -55 to $+80$ °C. A variety of material samples and joints were prepared and tested in order to provide a database for numerical simulation and sizing. One of the proposed solutions was developed until the physical sub-component level. Finally, morphing parts were prepared and delivered for assembly in ground test and true-scale wind tunnel demonstrators.

Nomenclature

- d Bond line thickness
- G Initial shear modulus
- i Index
- k Exponent parameter in strain-life law
- n Sample size
- N Number of cycles

C. Nagel (✉) · A. Fiedler · O. Schorsch · A. Lühring
Fraunhofer Institute for Manufacturing Technology and Advanced Materials (IFAM),
Adhesive Bonding Technology and Surfaces, Wiener Straße 12, 28359 Bremen, Germany
e-mail: christof.nagel@ifam.fraunhofer.de

A. Fiedler
e-mail: arne.fiedler@ifam.fraunhofer.de

O. Schorsch
e-mail: oliver.schorsch@ifam.fraunhofer.de

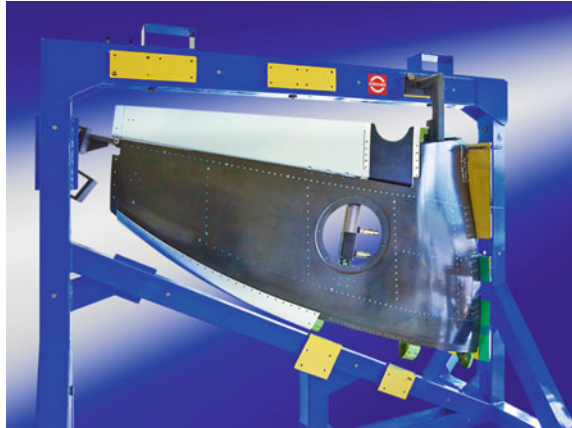
A. Lühring
e-mail: andreas.luehring@ifam.fraunhofer.de

N_f	Number of cycles to failure or fatigue life
P	Probability
R	Load ratio or stress ratio
S	Standard deviation
u	Displacement in mechanical test
γ	Amount of shear
ε	Nominal strain
ε_0	Prefactor in strain-life law
ε_1	Maximum principal strain (given as nominal strain if not stated otherwise)
α	Material parameter in hyperelastic Ogden potential function
λ	Stretch ratio
μ	Material parameter in hyperelastic Ogden potential function
ν	Poisson's ratio
θ	Rotational angle

1 Introduction

Adaptive wings are considered as a potential means to reduce fuel consumption of civil aircrafts. Solutions involving rigid body movements ('swing-wing') or camber variations ('mission adaptive wing') have been investigated and tested, but are restricted to military aircraft [1, 2]. Current research in civil aircraft production focuses on local solutions, which provide small shape changes but are expected to reduce fuel consumption. In this paper, an adaptive part is investigated which was designed to close a gap evolving between a movable tab and the rigid aircraft structure. This part was manufactured, tested, and delivered for assembly in a 'wingtip with active trailing edge' (WATE), as shown in Fig. 1. The WATE was designed as a part of the adaptive wing developed and tested within the SARISTU project. Since the scope of the adaptive part is to keep continuity between aerodynamic surfaces by elastic deformation, major challenges are to obtain a highly deformable, yet stable structure, which can be operated between -55 and $+80$ °C. Other mandatory requirements are stability against fatigue and physical aging, and low actuator capacity, as well as a concept for maintenance and repair. Commercial elastomers were tested as candidate materials for morphing wings by Kikuta [3]. Murray et al. [4] were able to produce and test a flexible matrix composite (FMP) with glass fibers and silicone. Bubert et al. [5] used flexible honeycomb, FMP, and additional reinforcement to make a morphing structure. Low-temperature flexible Hyperflex-03 elastomer developed within the SARISTU project has proved to provide high flexibility and good adhesion to aluminum over the aircraft operational temperature range [6, 7]. The current paper is focused on design and fatigue life of an adaptive part containing Hyperflex-03 elastomer.

Fig. 1 Wingtip with active trailing edge (source www.saristu.eu)



2 Design

More than nine design variants were investigated in the concept phase based on numerical simulation, as shown in Fig. 2. Concept variants V1, V4, V5, V6, and V7 consisted of a block of solid and elastic materials. Variants V4 and V5 were given cavities to reduce weight. Variant V6 had a semicircular cutout on the trailing edge to reduce actuator capacity, flutter effect, and strain. The wedge-shaped variant V7 was considered for reduction of weight and installation space. Variants V2, V3, V8, and V9 contained aluminum ribs and flexible segments, where the latter were given properties of silicone rubber (V3, V9) or elastomeric foam (V2, V8).

Numerical simulations were performed on a preliminary geometry in order to study deformations and strains occurring in the soft material, loads due to actuation of the morphing structure, and eigenmodes. The geometry shown in Fig. 2, with dimensions of 350 mm along chord, 200 mm along span, a maximum thickness of 70 mm, and a minimum thickness of 1.75 mm at the trailing edge, was considered. Boundary conditions were chosen such that one of the side faces could rotate around the rotation axis, while the other one was fixed, thereby simulating the deflection of the tab, as shown in Fig. 3. The air pressure distribution was approximated by a constant pressure acting on the top surface.

The deformation at the trailing edge, which is caused by the action of air pressure at zero tab deflection, is shown in Fig. 4. It can be seen that massive soft parts suffer from large deformations due to low stiffness against air pressure. This is effectively avoided by the introduction of ribs or a semicircular cutout on the trailing edge if no ribs are present.

The strains in the adaptive part at maximum tab deflection and maximum air pressure were found to be about 10–15 % on average, but could locally reach more than 30 %, specifically in the presence of ribs. Strains were lowest for homogeneous design with cutout on the trailing edge.

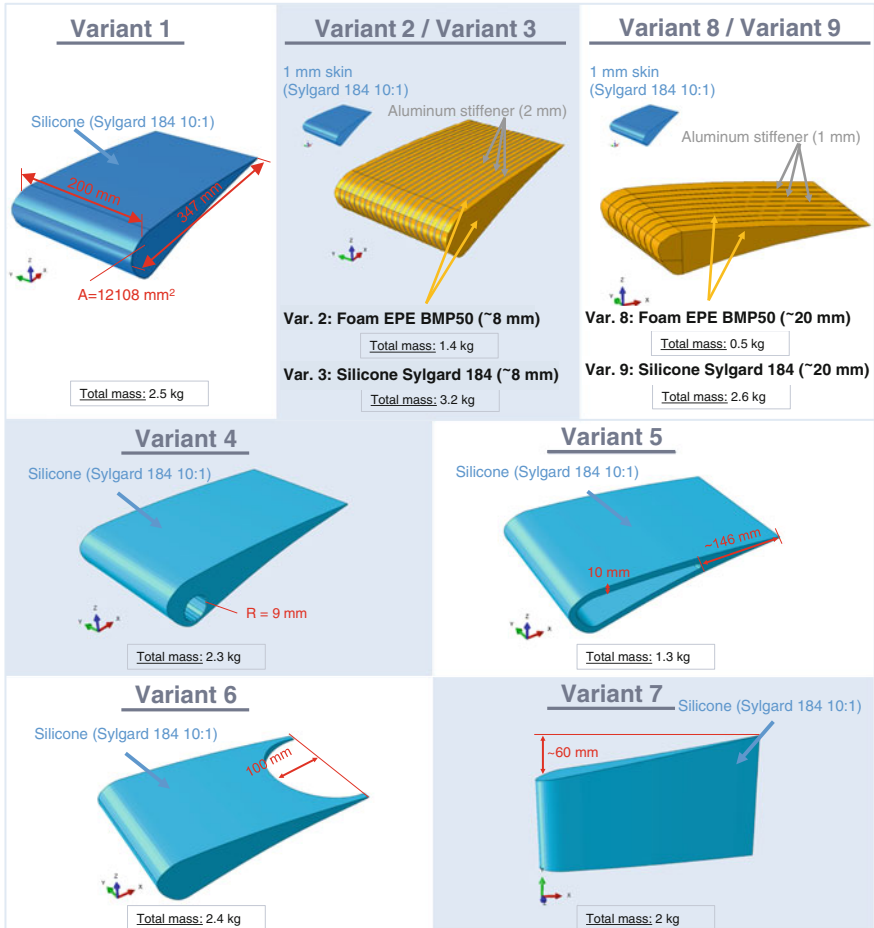


Fig. 2 Geometry of the investigated concept models

The reaction moment about the rotation axis is depicted in Fig. 5. The magnitude of this moment is a measure of the actuator capacity needed to drive the adaptive part. This is important since more powerful actuators add weight to the aircraft and consume more energy. The maximum available hinge moment of the actuator was limited to 70 Nm. As can be seen in Fig. 5, this requirement could be fulfilled with flexible solid variants (V1, V4, V5, V6), while the variants with ribs had significantly higher reaction moments.

The frequency of the first eigenmode is an important quantity to characterize the risk of dangerous oscillations in the structure. Below 10 Hz, there is a high risk that dangerous oscillations might be excited during flight operations. A modal analysis was performed in order to determine the eigenmodes and related frequencies of the design variants. It turned out that the values of the first eigenfrequencies were well

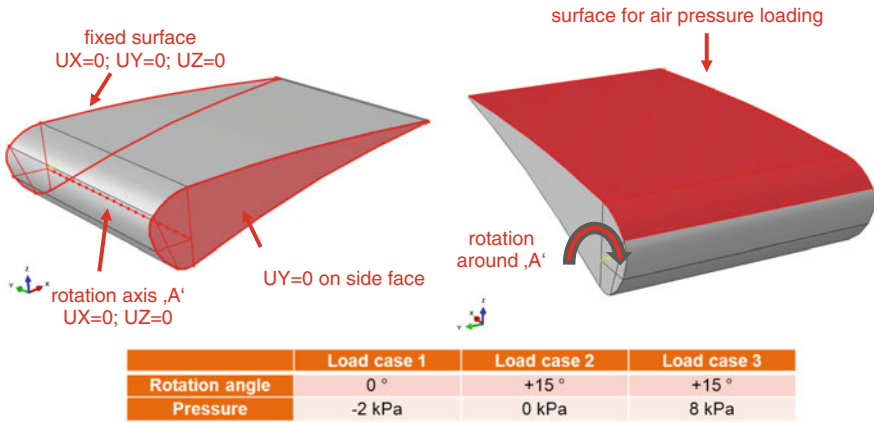


Fig. 3 Loads and boundary conditions

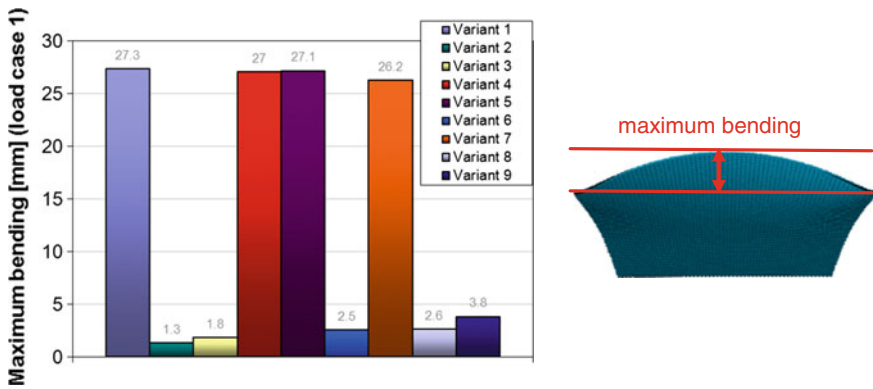


Fig. 4 Comparison of the deformation at the trailing edge caused by the action of air pressure

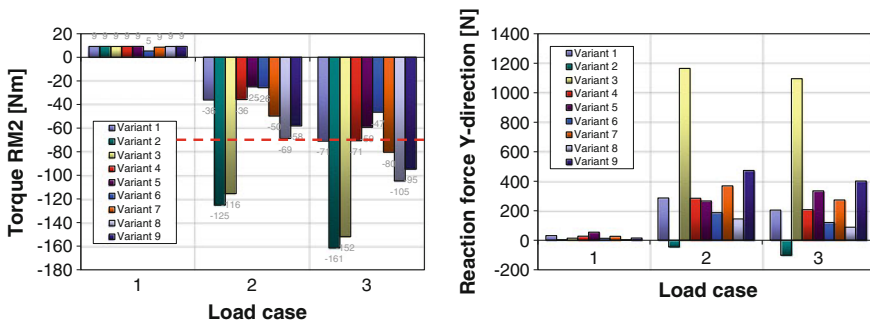


Fig. 5 Torque RM2 necessary to deform the morphing part (left) and reaction force acting normal to the interface (right)

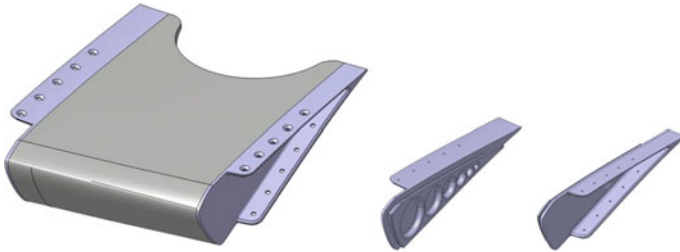


Fig. 6 Finalized geometry of the adaptive part (*left*); inboard and outboard frame (*right*)

above 10 Hz, so it could be concluded that the risk of eigenmode excitation is comparatively low.

In the end of the design phase, it was decided to elaborate on a ribless concept for sake of low actuation forces and ease of manufacture. The magnitude of loss in aerodynamic performance due to the cutout on the trailing edge was unknown at that time, but a loss could be tolerated if the overall performance of the WATE would be better than a conventional wing tip. In order to enable an evaluation of the aerodynamic performance, CAD data of the deformed adaptive part under flight load cases and wind tunnel test conditions were provided.

The finalized geometry of the adaptive part is shown in Fig. 6. One of the most important questions was the connection between the adaptive part and the aircraft structure. The major issues here are the soft-to-rigid transition, which causes a stiffness jump, and the design of a non-permanent joint, which is necessary for reasons of maintenance and repair. This was overcome by the use of assembly frames, which could be jointed to the structure by a number of fasteners.

The assembly frames were made of aluminum, and they were integrated in a casting process (Fig. 7). A mold was filled with a reactive mixture of the silicone components, and the elastomer was cured in the mold. The structural interfaces with cleaned and activated surfaces acted as a part of the mold. In this way, an adaptive part was obtained which was already equipped with the structural interface for connection with the airframe. The load transfer between the elastomer body and the interface was achieved by form closure and adhesion, which provided a stable joint due to smooth load distribution.

3 Mechanical Properties of Hyperflex-03

Flexible Hyperflex-03 elastomer was formulated specifically for application in civil aircraft adaptive devices. This material shows high flexibility in the temperature range between -55 and $+80$ °C and provides stable adhesion to aluminum in the presence of simulated exterior land and air conditions as well as in the presence of hydraulic fluid [6, 7]. The most important material properties were taken from Ref. [6] and are shown in Table 1.

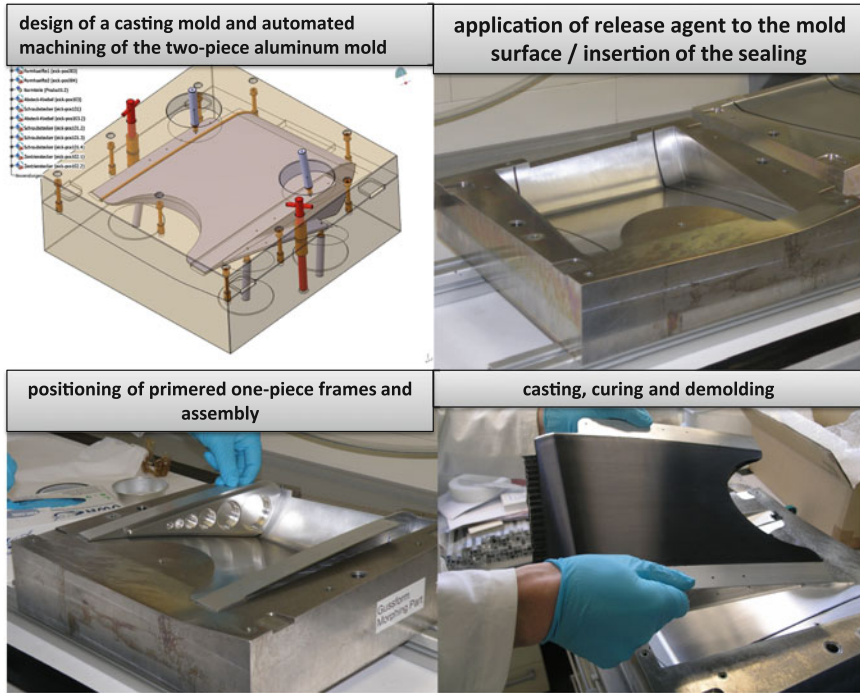


Fig. 7 Manufacturing process of an adaptive part for a wingtip with active trailing edge

Table 1 Mechanical properties of Hyperflex-03 at a strain rate of $\sim 0.1/s$ and indicated temperatures

Temperature (°C)	Initial shear modulus (MPa)		Strain at fracture (%)		Tensile strength (MPa)		Poisson's ratio (-)	
-55			309	± 66	10.08	± 1.78		
23	0.95	± 0.30	173	± 11	5.49	± 0.38	0.47	± 0.02
80			140	± 10	4.88	± 0.39		

Initial shear modulus and Poisson's ratio do not depend on temperature. Initial shear modulus equals to parameter μ of hyperelastic material model

Fatigue properties were tested at -55 , 23 , and $+80$ °C using single lap shear joints, harmonic loading, and displacement control. The aluminum adherends had a length of 100 mm, a thickness of 1.6 mm, and a width of 25 mm. The overlap length was 12 mm, and the bond line thickness was 2.8 mm. The asymmetric mismatch of the samples was balanced by spacers. In order to simulate upward and downward tab movements, a displacement ratio of $R = -1$ was chosen. A value of 50 % stiffness change was used as failure condition because no total failure was obtained under displacement control.

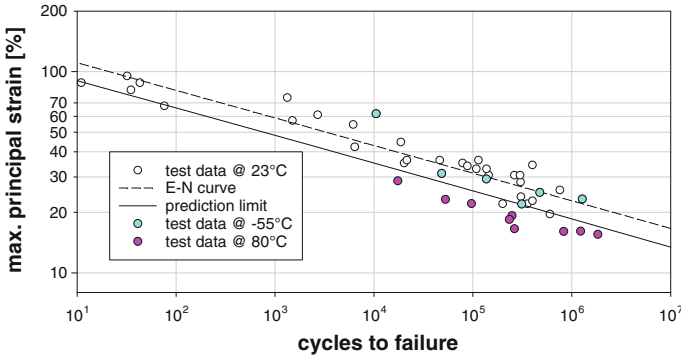


Fig. 8 Strain-life data from displacement-controlled, fully reversed fatigue test of Hyperflex-03 single lap joints with aluminum adherends, at a test frequency of 5 Hz and indicated temperatures

Results are shown in Fig. 8 using nominal strain amplitudes, which were calculated from the applied displacement u and the measured bond line thickness d based on the assumption of a simple shear deformation mode. The nominal strain is related to the stretch ratio by $\varepsilon = \lambda - 1$, and the maximum principal stretch in simple shear is defined as

$$\lambda = \sqrt{1 + \frac{\gamma^2}{2} + \gamma \sqrt{1 + \frac{\gamma^2}{4}}} \quad (1)$$

where γ denotes the amount of shear, which is equal to u/d . In addition to the data measured at -55°C and $+80^\circ\text{C}$, the results measured at 23°C , which were taken from [6], are given for reference. It can be seen that the data points measured at -55°C are close to the results found at 23°C , while data points measured at $+80^\circ\text{C}$ are below the 23°C and -55°C results.

The dashed line in Fig. 8 refers to the power law

$$\varepsilon = \varepsilon_0 N_f^{-1/k} \quad (2)$$

fitted to the data measured at 23°C , ε denoting strain amplitude, N_f the number of cycles to failure, and ε_0 and k are material-dependent parameters. The values of the material parameters as determined by nonlinear least squares fitting are $\varepsilon_0 = 10^{2.18 \pm 0.09} \%$ and $k = (7.29 \pm 0.39)$.

Based on the standard deviation S of the regression and the quantile t of a t -distributed $\log N_f$, the lower prediction limit of the strain-life curve was calculated for a chosen survival probability of $P = 90 \%$ and $n - 2$ degrees of freedom, n denoting the number of data points, using a one-sided tolerance limit, following the procedure outlined in ISO 12107:

$$\log N_{i,p} = k(\log \varepsilon_0 - \log \varepsilon) - S \cdot t \cdot \sqrt{1 + \frac{1}{n} + \frac{(\log \varepsilon - \overline{\log \varepsilon})^2}{\sum_{i=1}^n (\log \varepsilon - \overline{\log \varepsilon})^2}} \quad (3)$$

The lower limit is shown as a solid line in Fig. 8. It can be seen that the fatigue life for a chosen probability of survival of 90 % is reduced by about one order in magnitude as compared to the dashed strain-life curve, which corresponds to a probability of survival of 50 %. This means that the strain level which leads to the expected life at 50 % probability of survival has to be reduced by 15 % in order to achieve 90 % probability of survival.

It can be seen in Fig. 8 that at $-55\text{ }^\circ\text{C}$, the fatigue life values are above the prediction limit of the room temperature data, indicating that the fatigue life of the lap joint does not change if the temperature is lowered to $-55\text{ }^\circ\text{C}$. Fatigue life measured at $+80\text{ }^\circ\text{C}$ is below the prediction limit of the room temperature data. Considering the fact that a WATE will be preferably operated at low temperature, the majority of fatigue cycles will affect the joint at low temperature and the fatigue life will be governed by the properties measured at $-55\text{ }^\circ\text{C}$. At a temperature of $+80\text{ }^\circ\text{C}$, the number of fatigue cycles acting on the joint will be comparatively low because there will be just a couple of control movements before takeoff and a more or less constant deflection during takeoff and landing. Hence, no significant fatigue can be expected at high temperature.

4 Fatigue Properties of an Adaptive Part

As confirmed by test results, cohesive failure within the elastomer is the predominant failure mode [6]. It is hence most important to analyze the fatigue life of the elastomer block in the adaptive part accordingly. The fatigue life estimation was based on a locally computed value of the maximum principal strain ε_1 in the elastomer under cruise load conditions and the strain-life data shown in Fig. 8, where fatigue life refers to 50 % loss in stiffness, not fracture. The maximum principal strain was used as a comparative variable because it was shown that, in bonded joints, ε_1 approached the ultimate strain at fracture obtained in uniaxial tensile tests if the fracture load was applied to the joints [6].

Principal strains were calculated using ABAQUS 6.12 finite element analysis of the adaptive part shown in Fig. 6. Linear hybrid hexahedral elements with reduced integration C3D8RH were used for the elastomer block. Frames were meshed with linear, reduced integration hexahedral elements C3D8R. Aluminum parts were given linear elasticity, using an elastic modulus of 70,000 MPa and Poisson's ratio of 0.3. The elastomer was assigned hyperelasticity according to Eq. (3), using $n = 1$, $\mu = 0.95\text{ MPa}$, and $\alpha = 3.8$ as determined by nonlinear least squares fitting independent Hyperflex-03 data [6]. The model was loaded with an air pressure distribution of approx. 10 kPa, one-sided rotation about the hinge line, and temperature,

corresponding to the cruise load case. It was shown before that the stiffness of the adaptive part as well as the maximum values of the torque corresponding to rotational angles of 5° and -15° was well approximated by this model [6].

The calculated values of ε_1 at the location of the highest strain were 20.1 % at 5° and 14.9 % at -15° of rotation. In the following, ε_1 was assumed to be proportional to the rotational angle. The typical mission time of the SARISTU aircraft was given as 2.5 h. The number of cycles occurring in a 2.5-h mission was estimated as $N = 9000$, assuming a frequency of 1 Hz. Because the number of tab deflections as function of the rotation angle was not known, the following assumptions were made: The number of tab deflections as function of the rotation angle is a normal distribution. Mean rotational angles of -5° and 0° were chosen, and standard deviations were set to 2° , 3° , and 5° . In addition, a uniform distribution was considered. The scale of the rotational angle θ was spaced between -15° and 5° , using either constant or variable step width, resulting in 11–17 strain levels. Each of the assumed distributions contained a total of 9000 cycles, representing a 2.5-h mission.

The damage contribution produced in the elastomer on strain level i was calculated as the number of cycles N_i occurring on that level, divided by the number of cycles to failure $N_{f,i}$, according to Eq. (3). The probability of survival P was varied between 99.0000 and 99.9999 %. The damage contributions on strain level i were summed up to give the total damage D , depending on the shape of the angle distribution and the probability of survival. Assuming that the material fatigue limit is approached if D equals one, the number of missions which could be completed before the part must be exchanged was calculated as $1/D$ and the total time on mission was calculated as $2.5/D$. The choice of the θ scale spacing had no big influence on the results.

The total time on mission is depicted in Fig. 9 as function of the shape of the tab angle distribution and the probability of survival P . It can be seen that the total time on mission decreases if the width of the tab angle distribution increases, i.e. if the

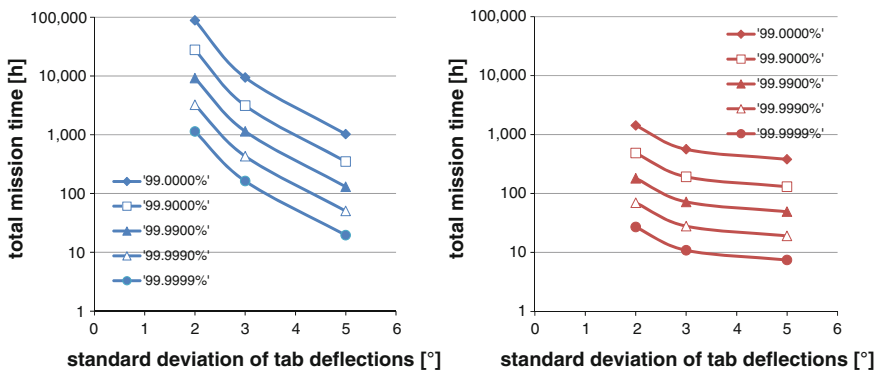


Fig. 9 Total mission time of an adaptive part under cyclic loading with variable rotational amplitudes, with an average rotational angle of -5° (left diagram) and 0° (right diagram)

fraction of tab deflections at high values of θ increases. It can be further seen that the total time on mission decreases if the average value of the tab deflection is shifted from -5° to 0° , while the standard deviation remains unchanged. This is due to the fact that, for the specific design, positive tab deflection involves higher strains and is thus more damaging than negative tab deflection. Finally, it can be seen that higher probabilities of survival produce lower total mission times because the lower limit of the strain-life curve decreases with increasing probability of survival. It can be inferred from Fig. 9 that the probability of failure is very low if the adaptive part is tested at ‘normal’ rotation angles. Estimated test times until failure at 1 Hz are 7 h for $P = 99.9999\%$ and 6000 h at $P = 50\%$ for a distribution with zero mean value and 5° standard deviation.

5 Prototype Fatigue Tests

A prototype of the bonded elastomer part was tested at room temperature in a servo-hydraulic testing system allowing for simultaneous tension and torsion loading. In the specified test, the part was loaded in torsion about the rotation axis using a constant rotation velocity, while the axial deformation was restricted. Under this condition, a tensile load is generated acting along the rotational axis and causing additional tensile stresses in the part. This is similar to the situation in service, where the part is mounted to a comparatively stiff structure, which does not permit deformation along the rotation axis.

Quasi-static tests of the part at rotational speeds between 0.25 and 0.5 degrees per second were described in Ref. [6]. Selected results will be repeated here since they are needed in the following discussion: The stiffness of the part was about 3 Nm per degree of rotation, and the torque values at minimum (-15°) and maximum (5°) rotation were 42 and -16 Nm, respectively, the sign of the torque value indicating the direction of rotation. From the quasi-static test results, it was concluded that the stiffness of the part was adequate in order to efficiently operate the part by a commercial actuator. Neither strain rate effects nor degradation effects were present at quasi-static loading. The stiffness as determined in quasi-static tests could be predicted by finite element modeling based on a hyperelastic material model for the underlying material, which was calibrated using independent test results.

Cyclic fatigue tests on the adaptive part prototype were performed at room temperature. The part was loaded in torsion about the rotational axis using constant rotational velocity throughout each individual cycle, while the axial deformation was restricted. Since the tests were performed at a constant frequency of 1 Hz, the rotational speed changed between different cycles due to non-constant angle deflection amplitudes. At the lowest deflection angle, the rotational speed was about 1 degree per second, whereas it was about 15 degrees per second at the highest deflection angle.

Block loading had to be used instead of load-time histories because the latter were not available. In order to achieve at least some degree of randomization, the

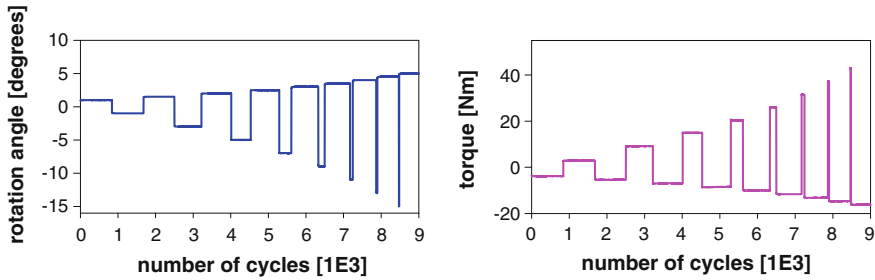


Fig. 10 Envelope of the block loading sequence (*left diagram*) and respective envelope of the measured torque function (*right diagram*), taken from the initial run of the loading sequence

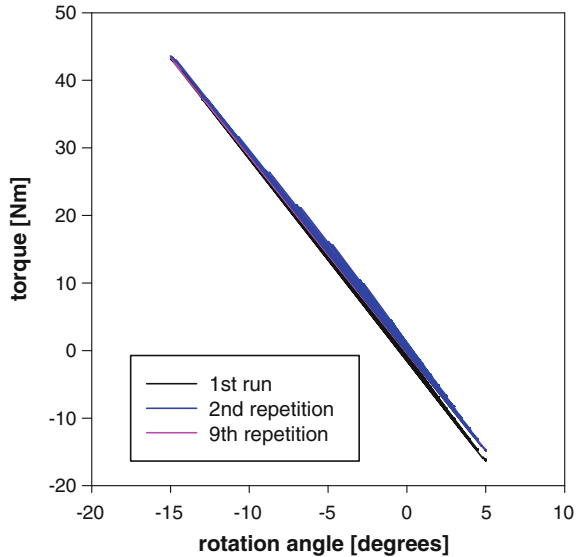
load sequence was sorted such that each block with a positive deflection angle was followed by a block with a negative deflection angle. Furthermore, blocks were sorted such that loading amplitudes occurred in ascending order. The loading sequence used in the fatigue test is shown in Fig. 10. This loading sequence contained a total of 9000 cycles and had a bell-shaped spectrum with a mean value of 0° and a standard deviation of 5° . The load sequence was repeatedly applied to the part. Rotation angle and torque were recorded, and the temperature of the part was controlled specifically within the blocks containing high deflection angles. The part was visually inspected after each completion of the 9000 cycle block loading sequence.

The envelope of the torque function measured in the first run is shown in Fig. 10. It can be seen that the absolute torque increases with increasing block number, as the absolute rotational angle increases. The highest absolute torque values were 43 Nm at -15° and 16 Nm at 5° . It should be emphasized that the extreme values of the torque, measured at a rotational speed as high as 15 degrees per second, which occurs in the last block, are very close to the ones measured in the static tests at rotational speeds between 0.25 and 0.5 degrees per second. This indicates that there is only a limited strain rate effect in the range of rotational speeds which can occur in service.

It can further be seen in Fig. 10 that the absolute torque value found within each block does not change with increasing cycle number, indicating that degradation effects due to repeated loading, which would reduce the stiffness of the part, were not present.

A correlation between the peak values of the applied rotational angle, θ , and the peak values of the measured torque, M , is depicted in Fig. 11. This plot also suggests that there is effectively no strain rate effect. If the $\theta - M$ correlation from the 2nd repetition is considered, a slight decrease in stiffness can be noticed as compared to the first run of the block loading sequence. This can be explained as a weak Mullins effect due to the preload imposed within the first run. The stiffness decrease is however very small and has disappeared after the 2nd repetition, as can be seen from the $\theta - M$ correlation of the 9th repetition. This indicates that the stiffness of Hyperflex-03 elastomer is quite insensitive to repeated loading at strain

Fig. 11 Correlation between the applied rotational angle and the measured torque (peak values) at indicated states of fatigue loading



amplitudes which can be expected in service. It is thus not required to describe the stiffness degradation within the material model of Hyperflex-03 elastomer.

The stiffness of the adaptive part as derived from the curves depicted in Fig. 11 (except the curve of the initial run) is about 2.9 Nm per degree of rotation. If only the initial run is considered, a value of 3.0 Nm per degree of rotation is obtained. In both cases, the stiffness is very close to the value of about 3 Nm per degree, which was observed under quasi-static loading conditions. This indicates that a unique material stiffness can be assumed in quasi-static as well as fatigue loading.

The 5th hysteresis of each block in the 2nd repetition of the block loading sequence is shown in Fig. 12. It can be seen that the hysteresis loop opens up once the rotation angle increases. This is due to the viscoelastic damping of the elastomer material. Because the viscoelasticity of the material contributes to the overall structural damping, it appeared to be important to evaluate the elastic energy, the dissipated energy, and the ratio between the dissipated and the elastic energy, which can be considered as a measure of the material damping.

The elastic energy of each cycle was numerically computed as the area below the loading branch of the hysteresis, whereas the dissipated energy was computed as the area within the hysteresis loop. Finally, the loss factor was computed as the ratio between both. The loss factor of the 2nd repetition of the block loading sequence is shown as a function of the rotation angle in Fig. 13. It can be seen that the loss factor ranges from zero to about 10 % if the rotation angle changes between 0° and 15°.

A slight change in loss factor can be noticed if the graph of the initial run is compared to that of the 9th repetition. This is due to the stiffness change within the first few cycles as mentioned above. No change was visible after the 2nd repetition.

The loss factor depends on the rotation angle because the test was performed using a constant test frequency of 1 Hz. A constant test frequency leads to an increasing strain rate once the rotation angle increases. Therefore, the apparent relation between loss factor and rotation angle is a consequence of the changing strain rate. At low strain rates, the adaptive part behaves like an elastic solid, while it becomes more and more viscoelastic at increasing strain rate. It can therefore be

Fig. 12 Fatigue test of the adaptive part at room temperature and a test frequency of 1 Hz. The 5th hysteresis of each block in the block loading sequence is shown

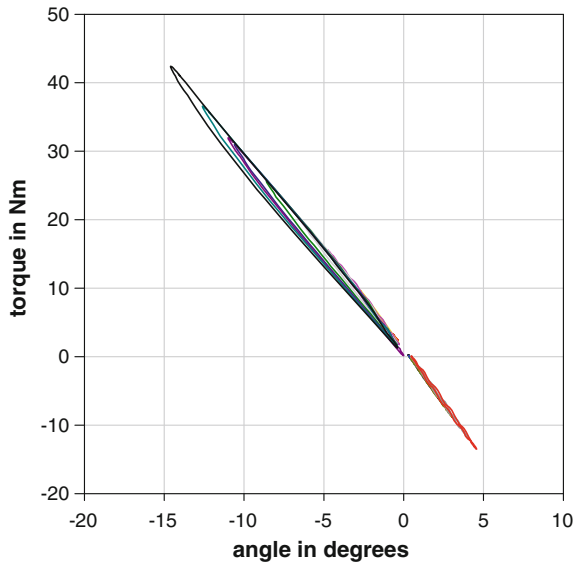
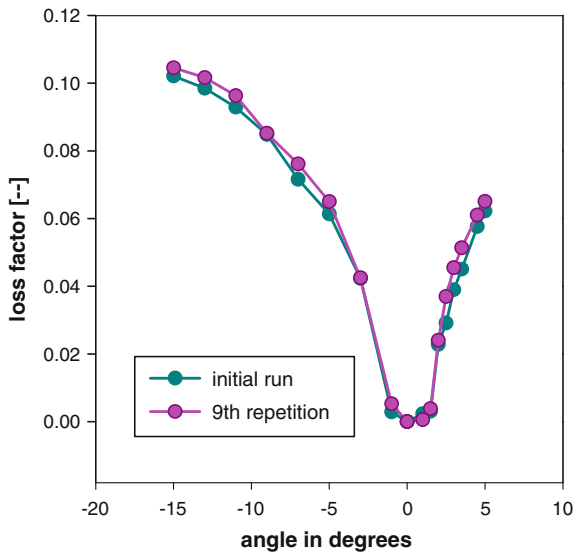


Fig. 13 Loss factor as a function of the rotation angle at indicated states of fatigue loading



expected that, under service conditions, the damping properties of the adaptive part will change if the rotational speed varies. This needs to be considered in the tuning procedure of the WATE feedback control loop.

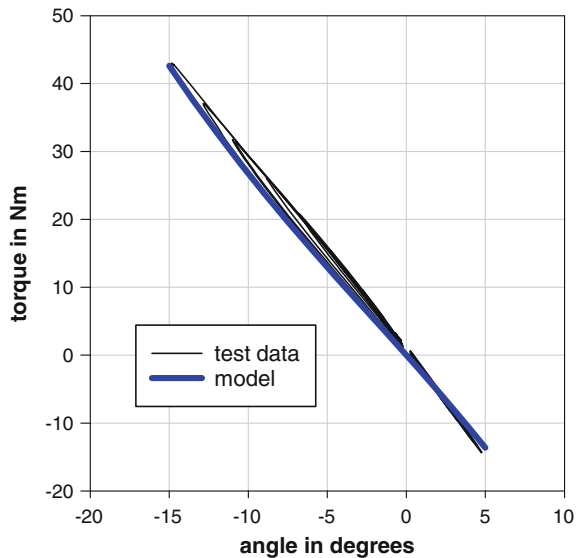
It was shown in Ref. [6] that the stiffness of the elastomer block in the adaptive part under quasi-static loading conditions could be described by an Ogden-type material model [8]

$$U = \sum_{i=1}^m \frac{2\mu_i}{\alpha_i^2} (\lambda_1^{\alpha_i} + \lambda_2^{\alpha_i} + \lambda_3^{\alpha_i} - 3) \tag{4}$$

where λ_i refers to the principal stretches, m is a material-dependent parameter ($m = 1$ for Hyperflex-03), and α_i, μ_i are temperature-dependent material parameters. The initial shear modulus is given by $G = \sum \mu_i$. Based on uniaxial tension and compression data, the parameters were determined to be $\mu = (0.95 \pm 0.30)\text{MPa}$, $\alpha = 3.80 \pm 0.30$. It should be emphasized that for Hyperflex-03, the material parameters do not depend on temperature.

A plot of the predicted stiffness is shown in Fig. 14 in comparison with the hysteresis data from the 9th repetition. It can be seen that at negative rotational angles, the loading branch is well described by the model, while the unloading branch is not, because viscoelasticity is not contained in the quasi-static model. The accuracy is yet acceptable since the deviations are small. This is useful because the consideration of material viscoelasticity on component simulation level is impractical due to model size. At positive values of the rotation angle, the stiffness is described sufficiently well by the model and no difference can be made between loading and unloading branches.

Fig. 14 Correlation between the applied rotational angle and the measured torque (peak values) at indicated states of fatigue loading



After completion of the 9th repetition, no visible damage could be detected. This is in agreement with the fatigue life estimation since 9 repetitions are close to estimated mission times of 20 h or 50 h as calculated for 99.999 % or 99.99 % probability of survival. In order to verify the assumptions made in the fatigue life estimation procedure, the part had to be tested until a 50 % loss in stiffness. According to current estimations, this requires tests lasting over several thousand hours.

6 Conclusion

Morphing concepts were investigated for a WATE in an adaptive wing. Concepts were discussed which would be adequate to take up geometric gap changes in order to maintain a smooth transition between connected parts. One of the proposed solutions was developed until the physical sub-component level, and the adaptive part was tested under fatigue loading. It was shown that Hyperflex-03 elastomer has excellent fatigue resistance and stable adhesion to aluminum within aircraft operational temperature range. The suggested solution for assembly has proved to be fatigue-resistant and suited for aircraft manufacture. The stiffness measured in cyclic sub-component tests was not sensitive to strain rate or degradation effects and could be accurately predicted by a hyperelastic material model. Based on the presented results, Hyperflex-03 is suggested as a candidate material for adaptive aircraft structures.

Acknowledgments The research leading to these results has received funding from the European Union's Seventh Framework Programme for research, technological development, and demonstration under grant agreement no 284562.

References

1. Thill C, Etches J, Bond I, Potter K, Weaver P (2008) Morphing skins. *Aeronaut J* 3:117–139
2. Smith JW, Lock WP, Payne GA (1992) Variable-camber systems integration and operational performance of the AFTI/F-111 mission adaptive wing. NASA Technical Memorandum 4370
3. Kikuta MT (2003) Mechanical properties of candidate materials for morphing wings. Virginia State University, Petersburg
4. Murray G, Gandhi F, Bakis C (2010) Flexible matrix composite skins for one-dimensional wing morphing. *J Intell Mater Syst Struct* 21:1771–1781
5. Bubert EA, Woods BKS, Lee K, Kothera CS, Wereley NM (2010) Design and fabrication of a passive 1D morphing aircraft skin. *J Intell Mater Syst Struct* 21:1699–1717
6. Nagel C, Fiedler A, Schorsch O, Lühring A (2015) Design, manufacture, and testing of a seamless morphing concept for a smart aircraft wingtip. In: Araújo AL, Mota Soares CA et al (eds) Proceedings of the 7th ECCOMAS thematic conference on smart structures and materials (SMART 2015), Ponta Delgada, Azores, submitted

7. Schorsch O, Lühring A, Nagel C, Pecora R, Dimino I (2015) Polymer based morphing skin for adaptive wings. In: Araújo AL, Mota Soares CA et al (eds) Proceedings of the 7th ECCOMAS thematic conference on smart structures and materials (SMART 2015), Ponta Delgada, Azores, submitted
8. Ogden RW (1986) Recent advances in the phenomenological theory of rubber elasticity. *Rubber Chem Technol* 59:361–383

Dynamic Aircraft Model with Active Winglet, Effects of Flight Mechanics and Loads Analysis

Toni Kanakis, Bimo Prananta, Hans van Tongeren and Rob Huls

Abstract This paper presents the background, development, and applications of simplified loads models for characterizing the loads related to SARISTU activities in application scenario AS03. The models have been developed from the initial SARISTU wing model of Alenia Aermacchi (AAM). A mass model of the fuel has been reconstructed from the aircraft data, and an aircraft model has been developed using an aircraft sizing tool. With the completion of the winglet design, the SARISTU winglet and the winglet active trailing edge (WATE) model have also been integrated in the loads model. The loads analysis for design purposes includes manoeuvre as well as gust loads. To support the evaluation of WATE device for the gust load alleviation system (GLAS), a state-space aeroservoelastic model of the SARISTU aircraft is developed. The methodologies and models developed within SARISTU have been successfully employed in the design of GLAS and WATE controller optimization and investigations to verify possible wing structure mass reductions. The approach and dynamic loads models developed in SARISTU can be applied straightforward in future R&D projects for structure loads assessments (aeromechanical), control design and optimization, loads, and Structural Health Monitoring (SHM).

T. Kanakis (✉)

Collaborative Engineering Systems Department, National Aerospace Laboratory—NLR,
Anthony Fokkerweg 2, 1059 CM Amsterdam, The Netherlands

B. Prananta

Flight Physics and Loads Department, National Aerospace Laboratory—NLR, Anthony
Fokkerweg 2, 1059 CM Amsterdam, The Netherlands

H. van Tongeren

Collaborative Engineering Systems Department, National Aerospace Laboratory—NLR,
Voorsterweg 31, 8316 PR Marknesse, The Netherlands

R. Huls

Gas Turbines and Structural Integrity Department, National Aerospace Laboratory—NLR,
Voorsterweg 31, 8316 PR Marknesse, The Netherlands

Nomenclature

A, B, C, D	State-space matrices, i.e. system, input and output matrices
A, D, R, E	Matrices representing rational approximation of the aerodynamic matrix Q in the state-space model
ATED	Adaptive trailing edge device
c	Chord
F	Force vector in the state-space model
k	Reduced frequency $k = \omega c / (2U_\infty)$
Q_{hg}	Generalized aerodynamic force of mode h due to gust input g
Q_{hj}	Generalized aerodynamic force of mode h due to gust striking aerodynamic panel j , extracted from NASTRAN as $QHJL$ matrix
QHHL	Matrix of generalized aerodynamic coefficients extracted from NASTRAN aeroelastic response
ϕ_s	Structural vibration mode
ϕ_{jg}	Delay function of aerodynamic panel j due to gust input g
GLAS	Gust load alleviation system
MKLIST	List of <i>Mach-k</i> data extracted from NASTRAN aeroelastic response
MTOW, MLDW	Mass configurations: maximum take-off weight and maximum landing weight
M, G, K	Mass, damping and stiffness matrices representing system dynamic of the aircraft
n_Z	Normal load factor
n_G	Vector normal to the direction of gust, i.e. vertical for normal gust and starboard for lateral gust
SHM	Structural Health Monitoring
V_D	Dive speed
WATE	Winglet active trailing edge
x, u	State and input vectors in state-space model
X_a	Aerodynamic lag state, part of rational function approximation of aerodynamic force in state-space model
ω	Circular frequency

1 Introduction

In this paper, dynamic loads models, which have been developed in the framework of AS03 of the SARISTU project, are presented. The model describes a regional jet equipped with an adaptive (morphing) winglet active trailing edge (WATE) device, and predicted loads and their effects have been studied on the rigid (flight mechanics) modes and a truncated set of the vibration modes. A description of the wing aeromechanical model will be provided, and the methodologies applied for dynamic loads identification for the WATE are given. Sectional wing loads have

been generated, and the aerodynamic forces have been taken into account with rational function approximation using Rogers' method. The loads model was rewritten in a state-space notation to enable development of gust load alleviation system (GLAS).

Within the SARISTU-AS03, loads computations are carried out to support the design group. The required loads typically include the shear force, bending moment, and torsion moment at various span locations, due to both aerodynamics and inertia. The effects of deformation on the loads distribution have to be taken into account. In a later stadium, the model will also be used to evaluate the design. The loads are evaluated for various load cases, Ref. [1], representing a predefined design space. To have realistic load levels, the boundary conditions for the loads computation should represent a free-flying aircraft, where a balance is maintained between the inertia and the aerodynamic loads. Further, the present work focuses on the characterization of the loads around the wing and winglet. The thrust forces are therefore not taken into account, and the degree of freedom of the aircraft in the longitudinal direction is constrained.

To obtain the required loads data as described in the beginning of this chapter, a loads model needs to be developed. The starting point for the development is the initial SARISTU wing finite element model (FEM) provided by Alenia Aermacchi (AAM) [1]. To enable proper loads computations, basically the model needs to include stiffness, inertia, and aerodynamic representations of the wing. Important inertia data concern the structural mass, systems, fuel, passengers, engines, etc. Moreover, the total mass of the aircraft is important for trim computation to determine the required aerodynamic force to balance the inertia loads. Modelling of aerodynamic control surfaces is usually also needed in trim computations to ensure proper aerodynamic moment.

In the next chapter, the initial wing model will be discussed. The necessary additional data will be identified. Subsequently, the strategy to obtain the missing data is detailed. The objective of the present work is to provide loads data through the development of a simplified loads model suitable for quick loads analysis of wing and winglet including WATE device and create a state-space description for controller synthesis. The following activities are covered in the present work:

1. Development of an aeroelastic wing model by generation of an aerodynamic panel model including a cross-check with the AAM results presented [1].
2. Reconstruction of fuel mass data based on IS12 general SARISTU aircraft data.
3. Application of the wing loads model for loads analyses at the wing-winglet junction to support the design group.
4. Application of the wing loads model for flutter analyses.
5. Development of aircraft model representing the SARISTU aircraft to account for rigid body/flight mechanics modes.

In the following chapters, detailed description of the models and their applications are discussed.

2 SARISTU Aircraft Loads Model

2.1 Wing Loads Model

The initial SARISTU wing model constitutes a structural dynamic FE model of the wing. The structures of the wing, i.e. spars, ribs and skin, are made of composite. Structural mass data are imposed through mass density in the description of element property. The FE model is in NASTRAN bulk data fraction (bdf) format. As far as the dynamic properties are concerned, this model can be considered a realistic representation of a wing without fuel.

The overview of the model is shown in Fig. 1. The supplied data contain only the structural model of the wing torsion box. Although for aeroelastic checks, both divergence and flutter analyses are also presented in [1], aerodynamic model to enable such analyses is not provided. Moreover, the flutter analyses consist of symmetric and anti-symmetric vibration modes, which means that the vibrations modes have been computed for a free-free or unrestrained boundary condition representing a free-flying condition. To implement such condition, the flexibility of the wing–fuselage connection and the inertia property of the rest of the aircraft are needed. Since the focus of the study is on the winglet area, these data are not provided either.

For a wing loads model with various functionalities required to support the WATE design, the initial model needs to be modified/added with additional data, such as non-structural masses and free-free boundary conditions. In the present work, a practical approach is followed which will be discussed in the following sections. The features that have been added to the initial wing can be summarized as follows:

1. Estimated inertia property of the half aircraft,
2. Boundary condition at the centreline,
3. Lifting surface aerodynamic panels,
4. Estimated fuel masses for full and half-full condition,
5. Control surface definition,
6. Fuselage–tail–engine model and updated inertia property, and
7. Mirror to full aircraft to enable asymmetric manoeuvre analyses.

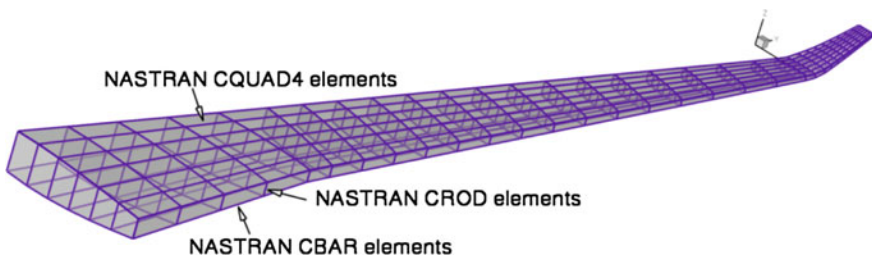


Fig. 1 Overview of initial dynamic model of the wing as provided by Alenia Aermacchi

In this chapter, points 1 to 5 are presented, while the rest will be discussed in the next chapter.

The free-free boundary condition is applied at the centreline of the aircraft at the location of the centre of gravity. The inertia property of the half aircraft is estimated from [1] and attached to a node defined at this location. Ideally, the wing should be connected to this node using a wing–fuselage connection model. Since this model is not provided by AAM, a rigid attachment of the wing root to the centreline node is used. In NASTRAN, this connection is implemented using RBE2 elements.

Normal mode analyses are carried out with symmetric and anti-symmetric boundary conditions at the centreline node. For symmetric boundary condition, the lateral translation, roll rotation and yaw rotation are fixed, while the longitudinal translation, vertical translation and pitch rotation are set free. The other way around is applied for the anti-symmetric boundary condition.

The mass of the fuel in the wing is estimated from the geometry of the wing structure and the global data of the aircraft as given in [1]. The following aspects should be considered:

1. The available geometric space is in the wingbox compartments, between front and rear spars, up to the location of the aileron.
2. Possible reduction of available geometric space by structural and system obstruction, e.g. deployment system for flaps and stowing space for landing gear.
3. Usable volume as defined by the selected tank concept, i.e. integral tank (about 85 %) or using bladder or bag tanks (about 65 %).
4. The total amount of fuel which is derived from the mission presented in [1], i.e. 14,841 kg.

In the framework of SARISTU, the baseline aircraft has been designed only up to a certain level of detail. For example, the layout of the system supporting the deployment of flap is not considered.

Therefore, not all aspects mentioned previously can be taken into account. In the present work, the following assumptions are used:

1. Three fuel tanks are defined: centreline tank, inboard tank up to the kink of the wing and outboard tank up to the location of aileron.
2. Integral tank concept is assumed to be adopted leaving usable space of 85 % with respect to the geometric volume.
3. The mass density of Jet-A or JP-8 fuel, i.e. 804 kg/m^3 , is used for mass computation.
4. The fuel mass for inboard and outboard tanks are computed based on the volume, while the centreline tank is computed so that the required amount of fuel is satisfied.

Based on these assumptions, the mass and mass moment of inertia data can be computed about the centre of gravity of a compartment. Subsequently, these data are implemented in the FE model using concentrated mass definitions and attached

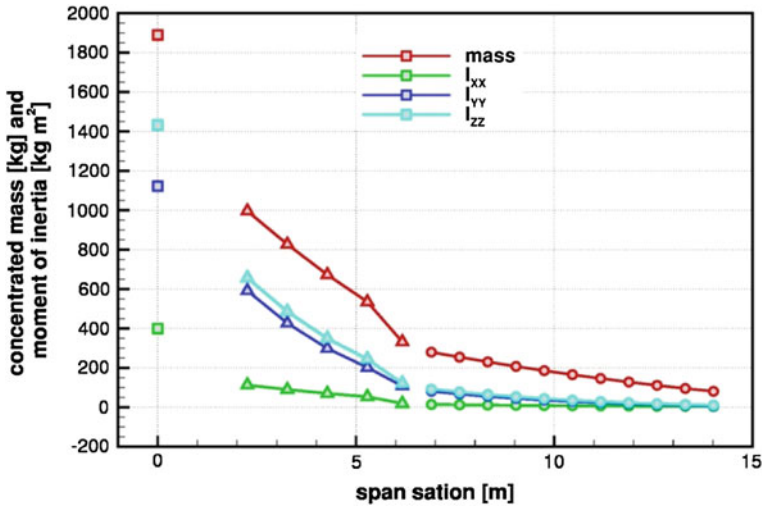


Fig. 2 Estimated inertia properties of the fuel expressed as concentrated masses along the span of the SARISTU wing

to the surrounding nodes using the RBE3 elements of NASTRAN. Figure 2 shows distribution of the concentrated fuel masses and moment of inertia along the span of the SARISTU wing. Figure 3 shows how these concentrated mass models are connected to the surrounding wing structure using rigid body elements..

In the present work, the doublet-lattice lifting surface method is applied for aerodynamic modelling. It is generally known that in its basic implementation, doublet-lattice method is not capable of modelling non-linearity in the flow, e.g. shock wave and flow separation, and geometric feature other than planform, e.g. twist distribution and airfoil thickness. The aforementioned features, however, are important for predicting loads. Therefore in the present work, a correction method is applied to include CFD data in a loads analysis using NASTRAN.

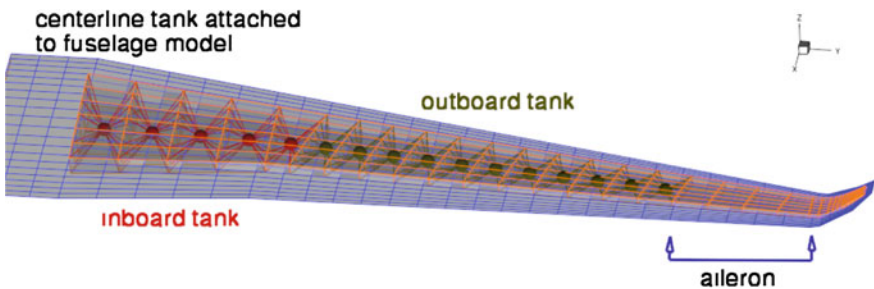


Fig. 3 Overview of the RBE3 connections between the concentrated masses and the surrounding nodes. Note that RBE3 elements have a property of multipoint constraint and therefore do not introduce additional stiffness to the system

The procedure to include CFD data into NASTRAN static aeroelastic computations can be summarized as follows:

1. A series of surface pressure data from the CFD computations are mapped into the doublet-lattice panel of NASTRAN. To enable conservation of the total force and to adhere to NASTRAN internal data format, the mapping is carried out as force distribution per dynamic pressure.
2. The mapped CFD force data are attached to a parameterization variable, for example angle of attack, angle of side slip, and pitch rotation.
3. The so-called controllers are defined in NASTRAN to represent the parameterization variable to be included as trim variable during static aeroelastic analysis. Note that for a certain situation, the parameterization variable of the CFD force data can be attached directly to an internal NASTRAN trim variable, instead of defining an extra controller.

During a static aeroelastic computation, a trim analysis is carried out where the values of the trim variables, e.g. angle of attack and deflection of control surface, are sought to achieve a balance between the inertia force, determined by the input load factors, and the aerodynamic force. The aforementioned procedure will ensure that correct CFD aerodynamic forces are selected during a trim analysis. If necessary, NASTRAN will automatically carry out interpolation between the available CFD input data to obtain the proper data for a certain value of trim variable.

In the present work, the CFD data as computed by PoliMi [2] have been used for correcting the loads computation using the doublet-lattice method of NASTRAN. The data concern CFD computations on the selected design load cases without taking into account the flexibility effects. To illustrate the effectiveness of the correction method, the distribution of the torsion moment along the span is used. Commonly, this type of load would suffer the most significant inaccuracy due to the inherent assumption of the pressure differential shape along the chord resulting from the linearized compressibility approach in doublet-lattice method. Figure 4 left presents the comparison of the torsion moment for design load case 4 ($V_D, n_{Z,max}$) computed using uncorrected doublet lattice and using CFD. Assuming that CFD

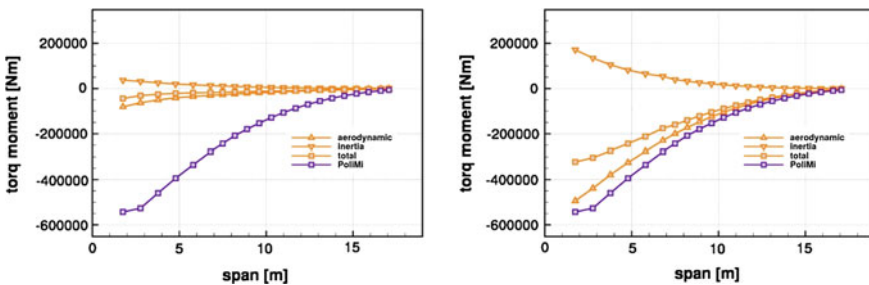


Fig. 4 Distribution of local torsion moment along the span computed using doublet-lattice method without (*left figure*) and with (*right figure*) CFD correction for one of the design load cases at $M = 0.605$, sea level and MTOW mass configuration

gives better results, the relatively large differences suggest the inaccuracy of the lifting surface method. Result obtained using the corrected doublet-lattice method is shown in Fig. 4 right. It can be seen that much better agreement is obtained with the CFD result. The remaining differences may be attributed to the fact that the CFD results are obtained without taking into account the flexibility of the wing. It may be concluded that the present aerodynamic modelling gives adequate accuracy.

2.2 Loads Analysis of Wing–Winglet Interface

During the design process of the WATE, the developed loads model has been applied for predicting the loads at the interface between the wing and the winglet. The analysis concerns 13 design load cases with various parameters of the WATE deflection and the fuel level. Conditions of normal operation, failure event, and jammed are investigated to support the decision on how to deploy the WATE.

In this section, this application is described only briefly. Detailed description of the exercise, the results and the conclusions are presented in [3]. Example of the results of loads prediction at the winglet root for various design load cases, various WATE deflection and various operation conditions is shown in Fig. 5. The shape of the symbols represents the deflection of the WATE, the fill colour of the symbols represents the load case number, and the outline colour of the symbols represents

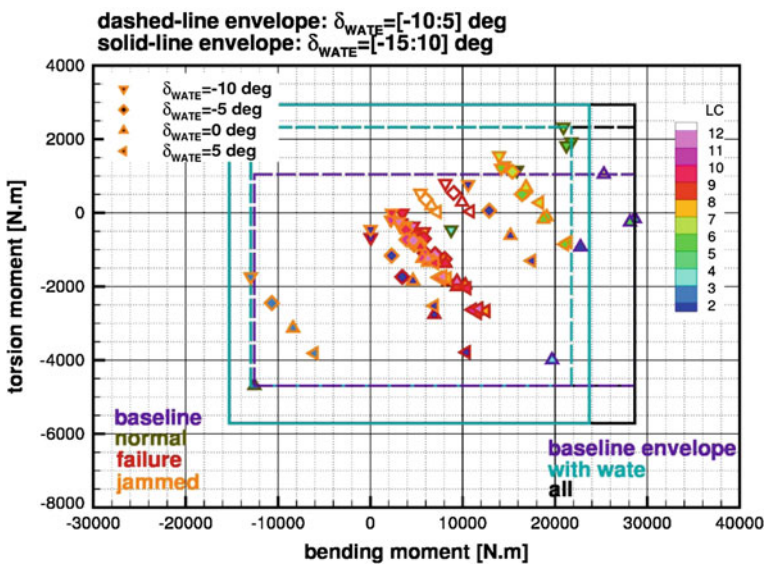


Fig. 5 Example of the results of loads prediction at the winglet root for various design load cases, various WATE deflection and various operation conditions

the operational condition. The study concludes that a restriction of the WATE envelope should be applied to reduce the winglet root loads.

For complete description of the exercise, [3] should be consulted.

2.3 Flutter Consideration

Application of the wing loads model with updated winglet and WATE model for flutter analyses is presented. An overview of the structural part of the model is shown in Fig. 6. The morphing part of the model has been removed. With regard to the effect of the aerodynamics, one can argue that when a fine aerodynamic model is used, e.g. CFD, it might be important to reproduce the correct shape of the morphing on the aerodynamic surface. In the present simplified loads model, however, doublet-lattice lifting surface is applied. The shape of the aerodynamic panel at the morphing part is defined by the surface spline approximation between the winglet and the WATE. The surface spline method is known to produce smooth surface which should provide a good approximation of the shape of the morphing part.

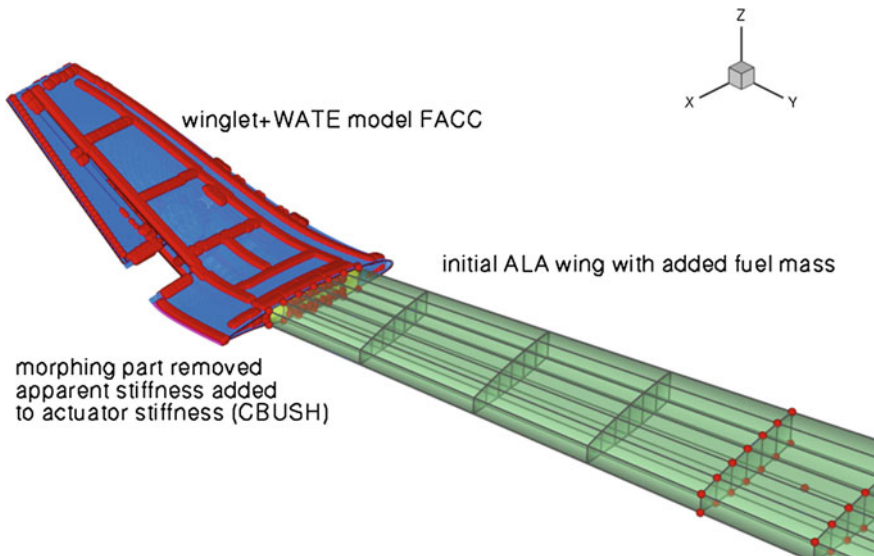


Fig. 6 Overview of the initial dynamic model of the SARISTU wing coupled with developed winglet model including WATE device. Note the morphing part is excluded from the model, but the stiffness is included in the definition of the WATE hinge moment

Table 1 Frequencies and type of anti-symmetric vibration modes of the SARISTU wing with initial and updated winglet and WATE model

Anti-symmetric modes	Updated	Initial
	wing + winglet (Hz)	wing + winglet (Hz)
1st wing bending	2.79	3.74
2nd wing bending	7.95	11.79
1st in-plane bending	12.37	14.99
3rd wing bending	14.20	25.74
4th wing bending	21.20	
1st wing torsion	25.65	35.36

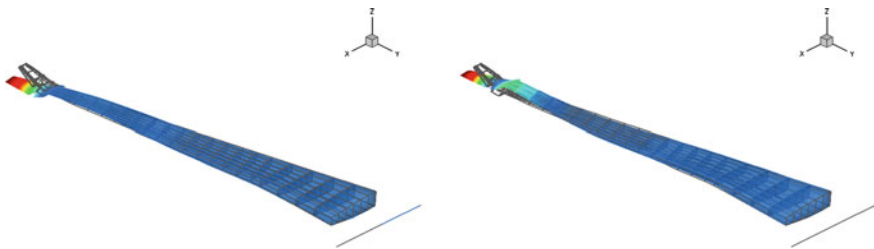


Fig. 7 Overview of the 3rd (*left figure*) and 4th (*right figure*) wing bending mode which in the case of updated winglet model also show significant winglet bending

The results of the normal mode analysis of the AS03 winglet with updated WATE FE model are shown in Table 1 for the anti-symmetric boundary condition. It can be seen that significant reduction of natural frequencies is observed. With regard to the vibration modes, the most significant differences are the contribution of winglet bending in the 3rd and 4th wing bending vibration mode, see Fig. 7. This was not observed in the initial winglet model. The result of flutter calculation is presented in Fig. 8 for $M = 0.695$ at sea level. In this computation, both actuator stiffness and additional stiffness from the morphing part are assumed to be present. Despite the significant natural frequency reduction compared to the initial winglet, the configuration is not sensitive to flutter.

2.4 Reconstruction of SARISTU Aircraft

The most important purpose of the aircraft mode is to facilitate loads analysis and control law design for loads alleviation. The actual reference SARISTU aircraft is defined through a design exercise. The resulting reference aircraft is reported in a reasonable detail in [1]. In the present work, the aeroelastic model of the SARISTU aircraft is developed based on the aircraft data as presented in [1].

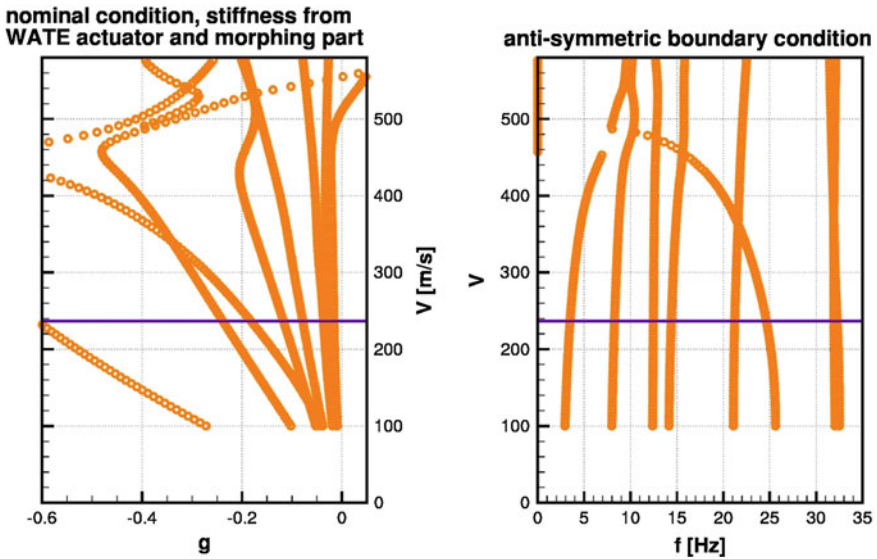


Fig. 8 Flutter diagram of the SARISTU wing with the updated FE model of the winglet including WATE. The blue line shows the matching velocity for the selected Mach number. In this nominal condition, both actuator and morphing part of the wing contribute to the stiffness of the WATE rotation mode

To estimate aircraft stiffness and masses for the specified mission, the NEOCASS tool has been used [4]. In the first step, the NEOCASS tool is applied to generate an aircraft model based on the specified geometrical arrangement, the layout of passenger seating and luggage compartments, position of the engines, etc. The results are shown in Fig. 9.

Subsequently, based on the required mission and other operational data, the structural stiffness and mass distribution are estimated based on the standard FAR 25 loads requirements. The underlying method of structural size and weight estimation of NeoCASS have been shown to be sufficiently reliable and accurate, see e.g. [5]. An aeroelastic model of the aircraft based on beam modelling is then

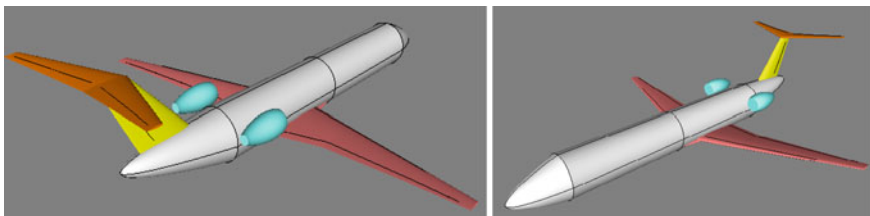


Fig. 9 Overview of geometrical representation of SARISTU aircraft in the NeoCASS environment

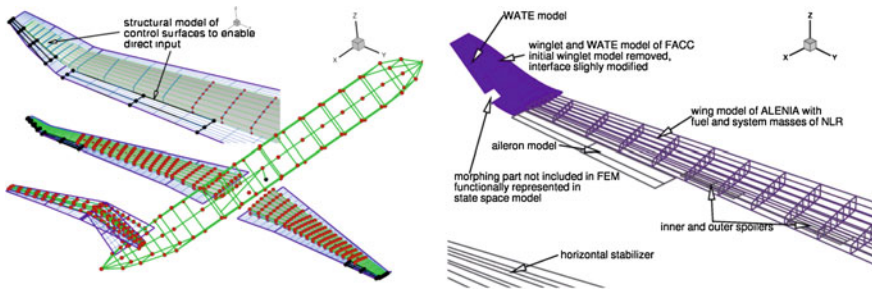


Fig. 10 Loads model of SARISTU aircraft suitable for aeroservoelastic analyses based on the initial wind model of ALENIA

generated. The format of the aeroelastic model is very similar to MSC/NASTRAN format which can be easily modified to be applied in a MSC/NASTRAN analysis.

Since a better definition of SARISTU wing is available, the wing part that is represented using beam elements is completely replaced by the SARISTU initial wing model, described in Sect. 2.1. The SARISTU wing is modelled using torsion box. The aircraft beam model with SARISTU wing is shown in Fig. 10.

The aircraft model is generated using a structural sizing tool based on the input defined in [2] in terms of mission, number of passenger, layout, predicted aerodynamic performance, propulsion system, predicted required amount of fuel, etc. The resulting aircraft model provides a realistic approximation of SARISTU regional jet aircraft in terms of mass distribution and structural flexibility.

As commonly done in NASTRAN, the loads model developed in the present work has five rigid body degrees of freedom. The longitudinal motion is not taken into account due to the lack of thrust and aerodynamic drag model in NASTRAN. Various control surfaces are modelled including ailerons, inner spoilers, outer spoilers, elevator, rudder and WATE. Since realistic inertia data of the control surfaces are not available, the control surfaces are only modelled as aerodynamic effectors.

The aircraft dynamic model consists of two mass configurations, i.e. the maximum takeoff weight and maximum landing weight. The only difference between these configurations concerns the outer wing fuel tank which is empty for the maximum landing weight configuration.

3 Aeroservoelastic Model for Gust Load Alleviation Design

In supporting the design of gust load alleviation (GLA), state-space model of the SARISTU aircraft loads model is generated.

3.1 *Modelling of Rigid Body Modes and Control Surfaces*

The final steps towards SARISTU full aircraft model are the addition of control surface models. Normally, control surfaces are defined only in the aerodynamic model. With the objective to use the aircraft model for aeroservoelastic analysis, it is desired to be able to manipulate the control surface deflection directly. In general, this can be done through a DMAP programming in MSC/NASTRAN. This method is however not preferable. Other more practical approach is to use dummy structures to represent the control surface. There are several methods to define a rotation of this dummy structure in MSC/NASTRAN, e.g. direct method and Lagrange multiplier method of large mass method. The aerodynamic panels of the control surfaces are then directly mapped to these dummy structures.

This modelling strategy facilitates a direct input to the control surface deflection during aeroelastic response analyses. A direct input to control surfaces is expected either from pilot input or from the output of the flight control system, e.g. gust alleviation system. Figure 10 presents the SARISTU loads model suitable for aeroservoelastic analyses.

To have the correct reference point in the NASTRAN model, i.e. at the centre of gravity of the aircraft, an initial run is carried out to determine the centre of gravity of the configurations. Subsequently, the so-called SUPORT point to define the rigid body mode in NASTRAN is moved exactly at the computed centre of gravity and connected to the aircraft reference point using RBE2 rigid body element. In this way, all rigid body modes will be computed by NASTRAN with respect to the centre of gravity implying also a correct reference for the aerodynamic forces and moments. The inertia data of the aircraft will also be computed and presented with respect to this reference point. By selecting Given's method as the eigenvalue solver in NASTRAN, the computed rigid body modes are in the global axis system and can be used directly to represent the flight mechanic motion of the aircraft with a proper scaling factor.

3.2 *Aerodynamic Data*

The state-space aerodynamic data are obtained by fitting the frequency domain aerodynamic data into a selected form of rational function approximation [6, 7], see Sect. 4.2 for more detailed description. The frequency domain unsteady aerodynamic data due to the structural motion can be generated using MSC/NASTRAN running SOL 146, i.e. aeroelastic response analysis, or SOL 145, i.e. aeroelastic stability analysis.

In MSC/NASTRAN, the unsteady aerodynamic data are generated in module *SEAERO*. Using a simple DMAP script, the following matrices are written to an output file for further processing:

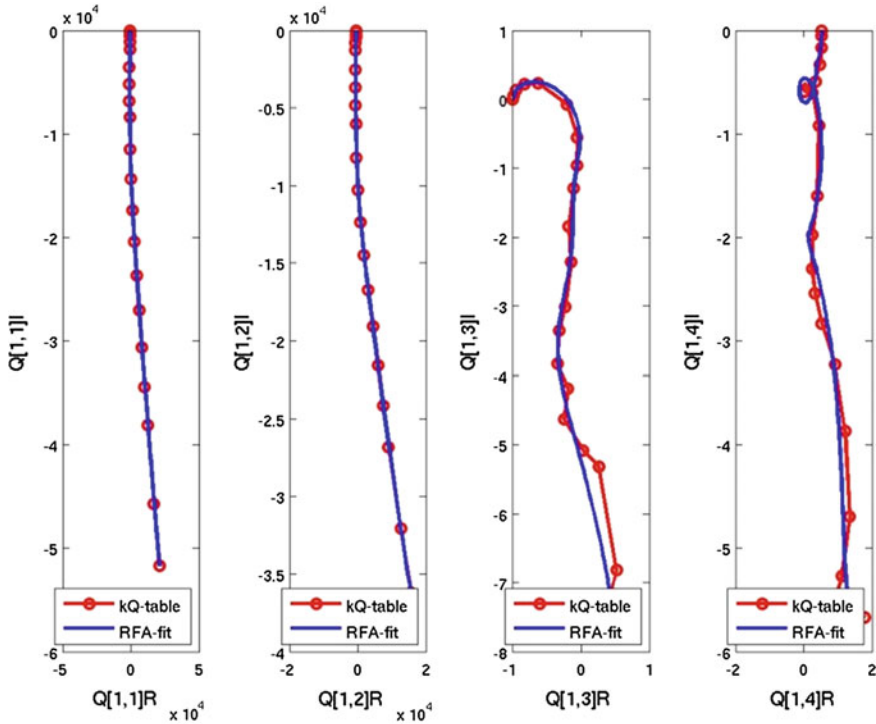


Fig. 11 Example of tabular data of generalized aerodynamic forces and the results of fitting procedure due to structural vibration modes

QHHL matrix that contains the generalized unsteady aerodynamic force per dynamic pressure $Q_{ij}(M_l, k_l)$ of mode i due to sinusoidal excitation of mode j , for all Mach-reduced frequency combinations. The letters H and L represent the size of the modal space *and* the size of the Mach-reduced frequency list, respectively.

QHJL matrix that contains the generalized unsteady aerodynamic force per dynamic pressure $Q_{ij}^G(M_l, k_l)$ of mode i due to sinusoidal gust excitation at aerodynamic panel j , for all Mach-reduced frequency combinations. The letter J represents the total number of aerodynamic panels.

MKLIST table that contains the Mach-reduced frequency combinations.

For the motion-induced unsteady aerodynamic forces, the fitting procedure is relatively straightforward. Figure 11 depicts an example of the tabular data of aerodynamic forces for the flexible modes and their reconstructed data. The first two modes show an excellent agreement between the tabulated data and reconstructed data. For modes with small magnitude of forces, i.e. the last two modes, the agreement is still very good.

The motion-induced unsteady aerodynamic forces are parameterized with respect to a set of normal modes. This means that the structure moves uniformly without phase lags between locations. The gust-induced unsteady aerodynamic forces on the other hand are instigated by flow disturbance which can arrive at various locations on the aircraft at different times.

The most general way to describe the flow disturbance encountered by an aircraft model is by defining the disturbance for each aerodynamic box separately. In this way, all kind of gust shape can be simulated. Moreover, the resulting aerodynamic force will be relatively similar to the motion-induced one. The drawback is that a large number of input have to be defined, i.e. the same with the total number of aerodynamic box.

Currently gust analyses are performed with an assumption that the gust shape is one-dimensional. This assumption is used based on the observation and also with the knowledge that such gust shape can produce worst-case scenarios.

The delay of a one-dimensional gust encounter for aerodynamic box j can be written in frequency domain as

$$\phi_{jG}(ik) = -\vec{n}_{Gj}e^{-ik[(x_j-x_0)/L_{REF}]}$$

where $k = \omega L_{REF}/2U_\infty$ is the reduced frequency and \vec{n}_G is normal component of aerodynamic box j in the direction of the gust, i.e. \vec{n}_{Zj} for a normal gust and \vec{n}_{Yj} for a lateral gust. It can readily be seen that if a large distance is covered by $(x_j - x_0)$ in this equation, the function will show periodicity or circular behaviour in the complex plane.

Therefore if the whole aircraft is treated at once, with a single reference point, the resulting aerodynamic force will also exhibit this circular behaviour which will hinder the fitting procedure. Figure 12 shows an example of gust-induced unsteady aerodynamic force of mode 4 computed for the whole aircraft at once. It can be seen that the tabular data clearly show circular behaviour resulting in an unsatisfactory fit data.

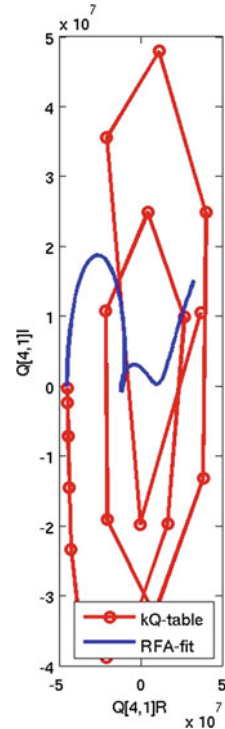
To overcome this problem, the approach presented in [3] is used. The aerodynamic model of the aircraft is divided into four zones, each with its own control point: inner wing, outer wing, vertical tail plane and horizontal tail plane. The gust-induced aerodynamic forces of mode h due to gust input g can be written as:

$$[Q_{hg}(ik)] = [Q_{hj}(ik)][\phi_{jg}(ik)]$$

The aerodynamic force data $[Q_{hj}(ik)]$ are obtained from NASTRAN SOL 146 run, i.e. the $QHJL$ matrix. The splitting of the gust input, including computation of delays $[\phi_{jg}(ik)]$, is performed outside NASTRAN.

The same gust-induced unsteady aerodynamic data as those presented in Fig. 12 are now computed through division into four zones and subsequently fitted individually using rational function approximation. The results are shown in Fig. 13. It can be seen that the data exhibit less circular behaviour and the fit procedure results

Fig. 12 Example of gust-induced aerodynamic force computed for the whole aircraft at once showing circular behaviour and the unsatisfactory fit result



in a much better agreement compared to Fig. 12. Note that the fourth data are zero since the vertical tail plane is tangential to the direction of normal gust.

3.3 *Output Model*

The required output concerns data to be used for feedback for the controller and other parameter of interest representing structural loads. These output parameters are functions of the state and input variables. The output models consist of:

1. rigid body modes: roll, pitch and yaw rotations; lateral and vertical velocities; roll, pitch and yaw rates; and rotational and translational accelerations,
2. wing tip and wing root accelerations,
3. sectional loads at 23 stations in each wing, and
4. angle of attack and angle of side slip at the location of the vanes.

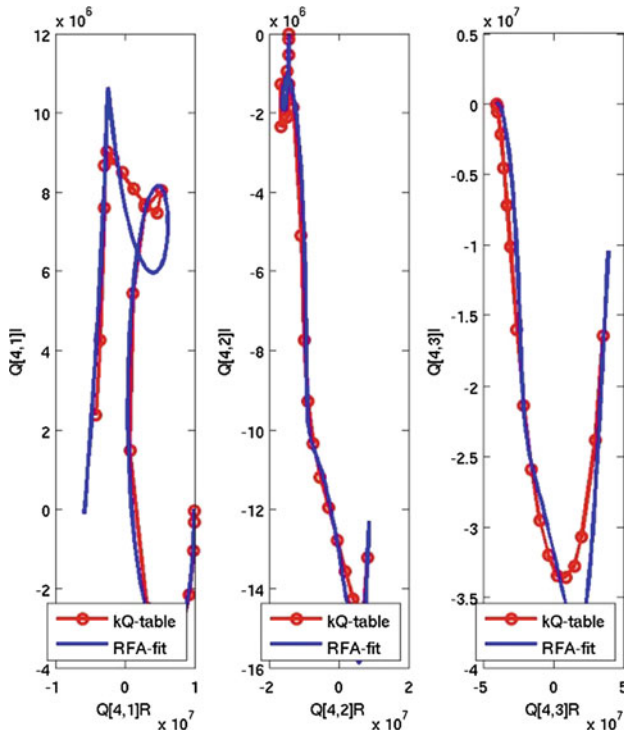


Fig. 13 Example of gust-induced aerodynamic force divided into four zones: inner wing, outer wing, horizontal tail and vertical tail, showing a much better fit result compared to Fig. 12

Most of these data can be reconstructed easily from the state response. The reconstruction of the sectional loads is explained below. The sectional loads data are extracted from the grid point forces associated with structural deformation due to trim state and those associated with the flexible part of the normal modes.

To extract the cross-sectional forces, all the nodes on a cross section are located first. The elements connected to one side of this point are then selected and their contributions to the node force are summed to yield the total force at this node. It should be noted that this implies that the boundary must follow the mesh faces and cannot cut through elements. The contribution of all the nodes is then summed to find the total cross-sectional loads. An example is shown in Fig. 14.

Both the three cross-sectional forces as well as the three cross-sectional moments are extracted with respect to the local coordinate axis. The cross-sectional loads are extracted from 46 locations, 23 in each wing, distributed over the wing, winglet and WATE. All these operations are performed in TMP Vision/SLIM.

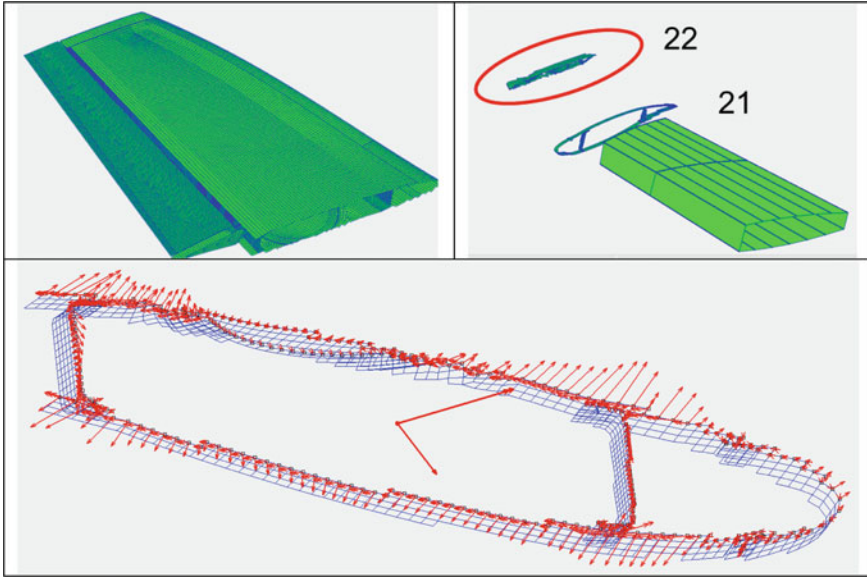


Fig. 14 Example of a wing (*upper left*) and the cross section used for extraction (*upper right*) and the resulting cross-sectional loads (*bottom*)

4 State-Space Model of the SARISTU Aircraft

To enable GLAS controller synthesis, the models developed above are rewritten in a state-space form. The governing equation describing the aeroelastic model as used in NASTRAN can be written as follows:

$$\begin{aligned}
 [M]_s \{\xi\} s^2 + [G]_s \{\xi\} s + [K]_s \{\xi\} - q[Q]_s \{\xi\} \\
 = [\phi_c]^T \{F\} + q[Q]_c \{\delta_c\} + q[Q]_g \{\eta_g\}
 \end{aligned}
 \tag{1}$$

where $[M]_s$, $[G]_s$ and $[K]_s$ are the generalized mass, damping and stiffness matrix, respectively; $\{\xi\}$ is the vector containing the generalized structural displacements; and q is the dynamic pressure. In the following, the structural model is rewritten first, followed by the aerodynamic loads, the control surface loads and the gust loads. This is followed by some model verification.

4.1 Structural Model

The mechanical model of the wing without aerodynamic forces can be described using the rigid and flexible modes as a subset of (1) as:

$$[M]_s\{\xi\}s^2 + [G]_s\{\xi\}s + [K]_s\{\xi\} = [\phi_s]^T\{F\} \quad (2)$$

The structural model is described in Sect. 2.1. The modes are normalized as such that it facilitates the interpretation of the response. The state vector $\{x\}$ for the structural model contains the generalized displacements and the derivatives thereof:

$$\{x\} = \begin{Bmatrix} \xi \\ s\xi \end{Bmatrix} \quad (3)$$

The matrix $[A]$ follows from (2), and the state equation is thus given by:

$$[A]\{x\} = \begin{bmatrix} [0] & [I] \\ -[M]_s^{-1}[K]_s & -[M]_s^{-1}[G]_s \end{bmatrix} \begin{Bmatrix} \xi \\ s\xi \end{Bmatrix} \quad (4)$$

where $[I]$ is the identity matrix. The first line defines the derivative (required for going from second-order to first-order differential equations) and the second line contains (2).

As opposed to Ref. [4], we also include direct actuation of the model by the external force vector $\{F\}$. Because the rotation on the control surfaces will be prescribed, the external force vector can be written as the function of the prescribed control surface rotations as:

$$\{F\} = [M]_c\{s^2\delta_c\} \quad (5)$$

The external inputs for the control surface movement are the angle δ_c , the angular rate and the angular acceleration, and thus, the input vector is given by:

$$\{u\} = \begin{Bmatrix} \delta_c \\ s\delta_c \\ s^2\delta_c \end{Bmatrix} \quad (6)$$

The $[B]$ matrix for the structural model can now be assembled from (2), (5) and (6) as:

$$[B]_s\{u\} = \begin{bmatrix} [0] & [0] \\ [0] & [0] \end{bmatrix} \begin{bmatrix} [0] \\ [0] \end{bmatrix} [\bar{M}]_s^{-1}[\phi_s]^T[M]_c \begin{Bmatrix} \delta_c \\ s\delta_c \\ s^2\delta_c \end{Bmatrix} \quad (7)$$

4.2 Aerodynamic Loads

The aerodynamic loads due to aircraft motion, i.e. the matrix $[Q]_s$, defined in the Laplace domain, are expressed as rational functions with coefficients obtained by

fitting against tabular data for purely oscillatory motion. The tabular data are computed using NASTRAN doublet-lattice method:

$$[Q]_s = [\bar{A}_0]_s + [\bar{A}_1]_s s + [\bar{A}_2]_s s^2 + \sum_{l=1}^{n_{ls}} [\bar{A}_{l+2}]_s \frac{s}{s + \bar{b}_{ls}} \tag{8}$$

where $[A_i]_s$ is the numerator coefficient matrix for the rational function approximation, b_{ls} are the denominator roots (the lag terms), and n_{ls} is the number of roots (the number of lag terms). The summation is often written in a more general manner:

$$[Q]_s = [\bar{A}_0]_s + [\bar{A}_1]_s s + [\bar{A}_2]_s s^2 + [D]_s ([I]_s - [R]_s)^{-1} [E]_s s \tag{9}$$

This is identical to (8) when the following definitions are used:

$$\begin{aligned} [\bar{D}]_s &= [\bar{A}_3]_s \quad \dots \quad [\bar{A}_{2+n_{ls}}]_s \\ [\bar{R}]_s &= \begin{bmatrix} -\bar{b}_1 [I] & & [0] \\ & \ddots & \\ [0] & & -\bar{b}_{n_{ls}} [I] \end{bmatrix} \\ [\bar{E}]_s &= \begin{bmatrix} [I] \\ [I] \\ [I] \end{bmatrix} \end{aligned} \tag{10}$$

The matrix $[D]_s$ is of size $n_s \times n_s n_{L_s}$, matrix $[R]_s$ is a square matrix of size $n_{ls} n_s$, and matrix $[E]_s$ is of size $n_s n_{ls} \times n_s$. Because matrix $[Q]_s$ is multiplied with the structural states $\{\xi\}$, matrix $[\bar{A}_0]_s$ contributes to the stiffness matrix, $[\bar{A}_1]_s$ to the damping matrix, and $[\bar{A}_2]_s$ to the mass matrix. These matrices are defined with a bar to differentiate them from the purely structural matrices so far and are given by:

$$\begin{aligned} [\bar{M}]_s &= [M]_s - q[\bar{A}_2]_s \\ [\bar{G}]_s &= [G]_s - q[\bar{A}_1]_s \\ [\bar{K}]_s &= [K]_s - q[\bar{A}_0]_s \end{aligned} \tag{11}$$

The equations of motion thus become:

$$[\bar{M}]_s \{\xi\} s^2 + [\bar{G}]_s \{\xi\} s + [\bar{K}]_s \{\xi\} - q[\bar{D}]_s ([I]_s - [\bar{R}]_s)^{-1} [\bar{E}]_s s \{\xi\} = 0 \tag{12}$$

When the aerodynamic loads are added to the state-space model, the mass, stiffness and damping matrix in (4) are replaced by the modified versions in (11). The other term introduces additional states in the model. These additional states (the lag terms) are aggregated in the aerodynamic state vector $\{X_a\}$. The total number of

aerodynamic lag states is $n_s n_L$. The components $\{X_a\}$ of this vector for each lag term are defined by:

$$\{X_{al}\} = \frac{s}{s + \bar{b}_l} \{\xi\} \tag{13}$$

The state-space matrix $[A]$ including the lag terms becomes:

$$[A]\{x\} = \begin{bmatrix} [0] & [0] & [0] \\ -[\bar{M}]_s^{-1}[\bar{K}]_s & -[\bar{M}]_s^{-1}[\bar{G}]_s & q[\bar{M}]_s^{-1}[\bar{D}]_s \\ [0] & [E]_s & [R]_s \end{bmatrix} \begin{Bmatrix} \{\xi\} \\ s\{\xi\} \\ \{X_a\} \end{Bmatrix} \tag{14}$$

Matrix $[A]$ is a square matrix of dimension $2n_s + n_s n_L$. The number of states is therefore also $2n_s + n_s n_L$. This matrix is also given in [5, 8] and describes the influence of aerodynamic loads on system dynamics. The first line defines the derivative of the structural modes, the second line contains the equations of motion, and the remaining lines define the aerodynamic states.

4.3 Control Surfaces

The control surface movement is added to the Eq. (1) as:

$$[M]_s \{\xi\} s^2 + [G]_s \{\xi\} s + [K]_s \{\xi\} - q[Q]_s \{\xi\} = [\phi_s]^T \{F\} + q[Q]_c \{\delta_c\} \tag{15}$$

The first term on the right-hand side described inertia effects and the second term aerodynamic effects. The former is often small compared to the latter, but can be used to verify the correctness of the structural model later. The external forces can be written as

$$\{F\} = [M]_c \{s^2 \delta_c\} \tag{16}$$

The $[M]_c$ matrix has dimension $n_c \times n_c$ and $[\phi_s]^T$ has dimensions $n_s \times n_c$. The matrix $[Q]_c$ is treated similar to the motion-induced aerodynamic force. The term with $[E]$ contributes to the $[B]$ matrix and the term with $[R]$ contributes to the $[A]$ matrix. The $[A]$ matrix has now in the form:

$$[A]\{x\} = \begin{bmatrix} [0] & [I] & [0] & [0] \\ -[\bar{M}]_s^{-1}[\bar{K}]_s & -[\bar{M}]_s^{-1}[\bar{G}]_s & q[\bar{M}]_s^{-1}[\bar{D}]_s & q[\bar{M}]_s^{-1}[\bar{D}]_c \\ [0] & [E]_s & [R]_s & [0] \\ [0] & [0] & [0] & [R]_c \end{bmatrix} \begin{Bmatrix} \{\xi\} \\ s\{\xi\} \\ \{X_a\} \\ \{X_c\} \end{Bmatrix} \tag{17}$$

After premultiplication with the inverted mass matrix and reorganization, the $[B]$ matrix becomes:

$$[B]_c \{u_c\} = \begin{bmatrix} [0] & [0] & [0] \\ -q[\bar{M}]_s^{-1}[\bar{A}_0]_c & -q\left(\frac{c}{u}\right)[\bar{M}]_s^{-1}[\bar{A}_1]_c & [\bar{M}]_s^{-1}[\phi_s]^T[M]_c \\ [0] & [0] & [0] \\ [0] & [E]_c & [0] \end{bmatrix} \begin{Bmatrix} \delta_c \\ s\delta_c \\ s^2\delta_c \end{Bmatrix} \quad (18)$$

This $[B]$ -matrix is similar to the one given in Refs. [4, 9].

4.4 Gusts

The gust loads are added to (15) following (1) as:

$$\begin{aligned} [M]_s \{\xi\} s^2 + [G]_s \{\xi\} s + [K]_s \{\xi\} - q[Q]_g \{\xi\} \\ = [\phi_c]^T \{F\} + q[Q]_c \{\delta_c\} + q[Q]_g \{\eta_g\} \end{aligned} \quad (19)$$

The matrix $[Q]_g$ defined in the Laplace domain in a similar manner as for vibration-induced and control surface-included aerodynamic. The only difference is the exclusion of gust acceleration data, i.e. the s^2 terms. With the gust terms, the $[A]$ matrix is therefore expanded as:

$$[A] \{x\} = \begin{bmatrix} [0] & [I] & [0] & [0] & [0] \\ -[\bar{M}]_s^{-1}[\bar{K}]_s & -[\bar{M}]_s^{-1}[\bar{G}]_s & q[\bar{M}]_s^{-1}[\bar{D}]_s & q[\bar{M}]_s^{-1}[\bar{D}]_c & q[\bar{M}]_s^{-1}[\bar{D}]_g \\ [0] & [E]_s & [R]_s & [0] & [0] \\ [0] & [0] & [0] & [R]_c & [0] \\ [0] & [0] & [0] & [0] & [R]_g \end{bmatrix} \begin{Bmatrix} \{\xi\} \\ S\{\xi\} \\ \{X_a\} \\ \{X_c\} \\ \{X_g\} \end{Bmatrix} \quad (20)$$

Furthermore, the gust modes act as external forcing and therefore contribute to the $[B]$ matrix similar to (18), creating an additional contribution $[B]_g$:

$$[B]_g \{u_g\} = \begin{bmatrix} [0] & [0] \\ -q[\bar{M}]_s^{-1}[\bar{A}_0]_g & -q\left(\frac{c}{u}\right)[\bar{M}]_s^{-1}[\bar{A}_1]_g \\ [0] & [0] \\ [0] & [0] \\ [0] & \frac{1}{u}[E]_g \end{bmatrix} \begin{Bmatrix} \eta_g \\ s\eta_g \end{Bmatrix} \quad (21)$$

And then, the $[B]_g$ and $[B]_c$ are joined according to:

$$[B]\{u\} = [B_c, B_g] \left\{ \begin{matrix} \{u_c\} \\ \{u_g\} \end{matrix} \right\} \tag{22}$$

It should be noted that another row of empty matrices must be added to B_c for the gust lag states that do not depend on control surface inputs.

4.5 Verification Cases

The model described in the previous chapter is verified in this chapter. If not mentioned otherwise, all results are for the MLDW mass case at Mach 0.39, 2.5 g at zero height. The pole zero map calculated directly in NASTRAN is first compared with that of the state-space model in Fig. 15 to check the $[A]$ matrix of the state-space model.

Figure 15 shows the pole zero map for the MLDW mass case at Mach 0.39. The figure shows the poles of the aeroelastic state-space model and the poles as they are given by NASTRAN. Many aero poles in Fig. 15 far from the imaginary axis are related to the lag terms introduced for the RFA approximation and therefore do not exist in the NASTRAN model.

The flexible modes for the structural model lie close to the imaginary axis, because damping is set to zero for the verification (not for the model used for controller synthesis). They indeed lie at the frequencies taken from the ‘mck’ file, indicating that the state-space description of the structure is correct. Another observation is that the poles of the state-space model closely match the NASTRAN

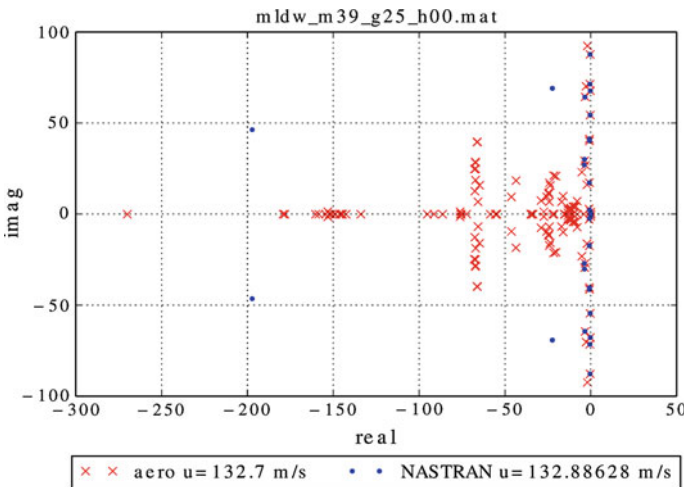


Fig. 15 Good agreement of pole zero map between NASTRAN and state-space model for MLDW, Mach 0.39 case. The additional poles of state space represent the lag states

results in both the real and imaginary part. This verifies that the implementation and evaluation of the RFA are correct. In conclusion, Fig. 15 verifies that the $[A]$ matrix correctly represents the NASTRAN model.

The response in the time domain to a normal gust is depicted in Fig. 16. The upper left figure shows the velocity of the gust. The other figures show the response of the translational modes (upper right), the rotational modes (lower left) and the flexible modes (lower right) from the state-space model. The figures show that the response of the state-space model (solid lines) closely matches that of the NASTRAN model (dashed lines). This verifies that the translation from NASTRAN to a state-space model is correct.

4.6 Application for Gust Load Alleviation Design and Analysis

The developed aircraft loads model in the state-space form has been successfully applied for the design of gust load alleviation (GLA) using a feed-forward approach, see Fig. 17 and [10]. A feed-forward controller is developed with an objective of minimizing the structural weight of the SARISTU wing. The wing

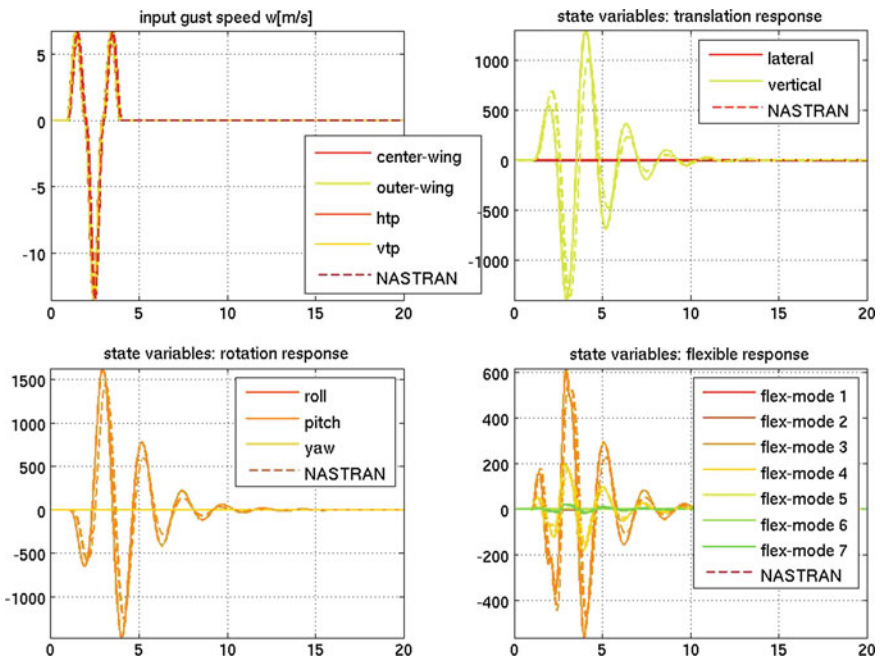


Fig. 16 Normal gust (upper left) and the response of the lateral/vertical displacement (upper right), roll/pitch/yaw (lower left) and flexible modes (lower right)

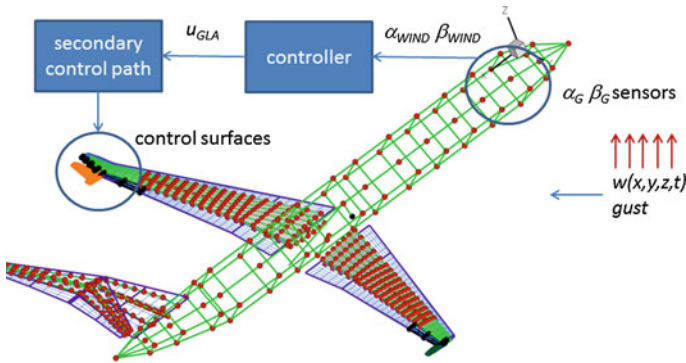


Fig. 17 Overview of the feed-forward controller for gust load alleviation developed in [10] using the loads model developed in the present study

mass model is represented by a rectangular wingbox. The controller is evaluated against various loads cases, and gust shapes in [10] show that wing weight reduction is possible, and moreover, the WATE device provides more effective gust load alleviation. The weight reduction is obtained through thinner wing skin.

5 Concluding Remarks

In this paper, an overall overview of the development of loads models to support the design team of AS03 and to support the evaluation of the WATE for gust load alleviation design is presented. It may be concluded that the following approaches have lead to a successful development of the loads model:

1. Doublet-lattice aerodynamics augmented with CFD results to have efficient loads evaluation with adequate accuracy during preliminary design of winglet and WATE.
2. Generation of aircraft aeroelastic model using preliminary design structural sizing tool NEOCASS to obtain realistic SARISTU fuselage and empennage coupled with the SARISTU wing loads model.
3. Generation of aeroservoelastic model in a state-space form with rational function approximation for the aerodynamic part.

The results of the present work have been successfully employed in the design of GLAS and WATE controller optimization. In addition, investigations have been performed to verify possible wing structure mass reductions. Around 2 % potential mass reduction has been predicted for the wing structure. The approach and dynamic loads models developed in SARISTU can be applied straightforward in future R&D projects for structure loads assessments (aeromechanical), control design and optimization and loads monitoring (a.o. ATED, SHM)

Acknowledgments We would like to thank all participating partners from the project-consortium SARISTU for the good teamwork and the support during the development and verification activities of the Adaptive Morphing Winglet. We especially enjoyed the work together in the AS03 team and to support during the design, optimization and evaluation activities of the WATE device for the GLAS. The research leading to these results has received partly funding from the European Union's Seventh Framework Programme through the SARISTU project for research, technological development and demonstration (GA/Nr.: ACP1-GA-2011-284562)

References

1. Baldassin E, Gifco MD, Gemma R, Carossa GM, Russo R, Ricci S, Gaspari AD, Peter F (2012) Reference baseline wing and morphing wing aeromechanical requirements. Deliverable D12.1.1 of SARISTU
2. Ricci S, De Gaspari A (2012) Morphed devices (TE; LE; WInglet) preliminary aerodynamic analysis. SARISTU Report D12.1.2
3. Prananta B, Herring M, Heinen C (2013) Aerodynamic and interface loads for design. SARISTU D3.2.1(a)
4. Cavagna L, Ricci S, Riccobene L (2009) Fast tool for structural sizing, aeroelastic analysis and optimization in aircraft conceptual design. In: 50th AIAA/ASME/ASCE/AHS/ASC structures, structural dynamics and materials conference. Palm Springs, CA, USA
5. Cavagna L, Riccobene L, Ricci S, Berard A, Rizzi A (2008) Fast MDO tool for aeroelastic optimization in aircraft conceptual design. In: 12th AIAA/ISSMO multidisciplinary analysis and optimization conference. Victoria, British Columbia, Canada
6. Wildschek A, Stroscher F, Klimmek T, Sika Z, Vampola T, Valasek M, Gangsaas D, Aversa N, Berard A (2012). Gust loa alleviation on a large blended wing body airliner. In: International Congress of the Aeronautical Sciences. Nice
7. Karpel M (1981) Design for active and passive flutter suppression and gust alleviation. NASA Langley Research Center, Langley
8. Tiffany S, Adams W (1988) Nonlinear programming extensions to rational function approximation methods for unsteady aerodynamic forces. NASA Langley Research Center, Hampton, Virginia
9. Baldelli D, Chen P (2006) Unified aeroelastic and flight dynamic formulation via rational function approximations. *J Aircr* 43(3):763–772
10. Prananta B, Tongeren J, Kanakis A (2013) Simplified loads model characterizing loads about wingtip morphing trailing edge tab. National Aerospace Laboratories (NLR), Amsterdam

Influence of H_2 and \mathcal{L}_∞ Criteria on Feed-Forward Gust Loads Control Optimized for the Minimization of Wing Box Structural Mass on an Aircraft with Active Winglets

Andreas Wildschek

Abstract This chapter presents the estimation of potential wing box mass saving enabled by means of active loads alleviation on a regional aircraft equipped with winglet control surfaces. As for the investigated aircraft, the inner wing is sized by maneuvers, and the minimization of structural weight of the wing box by active gust loads alleviation primarily affects the outer wing. Vice versa the minimization of structural weight of the inner wing can mainly be achieved by maneuver loads alleviation. The presented loads alleviation optimization directly minimizes the wing box mass required to sustain maneuver and gust loads. It is shown that the choice of the cost function has a significant influence on this optimum and the resulting wing box mass. Both H_2 and \mathcal{L}_∞ criteria are investigated. Based on the optimization results, a potential total wing box mass saving is proposed for further aircraft performance assessment.

Nomenclature

A/C	Aircraft
AIL	Ailerons
CG	Center of gravity
$\vec{d}(t)$	Disturbance response vector
dm	Mass of one wing segment
$\vec{z}(t)$	Vector of error signals
ELE	Elevators
$\mathbf{G}_c(s)$	Matrix of transfer functions of the SCP
GLAS	Gust load alleviation system
$\vec{H}(s)$	Vector of feed-forward controllers
h	Height of wing segment
i	Wing segment number
J	Cost function

A. Wildschek (✉)
Airbus Group Innovations, Munich 81663, Germany
e-mail: andreas.wildschek@airbus.com

k_e	Empirical compensation factor
L	Number of simulated samples
l	Total number of wing segments
Length	Span of one wing segment
M_b	Wing bending moment
m	Wing box mass
N	Filter length
n	Discrete time step
s	Laplace variable
SCP	Secondary control path
t_{eq}	Equivalent skin thickness
t_{sp}	Spar thickness
T_s	Sampling time
$\vec{u}_{GLAS}(t)$	Vector of controller commands
$w(t, x, y, z)$	Exogenous disturbance
w	Chord of wing box segment
z	Z-transform variable
MLA	Maneuver load alleviation
MLDW	Maximum landing weight
MTOW	Maximum takeoff weight
VA	Design maneuvering speed
VC	Design cruising speed
VD	Design dive speed
WATE	Wingtip active trailing edge
(x_0, y_0, z_0)	Reference point at cockpit location
ρ	Mass density
σ_{max}	Allowable stress at limit load

1 Introduction

The ability to minimize aircraft sizing loads by active control offers a great potential for reduction of weight of the primary aircraft structure and thus offers to improve fuel efficiency. The full benefit of active load alleviation systems can only be exploited if sufficient safety and reliability is proven to certification authorities [1]. This is one of the reasons why industry practice is to introduce load alleviation after conceptual design [2–4], although several studies exist that show that including active loads control at the earliest design stage can lead to a significantly improved fuel efficiency of the resulting aircraft design [5–8].

In this chapter, a method for the optimization of a feed-forward gust loads alleviation controller which directly minimizes the mass of the wing box required to sustain sizing loads is applied to the model of a regional aircraft equipped with

active winglets. The objective is to show the influence of choice of the cost function on the optimization result, i.e., the ability of an active winglet to reduce sizing loads. Both H_2 and \mathcal{L}_∞ criteria are considered. An adaptation algorithm for a gust loads controller using an H_2 criteria was derived in [9] for the SISO case, in [10] for MIMO case, and flight tested in [11]. Optimization of a gust loads controller based on \mathcal{L}_∞ criteria only was performed in [12] in order to perform a feasibility study on achievable loads alleviation performance on a blended wing body airliner. As controllers resulting from pure \mathcal{L}_∞ optimization generally do not fulfill the *continuous turbulence design criteria* (compare [1]), mixed H_2/\mathcal{L}_∞ optimization of a feed-forward controller for gust loads alleviation was performed in [13].

2 Synthesis Model

The coupled aero-elastic flight system dynamics models of a regional aircraft (see Fig. 1) are derived for several trim points (see Table 1) from a FEM consisting of beams for the fuselage and the empennage, and of shell elements and concentrated masses for the wings, coupled to a doublet lattice panel method. Inputs to these linear grid point models are control surface deflections, rates, and rate accelerations, as well as 1D-gust inputs. Outputs comprise flight mechanic states as well as sectional forces and moments at $i = 1 \dots 23$ wing sections. For simplicity, the thrust-drag equation is omitted (i.e., no need for thrust and drag model). In order to estimate aircraft stiffness and masses for the specified mission, the NeoCASS tool is used [14].

The aircraft is modeled for two mass configurations (MTOW and MLDW). The only difference between these configurations concerns the outer-wing fuel tank which is empty for MLDW configuration and full for MTOW. The output of the NeoCASS tool is an aero-elastic model of the aircraft based on beam modeling. The wings' beam model is replaced by a more accurate model based on shell elements and concentrated masses (e.g., for the fuel) including also the active winglets, see Fig. 2. Modeled control surfaces comprise of ailerons, inner spoilers, outer spoilers, elevators, rudder, and WATE. For each of the sizing load cases listed in Table 1, a state-space model of the flight system dynamics of the flexible aircraft is generated following the approach taken in [15].

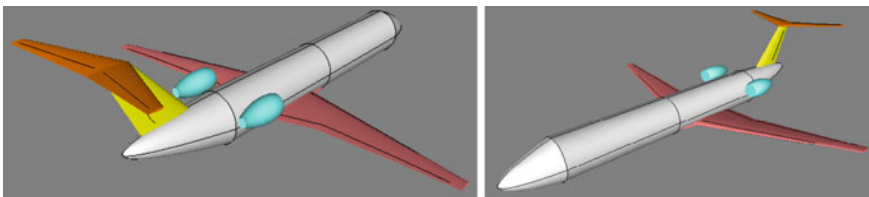
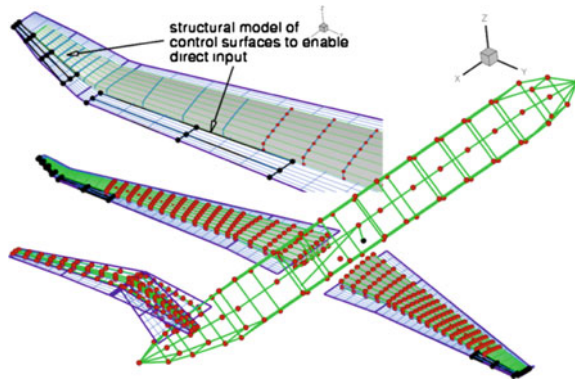


Fig. 1 Geometrical representation of the aircraft in the NeoCASS environment

Table 1 Sizing load cases used for GLAS validation

Flight case	Load scenario	Weight	Mach number	Altitude	Trim load factor (g)	Speed
1	Maneuver	MLDW	0.39	Sea level	2.5	VA [1]
2	Gust/Turbulence	MLDW	0.48	Sea level	1.0	VC [1]
3	Maneuver	MLDW	0.48	Sea level	2.5	VC [1]
4	Gust/Turbulence	MLDW	0.6	Sea level	1.0	VD [1]
5	Maneuver	MLDW	0.6	Sea level	2.5	VD [1]
6	Maneuver	MLDW	0.63	26,000 feet	2.5	VA [1]
7	Gust/Turbulence	MLDW	0.8	26,000 ft.	1.0	VC [1]
8	Maneuver	MLDW	0.8	26,000 ft.	2.5	VC [1]
9	Gust/Turbulence	MTOW	0.8	26,000 ft.	1.0	VC [1]

Fig. 2 Structural model including active winglets and replacing wings' beam models by shell elements

3 Gust Load Controller Optimization

Since the investigated airplane is inherently stable, no flight control system was designed. The actuators are modeled as PT_2 systems with rate command limitation and deflection command limitation. The feed-forward control system is considered to introduce a delay of 40 ms. In order to be able to use the aircraft with maneuver loads alleviation as baseline and exploit the full load alleviation potential, static deflections were applied to the control surfaces for all maneuver load scenarios in Table 1. With the objective function to minimize wing bending loads and the boundary condition that the load factor must not be influenced, a simple convex optimization problem is obtained which can be solved with commercial computer software. For straightforwardness, the optimization of maneuver loads alleviation is not shown here. Note that sections $i = 1$ through $i = 6$ are sized by maneuver loads.

For gust load alleviation with a feed-forward controller, a proper reference signal α is obtained by manipulating the alpha probe signal according to the procedure already described several times in the literature [11, 16, 17]. The GLAS control setup is shown in Fig. 3.

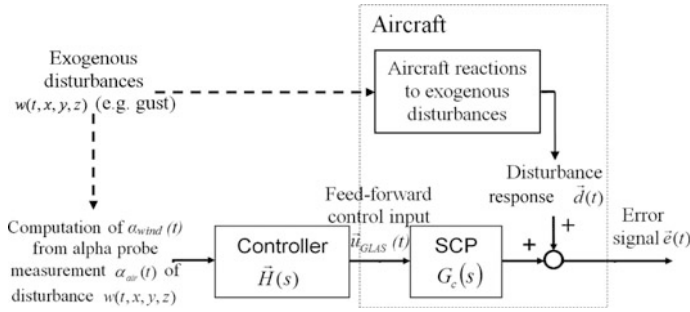


Fig. 3 Feed-forward GLAS control scheme [16]

The discrete feed-forward controller $\vec{H}(z)$ is implemented as a stack of FIR filters (one filter per actuated control surface pair), i.e.,

$$\vec{H}(z) = (H_{\text{WATE}}(z), H_{\text{AIL}}(z), H_{\text{ELE}}(z))^T \tag{1}$$

with e.g.,

$$H_{\text{WATE}}(z) = h_{0\text{WATE}} + h_{1\text{WATE}} \cdot z^{-1} + h_{2\text{WATE}} \cdot z^{-2} + \dots + h_{N-1\text{WATE}} \cdot z^{-N+1} \tag{2}$$

Thereby, z denotes the z -transform variable, and z^{-1} thus denotes a one sample delay. The vector of control commands $\vec{u}_{\text{GLAS}}(t)$ can be written as follows:

$$\vec{u}_{\text{GLAS}}(t) = (u_{\text{WATE}}(t), u_{\text{AIL}}(t), u_{\text{ELE}}(t))^T \tag{3}$$

with e.g.,

$$u_{\text{WATE}}(n) = \vec{h}_{\text{WATE}}^T \cdot \vec{\alpha}(n) = \vec{\alpha}^T(n) \cdot \vec{h}_{\text{WATE}} \tag{4}$$

with

$$\vec{h}_{\text{WATE}} = [h_{0\text{WATE}}, h_{1\text{WATE}}, h_{2\text{WATE}}, \dots, h_{N-1\text{WATE}}]^T \tag{5}$$

denoting the vector of FIR coefficients, and $\vec{\alpha}(n)$ denoting the vector of the sampled reference signal at time step n .

$$\vec{\alpha}(n) = [\alpha(n), \alpha(n-1), \dots, \alpha(n-N+1)]^T \tag{6}$$

For controller optimization, it is assumed that $\alpha(n)$ is just a delayed and high-passed version of the one-dimensional aircraft excitation $w(t, x_0, y_0, z_0)$, with (x_0, y_0, z_0) denoting the reference point at the fuselage nose. The advantage of using FIR filters is that they cannot become unstable as the filter's poles lie in the origin.

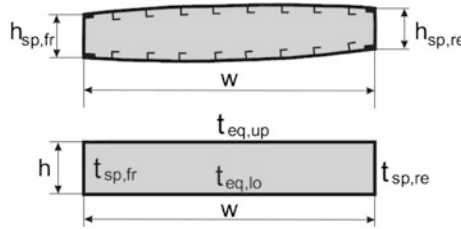


Fig. 4 Simplified wing box model [21]

Since a feed-forward controller also does not influence the poles of the plant, the feed-forward GLAS optimization cannot result in an unstable system [18, 19].

The controller $\vec{H}(z)$ is optimized in order to minimize a certain norm on the error signal vector $\vec{H}(z)$, which contains the wing bending moment at several selected wing box sections. Based on the method presented in [20], the mass of the wing box of one wing can be written as follows:

$$m = \sum_{i=1}^{i=l} \left(\frac{dm}{dM_b} \right)_i \cdot M_{b_i} \quad (7)$$

with M_{b_i} denoting the sizing wing bending moment in section i , and

$$\frac{dm}{dM_b} = \frac{\text{length} \cdot \rho \cdot 2 \cdot (w + h)}{h \cdot w \cdot \sigma_{\max} \cdot k_e} \quad (8)$$

Thereby, h and w are the height and chord of the simplified wing box section, see Fig. 4. The empirical factor k_e which compensates for the simplifications of the wing box is taken to 0.8. The allowable stress at limit load σ_{\max} is computed by dividing yield stress by a factor of safety. Note that, except for the mass density ρ , in general all variables in Eq. (8) will differ from one wing segment to the next. For controller optimization, it is assumed that $\alpha(n)$ is just a delayed and high-passed version of the one-dimensional aircraft excitation $w(t, x_0, y_0, z_0)$, with (x_0, y_0, z_0) denoting the reference point at the fuselage nose.

3.1 Mixed H_2/L_∞ Optimization of Feed-Forward Gust Loads Controller

The following cost function J considers both, *discrete gust design criteria* and *continuous turbulence design criteria*, compare specification in EASA CS-25 [1]:

$$\begin{aligned}
J = & \sum_{i=1,7,15,18,20} \left(\frac{dm}{dM_b} \right)_i \left(M_{b_{\text{static}}} \right. \\
& + \sqrt{\frac{1}{L+N-1} \sum_{n=1}^{L+N-1} \left(M_{b_{\text{turb}}} (n) + (\vec{h}_{\text{WATE}} * \vec{M}_{b_{\text{gust}} \rightarrow \text{WATE}}) (n) + (\vec{h}_{\text{AIL}} * \vec{M}_{b_{\text{gust}} \rightarrow \text{AIL}}) (n) + (\vec{h}_{\text{ELE}} * \vec{M}_{b_{\text{gust}} \rightarrow \text{ELE}}) (n) \right)^2} \\
& + \sum_{i=12,17,20} \left(\frac{dm}{dM_b} \right)_i A_i \left(M_{b_{\text{static}}} \right. \\
& + \max \left(M_{b_{\text{gust}}} (n) + (\vec{h}_{\text{WATE}} * \vec{M}_{b_{\text{gust}} \rightarrow \text{WATE}}) (n) + (\vec{h}_{\text{AIL}} * \vec{M}_{b_{\text{gust}} \rightarrow \text{AIL}}) (n) + (\vec{h}_{\text{ELE}} * \vec{M}_{b_{\text{gust}} \rightarrow \text{ELE}}) (n) \right) \\
& + \sum_{i=12,17,20} \left(\frac{dm}{dM_b} \right)_i A_i \left(M_{b_{\text{static}}} \text{abs} \left[\min M_{b_{\text{gust}}} (n) + (\vec{h}_{\text{WATE}} * \vec{M}_{b_{\text{gust}} \rightarrow \text{WATE}}) (n) \right. \right. \\
& \left. \left. + (\vec{h}_{\text{AIL}} * \vec{M}_{b_{\text{gust}} \rightarrow \text{AIL}}) (n) + (\vec{h}_{\text{ELE}} * \vec{M}_{b_{\text{gust}} \rightarrow \text{ELE}}) (n) \right] \right) \left. \right) \quad (9)
\end{aligned}$$

Thereby, the square root term represents the H_2 -criteria, and the max- and min terms represent the \mathcal{L}_∞ criteria. Note that the maximum and minimum are taken over $L + N - 1$ samples, and that the discrete time vector $\vec{M}_{b_{\text{turb}}}$ must be padded by $N - 1$ zeros, so that it has the same length ($L + N - 1$) as the vectors resulting from convolution of the FIR coefficient vectors with the bending moment sequences obtained when the reference signal measurement due to a discrete gust or continuous turbulence is fed to one of the control inputs, e.g., $\vec{M}_{b_{\text{gust}} \rightarrow \text{WATE}}$ for the WATE input. Thereby, L denotes the number of samples for which the continuous turbulence is simulated.

Adding constraints functions for command limits and rate command limits, the convex optimization problem for robust feed-forward GLAS controller synthesis is defined (The same equations are formulated for the WATE and for the elevators.)

$$u_{\text{AIL}}(n) \leq u_{\text{AIL-max}} \quad \forall n \in \left[0; \frac{t_{\text{end}}}{T_s} \right], \quad u_{\text{AIL}}(n) \geq u_{\text{AIL-min}} \quad \forall n \in \left[0; \frac{t_{\text{end}}}{T_s} \right] \quad (10)$$

$$\begin{aligned}
\frac{u_{\text{AIL}}(n+1) - u_{\text{AIL}}(n)}{T_s} & \leq \dot{u}_{\text{AIL-max}} \quad \forall n \in \left[0; \frac{t_{\text{end}}}{T_s} \right], \\
\frac{u_{\text{AIL}}(n+1) - u_{\text{AIL}}(n)}{T_s} & \geq \dot{u}_{\text{AIL-min}} \quad \forall n \in \left[0; \frac{t_{\text{end}}}{T_s} \right] \quad (11)
\end{aligned}$$

Thereby, subscript max denotes the maximum allowed deflection of the respective control surface, and subscript min denotes the minimum allowed deflection of the respective control surface, and T_s is the sampling frequency. Equations (9) through (11) state a convex optimization problem which can be readily solved with commercial optimization software. The feed-forward controller $\vec{H}(z)$ is optimized once without WATE (i.e., just using symmetrically driven ailerons), and once including the WATE. The filter length N was chosen to 16, because $N = 8$ gave significantly reduced performance for the GLAS with WATE. Figure 5 shows the bode plots of $\vec{H}(z)$ optimized without WATE (left) and with WATE (right).

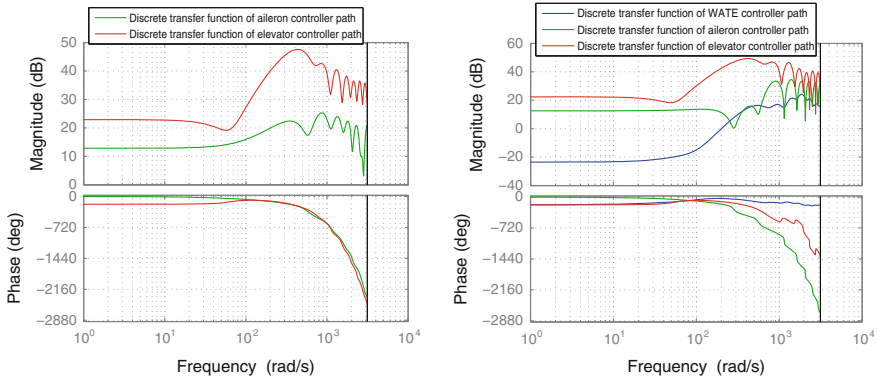


Fig. 5 Resulting controller for optimization without WATE (*left*) and with WATE (*right*)

Note that the high frequency gains of the controller transfer functions, which mainly result from the high weights A_i for the \mathcal{L}_∞ -norm terms, and from the significantly reduced bounds on command limits. This was done on purpose in order to obtain the maximum feasible load alleviation, well knowing however that such high frequency gain from an implementation point of view can cause problems such as sensor noise amplification and actuator fatigue.

3.2 Pure H_2 -Optimization of Feed-Forward Gust Loads Controller

In order to reduce the high frequency gain significantly and obtain an implementable controller, pure H_2 -optimization is performed using following cost function:

$$\begin{aligned}
 J = & \sum_{i=15,18,20} \left(\frac{dm}{dM_b} \right)_i M_{b_{\text{static}}} \\
 & + \sqrt{\frac{1}{L+N-1} \sum_{n=1}^{L+N-1} \left(M_{b_{\text{turn}}} (n) + (\vec{h}_{\text{WATE}} * \vec{M}_{b_{\text{gust}} \rightarrow \text{WATE}}) (n) + (\vec{h}_{\text{AIL}} * \vec{M}_{b_{\text{gust}} \rightarrow \text{AIL}}) (n) + (\vec{h}_{\text{ELE}} * \vec{M}_{b_{\text{gust}} \rightarrow \text{ELE}}) (n) \right)^2}
 \end{aligned} \quad (12)$$

Realizing that, even with maneuver loads alleviation, the inner wing is sized by maneuver, only the wing segments $i = 15$ (located at the aileron start), $i = 18$ (toward the end of the winglet), and $i = 20$ (located at the winglet/wing interface) are considered for the optimization. The idea thereby is to focus on gust load alleviation on the outer wing and check the load alleviation performance over the complete wing span in a subsequent simulation. The optimization is performed using the WATE, symmetrically driven ailerons, and elevators.

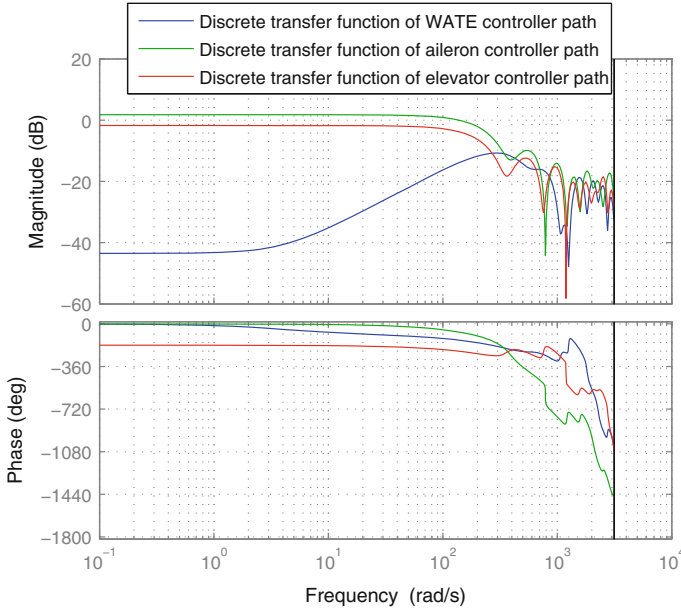


Fig. 6 Bode plot of purely H_2 -optimized GLAS controller

Moreover, the rate limits in Eq. (11) were chosen more conservatively in order to obtain a less aggressive controller. The bode plot of resulting $\vec{H}(z)$ is shown in Fig. 6. One can see that the resulting controllers for elevators and ailerons exhibit a roll-off, whereas the controller for the WATE has a band-pass characteristic. This controller is thus considered useful for implementation on a flying aircraft.

3.3 Performance Comparison

Also for GLAS validation, the turbulence input to the aircraft model is considered spanwise constant. In order to still consider the fact that in the real atmosphere, turbulence is distributed in space (most important distributed over wing span), and that the measurement of turbulence at one location (i.e., the alpha probe location) thus cannot perfectly predict the aircraft excitation due to space-distributed turbulence; the aircraft excitation $w(t, x_0, y_0, z_0)$ is now approximated by adding white noise to the von Kármán turbulence $\alpha_{wind}(t)$. This added noise represents the share of aircraft excitation which is not seen by the reference sensor. It must not be mistaken by sensor noise. The resulting quadratic coherence between reference signal $\alpha(t)$ and aircraft excitation $w(t, x_0, y_0, z_0)$ is plotted in Fig. 7. The reference point (x_0, y_0, z_0) is located at the cockpit location. Note that for discrete gust simulation, this additional noise is not considered.

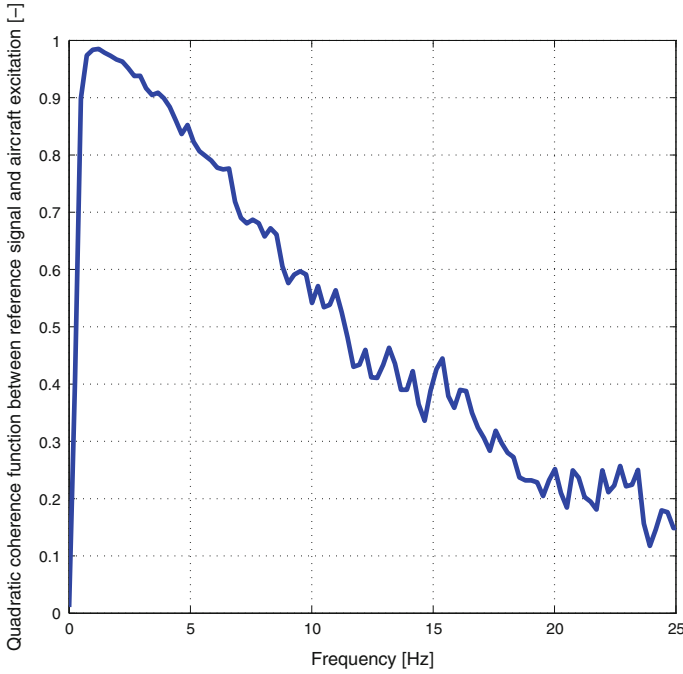


Fig. 7 Coherence function between α and w

Table 2 Wing box mass benefit for different GLAS configurations

Reference: A/C with MLA	Mixed H_2 / \mathcal{L}_∞ -optimal controller			Pure H_2 -optimal controller		
	Full GLAS	GLAS without WATE	WATE only	Full GLAS	GLAS without WATE	WATE only
Mass benefit w.r.t. reference (%)	2.26	1.80	1.76	2.30	1.82	0.72

Figure 8 illustrates that with the H_2 -optimal controller (using WATE, ailerons, and elevators), the obtained gust load alleviation performance over the complete gust loads envelope is slightly improved on the outer wing (see zoom) and significantly decreased on the inner and middle wing (see dashed black line with “+” marker) compared to the mixed H_2 / \mathcal{L}_∞ optimal controller, see red dotted line. For the inner and middle wing, however, maneuver loads are sizing, so the overall loads alleviation performance is improved.

Simulating the complete gust (including continuous turbulence) and maneuver loads envelope shown in Table 1, sizing wing bending moments M_{b_i} are obtained for all wing segments i . Using Eq. (7), the wing box mass required to sustain these

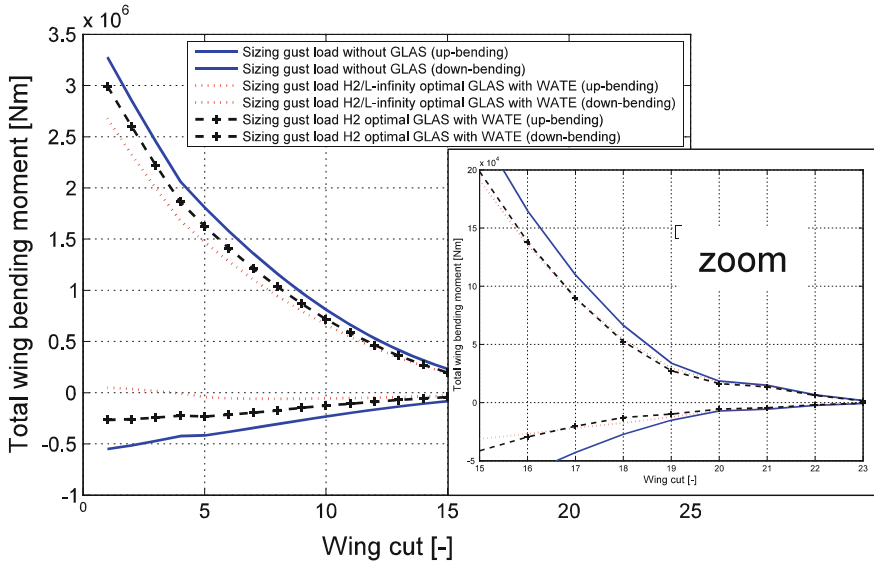
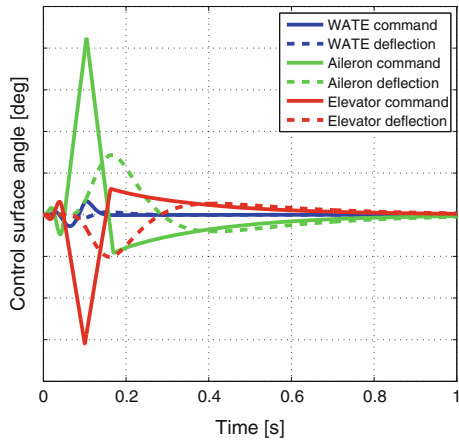


Fig. 8 Purely H_2 -optimal feed-forward GLAS controller performance (dashed black line with “+” marker) compared to mixed H_2 / L_∞ controller (red dotted line) considering only the gust loads envelope

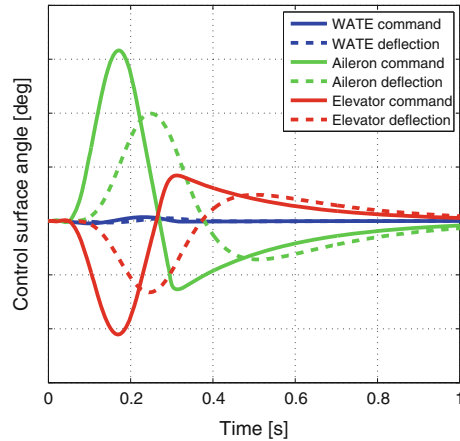
Fig. 9 GLAS control surface commands and deflections for a 30 ft. discrete sizing gust



loads is computed. Table 2 summarizes the obtained results. For the simulation of the H_2 -optimal GLAS without WATE, the WATE is just unplugged from the controller. For the simulation with WATE only, the ailerons and elevators are unplugged from the controller.

Figures 9 and 10 exemplarily illustrate control surface commands and deflections for a 30 ft. as well as for a 90 ft. discrete sizing gust for the H_2 -optimal

Fig. 10 GLAS control surface commands and deflections for a 90 ft. discrete sizing gust



controller. Commands to ailerons and elevators are moderate, except for the 30 ft. gust where commands exceed the rate limits without affecting potential wing mass saving.

4 Conclusion

The optimization of a feed-forward controller for gust load alleviation on a regional aircraft equipped with active winglets, with the objective of minimizing the mass of the wing box required to sustain sizing loads, is presented. Both mixed H_2/\mathcal{L}_∞ and pure H_2 -optimization are investigated. The mixed H_2/\mathcal{L}_∞ -optimization provides a more aggressive controller, which achieves higher gust load alleviation performance. Considering the complete loads envelope, however, pure H_2 -optimization achieves the highest wing box mass saving for the investigated aircraft. Moreover, the purely H_2 -optimized controller is less likely to cause actuator fatigue problems, or sensor noise amplification. A reduction of structural wing box mass of 2.3 % is computed and can be used for further investigations.

Acknowledgments The research leading to these results has gratefully received funding from the European Union Seventh Framework Programme (FP7/2007 2013) under Grant Agreement no 284562. Many thanks also go to all SARISTU partners for their invaluable contributions.

References

1. EASA CS-25 Amendment 14, dated 19 December 2013—Certification Specification for Large Aeroplanes
2. Airbus, A319/A320/A321 Flightdeck and Systems Briefing for Pilots, 1998
3. Airbus, A330 and A340 Flight Crew Training Manual, 2004

4. Flaig A (2008) Solutions to the aerodynamic challenges of designing the world's largest passenger aircraft. Royal Aeronautical Society Hamburg Branch Lecture Series
5. Suzuki S, Yonezawa S (1993) Simultaneous structure/control design optimization of a wing structure with a gust load alleviation system. *J Aircr* 30(2):268–274
6. Moulin B, Idan M, Karpel M (2002) Aeroservoelastic structural and control optimization using robust design schemes. *J Guid Control Dyn* 25(1):152–159
7. Haghight S, Martins J, Liu H (2012) Aeroservoelastic design optimization of a flexible wing. *J Aircr* 49(2):432–443
8. Xu J, Kroo I (2014) Aircraft design with active load alleviation and natural laminar flow. *J Aircr* 51:1532–1545
9. Wildschek A, Maier R, Hoffmann F, Jeanneau M, Baier H (2006) Active wing load alleviation with an adaptive feed-forward control algorithm. In: AIAA guidance, navigation, and control conference, Keystone, CO, 21–24 Aug 2006
10. Wildschek A, Bartosiewicz Z, Mozyrska D (2014) A multi-input multi-output adaptive feed-forward controller for vibration alleviation on a large blended wing body airliner. *J Sound Vibr*
11. Wildschek A, Maier R, Hahn K-U, Leißling D, Preß M, Zach A (2009) Flight test with an adaptive feed-forward controller for alleviation of turbulence excited wing bending vibrations. In: AIAA guidance, navigation, and control conference and exhibit, Chicago, Illinois, USA, 10–13 Aug 2009
12. Wildschek A, Haniš T, Stroscher F, “ \mathcal{L}_∞ -optimal feed-forward gust load alleviation design for a large BWB airliner. In: EUCASS 2011—4th European conference for aerospace sciences, St. Petersburg, Russia
13. Gowriedda-Sundaresh S (2013) Comparison of optimization methodologies for robust feed forward controller for gust load alleviation system. Master Thesis, Technische Universität München
14. Cavagna L, Ricci S, Riccobene L (2009) NeoCASS, a tool for aeroelastic optimization at aircraft conceptual design level. In: International forum on aeroelasticity and structural dynamics, Seattle, WA, 21–25 June 2009, pp. 1–15
15. Wildschek A, Stroscher F, Klimmek Th, Šika Z, Vampola T, Valášek M, Gangsaas D, Aversa N, Berard A (2010) Gust load alleviation on a large blended wing body airliner. In: 27th Congress of the International Council of the Aeronautical Sciences (ICAS 2010), Nice, France, 19–24 Sept 2010
16. Wildschek A (2008) An adaptive feed-forward controller for active wing bending vibration alleviation on large transport aircraft. Ph.D. dissertation, Munich
17. Hecker S, Hahn K-U (2007) Advanced gust load alleviation system for large flexible aircraft. In: 1st CEAS European air & space conference, Berlin, Germany, 10–13 Sept 2007
18. Moschytz G, Hofbauer M (2000) Adaptive Filter. Springer, Berlin
19. Elliott S (2001) Signal processing for active control. Academic Press, London, pp 51–61
20. Wildschek A, Prananta B, Kanakis T, Tongeren H, Huls R (2015) Concurrent optimization of a feed-forward gust loads controller and minimization of wing box structural mass on an aircraft with active winglets. In: 16th AIAA/ISSMO multidisciplinary analysis and optimization conference, Dallas, TX, 22–26 June 2015
21. Seywald K (2011) Wingbox mass prediction considering quasi steady aeroelasticity. Master thesis, Technical University of Munich

Evaluation of the Performance Benefits of the Winglet Active Trailing Edge in AS03

Martin Herring

Abstract An engineering demonstrator of the winglet active trailing edge (WATE) concept was manufactured by AS03 partners in SARISTU. In parallel, simulation activities were used to investigate the performance benefits of active winglets. A study made by AS03 partners (led by AGI-G) assessed the capacity of the WATE—with a suitably designed controller—to alleviate loads due to gust encounters, and this was used to estimate a structural mass saving of around 2 %. A separate study (performed by AGI-UK and ONERA) investigated the potential for an improvement of the lift-to-drag ratio for off-design conditions. This paper brings together the benefits of the structural mass reduction, and the lift-to-drag improvement, using a form of the well-known Breguet range equation to make estimates of the fuel that can be saved over a given mission. This has been combined with typical fleet operation statistics to estimate that the WATE concept (including the structural mass saving effects) could deliver a 1 % reduction in daily fuel costs for a representative airline fleet. For much of the analysis, simplifying assumptions and models have been used in order to meet the project time and cost objectives. Uncertainty in the precise level of benefit is a risk associated with further development of the WATE technology, but the activities in SARISTU AS03 have demonstrated the potential which makes the WATE concept interesting for further development.

Nomenclature

R	Range (or distance between start S_1 and start S_2 of mission segment)
V	True airspeed
f	Specific fuel consumption
C_L/C_D	Ratio of the lift coefficient to the drag coefficient (lift-to-drag ratio)

M. Herring (✉)

Airbus Group Innovations, TX3 Aeromechanics, 20, Golf Course Lane,
PO Box 5, BS34 7QW Filton, Bristol, UK
e-mail: martin.herring@eads.com

g	Gravitational acceleration
W_1	Weight (mass) at the start of mission segment
W_2	Weight (mass) at the end of mission segment
C_{Di}	Induced drag coefficient
C_{D0}	Parasitic drag coefficient
C_{Dw}	Wave drag coefficient

Abbreviations

AS03	Application scenario 3
WATE	Winglet active trailing edge
RANS-CFD	Reynolds averaged Navier–Stokes computational fluid dynamics
CFD-CSM	CFD coupled to a structural model (for flexible simulations)
MTOW	Maximum takeoff weight

1 Introduction

In the scope of SARISTU AS03, a number of detailed investigations were made into the potential benefits of the winglet active trailing edge (WATE) device. In particular, the ability to control gust and turbulence loads with the WATE was explored in deliverable D33.2C, and the opportunity to use the WATE to reduce induced drag (and improve the L/D ratio) by controlling span loading away from the design cruise condition was explored in D33.2E. In order to investigate the overall benefits and risks of the WATE technology, it is necessary to look at measures of performance that are meaningful in terms of airline operations, which means assessing the impact of the technology on fuel burn. By combining fuel burn data for different length missions with typical fleet usage statistics, it was possible to estimate the effect the WATE technology might have on a typical airline over the course of a single day. SARISTU deliverable D33.2F describes the full WATE fuel burn assessment.

To satisfy a customer request received towards the end of the project, a simple analysis to investigate the effects of removing the winglet and shortening the wing is presented. The analysis includes an assessment of the effect of using a planar wing extension to match the original canted winglet span. A short discussion on the impact on low-speed performance is also included.

In the final section of the paper, there is a summary of benefits and risks of the WATE technology as they are currently understood. This includes some conservative estimates of cost, weight, and maintainability metrics provided by FACC, who were the lead partner for the manufacturing of the WATE demonstrator in SARISTU.

2 Effect of WATE Lift-to-Drag Ratio Improvements on Fuel Burn

In AS03, the effects of varying the tab deflection angle on the drag on a SARISTU aircraft half model (excluding the empennage or rear-mounted engines and with improvised fuselage) was investigated using RANS CFD (DLR TAU code). Basic input data were taken from SARISTU deliverable D12.1.1. CFD simulations performed by Airbus Group Innovations were post-processed by ONERA using their *ffd72* code for a number of climb and cruise flight conditions. The ONERA code provided a detailed drag breakdown of the CFD solution into the main components of drag: induced drag, viscous drag, and wave drag. However, for the fuel burn analysis, simply the effect of the WATE deflection on the overall lift-to-drag ratio (C_L/C_D) was used, as this ratio is an important factor in the well-known Breguet range equation, as in Eq. (1). WATE deflection angles were varied in the range -8° (up) to 10° (down) as illustrated in Fig. 1. The principle exploited for performance benefit is shown in Fig. 2. Downward deflection of the tab trailing edge causes a local increase in camber, which increases the local lift, and leads to a spanwise redistribution of aerodynamic load with the centre of lift moving further outboard. This leads to a reduction in induced drag and an increase in the overall lift-to-drag ratio. Beyond a certain optimum angle, at around 5° for the cruise flight condition shown here, the viscous drag terms become more significant and the overall lift-to-drag ratio decreases again. Rearranging Eq. (1) for the weight fraction

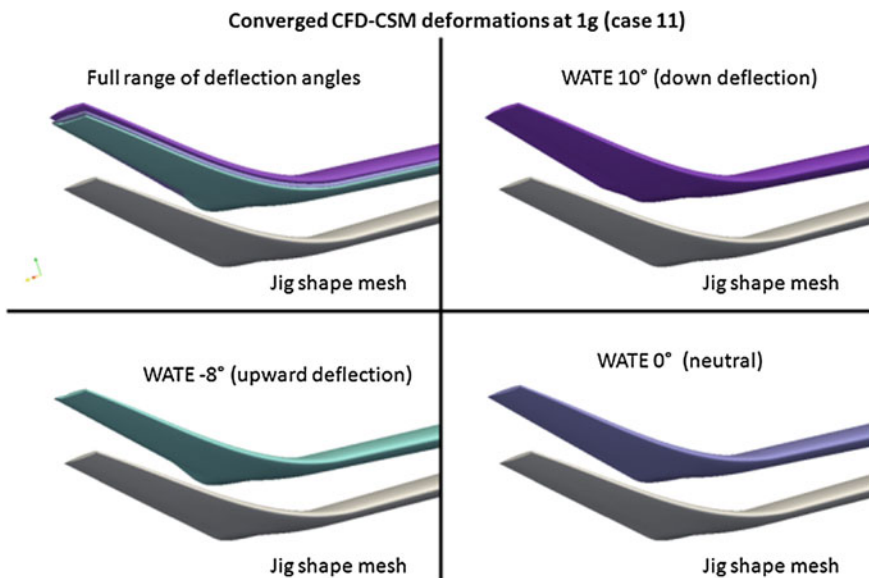
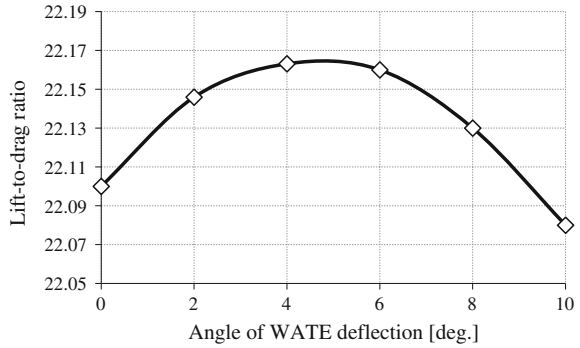


Fig. 1 Tab deflections for a range of deflection angles (shown for a flexible CFD-CSM case)

Fig. 2 Lift-to-drag variation with downward WATE deflection—cruise condition (Mach 0.75, 35,000 ft.)



(W_1/W_2), as shown in Eq. 2, allows the effect of an increase in lift-to-drag ratio on a reduction in weight delta ($W_2 - W_1$) for a given range segment ΔS to be calculated. The weight (or mass) delta is a quantity of fuel that is burnt.

$$R = S_2 - S_1 = \frac{V C_L}{fg C_D} \ln\left(\frac{W_1}{W_2}\right) \tag{1}$$

$$\frac{W_1}{W_2} = e^{\left(\frac{\Delta S}{V} \cdot \frac{f}{C_L/C_D} \cdot g\right)} \tag{2}$$

It is worth pointing out that the downward trailing edge deflection could be designed in as part of a fixed cruise shape definition, and this would lead to an optimum improvement in performance at one specific flight point. The main advantage of the WATE over a fixed geometry is the ability to tailor the spanwise load distribution for different Mach number and altitude combinations. The WATE is also available as a load alleviation device, which was investigated in AS03, and led to the structural mass savings described later in this paper. In theory, it would be possible to use the WATE to assist with handling qualities, but this was not investigated in AS03.

The CFD simulations performed for the cruise condition in Fig. 2 were repeated for several other flight points (e.g. climb conditions at different altitudes), and whereas the results in Fig. 2 were produced for a flexible CFD-CSM model, where deformation of the geometry under load is taken into account, the same study was also performed using a rigid mesh.

In each case, dividing the maximum lift-to-drag ratio by that at 0° deflection gave a similar scaling factor—or ‘aerodynamic improvement factor’—to that in Fig. 2 (where $AIF = 22.163/22.099 = 1.0029$). The fact that a lift-to-drag improvement is possible for the full range of considered flight conditions indicates that the baseline geometry is not optimized for drag. However, it should be remembered that a more inboard-loaded wing is better in terms of wing loads and may reduce the effort required to alleviate loads during the most extreme manoeuvres and gusts. The baseline design may have resulted from a trade-off.

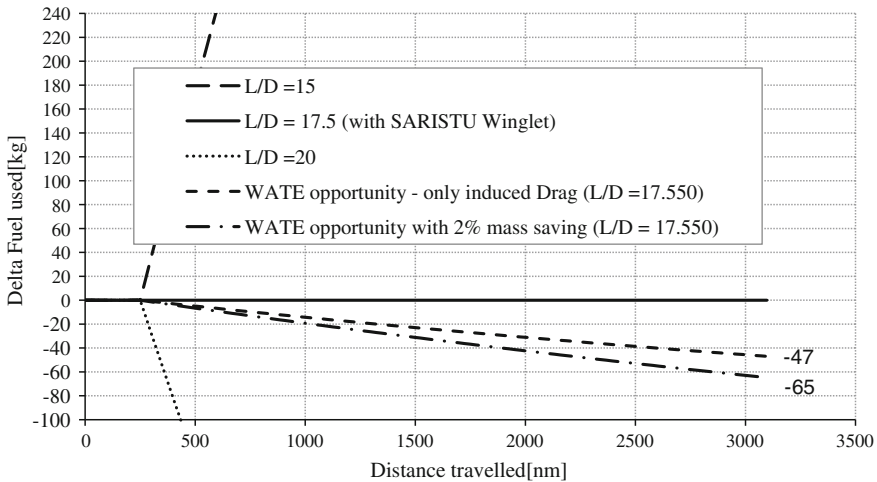


Fig. 3 Fuel increments for different lift-to-drag ratios (and 2 % structural mass saving)

The fuel burn calculations outlined in SARISTU deliverable D33.2F make use of Eq. (2) to compute the fuel used over a given distance travelled (range) for a baseline SARISTU aircraft, with a MTOW of 63,131 kg and a range of 3000 nm. The baseline aircraft was taken to have a lift-to-drag ratio of 17.50 (note that the higher values in the CFD results are for a geometry without engines or empennage), and the specific fuel consumption was taken to be 1.5579E-05 kg/N/s. By varying the assumed lift-to-drag ratios between 15 and 20 and calculating the effect on fuel burn, delta fuel burn figures with respect to the baseline aircraft can be plotted, as in Fig. 3. Applying the AIF of 1.0029 to the baseline lift-to-drag ratio yields a new lift-to-drag ratio of 17.550, which represents the opportunity provided by the WATE if the full benefit from the CFD study (cruise condition) is taken into account. The fuel burn curve associated with this lift-to-drag ratio is plotted in Fig. 3 and results in a fuel saving of 47 kg over a total distance of 3097 nm.

3 Effect on Structural Mass Reduction Due to WATE

The opportunity for a structural mass reduction stems from the application of the WATE as part of a gust load alleviation system. Deliverable D33.2C describes the development of an active gust load control system for the WATE, and the conclusions indicate that a net empty mass reduction of around 2 % is possible, after any penalties associated with systems installation have been taken into account.

There are different ways in which this can be exploited, e.g.

- i. Maintain the existing range performance and increase the payload slightly—note that the 2 % structural mass reduction is from an area of the wing where it is also providing some inertia bending relief, whereas the payload is in the fuselage, so the payload increase is likely to be significantly lower than the structural mass reduction.
- ii. Maintain the existing design weights, and replace some or all of the 2 % structural mass saving with fuel—up to the capacity limits of the fuel system—to increase the range.
- iii. Take advantage lighter take-off weight, and the influence this has on fuel burn over the course of the mission.
- iv. For a winglet retrofit, there is also the opportunity to offset the load increase caused by a more outboard centre of lift.

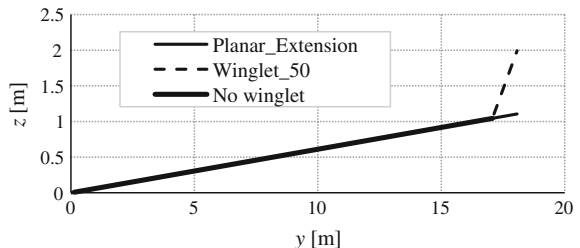
By adopting the third approach with a lift-to-drag ratio of 17.550 (i.e. including the WATE opportunity identified in the previous section), and repeating the fuel burn assessment, a 65-kg fuel saving is computed over the 3097 nm distance, as shown by the curve with 2 % structural mass saving in Fig. 3.

4 General Study on the Benefits of Winglets

The SARISTU winglet geometry was included for all detailed aeromechanical simulations in AS03, but to understand the performance benefit provided by the basic fixed winglet, a simple drag analysis was made using reference aircraft data from D12.1.1. The full study is presented in deliverable D33.2F. Three simplified wing/winglet configurations were considered, with geometry modelled as a two-dimensional trace (see Fig. 4).

The configuration labelled ‘Winglet_50’ represents the SARISTU configuration with a winglet canted at around 50°. The ‘No winglet’ case is with the winglet removed completely, and the ‘Planar_Extension’ is a configuration where the

Fig. 4 Configurations considered for the winglet analysis



winglet is extruded in the plane of the wing to have the same overall span as Winglet_50.

A program called ‘SpanOpt F111 v2’, as in Ref. [2], was used to model the induced drag of these configurations with optimized span loads. The program uses a discrete vortex Trefftz-plane analysis, and the parasitic drag contribution was estimated using the equivalent parasite area method, as in Ref. [3], applied only to the wing/winglet using wetted area estimations, as in Ref. [1]. Wave drag was assumed to depend only on C_L and estimated using a representative drag-rise trend for a fixed Mach number. If the analysis had been performed for the whole aircraft, these three drag terms alone could be combined to give the overall drag coefficient. For this analysis, it was assumed that the fuselage, empennage, and engines contribute the same amount of drag to all configurations, and an additional drag term was used for this purpose, so that the overall drag coefficient is as shown in Eq. (3).

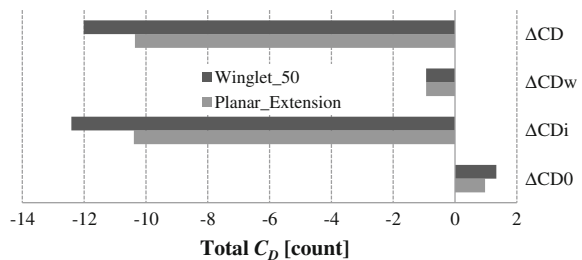
$$C_D = C_{Dadd} + C_{Di} + C_{D0} + C_{Dw} \tag{3}$$

The additional drag term was calibrated to lift-to-drag results given in D12.1.1. Figure 5 shows the difference in terms of Eq. (3) for the two extended configurations relative to the case with no winglet. It is clear from this comparison that the induced drag term is dominant and that the canted winglet (Winglet_50) has a lower drag than the planar extension. The resulting lift-to-drag ratios were as follows:

- Winglet_50: 17.47
- No winglet: 17.10
- Planar: 17.38

The impact on fuel burn is shown in Fig. 6, where it is seen that relative to the SARISTU winglet (Winglet_50), the planar extension increases the fuel burn by 53 kg over the 3097 nm distance, and the case with no winglet increases the fuel burn by 220 kg over the same distance.

Fig. 5 Incremental drag coefficients relative to no winglet or extension



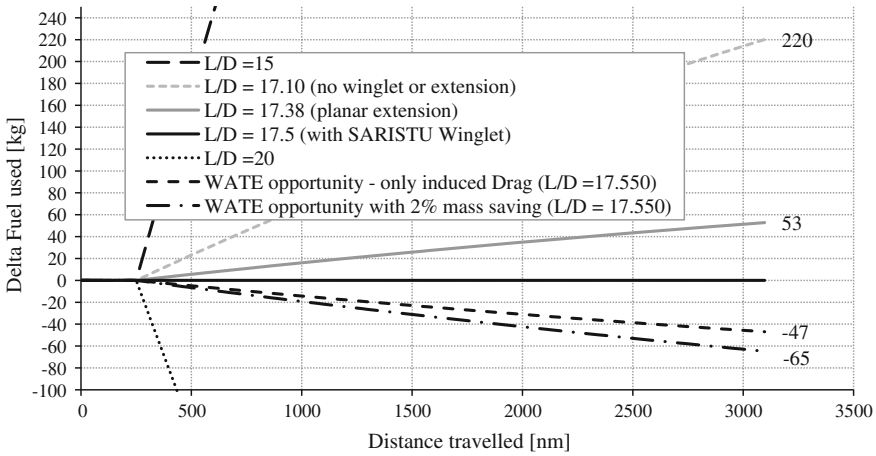


Fig. 6 Fuel increments for different lift-to-drag ratios including the penalty of no SARISTU winglet

5 Fleet Fuel Savings

In order to help better understand the impact of fuel savings on the operations of a typical airline, representative fleet survey data for a single day of operations were provided by the Airbus Future Projects Office, as shown in Fig. 7.

Fuel savings for single flights of a given range were multiplied by the number of flights from the fleet survey at that range to give a daily cost saving. Application of the data from the WATE opportunity case with 2 % structural mass saving—from Fig. 3 (and Fig. 6)—gives the distribution shown in Fig. 8. Summing these data across all mission lengths then gives a total daily fuel saving for the fleet. The mass and volume of this saving are stated in deliverable D33.2F and amount to a 1 % fuel saving for the fleet per day.

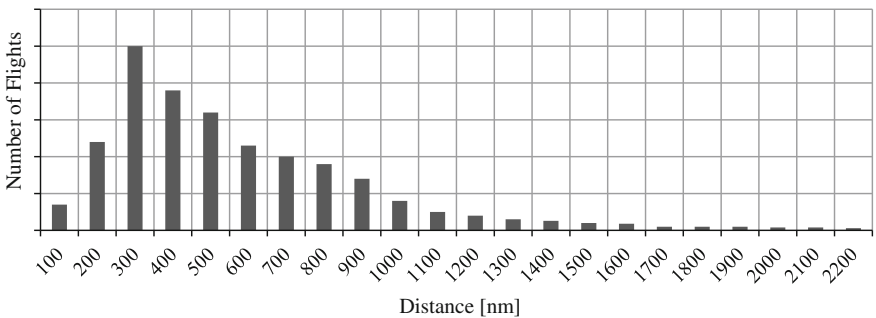


Fig. 7 Representative sample of daily fleet operations showing number of flights for a given range

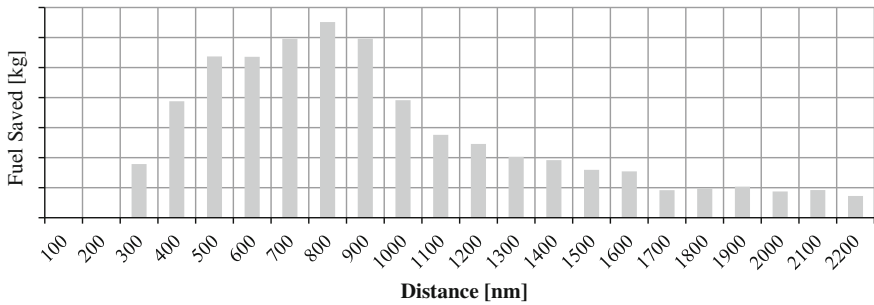


Fig. 8 Daily fleet fuel savings for flights of a given range

The same approach can be applied to assess the impact of the additional fuel costs associated with the removal of the winglet and with the replacement of the winglet by a planar tip extension. The planar wing extension is estimated to increase the daily fleet fuel cost by a little under 1 % relative to the SARISTU winglet. Complete removal of the winglet is estimated to increase the daily fleet fuel cost by more than 3 %.

6 Comparison of WATE Installation Technologies

The engineering demonstrator of the SARISTU WATE concept, manufactured by AS03 partners, was designed in the beginning of the project with a morphing filler material in mind. The idea was to ensure a clean wing geometry as shown in Fig. 9a and to avoid the opening up of a gap as shown in Fig. 9b. It was shown in the drag assessment report produced by ONERA—deliverable D33.2E—that the viscous pressure drag was 2.2 counts higher with the gap than for the morphing installation in Fig. 9a, and the gap provoked an increase of the total drag by 1.8 counts. D33.2E concluded that if drag reduction is one of the objectives of the WATE device, then only the morphing approach should be used.

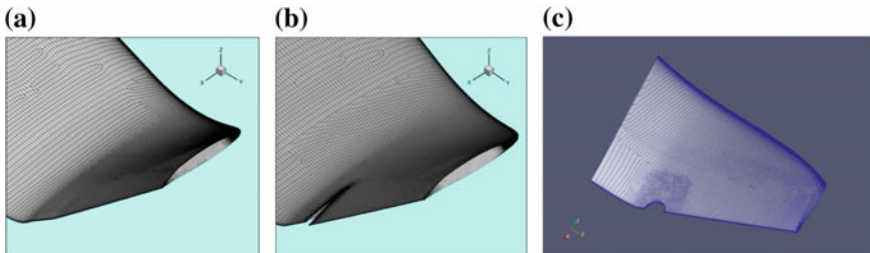


Fig. 9 a WATE with morphing, b WATE with gap, and c ATE with semicircular cutout

In practice, the elastomeric material used for the morphing part proved difficult to integrate for a continuous trailing edge, because the actuation forces required to cause sufficient WATE deformation were leading to problems with actuator sizing. The solution for the engineering demonstrator was to introduce a semicircular cutout (maximum strains in the morphing material were significantly reduced with this approach) as shown in Fig. 9c, but this created an aerodynamic problem that could not be solved within the tight manufacturing timescales. Deliverable D33.2E concluded that the semicircular cutout had a total drag around three counts higher than the continuous trailing edge. This would eliminate any benefits achieved through WATE camber variation, so this integration challenge remains to be solved in any further development of this technology.

7 Low-Speed Performance

The idea to study low-speed performance was considered too late in the project for new CFD simulations to be made. One idea for future investigation would be whether the WATE could provide additional lift during the approach and thereby allow a reduction in approach speed. Additional lift may also be beneficial during takeoff. Since the existing simulation data were generated for iso- C_L conditions, a further study is required to trade C_L with airspeed for a given lift.

An attempt was made in deliverable D33.2F to use the lift-to-drag trends derived from CFD to explore the potential for a drag reduction during the takeoff and climb. An analysis of the takeoff distance with different WATE deflection angles was performed, based on the method described in Torenbeek, Appendix K in Ref. [4]. The influence of WATE deflection on take-off distance is very small, because while the aircraft is still on the ground there is very little lift, and the WATE device acts predominantly on the lift-induced drag (see Fig. 5). In fact, even when the drag coefficient increments from this analysis were amplified artificially by a factor of 10, the distances saved were of the order of a few metres for a takeoff run of more than 1.4 km.

8 Summary of Opportunities and Risks

The SARISTU project partners who worked together on the WATE concept have collectively learnt a lot about the technology, and what it could deliver in terms of performance benefits for future aircraft. The design and manufacture of an engineering demonstrator has looked at the challenge of locating an actuator inside the loft line with only very minor changes to the aerodynamic profile, in order to control actuator forces. For the design and manufacturing teams, the WATE project was a challenging departure from previous winglet designs. A suitable elastomer was identified and tested, for the morphing part to meet the stringent CS-25

requirements. A control system was designed and built to alleviate in-flight turbulence loads, and a failure hazard analysis was performed with input from Airbus experts, leading to a good understanding of the possible failure conditions and prompting appropriate levels of redundancy in the design. The impact of the technology on aircraft in-flight performance—in particular on fuel burn—has also been assessed, as described in this paper.

Table 1 is a summary of the opportunities and risks for a range of performance metrics, as currently understood at the end of the SARISTU project.

Table 1 Risks and opportunities for the WATE concept

Performance metric	Opportunities/benefits	Risks
Mass of wing structure and systems	Estimated 2 % reduction (see D33.2C), with the mass penalty due to actuation and electronic systems included	The mass saving may be smaller if any significant load conditions were missed from the analysis and if these cannot be mitigated by the WATE control system
Drag reduction	Up to 0.3 % improvement in lift-to-drag ratio due to use of WATE to adapt span loading	Application of this benefit for the entire mission may be too optimistic—some of the shape improvement could potentially be designed into the undeflected geometry
Fuel burn	Up to 1 % reduction in daily fuel costs for a typical airline fleet	Potentially optimistic drag reduction figures are part of this analysis
Low-speed performance	Potential for WATE to improve high-lift characteristics, to reduce approach speeds and takeoff and landing distances	Analysis in AS03 was limited to drag reduction on takeoff—the improvement in takeoff distance was negligible
Handling qualities	Potential for WATE to complement other surfaces for manoeuvring and passenger comfort	Handling quality opportunities were not investigated in AS03
Morphing	Reduction in the viscous pressure drag (~2 counts improvement)	Challenge to integrate clean aerodynamic configuration with actuator sizing constraints and forces required to deform morphing material
Cost of manufacture		Up to 15 % greater than conventional winglet ^a
Cost of WATE repair		Up to 5 % greater than conventional winglet ^a
Cost of WATE repair when actuation system needs replacement		Up to 15 % greater than conventional winglet ^a

(continued)

Table 1 (continued)

Performance metric	Opportunities/benefits	Risks
Mass of actuation and electronic system integration		Up to 10 % of the mass of a conventional winglet ^a
Certification challenge	A failure hazard analysis was performed as part of D32.1D—some challenging areas such as the interaction of systems design and flight loads were already considered	Integration of technology onto a whole aircraft platform is much more challenging than the SARISTU demonstrator can show. More detailed consideration of the regulations and proof of compliance may begin to erode some of the benefits
Retrofit option	Gust load alleviation using the WATE could protect existing wing structure from loads increases due to a wing extension	A WATE system for retrofit would be significantly more challenging because the existing wing systems architecture would impose constraints on the design

^aConservative estimates made by FACC designers based on comparisons with conventional winglets

9 Conclusions

Some key benefits of active winglet technology and the morphing gap filler have been identified, and the potential magnitudes of these benefits have been quantified through simulation and understood through the experience of designing and manufacturing an engineering demonstrator. It is acknowledged that at the current level of maturity, there is still uncertainty about how the technology will perform on an aircraft platform, and this uncertainty is expressed as a set of risks to be understood during further development.

Highlights of the work performed in SARISTU include a 2 % reduction in the structure and systems mass of the wing due to WATE load alleviation and an analysis that shows how the WATE could adapt the spanwise distribution of aerodynamic flight during 1g flight, leading to a potential daily fuel cost saving of 1 % for a typical airline.

Acknowledgement The SARISTU project has received funding from the European Union's Seventh Framework Programme for research, technological development, and demonstration under Grant Agreement No. 284562.

Associated SARISTU Documents

Short name	SARISTU PRODAXS location	File
D33.2C	00-DOCUMENTS/03-AS/Documents/Deliverables	A_DEU_D33_2C_WATE_LoadsAlleviation_R2.pdf
D33.2E	00-DOCUMENTS/03-AS/Documents/Deliverables	A_DEU_D33_2E_WATE_DragAssessment_R1.pdf
D33.2F	00-DOCUMENTS/03-AS/Documents/Deliverables	A_DEU_D33_2F_WATE_FuelBurn_R01_sign_rep.pdf
D12.1.1	00-DOCUMENTS/12-IS/Documents/Deliverables	SARISTU 12.1.1 Iss_1.pdf—reference baseline wing and morphing wing aeromechanical requirements

References

1. Kroo I (2012, January 4) Wetted area calculations. Retrieved March 10, 2015, from Aircraft design: synthesis and analysis: <http://adg.stanford.edu/aa241/drag/wettedarea.html>
2. Miller A (2013) F111 v2 Technical Report, Airbus, Bristol
3. Roskam J (2005) Airplane design part I: preliminary sizing of airplanes. Design, Analysis and Research Corporation, Kansas
4. Torenbeek E (1982) Synthesis of subsonic airplane design. Delft University Press, Delft

Part IV

Technology Stream: Integrated Sensing. Fiber Optic-Based Monitoring System

Introduction and Overview

Application scenario 4 of SARISTU project deals with monitoring systems that are based on fiber optic sensors. The objectives are the design, optimization, and implementation of a strain monitoring system, based on a network of fiber optic sensors such as FBGs or distributed sensing. The system will be integrated on a generic wing structure and on a generic fuselage structure. On the wing, the system will have to monitor the shape on the morphing trailing edge and to monitor the strain at different positions. On a typical stiffened fuselage panel, the monitoring system will have to identify and locate debonding of the stringer from the skin and possibly to detect impact events on the skin. Each of these use cases is integrated in the overall application scenario (AS) and has different requirements when compared with the rest of the AS.

During the last four years, the team of partners working within scenario 4 managed to develop a modular monitoring system based on FBG sensors or distributed sensing approach and their integration to aeronautical structures. The development of a ribbon tape, carrying FBG sensors or a simple optical fiber, that is able to be co- or secondary bonded on the structure is one of the main achievements of this effort. Connection of several ribbon tapes in a single line (multiplexing) allows for the monitoring system to be sized according to the monitored part, while the nature of the ribbon tape and its integration method allow for repair of the ribbon and/or the structure itself. In addition to the above, partners have specifically developed a shape sensor, based on FBGs, that is able to monitor in real time the shape of the adaptive trailing edge of the wing. Based on these sensor types, the team designed, optimized, and integrated to the final demonstrators of SARISTU three different types of monitoring systems according to the main targets of this scenario. It should be noted that in order to achieve these goals, specific methodologies, static and dynamic, have been developed that are able to process and analyze the acquired data and to provide the user with the required feedback.

Four papers are included in this section that is related to the fiber optic-based monitoring systems. The first one is dedicated to the development of the ribbon

tapes, the shape sensors, and the required hardware to realize the above-mentioned monitoring systems, while the remaining three are dedicated to each different application target. Thus, the first of the remaining papers is dedicated to the methodologies developed (static and dynamic) and the design of the monitoring system for the damage detection in fuselage and wing structures, the second to the shape sensing of morphing structures (adaptive trailing edge) using FBGs, and the third to the load monitoring task of the internal loads of a wing box using fiber Bragg grating technology.

Ribbon Tapes, Shape Sensors, and Hardware

**Matthijs Bosboom, Martijn van Wijngaarden, Rolf Evenblij,
Paolo Bettini, Theodoros Loutas, Vassilis Kostopoulos,
Dimitrios Habas, Moshe Tur, Nahum Gorbato, Arik Bergman,
Uri Ben Simon, Iddo Kressel, Christos Koimtzoglou,
Monica Ciminello, Alexander Weisser and Christophe Paget**

Abstract For fiber optic sensors to be integrated in aerospace structures and for these sensors to provide data that can be used for structural health monitoring (SHM), development work has been performed in the SARISTU project. This particular chapter describes the inclusion of fiber optic sensors in a tape format, called ribbon tape, for damage detection and load monitoring with a secondary bonding procedure to install these in an aerospace structure. The ribbon tapes can be installed on composite structures either by co-bonding or secondary bonding techniques. Both procedures have been applied to composite coupons that have been tested in different environmental conditions. Moreover, a damaged tape repair

M. Bosboom (✉) · M. van Wijngaarden
KVE Composite Structures BV, Laan van Ypenburg 56, 2497, GB The Hague
The Netherlands
e-mail: bosboom@kve.nl

M. van Wijngaarden
e-mail: wijngaarden@kve.nl

M. van Wijngaarden
R&D, 2497, GB The Hague, The Netherlands

R. Evenblij
Aeronautics/Space and Automotive Testing, Technobis Fibre Technology,
Pyrietstraat 2, 1812, SC Alkmaar, The Netherlands
e-mail: rolf.evenblij@technobis.com

P. Bettini
Department of Aerospace Science and Technology, Politecnico di Milano,
Via La Masa, 34, 20156 Milan, Italy
e-mail: bettini@aero.polimi.it

T. Loutas · V. Kostopoulos
Department of Mechanical Engineering and Aeronautics, University of Patras,
Panepistimioupoli Patron 265 04, Greece
e-mail: loutas@mech.upatras.gr

V. Kostopoulos
e-mail: kostopoulos@mech.upatras.gr

procedure is developed. This chapter also describes the development of a fiber optic sensor to be used as a shape sensor inside a morphing aerospace structure to provide feedback on the structures shape. The hardware required to analyze and format the sensor readings for use in SHM is also provided in this chapter.

Nomenclature

AS0X	Application scenario nr in the SARISTU project
CTE	Coefficient of thermal expansion
DMI	Diamond microinterface
FBG	Fiber Bragg grating
FDM	Fused deposition modeling
FOS	Fiber optic sensor

D. Habas

Hellenic Aerospace Industry, Schimatari 320 09, Greece
e-mail: HABAS.Dimitrios@haicorp.com

M. Tur · N. Gorbatov · A. Bergman

School of Electrical Engineering, Tel-Aviv University, Tel-Aviv 6997801, Israel
e-mail: tur@post.tau.ac.il

N. Gorbatov

e-mail: gorbatov@eng.tau.ac.il

A. Bergman

e-mail: bergman.arik@gmail.com

U. Ben Simon · I. Kressel

Israel Aerospace Industries, Ben-Gurion Airport 70100 Israel
e-mail: ubensimon@iai.co.il

I. Kressel

e-mail: ikressel@iai.co.il

C. Koimtoglou

Integrated Aerospace Sciences Corporation—INASCO, Glyfada 16675, Greece
e-mail: c.koimtoglou@inasco.com

M. Ciminello

C.I.R.A. S.p.A. Centro Italiano Ricerche Aerospaziali,
Italian Aerospace Research Center, 81043 Capua, CE, Italy
e-mail: m.ciminello@cira.it

A. Weisser

Materials, Processes and Tests, AIRBUS Deutschland GmbH,
28199 Bremen, Germany
e-mail: Alexander.WEISSER@airbus.com

C. Paget

Materials and Processes Department, Airbus Operations Ltd, Bristol BS99 7AR, UK
e-mail: Christophe.Paget@airbus.com

FRP	Fiber-reinforced plastic
HDT	Heat deflection temperature
RT	Room temperature

1 Introduction

This document describes the design and manufacturing of both ribbon tapes and connector casing used in the AS04 work package.

SARISTU is a project subsidized by the European Union to enhance knowledge of Smart Intelligent Aircraft Structures. The project concerns the challenges posed by the physical integration of smart intelligent structural concepts. It addresses aircraft weight and operational cost reductions as well as an improvement in the flight profile-specific aerodynamic performance. One aspect of Smart Intelligent Aircraft Structures is applying active health monitoring of the structure using fiber optic sensors (FOSs).

Structures with embedded FOSs were proposed as early as 1989. But, twenty years later still faces significant challenges for monitoring aircraft structures: For fiber optic sensor manufacturing and characterization, there are commercial systems, and main limitations are brittleness, high cost, and certification issues. With regard to fiber Bragg grating (FBG) interrogation, conventional systems are commercially available and demonstrated in-flight tests. Integration of the sensing fibers into the structure is solved at laboratory scale, but the existing approaches are not robust enough to be used in industrial environments. Optical fiber ingress/egress from the laminate is a standing issue; miniature embeddable connectors are needed. In terms of methodology today, exploitation of the strain data is mostly done locally but not in a strain field for damage assessment. Therefore, dense sensor networks and new algorithms able to process the strain data from different points have to be developed in order to detect for example delamination caused by impacts. Looking at shape sensing, first attempts started in 2003. NASA launched in 2008 a program to develop and validate active shape control approaches.

A first goal for this project is to benefit from more than 10 years' experience by all partners to solve some of the standing issues, such as the robustness of the system, the embeddable connectors, and the reparability aspects. By doing the integration of the sensing network on real aeronautic structures, such as wing and fuselage stiffened panels, a maturation of the technology at system level will be achieved, together with a contribution to the qualification and certification requirements and to the standardization. It has to be pointed out that most of the foreseen works related to embedded FBGs have an added complexity for both, manufacturing and interpretation of the sensor response. Nevertheless, the approach of embedded optical fibers in terms of low cost manufacturing and robustness will be a step forward for the maturation of optical fibers for the targeted applications.

2 Ribbon Tape Development

2.1 Goal

The goal of the ribbon tape development was to design a supportive carrier for the optical fiber, which can be co-cured (initially secondary bonded) to the product to be monitored. In case the ribbon tape is damaged or needs to be removed due to a structural repair to the product, the ribbon tape needs to be easily removed and replaced.

2.2 Ribbon Tape Requirements

Several requirements are set up to define the boundary conditions for the design of the ribbon tape:

- Low cost production process, able to produce long tapes.
- Ribbon tape is used to attach the fiber optic sensor (FOS) to the structure to be monitored.
- Ribbon tape will protect the fiber optic sensor from handling and operational loads.
- Ribbon tape can be secondary bonded (co-curing for series production) to the structure.
- Initial structures are thermoset composites. Thermoplastic composite surfaces were taken into consideration, however, not developed within this project.
- The ribbon tape will not influence the structure it is attached to. Nor will it influence the measurement by the optical fiber.
- In case of co-curing, the ribbon tape and connector casing should be able to withstand the consolidation temperature (180 °C for 3 h) and pressure (7 bars) to form the structure.
- Ribbon tape needs to be removable from the structure in case of a repair to the structure or a damaged FOS.

2.3 Ribbon Tape Production Methods

Four ribbon tape production methods, based on a co-curing (prepreg) process, are considered:

1. Trapped rubber mold;
2. Compression molding;
3. Continues rolling process; and
4. Vacuum bag in autoclave/oven.

The concept ribbon tape is made out of 1 layer of prepreg and 1 layer of adhesive film, with the FOS between those two layers.

2.3.1 Trapped Rubber Mold

The first ribbon tape production method uses the difference of thermal expansion and hardness of the materials. The aluminum mold is heated by an oven or autoclave to the desired processing temperature. Since the CTE of the silicone rubber (340×10^{-6}) trapped inside the aluminum (23×10^{-6}) mold is a factor 15 higher pressure is therefore applied to the prepreg, consolidating it into a ribbon tape (Fig. 1).

The trapped rubber mold production method looked like a promising production method and was very easy to test. However, the hard mold damaged the fiber causing it to be unusable. Signal losses were measured that were out of tolerance (Fig. 2).

2.3.2 Compression Molding

The compression molding production method is based on the same principle as the trapped rubber principle, however, eliminating the rubber. The warm compression mold heats up the prepreg material and adhesive film under pressure. The melt temperature of the adhesive film is depended on the mold temperature (Fig. 3).

For the same reason as the trapped rubber production method, the compression mold principle is abandoned, since this will highly likely damage the FOS during the production process.

2.3.3 Continues Rolling Process

The production process is based on work rolls combining the prepreg material by heating and compression. The processing temperature depends on the materials selected. This principle has the same concerns on a hard metal mold pressing down on the fragile FOS. Next to that the initial setup cost to test this principle was out of

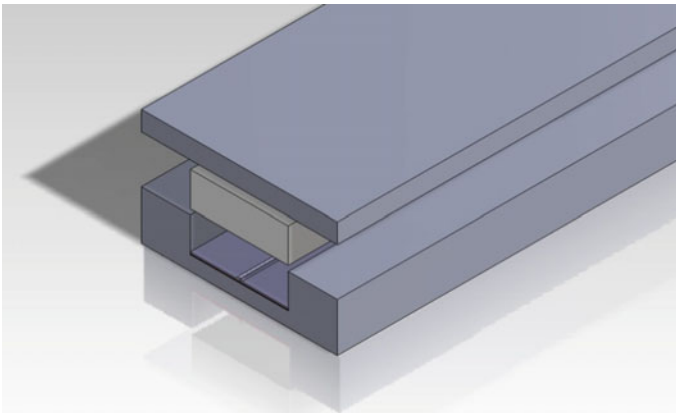


Fig. 1 Trapped rubber production process

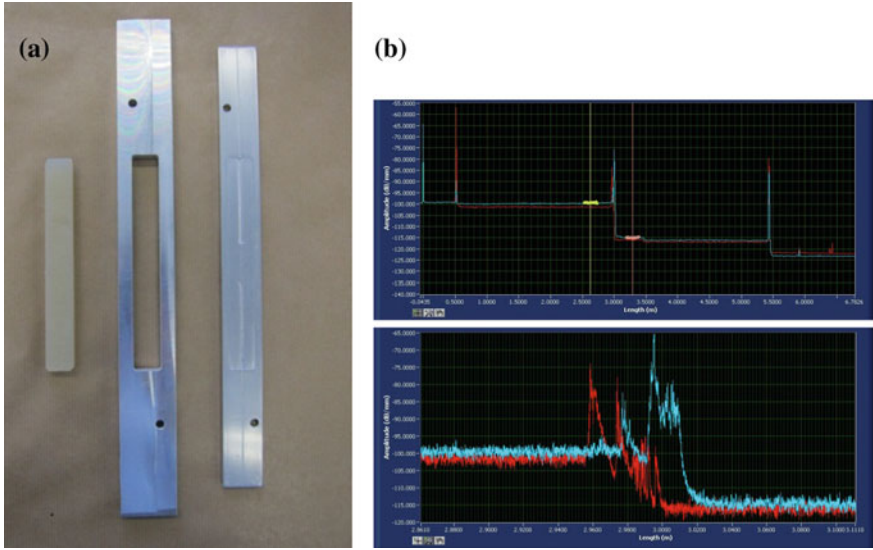


Fig. 2 Trapped rubber mold (a) and signal loss (b)

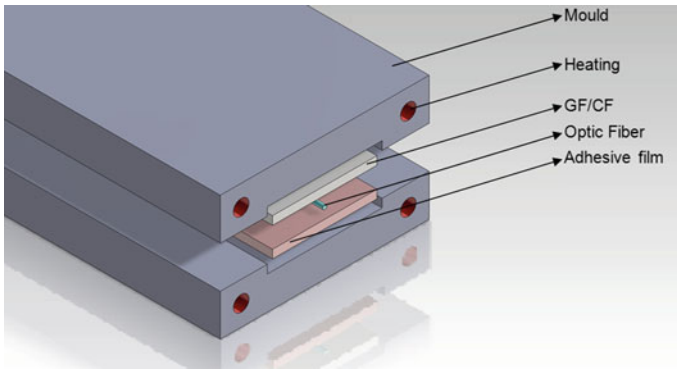


Fig. 3 Compressing molding production process

scope of this project. This principle can work well if the rollers are replaced by a soft(er) material in continuous production of vacuum bag-based ribbon tapes, as a preform process (Fig. 4).

2.3.4 Vacuum Bag in Autoclave/Oven

The fourth concept is based on using vacuum as compression method, in combination with an autoclave or oven. The ribbon tape is heated by the autoclave. With

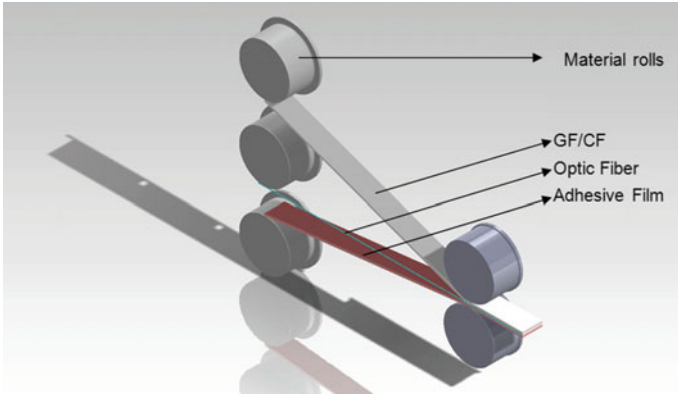


Fig. 4 Continuous rolling process

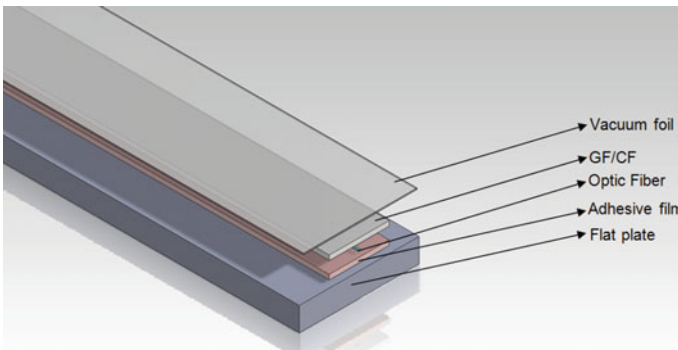


Fig. 5 Vacuum bag (prepreg) process

this production process, the ribbon tapes can be made to be secondary bonded or co-cured to the parent structure (Fig. 5).

Several ribbon tapes have been made by this principle and tested for signal losses. No signal losses were measured during investigation on the ribbon tapes produced by the vacuum processing method. For this reason, this production method is chosen and will be further investigated and optimized to suit the purpose of the ribbon tapes (Fig. 6).

2.4 Optimized Production Process

After production and testing of several ribbon tapes with the prepreg vacuum bag process, a number of improvements were made to the tapes. These improvements included the following:

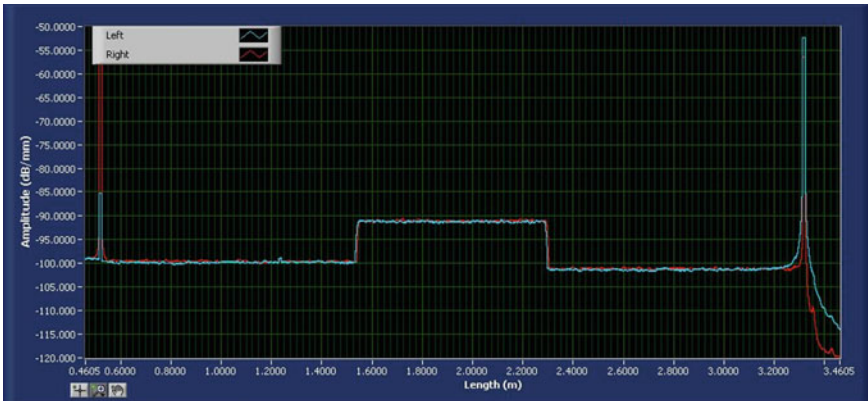


Fig. 6 Measurement of vacuum bag processed ribbon tape

- The width of the ribbon tape is optimized to 16 mm, since this fitted all the target mounting locations within the project.
- GFR prepreg is used both on top as underneath the FOS, instead of an adhesive tape on the bottom, since a GFRP layer will protect the FOS better.
- A peel-ply is used underneath the bottom layer to make it directly suitable for secondary bonding. Obviously, this is not applicable in case of co-bonding.
- Protection of the FOS at exiting locations from the cured prepreg, by adding PTFE tubing to the ribbon tape. The tubing will be embedded (~ 10 mm) into the ribbon tape prepreg and will function as a pull relief. This only needs to be used when no DMI connector casing is present.
- In case no connector casing is present and RT is used for secondary bonding:
 - Resin flow into the PTFE tubing caused the FOS to break, since the stress gradient became too large. The PTFE tubing is therefore closed-off by a fast setting flexible adhesive, 3M Scotch-Weld DP100, two-component epoxy adhesive.
 - The protective PTFE tubing has been cut to a taper ($\sim 10^\circ$) for a smooth stress gradient into the ribbon tape and be able to create a larger surface area for sealing-off the tubing by adhesive (Fig. 7).

2.5 Material Selection

The selected prepreg is an 80 and 160 °C curing toughened epoxy prepreg resin system from Cytec, called MTM49-3. The Cytec fabric code for the selected material is GF0100, which reverse to a readily available 300 gsm, 8ES weave. The resin weight of the selected prepreg is approximately 38 %. The resin system is both

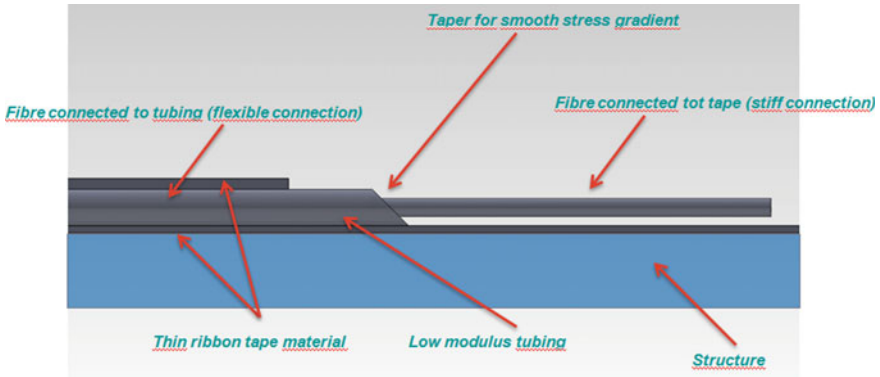


Fig. 7 Cross-sectional view of ribbon tape

autoclave and press curable and has a T_g of 190 °C. The high service temperature is chosen to be compatible with co-curing the ribbon tape onto the parent structure.

2.6 Ribbon Tape Removal Tests

During the life of an aircraft, it is likely that a component on which an FBG is installed will be damaged. To be able to monitor the repair and continues operation of the FBG network, it is essential that the ribbon tape is replaceable. Initial peel tests showed that the ribbon tape can be entirely removed from the structure. Whether is its con-cured of secondary bonded.

Within these initial tests, the flash breaker tape functioned like to be the designed connector casing. The development of the connector casing will be discussed in the following chapter. The connector casing protects the DMI connector during the production process of the ribbon tape, and afterward makes it possible to connect the sensor to the interrogation module (Fig. 8).

3 FORT Mounting Processes on a Composite Structure

Different viable technologies for integrating optical fibers into composite structures can be pursued. FO embedment during structural element production phases surely represents the most popular and appealing solution carrying the possibility of implementing a real from-the-cradle-to-the-grave monitoring strategy. Such an early integration allows us to investigate the buildup of residual thermo-elastic stresses, often responsible for damage onset and growth.

Questionable issues, mainly relating to the FO invasivity as well as to the reparability requirements of the monitoring system, make preferable the external

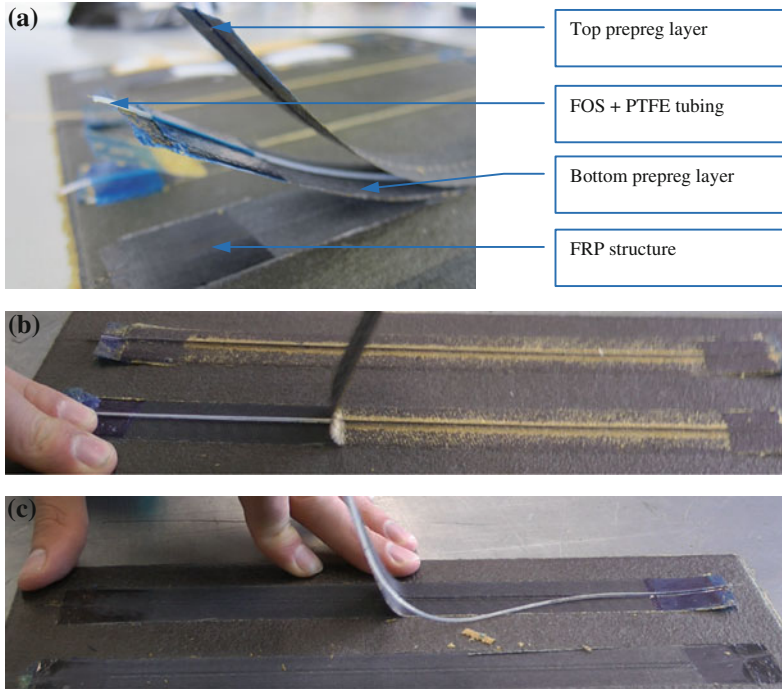


Fig. 8 Ribbon tape removal procedure: description of the assembly (a); removal of first (*top*) layer (b); removal of second (*bottom*) layer, including the FOS (c)

bonding. For such a solution, developed FORTs guarantee both FO protection and adequate bonding surface. Besides, being made of thin compliant glass fabric, they are also applicable to curved surfaces. In the following, two different developed bonding techniques for FORT are described.

The first one, named secondary bonding, consists in a simple procedure relying on low curing temperature paste adhesive according to standard bonding processes for composite adherends. In the second technique, named co-bonding, FORTs adhesion is granted by laminate uncured resin: No additional adhesive is required. As a consequence, both FORT materials and consumables must comply with (high) curing temperatures of composite part. However, even if more critical, the latter process guarantees higher strain transfer capability between monitored part and monitoring sensor.

Both the bonding techniques were developed for applying FORTs to carbon fibers-reinforced plates from which specimens for validation tests were cut (see Sect. 4).

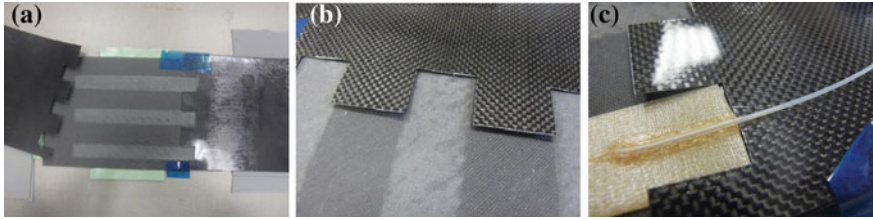


Fig. 9 Flexible caul plate developed for secondary bonding procedure: surface preparation only in selected areas (a); views of the mask profile for FORT positioning (b and c)

3.1 Secondary Bonding Procedure

FORTs can be bonded to the outer surface of composite laminates by means of low-temperature film or paste adhesives; vacuum bag and pressure pads can be used to guarantee a proper bonding pressure. Curing cycle of the adhesive can be performed in oven or by using electric heaters. Possible critical issues of this procedure refer to surface preparation, FOs protection, FORTs positioning, and adhesive amount optimization.

First, both mechanical and chemical adhesions of the adhesive layer have to be promoted on the adherends. In case of composites, a proper roughness is generally reached by applying peel-ply during curing process. In addition, wire netting pad was also applied to slightly roughing the surface of the carbon plates. Surface preparation was accomplished with the application of a Methylethylketone cleaner. The side of the laminate surface that does not process for surface preparation was covered as shown in Fig. 9a.

FOs exiting from the FORT must be protected during curing cycle avoiding any geometrical discontinuity along their path, which could lead to a dangerous shear state of stress due to manufacturing pressures. FOs breakage was avoided adopting a thin flexible caul plate able to bring out FOs from the laminate area avoiding discontinuities at laminate edges. A rubber pad with the same thickness of the laminate was put under the caul plate in order to obtain a better support. A special design of this caul plate granted also an easier and correct FORT positioning on the carbon plates as shown in Fig. 9b, c. The same figure highlights how the flexible caul plate can be put under FO without any problem thanks to its very low thickness.

FORTs were bonded on the surface of the carbon plates by means of Hysol EA9394; that is, a structural aerospace qualified adhesive paste which can be cured at room temperature. In order to determine the proper amount of adhesive, different quantities were tested on dummy ribbons. At the end, the quantity of 200 g/m^2 has guaranteed a uniform layer over all the bonding surface without a lot of excess of resin (case (b) in Fig. 10).

Curing cycle was performed in a vacuum-assisted oven with a vacuum level less than 500 mbar; an accelerated curing cycle was performed at $75 \text{ }^\circ\text{C}$ for 1 h which gives complete cure.

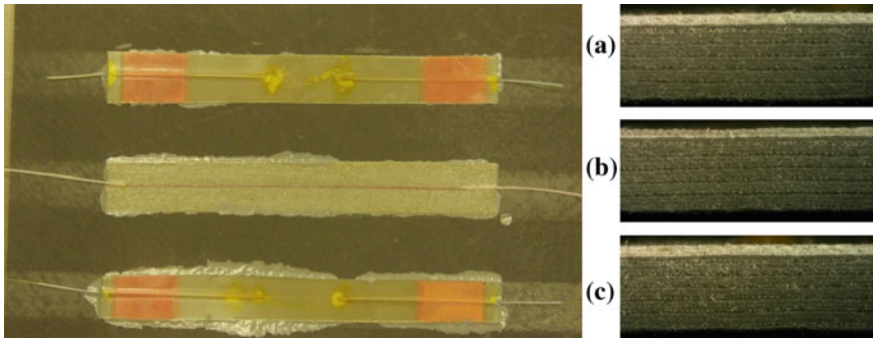


Fig. 10 Dummy ribbons bonded with different amount of adhesive: 150 g/m² (a); 200 g/m² (b); and 250 g/m² (c)

3.2 Co-Bonding Procedure

In the case of the co-bonding procedure, the FORT was placed on top of the uncured laminate and followed the same autoclave curing cycle of the carbon plate.

Adhesion of FORTs is granted by uncured resin in excess, no needing additional adhesive. Temperature compatibility of all materials used for FORT production as well as of consumables for FOs protection during curing process surely represents a problem to be overcome considering the high curing temperature (180 °C) and pressure (6 bar) of the prepreg adopted for carbon plate manufacturing.

Further difficulties may arise, consisting in FORT and FO tubing sinking into prepregs which may create undesirable indentations affecting the final laminate. Figure 11 shows deep signs on the laminate at the ribbon ends where FOs always failed during the technological evaluations. A thick layer of resin is visible on top of the ribbons (Fig. 11c).

As for the secondary bonding technique, special composite caul plates, with the half thickness of the FORT, were designed and produced in order to overcome these problems. After prepreg lamination over the mold is completed, peel-ply and

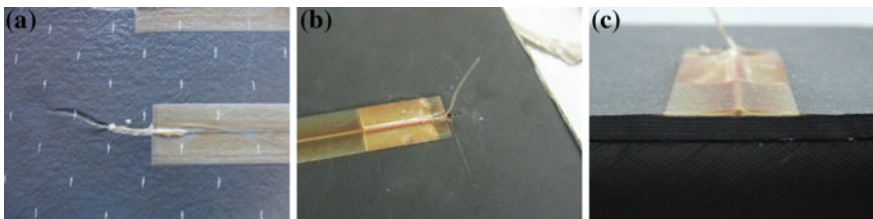


Fig. 11 Defects occurred in a nonoptimized co-bonding process: indentation of carbon laminate (a) FO breakage at the exit from FORT (b) and sinking of FORT into prepreg

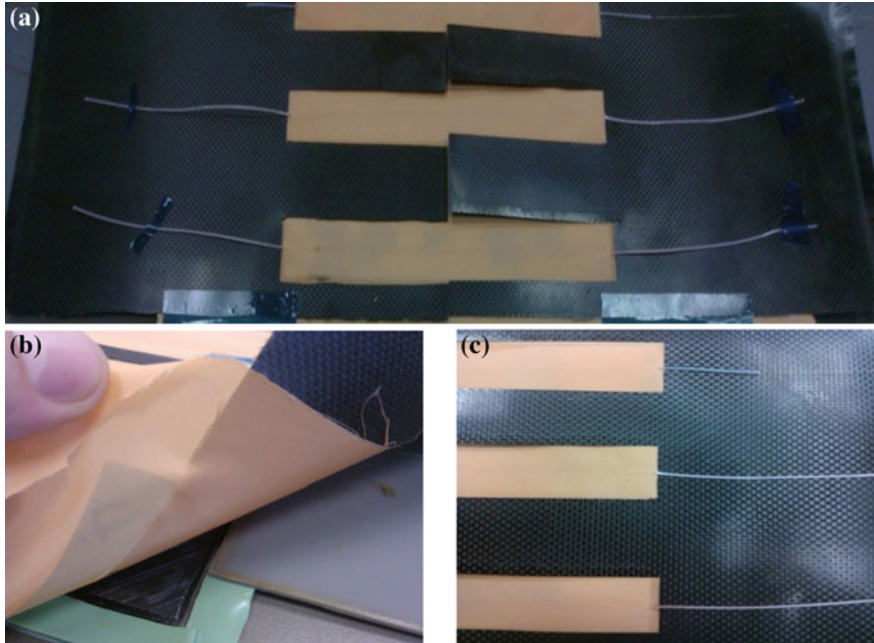


Fig. 12 Co-bonding technique: Flexible caul plate made of carbon fabric ($th = 0.2\text{ mm}$) (a); Peel-ply positioned on top of the FORT under the caul plate (b); caul plate used as mask for FORT positioning (c)

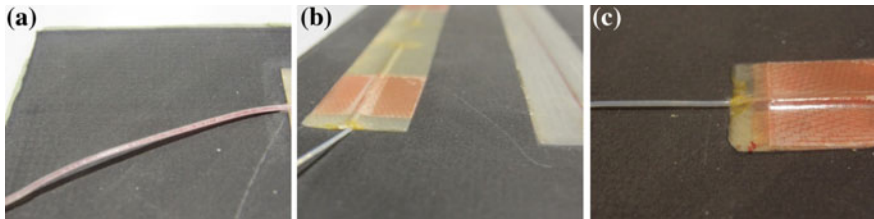


Fig. 13 FORT at the end of the developed co-bonding process: no visible indentations or FO breakage

FORTs are positioned on the laminate under caul plates. Peel-ply puncturing allows FO crossing. Some phases of the final setup of the procedure are reported in Fig. 12.

At the end of the process, a good protection of the FO was obtained without indentation and sinking on the laminate (see Fig. 13). The most delicate phase remains the passage of the FO through the peel-ply.

With reference to the setup shown in Fig. 14, the checklist of developed secondary bonding and co-bonding processes is summarized in Table 1.

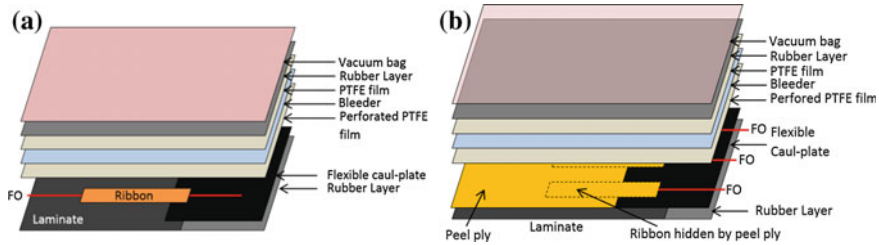


Fig. 14 Secondary bonding (a) and co-bonding (b) setup

Table 1 FORT mounting processes on a composite structure

Co-bonding process	Secondary bonding process
1. Laminate the carbon plies on the mold	1. Mark the ribbon position using adhesive tape on the laminate side where the FO exit
2. Mark on the peel-ply the exact ribbons position	2. Cover the side of the laminate surface that does not process for surface preparation
3. Hole the peel-ply for the passage of PTFE tubing	3. Use wire netting to slightly roughing the surface
4. Position the ribbons inserting PTFE tubing in the peel-ply holes	4. Use MEK to clean the laminate and the ribbon surface
5. Position the assembly (peel-ply + ribbons) on the laminate	5. Fix the laminate on the mold by using tacky tape
6. Insert the two flexible caul plates between peel-ply and FO (exiting from the holes) and apply a light pressure on the ribbons	6. Position rubber layers on the laminate side with FO
7. Apply the perforating PTFE film, bleeder, PTFE film, rubber layer, vacuum bag	7. Position the caul plate between the laminate/rubber and the FO and fix it
8. Apply the Cycom 977-2 curing cycle in autoclave	8. Remove all the adhesive tape
	9. Prepare the material for vacuum bag
	10. Preset the oven temperature at 75 °C
	11. Prepare the mixture of Hysol EA9394 (Part A 100, Part B 17)
	12. Spread a flat layer of the mixture on the ribbons surface
	13. Remove the excessive adhesive with spatula
	14. Fix the ribbons on the laminate and the FO on the mask by using adhesive tape
	15. Prepare the vacuum bag and apply the Hysol EA9394 curing cycle in oven

4 Reliability of FORTs for Strain Sensing in Composite Structures

4.1 Room Temperature Fatigue Tests

Three-point bending fatigue tests were scheduled in order to test the reliable long-term operation of the FORTs. The specimens were manufactured according to the ASTM D7264/D7264M-07 standard Test Method for Flexural Properties of Polymer Matrix Composite Materials. Carbon fiber-reinforced plates with dimensions of $300 \times 300 \text{ mm}^2$ were manufactured in-house via the autoclave technique, at a stacking sequence $[+45/-45/02/90/02/90/0/90/0]_s$ using unidirectional M21/34%/UD194/IM7-12k carbon fabric prepreg by Hexcel. Two plates were fabricated with a final average thickness of 4.09 mm.

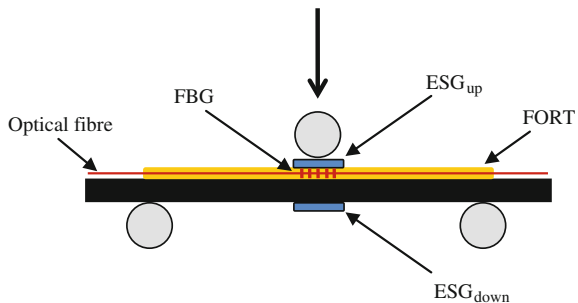
Two groups of coupons were cut at dimensions $400 \times 20 \text{ mm}^2$, and the first group was sensorized with FORTs via co-bonding and the other via the secondary bonding approach.

Single-mode optical fibers with polyimide coating were utilized and put inside the FORTs, with one FBG sensor of central wavelength at 1540 nm. The optical fiber has a core diameter of $9 \mu\text{m}$, cladding diameter of $125 \mu\text{m}$, and polyimide coating diameter up to $155 \mu\text{m}$, and the FBGs have a typical length of about 3–5 mm and were purchased by QPS Photonics Inc (Canada).

To mitigate the risk of optical fiber failure due to bending at the egress of the fiber from the FORT, special care was taken. A rubber layer surrounding the plate and an extra carbon fiber caul plate was used to ensure that the optical fiber will not fail or bend enough to jeopardize the proper light transmission (increasing too much the attenuation).

After having mounted the FORTs on the coupons, the next step was to attach electrical strain gauges (ESGs) to the specimens for comparison reasons and validation of the durability and proper function of the FBG sensor inside the FORT. The specimens were properly sanded and cleaned with acetone in the location where the ESG would be mounted for optimum adhesion. The ESG was placed on the upper layer of the FORT exactly on top of the FBG (ESG_{up} in Fig. 15). Model KFG-5-120-D16-11N30C2 of Kyowa was used. Two Kyowa DPM-611 B strain

Fig. 15 A schematic depiction of the positions of the FBG and the ESG



amplifiers were also used, as well as a National Instruments data acquisition board to record, digitize, and transfer the ESG measurements to LabVIEW. The sensors topology on a representative coupon is depicted schematically in Fig. 15. The distance of each sensor (FBG, ESG) from the specimen surface is measured and compensated for the correct and realistic interpretation of the measurement data. The loading nose has a special configuration so as not to exert load on the FORT in the area where the ESG is mounted.

The last step prior to test the coupons was to fusion splice the optical fiber with a pig-tail FC-APC connector in order to connect the FBG with a Micron Optics SM130 laser interrogator.

As mentioned above, the excess optical fiber length should be carefully placed and secured on the structure to avoid damage on the optical fiber during the autoclave process. Although this step looks easy for the given geometry, it can become extremely demanding for complex geometries and structures. On the other hand, the secondary bonded solution poses an ease of use. An issue of the procedure that can be improved is the amount and the uniformity of the adhesion layer. A system to provide a layer of uniform thickness and amount is under development. The use of adhesive in film form is also an interesting alternative. The greatest advantage of the secondary bonding approach is the ability to place FORTs anywhere upon the structure (even after manufacturing and assembly) offering thus the freedom and the versatility to design SHM tasks any time during the service life of the structure.

Upon the completion of the static and fatigue tests, a detailed analysis of the experimentally measured strain response was conducted and compared with strains obtained from analytical solution as well as FEA.

The data of the fatigue tests are presented in the form of graphs and of strain cycles during specific loading cycles.

Figure 16 depicts the strain measurements of the FBG and the ESG on a co-bonded coupon during the entire fatigue test. ESG values in Fig. 16 are not corrected for height difference and this explains why they are about 10 % higher compared to the FBG readings. The superiority of the FBG readings and of the

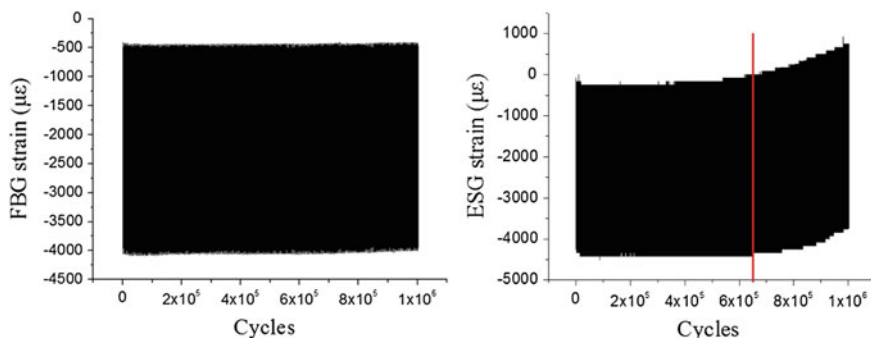
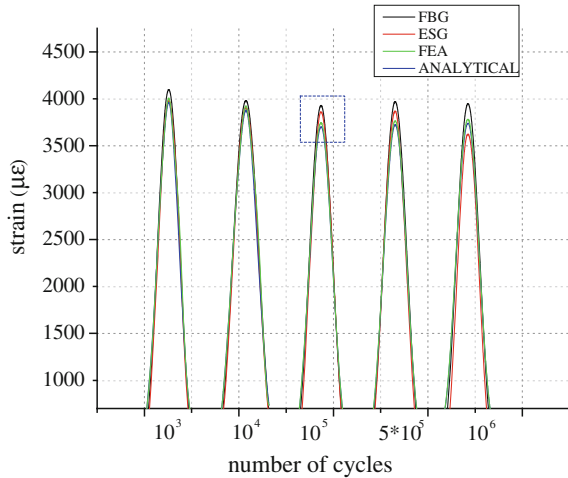


Fig. 16 Strain measurements during fatigue loading for the FBG and the ESG

Fig. 17 The secondarily bonded coupon’s strain response as recorded by all sensors and calculated analytically and with FEA



FORT operation in total is manifested via their stability and repeatability. The ESG on the contrary works properly up to ~640 kcycles when its values begin to deviate. Probably, the adhesion of the ESG to the surface of the FORT where it is mounted is compromised. The ESGs tended to de-bond from the coupon surface after approximately 600,000 cycles. This happened for 8 out of 10 tested coupons with a random pattern on the ESG “failure” cycle.

In Figs. 17 and 19, comprehensive graphs of the progress of the strain monitoring during fatigue test for the secondary bonded and the co-bonded FORT mounting technique are presented, respectively. Cycles 10^3 , 10^4 , 10^5 , 5×10^5 , and 10^6 were selected as a representative sample, analyzed, and presented. The evolution of the experimental (FBG and corrected ESG) as well as the theoretically and numerically calculated strain values is depicted. In order to assess how the FBG value is compared to ESG, theoretical, and FEA values, the root-mean-square deviation (RMSD) for the selected cycles is calculated and presented in Tables 2 and 3. For the calculation of the RMSD value, the following equation was utilized.

$$RMSD = \sqrt{\frac{\sum(x_i - y_i)^2}{\sum y_i^2}}$$

As shown in Table 2, the root-mean-square deviation between the FBG strain measurement and strain either measured using ESG or calculated remains well below 7 %. The large deviation of 15 % between FBG and ESG after 10^6 cycles is due to the ESG detachment from the coupon surface.

Zooming at the top of strain graphs during the 10^5 cycle (Fig. 18) provides a clearer view of the various measurements and numerical/analytical calculations. The deviation of the FBG value to the ESG (corrected value to compensate for the height difference between the two gauges) is a mere 2 % with the FE as well as the

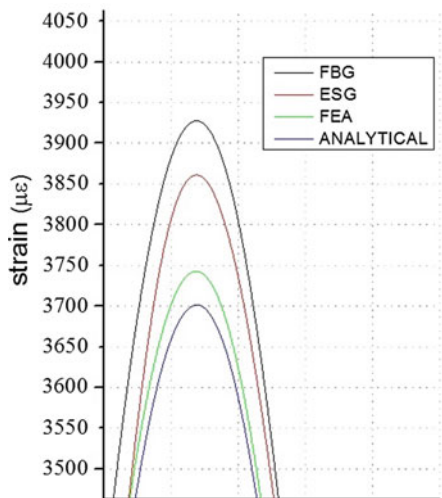
Table 2 RMSD between FBG and other values for all the cycles of secondarily bonded coupons

FBG versus ESG		FBG versus analytical		FBG versus FEA	
Cycle	RMSD %	Cycle	RMSD %	Cycle	RMSD %
10^3	4.98	10^3	5.99	10^3	4.82
10^4	3.39	10^4	5.13	10^4	3.59
10^5	5.35	10^5	6.21	10^5	5.41
5×10^4	5.74	5×10^4	6.36	5×10^4	5.44
10^6	15.13	10^6	6.62	10^6	6.24

Table 3 RMSD between FBG and other values for all the cycles of co-bonded coupons

FBG versus ESG		FBG versus analytical		FBG versus FEA	
Cycle	RMSD (%)	Cycle	RMSD %	Cycle	RMSD %
10^3	5.02	10^3	5.84	10^3	4.78
10^4	3.32	10^4	5.45	10^4	3.45
10^5	5.39	10^5	6.12	10^5	5.12
5×10^4	5.48	5×10^4	6.03	$5 \cdot 10^4$	5.31
10^6	19.75	10^6	6.54	10^6	6.17

Fig. 18 A zoom in the top of the 10^5 cycle



analytical value to deviate up to $\sim 6\%$, obviously due to the assumptions made in each case.

Similar behavior was observed for the co-bonded FORTs as demonstrated in Fig. 19. The problem of the ESG de-bonding is observed on the co-bonded coupons as well. In Table 3, the low RMSD values prove the reliable FORT operation in contrast to ESGs which seem to “fail” after a certain operational period.

Fig. 19 The co-bonded coupon’s strain response as recorded by all sensors and calculated analytically and with FEA (please refer to the online version for a colored version of the figure)

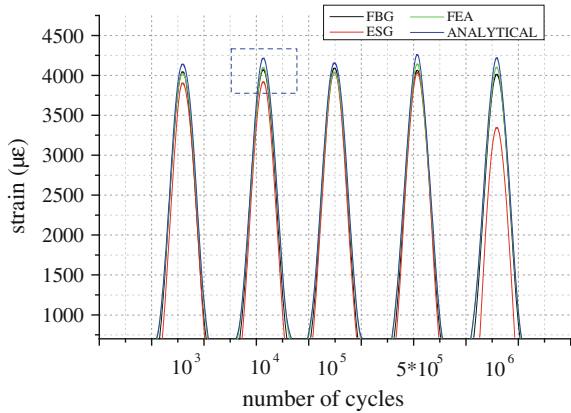
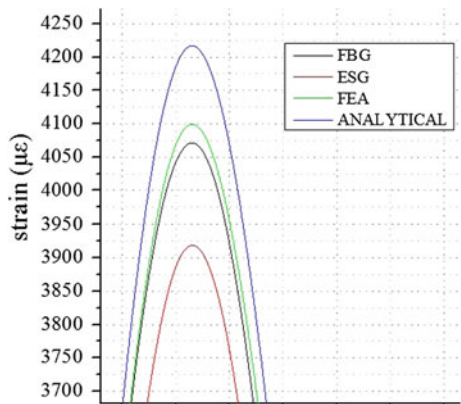


Fig. 20 A zoom in the top of the 10^4 cycle (please refer to the online version for a colored version of the figure)



Exemplary, a zoom in the top of the 10^4 cycle gives in Fig. 20 a clearer view of the various measurements and numerical/analytical calculations. The deviation of the FBG value to the ESG (corrected value to compensate for the height difference between the two gauges) is only 4 % with the analytical value deviating up to ~ 4 %.

4.2 High- and Low-Temperature Fatigue Tests

Reliable long-term operation of the FORTs was tested also at high- and low-temperature conditions. Three-point bending fatigue tests were scheduled in accordance with the ASTM D7264/D7264M-07 previously adopted for manufacturing and testing at room temperature. In detail, specimens were manufactured with the same material and stacking sequence as well as the FORTs was mounted following both the developed processes described in Sect. 3 (Fig. 21).

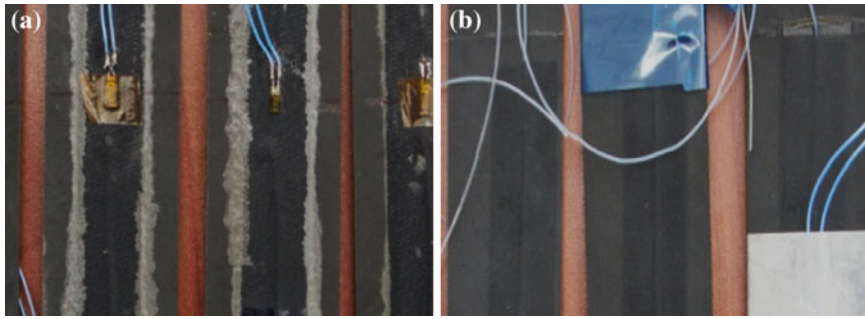


Fig. 21 Specimens for fatigue tests at controlled temperature: secondary bonding process (a) and co-bonding process (b)

Table 4 Specimens characteristics for high- and low-temperature fatigue tests

ID	Thickness (mm)		Width (mm)	Bonding procedure	Testing temperature (°C)	
	Specimens	Ribbon + Hysol ^a			Planned	Accomplished
410-408	4.26	0.60	40.20	Secondary bonding	100	100
410-409	4.35	0.60	40.03	Secondary bonding	100	100
410-407	4.25	0.55	40.20	Secondary bonding	-50	RT
415-423	4.34	0.54	40.25	Secondary bonding	-50	RT
415-422	4.37	0.59	40.22	Secondary bonding	100	100/-50
410-401	4.40	0.59	40.13	Secondary bonding	-50	-50
411-401	4.07	0.51	40.45	Co-bonding	100	100
411-402	4.02	0.48	40.14	Co-bonding	100	100
410-404	4.03	0.50	40.14	Co-bonding	-50	-50
415-431	4.04	0.57	40.00	Co-bonding	-50	-50
410-402	4.04	0.50	40.13	Co-bonding	100	Not tested
410-405	4.00	0.53	36.96	Co-bonding	-50	Not tested

^aOnly for the secondary bonding specimens

Fatigue tests were done at controlled temperatures of +100 and -50 °C. Specimens characteristics and testing conditions are summarized in Table 4.

Specimens were preliminary checked through RT static tests until a displacement corresponding to about -4000 $\mu\epsilon$ on the FBG. As it can be seen from the table, some planned tests were not carried out due to a FO breakage or FORT misalignment.

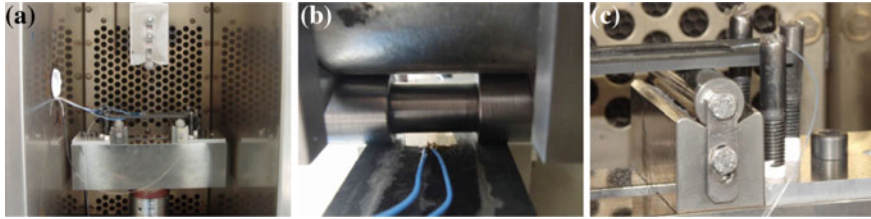


Fig. 22 Test equipment for high/low- temperature fatigue tests: view of the setup in the environmental chamber of the MTS machine (a); particular of loading nose (b) and pins to avoid specimen misalignment (c)

Two specimens produced by secondary bonding process were tested at RT in consequence of a sensors/ribbons malfunctioning occurred at planned low temperature.

Figure 22 shows the MTS[®] Testing Machine endowed with a temperature-controlled chamber used for the tests, which were performed in displacement control. The loading nose was centered between the outer support rollers and was provided with a groove in the central part of the cylinder in order to apply the loading pressure at the lateral edges of the specimen, without interfering with the central ribbon. The outer span between the support rollers was set at 128 mm. The standard fixture was integrated with lateral pins at both specimen ends in order to avoid undesired displacements during fatigue tests (Fig. 22c).

The optical fibers data acquisition system was integrated with a thermocouple, used to monitor the operating temperature as well as with strain gauges.

In particular, in addition to the strain gauge placed on the upper layer of the FORT and co-located with the FBG (ESG_{up}), a second ESG was attached on the lower surface of each specimen in back-to-back configuration (ESG_{down}), as shown in Fig. 15, in order to control the ribbon bonding quality.

After the test temperature was reached, fatigue tests up to 100,000 cycles were performed at the same maximum displacement level reached during preliminary RT static tests. Stress ratio $R = 0.1$ and frequency of 1.5 Hz were set. Static tests were run at 10/100/1000/10,000/100,000 cycles to check proper FORT working.

Experimental results obtained from a specimen produced by secondary bonding procedure are reported in Figs. 23 and 24.

The curves refer to deformation versus displacement measured by the FBG sensor and the strain gauges. Linear trends of all the deformation measurements with the displacement were obtained.

The same behavior was recorded during static tests at the beginning and at the end of the fatigue cycles demonstrating any effect of combined mechanical and thermal loading on the developed strain monitoring system occurred.

A synthetic representation of the results is reported in Fig. 24. FBG sensor values are compared with the expected ones, estimated by assuming the sensor position at 2/3 of the ribbon thickness including Hysol layer. For this specimen, the displacement imposed to achieve $-4000 \mu\epsilon$ on the FBG was equal to 2.6 mm. The

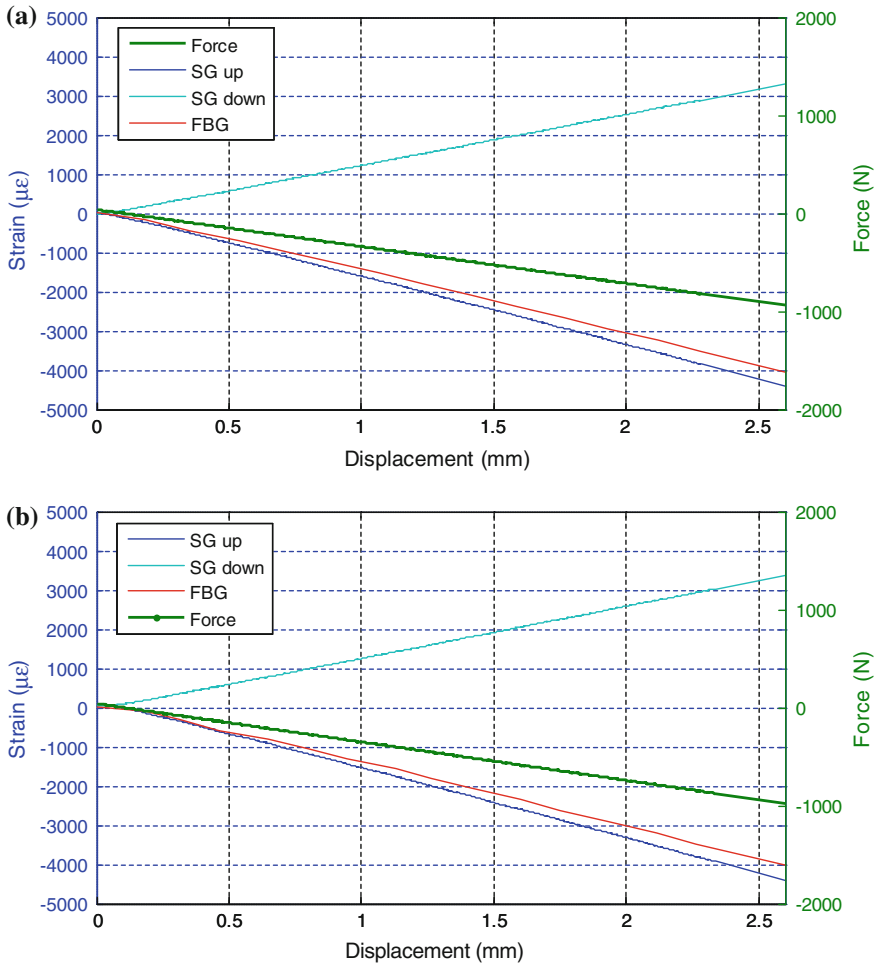


Fig. 23 The secondarily bonded coupons response during static tests performed at 100 °C after 0 cycles (a) and 100,000 cycles (b)

absolute value of the upper strain gauge was higher than the one of the lower strain gauges, as it can be expected from beam theory, considering that the upper strain gauge was applied at a distance of 0.6 mm from the specimen surface, corresponding to 30 % of the specimen semi-thickness.

The expected FBG values are very close to the FBGs measurements. This confirmed that sensor measurements were in agreement with a linear strain profile through the thickness.

As for secondary bonding, Figs. 25 and 26 report the results obtained from a specimen produced by co-bonding procedure. The displacement imposed to achieve $-4000 \mu\epsilon$ on the FBG sensor was equal to 2.8 mm.

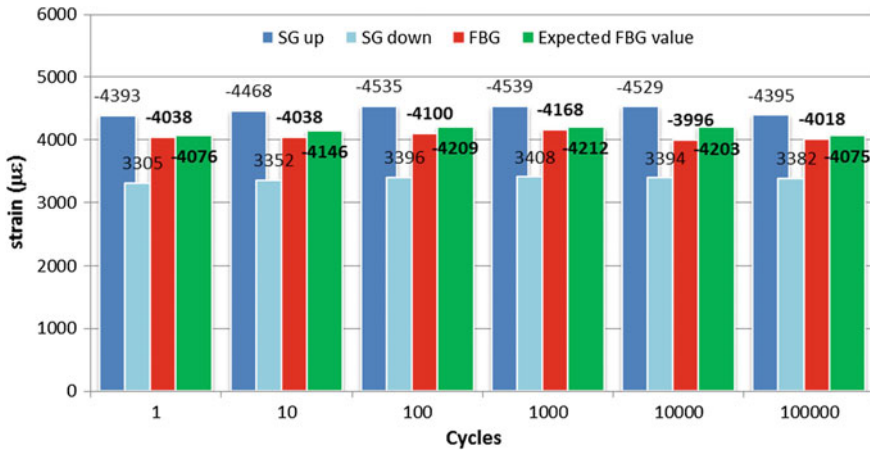


Fig. 24 Maximum strain measurements during static tests performed on a secondarily bonded coupon

Linear trends of all the strain measures with the displacement were obtained and the expected FBG values are very close to the FBGs measurements. It can be observed that the difference between the absolute values of the two strain gauges in back-to-back configuration is lower than in the case of secondary bonding tests. Such variation can be attributed to the absence of the adhesive layer. The behavior of the signals after the fatigue cycles did not show any significant variation with respect to the initial preliminary static test at 100 °C. One of the two strain gauges failed before the last fatigue cycle.

For the ribbons applied with secondary bonding procedure, the behavior of the sensor system during tests proved to be substantially unaffected by fatigue within the considered strain range and 100,000 cycles, all performed in harsh environmental conditions. The response provided by the two strain gauges applied in back-to-back configuration indicated that no significant alteration in strain transfer mechanism from the specimen to the ribbon was experienced during testing. Unfortunately, several strain gauges failed between 10,000 and 100,000 cycles. On the other hand, the strain measured by FBGs always remained constant in all the fatigue test performed as well as the difference between the measured strain and the value derived by applying beam theory to strain gauge data.

In the case of co-bonded ribbons, all the 4 specimens available for testing provided good results, both in high- and low-temperature conditions. No variations were observed in the measures taken at intermediate static acquisition up to 100,000 cycles. Discrepancies between expected and measured values were recorded and can be attributed to the uncertainties in the position of the sensor inside the ribbon. However, such discrepancies did not vary after the application of fatigue cycles, thus indicating that no inelastic mechanisms were activated at the interface between the ribbon and the composite specimen and at the interface between the ribbon layers and the optical fiber.

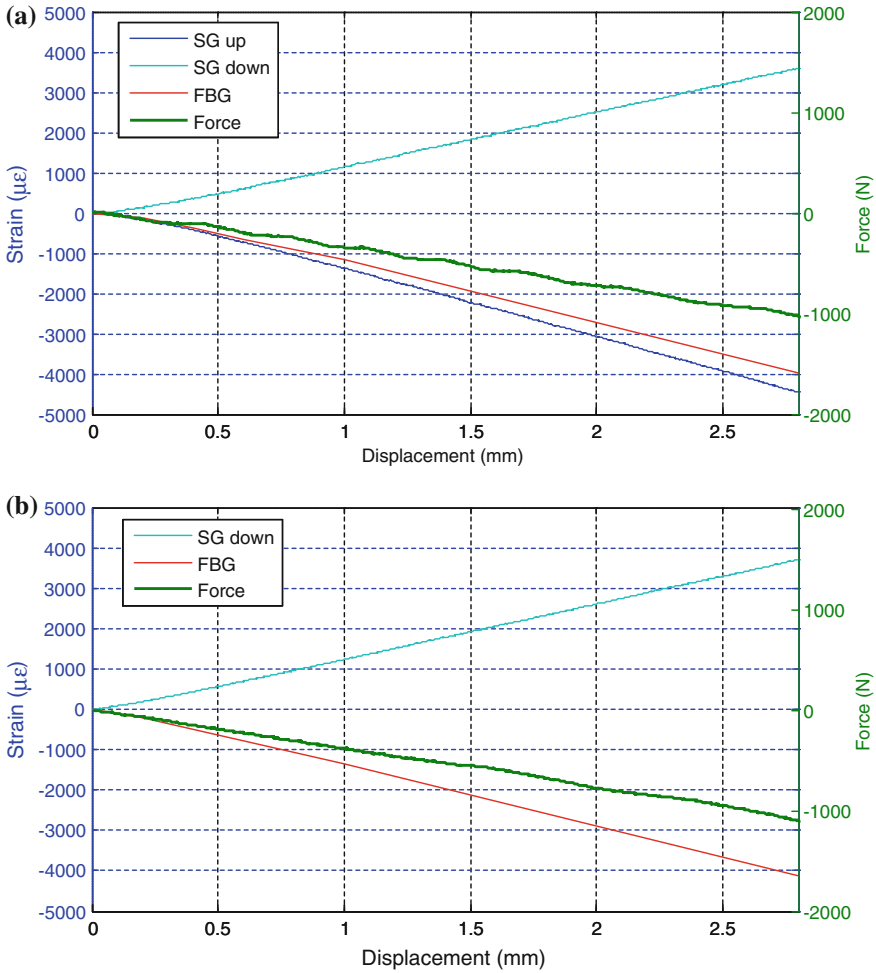


Fig. 25 The co-bonded coupon response during static tests performed at 100 °C after 0 cycles (a) and 100,000 cycles (b)

5 Connector Casing Development

5.1 Goal

The goal of this work package is to design a ribbon tape equipped with a robust connector casing that can be used industrially and on a large scale.

If an FOS malfunctions, it needs to be removed easily, so a new ribbon tape can be placed to continue the structural health monitoring (SHM). Integration of this repair functionality in the ribbon tape is desirable.

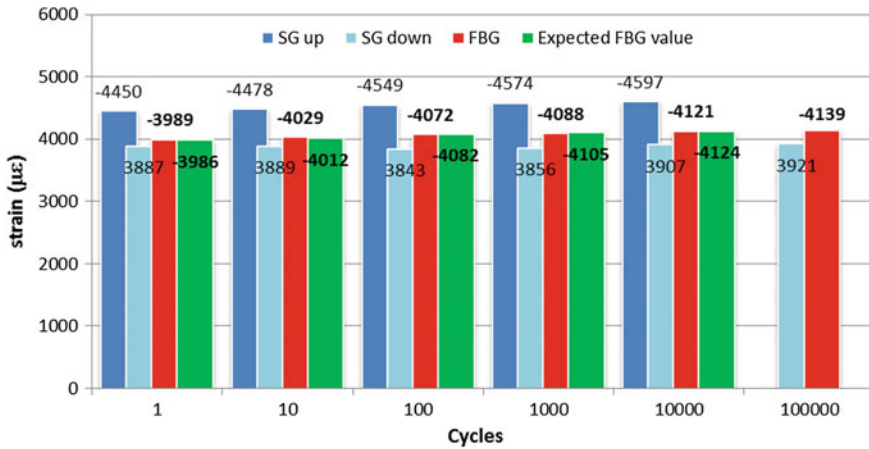


Fig. 26 Maximum strain measurements during static tests performed on a secondarily bonded coupon

5.2 Connector Casing Requirements

There are a few design requirements that need to be fulfilled regarding the processing of the connector casing in the ribbon tape:

- The connector casing needs to be able to handle a processing temperature of 180 °C and 7 bars (6 bar pressure + 1 bar vacuum) of pressure for a period of 3 h, which corresponds to the cure cycle of panels/stringers and co-bonding of the reinforcement stringers.
- The connector casing should be approximately the same width as the tape (16 mm) and long enough to safely house the DMI connector.
- The connector casing should be as flat as possible and rigid enough to accidentally step on it.
- Adhesively bondable to a FRP structure.

The selection criteria for the connector casing material are the following:

- Mechanically stable at elevated temperatures, HDT preferably >180 °C.
- Chemical resistant, though bondable to FRP structures.
- Preferably low-cost material.
- Electrically insulating.
- In the selection procedure, materials are selected which are preferably available in multiple forms, such as sheet, 3D printing by fused deposition modeling (FDM), and injection molding.

5.3 Material Selection

During a short literature study, there are multiple suitable materials selected for the connector casing. In the table below the selected materials suitable for the connector casing are listed with the characteristic features and heat deflection temperature (HDT) of the material.

Material	Material features		HDT (°C)	Remarks
PAI <i>Polyamide imide</i>	+	Extremely low coefficient of linear expansion	260–280	Not suitable for FDM
	+	Resistant to gamma- and X-rays		
	+	Excellent UV resistance		
	+	Excellent wear resistance and low friction		
	+	High dimensional stability at high thermal loads		
PEEK <i>Polyetheretherketon</i>	+	Very high maximum operating temperature	160 ^a –295	PEEK-HP3 for FDM technique
	+	Self-extinguishing		
	+	Excellent chemical and hydrolysis resistance		
	+	Suitable for high purity environments, sterilizable		
	+	High dimensional stability and suitable for close tolerances		
	–	High processing temperatures		
	–	Cost		
–	Anisotropic			
PEI (Amorph) <i>Polyetherimide</i>	+	Continuous use temperature of 180 °C	153 ^a –205	ULTEM* 9085 for FDM technique
	+	Excellent flame resistance		
	+	Good thermal and mechanical properties (slight reduction of mech. Properties to 250 °C)		
	+	Excellent electrical insulating		
	–	Cost		
PES (Amorph) <i>Polyethersulfone</i>	+	High temperature performance	203	Suitable for injection molding
	+	Dimensional stability		
	+	Inherently flame retardant		
	–	Chemical resistance		
	–	High process temperatures		
	–	Cost		
PPS (Amorph)	+	Dimensionally stable	174	

(continued)

(continued)

Material	Material features		HDT (°C)	Remarks
<i>Polyphenyleensulfide</i>	+	High mech. strength, stiffness and low coefficient of friction		Not suitable for FDM
	+/-	Excellent chemical resistance makes it difficult to bond		
	+	Good electrical and thermal insulator		
	+	Very high operating temperature		
	-	Brittleness		
	-	Cost		
PPSU (Amorph) <i>Polyphenylsulfon</i>	+	Excellent resistance to hydrolysis	189–207	–
	+	Virtually unlimited (steam) sterilized		
	+	Resistant to gamma- and X-rays		
	+	High toughness also at low temperatures		
PSU (Amorph) <i>Polysulfon</i>	+	High thermal oxidative stability	175	Not suitable for FDM
	+	Good hydrolysis resistance, sterilizable		
	+	Withstands microwave, X- and gamma rays		
	+	Very good creep resistance and stiffness over wide temperature		
	+	Good electricals		
	+	Self-extinguishing		
	-	Poor solvent resistance		
-	Processing difficulties			

^aLower temperature 3D printing variants

5.3.1 Material Trade-off

PEEK and PAI were preferred due to their high thermal resistance; however, the cost of these materials are far too high for this application and function of the connector casing.

PPS on the other hand is very difficult to bond, which require special pre-treatments, such as plasma or corona treatment/Etch in sodium dichromate-sulfuric acid solution. The HDT of PPS is at the edge of the material requirement, similar for PSU, therefore, these materials are ruled out for further investigation. Remaining materials, which are PPSU, PES, and PEI, suitable for the connector casing assembly have been further investigated. For PES, no 3D printing

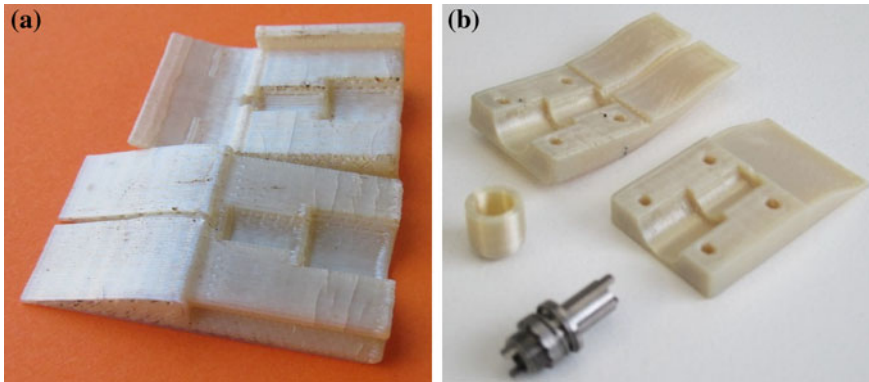


Fig. 27 3D-printed connector casing prototypes, *left* PPSU first prototype and *right* PEI second prototype

material could be allocated; therefore, this material is abandoned for further prototype investigation; however, if the connector casings will be machined or injection molded at a later stage, PES is a good alternative material.

PPSU, PES, and PEI are all amorphous of nature and have no sharp melting point; instead, amorphous materials soften gradually as the temperature rises, which helps to remain a rigid structure during high processing temperatures and temperature loads.

The first prototype connector casing was 3D printed using the PPSU material, which is available in all specified forms. The connector casings were 3D printed to check the functionality of the casing. Machining of the connector casing is interested for semi-large quantities, eventually the connector casings should be injection molded to reduce production cost.

The second prototype connector casing was also 3D printed using PEI (ULTEM* 9085), since it seemed like a more cost-effective option; however, the price difference between PPSU and PEI was little. The PPSU material had slightly elevated performance toward PEI; however, when comparing unfilled materials, PPSU has a higher impact strength (Fig. 27).

Within the SARISTU project, approximately 50 connector casings need to be produced, which makes injection molding far too expensive (>50 k nonrecurring cost, for the production mold) and 3D printing quality is not very accurate. Therefore, it is decided to machine the first 50 sets on a CNC milling machine.

5.3.2 Processing Tests

The 3D-printed ULTEM* 9085 (PEI, second prototype) connector casing was tested on mechanical stability at elevated temperature (180 °C for 3 h) and pressure (7 bars) in an autoclave. In the figures below, a pigtail with fully assembled connector casing is shown, before autoclave processing (Fig. 28).

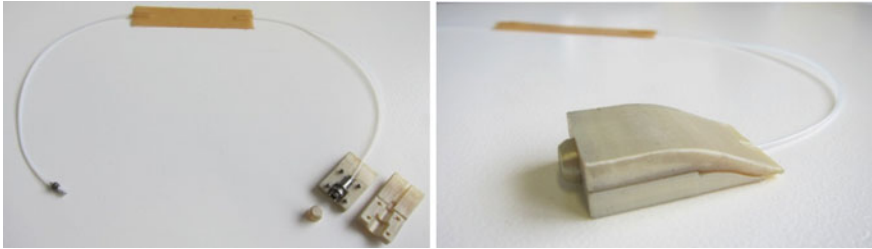


Fig. 28 3D-printed ULTEM* 9085 connector casing assy

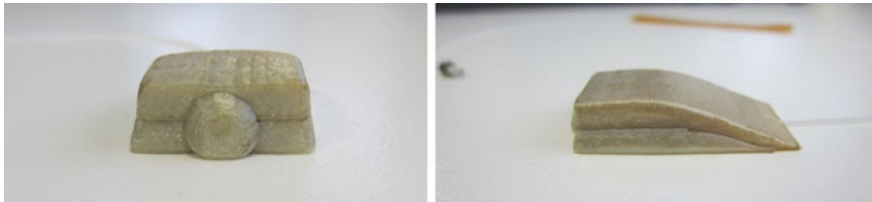


Fig. 29 Deformed PEI connector casing

The ULTEM* 9085 is NOT suitable for this high temperature combined with 7 bars of pressure. So, this material cannot be used neither for the connector casing nor for the direct bonding to the structure, see figures below for result after processing in the autoclave. The commercial available PEI in the form of sheet/rod has a much higher HDT, 205 °C instead of 153 °C for FDM material, and could therefore be perfectly suitable for these processing conditions (Fig. 29).

5.4 Connector Casing Design

The connector casing is specially designed to house a DMI connector. The current design is partially based on the first prototype design of the connector casing and additionally some new insights are integrated. Now the repair principle is integrated and the fitting of the DMI connector is optimized. In the figure below, the total ribbon tape assembly is shown, including the connector casing (Fig. 30).

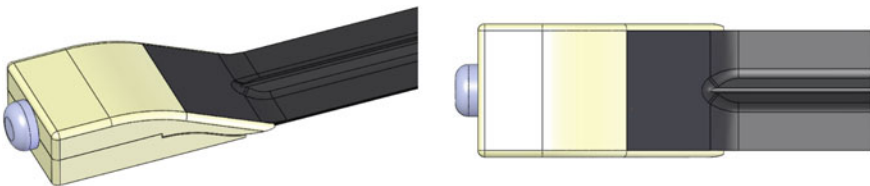


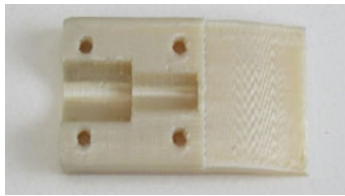
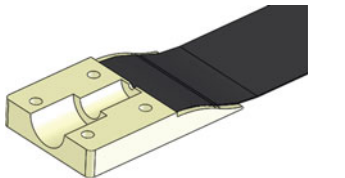
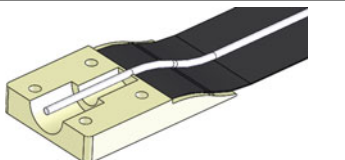
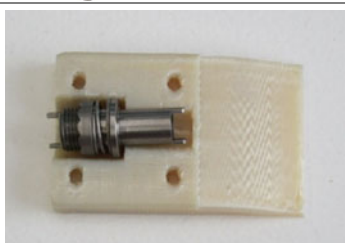
Fig. 30 3D CAD design connector casing

The connector casing consists of the following three parts:

Part	Use
Bottom	Alignment of DMI connector and lower prepreg layer
Top	Close-off the connector casing and protect the DMI connector
Cap	Additional close-off cap is designed, which will only be used to protect the DMI connector during processing in the autoclave


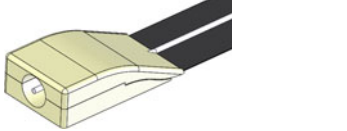

5.4.1 Assembly Procedure Connector Casing

In the steps below, the production sequence of the connector casing is described.

	<p>Place the lower half of the connector casing on top of the peel-ply. Make sure the 4 dowel pins ($\text{Ø}2 \times 5 \text{ mm}$) are placed in the designated holes. Not shown in the figure</p> <p>The bottom of the connector casing should be abraded (grain 80 or 100) before placing it on the peel-ply</p> <p>In the final design these dowel pins are replaced by integrated pins, into the upper connector casing half</p>
	<p>Place the bottom prepreg layer on top ($\sim 20 \text{ mm}$) of the lower half of the connector casing. Make sure it is not bridging near the mold surface. This can cause the FOS to break when pressure is applied during cure</p>
	<p>Place the optic fiber + PTFE tubing in the middle of the ribbon tape and make sure it is not bridging</p> <p>The DMI connector should be attached in this stage. Not shown in the figure</p>
	<p>Connect the DMI connector to the fiber (if not already done) and position the connector in the cavity of the lower connector casing</p>

(continued)

(continued)

	<p>Apply the close-off cap onto the DMI connector, to protect the connector during processing in the autoclave. This protective cap will be removed after processing</p>
	<p>Apply the upper half of the connector casing on the 4 dowel pins. Be careful not to crush the FOS nor the PTFE tubing. The FOS should be in aligned in the middle of the connector casing</p>
	<p>Apply the top prepreg layer on top of the upper connector casing (~20 mm). Make sure it is not bridging. Make sure the prepreg is not placed completely toward the front of the connector casing, since this will cause resin to flow into the front of the casing and thereby increasing the possibility of resin flowing into the DMI connector</p>

5.5 Ribbon Tape Repair Principle

The repair principle, e.g., easily removing of the ribbon tape is integrated in the design of the connector casing. This is done by making an initiation point to peel-off the ribbon tape. For testing the principle, the PPSU prototype connector casing was used.

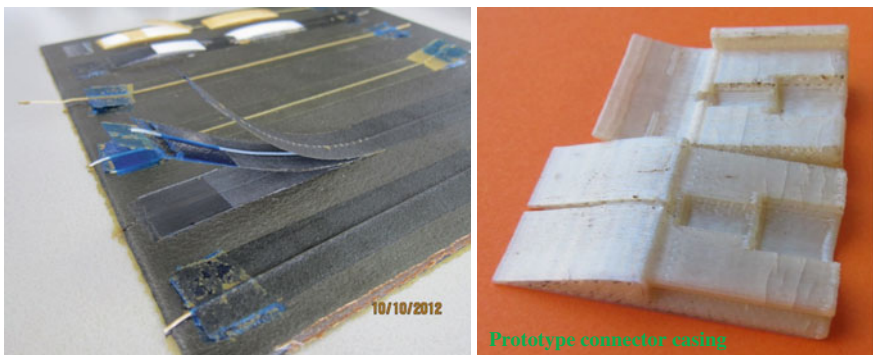


Fig. 31 Repair principle (left), prototype connector casing (right)

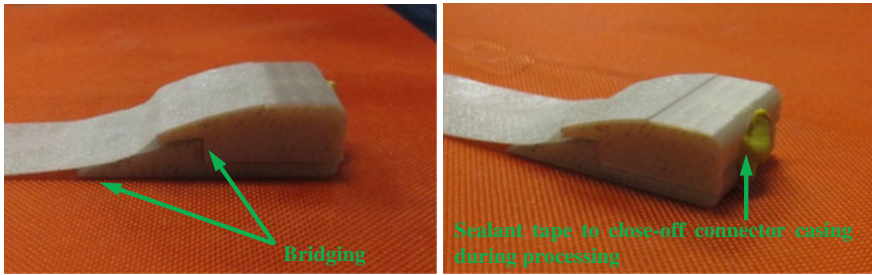


Fig. 32 Connector casing integrated in ribbon tape

The repair principle is based on the principle shown in the figure left below. Only now the connector casing itself is used instead of flash tapes for peel-off initiation. The prototype connector casing is slightly modified to accommodate the repair principle test (Fig. 31).

The figures below show the assembled ribbon tape with the PPSU prototype connector casing. This connector casing design was not fully suitable for the repair principle, since bridging occurred at the transition areas, from casing to peel-ply. After production of the prototype tape, the ribbon will be bonded to a structure, to test the functioning of the peel-off (Fig. 32).

5.5.1 Secondary Bonding of Ribbon Tape

The prototype ribbon tape is bonded, following the prescribed secondary bonding procedure, to a thin stringer made within the AS07 work package. The ribbon tape is bonded with a two-component structural epoxy paste adhesive, Hysol EA 9394. The only differences in the bonding procedure is that an oven is used to cure the adhesive instead of the prescribed heat blankets and the vacuum level was a little higher, 700 mbar instead of the prescribed 500 mbar (Fig. 33).

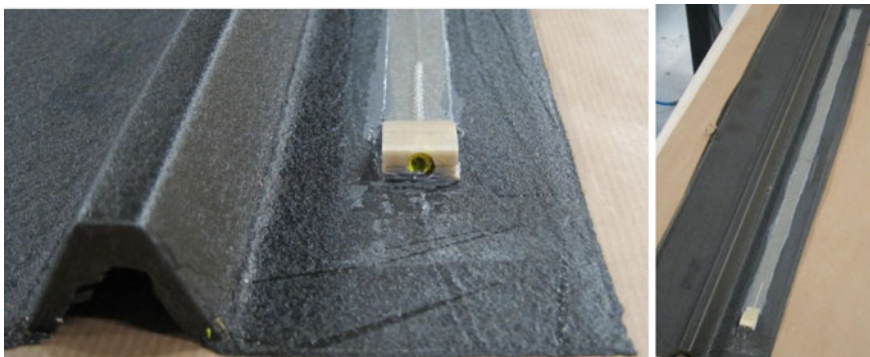


Fig. 33 Secondary bonded ribbon tape to AS07 stringer

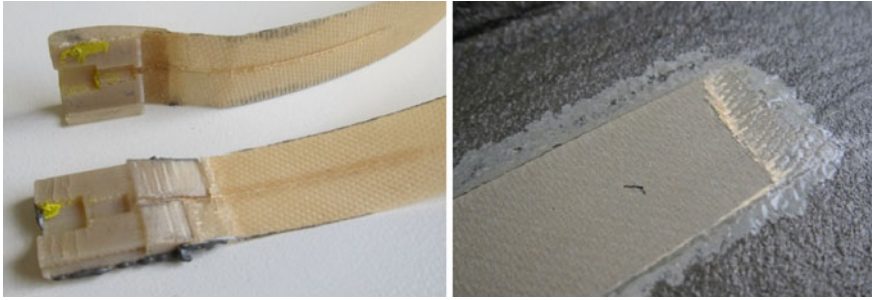


Fig. 34 Removed ribbon tape (*left*) and resulting surface after removal

5.5.2 Testing the Repair Principle

The removal of the ribbon tape is described in detailed steps below:

- Remove the yellow sealant tape from the connector cavity. Sealant tape was used to fill the gap since no actual DMI connector was present in the dummy ribbon tape during testing.
- Use a flat tool (screwdriver or alike) to remove the upper half of the ribbon tape. This initiates the pull-off of the upper prepreg layer.
- Carefully remove the upper prepreg layer. Pull parallel to the ribbon tape, so the GFRP ribbon tape does not tear-off.
- Use the flat screw driver to remove the lower connector casing half and initiate pull-off of the lower prepreg layer.
- Remove the lower prepreg layer. Pull parallel to the ribbon tape, so the GFRP ribbon tape does not tear-off. Reductant GFRP can be easily sanded down.

In the figure below, the removed connector casing with attached ribbon tape is shown in Fig. 34.

5.6 Final Design Connector Casing

Based on the results of the first 3D-printed prototypes, a final connector casing design is made, which includes all design optimizations. The 3D-printed connector casings were not suitable since they were neither temperature resistant nor pressure stable; therefore, the design is updated for a machined (translucent PEI) casing. The material used is SUSTAPEI from Röchling Sustaplast, which is an unfilled, translucent, amber-colored PEI. According to the datasheet, this material has a HDT (Methode A: 1.8 MPa) of 200 °C.

First 2 prototypes were machined, to perform the processing test (temperature/pressure), validate its functionality and fitting tolerances (Fig. 35).

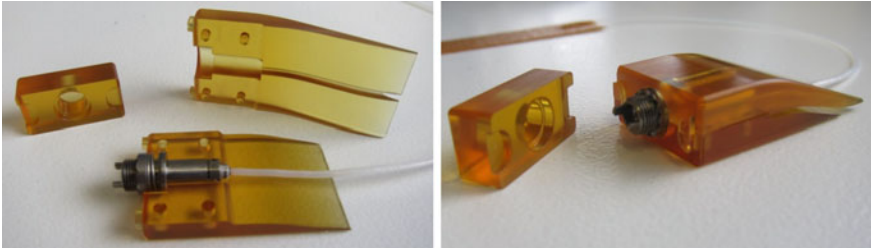


Fig. 35 Final connector casing design, machined PEI (translucent)

5.6.1 Processing Test

The machined PEI connector casing was tested in an autoclave under 180 °C @ 7 bars of pressure (6 bar AC pressure + 1 bar vacuum). No large deformations of the PEI connector casing could be measured.

5.7 Final Ribbon Tape Design

The ribbon tapes including the machined PEI connector casings have been successfully implemented in the connector assemblies for the SARISTU 5-Bay demonstrator (Fig. 36).

5.8 Connector Usage Within the SARISTU Project

During the project, ribbon tapes have been made with the target DMI connector and with an E-2000 connector. The E-2000 connector was used within the SARISTU project, since this was a more cost-effective option at the moment and the connector

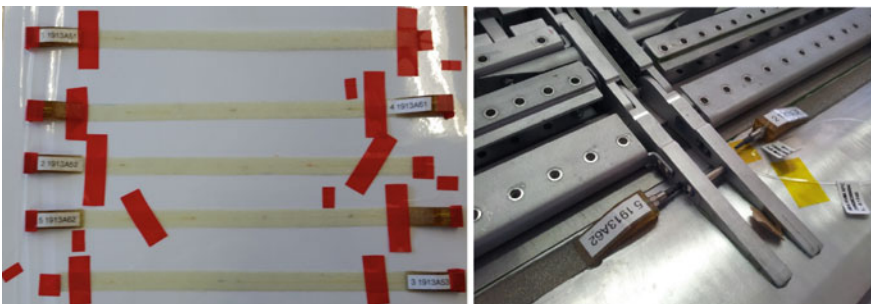
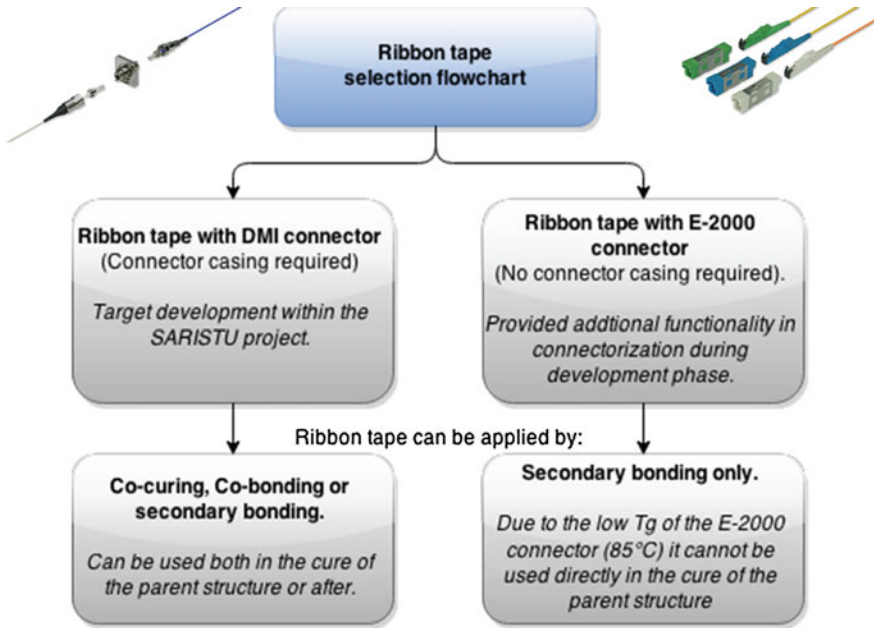


Fig. 36 5-Bay demonstrator ribbon tapes

casing development was not completely finished. Next to that the E-2000 provided additional flexibility in connectorizing the ribbon tapes. The images below show the types of connectors that can be used for the ribbon tape. Below the figure, a flowchart is provided that shows in which case which connector is chosen.



6 Ribbon Tape Qualification

6.1 Objective

Under the scope of developing a reliable and accurate sensor, the ribbon tape was subjected to multiple mechanical tests. The aim of these tests was not only to derive results regarding the bonding integrity of the ribbon tape on composite substrate but also to investigate the measurement’s efficiency in comparison with typical ESGs. Additionally, repeatability of ribbon tape’s recordings after several fatigue cycles was another parameter that was investigated.

6.2 Experimental Description

The composite coupons that carried the ribbon tape were manufactured from typical aerospace CFRP material (M21-T800S) and their dimensions were $L \times W \times \text{Thk}$: $200 \times 40 \times 4$ mm. The ribbon tape was bonded onto the coupon applying secondary bonding technique. For measurements' comparison reasons, strain gauges were also positioned on the top and bottom surface, as presented below (Fig. 37).

The coupons were subjected to three-point bending compressive fatigue test which parameters were defined as follows:

- The fatigue test was controlled by displacement.
- The cycles limit was defined to 10^6 .
- The frequency specified for the fatigue testing was 10 Hz.
- The upper and lower limit of the fatigue tests was derived from the measurements of the FOBG and was determined to $400\text{--}4000 \mu\epsilon$.
- Data were generated at preselected intervals, at every 10^n cycles (where $n = 0, 1, 2, \dots, 6$).
- At these intervals, two quasi-static cycles were performed with loading/unloading velocity of 1 mm/min (Fig. 38).

Fig. 37 Ribbon tape specimen

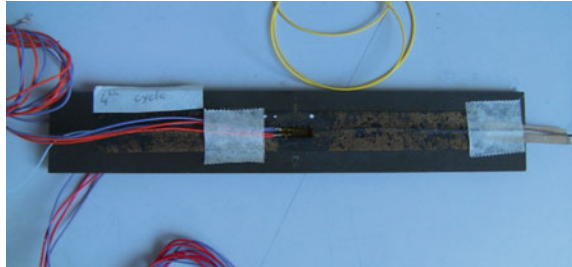
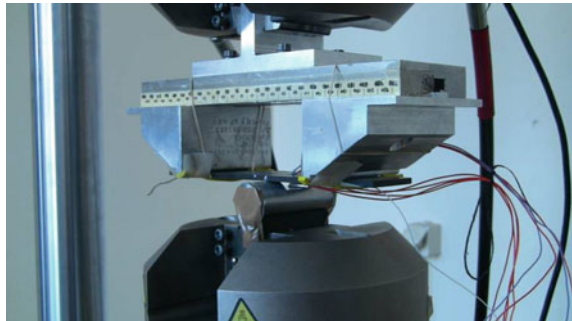


Fig. 38 Experimental setup



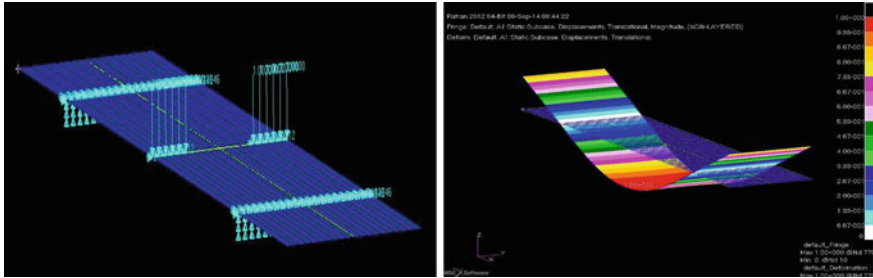


Fig. 39 Coupon FEM simulation

6.3 Results and Discussion

For the evaluation of both the ribbon tape’s accuracy and the bonding integrity to the composite substrate, two methodologies were followed. For the accuracy aspect, the ribbon tapes’ results were compared with the data obtained from the strain gauge mounted onto the top surface while for the sustainability of the bonding, the ribbon tape’s recordings were contrasted to the output of the strain gauge situated at the bottom surface.

In order to have a sufficient correlation of the results, a simulation of the experiment was initially performed, to derive the corrective factor related to the different through thickness positions of the sensors. This factor was incorporated into the data acquired from the strain gauges facilitating the post-analysis of the results (Fig. 39).

6.3.1 Evaluation of Ribbon Tape Accuracy

The requirement that should be satisfied concerning the precision of the Bragg gratings measurements in comparison with the strain gauges data was a 5–7 % deviation. The following figures depict the results gathered throughout the test campaign in different time intervals (after specific number of cycles). Trying to clarify the various graphs included into the figures and ease their understanding, it can be stated that the main objective was to envelope the retrieved data from the FOBGs inside the area formulated from the two limits defined by the upper and lower limit (7 % deviation) of the strain gauge’s readings (Figs. 40, 41 and 42).

6.3.2 Evaluation of Bonding Integrity

Similar correlation has been performed between the data obtained from the Bragg grating and the strain gauge attached at the bottom surface of the coupon. This comparison extracted beneficial results for the effect of the fatigue cycling to the

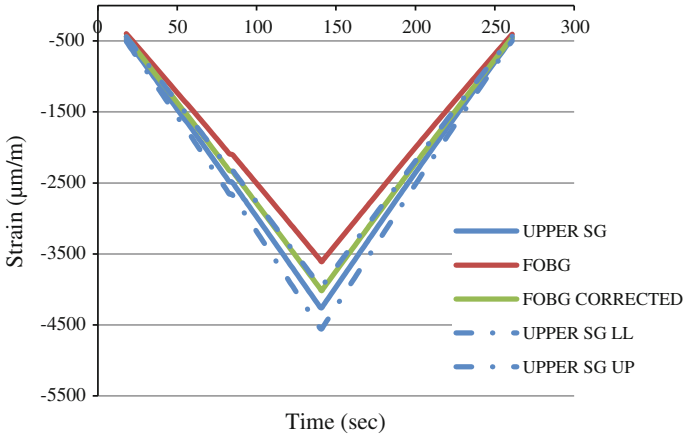


Fig. 40 Strain Comparison FOBG—Upper SG_0 Cycles_1520 nm

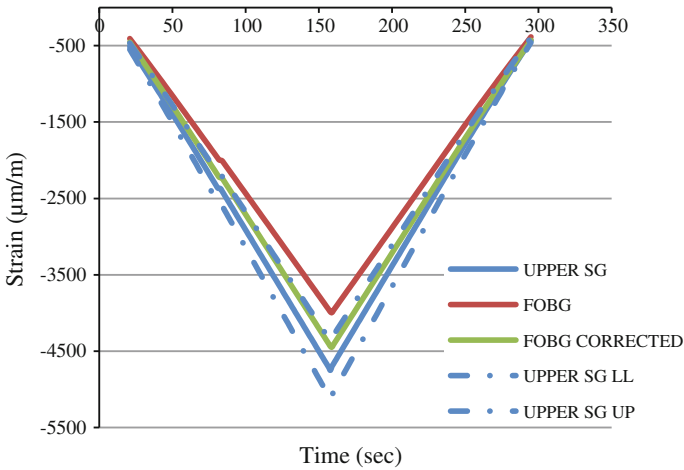


Fig. 41 Strain Comparison FOBG—Upper SG_10,000 Cycles_1520 nm

bonding layer between the ribbon tape and the composite substrate. Furthermore, this association could provide additional data for assessing the accuracy of the Bragg grating’s readings, identically with the first case, but now implementing the comparison with the lower strain gauge. Suggestively, some random graphs from the test campaign are presented in order to provide an overall picture of the experimental outputs (Figs. 43, 44, and 45).

The finalization of the three-point bending fatigue tests produced some fruitful and productive results regarding the mechanical properties of the ribbon tape. The reliability of the FOBG sensor can be assured, since as presented at the first analysis of the results, the data obtained from the ribbon tape are quite close to the

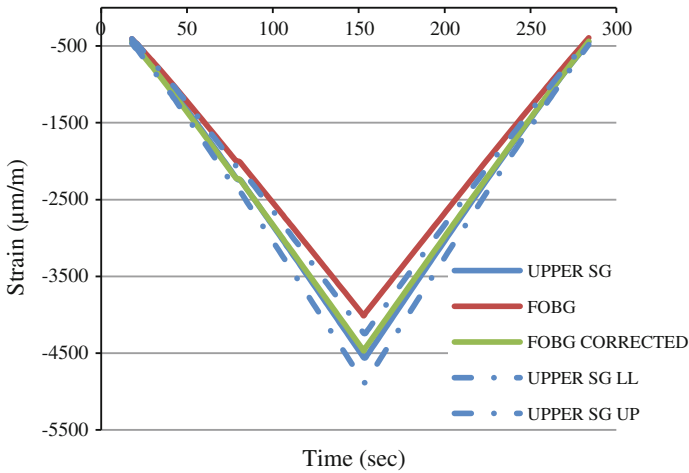


Fig. 42 Strain Comparison FOBG—Upper SG_1,000,000 Cycles_1520 nm

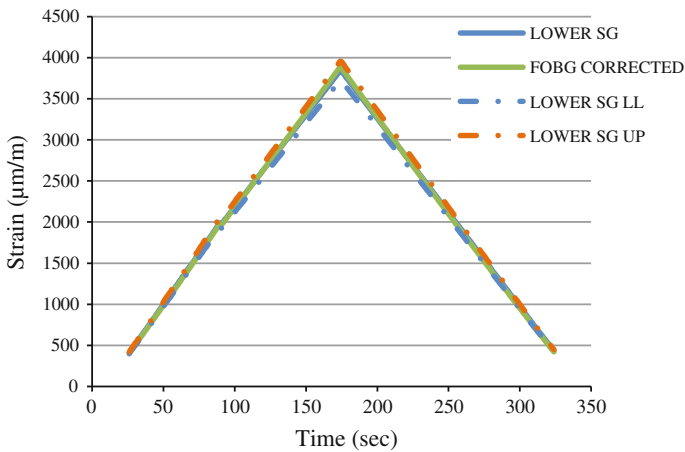


Fig. 43 Strain Comparison FOBG—Lower SG_0 Cycles_1520 nm

measurements of the strain gauges. The criterion initially set in the project, referred to a maximum 5–7 % strain deviation. This requirement is met, qualifying the optical fiber and the entire ribbon tape component as a reliable measuring method.

Furthermore, it is also evident that the quality of the bonding is not affected even after the covering of 10^6 fatigue cycles, since no alternations at the ribbon tape’s measurements are exhibited. Consequently, secondary bonding technique can be considered as an efficient methodology of ribbon tape’s placement on composite structures.

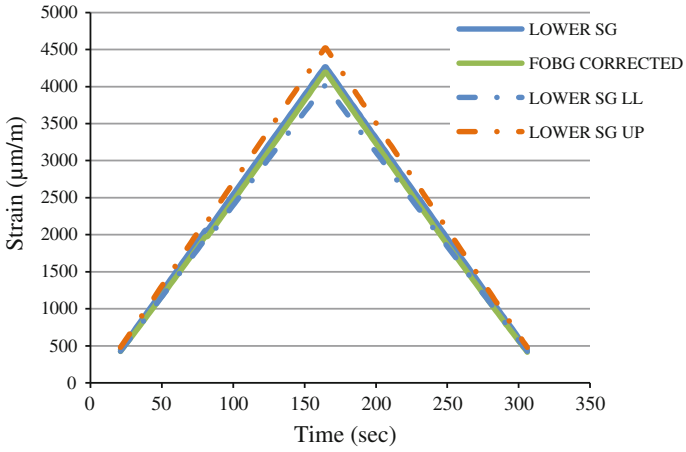


Fig. 44 Strain Comparison FOBG—Lower SG_100000 Cycles_1520 nm

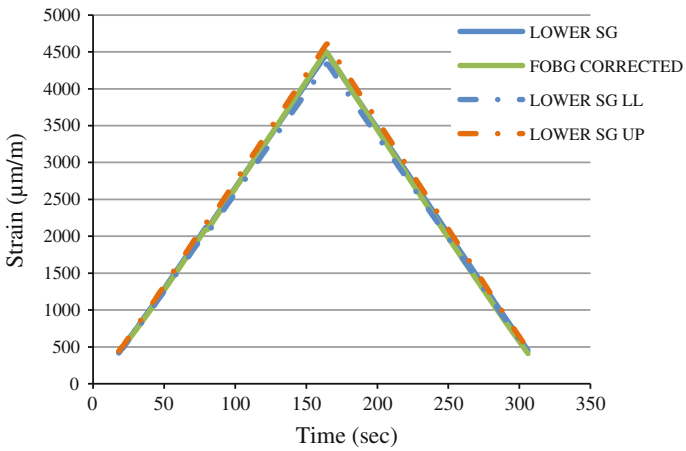


Fig. 45 Strain Comparison FOBG—Lower SG_1,000,000 Cycles_1520 nm

7 Shape Sensors

7.1 Goal

The goal of the shape sensor development is to design a mechanical sensing assembly utilizing FBG sensors to monitor morphing behavior of the ATED developed in AS02.

7.2 *Shape Sensor Requirements*

The ATED has a predefined morphing behavior in terms of maximum deflection. The required accuracy for the shape sensing system to determine the deflection is 0.5° with a maximum deflection range for the ATED tip of $\pm 10^\circ$. This means a shape monitoring accuracy of 2.5 %.

Next to the performance requirement, the shape sensor assembly's implementation needs to be compliant to the following conditions:

- The structural impact from the implementation of the shape sensor assembly should be kept to a minimum such that it does not affect the designed behavior and performance of the ATED.
- The shape sensor assembly needs to be removable from the ATED in case of structural maintenance or damage of the optical sensor assembly.
- The shape sensor assembly is to be bonded to the upper skin using an adhesive cured at room temperature.

7.3 *Material Selection*

The different materials used for the sensor assembly regard the sensor beam itself, the sensor beam support components, and the optical sensor fiber, including connector. The sensor beam was rapid prototyped using PE. The material for the support components for the 2-bay dummy demonstrator was standard aluminum and manufactured to spec by a milling machine, while the support components for the final 5-bay demonstrator were rapid prototyped as well using PE.

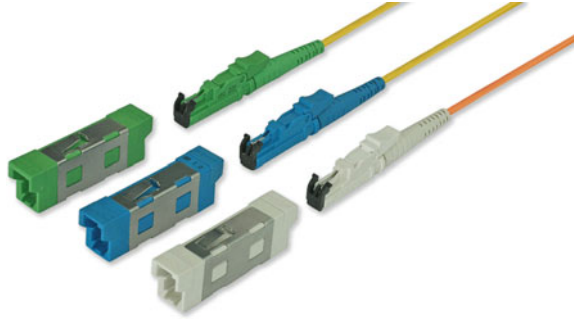
The optical fiber is standard ORMOCER[®] coated, SM 850-nm fiber provided by FBGS. The standard ORMOCER[®] coating is mainly designed for strain measurement applications and has the following features:



- High adhesion to the fiber glass enabling direct fixation of the FBGs
- High E-modules to generate a good strain transfer between the fiber and the glue
- Temperature operating range outperforming standard optical fiber coatings to support applications between -180 and $+200$ °C.
- Easy fiber manipulation allowing to remove the ORMOCER[®] coating for splicing without the use of chemical acids.

The optical fibers are bonded to the sensor beam using Epotech epoxy.

Fig. 46 E2000™ Simplex connectors and mating adapters



The optical fiber connector used is a standard E2000™ Simplex from Diamond. The E-2000™ incorporates numerous innovative features to address the needs of users. The connector has a positive latching mechanism with interchangeable color-coded and mechanically keyed thumb-latch, and a spring loaded protection cap. The E2000™ offers 0.1 dB maximum insertion loss at an operating temperature range of $-40/+85$ °C (Fig. 46).

7.4 *Manufacturing and Implementation Process*

7.4.1 **Shape Sensor Manufacturing Parts**

The shape sensor assembly is built to spec and consists of multiple parts (rapid prototyped); 4 support structures and the sensor beam itself. The sensor beam has a length of 300.0 mm (approximately, depends on the specific ATED bay), a width of 10.0 mm and a height of 3.0 mm. The sensor beam has engraving along the length on the upper and lower side of the beam to integrate the optical fiber (Figs. 47, 48, and 49).

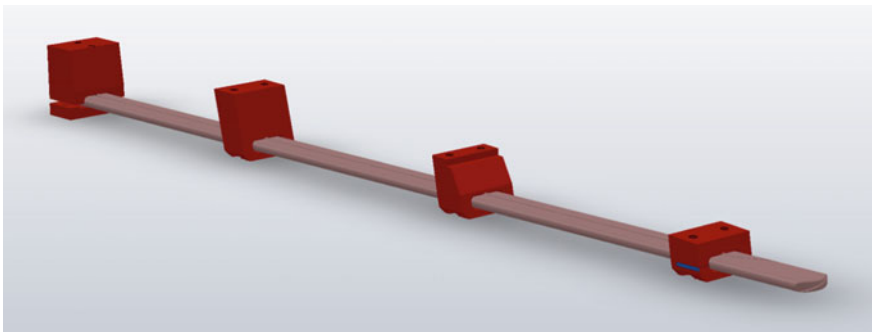


Fig. 47 Shape sensor assembly

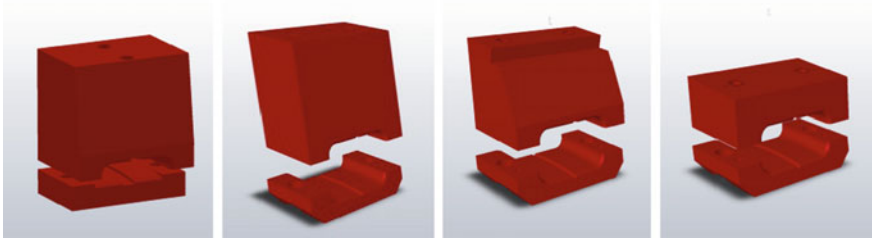


Fig. 48 Shape sensor beam support structures (from left to right, the first is used to fixate the beam)

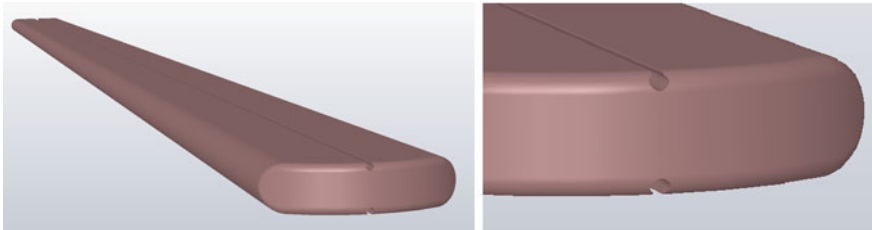


Fig. 49 The shape sensor beam

7.4.2 Shape Sensor Assembly Implementation Procedure

The following procedure describes the assembly steps for the implementation of the shape sensor assembly for the 2-bay and 5-bay demonstrator structure that includes bonding to the ATED skin. The skin itself is considered a system/subsystem, and its implementation requires supportive tooling to ensure efficient bonding of the subsystems to the aluminum parts of the skin structure.

The images above show the shape sensor assembly and its parts. The support structures (red) are to be bonded to the aluminum parts of the skin structure by means of specific adhesives. This adhesive bonding requires a 30–45 min of hardening. The first support structure fixes the beam. The other support structures allow the beam to slide through freely as the ATED morphs up and down. The support structures are to be bonded by means of an adhesive. The holes in the support structures (Fig. 48) are in case mounting are to be done by screwing. The images on the following page show how the beam is placed into the ATED structure (Figs. 50, 51, and 52).

The holes in the spars allow placement of the shape sensor beam. In order to assure a aligned placement on the skin structure of the sensor beam support structures, two additional stiff rulers (blue) are used to fixate the support structures with respect to each other and the skin structure, and the sensor beam itself is not stiff enough for that (see image below).

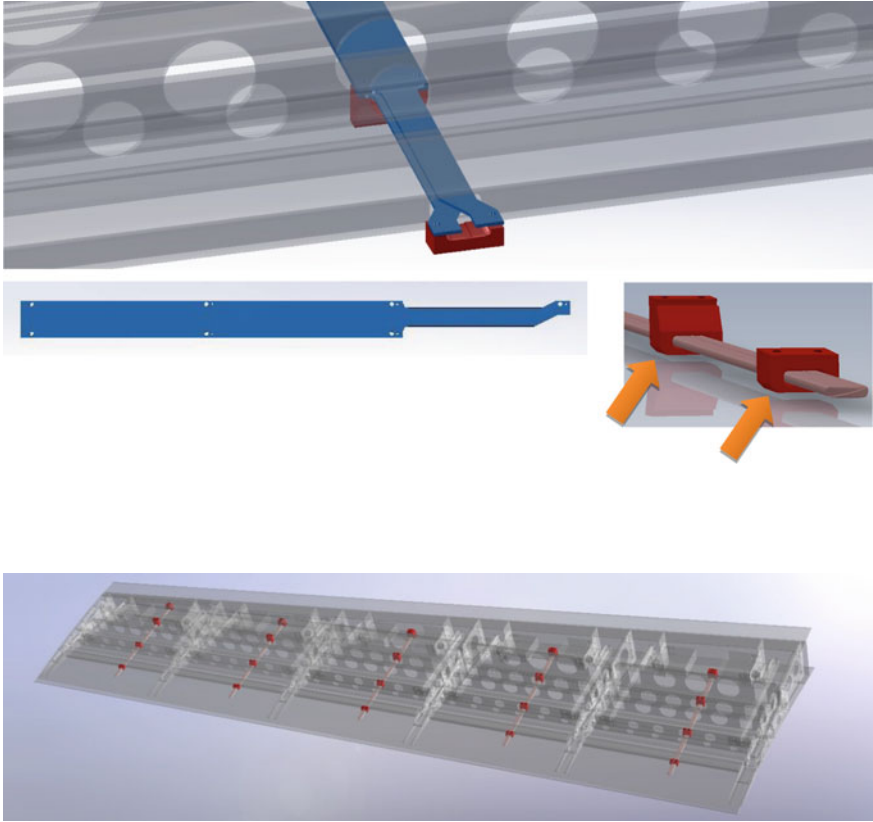


Fig. 50 Shape sensor implementation architecture 5-Bay demonstrator

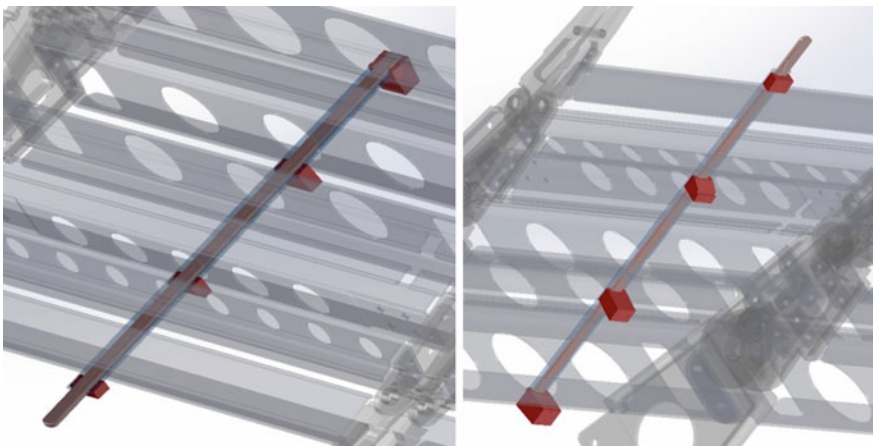


Fig. 51 Bottom-up (left) and Top-down (right) view of the sensor beam

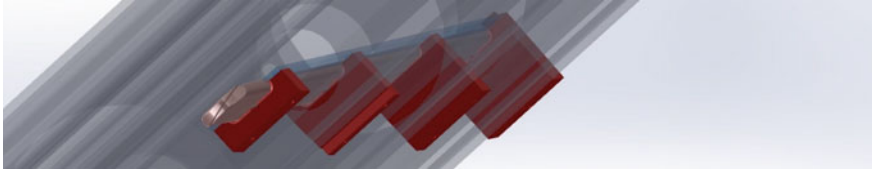


Fig. 52 Front view of the sensor beam

After bonding and hardening, the rulers are removed (hence the ruler shape). Then, the sensor beam is inserted and the support structures are closed (screwed) with small covers (green arrows). The following outline regards the assembly procedure:

1. Assembly of ATED rib and spar structure;
2. Pre-placement of the sensor beam and “open” parts of the support structures including the rulers;
(This can be done either before or after step 3, which is most efficient)
3. Placement of the upper skin structure on the ATED rib/spar structure;
4. Bonding/hardening of the sensor beam on the upper skin structure;
5. Placement of the lower skin structure.

8 Hardware

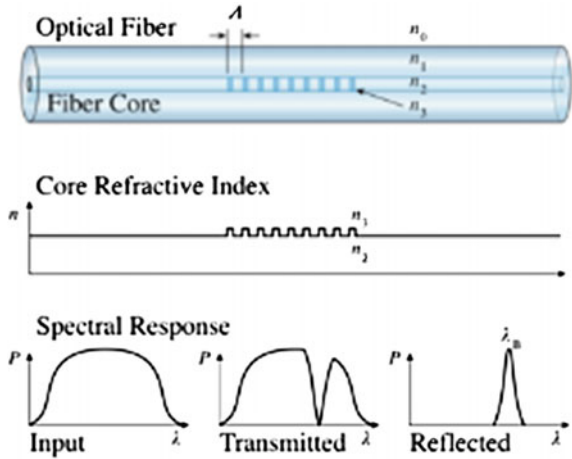
8.1 Fiber Bragg Gratings

The type of fiber optic sensor that is used for these sensor assemblies is the FBG. A fiber Bragg grating (FBG) is a type of distributed Bragg reflector constructed in a short segment of optical fiber that reflects particular wavelengths of light and transmits all others. This is achieved by creating a periodic variation in the refractive index of the fiber core, which generates a wavelength-specific dielectric mirror. A FBG can therefore be used as an inline optical filter to block certain wavelengths, or as a wavelength-specific reflector (Fig. 53).

The fundamental principle behind the operation of a FBG is Fresnel reflection. Where light traveling between media of different refractive indices may both reflect and refract at the interface.

The grating will typically have a sinusoidal refractive index variation over a defined length. The reflected wavelength (λ_B), called the Bragg wavelength, is defined by the relationship:

Fig. 53 FBG principle



$$\lambda_B = 2n_e \Lambda$$

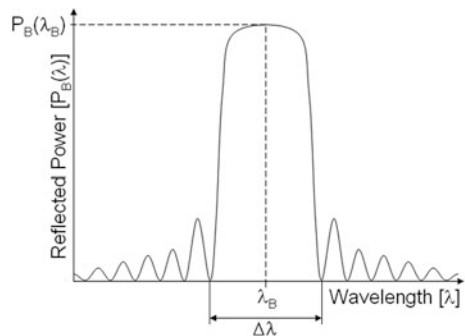
where n_e is the effective refractive index of the grating in the fiber core and Λ is the grating period. The effective refractive index quantifies the velocity of propagating light as compared to its velocity in vacuum. n_e depends not only on the wavelength but also (for multimode waveguides) on the mode in which the light propagates. For this reason, it is also called modal index (Fig. 54).

The wavelength spacing between the first minima (see image), or the bandwidth ($\Delta\lambda$), is (in the strong grating limit) given by:

$$\Delta\lambda = \left[\frac{2\delta\eta_0\eta}{\pi} \right] \lambda_B$$

where $\delta\eta_0$ is the variation in the refractive index ($\eta_3 - \eta_2$), and η is the fraction of power in the core.

Fig. 54 FBG spectral signature



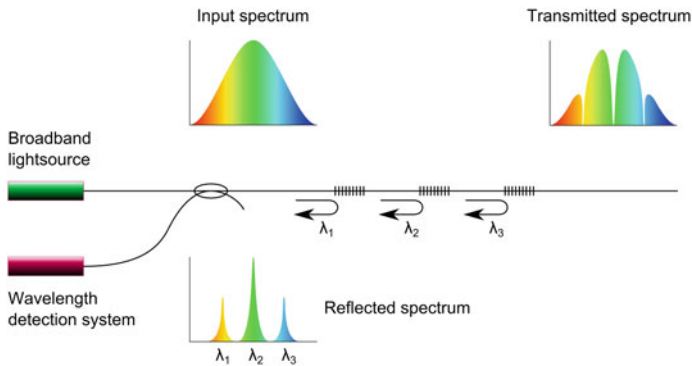


Fig. 55 Wavelength division multiplexing (WDM) principle

In practice, this can be applied as follows: using a broadband light source sending a signal spectrum into the fiber, only certain wavelengths according to the FBG sensors are reflected. By means of spectrometer, these wavelengths—and their shifts due to strain or temperature change—can be monitored and related to the strain levels picked up by the FBG sensors (Fig. 55).

8.2 System Overview

The diagram below sketches the general system layout for the fiber optic monitoring system taking both the initial and proposed system selection into account (Fig. 56).

From the perspective of the two system approaches, the following subsystems are described:

1. Background with regard to optical fiber types and FBG sensors;
2. The proposed interrogator systems:

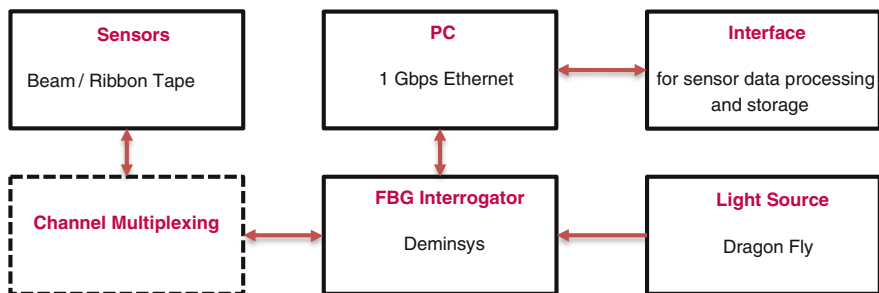


Fig. 56 FO monitoring system overview



Fig. 57 Final FOS system implemented

- a. **Initial system selection:** the free-space optics-based FBG interrogator called the **DEMINSYS** series;
 - b. **Proposed system selection:** the developments with regard to the integrated photonics-based interrogators the **GATOR and ANT** series, including the **DRAGONFLY** light source module;
3. Channel multiplexing: optical switches and ANT series;
 4. Sensor developments: Ribbon Tape and Shape Sensor;

The final system selection determined the **DEMINSYS** devices as the most appropriate; development progress and product manufacturing did eventually not match the planning for the proposed system selection. With regard to its measurements performance, the **DEMINSYS** proved more than sufficient for its purpose. Though for operational implementations (TRL9), the **DEMINSYS** is not likely to comply to aerospace requirements with regard to its device size, weight and power usage. Integrated photonics-based devices called **GATOR** series demonstrated a significant miniaturization capability in all its proportions and in addition proved to provide better performance, better specification flexibility, and subsequently higher reliability. The final implemented fiber optic sensing system overview is presented below (Fig. 57):

8.3 *FBG Interrogator: Deminsys*

8.3.1 General Specifications for the Deminsys

The Deminsys Ultra is a free-space optics-based quad channel FBG interrogator device providing 4 channels (fibers) with a typical maximum number of 8 FBG sensors per channel. The Deminsys uses SLED broadband light sources. The 1 Gbs Ethernet output can be connected to a single PC or (wireless) router in case more than one interrogator is required.



The Deminsys allows the use of an optical switch to multiplex signals and to increase the number of sensors to be interrogated through more than four channels.

The Deminsys provides a UDP protocol for data broadcasting, a Telnet interface for command control, and a HTTP server for configuration through an Internet browser.

8.3.2 Synchronization

The interrogator supports an active low synchronization input on a LEMO FGG.0B.306 CLAD 42 type connector. This allows for accurate synchronization of the acquired data with external events. Input voltage should be between 3 V minimum and 24 V maximum. Other pins on the connector should not be used. Typically, the maximum cable length is 2 m. For longer cables, additional measures are necessary.

8.3.3 Settings

The Deminsys system is a fully configurable sensor interrogation device. The Deminsys shows all necessary features for resample, data compression, light source control, network configuration, etc.

Internally, the Deminsys always operates at the sample rate of 20 kHz. Each device comes with a calibration file that includes the calibrated wavelength-to-strain conversion factors.

8.3.4 The Output of the Deminsys

The interrogation software can output several kinds of data in several formats. The data available are as follows:

- Raw data (CCD pixel data, i.e., the spectrum of the reflected FBG signals)
- Black level corrected data (corrected pixel data from the CCD array corresponding to the black level calibration procedure)
- Center of gravity (CoG) data (which proportionally relates to strain)

The data format is in time stamped binary format as broadcasted by the Deminsys interrogator to the CPU host or acquisition system. The Deminsys comes with extensive documentation on how to interpret and convert this binary data stream into engineering information.

Internally, the Deminsys always samples at a speed 20 kHz; however, a down sampling factor can set automatically—either averages or not—the data before broadcasting it. This way data can be obtained with a lower (averaged) sampling rate if the application should allow lower sample speeds.

8.3.5 Airborne Compatibility of the Deminsys System

The Deminsys series is tested and approved for TRL5 and assessed for TRL6/7. The supporting documentation for this is available on request.

8.4 Next-Generation FBG Interrogator Devices

One of the key requirements for the implementation of an SHM monitoring system on board of an aircraft is the ongoing process to miniaturize sensors and systems, to reduce their weight and their consumption of power to operate. Technobis is using integrated photonics technology to develop miniaturized fiber optic sensing systems for strain sensing that have relevant advantages over conventional systems.

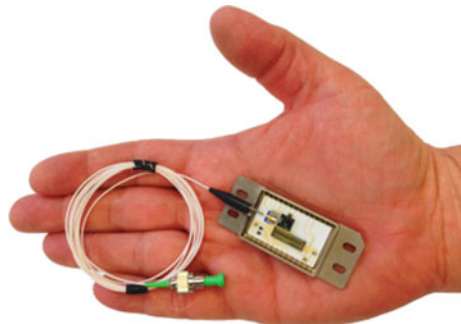
Devices based on integrated photonics are smaller, weigh less, and consume less power. And because of their smaller size they have improved mechanical and thermal stability and subsequently improved reliability, which will prove is ideal for aerospace applications. Technobis has been and still is involved in several aerospace projects taking part in the development of damage and impact detection, and load and shape monitoring applications for aircraft structures, also based composites materials.

Within the context of SARISTU, requirements and specifications were acknowledged. Technobis aims to further develop the integrated photonics-based FBG interrogator devices to support the SHM monitoring applications as damage and impact detection, load monitoring, and shape sensing.

The envisioned next-generation devices take off with the **GATOR** series, to be launched July 15. This regards a miniaturized device using application-specific photonic-integrated circuits (ASPICs). The advantages of being smaller, less weight, low power, and solid state make this a highly suitable and reliable candidate for future SHM in harsh environments as aerospace.

With similar specifications as a standard base, following multiple system designs and concept, a wide range of applications can be support: thermal (LadyGator), HighRel aerospace implementation (FlyingGator), combining high performances in resolution and speed (SuperGator), etc (Fig. 58).

Fig. 58 Ruggedized GATOR module



9 Methods to Evaluate the Integrity of Ribbon Tapes

The ribbon tape is a complex component from the optical fiber point of view. A tube-protected optical fiber enters the composite ribbon only to be stripped later to a vulnerable 140 micron in diameter, polyimide-coated glass fiber. In the process of the development of the finally successful ribbon tape, there was a need to assess the optical integrity of the optical fiber after embedding and to locate points of excessive loss or even complete failures.

To meet this nondestructive testing challenge, Rayleigh-backscattering-based distributed sensing was employed using coherent OFDR technology. One of the first not-so-successful embedding attempts is shown in Fig. 59. The figure shows red light, injected into fiber #1 being scattered from the fiber, indicating a problem. To identify the source of failure, we monitored the amount of Rayleigh back-reflected light from the sample, Fig. 60. In the fiber section up to the length coordinate of 3 m, we see reflection at a value of -100 dB/mm, which is the expected one for a healthy fiber (taking into account a few extra dB of connectors and splice losses from the measuring instrument up to the sample). However, at 3 m, which resides in the sample, suddenly the power of the back-reflected light drops to a much lower level, indicating a problem: a high scattering point, an intended sharp bending, or a partial internal break. All fibers exhibited very high optical losses.

As the embedding technology improved, optical integrity was achieved and optical losses minimized to a fraction of a dB. Figure 61 shows an advanced ribbon tape, still without FBGs. A typical back reflection curves are also shown, indicating optical continuity.

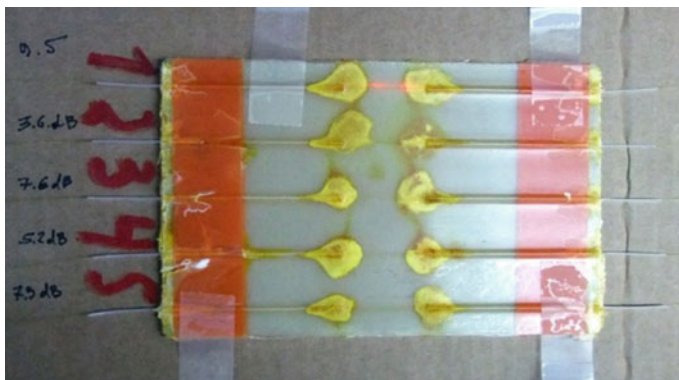


Fig. 59 One of the early attempts to embed fibers in a composite patch, later to be cut into ribbons. Red light was injected from one side and is seen being scattered, indicating an optical continuity problem

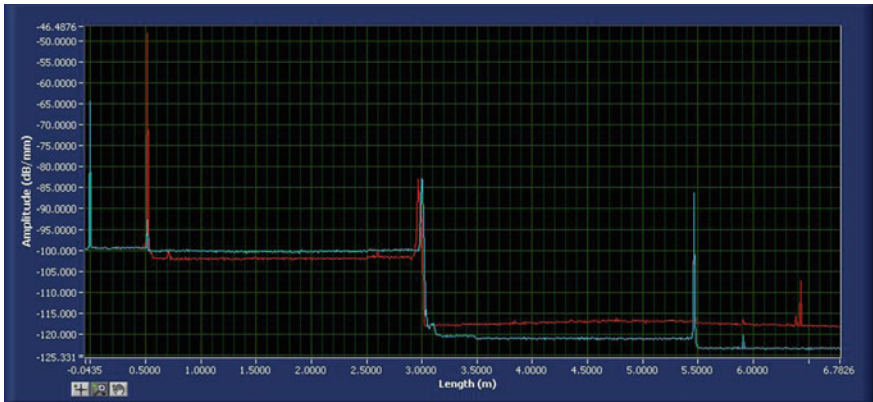


Fig. 60 Backscattering as a function of length along the fiber monitored from left (*blue*) and right (*red*). Something is happening at length coordinate of 3 m where backscattering seriously drops indicating a point of high scattering, high bending, or even a partial break

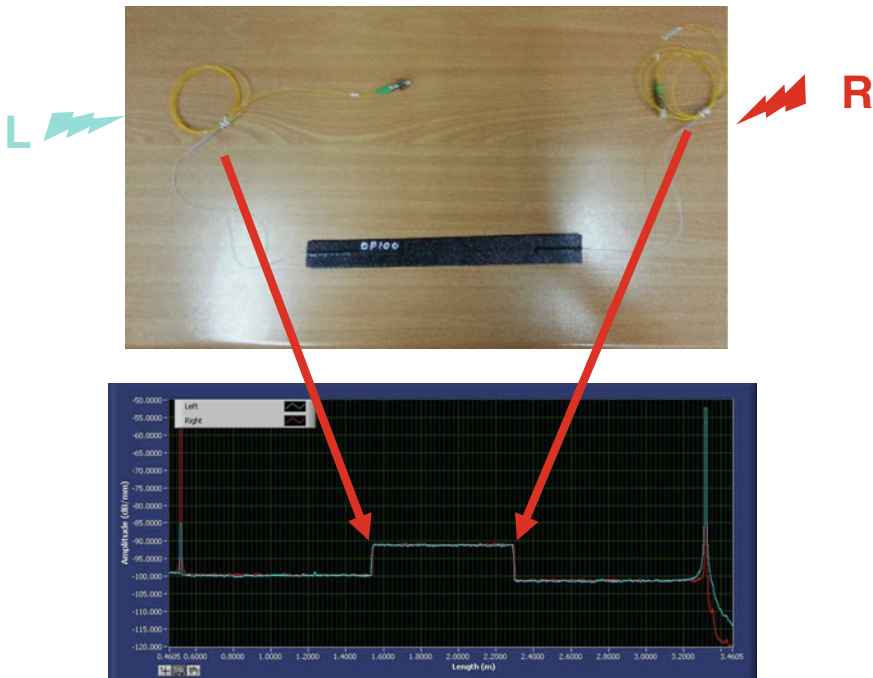


Fig. 61 A ribbon tape and its nice optical continuity. The fiber used for the ribbon tape has higher Rayleigh back reflection than that from the fiber pigtailed spliced to it

9.1 Experimental Evaluation

The ribbon tape performance, integrated as part of a typical aircraft wing and fuselages panels, was tested both statically and under cyclic loading. Strain readings were compared to electrical strain gauges with high correlation. Under fatigue loading, the ribbon tape remained bonded and strain readings were stable.

9.2 Panel Specimen Description

The panels include stringer runouts and ply drops. The panels were designed to represent the conceptual detail of the barrel circumferential joint (CJ). Two configurations were designed and manufactured: one with T-shaped stringers and the other with Omega-shaped stringers.

The first panel, with T stringers, is shown in Fig. 62. The panel includes a curved skin, with varying thickness and a joggle at one end. The panel has 4 T-shaped stringers, which were manufactured separately, and then co-bonded to the skin during the skin manufacture.

In addition, a second subcomponent, with Omega stringer, was designed and manufactured as shown in Fig. 63. This specimen has the same skin layup and features as the first panel. The difference is that this specimen has Omega-shaped stringer, which is manufactured by a co-cure process together with the skin.

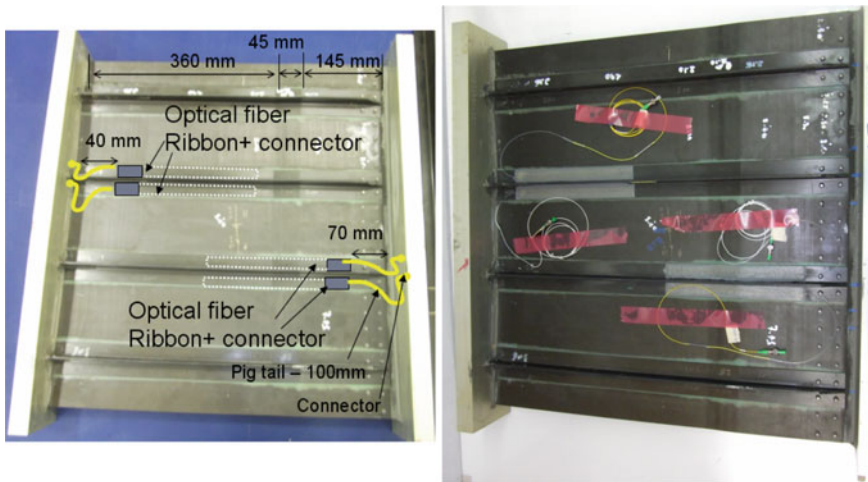


Fig. 62 Panel with four T stringers equipped with 4 ribbon tapes

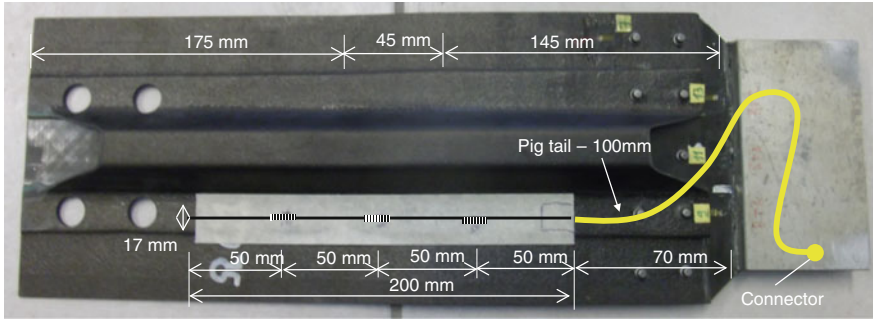


Fig. 63 The Omega stringer specimen equipped with a ribbon tape

9.3 Test Setup and Instrumentation

The panels were embedded in aluminum end blocks. The end blocks were machined with a groove according to the panel’s dimensions. Panels were potted in the groove, using special spacer rods to maintain parallel dimension of the outer loading surfaces of the end blocks. Load is introduced both on the panel ends and also on the end blocks, which transfer the load to the panels via shear (Fig. 64).

T Panel

In order to perform the testing in an Instron machine, special load introduction parts were manufactured by welding and machining. This is the gray-colored trapezoidal-shaped part in Fig. 65. In order to keep a constant load intensity along the specimen, shims were used (both regular and liquid shims) to make sure that the welded part contact surface together with the load end blocks is parallel.

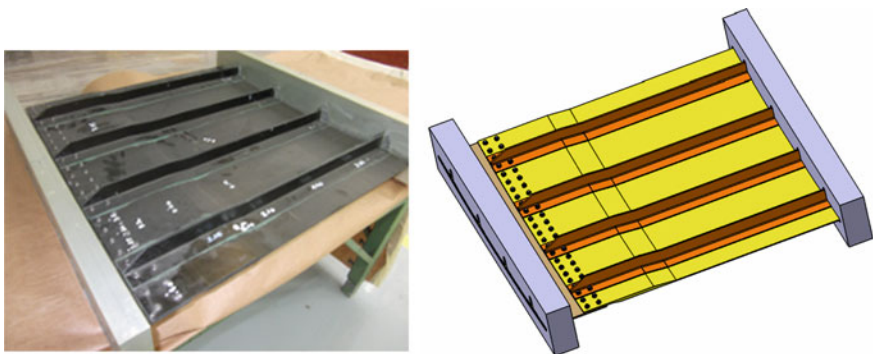


Fig. 64 T Panel, after assembly to strap and potting



Fig. 65 The T panel test setup, strain gauge, and ribbons locations

9.4 Test Description and Results

T Panel

The T Panel was first loaded and unloaded up to 4000 kgf for a few times, to check test setup, until finally loaded to failure. The panel final collapse occurred at about 22,000 kgf. The failure mode probably started at the edge stringer, due to its tendency to separate from the panel in the out-of-plane direction. The SG and FBG recording are shown in Fig. 66. An excellent agreement between FBG readings and conventional strain gauges is seen, indicating that a good load transfer exists between the ribbon tape sensors and the composite panel.

Omega Specimen

The specimen was first loaded up to limit load followed by constant amplitude compression cyclic loading. The SG and FBG recording during the static test are shown in Fig. 67. Again, like in the T panel, excellent agreement between FBG readings and conventional strain gauges is observed, demonstrating a good load transfer to the ribbon tape sensors. Typical FBG readings during the Omega specimen fatigue test are presented in Fig. 68. The FBG and ribbon bonding withstood 40 K fatigue cycles without any degradation.

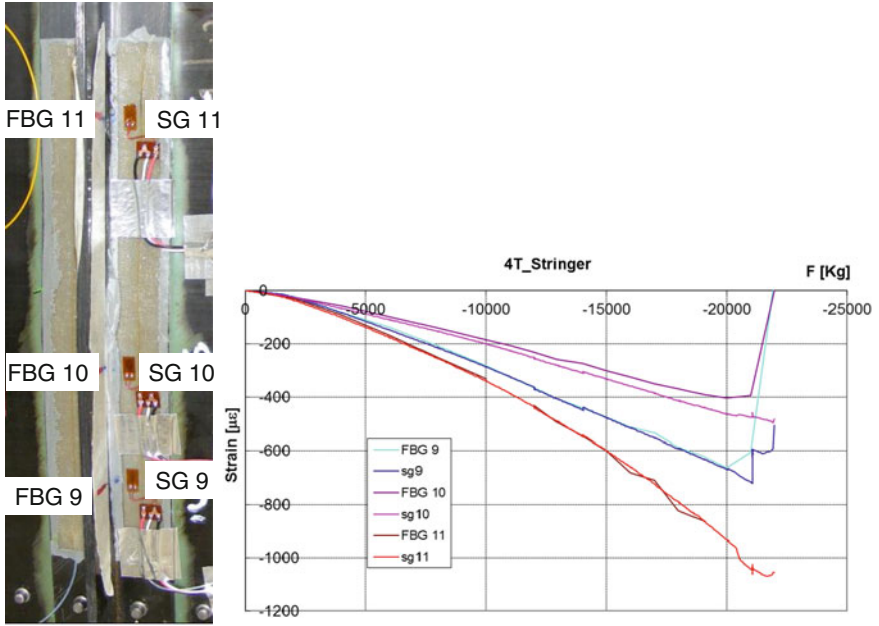


Fig. 66 T Panel strain gauges and FBG readings during the failure test

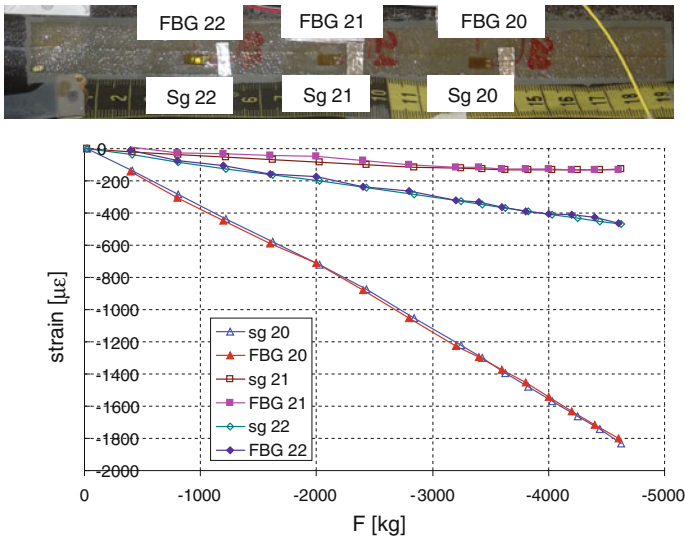


Fig. 67 T Omega specimen strain gauges and FBG readings during static compression test

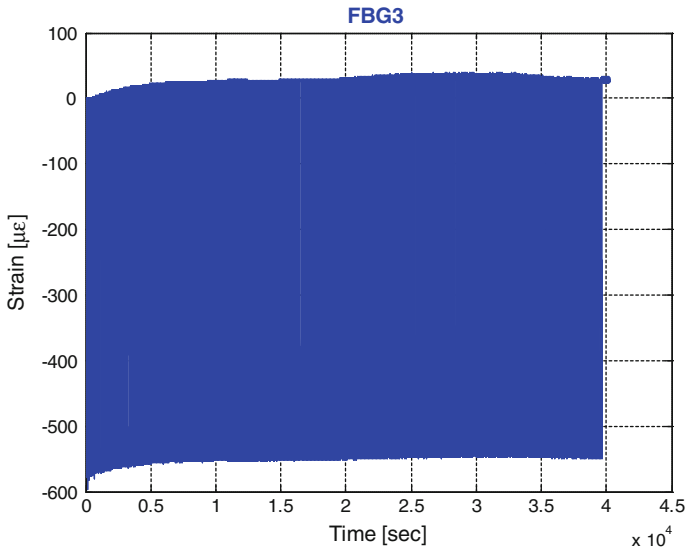


Fig. 68 Typical FBG readings during the Omega specimen fatigue test

10 Conclusion

Under SARISTU work package AS04 many achievements have been made very relevant for the entire SARISTU project and future success of SHM in aerospace application. For the integration of fiber Bragg grating optical sensors, a concept called ribbon tape has been developed to integrate the sensors in a tape with connector casing protection the fiber connectors during processing. Modern techniques like 3D printing have been used to test prototypes. The final concept has been integrated in project demonstrators like the 5-Bay demonstrator. Two concepts of mounting the sensors have been discussed, co-bonding during the autoclave process and secondary bonding using adhesive. Through extensive fatigue testing, it is shown that FORTs can be reliably used as they provide accurate strain measurements over an extended operating spectrum of 10^6 duty cycles. In addition, the FORT measurements are more consistent as compared to the ESGs that detach from the surface of the structure after a certain number of cycles. Furthermore, FORTs offer all the advantages of FBG sensors plus they are readily replaceable in case of sensor failure or for maintenance issues. The obtained FORT strain measurements are in logical agreement with ESGs and with numerically and theoretically calculated strain values at the same locations. Also fatigue testing at high and low

temperature provided acceptable responses of FORT strain measurements system demonstrating its proper working under combined mechanical and thermal loading.

Acknowledgments Many project partners have been involved in the development of the ribbon tape, shape sensor, and hardware for the SARISTU project. The success of the work package has been greatly influenced by the open and thoughtful lines of communication between all partners involved. The research leading to these results has received funding from the European Union's Seventh Framework Programme for research, technological development, and demonstration under grant agreement no. 284562.

Methodologies for the Damage Detection Based on Fiber-Optic Sensors. Applications to the Fuselage Panel and Lower Wing Panel

Alfredo Güemes, Julian Sierra, Frank Grooteman, Toni Kanakis, Pavlos Michaelides, Dimitrios Habas, Moshe Tur, Nahum Gorbatov, Christos Koimtzooglou and Nikolaos Kontis

Abstract Damages in aircrafts start as local cracks or delaminations, which, even though they do not change strongly the overall strain field, form initiation points for an eventual failure. Fiber-optic sensors act primarily as strain sensors, so unless damage happens to be close to the sensor location, the changes in the strain data may be very slight and damage may go undetected. Three main independent algorithms were developed for damage detection from strain measurements: (1) a strain field pattern recognition technique, based on principal component analysis,

A. Güemes (✉) · J. Sierra
Department of Aeronautics, UPM, Plaza Cardenal Cisneros, 3, 28040 Madrid, Spain
e-mail: alfredo.guemes@upm.es

J. Sierra
e-mail: juliansierrap@gmail.com

F. Grooteman · T. Kanakis
National Aerospace Laboratory NLR, Anthony Fokkerweg 2, 1059 CM Amsterdam, The Netherlands
e-mail: Frank.Grooteman@nlr.nl

T. Kanakis
e-mail: Toni.Kanakis@nlr.nl

P. Michaelides
NAsTech—Novel Aerospace Technologies, 64010 Ancarano, Italy
e-mail: p.michaelides@nastech.it

D. Habas
Research and Product Design Department, Hellenic Aerospace Industry S.A, 23, 320 09 Schimatari, Greece
e-mail: HABAS.Dimitrios@haicorp.com

M. Tur · N. Gorbatov
School of Electrical Engineering, Tel-Aviv University, 69978 Tel-Aviv, Israel
e-mail: tur@post.tau.ac.il

N. Gorbatov
e-mail: gorbatov@eng.tau.ac.il

from which damage indices were defined. The validity and accuracy of the approach was proven by experimental tests, as well as by simulations. (2) the extension of the Modal Strain Energy Damage Index algorithm, as a suitable method to identify skin–stringer debonds and optionally larger impact-induced damages in a CFRP composite structure with stiffeners, by using the strain data obtained during vibration tests from wisely distributed fiber Bragg grating (FBG) sensors; and (3) a strain difference-based algorithm which is threefold consisting of the following parallel methodologies: (i) strain difference limit method, (ii) Mahalanobis distance-based method, and (iii) statistical hypothesis testing-based method. These developments were put together on two realistic full-size aircraft structures, to validate the methodologies. In addition to the discretely located FBGs, distributed fiber-optic sensing was also used in the final testing, accurately measuring the strain signatures of damages caused by applied impacts.

1 Introduction

Fiber-optic sensors, and particularly fiber Bragg grating (FBG) sensors, have been used for the last 20 years with a built-up confidence on their performance. FBGs can measure the strain with accuracy similar to the conventional electrical strain gauges and extensometers, but with significant advantages over them, such as low size and weight, embeddability, non-electrical nature, and consequently no EMI and non-risks of sparking in fuel tanks and explosive atmospheres, no drifting for long-term measurements, and, very important, multiplexing capability: Tens to hundreds of sensors can be engraved at the same optical fiber, with the associated advantages for installation and interrogation. FBGs are currently used for strain measurements in aircraft structures under both static and dynamic conditions, even some certification issues remain to be solved. However, more work is still required, before their technical readiness level (TRL) is high enough for SHM applications. SHM is defined as the process of acquiring and analyzing data from on-board sensors to evaluate the health of a structure [1], and still new algorithms are needed to get information about local damages from strain measurements.

These additional activities were undertaken within the SARISTU project, mainly within Application Scenario 4, and the results are presented in this paper. Three main independent algorithms were developed: (1) a strain field pattern recognition

C. Koimtzoglou · N. Kontis
Integrated Aerospace Sciences Corporation—INASCO, 16675 Glyfada, Greece
e-mail: c.koimtzoglou@inasco.com

N. Kontis
e-mail: n.kontis@inasco.com

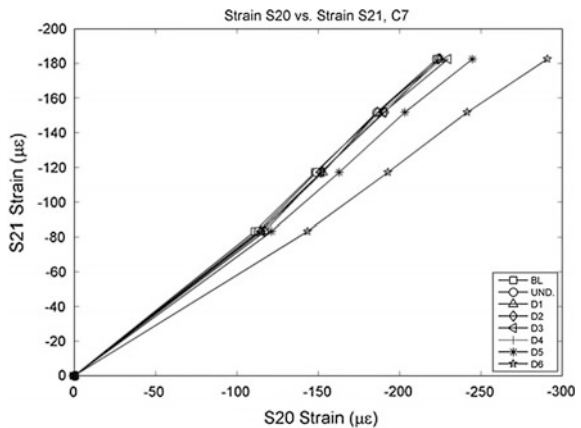
technique, based on principal component analysis, mainly done by UPM; (2) the extension of the Modal Strain Energy Damage Index algorithm, by using the strain data obtained during vibration tests from wisely distributed FBG sensors, mainly done by NLR; and (3) a strain difference-based algorithm which is threefold consisting of the following parallel methodologies: (i) strain difference limit method, (ii) Mahalanobis distance-based method, and (iii) statistical hypothesis testing-based method, developed by NASTECH and INASCO.

Strain signatures of damages caused by impacts applied to full-size fuselage panels were measured not only with discretely located FBGs but also by Rayleigh-based distributed sensing. Results were found to be in agreement with finite element (FE) predictions.

2 Principal Component Analysis

Just to focus the problem, in Fig. 1, the strains from two sensors bonded on a structure (details will be given later), under increasing loads, for the original undamaged structure, and after introducing slight damages (the largest damage D6 was a hole with 8 mm diameter, reducing the stiffness of a section by 7 %) are plotted. The influence of the damage on the strains is always negligible compared to the influence of the loads, the change in the numerical value of the strains is really small, but of course it is higher when damage is closer to a sensor (S20 in the former example). As shown in the figure, by plotting together these strains, the occurrence of damage can be identified. But such a manual procedure, called “differential strains,” can only be applicable to very simple structures with a reduced number of sensors [2]. For monitoring real aircraft structures, where the localization of damage initiation is unknown, it is needed to have a dense network of sensors and additionally some mathematical tools that can do automatically the

Fig. 1 The differential strain approach. The strains for two neighboring sensors under several load values, built for the healthy and damaged structures



comparison among all the strain data, to identify deviations over the original response. All the measurements must be studied together in order to increase the probability of damage detection. Then, it is necessary to use a multivariate statistical tool in order to get some valuable information about the system behavior.

PCA is a statistical technique whose main purpose is to identify the most important dynamics of a system, determining which data are redundant and which are just noise. By applying PCA to experimental samples, it is possible to reduce the complexity and size of the samples, revealing patterns and trends that may be hidden under the data. PCA is a mathematical procedure that uses an orthogonal transformation to convert a set of observations of possibly correlated variables into a set of values of linearly uncorrelated variables called principal components (PCs). This transformation is defined in such a way that the first principal component has the largest possible variance (i.e., accounts for as much of the variability in the data as possible). Usually, the number of PCs can be much smaller than the number of original variables. Each succeeding component in turn has the highest variance possible under the constraint that it should be orthogonal to (i.e., uncorrelated with) the preceding components.

The information of several sensors (J), during certain time interval (K) (for dynamic measurements) and, for a discrete number of experimental trials (I), can be arranged in a tridimensional matrix ($X3D$). In order to apply a PCA study, this matrix must be rearranged in a proper way. This procedure is called “unfolding.” Moreover, it is desirable to treat the data to reduce the “scale effects,” as this can hide important information about the system. The most usual way to do it is by normalizing the data. Normalization includes centering and scaling but is often called just “scaling.” For a detailed description of centering and scaling techniques, the reader is directed to [3].

Once the data matrix has been unfolded and normalized (X), its covariance matrix XTX is calculated. This square matrix measures the degree of linear relationships within the dataset. The subspaces in PCA are defined by the eigenvalues and eigenvectors of the covariance matrix. Usually, pj eigenvectors that form the transformation matrix P are sorted in descending order according to their associated eigenvalues. These are called the “PCs” of the experimental data. The eigenvector associated with the largest eigenvalue (first PC) represents the most important “pattern” in the data and contains the most representative information about the system behavior. For a more detailed description of PCA, the reader is directed to [3].

Once the covariance matrix is obtained, the matrix X can be transformed using a linear transformation in order to achieve the minimal redundancy. This transformation is achieved by means of the linear transformation matrix P :

$$T = XP.$$

The vectors formed by the rows of the transformed data matrix T (usually called T -scores) are uncorrelated, and their variances are given by the eigenvalues of the covariance matrix of the original data X .

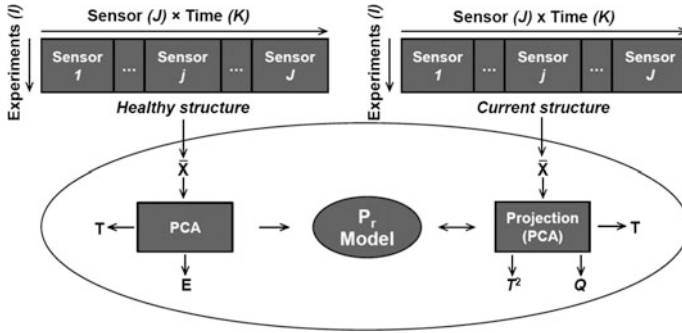


Fig. 2 Scheme of PCA methodology for SHM

There are statistical tools that allow, together with PCA, detection of anomalous behavior in systems. The two most common tools are the Q and $T2$ indices. The Q index indicates how well each sample fits into the PCA model. It is a measurement of the difference between a sample and its projection on the main components retained by the PCA model. $T2$ index is a measurement of the variation of each sample in the PCA model [4] (Fig. 2).

2.1 Experimental Setup

To validate the model and quantify its resolution, a simple experiment on an aluminum beam with a square cross section was carried out. The beam was 1500 mm long, attached to a testing bench in a cantilever mode. Four optical fibers were bonded to the beam, each one having eight FBGs. Thirty-two sensors were used in total, one of them for temperature measurement. The temperature sensor was used to verify that the temperature was constant during the experiments, also to have the possibility to do thermal compensations, if needed. A plain continuous fiber optic for distributed sensing was bonded besides the fiber optic having the FBGs. Both fiber optics (one with FBGs and another one plain for distributed sensing) were bonded in each face of the square section, located at $\frac{1}{4}$ of the face width (in order to avoid the neutral axis of the beam) (Fig. 3).

For interrogating the FBGs, a 4-channel Micron Optics SM130 was used. This equipment has a maximum acquisition rate of 100 Hz, wavelength stability of 2 pm (maximum 5 pm), and wavelength repeatability of 1 pm.

For the distributed sensing, a Luna Technologies OBR 4600 was used. This equipment allows measurements of up to 2000 m (in a long-range mode) with a spatial resolution of ± 1 cm and a maximum resolution for strain of $\pm 1 \mu\epsilon$.

Three different types of tests were performed. The first kind of test consisted of measurements under static loads by using the FBGs. The second one consisted of

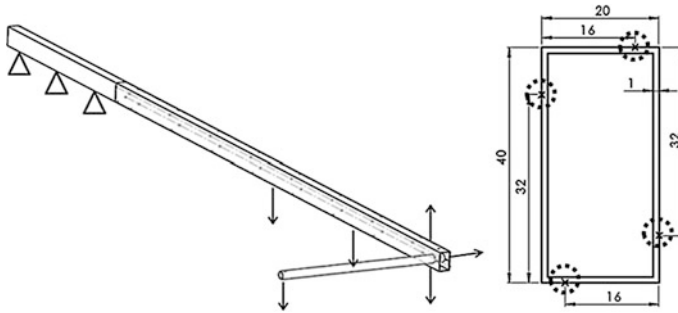


Fig. 3 Experimental setup. At *left*, scheme of beam used. *Arrows* represent the points of load application. At *right*, detailed scheme of fiber-optic locations at cross section. Each optical fiber has 8 FBG sensors, regularly spaced (150 mm). *Arrows* indicate points for load introduction. All dimensions are in mm

measurements under dynamic loads by using the FBGs. The last kind of tests consisted of measurements under static loads by using distributed sensing (OBR).

All the tests consisted of measuring the strains under different load configurations (load cases) using different load combinations and amplitudes for each load case. First, experiments were performed for healthy structure (initial condition) and, subsequently, after inducing different artificial damages in the beam (damage cases). The data obtained were used to conduct a PCA study.

Artificial damages were used in all experiments, as holes of increasing diameter, at several positions. It should be clarified that damages had cumulative character. In total, 6 damages were induced in the structure. A detailed description of damage locations is presented in Fig. 4.

2.2 Experimental Results

After projecting the gathered experimental data into the PCA model, projections of two PCs (*T-scores*) are plotted in Fig. 5. For each kind of experiments the results are presented only for one representative load case. Confidence intervals were calculated for the projections and are represented by the solid ellipse (99 % of confidence) and dashed ellipse (95 % of confidence).

The Q index, as mentioned before, quantifies change of the variations that are not explained by the PCA model. Usually, the T^2 index is bigger than Q index, but Q index is more sensitive because it explains how well each sample fits into the PCA model. The bigger Q index values mean the bigger unusual variations outside the PCA model (Fig. 6).

Similar experiments and data processing were done on other structures (wing of UAV, wind turbine blades) as described at Refs. [5, 6]. Reference [7] is an extension of the PCA to nonlinear cases, combined with ANN.

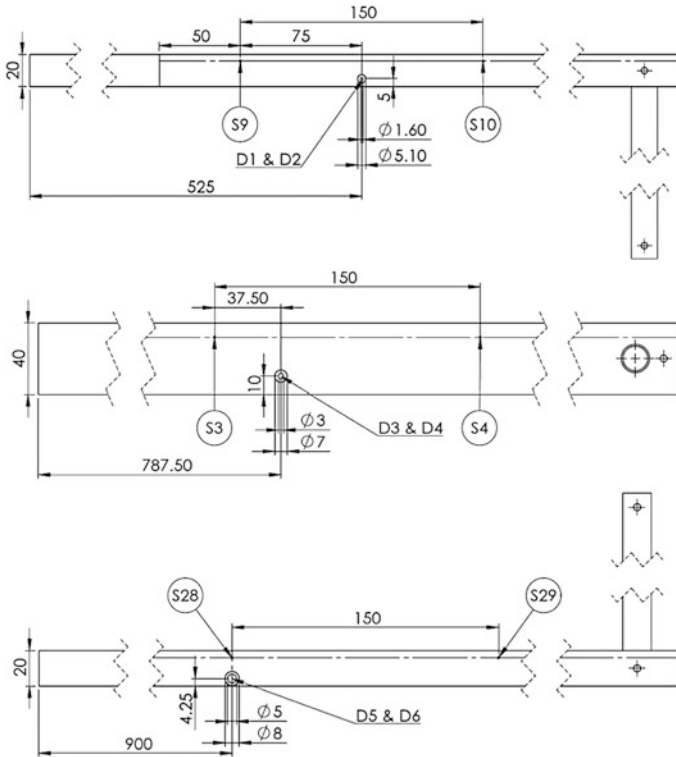


Fig. 4 Artificial damage locations. *Upper*, damages numbers 1 and 2 ($D1$ and $D2$). *Middle*, damages numbers 3 and 4 ($D3$ and $D4$). *Lower*, damages numbers 5 and 6 ($D5$ and $D6$)

Fig. 5 Projections into PCA model (first two principal components) with ellipses for 95 and 99 % of confidence for static tests by using FBGs for load case 2

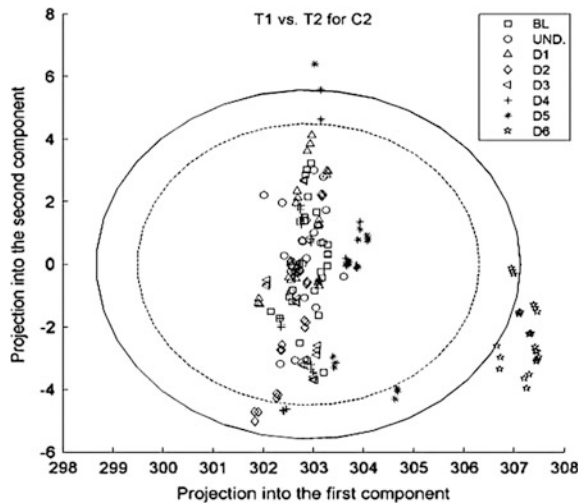
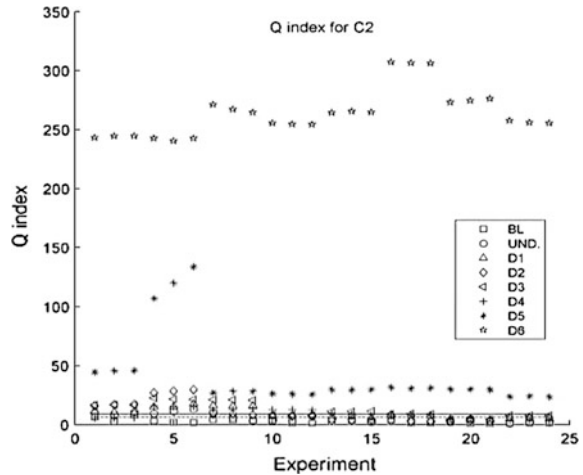


Fig. 6 Q index and control limits for 95 and 99 % of confidence for static tests by using FBGs for load case 2



3 Modal Strain Energy Damage Index Algorithm

A SHM system design tool for damage detection, developed by NLR [8] and extended within SARISTU, was applied to determine the number and position of the optical FBG sensors for two different fuselage panels. In general, four consecutive levels of damage identification can be distinguished of increasing complexity:

1. Determination that damage is **present** in the structure;
2. Determination of the **location** of the damage;
3. Quantification of the **severity** of the damage;
4. Prediction of the **remaining service life** of the structure.

The damage detection algorithm applied is based on a modal (vibration) approach and is able to detect the presence and location of the damage. The damage size can be determined as well but only when a large number of sensors are applied. This is (yet) unrealistic for a commercial SHM system and is therefore not pursued. Instead, it is expected that when the SHM system signals damage at a certain location, an inspector will inspect the structure in the vicinity of the signaling sensor by means of a suitable NDI technique to locate the exact position and size of the damage. The objective within SARISTU therefore was to minimize the number of sensors.

The SHM design tool is capable of fully automatically inserting the (impact, debond) damages in the FE model of the examined structure, even for complex models, and as such generates the damaged model, compute the modal responses, extract the strain value at the sensor locations, and derive the damage indicators (DI). Results are automatically generated and consisted of plots and pictures of the structure including the damage indicator values of the sensor network, depending on the damage indicator applied.

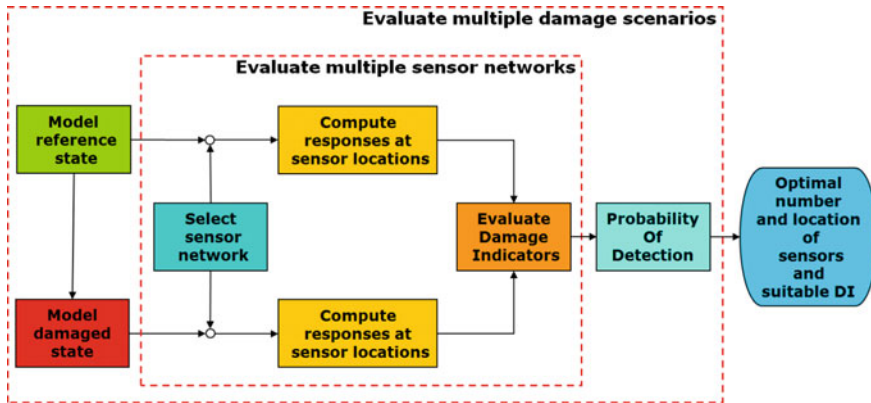


Fig. 7 Flow diagram of the SHM damage detection design tool

A flow diagram of the damage detection algorithm is depicted in Fig. 7. The algorithm is based on comparing the modal characteristics of the initial state with a damaged state of the structure. The modal characteristics are altered due to the presence of damage causing local changes in the stiffness of the structure. For both states, the modal frequency response function is calculated for the lowest modes at every sensor location for a given sensor network. The FBG sensor hereby measures the strain in the direction in which it is oriented. Hence, only limited information about the modal behavior of the structure is available in reality. Using the strain response measured by the sensor network in the initial and damaged states, a number of DI can be determined based on, for instance, changes in natural frequencies, mode shapes, and modal strain energy. The modal strain energy criterion is the most sensitive to small changes in the stiffness of the structure, making it a suitable indicator to detect small damages. Furthermore, the damage location is provided as well.

Besides skin–stringer debond damage detection, being here the primary objective, the FBG sensor network can also be applied as impact detection system during flight and even on the ground to determine the location of any significant impacts and as load monitoring system to record the strains (stresses) of the structure. Based on the results from the less accurate impact detection system (using the same sensor network), a damage detection can be performed on the part of the structure where the impact was located. Another option is to perform a damage detection on a regular basis. The damage detection system can be run on the ground by, for instance, application of a small shaker in the structural area of interest. The advantage of this approach is the known excitation force. The system can also be run during a flight, where structural loads are, for instance, gust loads, which are random in nature. However, the magnitude of the loads are then unknown, thus requiring a different modal approach.

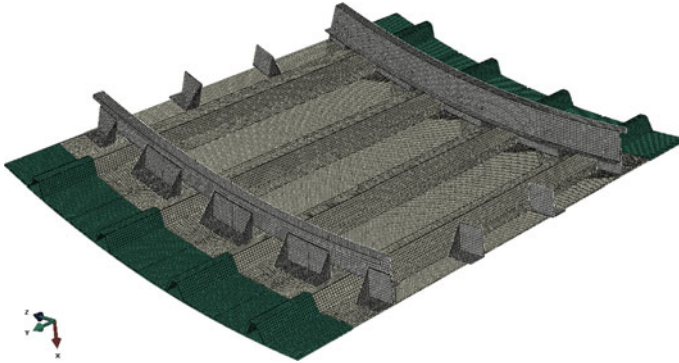


Fig. 8 Finite element mesh of the top fuselage panel

3.1 Fiber-Optic Sensor Network Top Fuselage Panel

The SHM design tool was applied on the composite top fuselage panel as designed within SARISTU to determine an optional FBG sensor network. The panel consists of 2 Z-frames and 4 hat stringers. A FE model of the panel was built as shown in Fig. 8.

The effectiveness of a number of sensor networks in detecting damage was analyzed. Within the project, it was decided that the main objective was the detection of stringer debonds and to install surface-mounted FBG sensors, by means of ribbon tape enabling the replacement of broken fibers, on both lower feet

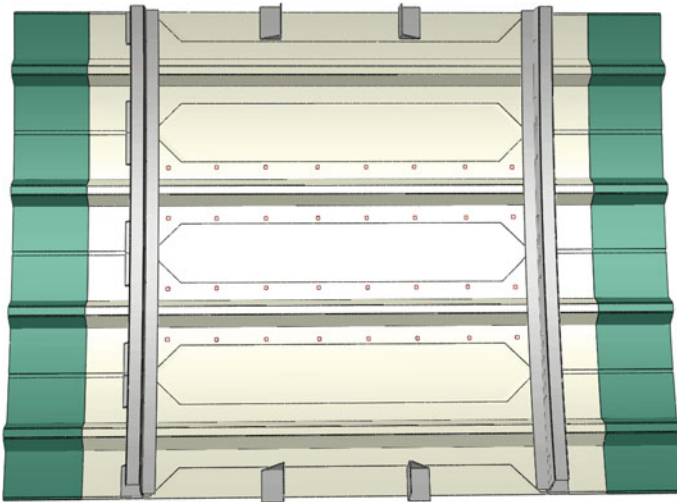


Fig. 9 FBG sensor locations

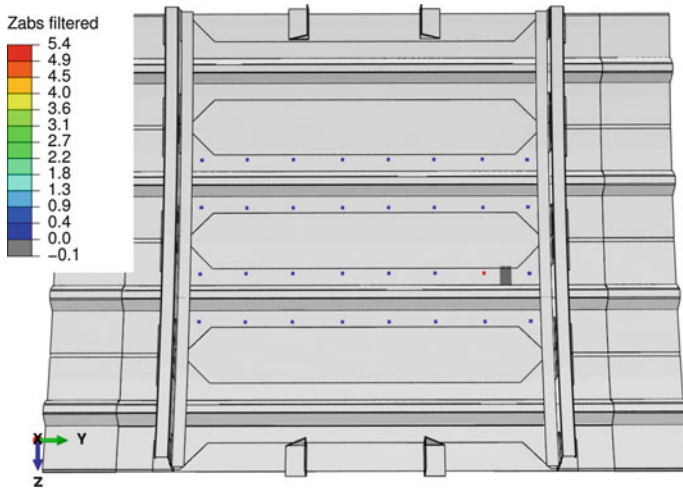


Fig. 10 Modal strain energy damage indicator for a stringer debond

of the two middle stringers, oriented in the direction of the stringer measuring the strain in flight direction. It was decided that the sensor network, as shown in Fig. 9, should be able to detect a stringer debond of 20 mm in one stringer feet. Analyses revealed that 8 FBG sensors per bay stringer foot sufficed. Besides the stringer debonds, the sensor network was also examined for its effectiveness in detecting impact damages of 20 × 20 mm in between the stringers.

The stringer debond and impact damage locations were all selected in between the sensors, being hardest to detect. Figure 10 is an example picture for a stringer debond scenario that is automatically generated by the SHM damage detection design tool. The dark gray area represents the location of the stringer debond area. The figure depicts the values of the modal strain energy damage indicator (MSE-DI) for the different sensors. The red-colored sensor shows a MSE-DI value more than 5 standard deviations away from the mean, correctly signaling the presence and location of the damage.

For several locations along the stringers, a debond was simulated in the upper or lower stringer feet of the two inner stringers, showing that all were correctly detected by at least one nearby sensor. For 4 locations in the middle bay area, an impact damage was simulated as well. Although no sensors were installed on the skin, the impact damage could still be successfully detected for all impact locations. To improve impact detection, an optical fiber should ideally be installed on the skin in between the stiffeners.

The analyses' results are based on the assumption that even small strains can be measured very accurately without any noise component. In reality, this will not be the case and noise will be present in the FBG time signals. Most of this noise will be averaged out by transferring to the frequency domain though, by taking a time average, of which the results are used to compute the damage indices. Hence, due to

the remaining noise, some damages may go undetected in reality. The signal-to-noise ratio (SNR) present in a realistic application may be simulated by adding a noise component to the computed responses. Other sources of uncertainty can in principle be added as well. The noise component influences the SHM system accuracy and reliability in timely detection of any damage before it becomes critical. This can be characterized by the system's probability of detection (POD), expressing the chance to detect a damage of a certain size within the structure, which is an important quantity for the certification of the SHM system. An experimental assessment of the POD is very expensive, because of the large number of damages that have to be tested on full-size components to obtain a statistically valid dataset. The presented SHM design tool offers a model-assisted approach to compute the POD. This can alleviate the costs significantly and only requires a limited amount of experimental data for its validation. For a reliable SHM system, the number of false calls should be minimized to reduce the costs of unnecessary inspections and affected aircraft availability, which is another important characteristic for acceptance of such a system.

4 Strain Difference-Based Algorithms

Using the static readings of FBGs (or the differences of neighboring ones), a SHM method is developed based on the differences between a healthy baseline set of measurements and a dataset at an unknown structural state of the structure. The method utilizes three algorithms which may be used separately or their outcomes merged to infer a "more confident" assessment on structural health state.

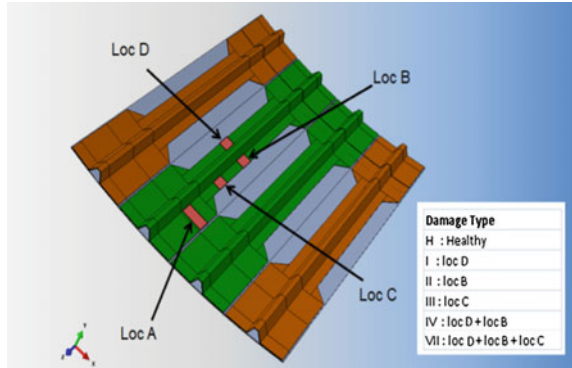
The method is applied to simulated datasets (FEM) of a stiffened fuselage panel. The first goal is to determine the minimum number of FBG sensors able to detect and possibly localize damage in the form of a 20-mm-length skin-to-stringer debonding.¹ After determining the minimum number of sensors, the methods are tuned to achieve a 90 % true detection rate and less than 5 % false detection rate.

4.1 Fuselage Panel FE Model

The current analysis is based on a FE model of a top fuselage panel. The model design is depicted in Fig. 11, presenting also the extent and locations of debondings that were considered (pink areas). Four health states are considered: one healthy and three damage cases comprising single or multiple debondings, namely damage cases *II*, *III*, and *VII*, also referred to as damage cases 1, 2, and 3, respectively, throughout this section.

¹Skin-to-stringer debonding spans along the whole width of the stringer foot.

Fig. 11 The FE model and the locations of the debonding cases



The FEA simulation results comprise the strain values at the stringer feet. More precisely, results refer to the right foot of the first stringer (from left to right in Fig. 11), both feet of the second and third stringers and the left foot of the fourth stringer. The naming of the stringers is given by the stringer number (1–4 from left to right), followed by an underscore and an index indicating the left (1) or right (2) foot. Hence, the stringer feet for which the strain data are extracted are named from left to right as follows: 1_2, 2_1, 2_2, 3_1, 3_2, and 4_1.

4.2 Strain Difference-Based Method

The goal of structural health monitoring (SHM) in general is to characterize the health state of a structure as *healthy or damaged* and possibly even define the type and location of damage. A method consisting of three distinct but closely related algorithms is developed and assessed in the current section. Each algorithm is based on the difference between healthy strain data and data² extracted from unknown structural state.

4.2.1 Strain Difference-Based Algorithm

The simplest of the methods used, the strain difference-based algorithm investigates the difference between the FBG readings of healthy and current state of the structure, producing a damage alert when this difference exceeds a predefined limit.

²Note that the same exact algorithms may also be applied to the normalized spatial derivative of the strain data (1st differences of the strain data), which is used in the “Tuning” section.

The algorithm is implemented in three steps: (1) Calculate the difference between the baseline and current strain measurements, (2) set a difference limit, and (3) produce damage alert if the difference falls out of the limit.

4.3 Mahalanobis Distance-Based Algorithm

In a similar manner to the above, the Mahalanobis distance algorithm is based on a metric of difference between strain data. This metric, the Mahalanobis distance, accounts for the stochastic nature of the measurements, by normalizing the difference between the signals and the sample standard deviation of the baseline signal, assuming that the standard deviation of the current strain measurement is the same as the baseline one.

In detail, the steps of the algorithm are: (1) Calculate the sample average and variance of the baseline (healthy) and current (possibly damaged) strain measurements, (2) calculate their Mahalanobis distance, (3) set an appropriate distance limit (user-defined), and finally (4) produce damage alert if the limit is exceeded.

The Mahalanobis distance DM of two datasets is given by:

$$D_M = \sqrt{\frac{(\overline{S_b} - \overline{S_c})^2}{\sigma_b^2}}$$

with s_b, s_c the baseline and current strain measurements, respectively, $\overline{(\cdot)}$ the sample average of a random signal, and σ_b^2 the variance of a random signal.

4.4 Normal Distribution-Based Algorithm

The cornerstone of the normal distribution-based algorithm is the assumption that the strain signals are normally distributed and the subsequent setup of a statistical hypothesis testing. The two signals, baseline and current, are merged into a single metric which follows a standard normal distribution. The final inference about the presence of damage or not is based on this metric and two alternative hypotheses for it:

Null Hypothesis (healthy structure): The metric equals zero. This means that the two datasets are statistically equal, and subsequently, there is no evidence for the presence of damage.

Alternative Hypothesis (damaged structure): The metric is not zero. This means that the two datasets are statistically non-equal, which means that there is a significant difference between the baseline healthy and the current states of the structure.

Fig. 12 The normal distribution-based statistical hypothesis testing



The steps of the algorithm are: (1) calculation of the baseline and current strain measurements sample average and variance, (2) subtraction of the averages and divide the difference by the sum of square roots of the corresponding variances, (3) selection of a confidence level and conduction of a statistical hypothesis testing based on the statistic calculated in step 2, and finally (4) damage alert if the statistic falls out of the confidence interval.

The quantity in the second step, given by the following formula, follows a standard normal distribution, under the assumption that each dataset is normally distributed:

$$N = \frac{\overline{s_b} - \overline{s_c}}{\sqrt{\sigma_b^2 + \sigma_c^2}} \sim \mathcal{N}(0, 1)$$

with N the test statistic, s_b, s_c the baseline and current strain measurements, respectively, $\overline{(\cdot)}$ the sample average of a random signal, σ_b^2, σ_c^2 the baseline and current strain measurements' sample variance, and $\mathcal{N}(\mu, \sigma^2)$ a normal distribution with mean μ and variance σ^2 (Fig. 12).

In the preliminary analysis, the main goal is to define the maximum distance between FBGs across the stringer feet that is able to detect damage with low false alarm and missed detection rates.

4.5 Investigation Plan

In order to assess the efficiency of the SHM algorithms, the following questions are set and answered:

1. What is the minimum number of FBGs that may be able to detect and localize damage?
2. How much noise can be tolerated by the damage detection system?
3. Does FBG positioning affect the damage detection performance?

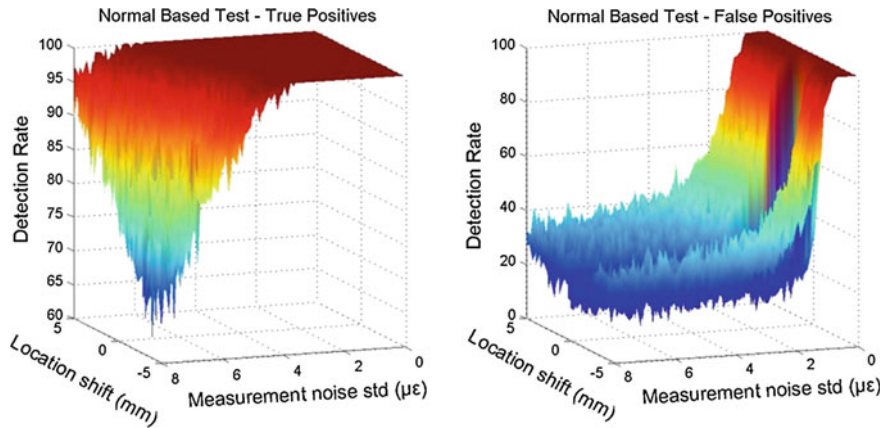


Fig. 13 Indicative results based on the hypothesis testing algorithm with 40.4 mm between FBGs

To answer the questions, the measurements are *artificially disturbed* with various noise levels, while the location of the FBGs is deviated as well. In particular:

- *80 different noise levels* are investigated: A random disturbance is added to the signal, with standard deviation from $0.1 \mu\epsilon$ up to $8 \mu\epsilon$ with 0.1 mm increments.
- *101 different FBG locations*, keeping the in-between distance constant: FBGs moved -5 up to 5 mm from their nominal location, with 0.1 mm increments (simulating manufacturing variability in FBG positioning).
- *100 Monte Carlo runs* for every noise level and every FBG location are conducted to calculate the corresponding statistics.

Hence, a total of 808,000 measurements are simulated based on the FEA results, based on which the SHM algorithms are preliminary assessed, based on the following criteria:

1. *True positive: Damage alert when damage actually exists.*
2. *False positive: Damage alert when there is no damage (false alarm).*

Indicative results are presented in Fig. 13.

The minimum distance between FBGs without jeopardizing the SHM system's ability to detect damage seems to be around 40 mm. The system is performing well under noise, while the uncertainty in FBG sensor placement does not significantly affect the results. Nevertheless, it should be noted that the false detection rate is very high (i.e., around 10 %). This problem is dealt with in the following section by properly tuning the algorithms.

4.6 Tuning

After defining the distance between FBGs, the algorithms are tuned to further enhance their efficiency. To achieve this goal, simulated datasets of fixed FBG distance are once more artificially disturbed with 400 different noise levels, ranging from $0.015 \mu\epsilon$ up to $6 \mu\epsilon$, while 100 Monte Carlo runs are conducted for each case to calculate the statistics.

Tuning refers to the damage indication limits of each algorithm, namely the strain difference limit, the Mahalanobis distance limit, and the hypothesis testing confidence level, for the first, second, and third algorithms, respectively.

The algorithms are assumed to perform well when at least 90 % true detection rate is achieved without the false detection rate surpassing 5 %. Tuning results are presented in Fig. 14 where the blue areas indicate the “noise level—tuning parameter” pairs that satisfy the above criterion. All algorithms achieve excellent performance for up to $2 \mu\epsilon$ noise amplitude, under a proper tuning.

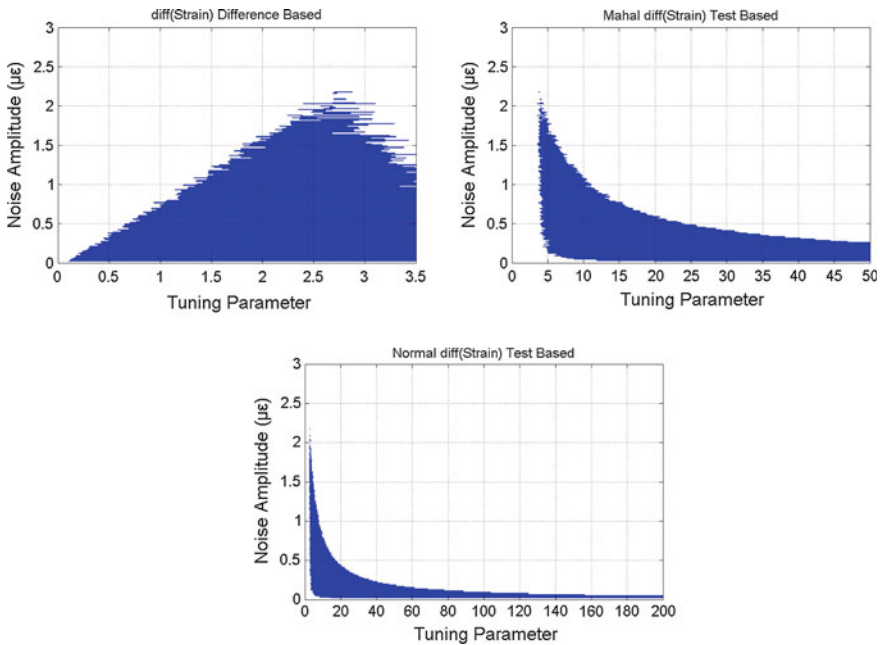


Fig. 14 Algorithm tuning. *Blue areas* indicate parameter values to achieve at least 90 % true and less than 5 % false detections. *Top left* Difference-based algorithm. *Top right* Mahalanobis distance-based algorithm. *Bottom* Hypothesis testing-based algorithm. All the algorithms are applied to the first spatial derivative of the strain readings

5 Experimental Validation of Theoretical Approaches

5.1 Objective

Under the scope of verifying and validating all the theoretical methodologies developed within AS04, an experimental building-up approach was defined at element and subcomponent level. Representative fuselage structures were designed and manufactured in order to evaluate the efficiency of the FE studies and algorithms in terms of satisfying criteria such as optimization of FOBG positioning onto the structure and system's capability of damage identification and detection.

5.2 Description of Composite Structures

The composite components that were proposed for the implementation of the test campaign, as already mentioned, referred to realistic fuselage structures. Typical combinations of CFRP skin with omega stringers attached were selected in order to perform a variety of experimental activities (static/fatigue compression, modal tests), setting as goal the qualification of the developed FOBG sensor system. In the following paragraphs, details concerning not only the design but also the selected production process of the components will be presented.

Having as reference the fuselage panels that were fabricated in AS12, the definition of the structures' configuration applied in AS04 was performed on the basis of material selection, components' thicknesses, stacking sequences, and stringer spacing. Some general characteristic of the panels that could be mentioned are as follows:

- The material that was utilized referred to a typical aerospace composite prepreg provided by Hexcel, named M21-T800S.
- Manual hand layup manufacturing process.
- Application of cobonding technique for the attachment of the omega stringers.
- Insertion of FM300 film adhesive at the area of the omega stringer feet to facilitate the bonding process.
- For both types of components (generic elements and subcomponents), the thickness of the skin and stringer was 1.656 and 1.834 mm, respectively.
- The metallic frames that were installed onto the structures were made from AL. AL. 2024-T351 having a "Z" section.
- The assembly of the metallic frame to the structures was performed applying blind rivets from steel alloy (MS90354S-0503D).

Design details addressed to each of the components are shown in the next sections.

5.2.1 Fuselage-Type Generic Elements with Assembly Details

The generic elements with assembly details comprised of a flat mono-stringer panel (Fig. 15).

Additional pads were installed under the metallic frame in order to increase the strength of the region in case 3-point bending test was performed.

Referring to the generic elements' test campaign, several configurations were investigated in terms of different damage sizes and locations. The positioning of the ribbon tape along with the various damage scenarios studied is shown in Fig. 16.

The placement of the FOBGs was derived according to the specifications resulted from a FE analysis implemented on similar panels. The outcome of this study recommended a sensor arrangement of approximately 35 mm distance from the damage so that the optical network will have the capability to detect debonding occurrences between the stringer foot and the skin. Information concerning this theoretical approach is available upon request. At the final stage, the optical fibers, taken into account the guidelines defined from the theoretical approach, were bonded, applying secondary bonding technique onto the generic elements.

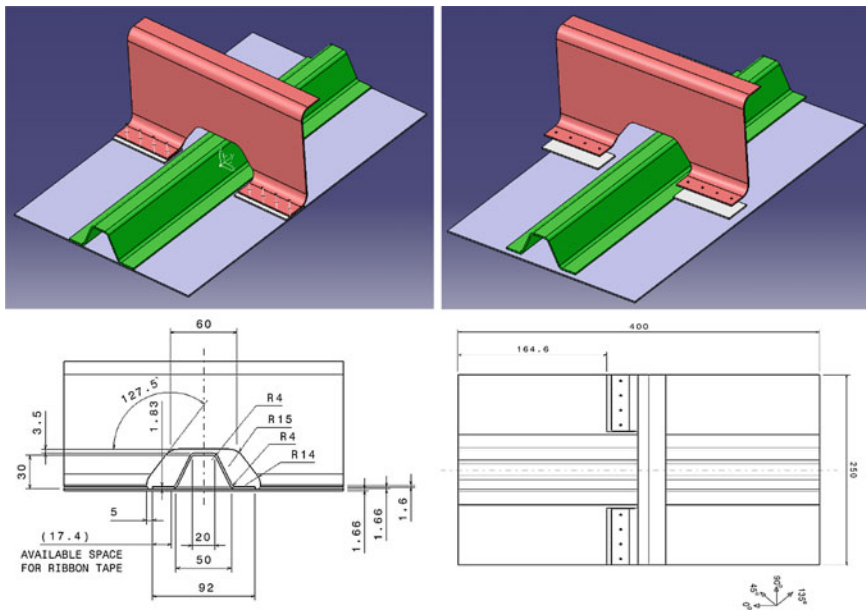


Fig. 15 Generic elements with assembly details

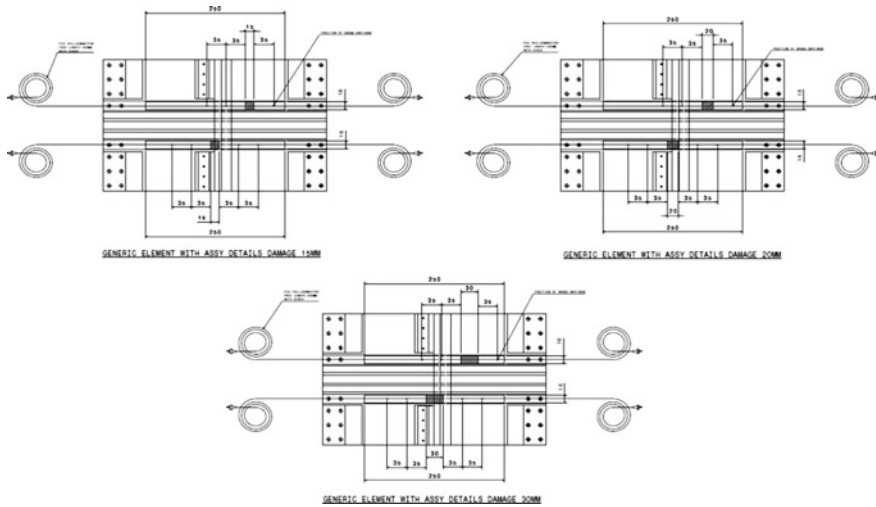


Fig. 16 Generic elements with assembly details—damages/ribbon tapes

5.2.2 Fuselage-Type Generic Subcomponents

Representative fuselage-type generic subcomponents were manufactured incorporating an optical fiber network, having as an objective the detection of potential damages developed in the structure. The tests will validate the Modal Strain Energy Damage Index algorithm, which is considered as a proper methodology to identify skin–stringer debonds in fiber-reinforced composite structures.

The conceptual design and the production route of the panels were similar to the techniques applied to the generic elements.

As shown, the generic subcomponent configuration refers to a flat panel carrying three omega stringers and two metallic frames. Details regarding geometrical features, such as stringers' and frames' spacing, were specified from AS12.

For the generic element, the full size panel (Fig. 17) various sizes of damages and locations were determined either in regions with high deformation, such as the middle bay area, or near regions with increased stiffness, such as the frame proximity. Again, in this case, a modal-based theoretical model was executed in order to tackle the number of the sensors along with their arrangement in each bay.

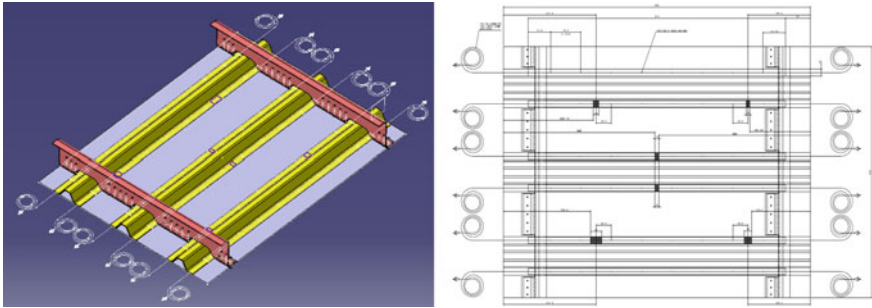


Fig. 17 Generic subcomponents—damages/ribbon tapes

6 Fiber-optic Distributed Sensing of the Effects of Impacts on Fuselage Panels

Two fuselage panels, as shown in Fig. 18, were subject to impacts before a compression test. The panels comprised a skin strengthened by four stringers. Twenty-four FBGs, spaced 40.4 mm apart, in the form of 4 ribbon tapes were

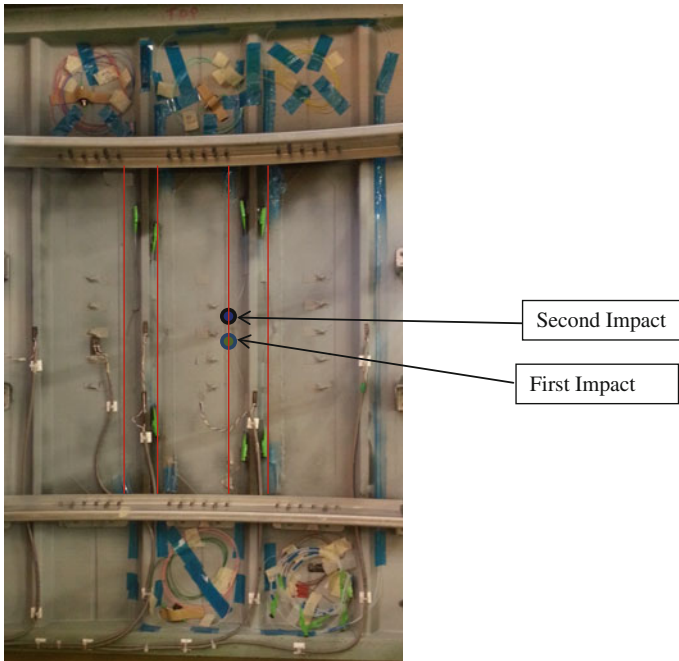


Fig. 18 The fuselage panel. The red lines denote the location of the fibers, used for the distributed sensing measurements. All these fibers sit on the two feet of the center two stringers. Also embedded onto each foot are 24 FBGs (spaced 40 mm apart) in 4 ribbon tapes



Fig. 19 Distributed measurement of the strain following impacts. **a** After one impact; **b** after 2 impacts, spaced 40 mm apart; **c** after two impacts, but references to the panel state before the first impact

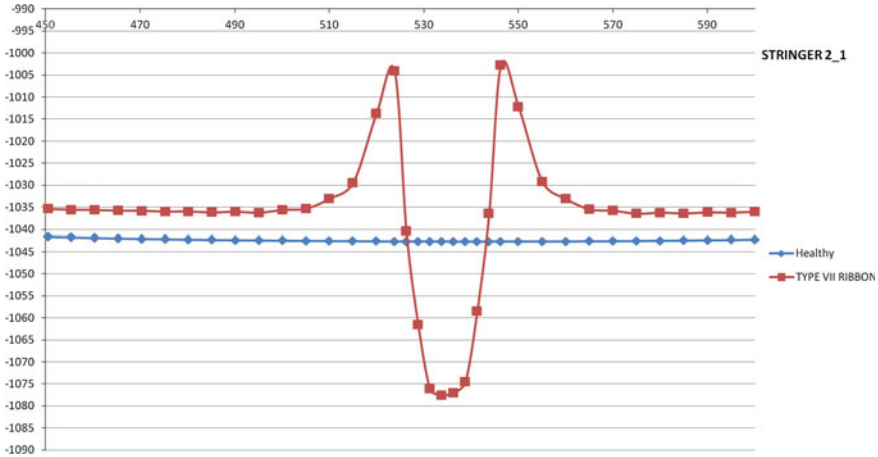


Fig. 20 The calculated effect of a 20×30 mm debond between the skin and stringer foot on strain distribution when high compressive load is applied

embedded on the two feet of the center two stringers. In addition, a standard, untreated polyimide-coated single-mode fiber was also glued along the same feet to serve for distributed sensing. All distributed sensing fibers, as shown in Fig. 18, were concatenated so that they could be interrogated from a single access point. Strain interrogation was performed using the Luna Technologies OBR 4600 optical backscattering reflectometer, on courtesy loan from Luna Technologies.

Strain measurements along the standard single-mode fiber (no FBGs) were performed using coherent frequency-domain reflectometry (OFDR) of Rayleigh backscattering. A reference reading was taken before any impacts. The strain induced by the first impact was calculated by comparing the reading after the first impact against the reading before the impact, Fig. 19a, b. The strain after the second impact, compared to the no impacts state, clearly showing two peaks Fig. 19c, reflecting the fact that the two impacts hit the plate 40 mm apart. The effect of the second impact alone was compared to the plate state before its application, showing a single displaced peak, as shown in Fig. 19b. Note that these significant strain signatures were obtained without any mechanical loading and they represent effects of impacts that left no visible traces on the outer surface of the plate.

The strain signatures in Fig. 19a, b look similar to those obtained from a FE calculation of the effect of compression on the strain field change from a healthy state when a debond of 20×30 mm is introduced between the skin and the stringer foot (see Fig. 20).

While the calculations and measurements were performed under different conditions, they show similar trends.

7 Conclusions

Concerning the first proposed methodology, the PCA method, since a small amount of damage slightly affects the global stiffness and the local strain field of the structure, very high sensitivity techniques for strain measurements must be used in order to maximize the resolution of the technique. FBGs have shown to be very sensitive to small strain changes in the structure, which makes them suitable for the proposed technique. In all the cases (T -scores, $T2$ indices, Q indices), it was possible to detect some deviations between the baseline (and the undamaged case) and the different damage cases. The Q index has shown more sensitivity in this study.

Modal strain energy damage indicator (MSE-DI). The DI are based on the changing modal characteristics between an initial and a damaged state. Results were shown for a three-stringer aircraft panel of successful detection for different damage scenarios, even for small damages. An approach was presented and applied to the same panel to determine the detection capability of the SHM system reflected by the POD curve, assuming a SNR. The applicability of the MSE-DI depends on the obtained SNR that can be reached in a practical application.

Concerning the third method, from the preliminary analysis, the following results are drawn from the numerical simulation: (I) A distance of 40 mm between FBGs seems adequate to have damage detectability and (II) the efficiency of the algorithms regarding the true damage detection achieved an 100 % *true positive rate for up to 3 $\mu\epsilon$ std.* Nonetheless, the false detection rate remained relatively high.

By tuning the algorithms, a better trade-off between false and true detection rates was achieved. In particular, all three methods may achieve the 90 % true–5 % false indication criterion when based on strain data difference for up to $\sim 1.5 \mu\epsilon$ noise amplitude (i.e., $\sim 0.5 \mu\epsilon$ noise std). When the strain spatial derivative is used instead of the raw strain data, the 90–5 % criterion is achieved for up to $2 \mu\epsilon$ noise amplitude.

Actual fiber-optic distributed strain measurements on fuselage panels show the potential of fiber-optic sensing for damage detection in future SHM applications.

Acknowledgments “The research leading to these results has received funding from the European Union’s Seventh Framework Programme for research, technological development and demonstration under grant agreement No. 284562.”

References

1. SAE-ARP6461 (2013) Guidelines for implementation of structural health monitoring on fixed wing aircraft
2. Fernández A, Menendez J, Güemes A (2007) Damage detection in a stiffened curved plate by measuring differential strains. In: International conference on composite materials, Kyoto
3. Sierra J (2014) Development and experimental validation of a structural health monitoring system for damage detection. Ph.D. thesis. Aerospace Engineering School, Polytechnic University of Madrid, Madrid, Spain

4. Mujica L, Rodellar J, Fernandez A, Guemes A (2010) Q-statistic and T2-statistic PCA-based measures for damage assessment in structures. *Struct Health Monit* 1–15
5. Sierra J, Guemes A, Mujica L (2013) Damage detection by using FBGs and strain field pattern recognition techniques. *Smart Mater Struct* 22:25011–25020
6. Sierra J, Güemes A, Mujica LE (2013) Damage detection by using FBGs and strain field pattern recognition techniques. *Smart Mater Struct* 22:1–10
7. Sierra-Pérez J, Torres-Arredondo MA, Cabanes G, Güemes A, Mujica LE, Fritzen CP (2014) Damage detection in metallic beams from dynamic strain measurements under different load cases by using automatic clustering and pattern recognition techniques. In: *EWSHM-7th European workshop on structural health monitoring*
8. Grooteman FP (2012) Damage detection and probability of detection for a SHM system based on optical fibres applied to a stiffened composite panel. *ISMA2012, Leuven*, pp 17–19

Load Monitoring by Means of Optical Fibres and Strain Gages

**Alessandro Airoidi, Giuseppe Sala, Rolf Evenblij,
Christos Koimtzoglou, Theodoros Loutas, Giovanni Marco Carossa,
Pasquale Mastromauro and Toni Kanakis**

Abstract This chapter describes the development of load monitoring systems integrated in the demonstrator of a smart wing structure. A monitoring system has been designed and installed on composite spars, with the aim of mapping the load conditions along the axes of such components. Such system is based on optical fibres embedded in ribbons, which have been externally bonded to the spars according to a specific optical architecture. A second system, based on conventional strain gages, has been designed to provide the sectional loads on the whole wing during wind tunnel testing and to interact with an aerodynamic load model. Both monitoring systems have been defined by using detailed FE models of the spar and of the whole wing box. Algorithms for the identification of internal and sectional loads have been developed. Finally, a third type of system is conceived to evaluate the possibility of damage detection into composite spars by using a denser network of sensors. The numerical procedures followed for the design and the calibration of the systems are discussed to assess a methodology for the development of health and usage monitoring systems to be applied in advanced aerospace structures.

A. Airoidi (✉) · G. Sala
Department of Aerospace Science and Technology, Via La Masa, 34,
20156 Milan, Italy
e-mail: alessandro.airoidi@polimi.it

G. Sala
e-mail: giuseppe.sala@polimi.it

R. Evenblij
Aeronautics/Space and Automotive Testing, Technobis Fibre Technology,
Pyrietstraat 2, 1812SC Alkmaar, The Netherlands
e-mail: rolf.evenblij@technobis.com

C. Koimtzoglou
Integrated Aerospace Science Corporation (INASCO), 18 N. Zerva St,
166 75 Glyfada, Athens, Greece
e-mail: c.koimtzoglou@inasco.com

1 Introduction

Health and usage monitoring systems may have a key role in the definition of new strategies for the design and the maintenance of modern aerospace composite structures. Design of composite components is notoriously determined by damage tolerance considerations, since both technological processes and load events occurring in service conditions can induce non-barely visible damages in composites. Indeed, additional uncertainties arise since innovative composite and hybrid structural architectures may behave in more complex ways than traditional metallic structures, under the action of thermo-mechanical loadings in service conditions. Moreover, the presence of damage does not only concern the behaviour of a damaged part, but potentially modifies load paths and local loadings on other primary parts, in difficulty predictable ways. Therefore, the application of damage tolerance strategies has to face a series of uncertainties that, eventually, opposes to a complete exploitation of the advantages of composites and increases the costs in the design phase and in maintenance operations.

Monitoring systems based on optical fibres (OF) can provide a substantial aid to address such issues. Fibre Bragg gratings (FBG) carried by OF can measure localized strains, being immune from electro-magnetic interferences, at a weight cost that is a small fraction of the one required by traditional strain gages, including all the auxiliary systems required for sensor interrogation [1]. Moreover, measuring networks based on OF's can be installed in composite structures by providing protection from external agents, with different levels of physical integration that depend on specific requirements.

Indeed, such characteristics of OF-based sensor networks make conceivable the integration of a relatively large number of sensors into a structural component. Such networks will be characterized by a moderate weight cost and could be reliably interrogated in flight conditions at adequate frequencies, so to make possible the reconstruction of the strain field evolution on the structural component in operative conditions.

T. Loutas
Department of Mechanical Engineering and Aeronautics,
University of Patras, 265 04 Panepistimioupoli Patron, Greece
e-mail: loutas@mech.upatras.gr

G.M. Carossa · P. Mastromauro
Alenia Aermacchi, C.so Francia 426, 10146 Turin, Italy
e-mail: giovanni.carossa@alenia.it

P. Mastromauro
e-mail: pasquale.mastromauro@alenia.it

T. Kanakis
Department of Collaborative Engineering Systems, National Aerospace Laboratory (NLR),
Anthony Fokkerweg 2, 1059 CM Amsterdam, The Netherlands
e-mail: Toni.Kanakis@nlr.nl

The spatial resolution and the level of physical integration of OF's into the structures required to extract meaningful information from sensor data depend on the scope of strain sensing. Indeed, if the objective is the identification of internal local damages in a composite structure, such as in the application described in [2–6], a very refined network is required and sensors embedded in composite laminates are likely to represent the best choice to detect the signatures of damage on the strain state. Conversely, few strain sensors can be required to know approximately the resultant of the external forces applied to a structure. Such monitoring systems are often used in testing the real-world aircraft structures and are implemented with conventional strain gages. At an intermediate level, a relatively dense network of sensors can be applied to a structural component to reconstruct the strain field for a more detailed evaluation of the internal loads and of the loads transmitted by the surrounding components. Such reconstruction can be based on algorithms similar to those developed for inverse FEM methodologies [7, 8].

In this work, all the three types of monitoring systems will be considered for application to the wing demonstrator developed in project Smart Intelligent Aircraft Structures (SARISTU), which integrates innovative solutions for the adaptation of the wing shapes to different flight conditions, such as morphing leading and trailing edges and an active winglet.

In the wing box of the demonstrator, two carbon-reinforced composite spars represent the main structural elements. They are well suited for the integration of a monitoring system based on OF, which can be placed along longitudinal paths and physically integrated according to different techniques. Such installation exploits the efficient multiplexing techniques that are available for optical fibre-based monitoring systems, such as wavelength division multiplexing, which allows several sensors on the same fibres [1]. Monitoring of detailed load conditions of the spars is considered in the first part of the paper, by developing a load monitoring system with an intermediate level of sensors density. The system is designed considering FBGs carried by external OF's, which are embedded into glass-fibre-reinforced ribbons that are bonded to the surface of the spars. The optical architecture is presented, as well as the algorithm for the identification of a parameterized load system, which was developed by using finite element models of the spars, taking into account the effects of uncertainties in numerical models.

Monitoring of internal forces (sectional loads) in the entire wing box is performed by developing a system based on conventional strain gages. Such system is presented in the second part of the paper, including the finite element model of the demonstrator, which has been used to evaluate the matrices that will allow the calculation of the internal forces in the wing section from the local strain signals.

In the third part of the paper, a study regarding the feasibility of damage detections on composite spars by means of strain sensing is reported. The effects of internal delamination on the strain field are examined for a generic C-shaped spar element and the influence of lamination sequence on such effects is outlined. A system based on OF's embedded in the spar is designed and the possibility of detection of the anomalies induced by damage on the strain field is discussed.

Finally, an example of aeroelastic model for load prediction is presented and the possible strategies to enhance the reliability of the presented monitoring systems based on the interactions among different numerical approaches are discussed. The interaction between the finite element models and the load monitoring systems developed for the spars and the wing box will be discussed in the final part of the paper.

2 FO-Based Load Monitoring Network for Composite Spars

At an intermediate level between the identification of global loads acting on a structural element and the identification of local damages, monitoring systems can be used to identify the detailed load conditions experienced by structural components.

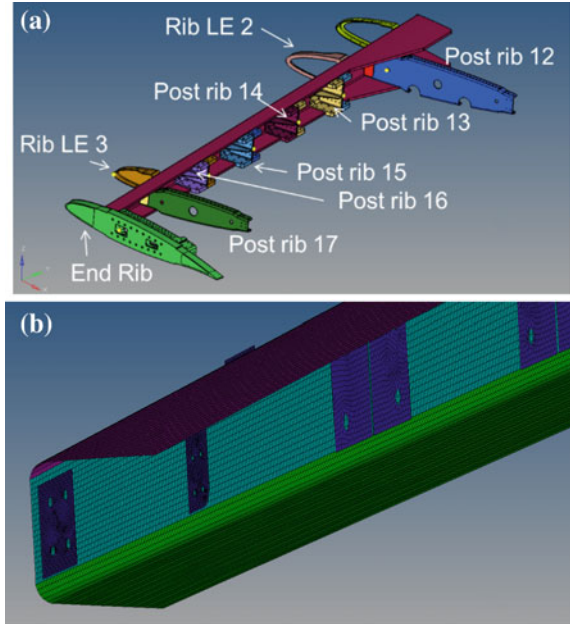
Such level of application becomes particularly interesting for innovative and complex structural architectures, which have been designed by adopting particularly conservative assumptions, due to difficulties in the prediction of their thermo-mechanical response. A detailed knowledge of load conditions in the most important structural parts would provide significant information to define and update maintenance operations. Moreover, the availability of a continuous monitoring of the structural response can be exploited to detect the modification of load paths derived from structural ageing, by the presence of damage in redundant parts and by the introduction of new flight configurations. Potential advantages are also related to the application of innovative morphing structures to perform load alleviation and to optimize the shape of aerodynamic surfaces for different missions or mission segments [9], which can increase the variety and the uncertainties of load conditions that can be experienced by the structural components of a flight vehicle.

Sensor networks based on OF are well suited to the identification of detailed load conditions on the spars of aircraft structures, since loading can be approximated by a parameterized system of concentrated loads, transmitted by ribs, and distributed loads applied through the junctions between the flanges and the skins. Such load distributions represent the discrete variables to be identified by using a procedure that minimize the residuals between the experimental strains and the strain distribution obtained by a model of the spar subjected to the parameterized load system.

2.1 *Load Identification Problem*

The spar considered for the development of the load monitoring system is presented in Fig. 1a. Some of the internal ribs in the wing box are connected by means of relatively bulky rib-posts, bolted to the web of the spar. The load identification

Fig. 1 Forward spar (a) and finite element modelling technique (b)



procedure that is implemented is based on two fundamental ingredients: the parameterization of the load system and the development of a finite element model of the spar, which is used to link the local strains to the load parameters. A detail of the model is shown in Fig. 1b. It was developed by using shell elements with typical size of 5 mm, for a total number of about 50,000 shells. The rib-posts were modelled by means of rigid plates, also shown in Fig. 1b, that were connected to the spar by rigid links in correspondence of the bolts.

The method used for the identification can be regarded as a part of an inverse FEM approach, aimed at the reconstruction of displacement and strain field in an element based on local strain acquisition [7, 8]. Indeed, a possible strategy to solve the problem can be based on a two-step solution procedure: a structural analysis based on a finite element model followed by a least square algorithm [8]. Such approach requires the identification of a reconstructed loading condition, which allows the final identification of the overall displacement and strain field.

Assuming a linear behaviour, the approximation of the loading conditions involves that the strain field can be regarded as the superposition of the strains induced by the M components of a parameterized load set, which can include both concentrated and distributed types of load, with amplitudes represented by a vector $\{F\}$. Considering a set of N local strains, $\{e^*\}$, acquired at given position by the sensor network, the application of a single term F_i of the load vector leads to a set of strain values that can be expressed as in Eq. 1, under the assumption of linear response.

$$\{\varepsilon^*\}_i = \{\alpha\}_i F_i \quad (1)$$

where $\{\alpha\}_i$ is a vector of influence coefficients, which provides the local strains for a unit value of the load term F_i . The superimposition of all the parameterized loads leads to a vector of strain measures that is expressed by defining a rectangular matrix of influence coefficient, $[\alpha]$, whose columns are the vectors $\{\alpha\}_i$, as indicated in Eq. 2.

$$\{\varepsilon^*\} = \sum_{i=1}^n \{\varepsilon^*\}_i = [\{\alpha\}_1 \quad \{\alpha\}_2 \quad \dots \quad \{\alpha\}_N] \{F\} = [\alpha] \{F\} \quad (2)$$

If the matrix $[\alpha]$ is known and the vector of strains $\{\varepsilon^*\}$ is given, the vector of the unknown loads $\{F\}$ can be evaluated by minimizing the squared norm of the distance between the experimentally acquired strains and the strains computed by using $[\alpha]$, as expressed in Eq. 3.

$$\|\{\varepsilon^*\} - [\alpha] \{F\}\|^2 = \sum_{j=1}^m \left(\varepsilon_j^* - \sum_{i=1}^n \alpha_{ij} F_i \right) \quad (3)$$

The minimization of the norm in Eq. 3 leads to a least square problem with the solution expressed in Eq. 4.

$$\{F\} = ([\alpha]^T [\alpha])^{-1} [\alpha]^T \{\varepsilon^*\} \quad (4)$$

The idealization carried out in the set-up of the identification problems involves several errors and approximations. A first aspect that can be analysed is referred to the definition of the parameterized load system.

From the engineering standpoint, spars are subjected to two types of loads, namely concentrated loads applied by the ribs and distributed loads applied through the junctions with the upper and lower skins. In the wing demonstrator considered in this work, the presence of the peculiar actuation system to morph the leading edge and the aerodynamic pressures applied to the winglet increases the importance of longitudinal forces applied to the spars. On the basis of such considerations, the parameterized load system shown in Fig. 1 was chosen, including:

- (a) vertical forces—applied to rigid bodies representing all the rib-posts;
- (b) longitudinal forces—applied to rigid bodies representing the bulky rib-posts and the end rib, which represent the forces introduced by the winglet and the actuation system of the morphing leading edge;
- (c) bending moments—applied to rigid bodies representing the bulky rib-posts, in order to consider a displacement of the force resultants;
- (d) uniformly distributed shear forces within all of the bays—applied along the upper and the lower flanges;

- (e) distributed torsional moments within all of the bays—applied to flanges by means of two distributions of forces with opposite signs along the chord directions;

Overall, the system consists of 29 load components. Considering the loads in a reference cruise conditions, a set of reference loads was defined, with the values reported in Tables 1 and 2, which are referred to concentrated and distributed loads, respectively. For distributed longitudinal loads, two versions of the reference load system were considered with resultants along the bays reported in Table 2.

The identification of the parameterized load system presented in Fig. 2, Tables 1 and 2 is considered the target of monitoring system. However, real loading can be considered as the sum of the parameterized loading system and of a corrective system, which can be represented by a vector of *m* components, with amplitude defined by the vector {*f*}. Accordingly, the strain in the physical system would be represented, still assuming the validity of the linear behaviour, by the following expression:

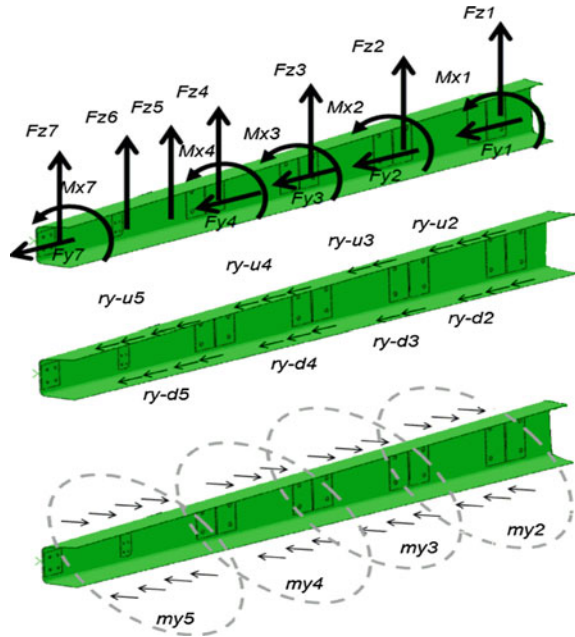
Table 1 Reference concentrated loads

	Vertical force (N)	Bending moment (N)	Shift of vertical force (mm)	Long. force (N)
Rib 13	1506	-176.5	117	-800
Rib 14	1871	-51.8	27	600
Rib 15	1716	-21.6	13	-400
Rib 16	1261	0.385	3	200
Rib LE3	673	-	-	-
Rib 17	740	-	-	-
Rib End	3072	18.5	6	-500
Total	10,893	272.25	166	2500
Total (abs)	10,893	268.78	166	2500

Table 2 Reference distributed loads

	Long. distributed load up (resultant) (N)		Long. distributed load down (resultant) (N)		Transv. distributed load (resultant) (mm)	
	a	b	a	b	a	b
Rib 13–Rib14	-510	255	-510	-255	255	112
Rib 14–Rib15	-765	204	-765	-204	255	-87
Rib 15–Rib16	-1020	153	-1020	-153	155	-173
Rib 16–End Rib	-600	240	-600	-240	258	504
Total	-2895	852	-2895	-852	923	356
Total	2895	852	2895	852	923	876

Fig. 2 Parameterized load system



$$\bar{\epsilon}_j^* = \alpha_{ij}F_j + \beta_{kj}f_k \tag{5}$$

Equation 5 provides an indication regarding the errors that can be introduced with the simplification of the load system. The accuracy in the identification of the load components depends on their influence on the local strains. If the omitted corrective system is characterized by low amplitude coefficient of the force components, f_k , or to a limited value of the influence coefficients β_{kj} , the simplification will not greatly affect the identification of amplitudes $\{F\}$ with the experimental strains, providing that the selected components have a significant effect on the strain field.

2.2 Architecture of the Monitoring System

The specification of the monitoring systems based on OF within project SARISTU took into considerations several issues regarding the physical integration of sensors, the reparability and maintainability of the monitoring system and the limitation of risks related to possible detrimental effects of OF's application on the structural response. Such considerations suggested that the external application of OFs was to be considered the preferable option for the development of the monitoring system. Moreover, owing to their small dimensions and intrinsic brittleness, direct handling of bare fibres is not conceivable; besides, the exiguity of bonding surface cannot

guarantee adequate load-transfer capability. To overcome these drawbacks, a special device should always be used, consisting in a thin, narrow and compliant laminate made of glass-fibre-reinforced plies, embedding OF's. Such a ribbon protects and insulates the OF, allows a perfect adhesion to moderately curved surfaces and does not prevent the adoption of high-temperature processes, being irrespective of possible low thermal stability of OF coating [10, 11]. In project SARISTU, a technology to produce sensorized ribbons was developed to be adopted for different applications [12]. Ribbons may have different widths and the embedded OFs may be endowed with several FBGs, according to the specifications of the monitoring system.

The integration of sensorized ribbons into the spars has to face problems regarding the presence of the ribs and of the rib-posts and to take into consideration the possible interferences with junctions lines with the skins and the auxiliary spars carrying the morphing leading and trailing edges. The most feasible solution was the bonding of ribbons to the inward surface of the C-shaped spars, within each of the bays, without requiring the passage of the ribbons through the ribs. Such choice avoids the need of ribs specifically designed for allowing ribbon applications, though it can complicate the routing of OFs, which have to connect different ribbons to maximize the exploitation of multiplexing capabilities of OF-based sensor networks.

The layout of the ribbons installation on the forward spars is shown in Fig. 3a. It can be seen that six sets of ribbons are considered along the spar axis. Each set is to be installed within a bay and consists of six 16-mm-wide ribbons positioned in the section as shown in Fig. 3b. On the bays 5 and 6 a longer ribbon is installed, since such bays are not divided a wing box rib, but by a rib nose at the end of the morphing leading edge. The optical architecture is exemplified in Fig. 3c in a generic case. Actually, each ribbon carries a variable number of FBG sensors.

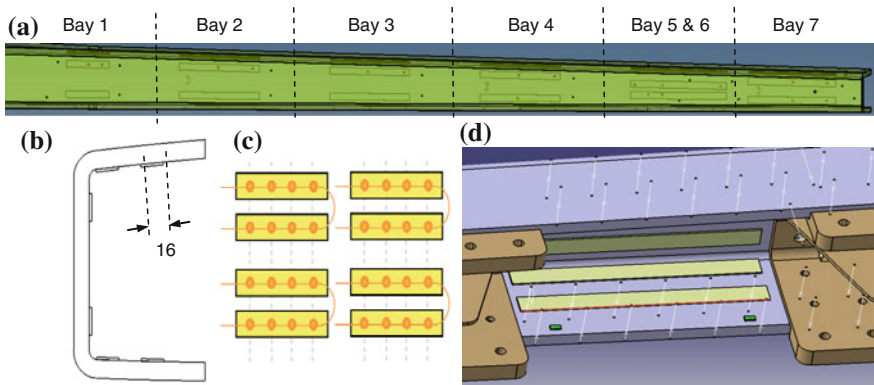


Fig. 3 Integration of monitoring system: layout of sensorized ribbon installation of the spar (a), optical architecture (b), details of ribbon installation (c) and typical position of ribbons in a section (d)

Interrogation procedure will be based on wavelength division multiplexing with a maximum of eight sensors per OF. Accordingly, several ribbons could be connected by the same OF, with the possible adoption of the connectors described in [12]. The availability of a return line actually constitutes a redundancy for the monitoring system, since it will be possible to interrogate the FBG sensors from both sides still maintaining the system functionality in case of an interruption in the optical fibre.

The detail shown in Fig. 3d is referred to a bay of the forward spar. The position of the ribbons was chosen in order to avoid the interferences with the post-ribs, the junction lines and the strain gages of the monitoring system for the sectional loads, which are represented by the green rectangles in Fig. 3d. The configuration presented in Fig. 3 is typical for all the bays of the forward spar, whereas for the rear spar, configuration is analogous but presents only four ribbons in each bay.

Strains will be acquired at 100 Hz frequency and all sensors belonging to a spar will be interrogated at same time, in order to achieve a complete information regarding the evolution of the strain field in the entire spar of the demonstrator during the tests.

2.3 Design of the Monitoring System

A numerical activity was carried out to design the monitoring system in order to achieve an appreciable trade-off between the number of sensors and the accuracy in the identification of the components of the parameterized load system. Such activity was aimed at designing the system in terms of number and positions of the sensors integrated in the ribbons bonded to the spars and was focused on the system installed on the forward spar.

The position of the ribbons was defined based on technological and engineering considerations, presented in the previous sections. The maximum number of FBG per ribbon was set to three, excluding the long ribbons applied to bays 5 and 6, where six FBG positions were considered. Such considerations lead to an available number of 126 positions for the FBGs installed on the spar. Considering equispaced sensors on the ribbons, the potential locations of the sensors in the forward spar are shown in Fig. 4.

The sensor configuration is described by means of an array of 18 flags, each one corresponding to a potential sensor position. Flags assume a value of 1 if the position is occupied by an active sensor; otherwise, the value is set to 0.

The strains to be identified are obtained by applying the reference loads to the finite element model of the spar. Hence, the output of such virtual test model is used to surrogate the strain vector to be acquired by monitoring system $\{\varepsilon^*\}$.

For a first verification of the algorithm, the *surrogate* model is the same used to calculate the matrix of influence coefficients $[\alpha]$ (*nominal* model), according to the procedure explained in Sect. 2.1. The influence coefficients are calculated for all the potential sensors positions. Thereafter, the selection of the rows of matrix $[\alpha]$ can be

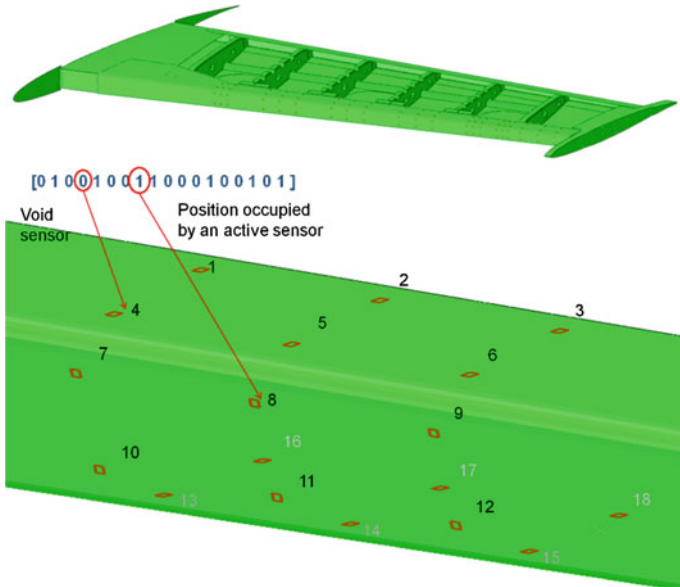


Fig. 4 Potential sensor positions and coding for active sensors identification

performed based on the coding array that describes the specific sensor configuration in the bay.

To evaluate the performance of the load identification system, an identical configuration of n_b active sensors per each bay was assumed. A Monte Carlo approach was applied by randomly generating sensor configurations, equal for all the bays. The root square mean error (RMSE) and the maximum error (MAXERR) were evaluated for each configuration.

Since the problem is linear, the adoption of a set of well-positioned sensors with a number equal to the one of the components of the load system should be adequate for a successful identification. Indeed, a small error is obtained for numerical reasons, and such error decrease as the number of sensor is increased as it is shown in Fig. 5, which reports RMSE and MAXERR percentage indices for the best 50 sensor configurations at five, six and eight sensors per bay after the exploration of 1000 configurations. The adoption of eight sensors per bay leads to an RMSE less than 0.15 % and to a MAXERR error lower than 0.4 %.

However, the development of the algorithm based on the spar finite element model involves difficulties related to the discrepancies between the physical properties of the spar and nominal model. For such a reason, the performance of the load identification algorithm was evaluated considering the strains obtained by applying the reference loads to a surrogated model with variations regarding the thickness and the orientation of the plies. Accordingly, the coefficients of influence are still the a_{ij} obtained by unit-load analyses on the nominal model, whereas the

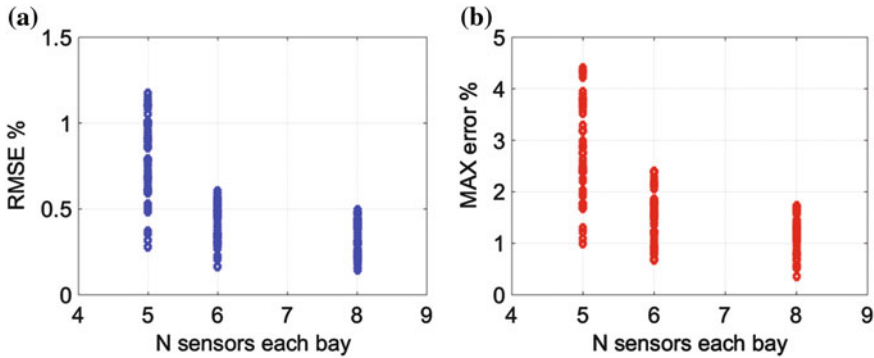


Fig. 5 Root mean square error and maximum errors in percentage for the best 50 sensor configurations using identical nominal and surrogate model

target strains can be represented as the combinations of effects acting on a surrogate model with coefficient of influence $a_{ij} + \Delta a_{ij}$.

Accordingly, the norm to be minimized for the identification of the parameterized load system is equivalent to the one obtained by introducing an equivalent disturbance in target strains, as it is represented in Eq. 6:

$$\begin{aligned} \min \|\{\varepsilon^*\} - [\Delta\alpha]\{F\} - [\alpha]\{F\}\|^2 &= \min \|\{\varepsilon^*\} - [\Delta\varepsilon^*] - [\alpha]\{F\}\|^2 \\ \Rightarrow \{F\} &= ([\alpha]^T[\alpha])^{-1}[\alpha]^T(\{\varepsilon^*\} - [\Delta\varepsilon^*]) \end{aligned} \tag{6}$$

The distribution of the equivalent disturbance is characterized by a mean value, which indicates that the overall response of the nominal model is different from the one of the surrogate models representing the physical spar, and by standard deviation (STD), which represents local variations between the nominal and surrogate model. The error due to such local variations is expected to be reduced by an increment in the number of sensors.

The evaluation of the influence of discrepancies between the nominal and the physical spar was considered by introducing in the surrogate model a variation in the thickness and in the orientation of the plies. The lamination sequence of the spar consists of about 70 carbon-reinforced plies, with unidirectional and fabric reinforcement. A variation in the ply thickness was introduced with a coefficient of variation (COV) of 3.6 %, whereas the orientation angles were modified with a variation having a null mean value and 1.5° of STD. A Monte Carlo approach was applied by exploring 10,000 configurations and the results reported in Fig. 6 provide the performances of the best 10 configurations with five, six and eight sensors per bay.

The results indicate that both types of errors in the identification of the parameterized load system decay as the number of sensor is increased. Maximum error can be below 27 % by using eight sensors per bay, whereas the RMSE index can be reduced to 11.5 % by choosing an adequate sensor configuration. However,

Table 4 Example of identification error for concentrated loads

	Vertical force (%)	Bending moment (%)	Shift of vertical force Δ (mm)	Long. force (%)
Rib 13	7.83	23.3	-34	19.5
Rib 14	6.20	17.1	-6	3.7
Rib 15	1.99	34.2	4	17.0
Rib 16	2.34	56.4	2	28.0
Rib LE3	5.19	-	-	-
Rib 17	4.85	-	-	-
Rib End	1.03	4.1	1	19.8
Mean	4.2	19.3	-4.7	12.5

Table 5 Example of identification error for distributed loads

	Long. distributed load up (%)		Long. distributed load down (%)		Transv. distributed load (%)	
	a	b	a	b	a	b
Rib 13–Rib 14	2.2	12.1	-6.2	-8.8	-5.1	13.5
Rib 14–Rib 15	3.5	22.8	-8.0	-24.9	-1.3	-7.2
Rib 15–Rib 16	-1.5	5.8	-3.7	-10.4	3.3	1.0
Rib 16–End Rib	-5.2	-12.8	-22.9	-65.0	16.6	1.9
Total	-0.25	6.97	-10.2	-22.3	3.37	2.3

Indeed, the accuracy in the identification of each load parameter is related to its influence of the longitudinal strain and to the number of sensors that are affected by the load value. Due to the constraint conditions, the loads applied towards the tips affect much more sensors than the ones applied to the wing root. Both observations are confirmed by the analyses of the *bending moment* and of the *shear forces* generated by the system of loads identified by algorithm. The internal forces obtained by applying the algorithm to the nominal model are correct and are compared in Fig. 7 with the ones obtained by using a surrogate model with COV of

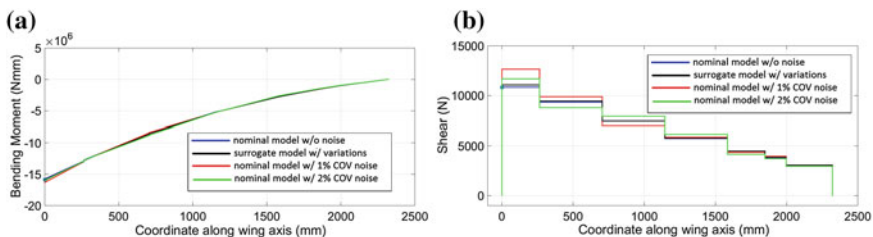


Fig. 7 Internal bending moment (a) and shear force (b) generated by the load system identified in different cases

5 % for ply thickness and a STD of 2° for ply orientations. Moreover, such solutions are compared with the internal forces obtained by superimposing two Gaussian noises to the strains $\{\varepsilon^*\}$, with a null mean value and a STD of 1 and 2 %, respectively.

It can be observed that the bending moments identified are very close to the correct solutions in all of the cases, whereas the shear force presents errors that increase from the tip to the root of the demonstrator. Moreover, the errors induced by the superposition of noise are higher than the ones originated by modelling errors, even if the variation of local strains is lower.

3 Monitoring System for Sectional Loads in the Wing Demonstrator

The second type of load monitoring system introduced in the wing box demonstrator is aimed at monitoring the internal forces in the entire wing box. The implementation of the system is based on strain gages, which are mainly installed in the spars of the demonstrators. The system was specifically developed to measure the evolution of internal forces during wind tunnel and ground testing of the wing demonstrator developed in project SARISTU. Although load monitoring capabilities are limited to the evaluation of internal forces in three sections, the methodology used to design the load monitoring system and to specify the load identification algorithm was based on the development of a detailed finite element model of the demonstrator. Such model represents a valuable tool to investigate the performance of the wing demonstrator and of the different monitoring systems installed in the wing box.

The following subsection describes the monitoring systems, the development of the finite element model and of the load identification algorithms, and the verification of the algorithm considering the load conditions obtained by aeroelastic models of the demonstrator.

3.1 Description of the Monitoring System

The monitoring system for the evaluation of internal forces is based on sets of strain gages, installed at three selected sections in the wing box of the smart wing demonstrator. The three sections endowed with monitoring strain gages are shown in Fig. 8.

Strain gages are installed on the forward and rear spar and on the upper and lower panels of the wing box. The single gages are connected in a half-bridge configuration that provides a set of channels, which are denoted with the symbol η , each one giving a strain measure.

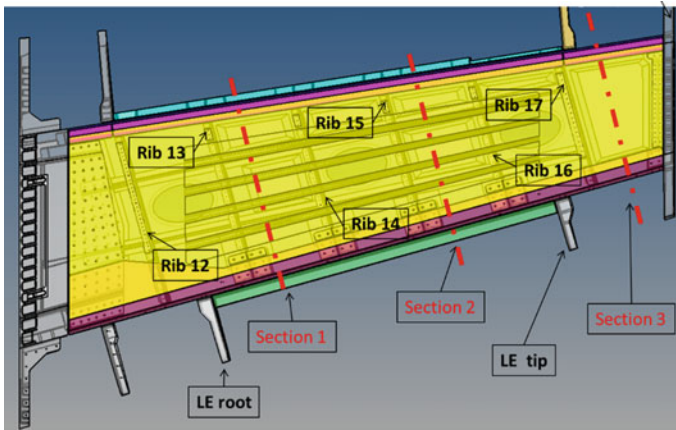


Fig. 8 Monitored sections

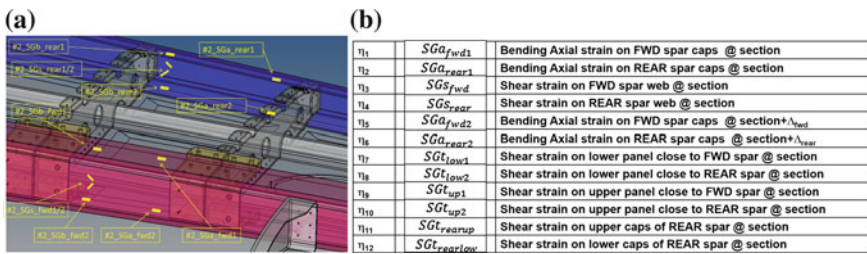


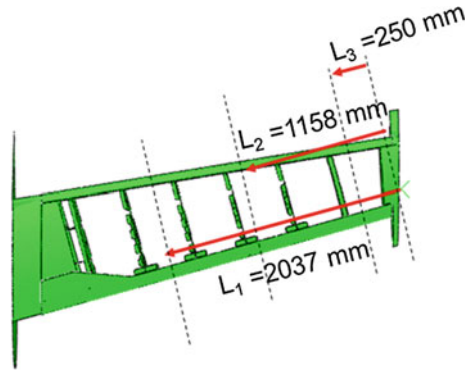
Fig. 9 Strain gages installed on the spars (a) and strain signals for each monitored section (b)

The strain channels available at such sections are reported in the table in Fig. 9b. Channels η_1 and η_2 provide the bending strain on the forward and rear spar, whereas channels η_3 and η_4 are installed on the webs of both spars to measure the shear strain. Channels η_5 and η_6 provide the bending strain on both spars at a small distance from the monitored section, but still on the same bay, to allow the evaluation of a bending gradient. The positions of such strain gages are exemplified in Fig. 9a, which is referred to section 2. Channels η_7 to η_{10} are used to acquire the shear strains on lower and upper panels. Finally, channels η_{11} and η_{12} are aimed at measuring the shear strains on the upper and lower flange of rear spars. The distance of the three monitored section from the rib at the tip is given in Fig. 10.

3.2 Identification of Internal Forces

The wing box of the demonstrator can be idealized as a beam loaded by different types of external loads. Each section of the wing transmits a system of three internal forces and three moments, which equilibrates the external loading. By assuming the

Fig. 10 Orientation and position of monitored sections



validity of beam theory, the stress and strain states at a given section directly depend on the values of internal sectional forces, neglecting the local effects of external loads and the stresses required to ensure the compatibility among the different parts of the structure. Within such hypotheses, local strain is a combination of the effects related to each component of the forces. This can be exploited to formulate an identification problem in the linear range, but the influence of some force components on the local strain can be negligible with respect to local effects, so that the problem could lead to unreliable solutions.

An efficient method for the identification relies on the definition of new variables, ζ_i , which are obtained by combining the signals of the strain channels. The aim of such combination is the identification of variables that are especially sensitive to only one of the most relevant internal forces, thus allowing a more robust identification of the internal force system. It can be assumed that they are influenced only by the value of shear force, bending and torsional moments, assuming that the other components of internal force system provide a negligible contribution. Such forces are defined at each monitored section, considering an axis that is perpendicular to the directions of the ribs in the wing box. Such axis should be conveniently positioned as close as possible to the elastic axis of the wing, so to avoid the coupling between the rotation of the sections about such axis, induced by torsional moment, and the bending deformation induced by shear and bending moment.

The monitoring sections are characterized by their distances from the tip of the wing box, L_k , measured along the reference axis, which are reported in 10. Variables ζ_i are defined in Eq. 7.

$$\begin{aligned} \zeta_i &= \gamma_{i1}\eta_1 + \gamma_{i2}\eta_2 + \dots + \gamma_{im}\eta_m \quad i = s, b, t \quad m = 1, 2, \dots, 12 \\ \Rightarrow \{\zeta\} &= [\gamma]\{\eta\} \end{aligned} \tag{7}$$

where γ_{ij} are a set of coefficients that define the specific combination. The index i is referred to the single component of the three internal forces that mainly affect the strain state in the wing demonstrator and can assume values s (*shear*), b (*bending moment*) and t (*torsional moment*). The combination has to be performed for each

monitored section. The index m is referred to the strain signals that are measured on each section.

The specific form of matrix $[\gamma]$ determines how strain signals are combined and defines a specific *method* for the identification of internal forces based on the installed monitoring system.

According to linear beam theory, the value of each combined signal ζ_i linearly depends on the internal forces in the wing structure, as indicated in Eq. 8.

$$\begin{aligned} \zeta_s &= \alpha_{ss}F_s + \alpha_{sb}\tilde{M}_b + \alpha_{st}\tilde{M}_t \\ \zeta_b &= \alpha_{bs}F_s + \alpha_{bb}\tilde{M}_b + \alpha_{bt}\tilde{M}_t \Rightarrow \{\zeta\} = [\alpha]\{F\} \\ \zeta_t &= \alpha_{ts}F_s + \alpha_{tb}\tilde{M}_b + \alpha_{tt}\tilde{M}_t \end{aligned} \quad (8)$$

Moments are normalized for numerical reasons, based on the distance of the sections from the wing tip:

$$\begin{aligned} \tilde{M}_b &= M_b/L_k \\ \tilde{M}_t &= M_t/L_k \end{aligned} \quad (9)$$

where the index k is referred to the specific section.

The inversion of the matrix $[\alpha]$ allows the identification of the force system, $\{F\}$, if the values of the combined signals are known. By substituting Eq. 7 in Eq. 8, the internal forces in each section can be evaluated from the strain channels $\{\eta\}$, as expressed in Eq. 10.

$$\{\zeta\} = [\alpha]\{F\} \Rightarrow \{F\} = [\alpha]^{-1}\{\zeta\} = [\alpha]^{-1}[\gamma]\{\eta\} = [\beta]\{\eta\} \quad (10)$$

Equation 10 defines a *calibration matrix*, $[\beta]$, which links the signals acquired by the strain gages in the half-bridge configuration to the internal forces in the section. Such matrix is generally rectangular and can be evaluated by means of experiments. However, the design of the monitoring system, including the choice of the method $[\gamma]$ for the combination of variables and a preliminary evaluation of the calibration matrix, can be carried out by means of a numerical approach.

3.3 Numerical Evaluation of Calibration Matrices

The numerical approach adopted for the development of the monitoring system was based on a detailed finite element model of the wing box, which is presented in Fig. 11. The model was developed for the solver code Simulia/Abaqus Standard [13] with a modular structure. Each part was separately meshed and then subsequently assembled. Conventional 4-noded shell elements were typically used, with the exception of rib-posts, which were modelled in different versions, by using also

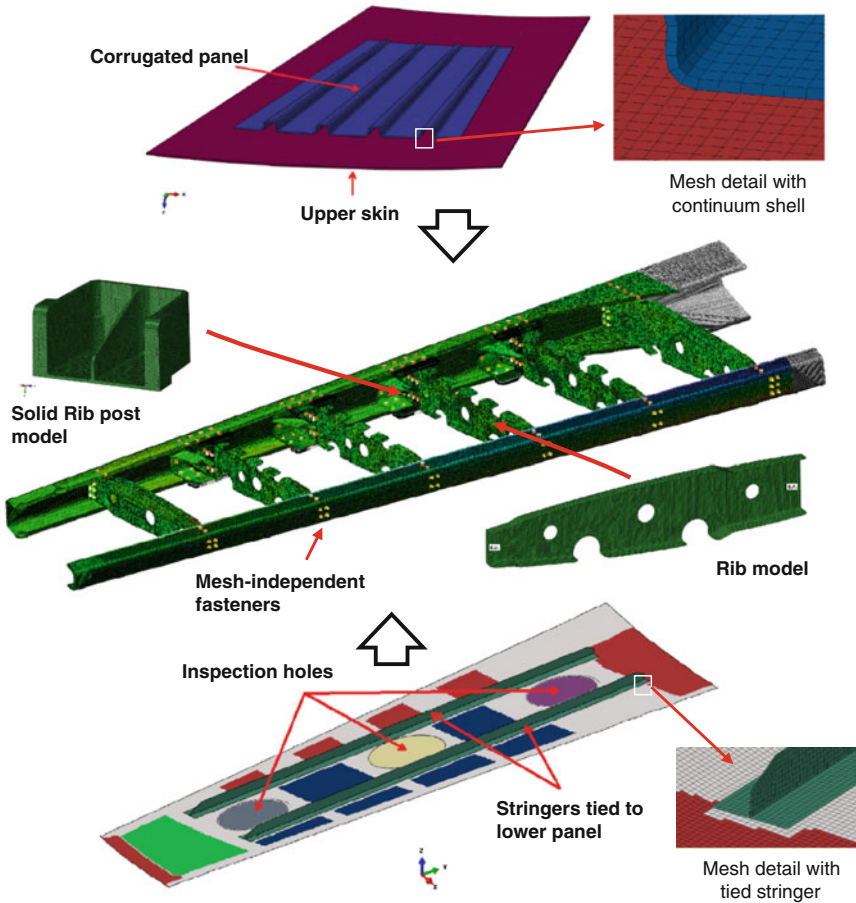


Fig. 11 Detailed finite element model of the wing box

tetrahedral solid elements, and some parts of the skins, which were represented by continuum shells to represent properly their thickness.

A typical element size of about 5 mm was used. Such size was assessed by means of a convergence study, which was performed on the model of the internal structure of the wing box, including ribs, rib-posts and spars. Attention was focused on the evaluation of the strain state along the spars, so to ensure that local strain levels were represented with sufficient accuracy.

The different parts were joined by using special connection elements, which model mesh-independent fasteners [13]. Such elements introduce a constraint between dissimilar meshes and distribute the constraint forces over an influence zone that can be defined by the user. Moreover, they are characterized by stiffness

properties that can be calibrated according to the physical properties of the junction element.

For the internal structure, the mesh-independent fasteners between the ribs, the rib-posts and the spars are shown in Fig. 11, but the method was actually used to model all the discontinuous junctions between the structural parts, including longitudinal junctions of the panels with the spars, and transversal junctions between panels and ribs. Stiffness properties were attributed by applying semi-empirical relations suggested by the solver code [13]. The corrugated reinforcement of the upper panel was modelled by continuum shells having common nodes with the panel, whereas the stringers in the lower panel were separately meshed and connected by means of a diffused mesh-independent connection (tie algorithm [13]) with the model of the panel. All composite parts were represented including ply properties and the detailed lay-up sequence in laminated shell elements.

The detailed wing box model was completed with the models of the root and tip metallic ribs. Finally, the models of the morphing surfaces were included: leading edge, trailing edge and winglet. The mesh refinement for such parts was kept at a coarse level. Indeed, the scope of the finite element model was the analysis of the strain states in the wing box and a detailed description of the complex structure of the morphing surfaces was not considered necessary. For such a reason, the mesh of the morphing surfaces was imported from an aeroelastic model developed for NASTRAN solver, converted in Abaqus and assembled with the main wing box model. However, connections were accurately represented by using mesh-independent fasteners, in order to model with adequate accuracy the transmission of forces between the morphing parts and the main structure of the demonstrator.

The complete model of the wing box is schematically represented in Fig. 12a, which also indicates the position of the strain gages. A specific output request was included for the strains in the elements that are in correspondence of such positions, so to make available, for an analysis in a generic load condition, the virtual estimation of strain gage signals. Preliminary analyses were carried out with the application of a vertical force, such as the one shown in Fig. 12a, in order to identify the elastic axis of the demonstrator.

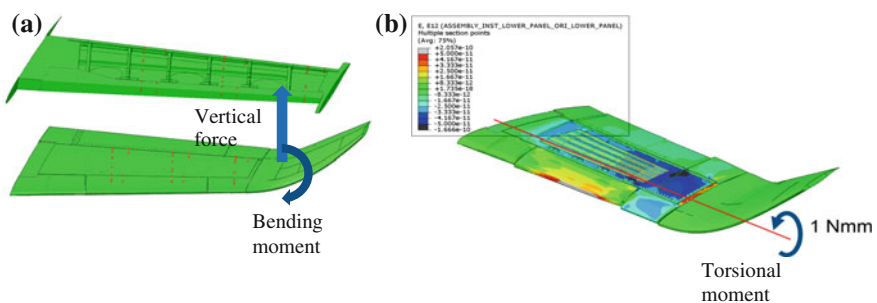


Fig. 12 Complete FE model (a) and contour of shear strain in an analysis with pure torque (b)

Thereafter, the model was used to calculate the matrix $[\alpha]$ and the calibration matrix $[\beta]$, for different methods, represented by different definitions of matrix $[\gamma]$. The procedure consists of the following steps, which were repeated for each section:

- (i) application of three load conditions resulting in a pure shear, pure bending moment and pure torsional moment in the monitored section; a pure shear condition is obtained by combining an upward vertical force with a bending moment the deflect the wing downward, so that the internal bending moment vanishes at the desired section;
- (ii) accomplishment of the numerical analyses and recovery of numerical strain values in the positions corresponding to the physical locations of strain gages; each load case will provide strain values related to a single internal force: $\{\eta_s\}$, $\{\eta_b\}$, $\{\eta_t\}$;
- (iii) application of matrix $[\gamma]$, defined according to the selected method for the combination of signals, to calculate the values of combined signals ζ , in the pure loading conditions:

$$\{\zeta\}^s = [\gamma]\{\eta\}^s \quad \{\zeta\}^b = [\gamma]\{\eta\}^b \quad \{\zeta\}^t = [\gamma]\{\eta\}^t \tag{11}$$

- (iv) once that such signals have been evaluated, the matrices of influences coefficient, $[\alpha]$, are obtained from the relations reported in Eq. 12, because only a single component internal force is non-zero in each analysis and the value of the combined variable is related to such internal force only;

$$\begin{aligned} \zeta_s^s &= \alpha_{ss}F_s & \zeta_s^b &= \alpha_{sb}\tilde{M}_b & \zeta_s^t &= \alpha_{st}\tilde{M}_t \\ \zeta_b^s &= \alpha_{bs}F_s & \zeta_b^b &= \alpha_{bb}\tilde{M}_b & \zeta_b^t &= \alpha_{bt}\tilde{M}_t \\ \zeta_t^s &= \alpha_{ts}F_s & \zeta_t^b &= \alpha_{tb}\tilde{M}_b & \zeta_t^t &= \alpha_{tt}\tilde{M}_t \end{aligned} \tag{12}$$

- (v) matrix $[\alpha]$ is evaluated from Eq. 12 and matrix $[\beta]$ is calculated by using the following Eq. 13, which derives from Eq. 10:

$$[\beta] = [\alpha]^{-1}[\gamma] \tag{13}$$

The definition of the algorithm for load identification was carried out by selecting the most efficient method to reduce the off-diagonal terms in matrix $[\alpha]$. In the method that was eventually selected, the combination of signals is prescribed as expressed in Eq. 14.

$$\begin{aligned} \zeta_s &= 3/4\eta_3 - 1/4\eta_4 \\ \zeta_b &= 1/2\eta_1 + 1/2\eta_2 \\ \zeta_t &= -1/4\eta_7 - 1/4\eta_8 + 1/4\eta_9 + 1/4\eta_{10} \end{aligned} \tag{14}$$

Hence, the variable related to the shear force is derived from the shear strains on the spars, which are differently weighted for the forward and rear spar; the variable related to the bending moment is evaluated by combining the bending strain on the

	shear	bending	torque		shear	bending	torque		shear	bending	torque
ζ_s	1.60E-08	-1.05E-09	-4.04E-09	ζ_s	1.60E-08	-1.05E-09	-4.04E-09	ζ_s	1.75E-08	7.05E-09	-6.20E-09
ζ_b	8.88E-10	-1.32E-08	-6.43E-10	ζ_b	8.88E-10	-1.32E-08	-6.43E-10	ζ_b	1.32E-09	-8.37E-09	3.08E-09
ζ_t	-3.31E-09	-2.54E-09	-4.35E-08	ζ_t	-3.31E-09	-2.54E-09	-4.35E-08	ζ_t	-7.55E-10	-2.38E-10	-3.57E-08
Section 1			Section 2			Section 3					

Fig. 13 Matrices of influence coefficients for the three monitored sections

spar flanges: finally, the variable related to the torsion is a combination of the shear strains on the panels. Such method obtained matrix $[\alpha]$ with off-diagonal terms that are one order of magnitude smaller than the diagonal one for all the three sections, as indicated in Fig. 13.

The method proposed in Eq. 14 turned out to be the most reliable one to define a set of variables, each one being particularly sensitive to only one of the internal force components. Such aspect enhances the reliability of the force identification and allows an easier final tuning based on experimental results, since discrepancies between the identified forces and the applied loads can be better interpreted from an engineering standpoint.

However, the flexibility of the approach could be exploited to apply different methods and to compare the results in order to improve the accuracy of load identification.

3.4 Virtual Assessment of Calibration Matrices

Numerical tests were performed to assess the capability of identifying the internal forces in realistic load conditions by using the calibration matrices evaluated in the previous sections.

The results of an aeroelastic model of the demonstrator were used to evaluate the internal forces in some relevant test conditions at Mach 0.294. In particular, a condition with positive angles of attack (+12°) and sideslip (+10°) and a completely different condition with negative angles of attack (-5°) and sideslip (-5°) were considered. The second condition also involves a deflection of -5° for the trailing edge.

The internal forces evaluated for such cases included vertical components as well as drag and longitudinal components. A simplified system of nodal forces was devised to obtain in the finite element model the same internal forces, including the bending moment originated by the vertical components. The bending moment originated by the horizontal forces and the torsional moment were only approximately reproduced.

Numerical analyses were performed to evaluate the virtual strains that were introduced in the identification algorithm based on the calibration matrices. The results for the bending moment and the shear force for the condition with positive

angle of attack are reported in Fig. 14, whereas Fig. 15 is referred to the torsional moment in the condition with a negative angle of attack.

It can be observed that the calibration matrices identified the internal forces with adequate accuracy, though some discrepancies have been obtained and can be attributed to imprecisions in the representation of the external loads as well as to the effects of internal force components that have not been included in the identification algorithm.

The application of identification procedure in real tests will probably require a correction of the matrices based on the experimental data. However, it should be

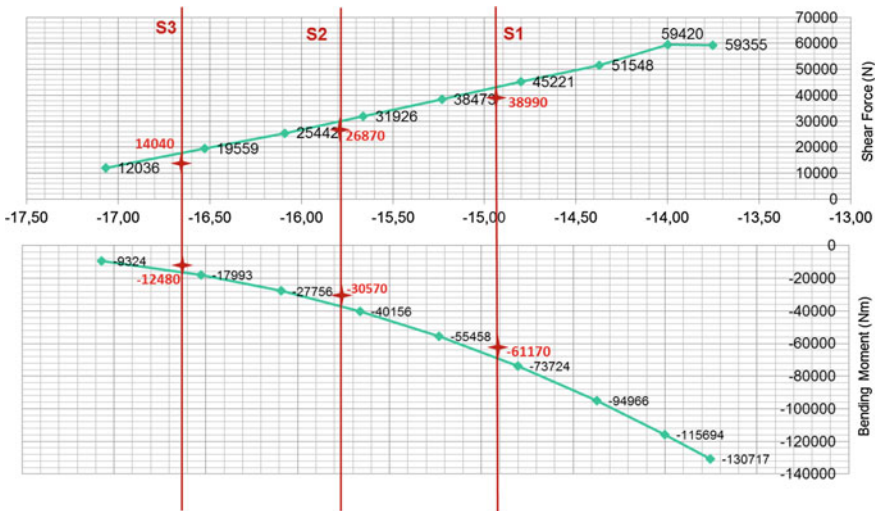


Fig. 14 Identification of shear force and bending moment in a condition with positive angle of attack

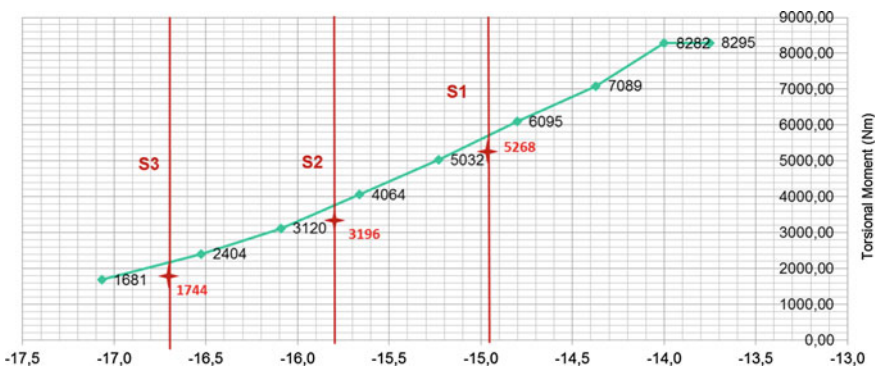


Fig. 15 Identification of torsional moment in a condition with negative angle of attack

noted that the virtual assessment of the method allowed the selection of the most promising combinations of strain signal to build the calibration matrices and an initial guess of calibration matrix that should result close to the optimal value. Additionally, the finite element model can be used to estimate the errors originated by discrepancies between the model and a real spar. Such evaluation was performed considering variations of the modelling parameters in the parts that were coarsely meshed, such as the leading and trailing edge. Large errors were separately introduced, such as increment of 30 % of the thickness referred to the metallic auxiliary spars of leading and trailing edge, increment of 30 % for the thickness of leading edge panels, reduction of 60 % for the thickness of trailing edge panels. Finally, all the variations were simultaneously considered. The maximum variation for the diagonal terms of matrix $[\alpha]$ with respect to the original matrix was of 3.8 %. Finally, all variations were introduced and the stiffness attributed to the mesh-independent fastener in the model was also increased of 30 %, obtaining a maximum variation of the diagonal terms of $[\alpha]$ of 3.75 %. Overall, the load identification algorithm turned out to be adequately robust with respect to possible large errors in the models of the morphing surfaces and to wrong estimation of the stiffness attributed to the junctions between the parts.

4 Feasibility of Damage Detection on Composite Spars Based on Strain Sensing

Sensing networks based on OF are often proposed to develop damage detection monitoring systems [2–6] that involve a large number of FBGs, typically applied to panels. In a previous section, the capability of a FBGs network to identify with sufficient accuracy the complex load conditions acting on composite spars has been assessed, if an adequate number of sensors are used. In this section, the possibility of damage detection on composite spars is numerically explored to investigate the feasibility of the technique for such type of component. It is well known that under structural loading, the presence of damage induces a variation in the local strain distribution, due to the variation of load path. Therefore, the damage itself can be detected by comparing such altered strain distribution with the strain field affecting the same undamaged structure. The main drawback of such a procedure resides in the intrinsically *local* nature of damage-induced strain anomalies, which makes damages only detectable in vicinity of strain sensors.

However, the strain field in many structural components is expected to present a smoothly varying distribution in the zones far from the application of concentrated loads. Such aspect can be exploited to detect anomalies that indicate a local alteration with respect to a smooth nominal solution. An example of such approach can be found in [14, 15], where an algorithm was devised to identify the failures in bonded junction. Comparison between the local strain signal and a set of strain acquisition in the same region is required to develop this type of damage detection

strategy. The apparent advantage is the elimination of a reference baseline and of a reference load condition, since anomalies are detected with respect to an instantaneous strain distribution, which can be originated by any load condition.

To investigate and validate this type of methods for a composite spar, a C-shaped carbon/epoxy wing spar is assumed and modelled as test bed, but added with two flanges on top and bottom surfaces (see Fig. 16).

The C-shaped spar initially considered for this study consists of 15 plies; its stacking sequence is made of 63 % $[45^\circ]_{\text{fabric}}$, 25 % $[0^\circ]_{\text{unidirectional}}$ and 12 % $[90^\circ]_{\text{unidirectional}}$. Each flange consists of 10 plies, whose lamination includes 58 % $[0^\circ]_{\text{unidirectional}}$, 21 % $[0^\circ]_{\text{fabric}}$ and 21 % $[45^\circ]_{\text{fabric}}$. Therefore, the lay-up of the spar web turns out to be dominated by $+45^\circ$ fabric plies, whereas the caps are characterized by a higher percentage of 0° oriented fibres.

Spar and flanges are modelled by using solid laminated elements and joined together through a layer of cohesive elements [13], inside which delaminations can be modelled by attributing no capability of stress transmission. The component is subjected to a three-point-bending-like loading condition. To check different damage scenarios, different sizes (Fig. 17a) of the same delamination (Fig. 17b) are considered.

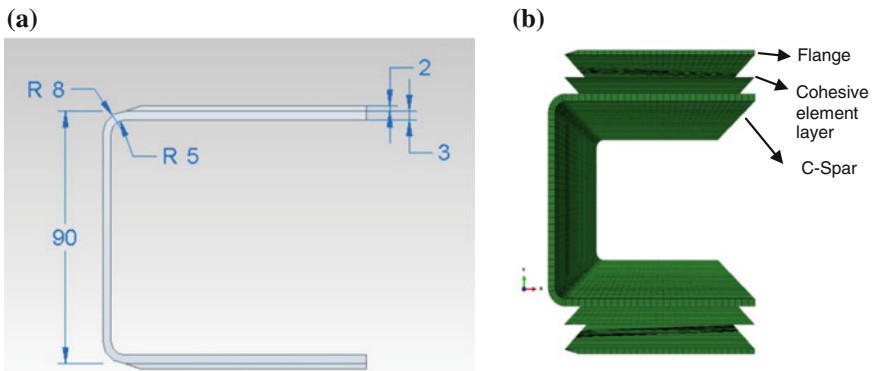


Fig. 16 Flanged C-shaped spar considered for damage detection

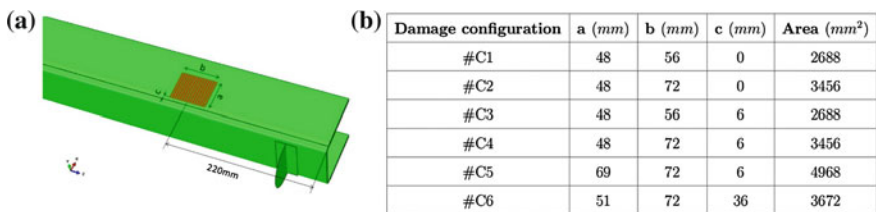


Fig. 17 Delamination position and size

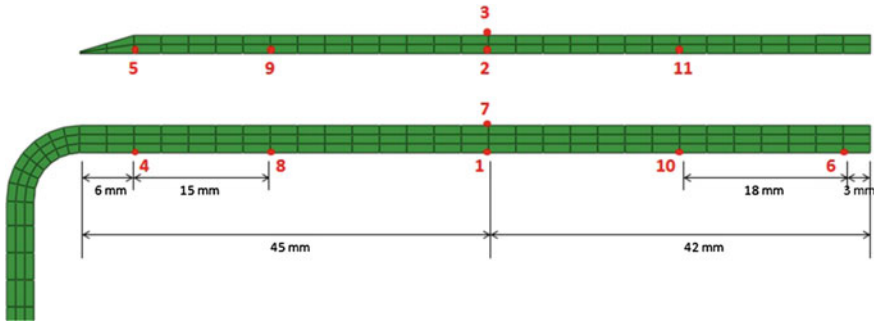


Fig. 18 Position of optical fibres carrying the sensing network

Strains are evaluated along paths (which correspond to the optical fibres carrying FBGs), whose traces are shown in Fig. 18. The model of the spar was subject to a three-point bending load condition and typical strain–span curves, for every combination of damage size and measuring path can be obtained, showing different degree of sensitivity. The examples reported in (Fig. 19) show that the alteration of the strain distribution along external paths, like paths 1 and 9 (see Fig. 18), is characterized by a moderate amplitude distributed along an appreciable span length. However, alteration is very sensitive to the position of the path with respect to the damage location, since path 1 shows very limited variation with respect to the undamaged conditions.

The alteration along the internal paths located in the flange, two plies above the layer of cohesive elements, is characterized by the higher amplitudes, though they are extended over a lower span. Moreover, internal paths appear less sensitive to damage localization.

Once completed such a screening procedure, a damage/path of the configuration shown in Fig. 20 is defined to assess the damage detection capability of different methods.

In the configuration represented in Fig. 20, the influence exerted by stacking sequence on damage detectability has to be evaluated. Comparing the four laminations reported in Fig. 21, it appears that the more spar and flanges laminations differ, the more easily damage can be detected (see typical curves shown in Fig. 21). It is worth noting that the lamination sequence of the spars used in the demonstrator of wing box of project SARISTU is identical for the flanges and the webs, as in Lay-up #1 reported in Fig. 21. Such a case is characterized by a negligible and undetectable alteration in the presence of delamination. Such consideration indicates that in such condition damage detection is unfeasible, whereas results indicate that the introduction of differences between the lay-up of webs and caps provides the possibility to measure the effect of delamination. Indeed, the adoption of different lay-ups involves the presence of ply drop-offs and thickness variations, which are often considered triggers for potential delaminations. Hence, the presented results indicate that delamination damage is more easily detected if

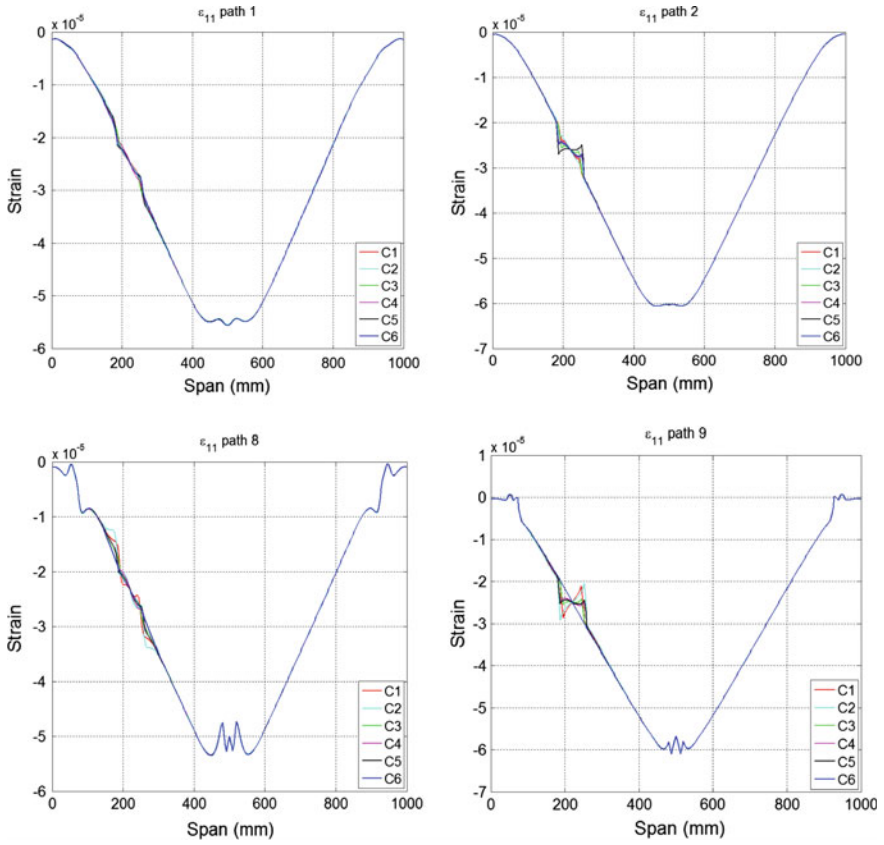


Fig. 19 Strain distribution along different paths for different damage scenarios

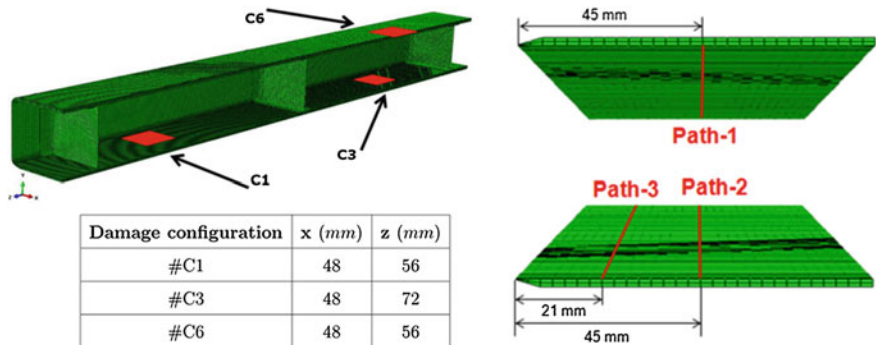


Fig. 20 Final configuration of damage scenarios and damage detection path

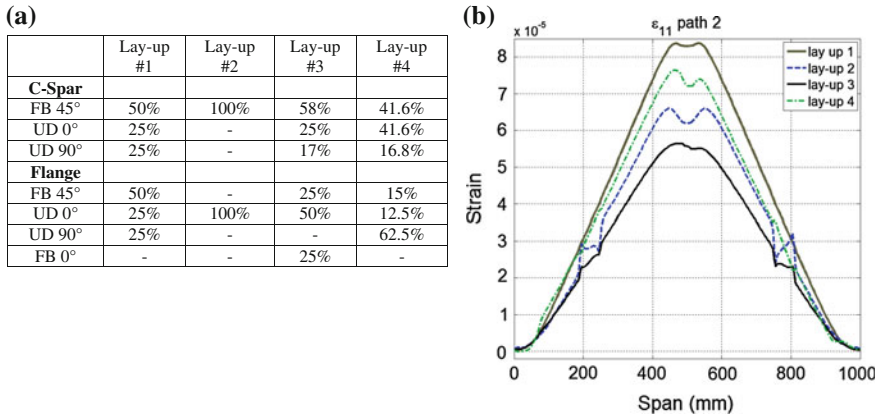


Fig. 21 Sensitivity of damage detectability to different lay-ups

the stress transfer function of interlaminar layer is exploited in the design of the spar, though this means increasing the risk of delamination induced in operative conditions. Conversely, a conservative design, where the interlaminar layers do not work to transfer stresses between the different lay-ups in web and caps, is not suited to install a damage detection system based on strain sensing.

In conclusion, global information about strain distribution can be processed for providing synthetic damage indexes. For this purpose, five points are extrapolated in the damaged area along measuring path #1, mimicking real FBGs: three ahead and two across damage itself, then residual strain indexes are evaluated.

Adopting the criterion reported in [16], strain anomalies can be computed through the formula:

$$R_{x_i} = \frac{2\varepsilon_{x_i}}{(\varepsilon_{x_i} + \varepsilon_{x_{i+1}})\Delta x} - \frac{1}{\Delta x} \tag{15}$$

The results reported in Fig. 22a are obtained for damage-type C6, along the path #1. The x -axis refers to the abscissa along the span of the second bay in spar element. Results are inconsistent since the basic hypotheses of this method have been violated, because the strain distribution is characterized by a significant gradient along the sensing path.

An alternative method can be based on the evaluation of the differences between measured local values and the values of a least-squares-approximation based on several measuring points along the path. Polynomial interpolation function can be used for the least square approximation, which will be characterized by polynomial coefficients k_n , where n varies from 0 to N , N being the order of the polynomial. The following formula is obtained:

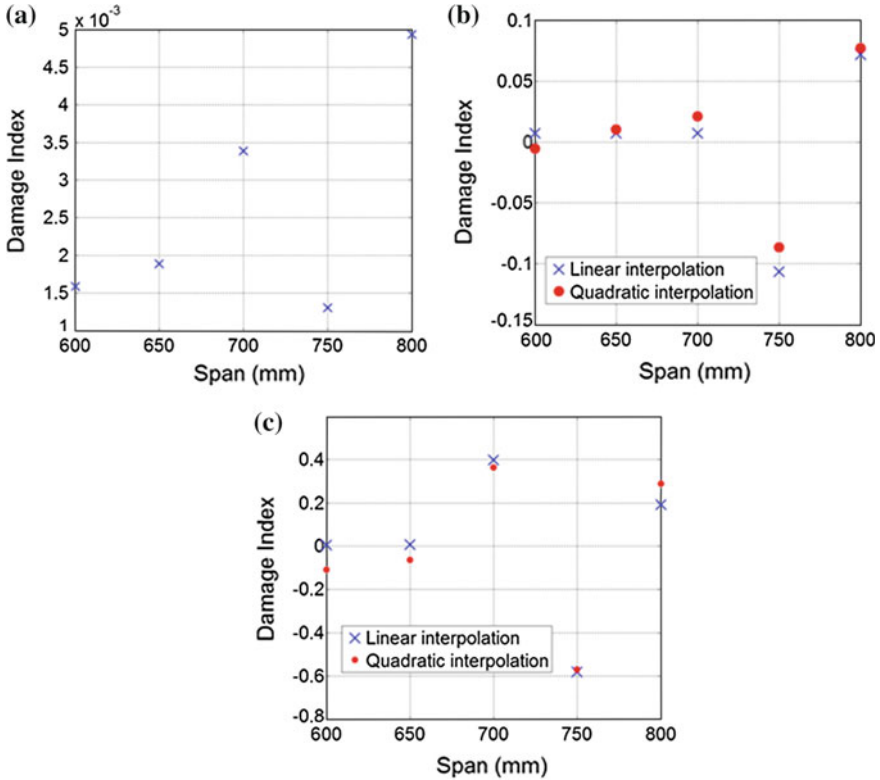


Fig. 22 Damage indices for damage C6 along path #2: normalized strains (a), strain interpolation (b), strain gradient interpolation (c)

$$S_{x_i} = \frac{\varepsilon_{x_i} - \sum_{n=0}^N k_n x_i^n}{\varepsilon_{x_i}} \tag{16}$$

Such formulation supplies the results shown in Fig. 22b, where the first three points (ahead damage) are characterized by almost null residuals, while the other two points (across damage) show residuals whose values are far away from zero. The results provided in Fig. 22b are obtained considering both a linear and a quadratic interpolation.

An additional approach, still based on a polynomial interpolation, can be devised considering the difference between the gradients of strains computed on a local basis and the gradients identified by the polynomial interpolation, according to the formula:

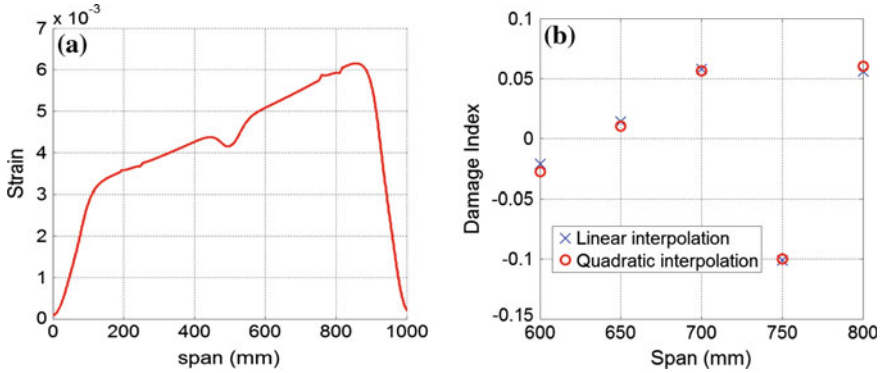


Fig. 23 Strain distribution along path #2 for the cantilever beam load conditions (a) and damage index based on strain gradients (b)

$$G_{x_i} = \frac{(\varepsilon_{x_{i+1}} - \varepsilon_{x_i}) - \frac{d}{dx} (\sum_{n=0}^N k_n x_i^n)}{\frac{d}{dx} (\sum_{n=0}^N k_n x_i^n) \Delta x} \quad (17)$$

The methods anticipate the effect of damage, which can be pointed out by the third strain residual already (see Fig. 22c). By all means, the two latter techniques prove to be efficient and able to supply consistent results.

Since the three-point-bending-like loading condition can be considered a sound test bed, but not truly representative of the real forces system acting on a wing spar, a second loading condition is taken into account, where the spar acts a cantilever beam, built-in at the root and loaded by vertical forces and bending moments at span mid-point and free edge.

In such a condition, typical strain–span distribution, as measured along path #2 for damage C3, is shown in Fig. 23a, while corresponding damage indices computed as the difference between measured and least-squares-approximated gradients of strain distributions are reported in Fig. 23b. Again, it appears that damage can be pointed out at a sufficient degree of accuracy, provided a suitable measuring path is preliminary chosen.

5 Prediction of Aerodynamic Loads and Strategies for the Assessment of Monitoring Systems

5.1 Example of Aeroelastic Models for Load Predictions

In the previous sections, three types of monitoring systems based on strain sensing have been presented. The development of the algorithms that extract the information to be monitored from the strain measures has been accomplished by using

different types of structural FE models, at different levels of mesh refinement. The numerical approaches allowed the design of the system and the evaluation of the expected performances. However, the finite element models and the algorithms based on their applications have to be assessed and calibrated by means of tests in order to improve the reliability of the monitoring systems.

For the activity of assessment and calibration of the different systems, the availability of an aeroelastic model is fundamental. The example here reported is referred to a full aircraft aero-elastic model that has been developed for required wing loads assessments, which have been carried out with respect to realistic flight operations. Several aspects have been considered, such as loads constraints and evaluation for relevant wing sections, as well as weight reductions.

Indeed, the reference SARISTU aircraft is defined through a design exercise. The resulting aircraft is reported in a reasonable detail in Ref. [14] and the development of the aeroelastic model is based on such data.

To estimate aircraft stiffness and masses for the specified mission, the NeoCASS tool has been used [17]. In the first step, the NeoCASS tool is applied to generate an aircraft model based on the specified geometrical arrangement, the layout of passenger seating and luggage compartments, position of the engines, etc. The results are shown in Fig. 24a.

Subsequently, based on the required mission and other operational data, the structural stiffness and mass distribution are estimated based on the standard FAR 25 loads requirements. The underlying method of structural size and weight estimation of NeoCASS has been shown to be sufficiently reliable and accurate, see e.g. [18].

An aeroelastic model of the aircraft based on beam modelling is then generated and shown in Fig. 24b. The format of the aeroelastic model is very similar to MSC/NASTRAN format, which can be easily modified to be applied in a MSC/NASTRAN analysis.

Since a better definition of SARISTU wing is available, the wing part that is represented using beam elements is completely replaced by the SARISTU initial wing model. The SARISTU wing is modelled using torsion box. The aircraft beam model with SARISTU wing is shown in Fig. 25a.

This modelling strategy facilitates a direct input to the control surface deflection during aeroelastic response analyses. A direct input to control surfaces is expected either from pilot input or from the output of the flight control system, e.g. gust

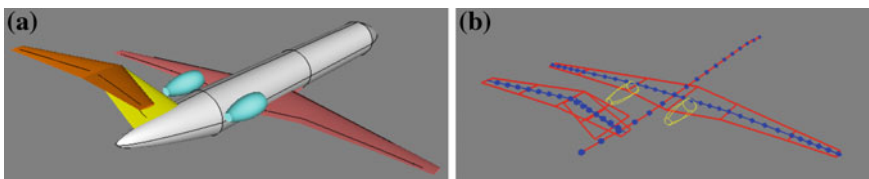


Fig. 24 Geometrical representation of SARISTU aircraft in the NeoCASS environment (a) and aeroelastic model generated by NeoCASS based on the required mission (b)

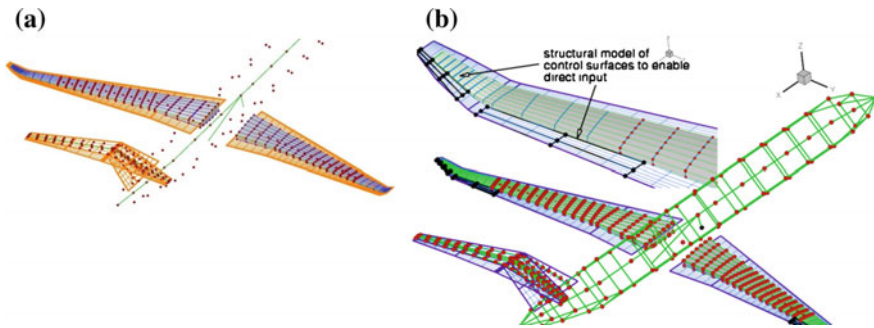


Fig. 25 SARISTU aircraft model consisted of ALENIA initial torsion box wing model and NeoCASS fuselage tail model based on beams (a) and model suitable for aeroservoelastic analyses (b)

alleviation system. Figure 25b presents the SARISTU loads model suitable for aero-servo-elastic analyses.

As commonly done NASTRAN, the load models developed in this work have five rigid body degrees of freedom. The longitudinal motion is not taken into account due to the lack of thrust and aerodynamic drag model in NASTRAN. Various control surfaces are modelled including: ailerons, inner spoilers, outer spoilers, elevator, rudder and WATE. Since realistic inertia data of the control surfaces are not available, the control surfaces are only modelled as aerodynamic effectors.

The aircraft loads model consists of two mass configurations, i.e. the maximum take-off weight and maximum landing weight. The only difference between these configurations concerns the outer-wing fuel tank, which is empty for the maximum landing weight configuration.

The loads model contains required functionalities for loads analysis for relevant wing sections of interest and is suitable for evaluation of structural wing loads with available data. The output of the loads models consists of (a.o.):

1. rigid body modes: roll, pitch and yaw rotations, lateral and vertical velocities, roll, pitch and yaw rates, rotational and translational accelerations;
2. wing (tip) and wing root accelerations;
3. sectional loads at 23 locations in each wing;
4. angle-of-attack and angle-of-side slip at the location of the vanes.

The reconstruction of the sectional loads is explained below. The sectional loads data are extracted from the grid-point forces associated with structural deformation due to trim state and those associated with the flexible part of the normal modes.

To extract the cross-sectional forces, all the nodes on a cross section are located first. The elements connected to one side of this point are then selected and their contributions to the node force are summed to yield the total force at this node. It should be noted that this implies that the boundary must follow the mesh faces and

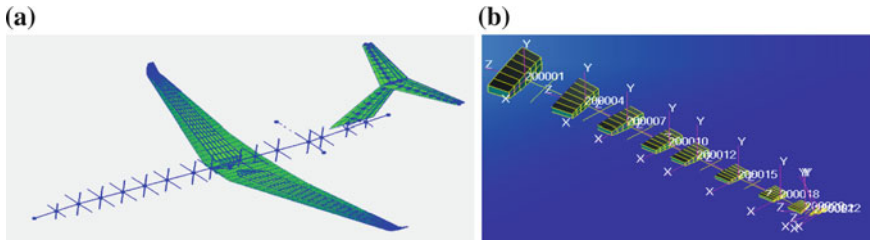


Fig. 26 Aeroelastic FE model (a) and cross section for the extraction of loads (b)

cannot cut through elements. The contribution of all the nodes is then summed to find the total cross-sectional loads (see Fig. 26). Both the cross-sectional forces and the cross-sectional moments can be extracted with respect to the local coordinate axis. All these operations are performed in TMP Vision/SLIM.

5.2 *Potential Interactions of Numerical Approaches for Calibration and Validation of Monitoring System*

The development of reliable monitoring systems requires a calibration and validation phase based on experimental tests. Such consideration is valid for the demonstrator considered in project SARISTU as well as for a full real-world aircraft endowed with a smart wing. In this phase, the interactions between the different numerical approaches that have been used for the development of the monitoring system play a fundamental role.

Indeed, the role of the monitoring systems presented in this work is different, and the interactions between tests and numerical approaches can be performed with different scopes.

- (a) the monitoring system for the identification of sectional loads, based on strain gages, which was presented in Sect. 3, has a limited role as usage monitoring system installed for in-flight operations, but represents a valuable tool for the calibration of finite element models and aeroelastic models used for the development of the other monitoring systems. Figure 27 presents a possible strategy to compare measured and predicted sectional loads as well as measured and predicted strain measures, based on the data acquired in wind tunnel and ground tests. Such processes could potentially be employed to adjust the finite element and the aeroelastic model and to tune the calibration matrices for the identification of sectional loads.
- (b) the monitoring system based on OF's presented in Sect. 4, designed for the identification of internal loads applied to the spars, can be assessed, enhanced and validated by using the numerical predictions that derive from reliable aeroelastic models and detailed structural finite element models; the scheme

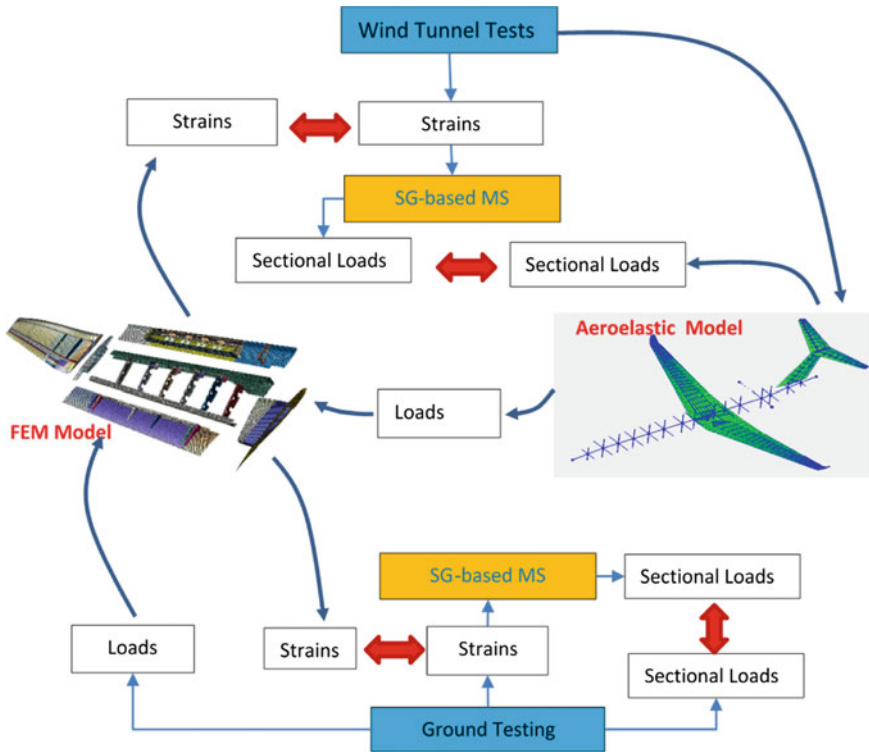


Fig. 27 Interaction of detailed FE model, aeroelastic models and monitoring system for the identification of sectional loads

reported in Fig. 28 shows that the predictions obtained by the load monitoring system for the spars can be compared with the predictions of validated structural model subjected to the external loads provided by an aeroelastic model.

- (c) finally, the potential for damage detection on the spars that was discussed in Sect. 5 requires the availability of a nominal strain field that can be reconstructed by using several strain measures; this could allow the identification of local strain outliers that can be related to damage; such reference strain field can be obtained through an interpolation of strain data acquired in a well-defined region; however, the process becomes more reliable and flexible if the nominal strain state was obtained through a finite element model of the subcomponent, subjected to the load system identified by a load monitoring system; such strategy is also included in the scheme presented in Fig. 28.

Overall, these considerations point out the importance of the numerical models and their interactions for the tuning of reliable monitoring systems that operate at various levels.

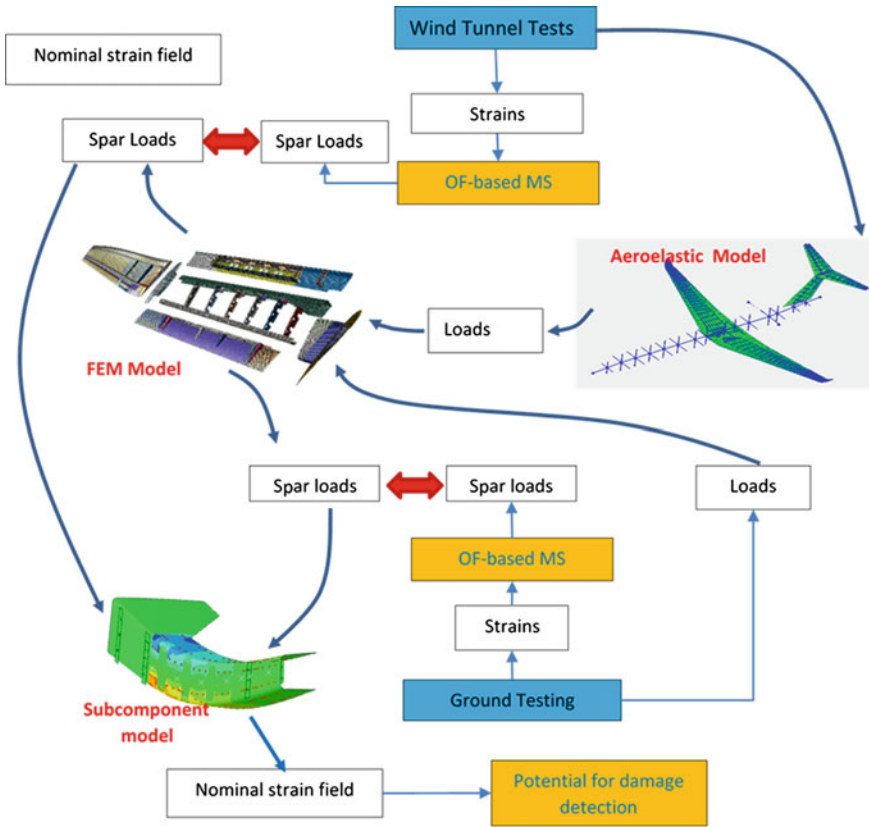


Fig. 28 Interaction of detailed FE model, aeroelastic models, subcomponent model and monitoring systems based on optical fibres

6 Conclusions

In this work, different monitoring systems based on strain sensing have been presented. The design of such systems was accomplished by applying different numerical approaches that were used to predict the strain fields in different load conditions and for different structural elements. Such approaches also allowed an evaluation of the expected performances for the different systems.

The first system considered is based on a relatively dense network of sensors carried by OF's. Such technology is characterized by inherent lightweight and insensitivity to electro-magnetic noise. The embedment of the fibres into ribbons that are externally bonded to the structure provides a system with adequate characteristics of maintainability and reparability. All such aspects allowed conceiving a system that is potentially able to reconstruct the strain field in a wing spar through the identification of a parameterized load system transmitted to the spar by the

surrounding structural components. The system appears sufficiently robust with respect to the effects of modelling errors and is able to reconstruct the strain field with appreciable degree of accuracy. The main drawback of the system is represented by the limited number of sensors that are available to identify load components close to the root of the demonstrator, so that noise could introduce errors in the identification of the load system, although the longitudinal strain state would be captured with acceptable precision.

A technology based on OF's was considered to study the feasibility of damage detection in the spars, focusing on delaminations nucleated on the caps of C-shaped sections. One of the main findings obtained in such a work is the impossibility of damage detection in case of identical lamination sequences for the web and caps of the spars, which is the solution adopted for the spars in the demonstrator of project SARISTU. Conversely, delaminations induce an alteration on the strain values and gradients along a longitudinal path if the lamination sequences are different. Such alterations can be detected by a network of sensors, particularly if OF are embedded in the composite material. The methods adopted to assess the potential of damage detection are based on the comparison of local strain measurement with a strain field that is reconstructed on the basis of interpolation or is based on the identification provided by a load monitoring system. However, the density of sensors required to guarantee the detection of damage can be quite high.

Traditional strain gages were considered to develop another type of monitoring system, aimed at evaluating the sectional loads in the wing box of the demonstrator. Such system has a limited role for in-flight operation and is based on a more conventional technology, but the methodology followed presents interesting aspects. The design of the monitoring system was carried out by using a detailed finite element model of the wing box, which is built according to a modular structure that can be exploited for model calibration. A method to combine different strain signals was selected through virtual tests in order to reduce the coupling between the effects of different sectional loads on the combinations. Such activity makes also available a complete finite element model of the demonstrator, which can be used in conjunction with aeroelastic models in order to set up procedures for the final calibration and assessment of the algorithm developed for the monitoring system, as it has been presented in the final part of the work.

Acknowledgments The research leading to these results has received funding from the European Union's Seventh Framework Programme for research, technological development and demonstration under grant agreement no. 284562.

References

1. Grattan K, Sun T (2000) Fiber optic sensor technology: an overview. *Sens Actuators, A* 82 (1):40–61
2. Zhou G, Sim LM (2002) Damage detection and assessment in fiber reinforced composite structures with embedded fibre optic sensors-review. *Smart Mater Struct* 11:925–939

3. Yashiro S, Takeda N, Okabe T, Sekine H (2005) A new approach to predict multiple damage states in composite laminates with embedded FBG sensors. *Compos Sci Technol* 65:659–667
4. Yashiro S, Okabe T, Takeda N (2002) Damage identification in a holed CFRP laminate using a chirped fiber Bragg grating sensor. *Compos Sci Technol* 67(2):286–295
5. Palaniappan J, Wang J, Ogin S, Thorne A, Reed G, Tjin S (2005) Use of conventional and chirped optical fibre Bragg gratings to detect matrix cracking damage in composite materials. *J Phys: Conf Ser* 15:55
6. Bettini P, Guerreschi E, Sala G (2015) Development and experimental validation of a numerical tool for structural health and usage monitoring systems based on chirped grating sensors. *Sensors* 15(1):1321–1341
7. Tessler A, Spangler JL (2005) A least square variational method for full-field reconstruction of elastic deformation in shear-deformable plates and shell. *Comput Methods Appl Mech Eng* 194:327–329
8. Shkarayev S, Krashantisa R, Tessler A (2001) An inverse interpolation method utilizing in-flight strain measurements, for determining loads and structural response of aerospace vehicles. In: *Third international workshop on structural health monitoring*, Stanford, CA
9. Barbarino S, Bilgen O, Ajaj RM, Friswell MI, Inman DJ (2011) A review of morphing aircraft. *J Intell Mater Syst Struct* 22:823–827
10. Bettini P, Sala G (2007) Preliminary assessment of helicopter rotor blades fatigue endurance through embedded FO sensors. In: *Proceedings of the 24th ICAF symposium*, Naples, 16–18 May 2007
11. Gaudenzi P, Olivier M, Sala G, Sciacovelli D, Wheelan M, Bettini P, Nosenzo G, Tralli A Development of an active composite with embedded piezoelectric sensors and actuators for structure actuation and control. In: *Proceedings of the 54th international astronautical*, IAC-03-I.4.03, Bremen
12. van Wijngaarden MJ, Bosboom MB, Evenblij R, Bettini P, Loutas T, Habas D (2015) Ribbon tapes, shape sensors and hardware. Paper presented at SARISTU final conference, Moscow, Russian Federation, 19–21 May 2015
13. Abaqus (2013) Analysis and user's manual version 6.13
14. Li HCH, Herszeberg I, Davis CE, Mouritz AP, Galea SC (2006) Health monitoring of marine composite structural joints using fibre optic sensors. *Compos Struct* 75:321–327
15. Herszeberg I, Mouritz AP (2006) Automated characterization of structural disbonds by statistical examination of bond-line strain distribution. *Struct Health Monit* 5:83–94
16. Baldassin E, Gifco MD, Gemma R, Carossa GM, Russo R, Ricci S, Peter F (2012) Reference baseline wing and morphing wing aeromechanical requirements. Deliverable D12.1.1 of SARISTU
17. Cavagna L, Ricci S, Riccobene L (2009) Fast tool for structural sizing, aeroelastic analysis and optimization in aircraft conceptual design. In: *50th AIAA/ASME/ASCE/AHS/ASC structures, structural dynamics and materials conference*, Palm Springs, CA, USA
18. Cavagna L, Riccobene L, Ricci S, Berard A, Rizzi A (2008) Fast MDO tool for aeroelastic optimization in aircraft conceptual design. In: *12th AIAA/ISSMO multidisciplinary analysis and optimization conference*, Victoria, BC, Canada

Shape Sensing for Morphing Structures Using Fiber Bragg Grating Technology

Rolf Evenblij, Frank Kong, Christos Koimtzoglou, Monica Ciminello, Ignazio Dimino and Antonio Concilio

Abstract Shape sensing is one of the versatile applications in a wide market spread, made practical with the use of fiber-optic (FO) sensors for strain sensing. The properties and capabilities of optical fibers with regard to both strain sensing and data transmission, their high endurance, and chemically inertness allow successful implementations in harsh environments such as aerospace. In the SARISTU project, a FO sensing-based approach for chord-wise shape reconstruction of an adaptive trailing edge device (ATED) is realized with the extrinsic implementation of fiber Bragg grating sensors. With this implementation, the capability is provided for a closed-loop control of the morphing mechanism for a given set of the target shapes. This paper describes the development and implementation of the FO sensing system as well as the applied methodology using Frenet–Serret formulas for shape reconstruction, including component and functional model testing results for validation.

R. Evenblij (✉) · F. Kong
Technobis Fibre Technologie, Pyrietstraat 2, 1812SC Alkmaar, The Netherlands
e-mail: rolf.evenblij@technobis.com

C. Koimtzoglou
INASCO, Integrated Aerospace Sciences Corporation, 18 Napoleontos Zerva street, 16675 Glyfada, Athens, Greece
e-mail: c.koimtzoglou@inasco.com

M. Ciminello
Adaptive Structures Department, CIRA, The Italian Aerospace Research Centre, Via Maiorise snc, 81043 Capua, CE, Italy
e-mail: m.ciminello@cira.it

I. Dimino
Smart Structures Technologies Laboratory, CIRA, The Italian Aerospace Research Centre, Via Maiorise snc, 81043 Capua, CE, Italy
e-mail: i.dimino@cira.it

A. Concilio
Smart Structures Department, CIRA, The Italian Aerospace Research Centre, Via Maiorise snc, 81043 Capua, CE, Italy
e-mail: a.concilio@cira.it

1 Introduction

This document describes the design, manufacturing, and implementation of fiber-optic (FO)-based shape sensors for a morphing structure, an adaptive trailing edge device (ATED) conceived in AS02. The FO shape sensors have been developed in the AS04 scenario of SARISTU and implemented in the AS02 scenario.

SARISTU is a project subsidized by the European Union to enhance knowledge. The project concerns the challenges posed by the physical integration of smart intelligent structural concepts. It addresses aircraft weight and operational cost reductions as well as an improvement in the flight profile-specific aerodynamic performance. One aspect of Smart Intelligent Aircraft Structures is applying active health monitoring of the structure using fiber-optic sensors (FOSs).

Conformal morphing technology is a new area to the aircraft industry. The ability of an aircraft to change the shape of its wings during flight allows it to perform a flight mission more efficiently than a fixed-wing aircraft (due to drag reduction and improved lift-to-drag ratios) and thus attracts much interest from both the military/government and the private aircraft industries. However, building a morphing wing presents new challenges in many aspects. One of the challenges is how to optimize the distribution of sensors and actuators to form a reliable control system.

The purpose of this work is to provide a means to track the ATED morphing behavior by using the fiber Bragg gratings sensors. The design and validation of the shape sensor as described in the following chapters are based on the ATED design as acquired by SARISTU.

2 Development of the Shape Sensor

2.1 Goal

The goal of the shape sensor development is to design a mechanical sensing assembly utilizing fiber Bragg grating sensors to monitor morphing behavior of the ATED.

2.2 Sensor System

The use of optical fibers as sensing elements comes with several advantages. Their properties and capabilities with regard to both strain sensing and data transmission, their high endurance, and chemically inertness allow implementations in harsh environments. Many studies and implemented models, during and prior SARISTU

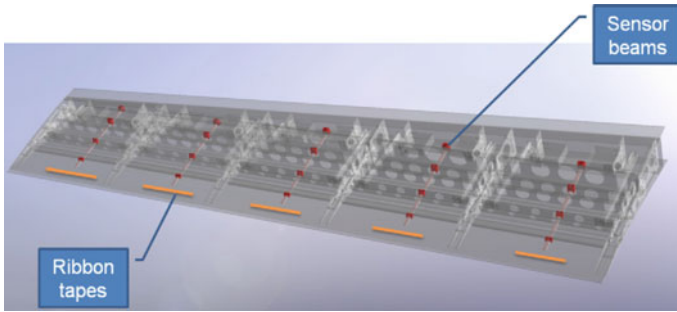


Fig. 1 ATED sensor system layout: span- and chord-wise layout for the 5-bay demonstrator

progress, validated the feasibility to a wide range of sensing applications. ATED measurement task is to reconstruct its shape from strain data, retrieved from both span- and chord-wise sections, using tailored solutions based on FO technology. To match the geometrical constraints, two kinds of sensorized structures were selected for chord-wise (sensing beam) and span-wise deformations (ribbon tapes) as indicated in Fig. 1. This paper only describes the design, manufacturing, and usage of chord-wise shape sensors.

A FO-based approach is utilized for chord-wise ATED shape reconstruction implementing fiber Bragg gratings (FBG). Based on a mechanical device, integrated with an optical fiber transducer, the shape information is translated into strain information and properly modulated. By specific data processing mathematics, these strain values are converted back into an approximation of the produced shape. The resulting error is compliant with the monitoring requirements. The solution is the result of a cooperation among structural (UniNa, CIRA), manufacturing (Aernnova), and sensor (Technobis, Inasco) technology partners.

2.3 Requirements and Specifications

The ATED has a predefined morphing behavior in terms of maximum deflection. The required accuracy for the shape sensing system to determine the deflection is 0.5° with a maximum deflection range for the ATED tip of $\pm 10^\circ$. This means a shape monitoring accuracy of 2.5 %.

Next to the performance requirement, the shape sensor assembly's implementation needs to be compliant to the following conditions:

- The structural impact from the implementation of the shape sensor assembly should be kept to a minimum such that it does not affect the designed behavior and performance of the ATED.

- The shape sensor assembly needs to be removable from the ATED in case of structural maintenance or damage of the optical sensor assembly.
- The shape sensor assembly is to be bonded to the upper skin using an adhesive cured at room temperature.

2.4 Material Selection

The different materials used for the sensor assembly regards the sensor beam itself, the sensor beam support components, and the optical sensor fiber, including connector. The sensor beam was rapid-prototyped using PE. The material for the support components for the 2-bay dummy demonstrator was the standard aluminum and manufactured to spec by a milling machine, while the support components for the final 5-bay demonstrator were rapid-prototyped as well using PE.

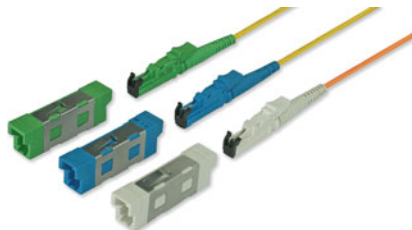
The optical fiber is standard ORMOCER[®] coated, SM 850 nm fiber provided by FBGS. The standard ORMOCER[®] coating is mainly designed for strain measurement applications and has the following features:

- High adhesion to the fiber glass enabling direct fixation of the FBGs
- High E-modules to generate a good strain transfer between fiber and the glue
- Temperature operating range outperforming standard optical fiber coatings to support applications between -180 and $+200$ °C.
- Easy fiber manipulation allowing to remove the ORMOCER[®] coating for splicing without the use of chemical acids.



The optical fibers are bonded to the sensor beam using Epotech epoxy.

The optical fiber connector used is a standard E2000[™] Simplex from Diamond. The E2000[™] incorporates numerous innovative features to address the needs of users. The connector has a positive latching mechanism with interchangeable color-coded and mechanically keyed thumb-latch, and a spring loaded protection cap. The E2000[™] offers 0.1 dB maximum insertion loss at an operating temperature range of $-40/+ 85$ °C.



2.5 Manufacturing and Implementation Process

2.5.1 Shape Sensor Manufacturing Parts

The shape sensor assembly is built to spec and consist of multiple parts (rapid prototyped): 4 support structures and the sensor beam itself. The sensor beam has a length of 300.0 mm (approximately, depends on the specific ATED bay), a width of 10.0 mm, and a height of 3.0 mm. The sensor beam has engraving along the length on the upper and lower side of the beam to integrate the optical fiber (Fig. 2).

2.5.2 Shape Sensor Assembly Implementation Procedure

The following procedure describes the assembly steps for the implementation of the shape sensor assembly for the 2-bay and 5-bay demonstrator structure that includes bonding to the ATED skin. The skin itself is considered a system/subsystem, and its implementation requires supportive tooling to ensure efficient bonding of the subsystems to the aluminum parts of the skin structure.

The images above show the shape sensor assembly and its parts. The support structures (red) are to be bonded to the aluminum parts of the skin structure by means of specific adhesives. This adhesive bonding requires a 30- to 45-min hardening. The first support structure fixes the beam. The other support structures allow the beam to slide through freely as the ATED morphs up and down. The support structures are to be bonded by means of an adhesive. Alternatively the screw holes at the top surface of support structures can be used in case screw

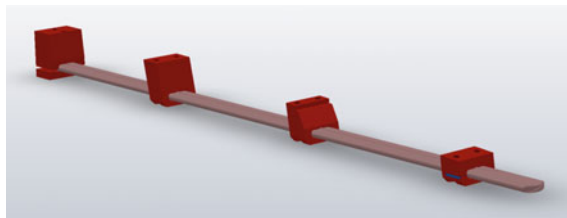


Fig. 2 Shape sensor assembly

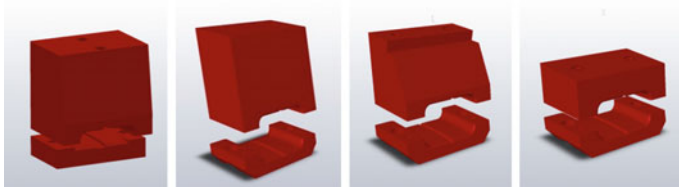


Fig. 3 Shape sensor beam support structures (from left to right, the first is used to fixate the beam)

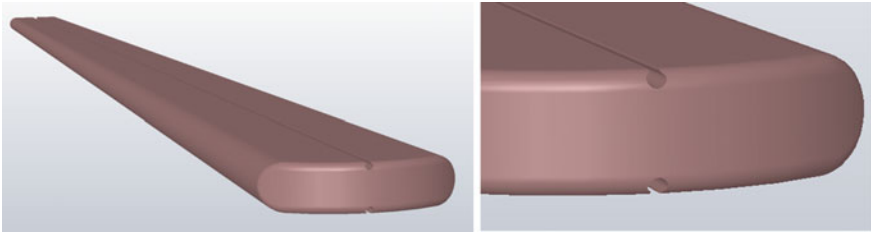


Fig. 4 The shape sensor beam

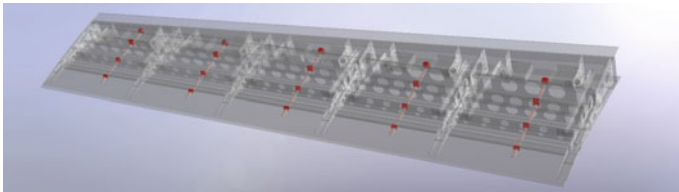
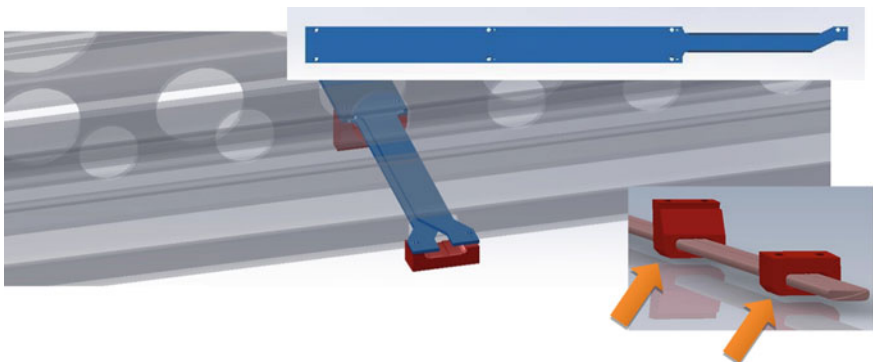


Fig. 5 Shape sensor implementation architecture 5-bay demonstrator

mounting appears more appropriate (Fig. 3). The images on the following page show how the beam is placed into the ATED structure (Figs. 4, 5, 6 and 7).

The holes in the spars allow placement of the shape sensor beam. In order to assure a aligned placement on the skin structure of the sensor beam support structures, two additional stiff rulers (blue) are used to fixate the support structures with respect to each other and the skin structure, and the sensor beam itself is not stiff enough for that (see image below).



After bonding and hardening, the rulers are removed (hence the ruler shape). Then, the sensor beam is inserted, and the support structures are closed (screwed) with small covers (green arrows). The following outline regards the assembly procedure:

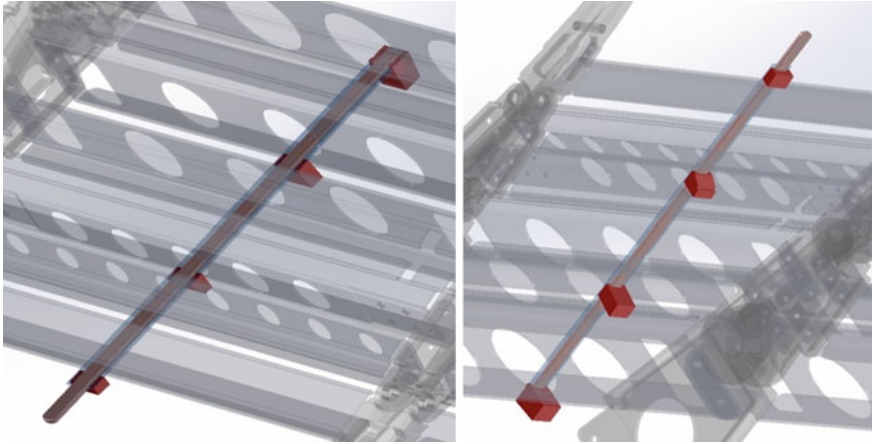


Fig. 6 Bottom-up (*left*) and top-down (*right*) view of the sensor beam



Fig. 7 Front view of the sensor beam

1. Assembly of ATED rib and spar structure;
2. Preplacement of the sensor beam and “open” parts of the support structures including the rulers; (*This can be done either before or after step 3, which is most efficient*)
3. Placement of the upper skin structure on the ATED rib/spar structure;
4. Bonding/hardening of the sensor beam on the upper skin structure;
5. Placement of the lower skin structure.

3 Principle of Operation

3.1 Non-contact Shape Monitoring

The shape sensor assembly is based on the principle of non-contact shape monitoring. This means that the optical fiber is mechanically not directly connected to the object of measurement, i.e., the ATED in this case. The sensor assembly is mechanically designed such that the deflection sensing beam is following the

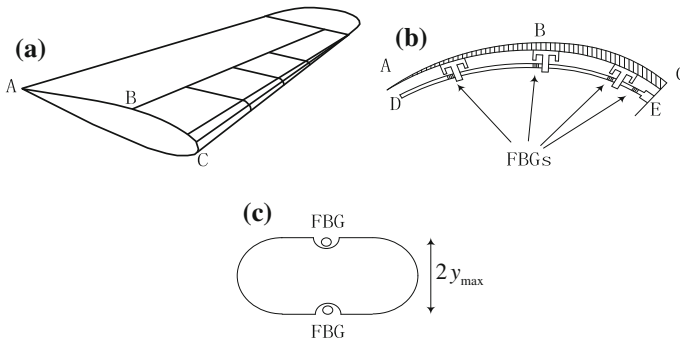


Fig. 8 Illustration of the ATED shape plan. **a** Morphing wing of an aircraft. **b** Sensing strip DE. **c** Cross section of the sensing strip

deflection freely—through the guiding support structures—of the ATED as it morphs through different shapes.

Figure 8 shows our concept sensing plan in principle. A morphing wing with its cross section is shown in Fig. 8a. Below the wing skin (ATED part; arc AB), several guides are attached (Fig. 8b), each with an opening to guide the sensing strip (arc DE). The purpose of these “strip guides” is to keep the sensor strip in position but still allow it to move freely in the chord-wise direction, following the morphing behavior of the ATED. The starting point (point E) of the strip is fixed relatively to the wing.

The openings of the guides are designed to be as smooth as possible so that the sensing strip can move freely in the longitudinal direction but restricted in the transverse direction. The cross section of the sensing strip is shown in Fig. 8c: The fiber is glued on the top and bottom, the Bragg gratings are made along the fiber, and the strain values on the strip surfaces can thus be measured.

3.2 Mechanical Analysis

In this section, the mechanics of the sensor assembly structure is discussed. From Fig. 8b, we know that our structure can be regarded as a modified cantilever problem in which the beam goes through a few strip guides. Unlike the classic cantilever, the positions of the guides are known, while the forces applied by them are unknown. Therefore, we will need a special way to find the deflection expression of the sensing strip.

3.2.1 The Strip Guides

According to the design in Fig. 8b, the strip guides are fixed relatively to the wing skin by mechanical connections.

Figure 9 shows us this geometrical relation in details. The above solid line is the shape of the wing skin, along which the strip guides (B_1H_1 , B_2H_2 and B_3H_3) are fixed on. The guides are perpendicular to the wing skin at the bottoms B_1 , B_2 , and B_3 . The sensing strip (dashed line) goes through the guiding points H_1 , H_2 , and H_3 . Given the wing skin expression, we can thus know the values of (x_{bi}, y_{bi}) . The normal vectors \vec{n}_i at these points can also be computed. The positions of the guiding points are then:

$$(x_{hi}, y_{hi}) = (x_{bi}, y_{bi}) + d \cdot \vec{n}_i, \quad i = 1, 2, 3 \tag{1}$$

in which “ d ” is the distance from the wing skin to the sensing strip.

3.2.2 Guiding Forces and the Strip’s Deflection Equation

The guiding positions found in Eq. (1) are also where the guiding forces are loaded to the sensing strip. Besides, since the strip guides allow the strip to move freely in the longitudinal direction, the forces will be applied only in the directions of \vec{n}_i .

Now, we have known the positions and directions of the forces; the only thing that we do not know is their amplitudes. We can thus give them a group of probation values (then we will know everything), but they have to bend the strip in such a way that it goes through all the guiding positions. It thus forms a “nonlinear equation” problem of finding proper force amplitudes. As the first step, we have to find the deflection expression due to a group of the “probation” guiding forces. Figure 10 shows how it is computed.

The forces generate bending moment along the strip [4],

$$(0, 0, M_z(x)) = \sum_{\text{forces to the right}} f_i \cdot (x_{hi} - x, y_{hi} - w_p(x), 0) \times \vec{n}_i \tag{2}$$

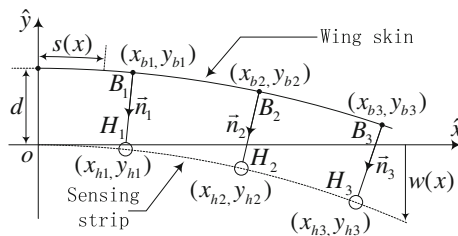


Fig. 9 The position of the strip guides

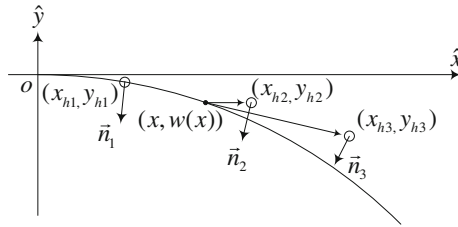


Fig. 10 Bending moment calculations

in which $f_i (i = 1, 2, 3)$ is the probation force amplitudes, and $w_p(x)$ is the strip’s (probation) deflection, and it is computed by the following differential equation [4]:

$$\frac{\frac{d^2 w_p}{dx^2}}{\left(1 + \left(\frac{dw_p}{dx}\right)^2\right)^{\frac{3}{2}}} = \kappa(x) = \frac{M_z(x)}{EI_z} \tag{3}$$

in which $\kappa(x)$ is the curvature, E the modulus of elasticity, and I_z the moment of inertia of the strip.

As long as we know $w(0)$ and $w'(0)$ (they are set zero in the coordinate system of Fig. 3), $w_p(x)$ can be solved by running iteration between Eqs. (2) and (3). But it might be that the strip’s deflection obtained for this force combination does not go through the guiding points, which means:

$$w_p(x_{hi}) \neq y_{hi}, \quad i = 1, 2 \text{ or } 3 \tag{4}$$

Then, we will need to change f_i until we find the best f_i that minimizes:

$$\delta(f_1, f_2, f_3) = \sum_{\text{all holders}} (w_p(x_{hi}) - y_{hi})^2 \tag{5}$$

in which δ is called the penalty function, and it would be zero if we have found the “right” f_i .

In our modeling, we have employed the “trust-region-dogleg” algorithm to minimize Eq. (5) and the optimization was done twice at different resolutions to guarantee both the speed and accuracy [5]. In the end, we will find a “right” $w(x)$, and the strain distribution along the strip surface is computed by:

$$\varepsilon(x) = \frac{\frac{d^2 w}{dx^2}}{\left(1 + \left(\frac{dw}{dx}\right)^2\right)^{\frac{3}{2}}} EI_z y_{\max} \tag{6}$$

in which y_{\max} is half of the sensing strip thickness (Fig. 8c).

Now, we have found the strain distribution on the strip surface for a particular wing shape. In the next chapter, we will reconstruct the wing shape with a few strain values on the strip surfaces.

3.3 Shape Reconstruction Procedures

The essence of a reconstruction is the recovering of the full knowledge from limited information. In our work, the same principle applies. Theoretically, if we have unlimited number of sensors, there will be a 100 % reconstruction. However, we are always limited to use as few sensors as possible. Therefore, we have to put the sensors in the most necessary positions and extrapolate/interpolate the strains in other places.

3.3.1 Sensor Positions and the Strain Value Extrapolation (Interpolation)

Before going into the sensing process, it is worthy to have a rough idea of the strain profile on the surfaces of the sensing strip. We know that the strain is proportional to the bending moment:

$$\varepsilon(x) = M(x) \cdot y_{\max} \tag{7}$$

Suppose the bending is relatively small compared with the total length, and the guiding forces are approximated as applied vertically (Fig. 11a).

And the corresponding bending moment is as follows:

$$M(x) = \begin{cases} (F_1 + F_2 + F_3)x - (F_1l_1 + F_2l_2 + F_3l_3), & 0 < x < l_1 \\ (F_2 + F_3)x - (F_2l_2 + F_3l_3), & l_1 < x < l_2 \\ F_3x - F_3l_3, & l_2 < x < l_3 \\ 0, & x > l_3 \end{cases} \tag{8}$$

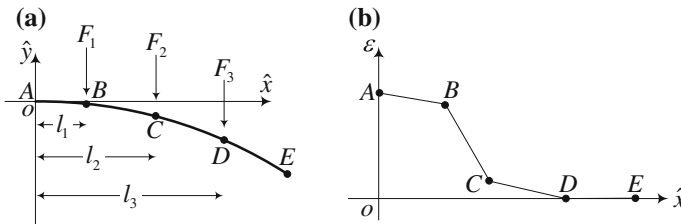


Fig. 11 Multi-forces cantilever and the bending moment. **a** Cantilever with three forces. **b** Strain along the beam

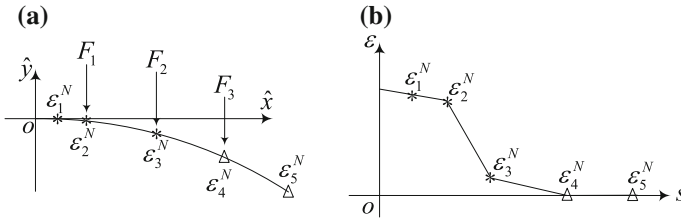


Fig. 12 The sensing and extrapolating (interpolating) plan. **a** Sensor positions. **b** Strain extrapolation and interpolation

The strain can then be computed and plotted in Fig. 11b. It is composed of four line segments: AB, BC, CD and DE. The points B, C, and D are places where the forces are applied. If we know in advance where the guides are, we can interpolate the strain distribution based on this knowledge.

Figure 12 shows our sensing plan. Three sensors are marked with “*”: The first sensor is placed in the middle between the starting point and the first load; the other two sensors are put in places where the forces are applied (only approximately, since the bending will shift the loading position longitudinally). For the last loading position and the strip end, we do not measure the strain values, but we know they are zero by Eq. (8). Therefore, a “guess” is made at these two points (marked with “Δ”). With all the strain values, we can now plot the strain distribution function by linking these points (Fig. 12b).

3.3.2 Strip Shape Reconstruction by Frenet–Serret Formula

With the interpolated strain distribution, it is now possible to recover the shape of the sensing strip. The Frenet–Serret formula will be used to complete the mission. Before going into the details of the shape reconstruction, we need to first clarify the exact definition of the word “shape.” The differential geometry tells us that the shape can be understood as a group of scalar and vector quantities along the curve: the curvature $\kappa(s)$, torsion $\tau(s)$, tangent vector $\vec{T}(s)$, normal vector $\vec{N}(s)$, binormal vector $\vec{B}(s)$ and position vector $\vec{r}(s)$. These quantities are related and the Frenet–Serret formula tells us that the vector quantities can be derived from the scalar ones.

Therefore, the strategy is to first recover $\kappa(s)$ and $\tau(s)$ from $\epsilon(s)$ and then all the other quantities. For the ATED application, the strip is bent in such a way that the symmetric plane is fixed. Therefore, the torsion is zero:

$$\tau(s) = 0 \tag{9}$$

The curvature is linearly proportional to $\varepsilon(s)$ and inversely proportional to y_{\max} :

$$\kappa(s) = \frac{\varepsilon(s)}{y_{\max}} \quad (10)$$

Now, we can employ the Frenet–Serret formula [6]:

$$\begin{aligned} \frac{d}{ds} \bar{T}(s) &= \kappa(s) \bar{N}(s) \\ \frac{d}{ds} \bar{N}(s) &= -\kappa(s) \bar{T}(s) + \tau(s) \bar{B}(s) \\ \frac{d}{ds} \bar{B}(s) &= -\tau(s) \bar{N}(s) \end{aligned} \quad (11)$$

An important feature of the Frenet–Serret formula is that the derivatives $\left(\frac{d}{ds} \bar{T}(s), \frac{d}{ds} \bar{N}(s) \text{ and } \frac{d}{ds} \bar{B}(s)\right)$ are expressed in terms of the primitive functions $(\bar{T}(s), \bar{N}(s) \text{ and } \bar{B}(s))$. Besides, we know that:

$$\begin{aligned} \bar{T}(s) &= \int_0^s \left(\frac{d}{ds} \bar{T}(s) \cdot ds + \bar{T}(0) \right) \\ \bar{N}(s) &= \int_0^s \left(\frac{d}{ds} \bar{N}(s) \cdot ds + \bar{N}(0) \right) \\ \bar{B}(s) &= \int_0^s \left(\frac{d}{ds} \bar{B}(s) \cdot ds + \bar{B}(0) \right) \end{aligned} \quad (12)$$

Therefore, as long as we have the initial values of $\bar{T}(0), \bar{N}(0)$ and $\bar{B}(0)$, we can reconstruct the shape by iterating between Eqs. (11) and (12). Finally, the position vector $\bar{r}(s)$ of the strip is computed by:

$$\bar{r}(s) = \int_0^s \bar{T}(s) \cdot ds + \bar{r}(0) \quad (13)$$

3.3.3 Wing Shape Reconstruction

Now, we have recovered the shape of the sensing strip, but our final goal is to reconstruct the shape of the wing. These two structures are simply connected by the strip guides.

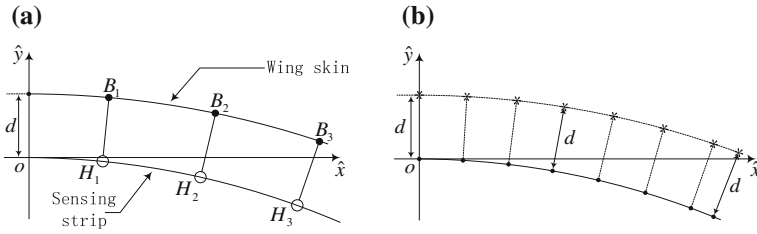


Fig. 13 Wing reconstruction from the shape of the strip. **a** Wing and the strip geometry. **b** Wing shape reconstruction

Figure 13a shows the geometry of this connection, and Fig. 13b shows our strategy to reconstruct the wing skin shape: We pick up a few points (marked with black dot) along the reconstructed sensing strip [the solid line in Fig. 13b, given by Eq. (13)]; the normal vectors at those points are calculated; the “*” points are obtained by going for “ d ” distance from the “black dots” along the normal vectors; and linking all the “*” points, the wing shape (the dashed line in Fig. 13b) is thus reconstructed.

3.4 Simulation Results

We will use the knowledge from the previous paragraphs and present a complete simulation of the wing shape reconstruction. In Sect. 3.4.1, we will define the “parabolic wing” and the reconstruction error. In paragraph 0, this error will be investigated for a series of wing configurations.

3.4.1 Problem Definition

Figure 14a shows the geometry of the parabolic wings, and they are of the form:

$$y = d + ax^2 \tag{14}$$

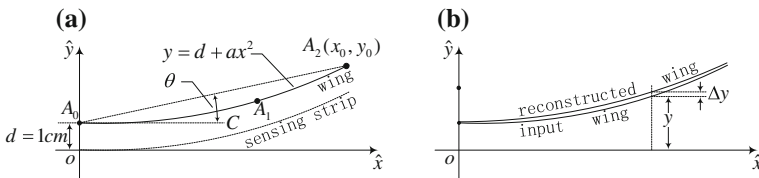


Fig. 14 Reconstruction error investigation setup. **a** Parabolic wing. **b** Reconstruction error

The sensing strip (dashed curve in Fig. 14a) is at 10 mm under the wing.

Changing the value of parameter “a” in Eq. (14), the end tip of the wing skin (point A_2 in Fig. 14a) will move vertically by “ ax_0^2 ” The angle between A_0A_2 and A_0C is thus defined as the deflection angle:

$$\theta = \tan^{-1} \left(\frac{ax_0^2}{x_0} \right) \tag{15}$$

For each angle, the strain on the strip is calculated according to Sect. 3.2. We pick up three strain values (of 100 mm separations) and reconstruct the wing shape according to Sect. 3.3. In the end, the reconstructed wing shape is compared with the original “input” wing and the “reconstruction error” is defined as the relative difference between these two shapes (Fig. 14b):

$$\delta = \left| \frac{\Delta y}{y} \right| \times 100 \% \tag{16}$$

3.4.2 Reconstruction Results

Varying the deflection angle θ from -30° to 30° , Fig. 8a shows the corresponding input and reconstructed wing shapes. The solid lines are the input parabolic wings, and the starred points are the reconstructed shapes (Figure 15).

We can see that the reconstruction is a good representation of the input shape. Further analysis shows that the reconstruction error is no more than 0.5 %. This small error is plotted in Fig. 8b, and it might arise from the following aspects: the approximation that the strain distribution is composed of line segments (Sect. 3.1); the longitudinal shift of the sensing strip (due to bending) that relocates the guiding forces; the error caused by the geometrical reconstruction of the wing from the sensing strip (Sect. 3.3.3).

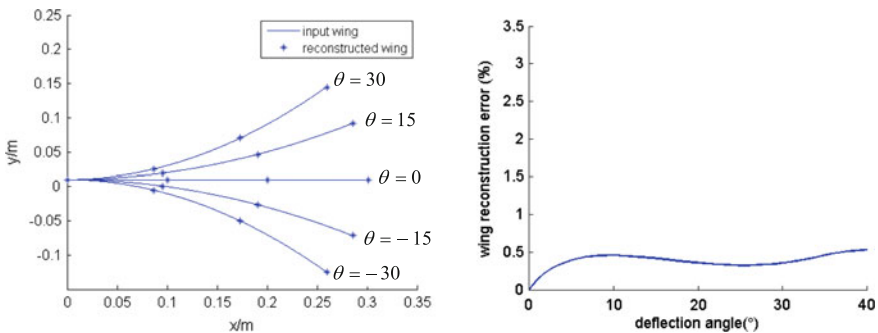


Fig. 15 Wing–wing comparison and the reconstruction error. **a** Comparison between input and reconstructed wings. **b** Reconstruction error

3.5 Experimental Results

In Sect. 3.4, we have validated our reconstruction method by simulations. Now, we will perform the measurements and validate the method by experiments. In Sect. 3.5.2, a setup is designed to evaluate the reconstruction efficiency for the sensing strip; in Sect. 3.5.3 a, morphing wing model is made as part of an internal student project and we will show the complete wing shape reconstruction in a demonstration.

3.5.1 Cantilever Experiment

The first rudimentary experiment performed was a cantilever system with an optical fiber with FBGs. Figure 16 shows the cantilever setup and the placement of the FBG sensors. The cantilever beam experiment was a part of an internal student project. The test results of this experiment were very promising and already showed an accuracy much better than required for SARISTU. Although the design was modified and specifications were relaxed for the final SARISTU design, the measurement results still remain well within the requirements (Fig. 17).

With a repeated deflection profile of ± 15 mm at the tip of the cantilever, the test results show a RMS value of less than 0.5 mm position accuracy at the tip. This means an error margin of less than 0.2 %.

3.5.2 Sensing Strip Reconstruction Measurement

From the discussion in Sect. 3.3, we know that the most important part of the wing shape sensing is the reconstruction of the sensing strip. The wing shape is then simply obtained by the geometrical relation between the wing skin and the strip. Therefore, it would be very interesting to investigate the reconstruction efficiency for the sensing strip alone.

Figure 18 shows the measurement setup. The strip is clamped tightly at the left side. A needle driven by a motor (together with a spring) is used to push the

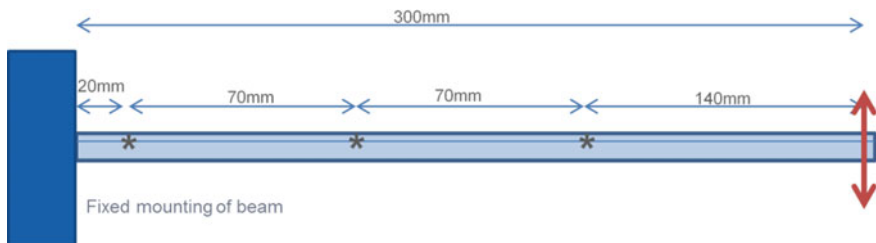


Fig. 16 Extended cantilever system with FOS

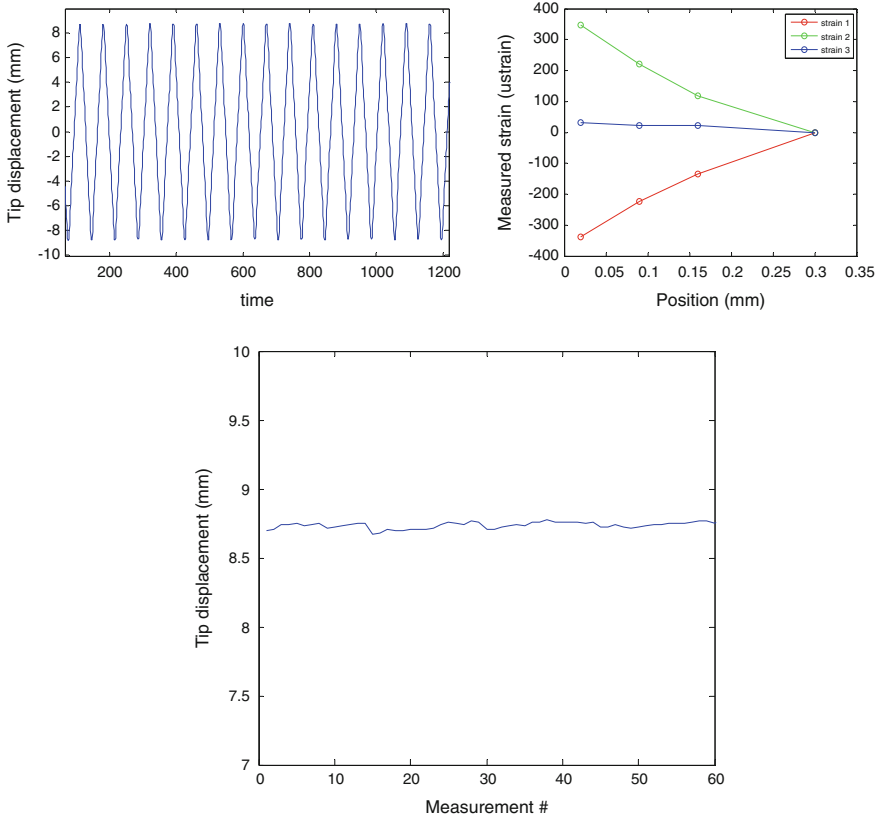


Fig. 17 Cantilever test measurement results

strip. This is to simulate the effect of the strip guides in a morphing wing. A ruler is placed to the right of the sensing strip, and therefore, the displacement of the strip end tip can be measured.

Two FBG sensors are made along the sensing strip, and therefore, the strain can be measured on its surface. From these strain values, we can recover the shape of the strip according to Sect. 3. The input and reconstructed “end tip displacements” are thus compared in Fig. 19.

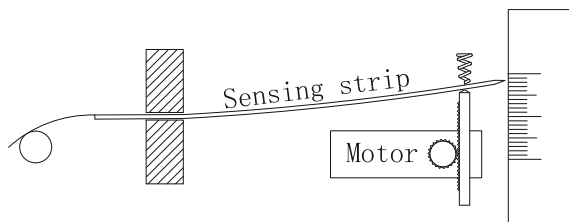


Fig. 18 Sensing strip end tip displacement measurement setup

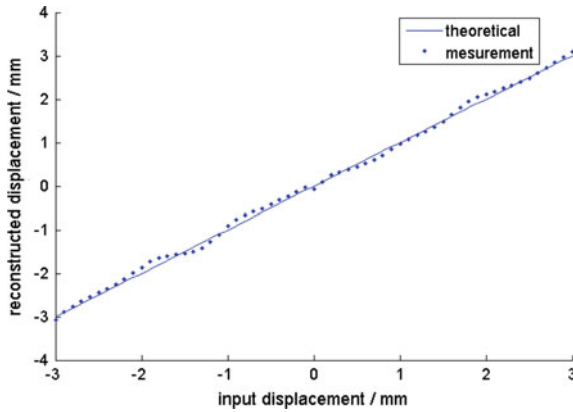


Fig. 19 Sensing strip reconstruction measurement data

Changing from -3 to 3 mm, we see that the reconstructed displacements flutter around the input displacements. A further analysis will show that the average reconstruction error is less than 4.3% .

3.5.3 Morphing Wing Demonstration

With the sensing strip in Sect. 3.5.2, we can now perform the complete wing shape reconstruction. Therefore, we have built a demo morphing wing. It is made of three rotation parts (each part is of 100 mm long), as shown in Fig. 11. At 10 mm below the wing skin, we made three openings to guide the sensing strip.

Bending the wing to three configurations (downwards, horizontal, and upwards), Fig. 20 shows both the positions of the sensing strip (the red solid curves) and the

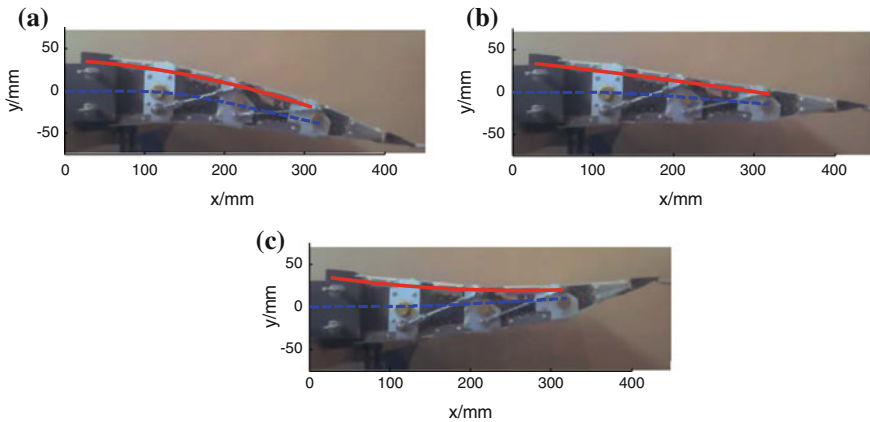


Fig. 20 Morphing wing demonstration setup and reconstruction. **a** Downwards. **b** Horizontal. **c** Upwards

shapes of the reconstructed wing (the blue dashed curves). We can clearly see that our method is able to recover the shapes of the wing. For a more accurate quantitative analysis, a better design and the actuation system of the morphing wing were needed, which will be the future task of collaborative research with other partners within SARISTU.

4 2-Bay and 5-Bay Demonstrator

Several 2-Bay demonstrators have been manufactured of which one integrated with the shape sensor assemblies. (Perturbed) Load tests, successfully lead by CIRA, were performed at Aernnova, Vitoria (Figs. 21 and 22).

Although no further numeric analysis has been performed on the results yet, the visualization clearly demonstrates an accurate representation of the shape reconstruction of the two shape sensors which were integrated.



Fig. 21 Test setup for the 2-bay ATED demonstrator

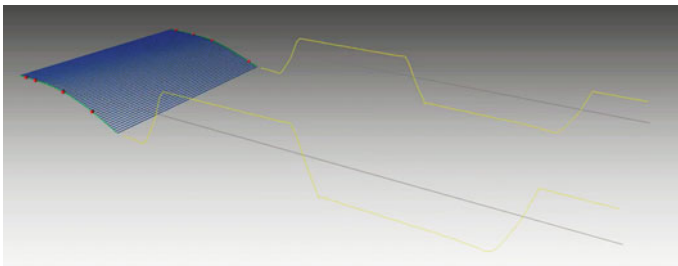


Fig. 22 Visualization of 2-bay deflection data

Eventually, this led to the implementation of the shape sensors in the 5-Bay demonstrator which will be tested May/June 15 at TsAGI in Moscow.



5 Conclusion

In general, the concept of utilizing optical fibers as sensing element is facing a bright future. Their properties and capabilities with regard to both sensing strain and transmission of data, their high endurance, and chemically inertness allow harsh environment implementations. The demonstrated studies and implementation models during and prior SARISTU progress, also through parallel assessments in other programs, validated the feasibility for generic sensing applications.

The mathematical model for the interpretation of strain and conversion into shape information has proven more than sufficient. The shape sensor system was overspecified on purpose to provide additional insights in behavior going beyond the requirements with regard to the ATED shape sensing capabilities. It surely will provide interesting insights for further developments.

The ATED shape sensor assemblies have been implemented successfully in the 2-Bay ATED dummy demonstrator and finally in the 5-Bay demonstrator to be tested at TsAGI Moscow. The experiments with the 2-Bay ATED Dummy demonstrated in Vitoria, Spain, already depicted compliance to the shape sensing requirements for the 5-Bay ATED.

Unfortunately, the wind tunnel tests did not take place yet to present conclusive results. These test will be performed in upcoming months May/June 15.

In preparation to these tests the operation of the shape sensors have been successfully verified during the assembly of the complete wing at Alenia, Napoli.

Acknowledgments Many project partners have been involved in the development of the shape sensor for the SARISTU project. The success of the work package has been greatly influenced by the open and thoughtful lines of communication between all partners involved. The research leading to these results has received funding from the European Union's Seventh Framework Program for research, technological development, and demonstration under grant agreement no 284562.

References

1. <http://www.saristu.eu/project/activities/as-02-structural-tailoring-of-wing-trailing-edge-device/>
2. Bowman J, Sanders B, Weisshaar T (2002) Evaluating the impact of morphing technologies on aircraft performance. AIAA Paper 2002–1631
3. Cesnik C, Last H, Martin C (2004) A framework for morphing capability assessment. AIAA Paper 2004–1654
4. Gere JM, Goodno BJ (2009) Mechanics of materials, 7th Edn
5. Dennis JE Jr, Schnabel RB (1996) Numerical methods for unconstrained optimization and nonlinear equations
6. Victor Andreevich Toponogov (2006) Differential geometry of curves and surfaces

Part V

Technology Stream: Integrated Sensing. Wing Damage Detection Employing Guided Waves Techniques

Introduction and Overview

SARISTU Scenario 5 has as main goals the design, manufacturing, and implementation of a composite wing damage detection system based on guided ultrasonic wave measurements techniques. The system must be able to detect BVID and VID on reinforced skin of a composite wing, integrating/installing the sensors within the structural subcomponents during the manufacturing phase and reducing drastically the inspection time of the selected part to be monitored, if compared to available NDT. A real reduction of life cycle costs related to maintenance and inspections, through reduced maintenance time and/or inspection intervals, is expected for sensorized structural components and SHM systems introduction. Clusters of high-frequency ultrasonic sensor arrays are located in critical areas of a structure to analyze the characteristics of the guided waves propagating from a controlled source. The appearance of a defect between the source and the receiver (pitch-catch) or between the source and a well-identified boundary (pulse-echo) modifies the elastic waves propagating between them. Analyzing the signals received by sensors is possible to correlate structural perturbations with acquired signals.

The main aspects investigated within AS05 are as follows:

- Experimental wave propagation characterization using piezoelectric patches;
- Sensorization of structural coupons and subcomponents (secondary bonded sensors; sensor location optimization);
- Development and testing of wave propagation-based damage detection algorithms and their implementation within SHM system (methodologies);
- Numerical simulation techniques development aimed at reproducing the wave propagation into composite structures;
- Investigation of integration aspects of SHM systems into full-scale subcomponents (wing demonstrator of IS12).

Three sets of panels have been produced (stiffened and unstiffened) from coupon to stiffened ones as well as one bigger panel with thicknesses and layup transition areas reproducing the IS12 wing demonstrator lower panel lamination sequences

and transitions between different thicknesses. These are the main activities presented within the following papers and the partners involved:

1. Production and reference NDT by phased-array C-scan after manufacturing (BAB)
2. Impact calibration by the mean of infrared thermography and phased-array C-scan. (UNINA)
3. Sensorization, signal acquisitions, analysis and methodology development, and application before and after impact damages (Aernnova, FhG, KULeuven, UNIBO, UNINA)
4. Development of specific electromechanical impedance-based device for sensors bonding and functionality reliability check (FhG)
5. Statistical evaluation procedure for detectable damage threshold assessment aimed at P.O.D. and P.O.F.A. definition of the methodologies (P.O.D. and P.O.F.A. assessment were beyond the scope of this scenario, but a preliminary investigation on possible definitions has been carried out.) (KUL, UNIBO, UNINA).

Methodologies for Guided Wave-Based SHM System Implementation on Composite Wing Panels: Results and Perspectives from SARISTU Scenario 5

Ernesto Monaco, Natalino Daniele Boffa, Vittorio Memmolo, Fabrizio Ricci, Nicola Testoni, Luca De Marchi, Alessandro Marzani, Jan Hettler, Morteza Tabatabaeipour, Steven Delrue and Van Den Abeele Koen

Abstract Within the SARISTU project, the Application Scenario 5 (AS05) was devoted primarily to the development of methodologies based on ultrasonic guided waves for Structural Health Monitoring (SHM) implementation on wing structural elements made of composite materials for detecting BVID or hidden flaws. These methodologies have been mainly developed by the authors of this paper,

E. Monaco (✉) · N.D. Boffa · V. Memmolo · F. Ricci
Department of Industrial Engineering—Aerospace section,
University of Naples “Federico II”, Via Claudio 21, 80125 Naples, Italy
e-mail: ermonaco@unina.it

N.D. Boffa
e-mail: natboffa@hotmail.com

V. Memmolo
e-mail: vittorio.memmolo@unina.it

F. Ricci
e-mail: fabricci@unina.it

N. Testoni · L. De Marchi
Department of Electrical, Electronic and Information Engineering—DEI,
University of Bologna, Viale del Risorgimento 2, 40136 Bologna, Italy
e-mail: nicola.testoni@unibo.it

L. De Marchi
e-mail: l.demarchi@unibo.it

A. Marzani
Department of Civil, Chemical, Environmental and Materials Engineering—DICAM,
University of Bologna, Viale del Risorgimento 2, 40136 Bologna, Italy
e-mail: alessandro.marzani@unibo.it

J. Hettler · M. Tabatabaeipour · S. Delrue · K. Van Den Abeele
Department of Physics, KU Leuven, Kulak, E. Sabbelaan 53, 8500 Kortrijk, Belgium
e-mail: jan.hettler@kuleuven-kulak.be

technologically integrated, and applied on small-scale structural elements within Scenario 5 (unstiffened and stiffened plates) focusing, at the end of the work, also on statistical assessment of damage thresholds levels for each methodology pro-paedeutic to a probability of detection (POD) evaluation of each approach. The paper will shortly present the methodologies developed and implemented, the main experimental and numerical results in terms of damage detection, and the statistical assessment of threshold damage detection levels. Finally, a short comparison about pros and cons of the methodologies as well as the migration strategy of the methodologies to the Integration Scenario 12 for full-scale wing implementation will be presented.

Nomenclature

SHM	Structural Health Monitoring
ToF	Time of flight
POD	Probability of detection
PFA	Probability of false alarm
WSM	Wave scattering method
TM	Tomographic method
K–S Test	Kolmogorov–Smirnov Test
SDC	Signal difference coefficient
RMSD	Root-mean-square deviation
DI	Damage index

1 Introduction

The next frontier of maintenance scenarios within the aeronautical industry concerns the development of Structural Health Monitoring (SHM) systems based on sensors permanently installed on aeronautical structural subcomponents to “interrogate” the health status of certain hot spots and to prompt maintenance interventions of these components only at times when necessary instead of at fixed intervals and by expert inspectors. Approaches based on guided waves excited and sensed by piezoelectric arrays of sensors are among the techniques under investigation. The

M. Tabatabaeipour
e-mail: morteza.tabatabaeipour@kuleuven-kulak.be

S. Delrue
e-mail: Steven.Delrue@kuleuven-kortrijk.be

K. Van Den Abeele
e-mail: Koen.VanDenAbeele@kuleuven-kortrijk.be

ultrasonic research community has studied guided waves for nondestructive evaluation of platelike structures for several decades. As a result, there exists a large spectrum of algorithms for analyzing the generated and acquired ultrasonic signals and the authors of the current paper have been investigating several possible implementations during the last years.

Guided waves are created by the constructive interference of bulk waves reflected between the top and bottom surfaces of the plate; these waves have a number of characteristics that are different from those of the bulk waves. First, they are, in general, multimodal and dispersive; the particle motion (symmetric or extensional and antisymmetric or flexural) and the velocity of each mode depend upon the thickness and the material properties of the plate, as well as on the frequency of the excitation of the wave. Second, they can propagate a much larger distance than the bulk waves without significant decay in their amplitude. Third, and most important, they are extremely sensitive to the presence of discontinuities in their path and carry information on certain properties of the flaws as they propagate away from the flaws. Finally, it is relatively easy to generate and record guided waves using (PZT) actuators and sensors that require very little power, which makes them suitable for online SHM. The research groups of KU Leuven (KUL), University of Bologna (UNIBO), and University of Napoli (UNINA) have worked within SARISTU AS05 toward the development of methodologies aimed at detecting delaminations and disbonds in flat composite unstiffened and stiffened panels via ultrasonic guided waves. In next paragraphs, these methodologies will be presented along with the results obtained by their application on structural coupon/small subcomponents developed within the dedicated scenario.

2 Guided Wave-Based SHM Methodologies Developed Within SARISTU Scenario 5: Classification and Description

The methodologies, employed by KUL, UNIBO, and UNINA to detect delaminations and disbonds in flat composite unstiffened and stiffened panels via ultrasonic guided waves, can be roughly divided in two classes: wave scattering methods (WSMs) and tomographic methods (TMs) (see Fig. 1).

The basic principle of a WSM consists in exciting a guided wave from an actuator and measuring the time of flight (ToF) of the wave traveling along the direct path actuator–sensor as well as the ToF related to the wave path actuator–defect–sensor. Referring to Fig. 1a, a guided wave actuated at the transducer 1 travels along the component. Sensor 2 will detect and register the wave propagating along the direct path 1–2 as well as the wave scattered by the defect D, i.e., for a traveling path 1–D–2.

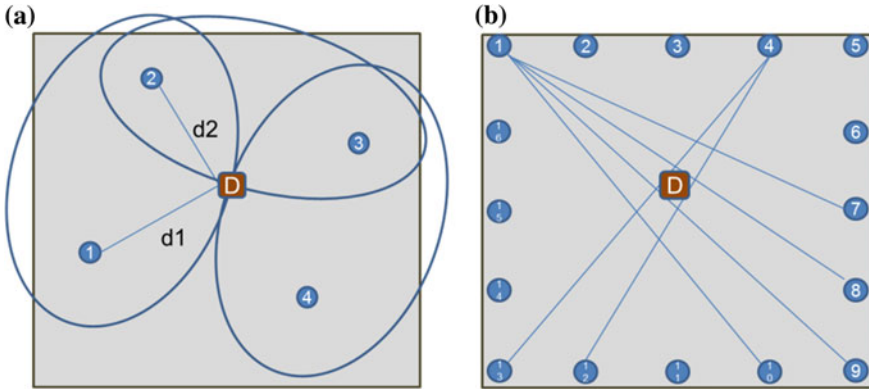


Fig. 1 Schematic representation of the operating principle of the **a** Wave scattering method (WSM) and **b** Tomographic method (TM)

The ToF of the scattered wave can be converted in a distance of propagation, once the speed of the wave or its dispersion curve is known, and then used to feed triangulation schemes aimed at revealing the presence of the defect as well as locating the defect position. For instance in Fig. 1a, the ToF for the path 1–D–2, converted in distance of propagation ($d_1 + d_2$), has been used to trace the ellipse with transducers 1 and 2 as foci. All the points of such ellipse, in fact, are characterized by a constant distance ($d_1 + d_2$) and are potential defect locations. By repeating this procedure in a multiple transducers system, the crossing of the various ellipses will be an indicator of the actual damage position.

The key operating principle of TMs consists in comparing the wave signal actuator–sensor detected on a pristine condition of the component (baseline signal), with the same signal detected after damage (current signal). Differences in the two signals are used to denote the presence of the defect in the actuator–sensor path. For instance, referring to Fig. 1b, transducer 1 is used as an actuator and transducers 7, 8, 9 and 10 as sensors. Since the wave paths 1–7 and 1–10 are less affected by the damage D with respect to the paths 1–8 and 1–9, the difference in the signals (damaged vs pristine condition) for paths 1–8 and 1–9 will be more pronounced than those at paths 1–7 and 1–10. Such difference can thus be converted into an indicator to denote the presence of the damage along the path. Increasing the number of actuators and sensors, and so the wave paths, and combining the indicators of all paths allow to detect and locate the defect.

In the following, the WSM and TM methodologies for identification/localization of damages that have been developed by the aforementioned AS05 partners of SARISTU are described in more detail.

3 Wave Scattering Methodologies: Application and Results

3.1 Background

The damage imaging proposed by UNIBO is a wave scattering procedure applied to the signals acquired in pulse-echo mode. The implemented procedure exploits a baseline to remove the scattering produced by structural reflectors. The whole procedure relies on the accurate estimation of the distance of propagation of the scattered waves. To this aim, the group velocity of the propagating wave at the selected frequency of operation is necessary. Such measurement is performed, for instance, detecting the peak of the cross-correlation between the actuated pulse and the acquired signal to estimate the ToF of the propagating wave and then dividing it by the distance of propagation to get the inverse of the group velocity. If the propagation is anisotropic, i.e., the group velocity at the selected frequency changes with the direction of propagation, the group velocity at different angles in the range 0° – 180° must be carefully evaluated because the proposed algorithm considers only one value of the group velocity.

Once the group velocity estimation is performed, the WSM-based defect imaging can be performed as follows:

1. First guided waves are generated from an actuator and received from the remaining sensors of the network;
2. A band-pass filtering of the received responses is applied in order to cancel out the effect of the transducer's resonances;
3. The signal's envelopes (modulus of the Hilbert transform) are detected in order to estimate the length of the wave propagation paths. In this step, either a baseline subtraction (if pristine signals are available and reliable) or a time gating (if the position of the geometric entities which may cause the principal reflections are known) can be applied to remove the effects of the incident wave and acoustic reflections generated by structural elements;
4. Finally, the delay-and-sum beamforming algorithm, designed to image an area related to the convex hull which is defined by the position of the sensors, is applied.

3.2 Results

The procedure has been tested on different dataset. The first dataset is related to the FEM simulation of a 5-mm-thick plate coupon. The size of the damage in this example is a $5 \times 5 \times 2.5$ mm square notch. Two different sensor configurations were tested, to analyze the performance of the implemented beamforming procedure. The results presented in Fig. 2a, b were achieved without using the baseline subtraction

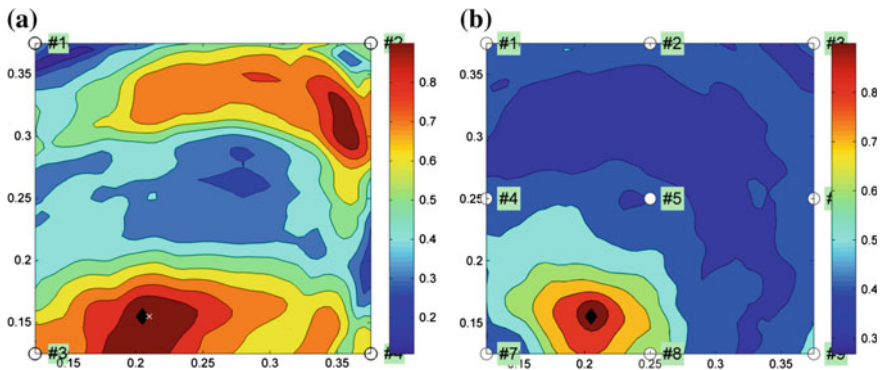


Fig. 2 Damage maps using WSM based on **a** 4 sensors/actuators and **b** 9 sensors/actuators. Input signals for the reconstruction algorithm are produced by finite element simulations

but only the time-gating approach. In these figures, as well as in Fig. 4, the damage position is represented with a black diamond, whereas the color (please note the color bar on the side of the figures) corresponds to the output of the beamforming approach intensity.

Next, the algorithm was tested on experimental data obtained on a flat composite panel (495×495 mm) produced by Bombardier and sensorized as described in the SARISTU Deliverable 51.2 “Design of SHM system.” The plate was impacted at UNINA as described in the same report.

The actuated pulse in this case is a 50 kHz, Hanning windowed, 1.5 cycle tone burst, and a setup constituted by a single actuator and two receivers has been used. The position of the delamination is detected at UNINA by means of a C-scan.

Two different settings for step 1 were evaluated: In the first case, the low and high cutoff frequencies were set to 30 and 100 kHz, respectively; in the second case, to 40 and 90 kHz. The first case produces an image with multiple peaks around the delamination borders, as can be seen in Fig. 3a. In the second case, visualized in Fig. 3b, a single peak could be observed. In both cases, there is a good agreement with the actual position of the delamination.

In addition, the UNIBO methodology was tested using a dataset acquired by KUL on a similar but different flat composite plate (505×505 mm), also impacted at UNINA. The position of the defect was detected at UNINA via C-scan. As it can be noted from Fig. 4a, similar results in terms of accuracy in the delamination position localization were achieved.

Finally, the procedure was tested on a stiffened plate. In this case, the damage, defined with a black diamond in Fig. 4b, was related to a partial disbond of the stiffener caused by an impact. Due to the numerous and strong reflections caused by the stiffener geometry itself, we learned that it very difficult, if not impossible, to image such defect when no baseline is subtracted, and when the sensors are not placed on the stiffener itself.

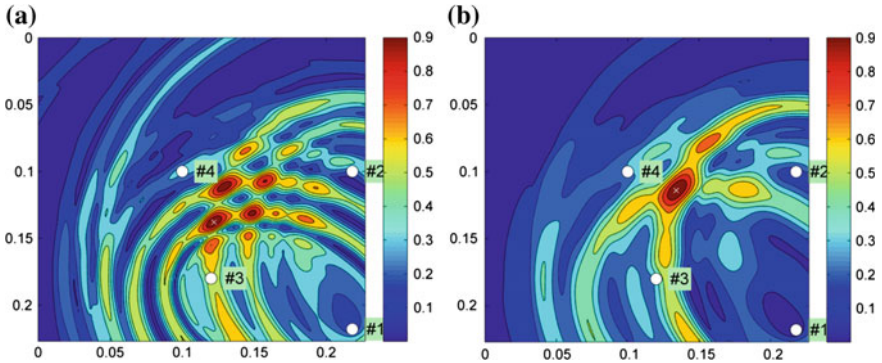


Fig. 3 Damage maps using WSM considering 1 actuator (#1) and 2 receivers (#2 and #3). Input signals were experimental data obtained on an unstiffened plate considering **a** first setting and **b** second setting as described in the text

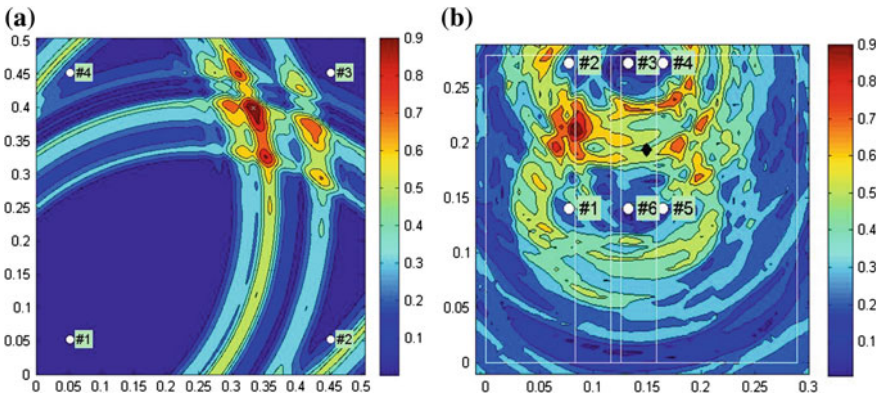


Fig. 4 Damage maps using WSM **a** Output of the proposed damage detection and localization method, using 1 actuator and 2 receivers (based on experimental signals obtained by KUL on an unstiffened plate); **b** Output of the proposed damage detection and localization method, using 6 actuators/receivers (based on experimental signals obtained on a stiffened plate)

By adding sensors on the stiffener, it is possible to detect the presence of the damage (see Fig. 4b) even without the baseline, but the localization is quite inaccurate.

4 Tomographic Methodologies: Application and Results

KUL’s SHM test within SARISTU AS05 is based on the multi-path analysis of a sparse array of transducers, before and after damage. “Baseline” measurements are acquired in a predamaged condition and stored for each path between two sensors

in pitch-catch using excitation signals consisting of sinusoidal burst at fixed frequencies or sweeps. After damage (delamination due to impact), these measurements were repeated using the same settings. The latter signals are called the “current” signals referring to the current state of the material. The baseline and the current signals are then used for the tomographic reconstruction of the damage position after impact using an algorithm called RAPID, which stands for “Reconstruction Algorithm for Probabilistic Inspection of Damage.”

4.1 Background of RAPID

The RAPID reconstruction algorithm is based on the baseline signals, $B_{ij}(t)$, before impact and the “current” signals, $C_{ij}(t)$, which are obtained after impact between all possible sensor pairs. Here, the index i denotes the transmitter and j is the representative of receiver. For each possible pair of sensors, we calculate the signal difference coefficient (SDC) which may be expressed in terms of either the root-mean-square deviation (RMSD) or the correlation coefficient, or any other alternative measure, as follows:

$$\text{SDC}_{ij}^1 = \text{RMSD}_{ij} = \sqrt{\frac{\sum_t [B_{ij}(t) - C_{ij}(t)]^2}{\sum_t [B_{ij}(t)]^2}}$$

$$\text{SDC}_{ij}^2 = 1 - CC_{ij} \quad \text{with} \quad CC_{ij} = \frac{\text{Cov}[B_{ij}(t), C_{ij}(t)]}{\sigma[B_{ij}(t)]\sigma[C_{ij}(t)]} = \frac{[\sum_t [B_{ij}(t) - \mu_{B_{ij}}][C_{ij}(t) - \mu_{C_{ij}}]]^2}{\sum_t [B_{ij}(t) - \mu_{B_{ij}}]^2 \cdot \sum_t [C_{ij}(t) - \mu_{C_{ij}}]^2},$$

where “Cov” is the abbreviation of the covariance and σ is the standard deviation. Subsequently, we apply these data to an imaging algorithm that uses these coefficients as weighting functions for the different directions.

Mathematically, the RAPID reconstruction algorithm can be represented by means of the following steps and relationships. The coordinates x_i , y_i and x_j , y_j are the planar coordinates of the i th and j th transducer in the sparse array.

We define

$$S_{ij}(x, y) = \frac{\beta - R_{ij}(x, y)}{1 - \beta} \quad \text{for} \quad \beta > R_{ij}(x, y)$$

$$S_{ij}(x, y) = 0, \quad \text{otherwise}$$

$$\text{with} \quad R_{ij}(x, y) = \frac{\sqrt{(x_i - x)^2 + (y_i - y)^2} + \sqrt{(x_j - x)^2 + (y_j - y)^2}}{\sqrt{(x_i - x_j)^2 + (y_i - y_j)^2}}$$

With this information, and with a weighting factor W_{ij} corresponding to a either $RMSD_{ij}$ or $1 - CC_{ij}$ as indicated above, the pixel intensity (probability) for each potential point on the reconstruction image is defined as

$$P(x, y) = \sum_{i=1}^{N-1} \sum_{j=i+1}^N W_{ij} S_{ij}(x, y) \quad \text{or} \quad P(x, y) = \sum_{i=1}^{N-1} \sum_{j=i+1}^N \frac{(W_{ij} + W_{ji})}{2} S_{ij}(x, y)$$

Note that the image can be constructed using one half of the signals, assuming reciprocity, or on the entire set of signals.

The details of the RAPID damage localization methodology (based on the mathematics explained above) have been implemented in an algorithm that has been programmed on a MATLAB[®] as well as on a LabVIEW platform. Different feature extractions as described above (RMSD or CC) have been implemented. Further, the user can exploit the constant/adaptive signal length feature in the program if the dispersion curve is known. In addition, the user has control over several inputs including plate dimension, number and position of transducers, filter specifications, excitation signal frequency and number of cycles, sampling frequency, feature extraction method, signal length, minimum and maximum group velocity in case of adaptive signal length (see later), baseline, and current file path. As a result, the software gives rise to a tomographic image of the plate and feature value versus propagation paths. There is also a possibility in the program to use all transducers at once or to use one/two less transducers in a round-robin selection. In the latter case, the user can eventually fuse a number of images.

In addition, recorded signals obtained at different excitation levels could be exploited in a methodology that eliminates the need for a baseline (defect-free) reference signal and focuses on the nonlinear components in the signals at various amplitudes (NL-RAPID). For this methodology, the “defect-free” reference signal could be substituted by the lowest amplitude response signal. After rescaling the lowest amplitude response with the proper amplitude ratio, this signal can be used in the above-described reconstruction methodology as the base signal, while the higher excitation signals represent the “current signals.” The SDC values to be used as weighting factors in the RAPID routine then correspond to the energy in the scaled subtraction of the signals at the various amplitudes.

4.2 *Experimental Implementation and Results of RAPID*

KUL’s SHM implementation within SARISTU AS05 uses a multi-path analysis of a sparse array of transducers, before and after damage, and the RAPID reconstruction algorithm for the reconstruction of the damage features. The SHM system uses DuraAct™ P876 SP1 sensors for the ultrasonic wave excitation and reception. These transducers can work as emitters and receivers and operate well in the frequency range of 20–400 kHz. Due to their low cost, a high number of sensors

can be employed on a sample providing a good coverage by the potential mutual propagation paths. The DuraAct™ P876 SP1 was glued to the sample using Loctite Hysol® 9466™ following the standard operational instructions and conditions. In the initial testing of a flat composite plate 16, sensors were used, which provides 120 different straight paths between the transducers. This set of 16 sensors is termed to be the “sparse sensor array” in the rest of the text.

The SHM system proposed by KUL is using DAQ cards from National Instruments for the acquisition of the signals (NI PXI-5122, 100 MS/s, 14-Bit Digitizer/Oscilloscope Data acquisition cards, 2 channel per card, 14-bit, with max sampling rate of 100 MHz). The sampling frequency used is minimal 1 MHz and limited to 100 MHz. Signal excitation is performed using the NI PXI-5421, 100 MS/s, 16-Bit Arbitrary Waveform Generator Card. For the signal amplification on excitation, 2350S-020-2 K power amplifiers from Tegam are used (2-channel amplifier with a frequency range up to 2 MHz, and an output up to ± 200 V). Burst and swept signals with frequency between 50 and 350 kHz are produced digitally in LabVIEW and transferred to the Arbitrary Waveform Generator. In most cases, single frequency burst signals of 3 cycles, Hanning windowed, are used at different frequencies (e.g., 50, 100 kHz) and different excitation amplitudes in the range of 10–150 V_{pp}. In addition, the same system also allows testing by using swept signals within the range of 20–350 kHz. All DAQ and AWG cards reside inside a single PXI system of National Instruments, together with a relay card for multiplexing between generator and sensor. LabVIEW is used for setting the experimental parameters, and for controlling the generation, multiplexing, and acquisition. Data in the form of acquired signals and analysis results are stored on a computer, which controls all operations. The data are available for further off-line processing using RAPID (programmed in either MATLAB or LabVIEW).

To avoid directionality of the signal generation, and different propagation velocities due to the anisotropy of the material (layout of fibers in different directions), the SHM system focuses only on the A0 mode at 50 and 100 kHz.

Using the recorded signals, a tomographic reconstruction of the defect location (RAPID: Reconstruction Algorithm for Probabilistic Inspection of Damage) was carried out based on the baseline signals (before impact) and the current signals (after impact) at low amplitude (0.01 V input before amplification) and low frequencies (50 and 100 kHz). The use of higher frequencies such as 350 kHz is not appropriate for the type of imaging algorithm proposed here due to the angular dependence of the velocity induced by the anisotropy of the composite and the complexity of the potential modes in the plate.

4.2.1 Flat Plate Results using RAPID

A first set of experiments was conducted on a flat composite plate of 500 by 500 mm, before and after impact. RAPID was used to analyze the signals. With proper thresholding and/or power scaling of the weights, probability images can be obtained which provide a mapping of the most probable location of the defect (In

the figures, the intersection of the cursors shows the predicted defect location in the plate, as visualized in Fig. 5 by B- and C-scan NDT): Fig. 6 illustrates the reconstruction image for an input frequency of 50 kHz, whereas Fig. 7 corresponds to an input frequency of 100 kHz. Finally, a combination of images at the two different frequencies by point-by-point multiplication provides a highly distinct image of the defect (Fig. 8). The real position of the defect agrees very precisely with the position obtained from the guided wave tomography. In conclusion, it seems that the above “linear” methodology can be used to identify the damage region with a good accuracy. A reduction of the number of transducers in the sparse array to eight provides similar, be it less unequivocal results for the damage localization, as shown in Fig. 9.

In the course of the development of the algorithm, two independent parameters have been profoundly considered: the length of the signal, which has an influence on the region coverage; and the β -factor, which may have an influence on the reconstructed defect size.

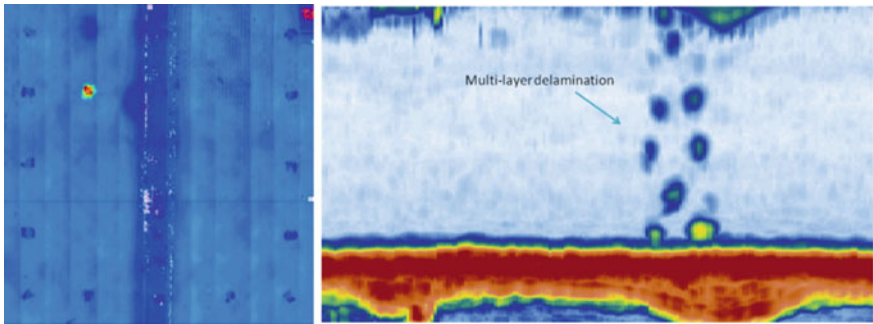


Fig. 5 C-scan (left) and B-scan image (right) of the defect in the plate (courtesy of BAM). The B-scan shows the presence of two delamination zones

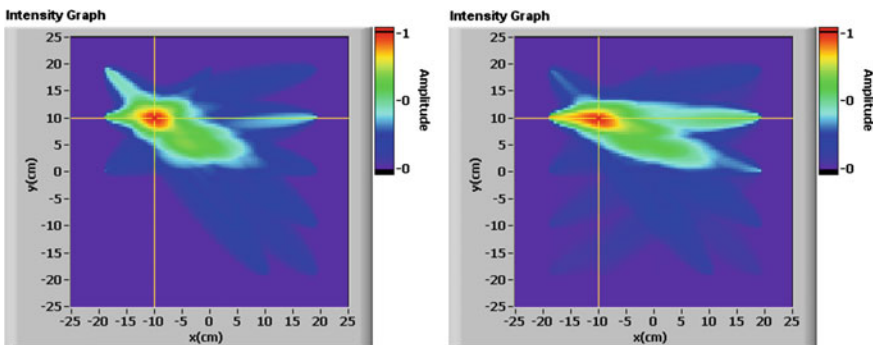


Fig. 6 Left RAPID reconstruction image obtained using power scaling of RMSD at 50 kHz right RAPID reconstruction image obtained using power scaling of correlation coefficients at 50 kHz

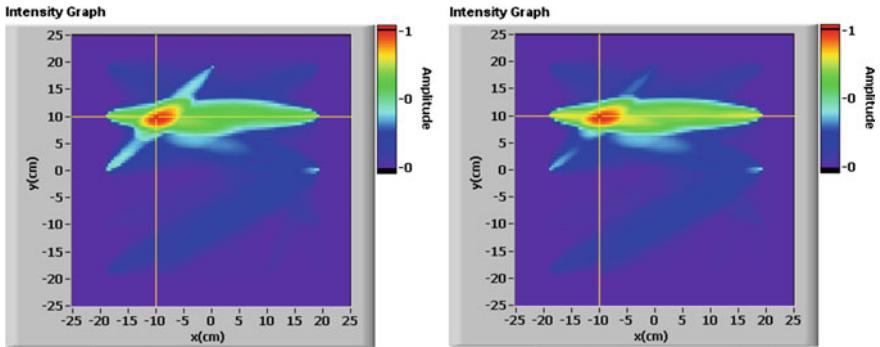


Fig. 7 *Left* RAPID reconstruction image obtained using power scaling of RMSD at 50 kHz *right* RAPID reconstruction image obtained using power scaling of correlation coefficients at 50 kHz

Fig. 8 Combined RAPID image at 50 and 100 kHz

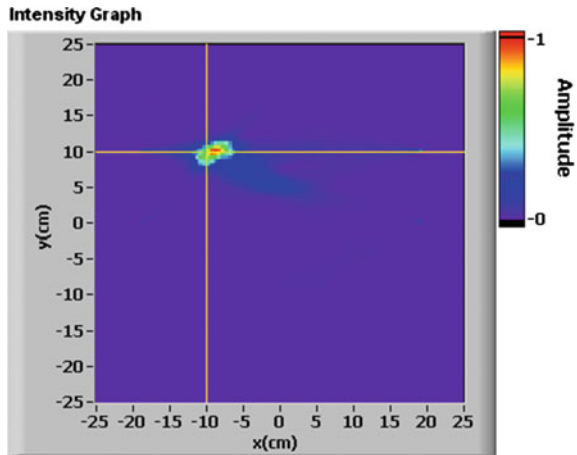
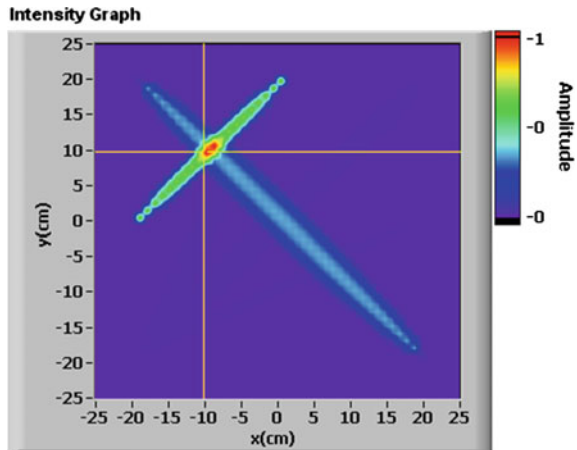


Fig. 9 RAPID reconstruction image obtained using power scaling of RMSD at 50 kHz using only the signals from 8 sensors in the array



Evaluations show that knowledge of the composite dispersion curve (group velocity vs. frequency) may improve the localization image contrast. For this purpose, adaptive signal length has been used. Knowing the minimum and maximum velocity of the involved modes in the measurement signals, one can extract a proper length of the signal for further investigation in each different propagation path according to the formula given below:

$$\begin{aligned} \text{Starting point of the signal} &= \frac{\text{Propagation path distance}}{V_{\max}} \\ \text{End point of the signal} &= \frac{\text{Propagation path distance}}{V_{\min}} + \text{Excitation signal length} \end{aligned}$$

4.2.2 Stiffened Plate Results using RAPID

A similar experiment using the same instrumentation as considered on the flat plate was repeated for a stiffened plate. The positioning of the sensor array on the stiffened plate is shown in Fig. 10, along with the position (and extension) of the impact damage with respect to the sensor array. A 60 J impact on the bay provided a quite localized impact damage (diameter of 35 mm), whereas a 70 J “under stringer foot” impact has created a comparatively extended area of debonding. Unfortunately, both impacts were realized at positions which are located outside the sensor network. The bay impact was close to sensor 10 and 11; however, the “under stringer” impact was completely outside the network.

We first focus on the analysis of the impact damage on the bay. Since the direct sound paths are not passing through the defect area, the image reconstruction algorithm is not able to detect the exact location of the damage. However, the analysis using the correlation algorithm shows a “difference” indication in the vicinity of the impact damage near to the path between transducers 10 and 11 (T10R11). The results for 50 and 75 kHz are shown in Fig. 11. For comparison, the cursor intersection on these figures shows the correct damage location.

The second impact location, under the stringer foot, is about 70 mm away and outside of the sparse transducers network. This impact has caused a large debonding area (see Fig. 12). However, the debonding defects are far from the transducer array, so that the influence of the damage is expected not to be so clear on the following images. In order to arrive at a plausible image, we had to make a small adjustment to the algorithm. Detailed investigation on the signals revealed that, if we select the later parts of the signal in combination with the RMSD analysis, it is possible to observe the most important signal changes along the right side of transducer network. This variation is most profound in the vicinity of the transducer 4 (see Fig. 13).

Finally, in Fig. 14, we have combined the reconstruction analysis for the bay impact and the foot debonding at 50 kHz. The early parts of the signals provide the

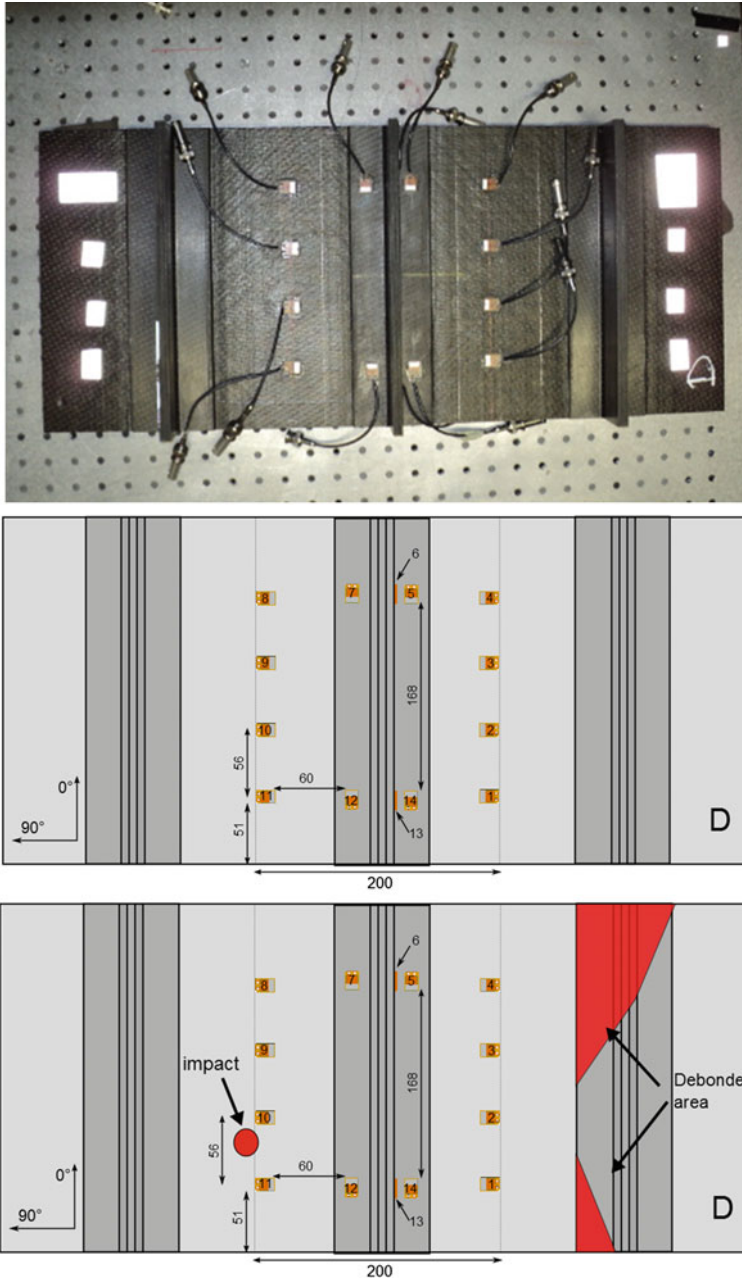


Fig. 10 Sparse array sensor positioning on the stiffened panel (*Top and Middle* figure); positions and extend of the damaged zones with respect to the position of the array transducers

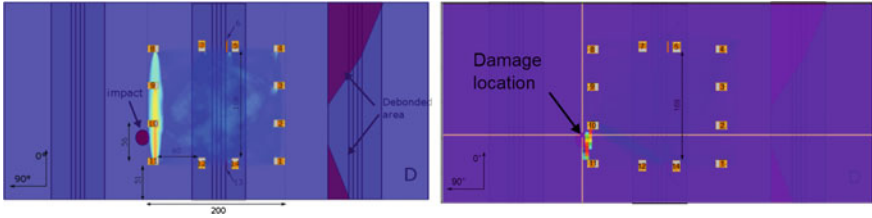


Fig. 11 Image obtained at the defect zone on the bay 50 kHz (left) and at 75 kHz (right), using the correlation algorithm

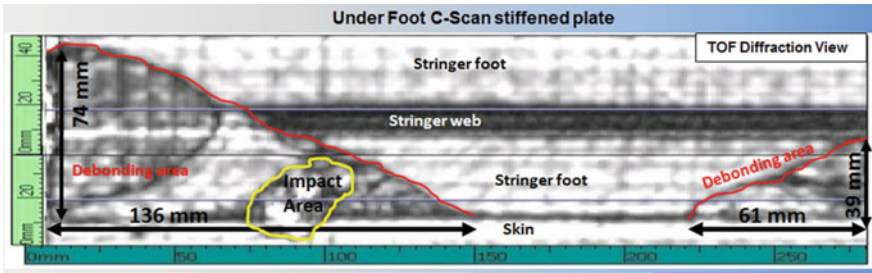


Fig. 12 Under foot ToF diffraction scan image of the stiffened plate

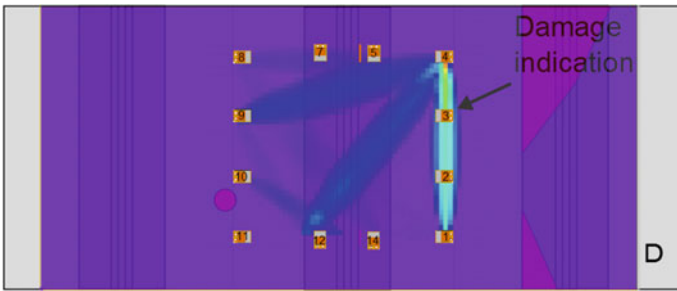


Fig. 13 Image obtained by the RMSD algorithm at 50 kHz, using the later parts of signals

indication of the damage near the network, while the later parts of the signals were used to give an indication of the damage further away from the network. The identified zone corresponds well with the direction to the highest probable defect as seen from the sensor network.

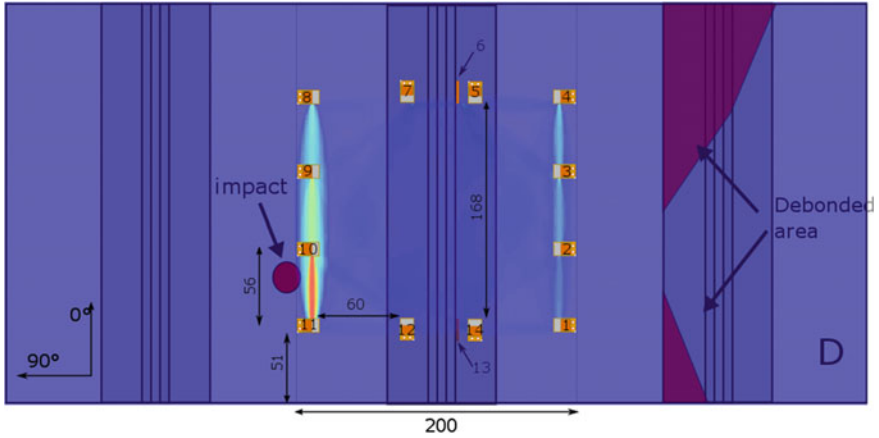


Fig. 14 Combining image at 50 kHz, the early parts of the signal provide the indication of the damage near the network (obtained using the correlation algorithm), while the later parts of the signals have been used to give an indication of the damage further away from the network (obtained using the RMSD algorithm)

4.3 Potential Extension of the RAPID Methodology

As mentioned in the background section of the above-discussed methodology, a baseline free version of RAPID can be considered by exploiting the nonlinear behavior of ultrasonic signals in the presence of defects at various excitation amplitudes (NL-RAPID). Till now, however, it turned out that a nonlinear analysis based on the scaling of signals with different input voltages was not successful for nonlinear-based tomography in the currently used experimental setup and conditions. The reason might be due to the fact that, despite the clear influence of the defect at the lowest input amplitude, it is not possible to activate its nonlinear response since the amplitudes are not high enough for the surfaces of the delaminations to start clapping. For the current delamination, the “linear” effect is orders of magnitude larger than the “nonlinear” effect. For the nonlinear effect to be visible, the severity of the delamination should be much smaller than what is currently induced, such that it can be activated at lower excitation amplitude. Further investigations are currently going on.

4.4 Conclusion of the RAPID Methodology

In conclusion, the developed RAPID reconstruction algorithm uses a probabilistic prediction of damage based on the difference between baseline signals and current signals. RAPID allows to easily investigate the region covered within sensor

networks, or at most features that are located on the boundaries of the arrays. The technique is incapable of detection of damage in the non-covered area.

UNINA's SHM analysis methodologies are based on tomographic approaches similar to KUL's: For each couple of actuator/sensor (or Propagation Path), a damage index is evaluated. The key event in SHM applications is the damage detection. A signal response must be computed/stored for identifying structural damage caused by a change in structural stiffness (i.e., damage occurrence). A damage index approach based on guided wave propagation excited by piezo-electric sensors is used here to detect the damage. The measurements consist of broadband signals due to the ultrasonic waves propagating in the structure.

4.5 Background of the Guided Wave based Damage Index Approach

Generally, given two wave signals of different structural configurations, a damage index (DI) could simply be defined as:

$$DI = \frac{|C.S. - B.S. |}{B.S.}$$

C.S. is the *current signal* and represents the computed/stored signal response of the structure after operational life. B.S. is the *baseline signal* and represents the computed/stored signal response of the structure when it is supposed in healthy state, generally after manufacturing. Changes in the characteristics of ultrasonic waves propagating across existing defects allow to detect damage through the DI computation. With a DI close to zero, the structure is in a healthy state; when the DI exceeds a certain threshold, this means damage appears; the greater the index, the more serious the damage should be. From previous equation, DI could vanish if there is no change in the structure and its value could increase with the severity and proximity of damage to the sensor locations.

Obviously, it is expected that most of the paths that cross the damaged area will be sensible to the stiffness variation and will show a different vibration response. For this reason, a damage index formulation based on the differences of signal intensity in time domain is computed for each actuator and receiver path.

Exploiting the intersection of the propagation paths characterized by the more elevated values of such differences, relatively to the average value evaluated on all the propagation paths, it has been possible to delimit a circumscribed area on a flat panel around the imposed damage which allowed a good identification of the defect zone in terms of position and surface extension.

4.6 Results of the Guided Wave based Damage Index Approach

The approach has been applied to several flat plates and to a stiffened plate. In the following, we present some results obtained on a typical wing composite layered panel with a tapered thickness which is instrumented with 39 PZT sensors permanently installed on the structure's surface. The plate has been manufactured by BAB, and the taper is obtained by means of two ramp links between the three bays with constant thickness, respectively, of 10, 8 and 6 mm. Each of the three bays of the panel is instrumented with 13 sensors (Fig. 15) to detect damage in the corresponding monitored area. Each bay is considered as an independent structure, and no interference phenomena between them are taken in consideration.

The excitation signal (source) is a 4.5 sine cycle, windowed with a Hanning function at a working frequency of 60 kHz. It is digitally amplified to have a peak-to-peak voltage of 80 V. Impacts of 85, 110, and 150 J were, respectively, applied to impact the 6-, 8-, and 10-mm-thick bays. The exterior surface of the plate was then inspected with C-scans around the vicinity of the impact locations. The obtained C-scan images clearly show the appearance of delaminations as illustrated in the Fig. 16.

The following figures present the results of the damage index analysis technique obtained by the described UNINA approach on the 6- and 8-mm-thick bays (Fig. 17).

In addition, the same approach has been employed for a stiffened panel damage analysis employing as damage index the differences in the propagation velocities on each propagation path. Despite the reduced number of sensors chosen for this configuration, the damage could be identified, even though the localization was not so detailed (see Fig. 18).

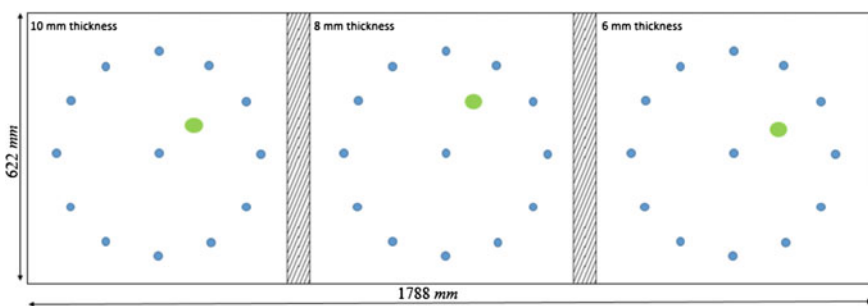


Fig. 15 Overall configuration of the tapered wing panel. The green area is the impact zone

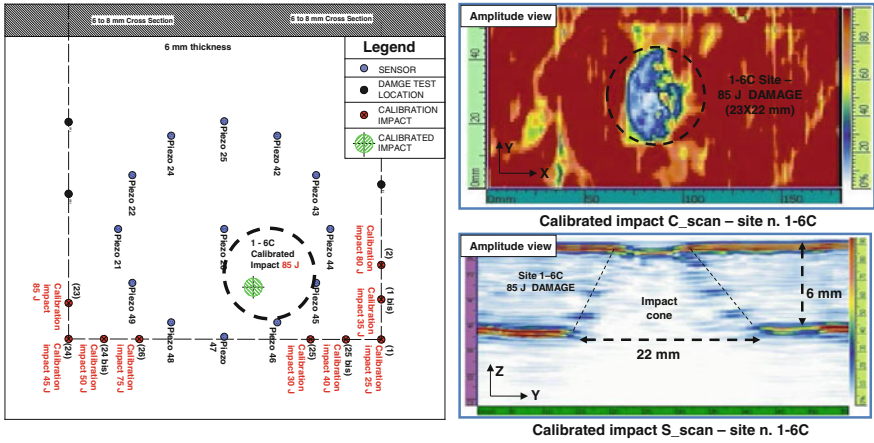


Fig. 16 Impact tests on the tapered panel—6 mm thickness bay

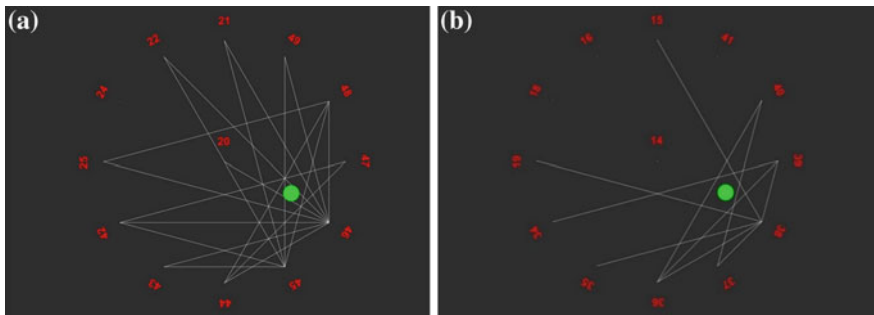


Fig. 17 Damage Index evaluation on the tapered panel—6 and 8 mm thickness bays

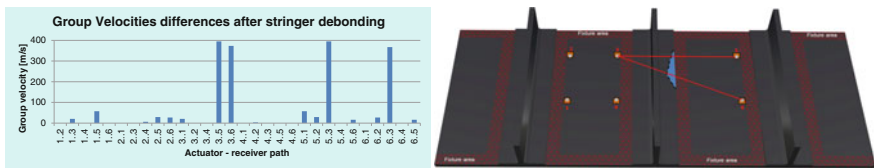


Fig. 18 Damage Index evaluation on the stiffened panel based on wave group velocity variation

5 Statistical Assessment of Threshold Level for Minimum Statistical Damage Assessment

SHM systems are generally able to detect the presence of damage. In some cases, they also provide its location and extension aside from the remaining life of the structure. According to the type of analysis that they can provide, two categories can be identified: (1) hit–miss analysis, if the system returns only qualitative information on the health of the structure, indicating only whether the crack is present or not; and (2) signal response analysis, where the system provides a continuous signal response correlated with the crack size (quantitative information). In this context, the POD method allows to quantify the efficiency of an NDE/SHM system; the reliability of an inspection system is thus obtained through rigorous and sophisticated statistics. As shown in Table 1, regarding the system reliability assessment, four different “compound events” have to be considered, which are correlated with as many conditional probabilities.

Each event where the system detects damage when it is present contributes to the positive predicted probability (PPP), well known as probability of detection (POD); the occurrence in which the system detects damage when it is not adds to the probability of false alarm (PFA); the event where the system fails to detect damage when it is present is correlated with the probability of false negative (PFN); and finally, each event where the system indicates no damage when the damage does not exist contributes to the negative predicted probability (NPP). Knowing these probability values, the system detection reliability can be determined. However, according to the Theorem of Bayes, only two probabilities need to be assessed as the sum of POD and PFN equals unity, as well as the sum of PFA and NPP. Typically, only the POD and the PFA are computed to assess the reliability of the system.

However, POD and PFA are not unrelated to each other, as the system decision threshold defines their bounds. In fact, a system response providing damage index value below the threshold would result in a free from failure structure; otherwise, the structure is considered damaged. Thus, the determination of the decision threshold is crucial for a better discrimination between noise and signal. Analyzing data from experimental research, it is possible to understand the relationship between the threshold of detection and the system response under monitoring conditions.

Figure 19 illustrates the overlapping of noise and signal distributions. The definition of conditional probabilities depending on the decision threshold is immediately evident. In order to optimize the damage detection and its reliability, the analysis of noise and signal distributions appears to be necessary.

Table 1 Probability matrix of detection: compound events and corresponding probabilities

Event	Flaw	No flaw
Detected	True call (POD)	False alarm (PFA)
Not detected	Missed call (PFN)	True no call (NPP)

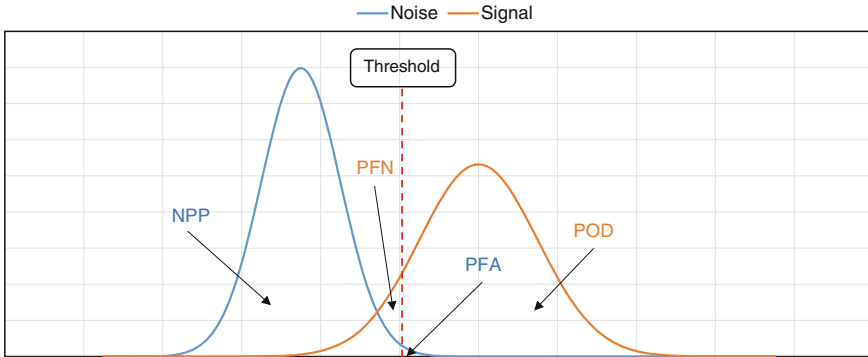


Fig. 19 Threshold definition links all the elements of the probability matrix of detection

RAPID uses a proper thresholding of the weights to create probability images which provide a mapping of the most probable location of the defect.

To illustrate how we have introduced statistics, we consider the following experimental procedure. We assume a total of N transducers, and we repeat the acquisition of signals between two transducers M times for every TR pair. Doing so, we obtain a set of baseline signals $B_{ij}^k(t)$ ($i, j = 1 \dots N, k = 1 \dots M$) and current signals $C_{ij}^k(t)$ ($i, j = 1 \dots N, k = 1 \dots M$), where i and j stand for the transmitting element and the receiving element, respectively; k denotes the acquisition number (repetition); and t is time.

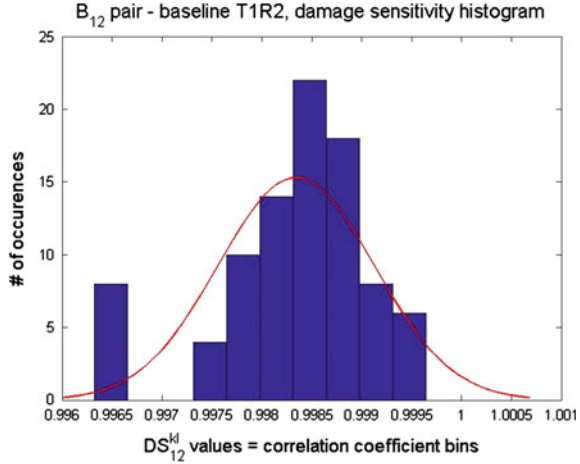
The calculation of the overall threshold index is based on the knowledge of the damage sensitivity (DS) parameter. DS describes the amount of noise and its variation due to the measurement apparatus. It is defined as the following scalar value, for either baseline signals or current signals:

$$DS_{ij}^{kl} = \text{corr} \left(B_{ij}^k(t), B_{ij}^l(t) \right) \quad DS_{ij}^{kl} = \text{corr} \left(C_{ij}^k(t), C_{ij}^l(t) \right)$$

Based on the DS values for each pair (keeping $i, j = \text{constant}$), we obtain a correlation matrix (size $M \times M$) with ones on the diagonal, which is telling us how well each pair of the acquired signals for one TR pair is correlated. In the ideal case, all values in the matrix should be close to 1, since the system has not been altered during the measurement, and each acquisition is just a plain repetition of the identical measurement. However, the deviation from unity helps us quantify the sensitivity of the setup with respect to measurement noise.

We assume that the values DS_{ij}^{kl} in the correlation matrix for fixed TR pair i, j correspond to a normal distribution. Therefore, the probability density function (and histogram) of the correlation matrix elements for a given ij TR pair should follow a Gaussian curve. As we are operating in pitch-catch and not pulse-echo, we may omit the diagonal elements, because they have no physical meaning (sending and

Fig. 20 Correlation coefficient histogram for one TR pair and 10 acquisition levels, with outliers



receiving with the same element at the same time). A typical histogram for one TR pair is shown in Fig. 20.

Using the histogram and data from the correlation matrix, we can calculate the mean value μ_{ij}^B and the variance σ_{ij}^B . After removal of the apparent outliers using the $2\sigma_{ij}^B$ criteria, we recalculate the mean value. If we repeat the same procedure for all of the TR pairs (ij indices), we obtain a matrix of the mean values for the baseline. From this matrix, we select the minimum as the worst-case scenario $\mu^B = \min_{i,j=1\dots N} (\mu_{ij}^B)$. Likewise, we repeat the entire procedure for the “current” dataset and obtain the $\mu^C = \min_{i,j=1\dots N} (\mu_{ij}^C)$.

To proceed further, we again assume the worst-case scenario and take the minimum of μ^B and μ^C , which we define as μ , i.e., $\mu = \min(\mu^B, \mu^C)$. The final threshold TSDC to be used for the signal difference coefficient thresholding is then calculated as $TSDC = 1 - \mu$.

The SDC values are then thresholded using the following formula:

$$W_{ij} = \begin{cases} SDC_{ij} & \text{if } SDC_{ij} > TSDC \\ 0 & \text{if } SDC_{ij} \leq TSDC \end{cases} \quad i, j = 1 \dots N$$

where $SDC_{ij} = RMSD_{ij}$ or $SDC_{ij} = 1 - CC_{ij}$ as defined earlier in Sect. 4. The W_{ij} values then serve as weighting coefficients for RAPID reconstruction algorithm to be used in the calculation of the pixel intensity of the probability of damage distribution.

The procedure with and without thresholding was applied to the data recorded on a flat composite plate measuring 400 by 400 mm. Thirteen ($=N$) transducers were attached to the plate, and before and after impact, 10 ($=M$) independent measurement sets were recorded containing the signals between each TR pair. The location of the transducers and the impact location are shown in Fig. 21a. The results of the

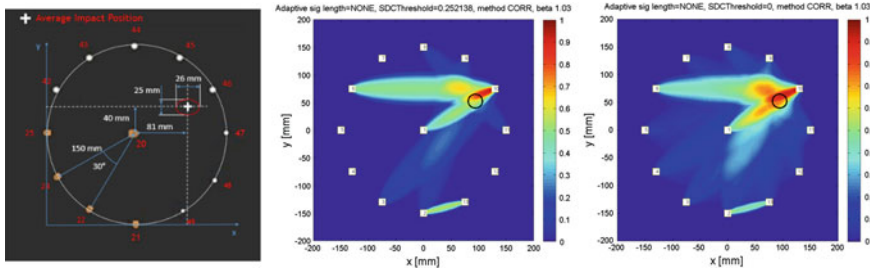


Fig. 21 *Left* Setup of the tomographic sparse array; *Middle* RAPID reconstruction algorithm using the thresholding method; *Right* RAPID reconstruction algorithm without the thresholding method

RAPID reconstruction algorithm with and without thresholding, based on measurement set with $k = 1$, are shown in Fig. 21b, c.

Repeating the analysis for measurement sets 2–6 provided very similar results. However, the same analysis on measurement sets 7, 8, 9 and 10 revealed that a particular error had occurred in the acquisition of signals between the sensor 42 and 45. By excluding this path, the reconstruction of the impact location could be reestablished in an unambiguous manner, as shown in Fig. 22.

Also for the WSM method considered by UNIBO, a threshold assessment can be proposed. In this case, experimental data on the so-called ramp panel manufactured by Bombardier are considered. To determine the threshold statistics, the group velocity for the frequency of interest at several directions of propagation must be evaluated on the pristine panel.

A Hanning window amplitude modulated, 4.5 cycle sinusoidal burst with a central frequency of 60 kHz was produced by a waveform generator and amplified by a high-voltage amplifier before being transmitted over the ramp panel. All the

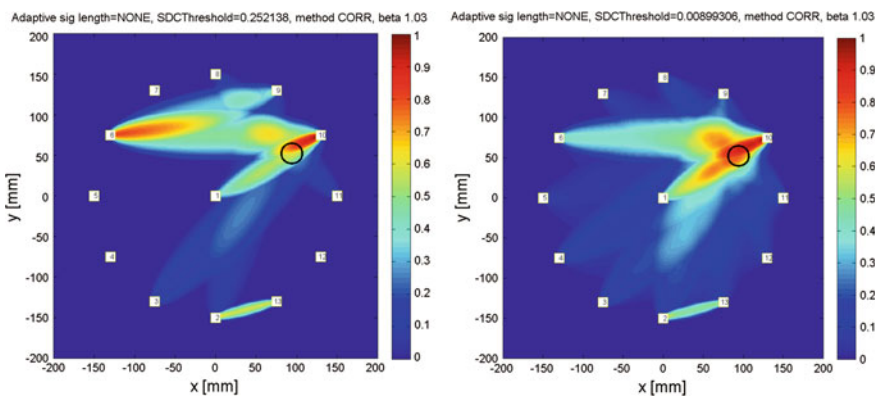


Fig. 22 *Left* RAPID reconstruction algorithm using the thresholding method on dataset 7 including the information in the faulty path; *Right* RAPID reconstruction algorithm using the thresholding method on dataset 7 excluding the information in the faulty path

possible transmission/receive paths are acquired by and recorded for further processing.

The follow-up signal processing comprises the following phases: (i) FFT-based band-pass filtering in the range (30–120 kHz), (ii) signal normalization in the range (-1, +1), (iii) transmitted to received signal cross-correlation envelope detection by taking the absolute value of the Hilbert transform, and (iv) correlation peak location by using a second-order local interpolation scheme. The peak position obtained in this way is used to estimate the group velocity, which is calculated as the product of the distance and the sampling frequency, dividing by the peak position.

The results, shown in Fig. 23b, highlight that the propagation at 60 kHz is weakly anisotropic. The mean group velocity on the 6-mm panel results in 1486 m/s, and this mean value will be considered in the WSM defect detection scheme.

In Fig. 24, the threshold definition procedure for the WSM by UNIBO is schematically depicted. The method is applied when baseline signals are available and consists in the following steps:

- (1a) compute the wave scattering images with the delay-and-sum algorithm described in Sect. 3 several times with all the baseline signals available;
- (2a) define a spatial-dependent threshold by selecting pixel by pixel the maximum value among the baseline images computed in step (1).

Once the spatial-dependent threshold is computed, it is stored and reused for the damage index computation which consists in two steps as well:

- (1b) computation of the wave scattering image with the delay-and-sum algorithm described in Sect. 3;

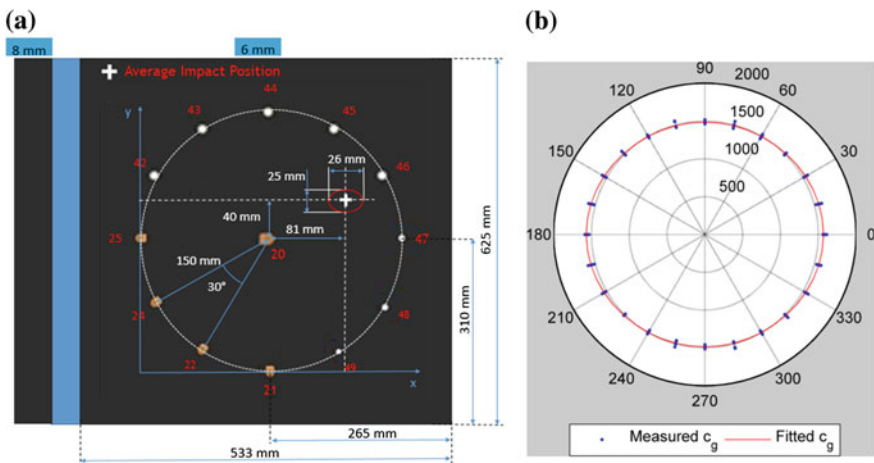
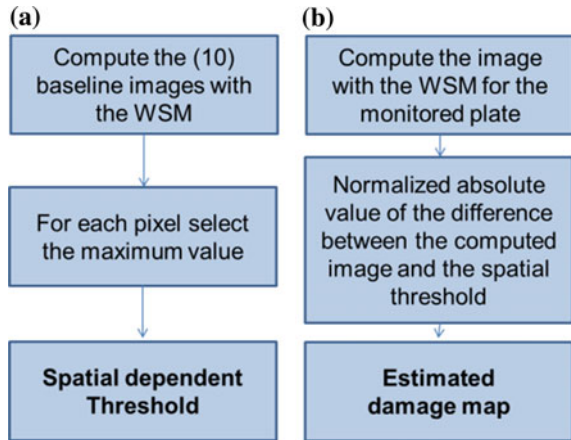


Fig. 23 **a** SARISTU ramp panel layout with sensor and impact location on the 6 mm thickness part, **b** group velocity experimental estimation at different angles for the 6-mm-thick ramp panel

Fig. 24 Thresholding procedure (a), Damage index map computation (b)



(2b) compute the difference between the image computed in step (1b) and the spatial-dependent threshold and divide this quantity by the spatial-dependent threshold.

It is worth noting that the baseline subtraction adopted in this algorithm is performed directly on the beamformed images rather than on the raw signals. The outcome of the above-described procedure is a damage index map which can be used both for defect detection and for localization. In Fig. 25, the result of the application of the procedure to the Bombardier ramp panel is shown for different sensor combinations.

It is worth noting that a reduction of artifacts and a better localization of the defect position can be achieved by increasing the number of sensors, but a satisfactory performance in terms of damage detection can be achieved also with a very limited number of sensors (just 3).

As stated in the description of the UNINA damage index formulation presented in paragraph IV, the value of the damage index (DI) could vanish if there is no change in the structure and its value could increase with the severity and proximity of damage to the sensor locations. However, using real experimental collected data, containing noise, it is not always like this. The experimental noise producing this effect can be statistically evaluated from the definition of a damage sensitivity (DS), which takes its foundation in the DI formulation considering small modifications of the baseline signals rather than the current signals:

$$DS = \frac{|B.S._i - B.S._j|}{B.S._k}, \quad i, j, k = 1, 2, \dots, n$$

The value of the damage sensitivity (DS) can be easily calculated by carrying out several measurements in the same representative condition. Starting from the hypothesis that all B.S. registered at a sensor location could be equal to each other, the subscript k can be either equal to i or equal to j , but also different from both.

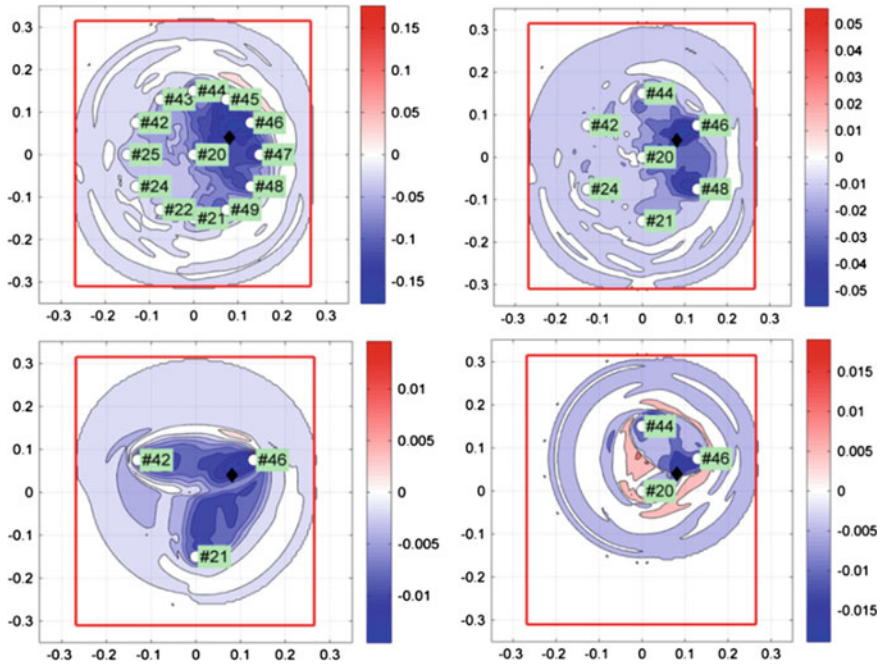


Fig. 25 WSM damage detection on the ramp panel considering 13 (*top-left*), 7 (*top-right*), 3 (*bottom-left*), and 3 (*bottom-right*) transducers

Repeating the procedure considering n baseline signals, one or more statistical DS populations could be obtained for a defined direction path. The collected data represent the experimental noise level, referred to a defined propagation path. From n signals, $n \cdot (n - 1)$ DS values are obtained with two different statistical considerations. The main assumption which is imposed is $k = i$ in the above equation for the damage sensitivity, in order to avoid altering the concept of the damage index itself. Considering all the collected data, a unique statistical population is obtained (Approach AI). Referring to the same k value for a single DS population, n DS statistical populations are given (Approach AII). The algorithms considered to obtain the samples and to discern the statistical populations for a define propagation path A–B is shown in Fig. 26. Differences among two approaches are easy to understand. In the first case, all the possible combinations are collected in a statistical population, consisting of $n \cdot (n - 1)$ samples. With the second approach, n different populations are discerned through fixing a reference signal; subscript i is fixed for each statistical population. In both cases, collected data are statistically processed as described next in order to evaluate the system detection threshold.

As stated earlier when discussing Fig. 19, the analysis of noise and signal distributions appears to be necessary in order to optimize damage detection and its reliability. In this work, only noise distribution is considered, proposing a fast method to define the threshold, but more experimental analysis is required to

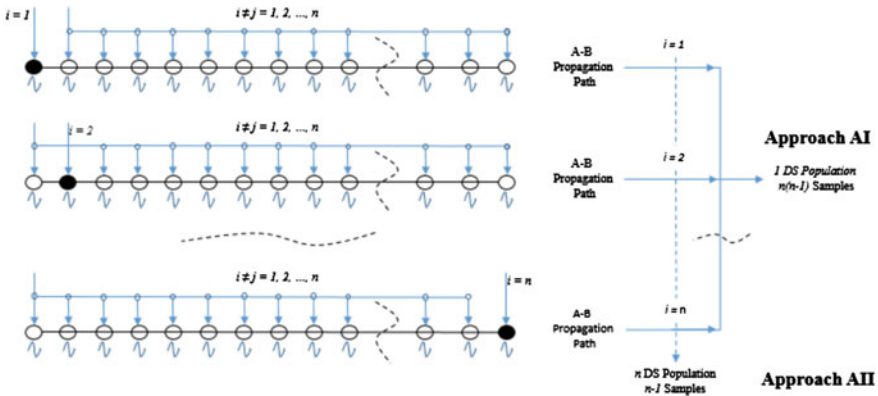


Fig. 26 Proposed procedures for evaluating experimental noise populations

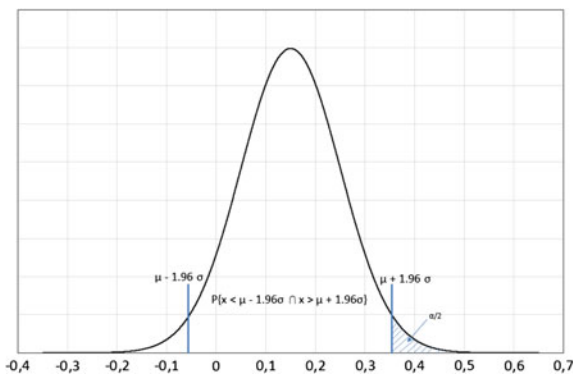
optimize the methodology. The Gaussian distribution is the most accepted hypothesis on measurements noise. However, when mathematical computations or data analysis is carried out after testing, it is not obvious. Generically speaking, this hypothesis is very sharp and it must be demonstrated via a rigorous statistical test. Then, if proven, it allows exploiting the power of parametric statistics. Parametric statistics assumes that the collected data have come from a type of probability distribution and make inferences about the parameters of the distribution. The hypothesis of Gaussian distribution of experimental noise allows to take advantage from its known probability properties. An upper confidence level can be developed in order to obtain the system threshold, based on the probability to find noise samples within the confidence bounds. The advantage of normal distribution results in the a priori known confidence bounds related to a specific probability, the “confidence level.” But first, the statistical population has to be characterized. The Kolmogorov–Smirnov (K–S) test is used to define the characteristics of statistical populations. As for every statistical hypothesis test, this test is used to establish whether certain outcomes of the experimental measurements would lead to a rejection of the null hypothesis. Using the K–S test, the null hypothesis consists in the absence of a Gaussian distribution for the collected data considered.

The set of all outcomes which cause the null hypothesis to be rejected in favor of the alternative hypothesis justifies Gaussian assumption. Starting from the above-mentioned procedure, for each propagation path, one or more populations are obtained. For each of those, the mean value and the standard deviation can be estimated, whether the K–S test showed its Gaussian distribution. We demonstrated that the collected data belong to Gaussian populations only using AII algorithm.

The estimations are carried out through the classical inferential statistics:

$$\mu = \bar{x} = \frac{1}{n} \sum_{i=1}^n x_i$$

Fig. 27 Statistical envelope of experimental noise under assumption of Gaussian distribution



$$\sigma^2 = s_{n-1}^2 = \frac{\sum_{i=1}^n (x_i - \bar{x})^2}{n - 1}$$

The “corrected” estimator s_{n-1}^2 is preferred to s_n^2 because it appears to have no statistical distortion; the smaller the number of samples, the better this preference. In fact, its expected value is the variance itself:

$$E\langle s_{n-1}^2 \rangle = \sigma^2(X) \neq E\langle s_n^2 \rangle$$

X is the population consisting of n samples x_i . From the definition of a confidence level, a threshold value can be easily found from the upper confidence bounds:

$$I_{th} = \mu + k \cdot \sigma$$

The k factor defines the confidence bounds, and it depends on the significance level chosen, as shown in Table 2.

With the probability of $(1 - \alpha)$, every sample x_i in the range is defined by the confidence bounds:

$$P((x_i \in X \geq \mu - k \cdot \sigma) \cap (x_i \in X \leq \mu + k \cdot \sigma)) = 1 - \alpha$$

Because the interest is in the upper confidence region (see Fig. 27), the confidence bounds can be simply expressed as:

$$P(x_i \in X \leq \mu + k \cdot \sigma) = 1 - \alpha/2$$

From these assumptions, the noise is included within the threshold I_{th} , as defined above, with the probability $(1 - \alpha/2)$.

Table 2 Significance level and confidence bounds of standardized Gaussian functions

Significance “ α ”	0.10	0.05	0.01
Factor “ k ”	1.65	1.96	2.58

Coming to the experimental procedure, as already stated, the methodology exploited for damage detection is based on a multiple propagation path approach. The acquisitions have been acquired on the same test article described in paragraph IV (varying thicknesses panel). Step by step, each sensor is actuated and the signal at each other PZT location is registered by using the classic pitch-catch method. Using N sensors, the baseline signals corresponding to $N*(N - 1)$ actuator and sensor paths are recorded at a known intact condition of the plate. Concurrent measurements are carried out for the statistical approach proposed, and then, measurements are repeated after impact. After processing of the collected data, all the paths that show a damage index that overcomes the defined threshold are considered to be used in the localization of the damage zone. Obviously, it is expected that most of the paths that cross the damaged area will be sensible to the stiffness variation and will show a different vibration response. For this reason, a damage index formulation based on the signal intensity in time domain is computed for each actuator and receiver path. Thus, the terms in the DI formulation can be replaced by the square signal amplitudes $\Phi_B(t)$ and $\Phi_C(t)$, respectively, evaluated for the baseline and the current configuration:

$$\text{B.S.} = \int_t \Phi_B(t) dt$$

$$\text{C.S.} = \int_t \Phi_C(t) dt$$

First, the baseline signals corresponding to 156 different actuator and sensor paths are recorded at a known intact condition of the plate. The measurements are repeated ten times with the same methodology in order to characterize the collected populations with the Approach AII. For each path, ten thresholds are now obtained computing a 0.5 % significance level ($\alpha = 0.01$). The maximum of these ten thresholds is considered as the path detection threshold. Thus, for every bay, 156 threshold values are obtained, one for each path. Next, the maximum of these 156 threshold values are considered as the reference threshold of the single system. In Table 3, the detection thresholds obtained are reported for the tree bays with different thickness.

Drawing only the propagation paths whose DI exceeded the evaluated threshold in each bay, Fig. 28 visualizes the selected damage paths that result from the above analysis.

Table 3 Detection thresholds of the bays. Statistical approach AII with significance $\alpha = 0.5$ %

Bay thickness “ t ” (mm)	6	8	10
Bay threshold “ I_{th} ”	0.39	0.45	0.22

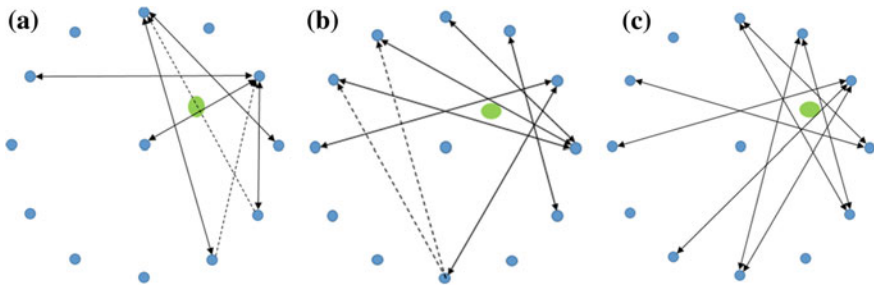


Fig. 28 Damaged paths. Results of 10 mm thickness section (a), 8 mm thickness section (b), and 6 mm thickness section (c). Threshold significance level $\alpha = 0.01$

6 Methodologies' Critical Comparison and Perspective for Their Integration Within the IS12 Experimental Platform

WSMs and TMs have their peculiarities, pros and cons, different degrees of reliability, and suitability for the upscaling on the IS12 wing box demonstrator. Some of the most significant observations from the laboratory implementation of WSM and TM can be summarized as follows.

WSMs rely on the ToF of the defect scattered waves. It is well known that the extraction of ToF data and its conversion to the distance of propagation for dispersive and multimodal signals are not an easy task, especially in such cases where the dispersive guided wave speed of propagation and attenuation for distance travelled are mode and propagation direction dependent. Such complexities can be alleviated by:

- considering non-dispersive or low dispersive modes;
- using short and narrowband pulses to actuate guided waves;
- limiting the number of actuated modes;
- exploiting baseline signals to remove the direct path components within the signals to be processed;
- exploiting structural geometrical data and transducers positions to remove the wave reflections originating from the structural component boundaries (edges, manholes, etc.); and
- exploiting guided modes and frequencies with characteristics that do not depend on the direction of wave propagation.

If the above suggestions are properly applied, the performance of WSMs is basically related to the maximum distance that can be travelled by a wave actuated by a certain transducer, scattered by the defect, and detected by a given receiver. This distance is generally affected by:

- the scattering of the defect (coherent, incoherent);
- the presence of structural reflectors (stiffeners, manholes, rivets, etc.);
- the mechanical attenuation of the guided waves; and
- the receiver electronics in terms of minimum detectable signal above the noise level.

To properly operate TMs, the area to be monitored must be properly covered by the sparse transducer array tracing approach (actuator–sensor straight link), and for all the considered actuator–receiver paths, the wave actuated should be detectable by the receiver (i.e., should have the proper energy) in the case of undamaged specimens. The technique is, in fact, incapable of detecting damages that lie outside the transducers convex hull. The limiting factor of these approaches is related to the baseline robustness versus changes in operative and environmental conditions, such as loads, fatigue, humidity, and temperature. Thus, the baseline should be acquired under many different conditions in order to properly support the defect detection/localization methodology in all prospected working conditions.

The table below summarizes the main advantages and disadvantages of the two imaging techniques.

	WSMs	TMs
Pros	• The possibility to map a defect using a limited number of sensors per given area to be monitored	• Velocity independent method
	• The imaging approach performs in nearly real time	• The method works even for a target material which is a composite plate and for which the dispersion curve (velocity vs. frequency) is not identical in different directions • The method is not so much sensitive to the environmental change compared to velocity-based algorithms
Cons	• Weak reflectors might not be detected since the scattered energy might not be sufficient to reach the sensors and be discriminate to other wave arrivals or signal noise	• Incapability of damage identification outside of the sparse sensors network since the image reconstruction is not based on the velocity but accounts on the diffusion of all potential points with probability value obtained from different propagation paths
	• If the imaging methods are used without the baseline, the position of wave reflectors such as stiffeners, manholes, and holes must be defined a priori in input, and a very precise knowledge of the wave group velocity is required	• The sensor network should be dense, since the defect can be more efficiently detected when it is in the line of sight from the actuator to the receiver
	• In general, the procedure is not capable to detect delaminations below stringers	• The ability to size the defect depends on the density of the transducer network

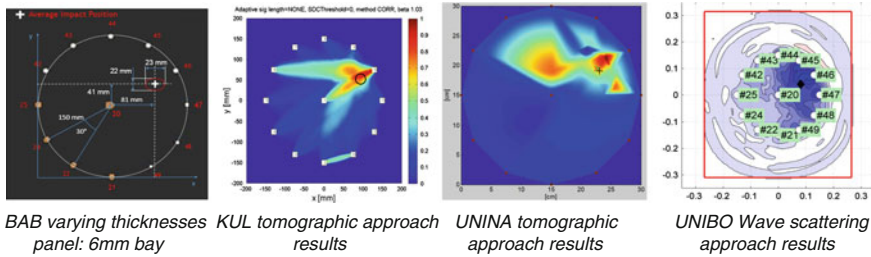


Fig. 29 Comparison of SHM experimental methodologies results on the 6 mm impacted bay of BAB varying thickness panel. Methodologies have been applied to the same acquired signals and «filtered» by the mean of the statistical thresholds approaches

In order to assess the performances of the WSMs and TMs for defect detection purposes, it is important to accurately estimate their individual limiting parameters. Obviously, these parameters play a key role for any methodology designed to define the optimal position of transducers over the structure.

7 Conclusion

The paper presents a summary of the main activities and achievement obtained by the involved SARISTU partners in the development and testing of methodologies aimed at the damage detection and SHM implementation on typical composite wing components.

Three methodologies have been presented, and experimental results for all three methods showed good potentiality for a future implementation of the methodologies into a SHM system based on guided waves.

A peculiarity of the AS05 activity is related to the damage statistical threshold definition which is a crucial point for a reliability assessment of the methodologies in view of POD and PFA evaluation. Only through a rigorous evaluation of elements of the probability matrix of detection, a realistic implementation of SHM into aircraft lifecycle could be envisaged.

As a final conclusion, a convincing image comparing the damage detection of the three developed methodologies is presented in Fig. 29 as an example of their application on the same test data (acquired by UNINA and then analyzed by the three involved partners autonomously). This comparison permits to imagine the potentialities of combining these methodologies for a more precise damage detection.

Acknowledgments The research leading to these results has received funding from the European Union's Seventh Framework Programme for research, technological development, and demonstration under Grant Agreement No 284562.

An Electromechanical Impedance-Based Mobile System for Structural Health Monitoring and Reliability Check of Bonded Piezoelectric Sensors

Mihail Lilov and Thomas Siebel

Abstract In many novel industrial applications, piezoelectric transducers (PZT) are used in sensing or actuating systems. These applications could be, for example, piezo-based structural health monitoring systems for aircrafts or active vibration reducing systems for automotive. Due to the fact that PZT materials are brittle, depolarize at high-temperature exposure or that the bonding layer to host structures for bonded transducers can degrade, monitoring of the reliability of these transducers is crucial to guarantee proper system operation. The electromechanical impedance (EMI) method allows monitoring of structural changes with only a single PZT applied to the surface of a structure. In the data analysis, it is furthermore possible to distinguish whether the host structure, the PZT material itself, or the bonding between PZT material and host structure is affected by damage. Object of this work is the implementation of the electromechanical impedance method on a compact, electronic node. Investigations of the EMI method and verification of the electronic node are conducted on an aerospace conform fiber reinforced plastic structure. Furthermore, the temperature effect on the measurement results is investigated, and methods for temperature effect compensation are applied.

Nomenclature

Y	Electrical admittance
Z	Electrical impedance
w_A, l_A, h_A	Dimensions of the piezo
$\bar{\epsilon}_{33}^T$	Permittivity
d_{31}^2	Piezoelectric charge constant
\bar{Y}_P^E	Young's modulus of piezoelectric transducer
Z_A	Mechanical impedance of piezoelectric transducer

M. Lilov (✉) · T. Siebel
Division Smart Structures, Fraunhofer Institute for Structural Durability and System
Reliability LBF, Bartning street 47, 64289 Darmstadt, Germany
e-mail: mihail.lilov@lbf.fraunhofer.de

T. Siebel
e-mail: thomas.siebel@lbf.fraunhofer.de

Z_S	Mechanical impedance of the host structure
Z_0	Baseline impedance measurement
Z_1	Current impedance measurement
\bar{Z}	Mean of the impedance
σ	Standard deviation
CC	Cross-correlation coefficient
n	Total number of frequency points
$\tilde{\omega}$	Effective frequency shift

1 Introduction

The use of piezoelectric transducers (referred to as: PZT) has found considerable attention throughout research and industry. A promising technique within the field of health monitoring of composite structures is the electromechanical impedance (EMI) method. The EMI method provides a monitoring approach that requires only a single PZT transducer to monitor a local part of a host structure. Bonding a PZT patch to a host structure establishes—due to the electromechanical transduction inside the PZT—a coupling between the mechanical impedance of the host structure and the electrical impedance measured at the PZT terminals [1].

However, beside the functional aspect of the piezo, i.e., sensing or actuating, the reliability of the piezomaterial is of major concern. Piezoelectric material is brittle, and breakage is likely to happen when the structure to be monitored is subjected to external loads which lead to deformation. A breakage affects the mechanical and electrical properties of the PZT and thus distorts the output signal. Further relevant failures influencing the measured output signal are debonding between piezoelectric material and the host structure or a depolarization due to heat exposure.

In order to prevent a monitoring system from misinterpreting the measured results, a procedure is required to separately identify the degradation of the piezoelectric material and damages of the host structure. This is realizable by separately analyzing the complex parts of measured electrical impedances. The mechanical properties of the host structure are mainly reflected in the real part of the measured electrical impedance [1]. The imaginary part of the admittance in turn is foremost sensitive to the geometric, electric and piezoelectric and mechanical properties of the PZT material [2].

A critical point concerning the application of EMI method to practical problems is the obtrusiveness of the required measurement equipment. Recent research activities are concerned with the development of electronic nodes based on EMI for the detection of structure damages on different materials and for different cases. Exemplarily, the realization of wireless SHM nodes based on EMI for monitoring the condition of CFRP laminated concrete structures, using piezoceramic sensors, was performed [3]. Bolt loosening within a metal fitting plug, which connects a

composite aircraft wing to a fuselage under realistic environmental conditions, was also successfully realized with an EMI-based system, especially developed for this purpose [4].

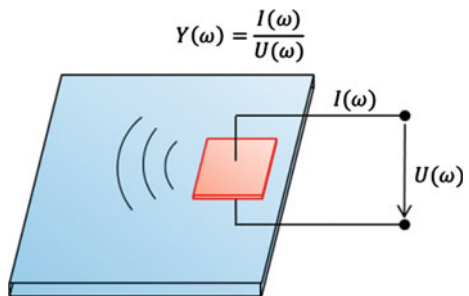
In this paper, the procedure for applying EMI for structural health monitoring and for checking the reliability of a piezoelectric sensor is presented and exemplarily demonstrated. A temperature compensation approach is applied to increase the damage sensitivity. Next, a compact and flexible impedance analyzer, based on centralized and distributed architecture concept, is presented. Due to its small physical dimensions, a full integration into the laminated piezoceramic transducer and in this way the increase of the robustness of the whole SHM system can be achieved [5]. Completely replacing a bulky laboratory impedance analyzer, the introduced compact node can achieve high-precision measurements and therefore realize a basis SHM platform, which can be easily adapted to specific application requirements. In the performed study, a verification of the monitoring node is successfully achieved under laboratory conditions.

2 Procedure for Structural Health Monitoring and Reliability Check of Piezoelectric Sensors

The EMI method requires only a single piezo applied to a host structure as shown in Fig. 1. The piezo excites the host structure to vibration, while simultaneously the electrical impedance—which is the inverse of the admittance—is measured. Due to the electromechanical coupling within the piezo, the mechanical properties of the host structure are reflected in the measured electrical impedance. The electrical admittance measured at a PZT attached to a host structure can be expressed as follows [6]:

$$Y(\omega) = Z(\omega)^{-1} = i\omega \frac{w_A l_A}{h_A} \left(\frac{e_{33}^T}{\epsilon_{33}^T} - d_{31}^2 \bar{Y}_P^E \frac{Z_s(\omega)}{Z_s(\omega) + Z_A(\omega)} \right) \quad (1)$$

Fig. 1 Principle of impedance measurement



where Y is the electrical admittance, Z is the electrical impedance, w_A , l_A , and h_A are the piezo dimensions, $\bar{\epsilon}_{33}^T$ is the permittivity, d_{31}^2 the piezoelectric charge constant, \bar{Y}_P^E and Z_A are the Young's modulus and the mechanical impedance of the piezo, respectively, and Z_S is the mechanical impedance of the host structure.

2.1 EMI for Local Damage Detection

In particular, the real part of the electrical impedance reveals a high sensitivity to modifications of the host structure and is hence appropriate for local damage detection. The cross-correlation coefficient (CC) assesses the difference between a baseline measurement Z_0 and a current measurement Z_1 for each frequency point in the following way:

$$\text{CC} = \frac{1}{n} \sum_{i=1}^n \frac{\{\text{Re}(Z_0(\omega_i)) - \bar{Z}_0\} \{\text{Re}(Z_1(\omega_i)) - \bar{Z}_1\}}{\sigma_{Z_0} \sigma_{Z_1}}, \quad (2)$$

where n is the total number of frequency points, \bar{Z} is the mean, and σ is the standard deviation of the corresponding impedances. In order to reduce temperature effects from the measurement data, a compensation approach is employed which is based on maximizing the CC between a baseline and a current measurement by a frequency shift [8]:

$$\max_{\tilde{\omega}} \text{CC} = \max_{\tilde{\omega}} \left\{ \frac{1}{n} \sum_{i=1}^n \frac{\{\text{Re}(Z_0(\omega_i)) - \bar{Z}_0\} \{\text{Re}(Z_1(\omega_i - \tilde{\omega})) - \bar{Z}_1\}}{\sigma_{Z_0} \sigma_{Z_1}} \right\}, \quad (3)$$

where $\tilde{\omega}$ is the effective frequency shift corresponding to the maximum CC coefficient.

2.2 EMI for Reliability Check of Piezo Materials

The imaginary part of the electrical admittance mainly depends on parameters related to the piezo and its coupling to the host structure and thus allows for piezo self-diagnostics. Analyzing the slope of the electrical admittance yields a measure for the health state of the bonding between host structure and piezo and for the properties of the piezomaterial. As illustrated in Fig. 2, the onset of a debonding would result in an increasing slope. In contrast, a fracture of the piezomaterial would result in a decrease of the slope.

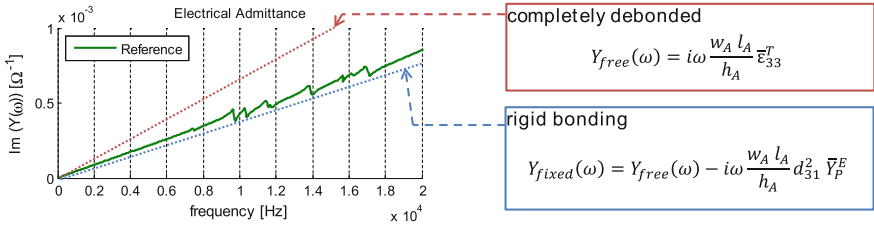


Fig. 2 Illustration of the imaginary electrical admittance slope

3 Experimental Investigation

3.1 Structural Health Monitoring

Experimental investigation for using EMI for structural health monitoring is carried out on an aircraft conform carbon reinforced fiber polymer (CFRP) panel with the dimension 500 mm × 500 mm × 5 mm. The panel is instrumented with PZTs of two different sizes, which are arranged according to Fig. 3. In this paper, only analyses of the bigger sized piezos from PI Ceramic GmbH, type DuraAct™ P-876.A15, referred to as A15, are addressed. These and other results of this investigation can be found in more detail in [7]. The active area of the regarded piezos is 50 mm × 30 mm × 0.5 mm. A number of ten A15 sensors are bonded to the structure by the means of two components glue, type EPOXY red from Hardman. The electrical impedance is measured with a precision impedance analyzer from Wayne Kerr, series 6500B. The measured data are collected on a personal computer (PC) which is connected to the measurement device by GPIB port. The structure is

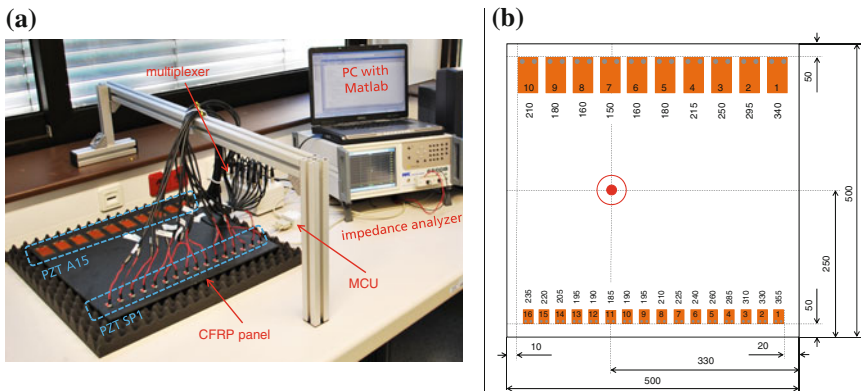


Fig. 3 a Experimental setup, b arrangement of PZTs and location of induced damage, each PZT assigned with number and distance to the damage location

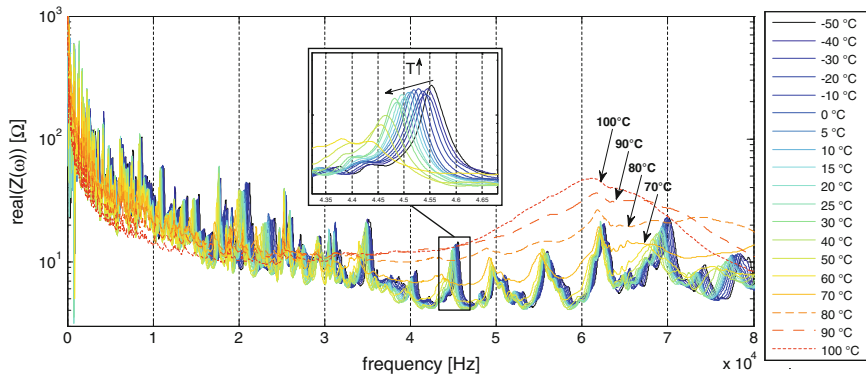


Fig. 4 Impedance spectra measured at PZT 5 (A15) for temperatures between -50 and 100 °C. Begin of softening of the bonding layer at 70 °C. Zoom display for temperatures -50 to 60 °C. Increasing temperature decreases frequencies of spectral peaks

excited by a swept sine with an excitation voltage of 1 V_{rms} in a frequency range up to 80 kHz.

In a first experimental test, the influence of varying temperatures is investigated. For this, the instrumented panel is subjected to temperatures between -50 and 100 °C. The measured impedance spectra for the big PZT on position number 5 (type A15) are exemplarily shown in Fig. 4. The representation illustrates that increasing temperature leads to a left shift of the spectral peaks and beginning from about 70 °C upward the spectra detract from the observable frequency characteristic. It is assumed that the high-temperature-induced spectral characteristic change of the bonded PZT is caused by a softening of the used adhesive.

For the assessment of the damage sensitivity of the EMI method, measurements are conducted in an air-conditioned laboratory room. First, measurements are acquired of the pristine panel at 22 and 16 °C. Next, an impact of 200 J is applied to the panel to induce damage. Measurements of the damaged panel are then conducted at 22 °C. The measurement of the pristine panel at 22 °C is selected as the reference measurement. The CCs between the measurement of the impacted panel and the reference measurement provide information about the damage sensitivity of each PZT. In order to discriminate the damage effect from the temperature effect, the CCs of measurements of the pristine panel at temperatures of 16 and 22 °C are additionally calculated. The results of two analyzed frequency bands are exemplarily illustrated in Fig. 5. From the analyzed frequency band 10 – 20 kHz can be deduced a high sensitivity of each PZT to the induced damage, which is more important than the temperature effect. In contrast, analyzing the 30 – 40 kHz range reveals that for most PZTs the temperature effect is more important than the damage effect, except for PZT 7 which is closest to the damage. Applying the effective frequency shift for temperature compensation reveals that the temperature effect can significantly be reduced which results in an increased damage sensitivity.

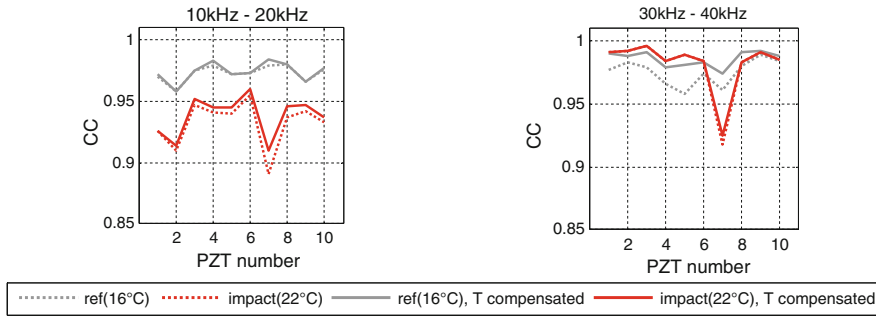


Fig. 5 CCs of measurement performed by the ten PZTs, type A15. CC between reference measurement of pristine panel at 22 °C and impacted panel at 22 °C. Closest PZT to damage is PZT 7. CC between measurements of pristine panel at 22 °C and pristine panel at 16 °C. Original data (*dotted lines*) and temperature compensated data (*solid lines*)

3.2 Reliability Check of Bonded Piezoelectric Sensors

A second experiment is carried out to investigate whether sensor damage and damage to the host structure can be separately detected. Three CFRP specimens of the size 240 mm × 40 mm × 2 mm are centrally equipped with laminated PZT from PI Ceramic GmbH, type DuraAct™ P-876.SP1, each with a piezo active area of the size 10 mm × 10 mm × 0.2 mm. The same measurement equipment is used as previously described. The impact of three types of damage on the EMI is analyzed based on the following test setup and procedure. To simulate breakage, a first measurement is conducted to acquire reference data. Next, the piezo is mechanically cut as shown in Fig. 6a, such that only 75 % of the active area remains before a second measurement is conducted. To simulate debonding, two piezotransducers are applied on opposite sides of the same specimen. One is bonded with 100 % of its area, while the second piezo is applied only along about 75 % of its active area. Measurements of both piezotransducers are compared to each other. To analyze the impact of host structure damage, a measurement is conducted at the pristine structure. Next, a hole is cut into the host structure in the vicinity of the piezo, and a second measurement is conducted.

Figure 6b reveals that for piezo breakage the real impedance spectrum tends to increased; however, the modal peaks of the spectrum remain unchanged. In contrast, the imaginary admittance yields a significant decrease of its slope. For the simulated debonding as shown in Fig. 6c, again there are no significant shifts in the peaks of the real electrical impedance, while the slope of the imaginary admittance changes. The observation is different, when host structure damage is induced, as shown in Fig. 6d. Here, frequency shifts of the real impedance peaks appear, while the slope of the imaginary admittance remains unchanged.

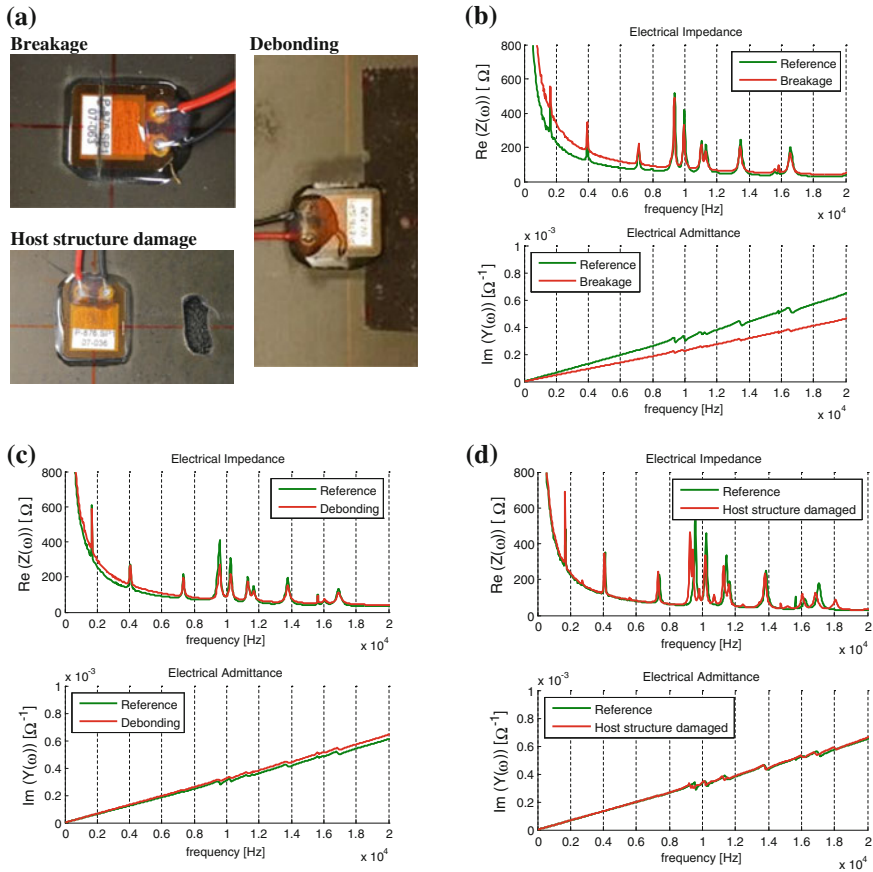


Fig. 6 a *Damage cases* breakage, debonding, host structure damage; EMI spectra for: b piezo breakage c debonding d host structure damage

4 EMILIA

Alongside several investigations based on EMI method and detection of host structure and piezoceramic damages, there is requirement to replace the bulky, standard used, and expensive laboratory impedance analyzer with a compact, lightweight, and much cheaper impedance analyzer, which can be implemented in a networkable SHM system on an airplane. Here, a compact impedance analyzer named EMILIA (Electromechanical Impedance for Local Integrity Assessment) is realized. For the development of the analyzer, low weight and compact design are the two pivotal requirements. The realization of two versions of the EMI node—one for centralized and a second for distributed topology—is taken into account during the node designing.

4.1 Electrical Characteristics

The electric specifications of EMILIA are mainly based on the core component in the node circuit, the impedance converter AD5933 from Analog Devices, and on the voltage regulator which is responsible for providing a stable supply voltage to the node as shown in Table 1.

The compact impedance converter AD5933 is the heart of the developed EMI node. It can precisely measure complex impedances connected to its output and input pins. Integrated on the chip are a frequency generator with 12-bit resolution and direct digital synthesizer, an internal clock, and also a temperature sensor. For each measured frequency, the response of the measured impedance is calculated by an onboard data signal processor, which computes the discrete Fourier transformation. As result, the real and imaginary parts of the measured impedance are sent back via two-wire communication Inter-Integrated-Circuit (I2C) bus to the control unit, e.g., a microcontroller (MCU) or another I2C-compatible device, which drives the AD5933. The settings for the impedance measurements, e.g., measuring point, start frequency, and output excitation range, are submitted to the register of the I2C converter. For a proper function, the AD5933 needs a feedback resistor on the receiving stage of the chip, which sets the gain of the transimpedance amplifier, followed by a programmable gain amplifier (PGA), antialiasing filter, and analog-to-digital converter. It has to be selected cautiously to ensure that the ADC is working in its linear range to achieve high accuracy. For calibration of AD5933, a justification measurement of a calibration resistor with known value is connected to the output and input stage.

4.2 Function Diagram

Figure 7 illustrates the basic function topology parts of EMILIA. The control of the impedance analyzer is realized by a PC and a USB to I2C bridge. This conversion element also delivers the supply raw voltage of 5 V to the node. EMILIA consists of

Table 1 System specifications

Parameter	Min	Max	Units/Note
Supply voltage	3.20	12.00	V
Load current	–	200	mA
Excitation freq.	1	100	kHz
No. of increments	1	511	–
Excitation ampl.	0.19	1.98	V _{p-p}
Imp. meas. range	1 k	10 M	Ω
System accuracy	0.50	–	%
Temp. sensor	–	–	on board
Temp. range	–40	+125	$^{\circ}\text{C}$

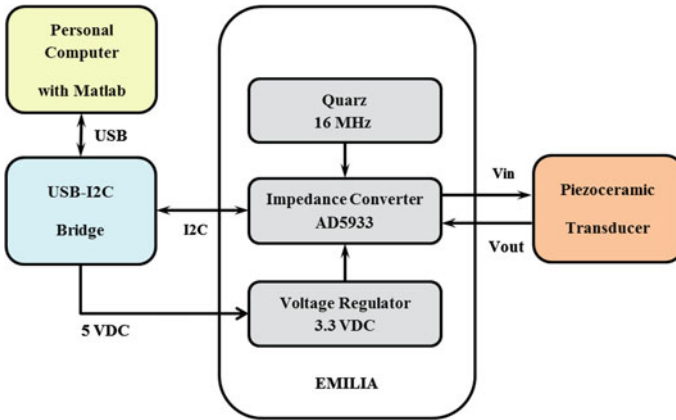


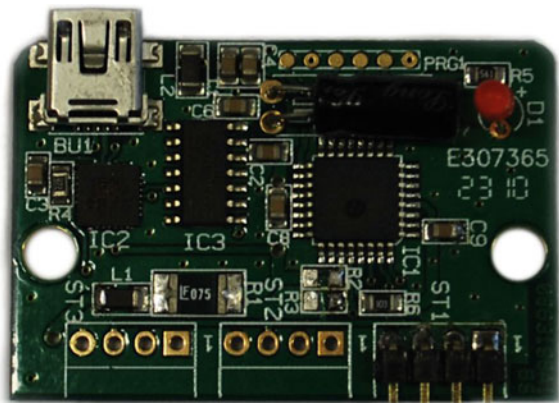
Fig. 7 Function diagram of EMILIA

three main circuits: the clock, impedance converter, and the voltage regulator circuit. Despite the onboard clock generator, for precise measurements under variable temperature, the usage of an external clock is highly recommended. The function of the voltage regulator is to transform higher than the recommended 3.3 V operational voltage for AD5933 and to ensure stable voltage supply required for proper operation.

4.3 Stages of Development

In first step, a central configuration of the EMI node named EMILIA-V01 is developed. Due to the I2C communication interface of the impedance converter, an external USB to I2C bridge from ELV Elektronik AG is used as shown in Fig. 8.

Fig. 8 USB-I2C bridge from ELV



This compact device utilizes CP210x USB to UART Bridge Virtual COM Port (VCP) drivers from Silicon Labs and in this way provides a basic possibility to control the impedance node via COM-port implementation in MATLAB or another programming environment. The bridge disposes three I2C connectors for external devices and can manage up to 128 nodes connected with a bus clock rate from 245 Hz until 400 kHz. The design of EMILIA-V01 is adapted to the dimensions and especially to the fixing of the I2C bridge as shown in Fig. 9. Thus, a mount of EMILIA-V01 to the bridge can be realized by plugging it on the top of the bridge, and in this way, simple housing can be achieved. In this first version, the voltage regulator circuit responsible for the supply of AD5933 with stable 3.3 V is placed on the bottom of a double-sided printed circuit board (PCB). As shown in Fig. 10, on the top of the node, the clock generator circuit and the AD5933 circuit are located. On the left side, connections for the needed feedback resistor are designed, while on the right side, the connections for the piezoceramic transducer or unknown impedance are placed. The size of EMILIA-V01 is 45×20 mm with weight of 2.8 g. Embedded into the housing of the USB-I2C as shown in Fig. 10, the developed EMI node acts as a compact and central impedance analyzer which offers

Fig. 9 Design of EMILIA-V01

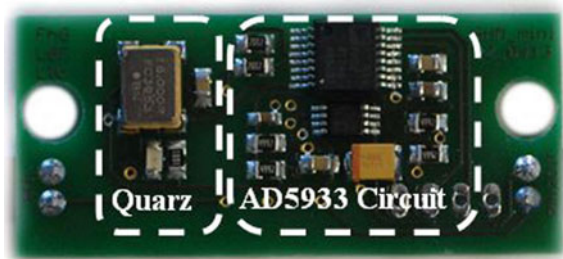
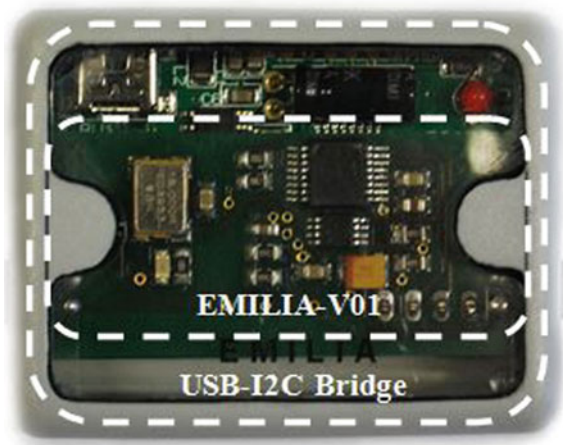


Fig. 10 Housed EMILIA-V01 with USB-I2C



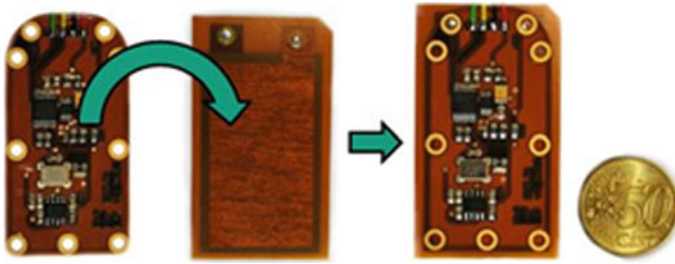


Fig. 11 Applied EMILIA-V02 on DuraAct™ SP-876.A13

connection to multiple piezos consecutively. The control of EMILIA-V01 is realized in MATLAB. In the next development stage, the impedance analyzer is realized by a flexible PCB named EMILIA-V02, which is designed and optimized for application on a piezoceramic module from PI Ceramic GmbH, series DuraAct™, type SP-876.A13. This configuration allows for a distributed solution for structural health or piezo monitoring purposes as shown in Fig. 11. Due to the flexibility, given by this concept, no influences on the piezoceramic module from the EMI node exist. An advantage of this concept is that the temperature at the piezo can be measured by AD5933 directly and be used for temperature compensation issues of the temperature-dependent piezo behavior. The concept of EMILIA-V02 provides positioning of all needed circuits on the top of the board. The size of the system is 58.5×30 mm with a weight of 1.5 g. The bottom of the PCB is kept free for later implementation purposes. At this realization status, short distance networks due to the used I2C-communication can be performed.

In the preparation of the system validation, impedance measurements with the system are realized and lead to following conclusions: (a) The calibration resistor needed for the initial calibration of the system should have the same value like the feedback resistor; (b) the calibration resistor should have the arithmetical average value of expected impedance; (c) the smaller the measurement resolution is, the higher is the system accuracy; (d) the usage of precise resistors as calibration and feedback resistor increases also the accuracy of the system especially at high frequencies.

4.4 *EMILIA Verification*

For the accuracy system verification, a comparison between measurements conducted with a laboratory precision impedance analyzer, Wayne Kerr 6500B, and the developed EMI node is performed as shown in Fig. 12. Here, the measurements with both systems are performed at identical environmental conditions and on the same CFRP-panel. The measurements are performed with an excitation voltage of 1 V_{p-p} due to the limitation of the laboratory impedance analyzer excitation

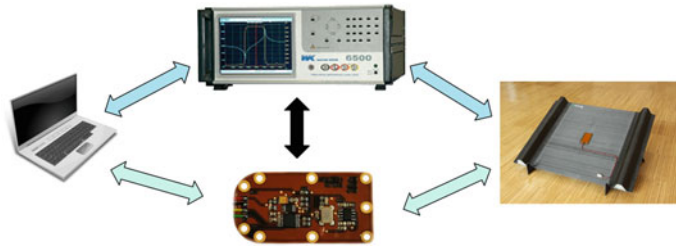
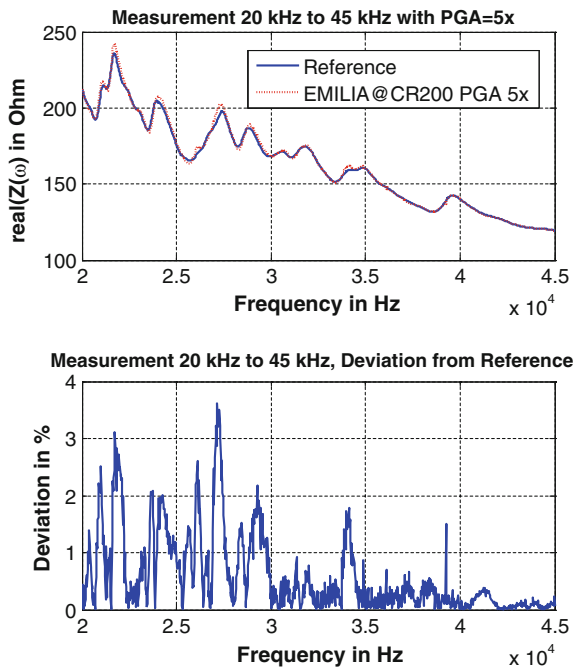


Fig. 12 Laboratory impedance analyzer versus EMILIA

Fig. 13 EMI data comparison

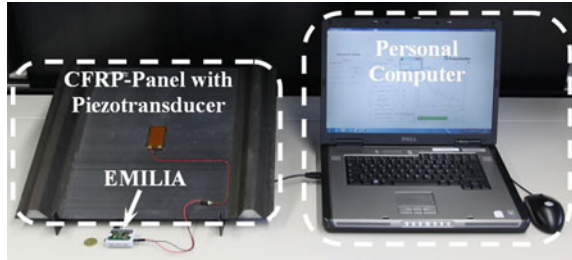


voltage. Figure 13 shows the EMI data comparison measured with the laboratory impedance analyzer (continuous line) versus EMILIA (dotted line) in the frequency range 20–45 kHz. The average deviation between the measurements is less 2 % in the investigated frequency range.

4.5 Detection of Structural Modifications

After investigation of the developed system and factors responsible for the precise function, measurements on an airplane conform structure under laboratory

Fig. 14 Test setup with EMILIA-V01

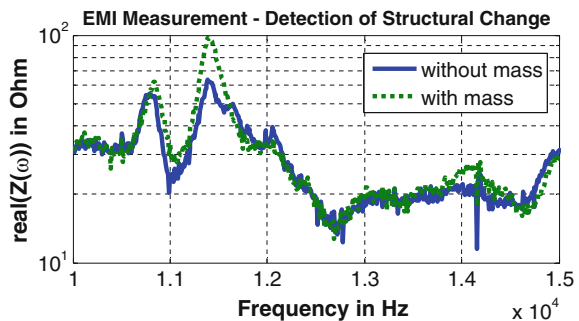


environment are carried out. Here, all investigations are realized with the first, centralized version of the node EMILIA-V01. For system verification, a setup consisting of control (PC), CFRP-panel with applied piezoceramic transducer, and EMILIA is conducted as shown in Fig. 14. The used CFRP-specimen has a size of 500 mm × 400 mm with a thickness of 2 mm and is manufactured of unidirectional prepreg material. Two stringers are bonded on the surface. The measurement performed to detect a structural change, here adding of 27.4 g heavy mass 20 mm distant from the piezo, was conducted in MATLAB on the control PC as shown in Fig. 14. First, the entire measurement frequency range between 1 and 100 kHz is measured. After data analysis, the most sensitive frequency band for the induced structure change detection is selected and a new set of measurements with higher frequency resolution within this frequency range are performed.

4.6 Experimental Results

The measured impedance analysis for the setup is illustrated in Fig. 14. The most dynamic frequency band is between 10 and 15 kHz for the realized setup configuration, and the raw data streams for the structure status without (continuous line) and with added mass (dotted line) are shown in Fig. 15. Obviously, characteristic and amplitude changes of the resonance peak at 11.4 kHz are observed after modifying the structural mass. The same observation exists for the resonance peak at 10.8 kHz and for the run of curve at 14 kHz.

Fig. 15 Detection of mass-adding



5 Conclusion

In this paper, first method for EMI-based structural health monitoring and reliability checks of PZT is introduced and experimentally investigated. It is demonstrated that the PZT breakage and debonding can be detected separately from damage of the host structure. Further, the development of a compact impedance analyzer node is presented. Two versions of the node are implemented: One version is appropriate for realization of a local impedance analyzer (EMILIA-V01) and second version (EMILIA-V02) for the integration on the surface of a piezoceramic module (PI DuraAct™ SP-876.A13). Both designs offer different advantages of an EMI system for realization of a monitoring system dependent of specific application requirements.

Successful detection of a mass modification on a CFRP structure is realized by the means of the developed EMI node. The comparison of measurements conducted with a laboratory precision impedance analyzer and EMILIA is carried out. This investigation reveals that the developed node offers precise measurements of a complex unknown impedance. The presented compact impedance analyzer can be used for structural health monitoring and also for piezo health monitoring purposes.

Acknowledgments The research leading to these results has received funding from the European Union's Seventh Framework Programme for research, technological development, and demonstration under Grant Agreement No 284562.

References

1. Giurgiutiu V (2008) Structural health monitoring with piezoelectric wafer active sensors. Elsevier Academic Press, Waltham
2. Park G, Farrar CR, di Scalea FL, Coccia S (2006) Performance assessment and validation of piezoelectric active-sensors in structural health monitoring. *Smart Mater Struct* 15(6):1673
3. Park S, Kim JW, Lee C, Park SK (2011) Impedance-based wireless debonding condition monitoring of CFRP laminated concrete structures. *NDT&E Int* 144:232–238
4. Lim HJ, Kim MK, Sohn H, Park CY (2011) Impedance based damage detection under varying temperature and loading conditions, *NDT&E Int* 44:740–750
5. Lilov M, Siebel T (2014) EMILIA—a compact impedance analyzer for local integrity assessment. In: IX international conference on structural dynamics (EURODYN 2014), Porto, Portugal
6. Liang C, Sun FP, Rogers CA (1994) Coupled electro-mechanical analysis of adaptive material systems—determination of the actuator power consumption and system energy transfer. *J Intell Mater Syst Struct* 5(1):12–20
7. Siebel T, Lilov M (2013) Experimental investigation on improving electromechanical impedance based damage detection by temperature compensation. *Key Eng Mater* 569–570:1132–1139
8. Koo KY, Park S, Lee JJ, Yun CB (2008) Automated impedance-based structural health monitoring incorporating effective frequency shift for compensating temperature effects. *J Intel Mater Syst Struct*

PAMELA SHM System Implementation on Composite Wing Panels

Angel Alcaide, Federico Martin, Eduardo Barrera and Mariano Ruiz

Abstract Aernnova developed a methodology for structural health monitoring (SHM) by use of multiple ultrasonic wave-based PAMELA SHM™ system wirelessly controlled. The possibility to perform automated NDT tests with no human presence required enables a large number of inspections and total test time reduction. The capability of this system to detect and characterize the effects on ultrasonic wave responses of several types of damages on different materials as metallic or composite structures is utmost importance for efficient and reliable SHM during structure life cycle. A study of this capability, tools descriptions, and damage detection results are presented in the paper, with the recommendations for future actions, aimed to make easier interpretation and identification of these structural damages. Several different damage detection methodologies and algorithms will be addressed attending to describe the advantages and particularities of each applied to both materials metallic and composites.

A. Alcaide (✉) · F. Martin
Structural Integrity Department, Aernnova Engineering Division,
Av. Manoteras, 20 B-5ª, 28050 Madrid, Spain
e-mail: angel.alcaide@aernnova.com

F. Martin
e-mail: federico.martindelaescalera@aernnova.com

E. Barrera · M. Ruiz
Instrumentation and Applied Acoustic Research Group,
Technical University of Madrid (UPM), Crta. Valencia Km. 7,
28031 Madrid, Spain
e-mail: eduardo.barrera@upm.es

M. Ruiz
e-mail: mariano.ruiz@upm.es

1 Introduction

Timely damage diagnosis and characterization in structures before failure is vitally important in the aeronautical sector, where the structural integrity must be constantly ensured. All structural components of a commercial aircraft are inspected at regular intervals using different evaluation techniques that are expensive, complicated, and costly. Currently, the service intervals are obtained statistically by taking into account the probability of failure. These methods are called predictive maintenance since repairs and overhauls are preprogrammed.

If continuous structure monitoring tools were available, predictive methods could be changed to the methods based on the assessment of real condition of the structure and the revisions could be made when and where they are necessary. Continuous monitoring of the location of the damage and the level of its severity enables implementing this strategy, which would save both direct maintenance costs and time spent on each revision. Moreover, the criteria used to minimize the weight of aircraft result in an increased use of composite materials. However, these materials have anisotropic mechanical properties, which seriously complicate the inspection process.

Many flaw types, such as, barely visible delaminations, detachment between layers, fiber breakage, or porosity may result in a serious loss of strength. All these defects could be monitored with structural health monitoring (SHM) techniques and systems, which would additionally permit for increasing the use of composite materials and using all their advantages. One of the main advantages would be significant savings in fuel and the corresponding decrease in CO₂ and NO_x emissions.

Structural testing of aircraft elements is generally a complex, costly, and time-consuming process. Typical primary components fatigue tests of aircraft structures usually last between one and two years. In addition, this process must be interrupted periodically to check the structure integrity, usually using nondestructive methods that increase more and more the total duration of the process. Therefore, the development of systems that simplify and reduce the currently used techniques and the cost of them has to be considered.

2 SHM System Description

The PAMELA SHM™ system [1, 2] (developed by Aernnova) provides a solution to automated structural integrity inspection by means of SHM technique employing ultrasound. This project has received funding from the European Union's Seventh Framework Program for research, technological development, and demonstration under Grant Agreement No. 284562.

The PAMELA SHM™ system consists of a number of portable autonomous units that communicate with each other and can be easily managed by one person.

With a multiple PAMELA SHM™ system units, it is possible to monitor continuously in an automated mode any aircraft structure during fatigue test processes, configuring each PAMELA III device to perform different test sequences at different instants of time. Besides the capability to monitor in an automated way, the current system offers the possibility of embedding a variety of algorithms for automatic control of signals and sensors that can be run onboard in real time. Those embedded algorithms enable autonomous scanning at concerned areas and recording the component functionality in a buffer storage that can be interfaced by a standard computer provided with a commercial operating system.

An ultrasonic wave-based SHM system consists of many piezoelectric transducers, one or more circuits to generate the actuator excitation signals, one or more circuits that acquire the ultrasonic signals from the transducers, and a processing system. In the system presented in this paper, these components (generation, acquisition, and processing) have been developed and integrated into the same electronic instrumentation. PAMELA III can generate any type of excitation signal for up to 12 piezoelectric transducers. Concurrently, it can acquire the response signals that propagate throughout the structure being tested and also perform the signal processing for damage detection in situ.

The processor module configures and controls the remaining modules in PAMELA III and performs the signal processing required for each analysis algorithm. This module is based on an embedded PowerPC processor, which is inside a Virtex 5 field programmable gate array (FPGA) device from Xilinx Inc.

The excitation module generates the excitation signals for each of the 12 output channels. The shape of the excitation signals is digitally synthesized for any desired signal inside the FPGA. An analog circuit converts the signals into analog voltages up to 40 V peak to peak. This module allows each channel to be excited independently of each other.

The electronic system is designed, manufactured, tested, and enclosed in a composite box. The fully assembled system is shown in Fig. 1. The printed circuit board has 12 layers and over 800 components when fully assembled. The overall dimensions are $161 \times 161 \times 24$ mm. PAMELA III weighs 283 g (box included). PAMELA III has been designed to carefully avoid any working issues. All of the chosen components and assembly process have been selected to be lead free and obey RoSH regulations. There is a patent pending on the system.

The other key component required for the SHM instrumentation is the piezoelectric transducer. This critical component is responsible for converting the electrical signals into ultrasonic waves. Piezoelectric transducers are also reversible and can convert ultrasonic waves from/into electrical signals. There are many types of piezoelectric transducers in many sizes that can be dispersed in a structure in many ways. They can be used with both metallic and composite materials (Fig. 2).

PAMELA III connects to the array of 12 piezoelectric disks mounted on the integrated PhA III transducer. The transducer is bonded to the structure using an appropriate epoxy adhesive. PAMELA III is then installed on a structure connecting the hardware to the transducer adapter and attaching the hardware without any



Fig. 1 The PAMELA III with all electronic components inside the composite box placed over the PhA transducer adapter and bonded to the structure to perform SHM testing

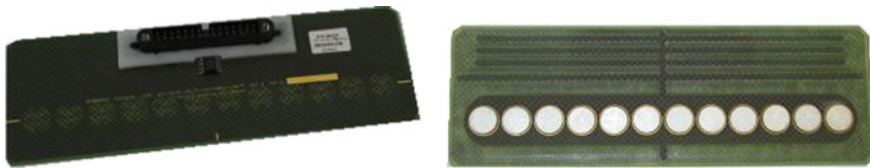


Fig. 2 Integrated PhA transducer showing underside and overhead views (*left*) and two different types of piezoelectric transducer sets: disk and rings (*right*)

cables. The hardware is electromechanically coupled to and supported by the transducer without requiring additional fixtures on the structure.

The actual system has a major advantage over other systems in the development today, consisting in the capability of excitate and acquire at all sensors simultaneously. This fact gives the system a huge power and development capacity on new NDT techniques.

The diverse number of SHM analysis techniques allows for the detection of many different types of defects. In metallic structures, it is possible to detect fatigue crack development, corrosion, joint debonding, stress corrosion cracking, or impact damage. In composite structures, it is possible to detect impact damage, delaminations (including growth), and bonding and debonding.

There are many techniques used for damage detection; PAMELA III can implement most of these damage detection techniques in any structure that has piezoelectric transducers. The flexibility and capacities of the FPGA, which constitutes the core of the electronic device, allow the system to adapt itself to different working modes and to perform several tasks in parallel.

The system is able to control multiple PAMELA III devices simultaneously. In addition, for each device, the operator can configure not only a single test type, but a sequence of several tests to be performed sequentially.

This way, the external computer manages the operation of all PAMELA III devices within the system and retrieves the temporal waveforms acquired by each device for every test performed. Thereby, different inspection sectors of an aeronautical component can be monitored simultaneously with identical PAMELA III devices, configured with different tests sequence lists. So, several PAMELA III devices can be running simultaneously checking continuously the structure integrity without human intervention.

However, in many occasions it is not necessary to transmit all the temporal acquired data from PAMELA III devices to the external computer, since PAMELA III devices offer local processing capabilities. In these cases, only the outputs of the processing algorithm must be transmitted.

One of the most important issues of the PAMELA SHM™ system is the communication performance. Devices could be connected by Ethernet or by wireless. The wireless connection of multiple devices creates a mesh net where data flow to the control PC above it. The environment of working (closed structures, metallic parts, and so on) must be taking into account. The system has been tested into closed 3-bay wingbox demonstrator provided with a small aperture between contiguous bays used to pass the power supply cables as shown in Fig. 3.

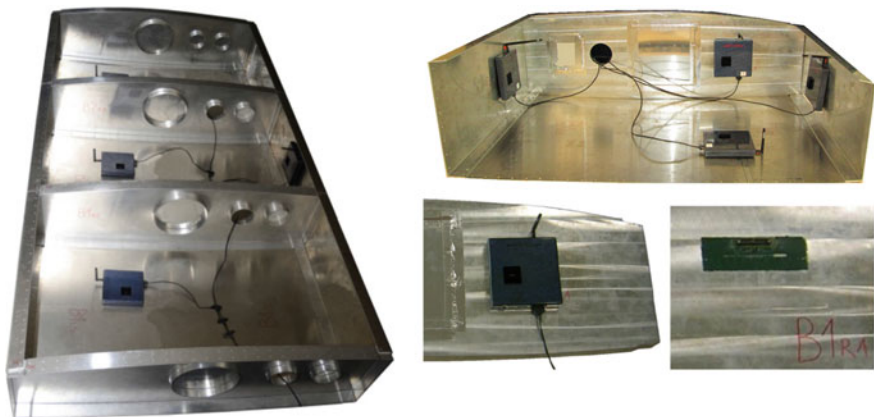


Fig. 3 PAMELA SHM system installed on a 3-bay wingbox demonstrator

3 Damage Detection Capabilities

PAMELA III is designed to be able to produce all types of excitation signals and route them to the piezoelectric transducers. Using the PAMELA control and configuration software, the signal characteristics and parameters to be sent to the hardware can be selected.

The system can perform several types of tests: passive, simple, round robin, transmitter beamforming, transmitter focusing, and plane front, with selectable wave velocities, sampling frequency, and number of samples per test. The excitation signals are fully configurable in shape, frequency, amplitude, and number of pulses. The type of excitation signals includes sine, sine sweep, impulse, uniform white noise, and arbitrary, with several windowing as Hamming, Hanning, and Flat.

Although Aernnova has developed an integrated transducer for the SHM system development, PAMELA device can work with any configuration and type of sensors/actuators just providing a connection thereof to the input/output channels of the device. This allows the system to adapt to a wide variety of applications.

Several PAMELA devices could be connected to work in pitch-catch mode where one device excites their transducers and one or more devices receive the direct signals propagated to them. This functionality allows to all the devices to work in pulse-echo mode as one single device increasing the number of effective channels.

SHM systems often include an impact detection capability, as sensors must be able to measure the energy generated by an impact to estimate the damage in the structure. When using ultrasonic waves, the previous requirement is no longer needed, as it is possible to measure damage in the structure afterward. In passive mode, PAMELA III listens on all the transducers for a signal with amplitude that is greater than a previously set threshold level. After an impact, any of the aforementioned SHM techniques can be used to determine the severity of the defect. Fig. 4 shows the results of a damage detection algorithm activated after a row of impacts. The front edge of the plate and four impact damages are clearly identified.

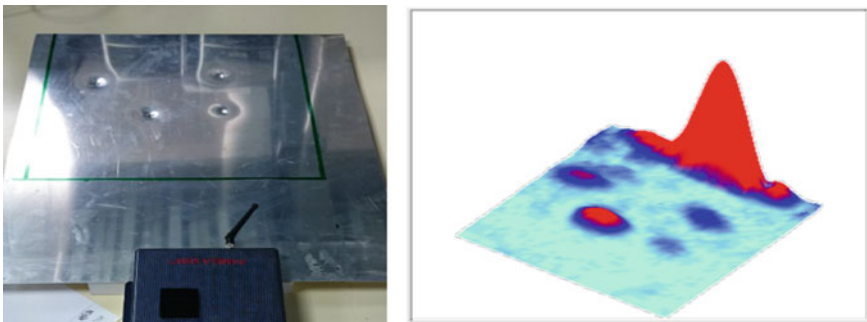


Fig. 4 Aluminum flat panel with 4 several impact damages (*left*) and an image obtained with the PAMELA SHM system (*right*)

PAMELA devices, in addition to the capability of performing tests and transmitting the collected data to the controller, have the capability of performing local data processing or preprocessing (reduction, normalization, pattern recognition, feature extraction, etc.). Local data processing decreases the data traffic over the network and allows CPU load of the external computer to be reduced. Even it is possible that PAMELA devices are running autonomously performing scheduled tests and only communicate with the controller in case of detection of structural damages or when programmed. Each PAMELA device integrates a software management application (SMA) that allows to the developer downloading his own algorithm code and adding the new data processing algorithm to the device. The development of the SMA is done in a virtual machine with an Ubuntu Linux distribution including all necessary software tools to perform the entire cycle of development. Eclipse Integrated Development Environment (IDE) is used to develop the SMA project and to write the code of each data processing algorithm [3].

Many different damage detection and characterization could be used with PAMELA SHM system because of its flexibility and capability to be reprogrammed to work on multiple different ways.

The SMA described before is used to integrate a damage detection algorithm where all acquisition data are processed in the device sending back just the image generated. Therefore, the damage index estimation for each observation point $O(x_o, y_o)$ of the grid is calculated using Eq. (1), where N is the number of piezoelectric transducers, R and E represent receiver and emitter respectively; $H(S_{ER}(t))$ is the analytic representation of the signal using the Hilbert transform, and $T_{ER}^1(O, t)$ is the theoretical signal associated with the observation point O (see [4] for additional details about each term in this equation).

$$D_1(O) = \left| \sum_{E=1}^N \sum_{R \neq E}^N \int_{-\infty}^{+\infty} H(S_{ER}(t)) T_{ER}^1(O, t) dt \right| \tag{1}$$

The result of the algorithm will be a 2D array with the damage index estimation assigned to each observation point of the grid. Figures 5 and 6 show the testing of this algorithm.

Similar algorithms have been developed for composite panels. In this case, algorithms require different signal conditioning because of the special characteristics of the material, and the anisotropy should be taken in count. Different directions of propagation have different velocities, so calculations require more complex algorithms. From material parameters, this velocity pattern could be accurately calculated by off-line applications before starting the tests and before using the real-time tools. In Fig. 7, an example of typical composite panel velocity pattern calculated just from the structure parameters of the panel is shown.

The mathematical treatment of the acquired signals and algorithms to obtain relevant information from each panel point from each of the signals received at the sensors allows the detection and visualization of the damage, although it is still

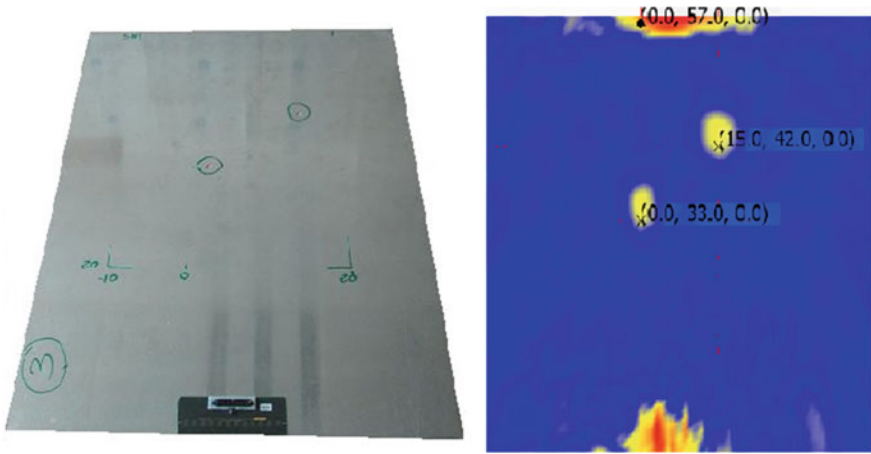


Fig. 5 Aluminum plate with transducer and ROI identified (left) and 2D image (right) obtained using PAMELA SHM system of the damaged panel on the left side

Fig. 6 3D image obtained using PAMELA SHM system of the damaged panel on Fig. 5

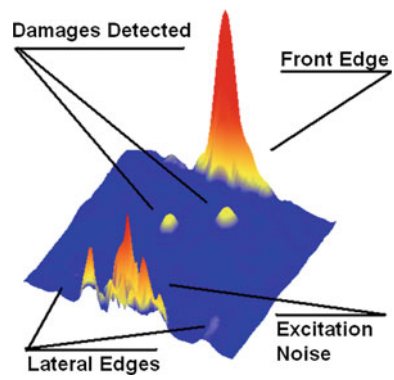
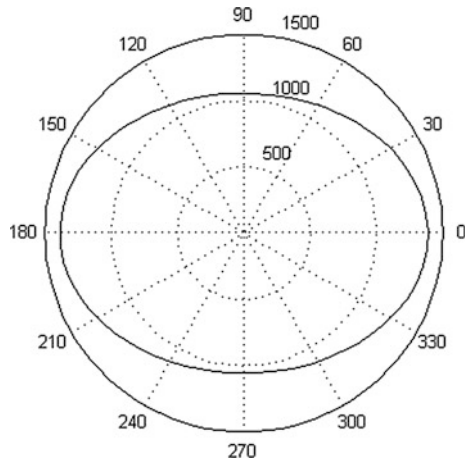


Fig. 7 Example of composite wave velocity pattern for all possible direction of propagation



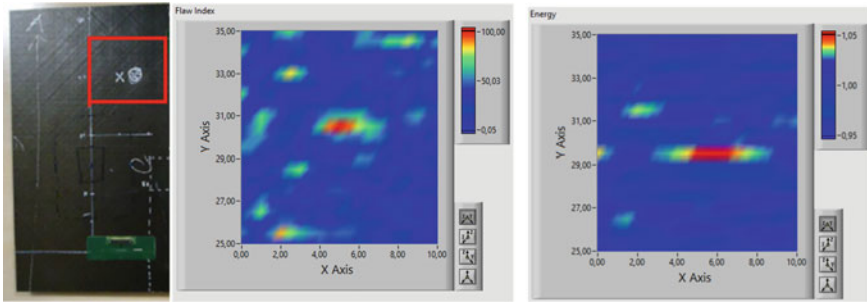


Fig. 8 Composite flat plate with transducer and ROI identified (*left*) and 2D images (*center and right*) obtained using several detection algorithms on damaged panel

necessary to face different problems that prevent generalization of these algorithms. The best results were obtained when using a basic data acquisition signal for the intact and looking panel and representing the changes shown by comparing the acquired signals for the post-panel impacted with those stored in the reference database.

The difficulty of detecting the impact produced starting only after the occurrence of acquired signals therein lies in the great attenuation that occurs in waves propagated in the panel. Rebounds corresponding to the reflection of guided waves to reach and pass through the damage caused by the impact are hidden under the large initial noise intensity produced by the transistor and interferences produced by the characteristics of the material is not homogeneous.

By using the differences between the panel and the panel intact damage, we can focus on the signal which has such changes, thus analyzing whether or not derived from damage or impact or that are false positives (Fig. 8).

PAMELA SHM system allows “ad hoc” solutions with no need of using the PhA III integrated transducer. As an example, a complex structure build with one aluminum stringer and a silicone skin has been analyzed. By using the A0 mode, just one piezoelectric is possible to detect mass loss or damage on the silicone skin as well as objects place on the structure. (See Fig. 9) This allows to analyze the union between this structure and the ribs where it is placed.

The selection of a proper propagation mode of the Lamb wave and the excitation signal needed allows to obtain accurate results without complex data process. In this case, just some noise filters and envelopes are used to obtain a representative image (Fig. 10) of the stringer analyzed where the damage on silicone layer and the superficial mass are identified.

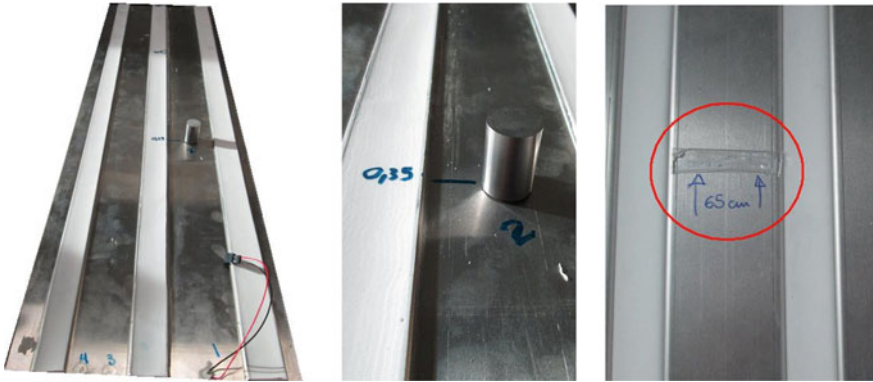


Fig. 9 Morphing skin (*left*) with a superficial object (*center*) and a damage on the silicone layer (*right*)

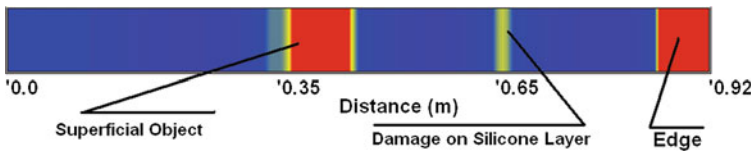


Fig. 10 2D image for inspection of morphing skin

4 Conclusions

This paper describes PAMELA SHM system as a fully integrated system capable of work in many different modes and configurations to perform NDT techniques for maintenance and SHM applications. Flexibility and adaptability of PAMELA device allow it to be use on a multiple PAMELA SHM system or as an advanced electronic tool for further developments on NDT field. This new approach provides multiple advantages, as described in this paper. All the features and the interesting preliminary results were obtained using several methods for detection in different materials, and geometries make the system very attractive for all kind of SHM applications and a powerful platform for further developments. The improvements that are actually been developed as a higher range of voltage on in/out channels will allow the system to be applied on different composite materials and geometries with no need of precalculations and less post-process effort.

Acknowledgments The research leading to these results has received funding from the European Union's Seventh Framework Program for research, technological development, and demonstration under Grant Agreement No. 284562.

References

1. Monje PM et al (2012) Integrated electronic system for ultrasonic structural health monitoring. In: 6th European workshop on structural health monitoring—Fr.1.C.1
2. Aranguren G, Monje PM, Cokonaj V, Barrera E, Ruiz M (2013) Ultrasonic wave-based structural health monitoring embedded instrument. *Rev Sci Instr* 84:125106
3. Ruiz et al M (2014) Integration of embedded data processing algorithms inside PAMELA devices. In: Proceedings of the 7th European workshop on structural health monitoring (Nantes, France)
4. Quaegebeur N, Ostiguy PC, Masson P (2014) Correlation-based imaging technique for fatigue monitoring of riveted lap-joint structure. *Smart Mater Struct* 23:055007

Toward the Upscaling of Guided Waves-Based NDE and SHM in Aeronautics

Nicola Testoni, Luca De Marchi and Alessandro Marzani

Abstract In this work, we report on some research developments to support the upscaling of nondestructive evaluation and structural health monitoring (SHM) approaches, mainly based on ultrasonic guided waves, for aeronautical applications. In particular, first a spiral-shaped piezoelectric sensor sensitive to the wave direction of arrival (WDA) of guided waves propagating in plate-like structures is described. Next, a miniaturized sensor node capable to perform locally signal processing algorithms, as those developed for the spiral sensors, is presented. The sensor node weights 4 g, measures approximately 20×24 mm, is characterized by a low power consumption and exploiting a data-over-power (DoP) network communication reduces to a minimum the need for cabling. At such the spiral sensors and sensor node result to be suitable for the upscaling of SHM approaches devoted to locate impacts as well as delaminations in aircrafts fuselage and wings. Next, impact and/or damage coordinates are passed to an augmented reality (AR) framework that allows the NDT inspector, if equipped with a proper visual device, to see in real time directly on the structure the position of the impact/damage. In the end, by guiding the technician directly to spots potentially damaged this could speed up the NDT visual inspection phase as well as it should reduce the possibility that damages would go undetected. Applications of the above methodologies/technologies for impact localization on an aluminum plate are presented.

N. Testoni · L. De Marchi

Department of Electrical, Electronic and Information Engineering—DEI,
University of Bologna, Viale del Risorgimento 2, Bologna 40136, Italy
e-mail: nicola.testoni@unibo.it

L. De Marchi

e-mail: l.demarchi@unibo.it

A. Marzani (✉)

Department of Civil, Chemical, Environmental and Materials Engineering—DICAM,
University of Bologna, Viale del Risorgimento 2, Bologna 40136, Italy
e-mail: alessandro.marzani@unibo.it

1 Introduction

Structural health monitoring (SHM) is becoming of interest as a possible mean to alleviate maintenance costs in aeronautics. One of the today aims is to develop guided waves-based SHM systems for the early detection of delaminations that might appear in composite structures due to impacts. Impacts can occur during manufacturing, in service (hail, flying flocks collisions, and impacts due to the presence of debris on the runway during take-off and landing), or at the same maintenance stage. This is because of, as well known, due to impacts, composite materials may be subject to different types of damages before the complete perforation, such as matrix cracking, fiber to matrix debonding, delamination, indenting, and fiber rupture. Among the mentioned, delamination deserve particular attention because even if it may appear not to be visible or scarcely visible at the structure surface (the acronym BVID—Barely visible impact damage is used to term this type of damage), a delamination may reduce the overall stiffness of the structure as well as its strength.

Basically, guided waves-based SHM systems consist in a network of tiny and low weight piezoelectric transducers, bonded or embedded into the structure (generally the skin), driven by a proper data acquisition system (DAQ). The DAQ is capable to actuate guided waves from one or more transducers (actuators) and receive from some others (sensors), when it operates in active manner, or simply to record waveforms at sensors when operates in passive mode [1, 2]. In both cases, the guided wave signals acquired at the sensors are next treated with signal processing tools with the aim of assessing the existence of damage, to localize the damage, and also aim at characterizing the shape of the damage.

Compared to other SHM approaches, SHM systems based on guided wave have some potential being characterized by the following peculiar and positive aspects:

- allow to monitor and inspect large areas from few accessible points of the structure (the transducers positions), including hidden parts of the structure as long as they can be well reached by the guided wave propagation;
- guided waves are characterized by an high speed of propagation (impacts and delaminations can be detected and located in almost real-time), have limited attenuation, and are sensitivity to multiple types of damage including those hidden in the structure [1, 2];
- allow to develop a permanently embedded monitoring system that can potentially operate in flight with no disturbance for the standard operations;
- are characterized by low-weight equipment.

However, today SHM approaches based on guided waves because of some methodological and technological limitations hardly meet the standards of the aerospace industry and their integration in the manufacturing process seem still far to come. Among the several, major limitations are as follows:

1. the developed methodologies for impact/damage detection, localization, and characterization allow to operate properly on regular geometries made of

isotropic materials, whereas their reliability on composite structures with the presence of stiffeners, rivets, manholes, and other geometrical anomalies has still to be proven; in addition, the majority of the developed methodologies need baseline measurements (it is proven that the baseline might change because of temperature, moisture, operative loads, aging, etc.);

2. the scalability from laboratories to aircrafts of the SHM system technology is still unproved (open issues related to weight, hardware power consumption, complex circuitry, life duration, and bulky signal processing);
3. absence of means to assess the SHM cost/benefit analysis.

Doubtless, the SARISTU project has contributed to advance the state of the art of all points (1, 2 and 3) above by increasing the TRL level of guided waves-based SHM in aeronautics, thus shortening the gap from demand and supply. On this direction, this chapter reports on some recent research developments carried out at the University of Bologna (UNIBO) by the authors to ease the upscaling of guided waves-based SHM for aircraft structural surfaces, wings, and fuselage skins, as well as to support the on-ground visual inspection phase. In particular, first a novel patent-pending dual-element spiral-shaped piezoelectric transducer for guided waves detection on metallic and laminate composite structures is presented. Thanks to its peculiar shape the sensor has an inherent capability to reveal the wave direction of arrival (WDA) of the guided waves. In brief, the sensor frequency response peaks at a frequency that depends on the WDA of the guided waves. At such, by analyzing the frequency response such direction can be estimated from a single sensor with a purposely designed signal processing. The sensor is thus suitable to operate in passive manner for impact/defect localization. Next, a miniaturized sensor node, meant as a basic building block for a passive sensor networks to be integrated in aircraft structures, capable to embed and perform dedicated signal processing algorithms, such as those developed for the spiral-shaped sensor, is described. Finally, an augmented reality (AR) framework that exploiting the outcome of the embedded SHM system supports the on-ground visual inspection phase of aircrafts surfaces, by virtually projecting eventual damages directly on the structure, is described. Some initial tests aimed at locating impacts on an aluminum plate are described to show the proposed developments and how they can be integrated.

2 Spira Mirabilis

The methodologies to locate impact based on guided waves can be mainly classified in three groups: (i) inverse methods that locate the impact via model updating, by using neural networks, genetic algorithms, or time reversal [3–6]; (ii) hyperbolic positioning algorithms that locate impact by using the difference in time-of-flight (ToF), i.e., time difference of arrival (TDoA), of the wavefronts captured by different sensors and proper triangulation algorithms [7–13]; and (iii) direct strategies

which allow to locate the wave source by capturing the wave direction of arrival (WDA) without recurring to the waves ToF [14–17].

Each approach has advantages and disadvantages, but it is true that strategies (i) are quite onerous in terms of computational resources, (ii) since ToA are measured with either threshold-based procedures, or peak detection techniques, they suffer from the multimodal and dispersive nature of guided waves, (iii) require ad hoc developed transducers. In the following, a spiral-shaped piezoelectric sensor sensitive to the WDA of guided waves propagating in plate-like structures is described [18]. In particular, the transducer has an anisotropic wavenumber filtering effect. Thanks to the link between frequency and wavenumber which characterize the guided propagation, the anisotropic transducer has a frequency response which depends on the WDA, and consequently the analysis of the frequency spectrum of the acquired signal can reveal the direction of the incoming waves.

2.1 Sensor Design

The sensor is composed by two electrodes ($E1$, $E2$) on the top surface of the device, plus a common electrode EC on the bottom surface, which is bonded to the structure to be inspected (see Fig. 1). $E1$ has a circular shape, while $E2$ is shaped either as a segment of a logarithmic spiral (Spira mirabilis) or as a segment of an Archimedean spiral so that the wavefront of an acoustic event generated by an impact hits $E1$ and $E2$ at two different time instants. For instance, in Fig. 1a, the geometry of the proposed sensor is represented along with two wavefronts $F1$ and $F2$ schematically depicted. Assuming that a wavefront, for instance $F1$, is moving toward the sensor (i.e., is moving in direction $-y$) it will reach first the electrode $E2$ in $P1$ and after a certain time the electrode $E1$ in $Q1$. The orthogonal projection of

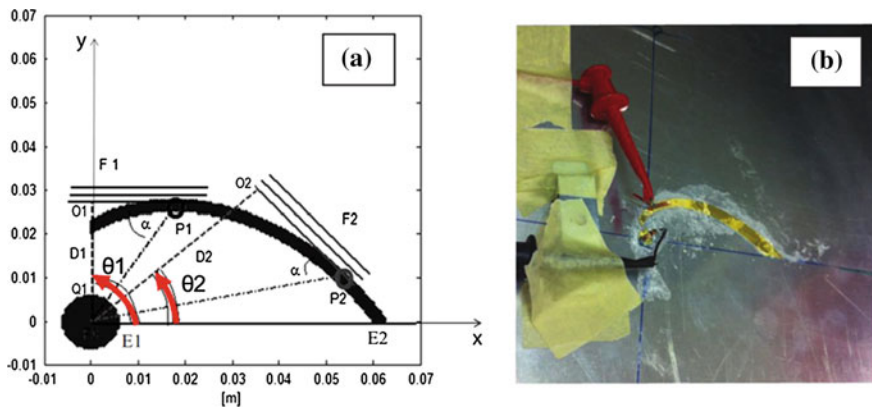


Fig. 1 Drawing of the transducer electrodes (a), and (b) their practical realization by shaping a 100- μ m-thick PVDF sheet

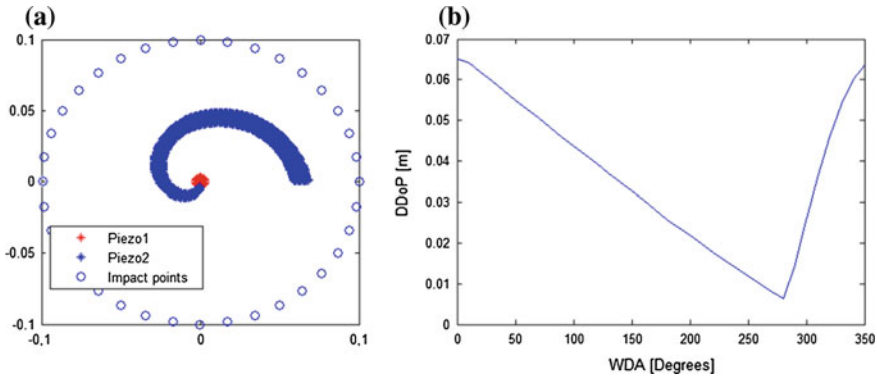


Fig. 2 Geometry of the patterned electrodes and considered potential impact positions (a). Subplot (b): difference in distance of propagation (DDoP) for the wave generated at the different impact positions and incident at the two electrodes. The WDA is the angle between the direction which connects the impact point to the center of electrode 1 and the x -axis of subplot (a)

$P1$ on the line which passes through $Q1$ is denoted as $O1$. Because of the asymmetric shaping of $E2$, the difference in distance of propagation (DDoP) for the wavefront to travel from $O1$ and $Q1$, i.e., the distance $D1$, varies with the wave direction of arrival (WDA) of the wavefront itself. Since the logarithmic spiral has the property that the angle between a radius vector ($r = ce^{a\theta}$ in polar coordinates) to a point on the curve and the tangent at the point is constant, and can be computed with the following relation $\tan(\theta) = 1/a$, there exists a trigonometric relation between the DDoP and the WDA. The DDoP for the two wavefronts $F1$ and $F2$ is denoted in Fig. 1a as $D1$ and $D2$, and their WDA as θ_1 and θ_2 .

As shown in Fig. 2b, the DDoP as a function of the WDA is monotonically decreasing in the interval $0^\circ < \text{WDA} < 280^\circ$, when $E2$ is shaped like an Archimedean spiral. With a dedicated signal processing procedure [19], the information about the distance DDoP (and the WDA) can be retrieved from the waveforms acquired and digitized at the two electrodes. More specifically, the DDoP can be extracted by the cross-correlation of the warped versions of the acquired signals at $E1$ and $E2$, as shown in Ref. [12]. Optimized selection of the sensor shape and size is under investigation to further improve the accuracy of the proposed approach.

2.2 Experimental Test

The experimental validation was carried out by bonding a Spira Mirabilis prototype PZT sensor to a 3-mm-thick Aluminum plate (see Fig. 1b). The practical realization of the proposed sensor was obtained by laser cutting a 100- μm -thick PVDF sheet (see Fig. 1b). Others geometries can be easily obtained [20].

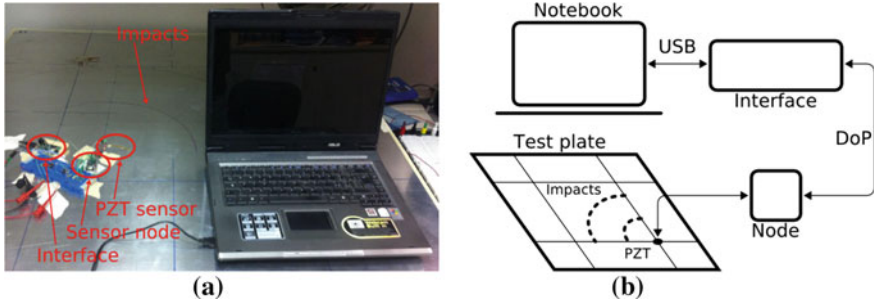


Fig. 3 A photograph of the experimental setup for the validation of the developed sensor's guided wave detection capabilities (a) and the schematic diagram (b)

The two electrodes were connected with a small footprint, low power, and light weight sensor node purposely designed to digitalize and process the waveforms acquired by the piezoelectric sensor. The sensor node was connected to an interface and via USB to a notebook PC. Due to the low power requirements, the DoP bus was powered through the USB connection (Fig. 3). An overall current consumption below 20 mA was measured.

Signals from the two electrodes in absence of stimuli were recorded exploiting the free running mode. A mean voltage of $1.54 \text{ V} \pm 0.44 \text{ mV}$ was recorded on channel one, while $1.84 \text{ V} \pm 0.84 \text{ mV}$ was recorded on channel two, this difference being most probably due a mismatch between the threshold voltage of the input transistors. Voltages are satisfactorily stable, the maximum deviation from the median value being at most 1 quantization level.

The impact detection experiment was designed as follows. Two concentric circular arcs centered on the PZT sensor of 20 and 40 cm of radius were drawn on the aluminum test plate from $\vartheta = 0^\circ$ to 120° , and subdivided into 12 segments 10° wide. Pencil breaks were performed on the ends of each arc segment, resulting in a total number of 26 impacts. The electrical signals generated by the PZT when reached by the elastic waves originated by the pencil breaks were recorded by the sensor node configured in trigger mode and transmitted to the controlling PC. The trigger was set on the channel connected to the larger electrode of the PZT sensor. The resulting signals are shown in Fig. 4.

The recorded waveforms are well behaved and do not show signs of voltage saturation. Comparing the signals generated by $E2$ (Fig. 4b, d) with the ones generated by $E1$ (Fig. 4a, c), a clear low-pass filtering effect due to the larger sensing area is appreciable. Also a delay pattern is visible in the signals generated by the smaller sensor, although more evident in the signals referring to the 20-cm arc (a). This pattern can be fruitfully used to distinguish the angle of incidence of incoming elastic waves.

Two sample waveforms acquired at $E1$ and $E2$ for an impact located at $\theta = 10^\circ$ of the 20-cm-radius arc ($x = 197 \text{ mm}$ and $y = 35 \text{ mm}$) are depicted in Fig. 5a. The DDoA estimation procedure is based on the design of a warped frequency transform

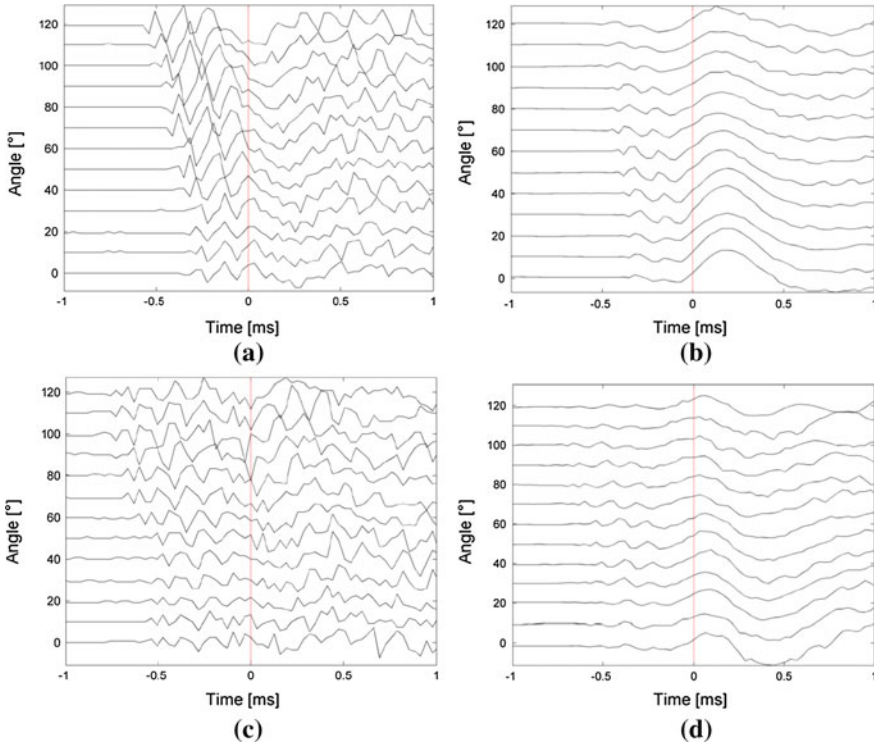


Fig. 4 Recorded signals from the pencil breaks experiment. Signals generated by *E1* are shown on the *left side* (a, c), while signals generated by *E2* are shown on the *right side* (b, d). The *top row* (a, b) refers to the 20-cm case, the *bottom row* to the 40 cm one. The *red dashed line* corresponds to the trigger event

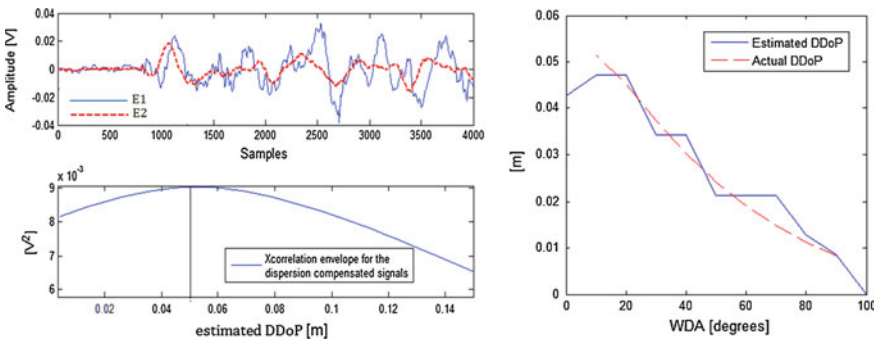


Fig. 5 (Top left) Waveform acquired by the shaped sensors; (Bottom left) Cross-correlation of the two warped signals acquired by the two electrodes *E1* and *E2*. The warped signals time axis has been converted to distance as described in Ref. [19]. (Right) Estimated and actual difference in distance of propagation as a function of the WDA

operator (WFT). In particular, the WFT operator is defined here according to the group velocity dispersion curve of the A0 mode that was computed according to the procedure described in [21], taking into account the material and geometrical properties of the considered specimen. Then, the two waveforms are processed with the WFT operator and their cross-correlation is computed along with its envelope.

The envelope of the cross-correlation between the warped signals acquired at $E1$ and $E2$ is depicted in Fig. 5 (bottom left).

The abscissa of envelope maxima reveals the difference in DDoP among the wave paths from the impact point and the 2 electrodes. The estimated DDoP is compared with the actual DDoP in Fig. 5 (right). As can be seen in this picture, the experimental characteristic follows the trend given by the geometry of the sensor. The average error in the estimation of the WDA is around 5° , and this result represents noticeable advance w.r.t. alternative solutions presented in the literature [22].

3 A Miniaturize Sensor Node for Guided Waves NDE and SHM

Active or passive guided waves-based SHM are characterized by different technological constraints. In particular, the energy consumption, weight, and space required for the circuitry involved in the actuation and processing of the signals connected to the active SHM is still a challenge to allow for a permanently installed, continuous real-time monitoring of the involved structures [23–25]. Conversely, if the target of the SHM system is the impact detection, such electronic equipment can be greatly simplified because the actuation circuitry is no longer required since the waves generated by the impact are exploited. Moreover, WDA transducers in place of traditional sensor arrays could allow reducing the number of signal channel to be recorded at the same time [17, 18, 26]. This complexity reduction is crucial toward the applicability of SHM systems in several current research fields due to the reduced dimensions, weight, and cost of the sensor nodes, which allows for the deployment of embedded monitoring systems.

To this aim, a small and light sensor node for guided wave detection on laminate composite and metallic structures was realized. A companion gateway device was also implemented as a mean to both interface and feed power to the sensor node through a two-wire data-over-power (DoP) network bus. Electrical power can be drawn either from the USB PC connection or from a low-voltage external power supply unit (PSU). The sensor node was designed to be connected to other similar devices to create a network of up to 256 nodes. Communication to a notebook PC or to an embedded platform like Intel Edison [27] is performed in a half-duplex fashion at an effective speed of 200 kbps by means of a low-voltage, high-speed, half-duplex RS485 transceiver.

The heart of the sensor node is an extreme low power, low-voltage, 8-bit microcontroller unit (MCU) with an integrated 12 channel, 10-bit analog-to-digital converter (ADC) with embedded voltage reference. Elastic waves generated from impacts and propagating on the structure are recorded by the innovative, patent-pending, dual-element Spira Mirabilis PZT [18] and stored in an external 1-Mbit serial peripheral interface (SPI) serial SRAM. Program instructions are stored in a 7-Kbit flash memory embedded within the MCU. Each sensor node is roughly 20×24 mm wide, consumes less than 10 mA at a supply voltage of 3.3 V, and weighs less than 20 g, making it attractive for aerospace systems where size, power, and weight reduction are crucial.

3.1 Interface Architecture

The network interface is built upon a four-building-block architecture as shown in Fig. 6a.

An FTDI FT231X USB to full handshake UART-integrated circuit (IC) is used to provide USB connectivity for an embedded controller or an external PC. This IC features a fully integrated clock generation with no external crystal required plus optional clock output selection enabling glue-less interface to an external MCU or FPGA. It also has a fully integrated 2048 byte multi-time-programmable

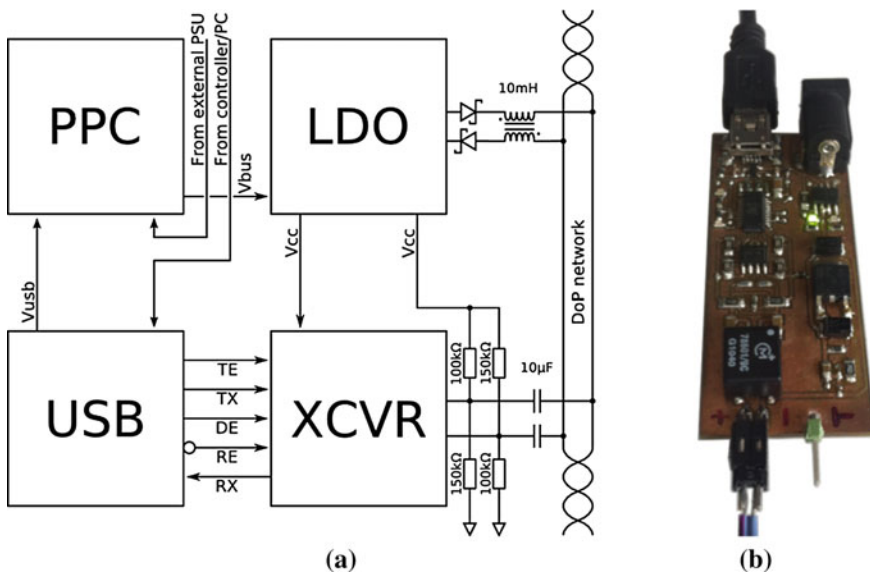


Fig. 6 Schematic diagram of the DoP network interface (a) and the implemented and tested prototype board (b). Connectivity to a PC is provided by the USB cable, while a twisted pair implements the DoP network bus

(MTP) memory, used for storing device descriptors and I/O configuration. The entire USB 2.0 full speed protocol is handled on the chip, allowing for data transfer rates from 300 baud to 3 Mbaud at TTL levels. It is operated by a +5.0 V single supply line taken directly from the USB bus and internally regulated to +3.3 or +1.8 V by integrated low-dropout (LDO) regulators. When active, it typically consumes 8 mA, but it can also enter a suspend state in which power consumption drops to 125 μ A. An industrial temperature range device was chosen in order to withstand temperatures in the range -40 to $+85$ $^{\circ}$ C.

A Linear Technology LTC4414 low loss PowerPath™ Controller (PPC) is used to control an external Pchannel MOSFET to create a near ideal diode function for power switchover. This permits the interface to perform a highly efficient management of the available power sources, namely the +5.0 V, 500 mA USB power supply line, and an external +3.5 to +36 V, 5A auxiliary PSU. When conducting, the measured voltage drop across the MOSFET is typically 20 mV with a typical R of 31 m Ω . The load is automatically disconnected from the USB power line when the auxiliary source is connected. This is signaled to the user by the turnoff of a red indicator LED. The wide supply operating range of the PPC supports operations from one to eight Li-ion cells in series or the 28VDC avionic bus power line as per MIL-STD-704F. The low quiescent current (30 μ A typical) is independent of the load current. An industrial temperature range device was chosen.

The PPC feeds the DoP network bus by means of two 5A Schottky diodes in series with two mutually coupled 695 μ H inductors in anti-parallel configuration. This aids filtering out common mode interferences on the DoP network bus, while allowing the flow of power supply current [28]. The PPC also feeds a Texas Instrument LM317 medium current 1.2–37 V adjustable LDO voltage regulator. This IC is designed to supply up to 500 mA of load current with an adjustable output voltage, taking power from an external supply unit providing up to +40 V. The nominal output voltage is programmed to +3.3 V by one 240–390 Ω purely resistive divider, also taking into account an adjustment pin current of 100 μ A. To reduce the sensitivity to input line impedance, a ceramic 100-nF input bypass capacitor was selected. The adjustment terminal was also bypassed to ground by a similar capacitor to improve ripple rejection as the output voltage rises. To assure stability and avoid excessive ringing, a 1- μ F ceramic output capacitor was employed. When powered through the +5.0 V USB source, quiescent current consumption never exceeds 1.5 mA; conversely currents up to 4.0 mA can be measured when a higher voltage is supplied through the auxiliary power line. A green indicator LED is lit whenever output power is present as shown in Fig. 6b. An extended temperature range device was chosen in order to withstand temperatures in the range -40 to $+125$ $^{\circ}$ C.

The LDO feeds a Linear Technology LTC2854 low power, 20 Mbps, RS485/RS422 transceiver (XVCR), used to interface the UART to the DoP network. The receiver includes a logic-selectable 120 Ω termination, one-eighth unit load [29] supporting up to 256 nodes per bus, and a failsafe feature that guarantees a high output state under conditions of floating or shorted inputs. The driver provides full RS485 compatibility. A half-duplex device was selected to reduce the wiring

while allowing for a high enough communication speed. When the driver is disabled, both outputs present high impedance, this term being dominated by the receiver input resistance which is guaranteed to be greater than 96 k Ω when the termination is disabled. The operating current typically is 470 μ A in transmit mode and 370 μ A in receive mode, but can be decreased to just 5 μ A in shutdown mode.

Additional current is required according to the number of nodes connected to the bus. An industrial temperature range device was chosen. A simulation of the effective input impedance of the interface, comprehensive of the additional circuitry for DoP networking, has been performed using LTspice IV, a high-performance SPICE simulator produced by Linear Technology. The total load seen by the driver is less than one unit load (15 K Ω) for frequencies higher than 250 kHz and is approximatively one-half unit load at 500 kHz, allowing for up to 58 similar devices on the same portion of line.

3.2 *Sensor Architecture*

The sensor node is also built upon a four-building-block architecture as shown in Fig. 7a. The XCVR section is identical to the one fitted on board the network interface and presented in the previous section. The LDO section is similar to the one already discussed, however, due to the much lower power requirements of the sensor node, a Texas Instrument LM3480 100 mA linear voltage regulator is employed instead of the LM317. A device with a fixed +3.3 V output voltage was selected to reduce the number of required external components. This IC features operation from an input voltage as high as 30 V and an ensured maximum dropout of 1.2 V at the full 100-mA load, which is compliant with a +5.0 V power supply of the entire DoP bus. The maximum input voltage is also compliant with the 28VDC avionic power supply. The low quiescent current (1.75 mA maximum) is inversely dependent from the load current. An extended temperature range device was chosen.

Beside the XCVR section, the LDO feeds a Microchip 23LC1024 1 Mbit Serial SRAM device and a Microchip PIC16LF1828 8-bit low-power microcontroller unit (MUC). The memory is accessed via a simple SPI compatible bus. The bus signals required are a clock input (SCK) plus separate data in (SDO) and data out (SDI) lines. Access to the device is controlled through a chip select (CS) input. All these lines are directly controlled by the MCU. The RAM IC features an unlimited number of read and write cycles and zero write time, allowing for data rate up to 20 Mbps in sequential access mode. This memory is used as a temporary storage for the acquired data samples, its access time being compatible with the continuous sampling period of the ADC embedded within the MCU. It features a very low power consumption: When in standby, only 2 μ A are absorbed from the +3.3 V power supply, while operative current is less than 2 mA. An industrial temperature range device was chosen.

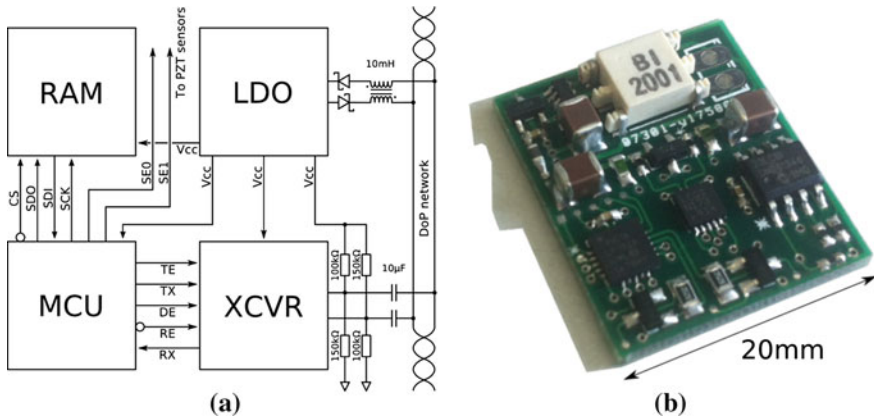


Fig. 7 Schematic diagram of the DoP sensor (a) and the implemented and tested prototype node (b). Connectivity to the DoP network is provided by a twisted-pair solder connection in the *top right* of the node

The chosen MCU belongs to the enhanced mid-range family and features an integrated 32 MHz oscillator, thus reducing the number of external components. A 12 channel, rail-to-rail ADC with selectable integrated voltage reference is available. It allows the conversion of an analog input signal to a 10 bit binary representation via successive approximation. At the maximum ADC clock period, a 10 bit conversion requires 11.5 μs , but an option for performing 8 bit conversions in 9.5 μs is present. Moreover, integrated SPI and Enhanced Universal Synchronous–Asynchronous Receiver–Transmitter (EUSART) contain all the clock generators, shift registers, and data buffers necessary to perform an input or output serial data transfer independent of device program execution. Automatic detection and calibration of the baud rate is also available, making it ideally suited to the task of sampling the acoustic signals generated from impacts, processing them, and communicate results back to the controller. The maximum current consumption in active mode at a system clock frequency of 32 MHz is 3.6 mA. An industrial temperature range device was chosen. The total current consumed by one sensor node amounts to 7.3 mA, which leads to a power consumption of 36.5 mW when the DoP bus is powered through the +5.0 V USB power line. Also accounting for the 10 mA current consumption due to the interface circuit discussed in the previous section, up to 67 such devices can be simultaneously connected to the same interface without violating USB 2.0 specification (Fig. 7).

3.3 Firmware Workflow

To detect and acquire the electrical signals generated by the PTZs in presence of guided waves, a firmware based on a five-state finite state machine (FSM) has been

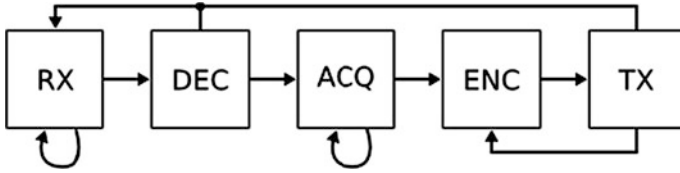


Fig. 8 Simplified work flow of the firmware developed for guided wave detection and acquisition. The architecture is based on a five-state finite state machine

developed, uploaded onto the MCU, and tested. The state sequence is shown in Fig. 4. After waking up and initialization, the FSM enters the reception (RX) state, where it polls the internal EUSART subsystem waiting the XVCR to detect a start package to be transmitted on the DoP bus. Whenever an incoming data stream is detected, it gets recorded on an internal buffer, waiting for decoding. If the maximum stream length is reached before a stop package is detected, the buffer is used and the FSM re-enter the RX state. Conversely, it moves to the decoding (DEC) state (Fig. 8).

Data on the DoP bus must be phase-encoded [30], so the DEC state is mandatory to recover the original information. Each byte in the decoded stream corresponds to 20 bits in the encoded one, giving an effective data rate of 200 kbps at a transmission frequency of 500 kHz. Information transmitted always includes the sensor node address the stream is destined to: If the decoded address does not match either the broadcast or the local host, the FSM simply ignore the message and re-enters the RX state. Conversely, if signal acquisition is requested, it enters the ACQ state.

Two forms of data acquisition were programmed: free running and triggered. A node configuration package can be sent to setup the acquisition mode, the total number of samples N_s to be acquired, the number of pretrigger samples N_p , and the trigger thresholds for each channel. In both acquisition modes, the MCU immediately starts acquiring samples from the PTZs, accumulating the recorded data in the external RAM. In free running mode, only the first N_s samples are kept. Conversely, in triggered mode, the MCU check each recorded samples: If they fall outside the given thresholds, N_p samples before and $N_s - N_p + 1$ after the current one are kept.

The FSM then enters a rapid sequence of encoding (ENC) and transmission (TX) stats. Recorded data are subdivided into shorter packages, destination address is appended, and then the resulting stream is phase-encoded and transmitted over the DoP bus. In this implementation, a naïve network ownership protocol was used, resulting in the fact that the controller/PC connected to the DoP interface always owns the channel. More complex protocols will be implemented to allow for simultaneous acquisition over the whole sensor network.

4 Augmented Reality Detailed Formatting Instructions

The output of the impact methodology is passed to an AR visualization technology that is meant to support the inspector during the on-field inspection/diagnosis as well as the maintenance operations. The inspector, in fact, can see interactively in real time the impact data directly on the surface of the structure. Here, the proposed approach is tested on the engine cowling of a Cessna 150 general aviation airplane. Preliminary results confirm the feasibility of the method and its exploitability in maintenance practice.

Following the definition by Atzuma [31], AR is a real-time technique in which real-world images are added by virtual objects in a defined position. The most critical issues related to this technique have been described and listed in a review paper by [32]; they are: tracking techniques, interaction techniques, calibration and registration, AR applications, and display techniques. Tracking is required to evaluate the position and the pose of the experimenter head about an external reference system: Several techniques can be applied depending on the need of final application, but all these methods can be grouped into two main types: sensor-based tracking and vision-based tracking techniques [32]. On the one hand, sensor-based tracking techniques include the application of GPS/accelerometers and magnetometers, acoustical, optical, or mechanical devices to detect the pose and position of an observer in open spaces: A detailed description can be found in [33]. On the other hand, vision-based tracking techniques can be divided into feature-based and model-based [34] techniques: The main idea is to frame a geometrical object (marker) in the images, whose features are known and to guess the relative position between the marker and the camera reference system. In case of model-based techniques, the model edges or contours are used to superimpose the virtual image. The calibration and registration [35] problems deal with the correct superimposition between the external image, and the virtual one. The experimenter perceives in fact immediately if the virtual image is not correctly aligned with respect to the external world or if an un-natural field of view is obtained, and an unpleasant sensation arises. About visualization, several techniques have been developed in recent years [36]: The high number of devices developed for AR applications can be divided into two main categories: head mounted displays (HMD), and see through displays. HMD are composed by a dark head helmet, in which a pair of projector displays the external world projecting images acquired from a camera pointing outside. See through displays, usually presents semitransparent lenses and a projector: The experimenter can see through the lenses, and the virtual scene is projected onto the lenses so that the virtual image is superimposed to the real one. According to [36], also new devices such as mobile platforms (e.g., Android) can be used for AR, but in this case, the augmented image is displayed onto the screen of a mobile phone or a tablet, using the device camera to acquire the external image.

4.1 Reference System

The mathematical framework lying below the AR deals with the techniques to detect markers and to correctly superimpose the virtual image to the real-world image, from the camera. In this application, a vision-based tracking technique is used, where a marker of known dimension is used to evaluate the relative position between the camera and the marker itself. As detailed in Ref. [37], three reference systems: the camera coordinate system (X_c, Y_c, Z_c), centered in the pinhole center, the screen coordinate system (x_c, y_c, z_c) centered in the center of the pc screen, and finally a marker coordinate system (X_m, Y_m, Z_m), centered in the center of the marker itself (Fig. 9), and proper relations among them are necessary to add virtual images and symbols to a real-world image.

4.2 Case Study

The experimenter wears a pair of Vuzix STAR™ 1200 (Fig. 10) glasses, which are specifically designed for such applications. These glasses include a camera in the front and two miniaturized projector projecting images on transparent lenses. Two USB plugs connect the Vuzix glasses with a notebook or a computer. The external view, framed from the frontal camera, can be elaborated following the steps: threshold image, detect connected objects, extract the marker, detect the distortion and dimensions of the markers, pose, and distance computations. In the following, a virtual symbol or image can be added to the frame and projected onto the glasses exploiting the glasses projectors. The resolution of the camera of

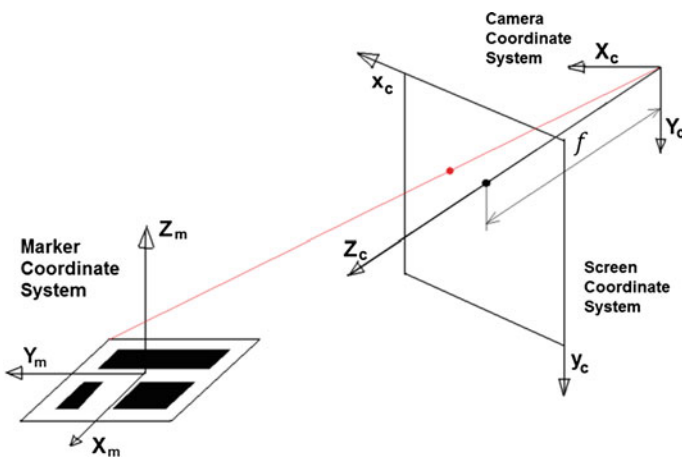


Fig. 9 Camera, screen, and marker coordinate system



Fig. 10 (Left) Vuzix STAR 1200 glasses used in the research, (center) marker features, (right) image of aluminum sheet with impact marker

this see through glasses model can be changed up to 1920×1080 pixels, and the two projectors support video display resolutions up to 1280×720 .

The Vuzix glasses are equipped with three gyroscopes also, so that they can provide the pose angles (pitch, roll, yaw) of the experimenter's head, but in this case, these data are not used since a vision-based tracking technique is used: The elaboration of the marker image taken from the camera allows to guess the rotation and translation of the camera reference system with respect to the marker reference system. The marker used in these tests to compute the distance and relative position between camera and marker coordinate system represented Fig. 10 (center) has been simply sketched with a graphical software and printed on a paper sheet. Different marker shapes could be used, provided they are asymmetric, black and white, and easily recognizable by the AR software. Once the marker has been sketched, a picture of the marker with a preset distance and attitude from the camera is made: In this way, the software possesses a model of the maker to compare the objects in the image and the calibration of the camera occurs.

All the operations of feature detection and pose determination are performed using the AR toolkit, which is an available library for AR shared by the University of Washington [38]. The calibration is obtained by framing a marker lying in a known position, with a camera whose features are known; in this way, it is possible to set the calibration matrix which is always related to a defined camera setting.

Figure 10 (right) shows in the left the aluminum panel with the marker in the low left corner; the experimenter wears the glasses while testing the display and image detection system. He hits the aluminum panel with a hammer, the impact detection procedure starts, and a point is defined in a reference system fixed with the plate. Two coordinates (horizontal and vertical distance of the impact point from the edge) are passed to the visualization algorithm. Figure 11 shows the image from the glasses camera is processed by the AR toolkit with the following steps: application of threshold, detection of connected objects, detection of objects contours, detection of marker, computation of image distance and pose with respect to the camera reference system by the evaluation of the marker distortion, detection of the impact point in the camera, and screen reference system.

Finally, a symbol represented by three squares centered in the impact point is added to the image: The red square shows the impact position, the yellow the impact proximity, and the green the impact surrounding area. The dimension of the

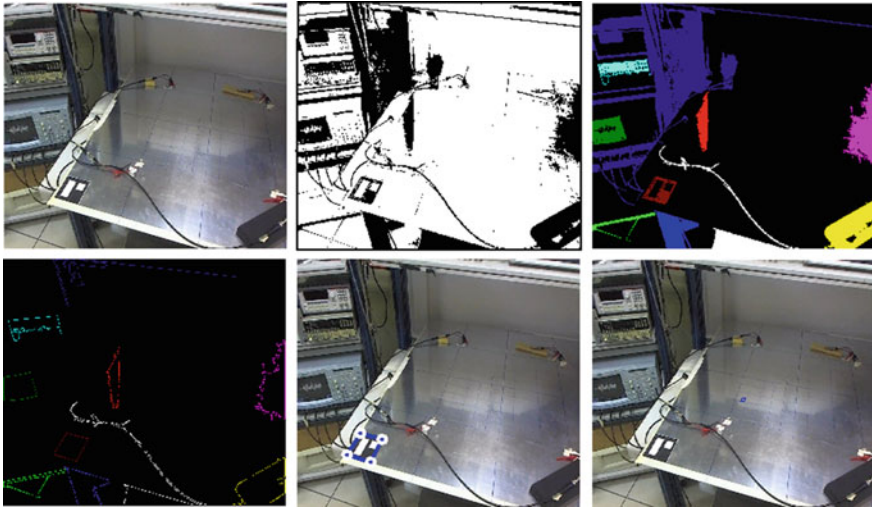


Fig. 11 Image analysis: image acquired by Vuzix camera (*top left*), thresholded image (*center top*), connection of pixel to detect objects (*top right*), contours detection (*down left*), marker edges detection and pose estimation (*down center*), impact point detection in AR (*down right*)



Fig. 12 Experimented with AR glasses (*left*) and image visualized by the experimenter with a virtual marker over imposed to the structure (*right*)

squares is not constant, but it depends on the strength of the impacts, so that the experimenter can visually evaluate the energy exchanged in the impact in an intuitive way, well before numerically evaluate the impact detection and evaluation results. Figure 12 shows the image projected on the glasses lenses by the computer, after the augmentation with the impact symbol.

5 Conclusion

In this work, some research activities toward the upscaling of guided waves-based SHM systems have been proposed. In particular, a novel piezoelectric sensor particularly suited to be employed for impact detection procedures in plate-like structures is shown. Thanks to its peculiar geometrical shape and the dedicated signal processing procedure, the sensor reveals the information about the incident wave direction of arrival (WDA). Pencil break impact detection experiments, where the signals were autonomously acquired by a small footprint, low power, and light weight sensor node and transmitted to a controlling PC for further processing, showed the capability of the Spira Mirabilis to estimate the angle of incidence of incoming elastic waves. Each node is roughly 20×24 mm, consumes less than 40 mW, and weighs less than 20 g, making it attractive for aerospace systems where size, power, and weight reduction are crucial. Such device is meant as a building block for smart structure passive sensor networks development and draws power from a two-wire data-over-power (DoP) network communication interface, which is also used for half-duplex communication.

Finally, a human-machine interface based on AR conceived to provide to maintenance operators the results of an impact detection methodology is shown. In particular, the implemented tool dynamically interacts with a head portable visualization device allowing the inspector to see the estimated impact position on the structure.

Acknowledgments The research leading to these results has received funding from the European Union's Seventh Framework Programme for research; technological development and demonstration under grant agreement no. 284562.

References

1. Zhongqing S, Lin Y, Ye L (2006) Guided lamb waves for identification of damage in composite structures: a review. *J Sound Vib* 295:753–780
2. Staszewski WJ, Mahzan S, Traynor R (2009) Health monitoring of aerospace composite structures: active and passive approach. *Compos Sci Technol* 69(11):1678–1685
3. Park J, Ha S, Chang F (2009) Monitoring impact events using a system-identification method. *AIAA J* 47(9):2011–2021
4. Staszewski WJ, Worden K, Wardle R, Tomlinson GR (2000) Fail-safe sensor distribution for impact detection in composite materials. *Smart Mater Struct* 9:298–303
5. Coverley PT, Staszewski WJ (2003) Impact damage location in composite structures using optimized sensor triangulation procedure. *Smart Mater Struct* 12:795–803
6. Ciampa F, Meo M (2012) Impact detection in anisotropic materials using a time reversal approach. *Struct Health Monit* 11(1):43–49
7. Kundu T, Jata K (2009) Detection of the point of impact on a stiffened plate by the acoustic emission technique. *Smart Mater Struct* 18:035006
8. Tracy M, Chang F (1998) Identifying impacts in composite plates with piezoelectric strain sensors, part II: experiment. *J Intel Mat Syst Struct* 9(11):929

9. Seydel R, Chang F (2001) Impact identification of stiffened composite panels: I. System development. *Smart Mater Struct* 10(2):354–369
10. Kosel T, Grabec I, Muzic P (2000) Location of acoustic emission sources generated by air flow. *Ultrasonics* 38(1–8):824–826
11. White P (1969) Cross correlation in structural systems: dispersion and nondispersion waves. *J Acoust Soc Am* 45:1118–1128
12. De Marchi L, Marzani A, Speciale N, Viola E (2011) A passive monitoring technique based on dispersion compensation to locate impacts in plate-like structures. *Smart Mater Struct* 20:035021-10
13. Perelli A, De Marchi L, Marzani A, Speciale N (2012) Acoustic emission localization in plates with dispersion and reverberations using sparse PZT sensors in passive mode. *Smart Mater Struct* 21:025010
14. Matt H, Lanza di Scalea F (2007) Macro-fiber composite piezoelectric rosettes for acoustic source location in complex structures. *Smart Mater Struct* 16:1489–1499
15. Salas K, Cesnik C (2009) Guided wave excitation by a CLoVER transducer for structural health monitoring: theory and experiments. *Smart Mater Struct* 18:075005
16. Salamone S, Bartoli I, Di Leo P, Lanza Di Scala F, Ajovalasit A, D’Acquisto L, Rhymer J, Kim H (2010) High-velocity impact location on aircraft panels using macro-fiber composite piezoelectric rosettes. *J Intell Mater Syst Struct* 21(9):887–896
17. Baravelli E, Senesi M, Ruzzene M, De Marchi L, Speciale N (2011) Double-channel, frequency-steered acoustic transducer with 2-d imaging capabilities. *IEEE Trans Ultrason Ferroelect Freq Control* 58(7):1430–1441
18. De Marchi L, Testoni N, Marzani A (2015) Spira mirabilis: a shaped piezoelectric sensor for impact localization. In: Lynch JP (ed) *Sensors and smart structures technologies for civil, mechanical, and aerospace systems 2015*, vol 94359, 4351S. Proceedings of SPIE, San Diego, California, United States, 8 Mar 2015
19. De Marchi L, Marzani A, Caporale S, Speciale N (2009) Ultrasonic guided waves characterization with warped frequency transforms. *IEEE Trans Ultrason Ferroelect Freq Control* 56(10):2232–2240
20. Intelligent Structures (2015) <http://intstruct.blogspot.it/>
21. Bocchini P, Marzani A, Viola E (2011) Graphical user interface for guided acoustic waves. *J Comput Civil Eng* 25(3):202–210
22. Nakatani H, Kundu T, Takeda N (2014) Improving accuracy of acoustic source localization in anisotropic plates. *Ultrasonics* 54(7):1776–1788
23. Hong M, Wang Q, Su Z (2014) A guided wave approach for real-time health monitoring of high-speed train bogie frames. In: Far East forum on Nondestructive evaluation/testing (FENDT), IEEE, pp 39–43
24. Monje PM, Casado L, Aranguren G, Cokonaj V, Barrera E, Ruiz M (2012) Integrated electronic system for ultrasonic structural health monitoring. In European workshop on structural health monitoring
25. Qing XP, Beard SJ, Kumar A, Li I, Lin M, Chang FK (2009) Stanford multiactuator-receiver transduction (smart) layer technology and its applications. *Encycl Struct Health Monit*, pp 1363-1388
26. Qiu X (2010) Patterned piezo-, pyro-, and ferroelectricity of poled polymer electrets. *J Appl Phys* 108(1):011101
27. I. Corporation. Intel Edison platform (2014)
28. Chin T-k, Tran D (2011) Combine power feed and data link via cable for remote peripherals
29. Gingerich K (2004) RS-485 unit load and maximum number of bus connections, tech. rep., Texas Instrument
30. Stallings W (ed) (2003) *Data and computer communications*, 7th edn. Prentice Hall, New Jersey
31. Azuma RT (1997) A survey of augmented reality. *Teleoperators Virtual Environ* 6:355–385
32. Zhou F et al (2008) Trends in augmented reality tracking, interaction and display: a review of ten years in ISMAR. In: Proceedings of the 7th international symposium ACM/IEEE ISMAR on mixed and augmented reality, pp. 193–202. IEE, Cambridge

33. Welch G, Foxlin E (2002) Motion tracking: no silver bullet, but a respectable arsenal. *IEEE Comput Graph Appl* 22(6):24–38
34. Pressigout M, Marchand É (2006) Hybrid tracking algorithms for planar and non-planar structures subject to illumination changes. In: *Proceedings of international symposium ACM/IEEE ISMAR'06 mixed and augmented reality*. Santa Barbara, California. France, pp 52–55
35. Pang Y, Yuan ML, Nee AYC, Ong SK, Youcef-Toumi K (2006) A markerless registration method for augmented reality based on affine properties. In: *AUIC '06. Proceedings of the 7th Australasian user interface conference*, pp 25–32
36. Yuen S, Yaoyuneyong G, Johnson E (2011) Augmented reality, an overview and five directions for AR in education. *J Educ Technol Dev Exch* 4(1):119–140
37. De Marchi L, Ceruti A, Marzani A, Liverani A (2013) Augmented reality to support on-field post-impact maintenance operations on thin structures. *J Sens* 619570:10
38. Artoolkit (2013) <http://www.hitl.washington.edu/artoolkit/>

Part VI

Technology Stream: Integrated Sensing. Impact Damage Assessment Using Integrated Ultrasonic Sensors

Introduction and Overview

AS06 focuses on 2 major pillars toward technical qualification of impact damage assessment using integrated ultrasonic sensors. The first pillar is the physical integration of sensors, whereas a co-bonding concept for two different sensors types has been verified including proof of non-disturbance and sufficient durability as well as appropriate electrical connecting and quality check. Additional preliminary repair concepts are presented. Second pillar is the damage detection approach. Within SARISTU AS06, an approach has been developed to prove the reliability of damage detection. It is a so-called MAPOD (model-assisted probability of detection) approach dedicated to SHM sensor network. For doing that a dedicated damage detection software has been developed.

Within AS06, three main achievements can be stated: First, a sensor integration concept has been developed and approved to large-scale structures; second, a damage detection concept using simulated data has been approved to be functional; and third, the coding of a damage detection software working with experimental and simulated data under laboratory conditions.

The following papers of AS06 reflecting upon described approach. First paper from I. Bueth et al. describes the approach how to transfer probability of detection (POD) approach from conventional NDI to SHM using simulation data. The MAPOD (model-assisted POD) approach is detailed on an example of an AS06 panel. Second paper from R. Loendersloot et al. describes the graphical user interface in detail and the third paper from M. Moix Bonet et al. evaluates its performance. Last but not least, the fourth paper describes the sensor integration approach using an example of two AS06 panels.

Damage Identification in Composite Panels—Methodologies and Visualisation

Richard Loendersloot, Inka Buethe, Pavlos Michaelides,
Maria Moix-Bonet and George Lampeas

Abstract A methodology for the identification of an impact damage using guided waves on a composite structure is implemented. Both numerical and experimental results are used, and a graphical user interface is developed to visualise the potentially damaged area. The latter allows, on top of detection, an assessment of the location and severity of the damage. The input can be experimentally based or calculated with the help of numerical models. Within this work, two numerical models are presented, based on stacked-shell finite element approach and on spectral element approach in time domain. The graphical interface allows the user to choose the most suitable approach from various damage identification methods using pitch-catch acousto-ultrasonics. The numerical models allow us to test a variety of damage locations with variable extents. The quality of the models is shown by a comparison of simulated and experimental data in time domain and respective damage indices. Finally, the visualisation allows to focus on specific areas, enhancing the analysis of multiple damages in a structure. The damage

R. Loendersloot (✉)

University of Twente, Engineering Technology, Dynamics Based Maintenance, P.O. Box 217, 7500 AE Enschede, The Netherlands
e-mail: r.loendersloot@utwente.nl

I. Buethe

Institute of Mechanics and Control Engineering—Mechatronics, University of Siegen, 57076 Siegen, Germany
e-mail: inka.buethe@uni-siegen.de

P. Michaelides

NASTECH—Novel Aerospace Technologies, Ancarano 64010, Italy

M. Moix-Bonet

Multifunctional Materials, Institute of Composite Structures and Adaptive Systems, German Aerospace Center, Lilienthalplatz 7, 38108 Braunschweig, Germany
e-mail: maria.moix-bonet@dlr.de

G. Lampeas

University of Patras, Laboratory of Technology and Strength of Materials, Department of Mechanical Engineering and Aeronautics, 26500 Rion, Patras, Greece

identification tool is a powerful tool in understanding the effects of various damage scenarios on the time response data and together with the numerical model provides a valuable input for model-assisted probability of detection (MAPOD).

Nomenclature

A_p	Ripple amplitude
A_{st}	Amplitude attenuation
D	Diameter
D	Damaged state (subscript)
DI	Damage index
E	Modulus of elasticity
F	Frequency
f	Filtered (subscript)
f_a	Actuation frequency
f_c	Cut-off frequency
G	Shear modulus
H	Thickness
H	Healthy state (subscript)
i, j, k	Index
$I(x, y)$	Damage intensity as function of spatial coordinates
L	Length
lpf	Low-pass filter (subscript)
N	Filter order or total number
N_p	Number of actuator–sensor paths
$R(x, y)$	Relative distance as function of spatial coordinates
$s(t)$	Time signal of piezoelectric transducer
$S(\omega)$	Frequency domain signal of piezoelectric transducer
T	Time
t_{layer}	Layer thickness
t_{PWAS}	Thickness of piezoelectric wafer active sensor
W	Width
x, y	Spatial coordinates
$X(\omega)$	Frequency domain function of low-pass filter
B	Scaling
N	Poisson ratio
P	Correlation coefficient
ρ_v	Volumetric density
ω	Angular frequency
A0	First asymmetric guided wave
AS	Application scenario
CFRP	Carbon fibre-reinforced plastic
GUI	Graphical user interface
IS	Integration scenario
MAPOD	Model-assisted probability of detection

PWAS	Piezoelectric wafer active sensor
S0	First symmetric guided wave
SEM	Spectral element method
SS-FEM	Stacked-shell finite element method

1 Introduction

The objective of application scenario 6 (AS06) of the SARISTU project is to develop a tool to assess an impact damage in a composite structure. The assessment relies on the use of integrated ultrasonic sensors, and the composite structures under investigation are representative for a door surrounding structure. The methods developed should be able to identify *barely visible impact damages*, effectively translated to delaminations with a minimum radius 20 ± 5 mm: all smaller delaminations are in principle considered to be too small to be detected reliably, but all larger delaminations are expected to be found as they pose a safety risk for the component. The accuracy in location is specified to be ± 10 mm.

The door surrounding representative composite structure is a quasi-isotropic, prepreg-based composite skin structure stiffened with Omega stringers that are cobonded to the structure. Within AS06, flat plates with and without stiffeners are investigated as well as curved plates with stiffeners. The full-scale door surrounding structure, as manufactured in the integration scenario (IS13), is also curved.

The tool has to have the functionality to support the inspection process and decision-making process regarding maintenance and repair of structures. A graphical interface is a prerequisite for this. The graphical user interface should allow the user to analyse data, choosing various options related to the type of analysis and region of interest, while not requesting in-depth knowledge on the algorithms implemented. It should also provide a clear output to be used in, for example (model-assisted) probability of detection—(MA)POD—analysis. Visualisation of the data and the potentially damaged area is an important element in the user interface.

The main principle of the damage assessment is that an acousto-ultrasonic signal is used to interrogate the structure. Typically, this implies a windowed wave packet containing a limited number (~ 3 – 10) of sine waves with a frequency in the order of 50–500 kHz. The signal is subsequently registered by a sensor positioned at some distance from the actuator. The way the signal is altered while travelling through the material forms the base of the damage assessment. The signal is also subjected to a number of environmental influences and noise. Signal processing techniques are applied to the raw data signals to reduce noise and eliminate crosstalk (the interference of signals of different channels, for example the actuation signal and the sensor signal channels).

Piezoelectric transducers are employed as actuators and sensors. Here, a network of transducers, referred to as a *workspace*, is considered, in which all transducers

can act as actuator and sensor. If one transducer is assigned as actuator, the others act as sensors. Each straight line from actuator to sensor is referred to as a *path*. A full coverage of paths for the area enclosed by the transducers is obtained by alternating the actuator. Note that each path provides information on the possible presence of damage close to the path, but only the combination of paths provides sufficient information to localise potentially damaged spot. This is partly caused by the reversibility assumption: it is assumed that switching the actuator and sensor for a path does not affect the resulting signal. Strictly taken, this assumption only holds for the pristine situation, since damage will introduce nonlinearities [1]. The assumption implies that the signal does not hold any information on the location of the possible damage on the path. For that reason, each path is only measured once, with each actuation frequency.

Damage assessment can be based on a single set of measurements (*unreferenced*) or on the comparison between measurements of the pristine condition and those of the current condition (*referenced*). The latter is used here, despite the fact that it may be difficult in practice to define the pristine state, as this state depends on environmental conditions: the pristine condition may not be representative if, for example, temperature, humidity or loading are different during the measurement of the current condition. However, the initial use of the tool is anticipated to be in the inspection phase, allowing to create a limited window of variability in the environmental condition: the aircraft will for example be on the ground, which provides some control on the environmental conditions.

Various algorithms are available to assess the presence of damage based on the comparison of pristine path signals and path signals from a structure potentially containing damage. The ability to identify damage depends on multiple factors, amongst which the frequency of actuation, the presence of stiffeners or transitions on a path and the location of the damage. An assessment of the performance of a large number of algorithms is therefore carried out. This assessment is briefly discussed in this paper.

Initially, flat panels without stiffeners are used to test the methods, both experimentally and numerically. This is motivated by the fact that the propagation of guided waves in a structure built from anisotropic layers is not well understood, in particular the response to the presence of damage and transitions such as a stiffener. Numerical models can assist in shedding light on the phenomena occurring when a wave travels through the material and encounters a flaw or transition in thickness or fibre orientation. Two numerical methods are implemented: the *spectral element model* (SEM) and a *stacked-shell finite element model* (SS-FEM).

2 Signal Processing and Damage Identification

The first task of the software developed for the acousto-ultrasonic damage identification is to load the data from a pristine and a potentially damaged case. This can either be data from experiments or from numerical models. In the first case, a

number of signal processing steps are required to prepare the data for the actual damage identification. This paper does not intend to discuss the origin of some of the distorting effects that are filtered during the signal processing phase, but merely presents the solution as it is implemented. There are three important signal processing steps:

1. Distortion of first few measurement points,
2. Zero offset and
3. Electro-magnetic crosstalk.

The first two are dealt with rather straightforwardly. The first few points (from experience, the default value is set to 5) are ignored by setting them to zero. Note that this corresponds to a time of 0.4 ns, given a typical sampling frequency of 12 MHz. The zero offset is corrected by subtracting the mean value (excluding the first few points that were already set to zero) from the signal.

The electro-magnetic crosstalk poses more challenges. Without going in further details, it can be stated that the length of the part of the sensor signal that is affected by the crosstalk is related to the actuation frequency and the number of cycles in a burst—be it not directly. A pragmatic approach would be to simply ignore the part of the signal that is affected by the crosstalk. However, in some cases, the real response of the sensor starts before the effect of the crosstalk has vanished.

To this end, a filter routine is implemented. It is assumed that the crosstalk signal mainly contains the actuation frequency. This is a reasonable, but not entirely correct assumption, as was shown by Moix-Bonet in a technical report issued in the SARISTU project [2]. The problem with using a more accurate representation of the actuation signal is that the number of cycles in the crosstalk signal does not correspond to the number of cycles in the actuation signal (6 against 5 cycles). Filtering only the actuation frequency will leave some high-frequency components behind, but these are small compared to the actual sensor signal. Evidently, the actuation frequency will also be present in the sensor signal, leading to a part of the actual sensor signal being unintendently filtered in case there is overlap between the crosstalk signal and the actual sensor signal. The overlap, if present, is small for the cases investigated, justifying the assumption that the filtering will not affect the damage identification. A flow chart of the filter routine is presented in Fig. 1.

The steps in the routine are visualised in Fig. 2. First, the raw signal (Fig. 2a) is loaded, after which a low-pass filter is applied with a cut-off frequency f_c of (by default) 150 % of the actuation frequency f_a (Fig. 2b). The software allows us to use different models for the low-pass filter—essentially, those offered by MATLAB. The filtered signal is shown in Fig. 2c, which is subtracted from the original signal (Fig. 2a), yielding the filtered signal in Fig. 2d. The experimental data from a flat panel with stiffeners are used for this illustration. An actuation frequency of 80 kHz was used, leading to a cut-off frequency of 120 kHz. The maximum ripple in the passband ($f < f_c$) is set to 1 dB, while the attenuation of 80 dB is used for the stop band ($f > f_c$).

Once the raw data are processed, the damage identification algorithms can be applied. The approach followed corresponds with the signal correlation analysis

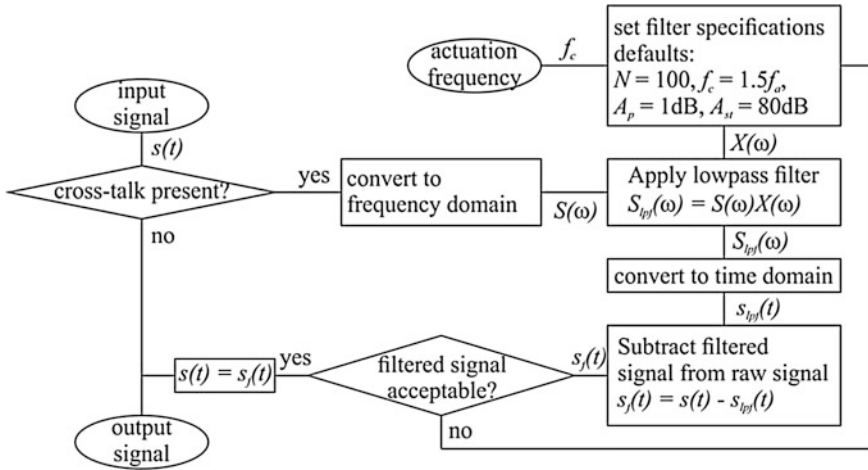


Fig. 1 Flow chart of the electro-mechanical crosstalk filter

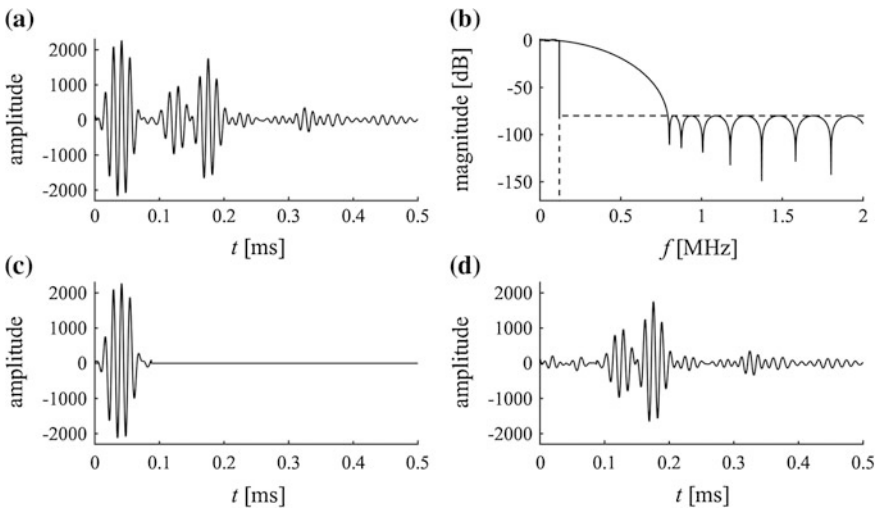


Fig. 2 Graphical overview of the crosstalk routine. Raw signal from experimental data from a flat test panel with Omega stringers, actuation frequency 80 kHz, cut-off frequency 120 kHz, passband ripple 1 dB and stop band amplitude attenuation 80 dB. **a** The raw signal; **b** the low-pass filter; **c** the low-pass filtered signal; and **d** the raw signal minus the low-pass filtered signal

technique as described by Su and Ye [1]. First, a grid is defined, overlaying the panel. The damage intensity $I(x,y)$ at each grid point (x,y) is calculated, by assuming a certain area of influence of the actuator–sensor paths. The damage intensity is defined as follows:

$$I(x, y) = \sum_{k=1}^{N_p} (1 - \rho_k) \left(\frac{\beta - R(x, y)}{\beta - 1} \right) \tag{1}$$

where ρ_k being the correlation coefficient of the k th actuator–sensor path, N_p the number of paths, β the scaling factor determining the area of influence and $R(x, y)$ defined as:

$$R(x, y) = \begin{cases} \frac{\sqrt{(x-x_i)^2+(y-y_i)^2} + \sqrt{(x-x_j)^2+(y-y_j)^2}}{\sqrt{(x_i-x_j)^2+(y_i-y_j)^2}} & \text{for } R(x, y) < \beta \\ \beta & \text{for } R(x, y) \geq \beta \end{cases} \tag{2}$$

where (x_i, y_i) and (x_j, y_j) indicate the locations of transducer i and j , respectively. Typically, β is equal to 1.05. Su and Ye [1] use the correlation coefficient as an indicator of damage. The correlation coefficient equals one if there is no damage and is lower than one if there is damage (as the correlation between the signals will be less).

The correlation function is not the only possible indicator of damage: there are many methods to calculate a damage index (DI). Fourteen methods are implemented and tested on their performance [3] next to the method based on the correlation coefficient. The damage indices are based on signal’s intensity, time of an event (e.g. time of flight), frequency domain expressions, signal energy, etc. In every method, attributes of baseline (healthy) and currently acquired (unknown health state) signals are compared to identify potential change in the structural characteristics, which in turn would be an indication of damage. The performance depends on the type of damage (i.e. how the signal is affected) and on the actuation frequency. It is therefore difficult, if not impossible, to formulate definite conclusions on the performance.

The methodologies implemented, along with their mathematical formulas, are presented in Table 1. This allows the user to mutually compare methods and select the best performing method for the case under investigation. An issue to address is that the damage index that is calculated in most methods gives a value of zero if no damage is present and tends to infinity (theoretically, in practice a large number) if there is damage. The following relation applies between the value of the correlation coefficient and the damage index:

$$\rho_k = \frac{1}{DI + 1} \tag{3}$$

The only exceptions are the signal amplitude peak ratio (SAPR) method and the ratio of covariance matrix eigenvalues (RCME) method. In case of the SAPR method, the damage index equals 1, rather than 0 in case of no damage, but also tends to infinity in case of damage: the ‘+1’ in the denominator of Eq. 3 is dropped. The RCME method gives a value between 1 and 0 for the healthy and damaged

Table 1 Damage identification algorithms implemented in the software

	Method name	Abbr.	Mathematical formula
1	Correlation coefficient	CC	$\rho = \frac{\sum_{i=1}^N S_{H,i} S_{D,i} - \sum_{i=1}^N S_{H,i} \sum_{i=1}^N S_{D,i}}{\sqrt{\sum_{i=1}^N S_{H,i}^2 - (\sum_{i=1}^N S_{H,i})^2} \cdot \sqrt{\sum_{i=1}^N S_{D,i}^2 - (\sum_{i=1}^N S_{D,i})^2}}$
2	Signal amplitude peak ratio	SAPR	$DI = \frac{\max[S_H]}{\max[S_D]}$
3	Signal amplitude peak squared percentage differences	SAPS	$DI = \left(\frac{\max[S_H] - \max[S_D]}{\max[S_H]} \right)^2$
4	Signal amplitude hilbert transform maximum	SAHM	$DI = \left \frac{\max[H[S_H]] - \max[H[S_D]]}{\max[H[S_H]]} \right $
5	Signal sum of squared differences	SSSD	$DI = \frac{\sum (S_H - S_D)^2}{\sum S_H^2}$
6	Welch-based power spectral density	WPSD	$DI = \frac{\left \int_0^{2/f_{ex}} PW[S_D] df - \int_0^{2/f_{ex}} PW[S_H] df \right }{\int_0^{2/f_{ex}} PW[S_H] df}$
7	Welch-based transfer function	WTF	$DI = \frac{\left \int_0^{2/f_{ex}} TF[S_D] df - \int_0^{2/f_{ex}} TF[S_H] df \right }{\int_0^{2/f_{ex}} TF[S_H] df}$
8	Parametric (AR-based) power spectral density	ARPSD	$DI = \frac{\left \int_0^{2/f_{ex}} PAR[S_D] df - \int_0^{2/f_{ex}} PAR[S_H] df \right }{\int_0^{2/f_{ex}} PAR[S_H] df}$
9	Parametric (AR-based) resonance frequency differences	ARRFD	$DI = \frac{\left f_{peak}^H - f_{peak}^D \right }{f_{peak}^H}$ $f_{peak}^{H,D} = \underset{f}{\operatorname{argmax}} [PAR[S_{H,D}(f)]]$
10	Parametric (AR-based) chi-squared statistic	ARCS	$DI = \delta P^T \cdot \delta C \cdot \delta P$ $\delta P = P_H - P_D; \delta C = C_H + C_D$
11	Cross-correlation-based TOF percentage difference	CCTOF	$DI = \frac{ t_{\max} CC^H - t_{\max} CC^D }{t_{\max} CC^H}$ $t_{\max CC}^{H,D} = \underset{t}{\operatorname{argmax}} [CC_{H,D}(t)]$
12	Cross-correlation maximum percentage difference	CCMPD	$DI = \frac{ \max[CC_H] - \max[CC_D] }{\max[CC_H]}$
13	Hilbert transform-based TOF percentage difference	HTOF	$DI = \frac{ t_{\max H}^H - t_{\max H}^D }{t_{\max H}^H}$ $t_{\max CC}^{H,D} = \underset{t}{\operatorname{argmax}} [H[S_{H,D}(t)]]$
14	Discrete wavelet transform approximation coefficient-based DI	DWTC	$DI = \frac{\sum (DWT[S_H] - DWT[S_D])^2}{\sum DWT[S_H]^2}$
15	Ratio of covariance matrix eigenvalues	RCME	$\rho = 1 - \frac{\lambda_2}{\lambda_1}$

state, respectively, like the correlation coefficient. Using Eq. 3 allows to use any damage indicator in combination with the damage intensity $I(x,y)$ as defined in Eq. 1.

3 Software with Graphical User Interface

The routines to convert the raw data signals to a coloured contour plot indicating possible damage locations are embedded in a software package with a graphical user interface (GUI). The user can quickly analyse a set of measured responses, without having to be an expert in the signal processing and damage identification algorithms. It is however also possible to tune many of the variables, allowing a more experienced user to perform a more detailed analysis of the data.

Both experimental and numerical data can be analysed with the GUI. It is therefore, for example, possible to run a series of numerical analysis to investigate the effect of specific damage characteristics on the capability of the damage identification process. A better understanding of these effects will enhance the interpretation of experimental results (Sect. 6). An example of the analysis of data from numerical models is presented in Sect. 5.

The GUI is structured in three sections: a section with buttons to toggle between the different user control panels; a section for the user control panels; and a section for graphical representations. There are five different user control panels, overlaying each other and allowing the user to control the operations applied to the data. These panels are as follows:

1. The file load panel,
2. The preprocessor panel,
3. The algorithms panel,
4. The data visualisation panel, and
5. The export panel.

Some additional functionality is embedded in the part with the graphical representation, as well as in the part of the menu block. Note that one can only proceed to the other sections of the software once a complete data set is loaded.

3.1 File Load

The software is developed to handle different types of input. Data that can be loaded are experimental data from the ScanGenie system as used by the DLR and especially Airbus, experimental data from measurements from the University of Siegen and numerical data from the models from the University of Siegen and the University of Patras. The format of the data is different. Hence, the user first needs to select the type of data. A distinction is made between geometrical data and

signals from the transducers. Although currently not implemented, an additional functionality is scheduled to be implemented to specify the geometrical properties (partly) manually.

The signals from the transducers are restructured to obtain a memory efficient and logical structure. The memory efficiency is significantly higher than the default structure of the ScanGenie MATLAB export; this contains a fair amount of redundancy, since the actuator signal is stored for each path, also if the sensor signal from another path is obtained from the very same actuator signal. In general, a number of transducer act as sensor each time a transducer is acting as actuator. All sensor signals of a single actuation cycle are saved together with the actuator signal of that cycle. This avoids redundancy and in the end allows the user to load multiple cases at once, without running into memory-related errors or slow functioning of the computer.



Fig. 3 File load panel. The file containing the geometric information is selected in the *top part*; once loaded, the *lower part* of the panel becomes active and the signal data files can be specified and loaded

The panel in the software with all the options for loading the geometry and data files is shown in Fig. 3. Note that a geometry file must first be loaded before it is possible to load data files. Moreover, it is possible to analyse data files without a reference or baseline file, although no damage identification algorithms are implemented for this case, leaving only a limited number of functions available in the visualisation section. Finally, one can also choose to load a configuration. A file saved from a previous analysis is then loaded. It can contain anything from just the geometry to the damage identification data. The ‘save’ button allows to save the data that is in the program at that moment, creating a configuration file. This allows the user to create a restart point at any time wanted.

3.2 *Preprocessor*

The signal processing steps described in Section 2 of this paper can be activated in this part of the software (see Fig. 4). The user can decide to skip these, as, for example, the numerical data do not show electro-magnetic crosstalk. It is also possible to change settings of the signal processing steps, although it is recommended to follow the default settings if one is not familiar with the signal processing concepts.

The crosstalk filter takes the largest part of the preprocessor panel. Most graphical elements are related to settings of the filter and will not further be addressed here. It is however important to note that the filtering is first applied to a copy of the data and shown to the user in the graphical visualisation panel on the right-hand side of the GUI. Initially, only a limited set of signals is shown, due to the large amount of signals. The user can select other signals to be shown by selecting the signals in the list box next to the main graphical area. The filter is only applied upon acceptance by the user; the original data are overwritten by the filtered data, and the temporary data are deleted.

Finally, the grid for the damage plot has to be created. The default is a (nearly) square grid, with a density based on the dimensions of the workspace; the number of elements must be an integer number, and therefore, the edge lengths are set as close as possible to a square grid by default. The ratio of the grid dimensions can also be unconstrained, resulting in a rectangular grid, and the grid can also be based on edge size rather than on a number of elements in each direction. Again, the edge lengths are adjusted to obtain the nearest integer number for the number of elements along the domain edge.

3.3 *Algorithm*

Once the data have passed through the necessary signal processing steps, a damage identification method can be selected. The pop-up menu in this panel (see Fig. 5)



Fig. 4 Preprocessor panel. The signal processing steps are defined in the three sections on the *top* of the panel, whereas the creation of the grid for mapping the damage intensity is controlled in the *bottom section* of the panel

provides the possibility to select one of the algorithms listed in Table 1. It is not possible yet to select more than one damage identification algorithm, although this is foreseen to be implemented in future versions. Moreover, it is not yet possible to change any of the parameters of the algorithms. Although not all algorithms have variables that can be set, it may be of interest to fine tune specific algorithms.

The damage identification algorithms are applied to all combinations of reference and current data sets. If multiple reference data sets are used, the difference between these data sets can also be analysed, which gives an indication of the

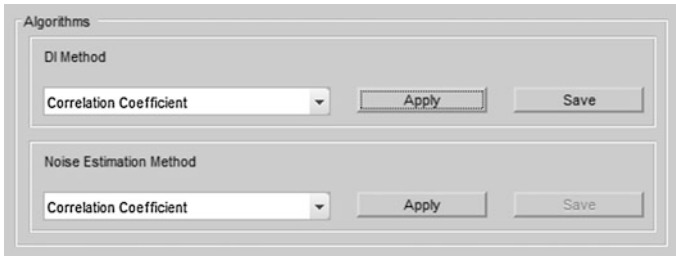


Fig. 5 Algorithm panel. The algorithms to be used for the damage identification and the noise estimation (if multiple reference files are loaded) can be selected individually

scatter of the measurements. The same algorithms are used for this noise estimation as are used for the damage identification, and again, all possible combinations of data sets are analysed.

3.4 Visualisation

Various aspects can be shown in the graphical representation area. The visualisation panel (Fig. 6) allows the user to control what is shown. First of all, the geometry can be shown. This means the geometry of the entire panel, but also that of (one of) the workspace(s). If a workspace is selected, the paths can be added to the plot.

Secondly, the raw data can be plot. The term ‘raw’ here refers to the time data of the transducers that are stored, after the signal processing if applied. The actuator and sensor signals are separated as are the reference and current state data, resulting in a set of four graphs. The raw data plot is the only plot that can be made if no reference data are loaded. In that case, only two graphs are shown.

The largest subpanel is the damage surface plot section. The damage intensity $I(x,y)$ is plotted as a coloured surface plot, using Eqs. 1 and 2. The colour indicates the intensity, where blue refers to a low intensity (no damage) and yellow to a high likelihood of damage. The absolute values of the damage intensities are given in the colour bar that is either positioned below or aside the main plot. It is possible to show the intensity for specific actuation frequencies, if multiple actuation frequencies are used. Note that in general only a single actuation frequency is used per actuator, such that an incomplete path coverage is obtained if not all actuation frequencies are included. Multiple damage indices per path are available if multiple actuation frequencies per actuator are used; the user can choose to plot the maximum, mean or minimum intensity in that case.

The intensity gives an indication of possible damage locations. However, it is up to the user to set a threshold, as the absolute value of the damage intensity depends on many variables, such as the type and location of the damage or the presence of other damages, and no physical interpretation is available to set a general threshold. A slider can be used to set the threshold. If a threshold is set, dynamic contour lines



Fig. 6 Visualisation panel. This panel permits the user to control the graphical output displayed on the right-hand side of the GUI (not visible here)

are plot, indicating the border between the intensities below and above the threshold. The contour lines are updated each time the threshold is changed. A potentially damaged area can be selected by choosing a proper threshold value. Square markers are added as well, indicating peaks in the damage intensity. A peak is defined as a damage intensity value that is higher than the damage intensity of all its surrounding points and higher than a preset (hardcoded) threshold. Once the threshold is set, an area enclosed by a contour can be selected. The damage index of the area is subsequently stored. The user can now either focus further on the area

enclosed in the contour, by isolating it, or focus on other areas by excluding this. The colour scaling of the intensity is updated after isolation or exclusion of the area enclosed by the contour. Thus, in case of the latter, secondary potentially damaged areas can more easily be identified: this procedure offers unique possibilities for assessing multiple damages in the structure.

3.5 Export

The damage intensity indicates *possible* locations for the damage: to investigate the likelihood that it concerns a real damage, the data need to be exported and subsequently imported in a probability of detection analysis. The data to export are controlled in the export panel (Fig. 7). Prior to be allowed to enter this section, at



Fig. 7 Export panel. Two different output files, both in ASCII format, can be exported. The content of the files can be adapted by (de)activating the checkboxes

least one damaged area must be identified, by setting a threshold for the damage intensity and selecting an area enclosed by a contour. Two different export files, both in ASCII format, can be exported:

1. Data file containing information on the damage intensity in the contour(s) selected and
2. Data file containing the damage indices for each path.

The files start with a header providing information on the data files used, the date the file was created and the dates it was appended (if). The damage extent file then contains by default four elements for each contour that is exported:

1. The damage intensity integrated over the area enclosed by the contour,
2. The area enclosed by the contour,
3. The coordinates of the peaks in the contour and their values, and
4. The centre coordinates of all grid elements in the contour and their damage intensity value

The user can chose to deselect each of these items to exclude them from being exported. The damage path file contains per path in a workspace the following information:

1. The transducer number of the actuator,
2. The transducer number of the sensor,
3. The actuation frequency,
4. The damage index of the path,
5. The x -coordinate of the actuator,
6. The y -coordinate of the actuator,
7. The x -coordinate of the sensor,
8. The y -coordinate of the sensor and
9. The length of the path

Again, the user can control which of these items are included in the export file.

3.6 *Graphs*

The data visualisation panel covers approximately 50 % of the GUI. It mainly contains space to display graphs, either from the geometry, the signals or the damage intensity. Some additional functionality is added to facilitate the export of graphs. The buttons ‘undock’ and ‘redock’ are used to transfer the data to a separate figure window and vice versa. The user can manipulate the graphical material in the separate figure, using the built-in MATLAB functionalities. The graphical visualisation panel is shown in Fig. 12.

4 Numerical Modelling

Developing a finite element (FE) model can contribute to the understanding of the scattering phenomena of Lamb waves upon encountering structural damage. Standard FE model has a number of limitations that should be taken into account:

- A fine FE mesh, comprising at least 10 or even more nodes per Lamb wavelength, is a prerequisite to deliver good spatial precision;
- A laminate may have to be divided into sublaminates in thickness, to properly represent interlaminar damage and damage into the individual laminas;
- The time step for dynamic calculation should be less than the ratio of the minimum distance of any two adjoining nodes to the maximum wave velocity (often the velocity of the S0 mode).

Two solutions to overcome these limitations are presented in this paper. The first method is the spectral element method (SEM), whereas the second relies on a stacked-shell FE model.

4.1 SEM

The spectral element method combines the advantages of global pseudospectral methods with the flexibility of finite element methods. One of the first use-cases can be found at [4], dealing with fluid dynamics. The use of the spectral element method in time domain for structural health monitoring in general is described in [5]. The SEM model used in this work is described in detail in [6]. The SEM model uses a flat shell spectral element, based on first-order plate theory (first-order shear deformation theory). As the structure is modelled with one element over the thickness for undamaged parts, the number of degrees of freedom is comparably small. The nodes for these elements are not distributed evenly, but follow the roots of a Gauss–Lobatto–Legendre polynomial. Their irregular distribution combined with the use of Lagrange interpolation polynomials as shape functions makes it possible to use less elements than necessary for traditional low-order FEM. In particular for higher frequencies and bigger structures, this is an advantage. Moreover, a band-like structure of system matrices (like mass matrix) enables a reduction of computational costs in time domain. Nevertheless to introduce delamination, the one element over the thickness has to be divided into two new elements, each comprising of multiple layers of the composite material; if a delamination is modelled between layer k and $k + 1$, then the bottom element contains layer 1 to k and the top element layers $k + 1$ to N , where N is the total number of layers. Note that this division causes more system matrix elements to differ from zero. The calculation of contact forces prohibits penetration of the two elements above and below the delamination. More information about the delamination introduction can be found in [7]. For the implementation of SEM, the

plate-like character has to be ensured. For this, the relation of size of the damage and plate thickness is important.

4.2 Stacked-Shell FEM

The three basic requirements mentioned above usually result in high demands in terms of computational cost, particularly for large composite structures. To balance the need for precision and computational efficiency, the ‘stacked-shell’ or ‘layered shell’ approach under the finite element method (SS-FEM) is investigated for the Lamb wave simulation. The explicit FE code LS-DYNA is used for this purpose. In the stacked-shell approach, the composite laminates are represented by a discrete number of sublaminates modelled as shell elements, which can be tied together with solid cohesive elements or contact interface elements with cohesive zone properties. These interfaces have the capability to behave as matrix interlayers which connect the plies and are capable to fail during the simulation when appropriate conditions are met, either by introducing a cohesive law in the interface, or by setting appropriate interface strength limits. A schematic of the stacked-shell approach is given in Fig. 8. It should be noted that the number of layers in the SS-FEM model does not need to correspond to the number lamina in the composite, although in the model implemented here, each lamina is represented by a shell layer.

The stacked-shell approach is capable of representing accurately the out-of-plane behaviour of laminated structures, while maintaining the higher computational efficiency and simplicity of conventional shell approaches. The main advantage comes from the disconnection of the mesh discretization requirements of the in-plane and the through-thickness directions of the structure; the mesh density of

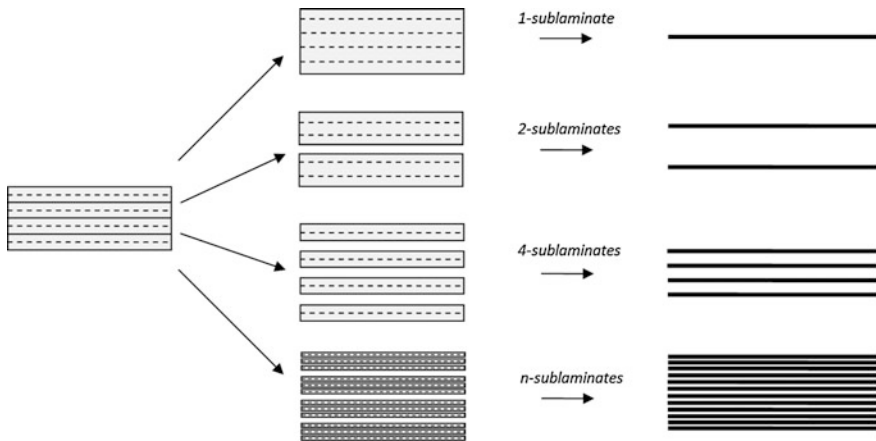


Fig. 8 Schematic of the stacked-shell approach. A 4-layer laminate is modelled by stacking 1-, 2-, 4- and n -sublaminates

the shell elements is independent of the through-thickness mesh density, whereas the latter normally dictates a significantly more dense mesh than the in-plane requirements demand. Furthermore, using the layered shell approach, an intrinsic delamination capability is introduced, i.e. delaminated areas can be easily and properly represented.

5 Use-Cases

Within the SARISTU project, a plate-like exemplary structure was used for experimental investigations, which can be compared to numerical simulations. This structure exhibits 11 layers of CFRP made from M21 matrix with T800S fibres. The properties of a layer of unidirectional composite material are listed in Table 2, the dimensions of the test panel and the piezoelectric transducers (PWAS—piezoelectric wafer active sensors), including their position in Table 3, whereas a schematic of the plate is presented in Fig. 9. The transducers are cobonded on the plate, making a shortening of the critical path on the production line possible. The actuator is excited by a five-cycle sinusoidal tone bursts, modulated utilising a Hanning window. Central frequency of 120 kHz (SS-FEM) and 250 kHz (SEM) is used.

5.1 Definition of the Test Cases

Various damage scenarios were implemented in the numerical models to test the damage identification algorithms in the software, as well as the capabilities of the

Table 2 Material properties of the CFRP [11 layers, (45, 0, -45, 90, 0, 90, 0, 90, -45, 0, 45), M21 matrix with T800 fibres]

E_x (GPa)	$E_y = E_z$ (GPa)	$G_{xy} = G_{xz}$ (GPa)	G_{yz} (GPa)	$\nu_{xy} = \nu_{xz}$ []	ν_{yz} []	ρ_v [$\text{kg}\cdot\text{m}^{-3}$]
157	8.5	4.2	2.2	0.35	0.53	1580

Table 3 Dimensions. Panel and the transducers including their location

	Symbol	Unit	Value			
Length	L	mm	500			
Width	W	mm	500			
Thickness	H	mm	2.024			
Layer thickness	t_{layer}	mm	0,184			
PWAS transducer	d	mm	6.35			
	t_{PWAS}	mm	0.25			
	x	mm	100	400		
	y	mm	100	200	300	400

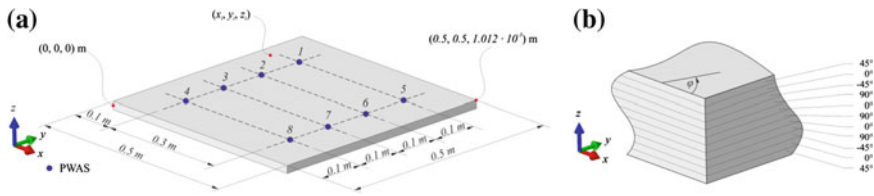


Fig. 9 Set-up of the SARISTU plate-like structure. Test structure for software, experiment and numerical simulations; **a** geometry with its dimensions and locations of the transducers; **b** the lay-up with orientation of the different layers

Table 4 Damage scenarios implemented in the numerical models

Scenario	Model	Shape	Dimensions	Location	Layer
1	SEM + experiment	Elliptical	$d_1 = 28 \text{ mm}$, $d_2 = 19 \text{ mm}$, $\theta = 45^\circ$	$(x,y) = (0.25,0.2)$	9–10
2	SS-FEM	Round	$d = 10 \text{ mm}$	$(x,y) = (0.25,0.4)$	1–2
3	SS-FEM	Round	$d = 10 \text{ mm}$	$(x,y) = (0.25,0.4)$	1–5
4	SS-FEM	Round	$d = 30 \text{ mm}$	$(x,y) = (0.25,0.4)$	10–11
5	SS-FEM	Round	$d = 30 \text{ mm}$	$(x,y) = (0.25,0.4)$	7–11

graphical representation of the damage offered by the software. The damage scenario of the SEM analysis is based on the experimentally introduced damage and differs from the damage scenarios in the SS-FEM model. The details are given in Table 4. Note that the composite layers are numbered from top to bottom.

5.2 Results of SEM Model

To validate the SEM model, measurements of the undamaged structure are compared with results from the SEM. An exemplary timeline is shown in Fig. 10. After a path independent scaling for all transducers, the wave packages of the different modes can be represented properly. To compare the results of the damaged structure, the software, described in Sect. 4, was used. The correlation coefficient has been exported for all paths. The path between PWAS 6 and PWAS 4 is directly crossing the damage zone, while all other paths starting at actuator 6 are not. As it can be seen in Fig. 11, the agreement between SEM simulation and experiment is fairly good.

The usage of SEM simulation data with the developed software is possible very easily. With its help, a damage localisation can be realised. As the simulation does not include noise, even from data of a single frequency, the localisation results are excellent. The output of the software is shown in Fig. 12. The red contour line is set by the user by increasing the threshold up to the desired level. It corresponds to the damage implemented in the numerical model, as defined in Table 4.

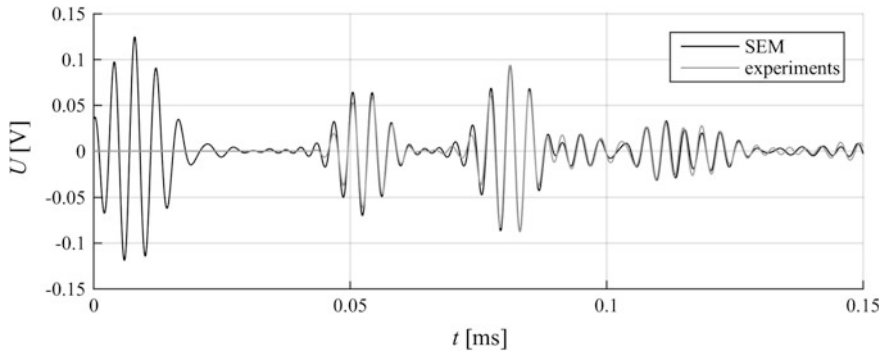


Fig. 10 Exemplary timeline to compare experimental and numerical SEM results. The different modes and their amplitudes can be simulated properly. An adaptation of the signal amplitude is necessary. This correction factor is the same for all sensing transducers

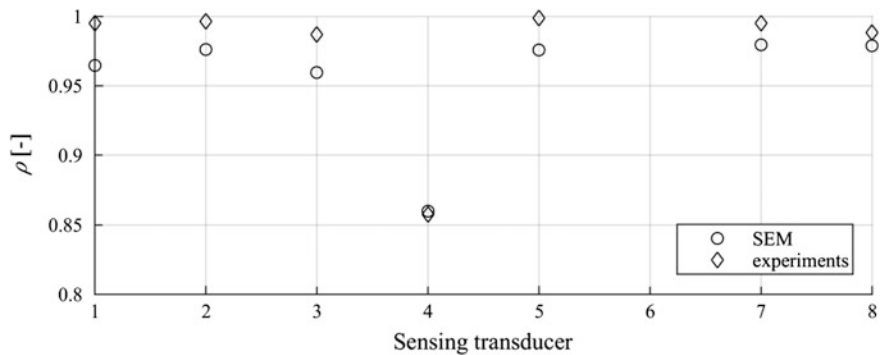


Fig. 11 Comparison of damage indices for SEM simulation and experiment. While for paths, which are not directly crossing the delamination, the experimental data results in slightly lower correlation coefficient, for the direct path, simulation and experimental results show an excellent agreement

5.3 Results of the SS-FEM Model

An indicative comparison of the numerical and experimental time response results for the undamaged case, in which transducer 1 is the actuator and transducers 2–8 are sensors, is presented in Fig. 13. The presented results refer to calculated strain values at the position of sensor 3.

From the indicative comparison of Fig. 13, it arises that the methodology seems effective for the simulation of Lamb wave propagation: a qualitative correspondence of the results is obtained. However, the need for further development and optimisation of the simulation parameters is obvious as well. Improvements are

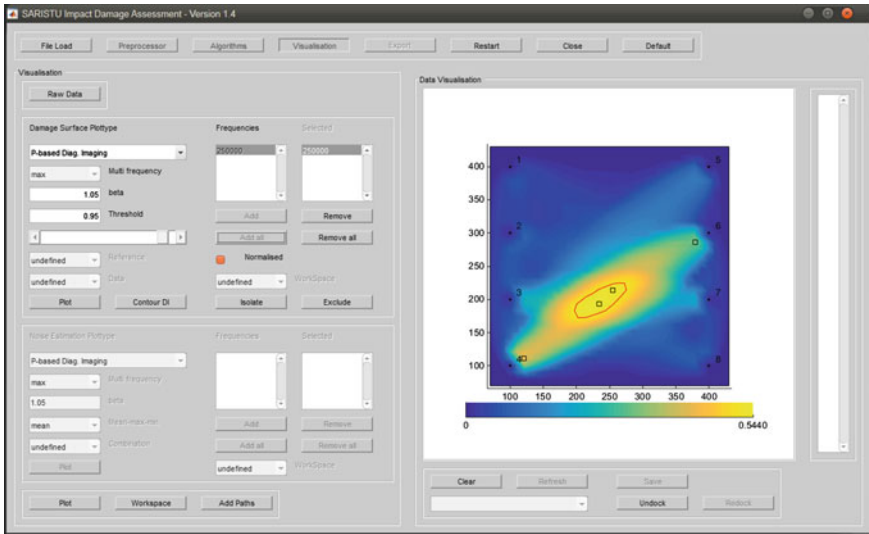


Fig. 12 Output of the software for damage localisation. Using the SEM simulations as input, the software detects the damage with the help of the correlation coefficient and localises it with path-based methods. The *red contour line* is set by the user by increasing the threshold level to the desired level. The *square markers* indicate maxima in the damage intensity

foreseen to be achieved by means of mesh convergence studies for the in-plane mesh density and an optimisation of the number of sublaminates. Finally, a calibration of the simulation parameters, to match the real properties of the panel from which the experimental results are obtained, will further diminish the differences between the simulation and the experimental results.

The time response results of transducer 5 for the various damage cases investigated are compared to the response of that transducer for a pristine structure. The results are depicted in Fig. 14. The ultrasonic wave generated by the actuator (here transducer 1) crosses the damage, that is located in the middle of the path from transducer 1–5.

It can be observed, from Fig. 14, that the signal from the damaged panels is slightly reduced compared to the signal of the pristine panel. The amplitude reduction is marginal; the only visible difference is from the case of a damage with a 30 mm diameter located at the top of the laminate (the side of the transducers).

5.4 Discussion of the Numerical Models

A first analysis of the two numerical models indicates that a higher accuracy is obtained using the SEM model. The SS-FEM model is less accurate when

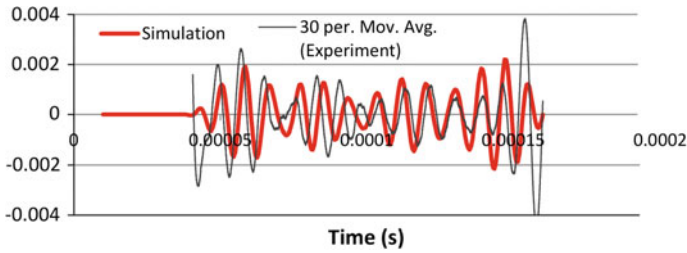


Fig. 13 Comparison of numerical and experimental time response. Results of transducer 3 for the undamaged flat panel case

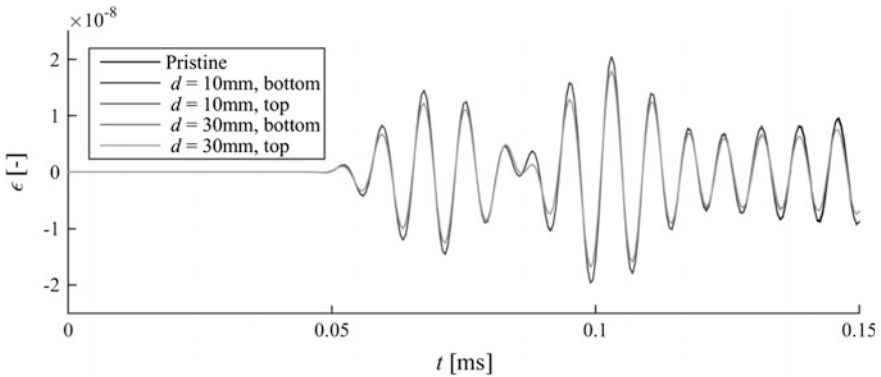


Fig. 14 Comparison of numerical responses between undamaged and damaged flat panels for transducer 5. The damage is located in the middle of the path from transducer 1 (which acts as the actuator) to 5. Only the response of the case with the 30 mm delamination located at the top differs visually from the pristine response

compared to the experimental results. However, the SEM model only allows for the modelling of a single-layer delamination in the material, whereas a complex, but far more realistic, multilayer delamination can be modelled in the SS-FEM model. This by itself offers valuable opportunities to enhance the damage identification, since it is to be expected that the response to a delamination with a certain area, located between two layers close to the surface, will cause a similar damage intensity, but different response when compared to a delamination spanning multiple layers, but with a smaller area. The SS-FEM indicates a difference in the response depending on the location of the damage, but unfortunately, the results show that the difference lies in being detected or not. However, it must be noted that the SS-FEM results are based on a limited set of paths, with only transducer 1 acting as an actuator. At this point, it is difficult to compare the numerical models in more detail, since a different type of damage is implemented (see Table 4).

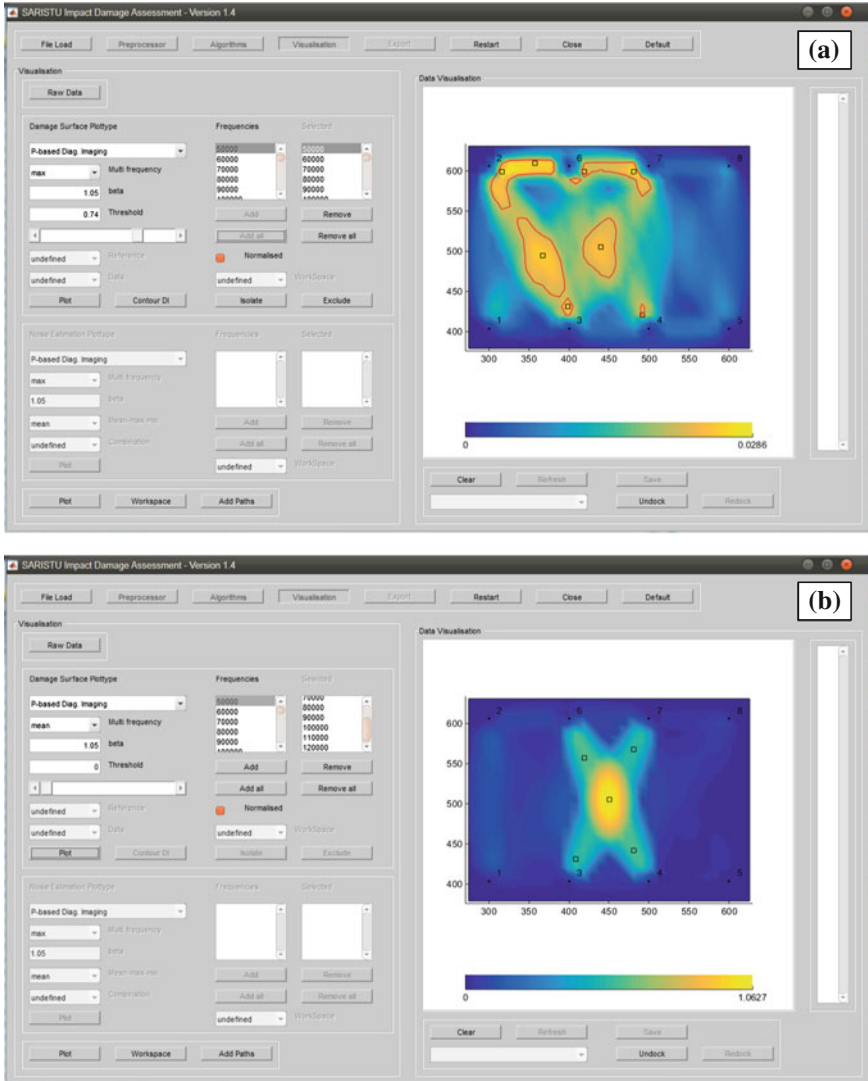


Fig. 15 Output of the software damage identification. Experimental data of a flat panel with Omega stringers is used. Actuation frequencies from 50 to 300 kHz are used. The *red contours* indicate potentially damaged area. The damage is located in the centre of the image. **a** Using all actuation frequencies and the maximum value of the correlation coefficient for each actuator–sensor path; **b** using a subset of the actuation frequencies and the mean value of the correlation coefficient for each path

5.5 Results of Experimental Data

The software is also tested on experimental results in order to assess the influence of environmental conditions on the capability of the damage identification algorithms. The environmental conditions are mainly limited to the higher level of noise that is observed in experiments compared to numerical models, since the experiments were performed in a relatively well-controlled laboratory environment. Instead of using a single actuation frequency, multiple actuation frequencies were used, ranging from 50 to 300 kHz. The resulting damage intensity plot, based on the correlation coefficient damage identification algorithm, is shown in Fig. 15. The difference between using all frequencies or a subset (all frequencies up to 120 kHz) and using the maximum or the mean of the correlation coefficient of each actuator–sensor path is highlighted clearly by the two damage intensity plots in Fig. 15: the top figure shows a lot of disturbance making it difficult to unambiguously identify the location of the damage, whereas the lower figure clearly indicates the location of the damage. The choices of the actuation frequencies, the damage identification method and other settings are clearly relevant, but sometime hard to make beforehand. The software allows to analyse the effect of these choices in a quick and convenient manner.

6 Conclusion

It has been shown that the software for the damage identification discussed in this paper offers a convenient manner of analysis of data from monitoring tests, based on a network of piezoelectric transducers. The software can handle both numerical and experimental data, making it suitable to be used in both the design phase of a monitoring system as well as in the use phase. The user can analyse the data without an in-depth knowledge on the signal processing algorithms that are implemented, but can at the same time adjust all kind of settings, making the software a powerful tool both for a quick scan of measured data and for a more elaborate investigation by an experienced user (in the field of signal processing).

The numerical models show different results: the SEM model is more accurate compared to the SS-FEM model in terms of correspondence to the experimental results. The SS-FEM promises a more detailed representation of the damage, by allowing the damage to span different layers. The accuracy of the SS-FEM method is however still not at the desired level.

Acknowledgments The research leading to these results has received funding from the European Union's Seventh Framework Programme for research, technological development and demonstration under Grant Agreement No 284562.

References

1. Su Z, Ye L (2009) Identification of damage using lamb waves—from fundamentals to applications. Lecture notes in applied and computational mechanics, vol 48. Springer, Berlin
2. Moix-Bonet M (2012) Guidelines for the signal processing algorithm. Technical Report of SARISTU project
3. Michaelides PG (2013) Pitch catch algorithms preliminary analysis. Technical Report of SARISTU project
4. Patera AT (1984) A spectral element method for fluid dynamics—laminar flow in a channel expansion. *J Comput Phys* 54:468–488
5. Ostachowicz W, Kudela P, Krawczuk M, Zak A (2012) Guided waves in structures for SHM—the time-domain spectral element method. Wiley, New York
6. Schulte RT (2010) Modellierung und Simulation von wellenbasierten Structural Health Monitoring – Systemen mit der Spektral-Elemente Methode. PhD thesis, University of Siegen (2010)
7. Jung H, Schulte RT, Fritzen, C-P (2011) Interaction of elastic waves with delaminations in CFRP structures: a numerical study using the spectral element method. In: Chang F-K (eds) Structural health monitoring, 8th international workshop on structural health monitoring, Stanford, September 2011, pp 2576–2583

Manufacturing of CFRP Panels with Integrated Sensor Network and Contacting of the Network

Dimitrios Habas, Daniel Schmidt and Nicolas Dobmann

Abstract Structural health monitoring systems are considered nowadays as ones of the most promising technologies for improving the economics of commercial aircrafts. An ideal SHM system could be capable of indicating the type of damage, its size, location, severity, and estimate the remaining lifetime of the structure. Until now, several technological approaches have been implemented under the scope of SHM systems. One of the most efficient methodologies is the application of guided ultrasonic waves (Lamb waves). This paper will focus on the Lamb wave technique and describe the road map followed along with the instrumentation developed to process the derived signals. For the implementation of such system, two types of piezoelectric sensors have been tackled. The “Smart Layer” provided by Acellent and the DuraAct™ sensors fabricated by Invent GmbH. The “Smart Layer” is based on polyimide layers. At specific spots, PZT are embedded in the layer and they are connected to the main connector by means of a copper circuit. On the other hand, DuraAct™ sensors are piezocomposites which consist of piezoceramic materials embedded in a ductile polymer. In order to study the performance of these systems, physical demonstrators have been manufactured. Representative composite fuselage structures incorporating curved skin panels with omega stringers made from CFRP materials have been designed and produced. Arrays of both types of PZT sensors have been integrated onto these structures inserting by this mean sensors at certain positions which could identify a potential damage. After the finalization of the

D. Habas (✉)

Engineering, Research, Design and Development Directorate, Hellenic Aerospace Industry,
P.O. Box 23, 32009 Schimatari, Greece
e-mail: HABAS.Dimitrios@haicorp.com

D. Schmidt

German Aerospace Center, Institute of Composite Structures and Adaptive Systems,
Multifunctional Materials, Lilienthalplatz 7, 38108 Braunschweig, Germany
e-mail: daniel.schmidt@dlr.de

N. Dobmann

Airbus Group Innovations, Structures Engineering, Production & Aeromechanics,
Airbus-Allee 1, 28199 Bremen, Germany
e-mail: nicolas.dobmann@airbus.com

production process, the panels were impacted and a damage detection analysis was performed based on the acquired data of the Lamb wave propagation through the manufactured panels. Under this analysis, the two different sensor networks were evaluated in terms of reliability, repeatability, and probability of detection by determining the allowable damage size ($a_{90/95}$), which will be detailed in associated papers of AS06.

Nomenclature

AS0X	Application scenario number in the SARISTU project
CFRP	Carbon-fiber-reinforced plastic
GFRP	Glass-fiber-reinforced plastic
IS1X	Integration scenario number in the SARISTU project
PZT	Lead zirconate titanate
SHM	Structural health monitoring

1 Introduction

This document presents the manufacturing activities performed and the aeronautical structures produced in order to support the evaluation and validation process of the different types of ultrasonic sensors developed within AS06.

Knowledge of the structural integrity is of significant importance in determining the operational status of a system, like an aircraft. Currently, the fundamental approach that is followed is the regular and scheduled inspections of the aircraft, a solution that is undoubtedly costly and time-consuming. Airlines often have to retire aircrafts from service for days or even weeks in order to perform maintenance, which clearly affects profit margins of the operators. According to economical studies, over 25 % of aircraft life cycle cost is due to maintenance and inspections of the airframe. Nowadays, the application of composite materials in primary structures is steadily increasing. CFRP incorporates a lot of competencies, but on the other hand, assessment of potential damage can often be more complex for CFRP structures. SHM systems may become a way to cope with these increased complexities while simultaneously decreasing costly maintenance inspections and provide a foundation for possible further savings.

SARISTU is a European research project that, among other topics, addresses the physical integration of smart intelligent structural concepts. Several sensing technologies are investigated and developed within the project under the objective of implementing a system with high level of maturity. Additionally, guidelines are defined in order to design a system that could be integrated to all aerospace structures. Within SARISTU and more specifically the activities undertaken in AS06, a SHM network has been analyzed based on ultrasonic wave propagation techniques. PZT sensors transmit and receive guided waves (Lamb waves) which

can be applied to detect defects in structural components. Arrays of built-in piezoelectric patches have been used as sensors and actuators to excite and receive ultrasonic waves in order to characterize the location and extent of structural damage in large structures by analyzing signal paths.

Within AS06 two types of sensors were used, the “Smart Layer” provided by Acellent Technologies Inc. and the DuraAct™ sensors fabricated by Invent GmbH. The objective of the work performed was to verify the functionality of the developed systems with respect to their damage assessment level, sensor integration, quality assurance, placement methodologies, etc. Meeting all these requirements, several structures were designed and manufactured. The conceptual approach, which will be thoroughly presented in this paper, was to develop representative and realistic fuselage aerostructures which could carry the aforementioned sensors. As a final goal, these structures would be subjected to impact testing in order to evaluate the behavior and performance of the entire monitoring system, activities described in associated documents.

2 Development of Composite Aerostructures

2.1 Goal

Designing and manufacturing composite structures that would address all the specifications set in a serial production was one of the major requirements that should be satisfied. On this basis, not only limitations/capabilities regarding the sensors’ placement would be identified but also beneficial results could be derived for the sensors’ sustainability in scaled aeronautical components.

2.2 Conceptual Design of Composite Aerostructures

The aeronautical structures that were manufactured referred to two identical curved panels made from CFRP. The material that was utilized applied to a typical aerospace composite prepreg provided by Hexcel, named M21-T800S. Trying to simulate a section of a fuselage from a regional aircraft, each panel incorporated a skin with five omega stringers. Furthermore, two metallic frames were attached to the structure assembled with blind bolts. The frames were fabricated from Al.Al. 7075-T62 (per QQ-a-250/13) formed to “Z” section. Since the overall configuration of the panels was based on the structures that were developed in IS13, details such as component thicknesses, stacking sequences and items (omega stringers and metallic frames) spacing were already defined (Fig. 1).

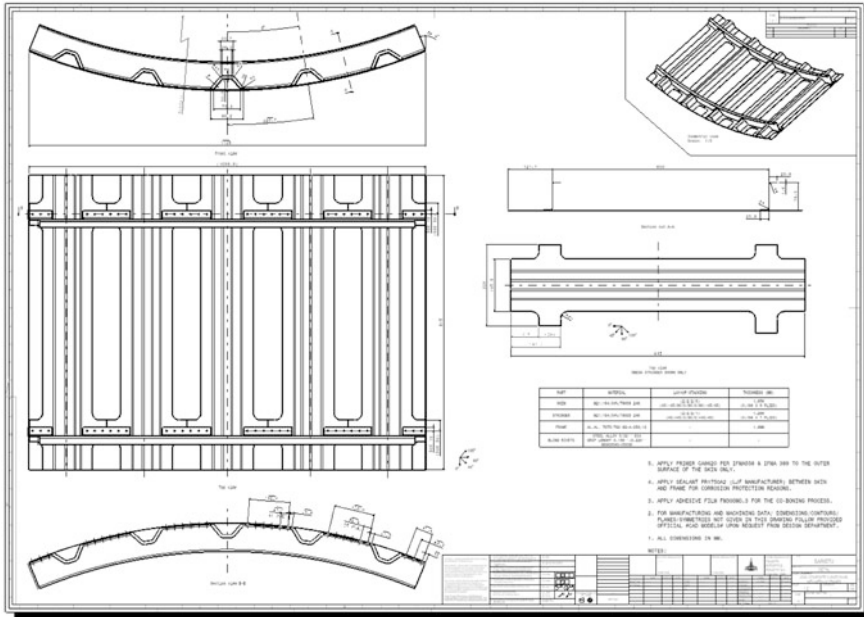


Fig. 1 Technical drawing of curved panel

Important information concerning both developed structures is as follows:

- Outer radius 1140 mm and panels’ dimensions are 1100 mm × 815 mm
- Stacking sequences:
 - Skin: [+45/−45/90/0/90/0/90/−45/ + 45] → Thickness 1.656 mm
 - Stinger: [+45/−45/0/90/0/−45/ + 45] → Thickness 1.288mm
- Type of blind bolts applied MS90354S-0503D (steel alloy)

For the integration of the omega stringers to the skin, cobonding technology was applied. This technique incorporated the placement of already cured stringers to soft (uncured) skin. To reassure the bonding integrity, FM300 film adhesive was also attached beneath the area of each stringer foot.

2.3 Manufacturing Process of Composite Aerostructures

For the needs of AS06, a mold with a metallic backing structure was manufactured in order to support all the production activities. Onto this structure, a bended plate was welded to get the necessary surface for all the manufacturing steps both for the omega stringers production and the cobonding process. The metallic framework incorporated tensors to provide the capability to manipulate and deform the

geometry and the radius of the panel. Also this deformation functionality of the mold could be used to prevent the estimated springback effect by modifying the surface from its theoretical final shape (Fig; 2).

At the first step, the open hat (omega) stringers were fabricated with the assistance of aligned metallic molds (Fig. 3). Manual hand layup technique was applied as manufacturing process.

The stringers were produced in two batches of five elements and maintained in storage before trimming them down to their final size. For this process, a dedicated trimming tool was manufactured (Figs. 4, 5 and 6).

The final step consisted of utilizing FM300 for the positioning of the stringers to the skin.

Fig. 2 Backing support structure for CFRP panels

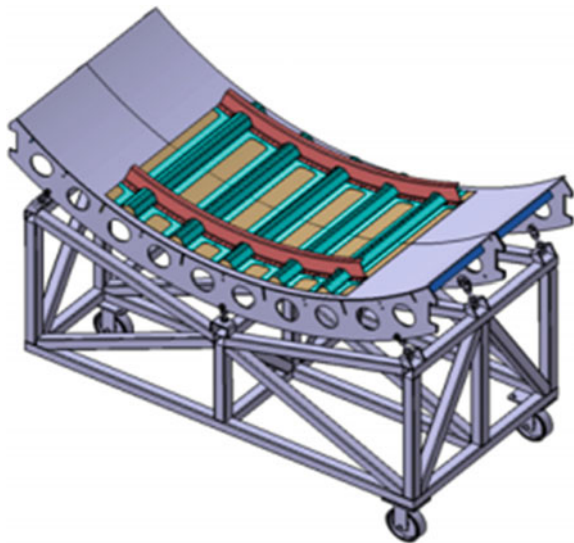
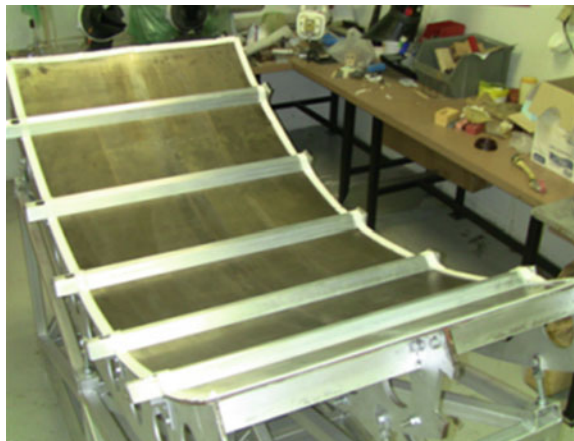


Fig. 3 Omega stringer mandrels situated on the mold



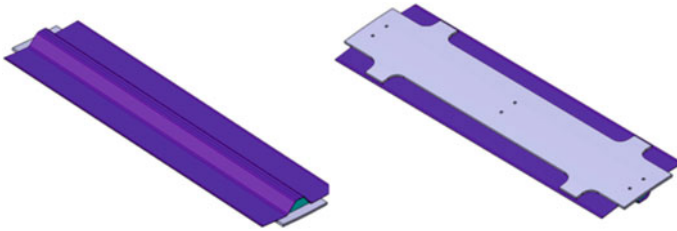
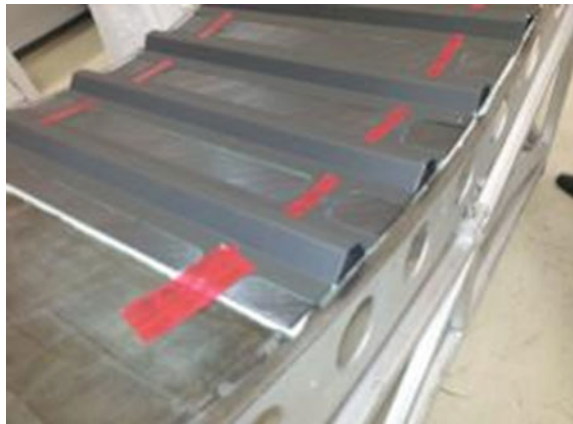


Fig. 4 Trimming fixture for omega stringers

Fig. 5 Film adhesive application



Fig. 6 Stringers' arrangement



2.4 Sensor Technology and Integration

As actuators and sensors, piezoelectric transducers are commonly used for Lamb wave-based structural health monitoring. These transducers are made of thin, monolithic piezoceramic plates or disks. For SHM applications, a sensor array is commercially produced and distributed by the company Acellent Technologies Inc. under the name Smart Layer®. This array consists of piezoceramic disks with a diameter of 6.35 mm. The disks are bonded to a polyimide film, which provides the electrical connection and a protection from the environment. The electrical connection is printed on the polyimide film, such as flexible circuits, and covered by another film for electrical insulation.

“Smart Layer” was prepared for cobonding by surface treatment and enclosure in strips of VICOTEX 6376/40 GFRP prepreg and release film. The GFRP enclosure provides insulation and a protective cover for the sensor layers, while the release film ensures the interface area of the layer remains unattached to the structure (Figs. 7 and 8).

A promising alternative is to utilize the DuraAct™ technology to increase the reliability of brittle piezoceramics [1, 2]. This piezocomposite consists of a piezoceramic completely embedded in a ductile polymer. Further components such as electrodes, electrical connection, and insulation are also embedded into the composite. This DuraAct™ piezocomposite technology is utilized for the manufacturing of the SHM sensor arrays. A piezoceramic disk with a diameter of 6 mm and a

Fig. 7 “Smart Layer” enclosed in VICOTEX 6376/40 GFRP prepreg



Fig. 8 Fully prepared “Smart Layer”



thickness of 0.2 mm is embedded into the piezocomposite. Each piezocomposite is connected by thin cables with a stranded. As shown in Fig. 9, five piezocomposites as well as the cables are embedded into an unvulcanized EPDM (ethylene propylene diene monomer). The EPDM holds the piezocomposites and the cables in place and is an elastic protection from the environment. After the application process, the EPDM vulcanizes within the curing process of the CFRP.

Before proceeding to the final curing of the structure, the “Smart Layer” and the DuraAct™ sensors were fixed to the panels (Fig. 10).

2.5 Sensors Quality Control

In order to investigate the behavior and durability of both sensor networks and the potential impact of the curing process on their performance, the capacitance of the “Smart Layer” and the “DuraAct™” sensors was recorded. The measurements were implemented with a typical ICR meter at the frequency of 1 kHz. The data acquired, illustrated that both types of sensors withstood the cobonding process, in terms of pressure and temperature (Fig. 11).

Since no significant deviation concerning the capacitance of the sensors was exhibited after the production process, the two monitoring networks can be considered as reliable and durable surface-mounted systems.

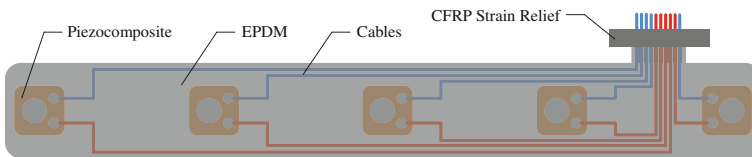


Fig. 9 Sensor array based on DuraAct™ piezocomposite technology

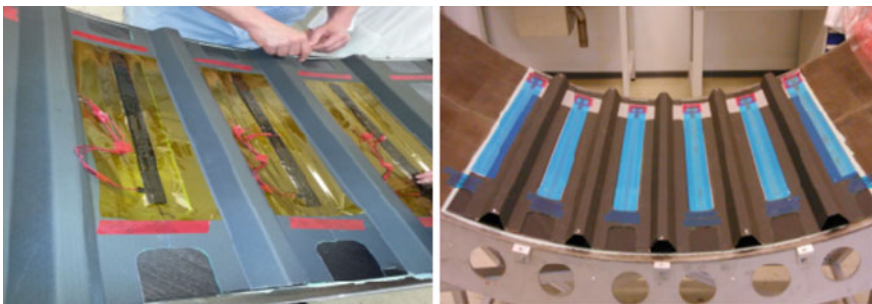


Fig. 10 Attachment of PZT sensors (*left* DuraAct™, *right* “Smart Layer”)

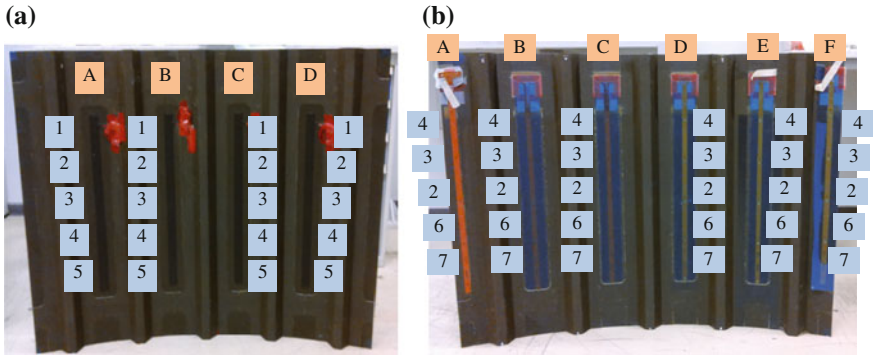


Fig. 11 Sensors numbering for capacitance measurements. **a** Capacitance data obtained for the DuraAct™ sensors range around 2 nF. **b** Capacitance data obtained for the “Smart Layer” sensors range around 1.7 nF

2.6 Finalization of Composite Structures

In continuation to the evaluation of the PZT after the autoclave process, the metallic frames were assembled with Huck “Unimatic” blind bolts and both panels were painted with a layer of primer, following the standard manufacturing procedures of aircraft structures (Fig. 12).

2.7 Contacting of the Sensor Network

The applied electrical interconnection to the “Smart Layers,” aims to permit quick installation and minimized effect on host structure and curing process. This is realized by a basic concept employing an entirely flat interface area on the layers, which is kept unattached to the host structure by a release film. Due to thickness



Fig. 12 Final composite structures

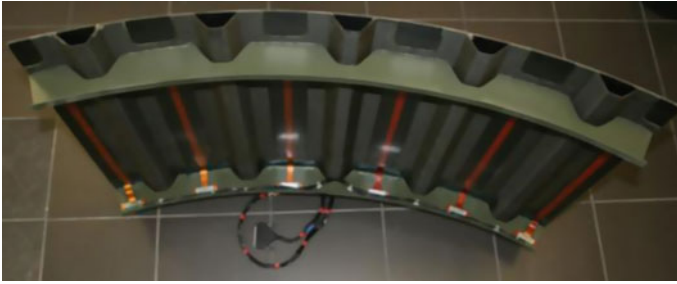


Fig. 13 Contacted sensor network “Smart Layer” panel

increases and flexibility in the interface area of “Smart Layers,” the pressure-varying effect on the host structure during the curing process is very low. As a result, the general effect on host structure properties is, respectively, minor.

Contacting of the sensor network established by “Smart Layers” is conducted by bolting the interface areas to a counterpart element. This counterpart element permits the transfer of all “Smart Layer” circuit paths to cabling connecting the sensor network to the interrogation unit.

For the cabling of the SHM network, wiring harnesses with a specific length are prefabricated. To connect the SHM network with the hardware system (ScanGenie®—Acellent Technologies Inc.), one end of the wiring harnesses is equipped with Sub-D 37 connectors. In case of the DuraAct™ arrays, the wiring harnesses are applied on the frames and connected to the SHM arrays using sealed crimp splices (Fig. 13).

3 Conclusion

Within this paper, the manufacturing activities performed within AS06 are highlighted. Two fuselage subcomponents have been produced in order to evaluate the efficiency and reliability of the sensors’ system. Under the scope of providing added value, results to the entire project the composite structures have been fabricated taken into consideration outputs of other AS, so that the final data to be easily correlated. The behavior of the SHM networks was closely monitored throughout the whole manufacturing process and fruitful outputs were derived. Utilizing standard production techniques, both types of sensors (“Smart Layer” and DuraAct™) exhibited sufficient performance to the curing process of the structures. The positioning and integration procedure were also smooth without any implications establishing a significant advantage to the application of the monitoring systems to the serial production of different aeronautical structures.

Moving the technology a step further, the composite structures will be impacted and multiple types of damages, in terms of location and size, will be induced. Based

on the guided ultrasonic wave methodology and the analytical approaches developed within AS06, the designed sensors will identify and assess the damages, either delaminations or debondings. The experimental results will be further elaborated and the benefits and drawbacks of the each damage identification algorithms will be recognized.

Acknowledgments The research leading to these results has received funding from the European Union's Seventh Framework Programme for research, technological development, and demonstration under Grant Agreement No 284562.

References

1. Wierach P (2002) Elektromechanisches Funktionsmodul, German Patent DE10051784C1
2. Wierach P (2010) Development of piezocomposites for adaptive systems. PhD-Thesis, Technische Universität Braunschweig, DLR-Forschungsbericht DLR-FB 2010-23

Damage Assessment in Composite Structures Based on Acousto-Ultrasonics— Evaluation of Performance

**Maria Moix-Bonet, Peter Wierach, Richard Loendersloot
and Martin Bach**

Abstract This work focuses on the damage detection and assessment of barely visible impact damages that occur after impacting a composite stiffened structure through the acousto-ultrasonics technique. Delaminations and debondings have been introduced in two stiffened panels and afterwards interrogated with an integrated structural health monitoring (SHM) network within the project. In order to perform the damage assessment, a methodology for the identification of damages along with a graphical user interface is developed. The performance of the developed methodology is evaluated and a damage assessment based on several damage indices and actuation frequencies is carried out. The most suitable parameters for the given structure and damage types are finally reported.

1 Introduction

Carbon-fibre-reinforced polymer (CFRP) is gaining ground as preferred material for the construction of aircraft structures for, among other benefits, its light weight, fatigue and corrosion resistance. Despite its multiple advantages, composite

M. Moix-Bonet (✉) · P. Wierach
Institute of Composite Structures and Adaptive Systems, Multifunctional Materials, German
Aerospace Center, Lilienthalplatz 7, 38108 Braunschweig, Germany
e-mail: maria.moix-bonet@dlr.de

P. Wierach
e-mail: peter.wierach@dlr.de

R. Loendersloot
University of Twente, Engineering Technology, Dynamics Based Maintenance, P.O. Box
217, 7500 AE Enschede, The Netherlands
e-mail: r.loendersloot@utwente.nl

M. Bach
Structures Engineering, Production and Aeromechanics, Airbus Group Innovations,
Airbus-Allee 1, 28199 Bremen, Germany
e-mail: martin.bach@airbus.com

laminates are prone to suffer delaminations as well as barely visible impact damages. The impact damage proneness is currently addressed with a damage tolerant design and an increase of the non-destructive inspections (NDI). Structural health monitoring (SHM) could be used as a complement of NDI, enabling a decrease in maintenance efforts.

A SHM technique is developed, based on acousto-ultrasonics applied in a permanently installed piezoelectric transducer network, which actuates and receives ultrasonic guided waves to provide information concerning the structure integrity [1]. A reliable damage detection procedure is currently under development so that AU represents a feasible alternative to the currently used NDI in aircraft structures.

Damage detection in aircraft structures based on ultrasonic guided waves has been extensively reported in the literature over the past decade. Matt monitored the bonded joint of a composite wing-to-spar with ultrasonic guided waves [2]. Zhao detected and localized rivet cracks and corrosion on an aircraft aluminium wing with a reconstruction algorithm for probabilistic inspection of defect [3]. Wu used the probability-based diagnostic imaging with a composite panel with bonded T-stringers, combining several frequencies for an improved damage assessment [4]. Despite the numerous studies, a method that achieves a reliable damage assessment on large composite structures with complex geometries has yet to be developed. The challenge relies on the multiple wave modes, wave reflections and conversions, non-isotropic behaviour or high wave attenuation that occurs during ultrasonic guided wave propagation in composite structures.

The presented work reports the results obtained with a developed methodology for the identification of damages along with a graphical user interface. A probability-based diagnostic imaging based on several damage indices and actuation frequencies is carried out on two stiffened composite panels, in which realistic BVID has been introduced.

2 Experimental Set-up: Manufactured Structures and Impact Campaign

Two identical composite structures, each with 3 cobonded omega stringers and 40 cobonded piezoelectric transducers, have been manufactured within the project. The skin presents constant thickness, a quasi-isotropic layup of 2 mm thickness and a slight curvature with an outer radius of 2075 mm. The stringers have a constant omega cross section and a 2-mm quasi-isotropic layup [5]. A schematic of the panel design with a detail of the stringer profile is shown in Fig. 1.

Each panel is equipped with different transducer types, SMARTLayer[®] and DuraAct[™], which conform the SHM network. The cobonding process as well as the durability of both transducer types has been previously studied [6]. The network is arranged in a total of 8 arrays containing 5 transducers each. The arrays are positioned parallel to the stringers and 2 adjacent transducers are 120 mm apart on

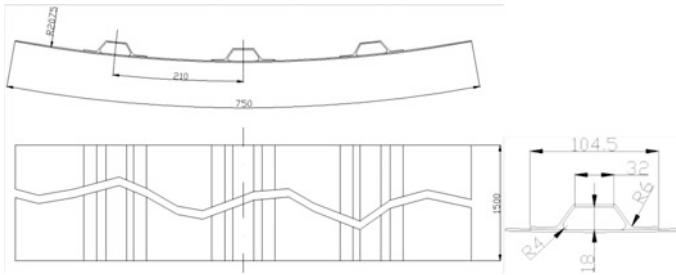


Fig. 1 Design of the CFRP panel without SHM network [5]



Fig. 2 Stiffened composite structure with 40 cobonded piezoelectric SMARTLayer[®] transducers

the direction parallel to the stringer and 200 mm on the direction perpendicular to it. The structure with the cobonded SMARTLayer[®] network is depicted in Fig. 2.

The impact campaign consists in several impacts introduced from the outer skin in each panel with energies between the 20 and the 34 J applied by means of a hemispherical projectile with a diameter of 25 mm. This amount of energy targets barely visible impact damages and debondings on the given structures. The area of the introduced damages measures between 518 and 690 mm²: The diameter of a round damage with this area measures 27.6 ± 2 mm. The introduced defects have been afterwards measured with traditional NDI methods. The NDI results are used as a reference to determine the performance of the damage identification algorithms. The geometry, SHM network and impact positions in one of the structures, as well as two of the defects inspected with NDI, are depicted in Fig. 3.

There are three types of damages, depending on their relative position within the structure:

- H-type damages are located under a stringer head
- S-type damages are located under a stringer foot and target a debonding between stringer and skin
- B-type damages are positioned on the skin, between SHM transducers

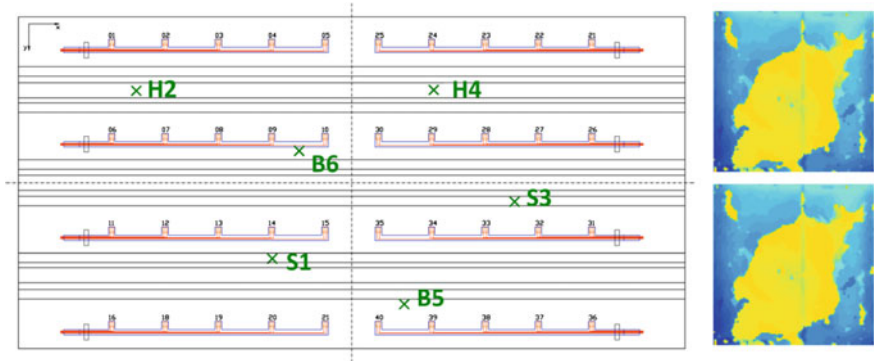


Fig. 3 Sketch of the structure and SMARTLayer[®] network with impact locations, indicated by the green crosses (left) and US scan of the damages (time of flight) H2 (right-up) and H4 (right-down)

The behaviour of the various damage types regarding the guided wave propagation is different in every case, and they have to be therefore considered.

3 Methodology: Signal Evaluation for Damage Assessment

In order to perform the damage assessment, a methodology for the identification of damages along with a graphical user interface has been developed within the study and is described in detail in Ref. [7]. The core of the damage identification algorithm is based on the probability-based diagnostic imaging method developed in Ref. [3]. First, a grid is defined, overlaying the panel. The damage intensity $I(x, y)$ at each grid point (x, y) is calculated, by assuming a certain area of influence of the actuator–sensor paths. The damage intensity is defined as:

$$I(x, y) = \sum_{k=1}^{N_p} (1 - \rho_k) \left(\frac{\beta - R(x, y)}{\beta - 1} \right) \tag{1}$$

with ρ_k being the damage index of the k th actuator–sensor path, N_p the number of paths, β the scaling factor determining the area of influence and $R(x, y)$ is defined as follows:

$$R(x, y) = \begin{cases} \frac{\sqrt{(x-x_i)^2+(y-y_i)^2} + \sqrt{(x-x_j)^2+(y-y_j)^2}}{\sqrt{(x_i-x_j)^2+(y_i-y_j)^2}} & \text{for } R(x, y) < \beta \\ \beta & \text{for } R(x, y) \geq \beta \end{cases} \tag{2}$$

where (x_i, y_i) and (x_j, y_j) indicate the locations of transducer i and j , respectively. Typically, β is equal to 1.05.

The damage assessment is carried out through comparison between a baseline, acquired with the structure in a pristine state, and the current signal, acquired in an unknown state of the structure. A change in the structure characteristics translates into a variation in the acquired signal, which shall be properly interpreted. In this chapter, it is supposed that the changes on the signal are only dependent on the appearance of damage.

The comparison between the two signals is quantified with a Damage Index (DI). In the developed damage identification tool, several DIs are implemented. The employed DI with their corresponding formulas can be found in the Appendix table and has been previously investigated in Ref. [8]. The DIs are based on various signal features, such as amplitude, time of flight, frequency domain features and signal energy. The methods implemented in the software are applied to the current case and the best performing DIs are afterwards reported.

The performance of the developed methodology is evaluated through comparison with the position and size of the damages observed with traditional NDT methods. An example of the analysis is depicted in Fig. 4. The structure and current impact being analysed are sketched on (a), while a comparison with the results obtained with traditional NDI and AU is presented in (b).

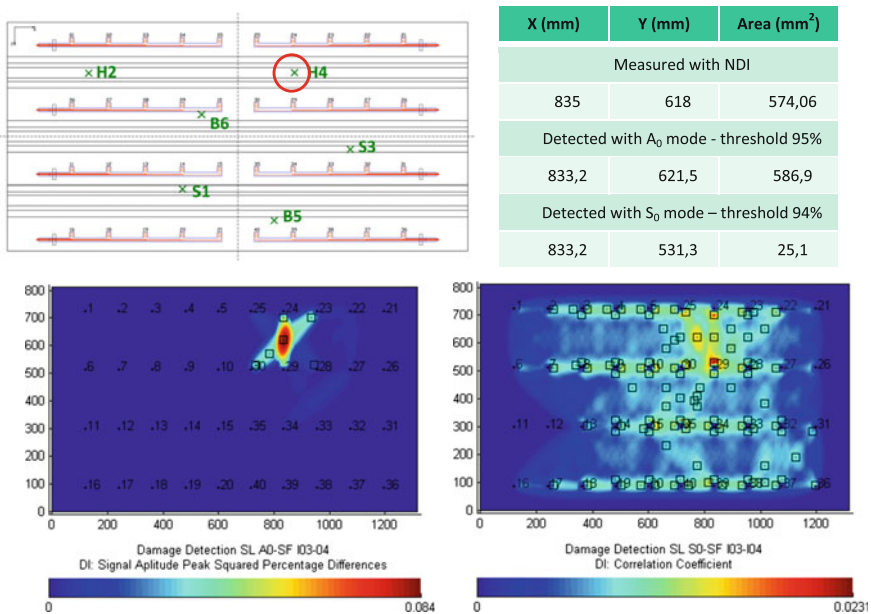
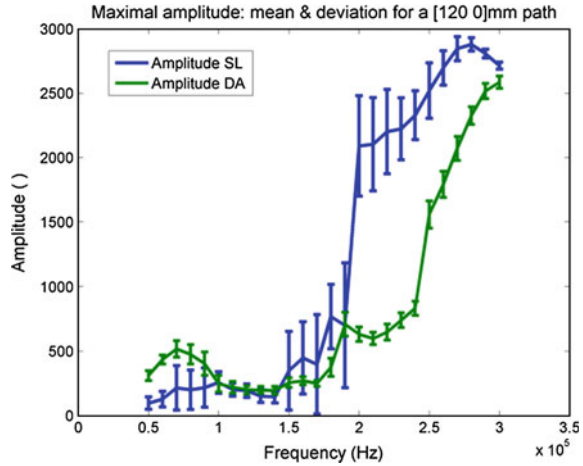


Fig. 4 SARISTU panel with SmartLayer[®] network and impact position (*up-left*). Damage detection between Impact 3 and Impact 4 at low (*down-left*) and high (*down-right*) frequencies

Fig. 5 Acquired Amplitude with SMARTLayer[®] and DuraAct[™] for a path parallel to stringer



The damage assessment in (c) is performed with signals acquired in a frequency range between 60 and 90 kHz, where the asymmetrical fundamental (A_0) mode is dominant, according to the Giurgiutiu theory of mode tuning [1]. The probability-based diagnostic plotted on the right is generated with the signal acquired between 200 and 250 kHz. In this frequency range, the symmetrical fundamental (S_0) mode has a dominant role.

The criteria to select the most appropriate frequencies were an appropriate-sensed amplitude, depicted in Fig. 5, and an isolated first arrival wave packet. Between 250 and 300 kHz, for example, in spite of the favourable received amplitude, the mode density is very high, hindering the damage detection with the selected damage identification method.

4 Results

4.1 Damage Index Selection

An initial research was carried out in order to evaluate the suitability of the implemented DIs. The analysis performed in Fig. 4 was reproduced for the 12 DIs and 8 damages. Two parameters were chosen to quantify the suitability of the DIs: the damaged-to-undamaged probability ratio and the damage localization error. The first consists of a ratio to evaluate the sensitivity of the DI in relation to the noise level. The ratio compares the maximal damage probability obtained with the identification algorithm when two baselines (no presence of damage) are compared and the maximal probability acquired when damage is present. The damage localization error, the second parameter, compares the damage locations in the x - and y -coordinates obtained with the traditional NDI methods and the ones obtained with the

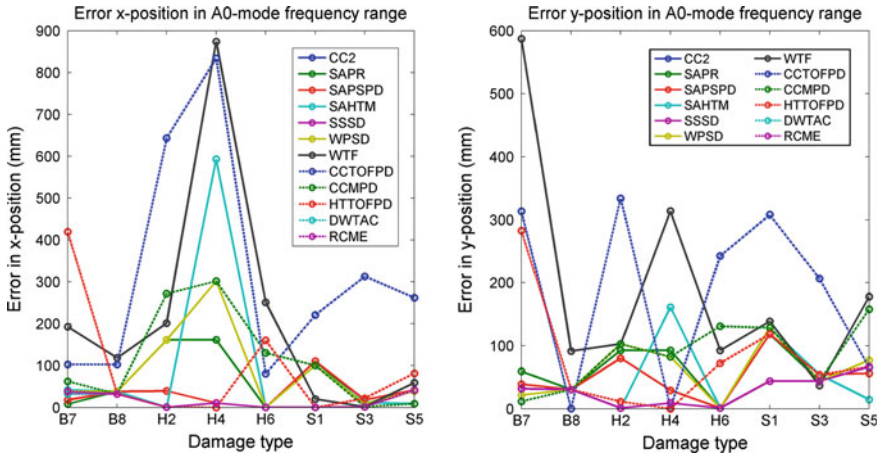


Fig. 6 Error in *x* (left) and *y* (right) location of the error depending on the damage type

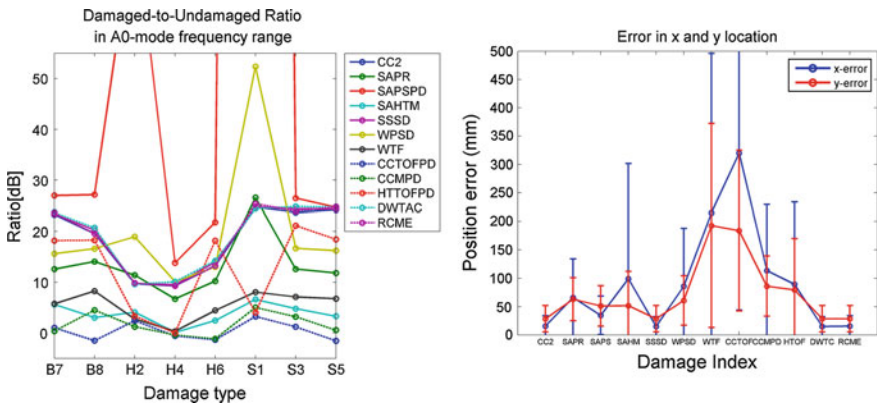


Fig. 7 Damaged-to-undamaged probability ratio (left) and error in location organized by DI (right)

damage identification algorithm. The damaged-to-undamaged probability ratio and the error of the defect location are plotted in Figs. 6 and 7.

The following DIs show a low sensitivity for all the damage types and high error in the damage localization for some of them and are therefore unsuitable to detect barely visible delaminations and debondings present in the given structure:

- Welch-based transfer function (WTF)
- Signal amplitude Hilbert transform maximum (SAHTM)
- Cross-correlation-based TOF percentage difference (CCTOFPD)
- Cross-correlation maximum percentage difference (CCMPD)

Moreover, two additional DIs present high errors in the location in specific damages:

- Hilbert transform-based TOF percentage difference (HTOFPD)
- Welch-based power spectral density (WPSD)

The 5 discarded DIs are based on 3 principles: the cross-correlation, the Hilbert transform and the Welch transfer function. The Hilbert transform is as sensitive to noise as to defects and is therefore not applicable for damage identification. The Welch transfer function is based on the spectral density. It is very challenging to find changes in a complex signal with multiple wave packets, solely considering the frequency domain information. The multiple wave packets present in the signal are affected differently by the presence of damages. Since time or phase shift is not uniform throughout the signal, the cross-correlation performed on the entire signal cannot be representative for damage identification purposes.

The DIs that effectively identify and locate damage are based on the maximal amplitude (SAPR, SAPS) or amplitude over the whole signal (SSSD, DWTC). The covariance matrix and the correlation coefficient are also sensitive to defects. Hence, these DIs are considered suitable for damage identification and employed in the following section.

4.2 *Parameter Optimization*

Only a single DI at a time has been taken into account in the previous section. In this section, the combination of parameters has been used in order to obtain a more reliable and sensitive identification algorithm. From the selected DIs in the initial research, the maximal DI value is taken for each path as input for the diagnostic imaging algorithm. The outcome is an improved ratio between the damage probability obtained in damaged and pristine states, as depicted in Fig. 8 (left). With this strategy, the location of the defect always corresponds to the most accurate from the available DI, as shown in Fig. 8 (right). The fusion of several DIs results in an improved sensitivity, maintaining the accuracy and the precision.

As shown in Fig. 8 (right), the error in the x -coordinate of the location is twice as low as that of the y -coordinate. This outcome can be caused by several reasons. Firstly, the density of transducers in the x -direction is 1.7 times higher than in the y -direction. The transducer density is a determining parameter for the localization accuracy. Secondly, the geometry of the structure has an influence on the damage detection capability of the algorithm: Between two adjacent transducers in the y -direction, there is always an omega stringer present.

Another general observation is especially low damage-to-undamaged probability ratio for the H-type damages detected in Fig. 8 (left). The detection of a H-type damage is mainly achieved through signals that travel across an omega stringers.

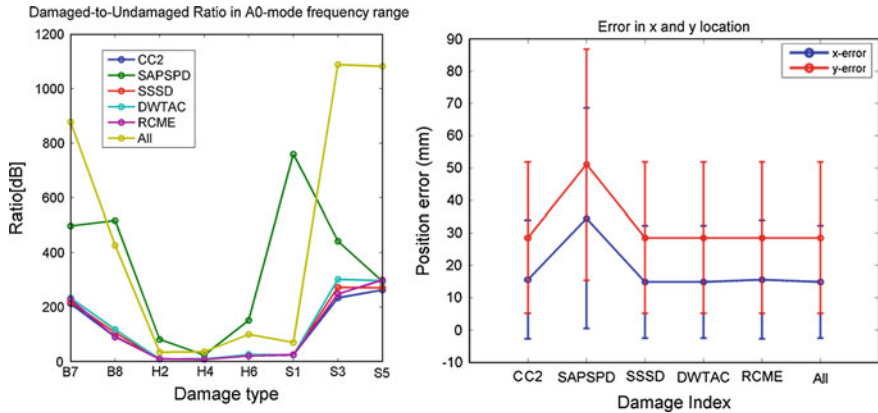
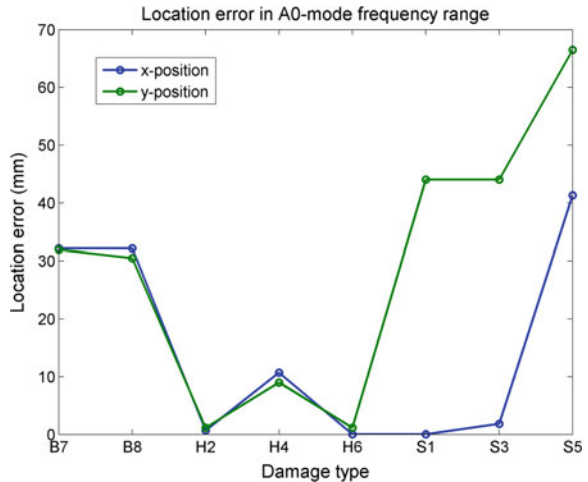


Fig. 8 Amplitude ratio between damaged and pristine signals (*left*) and mean and deviation of the localization error (*right*)

Fig. 9 Location error in *x*- and *y*-coordinates with maximal DI values



Waves propagating through the stringer have lower amplitudes and contain more wave packages due to reflections and mode conversions caused by the structure geometry, explaining the lower effect of the damage in the acquired signal. An example is depicted in Fig. 10 (right).

In Fig. 9, the accuracy obtained with the maximal value of DIs is shown. The localization of the B-type presents an error of more than 30 mm in both, the *x*- and *y*-coordinate. The B-type damage is mainly detected with horizontal paths; therefore, the *y*-location is normally erroneously estimated to be located at the transducer *y*-coordinate. The error in the *x*-coordinate is due to the tendency of the identification algorithm to show a higher amplitude near the transducers. These two effects

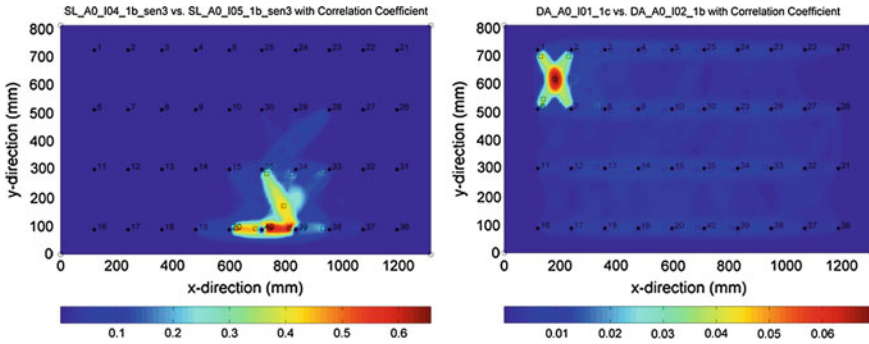


Fig. 10 Damage assessment of damage B7 (left) and H2 (right)

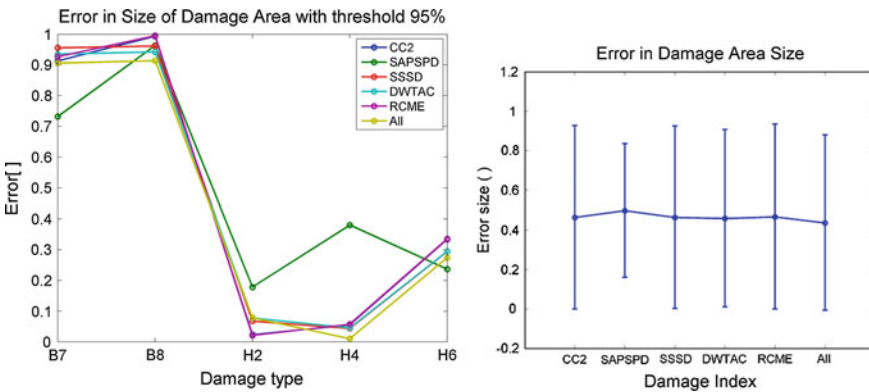


Fig. 11 Error in damage area size with a 95 % threshold (left) and error in damage area for each DI (right)

can be observed in the damage diagnostic of Fig. 10 (left). The y-location of the S-type damage, i.e. the debonding between skin and stringer, is also challenging for the algorithm. The cause lies again in the tendency to shift the maximal damage probability towards the transducer positions.

The identification and location of a damage can be performed in an unsupervised learning mode. However, a supervised learning mode is mandatory to carry out damage quantification [9]. Thus, a threshold shall be set in order to calculate the damage area. The best results have been obtained with a threshold of 94 %. This threshold means that the zone with probability values between the maximum probability and the 94 % of this maximum is considered the damaged area.

The average of the error made when estimating the size of a damage is higher than 40 % and the variation of the error is very high. The large dispersion is caused by the distinctive behaviour of the ultrasonic guided waves propagating through the

different damage types, as shown in Fig. 11. With the 94 % threshold, the H-type damages can be accurately quantified, with an error between 1 and 27 %, while the B-type has an error of around 90 %. The area of S-type damages could not be determined with traditional NDI and the results are therefore not presented. The high deviation indicates that a single threshold cannot suit all damage types.

5 Conclusion

The chapter exploits the possibilities of the developed damage identification methodology by applying it to the damage assessment of two stiffened composite panels. The methodology has been used to know and optimize the most suitable parameters for the analysis.

The damage identification algorithm is capable of identifying the 100 % of the introduced barely visible impact damages. It is possible to estimate the location of the damage with an error of approximately 15 mm in the x -coordinate and 30 mm in the y -coordinate. For the assessment of the damage size, a threshold is needed. An average of 42 % in the error of the damage area together with a high deviation indicates that the threshold should be set for each damage type.

The considerations and observations in this chapter can be a first step to improve the current damage identification algorithm and adapt it to the targeted structure. The amount of data from real damages was too limited to draw solid conclusions: the data generated during the impacting campaign of a door surrounding aircraft structure will be used to further analyse and improve the algorithm. The results obtained in this chapter constitute the experimental input data to perform a probability of detection (PoD) analysis on damage assessment of door surrounding areas by means of acousto-ultrasonics.

Acknowledgments The research leading to these results has received funding from the European Union's Seventh Framework Programme for research, technological development and demonstration under grant agreement no. 284562.

Appendix

See Table 1.

Table 1 Damage identification algorithms implemented in the software [7]

	Method name	Abbr.	Mathematical formula
1	Correlation coefficient	CC	$\rho = \frac{\sum_{i=1}^N S_{H,i} S_{D,i} - \sum_{i=1}^N S_{H,i} \sum_{i=1}^N S_{D,i}}{\sqrt{\sum_{i=1}^N S_{H,i}^2 - (\sum_{i=1}^N S_{H,i})^2} \cdot \sqrt{\sum_{i=1}^N S_{D,i}^2 - (\sum_{i=1}^N S_{D,i})^2}}$
2	Signal amplitude peak ratio	SAPR	$DI = \frac{\max[S_H]}{\max[S_D]}$
3	Signal amplitude peak-squared percentage differences	SAPS	$DI = 1 - \left(\frac{\max[S_H] - \max[S_D]}{\max[S_H]} \right)^2$
4	Signal amplitude Hilbert transform maximum	SAHM	$DI = 1 - \left \frac{\max[H[S_H]] - \max[H[S_D]]}{\max[H[S_H]]} \right $
5	Signal sum of squared differences	SSSD	$DI = 1 - \frac{\sum (S_H - S_D)^2}{\sum S_H^2}$
6	Welch-based power spectral density	WPSD	$DI = 1 - \frac{\int_0^{2f_{ex}} \mathbf{PW}[S_D] df - \int_0^{2f_{ex}} \mathbf{PW}[S_H] df}{\int_0^{2f_{ex}} \mathbf{PW}[S_H] df}$
7	Welch-based transfer function	WTF	$DI = 1 - \frac{\int_0^{2f_{ex}} \mathbf{TF}[S_D] df - \int_0^{2f_{ex}} \mathbf{TF}[S_H] df}{\int_0^{2f_{ex}} \mathbf{TF}[S_H] df}$
8	Cross-correlation-based TOF percentage difference	CCTOF	$DI = 1 - \frac{ t_{\max CC}^H - t_{\max CC}^D }{t_{\max CC}^H}$ $t_{\max CC}^{H,D} = \underset{t}{\operatorname{argmax}} [CC_{H,D}(t)]$
9	Cross-correlation maximum percentage difference	CCMPD	$DI = 1 - \frac{ \max[CC_H] - \max[CC_D] }{\max[CC_H]}$
10	Hilbert transform-based TOF percentage difference	HTOF	$DI = 1 - \frac{ t_{\max H}^H - t_{\max H}^D }{t_{\max H}^H}$ $t_{\max H}^{H,D} = \underset{t}{\operatorname{argmax}} [H[S_{H,D}(t)]]$
11	Discrete wavelet transform approximation coefficients-based DI	DWTC	$DI = 1 - \frac{\sum (\mathbf{DWT}[S_H] - \mathbf{DWT}[S_D])^2}{\sum \mathbf{DWT}[S_H]^2}$
12	Ratio of covariance matrix eigenvalues	RCME	$\rho = 1 - \frac{\lambda_2}{\lambda_1}$

References

- Giurgiutiu V (2005) Tuned lamb wave excitation and detection with piezoelectric wafer active sensors for structural health monitoring. *J Intell Mater Syst Struct* 16(4):291–305
- Matt H, Bartoli I, Lanza di Scalea F (2005) Ultrasonic guided wave monitoring of composite wing skin-to-spar bonded joints in aerospace structures. NDE & Structural Health Monitoring Laboratory, Department of Structural Engineering, University of California, San Diego
- Zhao X, Gao H, Zhang G, Ayhan B, Yan F, Kwan C, Rose JL (2007) Active health monitoring of an aircraft wing with embedded piezoelectric sensor/actuator network: I. Defect detection, localization and growth monitoring. *Smart Mater Struct* 16:1208–1217

4. Wu Z, Liu K, Wang Y, Zheng Y (2014) Validation and evaluation of damage identification using probability-based diagnostic imaging on a stiffened composite panel. *J Intell Mater Syst Struct* 1045389X14549873
5. Schmidt D (2013) CFRP panel with integrated SHM network. Technical report of SARISTU project
6. Moix-Bonet M, Buethe I, Bach M, Fritzen C-P, Wierach P (2014) Durability of co-bonded piezoelectric transducers. 2nd international conference on system-integrated intelligence. *Procedia Technol* 15:639–648
7. Loendersloot R, Buethe I, Michaelidos P, Moix-Bonet M (2015) Damage identification in composite panels—methodologies and visualisation. In: Wölcken PC, Papadopoulos M (eds) *Smart Intelligent aircraft structures (SARISTU)*. pp 581–606
8. Michaelides PG (2013) Pitch catch algorithms preliminary analysis. Technical report of SARISTU project
9. Worden K, Farrar CR, Manson G, Park G (2007) The fundamental axioms of structural health monitoring. *Proc R Soc A* 463:1639–1664

Path-Based MAPOD Using Numerical Simulations

Inka Buethe, Nicolas Dominguez, Henning Jung, Claus-Peter Fritzen,
Damien Ségur and Frédéric Reverdy

Abstract Probability-based methods for the consideration of detection rates and associated damage sizes have been state of the art in NDT. For structural health monitoring (SHM) systems, the quantification of detection capabilities needs to be addressed to enable the industrial implementation. Due to the fixed mounting of SHM systems on structures, experimentally based investigation is particularly difficult and resource consuming. Therefore, the use of numerical simulations is suggested to generate additional data for probability studies. Within this paper, two methods of model-assisted probability of detection (MAPOD) are presented. For the use case of carbon fibre-reinforced plastics (CFRP) panels, tested with acousto-ultrasonics, a path-based analysis was chosen. After a short description of the underlying numerical models, the used probability-based methods are explained. Their application is shown in detail using a 3D and a 2D model for a CFRP panel.

I. Buethe (✉) · H. Jung · C.-P. Fritzen

Institute of Mechanics and Control Engineering—Mechatronics, University of Siegen, 57076
Siegen, Germany
e-mail: inka.buethe@uni-siegen.de

H. Jung

e-mail: henning.jung@uni-siegen.de

C.-P. Fritzen

e-mail: claus-peter.fritzen@uni-siegen.de

N. Dominguez

Structure Health Engineering Department, AIRBUS Group Innovations,
Toulouse 31025, France
e-mail: nicolas.dominguez@airbus.com

D. Ségur · F. Reverdy

NDE for Aeronautics Application Laboratory, CEA List, Toulouse 31025, France
e-mail: damien.segur@cea.fr

F. Reverdy

e-mail: frederic.reverdy@cea.fr

Nomenclature

- a Area of delamination in mm^2
 \hat{a} Damage index as output from the SHM system for a structure with a delamination of a
 \hat{a}_{thr} Threshold over which a SHM system defines \hat{a} as delamination
 CC Correlation coefficient

1 Introduction

The application of structural health monitoring (SHM) methods for real-world use cases is not possible without a method of quantifying quality and reliability. SHM systems need to be evaluated based on a performance index. This index can be defined in different ways, based on physical quantities. Especially important are performance parameters, describing detection rates for exemplary damages and accuracies for processes evaluating the location of the damages.

Based on the methods of quantifying the quality of non-destructive testing (NDT) methods, this paper used the concept of probability of detection (POD). The POD describes the probability to find a damage of a given size with a given confidence level. The evaluation of the performance index $a_{90|95}$, which is the damage size which can be detected with a probability of 90 % at a confidence of 95 %, is based on statistical methods. Traditionally, the underlying data are generated with a number of experiments, conducted with several probes and multiple NDT engineers. The procedure is described in detail, e.g. in [1]. The effort for this procedure is high. Nevertheless, the effort is even higher for SHM systems. Their inherent feature of having the measurement system directly connected to the structure leads to much higher expenditures regarding the measurement equipment. The number of probes has to be equal to the number of necessary SHM systems. Moreover, the SHM system, fixed to the structure, exhibits the dependency of the defect location regarding the quality of defect detection, especially for anisotropic materials and real-world load-carrying structures.

Because of these reasons, it is necessary to find alternative solutions to evaluate the performance. One opportunity is based on artificial realizations of the system response at its structure with necessary defects. This is known as model-assisted probability of detection (MAPOD). Examples of previous works on this topic for conventional NDT can be found in [2–5]. In this proposal, we show two possible approaches, which are both based on numerical simulations. The investigated method of acousto-ultrasonics uses a network of piezoelectric transducers to introduce lamb waves. They interact with the structure and a possible defect before being captured by another piezoelectric transducer. The effect of damage is visible for a path between actuator and sensor within the network of transducers. The two methods, shown, permit a MAPOD based on a single path. While one method is

using a 3D model, the other method is based on a 2D model, representing the cross section of the structure for a given path. The aim of this paper is to show the application of these two approaches for a SARISTU use case, namely delamination caused by barely visible impacts, and compare the physical results as well as the resulting MAPOD-based performance indices. In a first step, the two models are explained shortly, and afterwards, the underlying statistical procedures to calculate the POD are given. The following description of MAPOD for the SARISTU use case shows the practical applicability including a detailed explanation of the results. The final conclusion also implies possible further steps to go beyond path-based MAPOD towards structure-based MAPOD.

2 Description of the Used Numerical Models

To describe the travelling of the lamb waves and their interaction with damage, two different approaches have been used. While the first method describes the travelling wave in all dimensions [spectral finite element (FE) method], the second approach (CIVA model) is limited to a cross section of the structure on the path between the actuating and the sensing transducer. To model the wave, this approach uses semi-analytical methods, while the first approach is based on numerical spectral FE methods in time domain. To describe the actuating and sensing of lamb waves with the help of piezoelectric transducers (PWAS—piezoelectric wafer active sensors), different methods exist. Most common is the use of a (varied) pin-force model to be able to describe the phenomena without using a detailed description of multiphysics within the piezoelectric element. A varied version has been used for both numerical models within this paper. The two models, used, are explained shortly in the following subsections.

2.1 *Spectral Finite Element Method*

With the spectral FE method, the wave field within a platelike structure can be calculated in three dimensions. The structure is represented by FEs, and the PWAS, including their structural effects, are modelled, too. To overcome the disadvantages of the FE method for platelike structures, such as a necessity of a very high number of elements and therefore degrees of freedom, this method uses first-order plate theory and FE nodes, distributed according to the Gauss–Lobatto–Legendre polynomials. The general approach of using spectral FEs in time domain is described in [6]. For the calculation of anisotropic layered structures, element matrices for stiffness, mass, damping, etc., are calculated, which describe the properties over the whole plate thickness. A big advantage of this method is based on the bandlike structure of the used matrices, which results in a noticeable reduction of

computational costs. The used spectral element is explained in detail in [7]. Its functionality as well as different applications can be also found in [8].

The delamination is implemented via a separation between two layers. The separation is realized with two different elements over the thickness. For both, separate element matrices are calculated. The nodes within the delamination area are not connected. A material penetration is checked and prevented within the calculation via adding additional contact forces in case of penetration. A detailed explanation of the used method to model a delamination is given in [9, 10].

2.2 *CIVA Model*

To provide efficient tools for predicting NDT guided waves, simulation tools are being developed at CEA LIST; they are based on semi-analytical (SAFE) [11] or hybrid semi-analytical/numerical techniques [12]. Both approaches lie on a modal decomposition and post-processing of these modes to account for transducer diffraction effects and flaw scattering. SAFE involves a FE computation in the guide section, allowing the computation of both wave numbers and modal displacements in the section as being the eigenvalues and eigenvectors (respectively) of a quadratic system of equations; this system is the discrete form of a variational problem in the guide section. As it is restricted to the section, it is computationally very efficient. The propagation is otherwise accounted for by means of analytic propagators in the guiding direction normal to the section considered. The computation of modal amplitudes emitted by a transducer is performed under the assumption that piezotransducers can be modelled as sources of normal or tangential stresses over their active surface. The module available in CIVA allows one to calculate the modes, the beam field and the interaction either with a crack oriented perpendicularly to the direction of guide (available in the first release: CIVA 10 GWT), or with a CAD-defined defect (available in the second release: CIVA 11 GWT). In the former case, the computation is based on a mode-matching technique that does not require the meshing of the zone surrounding the defect. To extend the capabilities of the first modules, hybrid techniques have been developed and integrated in the second release (CIVA 11 GWT). They can take into account the scattering by several defects or discontinuities such as a stiffener arbitrarily positioned in a part. For this approach, non-local phenomena (guided propagation) are modelled by modal decomposition in homogeneous portions of the piece using the SAFE method, while local phenomena are handled using FE modelling. The problem of interaction with any perturbation of the waveguide is written in the form of a scattering matrix. This matrix links an input vector constituted by the modal coefficients of the incoming wave, to an output vector constituted by those of the outgoing wave. To deal with arbitrary flaw shapes, guide inhomogeneities or junctions between several guides, a FE scheme has been developed with the goal to limit the computation zone to a minimal size for efficiency. The computation relies on the use of artificial boundary conditions with transparency. Radiation conditions

at infinity are brought back to the artificial boundaries by building an operator coupling the FEs inside the FE zone to modal solutions in guides. An original mixed formulation has been derived with the unknowns being the displacement field in the bounded domain and the normal component of the normal stresses on the artificial boundaries. The scattered field is then projected on modal solutions in guides through the use of biorthogonality relations. This method that we call “Hybrid Modal-FE method” has been established for 2D and 3D waveguides in Cartesian coordinates. The theoretical details of this method are provided in [12]. In the official version of CIVA (11 GWT), only the 2D (dealing with the scattering of lamb wave in isotropic guides) and axisymmetric version are implemented. In composite parts, specific attention must be paid to deal with a multilayered structure with anisotropic properties of plates considered here. Contrary to GW propagation in isotropic materials, the behaviour of GW in anisotropic materials depends on the direction of propagation. Standard formulae of the SAFE method to account for the θ dependency can be found in the literature [13] and have been implemented in CIVA.

3 Calculating the Probability of Detection

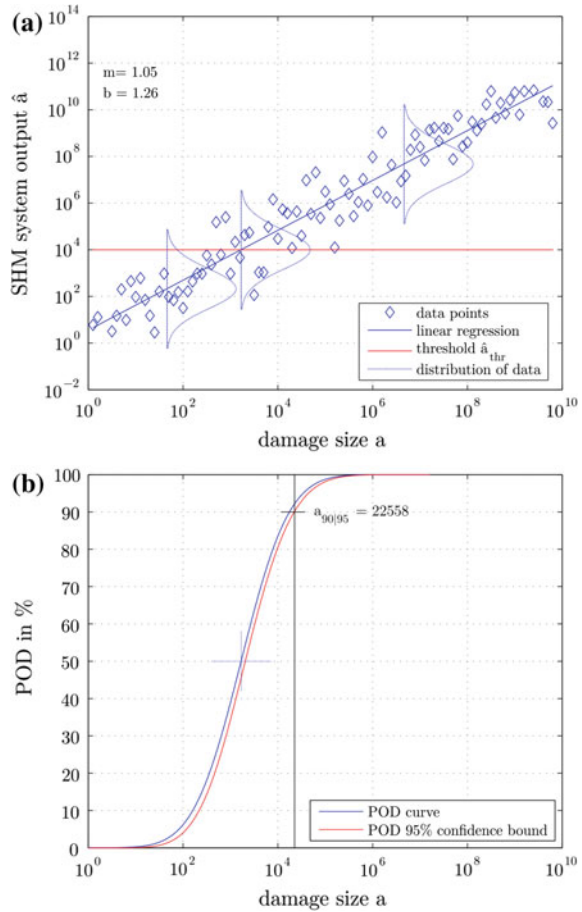
Different approaches for calculating POD curves and resulting performance indices are known, which can be distinguished in two main groups. The approaches within this paper represent one each. The first approach is based on the evaluation of a linear behaviour between a quantity representing the damage size and some quantity representing the measured output of the SHM system. The analysis is performed according to the military handbook MIL1823 [1]. Other methods especially regarding the calculation of confidence intervals exist (see, e.g. [14–17]).

3.1 *POD Based on Linear Regression Curve*

Within this application, the quantity, which represents the damage size, is the area of the delamination. In the following, this is called a . To describe the measured output of the SHM system, a damage index was used. This damage index is calculated by subtracting the correlation coefficient CC from one. CC is calculated as correlation coefficient of the baseline signal from the undamaged structure and the signal from the damaged structure.

The use of other damage indices is possible, and a detailed description can be found in [18]. The damage index is called \hat{a} from now on to be consistent with the MIL1823. Given that \hat{a} over a on logarithmic scales results in a linear dependency. For fixed values of a , values of \hat{a} show some deviation around the regression line (see Fig. 1a). The SHM system identifies a delamination if a measured \hat{a} is above a threshold \hat{a}_{thr} . The value of \hat{a}_{thr} can be calculated from the noise floor of \hat{a} , when

Fig. 1 POD based on linear regression curve. **a** Linear regression between a and \hat{a} . **b** POD curve generated from linear regression curve



there is no damage. As for the case of numerical calculations, the noise floor has to be added in a separate step and needs to be given, and \hat{a}_{thr} was evaluated from transducer paths distant to the damage area for the case of very small introduced delamination. When the regression line and the distribution of the scatter around the regression line are described mathematically with slope, intercept and scattering, these values can be used for calculating the POD curve. It describes the POD of a damage size a to be detected with the SHM method that is providing the value \hat{a} . From the POD curve, the $a_{90/95}$ value can be extracted as performance index. It gives the damage size a at which 90 % of the damages of this size can be detected with a confidence level of 95 %. The procedure is presented in Fig. 1b. The calculation of the confidence bounds is based on the delta method. For the calculations of the POD curve, the software *R* with the package *mh1823* POD is used [19].

4 Application of MAPOD for CFRP Structures

Within the SARISTU project, a platelike exemplary structure was used to show the possibilities of numerical approaches of path-based MAPOD. This structure exhibits 11 layers of carbon fibre-reinforced plastics (CFRP) made from M21 matrix with T800S fibres. The set-up is shown in Fig. 2.

To verify the models, used for MAPOD, the results can be compared to an experimental set-up, where a damage between PWAS 3 and PWAS 7 was introduced. The delamination can be considered as ellipse shaped with 19 and 28 mm as half-axes.

4.1 MAPOD Based on Linear Regression Curve and Spectral Element Method

To be able to use the SEM model for calculation of MAPOD, the similarity between experimental results and numerical results has to be secured. Figure 3 shows that for PWAS 6 as actuator, experimental and numerical time domain signals result in

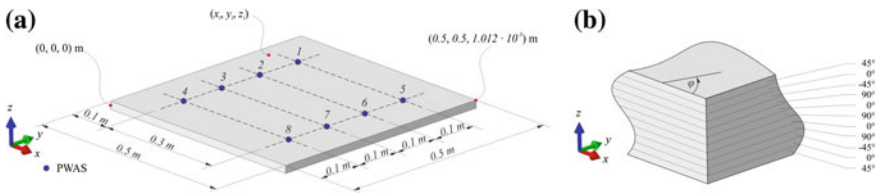


Fig. 2 Set-up of the SARISTU platelike structure to verify MAPOD concepts. The figure shows the geometry with its dimensions and locations of the transducers in (a) and the layup with orientation of the different layers in (b)

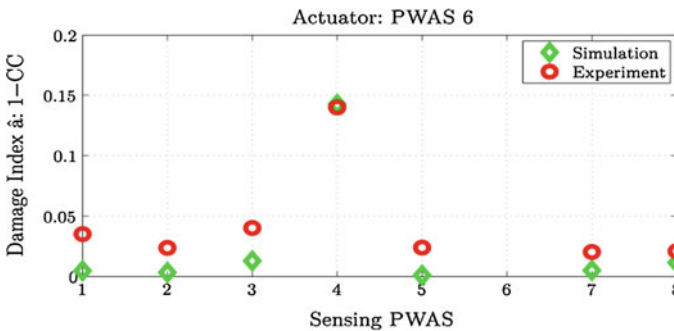


Fig. 3 Comparison of damage indices for 3D SEM simulation and experiment. While for paths, which are not directly crossing the delamination, the experimental data result in slightly higher damage indices, for the direct path, simulation and experimental results show an excellent agreement

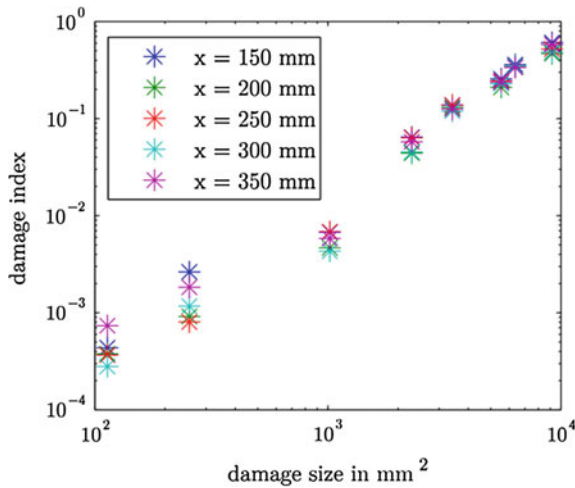


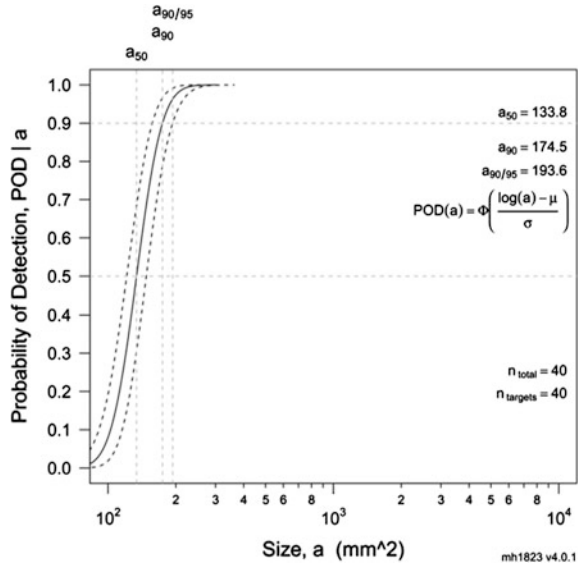
Fig. 4 Linear relation between damage index and damage size. For eight different damage sizes at five different locations, distributed evenly between the transducers, the damage index has been evaluated. With a double logarithmic scale, linear behaviour can be seen. An effect of the location is noticeable, but not independent of damage size

similar damage indices. As the damage is located central between PWAS 3 and PWAS 7, only the path 6–4 is directly affected by the damage, while for all other paths, reflections might have an effect on the receiving signal. While the damage index for numerical and experimental data on the direct path (6–4) is very much the same, the experimental data of all other paths result in slightly higher damage indices, compared to the damage indices calculated from the numerical data.

To generate data for a path-based MAPOD, the path between PWAS 3 and PWAS 7 was selected. Between these two transducers, five locations are distributed evenly ($x = 150, 200, 250, 300, 350$). For all five locations, damages of eight different extents have been chosen. The ellipse-shaped delaminations exhibit all but one a ratio of 2:3 for their half-axes. The path-based damage index was calculated. As damage size, the area of delamination was used. On a double logarithmic scale, a linear regression between damage size and damage index is shown in (Fig. 4). As expected, the damage index is not the same regardless of the damage location. Nevertheless, it is not always a special location, which exhibits the smallest or highest damage index for all damage sizes. Therefore, the location is taken as a disturbance parameter, influencing the scattering of the data.

Based on these 40 simulations, a calculation of MAPOD was carried out with mh1823 POD software [19]. As no threshold from experimental data was given, \hat{a}_{thr} was calculated from 15 measurements, using the paths 3–1, 3–2, and 3–4 for all five damage locations and the smallest damage. This results in \hat{a}_{thr} of 0.0006. Based on this value, the regression line and the scattering, an $a_{90|95}$ value of approximately 200 mm^2 is defined in the POD curve (see Fig. 5). This value is very low and substantiates the delamination detection possibilities with the used method of

Fig. 5 MAPOD with performance index $a_{90|95}$ for the path between PWAS 3 and PWAS 7. Based on the numerical results, the calculated MAPOD gives an $a_{90|95}$ value of approx. 200 mm^2



acousto-ultrasonics. It gives an estimation for damages, which are located on the direct path between two transducers.

The described calculations show a general approach on a conceptual level with an exemplary use case. For further improvement, a more detailed analysis of the threshold \hat{a}_{thr} based on the noise level for the used measurement equipment needs to be performed. A shift of \hat{a}_{thr} to higher values leads to a shift of the POD curve as well as of the $a_{90|95}$ value to the right, respectively, higher damage sizes.

4.2 MAPOD Based on Linear Regression Curve and 2D Hybrid Modal-Finite Element Method

A calculation of MAPOD was carried out with CIVA software based on the 2D Hybrid Modal-Finite Element method. Damages of eight different extents have also been chosen that would give the same area of the ellipse-shaped delaminations define in the previous MAPOD calculations. The delamination is located at the interface between the second and third layer. The uncertain parameters used in the MAPOD calculation are the defect location between the transducers and the density of the material. The locations of the delamination defect between PWAS 3 and PWAS 7 are described by a uniform distribution for x in the interval [150, 350], identical to the procedure in A. The density values are defined by a normal distribution with a standard deviation of 0.1 around a mean value of 1.58 g cm^{-3} . For each defect length, 5 draws of uncertain parameters taken in their corresponding distribution give a total of 40 simulations performed at 200 kHz for a bandwidth of

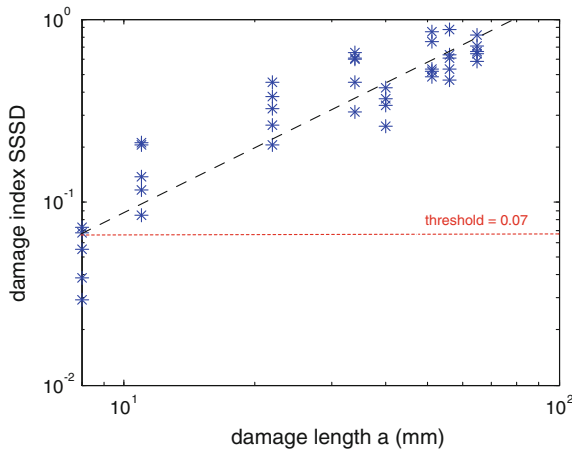
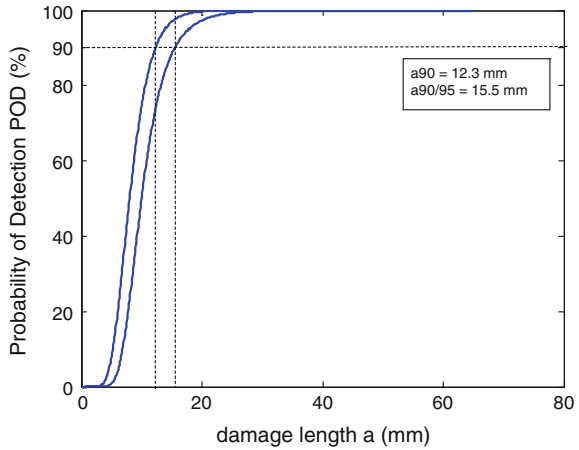


Fig. 6 Linear relation between SSSD damage index and damage length from the 2D CIVA model. For eight different damage sizes at uniformly distributed location between the two transducers, and a normal distribution of the density of the material, the damage index has been evaluated. With a double logarithmic scale, linear behaviour can be seen

40 %. The computation time for one simulation over the 72 frequency steps is about 6 min on an Intel® Xeon® CPU X5690@3.5GHZ 2 cores RAM 24 Go. The path-based damage index was calculated as the signal sum of squared differences (SSSD) algorithm given in [18] that focus on the whole signal and the differences between healthy and (potentially) damage state. On a double logarithmic scale, a linear regression between damage size and damage index is shown in (Fig. 6). As expected, the damage index varies regardless of the damage location and increases with the damage length.

In the previous SEM-MAPOD calculation, the damage index threshold is calculated from the measurements on indirect paths where the differences between the safe and damage samples arise from the wave reflections on the defect. In the 2D hybrid modal-finite element method modelling used in CIVA modelling, such reflections cannot be simulated because only direct path are taken into account in this 2D description. So, we define the threshold as the minimum value of the linear regression line that finally corresponds to the threshold defined in the SEM-MAPOD calculation (even if the value cannot be compared because of the different model and damage index algorithm). Based on this value, the regression line and the scattering, an $a_{90/95}$ value of approximately 15.5 mm is defined in the POD curve (see Fig. 7). Assuming that the damage length is an axis of an ellipse-shaped delamination to compare to the SEM-MAPOD result, one would find a damage size of $a_{90/95} \sim 500 \text{ mm}^2$. One advantage of the 2D CIVA-MAPOD calculations is the low computation time allowing to increase the number and the width of the uncertain parameter distributions.

Fig. 7 MAPOD with performance index $a_{90|95}$ for the path between PWAS 3 and PWAS 7. Based on the numerical results from CIVA model, the calculated MAPOD gives an $a_{90|95}$ value of approx. 15.5 mm



5 Conclusion

Model-assisted POD is a promising method to enable the estimation of detection rates for given damage sizes and types. Within this paper, two methodologies for path-based MAPOD are presented. Both are based on reliable modelling tools using numerical simulations. With two different basic approaches, the elaboration of POD curves for respective structures and application scenarios is described in detail. While one approach makes a detailed analysis of the generated wave field possible, but takes more time for computation, the other approach achieves lower computational costs via simplification within two dimensions. The presented methodologies can be used to assist in the conception of SHM systems as well as in following certification, necessary for acceptance tests. Therefore, they build one step on the way to use SHM systems in industrial applications.

For a detailed description of the performance of on SHM system, additional methods, which do not only include a path-based MAPOD, but give a structure-based MAPOD, build the next step. Therefore, it is necessary to develop enhanced statistical methods, including a statistical description of the location parameter. The path-based MAPOD builds an excellent fundament for the required future work.

Acknowledgments The research leading to these results has received funding from the European Union’s Seventh Framework Programme for research, technological development and demonstration under grant agreement no 284562.

References

1. Military handbook 1823. Nondestructive evaluation of system reliability assessment. Department of Defence, USA (2009)
2. Model assisted POD working group <http://www.cnde.iastate.edu/MAPOD>
3. Thompson RB (2008) A unified approach to the model-assisted determination of probability of detection. *Mater Eval* 66(6), 1685–1692
4. Jenson F, Iakovleva E, Dominguez N (2010) Simulation supported POD: methodology and HFET validation case. *Rev Prog QNDE* 30, 1573–1580
5. Dominguez N, Feuillard V, Jenson F, Willaume P (2011) Simulation assisted POD of a phased array ultrasonic inspection in manufacturing. *Rev Prog QNDE* 31, 1765–1772
6. Ostachowicz W, Kudela P, Krawczuk M, Zak A (2012) Guided waves in structures for SHM—the time-domain spectral element method. Wiley, New York
7. Schulte RT (2010) Modellierung und simulation von wellenbasierten structural health monitoring—Systemen mit der Spektral-Elemente Methode. PhD thesis, University of Siegen
8. Schulte RT, Fritzen C-P (2011) Simulation of wave propagation in damped composite structures with piezoelectric coupling. *J Theoret Appl Mech JTAM* 49:879–903
9. Fritzen C-P, Schulte RT, Jung H (2011) A modelling approach for virtual development of wave-based SHM systems. In: *Journal of physics, conference series*, 9th international conference on damage assessment of structures, DAMAS
10. Jung H, Schulte RT, Fritzen C-P (2011) Interaction of elastic waves with delaminations in CFRP structures: a numerical study using the spectral element method. In: Chang F-K (eds) *Structural health monitoring*, 8th international workshop on structural health monitoring, Stanford, Sept 2011, pp 2576–2583
11. Jezzine K, Lhémy A (2007) Simulation of guided wave inspection based on the reciprocity principle and the semi-analytical finite element method. In: *Review of progress in QNDE*, 26A, AIP conference proceeding, vol 894, NY
12. Baronian V, Bonnet-Ben Dhia AS, Lunéville E (2010) Transparent boundary conditions for the harmonic diffraction problem in an elastic waveguide. *J Comput Appl Math* 234, 1945–1952
13. Bartoli I, Marzani A, Lanza di Scalea F, Viola E (2006) Modeling wave propagation in damped waveguides of arbitrary cross-section. *J Sound Vib* 295:685
14. Berens AP (1988) NDE reliability data analysis *ASM metals handbook*, vol 17. *ASM Metals Handbook*, ASM International, Materials Park, 1988, pp 689–701
15. Forsyth DS, Aldrin JC (2011) Build your own POD. In: *Proceedings of 4th European-American workshop on reliability of NDE*
16. Rummel WD (2010) Nondestructive inspection reliability—history, status and future path. In *Proceedings of 18th world conference on nondestructive testing*
17. Gandossi L, Annis C (2010) ENIQ report No 41: probability of detection curves: statistical best-practices. ENIQ—European Network for Inspection and Qualification, Techreport
18. Pavlos M (2013) Pitch catch algorithm preliminary analysis. SARISTU Techreport ACP1-GA-2011-284562
19. Annis C (2013) Statistical best-practices for building probability of detection (POD) models, R package mh1823, version 4.0.1 <http://StatisticalEngineering.com/mh1823>

Part VII

Technology Stream: Integrated Sensing. Multi-site Damage Assessment of CFRP Structures

Introduction and Overview

The main objective of A07 is the development of a prediction method capable to assess the airworthiness of aeronautic structures (i.e., typical fuselage panels) by means of structural health monitoring system (SHM) developed in AS04 and AS06 in the presence of multi-site damages.

The work within AS07 is structured in 4 work packages: WP7.1 Specifications and Manufacturing; WP7.2 Methodologies and Testing; WP7.3 SHM-System Integration; WP7.4 Multi-site damage assessment of CFRP structures by means of CVM-TTT.

Standard pyramid approach was used to develop methodology to predict residual strength capability after multi-impacts (large test campaign at coupon level and reduced test at component level e.g., curved stiffened panels). The experimental results of coupons were used to validate a finite element mesomechanical modeling approach which accounts for both intralaminar and interlaminar damage. The FE models, which were based on a mesomechanical approach, showed a good agreement with both the impact damage and the subsequent compression performance at curved stiffened panel level. The manufacturing of 17 out of 21 curved stiffened panels is completed. Twelve curved stiffened panels were subjected to multi-impacts (3 and 4 impacts per panel) selecting the most critical impact scenario as predicted by FE analysis. All 12 panels were successfully tested under compression loading conditions until catastrophic failure. Two stiffened panels were equipped with SHM sensors using both acoustic ultrasonic and fiber Bragg grating systems. Signals from sensors were recorded during impact and compression after impacts. Data analysis is currently under investigation, and results will be included in the final report.

Paper named *Compression after multiple impacts: modelling and experimental validation on composite coupon specimens* described the investigation of the post-impact behavior of CFRP coupon specimens subjected to multi-site impacts. Both experimental results and FE prediction capability validated against test are included in the paper. Second paper titled *Compression after multiple impacts:*

Modelling and experimental validation on composite curved stiffened panels provides an overview of the investigation on the post-impact behavior of composite fuselage panels subjected to multi-site low-velocity impacts. Large curved stiffened panels (1.2 m × 0.8 m, with composite skins/stiffeners and aluminum frames) of two different skin thicknesses were subjected to sequential drop-weight impacts at locations previously determined to be critical in FE simulations and compression loading until final failure. Both experimental results and FE prediction of 12 curved stiffened panel tests are included in the paper.

Flat and Curved Panel Manufacturing

Martijn van Wijngaarden

Abstract This paper describes the manufacturing of flat test panels and curved stiffened test panels for the multi-site damage assessment of CFRP structures. Unidirectional carbon fibre prepreg has been used to laminate and autoclave the test panels. The flat panels in sizes 300 × 300 mm and 600 × 600 mm have been produced to provide a low-cost simple test article. The majority of the manufacturing effort has gone into the production of the curved test panels to be used for compression tests after having been subjected to multi-site damage. Tooling has been manufactured to be used in the various processing steps, which involve stringer autoclave consolidation, stringer machining, cobonding the stringers to the still-to-be-consolidated curved skin panel, application of reinforcement plies for load introduction, potting of the stringer ends, machining of the panel contour, potting the complete panel in a potting jig, machining the potting within tolerance for compression testing and quality control using NDI and dimensional verification. The finished panels have been shipped in custom crates which store the panel throughout its logistic and testing program. From KVE, the panels have been shipped to Premium AEROTEC GmbH (PAG) for assembly of the metallic parts also described in this report. PAG shipped the panels to the test location at Imperial College London (ICL).

Nomenclature

ABS	Airbus standard
AIMS	Airbus Material Specification
APII	Airbus Process Instructions
AS0X	Application scenario nr in the SARISTU project
CFRP	Carbon fibre-reinforce plastic
CNC	Computer numerical control
ICL	Imperial College London

M. van Wijngaarden (✉)
R&D, KVE Composite Structures BV, Laan van Ypenburg 56,
2497GB The Hague, The Netherlands
e-mail: wijngaarden@kve.nl

ID	Identification
KVE	KVE composite structures BV
NDT	Non-destructive testing
PAG	Premium AEROTEC GmbH
PTFE	Polytetrafluoroethylene
SARISTU	Smart Intelligent Aircraft Structures
UD	Unidirectional

1 Introduction

This document describes the design and manufacturing of both the flat panels and curved panels used in the AS07 multi-site damage assessment for CFRP SARISTU work package.

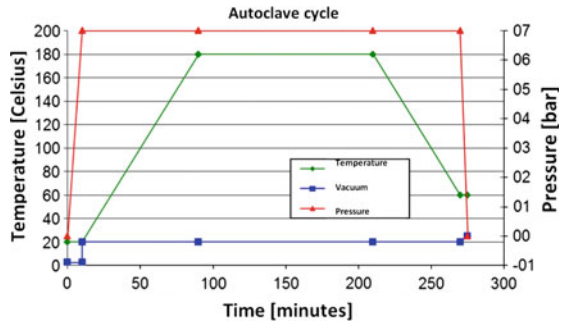
2 Flat Panel Manufacturing

To proceed the curved panels, simple low-cost 300×300 mm and 600×600 mm flat panels have been produced by KVE for impact and compression after impact testing at ICL. Carbon fibre-reinforced unidirectional Hexply UDM21\34%\294\T800S-24 K is used for these plates which is the same material as used for the curved panels and is supplied by Airbus. The four produced 300×300 mm thin 9 ply panels have the following lay-up [90/0/90/0/90/0/90/0/90].

The ten produced 600×600 mm thick 20 ply panels have the following lay-up [45/-45/90/-45/0/45/-45/0/45/0]s. The ten produced 600×600 mm thin 9 ply panels have lay-up [45/-45/90/0/90/0/90/-45/45]. The C-scan inspection prior and after impact, the testing and analysis of the coupons cut from the panels were performed at ICL (results described in other AS07 report). Processing was performed according to Airbus specification APIPI 03-02-019. The used autoclave cycle is displayed in Fig. 1.

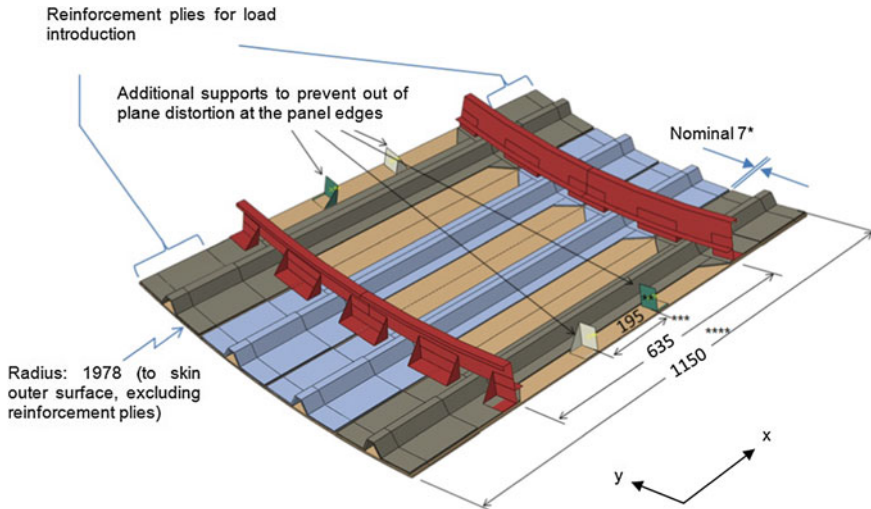
3 Curved Panel Design

The curved panel design used for multi-site damage assessment in AS07 is based on an existing Airbus-designed item adapted for SARISTU needs by Airbus. There is a thin and thick version of the panel, which is composed of a curved solid skin with four omega stiffeners. Reinforcement plies and potting material are used to introduce the compression load. Metallic frames and additional supports at the ends are added to prevent out-of-plane distortions at the edges (Fig. 2).



Heat up ramp	2	±0.5	[°C/min]
Pressure up ramp	0,2	-	[bar/min]
Curetemperature	180	±5	[°C]
Cure time	120	-0/+30	[min]
Heat down ramp	2	±1	[°C/min]
Autoclave pressure 1	7,0	±0,5	[bar]
Autoclave pressure 2 (cure)	7,0	±0,5	[bar]
Vacuum 1	-0,9	-	[bar]
Vacuum 2 (cure)	-0,2	-	[bar]

Fig. 1 Autoclave cycle flat panels (graph and data)



- * This dimension refers to the gap between adjacent stringer duck feet
- ** This dimension is the distance between opposing faces of the clip items
- *** This dimension refers to the offset between frame reference planes
- **** This dimension refers to the overall panel length before addition of the load introduction fixtures

Fig. 2 Overview curved panel design

The frames, clips and cleats are based on the designs of standard serial production parts, but have been adapted specifically for SARISTU, based on the principles of references.

Two versions of the clips are required for SARISTU:

- V1 items (wider) are used to secure the frames to the skin in the stringer bays
- V2 items (narrower) are used to secure the frames to the skin at the frame ends and also for the additional supports.

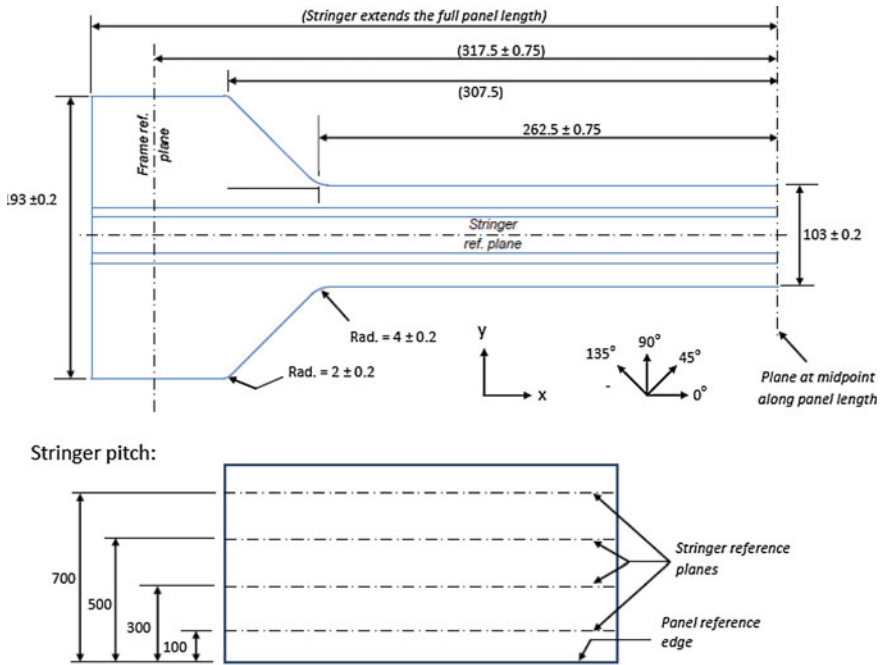
In order to reduce the number of different parts and to avoid the need for filler pieces, the clip and cleat designs are only representative of real aircraft parts, e.g. they are not weight optimised—they do, however, perform the same roles and satisfy the support requirements in the most effective manner.

There are four additional supports per panel, with each one comprising one of the v2 clips together with one of the cleats (Figs. 3 and 4).

Materials

The following materials are used in the production of the panels:

- Skin and stringers: medium grade T800/M21 prepreg.
 - AIMS 05-01-002.
 - ABS 5321.
 - IPS 05-01-002-03.
- Reinforcement plies: woven carbon fibre prepreg to ABS 5003N0000 (previous A-D material code ABS 5003A40EP350); this is material DAN1208A40.
- Adhesive: FM300M0.3 (reference Airbus specification number ABS 5320AM).
- Fasteners:
 - Clip/skin joints: EN6115K2-*
 - Clip/cleat/frame joints : EN6081KE5-*
- EN6115K2-* may be used in place of EN6081KE5-* if it simplifies assembly and does not increase cost.
- The appropriate grip length needs to be chosen depending on the total thickness being fastened.
- Frames: aluminium 2024 (ABS 5044A012; based on Airbus serial production parts).
- Clips (v1 and v2): aluminium 2024 (ABS 5044A014; based on Airbus serial production parts).
- Cleats: aluminium 2024 (ABS 5044A014; based on Airbus serial production parts).
- Shim: material options (liquid and solid) as per serial production assemblies.
- Potting materials:
 - Channels: aluminium 50ST (6060).
 - Resin: MLT219.



Stringer pitch tolerance: ± 1.0mm.

Stringer parallelism: ± 1.0mm.

For a stringer thickness ≥ 12 plies, feet shall include a chamfer:

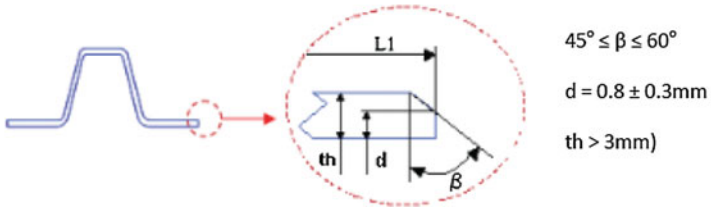


Fig. 3 Curved panel design details

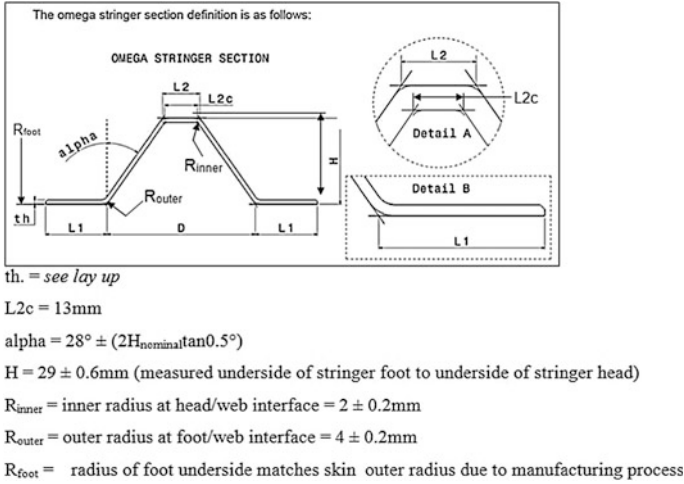


Fig. 4 Curved panel design details

Lay-up

Panels are produced in 2 configurations, with the following constant thickness lay-ups:

Thick panel:

- Skin: 3.680 mm: [45/-45/90/-45/0/45/-45/0/45/0/0/45/0/-45/45/0/-45/90/-45/45].
- Stringer: 2.944 mm: [45/-45/0/0/90/0/0/45/-45/0/0/90/0/0/-45/45].

Thin panel:

- Skin: 1.656 mm: [45/-45/90/0/90/0/90/-45/45]
- Stringer: 1.288 mm: [45/-45/0/90/0/-45/45]

These lay-ups account for the relevant Airbus design rules associated with stacking sequences, symmetry, etc.

Thickness tolerances:

- Thickness < 3 mm: $\pm 5\%$
- Thickness > 3 mm: $\pm 4\%$

Fibre orientation tolerance: $\pm 3^\circ$

Reinforcement plies

A total of four reinforcement plies are placed on both sides of the panel for load introduction (Fig. 5).

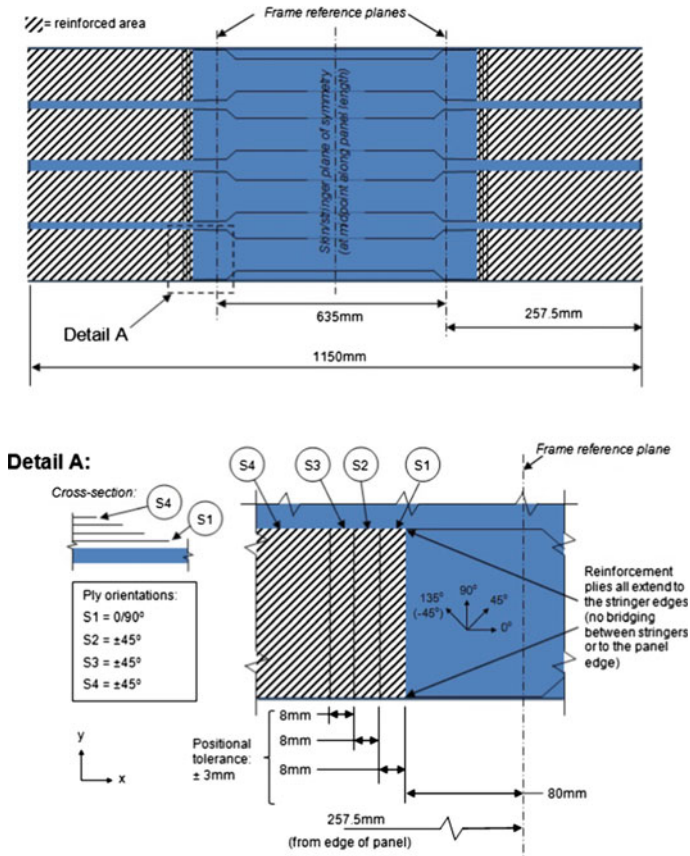
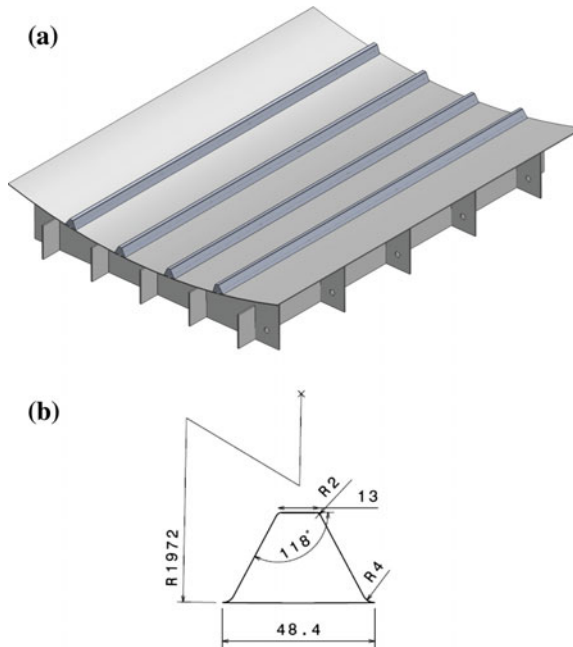


Fig. 5 Curved panel reinforcement ply locations

4 Curved Panel Tooling Design

A stainless steel 304 alloy female mould for the skin and aluminium 5083 moulds for the stiffeners have been designed and produced. Several sets of tooling have been made so that batches of skins can be combined in one autoclave cycle. Four stringers can be autoclave moulded on one skin mould. The stringer moulds are removed from the skin to mould the skin and cocure this to stringers that have been machined and prepared for the succeeding cobonding process (Fig. 6).

Fig. 6 Curved panel tooling with **a** complete mould CAD picture and **b** geometry stiffener tooling



5 Curved Panel Manufacturing

The curved panel manufacturing is performed in multiple steps. The manufacturing steps are described in chronological order.

Stringers

- Consumables used: Release film Airtech A7300, Vacuum film Airtech IPPLON KM 1300, Breather Ultraweave 1332, Breather N10 (debulk), Tacky tape Flash breaker, Release agent Frekote 700 NC.
- Ply cutting and storage: The plies for the stringers in the specified UD material are CNC cut and labelled and kitted for storage.
- Defrosting prepreg kit at least 2 h, register time and kit ID.
- Mould is prepared with release agent and covered with release film.
- Start lay-up and check every ply with signed product follow sheet.
- Debulk after every 1–3 plies according to Airbus specification.
- Use stringer moulds for debulking only to improve laminate quality in the radii (Fig. 7).

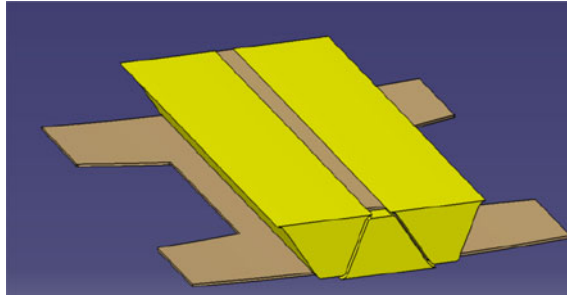


Fig. 7 Stringer debulking use of stringer cores to compress laminate

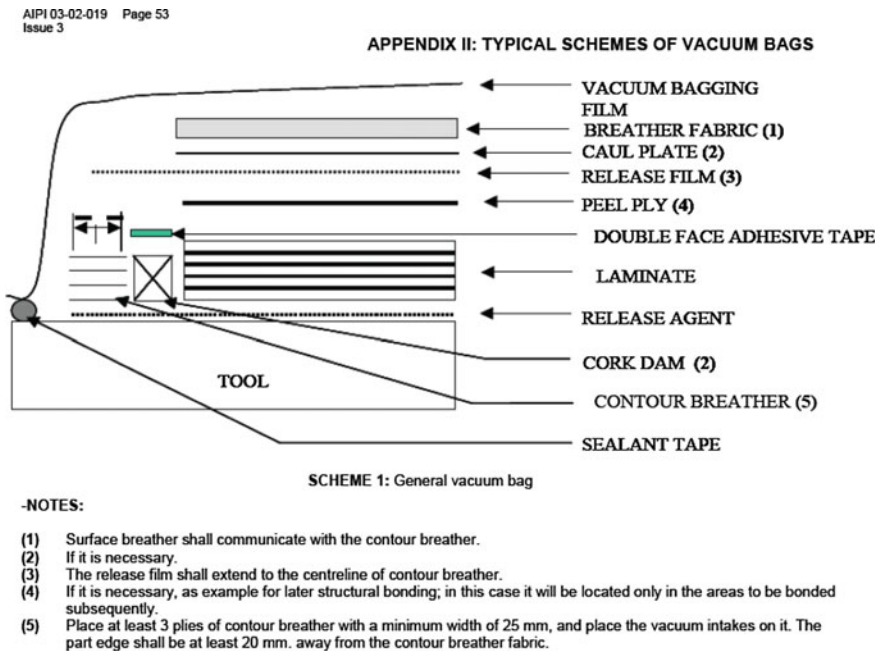


Fig. 8 Vacuum bagging procedure

- Apply product ID label on last ply.
- Use the AIPS 03-02-019 Airbus reference procedure for vacuum bagging the stringers (Fig. 8).
- Check completeness product follow sheet and vacuum leak test.
- Autoclave cycle according to the schedule below (Fig. 9).
- Release stringers from mould.

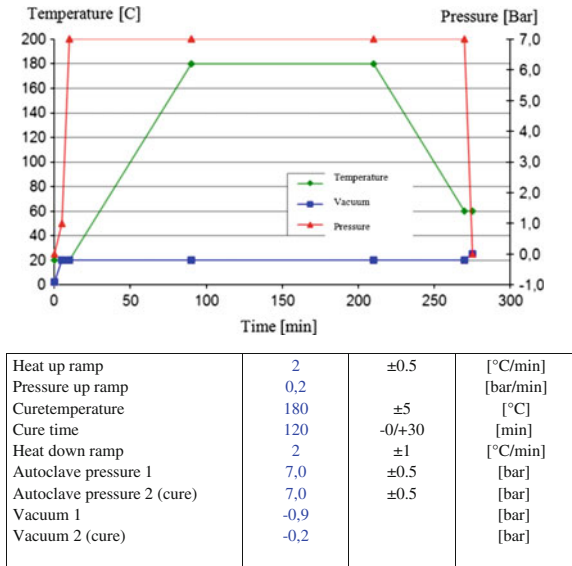


Fig. 9 Autoclave cycle details of stringer

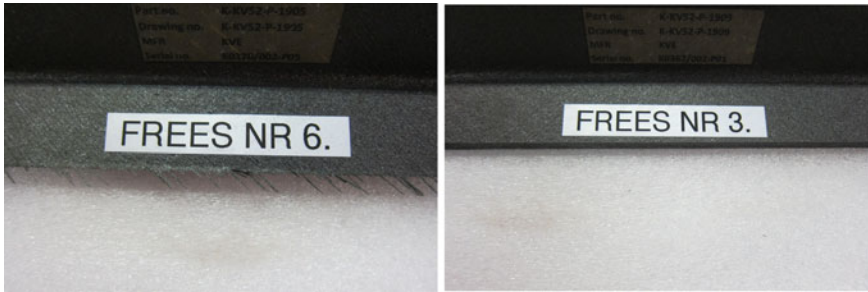


Fig. 10 Stringer mill-type test results and vacuum jig for machining

- Research has been performed in selecting the most optimum mill for machining unidirectional carbon epoxy material. In total, nine different mills were tested and evaluated for best machine setting, quality of the matching, fibre pull out and wear. Large differences were observed as the picture below shown (mill nr 3 was selected to be used in the SARISTU project) (Fig. 10).
- Machined stringers are cleaned and bagged according to specification until the cocuring procedure starts.

Panels

- Consumables used:
 - Release film Airtech A7300 non-perforated and perforated (for reinforcement plies and debulking)
 - Vacuum film Airtech IPPLON KM 1300
 - Breather Ultraweave 1332 and Breather N10 (debulk)
 - Tacky tape Flash breaker
 - Release agent Frekote 700 NC
 - Adhesive film Cytec FM300 M.03, PTFE tube
 - Reinforcement plies Fibredux 913C-926-40 %
 - Potting JB 219
 - Foam and sealer to close the stringers.
- Ply cutting and storage: The plies for the skins in the specified UD material are CNC cut and labelled and kitted for storage.
- Thawing of the prepreg kit and adhesive film for at least 2 h, register time and kit ID.
- Mould is prepared with release agent.
- Start lay-up and check every ply with signed product follow sheet.
- Debulk after every 1–3 plies according to Airbus specification.
- Prepare stringers for bonding according to Airbus specification (abrading, water break test, drying, cleaning).
- Apply adhesive film on the stringer foot.
- Place stringer pitch positioning tools to guarantee stringer location on the panel.
- Place stringers.
- Fix stringers using temporary flash tape and remove positioning tool.
- Apply flash tape on ends of stringers and remove temporary tape.
- Airbus procedure of inserting vacuum tube, PTFE tube and seal properly with tacky tape.
- Apply serial number on skin.
- Prepare for autoclave with perforated release film, surface breather and contour breather.
- Test for leaks.
- Install autoclave and connect vacuum, transducer and thermocouples.
- Second leak test (Figs. 11, 12 and 13).
- The autoclave cycle for the curing of the panel is identical to the autoclave cycle for the stringer displayed earlier in this report.
- Release panel from mould.
- Visual check for defects according to AIFI 03-02-019.
- Send panels to TU-Delft for C-scan (results shown in next section).

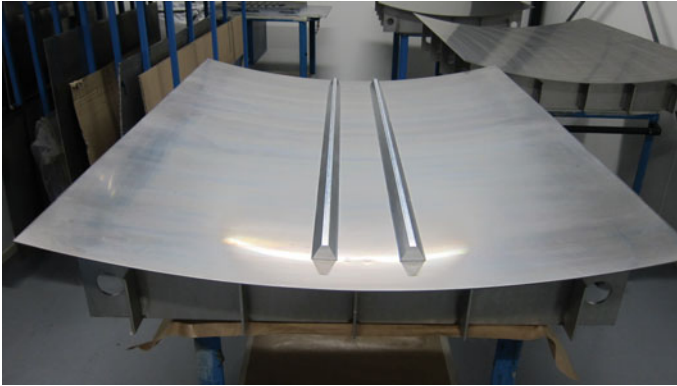


Fig. 11 Stringer mould

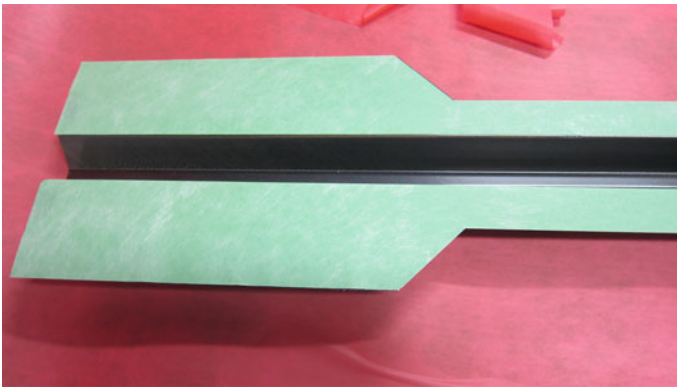


Fig. 12 Adhesive film on stringer with backing film still on

- Prepare for reinforcements plies by sanding the area, water break test and drying (AIPi 06-01-003)
- Thawing of the reinforcement ply kits.
- Laminate the reinforcement plies on both sides of the panel according to the following schedule:

Reinforcement ply	Orientation (degrees)	Dimensions (mm)
S1	0/90	182.5 × 193
S2	±45	174.5 × 193
S3	±45	166.5 × 193
S4	±45	158.5 × 193

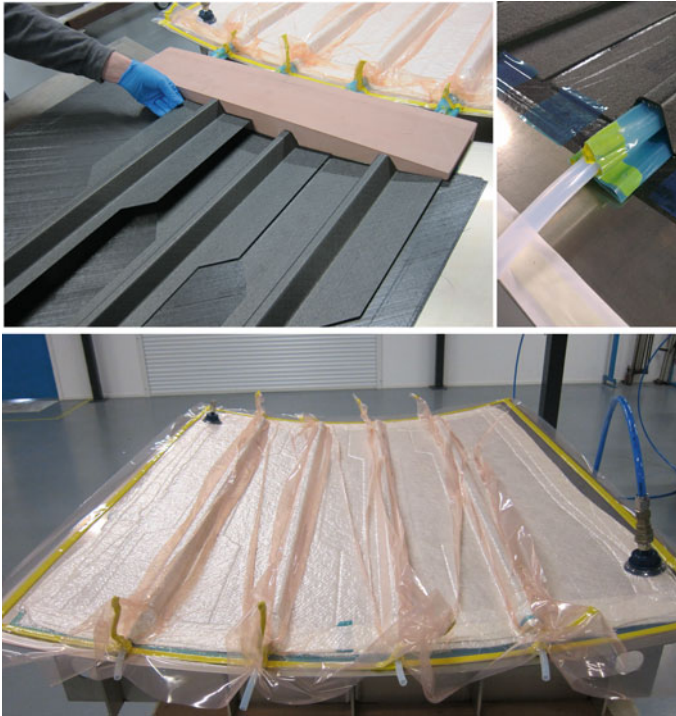
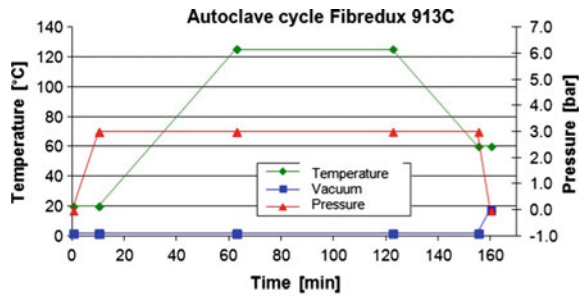


Fig. 13 Stringer positioning, vacuum tube installation and bagged panel

Fig. 14 Autoclave cycle reinforcements plies



Heat up ramp	2	[°C/min]
Pressure up ramp	0,2	[bar/min]
Paوزه	0	[min]
Interned temp	20	[°C]
Cure temperatur	125	[°C]
Curetime	60	[min]
Heat down ramp	2	[°C/min]
AC pressure 1	3,0	[bar]
AC press 2 (cure)	3,0	[bar]
Vacuum 1	-0,9	[bar]
Vacuum 2 (cure)	-0,9	[bar]

- Prepare for autoclave by bagging the entire panel using perforated release film and N10 breather (not on mould but free standing bagged all around) (Fig. 14).
- Release panel from vacuum bag.
- Perform inspection after reinforcement plies.
- The insides of the stringers are to be potted before the entire panel is potted to prevent air pockets that prevent the potting resin from filling the stringer cavity.
- The inside of the stringer is cleaned, and a small foam block is inserted 45 mm (before trimming) deep in the stringer. The potting resin will be poured into the stringer, and the foam block must prevent the resin from leaking into the rest of the stringer. To eliminate any risk of potting leakage, the edges of the foam block with the stringer are sealed with F16 resin which is made thixotropic with aluminium powder filler.
- The three resin components of the JB 219 are mixed in the ratio JB-L 219 200 g, JB 219 H NT 100 g and JB 219 A Green 20 g. The green component is needed to mix thoroughly before taking out of the container due to rigid deposit residue.
- The stringer ends are filled and cured for 24 h at room temperature.
- The panel contour is now CNC trimmed while the CNC program aligned with the stringers.
- Check trimming dimensions.
- The panel ends are potted in a potting jig. The jig has a vacuum pickup block in the contour of the panel. In the bottom of the potting jig, an aluminium channel is placed which has been pre-treated with release agent. The position of the panel in the aluminium channel and the vertical angle of the panel are checked when the panel is placed in the potting jig.
- To prevent exothermic reaction, the resin is mixed in batches of the following ratio JB-L 219 800 g, JB 219 H NT 400 g, JB 219 A Green 80 g and 80 g chopped glass added at the very latest possibility to prevent outgassing.
- After batches of resin have filled 40 mm of the channel, the potting is cured for a day at room temperature.
- The same procedure is followed for the alternate side of the panel.
- The aluminium channels are removed from the panel. Originally, remachining of the potting was not scheduled, but due to the thermal shrinkage and deformations of the potting material, the ends of the panel were approximately ± 0.5 mm. To prevent excessive liquid shimming in the panel test pressure bench and to make sure no potting resin film is between the carbon material and the test bench, remachining of the potting has been done within ± 0.1 mm using a specialized end mill. The first trial panels were machined by ICL using a diamond-coated end mill, which showed high wear during milling of the potting. At KVE, a total of five end mills have been tested for achieved milling quality. The end mill proving the highest quality of machining was a very hard metal TiAlN end mill (Fig. 15).



Fig. 15 Machining of potted panel tests of end mill type

- The end control document is checked and completed.
- Custom crates have been built to ship the panels to Premium AEROTEC for further panel assembly.
- Two thin panels have been equipped with structural health monitoring sensors in cooperation with work package AS04 including acoustic sensors, ribbon tape fibre bragg gating sensors and distributed sensing fibres (Fig. 16).

6 Curved Panel Inspection

All manufactured panels were through transmission C-scanned for any faults present due to the manufacturing process. None of the panels contained any delamination of production fault that could be detected by C-scan (Figs. 17, 18, 19, 20 and 21).



Fig. 16 Machined potting and panel with structural health monitoring sensors

Besides ultrasonic inspection, dimensional checks have been performed during various steps of the manufacturing process.

- Stringer manufacturing checked and recorded the following:
 - Width total and cut-out
 - Length total and cut-out
 - Thickness
 - Radii
 - Angles

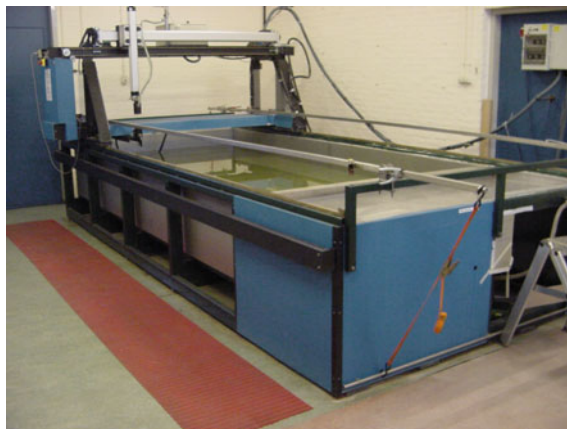


Fig. 17 C-scan setup TU-Delft



Fig. 18 Batch 1 C-scan top thin (nr 1 left) bottom thick (nr 1 left)

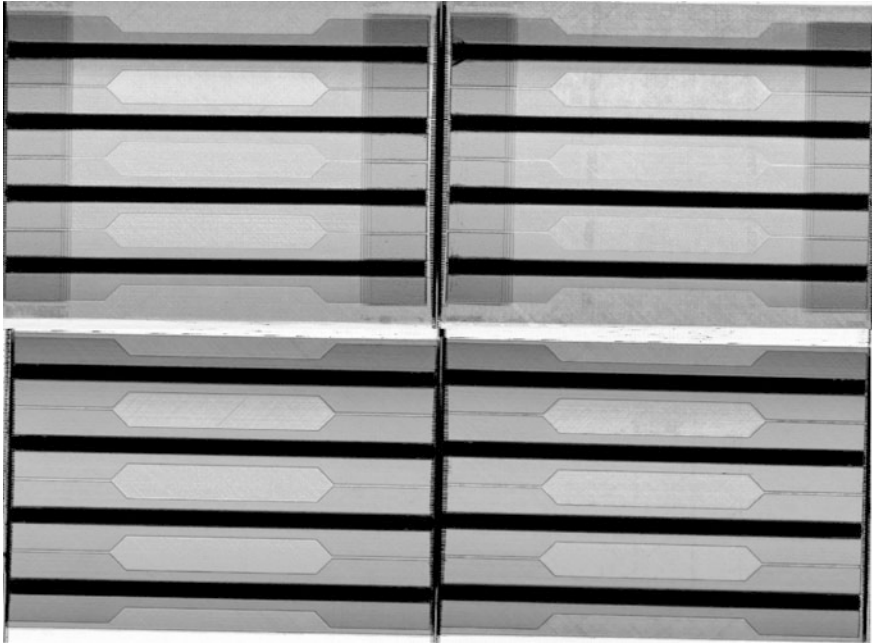


Fig. 19 Batch 2 C-scan top thin (nr 1 left) bottom thick (nr 1 left)

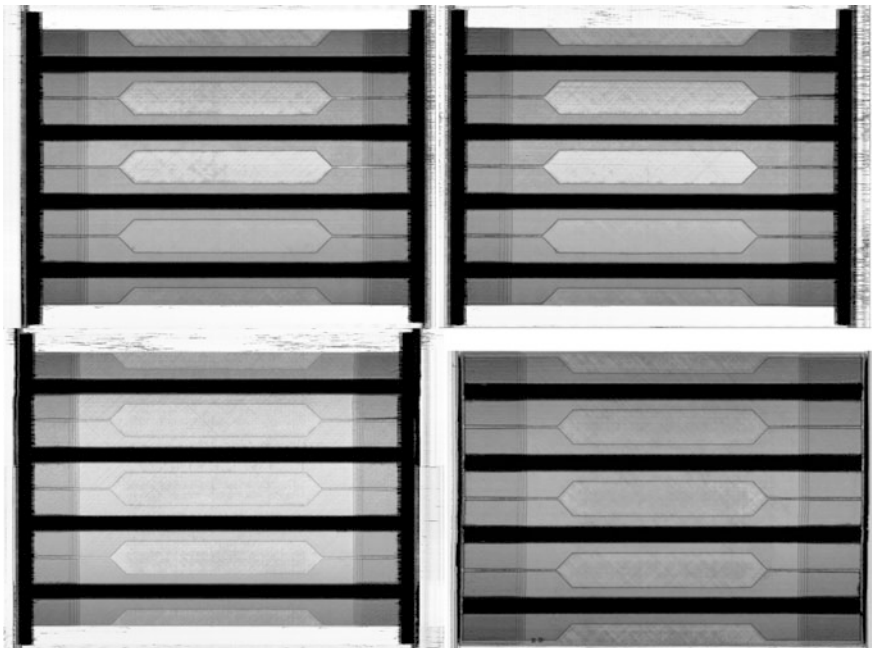


Fig. 20 Batch 3 C-scan top thin (nr 1 left) bottom thick (nr 1 left)

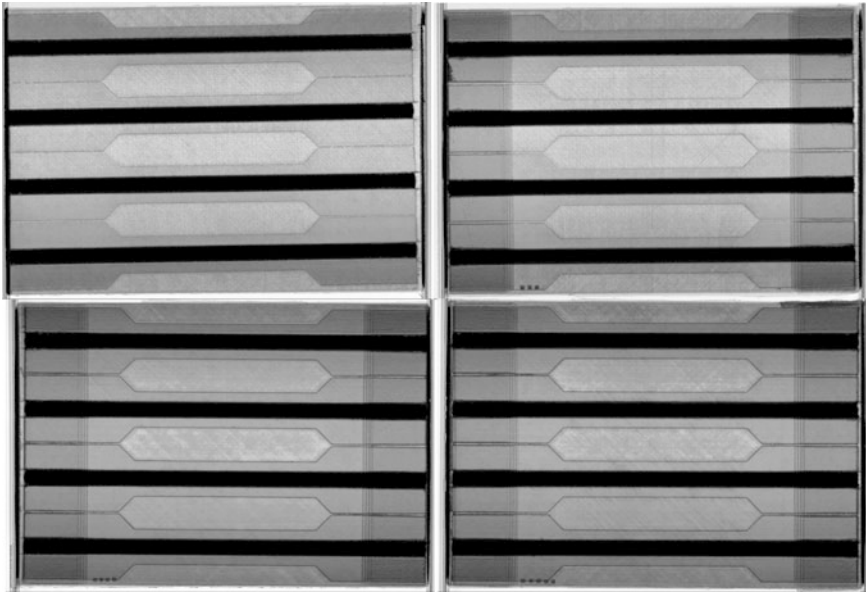


Fig. 21 Batch 4 C-scan top thin (nr 1 left) bottom thick (nr 1 left)

- Visual quality
- Product follow sheet filled out by responsible worker
- Panel manufacturing checked and recorded the following:
 - Stringer pitch
 - Thickness panel
 - Adhesive
 - NDT record
 - Dimensions after trimming (length, width)
 - Stringer and panel ID numbers
 - Visual quality
 - Product follow sheet filled out by responsible worker

Manufactured products not conforming to the dimensions were labelled, and a replacement product has been manufactured.

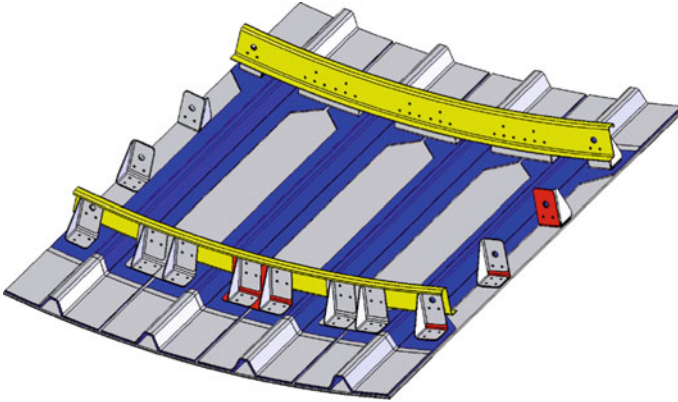


Fig. 22 CAD drawing of curved panels with metallic frames and clips

7 Curved Panel Assembly

After panels have been checked to be conforming to the specification, batches of these panels were shipped to Premium AEROTEC GmbH for assembly of metallic frames and clips required for containing the panel during testing (Fig. 22).

Fasteners:

- Clip/skin joints: EN6115K2-*
- Clip/cleat/frame joints : EN6081KE5-*
- EN6115K2-* may be used in place of EN6081KE5-* if it simplifies assembly and does not increase cost. The appropriate grip length needs to be chosen depending on the total thickness being fastened.

Frames:

- Aluminium 2024 (ABS 5044A012; based on Airbus serial production parts) (Fig. 23).

Clips (v1 and v2):

- Aluminium 2024 (ABS 5044A014; based on Airbus serial production parts).

Cleats:

- Aluminium 2024 (ABS 5044A014; based on Airbus serial production parts).



Fig. 23 Assembly in progress pictures from PAG

8 Conclusion

Several challenges have been encountered in producing the curved panels for the multi-site damage assessment. The envisaged tooling to be used has been replaced by smaller multifunctional tools for stringer and panel manufacturing. A special debulking procedure has been developed to obtain optimum stringer quality.

A range of mill types has been tested to deliver machined parts which have no fibre tear or requirement for any manual rework. A stringer positioning jig has been designed to conform to stringer position requirements. Potting of the panels proved to be very sensitive to exothermic and outgassing reactions of the resin. A procedure has been found to perform the potting even though the intended tolerances on the end faces could not be achieved from the potting support jig due to remaining thermal deformations. The panel ends with the potting were machined to the closest possible tolerance using a type of end mill that proved to deliver the best quality when milling the panel ends embedded in the softer potting resin. Custom panel crates have been built to transport the panel to Premium AEROTEC GmbH and to Imperial College London (ICL) after assembly.

Acknowledgments I would like to thank all partners involved in successful completion of this work package and for the support provided to solve the production challenges. The research leading to these results has received funding from the European Union's Seventh Framework Programme for research, technological development and demonstration under Grant Agreement No. 284562.

Compression After Multiple Impacts: Modelling and Experimental Validation on Composite Coupon Specimens

Spyridon Psarras, Raul Muñoz, Mazdak Ghajari, Paul Robinson and Domenico Furfari

Abstract This research investigates the post-impact behaviour of CFRP coupon specimens subjected to multisite impacts. Sequential low-velocity impacts at different locations were performed on coupons with different thicknesses. The impact load history was recorded, and the extent of damage was assessed by ultrasonic inspection. The residual strength in compression was then measured in a compression after impact rig which was specially modified for the testing of thin composites. High-speed video and digital image correlation records were taken for a number of specimens during testing. The experimental results were used to validate a finite element mesomechanical modelling approach which accounts for both intralaminar damage and interlaminar damage.

1 Introduction

Composite structures can be subjected to low-velocity impact during service, such as hail impact, which may cause a significant loss of stiffness and strength in compression. Impact-induced delaminations typically split the laminate into separate sublaminates, which are more susceptible to local buckling, leading to the premature collapse of the laminate [1–3].

The aim of this research was to investigate the post-impact behaviour of aircraft-grade carbon/epoxy laminates containing multisite impact damage. Sequential multisite impact tests were performed on composite coupons with different thicknesses. During experiments, the impact load history was recorded, and after each test, the extent of damage was determined by ultrasonic inspection.

S. Psarras (✉) · R. Muñoz · M. Ghajari · P. Robinson
The Composites Centre, Department of Aeronautics, Imperial College London,
South Kensington Campus, SW7 2AZ London, UK
e-mail: s.psarras@imperial.ac.uk

D. Furfari
Stress NSDW R&T—ESCRNS, Airbus Operations GmbH, 21129 Hamburg, Germany

After the impacts, the specimens were compressed up to failure and the failure loads were recorded. For testing thin composite coupons (2 mm thick or less), the compression after impact (CAI) fixture was modified to prevent global buckling. High-speed video and digital image correlation (DIC) records were taken for a number of specimens. The experimental results were used to validate a finite element (FE) modelling strategy that will be used to simulate the post-impact behaviour of stiffened panels.

2 Materials and Experimental Techniques

2.1 Low-Velocity Impact

The test program investigated two CFRP materials with two layups each, as detailed in Table 1. The specimens sized 150×100 mm and were impacted either along the horizontal centreline or along the vertical centreline of the specimen. As shown in Fig. 1, plates were subjected to either one impact or a sequence of two impacts at different locations. The same procedure was applied for both thin and thick coupons. Approximately, three specimens were tested for each impact scenario.

The impact tests were performed using a CEAST drop tower with CEAST 6.01 software controlling the test procedure and recording the test data. Each sample was placed in the preassembled rig in the base of the tower designed to ensure the correct location of the impact on each plate (Fig. 2). Four bolts secured the upper and lower portions of the rig around the specimen and were tightened to 25 Nm with a torque wrench. The actual impacting was automated and involved a 2.4-kg impactor being raised to the correct height corresponding to 10 J impact energy and then simply being released.

The test procedure (including inspection) was as follows:

- Measure and C-scan the specimens prior to test;
- Find the first impact of the specimens during which the force–time history was recorded;
- C-scan the specimens and measure the dent depth;
- Find the second impact during which the force–time history was recorded;
- C-scan the specimens and measure the dent depth.

Table 1 Materials and layups

Material	Name	Layup	Average thickness (mm)
T800/M21	Thin 1	[45, -45, 90, 0, 90, 0, 90, -45, 45]	1.65
	Thick 1	[45, -45, 90, -45, 0, 45, -45, 0, 45, 0] _s	3.7
HTS-6376C	Thin 2	[45, -45, 0, 90] _s	2
	Thick 2	[45, -45, 0, 90] _{2s}	4

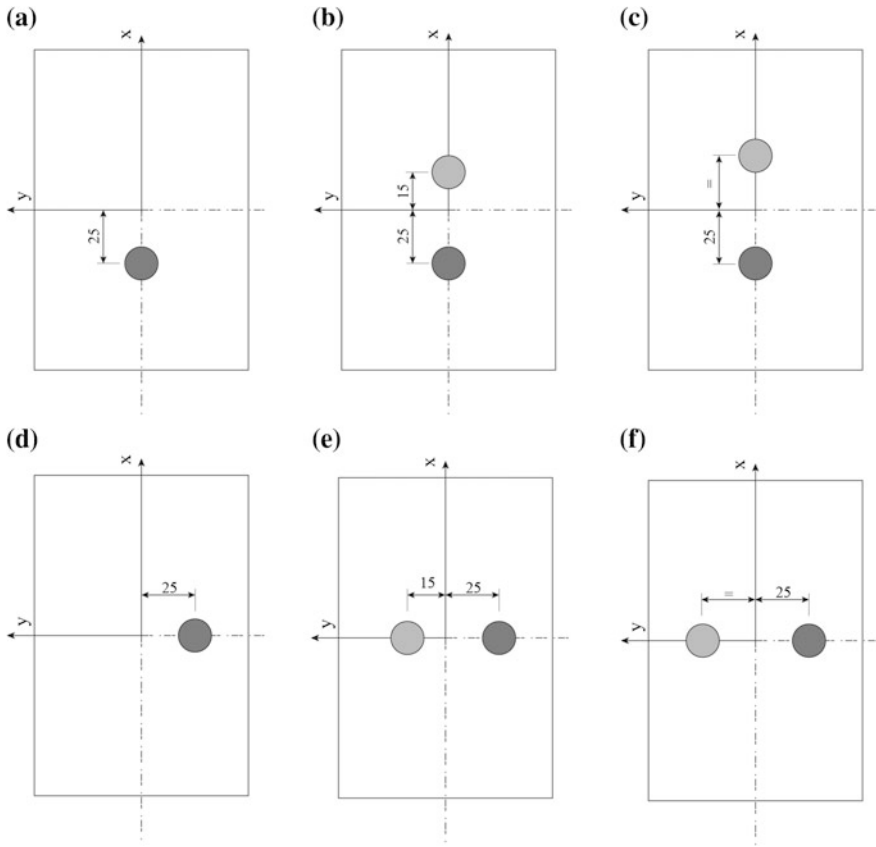


Fig. 1 Impact scenarios. The *dark grey circle* stands for the first impact, whereas the *light grey* stands for the second

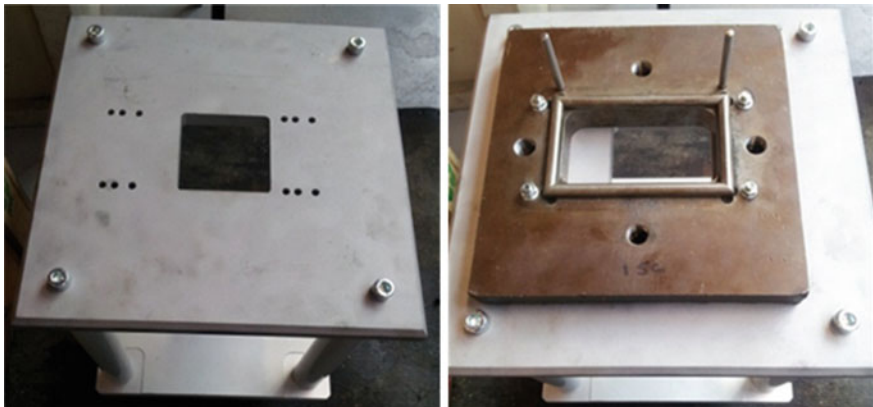


Fig. 2 Adapter designed to install the impact fixture with variable impact location in the drop-weight tower

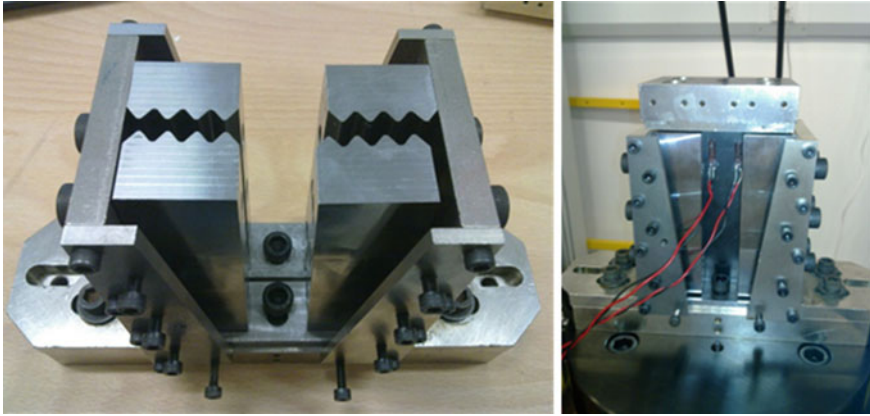


Fig. 3 CAI fixture designed to avoid global buckling of thin plates

On selected specimens, a time-of-flight ultrasound scan was taken to determine the through-thickness location of the impact-induced delaminations.

2.2 *Compression After Impact*

After impact testing, the specimens were tested using a CAI fixture [4] in an Instron testing machine with a 250-kN load cell at a rate of 1.5 mm/min under displacement control. For the current work, a modified testing fixture was designed and manufactured to avoid premature buckling of thin plates but also to allow the specimen to be observed during testing, as shown in Fig. 3. Strains were measured by using strain gauges and a digital image correlation system. High-speed cameras were used to record the onset of damage.

3 **Experimental Results**

3.1 *Low-Velocity Impact*

Low-velocity impact test results were very consistent for both thin and thick coupons. Force–time curves of specimens impacted at two different locations are depicted in Fig. 4. C-scan inspection revealed that the damage caused by the impacts is localized at each impact site with no overlapping or interaction between the two.

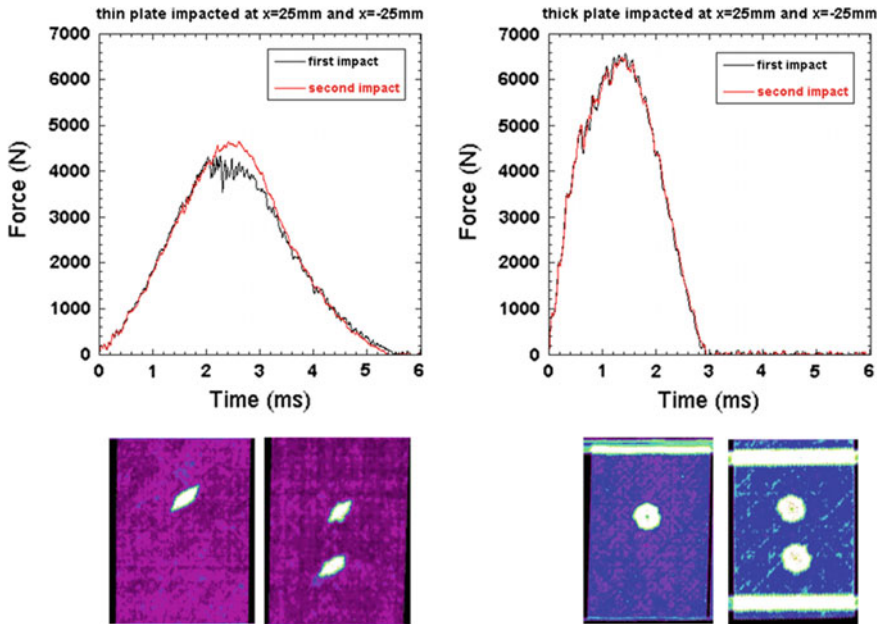


Fig. 4 Experimental force–time curves of the thin (*left*) and thick (*right*) plates subjected to a sequence of two impacts at $x = 25$ mm and $x = -25$ mm. The images under the curves depict the damage observed with a C-scan after each impact

3.2 Compression After Impact

Observation of the failed thin specimens confirmed that global buckling was avoided (Fig. 5).

The CAI strength test results are shown in Fig. 6. There are no clear trends that can be identified for all the material/thickness combinations. For the thin T800 specimens (Thin 1), a single impact reduces the strength, two impacts reduce the strength further, and increasing the separation of the two impacts reduces the strength even further (all the double impacts on the thin specimens were along the vertical axis). However, the level of scatter in the results means that the influence of the separation of the impacts may not be significant. For the thin HTS specimens (Thin 2), there seems to be little strength loss due to a single impact and two impacts which are separated by 40 mm along the vertical axis. Increasing the separation of the two impacts to 50 mm does produce a significant loss in CAI strength.

For the thick T800 specimens (Thick 1), the average data indicate a loss in strength due to a single impact, a further loss in strength for a double impact (along both the vertical and horizontal axes and with separation of 40 mm), but on an increase in the separation of the double impacts (along both the vertical and horizontal axes), the strength increases almost to that of the single impact case.

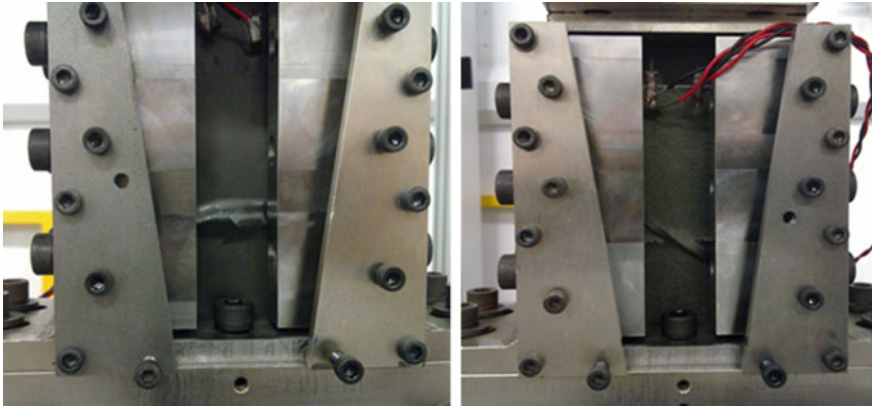


Fig. 5 Failure of thin specimens during CAI test

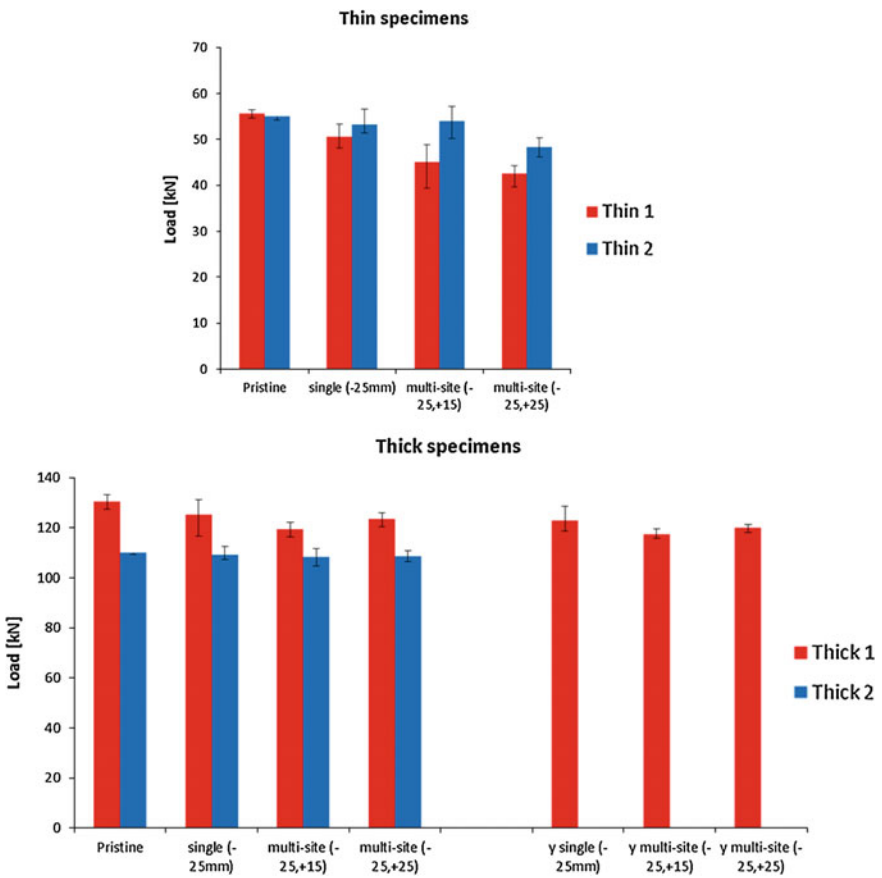


Fig. 6 Strength in compression of CFRP plates as a function of the number of impacts and the impact location (Thin 1 and Thick 1 are T800/M21, and Thin 2 and Thick 2 are HTS-6376C)

However, for this material, the changes in strength are not large compared to the scatter and so these trends may not be significant. For the thick HTS specimens (Thick 2), there is virtually no loss in strength due to a single impact or due to either of the two vertical axis double-impact cases. No horizontal axis double-impact cases were performed for this material.

4 FE Modelling

A finite element (FE) model based on a mesomechanical approach was developed to simulate the low-velocity impact and the compression after impact tests (Fig. 7). Each sublaminate of the plate was modelled with 8-node continuum shell elements with reduced integration (SC8R), whereas each ply within the sublaminate was represented with a through-thickness integration point. Cohesive elements were inserted between sublaminates to account for delamination onset and propagation during impact and compression. Thin coupons were modelled with two sublaminates, whereas thick coupons were modelled with four. The constitutive model of each ply was formulated within the continuum damage mechanics framework and was implemented via VUMAT in Abaqus/Explicit [5] to predict damage initiation and growth within each ply. The model, developed by Iannucci [6], accounts for four failure modes: tensile fibre fracture, compressive fibre fracture, coupled in-plane shear–tensile matrix fracture (quadratic criterion), and coupled in-plane shear–compressive matrix fracture. A unique feature of this model is that it has a nonlinear curve for in-plane shear stress–strain. Furthermore, with this model, it is possible to simulate irreversible strain (plastic strain) during unloading. The material properties were obtained from Airbus and the literature.

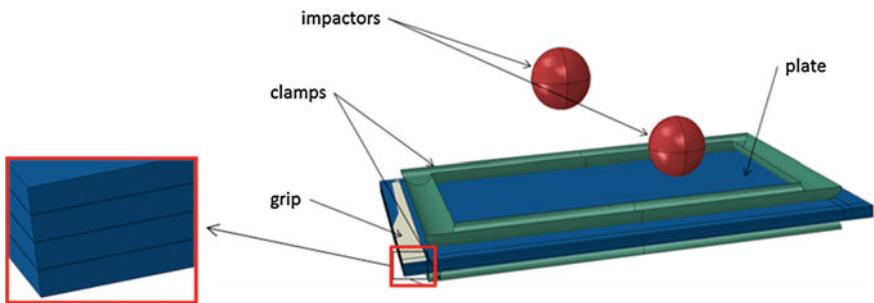


Fig. 7 FE model for simulating low-velocity multisite impact and CAI tests

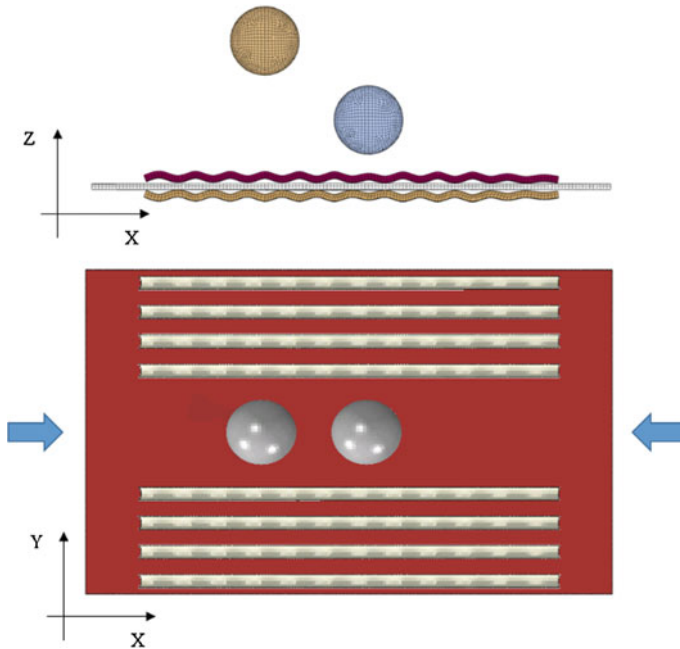


Fig. 8 Top and front views of the FE model of a thin plate impacted at two locations and supported during in-plane compression by wavy bars to account for geometric imperfections

The FE model was defined as a multistep analysis as follows:

1. First impact: A sphere defined as a rigid body (mass = 2.41 kg) was propelled onto the plate with an initial velocity of 2.88 m/s. To replicate the experimental tests, the clamping fixture (Fig. 2) was explicitly modelled.
2. Damping: To dissipate the kinetic energy of the plate, a viscous pressure was applied over the plate.
3. Steps 1 and 2 are repeated for each impact.
4. Compression: Once the plate stopped vibrating, the plate was compressed in the longitudinal direction at a rate of 1.5 m/s. The out-of-plane displacement of the thick plates was constrained during compression by a set of straight bars that represent the fixture. In the case of the thin coupons, the lack of flatness of the plates may have a significant influence on its post-impact behaviour, so geometric imperfections were introduced in the model by replacing straight bars with wavy ones (Fig. 8).

As is shown in Fig. 9, the FE model predicts a reduction of the compressive strength with a single impact and a much smaller further reduction due to a double impact.

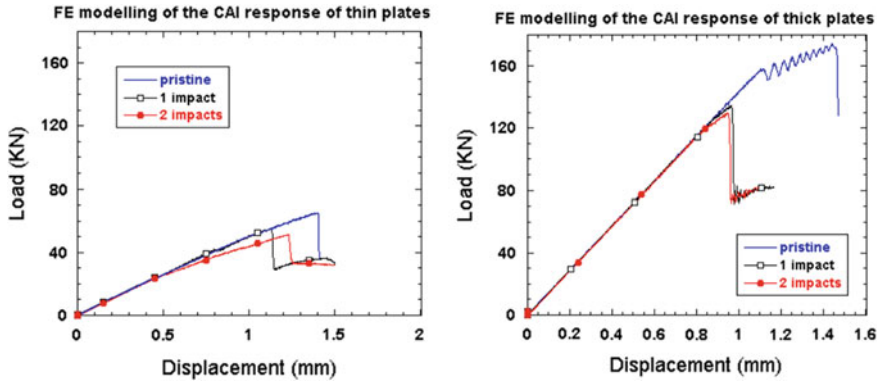


Fig. 9 Load–displacement curves obtained from CAI FE models of thin (*left*) and thick (*right*) plates (T800/M21). The plates were impacted along the vertical axis at the (x, y) coordinates $(-25, 0)$ for single impact and $(-25, 0)$ and $(25, 0)$ for two impacts

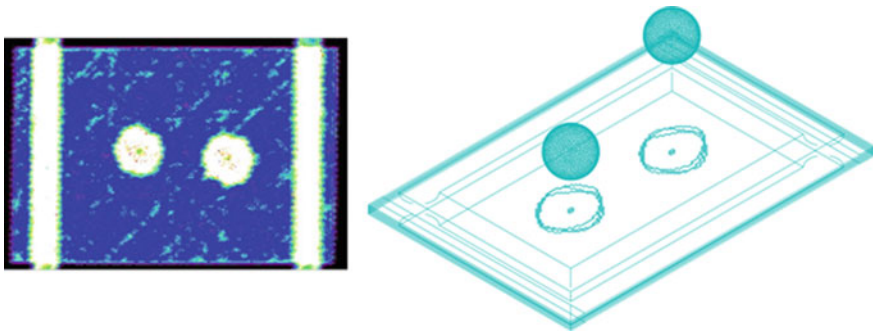


Fig. 10 Damage inspection on a thin coupon (T800/M21) after two impacts. C-scan (*left*) and delamination predicted by the FE model (*right*)

5 Correlation Between Simulations and Experiments

Comparison with experimental results revealed that the FE model predicts reasonable well the failure modes and patterns during low-velocity impact (Fig. 10) and CAI (Figs. 11 and 12), as well as the corresponding force–time and load–displacement curves (Figs. 13, 14, 15 and 16).

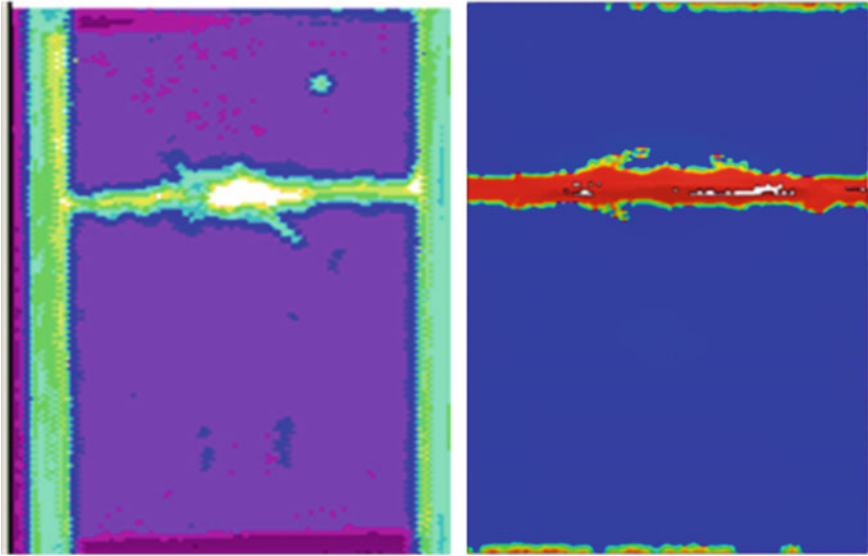


Fig. 11 Damage inspection on a thin coupon (T800/M21) after one impact. Comparison between damage detected by the C-scan (*left*) and fibre breakage predicted by the FE model (*right*)

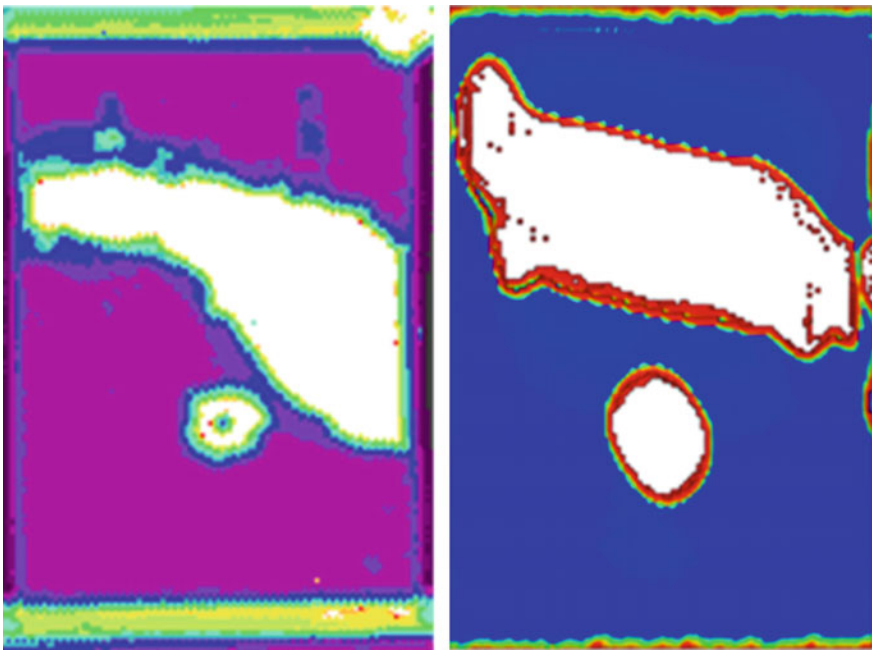


Fig. 12 Damage inspection on a thick coupon (T800/M21) after two impacts. C-scan (*left*) and delamination predicted by the FE model (*right*)

Fig. 13 Load–displacement curves of a thin plate (T800/M21) impacted at $x = 25$ mm. Comparison between numerical and experimental results

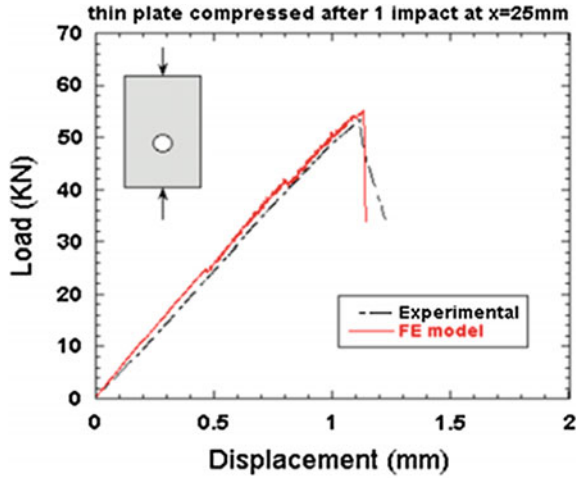


Fig. 14 Load–displacement curves of a thin plate (T800/M21) impacted at $x = 25$ mm and $x = -25$ mm. Comparison between numerical and experimental results

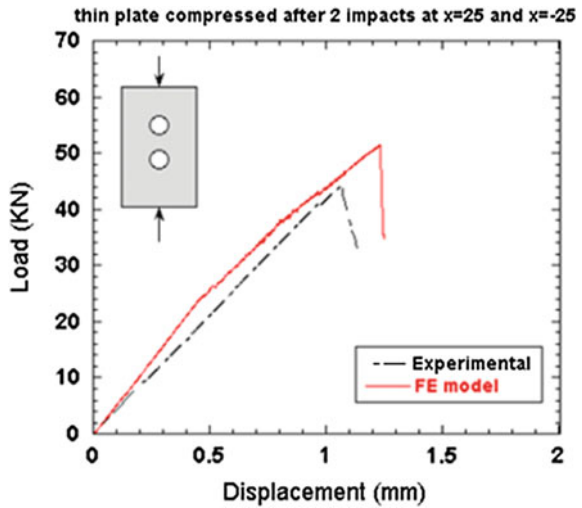


Fig. 15 Load–displacement curves of a thick plate (T800/M21) impacted at $x = 25$ mm. Comparison between numerical and experimental results

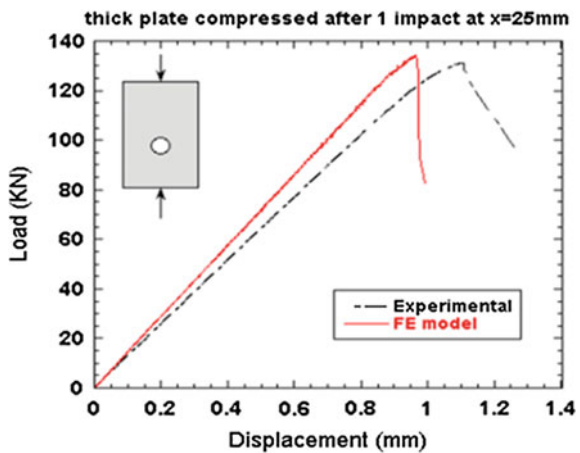
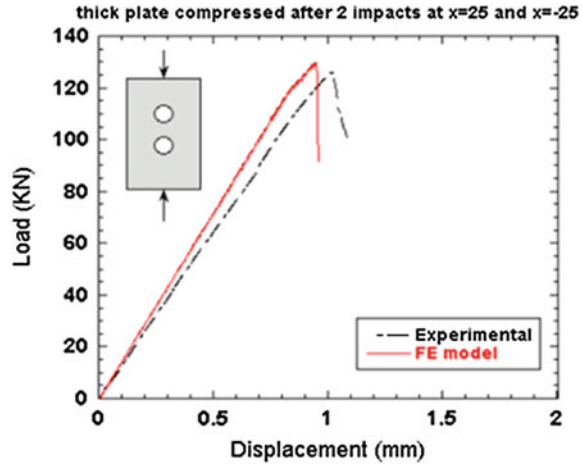


Fig. 16 Load–displacement curves of a thick plate (T800/M21) impacted at $x = 25$ mm and $x = -25$ mm. Comparison between numerical and experimental results



6 Conclusions

In this paper, the post-impact behaviour of CFRP plates was investigated by using experimental and numerical tools. In order to avoid global buckling when CAI testing thin specimens, a special support fixture was designed and manufactured. The experimental results were simulated by using a multistep FE model which accounts for both intralaminar damage and interlaminar damage. The FE predictions showed a good correlation in terms of damage size, failure modes, and load–displacement curves. It can be concluded that this modelling strategy can be used to predict the post-impact response of stiffened panels.

Acknowledgments This project has received funding from the European Union’s Seventh Framework Programme for research, technological development, and demonstration under Grant Agreement no. 284562.

References

1. Davies G, Olsson R (2004) Impact on composite structures. *Aeronaut J* 108
2. Baker N et al (2012) Damage tolerance of fully orthotropic laminates in compression. *Compos Sci Technol* 72:1083–1089
3. Sanchez-Saez S et al (2005) Compression after impact of thin composite laminates. *Compos Sci Technol* 65:1911–1919
4. ASTM-D7137/D7137 M-12 (2014) Standard test method for compressive residual strength properties of damaged polymer matrix composite plates

5. Pinho ST et al (2006) Physically based failure models and criteria for laminated fibre-reinforced composites with emphasis on fibre kinking. Part II: FE implementation. *Compos Part A Appl Sci Manuf* 37:766–777
6. Iannucci L, Willows M (2006) An energy based damage mechanics approach to modelling impact onto woven composite materials—Part I: numerical models. *Compos A Appl Sci Manuf* 37:2041–2056

Compression After Multiple Impacts: Modelling and Experimental Validation on Composite Curved Stiffened Panels

Spyridon Psarras, Raul Muñoz, Mazdak Ghajari, Paul Robinson, Domenico Furfari, Arne Hartwig and Ben Newman

Abstract This research investigates the post-impact behaviour of composite fuselage panels subjected to multi-site low-velocity impacts. Large curved stiffened panels (1.2 m × 0.8 m, with composite skins/stiffeners and aluminium frames) of two different skin thicknesses were subjected to sequential drop-weight impacts at locations previously determined to be critical in FE simulations. After assessment of the impact damage, each panel was tested in compression. High-speed video, strain gauges, digital image correlation and acoustic emission were used to monitor the failure development and to provide data for comparison with the FE simulations. The FE models, which were based on a mesomechanical approach, showed a good agreement with both the impact damage and the subsequent compression performance.

Nomenclature

FE Finite elements
LVI Low-velocity impacts
CAI Compression after impact
DIC Digital image correlation
HSC High-speed camera

S. Psarras (✉) · R. Muñoz · M. Ghajari · P. Robinson
Department of Aeronautics, Imperial College London, South Kensington Campus,
London SW7 2AZ, UK
e-mail: s.psarras@imperial.ac.uk

D. Furfari
Research and Technology, Airbus Operations GmbH, 21129 Hamburg, Germany

A. Hartwig
Structural Analysis Process and M&T, Airbus Operations GmbH, 21129 Hamburg, Germany

B. Newman
Altran GmbH and Co KG, Hein-Saß-Weg 30, 21129 Hamburg, Germany

AE Acoustic emission
HD High definition
KVE KVE composite structures BV
NDT Non destructive testing
PAG Premium AEROTEC GmbH

1 Introduction

The aim of this study is to investigate the post-impact behaviour of aircraft-grade carbon-/epoxy-curved stiffened panels containing multi-site impact damage that may arise, for example, in a hail storm. Delaminations and disbonding at the skin–stiffener interface created by impact can grow under compression leading to global collapse of the stiffened panel. This process can be significantly promoted by local buckling of sublaminates created by the delaminations and of the skin laminate separated from the stiffener by disbonding. Other compressive failure mechanisms include global buckling, local-global buckling and in-plane failure due to stress concentrations.

The study included an experimental programme consisting of multi-site impact and compression-after-impact testing of curved composite stiffened panels of two different thicknesses. The impact locations and energies were determined after detailed FE modelling, where a multistep analysis simulated the impacts and the CAI. After the impacts on the panels and the damage assessment, the panels tested to failure in compression. During the CAI, a variety of monitoring and data collection equipment was used aiming in different failure and damage aspects such as the damage initiation where a HSC was used. After, the experimentally observed behaviours were compared to the predictions from detailed finite element models.

2 Manufacturing of the Panels

An overview of a panel is shown in Fig. 1. The material of the panels and the omega hat stiffeners was the T800/M21. Panels with two different thickness sets of skin-stiffeners were manufactured as detailed in Table 1. The reinforcing plies of woven carbon fibre prepreg Fibredux 913C–926–40 % positioned in a strip at each end of the panel and were used to ensure that there was no premature failure due to stress concentrations associated with the load introduction.

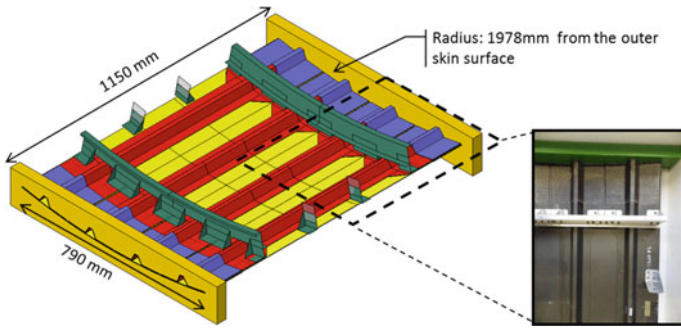


Fig. 1 Overview of the panel with its parts; skin (yellow), stiffeners (red), reinforcing plies (blue), potting (green) and aluminium frames and clips (grey)

Table 1 The thicknesses and the layups of the panels manufactured

	Part	Thickness (mm)	Layup
Thin	Skin	1.656	45/-45/90/0/90/0/90/-45/45
	Stiffener	1.288	45/-45/0/90/0/-45/45
Thick	Skin	3.680	45/-45/90/-45/0/45/-45/0/45/0/0/45/0/-45/45/0/-45/90/-45/45
	Stiffener	2.944	45/-45/0/0/90/0/0/45/-45/0/0/90/0/0/-45/45

The manufacture of the composite panels was performed by KVE and the aluminium ring frames and brackets were attached by PAG. The skin and the stringers were laid up from prepreg and autoclave cured separately. FM 300 film adhesive was used to bond the stringers to the skin using a jig to ensure their correct positioning. Reinforcement plies then were bonded on the end regions of the panels.

The ends of the panels were potted in a block glass fibre-reinforced epoxy resin using a mould formed of an aluminium alloy channel section. Prior to the end potting, the interior of the each omega stringer was sealed with a foam block at a suitable depth and filled with the potting resin which was allowed to cure. After each end of the panel was potted the frames, the clips and the cleats were installed. (The clips at the edges of the panels were to provide connections to an out-of-plane support jig used during the compression testing to prevent premature buckling at the free edges of the panel.)

3 Finite Element Model Predictions

Finite element (FE) models using ABAQUS were developed in order to simulate the low-velocity impacts (LVI), the interaction between multiple areas of damage and the compression-after-impact (CAI) performance of the composite panels. A FE model of the thin and thick CFRP composite panels was developed using continuum shell elements. Layers of cohesive elements were inserted between sublaminates in order to model delamination initiation and growth during impacts. An energy-based damage model developed at Imperial College [1] and implemented into the Abaqus FE system as a user material subroutine damage [2, 3] was employed to represent translaminar damage. This is based on a continuum damage mechanics approach and can predict four failure modes; tensile fibre fracture, compressive fibre fracture, coupled in-plane shear-tensile matrix fracture (quadratic criterion) and coupled in-plane shear-compressive matrix fracture [4].

The detailed FE model is shown in Fig. 2. The skin, the reinforcements and stiffeners were modelled as solid parts in order to mesh them with continuum shell elements. The frame was modelled as a shell part and meshed with conventional shell elements. The end regions of the panel, which were inserted in the resin, were tied to the reinforcements. A multistep analysis was used in order to simulate the impacts and the CAI. This consisted of a step for each impact, a rigid 20-mm-diameter sphere with mass according to the desired energy and a step for the CAI test. Between these steps, a damping step was defined during which a viscous pressure was applied on upper and lower surfaces of the panel to bring the panel to rest prior to the start of the next step.

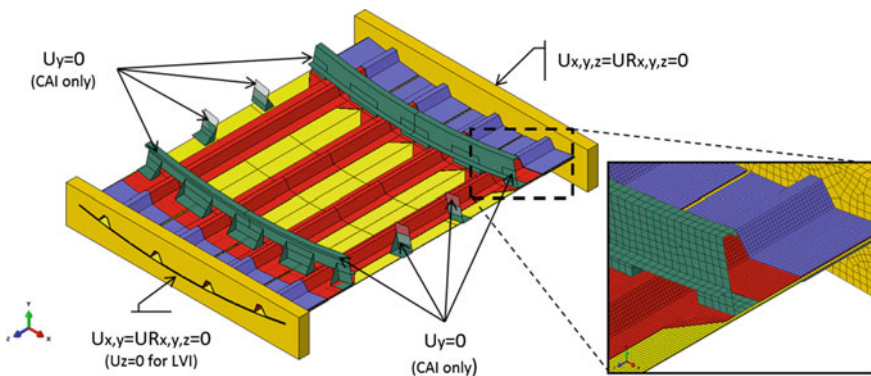


Fig. 2 Detailed FE model of the panel with the boundary conditions used during the multistep analysis

Table 2 Impact scenarios

	Panel	TN-pr	TN-sc0	TN-sc1	TN-sc2	TN-sc3
	Energy [J]	-	25	25	40	40
thin	Impact positions	-				
		-				
thick	Panel	TK-pr	TK sc1	TK sc2		
	Energy [J]	-	58	58		
	Impact positions	-				
		-				

Table 3 Summary of key tasks during the panel test campaign

Prior to testing	Impact testing	CAI testing
Perform ultrasound inspection	Record force-time history	Record applied load and displacement (LVDT)
Mount strain gauges	Perform ultrasound inspection	Record strain (strain gauges)
Spray speckle pattern for digital image correlation (DIC)		Capture images for DIC (for displacement and strain field)
		Record acoustic emission (AE) signals for damage classification
		High-speed camera recording (for crack initiation/propagation)
		High-definition video (to monitor overall behaviour)

4 Testing the Panels

The key tasks of the test campaign are summarised in Table 3. The first step was to prepare the panel; the panel was c-scanned; strain gauges were placed in the pre-defined positions, and a speckle pattern was sprayed for the DIC monitoring during the CAI testing. The impact tests were performed using a CEAST drop tower, Fig. 3, with CEAST 6.01 software controlling the test procedure and recording the test data. Each panel was placed in the base of the tower designed to ensure the correct location of the impacts. The locations of the impacts were determined from

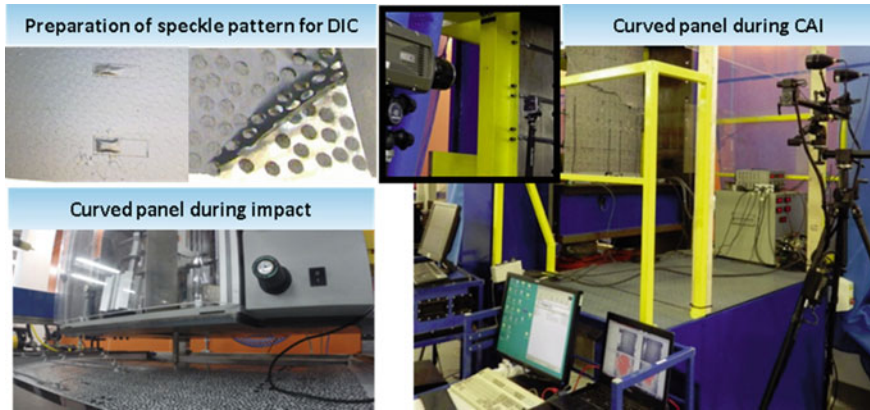


Fig. 3 Panel preparation and testing setup



Fig. 4 Designed framework to provide out-of-plane support to the panel

the FE analyses. The test scenarios that were investigated are summarised in Table 2. For scenarios TN-sc1 and TK-sc1, the impact centres have a distance of 50 mm and they are towards the web of the stiffener. For scenarios TN-sc2 and TN-sc3, the impacts have a distance of 40 mm and they are towards the edge of the stiffener. For TK-sc2, the impacts are in a zigzag pattern with 30 mm centre differences.

After each impact, the panel was inspected by using a portable ultra sound scanner to verify the damage size that was introduced to the panel. After assessment of the impact damage, each panel was subjected to a highly instrumented compression test to failure. A hyper-stiff 2500-kN compression machine was used for these tests. This has been modified with a specially designed framework to provide out-of-plane support to the ring frame members and to the free edges of the skin (Fig. 4).

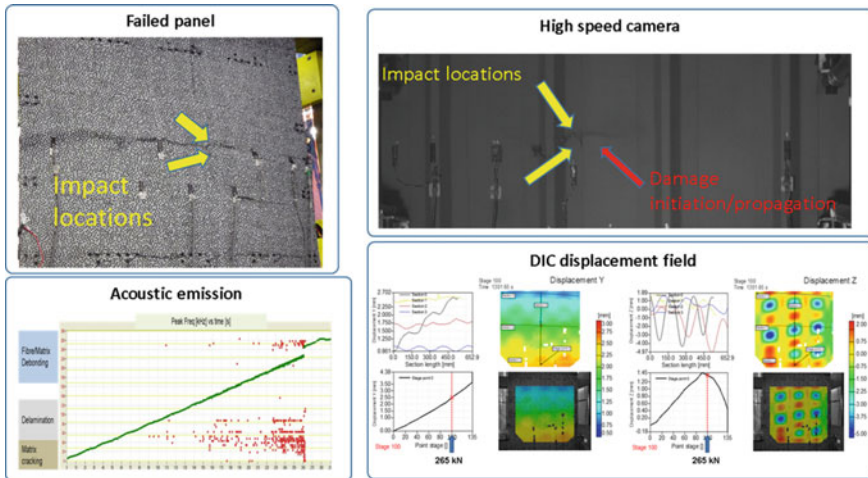


Fig. 5 Typical output from CAI testing: *top left*, a CAI-tested panel, indicating locations of the impacts, *top right*, the high-speed camera captures the initiation of the crack from the impacted area; *bottom right*, the DIC records of the skin vertical and out-of-plane displacements; *bottom left*, the classification of the damage made using the acoustic emission data

During the CAI tests, HD video and high-speed camera (HSC) recording, strain gauges, DIC and acoustic emission (AE) monitoring were used to monitor the failure development and provide data for comparison with the FE simulations. The HSC was used in order to capture the initiation and propagation of the cracks. The strain gauges were used to monitor the strain variations between the stiffeners and the skin and were correlated with the DIC data, which also provided information on the displacements and the local buckling. Finally, the damage classification during the CAI was assessed by using acoustic emission. Typical output of the CAI tests is shown in Fig. 5.

In Table 4, a summary of the CAI failure loads is presented. Comparing the failure loads of the pristine panels with the impacted panels, it is clear that the

Table 4 Experimentally measured and FE-predicted CAI failure loads

Scenario	CAI Failure load [kN]			FE prediction of CAI failure (kN)
	Test 1	Test 2	Test 3	
TN-pr	336			340
TN-sc0	324			320
TN-sc1	338	335		340
TN-sc2	298	311	308	300
TN-sc3	260			270
TK-pr	1210			1500
TK-sc1	1211	1233		1450
TK-sc2	1055			1400

extent to which the strength is reduced depends on the energy and location of the impacts. Not all impact damage leads to a reduction of the strength (for example, see test scenario TN-sc1). The strength of a panel is reduced more for higher energy impacts over the stiffener foot (e.g. scenarios TN-sc2 and TK-sc2).

5 Comparison of Test Results with the FE Models

Table 4 includes the FE-predicted failure loads for the CAI tests and Fig. 6 presents experimental and predicted data for both the impact and CAI behaviours. The FE models can accurately predict the damage size of the skin delaminations and the skin/stiffener debonding area caused by the impacts and the force–time response is also well predicted. For the CAI behaviour, the FE models successfully predicted the magnitude of the loss in strength of the panels and the local buckling is well predicted as is the location of the failure initiation and its propagation path. The CAI failure load predictions are more accurate for the thin panels as can be

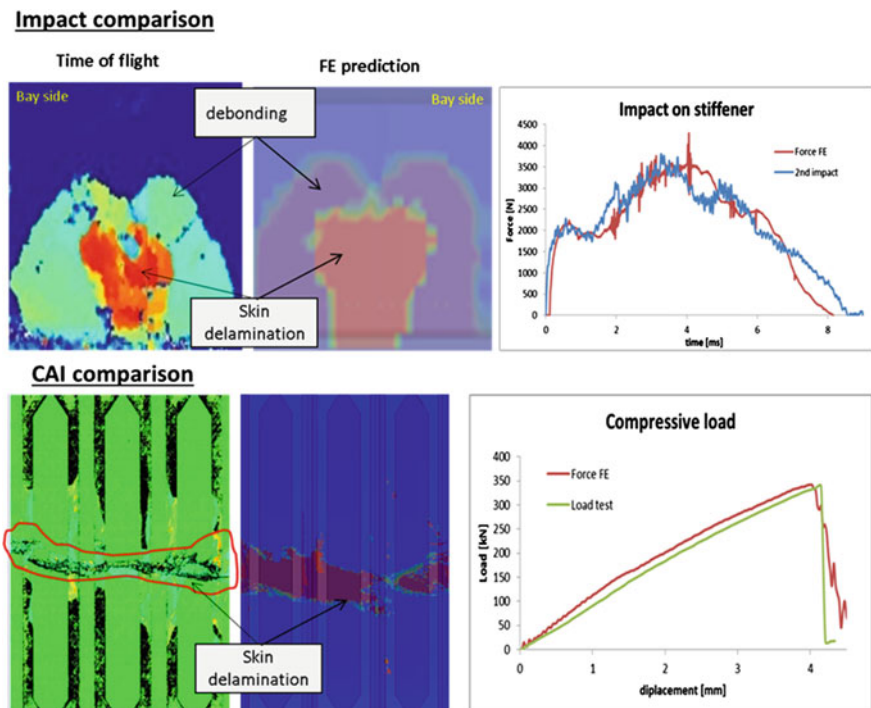


Fig. 6 Comparison between the FE prediction for impacts (example of an impact above a stiffener foot where delamination and disbond occurs) and CAI final failure of TN-sc1

seen in Table 4 and further studies are being conducted to explore the influence of various FE model refinements (such as cohesive elements to capture delamination growth within the stiffener feet).

6 Conclusions

This chapter presents the behaviours observed during multi-site impact and compression-after-impact testing of curved composite stiffened panels of two different thicknesses and compares these behaviours to FE predictions. The test jigs (including the specially designed anti-buckling fixture for the CAI testing) worked well and the panels failed in a valid manner. The experiments demonstrated the influence of energy, location and number of multi-site impacts on the compressive residual strength. FE model predictions showed good agreement with the experimental data for the impact response and for the subsequent compression behaviour, and can be used to identify critical multi-site impact scenarios.

Acknowledgements This project has received funding from the European Union's Seventh Framework Programme for research, technological development and demonstration under grant agreement no 284562.

References

1. Iannucci L, Willows M (2006) An energy based damage mechanics approach to modelling impact onto woven composite materials—Part I: numerical models. *Compos A Appl Sci Manuf* 37:2041–2056
2. Ankersen J (2011) Abaqus laminated composite damage 2D VUMAT guide for input parameters. Imperial College London
3. Pinho ST et al (2006) Physically based failure models and criteria for laminated fibre-reinforced composites with emphasis on fibre kinking. Part II: FE implementation. *Compos Part A Appl Sci Manuf* 37:766–777
4. Dávila CG, Camanho PP (2003) Failure criteria for FRP laminates in plane stress, paper 2003-1991

Multisite Damage Assessment Tool

Tulug Pince

Abstract Composites generally are not damage-tolerant, and impact damage can significantly degrade the compressive strength of a composite laminate. Even when no visible impact damage is observed at the surface (energies below barely visible impact damage (BVID)), matrix cracking and interlaminar failure can occur and the carrying load of the composite laminates might be considerably reduced (de Freitas et al in *Compos Struct* 42(4):365–373, 1998). The aim of the multisite damage assessment tool is to give quick answers with regard to remaining airworthiness and further investigations after hail strikes and reducing aircraft on ground time. To clarify the remaining airworthiness of an aircraft after multisite damage (MSD), mainly caused by hail strikes, an assessment tool is developed based on physical and virtual testing as well as accuracy factors of structural health monitoring (SHM) information.

Nomenclature

AOG	Aircraft on ground
AS	Application scenarios
AU	Acousto ultrasonic
BVID	Barely visible impact damage
CVM-TTT	Comparative vacuum monitoring through the thickness
DAT	Damage assessment tool
DET	Detailed inspection
DSG	Design service goal
FBG	Fiber Bragg grating
FEA	Element analysis
FC	Flight cycles
FH	Flight hours
GVI	General visual inspection
LVID	Large visible impact damage

T. Pince (✉)
Altran GmbH & Ko KG, Hein-Sass-Weg-30, 21129 Hamburg, Germany
e-mail: tulug.pince@altran.com

MSD	Multisite damage
MSDAT	Multisite damage assessment tool
NDE	Nondestructive evaluation
NDT	Nondestructive testing
OF	Optical fiber
PZT	Piezoelectric
RF	Reserve factor
SHM	Structural health monitoring

1 Introduction

Impact loading is known to cause extensive internal delaminations, matrix cracking, and fiber breaking in composite structures. Since composites, in general, are not damage-tolerant, impact damage can significantly degrade the compressive strength of a composite laminate. Even when no visible impact damage is observed at the surface (energies below barely visible impact damage (BVID)), matrix cracking and interlaminar failure can occur, and the carrying load of the composite laminates might be considerably reduced [1].

To clarify the remaining airworthiness of an aircraft after multisite damage (MSD), mainly caused by hail strikes, an assessment tool shall be developed based on structural health monitoring (SHM) information.

Areas prone to MSD will be equipped by a network of damage-detecting sensors. Eligible sensor technologies are fiber Bragg grating (FBG) sensors (AS04) and piezoelectric (PZT) sensors (AS06). As these technologies by nature of the measurement task are optimized for impacts from the outside, additionally CVM-TTT technology (AS07) will be integrated on stiffener element areas not directly adhered to the structure like stringer flanges or stringer hats.

2 Damage Types

Composites have unique damage sensitivities for both tension and compression loads.

There are different types of damages, which have to be considered:

- Fiber breaking
- Scratches, nicks
- Cracks
- Dents
- Delamination/Debonding

Broken fibers can be critical, because composite structures are typically designed to be fiber-dominant [2]. Fortunately, fiber failure is typically limited to the zone of impact contact and is constrained by the impact object size and energy. The resulting loss in residual strength is controlled by a relatively small damage size. One exception can be a high-energy, blunt impact over a large area, which breaks internal structural elements such as stiffeners, ribs, or spars, but leaves the exterior composite laminate skin relatively intact.

Scratches, gouges, and nicks are not critical if the damage is limited to the outer layer of resin. In case of fiber damage, they must be treated as a crack in the affected plies. Unlike metals, composite matrix nicks, scratches, and gouges are not likely to grow under repeated loads [3].

Cracks have a high stress concentration. The fibers in composite laminates act to inhibit tensile crack growth, which only occurs at relatively high stress levels. Consequently, damage growth, through the thickness, which progressively breaks the fibers in a composite, has generally not been a problem. Damages that include delamination or matrix damage along with cracks can have less severe stress concentrations and behave more like a soft inclusion in the laminate.

Dents are typically caused by an impact event. The dent is usually an indication of underlying damage, which can consist of fiber breakage, delamination, debonding and/or intramatrix cracks.

Delaminations occur on the interface between the layers in the laminate. Delamination after low-energy impacts causes only negligible effects on tensile strength, but may significantly reduce the compressive strength and lead to instabilities with shear loading [4]. The size of the delaminated zone increases with impact energy.

Results from FEA suggest that especially through thickness position of delamination plays an important role since the influence of damage is quite different [5, 6].

Delamination near the surface reduces the local buckling force by a great extent, while delamination that is deep in thickness does not (delamination of ~ 25 mm a sphere).

In regard to global buckling, the opposite effect was shown: Delamination deep in thickness reduced the critical buckling load significantly: The deeper the delamination, the lower the compressive failure load.

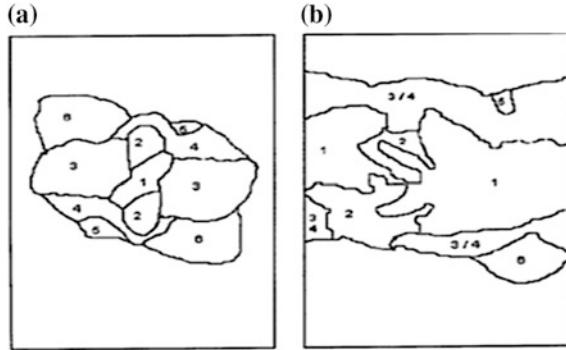
Typical delamination patterns after impact are shown in Fig. 1, which suggest an increase of delamination through the thickness [4].

Ply direction influences the delamination shape: The shape of the delaminated area for each interface between two plies is more pronounced in the ply orientation, which is at a larger distance from the impact zone.

An increased number of interfaces will, therefore, decrease the projected delaminated area. Since an increase of delamination during loading is possible before the ultimate strength is reached (depending on the stiffness of the material and depth of delamination) [6, 7], a continuous surveillance of the damage is of importance.

Next to the size of impact, the process of perforation of the panel affects the amount of damage [8]. Since the perforation process absorbs impact energy, the

Fig. 1 Delamination pattern for specimen D*II, T800/5245C: **a** after impact; **b** after CAI with a dent depth of 0.3 mm. 1–6 are different laminate interfaces [4]



reduction of the ultimate buckling force is smaller in comparison with a nonperforated laminate.

The damage location shows an influence on the effect of residual strength as well. The residual strength depends on the distance between the delaminated area and the lateral borders of the specimens [4].

Multiple damages are known to show an effect on residual compressive strength in dependency of the damage distance and loading direction [9]. For multisite damages with center-to-center distance of less than 1.7 damage diameters, it was found that multiple impacts can be treated as a single impact of twice the diameter.

2.1 Hail Strike

The largest threat for top panels, the region evaluated in this paper, is hail strike (Fig. 2).

In-flight hail strike is mainly found in the front fuselage, whereas on ground hail strike occurs at the upper fuselage panels [10, 11].

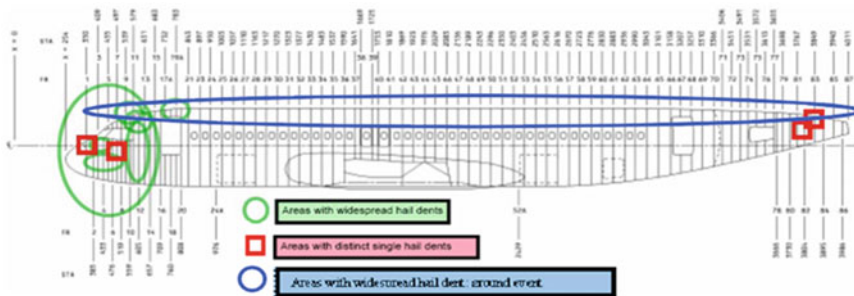


Fig. 2 Fuselage zonation for hail impact threat [10]

For impact of damage evaluation, it is important to estimate the size and energy of the impact.

Size of hailstones is as follows:

- Standard hailstorm (Ø 10 mm) for a *P* of 50 % of hailstorms
- Rare hailstorm (Ø 25 mm) for a *P* of 5 % of hailstorms
- Extremely rare hailstorm (Ø 50 mm) for a *P* of 0.1 % of hailstorms

Hail showers show a velocity of about 33 m/s with the impact energy of 32 J for aircrafts on ground. The concentration per unit area impacting a surface is also based on the size of the storm. For further information, please refer to [1].

Probability of hail strikes is hard to estimate due to high differences between region, season, and meteorological means of each country. In [1], all these variables established are discussed. In this report, the main focus is on Europe. Figure 3 shows the map of hail strike threat in Europe.

To convert the density color scale to “number of hail days per year per degree square,” the values need to be multiplied by 22 [1]. The probability of hail strike per FH over an aircraft lifetime is as follows:

$$\text{Probability of hail strike} = \frac{\text{density}}{\left(\frac{\text{DSG}}{\text{life time}}\right)} \tag{1}$$

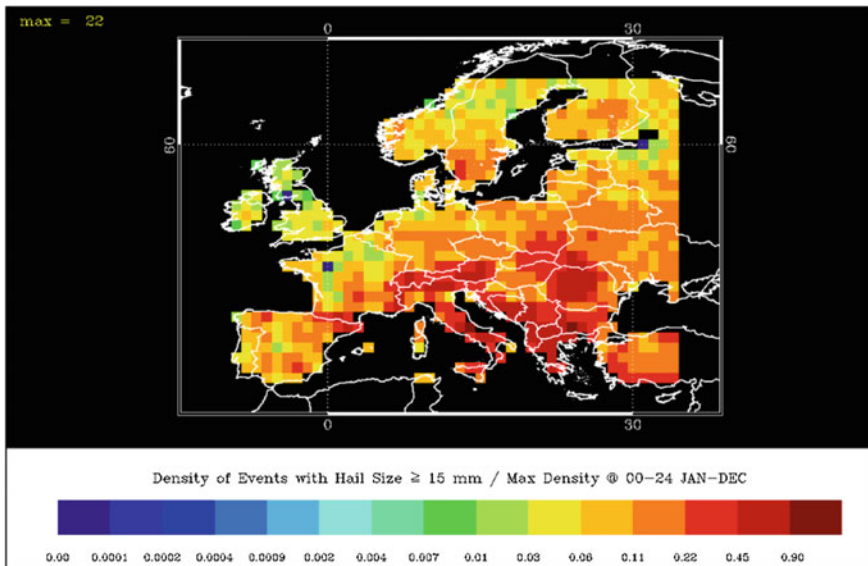


Fig. 3 Normalized density of hail days per year per degree square over Europe [1]

Assumptions:

- DSG = 100 000 FH [12]
- Aircraft lifetime = 30 years
- Average density of hail days = 0.11×220 (Fig. 3).

The probability of damage occurrence regardless of region and damage type is $2.4 \times 10^{-3}/\text{FH}$, which results in approximately 240 damages over 100,000 FH [13]; 85 % of the detected damages (whatever the maintenance task, A check, C check, daily, weekly, etc.) have dent depth below Airbus established detectability threshold (1.3 mm) [11].

3 Multisite Damage Assessment Tool

3.1 Benefit of an Assessment Tool

Within SARISTU, the MSDAT’s main objective is to save time and costs by avoiding unnecessary maintenance after obvious damage initiating incidents and during the scheduled maintenance steps. Benefits of the MSDAT are estimated under different aspects (Table 1).

Currently, the procedure for damage detection and evaluation is shown in Fig. 4.

With integrated sensing, the assessment can be performed in every airport. The utilization of the system shall be as simple as possible to avoid the necessity of inspectors’ level 2. The damage assessment process will become like in Fig. 5.

So, flights to special bases, which lead to spare day groundings which cost about 40,000\$ per day including the inspection and the access [12], can be avoided too.

Table 1 MSDAT benefits

Domain	Gain	Mitigation
Unscheduled maintenance	Damage assessment time	The SHM system must be able to assess damages in every airport
Scheduled maintenance	Access time + damage assessment time	The SHM system must be able to assess internal damages without access
Structural efficiency	Weight, concession, repairs	Long-term benefits

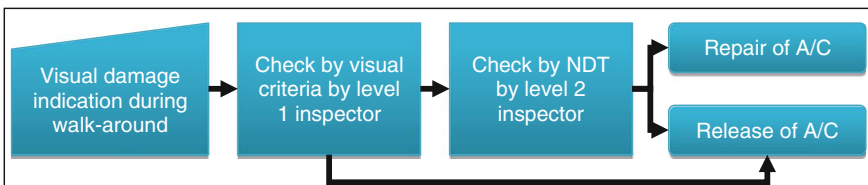


Fig. 4 Current damage assessment process (simplified) [12]

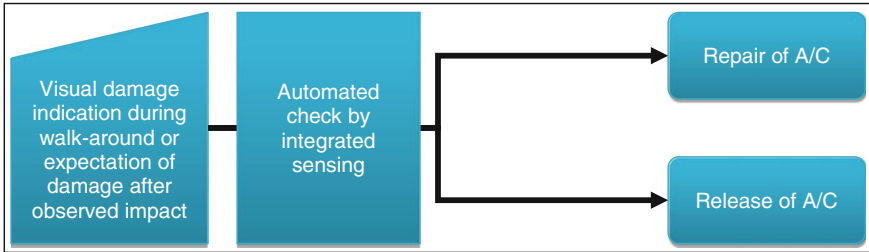


Fig. 5 Target damage assessment process (simplified) [12]

3.1.1 Philosophy

Ideal Damage Assessment Tool

The ideal damage assessment tool is supposed to provide data for guidance of the structural health of an aircraft to the customer and the repair team. The occurrence and characterization of damage (size, type, and location) are provided by NDE. The assessment tool is based on lookup tables, analytical algorithms, safety standards, and SRMs, which rely again on experimental data and FEA, to provide a quick decision. Next to the damage itself, essential input data would be the load-carrying data, strength of the aircraft structure, and current reserve factors (RFs) (implementing former damage and repair). Information as current flight cycles of aircraft, future flight route, and ground information may also be included in a further step (Fig. 6).

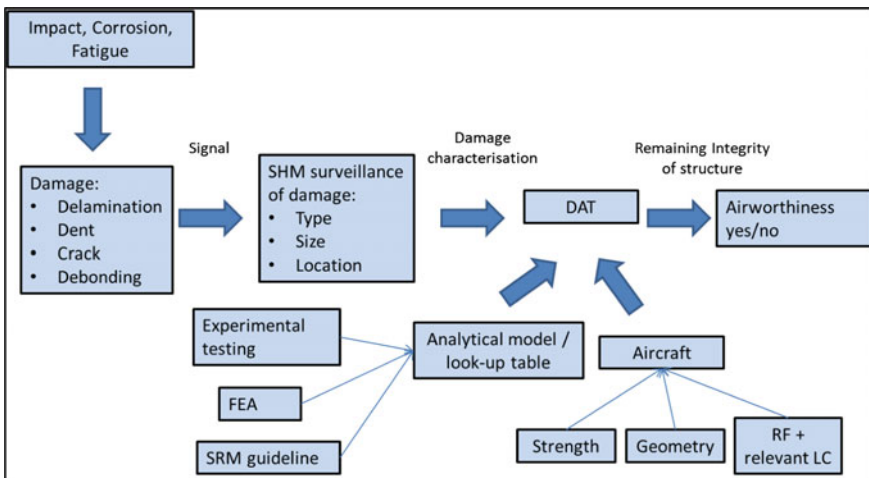


Fig. 6 Flow diagram of the ideal damage assessment tool (DAT)

SHM measurement would give the entire relevant damage characteristic to assess the damages and to draw recommendations regarding the airworthiness of an aircraft.

Current Damage Assessment Tool

The MSDAT evaluation is based on Guehrs’ parametric study [14], conducted with ABAQUS and validated by physical tests [15]. Nielen’s parametric study [16] is, at this time, not fully physically validated, and therefore, the results included in the database have to be handled with care. For more reliability of the MSDAT output, more detailed investigation such as extended coupon and panel testing as well as a full-scale test is crucial.

The MSDAT documents the type, size, and location of up to three damages on the test panel. The data can be entered manually or read automatically from an SHM system software output file (Fig. 7).

The tool is based on Excel VBA.

3.1.2 Structural Health Monitoring Systems

Optical Fibers (OFs)

A FBG sensor network consists of optical fibers with multiple FBG sensors and is a strain-based monitoring system. It uses the differences in the strain field due to flaws or defects in comparison with an ideal structure to detect and to locate defects.

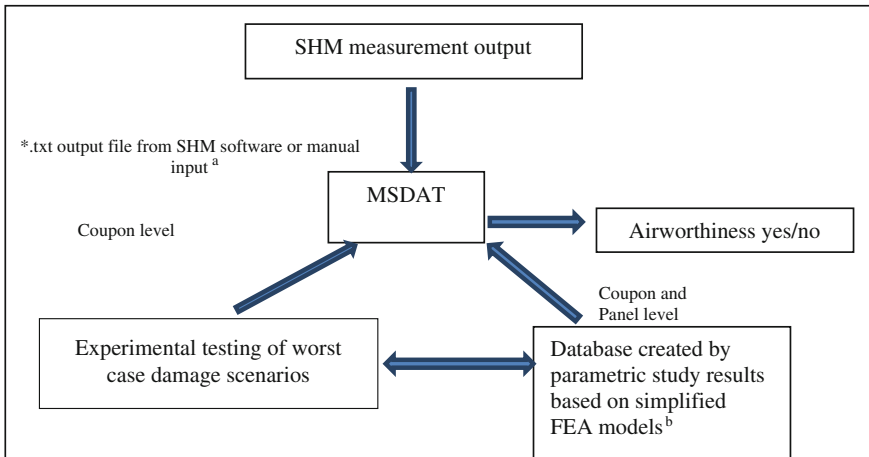


Fig. 7 Flow diagram of the current damage assessment tool MSDAT (^aCommercial software solutions generate *.txt outputs which can be read automatically by MSDAT. ^bValidation of FEA panel results by physical results currently not available due to delay in physical testing programme)

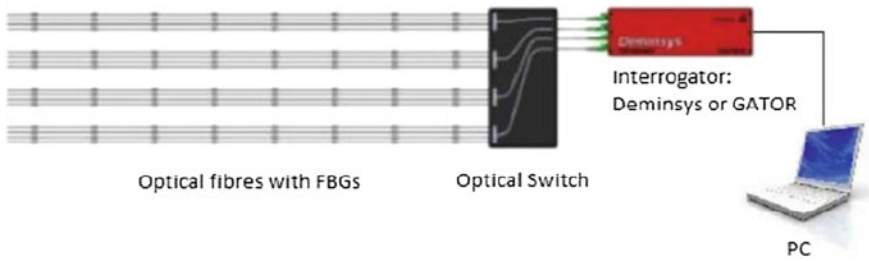


Fig. 8 General view of the FBG monitoring system [20]

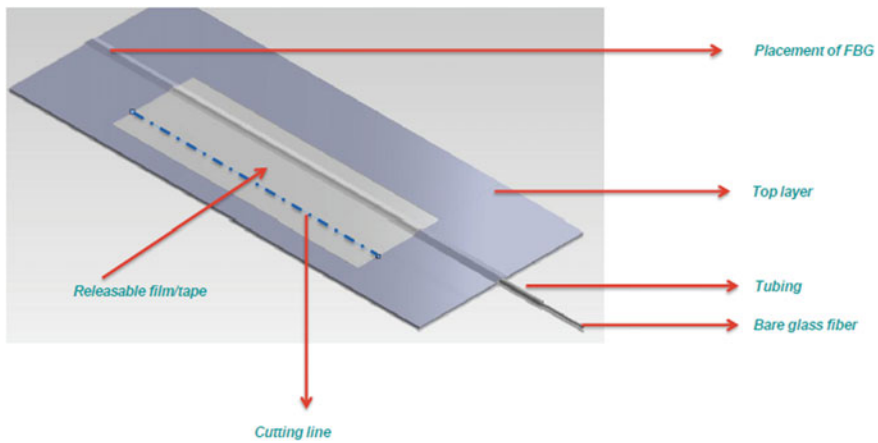


Fig. 9 Ribbon tape concept [17]

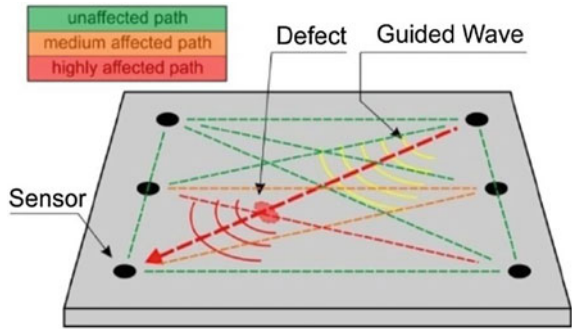
AS04 developed an innovative hybrid multiplexing methodology for the monitoring of several hundreds of sensors with only one interrogator (Fig. 8). It will be implemented on the wing to monitor the shape on the morphing trailing edge and the strain at different positions of the wing box and the lower wing panel. In the fuselage area, the monitoring system will have to identify and locate debonding of the stringer from the skin on the lower fuselage panel [17].

The optical fiber will be implemented to the structure with ribbon tape according to the scheme in Fig. 9.

3.1.3 Acousto Ultrasonic (AU)

The AU damage detection system is a network of piezoelectric ceramic sensors. These sensors are cobonded on the CFRP structure. It uses guided elastic waves to detect defects in the composite structure. All possible path communications are recorded to detect any kind of damage: impact, delamination, cracks, debonding,

Fig. 10 AU configuration—pitch-catch principle



corrosion change of material, etc. It has been investigated in scope of AS06 (Fig. 10).

The greatest advantage of this technique is that it can be used to record wide flat areas.

AS06’s aim is to develop a network of piezoelectric transducers, which will be permanently implemented onto door surround structures prone to in-service impact damages. Piezoelectric sensors are embedded in polyamide layers called SMART layers and are positioned (Fig. 11) on the panel inner surface.

Figure 12 shows an installation example with all components SMART layer with sensors.

3.2 Operation Mode

3.2.1 MSDAT Architecture

Figure 13 shows the architecture of the MSDAT.

The input for assessment calculation can be introduced differently as follows:

- Measured data (by NDE) entered manually by the user, or
- Measured data imported directly from file created by SHM.

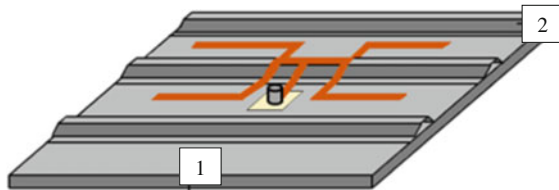


Fig. 11 Position of SMART layers over a stiffened panel [21]. 1: CFRP Skin; 2: Stringer

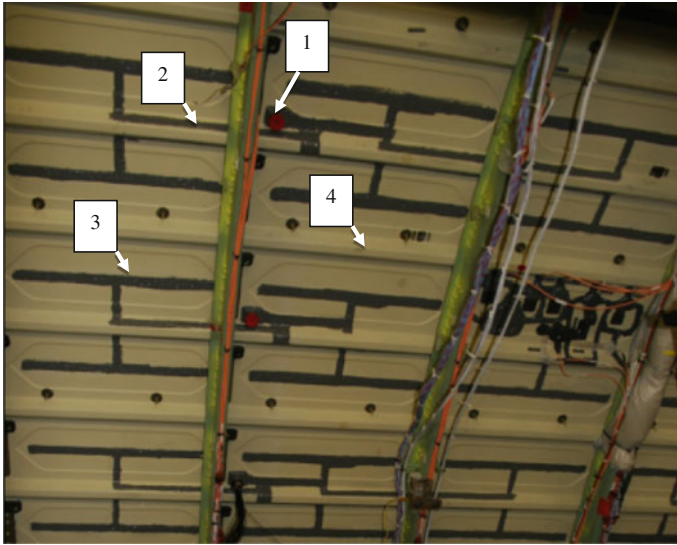


Fig. 12 Current SMART layer Design [21]. 1 Connector + Backing Plate; 2 interconnecting Kapton layer; 3 SMART layer with sensors; 4 stringer; 5 frame; 6 clip

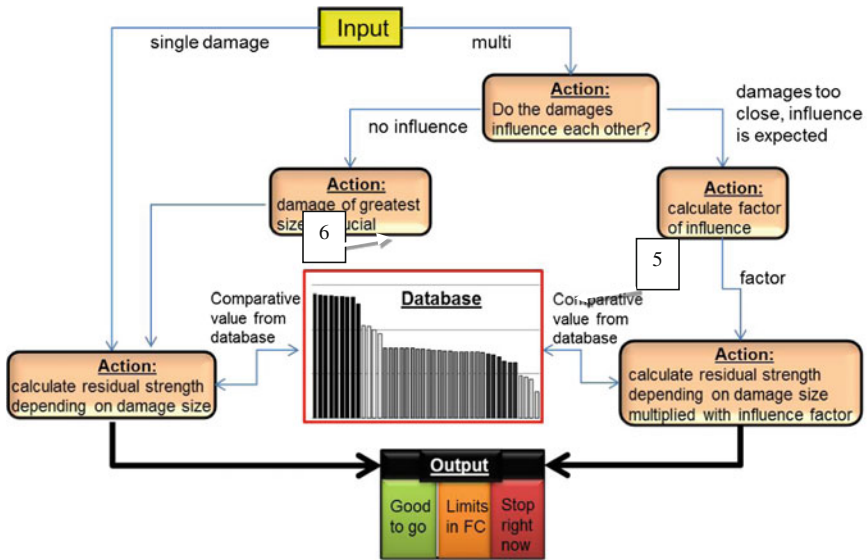


Fig. 13 MSDAT architecture

In the second case, a close interaction with structural health monitoring (SHM) systems that are applied to the respective structure is necessary:

- A potential damage is reported
- Type, size, location, and number of damages need to be identified and handed over to MSDAT

The MSDAT algorithm is capable of assessing up to three damages. Depending on the residual strength for the assessed number, size, location, and type of damages, a prediction concerning airworthiness is made. All evaluations are based on the database obtained by the parametric study [14].

3.2.2 Graphical User Interface

The user first has to choose the graphic resolution of the screen used (Fig. 14).

Then the “Start MSDAT” button has to be clicked (Fig. 15).

In this step, the data from the SHM software can be imported by hitting the “Import” button (1). Alternatively, the damage coordinates can be input manually. Therefore, the number of damages has to be selected first by the drop-down menu (2). According to the selected damage number, up to three lines for damage location and type will appear (3).

The user will also have to decide which database to use and which layout is to be considered (4).

By hitting the “Start” button (5), the evaluation will start. After having finished, the damage visualization (6) and result screens (7) will appear along with the residual strength and airworthiness suggestion (8) (Fig. 16).

Fig. 14 GUI screen solution definition



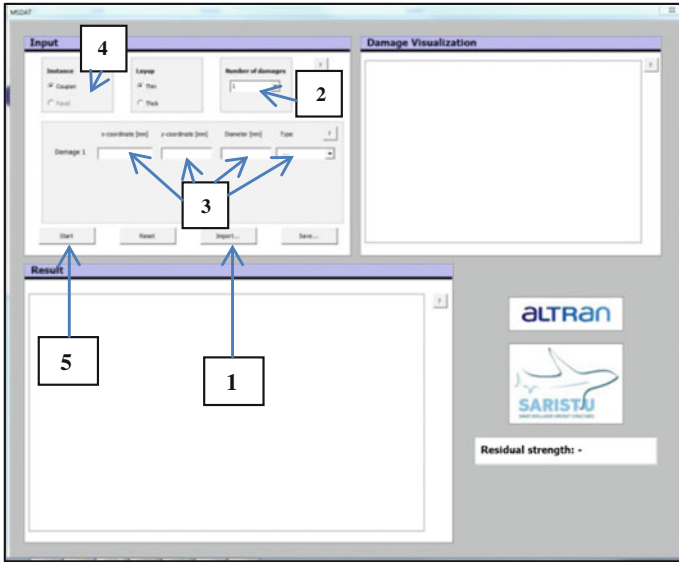


Fig. 15 GUI data input

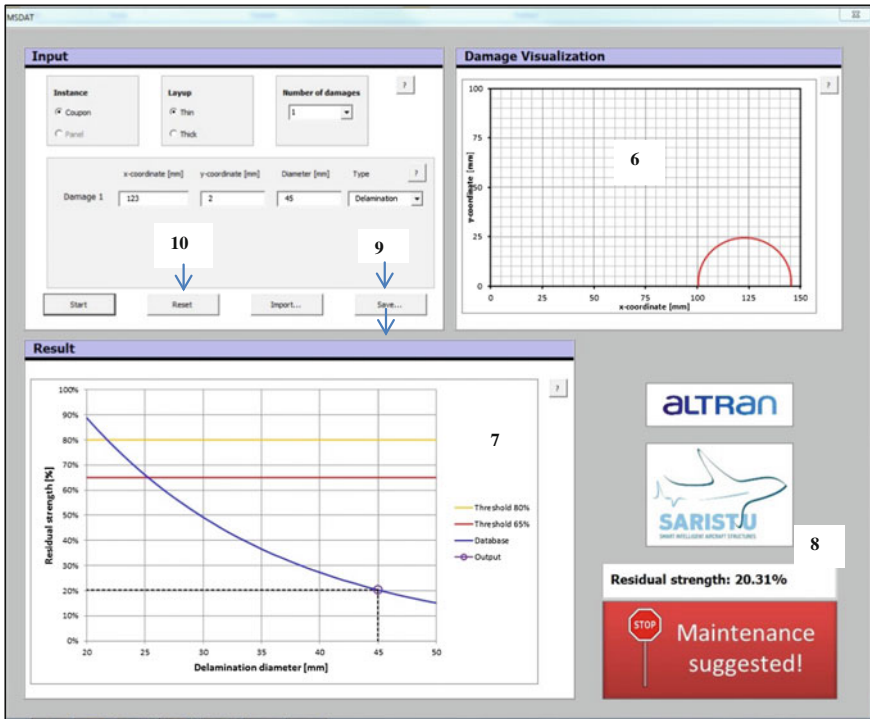


Fig. 16 GUI result output

This result can be saved by hitting the “Save” button (9). A new assessment can be started after hitting the “Reset” button (10).

3.2.3 Data Base

Test Matrix

In the scope of this work package, two different test programmes have been planned: firstly, a test series on coupon level and secondly on panel level. On both levels, different damage scenarios on different layups should be tested for the compression after impact (CAI) and shear after impact (SAI). Due to technical problems up to now, only the tests for CAI on coupon level are finished. The tests for CAI on panel level are ongoing. For details of the test programme, please refer to [18, 19].

Figure 17 shows the test programme for the coupon tests.

For the panel testing, four different damage scenarios have been developed: scenario 1 with impacts on mid-bay and stiffener foot; scenario 2 with impacts on different stiffeners’ feet; scenario 3 with impacts on same stiffener foot; and scenario 4 with impacts on mid-bay. The maximum amount of damages is limited to 3 damages.

FE simulation was used to down select scenarios and to rule out the less crucial ones, scenarios 2 and 4.

During testing, the decision was made to introduce an extended scenario 3a, which corresponds to scenario 3 and an additional fourth impact on the same stringer foot.

Table 2 shows the test programme for the panels (at the time of paper submission).

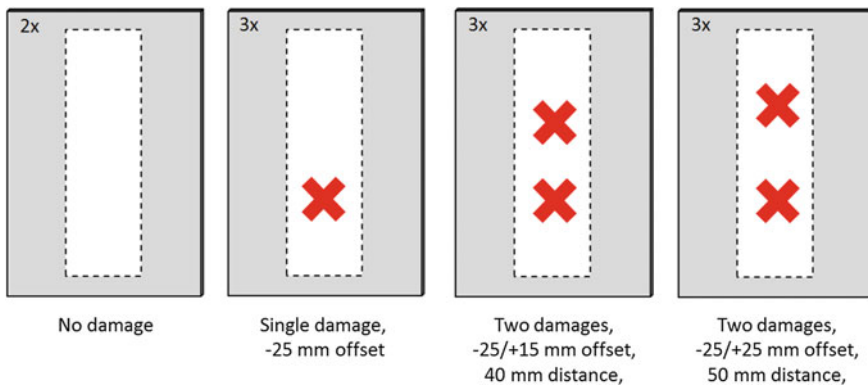


Fig. 17 Impact configurations investigated. The numbers in the *upper left corners* refer to the number of specimen in each group [14]

Table 2 Test matrix for panel tests

	Thickness	Scenario
Trial panel	Thin	1
Batch #1	Thin	3
	Thin	3
	Thick	3
	Thick	3
Batch #2	Thin	To be determined
	Thin	3
	Thick	To be determined
	Thick	To be determined
Batch #3	Thin	3
	Thin pristine	to be determined
	Thick	3a
	Thick pristine	To be determined
Batch #4	Thin	3
	Thin	1
	Thick	To be determined
	Thick	To be determined
Batch #5	To be determined	To be determined
	To be determined	To be determined
	To be determined	To be determined
	To be determined	To be determined

As the physical testing is very cost intensive and the ICL simulation is very time consuming, a simplified FE model of both coupon and panel has been created. In both cases, parametric studies of different damage scenarios have been conducted in order to obtain data for the database of the MSDAT (please refer to [14, 16]).

Simulation on Coupon Level

In order to investigate the influence of different single and multiple impact scenarios, several impact situations have been investigated by Gühns [14]. The varied parameters are the number of impacts, the damage diameter, and the distance between the center position of the delaminations and their angle with respect to the load axis. Three different damage diameters in the range from 20 to 30 mm are considered with a maximum number of three damages being inserted at a time. The middle diameter of 23 mm is extracted from C-scan data provided by Imperial College London (ICL) (Fig. 18). By changing the parameters, the variety of the different damage configurations that were considered can be derived from Fig. 19.

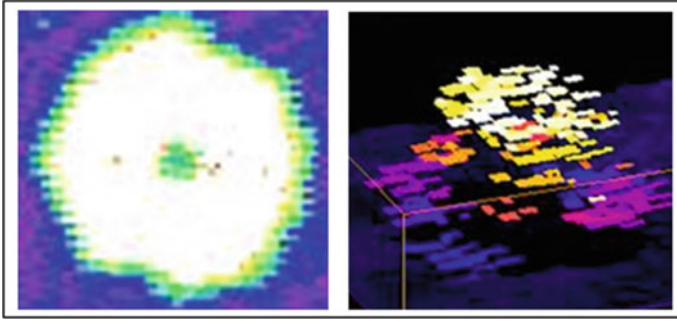


Fig. 18 C-scan data provided by Imperial College London (ICL), delaminated area projected through the thickness (*left*), and pseudo-3D time of flight shows a conical shape of the delaminations from the top to the bottom (*right*)

Simulation on Panel Level

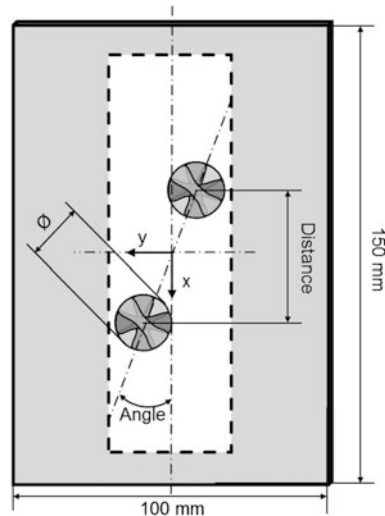
Nielen conducted a parametric study on panel level [16]. The parametric variations of damage distance and size for the different damage scenarios lead to 52 different results.

The structure of the damage scenarios is shown in Figs. 20, 21 and 22.

3.2.4 Results from SHM Systems

As proven in AS04 and AS06, the probability of detection for both acousto ultrasonic and fiber Bragg systems is almost 100 %. The question to be investigated

Fig. 19 Geometric specification of the four parameters investigated [14]



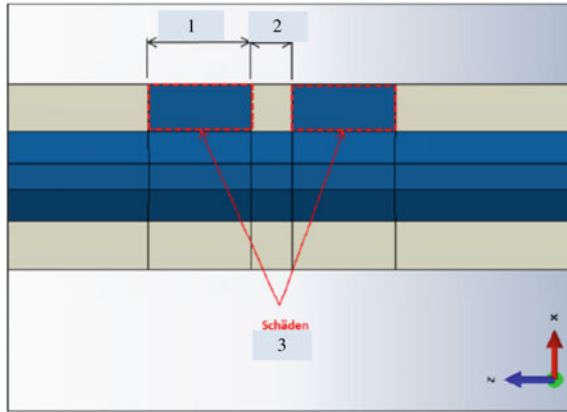


Fig. 20 Damage scenario 3. 2 damages on same stringer foot, 1 single damage size, 2 edge distance, and 3 damages

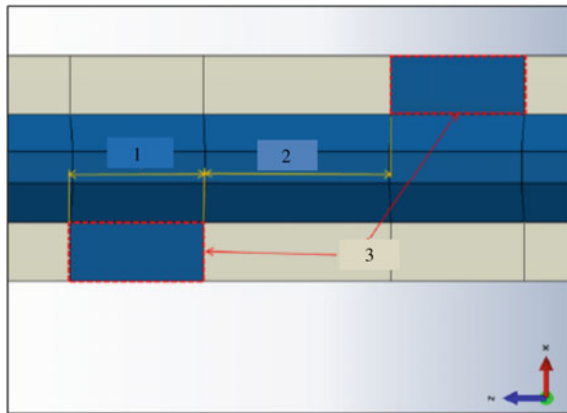


Fig. 21 Damage scenario 5. 2 damages on same stringer, both feet affected; 1 single damage size, 2 edge distance, and 3 damages

is the accuracy of the detected damages compared to C-scan findings. This will be solved until the end of the project in September 2015. The MSDAT is currently able to read and process automatically SHM system finding output data if they are in three-column scheme. Currently, no output data file samples are available for both systems. But the MSDAT can be adjusted according to the needs and demands of future files.

Meanwhile the measurement results can be entered manually as shown in Fig. 15, step 3.

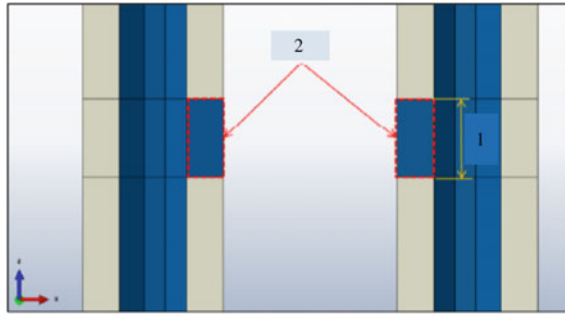


Fig. 22 Damage scenario 2. 2 damages on adjacent stringers, feet to mid-bay affected; 1 single damage size and 2 damages

4 Conclusion

The multisite damage assessment tool is able to provide a quick impression of the residual strength of the test panel with up to three BVID damages. So it can help to reduce aircraft on ground time after known impact incidents such as hail strike. Damage detection correlation between SHM systems and C-scan findings will be investigated and if necessary will lead to a correction factor implemented on the FE results in terms of accuracy. Also the parametric study on panel level will have to be validated. Moreover, a correlation between delamination size and debonding size of the impact damage has to be investigated.

In future steps of the research topic, a thorough cost and value evaluation should be made in order to decide which SHM system is more suitable. Moreover, as the tool is open to implementations, databases such as allowable damage information from repair handbooks can be added as well as information about earlier damages/repairs. In any case, future testing may focus on larger samples and combinations of predamaged frames and BVID on skin.

Acknowledgments I would like to thank all the partners involved for their kind support, especially Mr. Psarras from ICL.

The extraordinary support and dedication to the topic that my students, Mr. Gührs, Mr. Falkenberg, and Mr. Nielen with whom I had the honor and joy to supervise during their theses, showed, filled this work package with life. I would also like to thank Anne Gebert-de Uhlenbrock, who started the work package and built the fundamentals of the work we did.

The research leading to these results has received funding from the European Union's Seventh Framework Programme for research, technological development, and demonstration under Grant Agreement No. 284562.

References

1. Quineti Q (2010) Hail threat standardisation, EASA.2008.OP.25
2. MIL-HDBK17-3F (2002) Composite materials handbook
3. Air Traffic Organization Operations Planning Office of Aviation R&D (2009) Guidelines for the development of a critical composite maintenance and repair issues awareness course, DOT/FAA/AR-08/54
4. de Freitas M et al (1998) Failure mechanisms on composite specimens subjected to compression after impact. *Compos struct* 42(4):365–373
5. Robinson P, Tchambo H (2012) Validated specification for testing conditions
6. Yan H, Oskay C, Krishnan A (2010) Compression-after-impact response of woven fiber-reinforced composites. *Compos Sci Technol*
7. Short GJ et al (2001) The effect of delamination geometry on the compressive failure of composite laminates. *Compos Sci Technol* 61:2075–2086
8. Ahmet YAPICI, Mehmet METIN (2009) Effect of low velocity impact damage on buckling properties. *Engineering* 1(3):161–166
9. Galea SC et al (2010) The effect of multiple impact damage on the residual compressive strength of composite structures. *Int J Crashworthiness*
10. AIRBUS EDSASM (2010) A350 XWB composite fuselage—damage tolerance sizing process, V53RP0721437_EXP
11. ESAC (2010) Damage Tolerance Methodology, X029PR0608046
12. SARISTU AS06, (2012), RPR1/CCR2 Review AS06
13. AIRBUS (2010) Training report after immersion in air France (Roissy-CDG), D029ME0605272
14. Guehrs J (2013) Multi-site damage assessment of CFRP panels—a validated finite element analysis. Master thesis, TUHH
15. SARISTU (2014) AS07_multi site damage assessment tool
16. Nielen P (2014) Entwicklung einer Methode zur Beurteilung der Schädigungen von CFK-Flugzeugbauteilen bezüglich der Restfestigkeit. Bachelor thesis HAW
17. SARISTU AS04 (2012) RPR1/CCR2 review AS04
18. SARISTU (2014) AS07_SHM_Specification_D71.2_Final2
19. SARISTU (2014) AS07 curved panels: panel design, manufacturing requirements & inspection requirements, ACP1-GA-2011-284562
20. SARISTU (2012) Project periodic report, Grant : 2845562
21. SARISTU AS06 (2012) Sensor concept, ACP1-GA-2011-284562
22. SARISTU (2014) AS07 curved panel testing & analysis, ACP1-GA-2011-284562

Part VIII

Technology Stream: Integrated Sensing. Sensitive Coating for Impact Detection

Introduction and Overview

The objective of the 8th application scenario is to develop a smart coating that reveals impacts in order to ease the impact detection on composite structures. This solution would improve the barely visible impact damage threshold, reduce non-destructive testing actions and inspection time, and potentially reduce the design thickness margin and thereby weight. This sensitive coating has to reveal impacts only from a certain impact energy threshold in order to avoid false alarms and so trigger unnecessary ultrasonic inspection. Its application is limited to internal impacts that may occur during final assembly of the aircraft on frames or omega stringers. Several technical solutions have been investigated and improved during the project. The biggest identified challenge was to get much higher revelation threshold than related marketed solutions, but also to cope with drastic requirements on environment, health and safety, durability (adhesion, scratch resistance, aging...), and application process. Besides big chemical compatibility problems encountered between revealing agents and coating matrices, three final solutions have been selected for the prequalification tests (impact sensitivity and durability evaluation): Piezo-chromic pigments from CNRS integrated into epoxy primer or peelable paint, microcapsules from catalyze integrated into specifically developed coating, and brittle hybrid solgel elaborated by University of Aveiro. These sensing technologies have been drastically improved during SARISTU project to reach such high impact energy revelation threshold which was never seen elsewhere. However, the durability tests proved to be quite severe for all solutions. The related papers show part of the works performed during the project on the three technologies and give also an overview of the maturity in terms of impact revelation of the three solutions at the end of the project.

Piezochromic Compounds Able to be Used in Shock Detecting Paints

Manuel Gaudon, Alain Demourgues, Veronica Blanco-Gutierrez and Silvere Barut

Abstract The work of the ICMCB has dealt with the inorganic piezochromic pigments improvement. Our activities can be divided in three main points. From the state of the art on AMoO_4 piezochromic molybdates (this state of the art is described in the introduction paragraph), the first point has consisted in the synthesis and characterization of the piezochromic oxides and in qualifying pigments mixtures able to mark a shock (the pressure of the shock) without knowing the temperature at which has occurred the shock. In a second point, in order to vary the shock pressure inducing a change of color of the piezochromic pigments, new synthesis routes were developed in order to significantly vary the crystallites size of the piezochromic pigments. Indeed, it was shown that the crystallite size modifies in a large way the piezochromic behavior of the pigments. This point is very important for **SARISTU** project in order to get a palette of morphologies fitting with the requirements of the aeronautic piezochromic paints. In a last (third) point, the exploration of new potential systems was made. In particular, we have focused on doped calcium carbonates able to change their luminescent properties depending on the applied pressure and/or the temperature. This last part has opened new possibilities which have to be more investigated in a near future. The most important results obtained concerning the three above points are here summed up and discussed.

M. Gaudon (✉) · A. Demourgues · V. Blanco-Gutierrez
CNRS, ICMCB, Université de Bordeaux, 87 Avenue du Dr. Albert Schweitzer, 33608
Pessac, France
e-mail: gaudon@icmcb-bordeaux.cnrs.fr

A. Demourgues
e-mail: demourg@icmcb-bordeaux.cnrs.fr

V. Blanco-Gutierrez
e-mail: Gutierrez@icmcb-bordeaux.cnrs.fr

S. Barut
Airbus Group Innovations, 18 Rue Marius Terce, 31025 Toulouse, France
e-mail: silvere.barut@airbus.com

1 Introduction

One of the most interesting properties related with some inorganic compounds is their capacity to change their color under pressure. This phenomenon is exhibited by the so-called piezochromic compounds. Typically, for inorganic oxides, the piezochromic phenomenon can be originated from a first-order transition between two different structural phases. In this field, one of the most studied piezochromic oxides is the AMoO_4 ($A = \text{Co}, \text{Cu}, \dots$) molybdates that are easily prepared through the solid-state route [1–12]. In these compounds, the first-order transition was firstly mentioned by Sleight and Chamberland [1], pressure dependence phase diagrams were then established for some compositions as CuMoO_4 by Weitzel and coll [1–4], and for about 10 years now, their chromogenic properties are investigated by our team [5–10]. Indeed, it is found a drastic change of color with high optical contrast for some AMoO_4 compositions associated with the phase transition. The two “ideal compositions,” CoMoO_4 (from the monoclinic molybdates family) and $\text{CuMo}_{0.9}\text{W}_{0.1}\text{O}_4$ (from the triclinic molybdates family), exhibit a phase transition varying the temperature, as an hysteresis loop with an associated width of 500 and 100 °C, respectively. These transition loops frame the room temperature, i.e., in transition temperatures, are about 400 °C under heating and –100 °C under cooling for the cobalt oxide, and about 100 °C under heating and 0 °C under cooling for the copper one. This fact enables the piezochromic compounds to be potential candidates as shock markers around room temperature since the both allotropic forms are stable between 0 and 100 °C. Hence, the piezochromic phenomenon is associated to the possibility for both compositions to transit irreversibly from their high-temperature form (low-pressure form) to their low-temperature form (high-pressure form) when they are submitted to an external pressure.

This knowledge is the starting point of our implication into the SARISTU AS08 scenario.

2 Results and Discussion

2.1 *Inorganic Compounds Mixture as Universal Shock Sensors*

A mixture of two piezochromic compounds can be employed as universal shock detector. For such purpose, i.e., to be able to get the pressure of the shock without knowing at which temperature the shock has occurred, it is mandatory that both piezochromic compounds present a different temperature influence in their transition pressure values. The illustration is performed on two piezochromic compounds (CoMoO_4 and CuMoO_4 -type oxides), which exhibit first-order phase transition between their two allotropic forms associated with a drastic color change. The

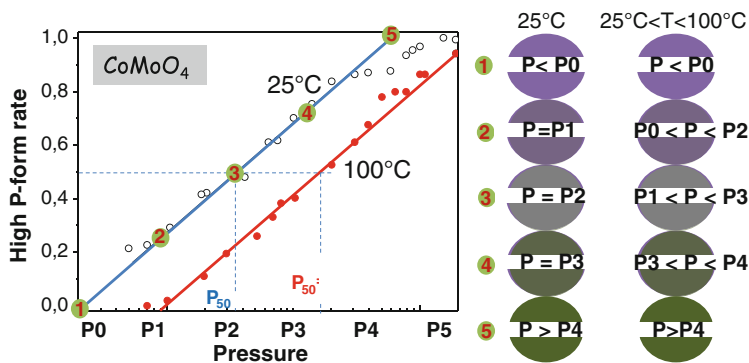


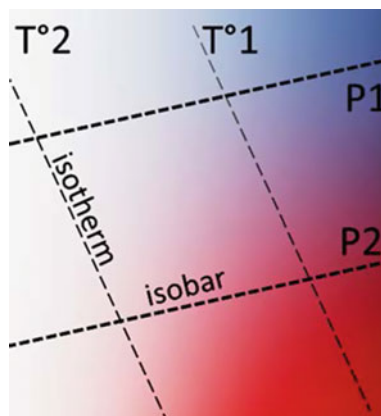
Fig. 1 CoMoO_4 change of color linked to the transition between the β (low-pressure) and the α (high-pressure) forms. It depicts the phase transition with pressure at 298 and 373 K

colorimetric coordinates of the used mixture well allows knowing the pressure of one shock as well as the temperature when the shock has occurred.

Piezochromic compounds can be described by two parameters: the transition pressure (P_{tr}) that is the pressure value corresponding to a 50 % of phase transformation of the compound, and the transition width (W), i.e., the pressure domain between the transition onset and the transition ending, in which the complete phase transformation occurs. Some of the performed studies concerning these compounds show the possibility of tuning up their P_{tr} and W values by modifying the particle size [7, 8] and/or the dopant ratio in the case of $\text{Co}_{1-x}\text{Mg}_x\text{MoO}_4$, [8, 10] or $\text{CuMo}_{1-x}\text{W}_x\text{O}_4$, [5, 6, 10–12] compositions. The phase evolution with pressure can be followed by measuring in each experimental point the L^* , a^* , b^* (or R, G, B) color coordinates of the compound and representing the normalized value of one of these coordinates versus the pressure. From such graph, it can be extracted the values corresponding to P_{tr} and W parameters.

Fig. 1 represents the color transition corresponding to the CoMoO_4 piezochromic compound from the low-pressure (β -phase, transition rate = 0) to the high-pressure (α -phase, transition rate = 1) form. Furthermore, it indicates the evolution between both phases with the pressure at 298 and 373 K. As it can be seen, an increment of the temperature leads to a displacement of the phase transformation to higher pressure values. It has been estimated that between the P_{tr} values (P_{50}) corresponding to 298 and 373 K, respectively, one order of magnitude of difference is reached. The W parameter is two orders of magnitude in pressure regardless the temperature. This experiment was performed as well in $\text{CuMo}_{0.9}\text{W}_{0.1}\text{O}_4$ piezochromic material which presents a transformation versus pressure between the α (low-pressure) and γ (high-pressure) forms. In this case, the temperature effect is more pronounced, and therefore, a larger displacement of the phase transition was observed when this parameter was increased.

Fig. 2 Color of our mixture after an impact corresponding to different (P, T°) couples



These phase evolution graphs offer the possibility to know the pressure at which one shock has occurred in a piezochromic compound by measuring its corresponding color coordinates after the shock, but for such purpose, it is essential to know the temperature at which it has occurred. However, as it will be explained below, the fact that two piezochromic compounds present a different temperature effect in their P_{tr} allows them to form a mixture able to indicate not only the pressure but also the temperature of the shock.

A 50 % in weight mixture formed by CoMoO_4 and $\text{CuMo}_{0.9}\text{W}_{0.1}\text{O}_4$ was prepared. They were the chosen compounds because their high-pressure and low-pressure polymorphs are stable at room temperature, and the temperature plays a different influential role on their P_{tr} value.

Through visible spectra, the color evolution with the temperature and pressure corresponding to the molybdate compounds and the mixture of both was studied. The mixture spectrum always remains between the spectra corresponding to the molybdate compounds, which is in agreement with the consideration of the color parameters of the mixture as an average of those corresponding to the molybdates.

The graph represented in Fig. 2 shows the effect which can be obtained for one mixture of CoMoO_4 and $\text{CuMo}_{0.9}\text{W}_{0.1}\text{O}_4$ subjected to several (T, P) values. a color evolution of the experimental points with the temperature and pressure leading to a grill-graph of isotherms and isobars can be seen ; that is, the visualization of the L^*-a^* plane is appropriated to deduce concrete (T, P) information. Other visualization planes such as L^*-b^* or b^*-a^* exhibit crossing points between different isotherms which implies two (T, P) values for a certain L^*-b^* (or b^*-a^*) value.

Hence, it has been experimentally demonstrated that the mixture of two piezochromic compounds can be employed as universal shock detector working at different temperatures. For such purpose, it is essential that the piezochromic compounds present a different temperature influence in their P_{tr} value so the color evolution of the mixture depends not only on the pressure but on the temperature as well. In a second experimental part, a mixture of two different molybdate compounds has shown its ability to mark pressure and temperature of a shock.

From our work, it is difficult to propose exact error bars for each T and P shock parameters extracted of the color mixture after a shock. Indeed, the accuracy of the determined parameter is mainly linked to the accuracy of the grill-graph positioning (isotherms/isobars) for the powder mixture. Furthermore, the accuracy differs depending on the T, P parameters. It was shown that the obtained color of the second mixture can be reasonably associated with a shock with a pressure of $\pm 10\%$ accuracy and a temperature of $\pm 10\text{ }^\circ\text{C}$ error bar. Optical contrast accuracy can be increased while optimizing the formulation of the mixture or modifying the composition of the piezochromic compound. As an illustration, our team works currently on the elaboration of luminescent molybdates and luminescent spectra allowing more sensitive characterizations of the shock parameters since the various changes of luminescence intensity, spectral distribution, and lifetimes can all be exploited as complementary data. Whatever, this work already constitutes a breakthrough would suppose a huge step in the research of smart paintings for shock detection. *This work was published with details in an ACS journal [13].*

2.2 Sub-micrometric $\beta\text{-CoMoO}_4$ Rods: Optical and Piezochromic Properties

Sub-micrometric $\beta\text{-CoMoO}_4$ rods have been obtained after thermal treatment of $\text{CoMoO}_4\cdot\text{H}_2\text{O}$ previously prepared by the precipitation method. The color of the sub-micrometric particles has been investigated through diffuse reflectance in the UV–VIS–NIR range, and the spectra have been compared with those corresponding to samples with larger isotropic particles. The $\text{O}^{2-} \rightarrow \text{Mo}^{6+}$ charge transfer band shifts to the UV region when decreasing the particle size revealing a more covalent bond. This can be justified under the consideration of a higher proportion of surface atoms in sub-micrometric particles that present lower coordination number. The piezochromic behavior of the sub-micrometric $\beta\text{-CoMoO}_4$ rods has been investigated. As the sub-micrometric size of the particles stabilizes the low-coordination phase (β -phase), the transition pressure to the α -phase is higher in comparison with that corresponding to larger particles. In addition, it was not possible to obtain a 100 % transformation of the β -phase in the sample with sub-micrometric particles. A similar temperature influence in the transition pressure regardless the particle size has been observed.

The study has been carried out considering five Co-molybdate samples with different sizes and morphology labeled as follows: RH, R β , R $\beta\alpha$, C β , and C α , where R and C refer to the sub-micrometric rods and samples obtained through the ceramic method, respectively. And H, β , and α refer to the hydrate, β - and α -phases, respectively.

The dehydration process of RH sample was studied by TGA under air from room temperature up to $700\text{ }^\circ\text{C}$. Two well-defined dehydration steps can be observed with the temperature. As the DTG curve suggests, the first one occurs in a broad temperature range between 100 and $300\text{ }^\circ\text{C}$, and the second one drastically

takes place at 340 °C. The total 7.4 % weight loss with a 5.9 and 1.5 % loss in the first and second step, respectively, indicates an almost monohydrate compound $\text{CoMoO}_4 \cdot \text{H}_2\text{O}$ instead of the $\text{CoMoO}_4 \cdot 3/4\text{H}_2\text{O}$. The two dehydration steps are related with the liberation of two different kinds of water molecules. According to the literature, those eliminated in the first step may correspond to the adsorbed molecules entrapped in the cavities of the structure, and those released in the second step are structural unities whose elimination leads to the hydrate \rightarrow β -phase transformation. Therefore, up to 300 °C, RH sample progressively loses the entrapped water in the structural cavities that represent the 80 % of the total mass loss, and at 340 °C, the structural water is drastically eliminated leading to the β -phase.

The X-ray diffraction patterns corresponding to RH, $\text{R}\beta$, and $\text{R}\beta\alpha$ samples exhibit broad diffraction peaks revealing a small crystal domain size, which in addition has been estimated by the Scherrer equation. A diameter value of 30 ± 7 , 25 ± 5 , and 27 ± 6 nm corresponding to RH, $\text{R}\beta$, and $\text{R}\beta\alpha$ sample, respectively, was found. In Fig. 3 representative TEM images of $\text{C}\beta$, RH, and $\text{R}\beta$ samples can be observed. As it can be seen, while in the case of the $\text{C}\beta$ sample the solid-state route leads to particles with irregular shape and dimensions larger than 2 μm (Fig. 3a), in

Fig. 3 TEM images corresponding to $\text{C}\beta$ (a), RH (b–d), and $\text{R}\beta$ (e and f) samples

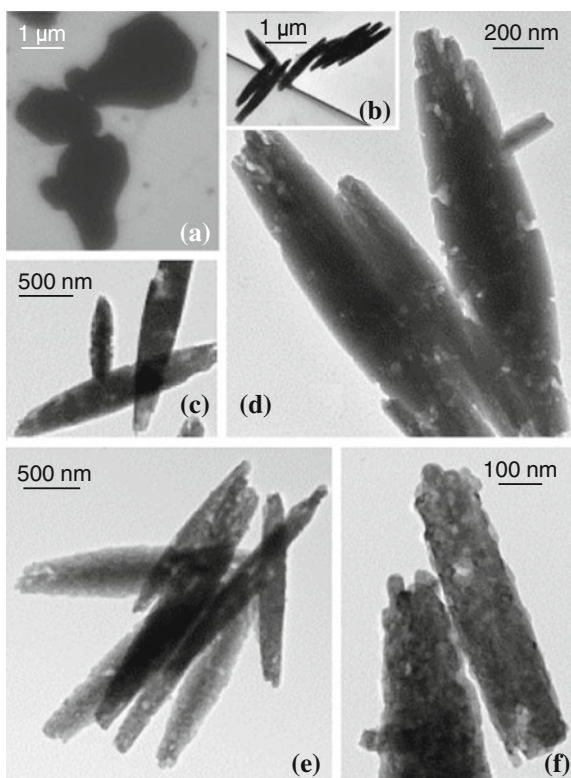
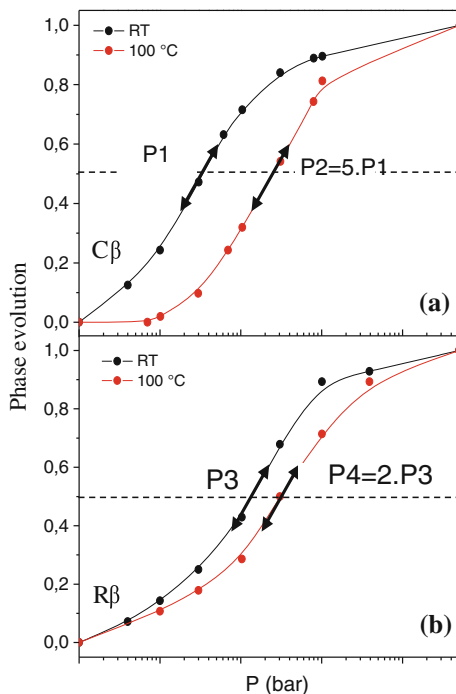


Fig. 4 Phase transformation vs pressure from β to α form at room T° and 100°C for $\text{C}\beta$ (a) and $\text{R}\beta$ (b) particles

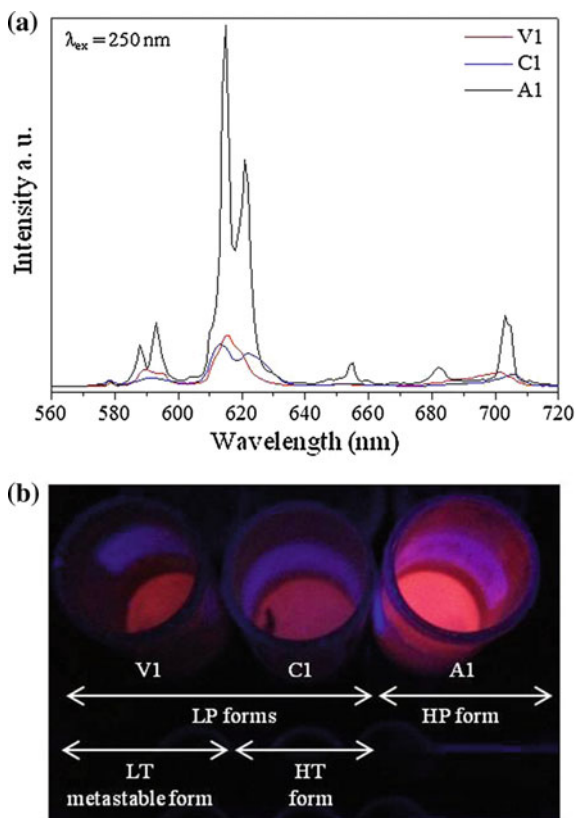


the case of RH and $\text{R}\beta$ samples the precipitation method allows not only decreasing the particle size (below $2\ \mu\text{m}$) but also obtaining regular morphology (Fig. 3b–f).

Thus, $\text{CoMoO}_4 \cdot \text{H}_2\text{O}$ rods were obtained with a diameter between 200 and 400 nm and a length over $1\ \mu\text{m}$ (Fig. 3b–d). This morphology is related with an intrinsic structural anisotropy that induces the particle growth along one of the axis in accordance with the X-ray diffraction patterns of RH sample. However, the high-temperature value employed in the ceramic route leads the sintering process overrides the particle growth in a preferred orientation, resulting in an irregular morphology (see TEM image of $\text{C}\beta$ sample in Fig. 3a). On the other hand, the thermal treatment employed in the dehydration process allows preserving the morphology of the precursor in the sub-micrometric $\beta\text{-CoMoO}_4$ sample according to a topotactic transition, with no trace of sintering (see TEM images Fig. 3e–f). It is worth mentioning as well, the rough surface, that $\text{R}\beta$ particles present in comparison with RH sample, as consequence of the dehydration process. On the other hand, TEM images reveal significantly larger particle dimensions in the case of RH and $\text{R}\beta$ samples than the crystal domains sizes estimated by X-ray diffraction. This clearly indicates that the sub-micrometric rods are composed by thinner unities of nanometric diameter as it can be visualized in the case of $\text{R}\beta$ sample thanks to the dehydration process.

Fig. 4 represents the phase transition variation with the pressure at room temperature and 100°C corresponding to the β -phase of CoMoO_4 compound with

Fig. 5 (a) Raw PLEm spectra for V1, C1, and A1 samples. (b) The three samples after being irradiated at 254 nm. LP, HP, LT, and HT refer to low-pressure, high-pressure, low-temperature, and high-temperature forms, respectively



micrometric and sub-micrometric particle size (Fig. 5a, b, C β and R β samples, respectively). The phase transition has been depicted after normalization of the α -/ β -phase ratio associated to the a^* color parameter variation with the pressure. From this curve, the transition pressure (P_{tr}) value can be estimated which corresponds to a 50 % of β - to α -phase transition. As it has been already seen from XRD, in the case of the sample composed by sub-micrometric particles, it is not possible to obtain a 100 % transformation of the β -phase into the α one. Therefore, the normalized curve has been done considering the a^* value for the maximum transformation. The different P_{tr} values corresponding to C β and R β sample, respectively, are in agreement with the already reported influence of the particle size in the transition pressure. When the particles become smaller, the low-coordination β -phase is stabilized resulting in a delay of the transition with pressure. On the other hand, it can be observed that regardless the particle size, a 75 °C increment in the temperature induces displacement of the phase transition due to the competition between typical pressure contraction and volume expansion with temperature (compare Fig. 4a, b). The same temperature influence in the P_{tr} is observed for both samples. Nevertheless, the effect is decreased for nanomaterials (P4 is only the

double of P3, whereas P2 is five times of P1). Thus, the effect seems preserved, but the P_{ir} versus the temperature evolves with the particle size whatever the temperature.

It is worth noting that the evolution curve of C β and R β samples presents a similar tendency as it is indicated by a double arrow in the graphs. The fact that two samples with very different particle size distribution illustrate such a similar shape for the evolution curve supports the already reported idea that the tendency of the curve is greatly dependent on the way of pressure application [10]. This phenomenon reported for large crystals could be extrapolated in the same magnitude for sub-micrometric particles justifying the same curve tendency irrespective of the particle size distribution.

It was shown that sub-micrometric CoMoO₄·H₂O rods have been prepared by a straightforward way employing the precipitation method. After the thermal treatment of the hydrate precursor, it was possible to obtain the β -phase with the same morphology associated with a topotactic transformation and any indications of sintering. It has been found that sub-micrometric particles do not transit in total into the α -phase due to the stabilization of the low-coordination form with the particle size reduction. Both the β -phase and hydrate compound present the Co²⁺ and Mo⁶⁺ located in octahedral and tetrahedral sites, respectively. However, by VIS-IR spectra, it could deduce more covalent Mo-O bonds of RH, R β , and R $\beta\alpha$ samples as the O²⁻ \rightarrow Mo⁶⁺ C.T.B. is shifted to higher energy regions in comparison with the C β and C α samples. The more covalent bond has been related with the sub-micrometric particle size for which surface atoms that present lower coordination become more important. In the case of RH sample, as well, the presence of water molecules in the vicinity of Co²⁺ has been taken into account. On the other hand, samples obtained after thermal treatment of the hydrate compound exhibit an extra band in their spectra that has been attributed to new coordination spheres of Co²⁺ related with the structural defects originated during the dehydration process. In the case of the phase evolution with pressure, it has been found a delay of the transformation in particles with sub-micrometric size and a similar tendency for the evolution curve regardless the particle size distribution, as it is greatly dependent on the way of application pressure that is the same in both cases. *This work was published with details in an Elsevier journal [14].*

2.3 *Eu(III)-Doped (Ca_{0.7}Sr_{0.3})CO₃ Phosphors with Vaterite/Calcite/Aragonite Forms as Shock/Temperature Detectors*

Pure metastable Eu(III)-doped (Ca_{0.7}Sr_{0.3})CO₃ vaterite phase has been obtained by the precipitation method. After the thermal treatment of this phase, the carbonate crystallizes with calcite structure. Thanks to the incorporation of 30 mol% of Sr in the composition that stabilizes the aragonite structure, both vaterite and calcite

phases are able to transform easily into this high-pressure form by mechanical treatment. Photoluminescence studies indicate the stabilization of the Eu ions at the trivalent oxidation state and found different luminescent properties depending on the carbonate structure, associated with the local environment of the doping element. This offers the possibility to employ this system as shock and temperature detector. In addition, thanks to the use of CaH_2 as reducing agent, it was possible to reduce at low temperature the main part of the Eu(III) content into Eu(II) in the three different carbonate forms. Photoluminescence studies were also performed in these samples and show different emission spectra for the different crystalline structures.

The photoluminescence studies confirm the location of the doping element in different environment depending on the allotropic form of the stabilized carbonate. Nevertheless, we will focus here on the most important point besides the SARISTU application: The luminescence intensity differs between the three allotropic forms. Hence, luminescence characterization on these carbonates pigments can be used to mark a shock. The luminescence intensity is provided for the various allotropic forms as shown in the Fig. 5.

The so low-emission intensity exhibited by V1 and C1 samples in comparison with that of A1 sample (Fig. 5a) could be justified under several considerations. On the various luminescence spectra recorded, it was shown that for V1 and C1 samples, the intensity ratio between the CTB and the 4f line is small. This can be explained by an internal configurational quenching due to a direct non-radiative transfer from the CTB down to the fundamental 7F3 manifold. The spectral distribution intensity between the CTB and the 4f is also strongly affected by the size of the luminescent particles. A nanometric size distribution can artificially enhance the 4f-4f transition in absorption due to successive absorption–reflection–transmission process through the whole particle. This can clearly contribute to a better excitation efficiency of the A1 sample. Also, many authors point out that structural vacancies (noted hereafter: \square) associated with the charge compensation $\square + 2\text{Eu}^{3+} \rightarrow 3\text{M}^{2+}$ may decrease the luminescence response due to the high effectiveness of the energy transfer, $\text{Eu}^{3+} \rightarrow \square$, that would not participate in the radiative de-excitation decay process. However, in the case of the prepared samples, the luminescence property may not be drastically affected by this process as this effect seems to be important for concentration of Eu higher than 15 %. Furthermore, it is not neither expected a concentration-quenching effect associated with high concentrations of Eu with an energy loss in a non-radiation process between proximal Eu atoms.

The metastable “low-temperature” phase (vaterite) and the high-temperature phase (calcite) could be experimentally differentiated by considering their spectral distribution and red/orange ratio. Therefore, by measuring this feature in PLEm spectra, raw vaterite material could be employed as thermal sensor to know if an increment of temperature has occurred in the 350–500 °C range. Also, the different luminescence properties observed between the high-pressure (aragonite) and low-pressure (vaterite, calcite) forms lead to believe raw vaterite (or calcite) material as useful shock detector by employing a 254-nm commercial UV light to radiate the carbonate material.

Pure $(\text{Ca,Sr})\text{CO}_3:\text{Eu}^{3+}$ vaterite was obtained by an original precipitation method. This metastable phase transforms with the temperature (at about 350 °C) into calcite phase and into the aragonite high-pressure phase when an additional ball-milling step is applied. These three different allotropic forms can be easily obtained thanks to the incorporation of 30 mol% of strontium in place of calcium. The structure of the three allotropic forms was studied by profile refinement of the corresponding X-ray diffraction patterns. Cell parameters are coherent with the literature data on the extreme compositions CaCO_3 and SrCO_3 considering a Vegard's law.

Luminescent measurements on the Eu(III)-doped materials allow differentiating not only between the “low-temperature” metastable vaterite and high-temperature calcite phase, but also between the low-pressure forms (vaterite and calcite) and the high-pressure one (aragonite). In this sense, different red/orange emission intensities ratio and different profile PL spectra have been found. The different luminescent properties found for each carbonate structure offer the possibility to employ this system as indicator for a temperature variation from 350 up to 500 °C and also for shocks. Developments have to be nevertheless performed to make this new generation of pigments able to satisfy the requirements of the SARISTU program. *This work was published with details in an Elsevier journal [15].*

3 Conclusion

This work has allowed the achievement of three main points: (i) the optimization of the molybdates piezochromic pigments, (ii) the study of the impact of crystallite size on piezochromic transition, (iii) the synthesis and characterization of europium-doped calcite samples for thermos and piezochromic properties (actually, piezo and thermoluminescent properties). These three studies were published in three different high impact factor journals: ACS Applied surfaces and interfaces, Journal of Material Chemistry and Dalton transaction, respectively.

Acknowledgments The research leading to these results has received funding from the European Union's Seventh Framework Programme for research, technological development, and demonstration under Grant Agreement No 284562.

References

1. Sleight AW, Chamberland BL (1968) Transition metal molybdates of the type AMoO_4 . Inorg Chem 7:1672–1675
2. Rodriguez F, Hernandez D, Garcia-Jaca J, Ehrenberg H, Weitzel H (2000) Optical study of the piezochromic transition in CuMoO_4 by pressure spectroscopy. Phys Rev B Condens Matter 61:16497
3. Hernandez D, Rodriguez F, Garcia-Jaca J, Ehrenberg H, Weitzel H (1999) Pressure-dependence on the absorption spectrum of CuMoO_4 : study of the green \rightarrow brownish-red piezochromic phase transition at 2.5 kbar. Phys B 265:181–185

4. Wiesmann M, Ehrenberg H, Mieke G, Peun T, Weitzel H, Fuess H (1997) P-T phase diagram of CuMoO_4 . *J Solid State Chem* 132:88–97
5. Gaudon M, Deniard P, Demourgues A, Thiry A-E, Carbonera C, Le Nestour A, Largeteau A, Létard J-F, Jobic S (2007) Unprecedented “one-finger-push”-induced phase transition with a drastic color change in an inorganic material. *Adv Mater* 19:3517–3519
6. Gaudon M, Thiry AE, Largeteau A, Deniard P, Jobic S, Majimel J, Demourgues A (2008) Characterization of the piezochromic behavior of some members of the $\text{CuMo}_{1-x}\text{W}_x\text{O}_4$ series. *Inorg Chem* 47:2404–2410
7. Gaudon M, Carbonera C, Thiry A-E, Demourgues A, Deniard P, Payen C, Letard J-F, Jobic S (2007) Adaptable thermochromism in the $\text{CuMo}_{1-x}\text{W}_x\text{O}_4$ series ($0 \leq x < 0.1$): a behavior related to a first-order phase transition with a transition temperature depending on x . *Inorg Chem* 46:10200–10207
8. Righetti L, Robertson L, Largeteau A, Vignoles G, Demourgues A, Gaudon M (2011) $\text{Co}_{1-x}\text{Mg}_x\text{MoO}_4$ compounds for pressure indicators. *ACS Appl Mater Interfaces* 3:1319–1324
9. Gaudon M, Basly B, Fauque Y, Majimel J, Delville MH (2009) Thermochromic phase transition on $\text{CuMo}_{0.9}\text{W}_{0.1}\text{O}_4@/\text{SiO}_2$ core-shell particles. *Inorg Chem* 48:2136–2139
10. Robertson LC, Gaudon M, Jobic S, Deniard P, Demourgues A (2011) Investigation of the first-order phase transition in the $\text{Co}_{1-x}\text{Mg}_x\text{MoO}_4$ solid solution and discussion of the associated thermochromic behavior. *Inorg Chem* 50:2878–2884
11. Yanase I, Mizuno T, Kobayashi H (2013) Structural phase transition and thermochromic behavior of synthesized w-substituted CuMoO_4 . *Ceram Int* 39:2059–2064
12. Benchikhi M, El Ouati R, Guillemet-Fritsch S, Chane-Ching JY, Er-Rakho L, Durand B (2014) Sol-gel synthesis and sintering of submicronic copper molybdate (α - CuMoO_4) powders. *Ceram Int* 40:5371–5377
13. Blanco-Gutierrez V, Cornu L, Demourgues A, Gaudon M. $\text{CoMoO}_4/\text{CuMo}_{0.9}\text{W}_{0.1}\text{O}_4$ compounds mixture as an efficient piezochromic sensor able to detect the temperature/pressure shock parameters. *ACS Appl Mater Interfaces*, Manuscript ID: am-2014-08652h.R1
14. Blanco-Gutierrez V, Demourgues A, Gaudon M (2013) Sub-micrometric β - CoMoO_4 rods: optical and piezochromic properties. *Dalton Trans* 42:13622–13627
15. Blanco-Gutierrez V, Demourgues A, Jubera V, Gaudon M (2014) Eu(III)/Eu(II)-doped $(\text{Ca}_{0.7}\text{Sr}_{0.3})\text{CO}_3$ phosphors with vaterite/calcite/aragonite forms as shock/temperature detectors. *J Mater Chem C* 2:9969–9977

Brittle Coating Layers for Impact Detection in CFRP

Frederico Maia, Kiryl Yasakau, Joao Tedim
and Mikhail L. Zheludkevich

Abstract The detection of possible impacts in carbon-fiber-reinforced plastic (CFRP) structures is important for the evaluation of structural integrity of CFRP. Sol-gel-based sensitive coatings for impact detection on CFRP substrates have been developed and investigated by University of Aveiro (UAVR). The coatings are based on hybrid sol-gel formulations with tunable mechanical properties, i.e., brittleness adjusted for a defined range of impact energy. This sensitive layer allows the identification and location of mechanical impacts under visible light and without supplementary tools or conditions for its detection. A systematic study was performed to enhance the coating response for the defined impact threshold. A set of different parameters such as composition, fillers, curing conditions, surface roughness, and chemistry of the surface were tested and optimized.

Nomenclature

SHM Structural health monitoring
NDT Non destructive testing
CFRP Carbon-fiber-reinforced plastic

F. Maia · K. Yasakau · J. Tedim (✉) · M.L. Zheludkevich
Department of Materials and Ceramic Engineering, CICECO-Aveiro Institute
of Materials, University of Aveiro, 3810-193 Aveiro, Portugal
e-mail: joao.tedim@ua.pt

F. Maia
e-mail: fred.maia@ua.pt

K. Yasakau
e-mail: kyasakau@ua.pt

M.L. Zheludkevich
e-mail: mzheludkevich@ua.pt

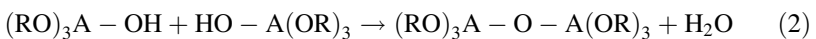
M.L. Zheludkevich
Helmholtz-Zentrum Geesthacht Centre for Materials and Coastal Research, GmbH Institute
of Materials Research, MagIC, Max-Planck-Strasse 1, 21502 Geesthacht, Germany

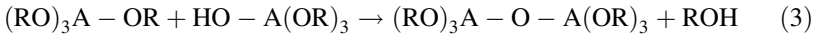
Sg Sol-gel
 BC Bar coater
 UAVR University of Aveiro

1 Introduction

The application of a coating to a substrate can have different aims, from a purely decorative purpose to more challenging and demanding characteristics such as protection but also other complementary functionalities, which can lead to the extension of service life of high-performance structures such as early-stage detection of damages. The replacement of metallic substrates by carbon-fiber-reinforced plastics (CFRP) in aeronautical structures has led to the reduction of fuel consumption, but has raised other problems. Being CFRP sensitive to impact damage and at the same time the existing non destructive techniques (NDT) used in structural health monitoring (SHM) complex and expensive, there is a need to develop more user friendly and intuitive ways of detecting whether a structure requires maintenance, ultimately making the whole process cost-effective without compromising safety.

One of the approaches for detection of mechanical impacts on CFRP may involve deposition of sol-gel-derived coatings. Sol-gel processes have been used in different applications to prepare homogeneous powders, bulk glass materials, xerogels, membranes, coatings, ceramic composites, fibers, and others. Silicon and/or metal containing precursors are commonly used in sol-gel synthesis to produce inorganic or organically modified oxide materials with tailored properties. The sol-gel method implies the evolution of precursors solution through a colloidal system (sol) followed by a highly branched system called (gel). Sols are dispersions of colloidal particles with diameters of 1–100 nm or 1–1000 nm in a liquid. Gel is an interconnected rigid network with pores of submicrometer dimensions and polymeric chains, whose average length is greater than a micrometer. The precursors for the sol-gel process can be different metals and silicon (Ti, Zr, Ce, Al, Si etc.) alkoxides with general formula $A(OR)_4$, where A is a metal or Si atom, OR is an alkoxy group, and R is typically an alkyl ligand. The common reactions of alkoxides upon contact with water are hydrolysis and polycondensation [1]. The hydroxyl ion attaches to the A atom producing alcohol and partially hydrolyzed precursor (1). Subsequently, two partially hydrolyzed precursors can link together in condensation reactions (2 and 3):





The reactions (2) and (3) can continue building branched network with $-O-A-O-$ bridges by the process of polymerization until the gel point where a continuous solid network is formed including liquid phase in pores.

Inorganic materials obtained through the chemical transformations described above possess high hardness, scratch resistance, though they are more brittle and have poor adhesion to polymeric surfaces. The addition of organic components to inorganic branched networks can provide increased flexibility, better adhesion, and higher coatings thickness. Inorganic and organic networks connected through chemical bonds form a new class of sol-gel materials, namely "ORMOCERS" (for ORganically Modified CERamics) [2]. Such hybrid materials can be classified into different types according to their chemical composition and chemical interactions in the hybrid network [3]. Properties of hybrid sol-gel materials can be adapted according to specific requirements of their applications. As an example, the amount of inorganic structures and the extent of organic cross-linking can have a dramatic influence on the mechanical properties. A high inorganic content leads to stiff but brittle materials. Many factors including preparation conditions, chemistry of monomers, and addition of nanoparticles or polymers can be adjusted in order to build hybrid sol-gel materials with desired properties.

In this work, University of Aveiro (UAVR) group developed mechanically sensitive hybrid sol-gel formulations to allow a visual observation of impact damages within certain energy ranges. Several sol-gel process parameters have been systematically studied for titania silica hybrid sol-gel formulations. The main developments done to improve sol-gel "brittleness" will be highlighted.

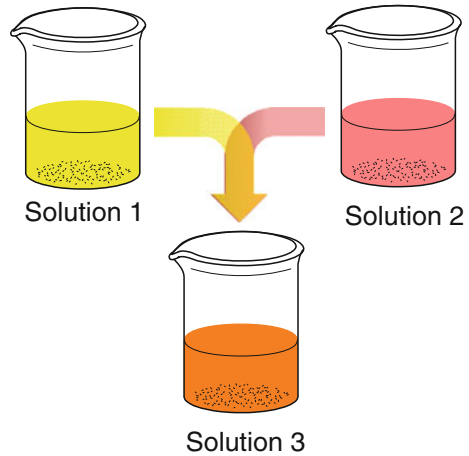
2 Development of Mechanically Sensitive Sol-Gel Coating

In the scope of this investigation, the first step consisted of evaluating the main requirements which the final sol-gel coating would have to exhibit in order to reveal impact damages within a specified energy range:

1. Good adhesion to the substrate,
2. Smooth and uniform layer, and
3. Brittleness within target impact energy range.

The selected sol-gel formulation was a titania-based formulation developed at UAVR, which already revealed good adhesion, wetting properties, and appropriate application methodology and allowed the production of a uniform, smooth layer. The sol-gel synthesis procedure is based upon the preparation of three different solutions, being the third one (solution 3) the result of mixing the first two (solutions 1 and 2), as represented in Fig. 1. Solution 1 is composed of a titanium precursor and an organic complexant, which was prepared under controlled

Fig. 1 Scheme of Sol-gel synthesis



temperature, time, and pH. Solution 2 is a mixture of silanes prepared under specific conditions. After solutions 1 and 2 being mixed for a specific time, the resulting sol-gel formulation (solution 3) is the one that will be applied. This synthesis is carried out at 22 °C and by the end of reaction the vessel containing solution 3 is let to age for 1 h. The sol-gel coating can be applied onto the substrate by dip-coating, bar coater, and with a brush- or spray coater. After being applied, the coated sample is let to stabilize during 30 min at room temperature for initial solvent evaporation and then subjected to curing treatment in oven. The curing step consists of 10 min at 60 °C, followed by gradual increase up to 120 °C (1 h 35 min).

To impart changes in the mechanical properties of this sol-gel formulation, several parameters were changed:

1. *Synthesis Temperature*
2. *Curing conditions*
3. *Aging time after synthesis*

The above-referred conditions were performed without altering the chemical composition of the base sol-gel formulation. One additional factor was investigated to promote brittleness and crack-formation upon impact, namely by increasing the inorganic content of the sol-gel formulation:

4. *Effect of type and concentration inorganic fillers.*

In the following section, the main results concerning the effects of these four factors on the impact tests will be described.

3 Results and Discussion

For the purpose of this study, the basic sol–gel formulation described above has been used. The main objective of this work was the improvement of the basic sol–gel matrix toward enhanced coating brittleness upon application of mechanical impacts with certain energy. The coatings were produced by a bar coater with a nominal wet film thickness of 20 or 40 μm , BC20 or BC40, respectively. CFRP substrates for laboratory studies have been prepared by abrading one of the sides with SiC sand papers in order to achieve a uniform roughness and defined chemistry of the surface. The latter effect was important to control due to its possible influence on sol–gel adhesion and reproducibility of impact test results.

3.1 Effect of Temperature

In order to assess the temperature effect on the sol–gel brittleness, several temperature conditions were tested, namely (i) curing and (ii) sol–gel synthesis temperature. The first parameter affects the rate of condensation reactions and solvents evaporation from a sol–gel matrix. Faster processes can lead to the formation of coatings with higher inorganic part and higher porosity. On the other hand, sol–gel synthesis temperature directly affects the kinetics of hydrolysis and condensation reactions. A higher condensation can lead to a more rigid sol–gel network and consequently to a higher brittleness.

Curing Temperature. Both heating ramp and maximum temperature of the curing step were varied. Common curing step is done starting from a lower temperature with a gradual heating rate until a higher temperature. From preliminary impact tests, a curing step without gradual heating results in brittle coating and it allows for the easier identification of the damaged area. Heating at constant temperature has been done for samples prepared at all other tested conditions (Fig. 2).

Synthesis Temperature. The temperature was also varied during the synthesis of sol–gel formulation. In particular, different temperatures of the initial three sol–gel solutions were tested in order to verify whether there was some connection between the synthesis temperature and the mechanical properties of the sol–gel coating.

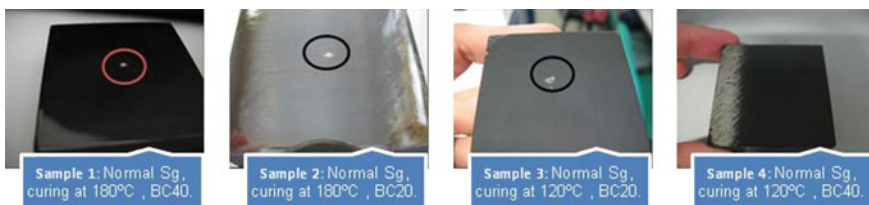


Fig. 2 Pictures of sol–gel-coated CFRP cured at temperature 180 °C (samples 1 and 2) and 120 °C (samples 3 and 4) after impact

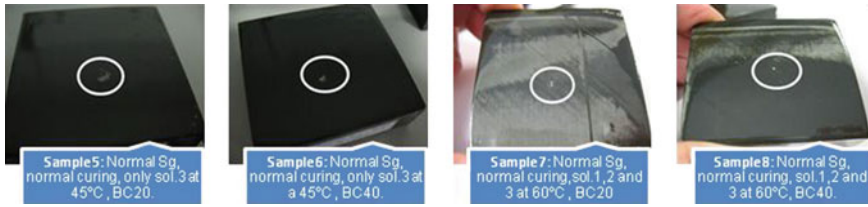


Fig. 3 Pictures of sol-gel-coated CFRP cured at temperature 120 °C; synthesis at 45 °C (samples 5 and 6); and at 60 °C (samples 7 and 8) after impact

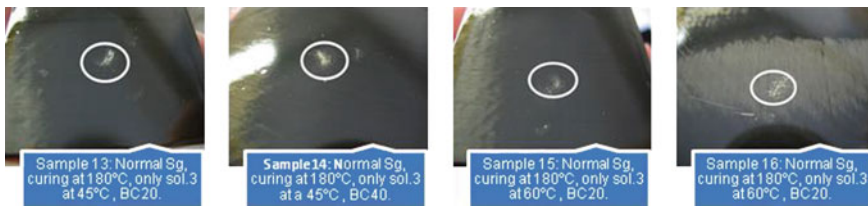


Fig. 4 Pictures of sol-gel-coated CFRP cured at temperature 180 °C; synthesis at 45 °C (samples 13 and 14); and at 60 °C (samples 15 and 16) after impact

From all the coatings prepared and tested, samples where only solution 3 was heated seemed to produce better visible marks of impact than others (Fig. 3). The combination of synthesis with curing temperatures was also tested. The results showed that the best system is the one where only solution 3 is heated at 45 °C and the curing temperature reaches 180 °C (Fig. 4).

3.2 Effect of Sol-Gel Aging

Sol-gel aging/storage time was an additional parameter which might affect mechanical properties of sol-gel coatings. Basically, all the tests performed in the previous section (3.1) were repeated using the same sol-gel formulations after one week of storage. The obtained results from impacts performed with targeted energy showed that samples coated with thinner wet films show better visible impact zones than samples coated with thicker films. However, the results were not significantly better with respect to 1 h of aging, so this effect was considered to have a minor effect on the brittleness.

From all the tests performed, the most promising were as follows:

1. Normal sol-gel synthesis at 22 °C with 1 h of aging and curing in the oven at 120 °C for 1 h 20 min (no ramp);
2. Normal sol-gel synthesis with 1 week of aging and curing at 120 °C for 1 h 20 min (no ramp);

3. Modified sol-gel synthesis where solutions 1 and 2 were kept at 22 °C and solution 3 at 45 °C, with 1 h of aging and curing in the oven at 180 °C for 1 h 20 min (no ramp).

3.3 Effect of Filler Addition

After studying the effects of temperature and aging on the brittleness of sol-gel coatings, some other strategies have been tested to improve the brittleness of sol-gel. As inorganic fillers commercially available, cationic exchange pigments on the basis of aluminosilicates denominated as pigment 1 and pigment 2 were used. The choice for use of inorganic fillers was somehow to impart a more “inorganic” content to the formulation of sol-gel, not at the expense of the sol-gel chemistry per se, but through addition of external pigments readily available and known within coating industry for development of composites. In this way, the aim was to decrease the flexibility of the sol-gel matrix and promote crack-formation upon external action, namely by mechanical impact.

The inorganic fillers were added in different percentages 1, 5, and 10 wt.% to sol-gel formulation. To improve the dispersion of the fillers in sol-gel, a few drops of isopropanol were added to the powder and then they were added to sol-gel and stirred before their application onto CFRP substrates.

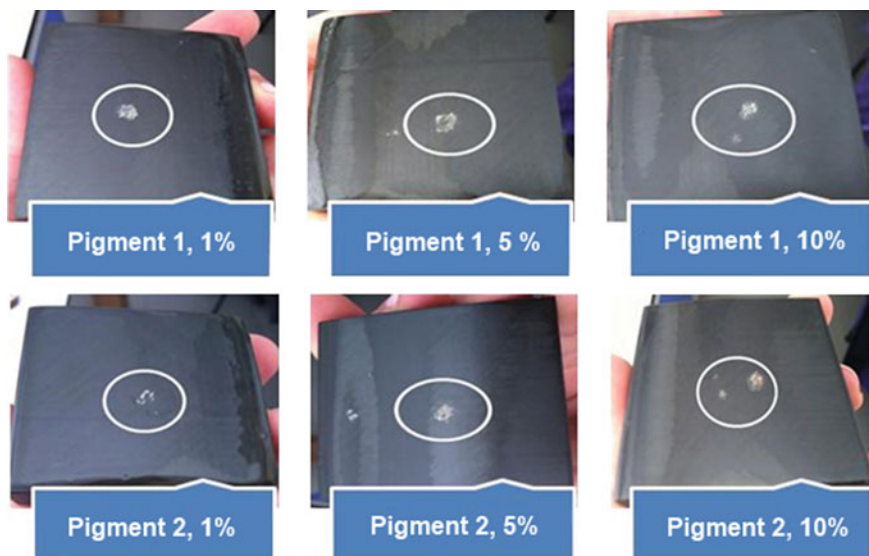


Fig. 5 Pictures of sol-gel coatings doped with pigments 1 and 2 after impact

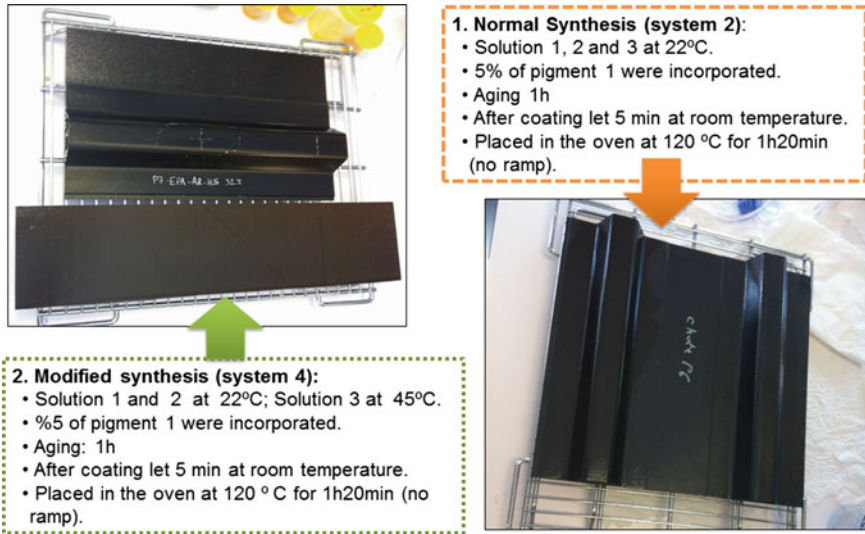


Fig. 6 Selected systems for validation at AIRBUS France

Coating damages resulting from mechanical impacts are shown in Fig. 5 for sol-gel coatings with pigments 1 and 2, respectively. From the observation of resulting damages in the sol-gel coatings filled with inorganic fillers, these systems seem to be more brittle, allowing for the identification and location of the damaged areas in a simple and expeditious way. The coatings with pigment 1 show a relatively better performance than those with pigment 2.

After careful analysis of all samples explored and taking in consideration the size of damage, the energy of impact, delamination, and coating removal, the selected systems were the ones containing pigment 1. Such samples have been applied on CFRP panels and sent for evaluation at the Airbus premises for validation of the impact sensitive coatings (Fig. 6).

4 Conclusion

In this work, the effect of different parameters on the synthesis and preparation of sol-gel coating formulations was investigated: synthesis temperature, conditions of curing, sol-gel aging, and addition of inorganic fillers. From all the conditions tested, the effect of temperature (no heating ramp) during curing and presence of inorganic fillers were the most influencing factors to achieve visible detection of damages within the specified mechanical impact energy range.

In spite of these promising results, there is still some possibilities not fully explored, including the substrate conditioning (polishing) and corresponding influence on coating adhesion, coating application methodology (spray, bar coater,

brush, dipping, etc.), and final coating dry thickness which, for the same formulation, can be used to further improve the coating brittleness.

From a commercial point of view, the use of sol–gel coatings as alternatives and/or complementary approach to NDT for SHM seem an attractive route because sol–gel technologies are readily available industrially at large scale, so the transfer of this knowledge to products would be a realistic scenario within a couple of years.

Acknowledgments The research leading to these results has received funding from the European Union’s Seventh Framework Programme for research, technological development and demonstration under grant agreement no 284562.

FM, KY, and JT thank FCT for PhD SFRH/BD/72663/2010, Post-Doctoral SFRH/BPD/80754/2011 and IF/00347/2013 grants, respectively.

References

1. Brinker CJ, Scherrer GW (1990) Sol–gel science: the physics and chemistry of sol–gel processing. Academic Press, San Diego
2. Schmidt H (1985) New type of non-crystalline solids between inorganic and organic materials. *J Non-Cryst Solids* 73:681–691
3. Sanchez C, Julian B, Belleville P, Popall M (2005) Applications of hybrid organicinorganic nanocomposites. *J Mater Chem* 15(35–36):3559–3592

Coating for Detecting Damage with a Manifest Color Change

Laura Monier, Karel Le Jeune, Isabelle Kondolff and Gil Vilaça

Abstract Carbon fiber-reinforced plastic (CFRP) structures are used in modern airliner. An impact may damage the inner structure of the composite without any visible marks on its surface. So, the solution that is investigated by CATALYSE is the application of a coating that would reveal impacts. This technology is based on microcapsules with a manifest color change (under visual and UV light). Different types of capsules were tested with different active components.

Nomenclature

CFRP	Carbon fiber-reinforced plastic
UV	Ultraviolet
IDL	Impact detection layer
LD	Leuco dye
IR	Infrared
μm	Micrometers
4-HR	4-hexylresorcinol

L. Monier (✉) · K. Le Jeune · I. Kondolff · G. Vilaça
CATALYSE Company, Marseille, France
e-mail: l.monier@catalyse-fr.com

K. Le Jeune
e-mail: k.lejeune@catalyse-fr.com

I. Kondolff
e-mail: i.kondolff@catalyse-fr.com

G. Vilaça
e-mail: gil.vilaca@kemone.com

1 Introduction

Carbon fiber-reinforced plastic (CFRP) structures are used in modern airliner. These materials could be damaged from inadvertent impacts. The damage on the surface is often not visible: Delaminations occur between the composite layers and may cause security problems. So, the solution that is investigated in AS08 is the application of a coating that would reveal impacts. In the literature, some impact detection systems are described, based on piezoelectric strain sensors [1, 2], vibration monitoring system with a fiber-optic vibration sensor [3] or other optical methods [4], and thermographic systems based on IR technology [5]. All these techniques are difficult to use in an industrial way. The checking of composite materials needs to be quick and reliable. What seemed to be the most interesting for us is a visual detection system, with the appearance of a colored task at the impact location. This technique could be based on dye-filled microcapsules introduced in a coating [6–8].

CATALYSE is in charge of encapsulating dyes in order to get a coating coloration once the capsules' shell is broken by the impact. The technology is based on a leuco dye/revealing agent system. The leuco dye is encapsulated, and the revealing agent is directly introduced in the coating binder. Firstly, CATALYSE has been working on the capsules size, its wall thickness, and the polymeric nature of the shell, in order to cope at its best with the requirements (threshold detection, final task coloration, etc.). Fluorescent compounds (fluorochromes) have been evaluated in order to optimize visual contrast in dark environment.

Many efforts have also been spent in order to avoid incompatibility between the IDL (impact detection layer) constituents and the coating matrix. Indeed, leuco dye or revealing agent tend to react with the matrix compounds and yield to an inhibition of the revelation. To solve this problem, CATALYSE proposed three solutions: encapsulation of the revealing agent before the introduction in the binder, a multilayer concept, or a new formulation of an entire coating.

2 CATALYSE Concept

CATALYSE objective is to develop an impact detection technology. The technology is based on a leuco dye/revealing agent system. The leuco dye, an invisible molecule which becomes colored in acid conditions, is encapsulated, and the revealing agent (a weak acid compound) is directly introduced in the coating binder, outside of the microcapsules. Before any impact, the two components are separated, and there is no coloration. When microcapsules burst upon impact, they free the product that comes into contact with the developer incorporated into the coating. A colored task appears at the impact location. This concept is illustrated in Fig. 1.

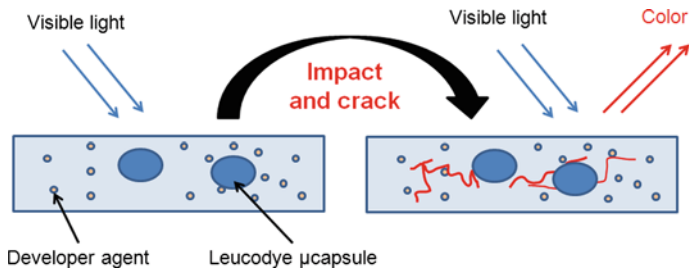


Fig. 1 CATALYSE concept for impact detection. On the *left*, the IDL containing microcapsules and the revealing agent before impact, on the *right*, an impact occurs

3 Microencapsulation

Initial studies focused on the synthesis of the leuco dye microcapsules. The leuco dye component, solubilized in an organic phase, will be encapsulated with following requirements: The shell must be proof from the outside of the coating (especially from the revealing agent), the capsules need to be resistant to pressure, to give a detection only if needed (impact detection threshold defined during the project), and the size is small enough to permit the classical use of the paint.

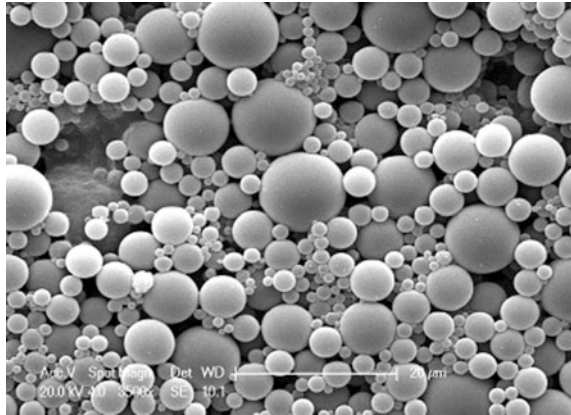
3.1 Impermeability Improving

The aim is to obtain impermeable microcapsules. A usual blue leuco dye has been dissolved in a hydrophobic solvent and encapsulated in a polyurea shell by an interfacial polycondensation process [9, 10]. To modify the impermeability, we can vary first the polyurea properties. By changing the reactional monomers (size, reactivity, functionalities, etc.), we obtain a compact cross-linked polymer. By changing the synthesis conditions (temperature, surfactants, etc.), we create a more crystalline and so a more impermeable polymer. Then, we can vary the thickness of the shell to adapt the impermeability of the optimized polyurea shell. Our best result is obtained for microcapsules as shown in Fig. 2.

The impermeability is checked with the following test: Microcapsules are introduced in a coating containing the revealing agent. No coloration is visible: Microcapsules are enough proof to the revealing agent. Then, microcapsules are impacted: A blue task appears. CATALYSE concept is available.

The size of microcapsules needs to be small enough to integrate them into a revealing paint: In Fig. 2, microcapsules obtained have an average diameter suitable to future applications.

Fig. 2 Impermeable microcapsules. SEM photography realized on dried leuco dye microcapsules



3.2 Adjustment of the Threshold Detection

Previous synthesized polyurea microcapsules are used for preliminary impact tests: They are too brittle to be used in an impact detection coating. The impact threshold defined for the project is not achieved. To solve the problem, we increase the thickness of the microcapsule shell. These new microcapsules are introduced in an impact detection coating and deposited on a metallic plate as shown in Fig. 3. Impact tests are realized, and the state of the surface is studied by confocal microscopy technology: Microcapsules have withstood the impact.

3.3 Use of a Fluorescent Leuco dye

Additional fluorescence on impact tasks would be interesting because it provides a security system to distinguish an accidental pollution color. So we replaced the usual

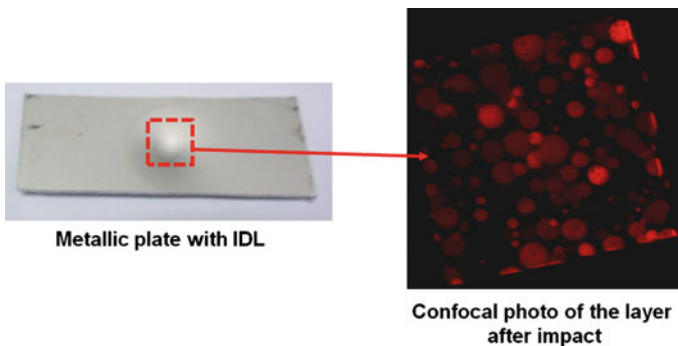


Fig. 3 Impact location studied by confocal microscopy technology. Microcapsules introduced in IDL are not destroyed

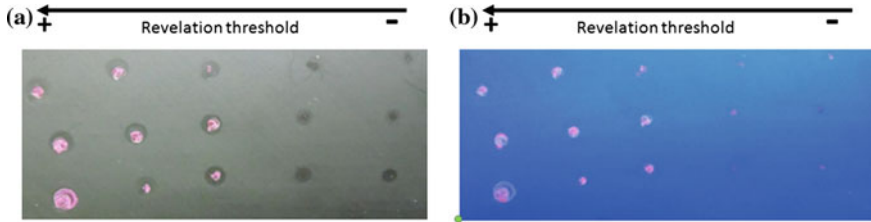


Fig. 4 Impacts made on IDL containing microcapsules with leuco-fluorochrome and tasks visualized under **a** visible light, **b** UV light. Various thresholds are tested: We obtain a nice *pink* task, under visible light and under UV light, at defined thresholds

blue leuco dye used until now by a fluorescent leuco dye: a leuco-fluorochrome. It is encapsulated by the previous interfacial polycondensation technique, in the optimized polyurea shell (good polyurea nature and properties, good thickness). Microcapsules are introduced in an IDL (with a revealing agent). Plates are painted and impacted with various thresholds. Results obtained are presented in Fig. 4. We obtain a nice pink task, under visible light or under UV light, at a defined threshold.

At the end of the first step of the study, CATALYSE managed to make microcapsules containing a fluorochrome, with suitable impermeability, resistance, and size, which give an adequate intensity after impact.

4 Coating Preparation

The couple microcapsules/revealing agent is introduced in conventional binders used in aircraft paints, but some flocculation and instability problems occur. The revealing agent is not compatible with these conventional binders. Despite literature searches, no known developer agents remain functional. Three solutions have been considered: encapsulation of the developer (first solution) and a multilayer system (second solution), which both permit to separate the revealing agent from the binder, and a new coating formulation with a compatible binder (third solution).

4.1 Double Microencapsulation

The selected developer to test microencapsulation is the 4-hexylresorcinol (4-HR), because of its non-toxic properties, and it gives a very nice pink color with the leuco-fluorochrome. It is encapsulated in a polyurea shell by a well-known interfacial polycondensation technique (Fig. 5). These new microcapsules are mixed with microcapsules containing a leuco-fluorochrome, in a suitable binder. This IDL is deposited on a metallic plate, and impact tests are performed: No revelation is

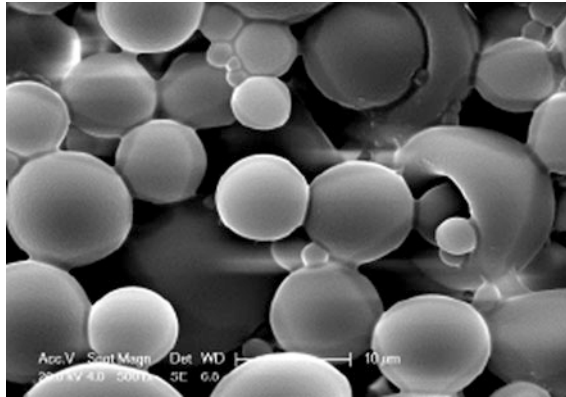


Fig. 5 4-HR microcapsules. No revelation after impact in the presence of microcapsules containing a leuco-fluorochrome

visualized. Other tests are realized without good results. It is assumed that the revealing agent, a weak acid molecule, reacts with monomers during the shell synthesis. The same problem will occur with other revealing agents, with this encapsulation process. This IDL way is blocked.

4.2 Multilayer System

The aim is to separate the IDL, containing leuco-fluorochrome microcapsules and the revealing agent, from the conventional non-compatible paint. A first (optional) layer can be a primer to increase adhesion properties. Then, a second layer, the IDL, must be deposited. Finally, the third layer will be the aircraft conventional paint which confers to the composite surface its definitive aspect.

A first test realized on a metallic plate (painting according to the multilayer system and impact tests) is presented in Fig. 6 and shows that the concept works.

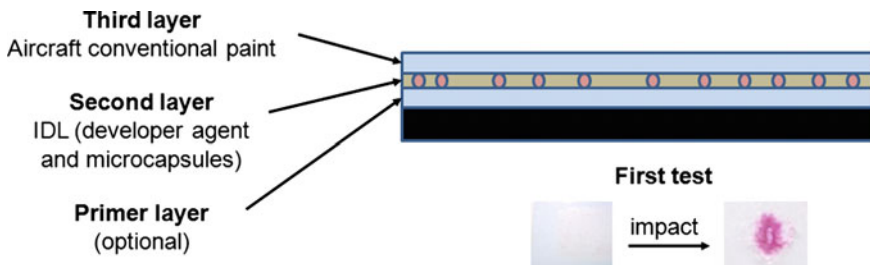


Fig. 6 Multilayer concept. A first test shows that multilayer concept works

4.3 New Coating Formulation

The objective is to replace the problematic conventional binder by another binder which can be compatible with the revealing agent. The new coating will contain the microcapsules with the leuco-fluorochrome, the revealing agent, and a new compatible latex. To be approved in aircraft technologies, it must have the following attended properties: good revelation after an impact, good mechanical properties and adhesion, and good water resistance.

4.3.1 Revelation After Impact

This problem had been already solved during the previous studies. We continue working with optimized microcapsules of leuco-fluorochrome described before, microcapsules 48.

4.3.2 Good Mechanical Properties and Adhesion

Microcapsules 48 are introduced in a binder n°8, with the revealing agent (the created IDL is named IDL 8-48). We add some compatible additives to improve adhesion on CFRP: cross-linker additives, to create cross-links in the IDL, and a high mechanical resistance varnish named Reshydrol.

Properties are measured by normalized crosscut tests. They are shown in Fig. 7. Mechanical properties and adhesion are improved by these additives. It is very important to note that adhesion properties depend on the substrate used.

4.3.3 Water Resistance

Properties are measured by immersion tests (samples are immersed directly in water) or by salt spray tests (with a specific machine which can disperse a determined quantity of drops of water, like a fog). IDL 8-48 does not resist to water.

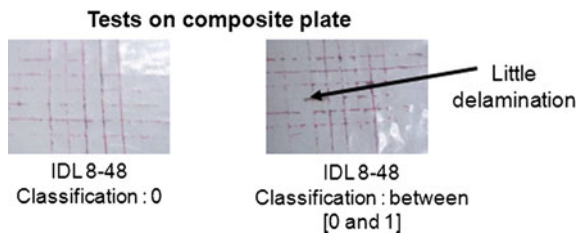


Fig. 7 Crosscut tests on a new coating formulation. IDL formulation contains microcapsules 48 and binder 8

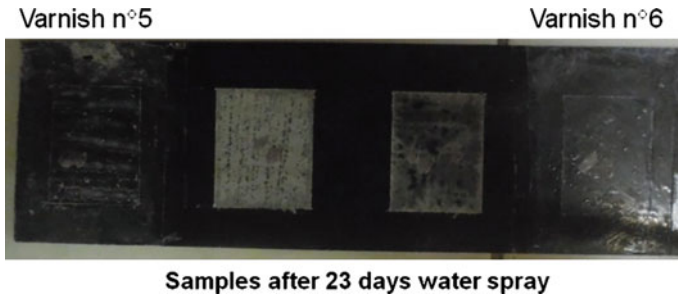


Fig. 8 Water resistance of IDL with protective varnishes. Varnishes n°5 and n°6 give a nice water resistance to IDL after 23 days of water spraying

We need to protect it and propose to deposit a varnish above. This concept could be associated with the multilayer concept.

Water spray resistance of multilayer samples is tested by water spraying for 23 days. The results are shown in Fig. 8. Varnishes n°5 and n°6 give a better resistance to IDL under water spray tests: Samples do not become white (no water infiltration).

After drying of the samples, classical impact tests are done: Impact detection still works.

5 Conclusion

CATALYSE IDL concept works well. It is constituted from a leuco-fluorochrome dissolved in a solvent and encapsulated in a polyurea shell by interfacial polycondensation, a revealing agent, and a compatible binder. The use of a leuco-fluorochrome compound permits a fluorescence detection. This system is especially interesting to avoid accidental pollution color and gives great results in terms of color detection intensity. CATALYSE polyurea shell microcapsules are optimized to obtain a suitable size and threshold impact strength detection. But this last characteristic depends a lot from the substrate.

To create an industrial IDL, the main problem is the compatibility between usual binders used in airplane paints and the revealing agent. Various technical solutions are considered. The double encapsulation way gives no results because of the chemical nature of the revealing agent, which is a weak acid and reacts with monomeric molecules used for the shell synthesis. The multilayer concept is a nice way to solve the problem. The most simple solution is to create a new coating formulation, with another binder. The last IDL proposed for the project gives a nice revelation after impact. Mechanical properties and adhesion are limited, but as we said before, it depends on the substrate and can be adapted. Water resistance is in good way to be solved. Some tests are in progress with varnishes n°5 and n°6.

Acknowledgments All the CATALYSE teams wish to thank the Workpackage 8 for this scientific adventure, which bring us knowledges in various subjects and permit us to discover very nice scientific staff. CATALYSE thanks Mr. Bruno Montagnier for his work during three years. The research leading to these results has received funding from the European Union's Seventh Framework Programme for research, technological development, and demonstration under grant agreement no 284562, so we are grateful for this.

References

1. Haywood J, Coverley PT, Staszewski WJ, Worden K (2005) An automatic impact monitor for a composite panel employing smart sensor technology. *Smart Mater Struct* 14:265
2. Coverley PT, Staszewski WJ (2003) Impact damage location in composite structures using optimized sensor triangulation procedure. *Smart Mater Struct* 12:795
3. Doyle C, Fernando G (1998) Detecting impact damage in a composite material with an optical fibre vibration sensor system. *Smart Mater Struct* 7(4)
4. Ambu R, Aymerich F, Ginesu F, Priolo P (2006) Assessment of NDT interferometric techniques for impact damage detection in composite laminates. *Compos Sci Technol* 66 (2):199–205
5. Thomas J, Harold B (1992) Thermographic detection of impact damage in graphite-epoxy composites. *Mater Eval* 50(12):1446–1453
6. Vidinejevs S, Strelalova O, Aniskevich A, Gaidukov S (2013) Development of a composite with an inherent function of visualization of a mechanical action. *Mech Compos Mater* 49 (1):77–84
7. Vidinejevs S, Aniskevich AN, Gregor A, Sjöberg M, Alvarez G (2012) Smart polymeric coatings for damage visualization in substrate materials. *J Intell Mater Syst Struct* 23:1371–1377
8. Odom SA, Jackson AC, Prokup AM, Chayanupatkul S, Sottos NR, White SR, Moore JS (2011) Visual indication of mechanical damage using core-shell microcapsules. *ACS Appl Mater Interf* 3:4547–4551
9. Yadav SK, Suresh AK (1990) Microencapsulation in polyurea shell by interfacial polycondensation. *AIChE J* 36(3):431–438
10. Wagh SJ, Dhuma SS, Suresh AK (2009) An experimental study of polyurea membrane formation by interfacial polycondensation. *J Membr Sci* 328(1–2):246–256

Sensitive Coating Solutions to Lower BVID Threshold on Composite Structure

Silvere Barut

Abstract The objectives of the 8th Application Scenario in SARISTU project is to develop sensitive coating for impact detection. This coating is to be applied on composite structural parts and reveal internal impacts from a certain threshold. Several solutions in terms of “sensors” and matrices have been investigated and improved in order to lower the BVID threshold while respecting durability criteria and environmental, health and safety constraints.

Nomenclature

BVID	Barely visible impact damage
SHM	Structural health monitoring
NDT	Non-destructive testing
AS	Application scenario
FAL	Final assembly line
EHS	Environment, health and safety
REACH	Registration, evaluation, authorization, and restriction of chemicals
CAI	Compression after impact
TRL	Technology readiness level
UV	Ultraviolet

1 Introduction

Composite material is now widely used in the aerospace industry for its good mechanical properties such as fatigue stress and corrosion resistance and light-weight. However, this material can be sensitive to impact which may initiate internal damage without any visible indication on the surface. That is why structure

S. Barut (✉)

Airbus Group Innovations, 18 rue Marius Terce, 31025 Toulouse, France
e-mail: silvere.barut@airbus.com

design is commonly oversized in order to keep aircraft flying with undetected but acceptable internal damage. Active structural health monitoring solutions are currently improving such as acousto-ultrasonic inspection using Lamb waves propagation. The goal of such technology is to localise and assess the damage size which would avoid manual ultrasonic inspection; however, these solutions require hardware and many sensors to monitor the structure, with the associated weight and system maintenance.

Another solution to detect and localise impact occurrence would be to get a visual revelation at the impact's spot, like a coating which would change colour under its pressure. It has the advantage to be a passive method (no hardware added) that will lower the BVID threshold and fasten the triggered NDT inspection. One of the biggest challenges of this type of technology is to limit false alarms where low-energy impacts could be revealed; however, when there is no induced internal damage, this would kill the business case by triggering unnecessary NDT inspections.

This topic is addressed in AS08 of SARISTU (Smart Intelligent Aircraft Structures) project, where this project, partially funded by European Commission under Seventh Framework Programme, aims at achieving reductions in aircraft weight and operational costs.

2 Application Requirements and Test Conditions

The scope of this application scenario is limited to internal impact detection that may occur during the final assembly of aircraft, like tool drop. Of course, small and safe impacts should not be revealed as well as man walk. The risk analysis confirmed that internal impacts are more likely from manufacturing to FAL, including handling and transportation. During in-service maintenance activities, protections are used locally to reduce the impact threat. Furthermore, the main concern in terms of damage tolerance for internal impact on composite fuselage is located on stringers and frames. Previous impact tests showed that these components can get internal damage from a medium range of energies, using a hemispherical impactor at low velocity.

From this prospect, the requirements for developing a sensitive coating for impact detection are established in details with other considerations such as EHS, durability, application and repair processes to ensure that the final solution(s) can be pushed to future commercialisation and integration in aeronautical production environment. The impact indicating function has to be valid for one or two years, but the standard requirements for internal paint are used as target for the coating itself such as adhesion and scratch resistance, water immersion or operative conditions within a predefined range of temperature.

In order to evaluate and demonstrate the solutions capabilities in terms of visual impact revelation threshold, and to be repetitive, impact tests are performed according to standard and normalised CAI procedure (see Fig. 1) using hemispherical impactor and the Dynatup machine at Airbus Group Innovations facility

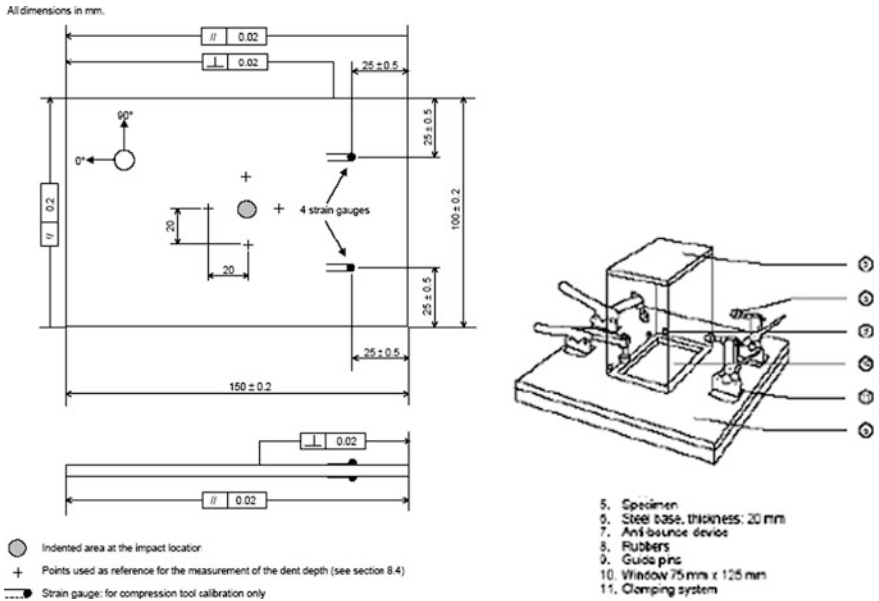


Fig. 1 Samples' definition and clamping conditions

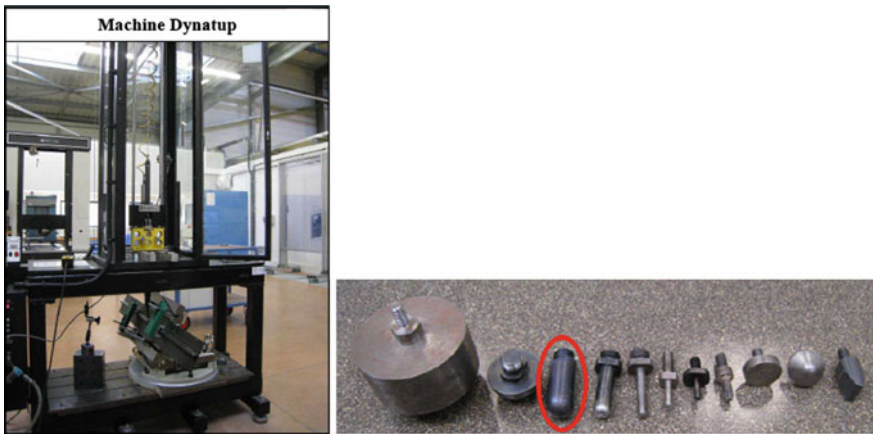


Fig. 2 Dynatup system and impactors

(see Fig. 2), which enables to record several parameters such as velocity, real impact energy and pressure during the impact.

Modelling using finite elements in quasi-static conditions was used to determine the CAI sample lay-up in order to make sure that the coupons are operated in conditions the most proximate as possible to realistic configurations: stiffness, impact duration and contact force history (see Fig. 3).

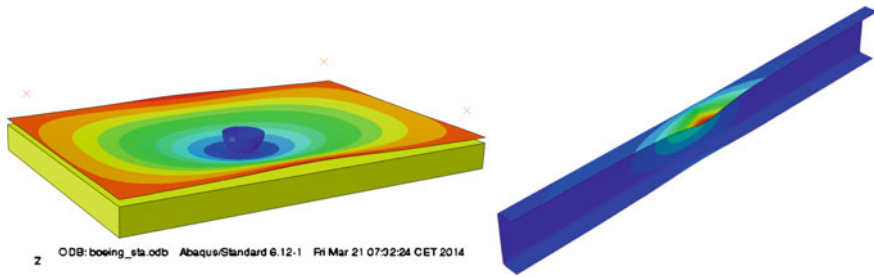


Fig. 3 Explicit dynamical computation on shell models

3 Technologies Improvement and Evaluation

Before SARISTU project, some similar or close solutions were underdevelopment [1] or already on the shelves [2, 3], but all marketed solutions were and still are very sensitive to pressure, and impacts at very low energy would be revealed and trigger many false alarms in the targeted applications.

Several identified solutions have been pushed forward through SARISTU project to get higher TRL and higher capabilities. Some of them have been abandoned or reoriented during the project due to technical boundaries. Finally, three different solutions have undergone the verification impact and durability tests:

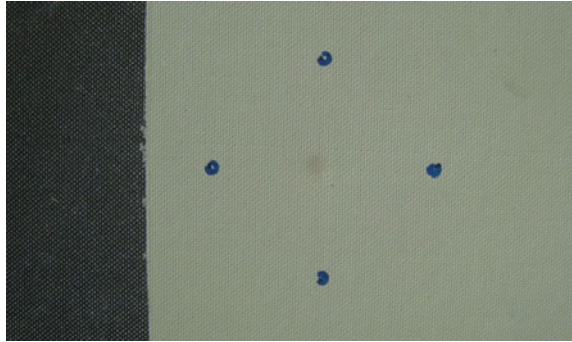
- One incorporating piezochromic pigments into primer coating or peelable coating;
- One incorporating microcapsules into specific coating; and
- One constituted only by sol-gel matrix.

3.1 Piezochromic Pigments

Piezochromic pigments have the ability to change colour when a pressure is applied. This colour change can be reversed by heating. During the project, CNRS worked on the modification of the synthesis of cobalt-based pigments and have been able to get tunable sensitivity to pressure, and one of the targeted impact thresholds has even been reached on a thick composite. But as cobalt is a possible candidate for the REACH list, copper-based pigments were investigated and proved to have similar sensitivity and revelation properties, but with lower temperature phase transformation close to the operational temperature range. The revelation contrast is not very high, but the impact is nevertheless revealed and the BVID optimised.

After several trials of pigments' incorporation into different matrices where agglomeration or chemical incompatibility has been encountered, processes have

Fig. 4 Impact revealed by piezochromic pigment in primer



been optimised and two types of matrices have been finally tested. The first selected coating is an epoxy primer which can additionally bring its intrinsic properties as permanent solution (see Fig. 4). The second selected coating is a paint which can be peeled off. This solution can be very interesting to avoid additional weight to the aircraft, but unfortunately, impact revelations were not conclusive during the verification impact tests.

The application process by spray can be applied in a production environment. The revelation can be erased by temporary local heating for a few minutes in case of no structural damage.

3.2 *Microcapsules*

Microencapsulation techniques are used in pharmaceutical industry or in research activities such as self-healing or corrosion protection. Previous works on impact revelation showed that the capsules can be used as shock revealer where a dye is released in a porous coating after the impact (capsule's breakage), but the capsules were too big and fragile at that time for aeronautical applications.

CATALYSE performed microencapsulation optimisation during SARISTU project and succeeded in having capsules of few microns with tunable and high pressure resistance. Besides these new breakthrough capabilities, the major challenge is the chemical compatibility between the tested revealing agents and the coating matrices. Finally, microcapsules with fluorochrome compounds introduced into specifically developed coating matrix are the solution with the best contrast in daylight and under UV light, and the revelation threshold can be largely tuned to satisfy the requirements (see Fig. 5). However, the host matrix is quite sensitive to scratch even with varnish on top. This solution is EHS compliant, and the application process can be done by bar coater or spray.

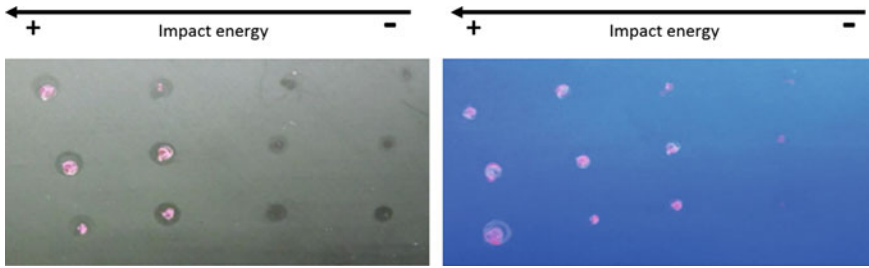
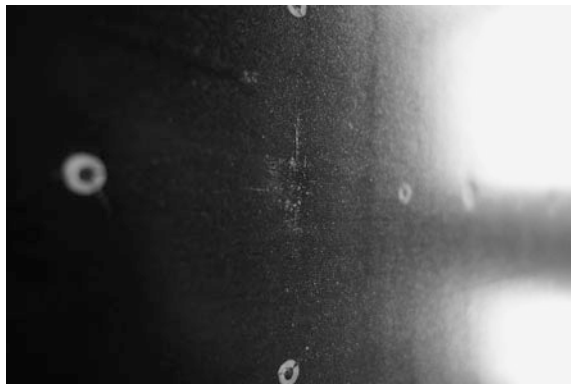


Fig. 5 Impact revealed by encapsulated fluorochrome compounds in specific coating in daylight or under UV light

Fig. 6 Impact revealed by dent and cracking sol-gel layer



3.3 Sol-Gel Matrix

The versatility of the sol-gel chemistry allows using various additional compounds to customise the coating properties. During the project, trials of impact revelation mixing this technology with different types of sensors were performed, but due to chemical compatibility problems or too complex process to be applied in industrial environment, those solutions were abandoned. Finally, University of Aveiro developed a solution made of sol-gel with additives to get it more or less brittle. This transparent and shiny coating reveals impacts through its layer dent and cracking (see Fig. 6). This coating is EHS compliant but requires to be slightly heated to polymerise.

4 Conclusion

The biggest challenge to get impact indicating coatings is the revelation threshold optimisation but not the only one. Chemical compatibility, revelation quality (contrast), mastering of processes (repeatability), EHS compliance and durability conditions are as many aspects as challenges to face. SARISTU project enabled to improve drastically the technologies and the knowledge of the investigated solutions, but also to get innovation breakthrough like impact revelation threshold capabilities that were never reached before. As a result, there is no fully compliant solution with the drastic initial requirements, but mitigations can be found.

Even though the solutions are to be sensitive to impact energy, they are fundamentally sensitive to pressure. In order to get future qualification of these solutions or their derivatives, their sensitivity qualifications will have to be established by pressure range, in order to be independent of the test conditions (local structure stiffness, impact conditions, etc.) and masterise the mechanical behaviour analysis.

Acknowledgments The research leading to these results has received funding from the European Union's Seventh Framework Programme for research, technological development and demonstration under Grant Agreement no. 284562.

The involvement, motivation and determination of the people and teams amongst the partners in the application scenario enabled to overcome the technology hurdles and get final solutions with upper TRL.

References

1. Air Force SBIR/STTR Innovation story. <http://www.afsbirsttr.com/Publications/Documents/Innovation-091908-Luna-AF04-133.pdf>. Accessed 04 May 2015
2. Sensors Products Inc. <http://www.sensorprod.com/pressurex-micro-green.php> (2015). Accessed 04 May 2015
3. Fujifilm Prescale. <http://www.fujifilm.com/products/prescale/prescalefilm/>. Accessed 04 May 2015

Part IX

Technology Stream: Multifunction Materials. Enhancement of Primary Structure Robustness by Improved Damage Tolerance

Introduction and Overview

Application scenario 09 aims to take forward to higher TRL-level technologies and methods that realize measurable improvements in aircraft damage tolerance and weight reduction. It aims to evaluate toughening of composite materials through additives such as multiwall carbon nanotubes (MWCNT) and various types of polymer interleaf veils. The development of strategies to effectively introduce toughening systems in common composite manufacturing processes has been successfully achieved. This scenario works alongside application scenario 10 in order to deliver multifunctional structures with enhanced damage tolerance and electrical isotropy. Several strategies were addressed, and their integration into composite materials and the influence on the damage tolerance were studied. The technologies were studied in terms of mechanical properties and electrical conductivity during the Phase 1. The best performing technologies (thermoplastic veils and MWCNT-treated prepreg) were further characterized in Phase 2 at RT and HW at coupon level and a sub-element level. This section includes four papers. The first paper, Enhancement of Infused CFRP Primary Structure Mechanical Properties using Interleaving Thermoplastic Veils, outlines the mechanical performance evaluation of a toughened fabric by addition of interlaminar thermoplastic veils infused with epoxy resin. The second paper, Use of Carbon Nanotubes in Structural Composites, presents developed multiwall carbon nanotubes (CNT) thermoset and thermoplastic carriers that allow the introduction of CNT in composite laminates having in mind the clear assumption adopted at the beginning of the project that not pristine powder CNT would be handle due to health and safety issues. The third paper, Enhancement of Primary Structure Robustness by Improved Damage Tolerance, gives an overview of the mechanical test campaign developed to evaluate and validate the different material solutions developed and provided by the partners to maximize the performance enhancements, particularly damage tolerance, while minimizing any knockdowns in hot/wet performance in infused as well

as prepreg panels. The last paper, Multiscale Reinforced Prepregs for the Improvement of Damage Tolerance and Electrical Properties of Aeronautical Structures, presents the multiscale CNT modification technology for conventional prepregs that allows the effective introduction of CNT into composite laminates and the work developed to scale up the process.

Use of Carbon Nanotubes in Structural Composites

Daniel Bonduel, Nadir Kchit and Michael Claes

Abstract Carbon nanotubes (CNT) possess excellent intrinsic characteristics such as exceptionally high mechanical and conductive properties which make them the prime candidate to reinforce high-performance composite structures. However, location and dispersion state of the CNTs are of particular importance to achieve the mechanical and electrical enhancement of carbon-reinforced composites. In the frame of European Project SARISTU, different approaches were investigated by the different partners (e.g., veils, powdered doped prepreg, and doped adhesives). Each approaches required specific dispersion solution. Along its existence, Nanocyl has developed a large experience in incorporation of CNTs in different resins (thermoplastics, thermosets, etc.) using improved innovative mixing process, CNT surface modification (functionalization) or by adding some dispersing agents or compatibilizers. Applying this expertise to SARISTU context, the requested products were delivered in the suitable form for each scenario. As an example, ground CNT/thermoplastics compounds were produced for powdered doped prepreg and different grades of doped thermoplastics for veils production.

Nomenclature

BET	Brunauer, Emmet, and Teller theory to determine specific surface area
CNTs	Carbon nanotubes
CFRC	Carbon fiber-reinforced composite
MVR	Melt volume flow rate
MWCNTs	Multiwalled carbon nanotubes
TEM	Transmission electron microscopy
TGA	Thermal gravimetric analysis

D. Bonduel (✉) · N. Kchit · M. Claes
Research and Development, Nanocyl S.A, Rue de l'Essor 4, 5060 Sambreville, Belgium
e-mail: Daniel.Bonduel@nanocyl.com

N. Kchit
e-mail: nadir.kchit@nanocyl.com

M. Claes
e-mail: michael.claes@nanocyl.com

1 Introduction

Since the first observation of CNTs in the early 1990s [1], huge progresses have been made in the understanding of this cutting-edge material. For a long time, carbon nanotubes were only categorized and used as “highly conductive fillers,” but nowadays this nanotechnology is starting to exhibit its true potential and proves that it can improve or even impart new properties to polymers (mechanical, chemical, or thermal properties). At the end, the composite will not only offer electrical conductivity but will also present better mechanical or chemical or heat resistance under operation, which will allow researchers and engineers to develop, create, and design breakthrough materials and unprecedented technologies.

Nanocyl is one of the first companies to be established in Europe for the commercial supply of this family of novel material. From 2002, Nanocyl has built up its worldwide recognition by providing high-quality products adapted to the customer’s needs. Its expertise in tuning the carbon nanotubes properties and morphologies to obtain the best out of their intrinsic potential has made Nanocyl one of the most recognized producers of specialty carbon nanotubes and of materials and technologies using carbon nanotubes. Moreover, this knowledge and expertise has led Nanocyl to exploit further the CNT advantages by preparing concentrates, dispersions, and semi-formulated products out of various material families (thermoplastics, thermosets, elastomers, silicones, liquids, etc.).

2 Carbon Nanotubes

Numerous different carbon nanotubes can be produced by playing with carbon sources, catalyst, process, and temperature. At Nanocyl, large volumes of thin MWCNT (NC 7000) are produced by catalytic chemical vapor decomposition. A primary interest of NC 7000 is low percolation threshold for electrical conductivity toward other conventional carbon-based fillers. In Fig. 1, a micrograph of NC 7000 is shown and their intrinsic characteristics are given in Table 1.

Nanocyl is also leading pro-actively health, safety, and environment matter all long the life cycle of product containing MWCNT NC 7000. Interaction with several key players and participation to different European projects has led to numerous data collection and positioning [2] on hazard [3, 4], exposure, use phase [5, 6], and end of life. As a consequence, registration dossiers under REACH have been filed and provide information on the safe uses of MWCNT.

Further, NC 7000 functionalized with amino groups (NH₂-NC 7000) was produced by a patented plasma process. The amino groups should improve the dispersion of the CNTs into the matrix leading to an increase of mechanical performances and a lower percolation threshold for electrical conductivity.

Fig. 1 Transmission electron microscopy of multiwalled carbon nanotube NC 7000

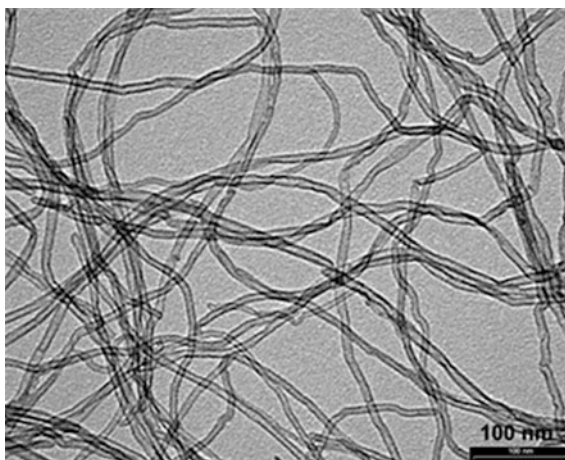


Table 1 Characterization of multiwalled carbon nanotube NC 7000

Property	Unit	Value	Method of measurement
Average diameter	Nanometers	9.5	TEM
Average length	Microns	1.5	TEM
Carbon purity	%	90	TGA
Metal oxide	%	10	TGA
Surface area	m ² /g	250–300	BET

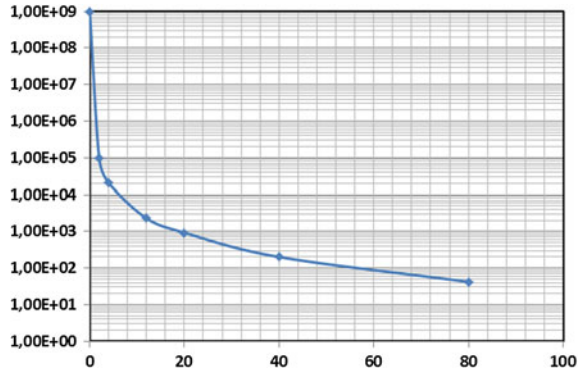
3 Carbon Nanotube-Doped Epoxy Concentrates

In order to enhance and achieve good performances, dispersion of CNTs in the matrix is from prime importance. Over years, Nanocyl developed knowledge on incorporation processes and good dispersion of CNTs. Based on this expertise, several grades of CNTs epoxy concentrates were developed (EpocylTM). Two of them are dedicated to mechanical reinforcement (grade name: Epocyl 128-02 and Epocyl 128-06) and one for electrical conductivity application (grade name Epocyl 128-05).

SARISTU project was targeting notably the electrical conductivity, and Epocyl 128-05 was therefore chosen. Dilution factor has to be calculated accordingly to the desired level of conductivity (see Fig. 2).

In order to enhance the mechanical performance, a modified grade of Epocyl 128-05 was also produced with amino groups functionalized CNTs. Studies undertaken by Fraunhofer and EADS with those two products show no significant effect on mechanical and electrical properties of amino groups functionalized CNTs in comparison with unfunctionalized.

Fig. 2 Resistivity ($\Omega\cdot\text{cm}$) versus parts of 128-05 in the final compound (100 parts in total). Properties measured on cast films



4 Carbon Nanotube-Doped Thermoplastics

Nanocyl’s expertise for the dispersion of CNTs in thermoplastics is used to produce high value masterbatches or compounds (PLASTICYL™ grades).

Plasticyl products provide easy to use masterbatches containing CNT already pre-dispersed. In some cases, for equal surface resistivity, a reduction up to 25 % of CNTs loading could be achieved by using Plasticyl masterbatch (see Fig. 3, surface resistivity threshold: $10^6 \Omega^{-2}$).

PLASTICYL™ is available in a wide range of thermoplastic resins, including PC, PP, PA, PET, HDPE, POM, and others. The knowledge for the production of PLASTICYL™ was used for the production of compounds and concentrates for veils and powdering applications.

Fig. 3 Effect of the incorporation method on the electrical conductivity performances

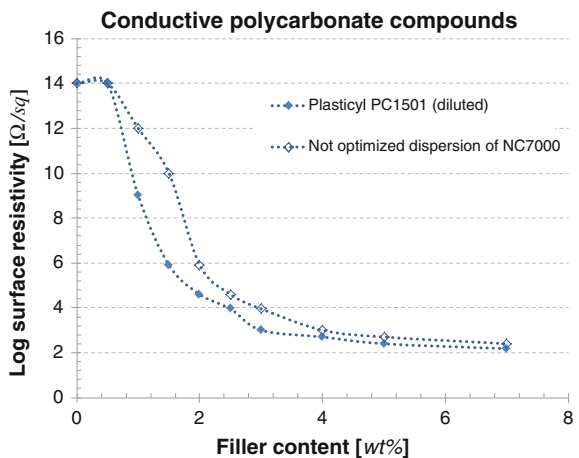


Table 2 Viscosity and melting range of the thermoplastics from same nature used for the veils

Commercial name	Melting range (°C)	Melt viscosity (Pa.s)	MVR (160 °C/2.16 kg (cm ³ /10 min)
Thermoplastic 1	125–135	1200 (190 °C/2.16 kg)	9
Thermoplastic 2	120–130	600 (160 °C/2.16 kg)	18
Thermoplastic 3	115–125	150 (160 °C/2.16 kg)	70
Thermoplastic 4	130–140	500 (160 °C/2.16 kg)	30
Thermoplastic 5	110–120	350 (160 °C/2.16 kg)	21

4.1 Veils Application

Thermoplastics with suitable compatibility regarding CFRC were selected. This selection was mainly based on the chemical nature of the thermoplastics.

A second selection was based on the physical properties of the thermoplastics. In order to melt during the curing cycle and migrate in CFRC, melt temperature of thermoplastic should be between 110 and 135 °C. Also, the melt viscosity and MVR should be adapted to industrial veils process. Table 2 shows the properties of the thermoplastics retained for the production of veils.

A first set of trials based on thermoplastic 1 was performed to identify the request loading of CNTs to reach the targeted electrical conductivity of 10–20 S.m.

A second set of trials has been performed on thermoplastic 1 with CNTs functionalized with amino groups. No significant effect of amino group functionalization was observed on electrical conductivity behavior [7].

Batches of both compounds were produced using industrial twin-screw extruder and suitable information was collected to conduct the cost/risk/benefit analysis in WP 132.

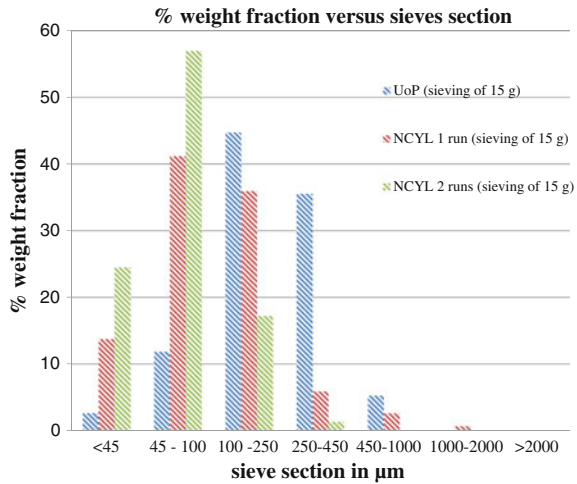
Lab scale veils were then produced by TECPAR and integrated in CRFC by TECNALIA. Evaluation of those CRFC doped with CNTs veils shows an increase of K_z electrical conductivity up to 18 S.m (baseline at 4 S.m). In terms of damage tolerance, about 30 % of compression after impact and 100 % increase of G1C are observed [7].

Due to high viscosity of CNT-doped thermoplastic 1, industrial production of veils was not possible yet. Therefore, other thermoplastics (thermoplastics 2–5 in Table 2) were doped with CNTs. Those materials are under veils production evaluation by TECPAR [8].

4.2 Powdering Application

For this application, thermoplastics with suitable compatibility regarding CFRC were selected. This selection was mainly based on the chemical nature of the thermoplastics. Thermoplastic 1 (properties are given in Table 2) was chosen for

Fig. 4 Particle size distribution for the different grinding trials



this purpose. As no specific limitations were observed for the powdering application, thermoplastic 1 was doped with a maximum loading of CNTs. The CNT-doped thermoplastic 1 was produced on a twin-screw extruder in pellet form.

The CNT-doped thermoplastic granules were ground with a lab scale grinder at University of Patras (UoP). The obtained powder was deposited on top of the prepreg. Those were then evaluated in CFRC by University of Patras and Tecnalia and showed significant increase in damage tolerance. Compression after impact was increased by 50 % [7, 9].

Unfortunately, the grinding equipment used by University of Patras showed limitation in terms of throughput and particles distribution. Indeed, productivity was very low (few grams per day) and particle size quite high (mean around 250 μm). In order to find alternatives, Nanocyl tested a selected industrial grinder. This industrial grinder showed a throughput one thousand times higher than the equipment used by UoP as shown in Fig. 4, a reduction of mean particles size from 100–250 μm (UoP) to 45–100 μm (NCYL 1 run). By regrinding the obtained CNT-doped thermoplastic powder, a significant increase of particles below 100 μm is observed. Figure 5 shows an increase of 25 % for twofold ground CNT-doped thermoplastic (NCYL 2 runs) toward one time ground CNT-doped thermoplastic (NCYL 1 run). Additionally, during grinding trials, suitable information was collected to conduct the cost/risk/benefit analysis in WP 132.

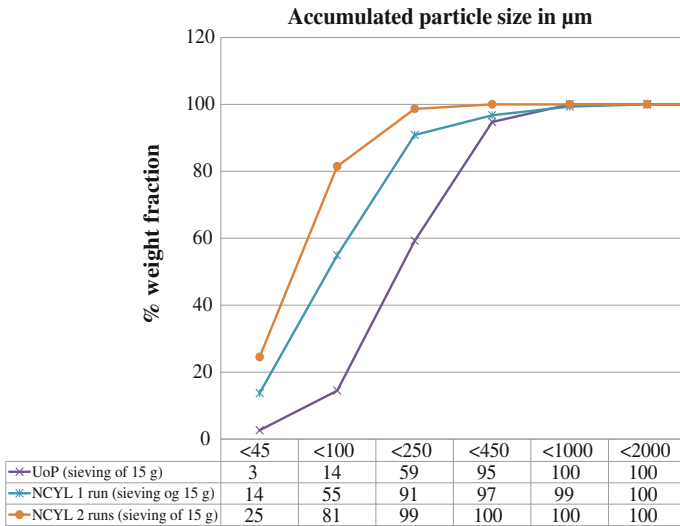


Fig. 5 Cumulative particles frequency versus particle size of ground CNT-doped thermoplastics using lab scale (UoP) and industrial (NCYL) scale grinder equipment

5 Conclusion

In the frame of SARISTU, Nanocyl has explored several approaches to increase the performances of carbon-reinforced composites. Therefore, based on Nanocyl knowledge, commercial multiwalled carbon nanotubes (NC 7000) were incorporated in different media (thermoplastics, epoxy resins) allowing some significant increase in damaged tolerance and electrical conductivity (*Kz*).

Furthermore, in order to increase CNT-doped thermoplastic grinding capacity, industrial grinder was positively evaluated.

Acknowledgments Nanocyl thanks AS 09 and 10 partners for their fruitful collaboration.

The research leading to these results has received funding from the European Union’s Seventh Framework Programme for research, technological development and demonstration under Grant Agreement No. 284562.

References

1. Iijima S (1991) Helical microtubules of graphitic carbon. *Nature* 354:56–58
2. <http://www.nanocyl.com/en/HS-E/Introduction>
3. Ma-Hock L, Treumann S, Strauss V, Brill S, Luizi F, Mertler M, Wiench K, Gamer AO, van Ravenzwaay B, Landsiedel R (2009) Inhalation toxicity of multiwall carbon nanotubes in rats exposed for 3 months. *Toxicol Sci* 112(2):468–481

4. Treumann S, Ma-Hock L, Gröters S, Landsiedel R, van Ravenzwaay B (2013) Additional histopathologic examination of the lungs from a 3-month inhalation toxicity study with multiwall carbon nanotubes in rats. *Toxicol Sci* 134(1):103–110
5. Wohlleben W, Brill S, Meier MW, Mertler M, Cox G, Hirth S, von Vacano B, Strauss V, Treumann S, Wiench K, Ma-Hock L, Landsiedel R (2011) On the lifecycle of nanocomposites: comparing released fragments and their in-vivo hazards from three release mechanisms and four nanocomposites. *Small* 7(16):2384–2395 (Aug 22)
6. Hirth S, Cena L, Cox G, Tomovic Z, Peters T, Wohlleben W (2013) Scenarios and methods that induce protruding or released CNTs after degradation of nanocomposite materials. *J Nanopart Res* 15:1504
7. Flórez S, Gayoso J. Enhancement of primary structure robustness by improved damage tolerance, Saristu final meeting
8. Latko P, Boczkowska A. Fabrication of carbon nanotube doped veils, Saristu final meeting
9. Vavouliotis A, Sotiriades G, Kostopoulos V. Multi-scale reinforced pre-pregs for the improvement of damage tolerance and electrical properties of aeronautical structures, Saristu final meeting

Enhancement of Primary Structure Robustness by Improved Damage Tolerance

Sonia Flórez and Jorge Gayoso

Abstract The aim of SARISTU is to take forward to higher TRL level from previous research of various technologies and methods that realize measurable improvements in aircraft damage tolerance and weight reductions. AS09 aims to evaluate toughening of composite materials through additives such as multiwall carbon nanotubes (MWCNT) and various types of polymer interleaf veils. This scenario works alongside AS10 to deliver multifunctional composite materials. The goal was the improvement in damage tolerance and electrical isotropy. The proposition is that nanoparticle introduction in materials could bring significant positive impact on environment. This positive impact would be by the way of weight reduction in structures and therefore would lead to a reduction in fuel consumption and gas emissions. Several strategies were addressed, and their integration into composite materials and the influence on the damage tolerance were studied. The technologies were studied in terms of mechanical properties and electrical conductivity during the Phase I. The best-performing technologies (thermoplastic veils and MWCNT-treated prepreg) were further characterized in Phase II at RT and HW at coupon level and a sub-element level. This paper reviews the technologies studied and their contribution to the improvement of damage tolerance.

Nomenclature

MWCNT	Multiwall carbon nanotubes
CNT	Carbon nanotubes
RT	Room temperature
HW	Hot-wet
CFRP	Carbon fibre-reinforced polymer
UD	Uni-directional
TP	Thermoplastic

S. Flórez (✉) · J. Gayoso
Aerospace Department, Tecnalia, San Sebastian 20009, Spain
e-mail: Sonia.florez@tecnalia.com

J. Gayoso
e-mail: Jorge.gayoso@tecnalia.com

gsm	Grams per square metre
ILSS	Interlaminar shear strength
CAI	Compression after impact
G _{ic}	Fracture toughness (mode I)
G _{iiic}	Fracture toughness (mode II)
OHT	Open-hole tension
FHT	Filled-hole tension

1 Introduction

The ability of composite materials, extensively used in the aerospace industry due to their high specific mechanical properties, to conform to required standards after damage is an issue of paramount importance for the industry: damage cannot be avoided, and the potential damaging events are high, so structures must be designed to work safely after damage happening. Impact damage is not an issue in metal structures, and the capability to absorb energy is large due to their ductility. However, in composites, impact means an important reduction of the structural integrity on the component [1].

Energy from impacts is absorbed by different mechanisms; usually, failure consists of matrix cracks produced by shear, resulting in delamination [2]. This kind of failure is typical in epoxy resins, especially for resins used in liquid composite moulding due to the brittle nature of the resin, as far as it is needed to modify their properties to improve their ability to flow. The use of thermoplastic veils as interleaf materials in composite laminates is widely used to enhance the damage tolerance behaviour of a composite material, leading to a significant improvement in the mode I and particularly mode II fracture toughness [3]. Another approach is, by means of a thermoplastic carrier, the inclusion of nanofillers: improvement on fracture energy has been reported to be higher than 100 % [4].

From the different approaches to fulfil the objective of improving composite damage tolerance, within SARISTU project, the inclusion of thermoplastic and CNT was explored in Scenario AS09. Several state-of-the-art and innovative solutions were selected as candidates to improve the damage tolerance of composite laminates. Their capability to be integrated in common composite manufacturing routes (LRI and prepreg) as well as the effectiveness to provide electrical conductivity was assessed. The work related to the later issue is compiled in the paper by Flórez S et al. presented at Saristu Final Conference (Moscow, Russia, 2015) 'Improvement of the electrical isotropy of composite structures—Overview'.

This paper is focused on the mechanical testing campaign developed to evaluate and validate the different material solutions developed and provided by the partners involved in SARISTU project—Scenario AS09. Table 1 summarizes the technologies addressed by partner.

Table 1 Partners versus technologies/process

Partner	Technology	Related manufacturing process
BOMBARDIER	Thermoplastic veils	Liquid composite moulding
TECNALIA	MWCNT-doped thermoplastic veils	Liquid composite moulding
SONACA	Thermoplastic veils	Liquid composite moulding
AIRBUS GROUP INNOVATION	MWCNT-doped epoxy	Liquid composite moulding
UNIVERSITY OF PATRAS	Spraying of CNT-doped substance	Prepreg

2 Experimental

In the scenario, AS09 different technologies were incorporated in the common composite manufacturing processes. Different raw materials were used by each laboratory for the manufacturing of several laminates integrating the technologies. The resin/fibre/nanomaterial combinations used in this work are summarized in Table 2. Each technology, developed by different laboratories, is described below:

(a) Bombardier

Baseline material combination for Bombardier was IMS60 fibre (Saertex) and Cycom 890 epoxy resin system (Cytec). The studied technology consisted of lower-weight-toughened commercially available thermoplastic veils.

Table 2 List of raw materials for the manufactured laminates

Manufacturer	Resin	Inclusion	CNT (gsm)	Fibre	Reference
Bombardier	Cycom 890	none	–	IMS 60	BS1
	Cycom 890	TP	–	IMS 60	BS1+toughened veil
Tecnalia	RTM 6	none	–	HTA 5131 6 K	BS2
	RTM 6	TP	0.63	HTA 5131 6 K	BS2 CNT-doped veil
Sonaca	RTM 6	TP	none	HTA 5131 6 K	BS2+toughened veil
Airbus Group Innovation	RTM 6	Binder	0.25	HTA 5131 6 K	BS2+CNT-doped binder
University of Patras	M21	none	–	T800	BS3
	M21	TP	2	T800	BS3+CNT-treated prepreg V1
	M21	TP	1	T800	BS3+CNT-treated prepreg V2
	M21	TP	1	T800	BS3+CNT-treated prepreg V2.1

(b) Tecnalia

Baseline material selected was Hexflow RTM6 epoxy resin and G1157D UD carbon fibre from Hexcel. Nanocyl and Tecpar developed MWCNT-doped thermoplastic carrier and doped veils respectively, suitable for liquid composite moulding. Veils based on CNT-doped thermoplastic were selected resulting in 0.63 gsm of CNT interleaved between each dry carbon fibre.

(c) Sonaca

Resin and dry carbon fibre selected for the baseline were Hexflow RTM6 epoxy resin and G1157D UD carbon fibre from Hexcel. The selected technology was based on the incorporation of a toughened commercially available thermoplastic veil, co-bonded on both sides of a dry carbon fabric.

(d) Airbus Group Innovation

Baseline selected was Hexflow RTM6 epoxy resin and G1157D UD carbon fibre, from Hexcel. The solution developed consisted of a MWCNT-doped epoxy binder system (CNT gsm = 0.25).

(e) University of Patras

Hexply M21/T800 (Hexcel) was selected as the prepreg system baseline, and the selected technology consisted of a CNT-treated M21 prepreg by means of a CNT-doped thermoplastic-based dry powder provided by Nanocyl. Depending on the thermoplastic inclusion, three different materials were developed: V1 (CNT gsm = 2), V2 (CNT gsm = 1) and V2.1 (CNT gsm = 1 optimized process).

Table 2 summarizes the list of raw materials for the manufactured laminates.

Each of the technologies was compared to its own baseline. As the baseline material for BS2+toughened veil and BS2+MWCNT-doped binder references was not manufactured, the results were related to the baseline reference manufactured at Tecnalia with the same raw materials (BS2).

Representative mechanical tests were conducted to evaluate the developed technologies. Table 3 summarizes the tests identified to assess the mechanical performance of the composite laminates.

Table 3 List of tests conducted

Test	Lay-up	Test standard
ILSS	[0]n	EN 2563
Compression after impact (CAI) (Impact 30 J)	QI [+45/0/-45/90] ns	AITM 1.0010-3
Compression	[0] n	EN 2850 Type B
Gic	[0] n	AITM 1.0005
Giic	[0] n	AITM 1.0006
Open-hole tension (OHT)	QI [+45/0/-45/90] ns	AITM 1.0007
Filled-hole tension (FHT)	QI [+45/0/-45/90] ns	AITM 1.0007

In each case, depending on the standard requirements, the number of plies (n) was adjusted. All the tests were conducted at room temperature conditions (RT). Open-hole tension, filled-hole tension and compression after impact tests were also performed at hot-wet conditions (HW) according to prEN3615 standard at 80 °C and 85 % HR. Conditioning time was at least 2000 h. The number of specimens per material was at least the minimum stated in the corresponding standard.

3 Results and Discussion

3.1 Phase I

In a first phase, interlaminar shear strength, compression after impact (impact = 30 J), in-plane compression and fracture toughness tests were conducted at RT conditions for the references listed (see Table 2). Once the Phase I was completed, a Phase II was initiated to further evaluate the most promising technologies: in Phase II, additional tests were conducted (RT and HW) to fully characterize the developed technologies.

3.2 Compression After Impact

CAI results showed an improvement from their baseline for all the materials tested with the exception of the laminates manufactured with CNT-doped binder (reference BS2+CNT-doped binder). In terms of damage area, the biggest improvement corresponded to BS1+toughened veil reference, reaching an improvement close to 80 %. The same result could be extracted from residual compression strength results.

Materials with references BS3+CNT-treated prepreg showed also a remarkable improvement, especially in their residual compression strength. Best performance (higher residual strength and lower damage area) was observed for BS3+CNT-treated prepreg V2 and BS3+CNT-treated prepreg V1.

Between the laminates manufactured by liquid moulding, the reference BS1+toughened veil showed the highest residual compression strength.

All the technologies tested used a TP carrier to, if it was the case, include CNTs. With the results obtained, high improvement in almost all the materials and being one of the best not using CNTs, it is not clear the influence of the CNTs in terms of improving compression after impact properties. However, it is remarkable also that the improvement is comparable, so their use can be considered to improve other properties such as conductivity (for reference see paper by Flórez S et al. presented at Saristu Final Conference (Moscow, Russia, 2015) 'Improvement of the electrical isotropy of composite structures—Overview'), improving mechanical properties related to damage tolerance (Fig. 1).

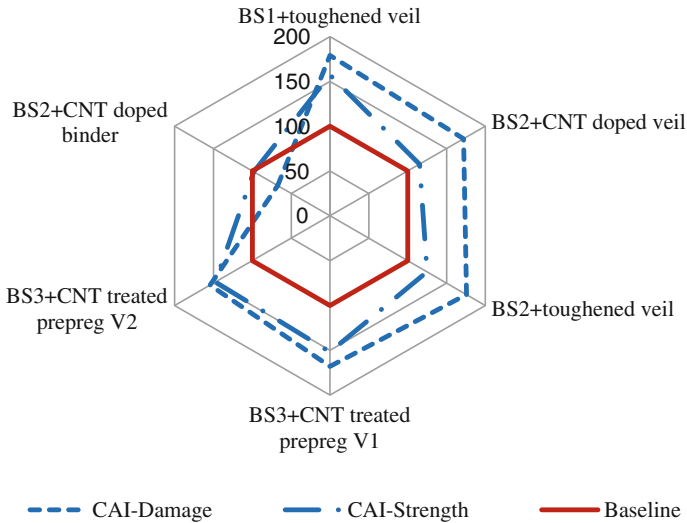


Fig. 1 CAI improvements (damage area improvement >100 % means a reduction of measured damage area after impact)

3.3 Interlaminar Shear Strength

A general decrease of this property was reported for almost all the materials tested, with the exception of BS2+CNT-doped binder reference. However, the decrease was moderate (in the range of 10 %), and most of the specimens crossed the threshold requirements for both liquid composite moulding and prepreg materials used by aeronautic industry.

Specimens tested revealed that in most cases, there was not a true interlaminar shear strength, being the plastic failure mode a common behaviour (almost 100 % of specimens which include TP inclusions with the exception of BS2+CNT-doped binder-based specimens). Plastic failure is usual in the case of materials with high toughness, and the results were considered correct (Fig. 2).

3.4 In-Plane Compression

With respect to in-plane compression strength, there were not significant variations in the case of BS1+toughened veil and BS3+CNT-treated prepreg V1 references. Major variations were observed in BS2+CNT-doped veil (-23 %) and BS2+CNT-doped binder (+20 %) specimens. Reference BS2+toughened veil showed also a significant increase (15 %). These data do not allow extracting clear conclusions about the influence of TP and/or CNT inclusions. Materials without CNT

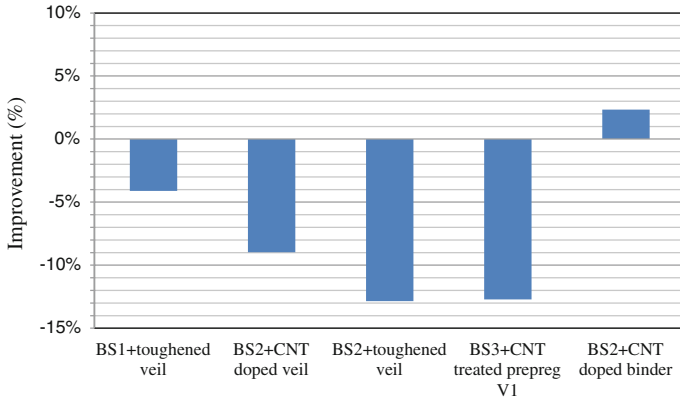


Fig. 2 ILSS results

inclusions seem to have not variation or a moderate increase. At the time, the best performance is shown by reference BS2+CNT-doped binder.

In-plane modulus results evidenced lower variations compared to the obtained strength values. Highest deviation observed (-16 %) corresponded to reference BS3+CNT-treated prepreg V1. Also, reference BS1+toughened veil showed a decrease (15 %).

The chart of the test results (Fig. 3) shows that the best improvement (combining modulus and strength variations) corresponds to reference BS2+toughened veil (no CNT inclusion) and to BS2+CNT-doped binder reference.

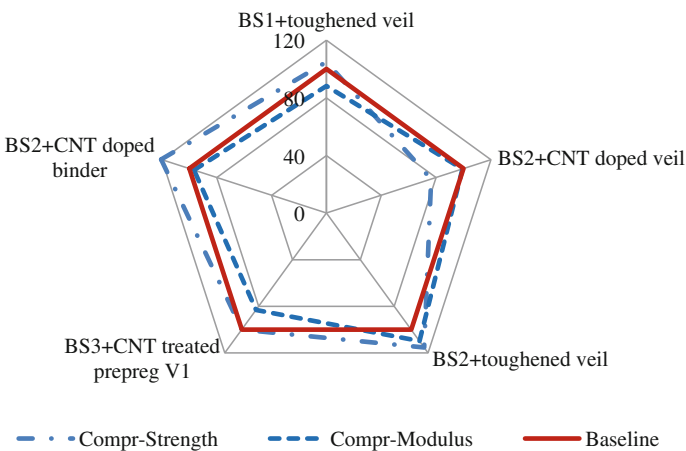


Fig. 3 In-plane compression results

3.5 Fracture Toughness (Modes I and II)

Remarkable improvement in mode I fracture toughness was found for almost all the materials tested reaching 150 % (mean value including outliers) in case of BS2+toughened veil and BS2+CNT-doped veil references and approx 50 % of improvement in the other materials. BS3+CNT-treated prepreg V2 reference did not show significant variations. In the case of BS2+CNT-doped binder laminate, it could not be tested properly (not possible to generate a stable crack growth through the centre of the laminate. Further tests needed).

Model II test was also performed (not results available for BS3+CNT-treated prepreg V1 reference), founding a remarkable improvement in the case of BS1+toughened veil material, but not so important than in mode I (+38 %). On the opposite, BS2+toughened veil reference decreased its mode II fracture toughness (-26 %).

In spite of a more extensive study would be needed, it seems that there is a relationship between the gsm of thermoplastic inclusion and the mode I fracture toughness (similar than it was found in CAI results). The higher the addition of the thermoplastic inclusion is, the higher improvement in the property is achieved. Relationship is also visible comparing BS2+CNT-doped veil (CNT gsm = 0.63) and BS1+toughened veil references. Further research would be needed to understand and establish the improvement rate per TP inclusion and material combination (Figs. 4 and 5).

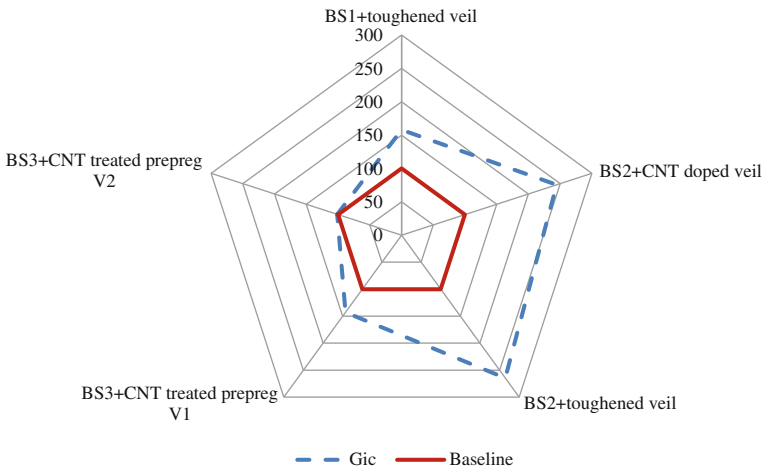


Fig. 4 Gic results

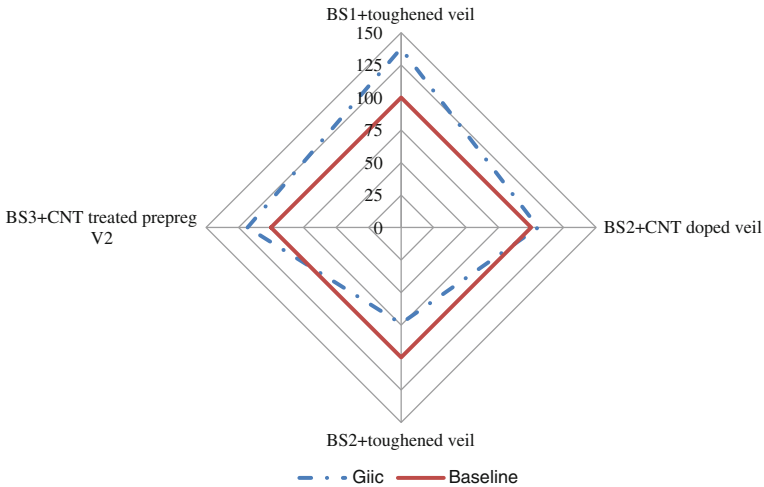


Fig. 5 Giic results

3.6 Phase II

After analysing the obtained results, the two best technologies were selected in order to continue with the test campaign, including RT and HW conditions and additional tests such as OHT and FHT. Related to liquid moulding and the integration of TP veils into composites, reference BS1+toughened veil was selected (Technology 1). In comparison with the other materials suitable for liquid moulding processes, this reference combined the best improvements in terms of compression after impact results, a good enhancement of fracture toughness with a moderate decrease of ILSS and in-plane compression. In the case of prepregs, BS3 +CNT-treated prepreg references were selected (Technology 2).

3.7 Technology 1: BS1+Toughened Veil

Fracture toughness (modes I and II) and compression after impact at HW were conducted. The results obtained were compared to the values previously obtained. Also, open-hole tension and filled-hole tension tests were performed, both at RT and HW conditions.

Fracture toughness results (Fig. 6) showed, at HW conditions, an improvement of 20 % in mode II and a decrease of 7 % in mode I in comparison with the baseline. In compression after impact, residual strength rised up to 16 %; meanwhile, damage area decreased to 54 % at HW in comparison with the baseline BS1. Comparing these values to the previously obtained, the improvement in Gic at RT

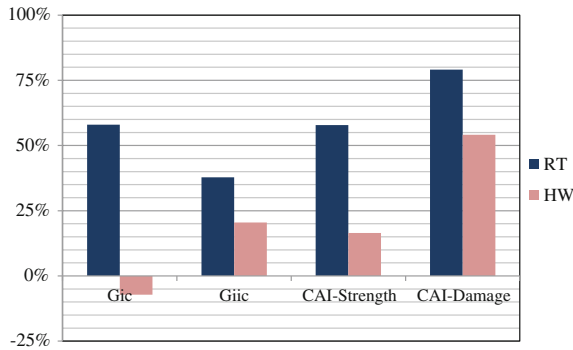


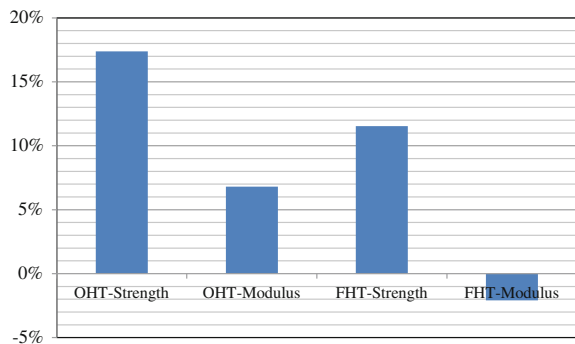
Fig. 6 BS1+toughened veil RT versus HW (Improvements compared to baseline). CAI damage improvement refers to the reduction of the measured damage area

was lost at HW, but the loss in the property was not too high. In case of Giic, the improvement remained, although not too high as at RT (58 %). On the other hand, damage area reduction after impact was still remarkable at HW (54 %). Residual compression strength was still improving after conditioning but not so high than at RT (16 vs. 58 %). In summary, the introduction of thermoplastic veils in the laminate improves the damage tolerance even at hot–wet conditions.

Open-hole tension and filled-hole tension tests were performed for BS1+toughened veil reference both at RT and at HW conditions (Fig. 7). In this case, as there were no available values for the baseline. The behaviour of the toughened material at RT and HW conditions is assessed. In the case of OHT, after conditioning and testing at HW, the behaviour was slightly better than at RT: 17 % improvement in strength and 6.81 % in modulus. FHT results showed a similar trend: 11.54 % of improvement in strength and a similar value than RT in modulus.

Summarizing all the results obtained for Technology 1, material showed remarkable improvements compared with their baseline both at RT and HW in residual strength and damage area after 30 J impact. Also, fracture toughness shows

Fig. 7 BS1+toughened veil —variation HW results versus RT



a significant improvement, with the exception of mode I at HW conditions. The overview of the whole test campaign only revealed two minor reductions in ILSS (RT conditions) and G_{ic} (HW conditions).

3.8 Technology 2: References BS3+CNT-Treated Prepreg V1, V2 and V2.1

Three gsm of CNT was studied in the Phase II: 2, 1 and 1 gsm (optimized). Although the later version was not studied during Phase I, the results obtained in the electrical conductivity (AS10) lead to include it during the last phase. Mode I fracture toughness test was performed from specimens were extracted from a plate made of this later material, and the results were compared with the previous values. The optimization of the process gives a significant improvement of G_{ic} , comparable to the results obtained by the same material treated in previous versions (Fig. 8).

Within Phase II, BS3+CNT-treated prepreg V2 was evaluated, both at RT and HW conditions (Fig. 9). Results obtained in this campaign showed an improvement of G_{ic} at HW conditions of 104 % compared with the same reference at RT conditions. In G_{iic} , a similar behaviour was observed: at HW conditions, G_{iic} mean value was 64 % higher than at RT conditions. This trend needs to be researched; a possible explanation could be the intensified plasticization effects from the presence of thermoplastic. Toughening at HW conditions was not observed in compression after impact test: damage area increases up to 7 %, and residual strength decreases up to 29 %, compared to the baseline.

OHT and FHT strength and modulus values remained quite similar at HW and RT conditions (Fig. 9). A small increase of 7 and 10 % was observed in OHT and FHT strength, respectively. In case of the modulus, variation was -4 % for OHT and +10 % for FHT.

In conclusion, Technology 2-based laminates showed significant improvements in relation to damage tolerance, with no significant variations at HW conditions, with the exception of fracture toughness, which increased.

Fig. 8 G_{ic} improvement in CNT-treated prepreg versus baseline

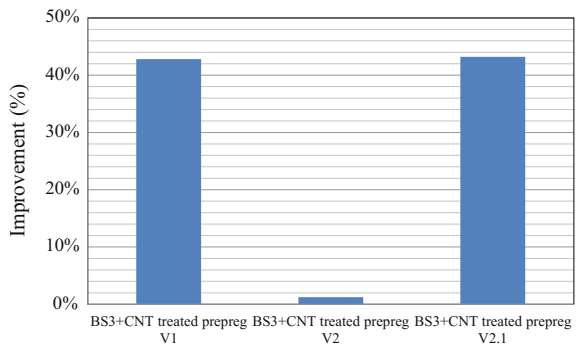
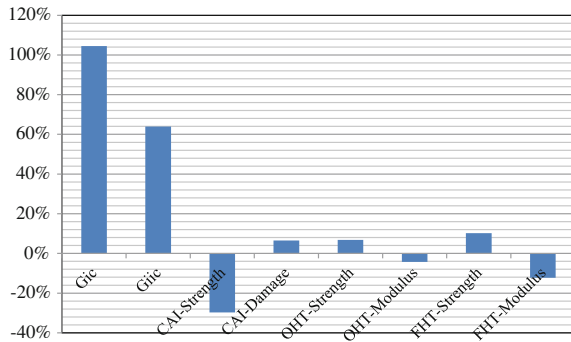


Fig. 9 CNT-treated prepreg V2—variations HW versus RT



4 Conclusion

Different approaches have been addressed to improve the damage tolerance of CFRP. The effect of the inclusion of TP and/or CNT in properties such as compression after impact or fracture toughness, which is closely linked to the delamination progress after an impact, was analysed.

In spite of further research is needed, it seems that there is a relation between the inclusion of TP and the improvement of after-impact properties and also mode I fracture toughness. It is not so clear the effect of CNT inclusions in these mechanical properties, but it can be stated that CNT inclusion does not penalize mechanical performance of the CFRP laminates. It is also remarkable the effect of TP inclusion in ILSS fracture mode, and most of the failures were plastic.

Two technologies were considered the best alternatives to move on from the coupon level to demonstrator manufacturing and consequently to be studied at a bigger scale: the first, interleaving TP veils without CNT inclusion suitable for liquid composite moulding; and the second, a CNT-treated prepreg. Further tests were conducted over those references, both at RT and HW conditions. Results showed that, even after conditioning, the improved mechanical performance remains.

Acknowledgments The research leading to these results has received funding from the European Union's Seventh Framework Programme for research, technological development and demonstration under grant agreement no 284562.

References

- Richardson MW, Wisheart MJ (1996) Review of low-velocity impact properties of composite materials. *Compos A* 27:1123–1131
- Gilbert EN, Hayes BS, Seferis JC (2002) Interlayer toughened unidirectional carbon prepreg systems: Effect of preformed particle morphology. *Compos A* 33:245–252

3. Ramirez VA, Hogg PJ, Sampson WW (2015) The influence of the nonwoven veil architectures on interlaminar fracture toughness of interleaved composites. *Compos Sci Technol* 110:103–110
4. Kostopoulos V et al (2010) Impact and after impact properties of carbon fibre reinforced composites enhanced with multi-wall carbon nanotubes. *Compos Sci Technol* 70:553–563

Enhancement of Infused CFRP Primary Structure Mechanical Properties Using Interleaving Thermoplastic Veils

Daniel Breen

Abstract Damage tolerance of aircraft primary structures is important to prolong the life of the structure and reduce maintenance costs. For composite structures, this is particularly crucial; unlike metallic structures which are largely made up of multiple components which can be easily visually inspected and replaced where necessary, advanced composite structures are frequently one piece, e.g. wingskins, fuselage sections, and therefore cannot be replaced. Inspection of these components require complex and time-consuming non-destructive inspection testing to check for delaminations within the laminates and any damage would require complex and costly repairs. Since this work focuses on infused CFRPs, it should also be noted that prepreg CFRPs in comparison are inherently more damage tolerant and hence one objective is to narrow the ‘performance gap’ between the two technologies. By including thermoplastic veils between the layers of a composite laminate stack, this reduces the brittleness of the matrix between reinforcement layers and also acts to reduce crack propagation, thus drastically reducing damage sizes as a result of an impact. Subsequently, residual CAI strengths are increased which for many aircraft structures is the primary design allowable. This paper outlines the mechanical performance evaluation of a toughened fabric by addition of interlaminar thermoplastic veils infused with epoxy resin. The objective of the toughened materials is to maximise the performance enhancements, particularly damage tolerance, whilst minimising any knock-downs in hot/wet performance, preform permeability for infusion and also electrical conductivity due to the additional insulating layers. This project work within AS09 evaluates the materials at coupon and sub-component level and feeds into IS12 for the materials of choice to manufacture the Bombardier lower wingskins.

D. Breen (✉)

Strategic Technology Composites Department, Bombardier, Airport Road,
Belfast BT3 9DZ, Northern Ireland
e-mail: daniel.breen@aero.bombardier.com

Nomenclature

CAI	Compression after impact
CFRP	Carbon-fibre-reinforced polymer
ATL	Automated tape laying
RTM	Resin transfer moulding
RTI	Resin transfer infusion
UD	Unidirectional fabric
NCF	Non-crimp fabric
RTD	Room temperature dry
H/W	Hot/wet
G1c	Mode 1 fracture toughness
G2c	Mode 2 fracture toughness
OHT	Open-hole tension
FHT	Filled-hole tension
OML	Outer mould line
IML	Inner mould line

1 Introduction

Composite aircraft primary structures have become more common over the past few decades and are fast continuing to increase due to their high strength to weight ratio, CFRPs being the most commonly used. There are generally two forms in which the material is supplied; as ‘wet’ carbon fabrics, tows or tapes already pre-impregnated with resin (prepregs) and as dry carbon fabrics or tows whereby the resin is infused into a stack of dry fabric layers known as a ‘preform’ as part of the component manufacturing process, e.g. RTM.

Prepregs have been around for decades and in most cases are currently applied to a mould via ‘ATL’ using a robot. Prepreg technology is very mature, well understood and hence is the more common process over infusion. Infusion technology albeit generally less commonly used particularly for large structures has many advantages over prepreg technology.

Bombardier, over the past two decades, has used its vast composite experience to develop and patent a novel infusion process called ‘resin transfer infusion’ (RTI). Unlike RTM which comprises of very expensive self-heating solid upper and lower moulds, RTI uses a solid lower mould and a semi-rigid upper mould specifically designed to enhance wet-out of resin and tailor fibre volume content using an autoclave. The resultant process is extremely repeatable and robust, produces parts of the highest quality (no porosity, inclusions or dryness) and has no limit to the size of the components that can be manufactured. Over prepregs, RTI has many advantages including reduced cost in storage of materials (prepregs must be kept frozen), significantly less raw material cost, stiffeners can be co-infused and

co-cured onto skins, i.e. only one cure cycle, matched lay-up times combined with less de-bulking and evacuation cycles results in faster process times, and extremely tight tolerance of thickness and fibre volume content.

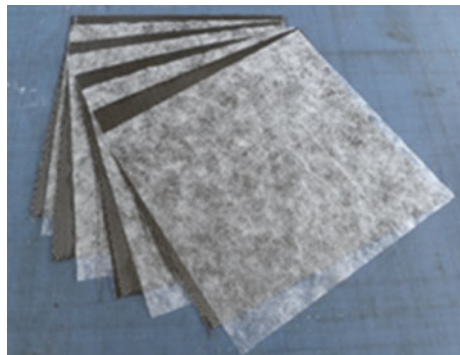
Since prepreg technology does not involve the infusion of large thick preforms, they can be pre-impregnated with tougher resin systems which specifically incorporate tougheners that generally increase its viscosity. Infusion resin systems are required to have a low viscosity, and particularly for large or thick structures, this has to be maintained for long periods to ensure complete wet-out of preforms, often increasing the cure cycle duration. This is generally only achieved by using resin which has no additives for improved toughness. Therefore, the mechanical properties of infused CFRPs, particularly damage tolerance, compression and fracture toughness will generally be slightly lower than prepreg composites. This paper outlines the work completed by Bombardier within AS09 which seeks to improve mechanical properties, particularly damage tolerance, of infused CFRPs.

Thermoplastic veils are layers of randomly spun fine thermoplastic filaments, e.g. co-polyamide, in the form of a web. The veils can be supplied in a range of areal weights and made from a range of polymers which vary properties such as melt temperature and moisture uptake. Figure 1 shows in simple terms how separate layers of carbon plies and thermoplastic veils interleaving each other would be laid up to create a preform.

Resin systems in pure form (without reinforcements) are typically very brittle. The concept behind thermoplastic veils is that the interlaminar regions between carbon layers within a laminate are resin dominated, and therefore, the toughness of this interface directly affects the tolerance to damage; by introducing a thermoplastic layer in these regions, both the brittleness and micro-crack propagation is reduced hence overall increasing the toughness of the laminate.

With the previous development work and experience going into the SARISTU project, along with a short down selection phase within AS09, Bombardier put forward for coupon testing a chosen toughened material system consisting of Bombardier's baseline RTI materials (UD and Biaxial NCF from Saertex infused

Fig. 1 Thermoplastic veils



with Cycom 890 epoxy resin from Cytec) but with the addition of a co-polyamide thermoplastic veil applied to all fabrics, henceforth known as ‘toughened’. For comparison, a repetition of all coupons was manufactured using Bombardier’s baseline RTI materials, henceforth known as ‘baseline’. Two-coupon mechanical test phase followed by a CAI sub-component test phase was carried out. The results and conclusions from the test campaign are outlined in this paper.

The subsequent objective of this work was that if the downselected toughened material was deemed successful, it would be used by Bombardier to manufacture the lower wingskins for IS12 as a part of two fully assembled demonstrator wing boxes. If unsuccessful, the material of choice for the wingskins would be the baseline material.

2 Phase 1 Coupon Testing and Results

Table 1 outlines the materials downselected at the beginning of AS09 for phase 1 coupon testing.

Table 2 outlines the phase 1 mechanical coupon test matrix. All of the testings within phase 1 were within a RTD condition. In order to ensure testing was repeatable and to spread the work load efficiently within the project, partners of AS09 were split into test houses per test type as outlined in Table 2.

Although not part of the AS09 phase 1 test matrix, Bombardier in the background also performed ‘in-plane’ and ‘through-thickness’ permeability tests on both the baseline and toughened materials to assess processability. The addition of thermoplastic veils between every layer could potentially act as a barrier and restrict or reduce the flow rate of resin through the preform and therefore are important processing parameters which needed to be evaluated.

The results from the phase 1 test campaign are outlined in the radar diagram in Fig. 2. At room temperature condition, the toughened material has shown a 79 % improvement in damage tolerance for a 30 J impact, 57 % increase in residual compression strength and a 58 % increase in G1c fracture toughness. In addition to these gains in mechanical performance, the toughened materials show only a negligible knock-down in permeability, -1 % for x and y directions and -3 % for z direction.

Table 1 Materials for coupon testing

Name	Fibre	Fibre density (g/cm ³)	Resin	Carbon areal weight (gsm)
Baseline	IMS 60	1.79	Cycom 890	274
Toughened (+veil)	IMS 60	1.79	Cycom 890	274

Table 2 Phase 1 coupon test matrix

Phase	Test ID	Test type	Test standard	Condition	Test organisation
1	00-01-03-IL	Short beam strength (ILSS)	EN 2563	RTD	Bombardier
1	09-01-04-CI	Compression after impact	AITM 1.0010-3	RTD	SONACA
1	00-01-06-CO	Compression 0	EN 2850 Type B	RTD	EADSIWG
1	09-01-07-G1	G _{IC}	AITM 1.0005	RTD	TECNALIA
1	09-01-02-SZ	Volume conductivity z direction	AITM 2.0065	RTD	TECNALIA

Phase 2 testing within AS09 has predominantly H/W within the test matrix and hence only materials that clearly show gains over the baseline at RTD, i.e. in phase 1 testing, would be put forward for phase 2 testing. The Bombardier toughened material was hence agreed by the consortium to follow into phase 2.

It should be noted, however, as Fig. 2 shows that the results of the volumetric electrical resistance (z) testing resulted in a 70 % increase in resistance ($\cong 70\%$

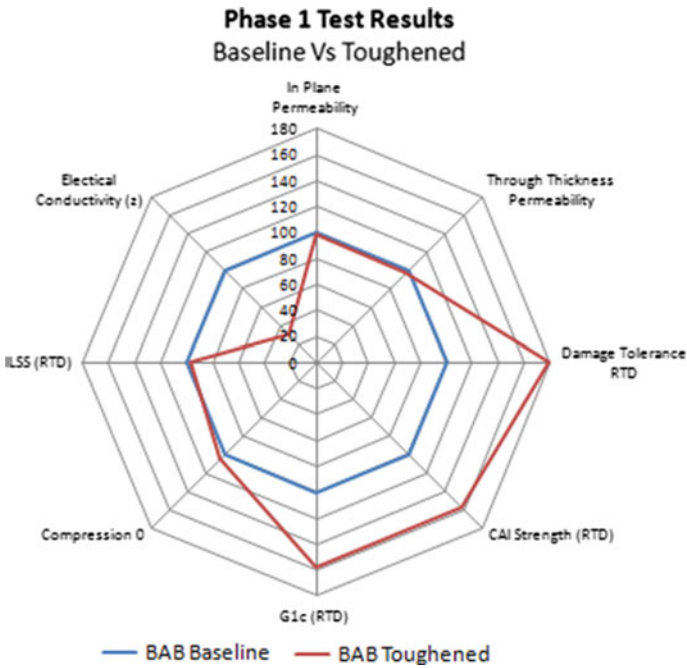


Fig. 2 Phase 1 coupon test results

decrease in conductivity) for the toughened material. A knock-down in volumetric conductivity is to be expected since the interleaving veils act as a resistor between the conductive carbon layers. It is unknown at this point, however, how much of a knock-down is acceptable for a structure to pass lightning strike and edge glow tests. Further investigation into this area will therefore be required post-SARISTU.

3 Phase 2 Coupon Testing and Results

Table 3 outlines the phase 2 mechanical coupon test matrix. All of the testing within phase 2 is within an H/W condition with the addition of a G2c test at RTD. All of the testing carried out in phase 2 was completed by Tecnalia.

The hot/wet condition of mechanical performance is a crucial measure used to generate worst-case scenario design allowables for aerospace structures. This is particularly important for composites where moisture uptake can cause resin systems to lose some of their performance.

Some thermoplastics are prone to moisture uptake, and hence, some thermoplastic veils can cause very large knock-downs in mechanical performance at H/W condition. The evaluation of H/W performance for this toughened material is therefore extremely important. In all cases of phase 2 testing, the hot/wet condition is 85 °C and 70 % relative humidity (RH).

The results from the phase 2 test campaign are shown in the radar diagram in Fig. 3. At H/W condition, the toughened material still maintains a 54 % increase in damage tolerance (again with a 30 J impact) over the baseline material and a 16.5 % increase in residual compression strength. Other increases in mechanical performance at H/W condition were also seen; G2c (+20 %), OHT (+27 %) and FHT (+3 %). The only resultant knock-down was for G1c (H/W) but was small in magnitude at -7.5 %.

Table 3 Phase 2 coupon test matrix

Phase	Test ID	Test type	Test standard	Condition		Test organisation
2	09-01-07-G1	G _{Ic}	AITM 1.0005	H/W	–	TECNALIA
2	09-02-01-G2	G _{IIC}	AITM 1.0006	H/W	RTD	TECNALIA
2	09-02-03-CI	Compression after impact	AITM 1.0010-3	H/W	–	TECNALIA
2	09-02-05-OT	Open-hole tension	AITM 1.0007	H/W	–	TECNALIA
2	09-02-07-FT	Filled-hole tension	AITM 1.0007	H/W	–	TECNALIA

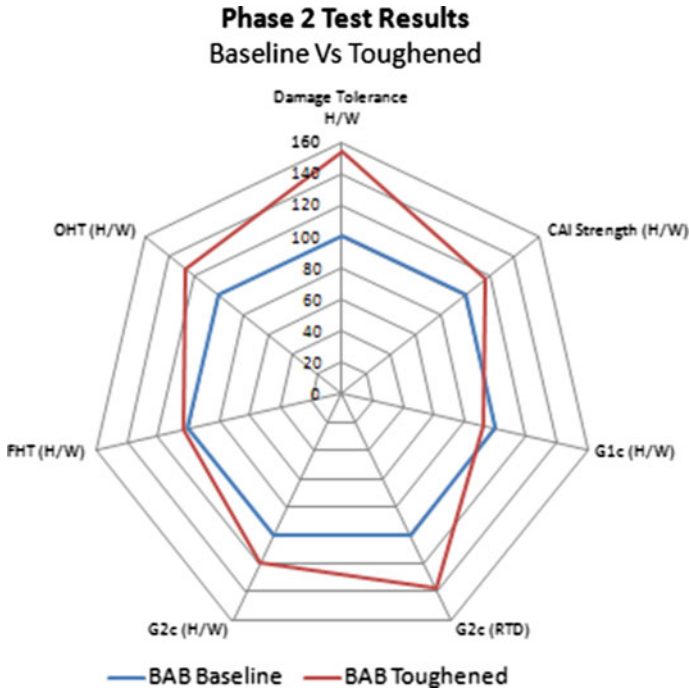


Fig. 3 Phase 2 coupon test results

4 Sub-Component Impact Testing and Results

With the success of the toughened material in both phase 1 and 2 mechanical testing, the final phase of the overall test campaign was to manufacture and test CAI sub-component test panels.

As the Bombardier downselected materials from AS09 are feeding into IS12 as the materials of choice to manufacture the lower wingskin demonstrator panels, it made sense to use sub-component test panels which are based on the typical wingskin design. Experimental sub-component test panels based on a typical wingskin was designed for the programme, as shown in Fig. 4. This consisted of a flat skin with 3 integral ‘T’ stringers, co-infused and co-cured in an autoclave using the resin transfer infusion process (RTI) (60 % VF). Using RTI, the achievable VF is independent of the veil thickness.

The compression sub-component panel is designed to evaluate CAI and is impacted in 6 locations before being compressed to ultimate failure:

- 4 × impacts on the outer skin surface (OML)
- 2 × impacts on stringer blade

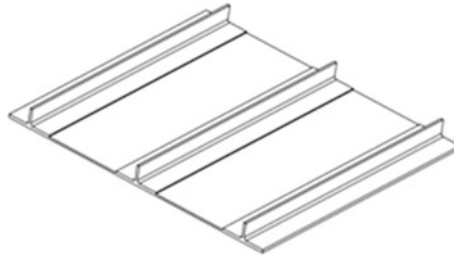


Fig. 4 Bombardier CAI wing sub-component test panel

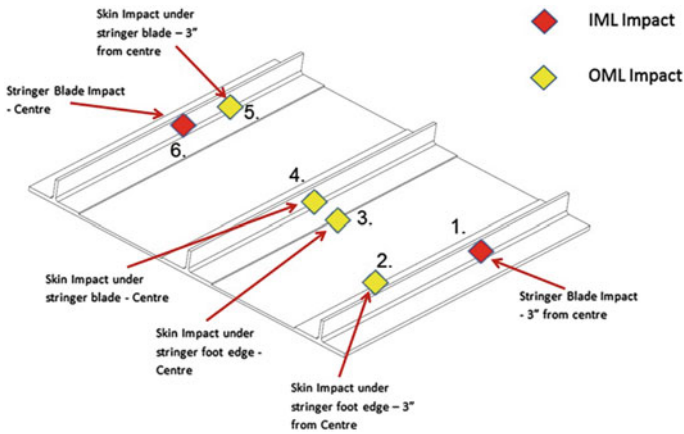


Fig. 5 Impact locations

The test matrix consisted of $3 \times$ baseline and $3 \times$ toughened panels in total. The $3 \times$ baseline panels were extracted from one long ‘master’ sub-component panel and the $3 \times$ toughened panels were manufactured in the same way. Thus, only 2 infusions were required to make all panels.

Using an instrumented falling weight machine, each panel was impacted in the 6 locations shown in Fig. 5. The dent depth was measured and marked on the panel.

It was decided that the impact energy applied to the test panel at all impact locations should be 37 J. By varying drop mass, height and tup diameter, the impact energy was evaluated and applied to the test panels.

Post-impacting, the panels were non-destructively tested using phased array ultrasonic scanning equipment to assess and measure the size of the damage induced at each impact location. The length in both x and y directions of the delamination region was recorded on each panel. The magnitude of the

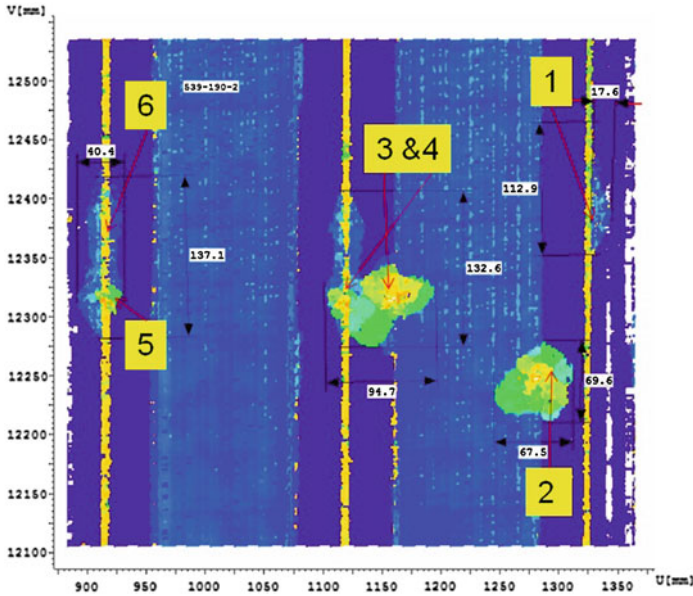


Fig. 6 D-scan showing delaminations from impacts

delamination areas are calculated by the product of the x and y lengths. Figure 6 shows a ‘D-scan’ of one of the baseline sub-component panels.

To get a better visibility and understanding of the resulting delamination areas across all panels, a line graph, Fig. 7, shows the level of damage for each impact location on each sub-component thus making a clear comparison.

Taking a look at either side of the dotted line in the centre of the graph which splits the baseline panels from the toughened panels, it would seem that the level of damage induced into both sets of panels is quite similar. This is surprising as the CAI coupon test results (RTD) from SARISTU AS09 phase 2 testing showed that the toughened coupons had 79 % less damage than the baseline for the same impact energy. However, this can be explained as there were issues during the impacting of the toughened panels;

- The repeat bounce prevention mechanism on the impact machine failed during all on the toughened panel’s impacts for locations 1 and 6 (stringer blade impacts).
- An attempt to overcome this at the time using a manual method of eliminating the repeat bounce was not successful.
- A repeat bounce of the impactor would certainly induce more damage and it was noted during the time of the impacts that the visible damage was much greater compared to the baseline panels where there was no issue with the repeat bounce prevention mechanism.

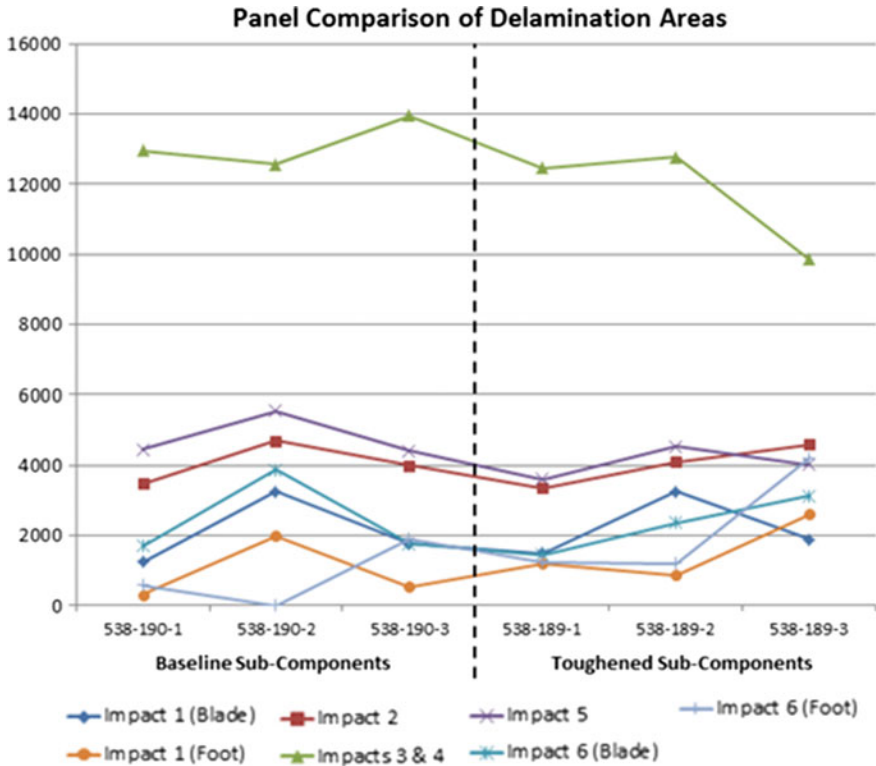


Fig. 7 Line graph of delamination areas of all Bombardier sub-component panels

The following information can be extracted from Fig. 7;

- Panels 538-190-1, 538-190-3, 538-189-1 and 538-189-2 overall have a relatively similar level of damage induced throughout.
- Baseline panel 538-190-2 shows a higher level of damage than baseline panels 1 and 3.
- Toughened panel 538-189-3 shows a much greater damage on the stringer foot (impact 6) compared to all other panels. On the contrary, the merged damage from impacts 3 and 4 is much less than all other panels.

5 Sub-Component Post-Impact Compression Testing and Results

The sub-component test panel options were wide and could vary not only in style but size and thickness. The specific compression sub-component panel for SARISTU AS09 was chosen for two reasons:

1. They are small enough (482 mm × 457 mm) so that they could be manufactured in the autoclave in the Bombardier R&D centre (NIACE) which was crucial to allow SARISTU deliverables to be achieved in time.
2. They are thin in comparison with most panel designs and this meant the test machine required to break the panels does not require huge capacities and so could be tested on site.

The only downside to the specific sub-component panel chosen is that it is prone to buckling because of its thin skin (3.55 mm). To counteract this in the best possible way without making the results unrealistic, a newly designed side only constraining anti-buckling guide was manufactured during SARISTU.

The guide, shown in Fig. 8, slides over the sides of the panel and rests on the lower potted end. Only very light contact is present with the guide in position, i.e. no clamping. The guide acts to stop the panel buckling during the compression test by preventing excess out of plane deformation, therefore ensuring ultimate failure is achieved.

Also noticeable is the steel clamping plates attached to the potted ends. These plates are placed on each side of the potting clamped together by large bolts which run right through the sub-component panel. This ensures the potting does not crack or crumble under heavy loads in the tests and also serves at the lower end to support the anti-buckling guide.

The compression testing of the specimens were conducted at the Bombardier ‘Experimental and Ground testing’ facility using the Avery 150 tonne compression test machine shown in Fig. 9. Load is applied to the panels until ultimate failure occurs. Strain readings are recorded from the gauges throughout the test.

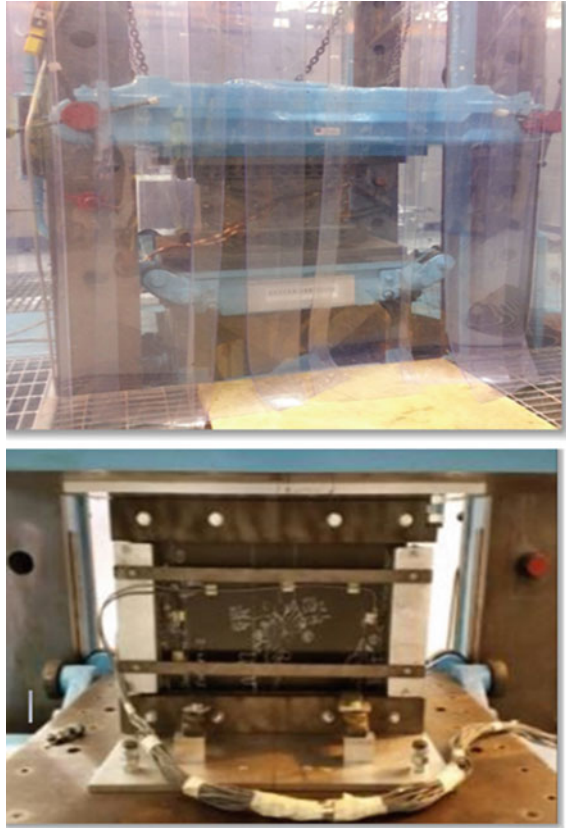
Loading increments are based upon the estimated failure loads in conjunction with decisions made during testing by the representatives of the stress department witnessing previous tests. The loading on these sub-component panels were applied as follows:

- 0–20 tonnes: 5 tonne increments*
- 20–30 tonne: 2 tonne increments*
- 30+ tonnes: 1 tonne increments until ultimate failure occurs



Fig. 8 Installation of anti-buckling guide to panel (*front and back*)

Fig. 9 150 tonne Avery compression machine and installed compression panel



*If at any stage from 0–30 tonnes the initial ‘crack’ was to be heard, which normally signals the onset of plastic deformation of the matrix, then the load increments were immediately be reduced to 1 tonne.

The lower plate of the test rig applies a continuous load to the panel in compression until ultimate failure has been achieved. The strain gauges applied to the panel monitors and records the strains experienced by the panel through a data logger. The data obtained from the test allow the following to be evaluated:

- Ultimate failure load,
- Compression after impact strength,
- Ultimate measured strain,
- Young’s modulus and
- Failure mode.

The ultimate failure loads of the compression tests are shown in Fig. 10.

All of the compression tests were successful and the failure modes were all in pure compression, i.e. no buckling. All breaking points occurred through the impacted locations as expected. Figure 11 shows toughened panel number 2 after

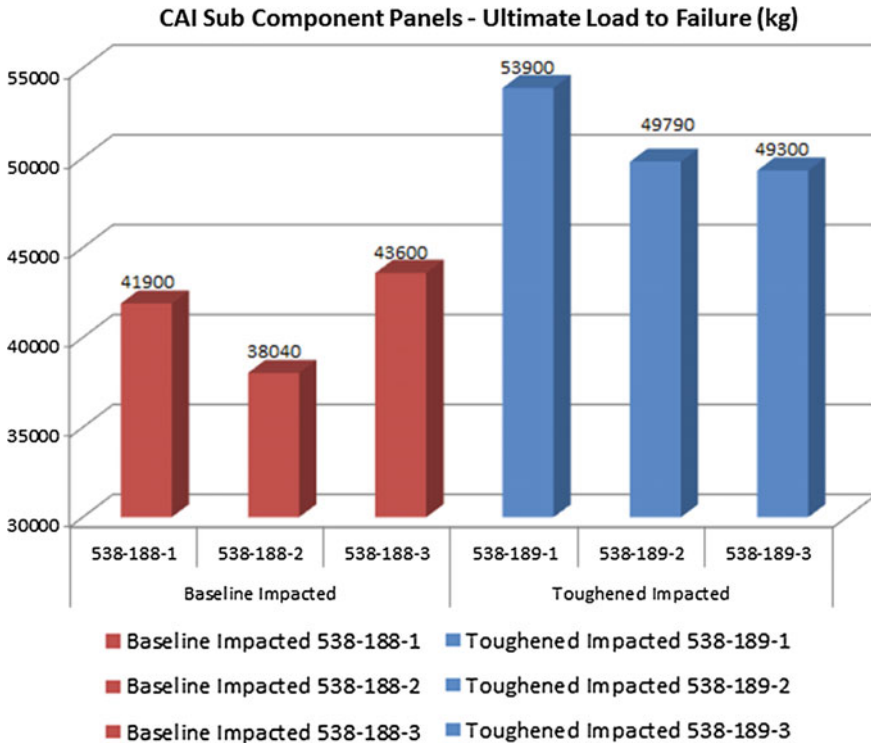


Fig. 10 Compression test results: ultimate failure loads

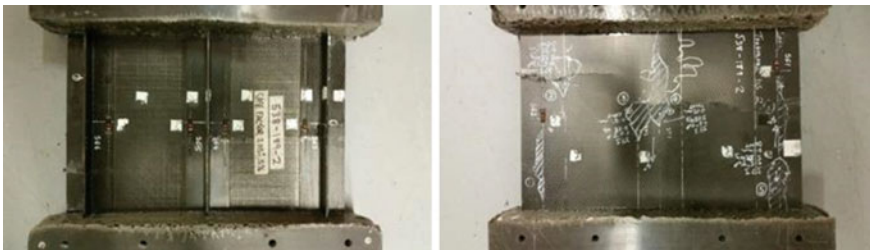


Fig. 11 Post-compression test of toughened panel 2

the compression test had been completed. The break line through areas of damage is clear from the OML side of the panel in the image on the right.

The average ultimate loads for the panels are as follows:

- Baseline Panels: 41,180 kg and
- Toughened Panels: 50,997 kg

The toughened panels therefore have on average a 23.84 % higher residual strength than the baseline panels.

6 Conclusions

The main aim for the use of interleaving thermoplastic veils within epoxy-infused CFRPs was to improve mechanical performance, particularly damage tolerance at RTD condition and to minimise any knock-downs that may occur at H/W condition.

Phase 1 coupon testing showed that the toughened material at RTD not only resulted in huge damage tolerance improvements (+79 %) residual compression strength (+57 %) and G1c fracture toughness (+58 %) over the baseline material (without veil), but showed vast improvements almost completely across the board of mechanical tests investigated. No knock-downs occurred in any of the mechanical tests at RTD.

The H/W condition was particularly important to investigate as some thermoplastics are prone to significant moisture uptake which can result in large knock-downs in mechanical performance. Phase 2 testing was H/W dominated and showed that compared with the baseline material, the toughened material again almost entirely across the board performed better, i.e. +54 % greater damage tolerance and +16.5 % residual compression strength. Only a slightly knock-down was shown for G1c fracture toughness (−7.5 %).

Since the interlaminar thermoplastic is non-conductive and can act as a resistor between the conductive carbon layers, electrical resistivity (through thickness) was also included in phase 1 testing and resulted in a large increase in resistivity (+70 %) compared to the baseline. Further investigations post-SARISTU, most likely full-scale lightning strike and edge glow testing, will be required to assess whether this resultant knock-down in conductivity is acceptable for a flying aircraft.

The interleaving veils could potentially also act as a resistance to resin flow, and therefore, Bombardier performed permeability tests for *x*, *y* and *z* directions to assess this. Negligible knock-downs were seen (1–3 %) across the results and hence the toughened material should perform similar to the baseline material in terms of processing times.

The sub-component testing, although inducing more damage than intended into the toughened panels due to repeat bounces occurring during malfunctions of the impact machine, still reiterated the results from the coupon testing and showed on average +24 % residual compression strength over the baseline panels.

Due to the processability and mechanical performance success concluded in this work, the toughened materials were used within IS12 by Bombardier to successfully manufacture the lower wingskin demonstrator panels.

Acknowledgments The research leading to these results has received funding from the European Union's Seventh Framework Programme for research, technological development and demonstration under grant agreement no 284562.

Multi-scale-Reinforced Prepregs for the Improvement of Damage Tolerance and Electrical Properties of Aeronautical Structures

A. Vavouliotis, G. Sotiriadis and V. Kostopoulos

Abstract Within the AS09 scenario, partners developed and investigated means by which the damage tolerance of carbon fiber-reinforced polymer (CFRPs) can be improved. This scenario worked alongside AS10 to deliver multifunctional composite materials. The goal was on the improvement in damage tolerance and electrical isotropy which in turn can produce a reduction in weight at the aircraft structure level. Nanoparticle introduction in composite materials compromised the main technological field studied, aiming to advance their Technology Readiness Level against more traditional methods (e.g., thermoplastic veils). Multi-scale modification technology for conventional prepregs developed by Applied Mechanics Laboratory at University of Patras was one of the investigated routes. The resulted MWCNT powder-treated prepreg proved to be one of the two best performing technologies during Phase 1 testing and was further selected to be further characterized (RT and HW) in Phase 2 at coupon level and at sub-element level. Moreover, the MWCNT powder-treated prepreg was down-selected to be used for lower panel production in IS13. In parallel, various industrialization aspects of the technology were investigated such as supply chain management, material handling, and process optimization during composites production. A laboratory production line was established and approximately 1000 m² of base prepreg material were treated and delivered. This chapter reviews the work performed on multi-scale modification technology for conventional prepregs during the course of SARISTU project (AS09, AS10 and IS13) summarizing key engineering developments and results.

A. Vavouliotis (✉) · G. Sotiriadis · V. Kostopoulos
Applied Mechanics Laboratory, Mechanical Engineering and Aeronautics Department,
University of Patras, Patras University Campus, 26500 Rion, Achaia, Greece
e-mail: vavoul@mech.upatras.gr

G. Sotiriadis
e-mail: sotiriad@mech.upatras.gr

V. Kostopoulos
e-mail: kostopoulos@mech.upatras.gr

Nomenclature

MWCNT	Multi-walled carbon nanotubes
RT	Room temperature
HW	HOT/WET p
CFRP	Carbon fiber-reinforced polymers
J	Waypoint index
K	Trailing-edge (TE) nondimensional angular deflection rate

1 Introduction

During the last decades, numerous research works reported that the incorporation of carbon nanotubes in carbon fiber-reinforced composites influence positively damage tolerance and electrical properties [1–9]. In order to further advance their Technology Readiness Level, nano-modification technologies needed to provide solutions compatible to industrial scaled—“production environment.” More specifically, concerning nanoparticle introduction in carbon fiber-reinforced polymer (CFRPs) composite materials, the challenge was to propose nano-modification routes taking into account the already established processing and manufacturing technologies in order to reach a seamless integration in current production facilities.

In Application Scenarios no. 9 and 10 of SARISTU project, the aforementioned challenge was taken. The goal was on the improvement in damage tolerance (AS09) and electrical isotropy (AS10) which in turn can produce a reduction in weight at the aircraft structure level. University of Patras (Applied Mechanics Laboratory) contributed with its scientific and technological experience on the improvement of damage tolerance and/or electrical conductivity of prepreg materials used by AIRBUS. Prepreg technologies consist yet the first choice for the majority of manufacturers. Pre-impregnated fibrous reinforcements (prepreg) provide significant benefits over other solutions, such as the readiness to use with no further treatment, ease of handling, uniform fiber alignment, accurate control of the resin content, ability to conform to intricate shapes, optimum polymeric composites integration, and very low void contents in the final products. The base prepreg material used in developments was HexPly[®] M21/T800 by HEXCEL.

From the initial stages of the project, it was evident that introducing the carbon nanotubes—via conventional doping techniques in multi-component resin systems used for the production of aeronautical-graded prepreg products will not be feasible due to restrictions on the availability of the bulk prepreg resin system formulation. University of Patras (Applied Mechanics Laboratory) was asked to provide an alternative solution omitting difficulties on bulk resin availability and aiming to ideas with direct and easy industrialization. To this end, the *multi-scale modification technology for conventional prepreps* was developed. A nano-formulation is prepared tailored for specific performance requirements and using various technologies it is deposited on the surface of the commercial prepreg. The properties of

the base prepreg are known and the nano-formulation is customized to meet its chemical, physical, and processing requirements. The procedure takes place in a controlled machine which has been developed specifically for this purpose. The process is modular capable of delivering customized nano-treated prepreg products. Conventional prepreg enters the machine and at the end of the process line it is packed again ready for the end-use. The new prepreg product can be readily used in manual and automated layup processes to be followed by autoclave curing according to its initial specifications.

Initially, a screening campaign was conducted in order to investigate the applicability of various nano-modification routes proposed by University of Patras for multi-scale modification technology for conventional prepregs in order to define the most suitable mainly in terms of process-ability and performance. *MWCNT-doped powder-treated prepreg* was selected as the most promising technology to be compared with other technologies with Phase 1 and Phase 2 testing campaigns of SARISTU project. Actually, the resulted MWCNT powder-treated prepreg proved to be one of the two best performing technologies during Phase 1 testing and was further selected to be further characterized (RT and HW) in Phase 2 at coupon level and at sub-element level. Moreover, the MWCNT powder-treated prepreg was down-selected to be used for lower panel production in IS13. In parallel, various industrialization aspects of the technology were investigated such as supply chain management, material handling, and process optimization during composites production. A laboratory production line was established and approximately 1500 m² of base prepreg material were treated and delivered. This chapter reviews the work performed on multi-scale modification technology for conventional prepregs during the course of SARISTU project (AS09, AS10 and IS13) summarizing key engineering developments and results.

2 Screening Phase

Within screening phase, three major routes were investigated: (a) the spray coating using various carbon nanotube filled solutions; (b) the deposition of various carbon nanotube-doped powders; and (c) the application of a carbon nanotube-doped b-staged epoxy film. The following table summarizes the results of the first iteration of the screening resulted the selection of the two most promising routes for further investigation. Two major criteria were established. The overall processability of the route under investigation and the applicability within SARISTU time frame are shown in Table 1.

Using the two selected route, small CFRP plates [0]₁₆ were produced in order to check the influence on interlaminar shear strength (ILSS) and through thickness electrical conductivity (k_z). As summarized in Table 2—compared with a baseline CFRP plate from conventional prepreg—the CFRP plate produced from the spray-coated prepreg kept electrical conductivity at the same levels while interlaminar shear strength was deteriorated. On the contrary, the CFRP plate produced

Table 1 Initial screening results on processability and applicability of proposed routes

Route	CNT material	Processability	Applicability	Decision
Spray coating	CNT aqueous solution	Bad	No	Rejected
Spray coating	CNT-cyanate ester-butanone solution	Good	Feasible	Accepted
Powder deposition	CNT-doped thermoplastic powder	Good	Feasible	Accepted
Powder deposition	CNT-doped thermoset powder	Bad	No	Rejected
Film application	CNT-doped b-staged epoxy film	FAIR	NO	Rejected

Table 2 Second iteration screening results on potential performance of two most promising routes. (influence vs. baseline CFRP properties)

Route	CNT material	K_z influence	ILSS influence	Decision
Spray coating	CNT-Cyanate ester-butanone solution	Negative	Negative	Rejected
Powder deposition	CNT-doped thermoplastic powder Produced by NANOCYL	Positive	Neutral	Accepted

from powder deposited prepreg almost doubled electrical conductivity and retained its ILSS properties.

Since powder deposition route resulted at least neutral or positive outcome in both properties, it was down-selected as the most promising to be compared with other technologies within phased testing campaigns (1&2) of SARISTU project.

3 Phase 1

The Phase 1 test plan of SARISTU Application Scenario no. 9 (AS09) and Application Scenario no. 10 (AS10) included the following tests (Table 3).

All tests were conducted at room temperature ambient conditions according to the respective test standard. University of Patras treated conventional prepreg in order to produce 6 (six) CFRP plates with 2 gsm of CNT per lamina for the aforementioned test protocol. The nanodoped thermoplastic was produced by NANOCYL. Powder transformation was performed at University of Patras. Reference specimens were also tested using non-treated—conventional—prepreg to extract the baseline properties enabling comparison. The following Table 4 summarizes the manufacturing efforts within this phase.

All produced CFRP plates were undergone a quality control protocol which included visual and tapping inspection, thickness/cured ply thickness measurements, and fiber volume fraction estimation. For the quasi isotropic plates aimed for

Table 3 SARISTU AS09 and AS10 Phase 1 test plan

Test type	Lay-up	Test standard	Number of specimens
Volume conductivity X - Y direction	(+45/0/-45/90) _{ns}	AITM 2.0064	3
Volume conductivity Z direction	(+45/0/-45/90) _{ns}	AITM 2.0065	5
Short beam strength (ILSS)	(0) _n	EN 2563	5
Compression after impact	(0/90/+45/45) _{ns}	AITM 1.0010-3	5
Compression 90	(90) _n	EN 2850 Type B	5
Compression 0	(0) _n	EN 2850 Type B	5
G_{IC}	(0) _n	AITM 1.0005	5

Table 4 Manufacturing efforts undertaken from University of Patras (Applied Mechanics Laboratory) under SARISTU AS09/AS10 Phase 1 test campaign

Plate usage	Size (mm)	Lay-up	Plates manufactured	Test center
Volume conductivity	500 × 500	(+45/0/45/90) _{3S}	1 Ref, 1 NANO	TECNALIA
Short beam strength	40 × 50	(0) ₁₁	1 Ref, 1 nano	Bombadier
Compression after impact	330 × 330	(0/90/+ 45/45) _{3S}	1 Ref, 1 NANO	SONACA
Compression 90	90 × 100	(0) ₁₁	1 Ref, 1 NANO	TAI
Compression 0	90 × 100	(0) ₁₁	1 Ref, 1 NANO	EADS-IW
G_{ic}	300 × 300	(0) ₁₆	1 Ref, 1 NANO	TECNALIA

Compression after Impact tests also Ultrasonic inspection was performed, while for quasi isotropic plates aimed for electrical test also optical microscopy inspection was performed. The following Table 5 summarizes the quality control efforts within this phase.

The results for CFRP produced with the nanodoped powder-treated prepregs confirmed the initial expectations for enhanced damage tolerance. More specifically, the Mode I Fracture Toughness was significantly increased while the measured damage area after impact is notably reduced. Moreover, the residual compression strength after the impact was increased. Nano-modification resulted not significant influence in material's compression strength (transverse and in-plane) while a negative effect on the electrical conductivity was observed (Table 6).

4 Phase 2

From Phase 1 test results, the process and material combinations developed by University of Patras was chosen to go forward along with interleaving thermo-plastic veil technology investigated by Bombadier. *Phase 2 test campaign aimed to*

Table 5 Quality control undertaken by University of Patras (Applied Mechanics Laboratory) on produced plates under SARISTU AS09/AS10 Phase 1 test campaign

Type	No.	Test type	Size (mm)	Lay-up	No. layers	Visual	Tapping	Vf (%)
Reference	1	Volume conductivity	500 × 500	QI	24	Pass	Pass	58 ± 2
	2	Short beam strength	40 × 50	UD	11	Pass	Pass	58 ± 2
	3	Compression after impact	330 × 330	QI	24	Pass	Pass	58 ± 2
	4	Compression 90	90 × 100	UD	11	Pass	Pass	58 ± 2
	5	Compression 0	90 × 100	UD	11	Pass	Pass	58 ± 2
	6	Gic	300 × 300	UD	16	Pass	Pass	58 ± 2
NANO-phase 1	1	Volume conductivity	500 × 500	QI	24	Pass	Pass	53 ± 2
	2	Short beam strength	40 × 50	UD	11	Pass	Pass	53 ± 2
	3	Compression after impact	330 × 330	QI	24	Pass	Pass	53 ± 2
	4	Compression 90	90 × 100	UD	11	Pass	Pass	53 ± 2
	5	Compression 0	90 × 100	UD	11	Pass	Pass	53 ± 2
	6	Gic	300 × 300	UD	16	Pass	Pass	53 ± 2

Table 6 Test results on reference and nano-CFRP plates under SARISTU AS09/AS10 Phase 1 test campaign

Property	Test center	Comparison NANO-1 versus Ref (%)
Through thickness electrical cond. K_z	TECNALIA	-63
In plate electrical conductivity K_{xy}	TECNALIA	-27
Short beam strength	BOMBADIER	-12
Residual compression strength	SONACA	52
Damage area after impact (30 J)	SONACA	-68
Transverse compression strength	TAI	21
In-plane compression strength	EADS-IW	6
Mode I fracture toughness G_{IC}	TECNALIA	43

investigate the influence of hot/wet environment on specific properties of the nano-CFRP plates. Before the Phase 2 panel manufacturing takes place, University of Patras, utilizing the experience gained during Phase 1, invested effort to further optimize the nanodoped powder treatment process providing a material with better compaction capabilities during curing (higher volume fraction). For Phase 2 testing, the panels were sent to TECNALIA for testing after production where the conditioning and the testing took place. The test matrix for Phase 2 is presented below (Table 7).

Tests were conducted at room temperature ambient conditions according to the respective test standard and also after conditioning according EN 3615 standard at 80 °C and 85 % HR. Conditions were checked using 3 travelers per each material and laminate. Conditioning time was at least 2000 h or material saturation. After conditioning, the specimens were tested at hot wet conditions: 80 °C and 85 % HR.

University of Patras using the optimized process treated the conventional prepreg in order to produce 4 (four) CFRP plates with 1 gsm of CNT per lamina for the aforementioned test protocol. The compaction of plates was enhanced exhibiting an average vf of 56 % (Phase 1 panels exhibited an average vf of 53 %). The following Table 8 summarizes the manufacturing efforts within this phase.

Table 7 SARISTU AS09 and AS10 Phase 2 test plan

Test type	Lay-up	Test standard	No. specimens	
			Ambient (RTA)	Hot/wet (HW)
Volume conductivity $X-Y$	(+45/0/-45/90)ns	AITM 2.0064	3	n.a
Volume conductivity Z	(+45/0/-45/90)ns	AITM 2.0065	5	n.a
G_{IC}	(0)n	AITM 1.0005	5	5
G_{IIC}	(00n)	AITM 1.0006	5	5
Compression after impact	(0/90/+45/45)ns	AITM 1.0010-3	5	5
Open hole tension	(+45/0/-45/90)ns	AITM 1.0007	5	5
Filled hole tension	(+45/0/-45/90)ns	AITM 1.0007	5	5

Table 8 Manufacturing efforts undertaken from University of Patras (Applied Mechanics Laboratory) under SARISTU AS09/AS10 Phase 2 test campaign

Plate usage	Size (mm)	Lay-up	Plates manufactured	Test center shipped
Volume conductivity <i>XY</i> and <i>Z</i>	300 × 300	(+/0/-/90) _{3S}	1 NANO	TECNALIA
Compression after impact	500 × 500	(+/0/-/90) _{3S}	1 NANO	
Open hole and filled hole tension	500 × 500	(+/0/-/90) _{3S}	1 NANO	
Gic and Giic	300 × 300	(0) ₁₆	1 NANO	

Table 9 Quality control undertaken by University of Patras (Applied Mechanics Laboratory) on produced plates under SARISTU AS09/AS10 Phase 2 test campaign

Type	No.	Test type	Size (mm)	Lay-up	No. layers	Visual tapping	C-scan	Vf (%)
NANO-Phase 2	1	Volume conductivity	300 × 300	QI	24	Pass	Pass	56 ± 1
	2	Compression after impact	500 × 500	QI	24	Pass	Pass	
	3	Open hole and filled hole tension	500 × 500	QI	24	Pass	Pass	
	4	Gic and Giic	300 × 300	UD	16	Pass	Pass	

All produced CFRP plates were undergone a quality control protocol which included visual and tapping inspection, thickness/cured ply thickness measurements, and fiber volume fraction estimation. For all plates, also Ultrasonic inspection was performed. Table 9 summarizes the quality control efforts within this phase.

The CFRP produced with the nanodoped powder-treated prepregs after hot/wet conditioning exhibits the ability to retain their good impact (damage area) and post-impact properties (residual compression strength). Hot/wet conditioning influenced positively the Mode I and Mode II performance possibly due to intensified plasticization effects from the presence of thermoplastic. Nano-modification resulted not significant influence in material's strength and modulus for open and filled hole tension testing. The optimized treatment process used in Phase 2 exhibited higher values (20 and 9 % reduction vs. baseline for K_z and K_{xy} respectively) of Z and $X-Y$ volume electrical conductivity compared with results from Phase 1 (63 and 27 % reduction vs. baseline for K_z and K_{xy} , respectively) nevertheless values are still lower than baseline material. Electrical conductivity is strongly linked with the volume fraction succeeded during manufacturing. Nano-modified composites exhibit lower volume fraction, and the presence of CNT-doped powder probably helps the composite to retain as much as possible the electrical performance (Table 10).

Table 10 Test results on nano-CFRP plates under RTA and HW condition for SARISTU AS09/AS10 Phase 2 test campaign

Property	Test center	Comparison NANO-2 versus REF from Phase 1	HW versus RTA comparison (%)
Mode I fracture toughness G_{Ic}	TECNALIA	1 %	104
Mode II fracture toughness G_{IIc}	TECNALIA	No ref from Phase 1	64
Damage area after impact (30 J)	TECNALIA	-55 %	7
Residual compression strength	TECNALIA	55 %	-30
Open hole tension strength	TECNALIA	No ref from Phase 1	7
Open hole tension modulus	TECNALIA	No ref from Phase 1	-4
Filled hole tension strength	TECNALIA	No ref from Phase 1	10
Filled hole tension modulus	TECNALIA	No ref from Phase 1	-12

5 Results and Conclusions

Results from Phase 1 and Phase 2 were analyzed in order to map the performance index of the nano-treated prepreg versus the conventional (baseline) prepreg (Fig. 1).

The analysis reports that the nano-treatment can improve up to 55 % the damage tolerance (reduction of damage area after impact). The compression after impact strength is improved up to 55 %. The optimized process of nanotreatment used in Phase 2 provided marginal improvement of Mode I fracture toughness G_{IC} in contrast to Phase 1. Furthermore, no significant deterioration of Mode II fracture

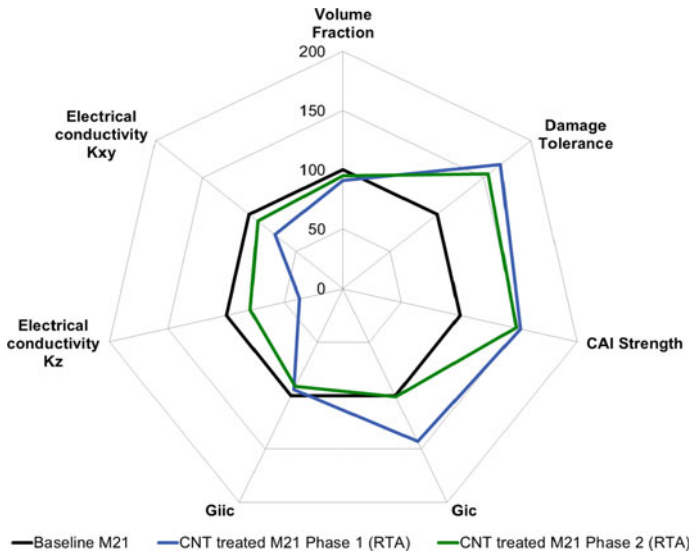


Fig. 1 Performance mapping in room temperature ambient conditions of nano-treated prepreg versus baseline prepreg

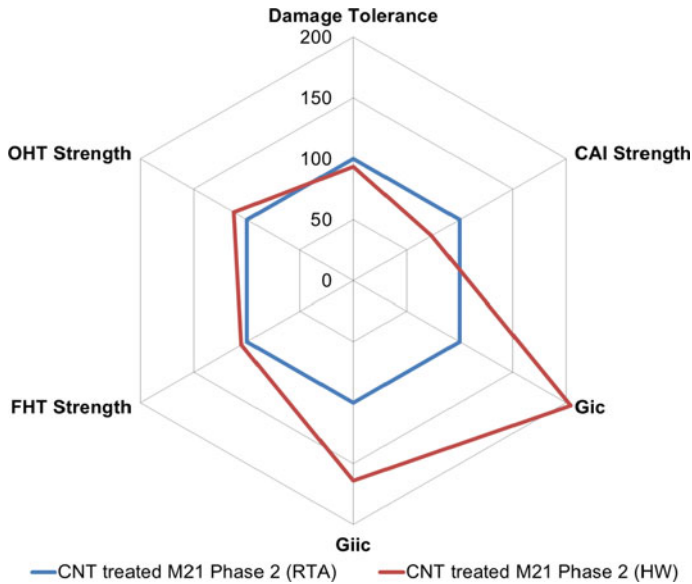


Fig. 2 Hot/wet influence mapping on key properties of nano-treated prepreg

toughness G_{2C} is reported in both phases. The K_z electrical conductivity during Phase 2 remains still lower compared with baseline but higher compared with Phase 1. Similar behavior is also shown for K_{xy} electrical conductivity (Fig. 2).

The analysis of results from the hot/wet test campaign performed during Phase 2 for the nano-treated prepreg material reported that the material retains its good impact properties since damage tolerance (damage area after impact) and CAI strength are reduced only by 7 and 30 %, respectively.

Interesting observation was that both fracture toughness properties (G_{ic} , G_{iic}) exhibit significant increase, possibly due to intensified plasticization effects from the presence of thermoplastic. Open hole tension and filled hole tension strength are kept at the similar levels after H/W (7 % for OHT, 10 % FHT).

Acknowledgments The research leading to these results has received funding from the European Union's Seventh Framework Programme for research, technological development and demonstration under grant agreement no 284562.

References

1. Joshi SC, Dikshit V (2012) Enhancing interlaminar fracture characteristics of woven CFRP prepreg composites through CNT dispersion. *J Compos Mater* 46(6):665–675
2. Siddiqui NA, Khan SU, Ma PC, Li CY, Kim J-K (2011) Manufacturing and characterization of carbon fibre/epoxy composite prepreps containing carbon nanotubes *Compos A Appl Sci Manuf* 42(10):1412–1420

3. Karapappas P, Vavouliotis A, Tsotra P, Paipetis A, Kostopoulos V (2008) Enhanced fracture properties of carbon reinforced composites by the addition of multi-wall carbon nanotubes. *J Compos Mater*. doi:[10.1177/0021998308097735](https://doi.org/10.1177/0021998308097735)
4. Kostopoulos V, Vavouliotis A, Karapappas P, Tsotra P, Paipetis A (2008) On the use of resistivity measurements for damage detection of CNT doped CFRPs. *J Intell Mater Struct Syst*. doi:[10.1177/1045389X08099993](https://doi.org/10.1177/1045389X08099993)
5. Vavouliotis A, Karapappas P, Loutas T, Voyatzi T, Paipetis A, Kostopoulos V (2008) Multi-stage fatigue life monitoring on carbon fibre reinforced polymers enhanced with multi wall carbon nanotubes. *Plast Rubber Compos Macromol Eng* 38(2):124–130
6. Karapappas P, Tsantzalis S, Fiamegou E, Vavouliotis A, Dassios C, Kostopoulos V (2008) Multi-wall carbon nanotubes chemically grafted on reinforcing carbon fibres. *Adv Compos Lett* 17:103–107
7. Barkoula N, Paipetis A, Matikas T, Vavouliotis A, Karapappas P, Kostopoulos V (2009) Environmental degradation of carbon nanotube modified composite laminates: an electrical resistivity study. *Mech Compos Mater* 45:21–32
8. Kostopoulos V, Baltopoulos A, Karapappas P, Vavouliotis A, Paipetis A (2010) Impact and after-impact properties of carbon fibre reinforced composites enhanced with multi-wall carbon nanotubes. *Compos Sci Technol* 70(4):553–563
9. Vavouliotis A, Paipetis A, Kostopoulos V (2011) On the fatigue life prediction of CFRP laminates using the electrical resistance change method. *Compos Sci Technol* 71(5):630–642

Part X

Technology Stream: Multifunction Materials. Improvement of the Electrical Isotropy of Composite Structures

Introduction and Overview

Editorial

Application scenario 10 aims to take forward to higher TRL-level technologies and methods that realize measurable improvements in electrical conductivity and weight reduction. AS10 aims to evaluate three technologies: multiwall carbon nanotubes (MWCNT), metallic strips, and metallic coatings for structural capability integration in order to demonstrate the manufacturability of CFRP parts with improved electrical conductivity. AS10 worked alongside AS09 in order to deliver multifunctional structures with enhanced damage tolerance and electrical isotropy. This section presents four papers. The first paper, *Metallic Strip Details for Validation of ESN Technologies*, presents the innovative development based on the metallic strip. Its design and manufacturing and the thermomechanical experimentation and modeling conclusion, the impact coupon test results and conclusion on damage tolerance and detectability of impacts, the electrical current distribution simulation and test, and finally the electro-thermal behavior results and conclusion. The second paper, *Finite Element Modeling of CNT-Doped CFRP Plates for Lightning Strike Damage*, reviews the coupled electrical and thermal analyses and the fully coupled electrical, thermal, and mechanical analyses to further understand the damage initiation and estimation of laminate failure as a result of the lightning strike. The third paper, *Fabrication of Carbon Nanotube-Doped Veils*, presents the work performed to develop MWCNT-doped veils as an effective way to introduce MWCNT into composite laminates for electrical isotropy enhancement. The last paper, *Improvement of the Electrical Isotropy of Composite Structures—Overview*, presents how nanotechnologies can help to enhance the electrical isotropy of composite laminates. It gives an overview of the electrical conductivity results obtained for laminates integrating MWCNT.

Improvement of the Electrical Isotropy of Composite Structures—Overview

Sonia Flórez, Idoia Gaztelumendi and Jorge Gayoso

Abstract The aim of SARISTU is to take forward to higher TRL level from previous research various technologies and methods that realise measurable improvements in aircraft damage tolerance and weight reductions. AS10 claims to evaluate three technologies: multiwall carbon nanotubes (MWCNT), metallic strips and metallic coatings for structural capability integration in order to demonstrate the manufacturability of CFRP parts with improved electrical conductivity. AS10 worked alongside AS09. The improved electrical conductivity should deliver composite laminates showing damage tolerance as it is pursued within AS09. This chapter reviews the technologies studied and their contribution to the improvement of electrical isotropy of CFRP laminates.

Nomenclature

CFRP	Carbon fibre-reinforced polymer
CNT	Carbon nanotube
RTM	Resin transfer moulding
UD	Unidirectional
MWCNT	Multiwall carbon nanotubes
TP	Thermoplastic
GSM	Grams per square metre
K_{xy}	X/Y or in-plane electrical conductivity
K_z	Z or through thickness electrical conductivity
FVF	Fibre volume fraction
CPT	Cured ply thickness

S. Flórez (✉) · I. Gaztelumendi · J. Gayoso
Aerospace Department, Tecnalia, 20009 San Sebastián, Spain
e-mail: Sonia.florez@tecnalia.com

I. Gaztelumendi
e-mail: Idoia.gaztelumendi@tecnalia.com

J. Gayoso
e-mail: Jorge.gayoso@tecnalia.com

1 Introduction

In recent years, the implementation of non-metallic materials in aircraft structures has been increasing in order to meet new requirements and ecological policies, which enables the manufacturing of not only environmentally friendly and light-weight components, but also integrated structures with multifunctional capabilities. The advantages of CFRPs over metallic materials in terms of specific stiffness and strength are clear. The epoxy polymers used as adhesives and as the matrices of composite materials are amorphous and highly crosslinked (thermo-setting) materials. This microstructure presents many useful properties, such as a high modulus and failure strength, low creep, and good performance at elevated temperatures [1]. Due to this, epoxy resins are widely used as the polymer matrix for high performance laminated composites as they also present a good processability, compatibility with most fibres, chemical resistance, wear resistance and low cost. However, this microstructured resin is relatively brittle, which is detrimental to the interlaminar properties of the composite, leading to a poor resistance to crack initiation and growth. On the other hand, one of the main drawbacks exhibited by composite materials relates to the lack of the necessary electrical conductivity required to cover different electrical functions such as edge glow, lightning strike, direct effect protection, short circuits and electrical bonding [2].

These mechanical and electrical drawbacks can be overcome by the use of nanotechnologies, by incorporating carbon nanotubes (CNTs) in the common composite manufacturing processes, which can then contribute to the development of improved materials with combined electrical, mechanical and thermal properties [3]. In the last two decades, the use of CNTs has become widely studied as a polymer reinforcement, due to its unique combination of superior properties [4]. In particular, the discovery of electrically conductive behaviour dominated by percolation at low filler loadings has led to wide interest in the interplay between the processing and the electrical response of CNT-based nanocomposites [5–8]. However, critical issues still need to be overcome especially when it comes to being processed by conventional CFPR composite manufacturing methods, such as liquid injection technologies (infusion, RTM). The incorporation of CNTs in the resin creates an increase of the viscosity, difficulting the resin flow which in turn can affect the impregnation of the fibre. On the other hand, CNTs can also be trapped in the carbon fibre during the infusion process causing a filtration effect, leading to defective laminates. Furthermore, the increase in temperature during the processing and curing steps reduces the viscosity of the doped resin, which can cause the re-agglomeration of the CNTs. To avoid these undesirable effects, different integration approaches can be used, as the thermoplastic materials based non-woven fabrics. The use of thermoplastic veils as interleaf materials in composite laminates is widely used to enhance the damage tolerance behaviour of a composite material, leading to a significant improvement in the Mode-I and particularly Mode-II fracture toughness [9]. The incorporation of CNTs in the thermoplastic material (that can act as a nanoreinforcement carrier) can improve not only the mechanical

performance of the composite laminate, but also the electrical behaviour, avoiding the above-mentioned processing problems. However, they present several limitations as the limit of the maximum amount of CNTs in the final laminate and the extra thickness that can provide. On the other hand, it is necessary to adjust the processing window of the parts with the melting temperatures of the carrier. Another approach is the use of thermosetting carrier, as the fabric binder, that can be CNT-doped and manufactured in a lower processing time than the thermoplastic based one. For the prepreg technology, similar approaches can be used, as the addition of CNT-doped powder (that can be based either on thermoplastic or on thermoset material) during lay-up or before. The advantages of this approach lie in the improved distribution of the CNTs in the laminate and also in the scalability of the process that can lead to an industrial level robust and stable process which fulfils the requirements and quality levels imposed by the aeronautic industry.

This work was performed in the frame of the AS10 Scenario within SARISTU FP7 project, where different strategies were studied in order to introduce CNTs in common composite manufacturing processes to provide the final laminate with electrical isotropy without a detrimental effect on the mechanical properties. Results for the mechanical behaviour, studied in AS09, are presented by Flórez et al. [10] in the paper “Enhancement of primary structure robustness by improved damage tolerance” at the SARISTU project final conference (Moscow, 19–21 May 2015).

2 Experimental

In Scenario AS10, different CNT integration technologies considering several raw materials were developed and incorporated in common composite manufacturing processes. The resin/fibre/nanomaterial combinations used in this work are detailed in Table 1. The properties of the carbon fibre for each case are included also, since the inherent electrical conductivity of each of the carbon fibre is different, so this can affect the final laminate properties. The laminates lay-up was set to be $[+45/0/-45/90]_{2s}$ for the tapes and $[(+45,-45)/(0,90)/(-45,+45)/(90,0)]_{2s}$ for fabrics. Each technology, developed by different laboratories, is described below:

(a) **Bombardier**

Baseline material combination for Bombardier was IMS60 fibre (Saertex) and Cycom 890 epoxy resin system (Cytec). The studied technology consisted on lower weight toughened commercially available thermoplastic veils.

(b) **Tecnalia**

Baseline material selected was Hexflow RTM6 epoxy resin and G1157D UD carbon fibre from Hexcel. Nanocyl and Tecpar developed MWCNT-doped thermoplastic carrier and doped veils, respectively, suitable for liquid composite moulding. Veils based on CNT-doped thermoplastic were selected (CNT

Table 1 List of raw materials for the manufactured laminates

Manufacturer	Resin	Inclusion	CNT (gsm)	Fibre	Conductivity of carbon fibre (S/m)	Reference
Bombardier	Cycom 890	NO	–	IMS 60	68,966	BS1
	Cycom 890	TP	–	IMS 60	68,966	BS1+toughened veil
Tecnalia	RTM 6	NO	–	HTA 5131 6K	66,667	BS2
	RTM 6	TP	0.63	HTA 5131 6K	66,667	BS2+CNT-doped veil-GEN1
	RTM 6	TP	0.63	HTA 5131 6K	66,667	BS2+CNT-doped veil-GEN2
	RTM 6	TP	0.63	HTA 5131 6K	66,667	BS2 +f-CNT-doped veil-GEN2
Airbus group innovation	RTM 6	Binder	0.25	HTA 5131 6K	66,667	BS2+CNT-doped binder
University of Patras	M21	NO	–	T800	71,400	BS3
	M21	TP	2	T800	71,400	BS3+CNT-treated prepreg V1
	M21	TP	1	T800	71,400	BS3+CNT-treated prepreg V2
	M21	TP	1	T800	71,400	BS3+CNT-treated prepreg V2.1

gsm = 0.63), interleaved between each dry carbon fibre. Three veils were studied with three fibre diameters: GEN1, GEN2 and f-GEN2 (with functionalized CNTs), in order to assess the effect of the veils fibre diameter on the processing and on the electrical conductivity of the laminate.

(c) **Airbus Group Innovation**

Baseline selected was Hexflow RTM6 epoxy resin and G1157D UD carbon fibre, both provided by Hexcel. The solution developed consisted in a CNT-doped epoxy binder system (CNT gsm = 0.25).

(d) **University of Patras**

Hexply M21/T800 (Hexcel) was selected as the prepreg system baseline and the selected technology consisted in a CNT-treated M21 prepreg by means of a CNT-doped thermoplastic-based dry-powder provided by Nanocyl. Depending on the thermoplastic inclusion, three different materials were developed: V1 (CNT gsm = 2), V2 (CNT gsm = 1) and V2.1 (CNT gsm = 1 optimised process).

Next table summarises the list of raw materials for the manufactured laminates:

Each of the technologies was compared to its own baseline. In the case of BS2 +CNT-doped binder, the comparison refers to BS2 as the baseline material, binder without CNT, was not manufactured.

The manufactured laminates were characterised in terms of electrical conductivity: The electrical conductivity tests were conducted according to Airbus AITM 2.0064 for X - Y or in-plane conductivity (K_{xy}), using the source/metre Keithley 2410. The electrodes were placed onto the edges of the laminate as shown in Fig. 1. The edges were metallized by thermal projection techniques using Zinc (in order to ensure a good and reproducible electrical contact, a metallisation of each end of the specimens is required). Specimen dimensions should nominally be 100 mm \times 20 mm \times 4 mm in thickness. It may become evident from initial testing that the fibre type has an overriding effect on conductivity values. Three samples were tested per reference, and two tests were carried out per sample.

AITM 2.0065 standard test was applied for Z or through thickness conductivity (K_z) (see Fig. 2) using the source/metre Keithley 2410.

Specimens dimension should nominally be 40 mm \times 40 mm \times 4 mm in thickness. Five samples were tested per reference and each sample was tested twice. Prior to testing, a comparison was performed using two different metallisation on the surface of the specimens: on one hand, a thermal projection based on zinc and on the other hand a commercially available silver paint. The metallisation based on the thermal projection of zinc is more conductive than the silver paint, but it is also a time consuming and costly process. The application of silver paint, in contrast, is an easier and faster method of metallisation and could be conductive enough to act as electrode. To assess the surface preparation method, the electrical conductivity was measured on samples prepared with silver paint. After the test, the silver paint was removed and the samples were thermally projected to be tested again. The FVF was calculated also for each K_z sample by measuring the thickness in each case.

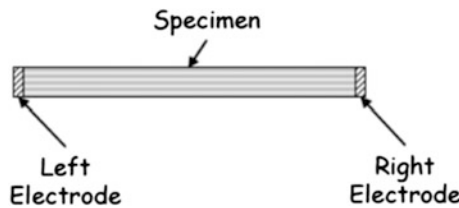
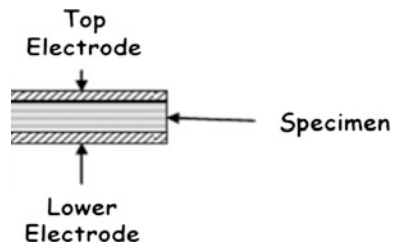


Fig. 1 X - Y conductivity measurement

Fig. 2 Z direction conductivity measurement



The technologies developed in the frame of this work were assessed for their capability to be integrated in composite laminates, their effectiveness to provide electrical isotropy and also to improve the damage tolerance of the laminate. The paper by Flórez et al. [10] “Enhancement of primary structure robustness by improved damage tolerance” refers more in detail to damage tolerance. The technologies that showed a positive influence on the damage tolerance and showed possibilities to be implemented in bigger size components were CNT-doped veils and CNT-treated prepreg. They were introduced in laminates and were characterised at a sub-component level for damage tolerance and electrical conductivity. (Finally, samples cut from a fuselage-related subelement, manufactured by TAI using CNT-treated prepreg, were measured also).

3 Results and Discussion

As shown in Table 1, the most conductive carbon fibres within this work were the T800 and the IMS60. Not only the inner conductivity of the fibre can affect the final electrical properties of the composite, but also the FVF can have a significant influence on the conductivity results, especially in the through thickness direction, since it is related to a higher probability of a contact between the fibres. Due to this, the FVF was calculated for each tested sample (K_z samples) by means of the CPT after measuring the thickness in each case. Figure 3 shows FVF mean values:

FVF established target value is 60 %. The reference BS3+CNT-treated prepreg V1 presented very low values (red columns). The reduction in CNT gsm (BS3+CNT-treated prepreg V2 and V2.1) allowed to increase the FVF value until 55 %. In the same way, a lower fibre diameter on CNT-doped veils (BS2+CNT-doped veil-GEN2 and BS2+f-CNT-doped veil-GEN2 versus BS2+CNT-doped veil-GEN1) led to the rise of FVF (orange columns).

Conductivity values in the XY direction were obtained for the references integrating CNTs even though this property is mainly influenced by the conductivity of the carbon fibres. Consequently, no measures were taken on laminates manufactured with non-doped thermoplastic veil (reference BS1+toughened veil). Figure 4 shows the obtained results. Laminates integrating CNT-doped veils (references BS2+CNT-doped veil GEN1, BS2+CNT-doped veil GEN 2 and BS2+f-CNT-doped veil GEN-2) showed an increase of XY conductivity even though the FVF value was lower than that of the reference (BS2). The highest increase was placed in a value of 30 % for the samples integrating veils manufactured having a lower fibre diameter (GEN-2), (see Table 1). A significant influence on the GEN-2 veils when functionalized CNT was used was not detected. Laminates integrating CNT-doped prepreg (references BS3+CNT-treated prepreg V1 and BS3+CNT-treated prepreg V2) showed a decrease in XY conductivity. However, the FVF value for V1 decreased in a 7 % while that for V2 remained the same. This drop down in the XY value becomes lower when the CNT gsm is reduced from 2 to

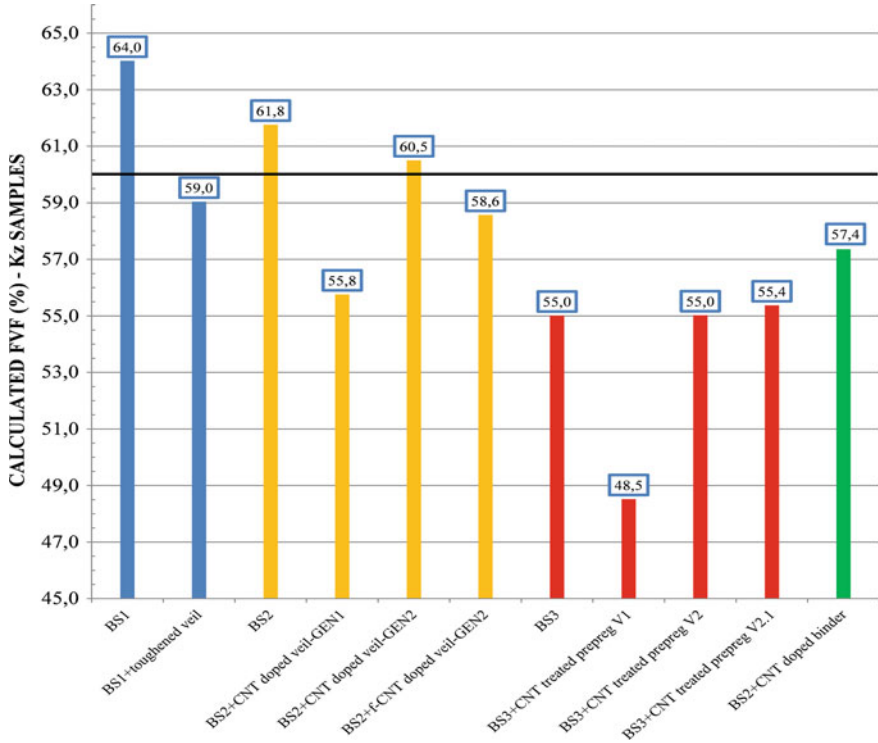


Fig. 3 FVF for K_z samples

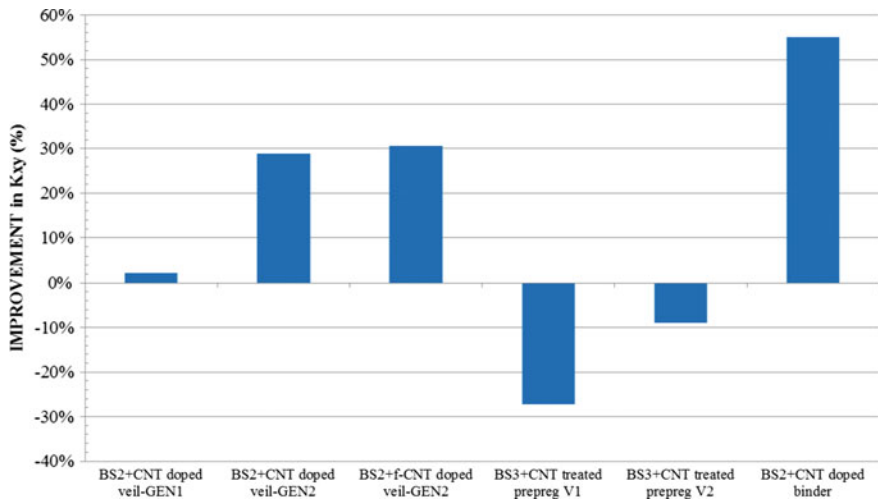


Fig. 4 K_{xy} results of composites for various material combinations

1. It has to be taken into account that the high conductivity provided by the fibre (Table 1) did not allow it to develop the in-plane electrical conductivity.

The highest K_{xy} improvement was observed for laminates including CNT-doped binder (reference BS2+CNT-doped binder), especially considering that the fibre used for their manufacturing was that showing the lower inner electrical conductivity (Table 1).

Taking into account the importance of the surface preparation (metallisation) of the samples before being tested in terms of electrical conductivity through the thickness [10], a comparison was performed on different samples, comparing two different surface preparations: on one hand the metallisation based on silver paint and on the other hand the metallisation based on thermal projection of zinc. The results revealed that no significant differences were appreciated using any of the metallisation processes. The Zn metallisation was selected as the surface preparation process to be applied to K_z samples, since it is considered more industrialisable.

Figure 5 shows the results for K_z . BS1+toughened veil technology, not having CNTs, was included in this study in order to asses the effect of the thermoplastic veil on the electrical behaviour of the composite laminate. Results revealed that the incorporation of non-doped veil in the laminate led to have lower electrical conductivity results as a result of the lower FVF values on samples including thermoplastic veils.

The scenario changed when the thermoplastic veils included CNT (references BS2+CNT-doped veil GEN1, BS2+CNT-doped veil GEN 2 and BS2+f-CNT-doped veil GEN-2). The presence of CNTs increased the through the thickness electrical conductivity up to 350 % even though the FVF value was lower as a result of the presence of thermoplastic material. For the doped versions, the higher the FVF is, the higher the conductivity, but there is always a need of an evenly distributed conductive material in between the fabric layers. The functionalisation of CNTs

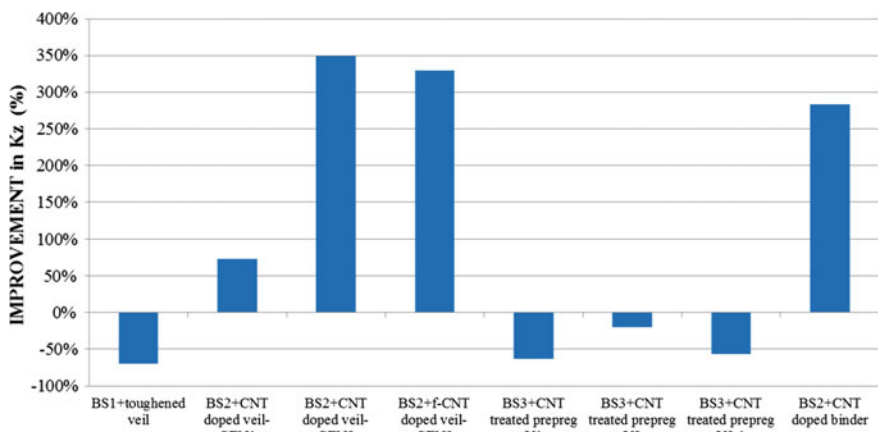


Fig. 5 K_z results of composites for various material combinations

(reference BS2+f-CNT-doped veil GEN2) did not give any advantage and it is a costly step that can be definitely avoided when through the thickness electrical conductivity is pursued.

Laminates integrating doped binder (reference BS2+CNT-doped binder) also presented a significant improvement even at lower FVF (referred to the baseline laminate manufactured by Tecnalina, BS2).

For the CNT-treated prepreg technology (reference BS3+CNT-treated V1 and BS3+CNT-treated prepreg V2), it can be concluded that the amount of CNTs affected the final electrical conductivity: In general, the addition of CNTs decreased the electrical conductivity values, especially using higher loading levels (CNT gsm 2 vs. CNT gsm 1). Higher amounts of CNTs (2 gsm) led to have also lower FVF, and in consequence, lower electrical conductivity values mainly due to the TP carrier. Optimised process (V2.1), studied at the second phase, did not show any improvement in the electrical conductivity behaviour.

4 Conclusion

In this work, different technologies were successfully incorporated in composite laminate manufacturing methods, for both, liquid injection technologies and prepreg based processes, with the aim of enhancing their electrical isotropy. From the testing conducted within, it can be concluded that nanotechnology can have a positive effect on the electrical conductivity of the laminate. Furthermore, the results from the testing also highlight the importance of ensuring that the conductivity results are viewed along side laminate quality, especially the fibre volume fraction, as it has a direct effect on both, the K_{xy} being the effect evident and K_z as the probability of contact between fibres is higher. In general, the results suggest that CNT-doped laminates, using either CNT-doped veils or doped binder-based technologies, can provide a step increase in through thickness conductivity for the same material and volume fraction. In particular, CNT-doped veil technology leads to a higher conductivity especially at lower particle size, compared to the non-doped commercial veil-based material. With regard to the treatment of prepreg by CNT-doped thermoplastic carriers, there is not a clear influence on the final electrical conductivity of the laminates, so further analysis is required to conclude the effect of CNTs on the electrical isotropy of laminates manufactured with prepreg.

Acknowledgments The research leading to these results has received funding from the European Union's Seventh Framework Programme for research, technological development and demonstration under grant agreement no 284562.

References

1. Kinloch AJ, Mohammed RD, Taylor AC, Eger C, Sprenger S, Egan D (2005) The effect of silica nano particles and rubber particles on the toughness of multiphase thermosetting epoxy polymers. *J Mater Sci* 41(4):1293–1293
2. Blanco MT, Pons F, Woelcken PC (2013) Nanotechnology for advanced composite airframes. In: Proceedings of SAMPE-SETEC 13 Wuppertal, Germany, 10–12 Sept 2013
3. Gojny FH, Wichmann MHG, Fiedler B, Bauhofer W, Schulte K (2005) Influence of nano-modification on the mechanical and electrical properties of conventional fibre-reinforced composites. *Compos A Appl Sci Manuf* 36(11):1525–1535
4. Moniruzzaman M, Winey KI (2006) Polymer nanocomposites containing carbon nanotubes. *Macromolecules* 39:5194–5205
5. Battisti A, Skordos AA, Partridge IK (2010) Percolation threshold of carbon nanotubes filled unsaturated polyesters. *Compos Sci Technol* 70:633–637
6. Sandler JKW, Kirk JE, Kinloch IA, Shaffer MSP, Windle AH (2003) Ultra-low electrical percolation threshold in carbon-nanotube epoxy composites. *Polymer* 44:5893–5899
7. Thostenson ET, Chou TW (2006) Processing-structure-multi-functional property relationship in carbon nanotube/ epoxy composites. *Carbon* 44(14):3022–3029
8. Kovacs JZ, Velagala BS, Schulte K, Bauhofer W (2007) Two percolation thresholds in carbon nanotube epoxy composites. *Compos Sci Technol* 67(5):922–928
9. Ramirez VA, Hogg PJ, Sampson WW (2015) The influence of the nonwoven veil architectures on interlaminar fracture toughness of interleaved composites. *Compos Sci Technol* 110:103–110
10. Seddon R, Gaztelumendi I, Flórez S, Pons F, Cinquin J, Korzhenko A (2013) Enhanced electrical conductivity of composite structures through integration of CNTs via bulk resin and/or buckypaper. In: Proceedings of SAMPE-SETEC 13 Wuppertal, Germany, 10–12 Sept 2013

Fabrication of Carbon Nanotubes-Doped Veils

Paulina Latko and Anna Boczkowska

Abstract Non-woven fabrics (veils) are structural materials consisting of randomly arranged thin fibres. They are used as an interlayer in the laminate fabrication process to improve mechanical properties of composites, especially their fracture toughness. A new role of such veils could be the enhancement of the electrical conductivity of laminate. For this purpose, veils should be doped with a conductive additive enabling them to maintain a high level of mechanical performance as well. Thermoplastic polymers doped with carbon nanotubes could be the best potential candidate materials for electroconductive veil fabrication. This is due to their low weight and the outstanding properties of carbon nanotubes. Moreover, there is no competitive material on the market yet. Commonly known are non-conductive veils produced from neat polymers or those obtained from carbon fibres covered by metal and stick together with chemical binder. From the technical point of view, the last two steps are undesired by product end-users. Hence, a much effort is focused on development of fabrication process of conductive veils from polymer and carbon nanotubes. The proposed technology is the melt blown manufacturing process. It allows fabrication of the final product (veil) through a highly cost-effective one-step route starting from polymer pellets/powder. There is no need to use solvents, processing compounds or binders for sticking fibres together. However, the incorporation of carbon nanotubes in the polymer network leads to a significant increase in the viscosity and decrease in the flow ability of the material. There are huge obstacles to its further processing. Therefore, it is necessary to make an appropriate selection of the polymer matrix and to control the properties of carbon nanotube-doped polymers at each stage of production. Especially, the polymer should have low viscosity (high MFI) and should be able to form fibres. As mentioned, conductive lightweight veils are not present on the market in an amount able to cover industry demand. Therefore, the next step is to

P. Latko (✉)

Technology Partners Foundation, ul. Pawińskiego 5A, 02-106 Warsaw, Poland
e-mail: paulina.latko@technologypartners.pl

A. Boczkowska

Department of Materials Science and Engineering, Warsaw University of Technology, ul.
Wolaska 141, 02-507 Warsaw, Poland
e-mail: anna.boczkowska@inmat.pw.edu.pl

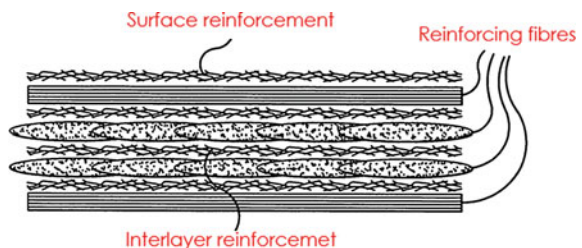
increase the existing pilot plant for doped veil production for composite parts in the relevant environment (from TRL 4 to TRL 6). A semi-continuous pilot line for the industrial production of doped veils will be designed and the manufacturing layout will be developed. The main area in which electroconductive veils are highly desired is the aerospace industry or electronic sectors. Such materials could be applied in electromagnetic shielding or in lightning strike protection instead of presently used metallic meshes or tapes. Due to their low weight, the total mass of the aircraft could be reduced and its mechanical properties, i.e. fracture toughness, may be improved.

1 Introduction

One of the risk to which the airplanes are exposed is lightning strike. According to the data, it can happen one time during the year and it causes the huge current affects the not well-protected parts of the plane. Lack of sufficient protection of the structure leads to the damage of electronic components which causes various destructions, for instance ignition, and finally crash of the machine. Nowadays, metallic (copper, aluminium, nickel) meshes or tapes are used for a lightning strike protection. However, the main disadvantage of those parts is introducing the additional weight for the whole structure. Therefore, the new idea is to replace the metallic components by low-dense materials with the same or better properties. In this case, the electrical performance is the most important feature. The straightening current should be discharge by carrying its through the plane without any damages and exit to the ground. Besides, the mechanical properties have to be maintained on the high level as well [1, 2].

In the beginning of the Project, the idea was to create something similar to copper mesh but with much more lower weight. For this purpose, the textiles materials made of polymer-based composites with electrical conductivity were taken into account. Mainly because of the lightweight, flexibility, lower price and easier fabrication [3]. Reinforcement of laminates by textiles components such as fibres or fabrics is known, especially in order to increase the fracture toughness (Fig. 1) [4, 5].

Fig. 1 Textile products in interlaminar reinforcement



Based on the experiences from the previous Project on Novel Self-Sensing Multifunctional Structures (acronym: ELECTRICAL, FP 7-AAT-2010-RTD-1), the produced conductive fibres did not give the desired results for electrical conductivity improvement. Therefore, the new approach is focused on non-woven fabrics made of special polymer doped with conductive filler. In order to fulfil all of the requirements given by end-users of these textiles materials thermoplastic polymer with adhesive properties was chosen. As a filler, the metallic particles were not taken into account due to their mass. Moreover, mats doped with conductive copper, silver or nickel particles are available on the market and they are not intended to be used in resin infusion process. There are not flexible and possess much higher areal weight than it was required for materials as an object of SARISTU Project. Hence, as a conductive filler, the multi-walled carbon nanotubes (MWCT) were chosen due to their low density and outstanding mechanical and electrical properties. In comparison with other carbon fillers, such as carbon black or carbon fibres, the percolation threshold for nanocomposites with MWCT is achieved at lower concentration than for mentioned fillers. In turn, the desired form of the product is one type of non-wovens called veil which is characterized by lower than 15 g/m^2 areal weight. It consists of thin fibres connected together by thermal, chemical or mechanical bonding. Preferably for resin infusion process, there is any additional chemical compound uses as a binder for fibres sticking [6]. There is plenty of different types of veils available on the market. On the one side, they are produced from neat thermoplastic polymers as polyamides, polyesters of polyolefines. On the other side, there are also veils consist of carbon fibres. Their main role in laminated fibre-reinforced composite materials is improvement of interlaminar toughness. Lack of sufficient resistance to interlaminar stresses causes further cracks in the structure leading to delamination of composite. According to the literature, thermoplastic veils are great materials which are utilized as interlayers in toughening of laminates. It was demonstrated that thin veils with small areal weight are the most effective for absorbing fracture energy [7–9].

As mentioned before, the main target during the Project was to fabricate textile material not only to increase mechanical properties like fracture toughness but primarily electrical conductivity of laminate. The proposed nanocomposites with carbon nanotubes and thermoplastic polymer are willingly studied because of the wide range of promising applications. In the aerospace industry, the usage of polymer-based composites is still growing and up to now they stand at 50 % of all materials used in aircrafts construction. In the case of composites fabricated from thermoplastic polymer and carbon nanotubes, the main obstacle is significantly increased in viscosity after carbon nanotubes addition. By this, processing of those materials into the desired shapes is extremely tough. There are many techniques used for thermoplastic polymers which can be applied in the field of nanocomposites processing. One of them is extrusion, which is easier and cheaper, due to the lack of additional chemicals required, than all spinning processes. What is more, this method leads to satisfactory distribution of carbon nanotubes in the length of fibres without bigger CNT agglomerates [10]. For improvement of electrical conductivity, this is a key factor. However, this property is analysed just in laminate after infusion, not in the veils after

fabrication because of the differences in state of dispersion of carbon nanotubes at each step of manufacturing process. Incorporation of MWCT into a laminate by applying of mats made by electrospinning process was successfully done but without describing electrical conductivity [11].

In this work, the fabrication of carbon nanotube-doped veils by pressing method will be described. The produced veils were used in resin infusion process as a interlayer of laminate. Despite that the improvement of electrical conductivity was observed, this method was rejected from further studied. Mainly due to the low productivity and significant deviations in fibre's diameter after extrusion, the first trials with melt blown method were started. At this stage of the work, five different materials were tested but without obtaining of veils. From the technical point of view, this type of material and technique are very promising and therefore will be developed in the new research Project.

2 Materials and Methods

Materials for veils fabrication were fabricated and supplied in the form of pellets by Nanocyl, Belgium. There are thermoplastic nanocomposites doped with multi-walled carbon nanotube (NC 7000, Nanocyl). The properties of neat thermoplastic polymers are listed in Table 1.

The materials were dried in a vacuum oven at 75 °C for 24 h before further actions. Fibres were extruded using a Haake MiniLab laboratory twin co-rotating screw mini-extruder (Thermo Scientific, Germany). The machine is equipped with a single circular with $d = 0.3$ mm to form fibres. Extruder is connected with a transport belt and winding reel allowing the formation of extrudate into fibres. Both velocity of transport belt and screws speed varied depending on the fibre's diameter. Samples for further tests were prepared using the HAAKE MiniJet injection moulder (Thermo Scientific). Successful mouldings were achieved using a barrel temperature of 210 °C, a mould temperature of 50 °C, a first pressure of 500 bars and a post-injection pressure of 400 bars.

Samples for rheological tests were fabricated by injection into rounds with a thickness of around 2 mm. An ARES rheometer (Rheometrics, Inc) was used to perform the rheological measurement in a parallel plate geometry. The linear elastic range was found by frequency sweep at low strain (0.1–10 %) and between 0.1 and 100 rad/s.

Table 1 Properties of polymers used as host matrix for nanocomposites

Material designation	Melting range (°C)	Melt viscosity 160 °C/2.16 kg (Pa·s)	MVR 160 °C/2.16 kg (cm ³ /10 min)
Thermoplastic 1	125–135	1200	9
Thermoplastic 2	120–130	600	18
Thermoplastic 3	115–125	150	70
Thermoplastic 4	130–140	350	30
Thermoplastic 5	110–120	500	21

Light microscope was used to analyse the macrodispersion of MWCT in polymer matrix. In turn, scanning electron microscopes were utilized for fibre's thickness and surface measurements. Samples for microscopic observations were prepared using a Leica UM6 equipped in a low-temperature chamber. Slides with thickness of 80–90 nm were sampled with DIATOME diamond knives dedicated for trimming and sectioning. The process was carried out at a temperature of $-100\text{ }^{\circ}\text{C}$ with speed of cutting set at 1 mm/s.

TGA was carried out using a TGA Analyzer Q500 (TA Instruments, USA). The 3 samples (ca. 8 mg) of each pellets and fibres were investigated at heating rate $10\text{ }^{\circ}\text{C}/\text{min}$ in the temperature range $20\text{--}1000\text{ }^{\circ}\text{C}$. Test was performed at nitrogen atmosphere at flow rates of 70 ml/min.

Electrical conductivity of laminates was investigated in both K_z and K_{xy} directions according to AITM2-0064 procedure.

3 Results

3.1 Veils Fabrication by Pressing

In the first stage of the Project, all of the works were focused on nanocomposites based on Thermoplastic 1 (Table 1). This polymer was doped with non-modified MWCT and amine-modified MWCT-NH₂. Materials in the form of pellets were produced using twin screws extruder by Nanocyl, Belgium [12]. The first approach to CNT-doped veils presumed the extrusion of fibres at first and then pressing them into veil. Following to this pathway, firstly thermal analysis was made to find the degradation temperature and melting point of doped thermoplastic polymers. It was found just tiny changes in characteristic temperatures for all polymers after MWCT addition. Afterwards, fibres were produced on the adjusted conditions. For both material, the screws velocity was 50 rpm, the speed of transport belt and winding reel was 9 and 500 rpm, respectively. However, the extrusion temperature differs for them. In the case of modified MWCT, the temperature was $20\text{ }^{\circ}\text{C}$ higher ($220\text{ }^{\circ}\text{C}$ for non-modified MWCT) which is related to difficulties during the process. It led to troubles with obtaining the desired diameter below $100\text{ }\mu\text{m}$ for Thermoplastic 1+MWCT-NH₂. Therefore, the diameter of those fibres was ca. $150\text{ }\mu\text{m}$. Finally, fibres were cut into 7 cm in length and spread on special paper and then pressed together. Such veil is shown in Fig. 2 [13].

The pressing temperature was $220\text{ }^{\circ}\text{C}$ and time 10 s just from one side for fibres made of Thermoplastic 1+MWCT. In the case of fibres made of Thermoplastic 1+MWCT-NH₂, the temperature was the same but the time was elongated to 50 s in order to decrease the thickness of fibres below $100\text{ }\mu\text{m}$. It was successfully made, and from both materials, veils with areal weight of $9\text{ g}/\text{m}^2$ were fabricated and send to the Tecnalia for further tests [14].

It is known from literature that dispersion of MWCT is the key factor affecting the electrical properties of nanocomposites. Therefore, the macrodispersion in

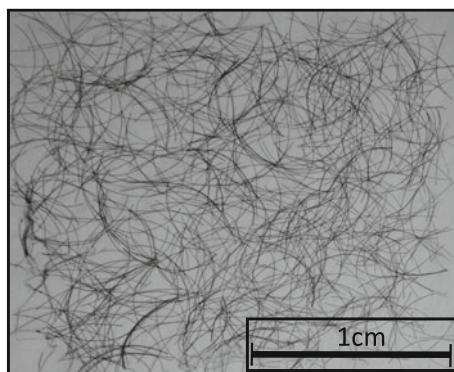


Fig. 2 CNT-doped veil prepared by pressing

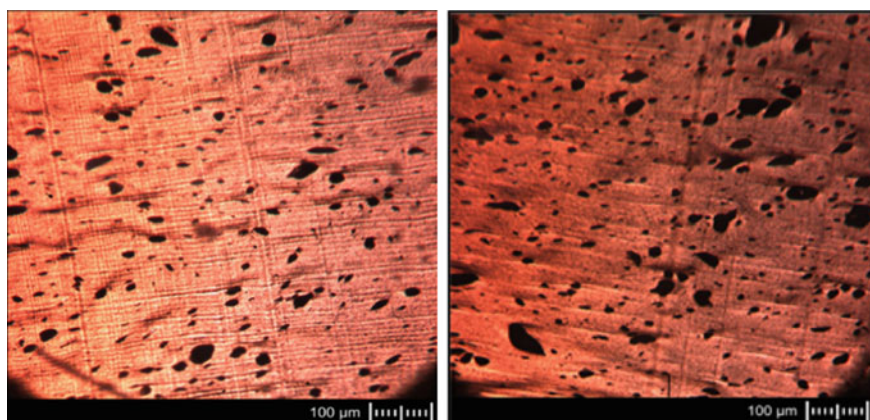


Fig. 3 Macrodispersion of starting pellets analysed by light microscopy. Thermoplastic 1+MWCT (*left*) and with MWCT-NH₂ (*right*)

starting pellets was analysed, and it is shown in Fig. 3. It can be stated that MWCT are well dispersed within the whole polymer matrix. Black dots represent the agglomerates of MWCT, and they are distributed uniformly in the host polymer. Obviously, the distribution of MWCT alters during the processing of starting material. Hence, the state of dispersion should be analysed on each step of the approach towards final product.

Following to Fig. 4, it is visible that MWCT in the fibres are arrangement in the direction of extrusion (red arrow). According to the theory that arrangement of MWCT improves the percolation threshold in the polymer nanocomposite fibres should possess higher electrical conductivity. However, due to the small diameter of fibres, the total MWCT in the measured area is very small, and therefore, the conductivity is lower than, for example, in bars after injection moulding.

Fig. 4 Arrangement of MWCT in extruded fibres

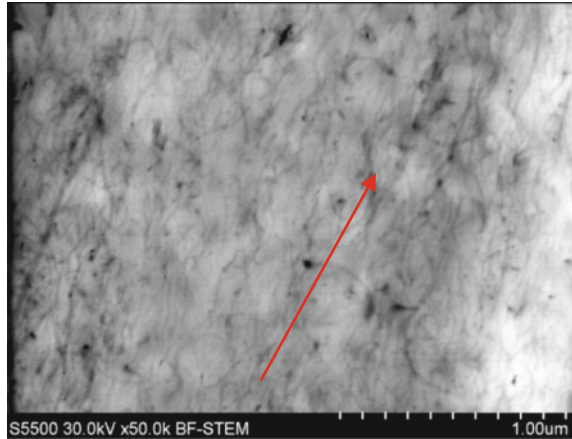
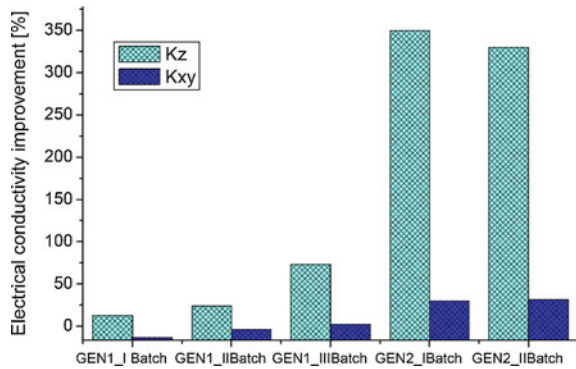


Fig. 5 Electrical conductivity of laminates with inserted veils. GEN1 = Thermoplastic 1+MWCT; GEN2 = Thermoplastic 1 +MWCT-NH₂



Two batches of veils prepared by pressing method were sent to Tecnia in order to check them in laminate infusion process. There were veils prepared from Thermoplastic 1 + MWCT (called GEN1) and Thermoplastic 1+MWCT-NH₂ (called GEN2). Both veils had GSM = 9 g/m² and fibres thickness around 80 µm. After infusion process where CNT-doped veils were used as interlayers the laminate’s cross section was made. It was found that used veils allowed to great connections between layers, although there were differences in thickness between layers caused by not uniform thickness of fibres in the veils.

The mentioned differences in fibre thickness affect the volume fractions of fibres in laminates when veils were inserted. This has effect on the further properties of the material, especially electrical conductivity as shown in Fig. 5. Electrical conductivity is dependent on volume fractions of fibres in veils. Hence, GEN 2 of veils (Thermoplastic 1+MWCT-NH₂) because of the obstacles during extrusion resulting in thicker fibres give the higher value of electrical conductivity of laminate in both directions. There are also tiny differences in obtained values for various batches of produced and used veils.

3.2 Melt Blown Process

According to the above, CNT-doped veils prepared by pressing method did not reach fully technical requirements mainly due to the differences in thickness of fibres. Moreover, despite that CNT-doped veils enhanced electrical conductivity, this technique was too slow to cover demand from partners. Therefore, the half-industrial technique—melt blown—was proposed as it will be faster and more useful for commercial applications. Firstly, attempts with Thermoplastic 1+MWCT were made but without any success. It happened due to extremely high viscosity of Thermoplastic 1 after addition of MWCT. Therefore in the next step, we tried to replace PA1 by others less viscous polymer as shown in Table 1. However, the choice was conditioned by the initial requirements. The comparison between complex viscosity of all polymers before and after MWCT addition is shown in Fig. 6. For all of the polymers, it is significantly increased in viscosity after nanotubes addition. Hence, the processability is going to be extremely tough and CNT-doped veil fabrication is not possible. By dilution of master batches by neat polymer, the problem with poor mixing of components due to the just one single screw appeared. By this, each trials with addition of processing additives ended in failure because of the technical deficiencies in equipment.

Based on the experiences reached in SARISTU Project related to CNT-doped veils fabrication, it was stated that much suitable will be melt blown method. Due to the fact that CNT-doped veil production is a very promising technology, the authors will continue its industrialization in the frame of recently approved H2020 Projects. Firstly, the new set of melt blown equipment will be designed what hopefully results in CNT-doped veil continuous manufacturing. Schematic graph of actions made in SARISTU and those planned for the future are presented in Fig. 7.

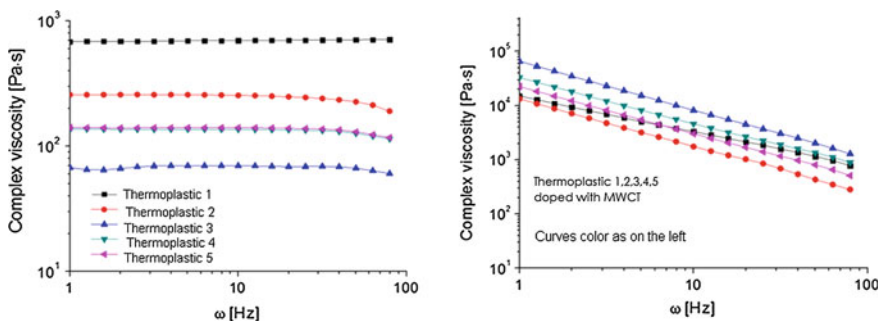


Fig. 6 Rheology behaviour of all types of materials. *Left* Neat polymers, *Right* Doped with MWCT

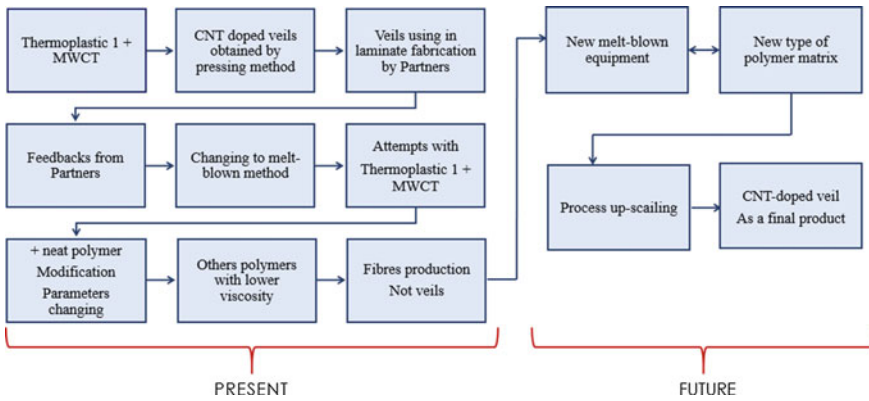


Fig. 7 The tested approach towards CNT-doped veil fabrication

4 Conclusions

CNT-doped veils were successfully obtained by extrusion and pressing method and used in laminate infusion process. In the presence of CNT-doped veils, the desired value of electrical conductivity—10 S/m—was achieved for veils doped with amine-modified MWCT. However, the differences in fibre’s thickness after extrusion cause the various volume fractions of fibres in laminates. Moreover, the slow production of veils according to this technique resulted in method changing and rejection of those veils as a CNT carrier. As a more promising, melt blown technique will be deeply investigated within H2020 Project.

Acknowledgments The research leading to these results has received funding from the European Union’s Seventh Framework Programme for research, technological development and demonstration under Grant Agreement No. 284562.

References

1. Gagné M, Therriault D (2014) Lightning strike protection of composites. *Prog Aerosp Sci* 64:1–16
2. Udmale V, Mishra D, Gadhave R, Pinjare D, Yamgar R (2013) Development trends in conductive nano-composites for radiation shielding. *Orient J Chem* 29:927–936
3. Brzeziński S, Rybicki T, Karbownik I, Malinowska G, Śledzińska K (2012) Textile materials for electromagnetic field shielding made with the use of nano-and micro-technology. *Cent Eur J Phys* 10:1190–1196
4. Hogg PJ (2005) Toughening of thermosetting composites with thermoplastic fibres. *Mater Sci Eng A* 412:97–103
5. Kuwata M, Hogg PJ (2011) Interlaminar toughness of interleaved CFRP using non-woven veils: part 2. Model-II testing. *Compos A Appl Sci Manuf* 42:1560–1570

6. Barkoula NM, Alcock B, Cabrera NO, Peijs T (2008) Fatigue properties of highly oriented polypropylene tapes and all-polypropylene composites. *Polym Compos* 16:101–113
7. Ramirez VA, Hogg PJ, Sampson WW (2015) The influence of the nonwoven architectures on interlaminar fracture toughness of interleaved composites. *Compos Sci Technol* 110:103–110
8. Zhu L (2013) Investigations on damage resistance of carbon fiber composite panels toughened using veils. *Chinese J Aeronaut* 26:807–813
9. Beckermann GW, Pickering KL (2015) Mode I and mode II interlamianr fracture toughness of composite laminates interleaved with electrospun nanofibre veils. *Compos A Appl Sci Manuf* 72:11–21
10. Potschke P, Brunig H, Janke A, Fischer D, Jehnichen D (2005) Orientation of multiwalled carbon nanotubes in composites with polycarbonate by melt spinning. *Polymer* 46: 10355–10363
11. Hamer S, Leibovich H, Green A, Avrahami R, Zussman E, Siegmann A, Sherman D (2014) Mode I and mode II fracture energy of MWCNT reinforced nanofibrilmats interleaved carbon/epoxy laminates. *Compos Sci Technol* 90:48–56
12. Bonduel D, Kchit N, Claes M (2015) Use of carbon nanotubes in structural composites. Paper presented at Saristu final conference, Moscow, 19–21 May 2015
13. Latko P, Boczkowska A (2012) Manufacturing of thermoplastic fibres and veils doped with CNTs, PL patent application P.401576, October 2012
14. Flórez S, Gayoso J (2015) Enhancement of primary structure robustness by improved damage tolerance. Paper presented at Saristu final conference, Moscow, 19–21 May 2015

Finite Element Modelling of CNT-Doped CFRP Plates for Lightning Strike Damage

Omer Soykasap, Sukru Karakaya, Yelda Akcin
and Mehmet Colakoglu

Abstract The neat and CNT-doped CFRP-laminated plates to be used in aerospace structures are considered for the behaviour of lightning strike damage. Material properties of both the neat and CNT-doped T800/M21 are obtained experimentally. Quasi-isotropic rectangular plates are modelled in ABAQUS finite element program. Coupled electrical and thermal analysis is carried out using multi-physics. Steady-state electrical analysis and transient heat transfer analysis are conducted at each time increment by the application of Joule heat generation. The damage region is estimated by considering the decomposition temperature of the resin. The coupled analysis shows that the damage region of the CNT-doped laminate substantially decreases when compared to the neat laminate. Next, fully coupled electrical–thermal–mechanical analysis is carried out in order to further understand the damage initiation and estimation of material failure before the decomposition of the resin. The damage initiation is estimated by considering thermal stress level and Tsai–Wu material failure criterion. The finite element simulations indicate that more electrical current can be applied to the CNT-doped laminate or that there would be less damage under the same electrical current because the electrical conductivity through the thickness of the plate plays a significant role for the lightning strike damage.

O. Soykasap (✉)

Department of Material Science and Engineering, Afyon Kocatepe University, A.N.S. Campus, Afyonkarahisar 03200, Turkey
e-mail: soykasap@aku.edu.tr

S. Karakaya

Department of Mechanical Engineering, Afyon Kocatepe University, A.N.S. Campus, Afyonkarahisar 03200, Turkey
e-mail: skarakaya@aku.edu.tr

Y. Akcin

Department of Metallurgical and Materials Science, Afyon Kocatepe University, A.N.S. Campus, Afyonkarahisar 03200, Turkey
e-mail: yeldaakcin@aku.edu

M. Colakoglu

Department of Mechanical Engineering, Adnan Menderes University, Main Campus, Aydın 09010, Turkey
e-mail: colakoglu@aku.edu.tr

Nomenclature

CFRP	Carbon fibre-reinforced plastics
CNT	Carbon nanotube
MIL-STD	United States Military Standard
IEC	International Electrotechnical Commission
JAXA	Japan Aerospace Exploration Agency
K_x	Electrical conductivity along the x direction
K_y	Electrical conductivity along the y direction
K_z	Electrical conductivity along the z direction

1 Introduction

Carbon fibre-reinforced plastics (CFRP) with considerable advantages have been preferred rather than traditional light-alloy metals in aircraft structures. However, CFRP is not good material to prevent the lightning strike damage due to its low electrical conductivity through the thickness [1]. Traditionally, there are some solutions to avoid the lightning strike damage such as laying of metallic strips, mesh, and foils on top surface of CFRP. There is a growing interest on the usage of CNTs and buckypaper for lightning strike protection [2]. The lightning strike damage depends on the electrical and thermal properties of the CFRP laminate. Extremely high temperatures during lightning strike may result a puncture, delamination of the composite due to decomposition of the resin, and fibre breakage due to sublimation of carbon fibre. MIL-STD-1757A and SAE ARP-5414 define the test standards for the qualification of lightning strike protection [3]. The waveforms defined in the standards can be used for the design of structures against lightning strike. There are a few studies on the experimental and numerical simulation for lightning strike damage of CFRP in open literature. The simulation of lightning strike damage is a complicated problem because it requires multi-physics analysis. Ogasawara et al. [1] at JAXA studied quasi-isotropic CFRP laminate experimentally and numerically for lightning strike damage. Considering the sublimation temperature of the carbon fibre and the decomposition temperature of the matrix, the number of damaged plies and the type of damage is estimated from the contours of temperature in plane and out of plane directions. A coupled electrical and thermal analysis using finite element method is carried out, the results of which agree with experimental values. Feraboli and Miller [4], Feraboli and Kawakami [5] and Hirano et al. [6] present experimental studies to determine the effect of the lightning strike on the damage area of CFRP. Both experimental studies and finite element analysis show that the shape of the damage is elongated in the direction of the fibres. The damage area and damage depth depend on the waveform and peak current. It is also found that low electrical and thermal conductivities of CFRP through the thickness are the main reason for the lightning strike damage. In order

to increase the electrical conductivity, some additives such as carbon black, CNT are applied into resin due to having good electrical conductivity [7–9].

In this study, the neat and CNT-doped T800/M21-laminated plates to be used in aerospace structures are considered for the investigation of lightning strike damage. First, the material properties of both the neat and CNT-doped T800/M21 are obtained experimentally. Next, coupled electrical and thermal analysis is carried out using multi-physics. Quasi-isotropic rectangular plates are modelled in ABAQUS finite element program. Steady-state electrical analysis and transient heat transfer analysis are coupled and conducted at each time increment by the application of Joule heat generation. The numerical model developed for lightning strike simulations is verified with the experimental data [10]. Last, fully coupled electrical–thermal–mechanical analysis is carried out in order to further understanding the damage initiation and estimation of material failure before the decomposition of the resin.

2 Finite Element Modelling

2.1 Coupled Electrical–Thermal Analysis

A rectangular quasi-isotropic plate is considered in finite element analysis. The plate is subjected to concentrated electrical current attributable to lightning strike under an electrical and thermal boundary conditions. The temperature dependency of electrical conductivity is also considered in the model. Coupled electrical and thermal analysis is carried out using multi-physics. Steady-state electrical analysis and transient heat transfer analysis are coupled and conducted at each time increment by the application of Joule heat generation to each finite element. The electrical breakdown after decomposition of matrix is considered by changing the electrical conductivity through the thickness direction. The electrical potential, electrical current, Joule heat generation, and temperature of the elements are obtained. The damage region is estimated by considering the decomposition temperature of the resin.

The thermal properties including thermal conductivity, specific heat, and coefficient of thermal expansion of CNT-doped and undoped materials are measured experimentally. The rectangular plate, 4 mm thick, 150 mm long by 100 mm wide, and 32 layered [45/0/–45/90]_{4s}, is made of unidirectional composite T800/M21 with a ply thickness of 0.125 mm. The plate is modelled as a 3D plate in ABAQUS finite element program as shown in Fig. 1 as a single part. Then, it is partitioned into a two section through the thickness for modelling ease: (i) the first 12 layers on the front side of the plate are orthotropic layers, and the rest is quasi-isotropic single layer. The orthotropic material properties and fibre orientations are assigned for the layers. The mesh density is increased in the central region where the electrical current is applied in order to increase the accuracy of the analysis. The quality of the mesh is then verified by shape and size metrics as well as analysis checks. The total number of the coupled thermal–electrical elements is 9600.

Fig. 1 Finite element model of the composite laminate

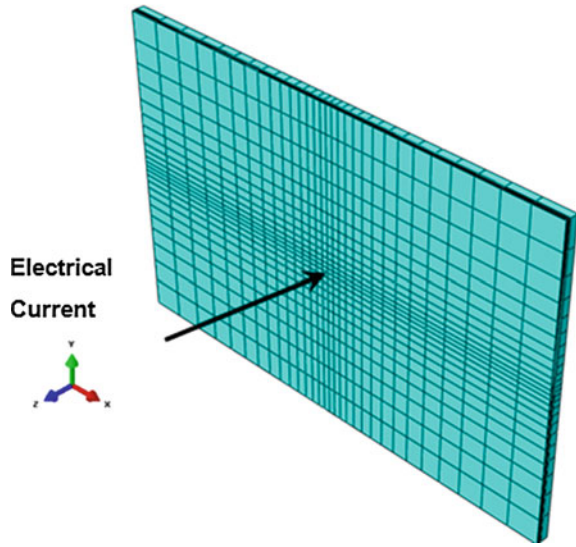


Table 1 Material properties of neat CFRP laminate

	Thermal conductivity (W/mK)	Specific heat (J/kg)	Density (kg/m ³)	Electrical conductivity [1] (S/m)
<i>Orthotropic part</i>				
Longitudinal	4.6	860	1520	29,300
Transverse	0.8	–	–	0.778
Thickness	0.7	–	–	7.94×10^{-4}
<i>Isotropic part</i>				
Longitudinal	2.7	860	1520	14,650
Transverse	2.7	–	–	14,650
Thickness	0.7	–	–	7.94×10^{-4}

Thermal radiation with an emissivity of 0.9 is applied to the front and side surfaces of the plate as the boundary conditions, whereas the back surface is assumed to be adiabatic. Environmental temperature is taken to be 25 °C. In addition, electrical potential is taken to be zero at the back and side walls of the plate because a copper plate under the back of a specimen was electrically grounded in experiments and the electrical discharge from the side surfaces to a back copper plate was observed during the tests. Extremely high value of 1×10^{11} kJ/kg for latent heat is applied to absorb the heat energy at 3000 °C [1]. The typical material properties of CFRP composite laminate used in the numerical model are shown in Table 1.

According to MIL and SAE standard [3], the lightning strike current waveforms are considered as four current components (A–D) as shown in Fig. 2a. T_1 shows front time parameter or the occurrence of the maximum current value in Fig. 2b. In addition, T_2 shows the nominal duration of wave tail from nominal origin to

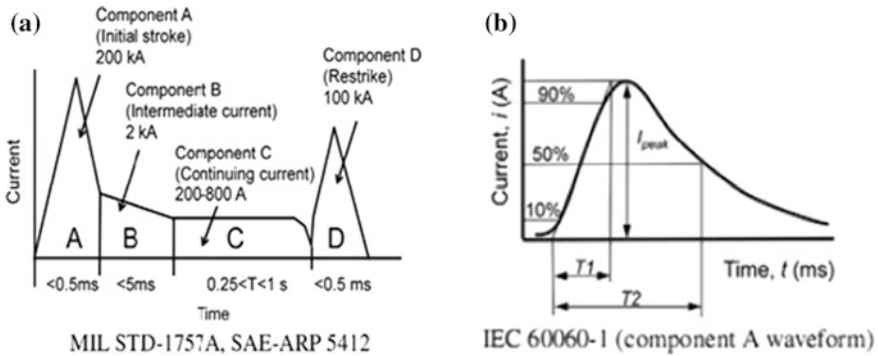


Fig. 2 a Standard lightning strike current waveform (SAE 5412) and b detailed description of component A for simulations [1, 3]

50 % of the peak current through the peak current. Although the peak current is 200 kA in component A, the waveform with reduced peak current is applied to verify the accuracy of the numerical results by the experiments.

The waveform with $T_1/T_2 = 4/20$ and peak current strike of 40 kA is applied to both undoped and CNT-doped T800/M21 plates. From TGA tests, it was observed that the mass loss starts at 400 °C being the decomposition temperature of the resin. Therefore, it is assumed that the material is failed after this temperature. According to studies in literature, depending on wt.% of CNTs doped into CFRP, K_z increases significantly. The electrical conductivity, K_z , increases as 0.01, 1, and 10 S/m for the resin with CNT wt.% of 0.5–1, CNT wt.% of 4–5, and CNT wt.% of 8–10, respectively [11, 12]. The manufacturing technique is also quite important because CNT doping might reduce K_z . In fact, CNT-doped thermoplastic dry powder was spread onto prepreg during the manufacturing of CNT-doped T800/M21, resulting lower fibre volume fraction and lower K_z due to thermoplastic carrier. On the other hand, K_z reaches up to 20 S/m when different manufacturing techniques such as CNT-doped veil and CNT-doped binder are used. In order to show the benefit of CNT doping, the typical electrical conductivity values of neat CFRP [1] and $K_z = 7.6$ S/m are assumed for the doped material during simulations. It is also assumed in the analysis that the carbon fibres are sublimated at 3273.15 K; hence, the K_z is taken to be increased linearly from 873.15 to 3273.15 K as given in Table 2. The damage areas of the first top eight layers of undoped T800/M21 and CNT-doped T800/M21 are shown in Figs. 3 and 4, respectively. When the damage areas, which are estimated by overlapping the damaged layers, of CNT-doped and undoped plates are compared, they are reduced three times for CNT-doped plate. At 30 μs when the current waveform is fully applied, the damage depth reaches 1 mm for undoped and 1.15 mm for CNT-doped plates.

Table 2 Electrical conductivity of CFRP material with CNT ($K_z = 1$ S/m)

Electrical conductivity, S/m			
<i>Orthotropic part</i>			
$K1$	$K2$	$K3$	Temperature (K)
29,300	1	1	298.15
29,300	1	1	873.15
29,300	100	100	3273.15
<i>Isotropic part</i>			
Kx	Ky	Kz	Temperature (K)
14,650	14,650	1	298.15
14,650	14,650	1	873.15
14,650	14,650	100	3273.15

2.2 Fully Coupled Electrical–Thermal–Mechanical Analysis

The finite element model is extended to implement mechanical field as well. Fully coupled electrical–thermal–mechanical analysis is more challenging because solutions need to be obtained for all three fields of displacement, temperature, and electrical potential, simultaneously. It requires temperature-dependent material properties in which assumptions are made especially after decomposition of the resin. Therefore, the material properties are taken to be temperature dependent. The damage in the composite plate during lightning strike can be divided into two parts: (i) the damage occurs from room temperature up to a temperature of starting mass loss and (ii) the damage after decomposition temperature of the resin. The currently fully coupled electrical–thermal–mechanical model does not capture the decomposition of the resin, fibre breakage, and delamination that occurs in the second part. Focusing the study in the first part, temperature dependency of the mechanical properties is ignored. However, it yields some physical insight into the damage initiation due to thermal stress by the applied electrical current.

Again a rectangular plate, 4 mm thick, 150 mm long by 100 mm wide, and 32 layered [45/0/−45/90]_{4s}, is considered and modelled. The waveform with $T1/T2 = 4/20$ and peak current strike of 40 kA are applied to both undoped and CNT-doped plates. When the electrical load reaches 1.5–2 kA, the temperatures can also reach the fully decomposition temperatures at 500–600 °C. The resin starts to decompose at 400 °C, and after this temperature, the mass losses occur. Therefore, the thermal stress levels and material failure conditions are estimated at 200, 300, and 400 °C, which occur in the plate depending on the magnitude of the applied electrical current. For material failure, Tsai–Wu failure criterion is considered as follows:

$$F_{11}\sigma_1^2 + F_{22}\sigma_2^2 + F_{66}\sigma_6^2 + F_1\sigma_1 + F_2\sigma_2 + 2F_{12}\sigma_1\sigma_2 \geq 1 \tag{1}$$

where $F_{11} = 1/(S_L^+1/S_L^-)$, $F_{22} = 1/(S_T^+1/S_T^-)$, $F_{66} = 1/S_{LT}^2$, $\sigma_6 = \tau_{12}$, $F_1 = 1/S_L^+ - 1/S_L^-$, $F_2 = 1/S_T^+ - 1/S_T^-$, $F_{12} = (F_{11}F_{22})^{0.5}/2$. S_L^+ , and S_L^- are

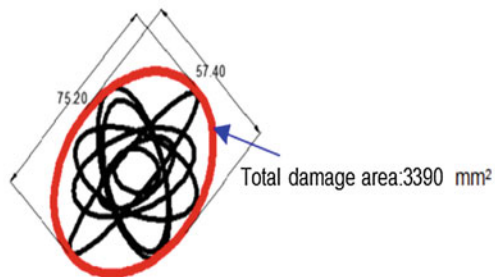
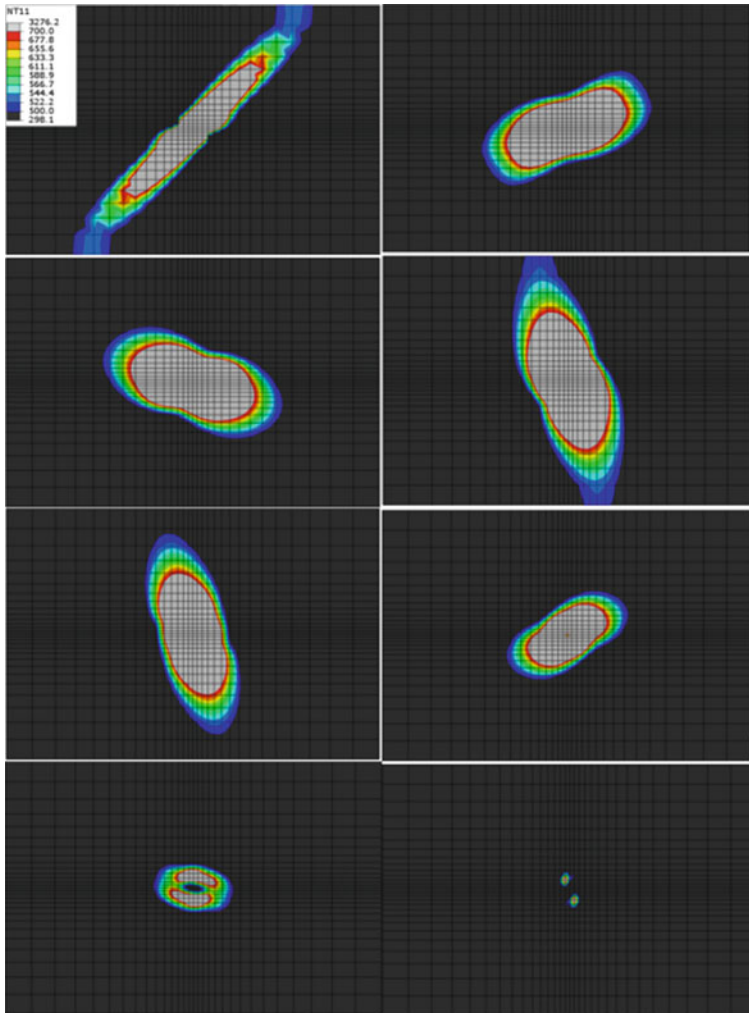


Fig. 3 The damage area of undoped T800/M21 plate at $30 \mu s$ for 40 kA, (black $< 200 \text{ }^\circ\text{C}$, grey $> 400 \text{ }^\circ\text{C}$), top eight layers from top left to bottom right

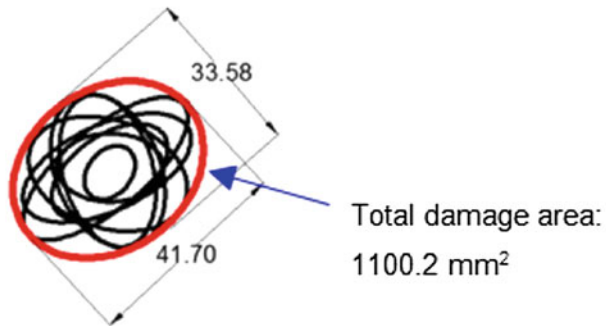
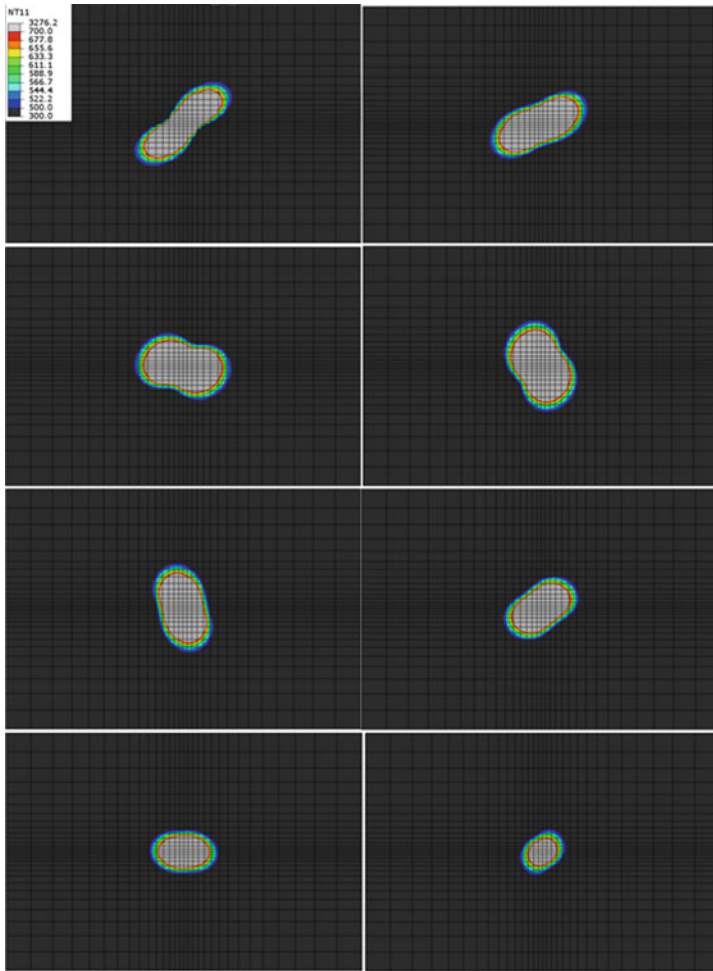


Fig. 4 The damage area of CNT-doped T800/M21 plate at 30 μ s for 40 kA, (*black* <200 °C, *grey* >400 °C), top eight layers from *top left* to *bottom right*

longitudinal tensile and compression strength; S_T^+ and S_T^- are transverse tensile and compression strength; S_{LT} is shear strength. Both compression strengths are taken as positive. The measured strengths of undoped T800/M21 material are $S_L^+ = 1380$ MPa, $S_T^+ = 30.8$ MPa, and $S_{LT} = 56$ MPa, whereas the strengths for CNT-doped T800/M21 material are $S_L^+ = 1476.6$ MPa, $S_T^+ = 37.8$ MPa, and $S_{LT} = 59.9$ MPa. The compression strengths of $S_L^- = 1051$ MPa, $S_T^- = 210$ MPa are taken from the literature [13] and are assumed to be the same for both the undoped and doped material.

Top surface stresses along fibres, perpendicular to the fibres, shear direction, S_{11} , S_{22} , S_{12} , and the applied electrical current called CECUR, are determined at 150, 300, and 400 °C. Next, Tsai–Wu criterion is obtained for both undoped and CNT-doped plates. Since K_z can reach up to 20 S/m depending on wt.% of CNT and manufacturing technique, the analyses are performed for $K_z = 10$ S/m and $K_z = 20$ S/m. The results are given for undoped plate in Fig. 5, CNT-doped plate with $K_z = 10$ S/m in Fig. 6, and CNT-doped plate with $K_z = 20$ S/m in Fig. 7 at 400 °C, respectively. According to the results, the stresses are localized in the central region where the electrical current is applied. S_{11} and S_{22} are in compression and both increase as the applied load increases and in turn the temperature increases.

Figure 8 shows the applied electrical current versus the maximum surface temperature for undoped and CNT-doped plates. CNT doping increases the K_z electrical conductivity; hence, there will be less temperature for the same applied electrical current. Tsai–Wu failure criterion is shown in Fig. 9 at 150, 300, and 400 °C for undoped and CNT-doped plates. The applied electrical current increases the surface temperature of the material; hence, it also causes thermal stresses. The criterion indicates that the material fails at 400 °C due thermal stress, which is also consistent with TGA analysis, where the mass loss starts due to decomposition of the resin.

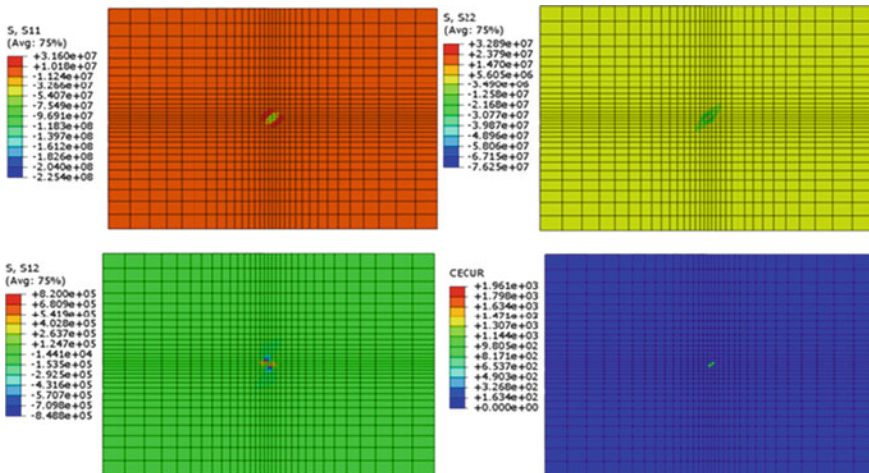


Fig. 5 Stresses S_{11} , S_{22} , S_{12} (Pa), and applied current CECUR (A) at 400 °C of undoped plate

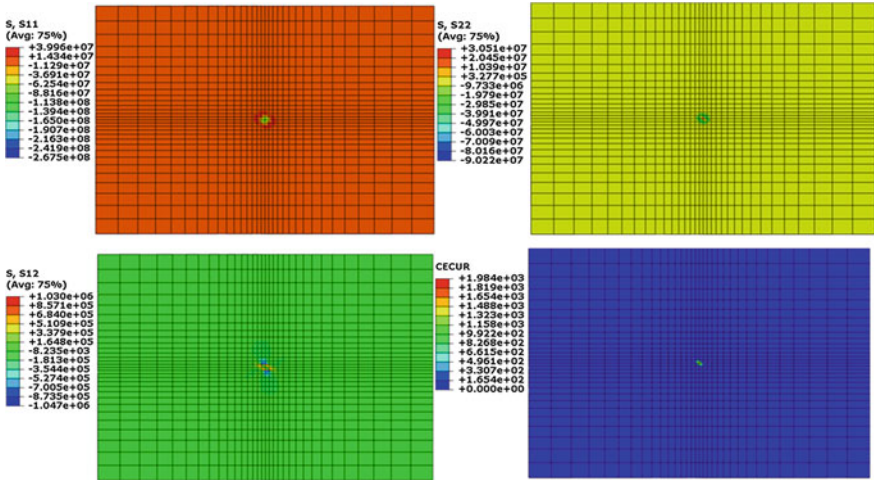


Fig. 6 Stresses S_{11} , S_{22} , S_{12} (Pa), and applied current CECUR (A) at 400 °C of CNT-doped plate ($K_z = 10$ S/m)

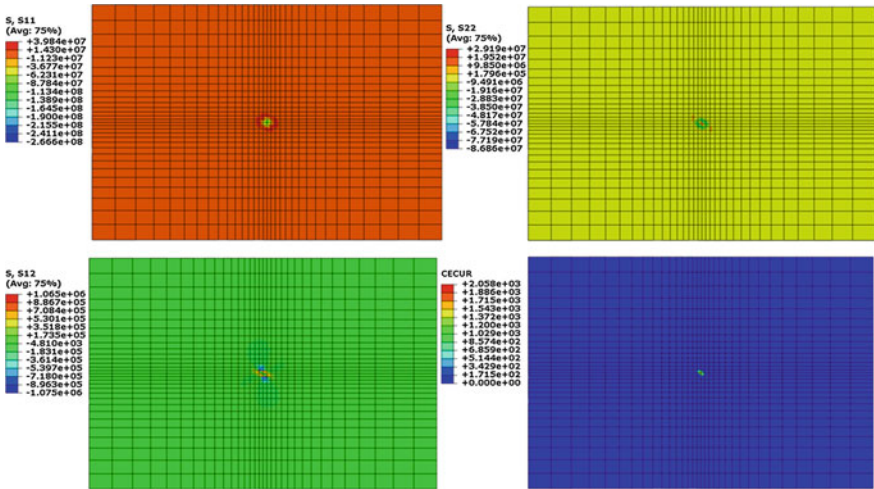


Fig. 7 Stresses S_{11} , S_{22} , S_{12} (Pa), and applied current CECUR (A) at 400 °C of CNT-doped plate ($K_z = 20$ S/m)

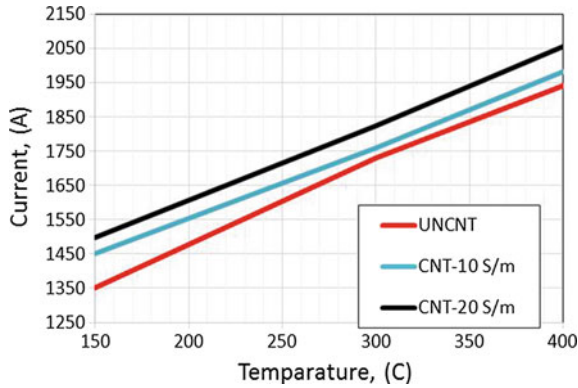


Fig. 8 Applied electrical current versus temperature, UNCNT (undoped), CNT-10 S/m (CNT doped, $K_z = 10$ S/m), CNT-20 S/m (CNT doped, $K_z = 20$ S/m)

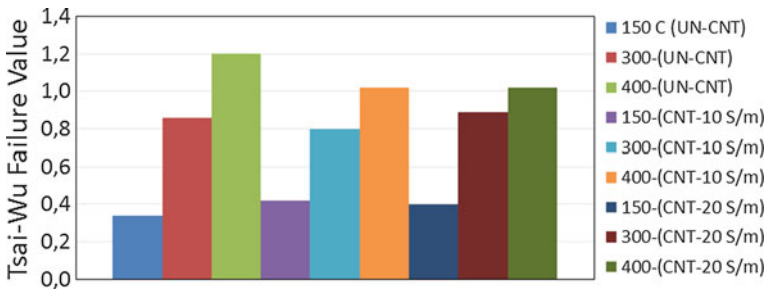


Fig. 9 Tsai-Wu failure criterion at 150, 300, 400 °C, UN-CNT (undoped), CNT-10 S/m (CNT doped, $K_z = 10$ S/m), CNT-20 S/m (CNT doped, $K_z = 20$ S/m)

2.3 Conclusions

Simulation of lightning strike damage is a complicated problem because it requires multi-physics analysis. Lightning strike damage depends on the electrical and thermal properties of the CFRP material. Extremely high temperatures may result in puncture, delamination of the composite due to decomposition of the matrix resin, and fibre breakage due to sublimation of carbon fibre. Considering the decomposition temperature of the matrix and the sublimation temperature of the carbon fibre, the number of damaged plies and the type of damage can be estimated from the contours of the temperature in plane and out of plane directions. Low electrical and thermal conductivities of CFRP through the thickness are the main reason for the lightning strike damage.

Material tests of undoped and CNT-doped T800/M21 are carried out to measure thermal properties and mechanical properties. Material tests show that CNT-doped T800/M21 has better electrical and mechanical properties than those of the neat material.

The numerical study is focused on understanding the damage behaviour caused by the lightning strike in CFRP used in aerospace industry. First, the coupled electrical and thermal model for undoped material is developed for simulations, and then, the effect of lightning strike is investigated. The damaged region is estimated by considering the decomposition temperature of the resin. The shape of the damage area tends to be elongated in the direction of the fibres. Next, CNT-doped laminates are considered using coupled analysis by increasing the electrical conductivity through the thickness. The effect of wt.% of CNT is also taken into account. The fibre orientation of the plies affects the size and shape of the damage area due to higher electrical conductivity of carbon fibres. In particular, the layer with 45° fibre orientation increases the total damage region. As the peak current or current waveform changes, electrical energy input to the system also changes and the damaged area varies accordingly. When the wt.% of CNT doped into the resin increases, the damage region substantially decreases because the electrical conductivity through the thickness of the plate plays a significant role for the lightning strike damage. Therefore, increasing the conductivity through the thickness reduces the damage region. Results of CNT-doped T800/M21 with increased K_z also show that the damage area reduces by 68 %.

Last, fully coupled electrical–thermal–mechanical analysis is carried out in order to further understand the damage initiation and estimation of material failure before decomposition of the resin. Undoped and CNT-doped T800/M21-laminated plates are studied with measured material properties. The damage initiation is estimated by considering the thermal stress level and Tsai–Wu material failure criterion. The criterion indicates that the material fails at 400 °C due to the thermal stress under the applied electrical current, which is also consistent with thermal tests that show the mass loss starts due to decomposition of the resin. CNT doping increases the K_z electrical conductivity; hence, it indicates that more electrical current can be applied to the doped material, and there will be less damage under the same electrical current.

Acknowledgments The research leading to these results has received funding from the European Union's Seventh Framework Programme for research, technological development, and demonstration under Grant Agreement No. 284562.

References

1. Ogasawara T, Hirano Y, Yoshimura A (2010) Coupled thermal–electrical analysis for carbon fiber/epoxy composites exposed to simulated lightning current. *Compos A* 41:973–981
2. Mall S, Ouper BL, Fielding JC (2009) Compression strength degradation of nanocomposites after lightning strike. *J Compos Mater* 43:2987–3001
3. Lightning Qualification Test Techniques for Aerospace Vehicles and Hardware, MIL-STD-1757A, Department of Defence, USA (1983)
4. Feraboli P, Miller M (2009) Damage resistance and tolerance of carbon/epoxy composite coupons subjected to simulated lightning strike. *Compos A* 40:954–967
5. Feraboli P, Kawakami H (2010) Damage of carbon/epoxy composite plates subjected to mechanical impact and simulated lightning. *J Aircr* 47:999. doi:10.2514/1.46486

6. Hirano Y, Katsumata S, Lwahori Y, Todoroki A (2010) Artificial lightning testing on graphite/epoxy composite laminate. *Compos A* 41:1461–1470
7. Sandler J, Shaffera P, Prasseb T, Bauhoferb W, Schultea K, Windle AH (1999) Development of a dispersion process for carbon nanotubes in an epoxy matrix and the resulting electrical properties. *Polymer* 40:5967–5971
8. Ruoff RS, Qian D, Liu KW (2003) Mechanical properties of carbon nanotubes: theoretical predictions and experimental measurements. *C R Physique* 4:993–1008
9. Berber S, Kwon YK, Tománek D (2000) Unusually high thermal conductivity of carbon nanotubes. *Phys Rev Lett* 84(20):4613–4616
10. Soykasap O, Karakaya S, Colakoglu M (2015) Simulation of lightning strike damage in carbon nanotube doped CFRP composites. Paper to be presented at ICCS18—18th International Conference on Composite Structures, 15–18 June 2015, Lisbon, Portugal
11. Allaoui A, Bai S, Cheng HM, Bai JB (2002) Mechanical and electrical properties of a MWNT/epoxy. *Compos Technol* 62:1993–1998
12. Heimann M, Wrist-Ruettters M, Boehme B, Wolter KJ (2008) Investigations of carbon nanotubes epoxy composites for electronics packaging. Paper presented at 58th (ECTC) Electronic Components and Technology Conference, 27–30 May 2008
13. Marín L, Trias D, Badalló P, Rus G, Mayugo JA (2012) Optimization of composite stiffened panels under mechanical and hygrothermal loads using neural networks and genetic algorithms. *Compos Struct* 94:3321–3326

Metallic Strip Details for Validation of ESN Technologies

Richard Perraud, Olivier Urrea, Thierry Pelegrin, Michel Bermudez, Michel Fouquembergh, Stephane Guinard and Christoph Breu

Abstract The aim of AS10 is to evaluate technologies that can be integrated directly into structures with the target of creating an electrical structural network (ESN) while reducing weight and improving survivability of composite structures. These investigations are based on various technologies and materials from nanomaterials to metallic strips and coatings. The metallic strip concept is based on the merging of materials at macro- and meso-element scale level, using conventional manufacturing technologies. The innovative development consists of a pre-assembled semi-product composed of an aluminium strip and a nonvulcanized rubber that is cobonded to the composite frame part while curing the structure.

R. Perraud · O. Urrea
EMC and Propagation, Airbus Group Innovations, 12, rue Pasteur,
92152 Suresnes Cedex, France
e-mail: richard.perraud@airbus.com

O. Urrea
e-mail: olivier.urrea@airbus.com

T. Pelegrin (✉) · M. Bermudez
Mechanical System Design, Airbus Group Innovations, 12, rue Pasteur,
92152 Suresnes Cedex, France
e-mail: thierry.pelegrin@airbus.com

M. Bermudez
e-mail: michel.bermudez@airbus.com

M. Fouquembergh
Heat Transfer Science, Airbus Group Innovations, 12, rue Pasteur,
92152 Cedex Suresnes, France
e-mail: michel.fouquembergh@airbus.com

S. Guinard
Computational Structural Mechanics, Airbus Group Innovations,
18, rue Marius Terce, 31300 Toulouse, France
e-mail: stephane.guinard@airbus.com

C. Breu
Preforming and Textile Technology, Airbus Group Innovations,
81663 Munich, Germany
e-mail: christoph.breu@airbus.com

This paper presents the metallic strip design and manufacturing choice, the thermomechanical experimentation and modelling conclusion, the impact coupon test results and conclusion on damage tolerance and detectability of impacts, the electrical current distribution simulation and test and finally the electrothermal behaviour results and conclusion.

Nomenclature

ABS	Airbus standard
AIMS	Airbus material specification
APII	Airbus process instructions
AS0X	Application scenario x in the SARISTU project
CFRP	Carbon fibre-reinforced plastic
NDT	Nondestructive testing
SARISTU	Smart intelligent aircraft structures

1 Introduction

This paper describes firstly the metallic strip design and manufacturing choice, secondly the thermomechanical experimentation and modelling, thirdly the impact coupon test results and conclusion on damage tolerance and detectability of impacts, fourthly the electrical current distribution simulation and finally the electro-thermal behaviour results.

2 Metallic Strip Design and Manufacturing Choice

2.1 Design Choice

The metallic strip design proposed in this study aims at challenging the traditional scheme of the electrical cable AD2 type attached to the composite structure owing to brackets. This cable fulfils electrical functions needed for instance for the current return or a provision of a common voltage reference. These functions are part of the electrical structural network (ESN) functions intrinsically covered by the former metallic structures. It is the case for the automotive or aerospace vehicles.

The concept proposed in this study is based on a very generic design called “Metallic Strip” which combines a composite carbon structure and a semi-product made of an electrical aluminium alloy and a thin layer of rubber [1–3]. This association allows for reaching a wide part of the benefits mentioned here above. The general requirements for achieving the design are classified following different main domains:

- The thermomechanical and structural aspects, covering the requirements of geometry (thickness, location, tolerances, etc.), surface protection (galvanic corrosion has to be prevented along with metallic materials have to be protected against the environmental corrosion), impact protection of the head of the CFRP frame and assembling (bonding of metallic component to the structure). One more major aspect of the concept is the mechanical behaviour decoupling as the metallic component should not change the mechanical behaviour of the composite structure.
- The thermal aspects, covering the requirements of the maximum temperature reached by the metallic strip and consequently by the composite structure under general and specific loads (short circuit, normal current flow, etc.).
- The electrical aspects, covering the requirements of conductivity for permanent functional current or for short-circuit currents up to 1500 A during one second. The other main electrical requirement deals with the electromagnetic impact. In fact, the new architecture has to use a routing and a geometrical configuration which do not magnetically affect the wires and other electrical metallic components in case of high current variations (ground reference fluctuation).

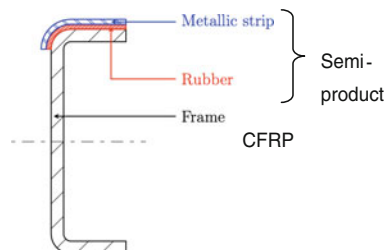
Secondary beneficial side effects are expected from metallic strips:

- Both metallic and elastomeric additional layers may act as absorbers with respect to accidental low energy and low velocity impacts on protected structures (typically, tools dropping on lower panels of fuselage sections during assembling or maintenance operations);
- Metallic additional layer may act as an impact tracker: metallic plasticity results in visible local dents when impacted; this would allow significative weight savings in the design of protected composite parts, since the current design policy with respect to impacts is conditioned by a threshold for impact damage detectability.

The generic design proposed (Fig. 1) uses the following:

- A 1050 H18 aluminium alloy strip of 1 mm thickness provides very high electrical conductivity and the best yield limit for this series of aluminium. But for supply problem on the material (not enough ordered material), the thickness was finally 0.8 mm. The most important is to keep the cross-area of 34 mm² necessary to conduct the current. The L-shape covers the radius and the head of the frame to protect against drop tool impact.

Fig. 1 Metallic strip concept



- A thin interface of SMACTANE FR60 RUBBER bonded to the metallic strip by bonding/vulcanization process under a thermomechanical press cycle (around 120 °C and >10 bars). This interface had different roles, first the accommodation of thermomechanical behaviours inside the multimaterial during the manufacturing process and the life cycle of the plane (-55 to 70 °C) to reduce the strength at the extremity of the metallic strip, secondly the electrical insulation between the metallic strip and the CFRP part and finally avoidance of the galvanic corrosion between the CFRP and the aluminium strip.

This couple constitutes a semi-product used in RTM/LRI process to facilitate the manufacturing. The rubber face sheet of semi-product is in contact with the carbon preform (Figs. 2 and 4).

The main challenge of this assembly is to warranty the good adhesion over the 30-year lifetime under severe environmental conditions such as a temperature ranging between -50 and 70 °C along with a high humidity level up to 80 %. The study plans to investigate the adhesion of the strip under several environmental conditions and thermomechanical solicitations detailed hereafter.



Fig. 2 Semi-product manufacturing process

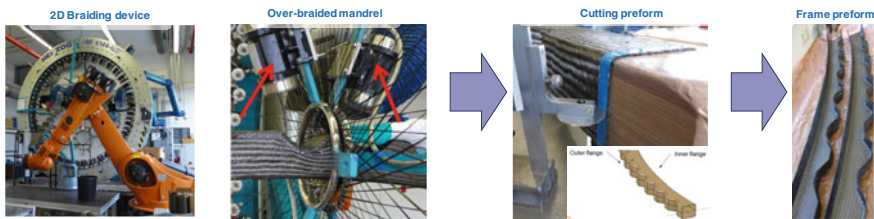


Fig. 3 Braided frame manufacturing process

2.2 Manufacturing Choices

The design suits with the braiding process which is the manufacturing technology retained into AS10 (Fig. 3). But it is also compatible with other conventional composite technologies, e.g. prepreg material. The general manufacturing procedure (Figs. 2, 3 and 4) is based on the conventional light resin infusion (LRI) process consolidating the dry carbon preform and a semi-product within the mould in order to combine the curing and the bonding phases of the process. The composite material system chosen for this investigation is a braid with HTS 40 E23 12K 800 tex fibre injected with the resin system RTM6 compatible with resin transfer moulding (RTM) processes.

The semi-product is composed of a 0.8-mm-thick aluminium 1050 alloy and a 1-mm-thick SMAC FR 60 rubber. The aluminium strip is cold-bended in a specific machine and treated with a tartaric sulphuric anodizing (TSA) for protection and assembling preparation with the rubber. Due to the project time constrains, the semi-product has been realized using an adhesive film AF136-2 for the bonding of the metallic strip and a preliminary vulcanized rubber (in this case, PSA and bonding primer surface treatment was used for better performance with adhesive film) (Fig. 2).

The semi-product is placed with the rubber face in contact with the dry carbon preform in the LRI mould in order to obtain a cobonding operation during the polymerization process. Finally, machining operations on the edges of the frame finalized the dimensions, and we could proceed to the assembly of the frame on the panel (Fig. 4).

The metallic strip structure, then fabricated, is controlled by NDI (Fig. 5) with the sensor in contact with the carbon side. This detailed inspection is required after

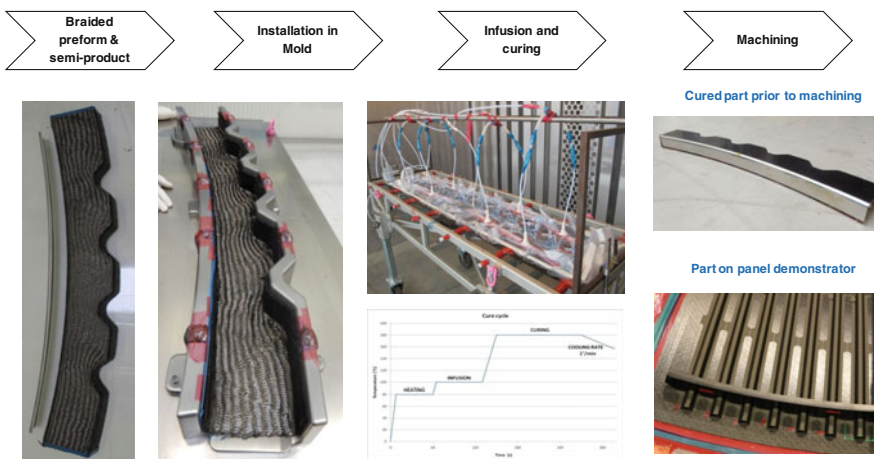


Fig. 4 Manufacturing of frame with metallic strip concept integration

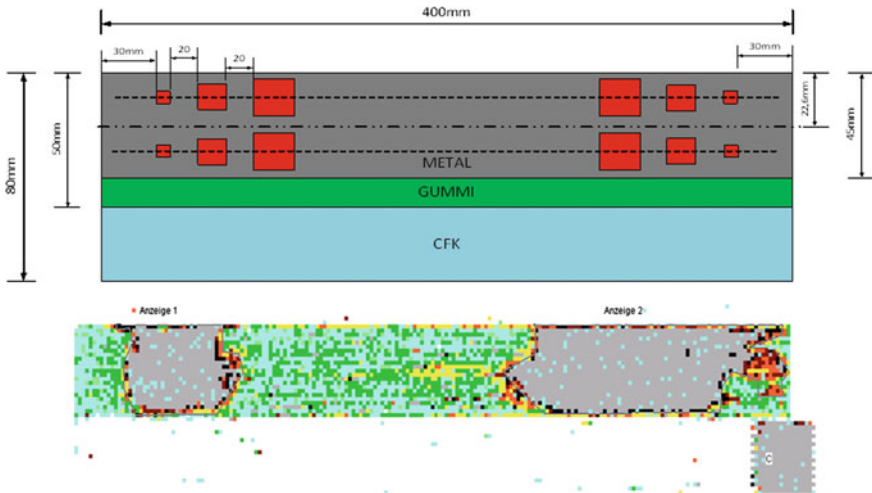


Fig. 5 Trial with incorporated defects for US inspection validation

infusion process to check the quality of the assembly. This NDI inspection includes an A-scan method to check local zone and a C-scan method for mapping the global level of porosity in the composite part and delamination between the rubber and the composite structure.

3 Thermomechanical Modelling and Experimentation

3.1 Thermomechanical Behaviour Experimentation of a ESC

Cooling and heating experiments and simulations have been performed on a CFRP/rubber/strip assembly in order to evaluate the risk of damaging under extreme temperatures. The specimen used for the tests is composed as follows:

- Metallic strip $1003 \times 50 \times 0.8$ mm made of aluminium 1050 H18
- Adhesive film $1003 \times 50 \times 0.8$ mm made of AF136-2
- Rubber layer 1 mm thickness on the surface made of SMAC FR60
- CFRP plate $1003 \times 50 \times 4$ mm prepreg carbon T700/M21

Thermal and strain sensors are placed on the assembly. Strain gauges are set partly on the metallic strip side to record its deformation with one additional gauge on the other side at the centre of the CFRP plate, while thermocouples are set on both sides to measure the homogeneity of temperature during the experiment. Two series of tests have been performed allowing for evaluating the thermomechanical behaviour: the first one, from room temperature to -55 °C and the second one, from

room temperature to 100 °C. The experiments performed, combining thermal and mechanical effects for a multimaterial architecture, are difficult to predict. Furthermore, information is missing on the rubber constitutive laws.

Under the conditions of the experiments, the system does not exhibit any damage and the aluminium strip remains in the elastic domain; however, a tensile stress develops at cold temperatures. It has been estimated at about 140 MPa upon cooling at -55 °C from a zero-stress state identified around 70 °C.

The experiment shows that the accommodation provided by the rubber is limited in the centre of the strip and is higher at the tips. This means that the rubber layer is stiff enough to constrain the metallic strip on the CFRP plate in the centre region of the assembly. Then, the maximum strain in the strip at lowest temperature does not depend on the rubber's stiffness.

3.2 *Thermomechanical Modelling*

Simulations of the cooling and heating experiments are then performed, for a better understanding of the thermomechanical phenomenon in the multimaterial architecture. This study helps getting a full understanding of what happened during the experiment and assesses quantitatively the rubber's constitutive law. Several mechanical tests have been realized in order to provide the right data needed for the simulation like quadruple lap shear specimen to determine the rubber shear module ISO1827 [4]. Specimens have then been manufactured, among which single lap shear specimen and perpendicular tension specimen according to the standards EN2243-1 [5] and EN2243-4 [6], respectively, to measure mechanical adhesion at room temperature, 70 and -55 °C.

Finite element simulations are performed using the software Abaqus, including the variations hereafter detailed for comparison and analysis.

- The first one is dedicated to the study of the geometry influence on the maximum stress in the strip. In fact, it is needed to explore the shape singularities and length capabilities, in order to identify the design limitations. The results show that above a 200 mm length, the maximum tension in the strip does no longer depend on the strip's length (Fig. 6).
- The second simulation aims at reproducing the experiments of cooling to -55 °C and heating to 100 °C. The resulting longitudinal strains are plotted in Fig. 7 and show a good match over the full range of temperatures. The agreement is almost perfect for the centre and tip strains (orange and blue), while the strains at half-sides are slightly overestimated (purple) (Fig. 7).

In conclusion, the experiments and simulations have allowed getting a complete understanding of the thermomechanical phenomenon in the system, as well as assessing quantitatively the rubber's constitutive law [7, 8] and the effect of the

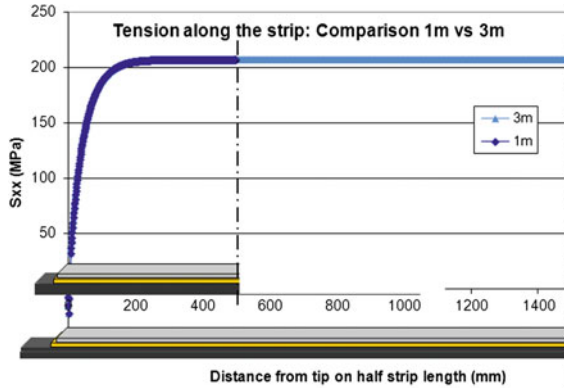


Fig. 6 Tension along the strip for 1- and 3-m-long assemblies

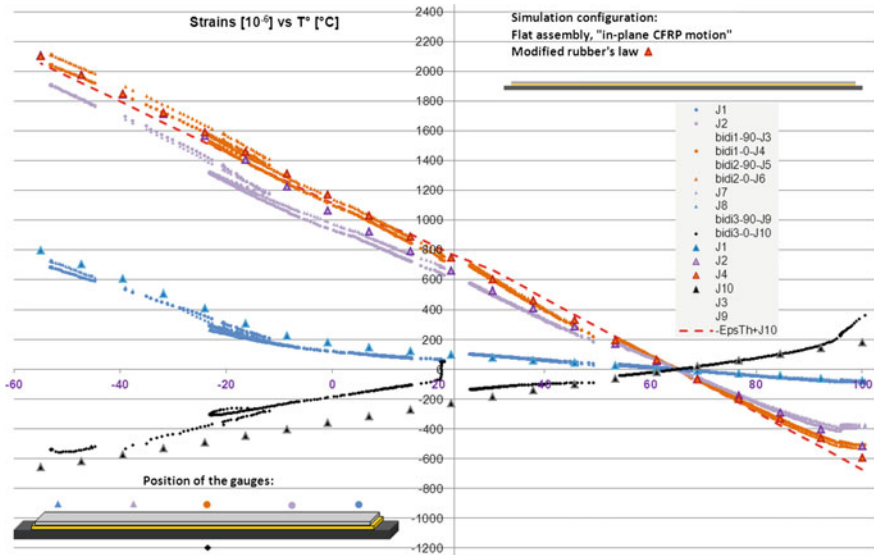


Fig. 7 Longitudinal strains calculated at gauge locations with the modified rubber's constitutive law (triangles), compared to the experimentally recorded strains (dots). The schematic indicates the gauge location corresponding to each colour

assembly length. It is shown that a stress greater than 200 MPa could develop in the metallic strip at $-55\text{ }^{\circ}\text{C}$, which would result in a plastic deformation for the aluminium alloy firstly chosen. Therefore, an optimization of the assembly design and/or the material choices is necessary in order to better withstand the thermo-mechanical constrains.

4 Impact Test Results and Conclusion on Damage Tolerance and Detectability of Impacts

Beneficial side effects are expected from additional layers: impact detectability, due to the ductility of aluminium, and impact damage tolerance, due to the energy-absorbing capability of both aluminium and elastomeric layers. In order to check such capabilities, impact tests are being conducted on both coupons (100 × 150 mm, AITM 1.0010) and structural details (representative fuselage frames). All specimens consist in a composite braided part (length 150 mm, width 100 mm, thickness 4.2 mm), on which a 1050H18 aluminium strip (thickness 0.8 mm) is bonded with a SMACTANE FR60 rubber layer (thickness 1 mm).

Experimental protocols for impact tests incorporate instrumented impacts (recording of contact force history, energy absorption of the impacted structure) and thorough measurements of dents and impact-induced delaminations within the laminate (laser profilometry, US inspections).

Though the impact test campaign is still in progress, evidence has been made already that:

- Detectability improves significantly: dent is visible through eye inspection for an impact less than 6 J (versus no visible dent on nonprotected composite before considerable damage occurs within the composite); a usual 0.3 mm dent depth is considered as the usual detectability threshold (Fig. 8).

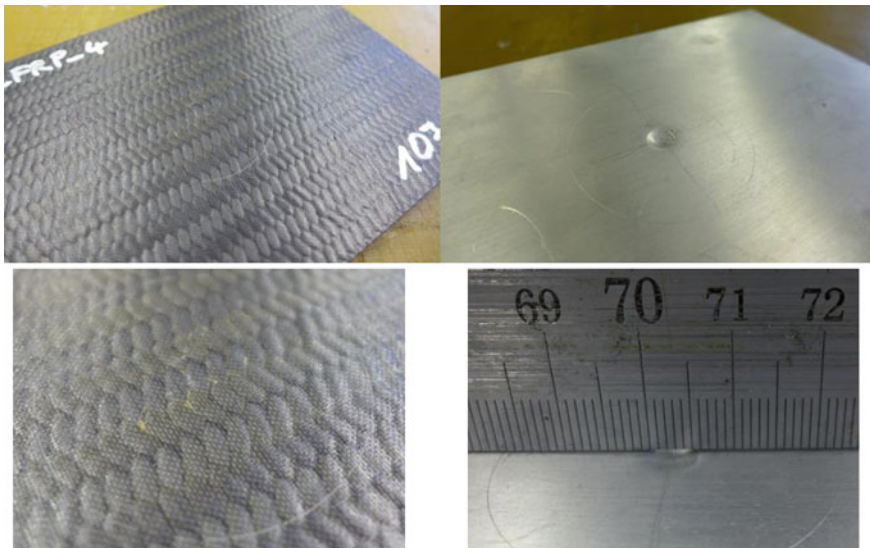


Fig. 8 Samples with 10 J impact. Poor visibility on CFRP, but good visibility on aluminium

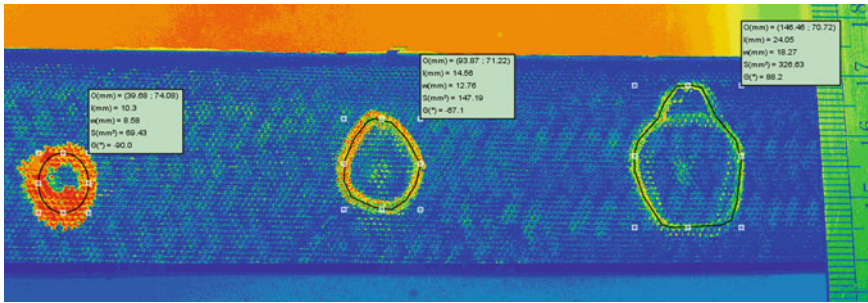


Fig. 9 Impact test on CFRP frame without metallic strip (10, 15 and 20 J)

Table 1 Comparison of damage on frame with and without metallic strip/rubber

Impact energy (J)	10	15	20
Frame with metallic strip and rubber (mm ²)	0	0	0
Frame without metallic strip and rubber (mm ²)	70	147	327

- Damage tolerance improves significantly: a preliminary estimate states that the protection increases the energy threshold for damage initiation within the composite of 10 J at least (Fig. 9 and Table 1). The improvement of damage tolerance can offer the opportunity to mass saving by CFRP frame resizing

5 Electrical Simulation and Experimentation

5.1 Electrical Current Distribution Simulation

AD2 cable is the current solution for ESN elements installed nearby composite structures. This solution is qualified for electrical and thermal aspects notably on current aircraft. To analyse the effect of change to a metallic strip in terms of current distribution, a 2D simulation model is developed and firstly validated with well-known metallic structures such as round wire. After validation, same simulation technique is applied to the metallic strip in order to check the current distribution and evaluate discrepancies with current cable solution. Skin effect phenomenon is well known when an alternating current (AC current) flows on the cylindrical wire. It depends on the nature of the material and the frequency of the AC current. At $f = 0$ Hz, DC current is uniformly distributed in the cylindrical form. But, in high frequencies, the current crowds to the surface and concentrates in a thickness on the order of the skin depth.

Skin effects for both cylindrical and strip models are depicted in Figs. 10 and 11.

Electrical current distribution has been computed for different structures, cable, rectangular strip and L-shape strip. For functional frequency of interest (until

Fig. 10 Current distribution at $f = 10$ kHz

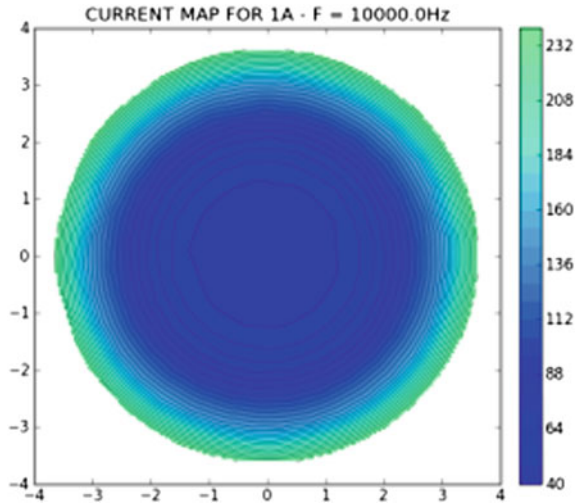
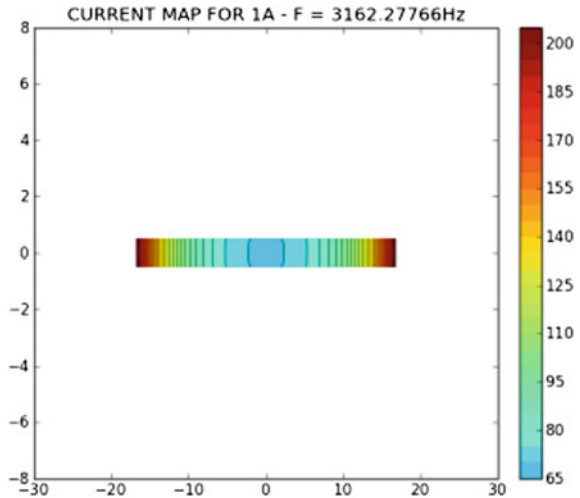


Fig. 11 Current distribution at $f = 3$ kHz



1 kHz), and L-shape strip chosen in SARISTU project, no skin effect is observed and resistance is quite constant until this frequency (Figs. 12 and 13).

5.2 Electrical Coupling Simulation and Experimentation

The aim of the simulations is to compare coupling functions (what amount of voltage V_{oc} for 1 Amp injected in the short-circuit wire) with AD2 and strip ($t = 1$ mm and $t = 0.8$ mm). For that, we take as a reference this geometrical configuration which is representative from the aircraft installation (Fig. 14).

Fig. 12 Current distribution at $f = 1$ kHz

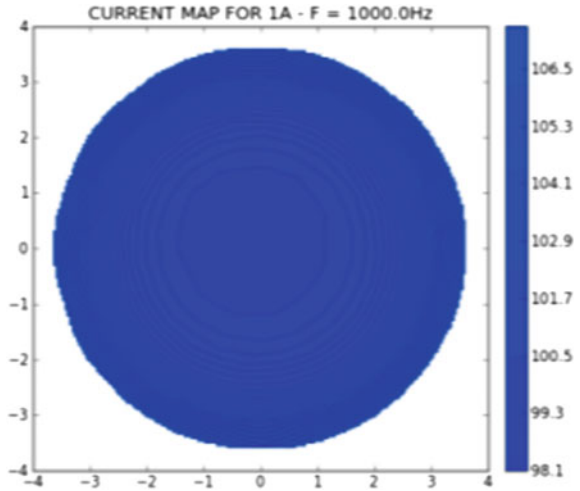
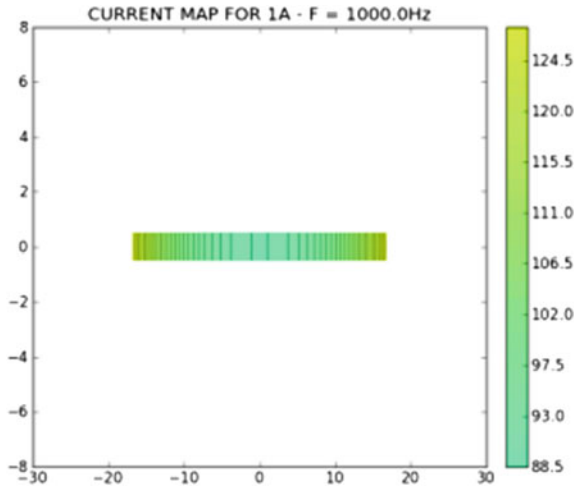


Fig. 13 Current distribution at $f = 1$ kHz



The red wire represents the short circuit. The green wire is the AD2 cable, and blue cables are victim cables (open-circuit cable). For the strip installation, we place the strip in the frame flange horizontally (Fig. 15).

Simulation models are built in 2D base on the above geometry considering two ESN cables or strips in the cross section corresponding to two frame paths. Distance between two AD2 cables or strips is 650 mm (interframe distance).

The simulation parameters are as follows:

- Electrical conductivity for AD2: 31095274 S/m
- AD2 radius: 3.3 mm
- AD2 resistance is then 0.94 mohm/m (@ $T^\circ = 20$ °C)

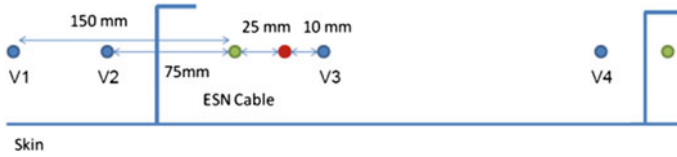


Fig. 14 Schematic from the reference document V92D11031379

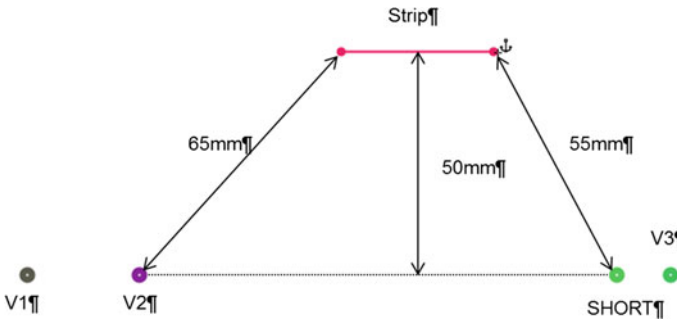


Fig. 15 Test configuration for metallic strip electrical coupling test

- Electrical conductivity for strip: 31289111 S/m
- Strip thickness = 1 mm or 0.8 mm
- Strip width: 34 mm

The examination of the result voltage of each simulation has shown the same coupling behaviour for the three configurations, and two main phenomena are identified as follows:

- Resistive coupling in low frequency below 100 Hz: this is a coupling due to the total amount of conducting resources (ESN elements). This coupling is the same for all victim wires V1–V4.
- Inductive coupling: this is the mutual effect between the injection wire and the victim wire (flux of injection loops inside the victim loop). A 20 dB/decade slope represents this coupling and is clearly seen for frequencies above 1 kHz. V3 victim wire has the highest coupling level because it is the nearest cable from the sources: on the contrary, V4, which is the further, observes the weakest.

As shown by the simulations and experimental test results, the strip installation versus AD2 cable does not induce high increase of coupling transfer functions (Fig. 16).

During experiments, we have seen that the introduction of braid or electrical connection between parts of a strip brings a resistive coupling more importantly due to the resistance of these elements.

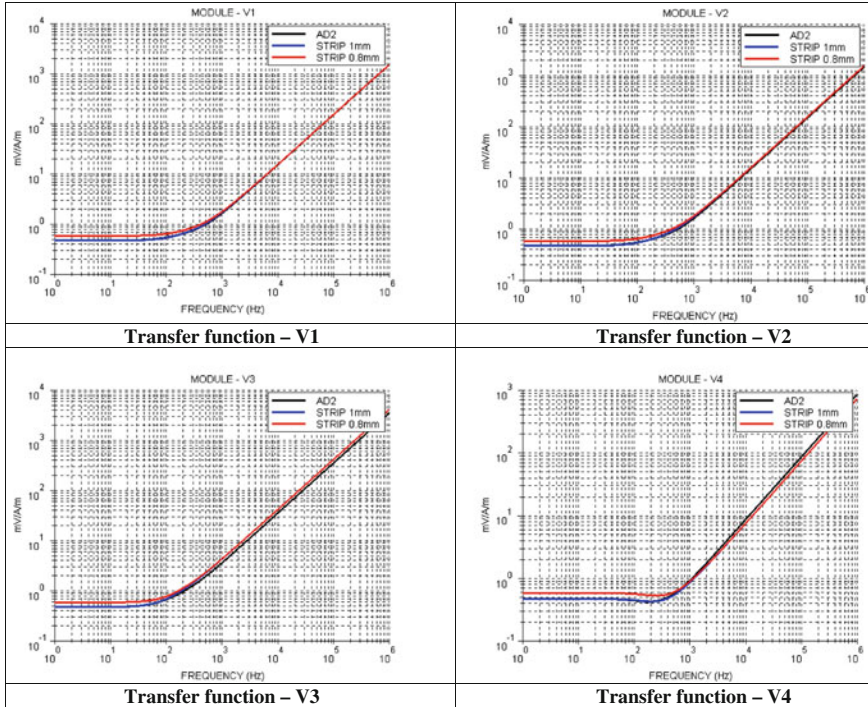


Fig. 16 Coupling behaviour comparison of 0.8 mm strip/1 mm strip/AD2 cable configuration in victim wires V1, V2, V3 and V4

For a real demonstrator or other, results obtained with braid connection between strips cannot be useful to determine the coupling function because we must know the number of braid per metre. Indeed, to transpose the coupling effects on greater lengths, we must add resistance and the inductive effects of each braid connected and not just multiply the above results per length. These first results will be confirmed on IS13 demonstrator for which real connexion between strips and longitudinal elements will be realized.

6 Electrothermal Experimentation, Modelling and Results

6.1 Electrothermal Experimentation

The effects of change from a cable to the metallic strip bonded to the composite structure have to be investigated in order to warranty the nonexcess temperature within the constitutive material of this architecture.

Two main criteria have to be respected:

Table 2 Mean temperature for each current step in °C

	Right T/C	Middle T/C	Left T/C	Ambient temperature
Baseline	70.3	70.3	70.3	70.4
800 Hz steady	73.5	72.6	74.4	70.7
800 Hz @ 15 min	73.3	72.3	74.1	70.6
400 Hz steady	73.5	72.6	74.4	70.7
DC steady	73.2	72.4	74.2	70.7
DC @ 15 min	73.1	72.3	74.1	70.7

- In a first case, the circulation of the specified current through the ESN elements shall not increase the temperature of these elements of more than 20 °C above the ambient temperature.
- In a second case, the temperature increase of the CFRP structure due to the current flow from the points of contact between ESN and the CFRP shall be lower than 10 °C. This requirement is mandatory to ensure staying below the resin’s glass transition.

Test has been setup for an AD2 cable (Fig. 17), and the wire might be subjected to current intensities up to 50 A DC, or 50 A AC up to 800 Hz during 15 min. A test is conducted at 70 °C, maximum temperature that will see the structure in normal conditions.

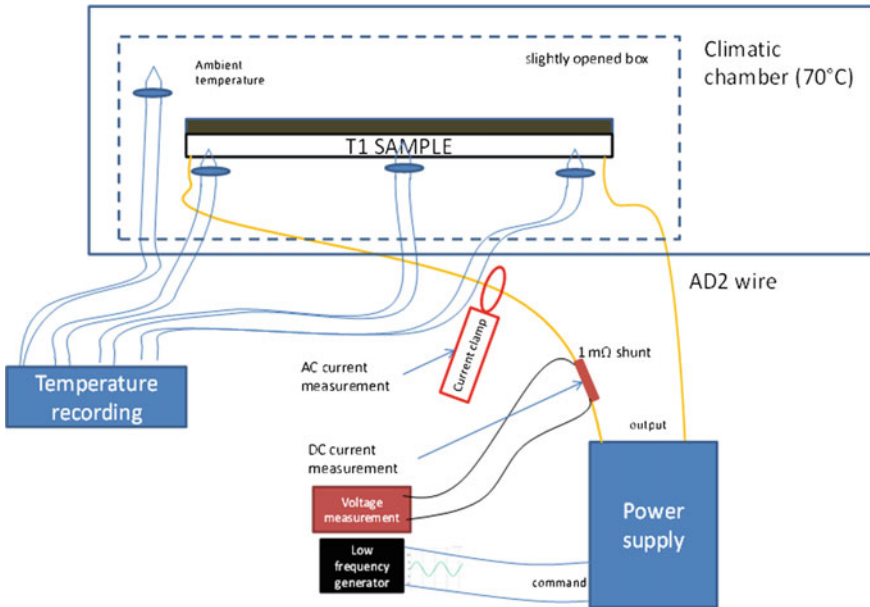


Fig. 17 Thermoelectrical test setup

The test consists in injecting a given current and in measuring temperature increase of the conductor during the test. Three thermocouples are pasted on the surface of the metallic strip to measure its temperature increase; a fourth thermocouple is used to record air temperature in sample vicinity. Left and right thermocouples are located at 40 mm from specimen ends. The three thermocouples have been installed on the central axis of the specimen.

The specimen is placed in a box in order to limit the effects of forced convection inside the climatic chamber.

The temperature increase has been evaluated relatively to baseline temperature at test beginning and to air temperature inside the box during test (Table 2). Steady states have been reached during the three tests. We can observe that temperature after 15 min is close to steady state temperatures.

As expected, the strip concept fulfils the electro-thermal requirement regarding structural temperature increase, while subjected to 50 A nominal current.

6.2 Electrothermal Simulation

Simulations have been performed with COMSOL MULTIPHYSICS®.

Two sizing scenarios linked with electrical properties have been identified for the thermal aspects under environment at 70 °C for neighbouring structures' sizing; in the steady state, the cable has to support 50 A at a frequency between DC and 800 Hz and must support transient currents, up to 1500 A during 1 s (corresponding to short-circuit conditions).

Considering for the first sizing scenario, a heat exchange by conduction, convection and radiation of a horizontal cylindrical cable, the temperature increase is 7.7 °C for DC current of 50 A in environment at 70 °C from heat balance, which can be written as

$$Q_{\text{Joule}} = \rho(T_{\text{mean}}) \int_{\Omega} j^2 = Q_{\text{convection}} + Q_{\text{radiation}} = (h_{\text{convection}} + h_{\text{radiation}})S(T - T_{\text{air}})$$

The configuration of the strip is quite different, and the assumptions lead us to consider a strip installed on bottom face of a composite beam (worst case with respect to convection configuration). The balance equation is the same as for cylindrical cable, except that we consider heat losses only on external face of the strip and we assume that contact face of strip with composite remains adiabatic, which is also the worst case with respect to heat diffusion in steady state. In this configuration, the nonlinear equation is solved for a strip of $34 \times 1 \text{ mm}^2$ in ambient at 70 °C with a current of 50 A and leads to a temperature increase of 7.9 °C. Therefore, according to the different assumptions (no heat transfer through composite and worst geometrical configuration for convection), we can conclude that the metallic strip has a temperature increase identical to corresponding gauge cylindrical cable.

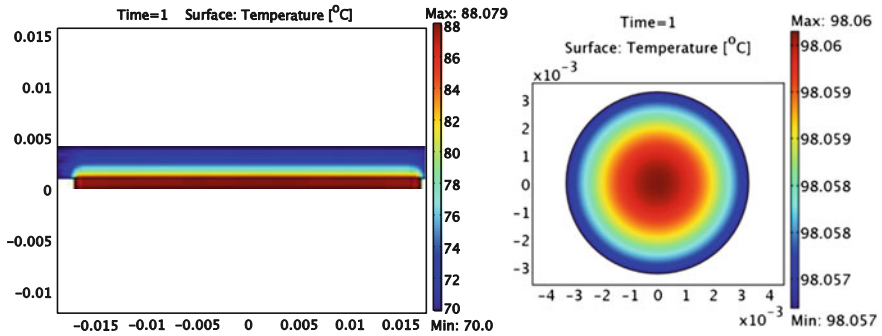


Fig. 18 Temperature for transient current of 1500 A, map at 1 s for metal strip and AD2 cable

The second sizing scenario leads to design a conductor for supporting transient currents up to 1500 A during 1 s at a temperature condition of 70 °C. Only the heat dissipation due to Joule effect is considered for the simulation. The cylindrical cable again represents the reference model and shows a temperature increase of 28.06 °C after 1 s. One can notice that the temperature is quite homogenous between the centre and the peripheral of the cylindrical cable. The metallic strip architecture allows considering thermal dissipation through the interface and the composite structure. As depicted in Fig. 18, the temperature increase of the strip is 18 °C and on the composite 10 °C for a duration of few seconds in the very first millimetres.

This shows also that the strip configuration leads to a lower temperature increase than the cable. This is explained by the dissipated heat partly diffused into the composite and highlights the need to adapt the interface in order to ensure staying below the resin's glass transition temperature of the composite structure.

Acknowledgments We would like to thank all partners involved in successful completion of this work package and for the support provided to solve challenges. The research leading to these results has received funding from the European Union's Seventh Framework Programme for research, technological development and demonstration under Grant Agreement No. 284562.

References

1. Telgkamp J, Schulze W, Kruse T (2011) Structural component with improved conductivity and mechanical strength, and a method for its manufacture. Patent US 2011278395 (A1), 17 Nov 2011
2. Aspas Puertolas J, Bermudez M, Thomas B (2013) Guinard S. Procédé et dispositif de protection contre l'impact d'éléments de structure primaire composite. Patent WO 2013004553 (A2), 10 Jan 2013
3. Aspas Puertolas J, Bermudez M, Fouquembergh M, Maisonnave N (2012) Pièce composite avec interface métallique. Patent WO 2012164210 (A2), 06 Dec 2012
4. International Standards ISO1827 Rubber, vulcanized or thermoplastic: determination of shear modulus and adhesion to rigid plates. Quadruple-shear methods

5. European Standards EN2243-1 Structural adhesives. Tests methods part 1: single lap shear
6. European Standards EN2243-4 Structural adhesives. Tests methods part 1: single lap shear
7. Treloar LRG (1975) *The physics of rubber elasticity*, 3rd edn. Clarendon Press, Oxford
8. Yeoh OH (1993) Some forms of the strain energy function for rubber. *Rubber Chem Technol* 66:754–771

Part XI Technology Stream: Integration and Validation. Implementation of Morphing, Structural Health Monitoring and Nanomaterials on an Outer Wing Box

Introduction and Overview

The main target IS12 was to validate the technical and economic feasibility of self-sensing and morphing structures. Two main objectives were pursued: self-sensing structure and morphing structure; for self-sensing structure, the objective was a real reduction of life cycle costs related to maintenance and inspections by using SHM systems. The SHM is included within a damage tolerance scenario; morphing structures the IS12 target was to deal with detailed aerodynamic shape seamless controlled structures throughout the entire lifetime of the aircraft. IS12 has focused on the structural integration of needed part capabilities. For this purpose, piezo, optical fiber and three major devices have been defined for joint integration in the outer wing; piezo for damage detection, optical fiber for internal load evaluation and delamination under the stringer, Leading edge offering improvements in aerodynamics and aircraft noise during take-off and landing—Trailing edge, offering cruise fuel consumption reductions—Winglet trailing edge offering local airfoil optimization during take-off and landing for controlled drag and noise reductions. The main achievement of IS12 has focused on integration activities concerning both conformably morphing and self-sensing structures, improved damage tolerance of composite materials using nanomaterial, and mapping of the load conditions along the axes of the wing box.

Morphing Value Assessment on Overall Aircraft Level

**Fabian Peter, Eike Stumpf, Giovanni Marco Carossa,
Markus Kintscher, Ignazio Dimino, Antonio Concilio, Rosario Pecora
and Andreas Wildschek**

Abstract In order to assess the benefit of the morphing devices developed in the framework of SARISTU, integration in an overall aircraft model is required. For this purpose, the relevant input data regarding the adaptive leading-edge, trailing-edge and winglet devices are gathered with specific focus on weight and aerodynamic performance. Different levels of detail are applied. For weight and actuation power, the methods range from geometry (e.g. span and chord)-dependent methods to absolute delta values which are for instance subtracted from components weights as wing structure weight. Methods for aerodynamic data reach from subtractions of absolute values from the lift to drag ratio, constant for the flight

F. Peter (✉) · E. Stumpf

Institute of Aerospace Systems, RWTH Aachen University, Wuellnerstrasse 7,
52062 Aachen, Germany

e-mail: peter@ilr.rwth-aachen.de

E. Stumpf

e-mail: stumpf@ilr.rwth-aachen.de

G.M. Carossa

Air Vehicle Technology, Alenia Aermacchi S.p.A., C.so Francia 426, 10146 Turin, Italy

e-mail: giovanni.carossa@alenia.it

M. Kintscher

German Aerospace Center, DLR Institute of Composite Structures and Adaptive Systems,
38114 Braunschweig, Germany

e-mail: markus.kintscher@dlr.de

I. Dimino · A. Concilio

CIRA, The Italian Aerospace Research Centre, Via Maiorise, 81043 Capua, CE, Italy

e-mail: i.dimino@cira.it

A. Concilio

e-mail: a.concilio@cira.it

R. Pecora

Industrial Engineering Department, University of Naples “Federico II”, Via Claudio, 21,
80125 Naples, Italy

e-mail: rosario.pecora@unina.it

phases (i.e. climb, cruise, decent), towards changes to the induced drag polars specific for each mission increment and dependent on the explicit lift coefficient. For an objective assessment, several aircraft models are compared. The assessment and comparison of these aircraft AC models take place on standard overall aircraft-level parameters as block fuel or maximum take-off weight.

Nomenclature

ATED	Adaptive trailing-edge device
EADN	Enhanced adaptive droop nose
LoD	Lift over drag
MTOW	Maximum take-off weight
MICADO	Multidisciplinary integrated conceptual aircraft design and optimization
NLF	Natural laminar flow
TLAR	Top-level aircraft requirements
VC	Variable camber
WATE	Winglet active trailing edge

1 Introduction

Highly matured conventional aircraft systems and designs make it necessary to closely evaluate the potential benefit of new technologies before detailed and expensive effort is put into product development. Comparison on system level often lacks the ability to capture the full potential of technologies due to the restriction that not the entire aircraft model is fully sized with respect to the changes inflicted by the system. Conceptual aircraft design is well suited for this application. Its main goal is to assess the performance on overall aircraft level while being able to implement changes on a detail level sufficient to capture the necessary sensitivities.

The morphing technologies developed in the SARISTU project are aimed to increase the aircraft performance mainly in economical regard while increasing the mass of specific subsystems. For this purpose, an assessment on overall aircraft level is unavoidable in order to give a true evaluation of the performance impact. The application scenarios findings have therefore been incorporated in several conceptual aircraft design models and their performance has been evaluated.

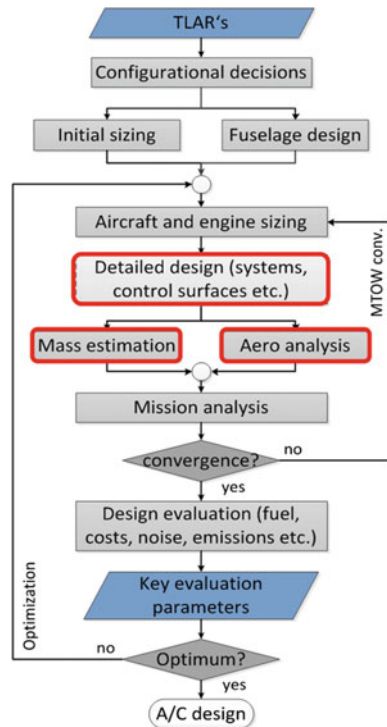
A. Wildschek
Airbus Group Innovations, 81663 Munich, Germany
e-mail: andreas.wildschek@airbus.com

2 Assessment Platform

During recent years, a software environment has been developed at the RWTH Aachen University Institute of Aerospace Systems (ILR). The software is named multidisciplinary integrated conceptual aircraft design and optimization (MICADO) and fulfils the above-mentioned requirements necessary for the evaluation of the morphing technologies of SARISTU and has been used for the assessment of morphing devices in previous publications [1, 2]. The software is capable of designing an entire aircraft from a set of top-level aircraft requirements (TLARs) on a detail level which makes performance predictions as, e.g., mission block fuel on a high level of accuracy possible. The structure of MICADO [3] is shown in Fig. 1. The loop structure for the main design tool, named maximum take-off weight (MTOW) convergence in Fig. 1, ensures that design changes are propagated through all aspects of the aircrafts design. The herein included modules are iteratively executed until convergence of a set of important design parameters (e.g. MTOW) is reached. The programme modules impacted most by the SARISTU morphing technologies are as follows:

- *Systems design*
 Since the flight control actuation is part of the aircraft systems, the morphing devices actuation will be incorporated in this tool.

Fig. 1 MICADO program structure



- *Mass estimation*
Mass changes of the structural components of the wing structure, the leading and trailing-edge devices will be taken into account in this module.
- *Aero analysis*
Each of the morphing technology will impact the aerodynamic performance of the aircraft which is implemented in these modules functions.

A sophisticated mission simulation is conducted in the mission analysis module. The equations of motion are solved for the mission increments and engine characteristics as fuel flow are calculated. Also flight condition-specific data as atmospheric values are taken into account. The summation of the mission increments and the iterative execution of this module allows for an accurate estimation of the fuel consumption and other performance data. In the following, the methods implemented in the single modules for the integration of the SARISTU morphing technologies are described.

3 Integration of Application Scenarios

The different technologies developed by the application scenarios lead to different methods of implementation. These methods will be described in the following specific to each application scenario. The presented methods for the weight estimation for the SARISTU morphing technologies are limited in their representativeness for an application in an aircraft. The focus of the investigations of SARISTU was on functional integration. In most cases, there is potential for weight savings if a detailed product design is conducted or aspects of series production as custom made motors and sensors are implemented in the design. Furthermore, the extrapolation of the mass of the wind tunnel components to full-scale wing components is limited by the lack of data. For this reason, the scaling by span has been chosen as first guess and practical but rough estimation.

In the following sections, the models are as follows:

(A) Application Scenario 1 (EADN)

The enhanced adaptive droop nose (EADN) developed by application scenario 1 is a leading-edge device which significantly reduces or eliminates the step between the leading-edge device and the wing box. With conventional slat, this step leads to transition from laminar to turbulent flow. Other aspects are actuation of power off-takes, system mass and high-lift performance. The incorporation of the mass aspect is discussed later in this section. The influence of high-lift performance could not be evaluated since no studies for the complex analysis of low-speed aerodynamics were conducted. However, the requirements of take-off and landing distance were not exceeded with estimations for reduced maximum lift coefficients. The actuation power impact will be included after the results of the wind tunnel experiments are available.

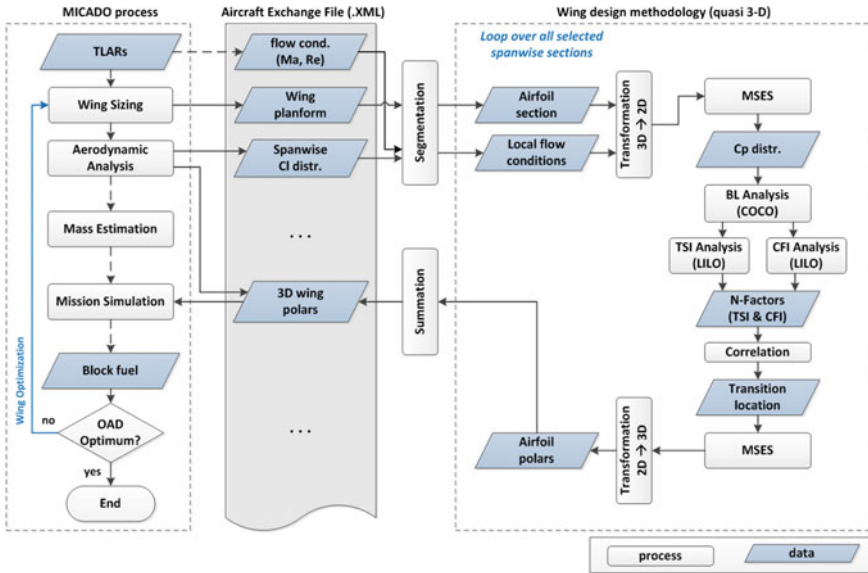


Fig. 2 Transition determination process

The main aspect which has to be integrated in MICADO is the increased area of laminar flow. MICADO has a tool chain implemented which includes the MSES [4] flow solver and tools for transition point determination. Dedicated publications for the corresponding tool chain are available [5]. The general process is visualized in Fig. 2.

On the left-hand side of Fig. 2, the overall aircraft design process stores data as flow conditions, wing planform and lift coefficient distributions in a parametric data file which is used by all modules. From this file, airfoil sections are extracted from the three-dimensional wing geometry and the corresponding local flow conditions are calculated. These data are used for a transformation into two-dimensional data. With the two-dimensional data, the MSES code can be executed and a pressure distribution is generated. This is the input for a tool chain which determines the transition location. The process is iterated since the transition location influences the pressure distribution. After reaching convergence, a transformation to three-dimensional data takes place creating the airfoil polars. These are incorporated in the three-dimensional wing polars which are then used in the mission analysis module for solving the equations of motion. For a representative result, several airfoil sections are chosen (e.g. root, kink and tip) and their results are combined.

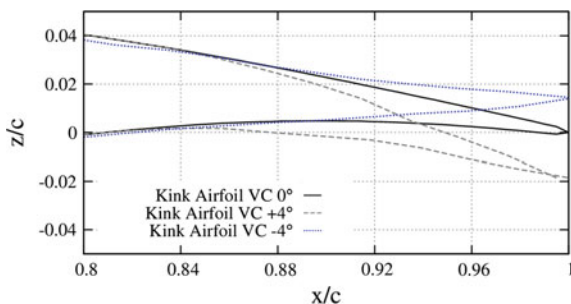
For the mass implementation, the mass of the wind tunnel demonstrator EADN is scaled to the full span of the leading-edge devices. This mass is distributed not only to the structural mass of the leading-edge devices, but the motor mass of the EADN is incorporated in the flight control system mass according to the

ATA-Chapter definition. The design of the wind tunnel demonstrator has potential for mass optimization and can be expected to be lighter if a detailed design is conducted. On the other hand, additional mass for controlling and redundancy-driven mass increases are also likely. Furthermore, an electrical anti-icing system has been implemented in MICADO as it has been in the EADN wind tunnel demonstrator. This leads to a decrease of bleed air off-takes and an increase in electrical power demand which also impacts the mass of the electrical generators.

(B) Application Scenario 2 (ATED)

The goal of the adaptive trailing-edge device (ATED) developed in application scenario 2 is to realize a variable camber (VC) function during cruise. The VC concept is to change the airfoil shape of the wing during cruise. Conventional wing control surfaces are operated during take-off, climb, decent and landing and are not suited to be operated during cruise. Since the lift coefficient changes during cruise, the wing, more specifically the airfoils, cannot always operate at their aerodynamic optimum. The lift coefficient cannot be altered without altering the flight condition, which is not feasible except by flight-level changes. Therefore, it is desirable to optimize either a fixed airfoil shape for a large range of lift coefficients or to have the possibility to change the airfoil shape according to the present flight condition. The latter is the aim of VC. Figure 3 shows the ATED’s geometric permutations for three different droop angles. The integration in MICADO is realized by calculating polars for the possible geometric permutations of the airfoil (i.e. the airfoil changes the VC system is able to create). These polars are then merged according to different criteria. For a fully functional VC system, this is done by selecting the best lift to drag ratio (LoD) of all the polars of the geometric permutations for the specific flight condition. This merging must be conducted for all polar points, which are dependent on the configuration (e.g. climb or cruise), lift coefficient, altitude and Mach number. For an operational mission assessment, a dysfunctional VC system can be represented by selecting the lowest LoD, which of course is a very conservative assumption. This concept has been analysed in previous publications [6]. For the mass of the ATED, the mass of the wind tunnel demonstrator is scaled with the span of the flaps, as the device is planned to replace the panel of the fowler flap.

Fig. 3 SARISTU ATED shapes for different droop angles



(C) Application Scenario 3 (WATE)

There are two main goals for the winglet active trailing-edge (WATE) device in SARISTU. The first is the improvement of the LoD by the adaptive camber of the WATE's trailing edge, and the second is the gust loads alleviation. For both aspects, application scenario 3 has conducted numerical investigations. Since the results of these investigations can be expected to have a higher accuracy than the methods commonly used in conceptual aircraft design, these results are taken as direct input parameters for the design of the WATE aircraft models. Specifically, this means LoD percentage improvements and reduction of structural wing mass.

4 Aircraft Models for Comparison

A set of top-level aircraft requirements (TLAR) was defined in the beginning of SARISTU. These TLARs and general configuration decisions were used as input for all of the designed aircraft models. The most important TLARs are shown in Table 1. The TLARs are comparable to the requirements of an AIRBUS A320-200 with a reduced cruise Mach number which is common for designs which aim at realization of natural laminar flow (NLF). The number of passengers leads to an aircraft of the single aisle class.

In order to compare the benefit of each SARISTU morphing technology, several aircraft models are designed and assessed. Furthermore, the integration of the technologies is successively introduced to analyse the impact of the specific implementation aspects. For each application scenario, the aerodynamic impact of the system is incorporated in a model first. Of course, these models do not represent viable aircraft concepts since they do not include the other aspects of the SARISTU morphing technologies. These other aspects (e.g. mass changes and changes in system architecture) are incorporated in an additional model for each application scenario.

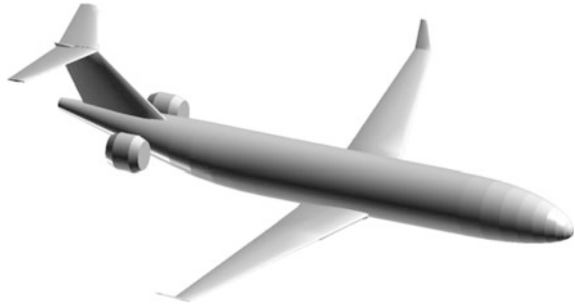
(A) Fully turbulent baseline model

The first model represents the configuration chosen for SARISTU which is shown in Fig. 4. This configuration has fuselage-mounted engines in order to avoid

Table 1 SARISTU top-level aircraft requirements

Requirement	Value
Max. altitude	40,000 ft
PAX-number	185
Max. payload	18 t
Design range	3000 NM
Design payload	16.8 t
Mach number in cruise	0.74

Fig. 4 SARISTU aircraft configuration



flow disturbing influences of wing mounted engines. The planform of the wing features a high aspect ratio wing with small leading-edge wing sweep in order to support a large surface fraction with laminar flow. The control device set-up is conventional with slats along the entire leading edge of the wing and single slotted flaps on the trailing edge. In this first model, the flow over the airfoils is calculated fully turbulent in order to quantify the benefit of the laminar flow areas introduced in the aircraft models for application scenario 1. The aircraft model A will be the baseline and reference of all aircraft models.

(B) Laminar slat model

The second model introduces areas of laminar flow. These areas, however, are restricted by the step between slat and wing box to 20 % of the chord. A reduction in viscous drag and thereby a reduced fuel burn can be expected and consequently a reduction in the overall aircraft mass as well.

(C) Transition determination model

For the third aircraft model, the transition from laminar to turbulent flow is determined for the SARISTU wing geometry. These transition locations lie well beyond the slat step, which justifies the assumption of the second model that laminar flow can be expected until the slat step. The larger areas of laminar flow are likely to lead to a further reduction of block fuel. The assumption of laminar flow beyond the slat step requires step-less leading-edge devices as the EADN. The necessary system impacts of the EADN are incorporated in the next aircraft model.

(D) EADN model

The EADN model incorporates the aforementioned aspects. The present mass estimations could lead to a small mass reduction for the EADN system compared to slat leading-edge devices if the kinematic chain and hydraulic components as the power control unit are considered. It is possible that the reduction is more than compensated by the increase of generator mass due to the electrical anti-icing systems. If so, the overall increased mass will reduce the block fuel reduction gained by the laminar flow.

(E) ATED VC model

The implementation of the VC airfoil shapes is conducted as described above by the usage of the merged polars with the best LoD for each polar point. This can be expected to lead to a total increase of LoD and therefore to a reduction in block fuel.

(F) ATED model

The ATED additional mass is assigned to the structural mass of the wing trailing edge, which will thereby be increased and thereby block fuel will increase as well.

(G) WATE LoD model

For the integration of the LoD improvement, the polars of the fully turbulent baseline model (A) are modified according to the results of the numerical investigations of application scenario 3. As described before, a higher LoD most likely leads to a reduced fuel burn.

(H) WATE model

This model combines the LoD improvements and the structural wing mass reductions and represents the design of the WATE implemented without the other application scenarios. Since the results of the numerical investigations predict a wing weight reduction, it can be expected that the fuel burn is further reduced.

(I) SARISTU combined AS model

In this model, all of the above-described modifications are implemented, comprising all of the SARISTU morphing technologies.

5 Results and Comparison

The results of the model comparison are shown in Table 2. As described before, the values are percentage values relating to the fully turbulent baseline model (A). It is important to keep in mind that all of the aircraft models are converged, meaning that changes (e.g. mass changes) are propagated throughout the design. Thereby all of the listed parameters are connected which is the reason why for almost every model every parameter changes. The discussion of the designs will therefore be focused on the most important changes (bold in Table 2).

For the laminar slat model (B), MTWO and block fuel are reduced as was expected. This reduction is even stronger for the transition determination model (C). For the EADN model (D), the strong increase of the electrical load and corresponding generator mass due to the electrical anti-icing system is dominating. Thereby, the MTOW reduction is smaller compared to the model (C). Consequently, the block fuel reduction is smaller as well. However, the block fuel reduction is still bigger than for the laminar slat model (B).

For the ATED device, the change in LoD due to the VC system is smaller than the LoD improvement due to laminar flow. Also the MTOW is increased. This is due to the increase of the trailing-edge mass. The resulting ATED model (F) still offers a block fuel improvement compared to the baseline model (A).

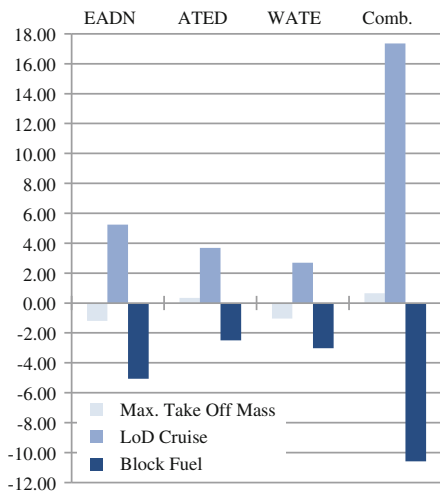
The LoD improvement of the WATE is slightly smaller than for the ATED. In contrast to the ATED, the WATE leads to a reduction of the aircraft mass and the WATE model (H) achieves a larger block fuel reduction.

The combined model (I) mass is slightly increased compared to the baseline model. However, due to the very large increase of LoD achieved by the combination of the SARISTU morphing technologies, a high block fuel reduction is possible. For a better visualization, the main parameters are shown in Fig. 5.

For an assessment on fleet level, a parameter study has been conducted based on the representative flights per day versus mission range distribution for a fleet of aircraft. Figure 6 shows the distribution of a generic fleet for one day in black columns. The maximum number of flights, more than 19 %, is conducted with a mission range of 300 nm. The grey columns show the block fuel for model (A) as percentage from the longest mission in the study (2200 nm). The blue columns show the block fuel for model (I) as percentage related to 2200 nm of model (A).

For the models (A) and (I), naturally the block fuel consumption increases with mission range. The reduction from model (A) towards model (I) increases with mission range which is due to the fact that the improved aerodynamic performance of the morphing SARISTU technologies is most beneficial during cruise flight conditions. The data in Fig. 6 can be combined to calculate the block fuel reduction for the analysed fleet. This results in a block fuel saving of 6.5 % of the SARISTU model (I) compared to model (A).

Fig. 5 Percental changes towards model (A)



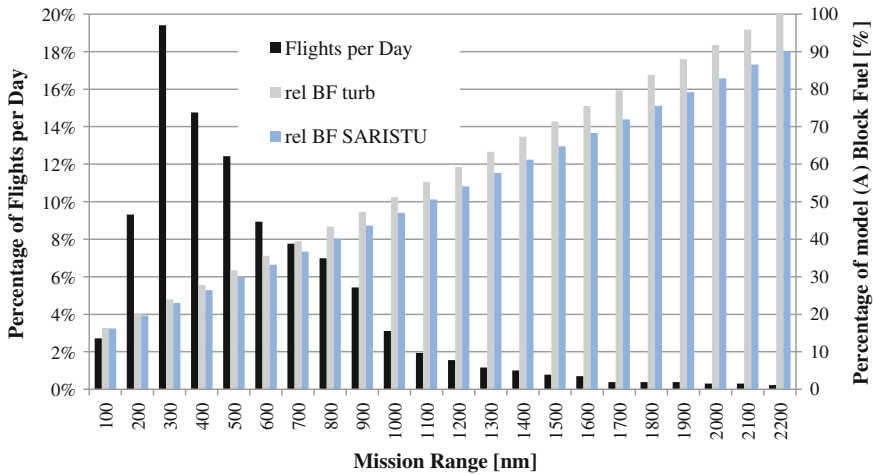


Fig. 6 Block fuel reduction on fleet level

6 Conclusion

The presented assessment proves that morphing technologies are able to improve fuel consumption significantly. The biggest single contributor is the enabling of large areas of laminar flow on the wing by NLF. All of the application scenarios achieve a reduction in fuel burn on their own. For each application scenario, this is accomplished by:

- EADN: Increase of LoD due to enabling of larger areas of laminar flow and reduction of leading-edge device mass,
- ATED: The increase of trailing-edge device mass is more than compensated by the increase of LoD due to optimization of the airfoil
- WATE: Results of numerical investigations show improvements for wing structure weight and LoD leading to an overall induced fuel burn

Consequently, the combination of the SARISTU morphing technologies yields a high reduction in block fuel.

The assessment on fleet level was done with a representative distribution of mission ranges for aircraft of the class defined by the TLARs. The parameter study conducted for these mission ranges together with the information of the frequency of these mission ranges resulted in a block fuel reduction for the fleet of 6.5 %.

Further potential lies in mass savings which could most likely be achieved especially for EADN and ATED. Moreover, the focus of SARISTU was on the integration of the technologies on an industrial level. Further aerodynamic optimization taking into account the gained knowledge of the boundaries, e.g. material stresses, available design space and scaling of components, poses a potential to

increase the fuel burn reduction even further. Improvements of the incorporated estimations for the mass of the morphing devices can also lead to an increase in confidence in the comparison results.

Acknowledgments The authors would like to thank the whole SARISTU consortium for the very good support and teamwork. The challenging task to integrate complex technologies on an international level has led to a large gain in experiences and interdisciplinary knowledge.

The research leading to these results has received funding from the European Union's Seventh Framework Programme for research, technological development and demonstration under grant agreement no 284562.

References

1. Peter F, Lammering T, Risse K, Franz K, Stumpf E (2013) Economic assessment of morphing leading edge systems in conceptual aircraft design. Paper presented at the AIAA 51st aerospace sciences meeting (ASM), AIAA, Fort Worth, Jan 2013
2. Franz K, Lammering T, Risse K, Anton E, Hoernschemeyer R (2012) Economics of laminar aircraft considering off-design performance. Paper presented at the 8th AIAA multidisciplinary design optimization specialist conference, AIAA, Honolulu, HI, Apr 2012 (submitted for publication)
3. Risse K, Lammering T, Anton E, Franz K, Hoernschemeyer R (2012) An integrated environment for preliminary aircraft design and optimization. Paper presented at the 8th AIAA multidisciplinary design optimization specialist conference, AIAA, Honolulu, HI, Apr 2012 (submitted for publication)
4. Drela C, A users guide to MSES 3.05. Technical report, Department of Aeronautics and Astronautics, MIT
5. Risse K, Schuelcke F, Stumpf E, Schrauf G (2014) Conceptual wing design methodology for aircraft with hybrid laminar flow control. Paper presented at the AIAA 52nd aerospace sciences meeting (ASM), AIAA, National Harbor, MD, Jan 2014
6. Peter F, Schuelcke F, Risse K, Stumpf E (2015) Variable camber impact on aircraft mission planning. Paper presented at the AIAA 53rd aerospace sciences meeting (ASM), AIAA, Kissimmee, FL, Jan 2015

Implementation of Morphing, Structural Health Monitoring and Nanomaterials on an Outer Wing Box

Giovanni Marco Carossa, Michelangelo Giuliani, Alan Johnston, Christina Altkvist, Alessandro Airoidi, Zahra Sharif Khodaei and M.H. Aliabadi

Abstract This paper presents the implementation of morphing, structural health monitoring and nanotechnology on the demonstrator wing. The goal is to reduce aerodynamic drag and improve bearing capacity, damage detection, damage tolerance allowable and internal load control. The morphing system developed intends to minimize the impact on the aerodynamic drag through variation in shape and help increase the overall efficiency of the wing and the plane. The structural health monitoring system can control a network of piezoelectric transducers and optical fibres that are surface mounted on the structure, to control damage, internal load and the shape of the morphing surfaces. Furthermore, the paper describes the construction and assembly of the wing demonstrator and outer manhole design/

G.M. Carossa (✉)
Alenia Aermacchi S.p.A., 10146 Turin, Italy
e-mail: giovanni.carossa@alenia.it

M. Giuliani
REDAM—Research and Development in Applied Mechanics, Parco Abate, 9C,
83100 Avellino, Italy
e-mail: info@redam.it

A. Johnston
Bombardier Aerostructures and Services, Belfast, Northern Ireland, UK
e-mail: alan.johnston@AERO.BOMBARDIER.COM

C. Altkvist
Saab AB, 581 88 Linköping, Sweden
e-mail: Christina.Altkvist@saabgroup.com

A. Airoidi
Department of Aerospace Science and Technology, Politecnico di Milano, 20156 Milan, Italy
e-mail: alessandro.airoidi@polimi.it

Z. Sharif Khodaei · M.H. Aliabadi
Imperial College London, London SW7 2AZ, UK
e-mail: z.sharif-khodaei@imperial.ac.uk

M.H. Aliabadi
e-mail: m.h.aliabadi@imperial.ac.uk

manufacturing for improved damage tolerance. This is achieved by using CFRP in combination with nanotechnology and the monitoring of the load in the wing box by means of optical fibres integrated on the spars of the wing box.

1 Introduction

IS12 focuses on integration activities concerning both conformably morphing, self-sensing structures, improved damage tolerance composite materials using nanomaterial and mapping of the load conditions along the axes of the wing box. It will allow (1) shape change without the generation of discontinuities; (2) damage detection without the need for visual inspection; (3) improved operative costs, using highest material allowable “nanomaterial”; (4) internal load monitoring; and (5) outer wing box manufacturing. In other words, without producing aerodynamic gaps during morphing and providing integrated optical fibre/piezoelectric for damage detection and load monitoring. A first in smart material concepts, this IS12 outer wing physically combines and evaluates different technological solutions and their combined effects at aircraft level. For these purposes, two demonstrators have been manufactured and will be tested. The first will be tested in a low-speed wind tunnel to validate functionality and system integration of the morphing devices: the second will be tested, to validate functionality, structural health monitoring (SHM) system, improved damage tolerance and internal load control.

IS12 Technologies:

1. Three morphing devices: winglet, leading edge and trailing edge were designed, manufactured and installed on the IS12 outer wing, with the aim to assess A/C level performance of the morphing configurations. Relevant device characteristics (weight, complexity, safety) will be tested in the wind tunnel to investigate their aeroelastics characteristics when integrated into the wing box. Finally, structural load alleviation and their effectiveness will be finalized into a value for risk analysis.
2. Self-sensing structure such a platform is based on three independent forms: (A) SHM data acquisition in which signals are acquired and analysed, removing errors on statistical basis. (B) FEM-based platform in which the RAPID algorithm was shown to be the most robust method of the developed methodologies (AS05) for all three levels of assessment, which included coupon, mono-stringer panel (experimental data). The platform also provides self-diagnostic capabilities using EMI to detect faulty sensors. A numerical model of the full wing demonstrator including all the details has been developed and validated for guided wave simulation of the full wing demonstrator prior to the final test. (C) Reliability-based optimization of the life-cycle cost of a smart aircraft component is developed in the framework of a Bayesian damage update

methodology by following a damage tolerant approach (FAA AC No: 20-107B). SHM effectiveness will be finalized into a value for risk analysis.

3. Three outer manhole covers were designed and manufactured for improved damage tolerance by using CFRP in combination with nanomaterials. The damage tolerance performance will be demonstrated on separately manufactured specimens and instrumented impact on a flat CFRP panels. The panels represent the slightly curved cover. The residual compression strength of baseline and new outer manhole covers will be compared.
4. A monitoring system was designed and installed on composite spars, with the aim of mapping the load conditions along the axes of such components. Such system is based on optical fibres embedded in ribbons, which were externally bonded to the spars according to a specific optical architecture. An algorithm for the identification of a parameterized load system was developed to define the network of sensors and assess potential performances in the presence of uncertainties.
5. Outer wing box design and assembly of parts were performed by Alenia with state-of-the-art technologies regarding integrated CFRP components and assembly (such as hot-forming process, flexible jigs, positive feed motors and one-shot drilling). Manufacturing was carried out by the following: EADS IW G winglet, CIRA/Aernnova trailing edge, DLR leading edge, INASCO ribs, BAB lower panel, RDM front/rear spar, top panel, rib post and interface ribs.

2 Demonstrator Morphing

G.M. Carossa

Alenia Aermacchi, Turin, Italy

The aim of morphing device studies in SARISTU, IS12, is to demonstrate the mechanical functionality, under aerodynamic loads, of three innovative components: morphing winglet, trailing edge and droop nose when integrated into a full-scale wing section. The device concepts, developed in the dedicated application scenarios, have been designed, sized and manufactured following aeromechanical requirements such as A/C and reference wing geometry, required morphed shapes, relevant structural loads and device extensions. All these data have been defined in IS12 at beginning of the Project. Following the development of project, the full-scale wing demo (a real wing section equipped with full-scale active morphing devices) for functional demonstrations has been realized. Wind tunnel instrumentation and test (low speed) requirements have been defined. Project “value” high-level parameter assessment is the aim of the final project phase for morphing devices. This goal is planned to be reached by means of an articulated process based on two main workflows. First, a multidisciplinary aeromechanical assessment (loads, aeroelasticity, aerodynamics) at A/C level, comparing the wing morphing

concept responses with the initial requirements, is going to be performed. Second but fundamental step for “Value” demonstration phase is the wind tunnel full-scale wing demo tests. Objectives of tests are morphing device functional test under loads, actuation, sensors and mechanical aspect verification of the developed morphing devices. This to verify the morphing actuation power needs and actuation loads initial predictions, morphing reached shapes quality, to investigate their aeroelastics characteristics when integrated into wing box, to verify structural loads alleviation effectiveness (for WATE) in open loop. An A/C level performance assessment of the morphing configuration shall be performed so to finalize the project “value”. The assessment will be based on results of both of previously described steps: weight, complexity, safety issues, experimental validation about actuation performances, loads alleviation effectiveness and aero-elastic issues.

3 Wing Box Top Panel Spar Steel and Aluminium Parts

Michelangelo Giuliani

REDAM, Avellino, Italy

In IS12, REDAM has controlled the development of the project, the structural analysis of the assembly of the demonstrator and the manufacturing process of different parts. Particularly, REDAM designed, sized and manufactured two top panel wing skins and two rear spars. Also in this phase of the project, REDAM acquired the original 3D models of the entire demonstrator, without any geometric information. REDAM had to remodel all parts and produce related drawing in order to support industrialization. REDAM had to convert original metric measure (especially for fasteners) in US measure in according with 2D DWG SARISTU wind tunnel test and 2D DWG SARISTU structural test (made by REDAM under ALENIA responsibility).

Finally, REDAM produced.

- For the wing tunnel demonstrator:
 - CFRP parts—Top panel, rear spar, front spar, fairing LE root, fairing TE root, fairing LE tip and fairing TE tip.
 - Steel part: Root rib
 - Aluminium part: TE root fairing, Rib TE and LE (root and tip), Rib post, shim, end rib and saddles for lifting.
- For the integrated SHM testing demonstrator,
 - CFRP parts—Top panel, rear spar, front spar,
 - Steel part: Root rib
 - Aluminium part: Angle root Rib, Rib post, shim, end rib and saddles.

- The top panel formed by two parts: panel + stringer panel; parts are fibre tape (CYCOM 977-2-34-24KIMS-196-T1-150), fabric (CYCOM 977-40-3KHTA-PW-193-1067) and glass fabric (GT25810;SPEC-J-513-E-3033;HEXCEL); it was cured in autoclave using a dedicated mould.
- Rear spar is manufactured in fibre tape (CYCOM 977-2-34-24KIMS-196-T1-150), fabric (CYCOM 977-40-3KHTA-PW-193-1067) and glass fabric (GT25810;SPEC-J-513-E-3033;HEXCEL); it was cured in autoclave using a dedicated mould. The tool is composed of two aluminium plates base + mould CNC machining (base mat. 5083 3380 × 300 × 20, mould mat. 5083 3220 × 130 × 110), on which will be laminated the rear spar. The mandrel has been made taking into account a possible spring back of the material after cure. The thermal expansion coefficient was applied on the tool to avoid dimensioning errors of part after treatment in autoclave.
- Front spar is manufactured in carbon fibre tape (CYCOM 977-2-34-24KIMS-196-T1-150) and fabric (CYCOM 977-40-3KHTA-PW-193-1067), glass fabric (GT25810;SPEC-J-513-E-3033;HEXCEL), it was cured in autoclave using a dedicated mould. The tool is composed of two aluminium plates base + mould CNC machining (base mat. 5083 3500 × 300 × 20, mould mat. 5083 3300 × 307.5 × 200), on which will be laminated the front spar. The mandrel has been made taking into account a possible spring back of the material after cure. The thermal expansion coefficient was applied on the tool to avoid dimensioning errors of part after treatment in autoclave.

4 Wing Box Lower Panel

Alan Johnston

BAB, Belfast, Northern Ireland

In IS12, Bombardier designed, sized and manufactured two off resin transfer infused (RTI) patented lower wing skins for the wing demonstrator's.

The first panel used on the wind tunnel demonstrator consisted of a dry carbon fibre matl toughened with a thermoplastic veil down selected from trials in WP9. This enabled Bombardier to conduct process optimization trials on a small-scale demonstrator.

The second lower panel which was used for integrated SHM testing was manufactured with Bombardiers' baseline RTI dry carbon fibre matl and resin matrix as this was the material used to manufacture the flat plaque and three-bladed panels supplied to the WP4 and WP5 partners during the SHM development phase.

Bombardier will also be conducting sensor cure monitoring trials during the infusion of a third SARISTU lower panel to conclude Bombardier deliverables within SARISTU.

Bombardier SARISTU project achievements

- Dedicated strategic technology research wing panel demo tooling for future wing development
- Access to project results on SHM and morphing structure as a potential end user
- Toughened non-crimp fabric material manufacturing and NDT trials to TRL5
- Step closer to producing net size apertures on RTI panels to reduce 5 axis machine time
- Alternative methods of preforming dry carbon fibre wing skins to reduce autoclave bottlenecks (heated tool, infrared lights, hot air recirculation)
- Process trials of new IML bagging elastomer materials
- Application and testing of water-based release agents on SARISTU tooling
- Sensor monitoring during cure (resin arrival and cure)
- Wing panel design for future automated fibre placement trials
- Preform tool to cure tool transfer trials of wing skins without overhead cranes

5 Design and Manufacturing of Manhole Covers

Christina Altkvist

SAAB, Linköping, Sweden

Concept:

- Outer Door—designed for improved damage tolerance by using CFRP in combination with Saab existing nanotechnology (background knowledge)
- Inner Door—to meet design requirements but will not contribute to damage tolerant improvement

Design:

- Outer door—monolithic CFRP laminate design with constant thickness. Bronze mesh for bonding and GFRP strip for galvanic protection included.
- Inner door—Simplified machined aluminium including sealing slot and pressure proof fasteners.

Manufacturing:

- Tool concept to include manufacturing of two doors simultaneously, same geometry used for all covers.
- 2 shipset, 3 + 3 covers manufactured.
- Predrilled holes in inner door used for assembly to drill in suit holes in outer door. All fasteners “temporary” installed prior to delivery.

Nanotechnology for damage tolerance improvement:

- Demonstrated on separately manufactured CAI specimens and instrumented impacts on a flat CFRP panel representing the slightly curved door
- CAI specimens will be cut from the impacted flat door panel and residual compression strength of baseline, and damage tolerant sections will be compared

6 Wing Box Load Monitoring System

Alessandro Airoidi

Politecnico di Milano, Milan, Italy

Optical fibres represent a feasible technology to install health and usage monitoring systems that may have a key role in the definition of new strategies for the design and the maintenance of modern aerospace composite structures. Indeed, fibre Bragg gratings (FBG) carried by optical fibres can measure localized strains, being immune from electromagnetic interferences, at a weight cost that is a small fraction of the one required by traditional strain gauges, including all the auxiliary systems required for sensor interrogation.

A relatively dense network of sensors can be applied to the main structural components of a wing box to reconstruct the strain field for a more detailed evaluation of the internal loads and of the loads transmitted by the surrounding components. Such system could provide a detailed knowledge of load conditions in the most important structural parts, with significant information to define and update maintenance operations. Moreover, the availability of a continuous monitoring of the structural response can be exploited to detect the modification of load paths derived from structural ageing, by the presence of damage in redundant parts and by the introduction of new flight configurations.

Such objectives were considered to design a load monitoring system for the spars of the wing demonstrator developed for project SARISTU. Physical integration was based on ribbons, made of glass fibre-reinforced composite plies and endowed with FBGs', which were bonded to the surface of the C-shaped spar. Up to six ribbons were installed in all the 7 bays of both rear and forward spar, as it is exemplified in Fig. 1. Each spar can typically carry three FBG sensors, thus leading to a number of about 120 available positions for each spar, which are represented by the red dots in Fig. 2.

An algorithm was developed to allow the identification, from the signals acquired by the FBGs, of a parameterized system of loads. Such system includes both concentrated loads, transmitted from the rib posts to the spar and distributed loads, applied by the lower and upper skins, for a total number of 29 components,

Fig. 1 Installation of sensorized ribbons in the spars

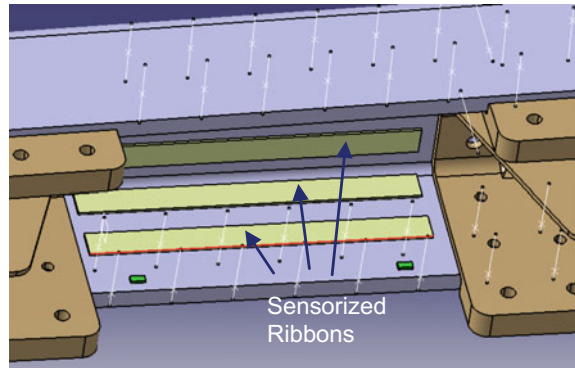
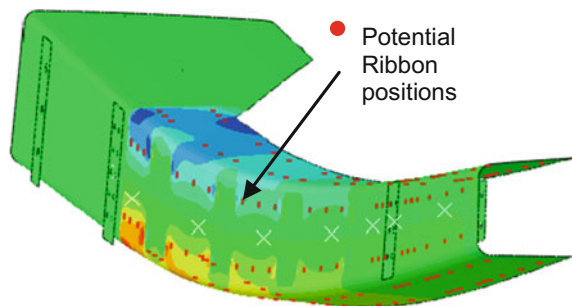


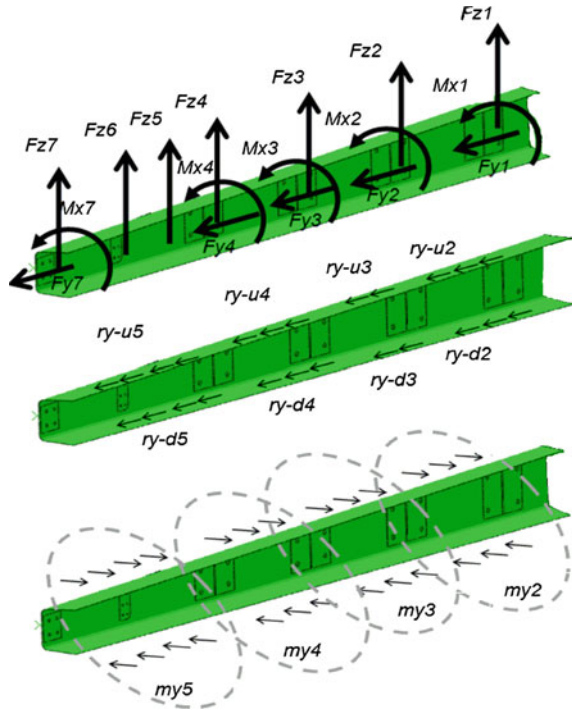
Fig. 2 Numerical strain field and available sensor locations



which are presented in Fig. 3. The local strain is considered as a superposition of the effects induced by each load component, which can be expressed by a vector of influence coefficients $\{\alpha\}_i$, such that $\{\varepsilon^*\}_i = \{\alpha\}_i F_i$. For the development of an identification algorithm, the knowledge of such influence coefficients is required and this can be obtained by developing a finite element model of the spar, as it is shown in Fig. 2.

Once that the influence coefficients are known, an algorithm based on a least square approach is used to identify the load condition from the strain signals acquired by the monitoring system. The number of active sensors and their positions was chosen considering possible discrepancies between the models used to calculate the coefficient $\{\alpha\}_i$ and the rear spar. A numerical activity showed that, in case of discrepancies of ply thickness and orientation, an increment of the number of sensors does lead to a reduction of the mean error and of the maximum error that is done in the identification of load parameters. For such a reason, a number of about 80 sensors were chosen, with positions selected among the potential available positions in the ribbons bonded to the spar. Expected performances indicate the possibility of identifying the main vertical components with an error lower than 10 %, in the presence of discrepancies that were assigned according to a Gaussian distribution with a coefficient of variance of 5 % for ply thickness and 2° for ply orientation.

Fig. 3 Parameterized system of loads



7 Damage Detection Platform for Composite Wing Box Demonstrator

Z. Sharif Khodaei and M.H. Aliabadi

Imperial College London, London, UK

Abstract: This paper reports on the development of a SHM methodology and technology platform as part of the wing design platform. The aim of the SHM platform is to integrate suitable damage detection methodologies from the application scenario 5 (AS05) into a single design architecture which will allow optimization of sensor positions, technologies and system fault analysis for test. The integration strategy is divided into two main steps: (1) methodology integration and (2) technology integration. The methodology selection was carried out in 3 different levels representing coupon, element and component levels to select the most appropriate and reliable methodology for a large complex structure such as a wing demonstrator. This step constituted an independent assessment of the damage detection methodologies and their potential for up-scaling to complex configurations. As a result, the most appropriate techniques were chosen and implemented into the platform which then is used to assess their applicability to a full-scale demonstrator. The focus of the paper will be on the selected methodology and its

application to the wing demonstrator. Detailed description of the damage detection methodologies is provided in papers by the partners in application scenario 5 and will not be reported here. After methodology selection, sensor number and positions are optimized based on maximum area coverage (MAC) applying genetic algorithm to maximize the most probable likelihood detection.

This paper is focused on the methodology selection, verification and integration together with the technology platform to be tested on a full-scale demonstrator. The full-scale demonstrator is modelled numerically using a finite element model validated at levels 1 and 2. The developed platform however has the capability to run with virtual model as well as signals coming from real test scenario.

The first part of the paper is devoted to the detailed description of the platform architecture and its functions, followed by the methodology integration and verification. To demonstrate scale-up of the integrated technique for a full-scale wing demonstrator, numerical signals are generated using (previously validated) advanced numerical techniques. The full description of the technology platform is also included describing the specifications of the data acquisition system (DAQ) based on guided wave technology for damage assessment. The architecture of the DAQ system is designed to be capable of providing sensor data in the format applicable to the integrated SHM methodologies and to allow the simultaneous acquisition of multiple PZT sensors (up to 160 sensors).

8 Conclusion

The IS12 major innovation in aircraft wing production is achieved by initiating a step change in the inherent capabilities of aircraft structures. Each of the two technology streams (morphing, SHM) offers great product improvements. Optimizing aircraft aerodynamic performance and weight leads to less fuel consumption. Aircraft operational cost will be reduced by increased availability and reduced inspection times. The general objective of the SHM work is to develop built-in real-time structural health monitoring systems, manufactured and assembled for an outer wing box. The developed technology could potentially result in higher structural safety and reduced inspection time for impact damage identification. Specifically, IS12 will target operating cost reduction through a first level of automatic inspection. The combination of shape and strain sensing with morphing concepts which include inherent damage detection capabilities at full-scale level is a significant innovation in the context of the competition in the worldwide civil aircraft industry.

Implementation of a Structural Health Monitoring System for a Composite Wing Box Skin

Alessandro Marzani, Nicola Testoni, Luca De Marchi, Ernesto Monaco, Zahra Sharif Khodaei, M.H. Aliabadi and Julio Viana

Abstract This paper reports on the implementation of a structural health monitoring (SHM) system devoted to delamination detection on the wing box demonstrator. The developed SHM system is capable to control a network of up to 160 piezoelectric transducers that are surface mounted on the structure. The SHM system is able to perform both electromechanical impedance (EMI) measurement at each transducer to check their reliability and their bonding strength to perform an active guided wave (GW) screening. This latter operation exploits the damage detection methodologies that have been developed in the AS05/IS12 scenario to

A. Marzani (✉)

Department of Civil, Chemical, Environmental and Materials Engineering—DICAM,
University of Bologna, Viale del Risorgimento 2, 40136 Bologna, Italy
e-mail: alessandro.marzani@unibo.it

N. Testoni · L. De Marchi

Department of Electrical, Electronic and Information Engineering—DEI, University of
Bologna, Viale del Risorgimento 2, 40136 Bologna, Italy
e-mail: nicola.testoni@unibo.it

L. De Marchi

e-mail: l.demarchi@unibo.it

E. Monaco

Department of Aerospace Engineering, University of Naples Federico II, Via Claudio 21,
80125 Naples, Napoli, Italy
e-mail: ermonaco@unina.it

Z. Sharif Khodaei · M.H. Aliabadi

Department of Aeronautics, Imperial College London, South Kensington Campus, London
SW7 2AZ, UK
e-mail: z.sharif-khodaei@imperial.ac.uk

M.H. Aliabadi

e-mail: m.h.aliabadi@imperial.ac.uk

J. Viana

Critical Materials, Science and Technology Park, Caldas das Taipas, 4806-909 Guimares,
Portugal
e-mail: jviana@critical-materials.com

detect damages. Some information and results of a first experimental test carried out at the ALENIA facilities will be given.

1 Introduction

This work reports on the implementation of a structural health monitoring (SHM) system based on electromechanical impedance (EMI) and guided wave (GW) diagnosis for the composite lower wing panel of the wing box. The development of the system is based on a virtual design platform (Sect. 2) and on a technological platform (Sect. 3) as core parts of an SHM methodology platform developed as part of the wing design platform. The aim of the SHM platform is to integrate damage detection methodologies, which are being developed in other application scenarios, into a single design architecture which will allow optimisation of sensor positions, technologies and system fault analysis for test. The integration strategy is divided into two main steps: (1) methodology integration and (2) technology integration. An extensive research has been conducted in AS01-07 on various SHM tools and procedures. As a result, the most appropriate techniques are chosen (as recommended by scenario leaders) and implemented into a single reliability-based platform which then used to assess their applicability to a full-scale demonstrator

The document will pave the path for the integration of the SHM methodologies in the wing demonstrator for the experimental verification of their performance as well as for the experimental evaluation of the finally considered SHM system.

2 Virtual Design Platform

The main objective of the platform is to design and develop a SHM platform for the integration of the methodologies and technologies established in AS01-05 for damage detection at demonstrator level, as shown in Fig. 1.

The methodologies were developed and tested at coupon and component levels in AS05. However, there will be scale-up issues when applied to a full wing demonstrator. In addition, the geometry and lay-up of the demonstrator could lead to some of the methodologies not being applicable in parts or sections of the wing. An output of the SHM platform is to identify these issues and assess the applicability of the developed methodologies.

The following objectives are covered:

1. Integration and verification: each methodology developed in AS05 is assessed at three different levels. Levels 1 and 2 involve methodology assessments using the experimental results from AS05 with the coupons manufactured by Bombardier

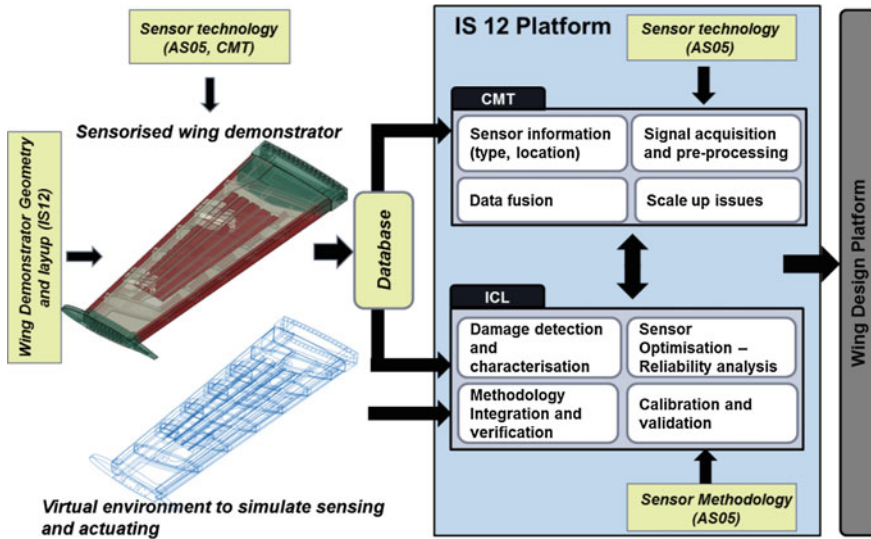


Fig. 1 Architecture of the integration platform

(throughout the report, these panels are referred to as flat and/or stiffened BAB panels). Level 3 consists of testing the methodologies on different bays of the wing demonstrator model. As a result of the assessment, the methodologies to be integrated in the final version of the platform (allowing for optimisation) are selected.

2. Robustness: it is addressed in two ways: (a) robustness of the integrated methodologies and (b) robustness of the multilevel damage detection platform. Robustness of the integrated methodologies is addressed in this report in assessment levels 2 and 3 by identifying the factors influencing the output of the damage detection methodologies such as threshold for damage index (DI), range of frequencies and applicability to different geometry. Robustness of the SHM platform is assessed by testing the platform in several bays with various damage size, location and severity, for levels 1 and 2 damage detection when one or more sensors fail and the effect of sensor positioning tolerance on the output.
3. Development of SHM methodologies at demonstrator level: This step is carried out after assessing the methodologies from AS05 by tailoring them to comply with the complex geometric features of the demonstrator and allowing for a multilevel detection.

There needs to be information flowing back and forth between the technology and methodology platforms. After the final number and position of the sensors are decided as the result of optimisation, the baseline signals for a range of frequencies will have to be obtained and stored in a database library. This step is done by the technology platform. After an impact test, the users have the choice to decide which part of the structure will have to be interrogated (all bays or some parts). The

platform architecture is designed in order for the user to choose an interrogated area; this information will be shared with the technology platform; and consequently, the baseline and current signals corresponding to the appropriate sensors in the interrogation region as well as relevant section properties will be the input to the methodology platform for damage detection diagnosis.

The platform is established in a virtual environment to enable an optimisation analysis for sensor positioning. Therefore, the first step was to establish a valid and accurate FE model. However, the main objective of the platform is damage detection. As a result of the methodology assessment (carried out in 3 levels), the most appropriate methodologies are chosen for integration into the final SHM platform to allow for optimisation of sensor positions. Damage detection is carried out in 2 different levels: (1) level 1 using the minimum number of actuators and sensors to detect the presence of damage and localise it to a certain bay and (2) level 2 using an array of transducers to detect and characterise damage locally. The inputs to the damage detection platform are baseline and current state Lamb wave signals which are possible with both numerical and experimental data. The experimental signals will be input from the technology platform. To allow for optimisation, the virtual model of the wing demonstrator is used to replicate numerous sensing and actuating using the developed SMART elements. At the final stage of the project, the SHM platform will be tested after impacting the demonstrator in several locations as shown in Fig. 2. These damage scenarios will be used for optimisation and finally in assessing the reliability of the final platform.

2.1 Methodology Integration from AS05

Various methodologies for damage detection and characterisation have been developed in AS05 for coupon and component levels. The aim of the IS12 platform is to integrate the methodologies reported to verify their applicability on the full

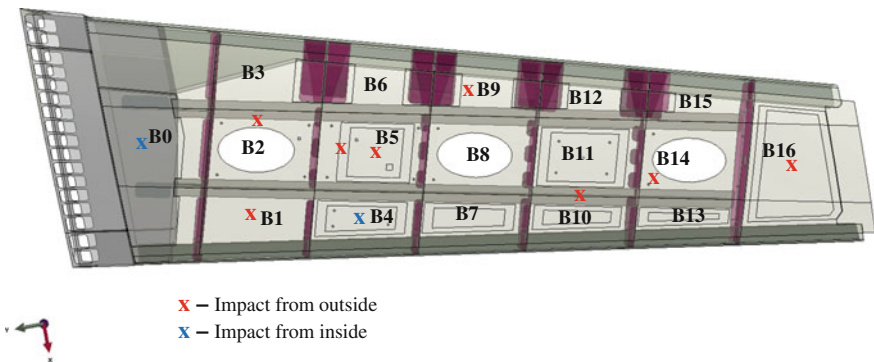


Fig. 2 Impact locations to be tested for damage detection on the demonstrator

demonstrator and identify scale-up issues. The assessments of methodologies are carried out in three different stages:

1. To test and verify each methodology with the sample signals sent by the developers.
2. The second level of assessment is to integrate the AS05 methodologies into the damage detection platform and test them with other signals (different frequencies, signal length, sensor positions, etc.) to further assess their applicability for flat and stiffened panels at component level. For example, signals from KU Leuven (KUL) were used to test the methodology developed by UNINA. As a result of level 2 assessment, a decision was made on the methodologies to be integrated and tested on the full demonstrator panel.
3. Last stage is to assess the final version of the integrated methodologies on various sections of the demonstrators and for a number of damage scenarios (100, 300 and 625 mm²). The 300 mm² damage has been considered as a result of minimum damage size from AS05 impact tests, although the final size of BVID has not been confirmed yet. The details of the numerical test (sampling frequency, excitation frequency, number and location of sensors, etc.) have been agreed on with the AS05 partners for each methodology.

All three partners in AS05, UNINA, KUL and UNIBO have tested flat and stiffened panels manufactured by Bombardier. They have provided ICL with their sensor signals together with the source code/executable for damage detection. So the first step was to run each methodology with the examples tested and provided by each partner to ensure the correct data handling and execution of the methodologies. This step was done in collaboration with each partner. After level 1 and level 2 assessments, it was concluded that the RAPID algorithm developed by KUL had the maturity level to be integrated into the full platform. Only, level 3 results are presented in this paper.

2.2 Numerical Modelling of the Full Wing Demonstrator

The final level of methodology assessment is to verify the integration methodologies (developed by KUL) in the final IS12 reliability-based platform for different damage sizes (100, 300 and ~600 mm²) and location (centre of the bay, close to an opening, etc.) on the full wing demonstrator model, to assess their reliability. The full wing demonstrator will be tested experimentally at the end of the project; therefore, at this stage, for development purposes and to allow for reliability analysis and sensor placement optimisation, a valid numerical model is required.

To be able to assess the developed damage detection methodologies for the wing demonstrator, the Lamb wave actuation and propagation in the full wing need to be modelled numerically. For numerical simulation of Lamb wave propagation, commercial code ABAQUS is used.

Wave propagation in plates is a dynamic problem and highly mesh dependent. To solve the equation of motion, ABAQUS software provides two solver options: (1) direct integration dynamic procedure provided in ABAQUS standard with the choice of implicit solver and (2) ABAQUS explicit procedure which uses the central-difference operator. Because the central-difference operator is only conditionally stable, the size of the time increment in an explicit analysis is limited in comparison with implicit analysis which is unconditionally stable. Therefore, an algorithm has been developed to calculate the stable time increment and appropriate mesh size. The numerical modelling technique developed has been extensively investigated and validated against experimental results which include (i) types of elements and meshing technique, (ii) convergence study, (iii) change in thickness, (iv) Lamb wave attenuation, (v) damage modelling approach and (vi) verification and calibration at demonstrator level. Some of the results are presented in this paper.

Due to the size and complexity of the demonstrator (change in thickness of the lower wing plate, large manholes, etc.) and the requirements on the mesh size and stable time increment, to keep the size of the model realistic, layered shell elements (conventional shell) are used for modelling the lower skin panel as composite laminate, as it was validated at the component level. The SMART FE option in the platform allows the user to find what are the min mesh size and the corresponding stable time increment for any actuation frequency. Convergence study was carried out on the composite plates provided by Bombardier (BAB) representing sections of the final wing demonstrator (6.4 mm thickness and size $300 \times 225 \text{ mm}^2$). It was confirmed that for 100 kHz excitation frequency, the converged solution was reached at 30 NPW mesh size in the plate. The result of the convergence study is shown in Fig. 3 where 10, 20, 30 and 40 NPW correspond to 5.6-, 2.8-, 1.9- and 1.4-mm mesh, respectively. The sensor signals from 30 and 40 NPW mesh size match exactly; therefore, 30 NPW was chosen as the converged mesh (for simplicity, 2 mm mesh size was chosen and results matched with 1.9 mm).

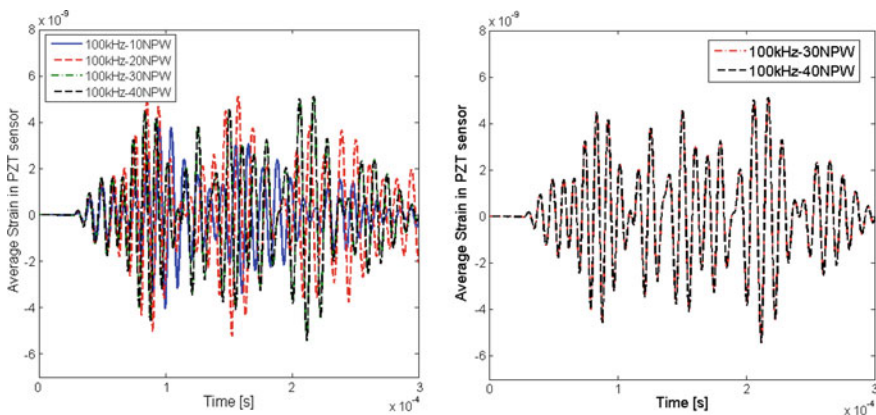


Fig. 3 Mesh convergence for 100 kHz excitation and different mesh size

For a 2-mm mesh (corresponding to 30 nodes per wavelength, NPW, for 100 kHz of excitation frequency) for the lower wing panel, the total number of the DoF in the whole model results in 4,163,097 which can only run on a high-performance computing (HPC) unit. The corresponding stable time increment was calculated to be $1.7e-7$ s which shows how demanding the simulation will be for a running time of $3e-4$ s. The total time period for each simulation is dependent on the excitation frequency. Once the excitation frequency is chosen, the velocity of first mode can be calculated, and depending on the interrogation area, the appropriate time period will be decided for each analysis. The wave propagation in complex parts of the panel such as bays with large openings, changing cross section and across stiffener and frames will be investigated to assess the application of SHM methodologies in those regions (Fig. 4).

The lower panel is modelled as composite laminate with difference thickness and lay-up for each section and bay as it is provided by BAB. To give a better representation of the developed FE model, Fig. 5 shows the lower wing panel with varying thickness and lay-up together with its structural mesh. Each different colour represents different cross-sectional lay-up and thickness.

Types of damage which result from impact on composite structures are delamination and fibre/matrix breakage. What has been carried out so far numerically was to model an impact event which caused 100 mm^2 BVID damage on the lower skin panel.

Two different impact energies were tested on the demonstrator, 35 and 50 J. A nonlinear contact algorithm was developed to accurately model the interaction between impactor and the lower skin. An explicit analysis was created by ABAQUS and run on an HPC unit due to its high computational cost. The 50 J

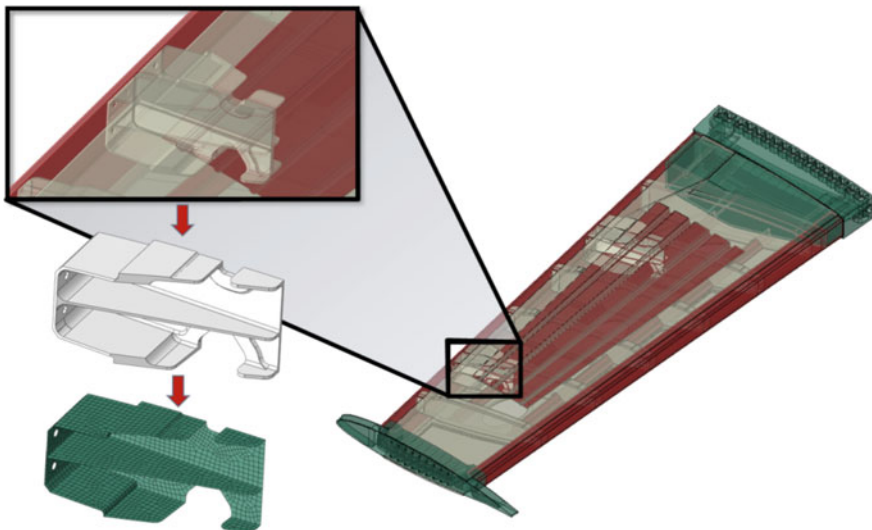


Fig. 4 Generating full FE model of the demonstrator

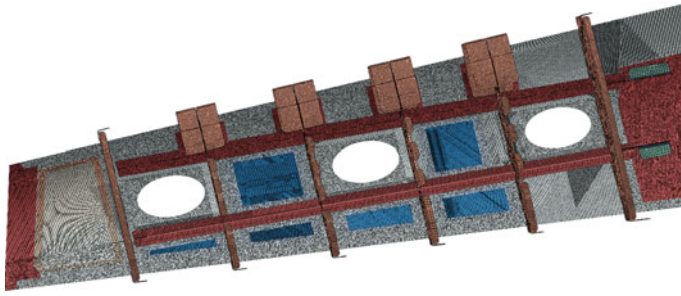


Fig. 5 FE model of the lower wing panel with various sections

impact energy resulted in around 100 mm² of damage. In the absence of real damage parameters of the material, similar material models published in the literature were used. The material damage model used includes four different damage initiation mechanisms plus damage in shear: fibre tension, fibre compression, matrix tension, matrix compression and shear damage. As it can be seen in Fig. 6, the damage can be predicted in each ply. The output of the analysis is a DI for each type of damage, going from 0 to 1 meaning no damage and completely damaged. Therefore for each damage scenario (fibre compression, matrix tension, matrix compression and shear damage), the corresponding material degradation factor can be computed and the material with reduced properties will be introduced. Afterwards, the reduced material properties will be assigned to an area to represent damage in the corresponding plies. However, in the absence of accurate and reliable damage parameters for the materials used in the production of BAB panels, it will be unreliable to run a full impact analysis and find the corresponding damage. It is worth mentioning that the numerical representation of damage is a simplification of a real damage. Therefore, there will be significant differences between the scattered waves which will be recorded experimentally and numerical ones. One main reason for this will be the severity of damage (reduction in material properties) which is an

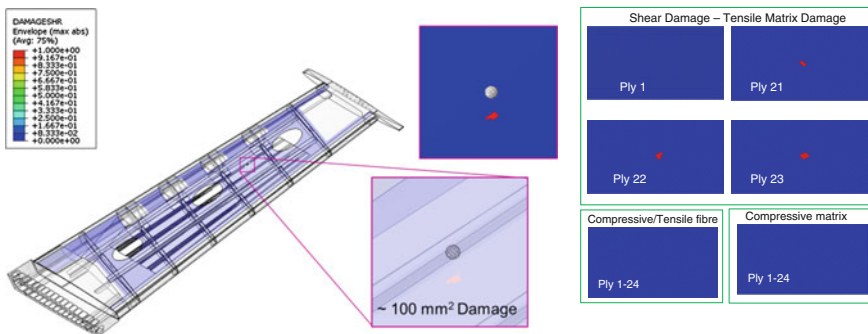


Fig. 6 Impact—50 J energy and the corresponding damage

unknown in the experiment. Moreover, in numerical models, the damage area will be modelled with clear edges which will reflect the wave much stronger than the real damage situation in the specimen.

2.3 Methodology Assessment at Level 3

Following the development of a validated numerical model, the next stage is to test the methodologies on different sections of the full wing demonstrator. Three different damage sizes (100, 300 and 625 mm²) and two different bays have been considered for this purpose (Bays 2 and 5), see Fig. 7a, b. All four damage scenarios have been assessed with both KUL and UNINA methodologies, and the results are presented in this section. It is worth mentioning that in Bay 5 where the lower panel consists of 24 plies (6.4 mm thickness), damage has been introduced as 50 % material degradation (softening) in plies 9–16. In Bay 2 (8.4 mm thickness), damage at position 4 close to the manhole was introduced as 50 % material degradation throughout all the plies.

C1-4 are the four reference points used for plotting the damage detection output as indicated in the following figures, and the coordinate axis shows the x- and y-directions of the result plots.

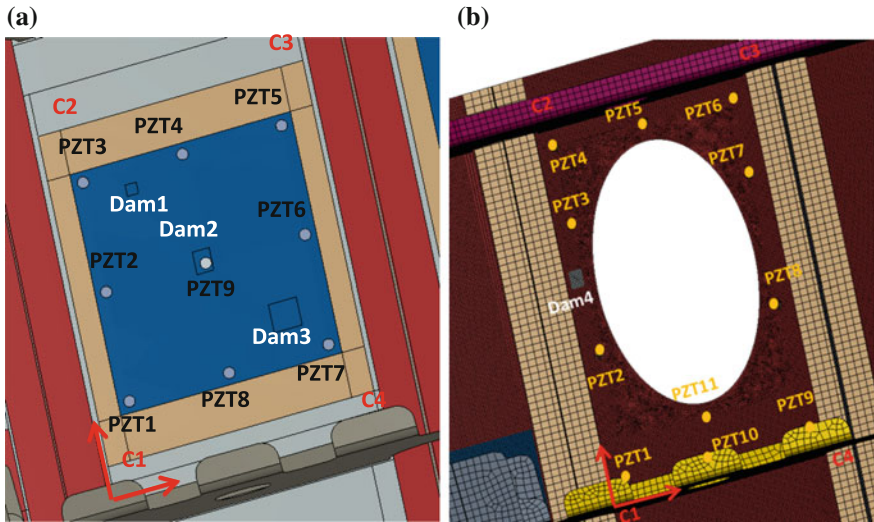


Fig. 7 Sensor lay-up and damage positions in Bays 2 and 5—Full wing demonstrator. **a** Bay 5. **b** Bay 2

2.3.1 Tomography Algorithm—KUL

The first part of the panel which was assessed is Bay 5 with three damage sizes and positions as shown in Fig. 7a. The tomography algorithm has several optional parameters to be changed such as the adaptive length and a threshold for the SDC value. Both options have been tested to find the best result. The results of the damage detection in Bay 5 are presented in Figs. 8, 9, 10, 11 and 12. The rectangle represents the simulated damage location and size. In all cases, it can be concluded that using 9 transducers, damage was successfully detected and located. To test the robustness of the methodology, the influence of removing some sensors on the output of the platform has been investigated. Figure 9 shows the results of the tomography approach when both sensors 1 and 9 have both been removed from the sensor array.

The next step is to test the methodology on a more complex bay: Bay 2 with a large manhole. The geometry of the section with the inserted damage and the sensor lay-up is shown in Fig. 7b, and the results of the damage detection using tomography approach are depicted in Fig. 12. The tomography approach is based on probability distribution of damage on a direct path between two transducers. As it can be seen from Fig. 12, even though damage can be detected in sections with large openings, because the algorithm does not consider the wave path going around the opening, the damage location is misdetected.

Another factor that has been considered in analysing the robustness of the platform is the effect of sensor placement on the output. Sensor 9 (in the middle of the bay) was given a tolerance of 5 % in both x - and y -direction, and it was observed that the result of the detection methodology remains unchanged, as shown

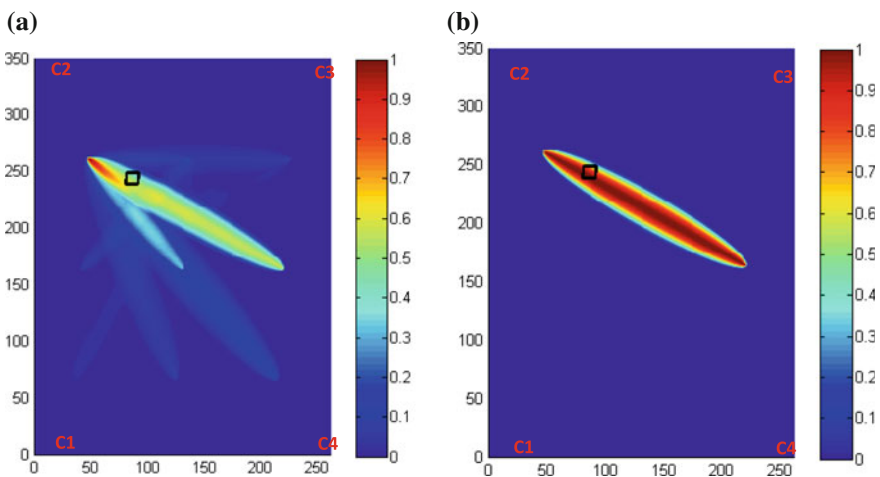


Fig. 8 Methodology platform using KUL tomography approach using all 9 transducers—Pos 1, 100 mm² damage in Bay 5, rectangle represents the damage area. **a** No adaptive length, no SDC threshold. **b** Adaptive length, SDC threshold

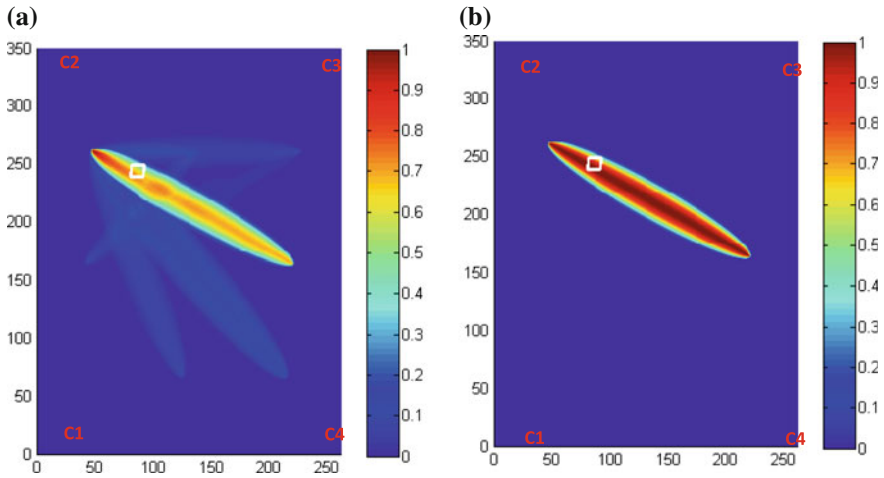


Fig. 9 Methodology platform using KUL tomography approach using all transducers (2:8)—Pos 1, 100 mm² damage in Bay 5. **a** No adaptive length, no SDC threshold. **b** Adaptive length, SDC threshold

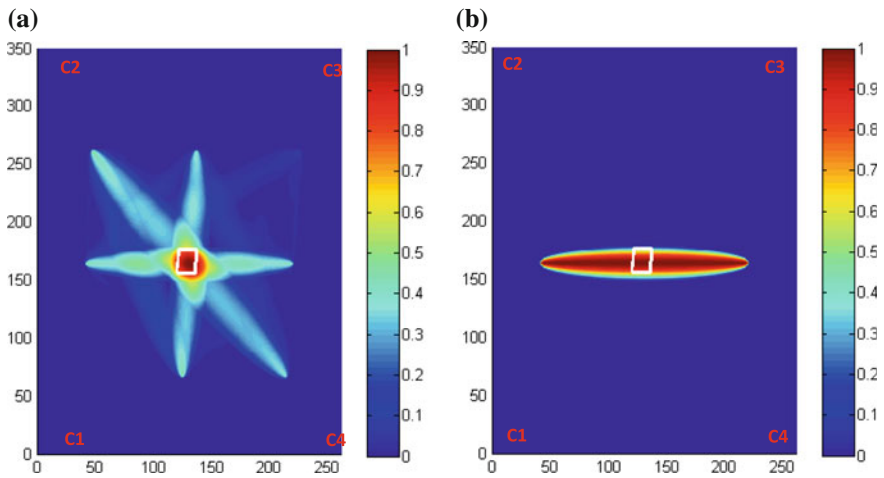


Fig. 10 Methodology platform using KUL tomography approach using some of the transducers (1:9)—Pos 2, 300 mm² damage in Bay 5. **a** No adaptive length, no SDC threshold—sensors 1 and 9 removed. **b** Adaptive length, SDC threshold—sensors 1 and 9 removed

in Fig. 11. One reason to have minimum effect on the detection is that the group velocity of the wave is defined as an input and the tolerance in the position of the sensor did not affect the velocity of the propagation.

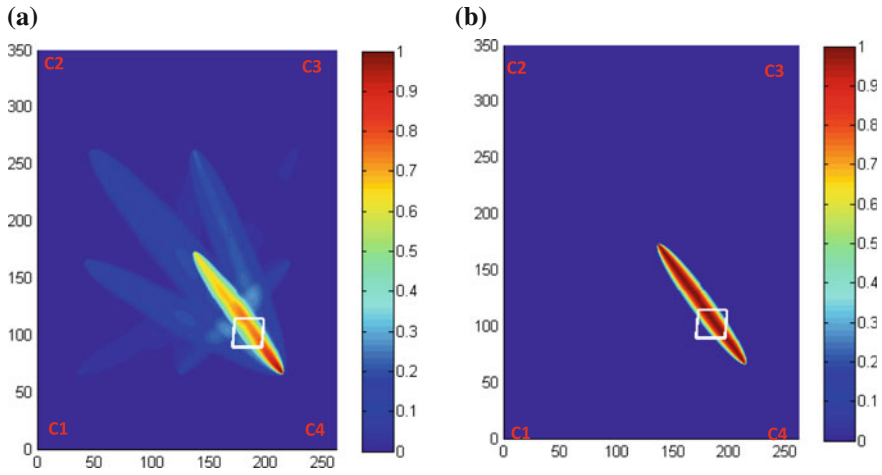


Fig. 11 Influence of the sensor positioning (sensor 9) on the detection results—robustness. **a** No adaptive length, no SDC threshold. **b** Adaptive length, SDC threshold

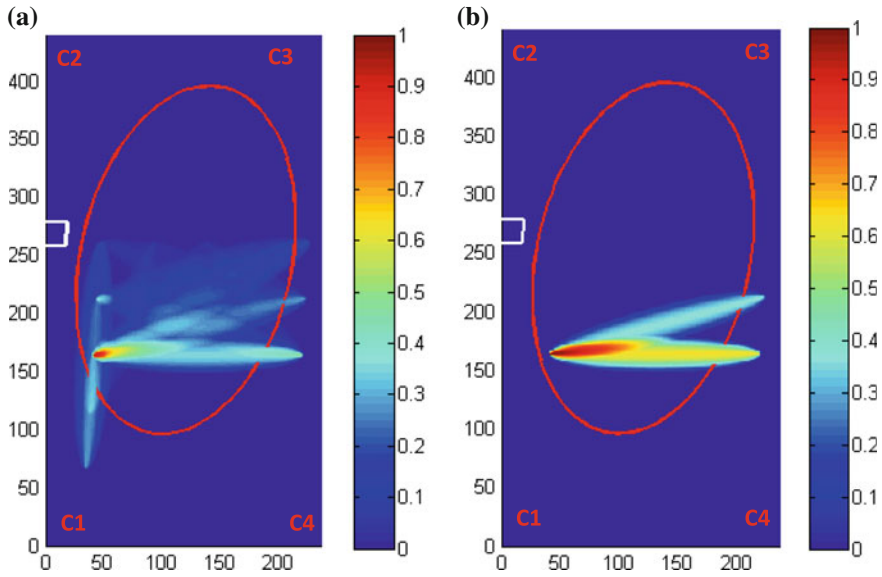


Fig. 12 Tomography Pos 3, 625 mm² damage in Bay 5—rectangle represents damage area. **a** No adaptive length, no SDC threshold. **b** Adaptive length, SDC threshold

2.3.2 Self-diagnosis—ICL

To assess the self-diagnosis application on the wing demonstrator, the midsection of Bay 5 with uniform thickness of 6.4 mm has been numerically assessed with 4 transducers placed in the corners, see Fig. 13.

Damage has been introduced as different degrees of debonding (25 and 50 %) between the transducer and the plate. Both RMSD values calculated from the real and imaginary part of the EMI measures are presented in Fig. 14. It is observed that the imaginary part of the impedance only shows RMSD values in PZT1 where debonding is simulated; therefore, it can be used for self-diagnosis of the sensor system.

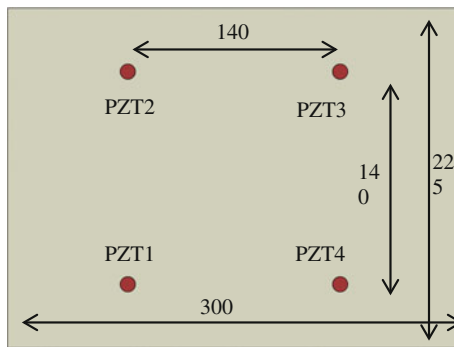


Fig. 13 Geometry and sensor positions

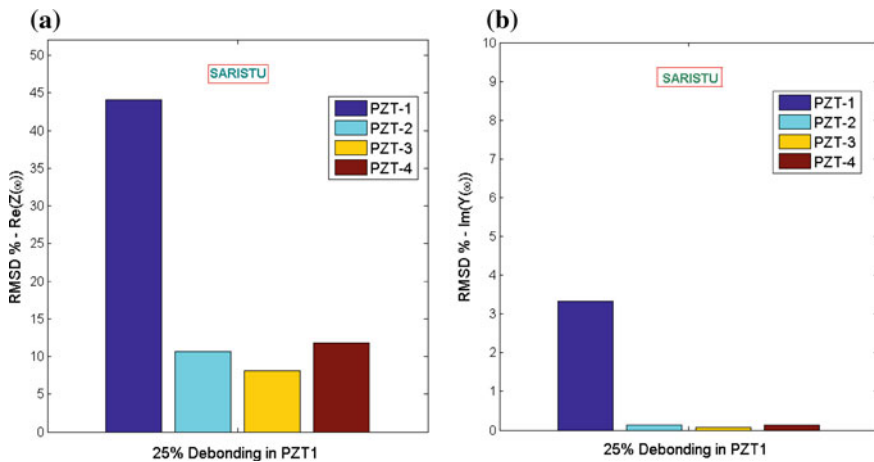


Fig. 14 Plots of RMSD for 25 % debonding in PZT1—Bay 5 demonstrator model. a Real part of impedance. b Imaginary part of impedance

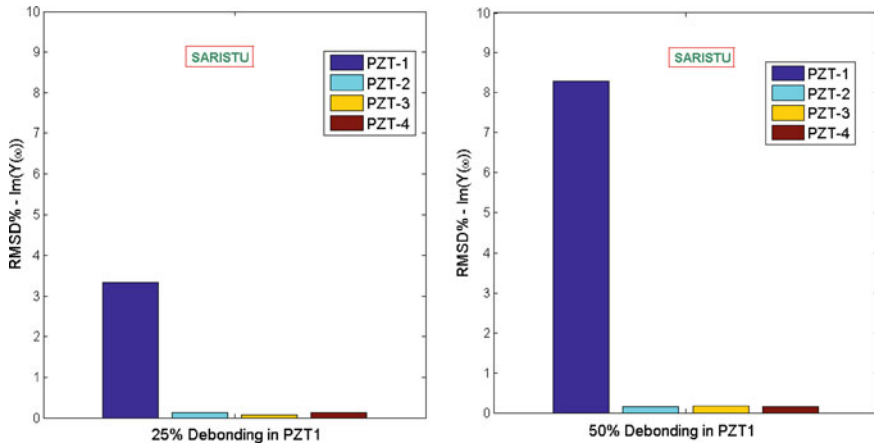


Fig. 15 RMSD value for different extend of damage

Figure 15 shows the output of the platform for both damage scenarios, obtained numerically from the imaginary part of the impedance. In both scenarios, the faulty sensor is detected successfully. Moreover, there is relationship between the extent of debonding and the damage index (RMSD), with higher values showing a more severe debonding. Therefore, the self-diagnosis directly contributes to the robustness of the platform and it eliminates false detection due to faulty sensors.

2.4 Conclusion

After a detailed assessment of all the developed methodologies in AS05, it was reported and concluded that the RAPID algorithm developed by KUL has shown to detect and localise damage with minimum of 8 transducers on the coupon level experimentally and different location and sizes of damage on different bays of the demonstrator level, although increasing the number of sensors to 16 will improved the robustness and reliability of the algorithm and other available techniques have demonstrated to detect BVID with fewer sensor numbers. Therefore, the RAPIS algorithm is integrated as the damage detection methodology for detection and characterisation.

In addition, the robustness of the platform was assessed by detecting various size and location of damage in different bays and by investigating the influence of failure of one or more sensors on the output of the damage detection. It can be concluded that the robustness is directly related to the optimum sensor number and position which will be the output of the optimisation analysis. The self-diagnosis capability of the damage detection platform (through EMI method) contributes directly to the robustness of the platform.

3 Experimental Platform

The proposed experimental platform is designed to operate guided wave-based methodologies developed in AS05/IS12 aimed at detecting defects, mainly delaminations, in structural components. Such methodologies generally exploit a network of piezoelectric transducers in which each transducer can act as actuator or sensor, alternatively. Thus, the experimental apparatus must be able to actuate and receive stress guided wave signals from the network of piezoelectric transducers bonded to the structure under inspection, whereas the processing phase, meant to translate the acquired signals into damage metrics, will be performed on a personal computer.

Since the adopted piezoelectric transducers are capacitive by nature, their use adds extra challenges in the development of a proper hardware system. For instance, common signal amplifiers used in standard ultrasonic applications are not suitable for this purpose due to the fact that the impedance of the transducers changes with frequency. A special amplifier is therefore needed to handle piezoelectric transducers used to actuate guided waves.

Furthermore, when the transducers are used as sensors, care must be taken because the low impedance inputs or high-value capacitive inputs change the behaviour of the sensors. Basically, there are two modes of reading piezoelectric sensors: voltage and charge. When the sensor is read as a voltage source, care must be taken on the parasitic capacitance of the cables and the input DAQ impedance. Input impedance must have high value of resistance and a low value of capacitance in order not to degrade the signals. The DAQ inputs must handle values of some micro-volts to hundreds of volts. A major advantage in reading the voltage of sensors is that any universal analogue input can be used to handle this kind of signals. Alternatively, reading the charge of the sensors has also some advantages, such as the elimination of the capacitive effect of the cable, but a major drawback that each input must have is a charge converter circuit and this is the reason why this approach is not popular on data acquisition systems and modular instruments. In addition, currents could be high on the cables compared with the voltage mode.

In guided wave analysis, each piezoelectric transducer acts sometimes as an actuator and other times as a sensor. This gives extra complexity to the system because the actuation and sensing architecture must be designed to handle both these operative modes. Also, care must be taken on the selection of the cables because they must handle big voltages and currents up to one ampere (Amp). The use of very thin section cables, in fact, could be sufficient to read the signals but not to excite the piezoelectric actuators. In addition, all cables should be shielded to reduce interference between channels (crosstalk).

All these issues have been taken into account in the development of the DAQ and will be described in the following.

3.1 Hardware

The proposed DAQ systems are composed by:

- a PXIe-1078 9-slot chassis unit from National Instrument (NI) embedding;
- a NI controller PXIe ExpressCard 8820;
- a PXI-6115 S Series Multifunction DAQ Module;
- a 5x PXIe-2529 High-Density Multiconfiguration Matrix;
- a TB-2636 Screw Terminal Block for NI PXI-2529 4×32 Matrix;
- an external electromechanical impedance measurement device (EMILIA);
- an external high-voltage amplifier.

The DAQ exploits LabVIEW Full Development System for Windows, and it is controlled by MATLAB.

The DAQ can be used to control at least 160 piezoelectric transducers to perform the guided wave-based screening. Each transducer is connected to the DAQ via proper cabling. Technically, the switching matrix will allow for dynamically selecting the transducer that will act as actuator and the ones (up to 3) which will be used as sensors to acquire the propagating waves. Thus, in the proposed architecture, the DAQ operates on 4 transducers at the same time instantly. Every time it is necessary to read a new group of 3 transducers, the switching matrix is reprogrammed. By means of the proposed architecture, all the transducers can be controlled by the DAQ system, so that the entire network of transducers can be considered as a whole, whereas the cost of the apparatus is controlled since it is not necessary to have multiple dedicated actuating and sensing devices connected to the transducers.

The DAQ is connected to an external personal computer with proper software (MATLAB) for the signal processing and damage metrics phase. It is worth noting that with the proposed configuration, it is possible to emulate phased array solutions by exploiting the fact that all the considered methodologies operate in the linear regime and by properly combining the results related to multiple acquisitions via software.

The DAQ control system integrates four main modules: an impedance analyser (EMILIA), an acquisition card (NI TB-2708), a high-voltage amplifier (RITEC) and an array of five switching matrixes (Fig. 16).

3.1.1 EMILIA

EMILIA is used to measure the impedance of one PZT. The EMI estimation procedure developed by FhG suggests to measure the piezoelectric transducer impedance as a function of the frequency in order to detect partial and/or total detachment of the transducer from the structure as well as transducer malfunctioning. EMILIA connectivity is based on the I2C bus, such that up to 112 devices

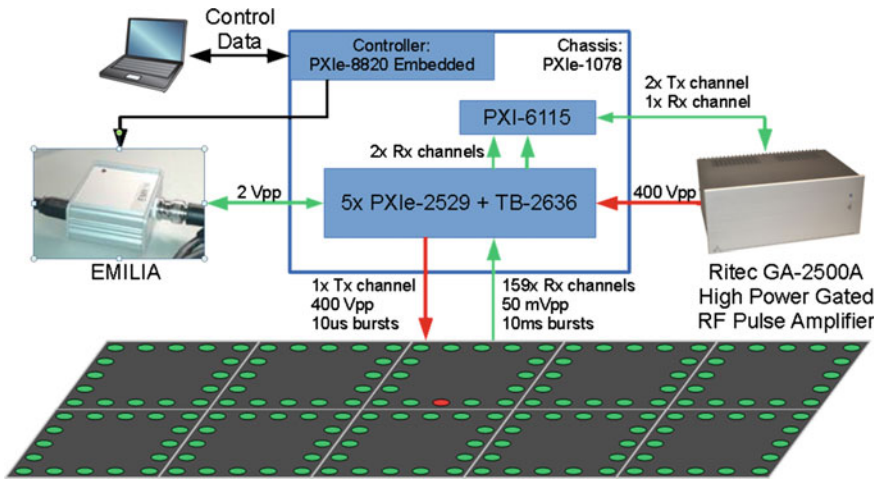


Fig. 16 Proposed DAQ architecture

can be connected to a single bus without requiring any additional hardware for network partitioning.

Specific care shall be placed to ensure the compatibility between the small signals measured by the EMILIA sensor node and the high-voltage actuation signals adopted in the guided wave measurements. Such a dedicated sensor-near circuitry is implemented to switch between the different measurement modalities and protect the EMILIA components from high-voltage signals. The EMILIA connects to the switching matrix on channel R0.

3.1.2 Acquisition Card NI TB-2708

According to document D51.2 (Design of SHM system), the overall highest sampling frequency is 100 MS/s and the highest bit rate is 14 bits. Based on recent activities, KUL can effectively operate also at 12 bits. Therefore, taking into consideration that the highest excited frequency used by all partners in AS05 is 400 kHz, it is possible to relax the sample rate to 10 MS/s and the bit rate to 12 bits, with a significant reduction of hardware cost. Considering the aforementioned linearity of the test problem, a digitising board with a minimum of 3 simultaneous sampling in DACs will be employed. A minimum of 16 MS data storage memory will be needed to cover up to 500 ms of recording on each channel. Hardware-implemented anti-aliasing filters with a cut-off frequency of at least 500 kHz will be used to reduce out-of-band noise and allow for better results during the interpolation and smoothing procedures that will be carried out to produce a virtual sampling frequency of 100 MS/s. Optionally, a virtual bit rate of 14 bits can also be obtained by applying proper signal processing techniques.

To such purposes, the acquisition card used is the NI TB-2708. The card has four analogue inputs (only three are used) and 2 analogue outputs. The acquisition card is responsible to control and monitor the amplifier output voltage and to read the response of the PZTs. The channels AI-0 and AI-1 are connected to the switching matrix's channels R1 and R2, respectively. The channels AI_2, AO_0 and AO_1 are connected to the amplifier on the ports: Tx Monitor output, LV signal input and Gate in. The channel HV_out connects to switching matrix's channel R3.

3.1.3 High-Voltage Amplifier

To deliver high-frequency, high-voltage systems to the piezoelectric transducers, a dedicate ultrasonic pulser shall be employed. According to the specifications discussed in section 4, this device shall be able to deliver at least 400 V_{pp} to the transducers at a frequency of 350 kHz by delivering a current of at least 1.8 A. As a consequence, considering a load of 4 nF and a continuous sinusoidal excitation, power amplifier featuring a slew rate of 450 V/ μ s and capable of delivering 35 W at least is required. To this purpose, an arbitrary waveform generator from NI (PXI-6115 S Series Multifunction DAQ Module) will be used to feed an high-voltage amplifier. A Ritec GA-2500A high-power gated RF pulse amplifier is adopted. This one-channel amplifier features an output voltage range in excess of 600 V_{pp}, an output current of 3.6 A, a slew rate of 6600 V/ μ s and a maximum RF pulse power of 400 kW over a full power frequency range of 30 kHz–2.5 MHz. This instrument is suited to drive DuraAct™ P-876.SP1 and DuraAct™ P-876.A15 transducers. By using this instrument, a particular attention shall be given to the baseline construction as, being the Ritec GA-2500A a gated amplifier, feedthrough is expected in correspondence of the opening and closing of the high-power drivers. Such undesired voltages can reach up to 35 V and in some cases may be intense enough to excite ultrasound waves in the driven piezoelectric transducers. A proper signal processing can be used to mitigate this problem by properly filtering the recorded signals. The amplifier amplifies the input signal (LV) generated by the acquisition card, and the output power signal is applied to the PZTs by the switching matrix.

3.1.4 Switching Matrix

In order to connect each transducer in the outer wing to the signal generation and acquisition equipment (DAQ), and to automate the baseline generation as well as the damage detection, a switching matrix (5x PXIe-2529 High-Density Multiconfiguration Matrix) is employed. State-of-the-art switching matrices have a switching bandwidth from DC to 500 MHz. Their configuration can be determined by terminal blocks allowing for multiple configurations on the same hardware, and they are ideal for flexible, high-channel-count applications where signals need to be routed from oscilloscopes, digital multimeters, arbitrary waveform

generators and power supplies to various test points on the demonstrator. The primary benefit in using a switching matrix consists in a simplified wiring since the overall test system can easily and dynamically change the internal connections path without any external manual intervention. This capability eliminates the need to duplicate instruments and thus reducing testing cost.

The switching matrix shall be able to withstand a maximum switching voltage of at least 400 Vpp (141 Vrms) and a maximum carry current of at least 1.8 A (required to drive a capacitance of 4 nF at 400 Vpp at the frequency of 350 kHz) and be characterised by a bandwidth of at least 3.5 MHz. A scan rate of at least 100 cycles/s will help in reducing the total amount of time required for acquiring a baseline for the whole outer wing.

The switching modules are five TB-2636 cards. The switching matrices are configured to 4 × 32 channel, where all matrices are connected in parallel on the side of the four channels, i.e. the R0 of all matrices are connected to each other, the same for R1, R2 and R3 channels. The channel R0 is connected to the EMILIA impedance measurement port. The channels R1 and R2 are connected to the channels AI_0 and AI_1 of the acquisition card, and finally, the R3 channel is connected to the HV out of high-voltage amplifier. In Fig. 17 is shown a summary of the connections explained above.

The PZTs are grouped into 10 sections of 16 elements. Each section corresponds to 16 consecutive channels of a switching matrix. The connections of each section to the switching matrix are shown in Fig. 18. Each PZT will be addressed by the section where it is belonging and by the channel in that section. The sections range from 0 to 9 and the channels from 0 to 15. Note that a section that starts in a C0 channel of a one of the matrix module, the PZT channels will be addressed with the same number (C0 = PZT 0, CN = PZT N), and sections starting in a C16 channel

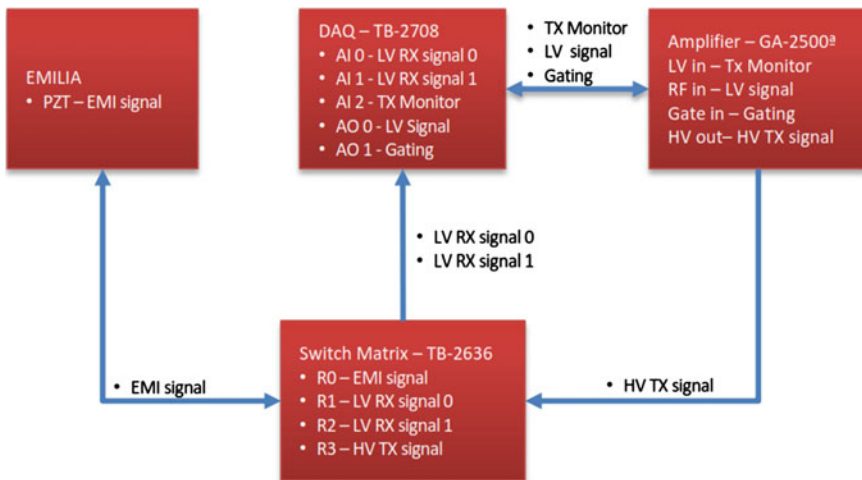


Fig. 17 Inter-module signal connections

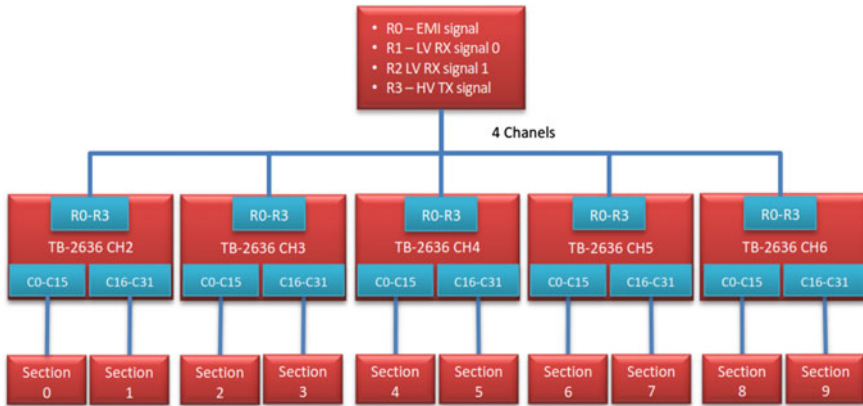


Fig. 18 PZT's connections

will be addressed with the number of matrix channel minus 16 (C16 = PZT 0, CN = PZT N-16) (Fig. 18).

3.2 Software

The acquired data will be retrieved from the DAQ system by means of a DAQ control software based on LabView and MATLAB. This software features a graphical user interface (GUI) to ease the filling of the required data. The GW-based methodologies are implemented in MATLAB; therefore, a MATLAB-based application program interface (API) has been developed for seamless information retrieval and automated interfacing with the stored data. The Saristu DAQ control system is composed of three parts: the DAQ application, the control application and the remote viewers (see Fig. 19).

The DAQ application is called Saristu DAQ, and it runs on the PC integrated on the NI-PXI chassis. This application is responsible to control all of the hardware installed on DAQ. The chassis should be connected to a wired local network. The control application is called Saristu Sequence Generator. It can be installed on any computer with Windows Vista or 7. To control the DAQ system, it is necessary to have a network connection between the two machines and access to a shared folder. On of the applications is configured the test sequence to be run on the DAQ. The application could be run offline and has all the functionalities enabled, and the only limitation is the interaction with the DAQ hardware. It is possible to generate a test sequence offline generating a XML file to be uploaded later to the DAQ system. The data viewer is a Web-based page that can be viewed in a Web browser (Chrome, Firefox). It presents the configuration parameters, the resulting waves and the historic of the warning messages of the last acquisition step. The data files

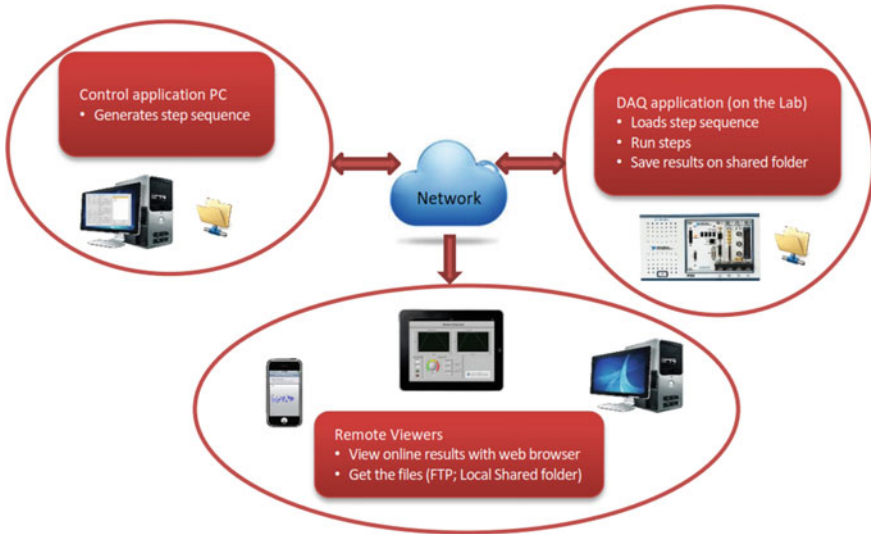


Fig. 19 DAQ control system

created from each acquisition step can be accessed remotely via a network shared folder on the computer running the DAQ application. There is no limitation on the number of Web clients connected to the DAQ hardware (Fig. 19).

The Saristu DAQ application controls the DAQ system, acquiring and preprocessing data from the DAQ hardware. This application is continuously monitoring two files for changes. The monitored files are as follows: `sequence.xml` and `step.xml`. These files are updated by the Saristu Sequence Generator application. When an update on files is detected (new configuration data), the application reads the file that was changed and queues the step defined in the file. Note that the results of the acquisition step defined in the file `step.xml` file will not be saved to memory. The results of the acquisition steps defined in the `sequence.xml` file are saved to a file as soon as the step is finished. In the section Step Parameters, the user can see the configuration of the last acquisition step and a warning for each of the input channels. Parameters that are not relevant for the step will be greyed out, thus during the pitch-catch step all the EMILIA parameters will be grey. The Status section has the current hour, an indicator signalling if the application is running or not an acquisition step or not and the sequence number of the last step. The step number for a step originating from the `step.xml` file will always be zero. The step number for steps originated from the `sequence.xml` file starts with 1 and is incremented for each step of the same sequence. In the Graphs section are shown the results for the last step. The type of results varies with the type of the step. For the pitch-catch and loop test step, the upper window has the Tx Monitor voltage, and

for the EMILIA step, the magnitude of the measured impedance. The lower graph has input 1 and input 2 voltages for the pitch-catch step, input 1 voltage for the loop test and phase of the impedance for the EMILIA step. Sections section is a graphical representation of the PZT used in the last step. PZT in red is the PZT connected to the excitation voltage, light green PZTs are inputs, and dark green are unconnected PZTs. The Messages section is for recording the activity of the DAQ. It has messages for reporting that files were loaded for various errors. All messages start with the date of the message.

3.2.1 Step Result Files

After executing a step from a sequence of steps, the results are automatically transferred to the data folder. The location of the files is the “Data Files Folder \Subfolder”, and the Subfolder is defined by the user that created the sequence of steps in the step sequence generator application, and the Data Files Folder is defined in the Saristu DAQ application.

The output filename will depend on four parameters, the filename, the step number within the sequence, the step type and a four digit number. The resulting filename will be “Base filename”_“four digit number”_“Step number”_“step type”.txt. The parameters for the file name are as follows:

- Base filename—This is defined in the Base Filename parameter of the configuration
- window.
- Four digit number—The next available number within the selected folder.
- Step number—Step number in the sequence.
- Step type—Step type. Will add “pc” for pitch-catch, “lp” for loop test and “emi” for EMILIA.

The resulting file is a tab separated text file using the system decimal separator. In the top of the file are a set of parameters used on the acquisition step followed by the results of the measurement.

3.2.2 Saristu Sequence Generator

The Saristu Sequence Generator application is responsible for generating the XML files with the acquisition steps for the Saristu DAQ system. In this application, acquisition steps are configured and grouped together in order to create a sequence of steps. The user can run the sequence or save it as a template for future use. The application also can run a single step. When running a single step, the results are not saved. This operation is useful for tests. In the Step Parameters sections are the configuration parameters for the acquisition step currently selected. In the Steps of

Table 1 Measured cable attenuation

Cable length (m)	Attenuation Tx (db)		Attenuation Rx (db)	
	100 kHz	1 MHz	100 kHz	1 MHz
1	1.67	2.11	1.87	1.86
2	3.07	3.62	3.23	3.22
3	4.28	4.94	4.41	4.38
4	5.32	6.16	5.45	5.40

Sequence section is the list of the acquisition steps in the sequence, indicating some of the parameters of the step. In the Step Control section are controls related to the current Step Parameters. The Preview Output button opens a window showing the wave that will be generated using the Output Configuration parameters; the View Error List button opens a window with messages for all the invalid parameter values; and the Run Step button commands the DAQ to run an acquisition step with the current Step Parameters. The Sequence Control section has controls to manage sequences. The Subfolder and filename controls where the results for the current sequence of steps will be saved and the name of the files. The Save Template button saves the current step sequence so that the template can be later loaded using the Open Template button. The Add Step button adds a new step to the list with the configuration in the Step Parameters section. And finally, the Run Sequence button sends the step to the DAQ computer so that it runs the sequence.

3.2.3 Data Viewer

The data viewer is a network link that can be viewed on a Web browser using a PC, tablet or other equipment that has a network connection to the DAQ hardware and support to Web contents. On the page are shown the configuration parameters, the test results and warning messages of the last acquisition step.

To load the data viewer simply browse the link http://daq_address:8002/SaristuDAQ.html. The `daq_address` is the IP address of the machine running the Saristu DAQ application (DAQ chassis PC), e.g. if the machine has the IP address 192.168.28.7, the link must be <http://192.68.28.7:8002/SaristuDAQ.html>. The page contains an image of the Saristu DAQ application, and its content is automatically updated every second. For more details, go to Chap. 4 Saristu DAQ application.

3.3 Cables and Transducers Bonding

To reduce electromagnetic interference on the recorded signals generated by external sources as well as crosstalk between the actuated sensors and the ones used for recording the incoming signals, the proposed transducer cabling assembly

makes use of shielded cables as an alternative solution to the usage of twisted pairs. To further increase the crosstalk attenuation, the mini coax cables of type RC178 (M17/93-RG178, see Fig. 20), are preferred. The impedance of this cable is 50Ω , which is optimal for delivering the maximum amount of power from the amplifier to the transducers used as actuators, less than 6.2 dB attenuation over 4 m at 1 MHz, and to reduce to the minimum the attenuation of the received signals on the path from the sensors to the acquisition equipment, less than 5.5 dB over 4 m at 1 MHz.

According to the best known global optimisation methods for finding dense packing of equal circles, considering a cable diameter of 1.8 mm and a total of 160 cables, the interface hole for cable exit should have a diameter of at least 27.9 mm, as shown in Fig. 2b. Alternatively, a square shaped hole of at least 24.4 mm side length can be considered by packing the 160 cables (Fig. 20).

The cables are grouped into 5 bundles (group A for a total of 32 cables, group B for a total of 26 cables, group C for a total of 12 cables, group D for a total of 31 cables and group E for a total of 32 cables). The bundles should have a free length (outside of the demonstrator) of 1 meter (Figs. 21 and 22).

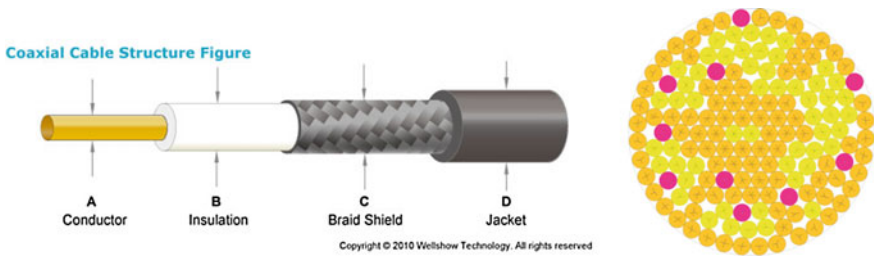


Fig. 20 a mini coax cable type RG178 (M17/93-RG178), b minimum size packing of the 160 cables for a circular hole

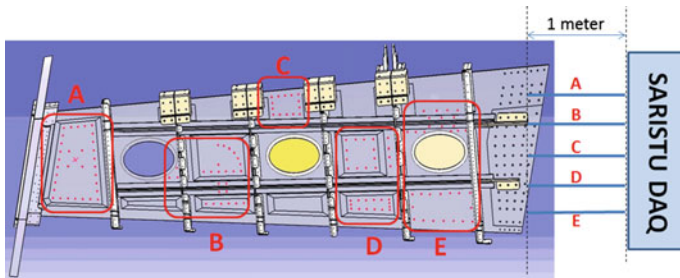


Fig. 21 Cabling Schematic representation of transducers position and transducers grouping (A, B, C, D and E)



Fig. 22 Cabling implementation on the lower wing panel. **a** group A and **b** overall view

4 Conclusion

This paper provides technical information for the implementation of a SHM system architecture designed to apply the damage detection methodologies based on ultrasonic guided waves. In particular, it proposes a technological solution based on a switching matrix for which at least 160 transducers are controlled and where 4 transducers at a time can be used to screen the structure, with a significant cost saving and with no loss of SHM capabilities.

Some important parameters are as follows:

- weight and physical dimensions of the whole apparatus, with specific reference to cabling issues;
- compatibility with the proposed methodologies: maximum number of channels that can be acquired and sampling rate;
- connectivity of the transducer network and the protocol for data gathering to a central processing unit, considering issues related to calibration, maintenance and inspection of the system, and EMI.

Moreover, it must be remarked that all the methodologies proposed in AS05/IS12 are linear, active methods. As a consequence, it is possible to further reduce the measurement equipment complexity by taking into consideration the superposition principle. In fact, by considering a maximum number of 16 transducers per bay, only one of which is being used as actuator, while the other 15 are used as sensors, and it is possible to repeat the same excitation 5 times from the same actuator and recording the propagated elastic wave choosing each time 3 different receivers. As long as the cabling assembly provides a sufficiently low noise and crosstalk level, this procedure will provide the same results that would have been obtained by recording all the 15 signals at the same time. While requiring a longer acquisition time, this approach will prove beneficial in terms of cost reduction. Additional useful details for the SHM implementation can be found in AS05 and IS12 project deliverables [1–3].

Acknowledgments The research leading to these results has received funding from the European Union's Seventh Framework Programme for research, technological development and demonstration under Grant Agreement No 284562.

References

1. Deliverable D52.1
2. Deliverable D52.2
3. Deliverable D123.3

Value at Risk for a Guided Waves-Based System Devoted to Damage Detection in Composite Aerostructures

Luca De Marchi, Alessandro Marzani, Nicola Testoni,
Ulrike Heckenberger and Alfonso Apicella

Abstract The need of reducing aircrafts' fuel consumption and emissions has led the aircraft industry to the design of smart structural elements, which are composite panels with built-in multisensors monitoring systems. The potential economic benefit in terms of maintenance and inspection planning strongly depends on the performances of the built-in monitoring system. The discrimination between damaged and not damaged structural components based on monitoring outcomes is indeed the result of a decision process, in which the state of the structure is assessed based on observations, affected by uncertainties. These might lead to erroneous estimation of the structural damage with consequent strong influence on the maintenance portfolio. In this paper, a reliability-based optimization of the life cycle cost of a smart aircraft component is proposed in the framework of a Bayesian damage update methodology by following a damage-tolerant approach. The methodology is applied to the delamination detection due to impacts on a composite component. The statistical models for the monitoring performance depend on a multilevel defect classification based on the five classes of events in accordance with the FAA AC No: 20 107B. Multiclass ROC analysis and threshold optimization are introduced in the perspective of the maintenance portfolio. A cost model accounting for the calculation of the value at risk (VAR), meant as the potential loss associated with the maintenance portfolio, is implemented.

L. De Marchi · N. Testoni

Department of Electrical, Electronic and Information Engineering—DEI, University of Bologna, Viale del Risorgimento 2, 40136 Bologna, Italy

A. Marzani (✉)

Department of Civil, Chemical, Environmental and Materials Engineering—DICAM, University of Bologna, Viale del Risorgimento 2, 40136 Bologna, Italy
e-mail: alessandro.marzani@unibo.it

U. Heckenberger

Technical Material Physics, TX2B—Metallic Technologies and Surface Engineering, Airbus Group Innovations, 81663 Munich, Germany

A. Apicella

Ingegneria di Progettazione, Airframe, Alenia Aermacchi S.p.A., Viale Aeronautica, 80038 Pomigliano d'Arco, Naples, NA, Italy

1 Introduction

Built-in health monitoring systems in structural components of airplanes allow to assessing the damage state and the consequent structural capacity. There is a strong interest to optimize and customize maintenance activities, aiming at the reduction of costs directly and/or indirectly associated with unnecessary inspections and replacement actions. In this setting, recent developments in structural health monitoring (SHM) do provide new possibilities.

Performance evaluation is crucial in SHM system development. In this paper, performance of an SHM system for impact detection will be computed in terms of its effectiveness in minimizing the service life costs of the structure, which shall be estimated via a Bayesian strategy that accounts for statistical model of impacts, their localization, and the category of damage they may cause.

2 Methodology

Impacts on composite structural panels are a major concern in the aircraft maintenance planning because they can be cause of capacity reduction without any evident sign of damage to a visual inspection. These “barely visible” impacts might indeed cause delamination or matrix cracking with consequent degradation of the structural properties of the laminate. Modern structural health monitoring systems that rely on ultrasonic guided waves aim to size and localize damages with one or more network of sensors which are able to give indication of a delamination. There are many different methodologies/technologies nowadays available, though the research in this field is still ongoing to find the most reliable and economical solution. Despite the kind of monitoring system built-in in the panel, the uncertainties involved in the outcome of the monitoring results must be always taken into account in a proper probabilistic setting. Uncertainties, such as environmental random noise (temperature, humidity, vibrations) on the SHM operations, might influence the identification of the damage, leading to false or missed detection.

The methodology used in this research to properly account for the statistical properties of the monitoring system is depicted in Fig. 1.

The probabilistic description of the loads, the capacity, and the impacts are inputs of the model and characterize the failure domain Ω_F

$$\Omega_F = \{R(t) - L(t) \leq 0\} \quad (1)$$

in which $R(t)$ is the capacity and $L(t)$ are the loads varying in time t .

In this paper, a damage tolerance approach is considered. This requires that damaged components will not lead to failure before they are detected and repaired. In probabilistic terms, the requirement is that the probability of failure p_f due to a

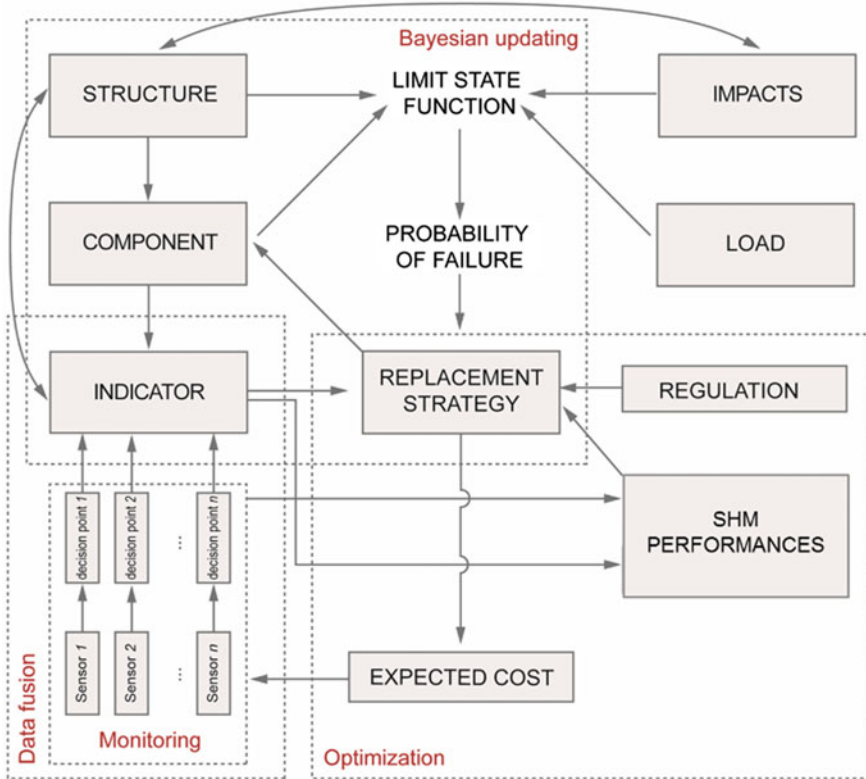


Fig. 1 Optimization of the replacement strategy subjected to reliability constraints

critical damage not being detected must be less than the target probability p_T , usually 10^{-9} per flight hour (FH). The probability of failure can be written as

$$p_f(t) = \Pr[R_0[1 - D(t)] - L(t) \leq 0] \tag{2}$$

where R_0 is the capacity of the undamaged component and $D(t)$ is the damage. Indicating with $f_L(x, t)$ the marginal density of the load and with $F_R(x, t)$ the cumulative distribution function of $R(t) = R_0(1 - D(t))$, and assuming independence between R and L , the probability of failure can be evaluated by the integral

$$p_f(t) = \int_0^{\infty} F_R(x, t) f_L(x, t) dx \tag{3}$$

This integral can be calculated via methods of structural reliability implemented in commercial software such as STRUREL once the complete probabilistic description of the variable involved is provided. Equation (2) explicitly involves the decrement of resistance due to impact damages $D(t)$ which must be calculated by

the mechanical model of the structural component. This model (either FEM or empirical model) must be able to give the post-impact strength of the panel which is a stochastic process with marginal density function $f_{D(t)}(d)$.

The accumulation of damage in time will cause the condition $p_f > p_T$ implying the necessity of maintenance. Engineers usually use this methodology, called condition-based maintenance (CBM), to evaluate the optimal inspection time for degrading systems.

The novelty of this paper is to propose a method for including SHM measurements into the CBM, in case of a multilevel damage characterization. In this framework, a Bayesian updating strategy is used. Given a set of indicators from the SHM system $Y(t)$, a Bayesian formula is used to calculate the posterior probability density function of $D(t)$, called $f'_{D(t)}(d)$, for given likelihood of the SHM performances and prior knowledge of the structural damage state $f_{D(t)}(d)$, that is

$$f'_{D(t)}(d) \propto \Pr(Y(t)|D(t) = d)f_{D(t)}(d) \quad (4)$$

For the evaluation of the likelihood function in the latter, a characterization of the multilevel damage classification and a proper statistical treatment of the monitoring system are discussed in the following.

3 Multilevel Damage Classification

The classification of the damage on composite material used in the aircraft industry is an issue in the certification of airplanes. Guidance on the design and maintenance strategy with respect to impacts is given in the Advisory Circular of the Federal Aviation Administration AC 20-107B. Although following such circular is not mandatory for the aircraft industry, we have adopted the damage classification therein described in this work. In particular, the circular identifies 5 categories of damage related to both their detectability and repair action. It is remarkable that this is not the only possible multilevel damage description. Other and older guidance circulars proposed classification with respect to the probability of occurrence of the impact (AMC25.1309 and ICAO Airworthiness Manual, IIA-4-I). Referring to the circular for further details, we briefly indicate the five categories as A_1, A_2, A_3, A_4, A_5 , being the category A_5 associated with the most catastrophic event. A maintenance action is related to categories A_2, \dots, A_5 . Maintenance action for A_2 is due within few flights, while for A_3 action must be taken before the airplane is allowed for the next flight. Other categories require immediate inspection action.

3.1 Classical ROC and Multiclass ROC Analysis

Statistical description of classifier is usually achieved through the so-called receiver operating characteristic (ROC) analysis. The ROC analysis is suited to characterize, from a statistical viewpoint, a binary choice. A point in the ROC curve identifies the relation between the true-positive and the false-positive conditional probabilities for a given value of the threshold decision variable. The threshold reflects the confidence that the identification is successful and the defect is actually present. ROC has been successfully applied to the inspection planning of composite panels monitored by SHM system [1].

Indicating with P_j the event that the SHM detects a category of damage A_j and with $N \equiv P_1$ the negative detection (no damage event), the confusion matrix associated with the aircraft damage scenario is given in Table 1.

The symbol $\#(P_j|A_k)$ indicates the number of times that the SHM system identifies the damage category P_j being the real damage A_k . Thus, the entire damage scenario can be described by a multiclass ROC analysis, P_j being the classifier classes. Recently, in the literature, attention has been focused in finding the optimal class' thresholds, extending the concept of area under ROC (AUC) into the volume under ROC hypersurface (VUS). Because of the complex nature of the problem, multithreshold optimization is still very challenging. In this paper, motivated by the state of the art in SHM and keeping in mind the sake of optimal inspection planning, some simplification will be done.

With regard to the influence of the SHM system measurements on the maintenance and inspection planning, the category classification is simplified to just two classes, A_2 and A_3 , being the higher categories related to damages evident to the airplane crew. Moreover, in this paper, we consider a SHM that is able to detect the presence of damage, event P , but not of estimating the size of the damage. This results in a simplification of the confusion matrix given in Table 2.

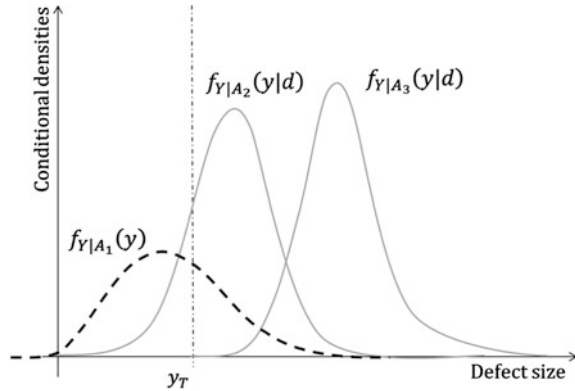
Table 1 Confusion matrix for the multilevel damage

	A_1	A_2	A_3	A_4	A_5
$P_1 \equiv N$	$\#(P_1 A_1)$	$\#(P_1 A_2)$	$\#(P_1 A_3)$	$\#(P_1 A_4)$	$\#(P_1 A_5)$
P_2	$\#(P_2 A_1)$	$\#(P_2 A_2)$	$\#(P_2 A_3)$	$\#(P_2 A_4)$	$\#(P_2 A_5)$
P_3	$\#(P_3 A_1)$	$\#(P_3 A_2)$	$\#(P_3 A_3)$	$\#(P_3 A_4)$	$\#(P_3 A_5)$
P_4	$\#(P_4 A_1)$	$\#(P_4 A_2)$	$\#(P_4 A_3)$	$\#(P_4 A_4)$	$\#(P_4 A_5)$
P_5	$\#(P_5 A_1)$	$\#(P_5 A_2)$	$\#(P_5 A_3)$	$\#(P_5 A_4)$	$\#(P_5 A_5)$

Table 2 Simplified confusion matrix

	A_1	A_2	A_3
N	$\#(N A_1)$	$\#(N A_2)$	$\#(N A_3)$
P	$\#(P A_1)$	$\#(P A_2)$	$\#(P A_3)$

Fig. 2 Example of conditional densities of the damage detection for a given damage in the panel



The events can be grouped as the following:

- the events $(N|A_1)$, true negatives (TN);
- $(P|A_2)$ and $(P|A_3)$, true positives (TP);
- missed detections, false negatives (FN), are the events $(N|A_2)$ and $(N|A_3)$;
- the event $(P|A_1)$ is a false alarm or false positive (FP).

To each element in this classification is associated a cost, namely C_{TP} , C_{TN} , C_{FP} , C_{FN} .

The decision process associated with the simplified confusion matrix in Table 2 is to select the optimal discriminant threshold between the events N and P . To explain this concept, the conditional densities of the damage detection for given damage in the panel are plotted in Fig. 2, y_T being the threshold.

4 Statistical Performances of the SHM System

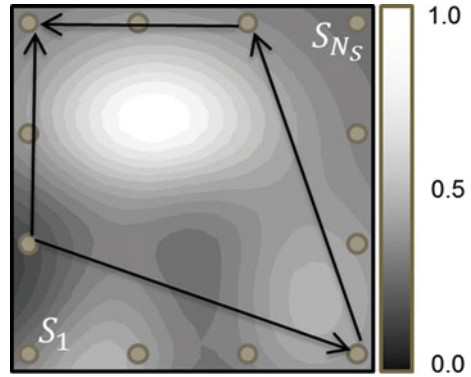
From the confusion matrix, one can derive one point in the ROC curve. This is usually not sufficient to statistically describe the performances of the SHM system. The probability of detection (POD) and the probability of false alarm (PFA) are defined as

$$POD(d) = 1 - \Pr(y < y_T | \text{damage}) \tag{5}$$

$$PFA = \Pr(y > y_T | \text{no damage}) \tag{6}$$

Let us consider a network of N_S transducers and N_R sensing calls. Each sensing call corresponds to a particular sequence of sensors/actuators calls for the SHM system to take a decision on the damage state. Due to the sensor position as well as the presence of stiffeners in the panel or the particular lamination, the SHM outcome will depend on the location of the actual damage. There will be parts of the

Fig. 3 Example of POD map for a network of S_{N_s} sensors and a particular sensing path



panel in which it will be more likely to find damage if it is present and parts with lower probability of POD. Same concept can be applied to the probability of failure. Thus, it makes sense to define POD/PFA maps in which every point of the panel is characterized by its coordinates and the local value of the POD and PFA. Figure 3 shows an example of POD map for a particular sensing path. Indicating with $j \in I$ the index identifying the j -th sensing strategy, the $POD_j(A_r)$ is a map indicating the probability of the SHM to detect a damage of class A_r by the sensing strategy I . In general, for more sensing strategies, assuming independence between $POD_j(A_r)$, the final POD can be expressed as follows:

$$P\left(\bigcup_{j \in I} y_j > y_T | d \in A_r\right) = 1 - \prod_{j \in I} [1 - POD_j(A_r)] \tag{7}$$

5 Bayesian Updating and Threshold Optimization

The failure probability evaluated from Eq. (3) can be updated by the SHM system outcome. To this aim, it is recognized that the likelihood function in Eq. (4) is the complement to the POD map of the monitoring system. The updated damage density $f'_{D(t)}(d)$ is estimated from the SHM information by Bayes' formula

$$f'_{D(t)}(d) \propto \prod_{j \in I} [1 - POD_j(A_r)] f_{D(t)}(d) \tag{8}$$

Once the damage is updated, the distribution of the capacity $R(t) = R_0(1 - D(t))$ is also updated, and the probability of failure, which is the probability of the outcome of the event $R(t) - L(t) \leq 0$, is evaluated.

5.1 Expected Cost Analysis for Threshold Optimization

The optimization of the threshold y_T can now be implemented by the minimization of a cost functional, which accounts for the monitoring system ability to detect the damage. As the events TP and FP both imply an inspection, assuming negligible the repair costs compared to the out-of-service costs of the airplane (longer for a TP), the costs associated with these will be assumed to be C_I and ξC_I , respectively. The event FN is associated with the cost of the component failure C_{II} , and no cost is associated with the event TN. For a given time window (usually one year), the cost functional

$$C_T(y_T) = C_I n_{TP}(y_T) + \xi C_I n_{FP}(y_T) + C_{II} n_{FN}(y_T) \tag{9}$$

where each cost term is multiplied by the expected number of the event outcome within the time frame. The cost-based optimization problem is now formulated as

$$y_{T,opt} = \arg \min_{y_T} C_T(y_T) \quad \text{with} \quad p_f < p_T \tag{10}$$

5.2 Value at Risk Approach for Threshold Optimization

The optimization of the threshold parameter y_T is based on the evaluation of the expected cost, which is valuable information to compare different maintenance strategies, in accordance with [2]. The assessment of the financial risk associated with the maintenance portfolio can be evaluated by financial risk measures such as the value at risk (VAR). This quantity can be calculated as the percentile of the cost, meant as random variable, i.e.,

$$VAR_p(C_T) = \inf\{x: P(C_T \leq x) \geq p\} \tag{11}$$

In order to calculate the VAR, the full probabilistic description of the variable $C_T(y_T)$ must be achieved. Usual values for the percentile p are 95 that means a 5 % probability that the maintenance cost will exceed the $VAR_{95}(C_T)$. Details on analytical procedure to find the distribution of the cost have been given in [2], and the reader is therein referred to.

Acknowledgments The research leading to these results has received funding from the European Union’s Seventh Framework Programme for research, technological development, and demonstration under grant agreement no 284562.

References

1. Cottone G, Gollwitzer S, Straub D, Heckenberg U (2013) Reliability-oriented optimization of replacement strategies for monitored composite panels for aircraft structures. In: Structural health monitoring 2013: a roadmap to intelligent structures. Stanford, California
2. Cheng T, Pandey MD, Van der Weide JA (2012). The probability distribution of maintenance cost of a system affected by the gamma process of degradation: finite time solution. Reliab Eng Syst Safety 108:65–76

Part XII

Technology Stream: Integration and Validation. Fuselage Assembly, Integration and Testing

Introduction and Overview

Introduction and Overview Integration Scenario 13 (IS13) takes the most promising technologies from Application Scenarios 04, 06, 07, 08, 09, and 10 and clusters them for integration into one of four generic fuselage panel types:

1. Door surround structure and mini-door, focusing on acousto-ultrasonic structural health monitoring (SHM);
2. Lower panel, focusing on damage tolerance and low-level electrical conductivity from nano-reinforced resins;
3. Side panel, focusing on a low-cost alternative to current electrical structure network solutions; and
4. Upper panel, focusing on multiple SHM capabilities and multi-site damage detection and evaluation.

By moving from test coupons in the Application Scenarios into full-scale generic fuselage panels, the selected technologies can be assessed in representative “real aircraft structures”—it is the ultimate goal of IS13 to evaluate the potential of these technologies to deliver the following SARISTU targets:

1. Multi-site damage detection capabilities for operational cost reductions regarding structure inspection by 1 %;
2. Improved damage characterization through advanced algorithms for operational cost reductions regarding structure inspection by 1 %;
3. The feasibility of combining SHM with nano-reinforced resins for damage tolerance improvement for weight savings exceeding 3 %; and
4. Electrical structure network installation cost reduced by 15 %.

Moving into the final stages of the SARISTU project, IS13 has reviewed and downselected from the candidate technologies, has integrated these into bespoke designs and has delivered the large demonstrators ready for their respective test campaigns. The papers that follow detail how this was achieved and some of the work that remains.

Fuselage Demonstrators: An Overview of the Development Approach

Ben Newman

Abstract Effective technology development relies on data in order to make informed decisions. In moving through the levels of a test pyramid, from small-scale initial investigations up to large, and ultimately (in the case of aerospace) flight test or full-scale static and fatigue test, demonstrators, the cost and criticality of generating these data increase accordingly. This paper reviews the approach taken in the work linking, and delivering, to the SARISTU fuselage demonstrators, and some of the key decisions taken to minimize risk, to exploit synergies and opportunities, and to streamline the development.

Nomenclature

ASxx	Application scenario xx
CCR	Critical concept review
CDR	Critical design review
CPM	Cold process metallisation
DSS	Door surround structure
ISxx	Integration scenario xx
MAAXIMUS	More Affordable Aircraft through eXtended, Integrated and Mature nUmerical Sizing
PDR	Preliminary design review
QTC	Quality, time and cost
R&T	Research and Technology
RPR	Regular progress review
SARISTU	Smart Intelligent Aircraft Structures
SHM	Structural health monitoring
SME	Small-/medium-sized enterprise
TRL	Technology readiness level
WPxx	Work package xx

B. Newman (✉)

Aerospace and Defence—Flight Physics and Innovation, ALTRAN GmbH & Co KG,
Hein-Sass-Weg 30, 21129 Hamburg, Germany
e-mail: ben.newman@altran.com

1 Introduction

The technology readiness level, or TRL, process is a well known, and oft-used, approach to monitoring and steering research and technology (R&T) development; this, in turn, can help to ensure progress delivery to quality, time, and cost (QTC) requirements. Via the use of wide-ranging questions and peer review, the Smart Intelligent Aircraft Structures, SARISTU, project uses a version of this process adapted to meet the specific project needs and also account for the wide range of starting points that each technology had. Given that the SARISTU consortium comprises 64 partners from research institutions, through small-/medium-sized enterprises (SMEs) and up to large airframers, the TRL-based approach is also an important tool to enable all sides to better understand each other’s ways of working towards common goals.

Before looking further at the adapted TRL process, the project structure and test pyramid should firstly be reviewed.

1.1 SARISTU Project Structure and Test Pyramid

The SARISTU project structure shown in Fig. 1 is referred to as the ‘Temple’ due to its depiction of how various technologies support and deliver to the larger, integrated demonstrators and how lower than expected results in one area need not

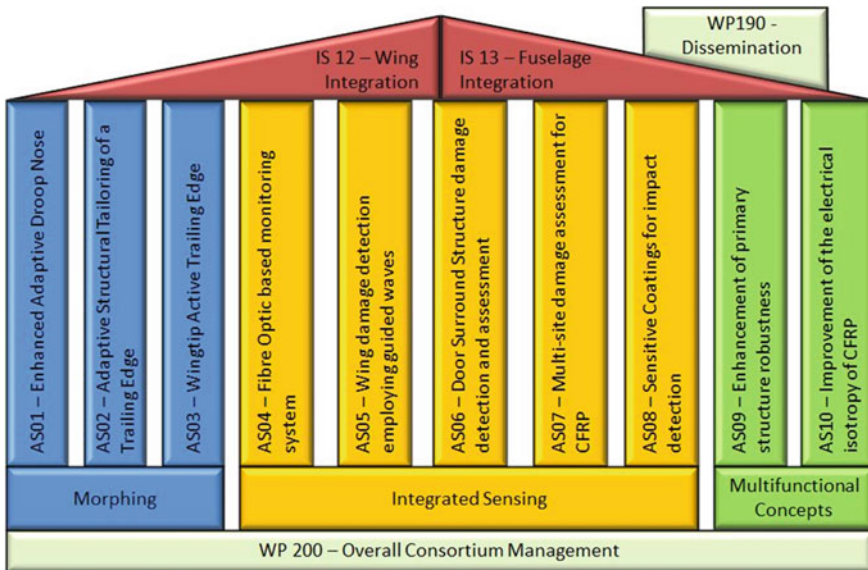


Fig. 1 The SARISTU project structure, referred to as the ‘Temple’

result in total failure of the project. Building on the overall consortium management of work package 200 (WP200), there are ten application scenarios (AS) addressing the three technology streams of morphing structures, integrated sensing, and multifunctional concepts; above these then sit the two integration scenarios (IS) which focus on taking the most promising AS technologies and clustering them into larger demonstrators. WP190 completes the structure as a dedicated work package to support dissemination activities across the entire project and ensure that the agreed procedures are adhered to.

A typical test pyramid, of the type shown in Fig. 2, builds on a wide range of small-scale tests at the bottom and moves up to a limited number of large, expensive tests at the top. In the case of aerospace, the top level typically covers flight tests or full-scale static and fatigue tests which may run into the many millions of euros each.

Within the ASs, work is focused primarily at coupon and element level, allowing various options to be investigated and a downselection to be made based on results and data. In the two Integration Scenarios, larger demonstrators are manufactured at detail (moving towards sub-component) level to further investigate, in parallel where feasible, the most promising technologies. SARISTU does not fully reach the sub-component or component levels.

Within this overall pyramid structure, each Application and Integration Scenario then has its own individual test matrix detailing exactly the scope of the study. Here it should be noted that, although generating suitable key data to perform initial evaluations and make downselections, the test campaigns do not fully complete the

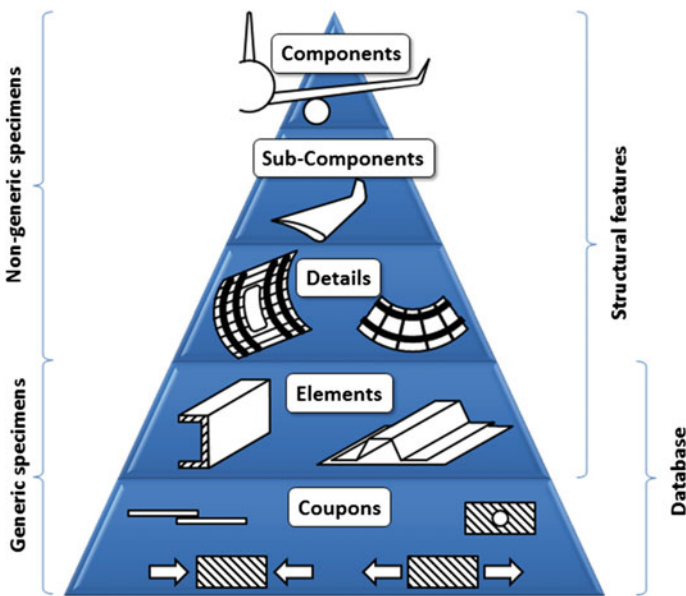


Fig. 2 Typical test pyramid

requirements that would normally be needed at each level, e.g. for development and qualification of a new structural material, hundreds of coupons may be required to enable statistical analysis of various properties followed by the generation of design values that can be used in component design and analysis.

1.2 SARISTU Adaptation of the TRL Process

Prior to starting of the project, it was clear that the TRL process would need to be adapted to suit SARISTU needs. To this end, a timetable of 6 monthly formal reviews was established, along with criteria for each session grouped under the following headlines: Performance, Engineering Readiness, Manufacturing Readiness, Aircraft Operations, and Concept Value & Risk; these were also supplemented by the categories Dissemination and Intellectual Property to cover promotion of results both within and beyond the project consortium. Referred to as ‘Critical Concept Reviews’ (CCRs) and ‘Regular Progress Reviews’ (RPRs), these peer evaluations were prepared and presented by the AS teams and assessed by expert panels drafted from the IS teams. During the first two years of SARISTU, four reviews covering a total of 163 criteria were held for each AS. Using these reviews, development work could be steered and downselection decisions could be taken based on results.

Whilst suitable for the Application Scenarios, the lack of further non-IS peer review teams meant that this approach was further modified for the Integration Scenarios. Taking the form of (bi-)weekly update of teleconferences and more formal Preliminary and Critical Design Reviews (PDRs and CDRs respectively), there was a focus on specific design and testing needs, in particular integration of the selected technologies into the final demonstrators. By coupling this regular communication with appropriate documentation, progress could be tracked and challenges could be identified and addressed immediately (an example of which is given in Sect. 3.).

2 Integration Scenario 13: Fuselage Assembly, Integration and Testing

IS13 expands on the fuselage-relevant technologies developed in AS04 and AS06-AS10 and incorporates them into the larger demonstrators produced in four work packages (Fig. 3). However, this is not a direct customer–supplier relationship; IS13 and the Application Scenarios have worked together from the start of the project to ensure that the requirements and expectations from each side are known and understood, thus allowing the value and risk analysis to deliver well-founded conclusions (Fig. 4).

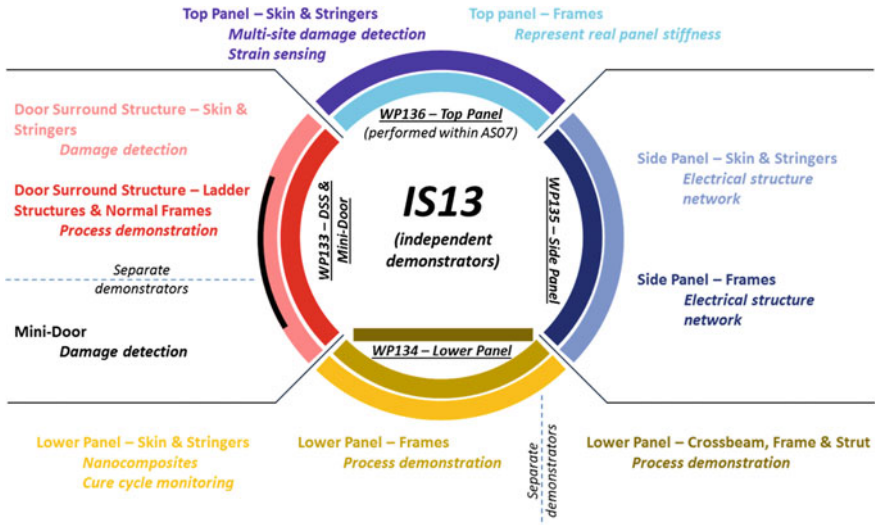


Fig. 3 Overview of the IS13 work packages that produce the demonstrators to be tested

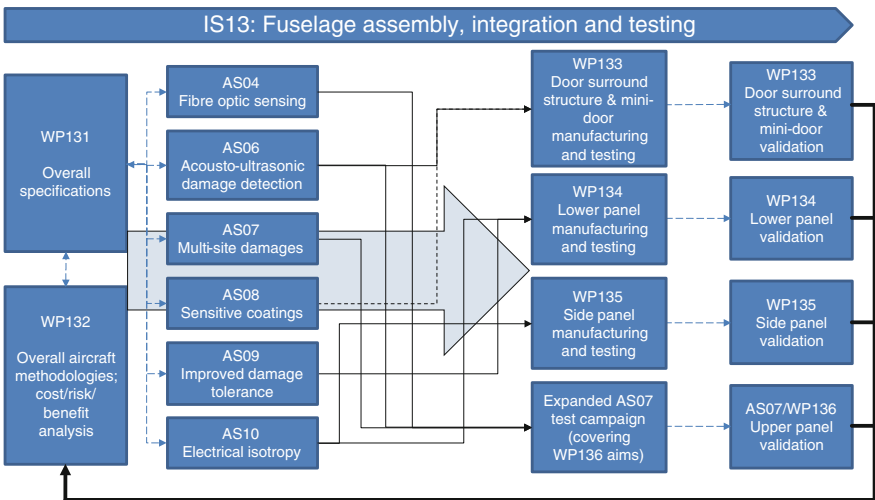


Fig. 4 Interactions between IS13 work packages and the application scenarios

3 Risk Minimizing and Mitigation

One of the key risks in developing technologies over an extended period of time is that of overrun in the early stages leading to irrecoverable delays later on. To mitigate this, a number of techniques were employed.

The first decision, noted in Fig. 3, was to keep the four demonstrator work packages independent of one another: this meant that a design change, manufacturing delay, or other such interruption to the time plan in one demonstrator would have no effect on the others. Common design features, such as outer radius or stringer design, would have been desirable in order to allow, in theory, assembly of the panels into a barrel section, but, if anything, this could have hindered testing rather than providing useful data (as none of the investigated technologies look specifically at assembly- or barrel-level integration issues).

Due to the inherent variability arising from a large range of process parameters and available techniques, material developments commonly suffer overrun compared to the original planning. A close link was therefore established between AS09, AS10, and WP134 at the start of the project to define the critical path from early stages through to the lower panel demonstrators. With this, two key decisions could then be taken:

1. Base the design and test plan for the final lower panels on a known and tested reference item.
2. Drive back from point 1 to define suitable element level test pieces.¹

With this approach, design and sizing of the WP134 panels did not have to wait for the conclusion of all lower-level testing before it could begin; in turn, work on tooling design and production could be launched on time. By modifying the scope of work to include the production of a reference panel without the material enhancements, WP134 also created its own baseline against which comparisons can be made (Fig. 5). Ultimately, the first lower panel demonstrators were completed and ready for testing before the expanded AS09 and AS10 test matrices had drawn to a conclusion.



Fig. 5 The baseline lower panel during final assembly

¹Coupon level test pieces were defined in the associated specifications, e.g. Airbus or internationally approved test documents.

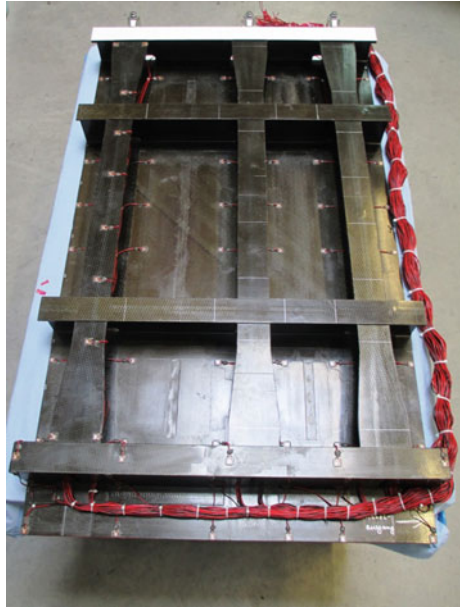
One of the most significant risk mitigation activities took place within the door surround structure part of WP133. The original work package definition called for the design to be an adaption from the work performed in the EC 7th Framework project MAAXIMUS,² modified to include the acousto-ultrasonic sensors being investigated in SARISTU. Cooperation with the MAAXIMUS project coordinator allowed the key risk of overlapping timelines to be identified at an early stage—this allowed the SARISTU partners to discuss and agree a mitigation plan, secure the appropriate internal resources, and then implement the plan once it was clear it was needed, i.e. before the wait for data had removed any chance of SARISTU delivering on time. The solution was the creation of a simplified panel design to meet the testing needs. However, the separation was not total as lessons learnt from MAAXIMUS work were employed by those partners involved in both projects. In addition, development work on the mini-door, the second demonstrator in WP133, was able to evolve as foreseen from MAAXIMUS as the baseline work in this area was already at a more advanced stage. The resulting door surround structure panel and mini-door are shown respectively in Figs. 6 and 7.



Fig. 6 The completed door surround structure panel in its dual purpose transportation and testing rig

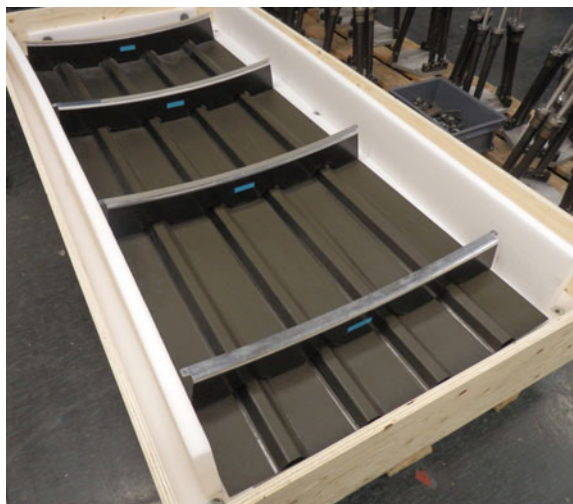
²The MAAXIMUS (More Affordable Aircraft through eXtended, Integrated and Mature nUmerical Sizing) project is running under the Grant Agreement number 213371.

Fig. 7 The completed mini-door



The review and regular communication approach bore fruit with the work being done in AS10 on cold process metallisation (CPM). Although the development and trials had yielded results, several months ahead of the latest decision date, it could be seen that the required performance was at risk of not being achieved. Open discussion amongst the associated partners enabled the remaining time to be focused not only on investigating possible solutions, but also on identifying alternative test opportunities. As such, when a data-based consensus was reached to

Fig. 8 The completed side panel



discontinue the CPM development, a plan was on standby for immediate implementation with no effect on the timescale (preparations for testing were actually completed before the WP135 side panel was completed and delivered; Fig. 8)—in this case, the solution was still to look at the electrical structure network, as originally defined, but to study the coupling effects between metallic strips and adjacent cables rather than the performance of the surface coating and metallic strips in a lightning strike or short-circuit scenario.

4 Exploitation of Synergies and Opportunities

During the first half of SARISTU, the need to significantly de-risk the wing demonstrator work in IS12, by building a second wingbox, was identified. This, however, required resources to be secured from within other areas of the project. The earlier technical decision to stop the development of the originally planned AS07/WP136 hail strike generator had released some of the budget, but still left a shortfall that needed filling. It was at this point that inter- and intra-work package synergies had to be sought, as an increase in the overall project budget was not feasible.

Staying firstly with AS07 and WP136, it was found that, from a technical point of view, the aims and activities of the latter could be merged into the former (Fig. 9); however, this required three agreements: firstly, that the partners implementing their structural health monitoring (SHM) systems for damage detection would do so in AS07 rather than WP136; secondly, that the AS07 partners agreed to a relatively straightforward expansion of the, by this stage, defined test matrix;

Original WP136 activity	New activity in AS07
Panel design with sensing technology	Curved, stiffened panel design
Tooling for skin, stringers and frames	Tooling for skin and stringers; frames produced by specialists under subcontract
Panel manufacture and assembly	Panel manufacture (subcontracting for mechanical assembly)
SHM sensor integration	2 panels will be equipped with both acousto-ultrasonic and fibre optic sensors
Adaptation of the hail impact generator	Hail impact activities stopped during Period2
Impacting, NDT and sensor interrogation	Impacting, NDT and sensor interrogation
Mechanical testing	Impacted panels compression tested to failure
Evaluation, including comparison between NDT and sensor signals	Evaluation, including comparison between NDT and sensor signals; data delivery to MSDA tool

Fig. 9 Synergies allowed nearly all of the work originally planned for WP136 to be performed within a slightly expanded AS07 test campaign

and thirdly, and most significantly, that the AS07 partners agreed to take on the additional financial burden for the extra work as the funding rates were less than 100 %. In all cases, all involved parties were quick to come to a positive conclusion, meaning that a significant IS12 risk could be mitigated at no extra overall cost and without reducing the scope of work—this proposal was submitted for formal approval by the project’s European Commission Technical Officer and was implemented in the third Grant Agreement Amendment, effective as of 11th of March 2014.

Arising from AS04 studies were the techniques of modal analysis and distributed sensing for both impact detection and strain monitoring using fibre-optic systems. What had not been investigated in SARISTU was the performance of these techniques on a larger structure, under load, and monitoring in real time. With the changes relating to SHM in AS07, the chance arose to fill this knowledge gap, and it was seized by the AS04 partners: in the case of distributed sensing, there were only seven weeks between first discussions, at which point panel manufacturing was well underway, and test execution (Fig. 10). During testing, initial analysis and cross-correlation could be made very quickly such that the functionality of both systems could be verified; there was also another unexpected benefit when it was found that the sensors identified a problem with the drop tower (used for panel impacting) which could then be remedied before proceeding.

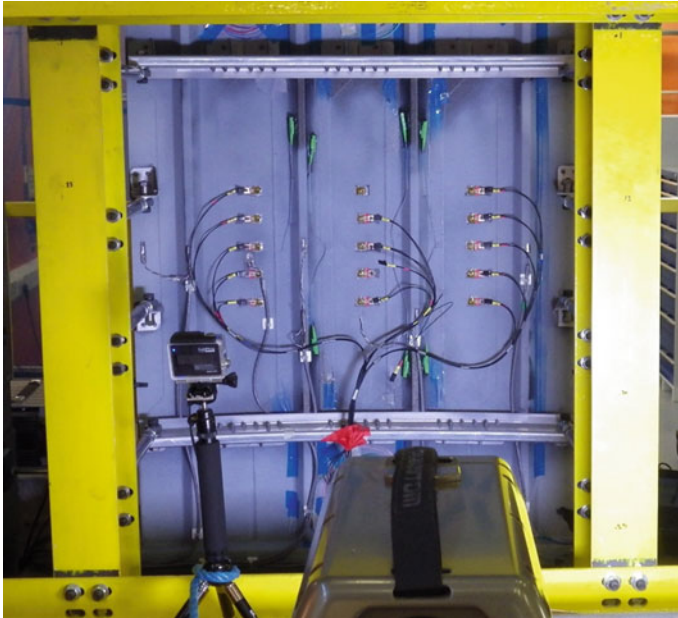


Fig. 10 An AS07 panel, incorporating strain gauges, acousto-ultrasonic sensors and two types of fibre-optic cables, being finalised for compression after impact testing

An earlier part of the redefinition of WP133 was the decoupling from the final demonstrator of the work on damage indicating surfaces being performed in AS08. However, once again the split was not 100 % as items from the frame manufacturing trials could be supplied to the AS08 partners to enable testing on structures representative of aircraft parts. This approach was taken, rather than testing on the final door surround structure panel, to enable the respective impacting and evaluation campaigns to run in parallel.

5 Streamlining of the Development

One of the simplest ways of streamlining development is one that is often either overlooked or implemented in the wrong sequence: in order to best know which plan, component(s) and test campaign are needed, one must first clearly know and understand what is to be investigated and demonstrated. In theory, it is obvious, but time, effort, and resources are often wasted by focusing on non-essential tasks due to the lack of understanding of the requirements. Within IS13, two slightly different approaches had to be taken: for both the door surround structure and the side panel, the approach was exactly as just detailed, resulting in generic panel designs specific to the study needs—in the case of the door surround structure, this meant that, as it was not a significant variable, state-of-the-art stringer co-bonding (cured stringers on uncured, or ‘wet’, skin) was substituted with secondary bonding (cured stringers on cured skin) in order to both minimize the risk of problems during curing (stringer infringement onto sensors) and allow the assessment of sensor performance after a second autoclave cure cycle. For the lower panel, on the other hand, a specific design was a key requirement for the material evaluation, so a proven reference was used as the basis for definition of both the final component and the test plan.

The inclusion of fibre-optic SHM systems with fibre Bragg gratings into the panels for AS07 also presented an opportunity to streamline IS13. By incorporating the strain monitoring task originally planned for the WP134 compression after impact tests into the similar AS07 tests (the differences being in panel design and materials rather than implementation of the SHM), the efforts of several partners, at one of the busiest times of the project, could be concentrated on one area with no reduction of overall scope.

As for the door surround structure, a number of manufacturing trials were performed for the frame pieces of the side panel, although in this case including co-cured rubber and metallic strips. Coupon level results assessed during the formal AS10 CCR and RPR reviews had not been promising regarding damage tolerance improvements resulting from this approach, but there were still open questions as to whether this was due to geometry and boundary condition effects rather than lower than expected performance. It was therefore not clear whether or not corresponding tests should be kept in the plan for the final demonstrator. By applying lessons learnt from WP133 trials, the first WP135 component was of a high enough quality

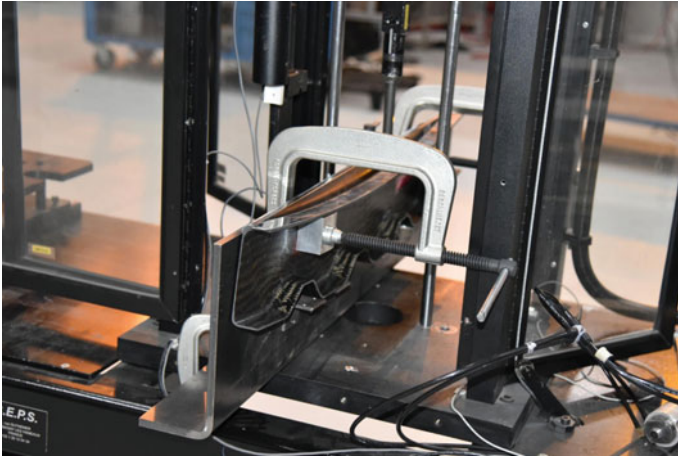


Fig. 11 Preliminary tests using a trial frame piece allowed the rest of the WP135 test campaign to be optimized and expanded without any impact on timing

that it could be made available for impacting tests ahead of panel completion; this in turn allowed a performance evaluation to be made, and the test plan to be optimized, and even expanded, without any impact on timing (Fig. 11).

6 Conclusion

Any number of approaches can be taken to minimize risk and maximize output, but ultimately new challenges and opportunities will always arise. The most important factor is how to respond in these situations. A process of structured regular communication is probably the most helpful means of fostering a feeling of ownership for all activities by all participants; this additional motivation then naturally drives towards quicker reaction times and a willingness to achieve more. As progress is discussed and reviewed frequently, formal reviews can also be simplified somewhat as they tend more towards being acceptance gates and are less likely to result in critical actions or change requirements.

In having delivered the demonstrators ready for testing, the IS13 partners, and indeed all SARISTU partners, have shown an extreme will to succeed: to perform above and beyond the call of duty to hit deadlines, to provide the data on which decisions could be effectively made, and to drive the project towards what is expected to be a successful conclusion.

Acknowledgments Thanks are due to the European Commission and Independent Assessors for supporting the project with their invaluable feedback and guidance. Sincerest thanks are also due to the teams of all SARISTU partners for their flexibility, dedication and tireless efforts to overcome challenges and deliver results.

The research leading to these results has received funding from the European Union's Seventh Framework Programme for research, technological development and demonstration under Grant Agreement No. 284562.

Development of a Door Surround Structure with Integrated Structural Health Monitoring System

Daniel Schmidt, Andreas Kolbe, Robert Kaps, Peter Wierach, Stefan Linke, Stefan Steeger, Friedrich von Dungern, Juergen Tauchner, Christoph Breu and Ben Newman

Abstract Structural health monitoring (SHM) based on Lamb waves, a type of ultrasonic guided waves, is a promising method for in-service inspection of composite structures. Lamb waves can be excited and received using a network of actuators and sensors, which are permanently attached to the structure. By analysing the sensor signals, different kinds of structural defects can be detected and located through the interaction of the Lamb waves. This paper presents the development and manufacturing of a full-scale composite fuselage panel with a

D. Schmidt (✉) · A. Kolbe · R. Kaps · P. Wierach
Institute of Composite Structures and Adaptive Systems, German Aerospace Center,
Lilienthalplatz 7, 38108 Braunschweig, Germany
e-mail: daniel.schmidt@dlr.de

A. Kolbe
e-mail: andreas.kolbe@dlr.de

R. Kaps
e-mail: robert.kaps@dlr.de

P. Wierach
e-mail: peter.wierach@dlr.de

S. Linke · S. Steeger · F. von Dungern
INVENT GmbH, Christian-Pommer-Straße 34, 38112 Braunschweig, Germany
e-mail: stefan.linke@invent-gmbh.de

S. Steeger
e-mail: stefan.steeger@invent-gmbh.de

F. von Dungern
e-mail: friedrich.vondungern@invent-gmbh.de

J. Tauchner
FACC Operations GmbH, Breitenbach 52, St. Martin im Innkreis 4973, Austria
e-mail: j.tauchner@facc.com

C. Breu
Airbus Group Innovations, 81663 Munich, Germany
e-mail: christoph.breu@airbus.com

door surround structure and integrated SHM system. The SHM system consists of piezoceramic sensor arrays, which are integrated into the composite manufacturing process in the form of semi-finished parts. With this approach, the manufacturing steps and costs can be reduced.

Nomenclature

A_i	Anti-symmetric modes
AFP	Automated fibre placement
ATL	Automated tape laying
CFRP	Carbon fibre-reinforced plastic
EPDM	Ethylene propylene diene monomer
S_i	Symmetric modes
SHM	Structural health monitoring

1 Introduction

Composite materials are increasingly used for aircraft structures due to their lightweight potential. But these materials are very sensitive to impacts which cause delaminations. The delaminations are often barely visible and cannot be reliably detected by visual inspection. Other inspection methods, such as conventional ultrasonic techniques, require a time-consuming scanning of the structure. A promising method for in-service inspection of composite structures is an integrated structural health monitoring (SHM) system based on Lamb waves. With such a SHM system, the structure can be more frequently inspected for damage events during the operation of the aircraft and the maintenance costs as well as the ground time of aircrafts can be reduced. Lamb waves are able to propagate over long distances in platelike structures and are highly sensitive to a variety of structural damages. These waves can be excited and received using a network of piezoceramic actuators and sensors, which are permanently attached to the structure. By analysing the sensor signals, different kinds of structural defects can be detected and located [1, 2]. However, the presence of at least two different Lamb wave modes (symmetric modes, S_0, S_1, S_2, \dots , and anti-symmetric modes, A_0, A_1, A_2, \dots) and their interaction at structural discontinuities (e.g. stringers, frames,

B. Newman

Altran GmbH & Co KG, Hein-Saß-Weg 30, 21129 Hamburg, Germany

e-mail: ben.newman@altran.com

thickness changes and damages) produce complex wave propagation fields and sensor signals which are difficult to evaluate. Due to the multimodal character of the Lamb waves, the wave interactions increase disproportionately with rising structural complexity.

The aim of the present work is to prove the damage detection and localization capability in complex and realistic composite structures. Furthermore, a sensor network and manufacturing process are developed in order to integrate the SHM network into the manufacturing process of the structure (cobonding) and to reduce the overall installation effort and costs. As a suitable aircraft structure for implementation, the door surround region is chosen because of its high impact probability during aircraft operation and its high structural complexity. In the following, the development and the design of the door surround structure including the sensor network as well as the complete manufacturing process are described. Various manufacturing processes are chosen and described to produce the different parts of the door surround structure.

2 Design of the Door Surround Structure

To test the SHM network in a complex structure, a full-scale door surround structure is chosen. Because a mechanical test is not requested, the door surround structure exhibits a representative design and detailed sizing is not needed. However, the detection of damages by the SHM system, especially the wave propagation and interaction with structural elements, should be comparable to an aircraft fuselage. Therefore, the door surround structure exhibits representative structural components, lay-ups, material thicknesses and thickness changes.

The door surround structure is symmetrical in both the horizontal and vertical directions in order to minimize the amount of tools and manufacturing costs. The structure exhibits a length of 5.1 m, a width of 3.5 m and an outer radius of approximately 3 m. The following Fig. 1 shows the design of the door surround structure without SHM network.

Because of the representative design, the skin exhibits a quasi-isotropic lay-up and thickness of 2 mm. Around the door cut-out, a thickness change from 2 to 8 mm occurs via a ramp of gradient 1:20. Apart from the door cut-out, further cut-outs (e.g. windows) are not considered to increase the number of sensors integrated into the structure. The skin is stiffened by stringers, which have an omega-shaped cross section like state-of-the-art composite fuselages. The stringer feet are provided with so-called duck feet onto which the normal frames are attached. These frames consist of C-profiles with integrated mouseholes, which allows the stringers to pass under the frame in longitudinal x-direction. The mouseholes are incorporated into the frame profile rather than being machined out after production. This contributes to a lower amount of material scrap and machining. The door surrounding is designed in the form of a ladder structure on either side of the cut-out. Each ladder structure comprises two opposing C-frames

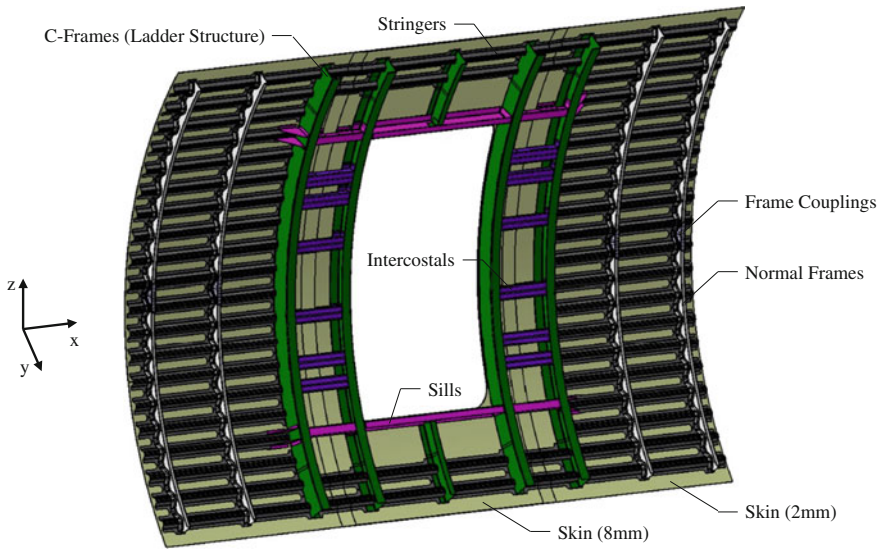


Fig. 1 Design of the door surround structure without SHM network

joined by frame supports (intercostals) to form a single piece. The intercostals exhibit an I-section. The ladder structures are differentially designed in order to minimize the amount of tools, the manufacturing complexity and the tolerance requirements of the later assembly step. Between the two ladder structures, the sills (C-section) are attached above and below the door cut-out.

The SHM network is applied on the inner surface of the skin and arranged in the form of arrays. These arrays are positioned in parallel with the stringers, in the middle between two stringers and two normal frames. Around the door cut-out (ladder structure), further sensor arrays are applied in the same circumferential position.

3 Structural Health Monitoring Network

Both actuators and sensors of piezoelectric transducers are commonly used for Lamb wave based SHM. These transducers are made of thin, monolithic piezoceramic plates or discs. For SHM applications, a sensor array is commercial produced and distributed by the company Acellent Technologies Inc. under the name Smart Layer[®] [3, 4]. This array consists of piezoceramic discs with a diameter of 6.35 mm. The discs are bonded to a polyimide film, which provides the electrical connection and a protection from the environment (see Fig. 2, left). The electrical connection is printed on the polyimide film, like flexible circuits, and covered by another film for electrical insulation. The disadvantage of the Smart Layer[®] is that

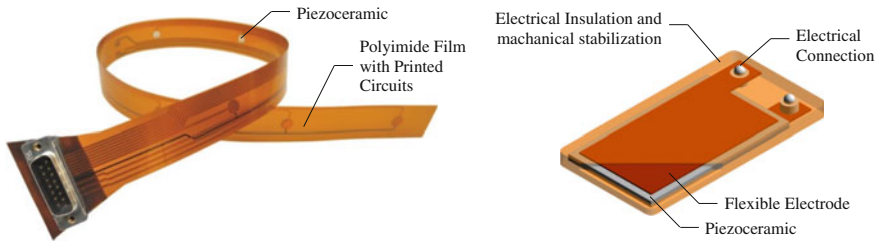


Fig. 2 Smart Layer[®] (*left*) [4] and schematic design of DuraAct[™] piezocomposites (*right*) [6]

the piezoceramic is provided with a wrap-around electrode to connect the piezoceramic from one side by the polyimide film. This wrap-around electrode exhibits a low reliability. Furthermore, the brittle piezoceramic is not protected against tensile loads so that the ceramic can be easily damaged within the application process or during operation. In addition, the printed circuits on the polyimide film tolerate only low strain levels and can be damaged during operation.

A promising alternative is to utilize the DuraAct[™] technology to increase the reliability of brittle piezo ceramics [5, 6]. This piezocomposite consists of a piezoceramic completely embedded in a ductile polymer (see Fig. 2, right). Further components such as electrodes, electrical connection and insulation are also embedded into the composite. Within the embedding process, the polymer is typically cured at a temperature of 180 °C. Due to the different coefficients of thermal expansion of the polymer and the piezoceramic material as well as the shrinking of the polymer during curing, the piezoceramic is provided with a mechanical pre-compression. This pre-compression protects the brittle piezoceramic material and allows tensile loads on the piezocomposite, which is an essential requirement for their application on curved structures. Further advantages of piezocomposites are defined electrical contacts and electrical insulation as well as high durability under variable environments.

SHM applications require a robust and reliable sensor technology to ensure that damages can be detected over the lifetime of the aircraft without any defect of the sensor network. Therefore, the DuraAct[™] piezocomposite technology is utilized for the manufacturing of the SHM sensor arrays. A piezoceramic disc with a diameter of 6 mm and a thickness of 0.2 mm is embedded into the piezocomposite. These dimensions are chosen in order to compare the results of the wave propagation with the Smart Layer[®]. The final piezocomposite has the dimensions of 12 mm × 12 mm × 0.45 mm.

Each piezocomposite is connected by thin cables with a stranded core and an outer diameter of 0.55 mm. Because of the stranded core, this cable type can tolerate high strain levels. As shown in Fig. 3, the piezocomposites as well as the cables are embedded into an unvulcanized EPDM (ethylene propylene diene monomer) layer. The EPDM holds the piezocomposites and the cables in place and is an elastic protection from the environment. The sensor array is covered with a transfer foil made from polyimide that holds the unvulcanized EPDM in shape and

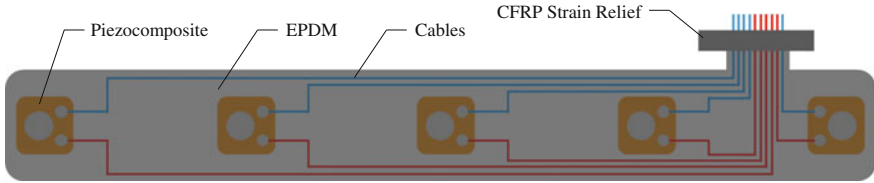


Fig. 3 Sensor array based on DuraAct™ piezocomposite technology

is removed after the array application onto the carbon fibre-reinforced plastic (CFRP) structure.

Within the application process onto the structure surface, a small strip of uncured prepreg is applied over the end of the cables at their exit point from EPDM. This strip acts as a strain relief and increases the reliability of the sensor array. After the application process, the EPDM vulcanizes within the curing process of the CFRP.

The distance between the piezoceramics within the sensor arrays is set to 120 mm. Various types of sensor arrays with a different amount of sensors are manufactured due to the available space on the door surround structure. The manufactured sensor arrays consist of 3, 4 or 5 piezoceramic sensors.

4 Manufacturing of the Door Surround Structure

4.1 Skin Manufacturing

The skin is made from CFRP prepreg material and is laid up by an automated fibre placement (AFP) robot, as shown in Fig. 4 (left). The robot lays up 16 prepreg slit tows, each with a width of 6.35 mm, in one course. The mould tool is installed in a vertical position so that the robot can reach all regions. Compared to automated tape laying (ATL), the AFP process allows the lay-up of more complex structures with reduced scrap. Especially in the present case, the thickness change of the skin can

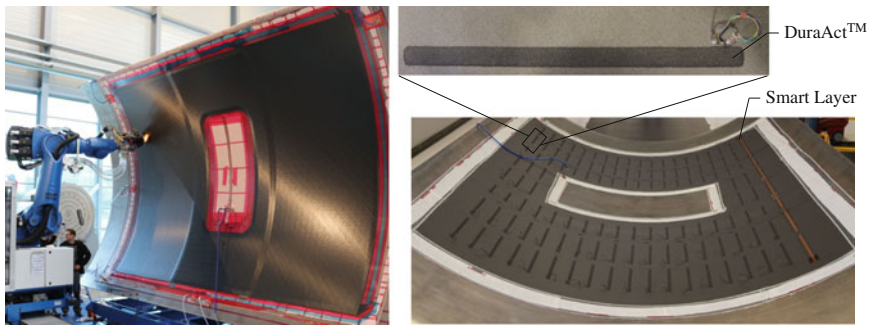


Fig. 4 Skin lay-up by automated fibre placement robot (left), manufactured skin with integrated sensor network (right)

be laid up very uniformly. The main challenge within the AFP process is the lay-up of the first ply because the release agent prevents the bonding of the prepreg material on the mould tool. Even though the slit tows are heated and pressed on the mould tool to improve the tack, they still do not adhere to the surface. This problem is solved by equipping the mould tool with a release film, which increases the tack of the first ply. The release film is applied in vacuum build-up to keep it in position without any wrinkles. After the lay-up completion, the mould tool is turned into a horizontal position to apply the sensor arrays on the uncured skin. The position of each sensor array is displayed by a laser projector, which is installed above the mould tool. Each sensor array is positioned and applied by hand. The whole door surround structure is equipped with DuraAct™ sensor arrays apart from one row, which is equipped with Smart Layers® in order to compare the actuation and sensing performance between the two types (see Fig. 4, right).

In total, 126 arrays with 584 sensors are applied. The skin is cured together with the sensor arrays in an autoclave process at 180 °C and 7 bar as per the prepreg material specification. The manufactured skin with the integrated sensor networks is shown in Fig. 4 (right).

4.2 *Stringer Manufacturing and Bonding*

The stringers are made from CFRP prepreg material in a quasi-isotropic stacking sequence and are laid up by hand on an aluminium tool. The stringers are cured in an autoclave process at 180 °C and 7 bar, and this is followed by milling to the final contour. Using this approach, 4 different stringer types, totalling 44 individual pieces, are manufactured. The stringer types show only differences in their length and stringer foot contour.

On aircraft composite structures, cured stringers are typically cobonded to the wet skin in one cure cycle. In the present case, the stringers are secondary bonded in an additional manufacturing step in order to reduce the risk of clashes between stringers and arrays and also to simplify the vacuum bagging. Therefore, the stringers are bonded to the cured skin using an epoxy film adhesive with a thickness of 0.32 mm. A uniform thickness distribution is guaranteed by a polymer mesh, which is integrated into the film adhesive. The disadvantage of the secondary bonding is that the cured skin needs to be sanded and cleaned for the bonding process. Within the bonding process, the film adhesive is applied on the stringer foot using a heating mat (45 °C) to improve the tack. Then, the stringer is positioned on the skin by the laser projector. To keep the stringers at its designated position, the film adhesive is heated up again to 45 °C using localized induction heating. The induction probes are placed on the stringer feet, as shown in Fig. 5. The advantage of the induction heating is that this process takes only 1–2 s to heat up the film adhesive to 45 °C, after which the process can be repeated periodically along the full stringer length. With all stringers positioned, the structure is vacuum bagged and the film adhesive is cured in an autoclave process at 150 °C and 3 bar.

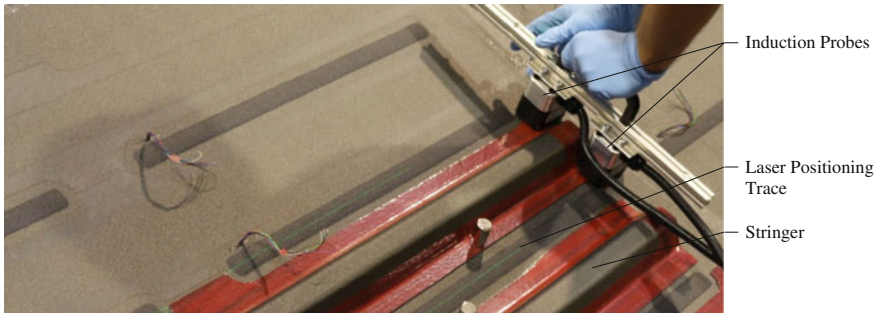


Fig. 5 Tack bonding of the stringers by induction heating

4.3 Manufacturing of the Ladder Structure

The complete ladder structure consists of 5 frames, 16 intercostals, 2 sills and 8 brackets. Due to the simple geometry (I-section or C-section) of the intercostals, sills and brackets, these items can be built up in prepreg technology by hand lay-up on male tools made from aluminium. All items are cured in an autoclave process at 180 °C and 7 bar. Compared to these items, the frames exhibit a more complex design and are therefore manufactured by preforming dry textiles and resin infusion. The frames are made from 12 layers of a biaxial CFRP laminate in a symmetrical $\pm 45^\circ$ lay-up. Since the door surround structure acts as a representative structure to test the SHM system, the frames can be infused and cured at room temperature. This procedure reduces the spring-in effects, so that shrinkage and warping of the frames are minimized. The frames are laid up by hand on a preform tool made from wood. After preforming, the complete laminate is transferred to the mould tool, which is made from Ureol[®] and has integrated infusion channels to improve distribution of the resin. Both the preform and the mould tool have a male form. To produce a uniform surface of the frames, caul plates are applied on top of the laminate. For the infusion process, two vacuum bags are applied: the first vacuum bag is necessary for the infusion process, whilst the second vacuum bag guarantees a uniform pressure distribution on the laminate. The infused lay-up is cured at room temperature. An additional post-curing process in an oven at 35 °C raises the glass transition temperature of the frames up to 90 °C.

4.4 Manufacturing of the Normal Frames

For the manufacturing of the normal frames, a combination of braided preforming and infusion technology is chosen. Compared to the frames of the ladder structure, these frames are produced with a different technology in order to demonstrate various manufacturing processes within one structure. Because the door surround structure is

a representative aircraft component to test the SHM system, no specific lay-up is required. Therefore, the thickness is set to approx. 2 mm at the frame web and to 3 mm in both flange areas. The higher flange thickness is realized by additional woven fabric plies. The nominal braiding angle is approximately $\pm 60^\circ$. Due to the large overall dimensions of the door surround structure, the arc length of the frames is too long for the available braiding machine. Therefore, the frames are split into two equal parts and joined together by frame coupling elements (see Fig. 1). These elements consist of two machined aluminium splice plates as per state-of-the-art principles.

The first manufacturing step is the braiding and preforming of the frames. This is realized by over-braiding a mandrel in a braiding machine, which is shown in Fig. 6 (left). The mandrel is made from beech plywood, because it can withstand the preforming temperature of 120 °C and it exhibits a low coefficient of thermal expansion. Within the braiding process, the mandrel is controlled by a robot and the stacking is stabilized by thermoplastic binder. After the braiding process, the preform is cut in the middle, thus enabling two frames preform to be manufactured in one braiding loop.

The second manufacturing step is the infusion and curing process. The infusion and curing are done within an oven (curing at 180 °C). Due to the component length and the number of mouseholes, the thermal expansion of the mould tool highly affects the part dimensions and tolerances; therefore, a composite mould tool (CFRP) is considered. As shown in Fig. 6 (right), a female tool is designed to control the dimensions of the outer frame surface, which is essential for the panel assembly. When the preform is inserted into the mould tool, it needs to precisely draped into the mouseholes profile (outer flange). However, the stiffness and the fibre tension in the mousehole profile prevent the draping, so that bridging and resin-rich areas could be occurred. To counter this, at least partially, an additional preforming process in the autoclave at a temperature of 120 °C and a pressure of 3 bar is used followed by the infusion and curing process in an oven at 180 °C.

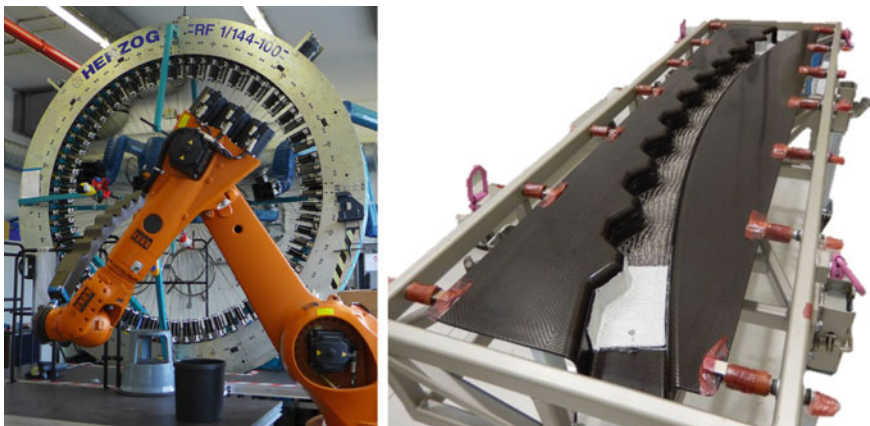


Fig. 6 Robot braiding device (*left*), frame mould tool (*right*)

4.5 Assembly and Cabling of the Door Surround Structure

The final stage within the manufacturing of the door surround structure is the assembly of all components and the cabling of the SHM network. Because the ladder structure is differentially manufactured, it is jointed in a subassembly stage by adhesive and rivets. The ladder structure subassemblies, the normal frames and the sills are assembled to the stringer-stiffened panel using fasteners and shimming due to the high part quality and excellent geometrical match up, only liquid shimming is required.

For the cabling of the SHM network, wiring harnesses with a specific length are pre-fabricated. To connect the SHM network with the hardware system (ScanGenie[®] Acellent Technologies Inc.), one end of the wiring harnesses is equipped with Sub-D 37 connectors. The wiring harnesses are covered by shielding braids for electromagnetic shielding and fixed to the frames. Connection of the wires to the SHM arrays is made using sealed crimp splices (DuraAct[™] arrays). These sealed crimp splices are intended for aircraft applications. Compared to aircraft connectors, these crimp splices are a more lightweight, time- and cost-saving solution. The contacting of the Smart Layers[®] is realized by bolting their electrical interface area to a counterpart element. The counterpart element connects the electrical circuit paths of the Smart Layer[®] with a female connector. A male connector on the wiring harnesses finally connects the Smart Layers[®].

After connecting the SHM arrays, the function of every sensor is tested by measuring the capacitance. It is proven that all 584 piezoceramic sensors survived the different manufacturing steps. The final door surround structure with integrated SHM network is shown in Fig. 7.



Fig. 7 Manufactured door surround structure with integrated SHM network

5 Conclusion

In this paper, the design and the manufacturing of a full-scale door surround structure with integrated SHM network are presented. The design of the structure, which is based on a state-of-the-art composite fuselage rules and requirements, is described. A sensor network and manufacturing process are developed in order to integrate the SHM network into the manufacturing process of the structure. The presented sensor network is based on the DuraAct™ piezocomposite technology and supplemented with commercially available Smart Layers® in order to allow direct comparison of the two sensor types. Furthermore, the complete manufacturing processes of the door surround structure regarding skin, stringers, ladder structure, normal frames, assembly and wiring harness installation are described. It is demonstrated that a door surround structure can be manufactured with the proposed materials and processes. The developed sensor arrays show reliable properties, because all sensors survived the different manufacturing steps without any failure.

Acknowledgments The research leading to these results has received funding from the European Union's Seventh Framework Programme for research, technological development and demonstration under Grant Agreement No 284562. The authors would like to thank the European Union as well as all project partners for their support.

References

1. Giurgiutiu V (2008) Structural health monitoring with piezoelectric wafer active sensors. Academic Press, Elsevier, Amsterdam
2. Rose JL (2004) Ultrasonic waves in solid media. Cambridge University Press, Cambridge
3. Lin M, Chang F-K (2002) The manufacturing of composite structures with a built-in network of piezo-ceramics. *Compos Sci Technol* 62(7–8):919–939
4. Acellent Technologies Inc (2015) Smart Layer®. <http://www.acellent.com>. Accessed 14 May 2015
5. Wierach P (2002) Elektromechanisches Funktionsmodul, German Patent DE10051784C1
6. Wierach P (2010) Development of piezocomposites for adaptive systems, DLR-Forschungsbericht DLR-FB 2010-23. PhD-thesis, Technische Universität Braunschweig

Damage Introduction, Detection, and Assessment at CFRP Door Surrounding Panel

Martin Bach, Nicolas Dobmann and Maria Moix-Bonet

Abstract Acousto-ultrasonics (AU) is a Structural Health Monitoring (SHM) technique based on a permanently installed piezoelectric transducer network, which actuates and receives ultrasonic guided waves to provide information concerning the structure integrity. In order to verify AU approach, a full-scale CFRP panel is manufactured including a co-bonded transducer network. In this paper, the verification approach is described, starting with the test procedure including damage introduction and reference NDI. The verification procedure is followed by data interrogation of the transducer network using a commercial interrogation unit and respective data evaluation by probability-based imaging methodology, which has been integrated into a Graphical User Interface (GUI) in the SARISTU project. In this paper, the methodology is verified against requirements concerning the minimum damage size to be detected, the accuracy of damage size assessment, and the accuracy of localization of damage. Damage-type differentiation, like delamination or debonding is not aimed in the course of the methodology.

1 Requirements and Specifications

A large number of requirements have been specified within SARISTU in order to verify the functionality of acousto-ultrasonic (AU) technology at CFRP fuselage structures [1]. Most of the requirements have been verified within AS06 by coupon

M. Bach (✉) · N. Dobmann
Structures Engineering, Production and Aeromechanics, Airbus Group Innovations,
Airbus-Allee 1, 28199 Bremen, Germany
e-mail: martin.bach@airbus.com

N. Dobmann
e-mail: nicolas.dobmann@airbus.com

M. Moix-Bonet
Multifunctional Materials, Institute of Composite Structures and Adaptive Systems,
German Aerospace Center, Lilienthalplatz 7, 38108 Braunschweig, Germany
e-mail: maria.moix-bonet@dlr.de

testing, e.g., the non-disturbance or durability of sensors. For some requirements, further specification for verification test became necessary during the course of AS06, in order to specify WP133 tasks “Fuselage assembly integration and testing Physical integration: Doors Surround Structure.” The focus is laid on two aspects which can be only verified on large-scale components, firstly the physical integration of the sensor network and secondly the verification of the main function of AUs: damage assessment.

The requirements verified on large scale in WP133 are as follows:

1. *Physical integration:*

- Sensor components included in the autoclave process shall not exude substances detrimental to the host structure,
- The sensor bonding surfaces shall be designed match corresponding host structure surfaces without cavities,
- The position of sensor layers on the fuselage panel shall be verifiable during positioning as well as after the bonding process by a laser positioning device,
- The installation process of the sensor layer shall not impede other production processes,
- Prolongation of the production cycle due to sensor layer installation shall be minimized,
- Production infrastructure required by the sensor layer installation process shall be minimized, and
- The sensors shall be fully functional after co-bonding process.

2. *Verification of damage assessment:*

- The types of structural damages detectable by the SHM system shall include at least skin delamination and stringer debonding,
- The SHM system shall have the capability of detecting and assessing structural damage in CFRP. The minimum damage size to be detected is for delamination 25 mm in diameter of the reference damage and for debonding 20 mm of length over the whole width of a debonded element. The assessment shall be with an accuracy of ± 5 mm in damage size and ± 10 mm in location,
- The damage analysis software shall have a GUI.

2 Verification of Manufacturing and Implementation Process

The process developed within SARISTU for the sensor network installation provides a structural integration during manufacture of the prepreg-based host structure by co-bonding. The sensor network is established by a number of individual

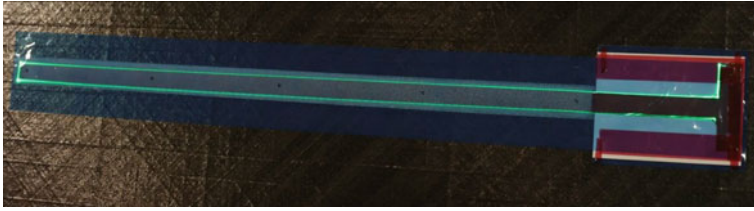


Fig. 1 Positioning of MSSL on uncured host structure according to projected contours

DuraAct™ and SMART layers™ designed for each individual plain-skin area of the monitored zone. Electrical interface components of the sensor layers as well as the interconnection to interrogation hardware by a cable harness are installed in subsequent production steps.

Positioning of sensor layers on the uncured skin of the panel is supported by a laser projection system. As illustrated in Fig. 1, the sensor layers are positioned according to contours projected in the designated locations. Slight pressure exerted on the enclosure of sensors has shown to provide sufficient tack to reliably keep them in position during layup. Positioning accuracy is considered to be increasable by applying reference points on the sensor layers which can be aligned with designated positions generated by the laser projector. Positioning of the layers is considered to be conducted by two workers in parallel using a crossbar to provide access to the installation area.

Reference [1] will detail the manufacturing and sensor integration process.

Figure 2 represents measurements between two pair of sensors, one parallel to a stringer and one perpendicularly across a stringer at different frequencies. By checking the waveforms for every used sensor combination, the full function of the sensors has been verified. For faster assessment, also capacity and EMI measurements were performed.

Verification of requirements:

- Sensor components included in the autoclave process shall not exude substances detrimental to the host structure.

Status: Shifted to coupon level

Proof: N/A

- The sensor bonding surfaces shall be designed match corresponding host structure surfaces without cavities.

Status: Shifted to coupon level

Proof: N/A



Fig. 2 Waveforms at different frequencies between two pair of sensors (*top* parallel to stringer, *bottom* across stringer)

- The position of sensor layers on the fuselage panel shall be verifiable during positioning as well as after the bonding process by a laser positioning device.

Status: Fulfilled

Proof: see Ref. [1] and Fig. 1

- The installation process of the sensor layer shall not impede other production processes.

Status: Fulfilled

Proof: Ref. [2]

- Prolongation of the production cycle due to sensor layer installation shall be minimized.

Status: Fulfilled

Proof: see Ref. [2]

- Production infrastructure required by the sensor layer installation process shall be minimized.

Status: Fulfilled

Proof: see Ref. [2]

- The sensors shall be fully functional after co-bonding process.

Status: Fulfilled

Proof: see Ref. [2] and Fig. 2

3 Verification of Damage Assessment

3.1 Impact Introduction

The damage introduction is performed with two types of portable impactors, an air pressure-driven impactor gun (cf. Fig. 3 top) and a spring-actuated impactor (cf. Fig. 3 bottom), both using hemispherical projectiles with a diameter of 16 and 25 mm, respectively. The pressure available in the impactor air tank and the compression of spring can be set with respect to the desired energy for impact.

The verification if necessary the adjustment of impact energies to obtain the targeted damage sizes is done on the basis of test results from specimen of similar material and structural configuration as shown in Fig. 7. If an impact does not cause at least the minimum targeted damage size, an additional impact is introduced at the same position.

NDI is conducted after each impact in order to validate a delamination or to decide the reintroduction of another impact. Conventional ultrasonic measurements (hand-ultrasound device) allow quick but no precise determination of the extended damage. Then, phased array inspection is used to get better imaging and results.

In total, 112 impact locations are planned on the door surround panel. Different types of impacts will be performed as follows:

Impact on stringer head (H),

Impact on bay-skin (B(2) and B(8) for 2 and 8 mm thickness),

Impact on stringer foot (S),

Impact on ramp (R), and

Impact on skin with stiffener (St).



Fig. 3 Mobile impactor

The panel is subdivided into two areas. During the impacting, first the lower part will be impacted. After having impacted it, the panel will be turned and then the second half will be also tested (Figs. 4 and 5).

For each impact, several parameters are defined: number, type, area, position, distance, and energy. To allow the necessary NDT inspections before impact introduction, multiple zones are defined. These zones have a size of 200 mm × 200 mm. Figure 6 gives an overview on impact zones.

3.2 Reference NDI

Non-destructive testing (NDT) is needed after each impact introduction in order to analyze the state of the structure and to determine sizes and positions of introduced damage.

Figure 7 represents the impact introduction at CFRP structure, while Fig. 8 represents the C-scan result. With this C-scan image, the damage size can be determined and directly compared to the damage size assessed by the SARISTU software.

Conducted impacts are summarized after introduction with the date, zone, impact energy, and the damage sizes evaluated by NDT.

Fig. 4 One half of the IS13 panel

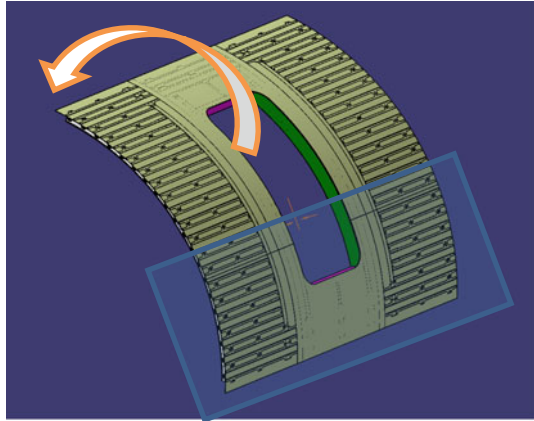
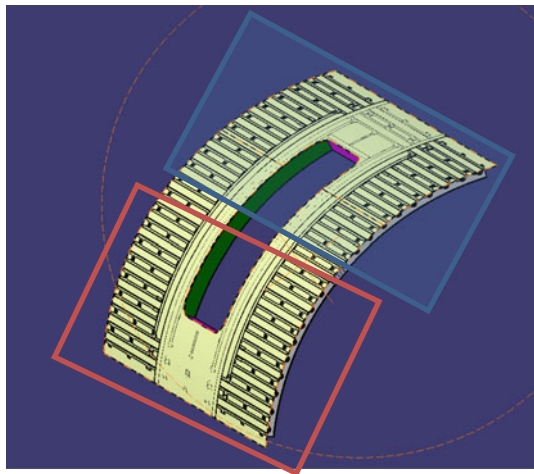


Fig. 5 Other half of the IS13 panel



3.3 SHM Measurement

- **ScanGenie**

The data acquisition system based on ScanGenie devices is developed by Acellent Technologies Inc. This hardware platform is designed for signal generation and data acquisition. As an USB-interfaced portable device, it can be connected to the computer. User-defined actuation signals can be generated on demand and sent to neighboring transducers. As all transducers monitoring the structure are connected through specific cables to the hardware platform, the acquisition of their respective responses can be performed by the device. Subsequently, specific software evaluates acquired data in terms of damage location and size or material property changes within the structure (see below).

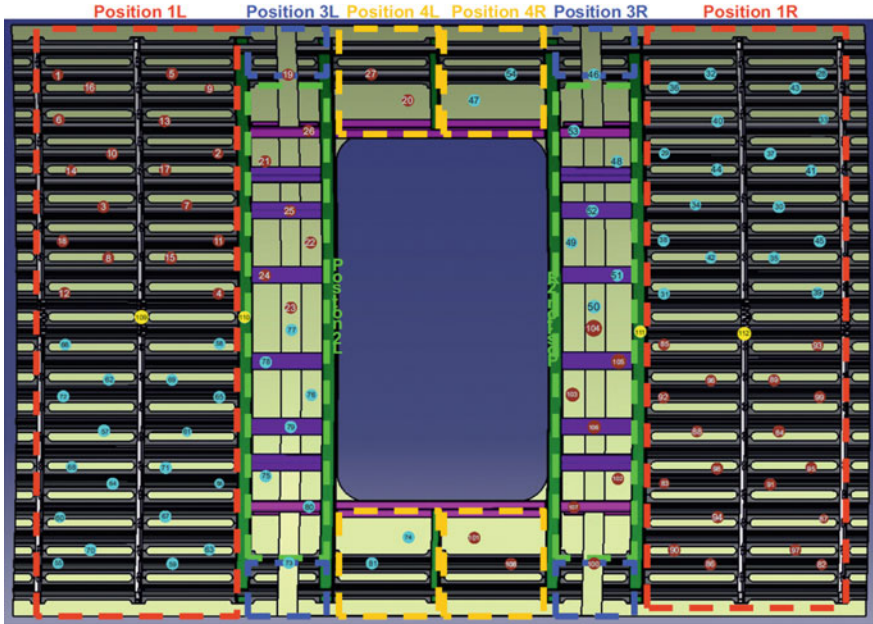


Fig. 6 Position of impacts on the panel



Fig. 7 Introduction of impact at CFRP panel (structure representative to door surround panel)

• **Data Analysis Software—Ref. [3]**

The damage analysis software, developed within the SARISTU project and described in detail in Ref. [3], converts raw data signals to a colored contour plot indicating possible damage locations, embedded in a software package with a GUI. The user can analyze the data without an in-depth knowledge on implemented signal processing algorithms, but can at the same time adjust multiple settings make the software a powerful tool for both a quick scan of measured

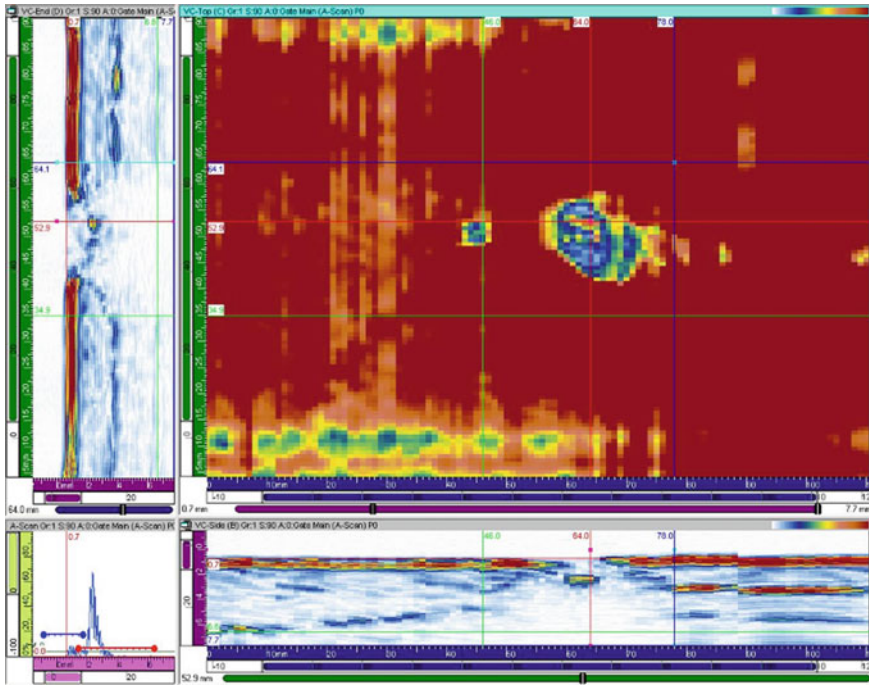


Fig. 8 Phased array C-scan

data and a more elaborate investigation by an experienced user (in the field of signal processing).

- **Comparison of NDT and SHM results**

The final step of the test plan will be to compare both technologies by means of different parameters such as damage localization (x - y coordinates) and damage size (mm^2). The Fig. 9 showing an example of the available results. The picture on top represents a quarter of the door surrounding panel. The damage can be clearly detected at position $(-4.000; 2.800)$ and the Fig. 9 represents a zoom in the affected area, including the calculation of damage size of $(-3982; 2718)$ mm and a damaged area of 7493 mm. The area was calculated with 66 % threshold, which would be approximately a round damage with a 100 mm diameter.

3.4 Verification of Requirements

- The types of structural damages detectable by the SHM system shall comprise at least skin delamination and stringer debonding.

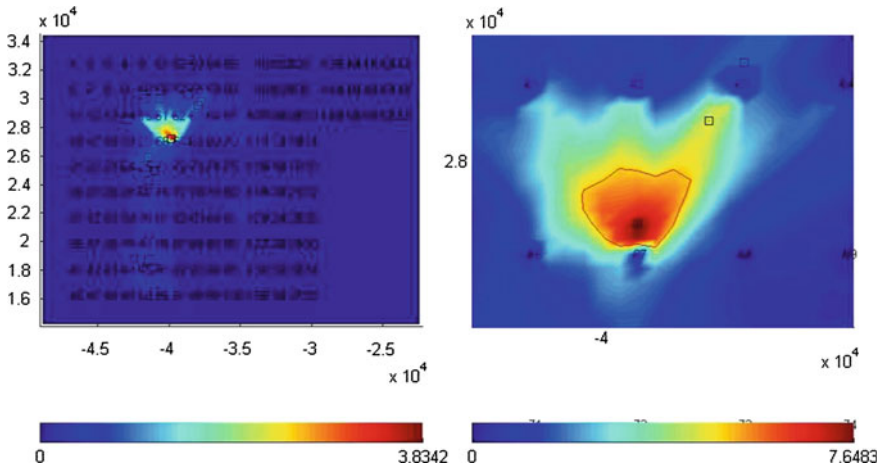


Fig. 9 Damage probability of quarter 1 of door surrounding panel (*left*) and zoom on the damaged area (*right*)

Status: Fulfilled on component level

Proof: Ref. [4]

- The SHM system shall have the capability of detecting and assessing structural damage in CFRP. The minimum damage size to be detected is for delamination 25 mm in diameter of the reference damage and for debonding 20 mm of length over the whole width of a debonded element. The assessment shall be with an accuracy of ± 5 mm in damage size and ± 10 mm in location.

Status: Partially fulfilled

Proof: see Ref. [4]

- The damage analysis software shall have a GUI.

Status: Fulfilled

Proof: see Ref. [3]

4 Conclusion

Within SARISTU Integration Scenario 13, a suitable verification platform for the requirements has been defined. The structure represents a majority of features which are specific for a door surrounding structure in terms of damage assessment using AU technology. The manufacturing integration of the sensor network has been verified with full success on this large-scale structure. The verification of the damage assessment functions of AU is currently ongoing and will be finished

within the SARISTU project. The first results of the system, which comprise the structure with integrated sensors, the data acquisition unit, and the damage assessment software, are strong indicators that the verification of the stated requirements will be successful.

Acknowledgments The success of the work package has been greatly influenced by the open and thoughtful lines of communication between all partners involved. The research leading to these results has received funding from the European Union's Seventh Framework Program for research, technological development, and demonstration under grant agreement no 284562.

References

1. Bach M, Moix Bonet M, Hayo T, Furlani F, Boudjema N, Deliverable D611 (2013) SARISTU internal report
2. Schmidt D, Wierach P (2015) Development of a door surround structure with integrated structural health monitoring system, submitted for publication, SARISTU final conference, Moscow
3. Loendersloot R, Bueth I, Michaelidos P, Moix-Bonet M (2015) Damage identification in composite panels—methodologies and visualisation. In: Wölcken PC, Papadopoulos M (eds) Smart intelligent aircraft structures (SARISTU), pp 581–606
4. Moix-Bonet M, Wierach P, Loendersloot R, Bach M (2015) Damage Assessment in Composite Structures based on Acousto Ultrasonics—Evaluation of Performance, submitted for publication, SARISTU final conference, Moscow

Installation of Metallic Strip on CRFP Frames: Assessment of IS13 Mechanical and Electrical Performance

Richard Perraud, Olivier Urrea, Thierry Pelegrin, Michel Bermudez, Stephane Guinard and Christoph Breu

Abstract The extended use of CFRP material in airframes led to a loss of the ability to use the aircraft superstructure for electrical tasks such as lightning strike protection, systems bonding and grounding. So, to replace metallic fuselage inherent electrical functions in composite aircrafts, an internal metallic structure called electrical structure network or ESN is introduced. The aim of AS10 is to evaluate technologies that can be integrated directly into structures with the aim of creating an electrical structure network (ESN) whilst reducing weight and improving survivability of composite structures. The innovative development consists of a pre-assembled semi-product composed of an aluminium strip and a non-vulcanized rubber that is co-bounded to the composite frame part early at the manufacturing stage. Evaluations of the technology were done at coupon level to check thermal, mechanical and electrical requirements. This paper presents the activity related to IS13 demonstrator and its damage tolerance and electrical

R. Perraud (✉) · O. Urrea
EMC and Propagation, Airbus Group Innovations, 12, rue Pasteur,
92152 Suresnes Cedex, France
e-mail: richard.perraud@airbus.com

O. Urrea
e-mail: olivier.urrea@airbus.com

T. Pelegrin · M. Bermudez
Mechanical System Design, Airbus Group Innovations, 12, rue Pasteur,
92152 Suresnes Cedex, France
e-mail: michel.bermudez@airbus.com

M. Bermudez
e-mail: thierry.pelegrin@airbus.com

S. Guinard
Computational Structural Mechanics, Airbus Group Innovations,
18, rue Marius Terce, 31300 Toulouse, France
e-mail: stephane.guinard@airbus.com

C. Breu
Preforming and Textile Technology, Airbus Group Innovations, 81663 Munich, Germany
e-mail: christophe.breu@airbus.com

performance assessment. For electrical aspects, a numerical model is built, allowing analysing the impact of strip installation versus current solution with the AD2 cable. Numerical results will have to be confirmed with measurements.

Nomenclature

ABS	Airbus Standard
AIMS	Airbus material specification
APII	Airbus process instructions
AS0X	Application scenario x in the SARISTU project
CFRP	Carbon fibre-reinforced plastic
ECF	Expanded copper foil
NDT	Non-destructive testing
SARISTU	Smart intelligent aircraft structures

1 Introduction

This paper is about the mechanical and electrical testing or simulations that have been performed at IS13 level, i.e. when metallic strip is installed on IS13 demonstrator. Metallic strip design and manufacturing have been detailed in another paper “Metallic strip concept overview and results—T. Pelegrin et al.”

The metallic strip design proposed in SARISTU aims at challenging the traditional scheme of the electrical cable attached to the composite structure owing to brackets. This cable fulfils electrical functions needed for instance for the current return or a provision of a common voltage reference. These functions are part of the electrical structure network (ESN) functions intrinsically covered by the former metallic structures. It is the case for the automotive or aerospace vehicles.

The “metallic strip” combines a composite carbon structure and a semi-product made of an electrical aluminium alloy and a thin layer of rubber. This association allows for reaching a wide part of the benefits mentioned here above.

For mechanical aspects, secondary beneficial side effects are expected from metallic strips:

- Both metallic and elastomeric additional layers may act as absorbers with respect to accidental low-energy, low-velocity impacts on protected area;
- Metallic additional layer may act as an impact revelator: metallic plasticity results in visible local dents on the strip when impacted, which lead to significant weight savings in the design of composite parts (the current design policy is conditioned by a threshold on impact damage detectability).

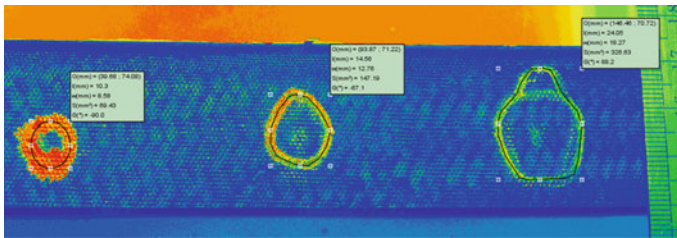
For electrical aspects, requirements are dealing with conductivity for permanent functional current or for short-circuit currents up to 1500A during one second. Moreover, another main electrical requirement deals with the electromagnetic

impact. In fact, the new architecture has to use a routing and a geometrical configuration which do not magnetically affect the wires and others electrical metallic components in case of high current variations (ground reference fluctuation). The aim of the model presented here is to assess the common mode coupling in different situations and compare the results obtained with the strip and the cable for installation near frames.

2 Damage Tolerance Testing

In order to quantify the potential beneficial effects on damage tolerance and damage detectability, impact tests are being conducted on coupons (100 × 150 mm plates, standardized AITM-10010) and structural details (representative structural frames). Impacted specimens consist in a composite braided part (length 150 mm, width 100 mm, thickness 4.2 mm), in which a 1050H18 aluminium strip (thickness 0.8 mm) is bonded with a SMACTANE FR60 rubber layer (thickness 1 mm).

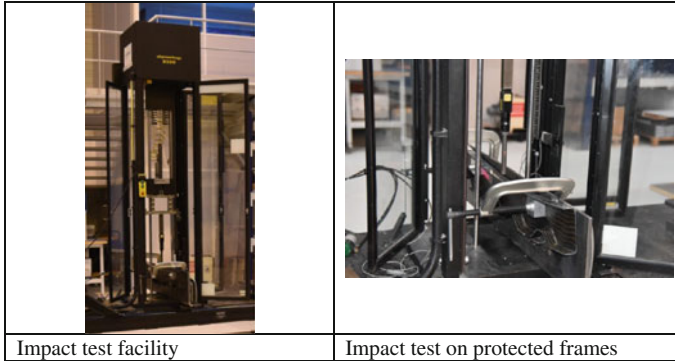
Experimental protocols for conducted impact tests incorporate a specific instrumentation (recording of contact force history and energy absorption of the impacted structure) and thorough measurements of dent depths (laser profilometry) and delaminations (ultrasonic inspections).



Measured delaminated areas for reference impacts (10, 15 and 20 J) on unprotected frame

Though the test campaign is still in progress, evidence could already be made that:

- Detectability improves significantly: dents are visible through eye inspection for an impact less than 6 J versus no visible dent on non-protected composite specimens at 20 J;
- Damage tolerance improves significantly: the protection increases the energy threshold for damage initiation by 10 J at least (complementary tests are planned to reach better estimates of the gain).



3 Electrical Performance Assessment

3.1 *State of the Art*

In aeronautic industry, metallic structure and fuselage handle the following important roles or functions: signal and fault current return, voltage reference for all electrical equipments, personal protection against electrical shocks, lightning and high-intensity radiated field (HIRF) protection and antenna ground plane reference for the main electrical ones. The use of CFRP materials for fuselage and internal structural elements of an aircraft imposes to assess the correct handling of these functions when all were more easily achieved due to the high electrical conductivity of aluminium and titanium alloys. For the functional current (corresponding to the current of functioning equipments that returns through the structure), this results in two main issues. First, poor conducting structure (conductivity is 1000 times lower for CFRP than metallic) induces a voltage drop that may be unacceptable for equipments. Second, depending on the frequency, a certain critical amount of current will flow through CFRP assemblies, or junctions, resulting in local temperature increases with possible mechanical damages. The management of current return distribution over different elements of a large aeronautical structure should be tackled with care especially for the aircraft weight optimization. The numerical modelling has been proved to be a helpful way for current distribution prediction, with the objective to size and optimize the so-called electrical structure network (ESN).

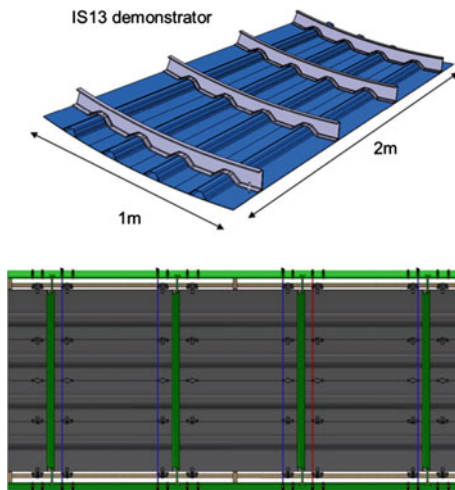
Some experiments on scale 1 demonstrator were done at different stages of aircraft development for ground reference fluctuations (common mode couplings), and some questions remain about the complete understanding of common mode

couplings near frames. The main reason is that, near frames, the metallic resources are not so dense as for longitudinal sections (RW, Seat Tracks) and redistribution is more complex between frames and skin which could be somehow connected to the structure with poor conductive junctions.

SARISTU, by developing a new technology for the ESN near frames, presents a real opportunity to compare the results obtained with the current solution (aluminium cables) with the strip solution. First, results have been presented on the former paper, and here, additional results will be obtained considering the scale 1 panel, IS13. From the electrical analysis, we have proposed to make some measurements and simulations to validate our capability to predict the common mode couplings and also to be able to quickly compare this solution to the one with the cable.

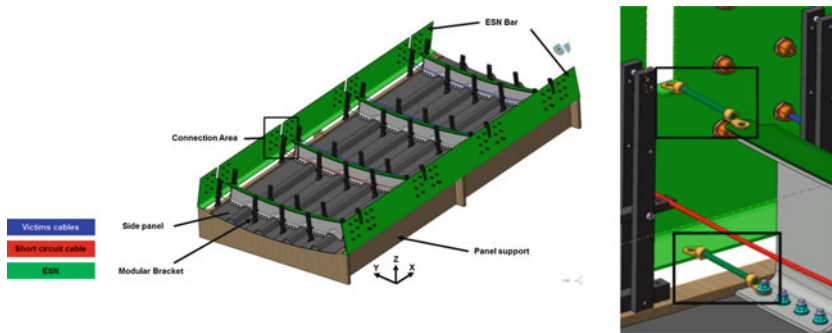
3.2 IS13 Panel and Electrical Support Definition

The composite panel is equipped with four frames on which metallic strips are installed. Metallic strips are isolated from the composite frames with rubber, and skin is made with expanded copper foil. The length of the panel is 2 m and the width is around 1 m. As the objective of the measurement or simulation is to assess the current distribution in the structure as well as the common mode couplings, we need to add to this panel a fixture that will allow injecting and measuring the current with installed cables.



The special fixture has been designed in order to represent a scenario where currents are able to flow on longitudinal elements such as real-life elements: raceways and seat tracks. The typical value for the resistance of these elements is around 0.1 mohm/m. The fixture will allow connecting the strips, cables and skin on the longitudinal part. In the side figure and the one below, the ESN elements (metallic) are represented in green: strips, longitudinal bars, and junctions between them.

For the aim of performing electrical tests, we need to install different cables that represent internal functions. The red wire represents a culprit cable such as a power supply driving a current corresponding to the function. The blue cables represent victim cables that will collect some energy from the red one by common mode coupling and inductive coupling. The position of the cables versus the culprit cables and the ESN is of great importance, and they are specified in requirements.



Junctions are made to connect strips to ESN bars with a maximum resistance of 0.15 mohm/m. the connection to the skin is made only with the first rivet. They will be connected to assess the influence of skin resistance in parallel with the frames.

3.3 Modelling Strategy

For numerical aspects, we chose from a long time a frequency domain technique [1, 2] that allows us to describe the metallic and CFRP structure inside the same tool capable to deal with a wide frequency band. This method is based on Electrical Field Integral Equations (EFIE) and is a boundary element method where you only describe linear or surface structure, thus avoiding dealing with volume elements. The technique developed in Airbus allows performing low-frequency analysis. This choice has been done according to the method capability to model:

- CFRP skin covered by metallic mesh;
- Internal metallic elements;
- Internal CFRP elements;

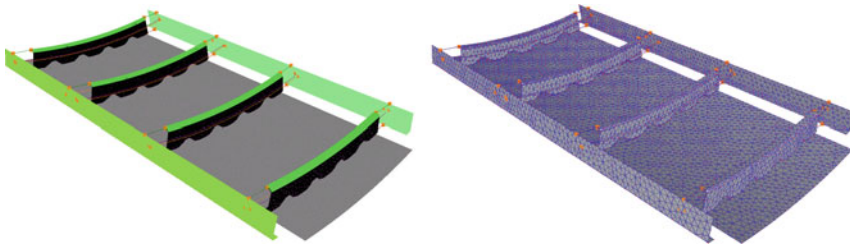
- Several sources with their amplitude and phase; and
- Non-perfect connections (junctions) between internal, interface elements and skin

Several critical constraints have also influenced the selection of the method, the main ones being the capability to handle the very low-frequency range, the capability to determine current in junctions (individual rivet or a set of junctions) and the predictive and operative aspects. Thus, the parallel computing capability on multiprocessors has been an important factor in the selection of the BEM/MOM methods. As an example, the treatment of a 35000 unknown's problem takes less than 10 min on a cluster of 64 processors (for one frequency).

Another aspect of the methodology is the multiconfiguration analysis that is accessible with the so-called multiport technique that is very powerful to deal with scenario analysis, typically corresponding to different ways to connect elements between themselves or to assess the impact of the loose of certain connections. Multiport technique is in fact a linear reduction technique that consists in finding a matrix relation between electrical quantities (voltages and currents) on identified ports, thus producing a small size model in the form of Y or Z matrix. The 3D code produces these matrices in the frequency domain.

3.4 IS13 Electrical Model

From the IS13 panel CAD data definition and its associated fixture presented above, a numerical meshing for BEM Solver is produced, as presented below. The electrical properties of each conductive element are set: linear resistance for cables, surface impedance for skin, and ports placed for junction local resistances or for local sources/sensors where we need to inject or measure current/voltages. In the model, there are 21 ports and so a 21×21 Y matrix is computed. Some scenarios are described hereafter.



3.5 *First Results*

At the time of redaction of this paper, the panel is not yet received in Airbus Group Innovations to perform the electrical measurements and so comparison with simulation results is not possible. The input parameters of the model (junction resistance) are then estimated for numerical evaluation, and some first results obtained by simulation by comparing strip and AD2 solution are given.

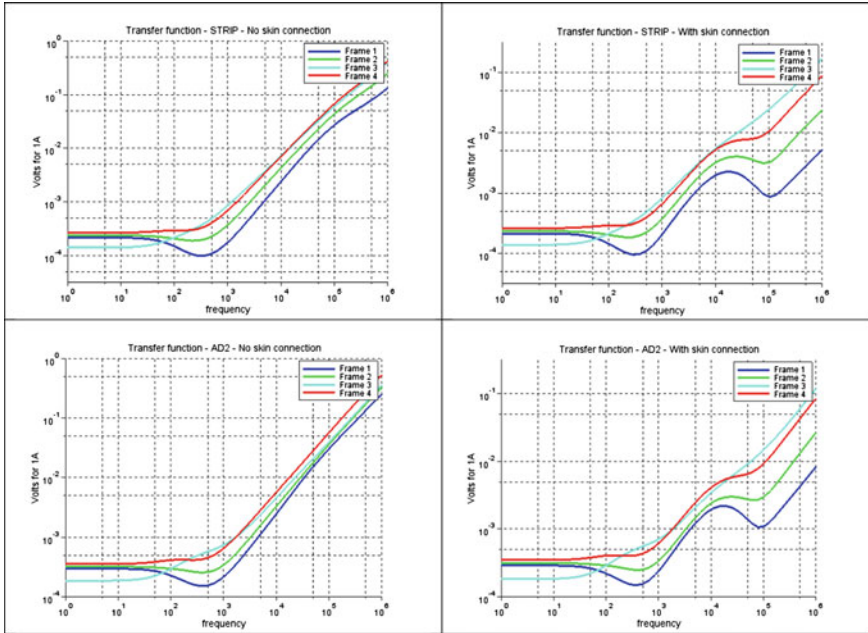
The ports are placed on the structure so that it is convenient to study difference injection scenarios. The results presented here consider a 1 Amp injection (normalized current) near the Frame 3 (Frames are numbered 1–4; Frame 3 is one of the internal frames). As no measurement data are available, all junctions' resistance is set to 0.1 mohm/m (junctions between frames and skin, junctions between strip and ESN). This parameter could be updated as soon as the panel is available.

The four scenarios are described here:

- Scenario 1: Strip connected to the ESN bars and no skin connection;
- Scenario 2: Strip connected to the ESN bars and skin connection;
- Scenario 3: AD2 connected to the ESN bars and NO skin connection; and
- Scenario 4: AD2 connected to the ESN bars and skin connection

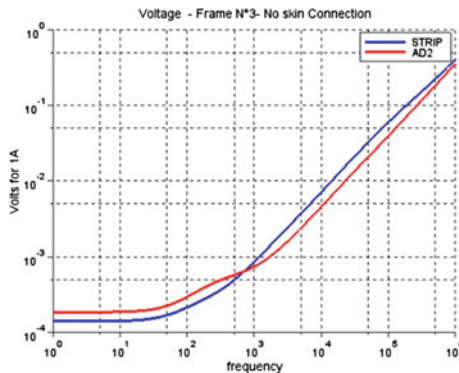
The following figure gives the transfer functions on four cables placed near frames, i.e. the amount of voltage induced for 1A injected in the frequency range (1 Hz, 1 MHz).

The typical behaviour for transfer function is a resistive coupling for frequencies below 100 Hz (flat curves) and inductive couplings in higher frequencies (20 dB/decade); those levels depend on the geometrical position of the victim wire versus the source. For the cable placed just near the source, the resistive coupling is very low as there is no resistive contribution of ESN longitudinal elements. For frequencies between 100 Hz and 10 kHz, there is a redistribution of current inside the structure due to inductive paths. Below 10 kHz, skin has no influence on current distribution because its resistance is quite high compare to the strip/AD2 resistance. For frequencies above 10 kHz, skin connexion has a strong impact on couplings. These effects will have to be confirmed with measurement.

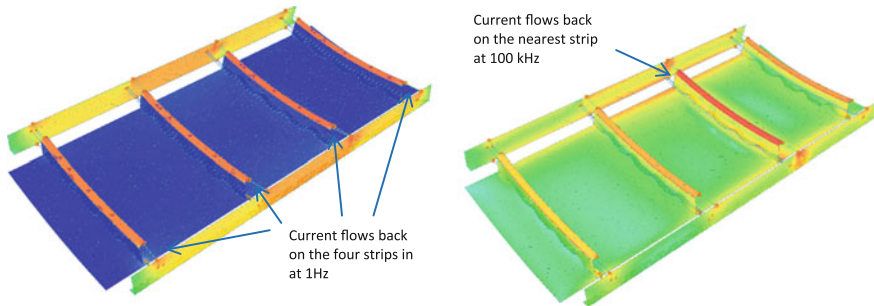


Transfer functions for 1A injected—AD2 and STRIP configurations (skin connected or not)

To clearly see the difference between strip and AD2 configuration (no skin connexion), we plot the transfer function for voltage near Frame 3. This is clear here that strip configuration is quite similar to the AD2 (even better for $F < 800$ Hz), but we have to mention that there is no junction resistance considered in this model. The strip needs more junctions between ESN elements, and this impact will be checked on the real structure when measured resistances available.



The following figure explains the redistribution effect between different elements for the strip configuration (current density mappings). At 10 Hz, the amount of current return is the same between all strip, and at $F = 100$ kHz, the current is no more equally distributed but flow back to the source by the nearest elements.



Current densities for $F = 1$ Hz (*left*) and $F = 100$ kHz (*right*)

4 Conclusion

This paper presents the first results of mechanical testing on frames equipped with metallic strips as well as the electrical performance. For mechanical tests, the strip solution improves significantly the detectability and the damage tolerance. For detectability, dents are visible through eye inspection for an impact less than 6 J versus no visible dent on non-protected composite specimens at 20 J. For damage tolerance, the metallic protection increases the energy threshold for damage initiation by 10 J (to be confirmed). Electrical assessments have been done by numerical simulation, and first, results show that strip solution is comparable with AD2 solution when junction resistances are low. The skin connection does not seem to impact transfer functions for current return below 10 kHz. Those results will be confirmed with the real measurements coming up soon.

Acknowledgments The research leading to these results has received funding from the European Union's Seventh Framework Programme for research, technological development and demonstration under grant agreement no 284562.

References

1. Revel I et al. (2008) Modeling strategy for functional current return in large CFRP structures for aircraft applications. EMC Europe
2. Piche A et al (2010) Electromagnetic modelling of large scale structures with non linear devices. EMC Europe

Benefit Analysis Value and Risk Assessment of New SARISTU-Technologies

Sevgi Batal and Stephne du Rand

Abstract The value and risk assessment investigates whether the SARISTU aim of improving aircraft efficiency has been met by achieving a reduction in the total weight and operating costs. Process times for manufacturing steps, together with pertinent weight data and weight impact calculations, are used to enable this assessment. The focus lies on processes established in the manufacturing of coupons, elements and details of the SARISTU-test pyramid in AS04 and AS06-10, as integrated into the sub-component technology demonstrators in IS13. A tool has been developed that allows results to be upscaled to component level and allows a comparison of SARISTU-technologies against state-of-the-art manufacturing methods for carbon fibre reinforced fuselages. Serial production and operational impacts have been considered. Additional technologies have been included, such as structural health monitoring (SHM), which was utilized for improving damage detection capabilities.

Nomenclature

Δ	Delta/change
AD	Accidental damage
AoG	Aircraft on ground
AS	Application scenario
AU	Acoustic ultrasonic
BMH	Braided mousehole
BVID	Barely visible impact damage
CFRP	Carbon fibre reinforced plastics
CVM-TTT	Continuous vacuum monitoring—through the thickness
CNT	Carbon nanotube

S. Batal (✉)

Aerospace, Defence and Rail—Airframe Structure, ALTRAN GmbH & Co. KG,
21079 Hamburg, Germany
e-mail: sevgi.batal@altran.com

S. du Rand

Aerospace, Defence and Rail—Flight Physics and Innovation, ALTRAN GmbH & Co. KG,
21079 Hamburg, Germany
e-mail: stephne.durand@altran.com

CPM	Cold process metalization
DE	International country code for Germany
DLR	Deutsches Zentrum für Luft- und Raumfahrt (German Aerospace Center)
DSS	Door surround structure
DT	Damage tolerance
ESN	Electrical structure network
FBG	Fibre Bragg grating
FEoPT	First estimation of process time
FO	Fibre optic
FuBu	Full bottom-up
GFRP	Glass fibre reinforced plastics
IS	Integration scenario
LSP	Lightning strike protection
MS	Metallic strip
MWCNT	Multi-walled carbon nanotubes
NDT	Nondestructive testing
Nr.	Number
NRC	Nonrecurring costs
OC	Operational costs
OEM	Original equipment manufacturer
RC	Recurring costs
Ref	Reference
SARISTU	Smart intelligent aircraft structures
SEM	Scanning electron microscope
SHM	Structural health monitoring
UD	Unidirectional
UV	Ultraviolet
WP	Work package

1 Introduction

The quintessence of the current approach of the benefit analysis for SARISTU IS13, “Fuselage Assembly, Integration and Testing”, has been captured in this document.

This includes an overview of the following:

- Applicable new technologies;
- Risk analysis;
- Methods used in the value and risk assessment;
- Process time impact assessment;
- Weight impact assessment; and
- Cost impact assessment.

As the SARISTU project will still be ongoing at the time of the *End of Project Conference*, this report's scope has been limited and the full scope will be addressed in the final report. The associated technologies and their impacts were analysed and the results are provided here as an exemplar of the scope of the analysis that will be found in the final benefit analysis report.

Within the last years, various technologies were developed in SARISTU. The first step of the benefit analysis focusses on identifying which technologies are linked to potential improvements, when implemented in future aircraft designs. The improvements are measured through comparisons of weight, process time and the overall operating cost to implement the technology.

The evaluated technologies were separated by main technology topics as well as the relevant and required tests that were defined and performed. Work package 132 (WP132) focusses on the benefit analysis for the fuselage-related technologies, and therefore, a breakdown has been made into the following technology topics:

- **Structural health monitoring (SHM):** Systems developed to enable the timely measurement of damages on the aircraft structure, by comparing the actual and relative capabilities.
- **Electrical isotropy:** Technologies summarized for electrical isotropy consider the improvement of the electrical current flow in a composite aircraft structure taking into account the bonding or grounding and lightning strike protection (LSP).
- **Damage tolerance (DT):** Related technologies concentrate on improving the structural performance of carbon fibre reinforced plastic (CFRP) elements as this is a key enabler for reducing component thickness and therefore saving mass.

For all of these topics, not only just the technology itself was developed, but also the method of implementation was identified.

The benefit assessment requires continuous comparison with the results coming from the test campaigns and includes considerations regarding upscaling. To enable the upscaling, a fundamental understanding of the principles of CFRP-aircraft design, manufacturing, maintenance and the existing challenges is needed.

Business cases related to implementing the investigated and developed technologies need to be defined individually. These are to be differentiated into those applicable to original equipment manufacturers (OEM), as well as operator-related business cases.

To enable the needed analyses, process time estimation and risk assessment tools were developed and an Airbus tool was both extended and updated. This allows for a fair and reproducible comparison between the different items within a technology topic, as well as for the comparison between all technologies and the resulting benefit for both the applicable OEMs and operators.

2 New SARISTU-Technologies

The scope of the application scenarios (AS) and work packages (WP) applicable to this chapter is presented in Fig. 1. A brief description of the target benefits and applicable technologies for each is to be found in the sections to follow. These are provided to enable the reader to better understand the work in this chapter, if the technologies or topics are unfamiliar.

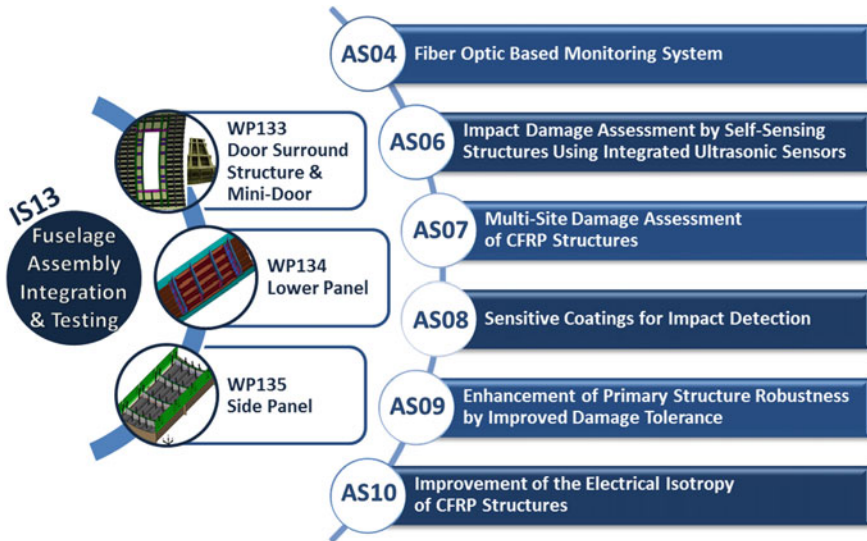


Fig. 1 ASs and WPs linked to and within the IS13 fuselage demonstration activities [1]

2.1 AS04—Fibre Optic-Based Monitoring System [1, 2, 3]

Target Benefits

- Design, optimization and implementation of a fibre optic (FO)-based SHM system in composite stiffened aircraft structures;
- System that enables strain sensing on fuselage applications; and
- System that enables the detection of debonding of stiffeners.

Objective Design, optimization and implementation of a strain monitoring system, based on a network of FO sensors, such as fibre Bragg gratings (FBG), that will be integrated into the structural parts during the manufacturing phase as a modular network of ribbon tapes. To obtain the benefits, the research has been focused on

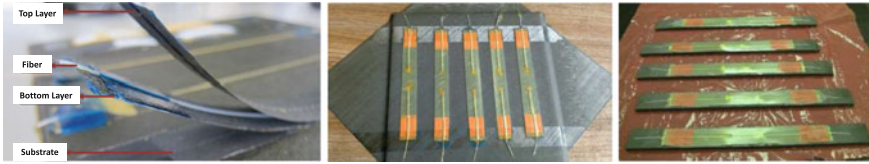


Fig. 2 *Left* Ribbon tape illustration. *Middle* Co-bonded ribbon tapes. *Right* Secondary bonded ribbon tapes [3]

the realization and testing of the ribbon tape concept, integration and functionality testing. Additionally, the appropriate raw data manipulation methodologies and a FBG-based SHM system are being researched and developed. See Fig. 2.

2.2 AS06—Impact Damage Assessment by Self-sensing Structures Using Integrated Ultrasonic Sensors [1, 2]

Target Benefits

- Assessing the damage detection, sensor integration, quality assurance, contacting and data transfer capabilities and functions of self-sensing structures;
- Introducing self-sensing functionality to the fuselage structure by implementing piezo-electrical transducers; and
- Enable damage detection and assessment functionalities to the fuselage through actuated and sensed guided waves in the “pitch-catch” mode.

Objective The objective was to enable the installation of a large-scale sensor network under serial production manufacturing conditions. The damage detection is to include the detection of delaminations after impact. The targeted demonstrator for this technology has been the WP133 door surround structure (DSS), Fig. 3, and mini-door.

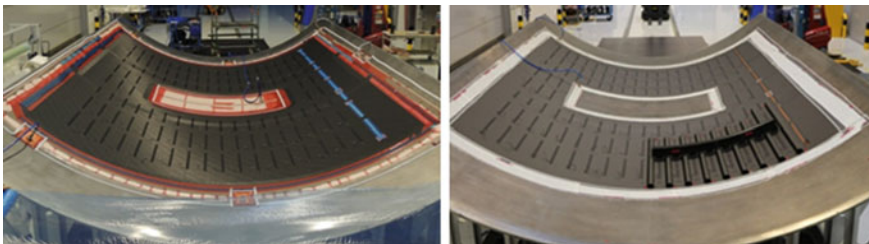


Fig. 3 Large-scale integration of sensor networks shown. *Left* Prebonding. *Right* Co-bonded [2]

2.3 AS07—Multi-Site Damage Assessment of CFRP Structures [1, 4]

Target Benefits

- Assessing airworthiness in the presence of multi-site damages through prediction method development, thereby enabling improvements in the maintenance aspects of CFRP structures;
- Specification of SHM system monitoring tasks for assessing multi-site damages;
- Down-selection of suitable SHM systems (from AS04-06);
- Enable damage assessment decision support through tool development to combine SHM system information and the prediction method;
- Integration and validation of both SHM-technology and the damage assessment tool; and
- Obtain additional information on stiffener health through the integration of continuous vacuum monitoring—through the thickness (CVM-TTT) technology.

Objective Development of prediction method and tool capable of assessing the airworthiness of aeronautic structures by means of SHM in the presence of multi-site damages. Primary technologies include the down-selected acoustic ultrasonic (AU) and FO SHM systems as shown in Fig. 4.

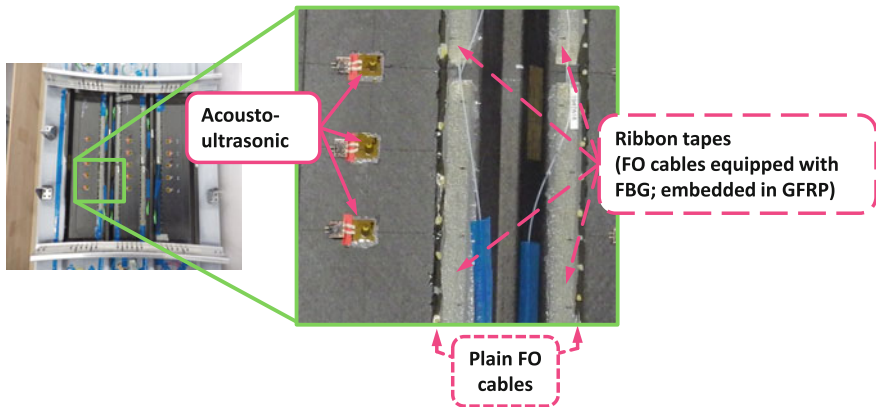


Fig. 4 Curved stiffened demonstrator panel with three types of incorporated SHM systems [4]

2.4 AS08—Sensitive Coatings for Impact Detection [1, 5]

Target Benefits

- Improve impact detection on composite structures by developing sensitive coatings that can increase the barely visible impact damage (BVID) threshold; and
- Assess further aircraft design optimization by reducing the structural thickness margin, resulting in weight savings.

Objective Objective was to develop a coating, including either pigments or microcapsules, that is pressure sensitive and will change colour after having experienced the material stress caused by a structural impact. The impact is to be indicated by a colour change which is observable in the visual or ultraviolet (UV) range. See Fig. 5.

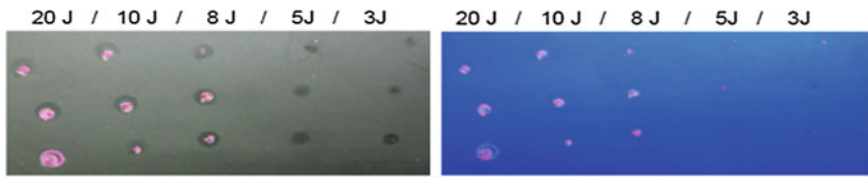


Fig. 5 Matrix separation with clearcoat applied to the top layer of the coupon, shown with impacts correlating to 3–20 J. *Left* Impact damage viewed in the visible spectrum (daylight). *Right* The same under UV-light [6]

2.5 AS09—Enhancement of Primary Structure Robustness by Improved DT [7]

Target Benefits

- Composite material and adhesive toughening via the introduction of carbon nanotubes (CNT) and thermoplastic interleafs; and
- Achieve an increased maturity level for technologies that can realize measurable improvements in aircraft DT and achieve consequent weight reductions.

Objectives

- Evaluate toughening of composite materials and adhesives;
- Integration of “commercial” thermoplastic veils into CFRP manufacturing processes;

- Development of methods and processes to integrate multi-walled carbon nanotubes (MWCNT) into CFRP;
- Investigation of MWCNT-doped structural film adhesives; and
- Production and testing of sub-elements representing the fuselage’s lower panel.

See Fig. 6 for graphical elaboration.

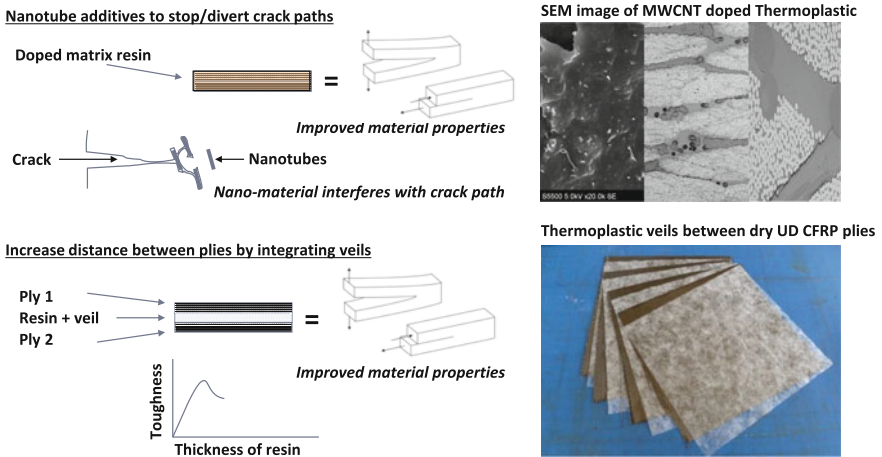


Fig. 6 Mechanisms of enhancing the primary structure and examples thereof [8]

2.6 AS10—Improvement of the Electrical Isotropy of CFRP Structures [1]

Target Benefits

- Demonstrate manufacturability of CFRP parts with improved electrical conductivity;
- Increase the z-direction electrical conductivity of third generation toughened prepreg CFRP laminates and adhesives by ten orders of magnitude; and
- Improve CFRP surface conductivity and thereby improve the damage mechanisms in place against accidental damage (AD), e.g. short circuiting and lightning strike.

Objectives

- Evaluate technologies that demonstrate structural integration capability and the manufacturability of CFRP parts with improved electrical conductivity;

- Introduction of CNT to increase the z -direction electrical conductivity of third generation toughened prepreg CFRP laminates and adhesives;
- Integration of metallic strips (MS) on the CFRP surface, providing insulation from the CFRP structure by introducing glass fibre reinforced plastic (GFRP) or rubber layer(s); and
- Research and develop metallic coatings to improve the CFRP's surface conductivity.

See Fig. 7 for graphical elaboration.

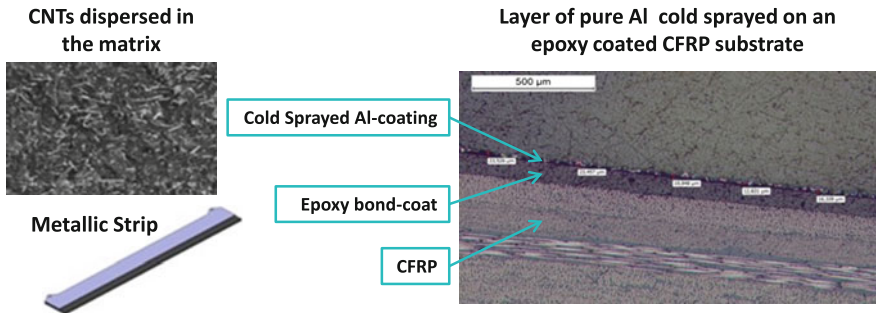


Fig. 7 *Top left* Example of CNTs dispersed in the matrix to increase z -direction electrical conductivity. *Bottom left* Metallic strip part design. *Right* Cold process metalization example [9]

2.7 Correlation of Application Scenario Technologies to the IS13 Work Packages

The various ASs briefly discussed in the preceding sections are integrated into demonstrators for further testing and evaluation. An overview of the correlation of ASs and IS13 WPs is shown in Fig. 8.

The WPs are briefly elaborated in the next sections to provide the reader with an understanding of the technology demonstrators utilized to benchmark many of the manufacturing processes that have been evaluated in this chapter.

An elaboration of the WPs and their components is provided in Sect. 2.8.

2.8 Demonstrator Naming and WP Primary Research Focus

The demonstrators have been named according to the fuselage components they represent. An overview of their names, location on a schematic fuselage cross section and the primary focus of the research they were built to facilitate is provided below in Fig. 9.

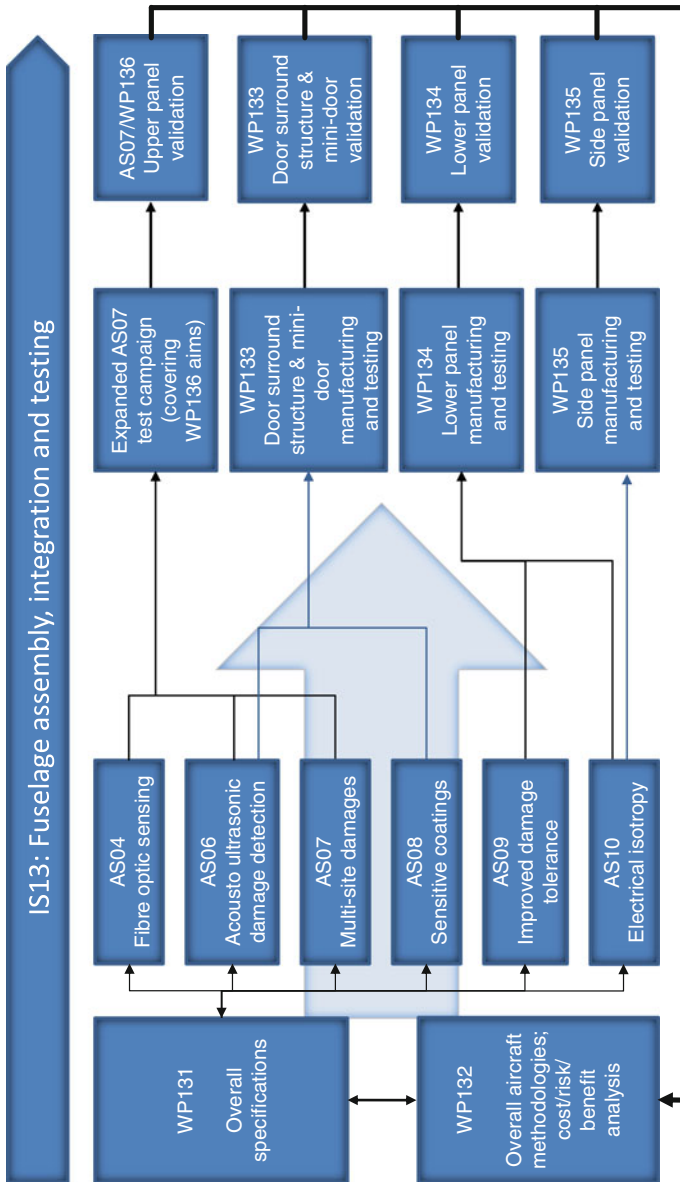


Fig. 8 Interrelation of ASs and IS13 WPs (Source B. Newman)

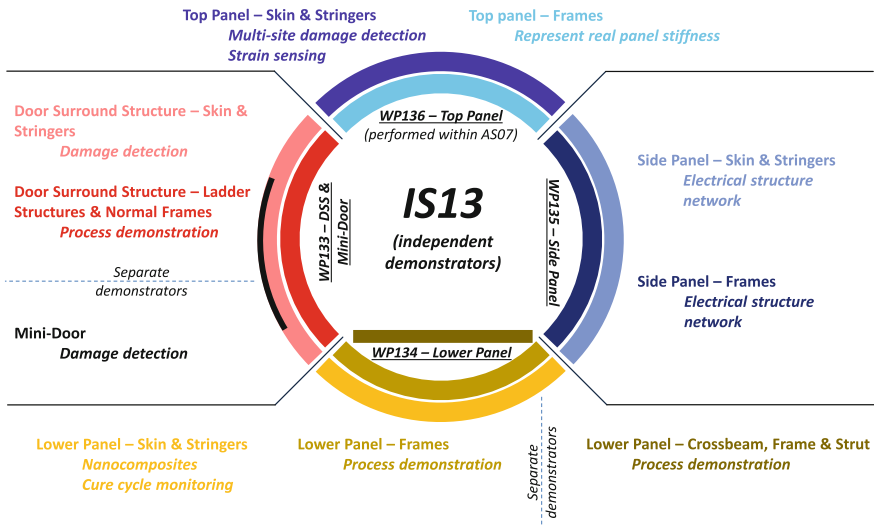


Fig. 9 Schematic fuselage cross section with correlating WP, demonstrator names and primary research focus indicated (Source B. Newman)

2.9 WP133—Door Surround Structure (DSS)

The DSS is a full-scale technology demonstrator, representative of a section of the fuselage panel that includes two frame bays to each side of a door reinforcement structure, as well as the door cutout.

The DSS has been assembled out of several major components, with the assembly shown in Fig. 10:

- Skin;
- Normal frames with Braided mouseholes (BMHs), connected with metallic couplings;
- Door frames;
- Omega stringers;
- Ladder structures; and
- SHM system.

Note: All component materials are composites, except for the SHM system, unless otherwise stated.

2.10 WP133—Mini-Door

The mini-door has been built as a half-scale model of a representative door. The assembled mini-door is shown in Fig. 11 and has been assembled out of several major components:

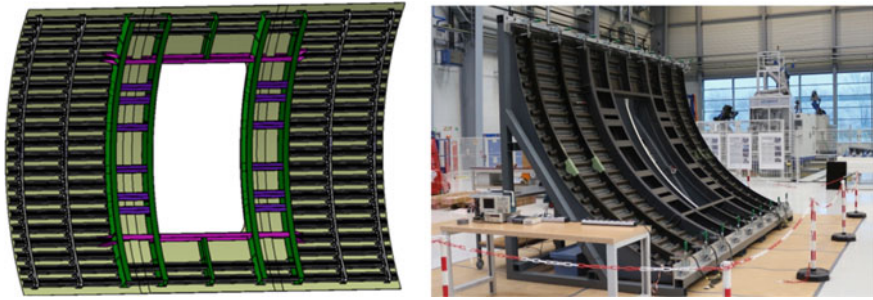


Fig. 10 *Left* DSS CATIA model [2]. *Right* DSS in DLR laboratory, Stade (DE)



Fig. 11 *Left* Mini-door after resin transfer moulding (inner surface, unpainted). *Middle* Mini-door (inner surface, painted). *Right* Mini-door (outer surface, painted) [2]

- Skin;
- Beams;
- Frames; and
- SHM system.

Note: All component materials are composites, except for the SHM system, unless otherwise stated.

2.11 WP134—Lower Panel

The lower panel has been built as a representative lower section of the fuselage. It has been assembled out of several major components, with the assembly shown in Fig. 12:

- Skin;
- Omega stringers; and
- Frames with metallic cleats.

Note: All component materials are composites, unless otherwise stated.

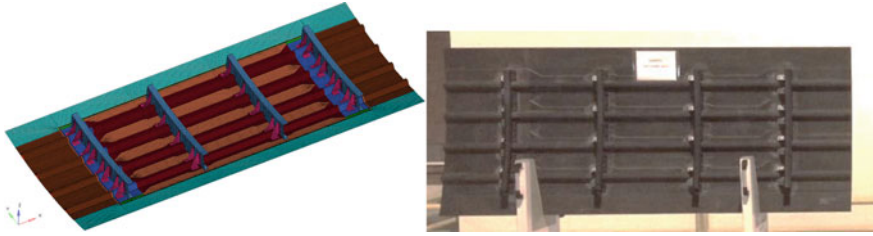


Fig. 12 *Left* Lower panel CATIA model [2]. *Right* Manufactured lower panel [10]

2.12 WP135—Side Panel

The side panel has been built as a representative fuselage side panel across several stringers and frames. It has been assembled out of several major components (the assembly is shown in Fig. 13):

- Skin;
- Braided mousehole (BMH) frames incorporating co-cured MS; and
- Stringers.

Note: All component materials are composites, unless otherwise stated.



Fig. 13 Side panel assembled into its electrical testing rig [11]

2.13 Technology Research and Development Status

An overview of the technology investigation status, as measured by the percentage of tests completed per AS, is provided in Fig. 14. This status reflects the testing completed by the end of project meeting (April, 2015).

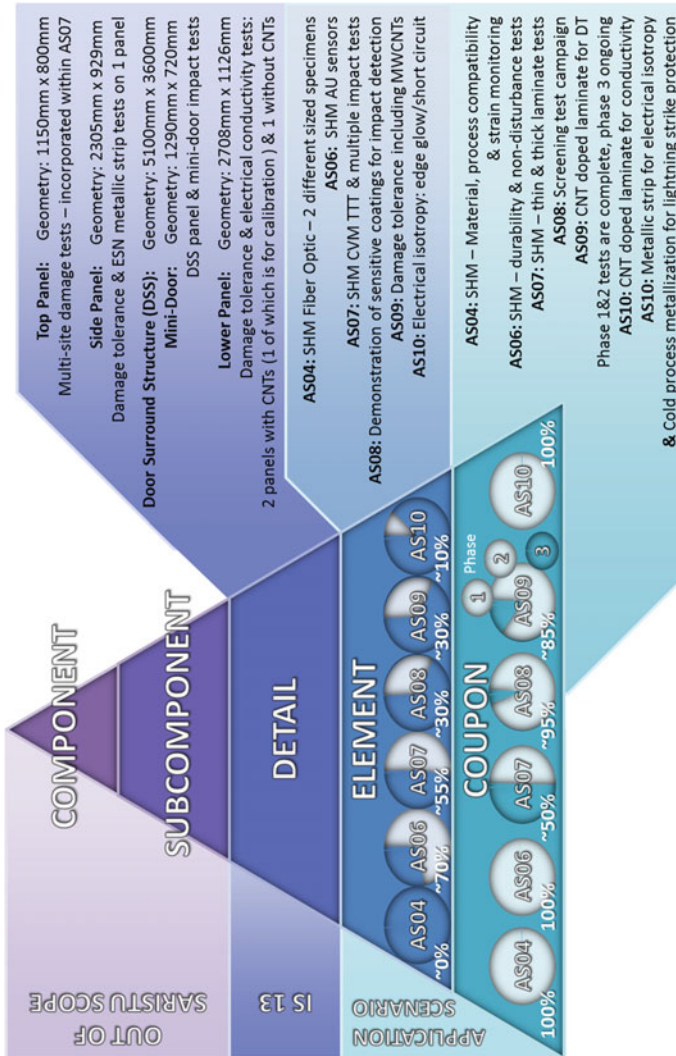


Fig. 14 Technology investigation status based on tests completed, indicated in %

2.14 Technology Topics

The investigated technologies have further been grouped into three topics, as illustrated in Fig. 15.



Fig. 15 Technology topics and their researched solutions

The current status of the SARISTU-technology research and development is illustrated below in Fig. 16, based on the percentage of tests completed (indicated on the figures) per technology topic. As all research has not yet been concluded, the benefit analysis that has been presented in the subsequent chapters may still change accordingly over the coming months.

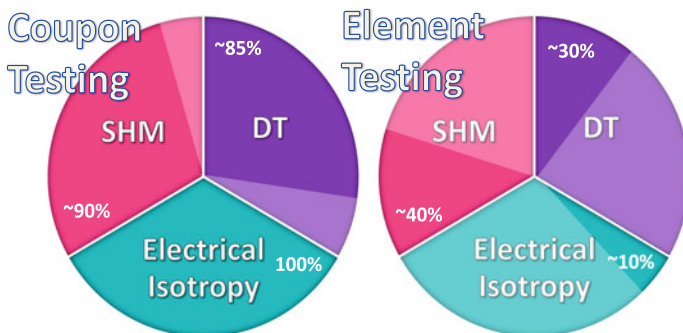


Fig. 16 Percentage of tests completed per technology topic, indicated in %. Coupon testing completion is illustrated in the left and element testing completion is indicated in the right

3 Technical Risk Analysis

Risks associated with the implementation, manufacturing and maintenance of the various technologies have been captured, along with their respective mitigation plans and actions. It should be noted that these risks are technical in nature.

The analysis primarily focusses on the following factors:

- Design optimization;
- Manufacturing (including serial production and ergonomic considerations);
- Functionality;
- Reliability;
- Durability;
- Maintenance; and
- Impact on SARISTU goals (e.g. whether the risks are estimated to be “showstoppers”).

The risk analysis presented in this chapter has been based on input received from the focal points of WP133, WP134 and WP135. The risks are presented based on a preliminary weighting that takes into account the complexity, probability of occurrence, impact severity, impact on health and safety (as applicable), as well as whether the risk is seen as a “showstopper” within SARISTU. The latter factor has been taken into consideration as some technical risks indicate facets of the technologies or associated manufacturing processes that are known to occur, yet have been mitigated or might fall outside the scope of the SARISTU project. A table of the received risks and their associated mitigations is provided following each risk assessment matrix.

A full technical risk analysis of the applicable technologies and processes is to be presented in the final report. This activity is currently ongoing and is partially dependent on the outcome of the ongoing test campaigns mentioned in Sects. 2.13 and 2.14.

3.1 General

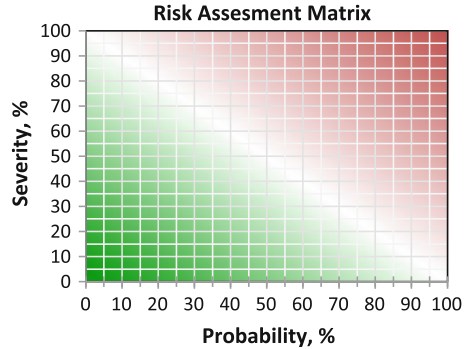
The technical risks have been grouped according to the technology topics and are presented in the subsequent sections together with a matrix of the received technical risks and their mitigations.

Weighting factors have been used to indicate the relative impact of the technical risks. It is expected that a re-evaluation of the weighting, as well as an addition or refinement of weighting factors, will be found in the final report.

Risks found at the bottom left (green area) of the visualized risk assessment matrix (see Fig. 17) are associated with a minor impact on the adoption of the particular technology or process they relate to. Risks indicated towards the upper

right-hand corner indicate that additional research and development may be needed to mature technologies for serial production or in-field service (which lies outside the scope of the SARISTU project).

Fig. 17 Generic, empty risk assessment matrix provided for explanation purposes



Some risks have been identified and mitigated within the scope of SARISTU for technologies which do not yet have a high maturity level. These will need to be revisited for serial manufacturing or line maintenance scenarios. In order to ensure that the associated technical risks are not shown as critical within the risk assessment matrices, the “showstopper” weighting factor was introduced. This factor allows the risks to be accurately reflected with respect to their impact, that is to say the probability and severity of their occurrence. As all these risks have been mitigated (or currently have mitigation in place), no risks have been indicated as “showstoppers” for any of the technology topics.

3.2 Structural Health Monitoring Risk Assessment

The risks associated with SHM-related WPs are listed in Table 1 and their impacts are indicated in Fig. 18.

No risks are identified as “showstoppers”.

3.3 Electrical Isotropy Risk Assessment

The risks associated with electrical isotropy-related WPs are listed in Table 2 and their impacts are indicated in Fig. 19.

No risks are identified as “showstoppers”.

Some risks were shared with the DT technology topic (Sect. 3.4) as the technologies involved were applicable to both topics.

Table 1 SHM risks and mitigations

Nr.	Grouping	Description	Risk	Mitigation	References
B.1	Manufacturing	Preform braiding	Difficulties in preform braiding to match a female mould tool	Additional development required to attain desired tolerances for integrated mousehole frames	[12]
B.2	Cost	BMH frames	Cost intensive manufacturing process	Additional development of manufacturing process and tool advances to optimize the process and eliminate expenses such as autoclaves or complex infusion processes	[12]
B.3	Performance	Stress analysis	Stress analysis needed to determine whether the performance requirements have been met	Planned stress analysis, outside SARISTU scope	[12]
B.4	Performance	Stress analysis	Stress analysis needed to enable optimization	Planned stress analysis, outside SARISTU scope	[12]
B.5	Manufacturing	Warping	Normal frames prone to warping	Further manufacturing trials and subsequent process/tool iterations, outside SARISTU scope	[12]
B.6	Manufacturing	Material properties	Frames with varying cross sections and material properties due to lay-up process and design	To be taken into account during part sizing	[13]

Fig. 18 SHM risk assessment matrix indicating weighted technical risks, based on their severity and probability of occurrence

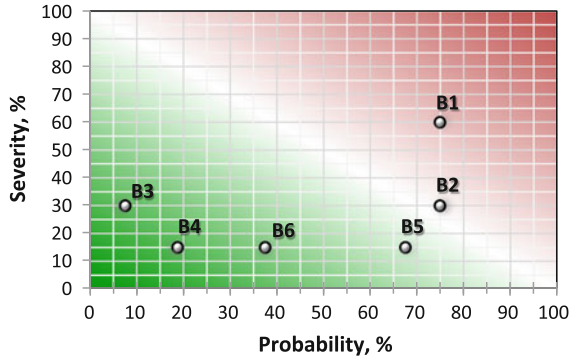


Table 2 Electrical isotropy risks and mitigations

Nr.	Grouping	Description	Risk	Mitigation	References
C.1	Manufacturing	Metallic strips	Industrialization of manufacturing process requires additional research (envisioned process is untried): Roll forming was used in SARISTU, with vulcanized rubber, having necessitated an additional layer of adhesive film to ensure bonding of metallic strips to the CFRP material	Process to be researched and developed to enable and streamline the following production effort: use single cutout flat strips, which would be formed afterwards	[14]
C.2	Cost	Frames	Cost intensive manufacturing process	Additional development of manufacturing process and tool advances to optimize the process and eliminate expenses such as autoclaves or complex infusion processes	[14]

(continued)

Table 2 (continued)

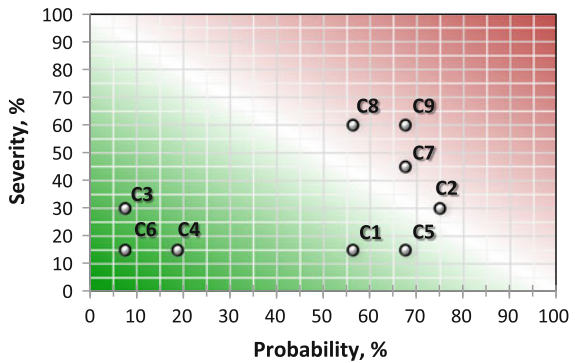
Nr.	Grouping	Description	Risk	Mitigation	References
C.3	Performance	Stress analysis	Stress analysis needed to determine whether the performance requirements have been met	Planned stress analysis, outside SARISTU scope	[14]
C.4	Performance	Stress analysis	Stress analysis needed to enable optimization	Planned stress analysis, outside SARISTU scope	[14]
C.5	Manufacturing	Warping	Normal frames prone to warping	Further manufacturing trials and subsequent process/tool iterations to be conducted, outside SARISTU scope	[14]
C.6	Manufacturing	CNT-doped veils	CNT-doped veils made via the melt-blown process need to consider the polymer's viscosity during the melt-blowing process to eliminate fibre breakage	Additional development of the manufacturing process led to a polymer change, additive usage and adjustments to the processing conditions, which successfully mitigated the risk	[15]
C.7	Performance	CNT-doped veils	Electrical conductivity highly dependent on thermoplastic used	Appropriate thermoplastic to be selected, outside SARISTU scope	[15]

(continued)

Table 2 (continued)

Nr.	Grouping	Description	Risk	Mitigation	References
C.8	Performance	CNT master batch for resin	Producing high CNT concentration master batch to be diluted for veil production that has the target electrical conductivity (MWCNTs in thermoplastic)	Doped resin systems were evaluated for a down-selected resin (to be used in the infusion process) to ensure the target electrical conductivity could be attained	[16]
C.9	Performance	CNT master batch for adhesive	Producing high CNT concentration master batch to be diluted for veil production that has the target electrical conductivity (MWCNTs in thermoplastic)	Doped resin systems were evaluated for adhesives to ensure the target electrical conductivity could be attained	[16]

Fig. 19 Electrical isotropy risk assessment matrix indicating weighted technical risks, based on their severity and probability of occurrence



3.4 Damage Tolerance Risk Assessment

The risks associated with DT-related WPs are listed in Table 3 and their impacts are indicated in Fig. 20.

No risks are identified as “showstoppers”.

Some risks were shared with the electrical isotropy technology topic (Sect. 3.3) as the technologies involved were applicable to both topics.

Table 3 Damage tolerance risks and mitigations

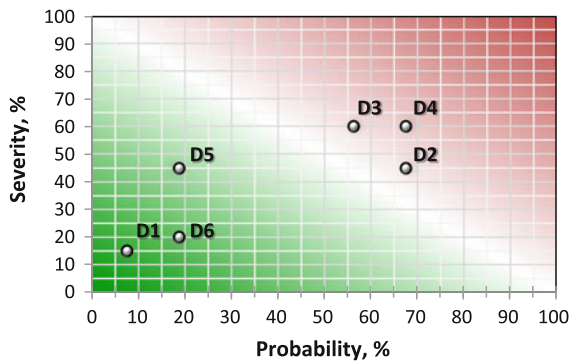
Nr.	Grouping	Description	Risk	Mitigation	References
D.1	Manufacturing	CNT-doped veils	CNT-doped veils made via the melt-blown process need to consider the polymer’s viscosity during the melt-blowing process to eliminate fibre breakage	Additional development of the manufacturing process led to a polymer change, additive usage and adjustments to the processing conditions, which successfully mitigated the risk	[15]
D.2	Performance	CNT-doped veils	Electrical conductivity highly dependent on thermoplastic used	Appropriate thermoplastic to be selected, outside SARISTU scope	[15]
D.3	Performance	CNT master batch for resin	Producing high CNT concentration master batch to be diluted for veil production that has the target electrical conductivity (MWCNTs in thermoplastic)	Doped resin systems were evaluated for a down-selected resin (to be used in the infusion process) to ensure the target electrical conductivity could be attained	[16]
D.4	Performance	CNT master batch for adhesive	Producing high CNT concentration master batch to be diluted for veil production that has the target electrical conductivity (MWCNTs in thermoplastic)	Doped resin systems were evaluated for adhesives to ensure the target electrical conductivity could be attained	[16]

(continued)

Table 3 (continued)

Nr.	Grouping	Description	Risk	Mitigation	References
D.5	Performance	CNT production	Feasible industrial grinding process	For the doped M21 prepreg several materials were produced to increase the volume fraction and were evaluated	[16]
D.6	Manufacturing	Material availability	The SARISTU approach to powder grinding has a yield that is too low for industrial requirements.	Industrial cryogenic grinding was evaluated	[16]

Fig. 20 DT risk assessment matrix indicating weighted technical risks, based on their severity and probability of occurrence



4 Benefit and Impact Assessment

The weight impact assessment has been executed utilizing an expanded version of Airbus’ “full bottom-up” (FuBu) weight estimation tool. Concisely explained, the weight calculation is based on a global finite element model for a CFRP-aircraft structure. This structure includes the skin, stringers and frames, with additional data such as those associated with clips, cleats and rivets.

Combined with the manufacturing time impact calculated by the internal first estimation of process time (FEoPT) tool, these values determined the implementation results that were taken as the assessment basis when applying the developed SARISTU-technologies on the aircraft structure.

The critical point for a manufacturer-related comparison is to define a representative basis for weight and process time calculation in close collaboration with an OEM. For the analysis presented here, this basis includes the following (as applicable in each case):

- Purchasing raw material;
- Material handling and manufacturing;
- Part manufacturing and assembly;
- Applying protective coatings; and
- Nondestructive inspection and testing.

This kind of calculation run was performed for all developed fuselage-related technologies and compared with the baseline. Once the impact of the technologies on the baseline model was identified and implemented in these tools, several calculation runs were executed. Continued refinement of these calculations will be executed over the final months of this project and a minimum of one additional run is required for the final report due to the fact that some test results are still missing (see Sect. 2.13) and the scope of all technologies is to be included.

In the subsequent figures, an overview of the delta weight, time and cost impacts is provided in comparison with the case of implementing SARISTU-technologies in the new CFRP-aircraft design. These values are used in order to enable the benefit analysis calculations. For example, an implementation¹ weight impact will influence the direct operating cost, which will influence the benefit, along with other cost factors, such as recurring costs (RC) and nonrecurring costs (NRC).

Due to the maturity of some technologies being further away from serial production than others, please consider that the delta values are currently not as detailed as required for all technologies as the benefit analysis activities are still ongoing and will be iterated over the next months. Additionally, upscaling is an ongoing process which will be completed and described in detail within the final delivery report.

The discussion regarding operator implementation and maintenance costs is currently in progress with both a legacy and a low-cost airline. The results of these discussions are expected to be significant due to many differences that need to be considered during the business case analysis, for example:

- Aircraft utilization—flight cycles, e.g. short-range versus long-range aircraft;
- Environmental aspects—climate-based influences, e.g. operations in cold or hot climate zones;
- Environmental aspects—damage sources, e.g. destination airfield types that influence the type of damages expected to be experienced by the aircraft, such as the runway condition or whether there are other debris sources; and
- Ground support equipment and maintenance facility availability.

¹Deltas (% values) are provided in this chapter in order to protect sensitive information.

It is expected that benefits will be shown in the final report based on a baseline for the manufacturer or the operator. The baselines utilized for presenting the results, per technology topic, are as follows:

- **SHM benefit analysis:** Saving shown for an operator, with the benefit indicated as for one aircraft with one occurrence of incident. The potential for SHM systems to be used in the design phase as an enabler for reduced DT criteria, and therefore reduced component thicknesses or masses and resultant weights, is not considered.
- **Electrical isotropy benefit analysis:** Shown as the benefit provided by the manufacturing process, which is linked to the OEM.
- **DT benefit analysis:** Calculations are directly linked to the design captured within the global finite element modelling used for the calculation by FuBu. The pending test results from WP134 are fundamental to make a new calculation run by changing some values mainly regarding robustness, e.g. decreasing the minimum skin thickness while keeping the same reserve factor, or the post-buckling policy linked to changing the stringer pitches.

4.1 Weight Assessment

The results shown here in Fig. 21 are based on the SARISTU development work, feeding into Airbus' weight assessment tool (FuBu) to be used as input in upscaling the results from laboratory-scale to full-scale in order to enable a fair evaluation. Technologies are evaluated individually against their own baselines.

Values have been colour coded according to the applicable technology topic. The weight benefits are still to be refined for the SHM and DT technologies and are highly dependent on the operator business case (as discussed in the introduction of this chapter).

The potential benefits shown for cold process metallization (CPM) assume that the challenges faced in coating application can be overcome during further development.

4.2 Process Time Assessment

Process times are to be evaluated in order to provide an accurate assessment, for the manufacturing and maintenance of all components related to the SARISTU-technologies. This section provides an overview of the methodology and results related to the various SARISTU-technologies, as well as several examples to demonstrate the influence that can be found when selecting different processes in the manufacturing of a single component. A full accounting of all technologies is to be provided in the final report in 48-month project.

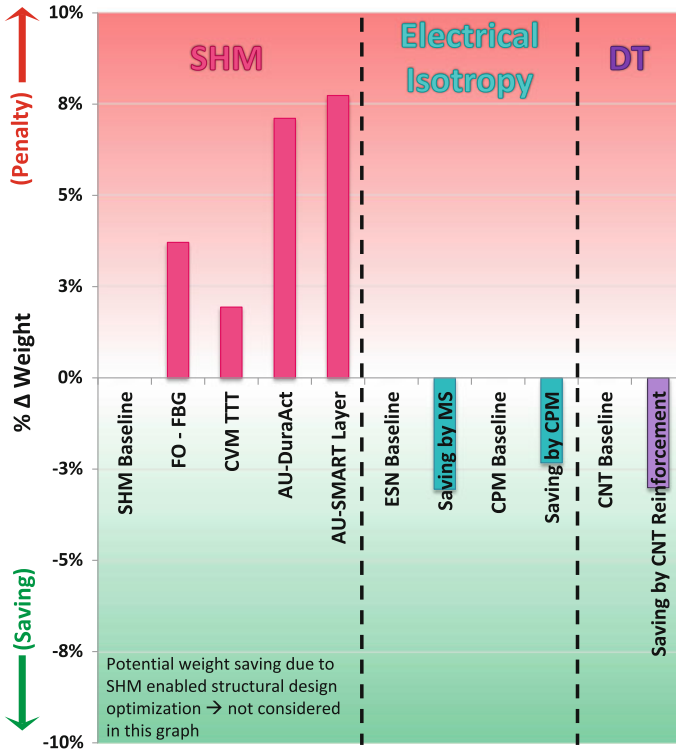


Fig. 21 Technology implementation weight impact on the fuselage; technologies are evaluated individually against their own baselines

Tools are under development to fully capture the spectrum of technologies and process influences that were investigated in SARISTU. The time assessment tool is based on its predecessor FEOPT, version 1, which is being expanded upon to enable the final report. FEOPT has been used in establishing the technology implementation time impact presented in this chapter.

4.2.1 Methodology

Process times have been calculated based on expert input from within the consortium. The difference between these calculated values and current state-of-the-art manufacturing and maintenance process times have been determined as delta (Δ) times, as originally measured in either man- or machine hour. The process time impact assessment is based on these values. The delta time results have further been utilized in the cost impact assessment (Sect. 4.3).

4.2.2 Impact of Manufacturing Processes Selection

As various manufacturing processes have different steps and durations associated with them, their accumulative manufacturing times will differ. A comparison of several manufacturing process times is given here to provide the reader with a reference of the impact that the selection of different manufacturing processes could have.

It can be noted that the processes do not always have the same steps, and when they do the steps often have different process times associated with them, e.g. the time needed to prepare for curing may vary by several hours.

In selecting specific technologies, methods or processes, the full impact on the manufacturing process needs to be considered, including the availability of specific tools and machines, the potential impact on in-service maintenance activities and the associated costs.

The selection of a specific process, method and technology has an effect on the benefit/impact assessment. All impacts are to be evaluated in the context of the full benefit or cost of implementation, not only the delta time, or weight. An investigation of the combinations leading to the greatest benefit is to be further explored and will be presented in full in the final report deliverable at the project's conclusion.

4.3 Cost Assessment

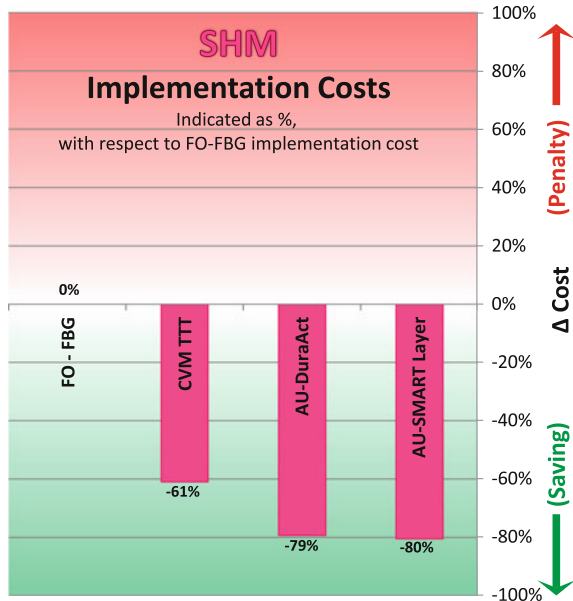
The input values to enable the cost benefit assessment were taken from discussions with industry experts and sources (both at a European OEM and a major European airline). As was mentioned in the introduction of this chapter, the discussions with the operators are still ongoing, yet the preliminary results based on the SHM results provided below, presented in Fig. 22, should serve to provide the reader with a first indication of the analysis and results to come in the final report.

It can be seen that while SHM systems do carry associated implementation costs, they could offer a reasonably quick breakeven based on the potential savings offered during maintenance.

Maintenance cost savings will be found *every time* the SHM system is able to provide indicative results that eliminate the need for nondestructive testing (NDT) or for an inspector to evaluate the AD. Eliminating as few as four 24 h AoG level two inspections, or five 10 h AU investigations, could provide a breakeven for the implementation costs of the AU SHM technologies on an aircraft. Taking into account the aircraft's design life of 100,000 flight hours, attaining the breakeven point seems quite likely under the current assumptions regarding the AU system's functionality.

Please note that the exact breakeven time frame will depend on the airline's mission profile and environment. For example, aircraft operating at airports where airstairs are used in favour of passenger boarding bridges are expected to see a difference in incidences of related ADs. Similarly, the flight duration, airport conditions and maintenance facility capabilities could have an influence on both the

Fig. 22 Technology implementation cost impact and benefit for SHM. Provided as material and installation cost and savings, as shown in % with respect to the material and installation costs of the FO-FBG



frequency that the SHM system is needed, and the maintenance planning, which could impact the breakeven time frame and SHM benefit.

Further estimations of the integration costs (both NRC and RC) and operational costs (OC) will be provided in the aforementioned final report.

5 Conclusion

The current status of the following analyses has been provided:

- Technical risk assessment at top and intermediate levels (for sub-components, elements, details and the associated manufacturing and maintenance processes)
- Process time, weight and cost impact assessment overviews

It is important to note that the final analysis must take all assessment types into consideration, from both a supplier and an end user’s point of view. A prime example of this relates to SHM systems: for an OEM, SHM systems complicate the manufacturing chain, increase costs and make the aircraft heavier²; however, the in-service benefits for airlines in terms of reduced AoG or inspection times, and therefore costs, are such that SHM is a premium system/service for which they may be willing to pay.

²This assumes the SHM system is not used in the design phase as an enabler for reduced damage tolerance criteria, and therefore reduced component thicknesses/masses.

The results indicate overall (net) benefits associated with the implementation of SARISTU-technologies on aircraft. The analysis presented here for the technologies will be updated and provided together with the technology implementation time-lines in the final benefit analysis report.

A major task that will be addressed in the final report is providing an implementation impact analysis that takes into account the various materials, methods and processes that can be selected in the manufacturing of pertinent components. Additionally, the analyses are to include the full maintenance steps and impact of all these technologies.

Acknowledgments The work presented in this paper relied heavily on input provided by the many specialists that so patiently answered our questions, showed us their facilities and contributed to the SARISTU-technologies evaluated here. The authors wish to sincerely thank all the partners and colleagues that have so generously contributed to our work, providing us with the input and feedback that assisted us in the compilation of this report.

Additionally, we would like to thank our focal points in our SARISTU partner organizations and our colleagues involved in the management of both the project and technical activities, whose continued support we greatly appreciate.

A special thank you goes out to our ALTRAN colleagues, families and friends who provided us with both direct and indirect support. Especially the coffee.

The research leading to these results has received funding from the European Union's Seventh Framework Programme for research, technological development and demonstration under grant agreement no 284562.

References

1. Seventh Framework Programme, AAT.2011.4.4-3, Integrated approach to smart airframe structures, Annex I—"Description of Work", (2014) Ref Ares (2014)3464235, 20 Oct 2014
2. SARISTU Partners (2014) SARISTU project periodic report—3rd reporting period (01 Sept 2013–31 Aug 2014)
3. Koimtzoglou C, AS04 Partners (2014) SARISTU AS04—CCR3 review
4. Newman (2015) SARISTU AS07 and IS13—scenario leader assembly report
5. Barut S (2014) SARISTU AS08—sensitive coatings for impact detection, CCR3 review
6. Barut S, Senani S, Nixon S, Kondolff I, Montagnier B, Tedim J, Zheludkevich M, Gaudon M, Blanco V, Gradert I (2014) SARISTU AS08—meeting for period 3 report
7. Pandya S, AS09 Partners (2013) SARISTU AS09—mid-term review poster
8. AS09 Partners, (2014) SARISTU AS09—CCR3 review
9. AS10 Team, (2014) SARISTU AS10—period 3 review meeting
10. Newman B (2015) SARISTU end of project meeting: IS13 presentation, day 1
11. Newman B (2015) SARISTU end of project meeting: IS13 presentation, day 2
12. Tauchner J, FACC (2015) Expert input: frame manufacturing risk mitigation—WP133. Email
13. Breu C, AIRBUS DS-D (2015) Expert input: risk mitigation—WP133, email
14. Tauchner J, FACC (2015) Expert input: frame manufacturing risk mitigation—WP135, email
15. Latko P, Technology Partners (2015) Expert input: CNT doped veil production—AS09. Status update of TECPAR CNT research, email and attachment
16. Bonduel D, Nanocyl (2015) Expert input: SARISTU CNT to increase DT—Evaluation and down-selection of processes and materials and expert input: nanocyl risk mitigation—WP134, email and attachment

Manufacturing of Nano-treated Lower Panel Demonstrators for Aircraft Fuselage

Feride Nur Sasal, Aysun Dogangun Akın, Ayhan Kılıç, Guray Erteği, Caglayan Duygu, Emre İşler, Ben Newman, Christos Koimtzoglou, Panagiotis Maroulas, Patrick Bara, Antonios Vavouliotis, George Sotiriadis and Vassilis Kostopoulos

Abstract Improved robustness is seen as a key technology enabler for reducing the required thicknesses of composite structural parts; this reduction would, in turn, lead to direct savings in the structural mass. The aim of this study was to produce one reference and two nano-treated lower panel demonstrators for investigating the effect of nano-reinforcement on the damage tolerance behaviour of skin, stringers, bondline and on the electrical conductivity of CFRP. The selected technology, resulting from development and experiments undertaken within the SARISTU project, is carbon nanotube (CNT)-integrated prepreg material M21/34%/UD194/T800S, which is treated by University of Patras. The studies on damage tolerance improvement performed within the scope of Application Scenario 09 were used as input during determination of the manufacturing parameters for the selected

F.N. Sasal (✉) · A. Dogangun Akın · A. Kılıç

Material and Process Technologies, Turkish Aerospace Industries Inc, 06980 Ankara, Turkey
e-mail: fersarac@tai.com.tr

A. Dogangun Akın
e-mail: adogangun@tai.com.tr

A. Kılıç
e-mail: akilic@tai.com.tr

G. Erteği
Forming Tools Design Engineering, Turkish Aerospace Industries Inc, 06980 Ankara, Turkey
e-mail: gertegi@tai.com.tr

C. Duygu · E. İşler
Manufacturing Engineering Department, Turkish Aerospace Industries Inc, 06980 Ankara, Turkey
e-mail: caglayan.duygu@tai.com.tr

E. İşler
e-mail: emisler@tai.com.tr

B. Newman
Aerospace and Defence—Flight Physics and Innovation, Altran GmbH & Co KG, 21129 Hamburg, Germany
e-mail: ben.newman@altran.com

co-bonding process. The demonstrators are curved panels whose overall dimensions are 2868 mm length and 1120 mm width, and that are stiffened with four omega stringers and four mechanically fastened frame pieces. This chapter reviews the design and fabrication of manufacturing tooling, the design and production of the various individual components, integration of the DiAMon Plus™ online cure monitoring system by INASCO and the assembly at TAI of the stiffened skin with the composite mousehole frames designed and manufactured by SABCA.

Nomenclature

ABS	Airbus standard
AIMS	Airbus material specification
AIPI	Airbus process instruction
AS	Application scenario
CAD	Computer aided design
CFRP	Carbon fibre reinforced plastics
CNT	Carbon nanotube
CPD	Composite part design
DEA	Dielectric analysis
EOP	Edge of the part
ESN	Electrical structural network
GSM	Grams per square metre
INASCO	Integrated aerospace sciences corporation
IPS	Individual product specification
IS	Integration scenario
LATO	Lay-up tool
RTM	Resin transfer moulding

C. Koimtzoğlu · P. Maroulas
Integrated Aerospace Sciences Corporation, 166 75 Glyfada, Greece
e-mail: c.koimtzoğlu@inasco.com

P. Maroulas
e-mail: p.maroulas@inasco.com

P. Bara
New Structural Developments, Société Anonyme Belge de Constructions Aéronautiques,
1130 Brussels, Belgium
e-mail: Patrick.Bara@sabca.be

A. Vavouliotis · G. Sotiriadis · V. Kostopoulos
Applied Mechanics Laboratory, Mechanical Engineering and Aeronautics Department,
University of Patras, Patras University Campus, 26500 Rion, Achaia, Greece
e-mail: vavoul@mech.upatras.gr

G. Sotiriadis
e-mail: sotiriad@mech.upatras.gr

V. Kostopoulos
e-mail: kostopoulos@mech.upatras.gr

SARISTU	Smart intelligent aircraft structures
SABCA	Société Anonyme Belge de Constructions Aéronautiques
TAI	Tukish aerospace industries
UD	Unidirectional
UNIPA	University of patras
WP	Work package
C_{Te}	Coefficient of thermal expansion
ΔL	Change in length
L_0	Initial length
T	Temperature, °C
T_0	Initial temperature, °C
T_g	Glass transition temperature

1 Introduction

This chapter describes the generic lower fuselage panel design adaptation, manufacturing and composite frame assembly studies performed within the scope of the SARISTU project's work package (WP) 134. The main goal of this study was to increase the multifunctional nature of aircraft composite structures, via simultaneous improvements in key properties such as damage tolerance and electrical conductivity, through the use of carbon nanotube (CNT) reinforced prepreg material. By combining features of the electrical structure network (ESN) into more robust structural elements, future aircraft could save on the need for both types of component, thereby saving weight and increasing efficiency.

CNTs are cylindrical rolled graphene layers with nanometre-sized diameter and micrometre-sized length. Planar sp^2 bonding, which is a graphite characteristic and provides excellent mechanical properties, is seen in CNTs [1]. CNTs have many promising mechanical and electrical properties; therefore, they have come to prominence in the past years, especially in multifunctionality studies [2]. Compression testing after impacting and electrical resistivity measurement analysis are designed by Airbus Germany to investigate the effect of nano-treatment in detail level parts from a typical test pyramid. To enable this, two CNT-treated and one reference panels are produced within the scope of this study. As it is prone to impacts from debris or ground vehicles, and it may also experience electrical currents, the fuselage lower shell is considered as the design scenario.

This chapter reviews all activities involved with creation of the demonstrators, namely design adaptation, tool design and manufacturing, component production, integration and use of the DiAMon Plus™ online cure monitoring system and assembly to the curved stiffened panels of composite mousehole frames. The observation of composite lower panel manufacturability by the use of CNT-integrated material is mentioned in this report.

2 Design Adaptation

2.1 Materials

The selected technology, resulting from the development and experiments undertaken within the SARISTU project in Application Scenario 9 (AS09), was the CNT-doped prepreg developed by the University of Patras (UNIPA) [3]. For this, the baseline material is M21/34%/UD194/T800S from Hexcel (Table 1). The manufacturing of the skin and stringers for two nano-treated lower panel demonstrators required 700 m² of this material, supplied by TAI, to be doped using UNIPA's powder grinding and depositing technique; this was no small undertaking as the equipment designed and built for the processing was laboratory scale, and was therefore very time and labour intensive (grinding of the CNT carrier material delivered by Nanocyl was particularly demanding as a yield of approximately 50 % resulted in only a few grams of usable powder per day) (Fig. 1 and Ref. [3]).

Table 1 Properties of M21/34%/UD194/T800S

Feature	Value
Airbus Ref. Specification	AIMS05-01-002, IPS05-01-002-03
Fibre volume fraction	58 % (nominal)
Fibre mass/unit area	198 gsm (nominal)
Theoretical composite density	1.58 g/cc (nominal)
Fibre type	Unidirectional
Cured ply thickness	0.184 mm
Fibre type	T800S
Fibre density	1.8 g/cc
Resin type	M21
Resin density (cured)	1.28 g/cc
Dry T_g	198 °C

Fig. 1 CNT treatment of prepreg



Special attention was paid to monitor the status of the prepreg material during processing, storage and shipping. During these steps, UNIPA measured and optimised various parameters linked with scalability of the technology (e.g. rates, capacity, quality) towards meeting end-user production requirements [3].

The epoxy film adhesive which was used during the coupon level development to investigate the effect of CNT doping on the mechanical and electrical properties was Hysol EA 9695 0.05 K (Henkel). Henkel produced the adhesive at laboratory scale, in collaboration with the Fraunhofer Institute, in both reference (non-doped) and CNT-doped forms. Analysis of the test results of CNT-doped film adhesive (SARISTU code AD 05, Ref. [4]) showed no significant change in mechanical properties, but a large scatter in the results indicating process sensitivity [4]. Although the electrical conductivity improved, the values were still much lower than the carbon fibre reinforced plastic (CFRP), meaning little current transfer across the bondline could be expected [4]. As a result, non-doped adhesive was selected for all generic lower fuselage panels.

During development activities, the shelf life of the modified Hysol EA 9695 0.05 K (SARISTU code AD 03; Ref. [4]) film adhesive expired and the delivery of a new order delayed significantly the sub-element level studies until lower panel manufacturing starts. As a risk mitigation plan, the alternative non-doped material FM300 K.05, which was available in TAI stock, was used in both subelement and lower panel manufacturing. This was considered a low risk change as both materials are qualified for series production use and the direct link between the two levels of the test pyramid would remain. The features of both adhesives are compared in Table 2.

2.2 Lower Panel Design

As a key risk mitigation action for WP134, the design of a tried and tested panel was used as a reference. Four omega stringers were designed as stiffeners for the skin of each demonstrator panel. These 2858-mm-long pre-cured items were placed, with a layer of adhesive, on freshly laid up skin for joining by a series production co-bonding process (Fig. 3a). Each stringer comprises seventeen plies of prepreg, giving a total nominal thickness of 3.128 mm. In addition, peel ply was used on the feet undersides to improve the surface preparation prior to bonding. The skin comprises 12 plies of prepreg plus an outer layer of ABS5381HA02 qualified copper foil (non-CNT-doped) to give a nominal thickness of 2.338 mm. For the skin and stringers, respective thickness tolerances of ± 9 and ± 7 % are applicable as per ABS5797.

A sample picture of a stringer drawing is given in Fig. 2, which also shows the tension and compression traveller specimens produced for each part. Similar travellers are included in the drawings for the co-bonded part, a sample of which is shown in Fig. 3a.

Reinforcement plies are necessary to support the panel extremities and minimise the risk of unwanted failure during compression after impact testing. For this, four

Fig. 2 Sample stringer design

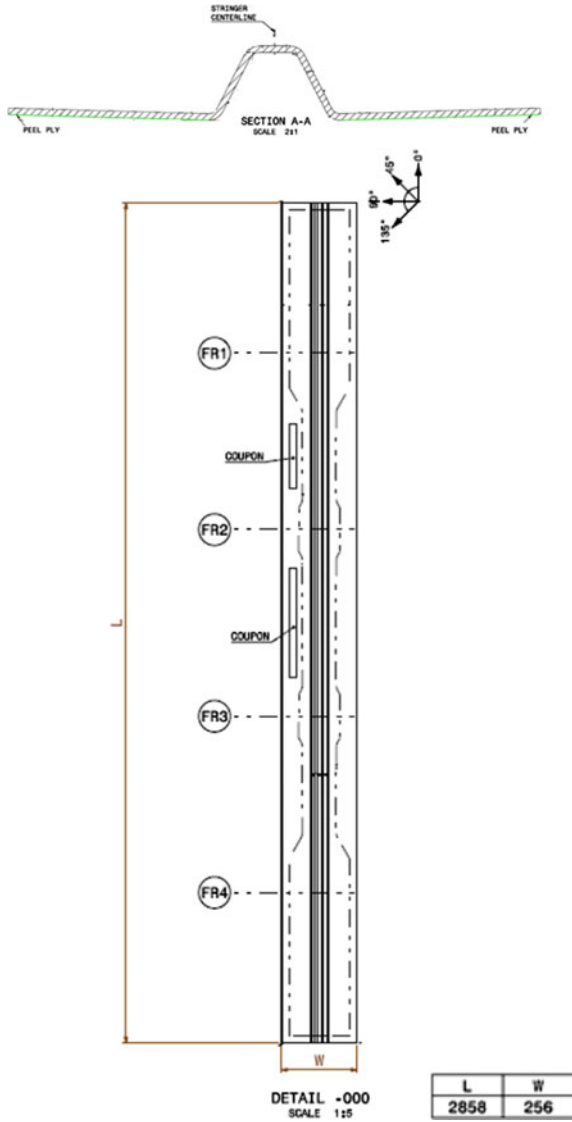


Table 2 Epoxy film adhesive comparison

Feature	FM300 K.05	Hysol EA 9695 0.05 K
Areal weight (lb/ft ²)	0.05	0.05
Nominal uncured thickness (mm)	0.20	0.25
Carrier	Polyester knit	Polyester knit
Ref. Airbus spec. number	IPS10-01-006-02	IPS10-01-006-01

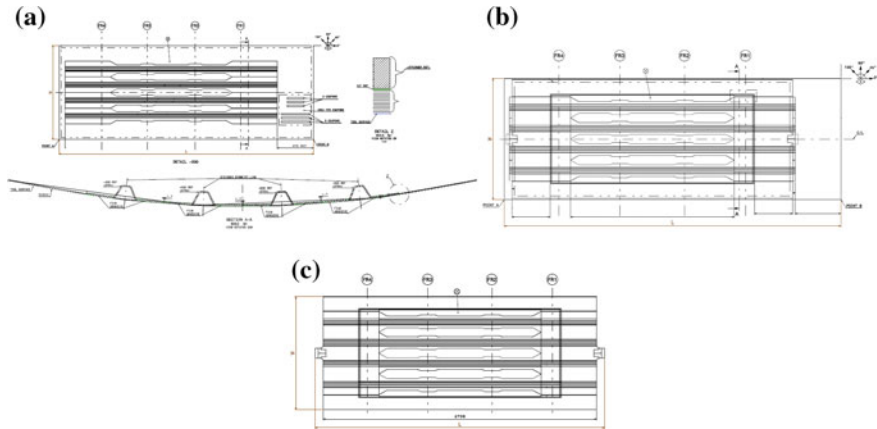


Fig. 3 Sample lower panel drawings. **a** Co-bonding. **b** Reinforcement application. **c** Machined part

plies of ABS5003A40EP350 woven fibre prepreg are included on both the inner and the outer surfaces of the stiffened panel as a “picture frame” around the study area. $0^\circ/90^\circ$ and $45^\circ/135^\circ$ orientations were used in a symmetrical manner (Fig. 3b).

The final length of the panels is 2868 mm with machining tabs and 2708 mm without them (Fig. 3c). To ensure that the machining tolerance was met, thermal expansion of the part was taken into account while writing the machining programme due to the location of the prick punch imprint moving.

2.3 Frame Design and Manufacturing

The frame segments’ main function is, by providing adequate and representative intermediate support and boundary conditions, to ensure the stability of the stiffened skins during compression after impact tests.

Braiding and resin transfer moulding (RTM) were selected as baseline technologies for the design and production of the frames. These choices simultaneously promote homogeneous characteristics along the complete component length (thanks to constant fibre alignment or orientation all along the preform), cost efficient automated production of preforms and reproducible high quality.

The preform architecture is a two-dimensional braiding with three fibre directions ($0^\circ, \pm 60^\circ$). In order to maximise part quality, it was decided to avoid preform transfers which can affect the homogeneity of properties such as fibre orientation and pitch. Therefore, dual-use mandrels were developed which are used first for the braiding operation (Fig. 5), and then transferred with their preforms directly to the curing mould. Mandrels are released and reused after demoulding (Fig. 6) and trimming operations have been performed. The sequence is illustrated in Fig. 4.

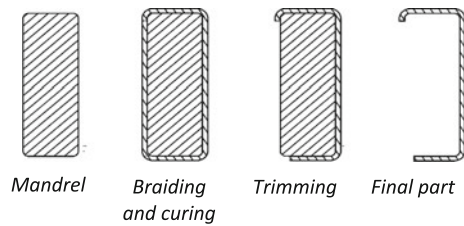


Fig. 4 Frame manufacturing—sequence of operations starting from the bare mandrel until the final part



Fig. 5 Braiding prepared on its mandrel

Fig. 6 Cured preform after extraction from mould



Two types of frames were produced which, depending on the stringer feet width at the attachment point, either do or do not have joggles in the outer flange (Figs. 7, 8). Injection of RTM6 resin and curing were performed in double closed moulds with heating plates and thermal insulation. The C-section and mousehole contours were achieved using a two-stage machining process, the first of which allowed the mandrel to be released and the second of which trimmed to final size (Fig. 7).

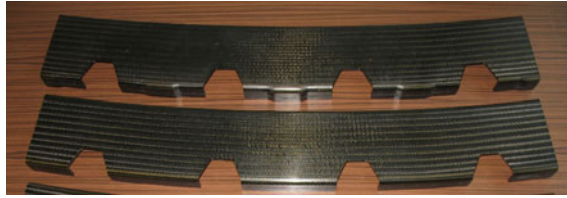


Fig. 7 Trimmed frames in 2 configurations: with (*top*) and without (*below*) outer flange joggles

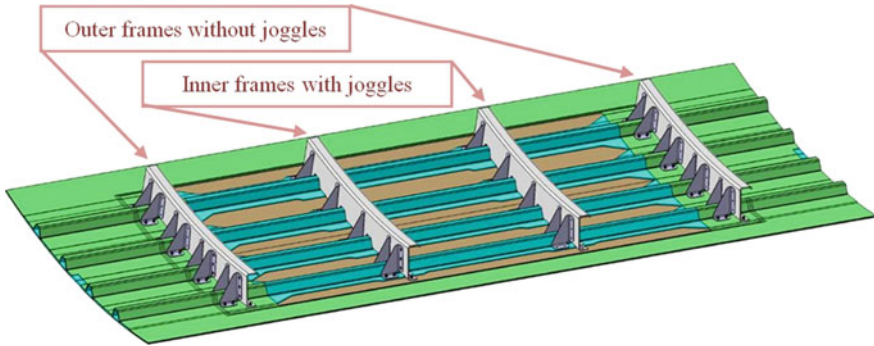


Fig. 8 CAD model of the assembled lower panel showing position of frames (with joggles for the inner ones), and the differing cleats arrangement (more required for the outer frames)

2.4 Assembly Design

Assembly drawings were prepared by SABCA taking TAI CAD models as reference.

Cleats were required for the frame installation; however, as they were not a key focus of investigation for SARISTU, these were made out of aluminium alloy using series production techniques to reduce manufacturing costs.

The input to design and development from early manufacturing trials resulted in high-quality parts right from the first run; this, in turn, enabled hole-to-hole final panel assembly and avoided the need for a costly assembly fixture.

3 Tooling

Three main tools were designed and produced for manufacturing of the curved stiffened panels: one lay-up tool for omega-shaped stringers, one holding fixture for stringer machining and one lay-up tool for lower panel skin lay-up and stringer co-bonding. Tools were produced by machining of aluminium 6061 T6 plate material. As the lay-up tools were to be used for 180 °C cure cycles, the following

calculations (Eq. 1) were made to ensure that they had the correct size and shape when the component set.

$$\text{Thermal Expansion Factor } \frac{\Delta L}{L_0} = (1 - (T - T_0) \times C_{Te}) \quad (1)$$

$$C_{Te} \quad 23.6 \times 10^{-6} \text{ } ^\circ\text{C [5]}$$

$$T \quad 180 \text{ } ^\circ\text{C}$$

$$T_0 \quad 20 \text{ } ^\circ\text{C}$$

$$\text{Thermal expansion factor } 0.9962$$

For routing the edge of the omega stringer part (EOP), a holding fixture was designed. The part is located with pins and clamped to secure it while the machine is running (Fig. 9).

The lay-up tool for the lower panel has two functions. Firstly, it is used as a lay-up surface for the skin panel. The second function is to position and co-bond the stringers on the skin. There are three locaters for the omega-shaped stringers. Each locator is manufactured with tolerances to correctly position the stringers in three dimensions. The total weight of the lower panel tool is about 820 kg. The detail of overall tool design is shown in Fig. 10.

An important feature of the panel lay-up tool was the incorporation of the dielectric sensors used by the DiAMon Plus™ system for online cure monitoring (with an intermediate glass ply layer between the prepreg and the sensor surface, the system is able to monitor the degree of ion mobility and translate it in real time into degree of cure, viscosity and glass transition temperature, T_g). In a process that started with the use of disposable sensors on a specially made trial tool, four sensors were mounted onto the final tool (Fig. 13) at key locations identified from thermal mapping (Fig. 12). In addition, modifications were also required to the autoclave to allow cabling to run through the pressure wall from the sensors to the DiAMon Plus™ system placed alongside (Fig. 11).

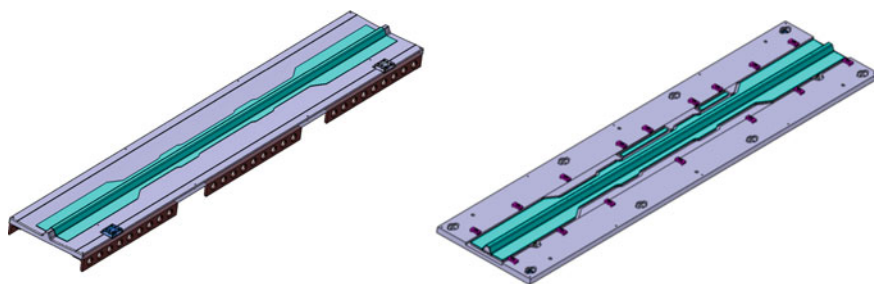


Fig. 9 Omega stringer manufacturing tool and machining fixture design—sample pictures

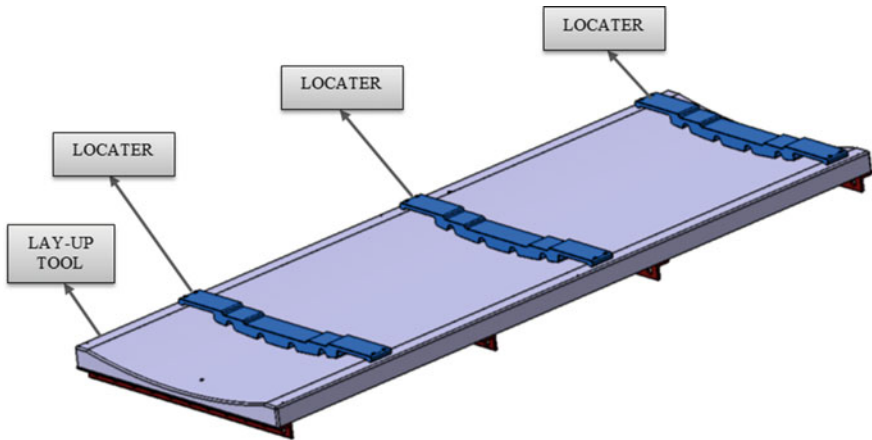
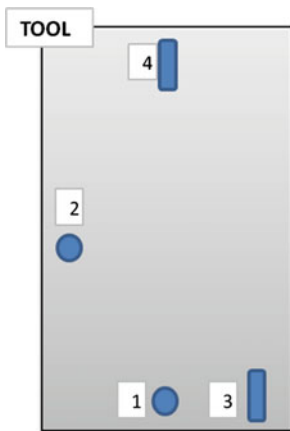


Fig. 10 Lower panel manufacturing tool design—sample picture



Position	type	code name
1	Tool	C0005
2	Tool mounted	C0001
3	single use	Flat/V 25pF
4		Flat/V 25pF

Fig. 11 Sensor type and configuration

4 Manufacturing

The requirements for composite manufacturing defined by Airbus specifications (AIPS 03-02-019 and AIPI 03-02-019) were met in the co-bonding of four stringers to the skin in both CNT-treated and reference versions. All the materials were stored according to the conditions stated in the material specifications, and any materials exceeding their shelf life were not used in production unless they passed the applicable storage life extension analyses. Cutting, lay-up and forming of uncured prepregs and adhesive film were performed in an isolated clean room

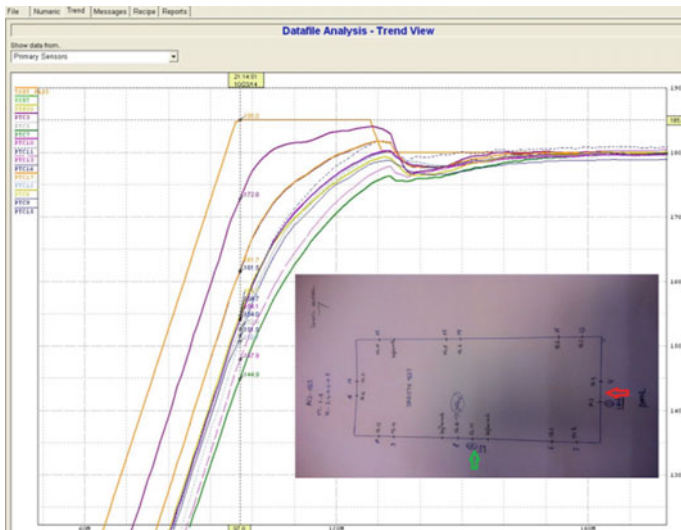


Fig. 12 Thermal profile identification—trial autoclave run with the skin tool

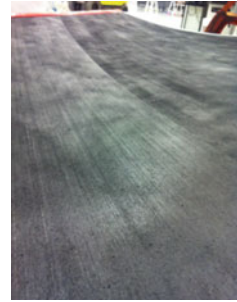
Fig. 13 DiAMon Plus™ integrated to the autoclave monitoring in real time the curing of the lower panels



(Class 100,000) to protect the materials from contamination. All required health and safety precautions were taken, especially for CNT usage.

One significant difficulty arising during manufacturing was that CNT removal from the plies during hand lay-up. Due to the very low material tack resulting from the CNT powder layer on the surface, the operator needed to apply hand pressure to get the plies to sit. During this hand placement, visibly detectable amounts of CNT-doped powder were removed from the treated plies. In addition, and despite the efforts to homogenise and stabilise the depositing process, the treated prepreg showed an apparent uneven distribution of powder before hand lay-up began

Fig. 14 CNT-treated prepreg —nonhomogeneity in production



(Fig. 14). Further improvements to both the CNT treatment process and the material tack have therefore been identified as key areas for improvement in the future work.

Due to the tight radii multiplying the low tack problems, the most challenging work was the lay-up of the omega stringers using CNT-treated prepreg. Vacuum compaction, which helps pull the layers to adhere onto each other and the tool surface, was applied after each ply instead of the usual three, thereby significantly increasing labour cost and manufacturing time (Fig. 15).

The sequence applied in lower panel manufacturing is briefly given as below. Similar steps were performed during stringer manufacturing.

4.1 Tool Cleaning—Release Agent Application

LATO (Lay-up tool) cleaned and release agent applied to tool surface with all steps are recorded as per AIPI 03-02-019 (Fig. 16). FREKOTE 700NC was used as the release agent material.

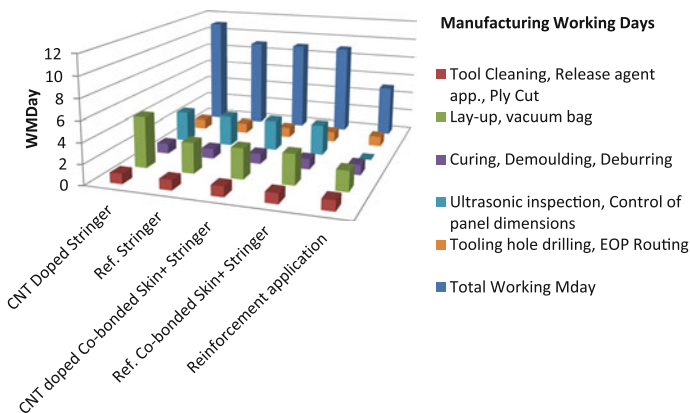


Fig. 15 Manufacturing periods in terms of component and production steps

```

RECORD THE FOLLOWING:

MATERIAL SPEC FOR PARTING AGENT : _____
BAKE TEMPERATURE                 : _____
BAKE TIME                         : _____
RELEASE AGENT RENEWAL             : _____

.....
*   *   *   *   *   *   *   *   *   *   *   *   *   *   *   *   *   *   *   *   *   *   *
* RELEASE * NUMBER * TOOL * TIME OF SOLVENT * T OF * TIME OF *
* AGENT * OF COATS * T (°C) * EVAPORAT BETWEEN * FINAL * FINAL *
* * * * * * * * COATS (minutes) * CURE (°C) * CURE (MINUTES) *
* * * * * * * * * * * * * * * * * * * * * * * * * * * * *
* * * * * * * * * * * * * * * * * * * * * * * * * * * * *
* PREKOTE * * * * * * * * * * * * * * * * * * * * * * * * * * * * *
* 700NC * * * * * * * * * * * * * * * * * * * * * * * * * * * * *
* * * * * * * * * * * * * * * * * * * * * * * * * * * * *
* * 3 * * * * * * * * * * * * * * * * * * * * * * * * * * * * *
* (Solvent * * * * * * * * * * * * * * * * * * * * * * * * * * * * *
* Base) * * * * * * * * * * * * * * * * * * * * * * * * * * * * *
* * * * * * * * * * * * * * * * * * * * * * * * * * * * *
.....
    
```

Fig. 16 Sample shop order view—tool cleaning and release agent application

4.2 Ply Cutting

Unidirectional (UD) plies were cut by a ply cutting machine using a programme prepared according to flat patterns of plies as per AIPI 03-02-019. Key process parameters were recorded in this operation (Fig. 17). A butt splice philosophy was applied since the material is in UD form.

4.3 Lay-up Operation

Lay-up of copper mesh and UD plies performed as per AIPI 03-02-019.

After lay-up of the copper mesh and UD plies was completed, adhesive was tack bonded to the pre-cured stringers (Fig. 18c) and these were positioned onto the

```

RECORD THE FOLLOWING - ASAGIDAKILERI KAYDET:
MATERIAL TYPE - MALZEME TIPI: IPS05-01-002-03 UD PREPREG
MANUFACTURER DESIGNATION-ÜRETİCİ ADI : _____
MATERIAL SPEC- MALZEME STANDARDI : _____
OUT OF FREEZER DATE-SOGUTUCUDAN ÇIKIŞ TARİH : _____
OUT OF FREEZER TIME- SOGUTUCUDAN ÇIKIŞ SAAT : _____
REMAINING LIFE ABOVE 18°C (HRS) : _____
18°C ÜZERİNDE KALAN ÖMÜR (SAAT) : _____
BATCH NBR : _____
LOT/ ROLL NBR : _____
EXPIRATION DATE/SON KULLANMA TARİHİ : _____

PLY CUT NC PROGRAM NO/NAME/REV : _____
PLY KESİM NC PROGRAM NO/ADI/REV : _____
    
```

Fig. 17 Sample shop order view—ply cutting

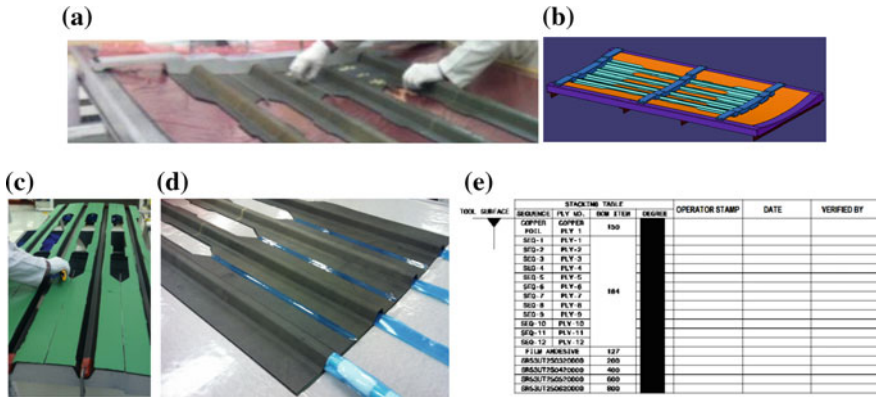


Fig. 18 Lay-up of lower panel and stringer positioning—**a** Stringer positioning. **b** Stringer locators. **c** Film adhesive application. **d** Tube-shaped vacuum bag. **e** Lay-up check and verification uncured skin. Bridges (stringer locators) were used for positioning of stringers (Fig. 18a, b). Each lay-up orientation was stamped by the operator and verified by an inspector (Fig. 18e).

4.4 Vacuum Bag Operation

Vacuum bag operation was performed and recorded in a shop order document (Fig. 19) as per AIPI 03-02-019. Tube-shaped vacuum bags were used in the omega stringers to allow the elevated autoclave pressure to also reach the skin regions underneath the stringer heads (Fig. 18d).

4.5 Curing

The part was co-bonded at 180 °C and 4 bar pressure in an autoclave as per AIPI 03-02-019. Applied parameters were recorded (Fig. 20). For the non-doped and the

RECORD THE FOLLOWINGS (AŞAĞIDAKİ DEĞERLERİ KAYDET) :

DATE OF PART IS BAGGED FOR CURE : _____
 (KÜR İÇİN TORBALAMA TARİHİ)

TIME OF PART IS BAGGED FOR CURE : _____
 (KÜR İÇİN TORBALAMA SAATI)

VACUUM LEAK VALUE (VAKUM KAÇAK DEĞERİ) : _____

CURE BEFORE DATE : _____
 (KÜR OLMASI İÇİN SON TARİH)

Fig. 19 Vacuum bag operation recording

RECORD THE FOLLOWING - ASAGIDAKI DEGERI KAYDET :

VACUUM DROP/MIN - VAKUM KAYBI (KPA) : _____

- APPLY PRESSURE TO AUTOCLAVE
- APPLY HEAT AFTER FULL PRESSURIZATION OF AUTOCLAVE.
- HEAT UP AND COOL DOWN RATES FOR THE PART PER CMR CURE CYCLE METHOD 3.
- HOLD PARTS IN AUTOCLAVE PER THE TIME AND TEMPERATURE SPECIFIED, ON THE CMR CURE CYCLE (LAMINATE METHOD 3).
- INCLUDE TEST COUPONS IF REQUIRED AND CURE PART IN AUTOCLAVE.

RECORD THE FOLLOWINGS-ASAGIDAKI DEGERLERI KAYDET:

DATE & TIME OF CURE START - KÜR BASLAMA TARİH VE SAATI : _____

DATE & TIME OF CURE END - KÜR BITİŞ TARİH VE SAATI : _____

AUTOCLAVE NUMBER - OTOKLAV NO : _____

AUTOCLAVE LOAD NUMBER - OTOKLAV LOT NO : _____

Fig. 20 Cure information recording

first CNT-doped panels, the cure cycle was also monitored using the DiAMon Plus™ system (see also Sect 4.11).

4.6 Demould Operation

Demould operation was performed as per AIPI 03-02-019.

4.7 Deburr Operation

Deburring and removal of excess resin was performed as per AIPI 03-07-002.

4.8 Ultrasonic Inspection

Ultrasonic Inspection was performed as per AITM 6-0011. See Fig. 21.



Fig. 21 Ultrasonic inspection of components—**a** Stringer inspection. **b** Lower panel inspection

4.9 Control of Panel Dimensions

Inspection of panel dimensions as per APII 03-07-002.

4.10 Reinforcement Application on Cured Part

The LATO (lay-up tool) was cleaned, and release agent was applied to surface. Fabric plies were cut by the ply cutter similar as for the prepreg, and these were laid up as per the technical drawings (overlap splicing was designed in as the material has a woven fabric form). Laser projection using a Virtek laser projector was used for specifying ply EOP's on the tool. The laser projection file was prepared by using the composite part design (CPD) module of CATIA (Fig. 22b), with projection locations checked according to the blueprint and approved at first trial part manufacturing. After laying up the inner and outer reinforcements (Fig. 22c, d), a vacuum bag was applied around the complete part independently of the tooling. The part was then cured in an oven on the lower panel skin tool at 125 °C. Demoulding, deburring and excess resin cleaning were performed as previously. Tooling holes were drilled per prick punch locations on the part before the trimming. Final routing to net EOP and the drilling of the pilot holes used for frame assembly was performed by five axes milling and a water jet cutting machine (Belotti MDL 14040, Fig. 23). Cleaning of excessive peel ply on reinforcements, excessive resin and chips from routing were completed as required as minor repair steps. The finished part was then forwarded to the assembly area for the next operations.

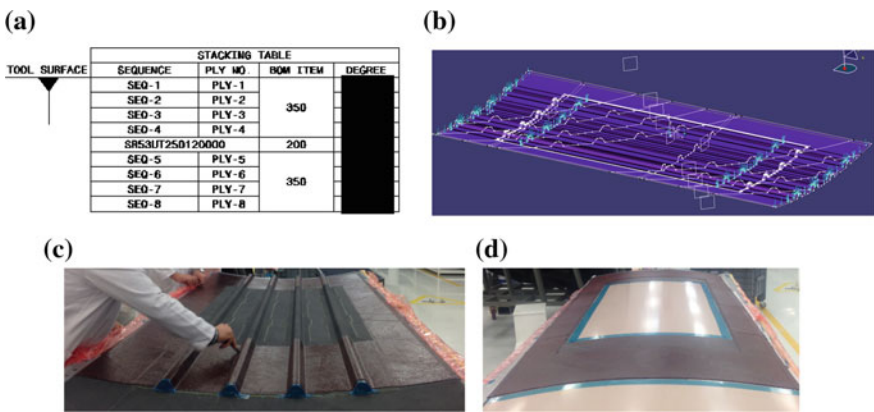


Fig. 22 Reinforcement application in summary—**a** Lay-up check. **b** Splicing. **c** Inner reinforcements. **d** Outer reinforcements

Fig. 23 Routing of the first lower panel



4.11 Results of the DiAMon Plus™ Cure Monitoring

For the needs of the dielectric analysis (DEA), it was necessary to monitor the temperature of the part at the position where the dielectric measurements were taken. Thus, a J-Type thermocouple was positioned next to each dielectric sensor. Temperature measurements at all 4 positions on the tool indicate that No. 1 and No. 2 (Fig. 13) are the hottest and coldest parts of the tool, respectively. Signal analysis of the dielectric measurements from all panels is in agreement with these facts since minimum viscosity (resin contact with the sensor) occurs firstly at sensor 1 and finally at sensor 2 (Fig. 24).

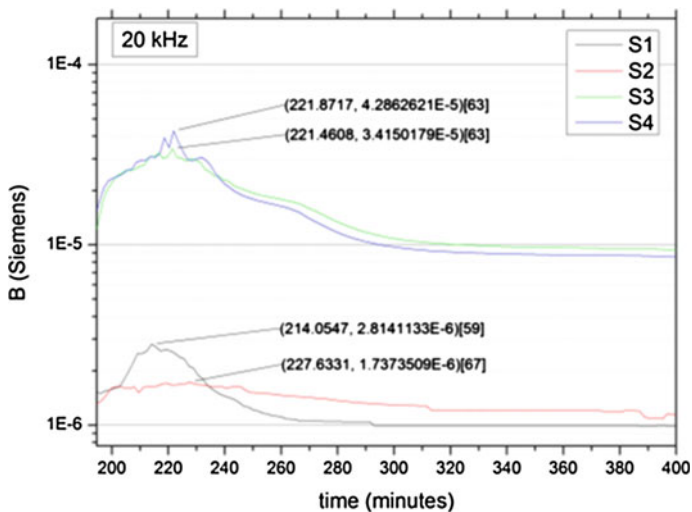


Fig. 24 Analysis of the dielectric signal of all sensors shows that the minimum viscosity is reached in the area of sensor 1 at 214 min and in the area of sensor 2 at 228 min after initiation of measurements

Fig. 25 Values of degree of cure as calculated for the position of all sensors and all panels using the DEA and DSC measurements

		DSC			DEA
		%cure	SD	±err	%cure
PANEL 1	C5	86.7*	1.3	0.3	95.7
	C1	95.4	0	0.4	x
PANEL 2	C5	95.8	0.4	0.4	95.8
	C1	94.3	0.5	0.3	81.6
	V	94.4	1.4	0.3	94.4
PANEL 3	V	95.5	1	0.4	95.2
	C5	96.02	0.44	0.6	95.9
	C1	95.12	0.06	0.6	91.6
	V	97.73	0.55	0.6	95.3
	V	96.33	1.3	0.6	92.7

Given the above facts, it is expected that degree of cure at position 1 is the highest and at position 2 is the lowest since the cure is partial as also indicated by DSC measurements from the finished panel next to the sensor positions. Cross-correlation of the degree of cure values, as estimated from the DEA measurements, with the values from the DSC results leads to the following results (Fig. 25):

1. All curing cycles for the manufacturing of the 3 panels have been performed successfully without the occurrence of any unforeseen events, as shown in the readings of the DiAMon Plus™ system.
2. The calculated degree of cure for all panels at position 2 is the lowest, as expected.
3. Position 1 always retains the highest degree of cure at around 96 %. DSC results for the case of panel 1/position 1 (marked with a * in Fig. 25) are considered problematic.
4. As a result of this analysis, the quality check of the part's cure should be based upon measurements at the coldest point (position 2).

Where material and process specifications give guidelines and requirements that are independent of design and may therefore be over- or under-estimated, the DiAMon Plus™ system allows real-time monitoring of predetermined critical tool locations. This can allow a feedback loop to the autoclave controller to optimise and end the run once curing is complete rather than at the end of a set dwell time (not covered in SARISTU). However, the benefit of such a system would have to be made on a case-by-case basis, as, for example, the additional sensors require cabling and connection, all of which increases the preparation time for what may be a small improvement in curing time.

5 Frame Assembly

Pilot holes were drilled into the curved stiffened panels during final machining. After positioning the frames onto the panel, the pilot holes (2.5 mm diameter) from the frames were transferred to the skin and fastened with temporary fasteners (Fig. 26a). During all operations until final assembly, appropriately sized temporary fasteners were used to keep parts in position. The next step was the placement of cleats against the frames and panel by the help of hand clamps (Fig. 26b); once again, the 2.5-mm diameter pilot holes were transferred, this time from the cleats to both the skin and the frames. After all pilot hole transfer operations, all fastener holes were opened up to 3.25 mm diameter. Liquid shimming was then applied to all interfaces between panel, frames and cleats (Fig. 26c). After curing of the liquid shim, all fastener holes were further opened up to 4.49 mm diameter and then reamed to the final 4.80 mm diameter. Although long, this step drilling method meets the requirements of inside hole quality. The last assembly operation was wet installation of the fasteners (Fig. 26d). As a result of the aerodynamic outer surface of the panel, fasteners used on skin were countersunk, with the head on the skin outer surface. For fastening of the cleats to the frames, protruding head bolts were used. The first of the completed panels is shown in Fig. 27.

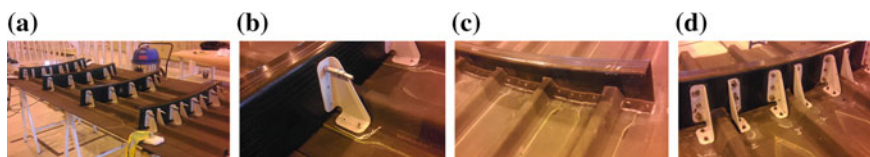


Fig. 26 Frame assembly sequence on lower panel—**a** Frame positioning (dry fit check). **b** Cleat placement. **c** Liquid shim application. **d** Wet installation of fasteners

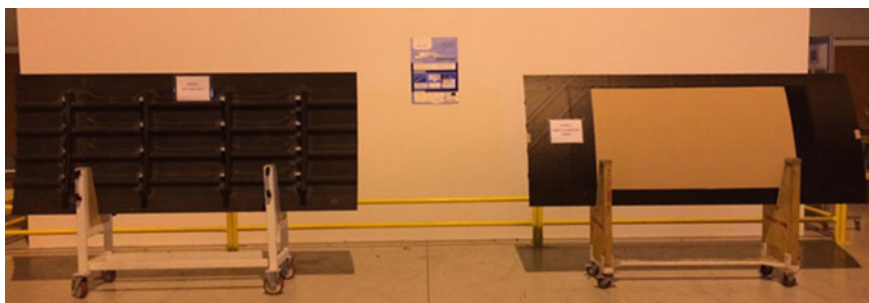


Fig. 27 Completed lower panel demonstrators

6 Conclusion

Following manufacturing trials, one reference and two CNT-treated lower fuselage panels were produced to enable improvements in damage tolerance and electrical isotropy to be assessed via appropriate test campaigns. It was observed that the lay-up phase using CNT-doped prepreg was significantly longer than for non-doped prepreg due to the low tackiness of the treated material. Hand lay-up may also not be the right manufacturing method for CNT-treated materials, since an unpredictable amount of CNT-doped powder was removed by placing and pressurising the plies via hand; this is in addition to tighter health and safety requirements. Cure monitoring using the DiAMon Plus™ system demonstrated the system's capability to be integrated in composite manufacturing routes without affecting the flow of the process, to evaluate in real time the degree of curing of the produced part and finally the potential to optimise the length of cure runs based on the system's ability to provide in real-time material macroscopic properties (degree of cure, T_g, viscosity) based on material data from the process rather than potentially overestimated material specifications.

Acknowledgments The research leading to these results has received funding from the European Union's Seventh Framework Programme for research, technological development and demonstration under grant agreement no 284562.

References

1. Dresselhaus M (2001) Relation of carbon nanotubes to other carbon materials. Springer, Berlin, pp 11–28
2. Ersarac FN (2012) Preparation and characterization of shape memory polymer based composite materials for aerospace applications. Middle East Technical University, Ankara
3. Vavouliotis A et al (2015) Multi-scale reinforced pre-pregs for the improvement of damage tolerance and electrical properties of aeronautical structures. University of Patras, Moscow, 19–21 May 2015
4. Ruetters M (2015) Influence of CNT-doping on mechanical behaviour of adhesive joints in aerospace applications. Fraunhofer –Gessellschaft Zur Foerderung Der Angewandten Forschung E.V., Moscow, 19–21 May 2015
5. ASM, Properties and selection: nonferrous alloys and special-purpose materials, vol 2. ASM HANDBOOK, p 222

Design and Manufacturing of WP135 Side Panel for Validation of Electrical Structure Network (ESN) Technologies

Christina Altkvist, Jonas Wahlbäck, Juergen Tauchner
and Christoph Breu

Abstract Design and manufacturing of a curved stiffened panel has been carried out within WP135 in SARISTU Integration Scenario IS13. The aim of this fuselage panel is the integration and validation of electrical structure network (ESN) technologies developed within Application Scenario AS10. The assembled panel includes premanufactured braided frames with cocured metallic strips aimed at improving electrical performance, impact detectability and damage tolerance. The panel will be subjected to electrical testing to verify the ESN solution, with additional frames used for impact testing and evaluation.

Nomenclature

AS10	Application Scenario 10
BMH	Braided mousehole
CFRP	Carbon fibre-reinforced plastics
CVD	Cold vapour deposition
CTE	Coefficient of thermal expansion
ECF	Expanded copper foil
ESN	Electrical structure network
IS13	Integration scenario 13

C. Altkvist (✉) · J. Wahlbäck
Saab AB, SE-581 88, Linköping, Sweden
e-mail: christina.altkvist@saabgroup.com

J. Wahlbäck
e-mail: jonas.wahlback@saabgroup.com

J. Tauchner
FACC Operations GmbH, A-4973 Sankt Martin im Innkreis, Austria
e-mail: j.tauchner@facc.com

C. Breu
Airbus Group Innovations, 81663 Munich, Germany
e-mail: christophe.breu@airbus.com

LSP	Lightening strike protection
NDI	Non-destructive inspection
PVD	Physical vapour deposition

1 Introduction

This document describes the design and manufacturing of WP135 curved stiffened panel to be used for integration and validation of AS10 electrical structural network (ESN) technologies. The assembled panel includes premanufactured braided frames with cocured metallic strips aimed at improving electrical performance, impact detectability and damage tolerance. The panel will be subjected to electrical testing to verify the ESN solution, with additional frames used for impact testing and evaluation (Fig. 1).

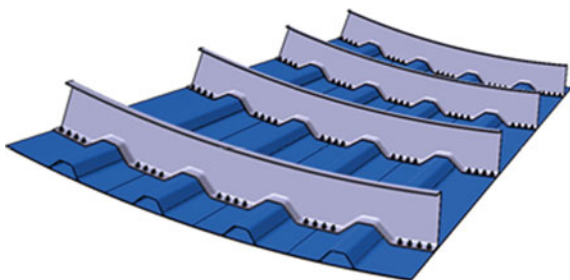
2 Cold Process Metallization

ESN technologies intended to be demonstrated on the WP135 side panel were metallic strips and metallic coatings solution. A brief description of cold process metallization is given in this chapter. Metallic strip design and manufacturing has been detailed in another paper “Metallic strip concept overview and results—T. Pelegrin et al.” Furthermore mechanical and electrical testing when metallic strips are installed on IS13 demonstrator has been presented in paper “Installation of metallic strip on CFRP frames: assessment of IS13 mechanical and electrical performance—R. Perraud et al.”

The aim of the research work conducted on metallic coatings was to replace the traditional bronze mesh or expanded copper foil on the exterior surface of the side panel with a metallic layer with only a moderate increase of the temperature at the surface.

The work carried out by Saab on cold metallization of CFRP was aiming at finding a metallic coating that met the requirements on conductivity and damage

Fig. 1 Side panel—CAD view



protection (short circuiting and lightning strike). Besides conductivity, there were also requirements on adhesion of the coated layer and resistance to thermal cycling, moisture and wear.

Two different cold metallization processes have been investigated:

- Thin-film coating process, for up to 10 μm metal coating thickness. This process is based on cold vapour deposition (CVD) technique and requires vacuum at the deposition point.
- Thick coating process, for thicknesses from 10 to 1000+ μm . This process is based on gas dynamic (supersonic) cold spray of metal particles in air.

2.1 Cold Vapour Deposition Metallization

The metallic coating is deposited at the CFRP substrate by condensation of a metal vapour (PVD technique) and requires vacuum at the deposition point. The metal vapour is generated within vacuum and diffuses within vacuum. It is then condensed on the object to be coated. The specific process developed by a subcontractor to Saab and used in AS10 is a filtered cathodic arc plasma accelerator deposition (FCAPAD) method (Figs. 2 and 3).

The work in AS10 was focusing on finding a metal coating that fulfilled the requirements on electrical surface conductivity, adhesion to CFRP and environmental durability. Testing was performed on Al-, Cu-, Ti- and Ni-coatings with varying surface preparations of the CFRP prior to coating and with varying coating thickness (Figs. 4 and 5; Table 1). Besides testing to determine scratch resistance and surface resistivity, additional testing was carried out to examine adhesion when tested in flexure and after drilling in coated laminate. Furthermore, coating thickness was measured, and possibility to perform NDI on coated specimens was checked

Fig. 2 Equipment for FCAPAD method



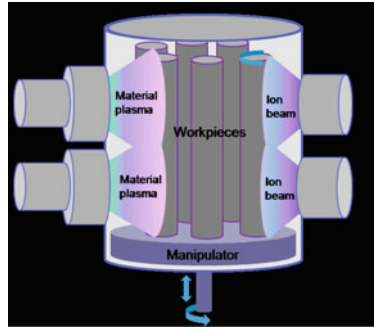


Fig. 3 Description of the coating process. Surface cleaning by ion beam etching prior the thin film deposition. Kinetic material plasma is created in the plasma accelerator. The filtered plasma forms a dense coating layer on the workpieces at room temperature

Fig. 4 Scratch test of Cu, 2 μm , surf prep 4

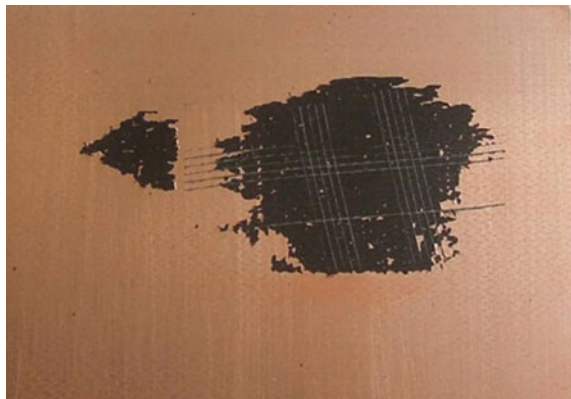


Fig. 5 Scratch test of Al, 2 μm , surf prep 3

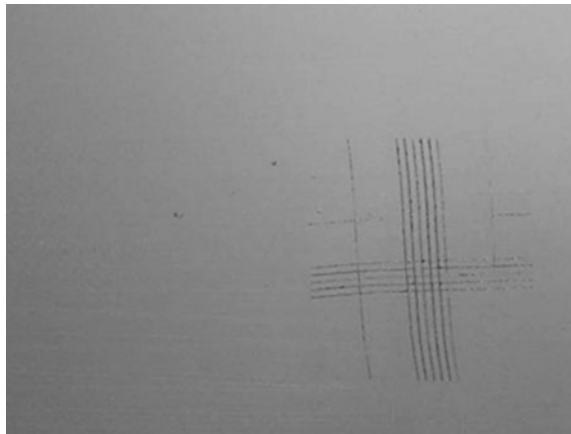


Table 1 Test results cold metallization, deposition method

Test Results SARISTU AS10 Cold metallization, deposition method																				
Coating material, thickness and surface preparation																				
Cu						Ni						Ti				Al				
0,5 μm			2,0 μm			0,5 μm		2,0 μm		0,5 μm		2,0 μm		0,5 μm		2 μm	3,5 μm			
Scratch Resistance ^a	Surf prep 1	Surf prep 2	Surf prep 4	Surf prep 1	Surf prep 2	Surf prep 4	Surf prep 1	Surf prep 2	Surf prep 1	Surf prep 2	Surf prep 1	Surf prep 2	Surf prep 1	Surf prep 2	Surf prep 1	Surf prep 2	Surf prep 3	Surf prep 4	Surf prep 3	Surf prep 3
As received	0	2	4-5	5	2-4	5	0	0		2	0	2-3		4	0	0				0
Therm cycling ^b	0-1		4-5		0	5	0			0-1	0			5	0	0				
Wet conditioned ^c		0						0					5							
Surf. res, mΩ/sq			10	5,4		3,4											45, 3	46, 7	5,4	6,3

Surface preparation 1 Cleaning method, as prior to painting
 Surface preparation 2 Cleaning and blasting method, as prior to painting
 Surface preparation 3 Ion etching
 Surface preparation 4 Carbon interlayer

Meets requirements
 Does not meet requirements
 Close to requirements

^a ISO 2409 Class 1-5 where 0 is very good and 5 no adhesion
^b 1 hrs at - 50°C, 1 hrs at +120°C, 3 cycles
^c 168 hrs at 40 ±2°C and 95 % RF

Summary of CVD testing is as follows:

- Al-coating was the best candidate and gave good adhesion with all tested thicknesses (0.5, 2 and 3.5 μm) as well as low resistivity at $t \geq 2 \mu\text{m}$ (5–6 mΩ/square).
- Cu gives good adhesion only at the thinnest tested thickness (0.5 μm). Surface resistivity was low (appr. 3–10 mΩ/square).

The process can be upscaled for coating of larger and curved panels, but thicker coatings for LSP are not suitable due to manufacturing cost. Therefore, the work was closed after mechanical, environmental and electrical characterization, and no LSP test was performed.

2.2 Cold Spray

The cold spray process uses the energy stored in high-pressure compressed gas to propel fine powder particles at very high velocities (500–1500 m/s). Compressed gas/air is fed via a heating unit to the gun where the gas exits through a specially designed nozzle at very high velocity (Fig. 6). A powder feeder is used to introduce powder material into the high-velocity gas jet. The powder particles are accelerated and moderately heated to a certain velocity and temperature and deform and bond to form a coating on impact with a substrate. The particle size, density, hardness,

temperature and velocity are varied to achieve the desired coating. The particles remain in the solid state and are relatively cold so the bulk reaction on impact is solid state only.

When using the cold spray technique on metal surfaces, a metal oxide is used as a processing aid to inhibit the metal powder to clog inside the equipment and the spraying nozzle. When spraying on bare CFRP surfaces, a blasting effect occurs when metal oxide powder is used and the surface is eroded. To solve the problem, the coating has been applied in two steps. A first layer, the bond-coat, consisting of a mix of a metal powder and a polymer material is applied to the CFRP, and the second layer is then sprayed on the bond-coat. Zn/Al₂O₃ was successfully sprayed on a bond-coat of epoxy adhesive mixed with metal powder of Al and Cu. Trials were also made with the aim to spray pure metal powders instead of oxides. Al was initially sprayed on a bond-coat of Cu/epoxy and on pure epoxy adhesive without metal particles (Fig. 7). After these initial results, the build-up of a coating layer could not be repeated. The most likely reason is that the spraying equipment parameters were not stable and the equipment is not sufficient to reach the high particle velocity needed for adhesion.

The test result from Al sprayed on an epoxy adhesive layer indicates however that when finding the required spraying parameters in combination with the substrate modulus, a metal coating on a CFRP substrate can be achieved. Since time and resources were insufficient to provide a suitable process to WP135, a decision was taken that the development should not continue within AS10.

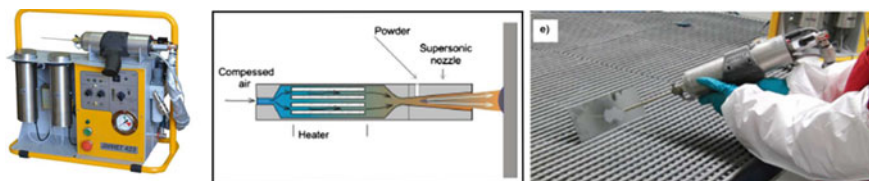


Fig. 6 Cold spray equipment and process

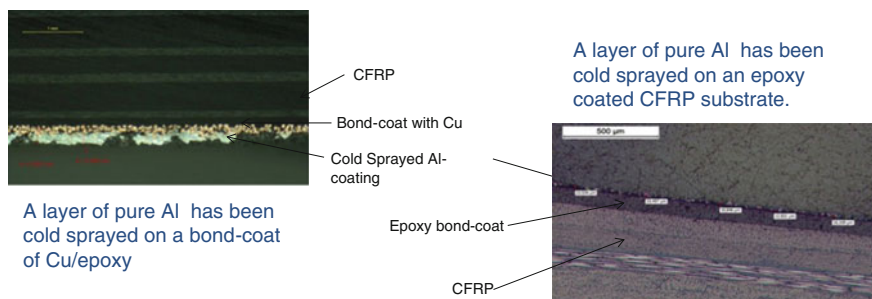


Fig. 7 Microscopic pictures of the layers

3 Side Panel Design

For the manufacturing of the skin, an existing mould tool was identified at Saab. The size of the stiffened panel was thereby driven by this in-house tool. It was decided to use only the tool area with a constant radius for layup which resulted in reduction of number of stiffeners from initially five down to four (Fig. 8). Further, this simplified, which was the main design driver, the frame design as well as the assembly of the frames. Final solution was a single curved panel with a size of approximately 2300 mm × 900 mm and with a curvature radius of 2800 mm

Hat stringers were defined as the baseline solution. To reduce manufacturing cost, all stringer were cocured with the skin. Additional guide tools to locate the stringer during layup and curing were designed. For positioning of the four hat-stiffeners Airbus recommended stringer pitch was used. Cross section of the hats was extracted from Airbus T-stringer recommendation with respect to height and width.

The layup of the skin and stringers has taken reference data for an Airbus cobonded design and has been updated to account for the fact that the stiffened panel will be cocured. Figures 9 and 10 show the design concept for the panel. The layout and spacing of the four stringers and four frames will follow Airbus requirements. Since the panel will not undergo mechanical testing and to simplify the manufacturing and thereby reducing cost, duck feet was not included in the stiffeners design. This design appears heavy, but weight optimization has not been a design driver for the panel design.

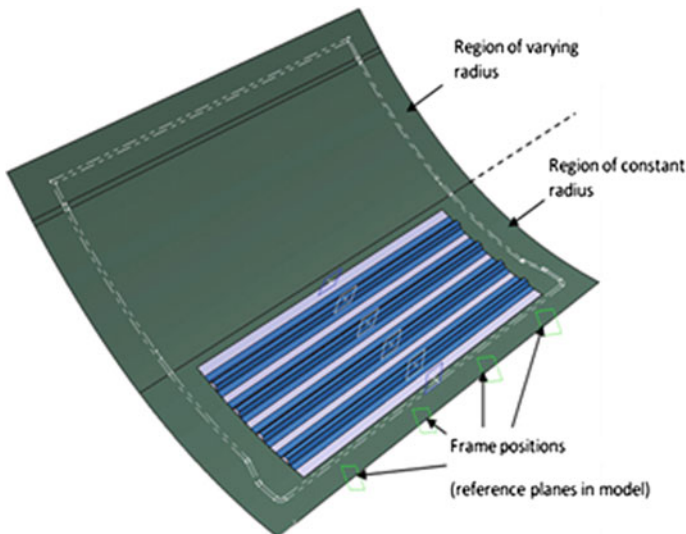


Fig. 8 Tool extension and side panel layout

Material used for manufacturing of the skin and the stringers was T800/M21 prepreg, and the layup stacking sequence for skin and stringers can be found below (Figs. 11 and 12). When it was decided not to apply a cold process metallization coating on the outside of the panel, the design was updated to include an expanded copper foil as the outer layer (current state-of-the-art).

- Prepreg: UD/M21/35%/194/T800S-12K.
- Lightning protection: ECF 3CU7-100FA.

The CFRP prepreg stack up sequence follows the principle of 1 + 9 + 2 + 5. These can be summarized as follows:

- 1 expanded copper foil as the most outer surface.
- 9 fully covering skin plies.

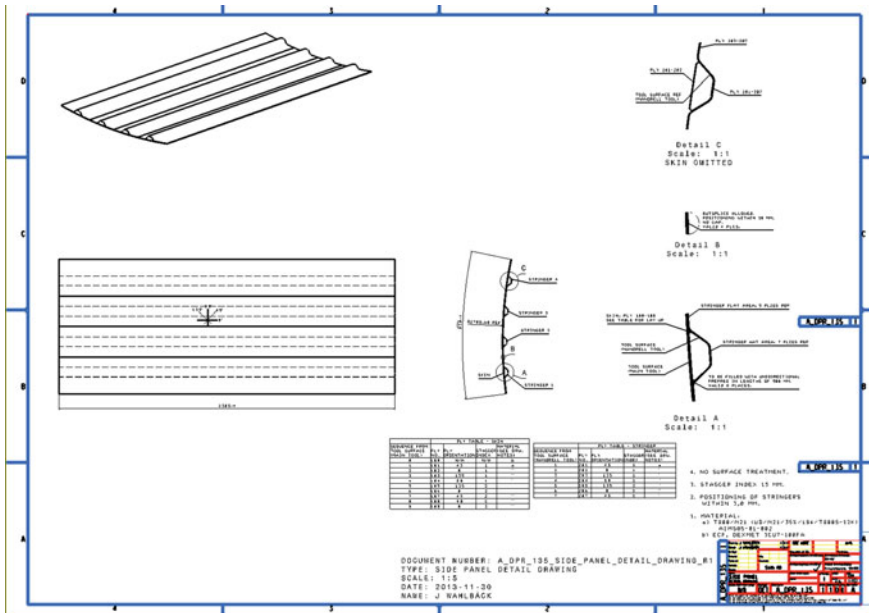
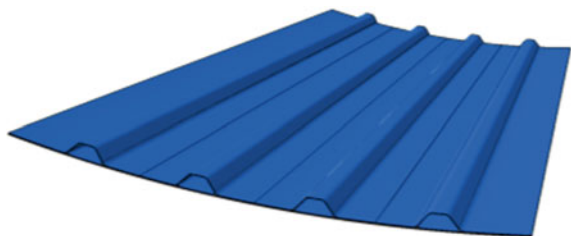


Fig. 9 Design drawing

Fig. 10 Side panel, CAD solid model



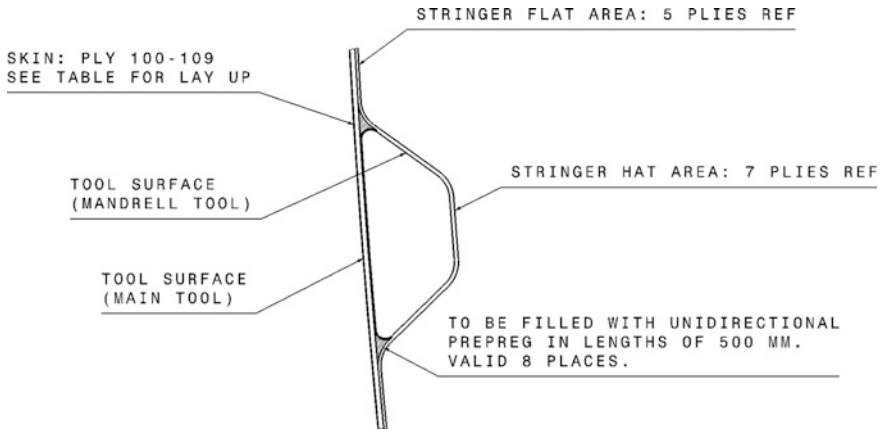


Fig. 11 Layup definition—skin

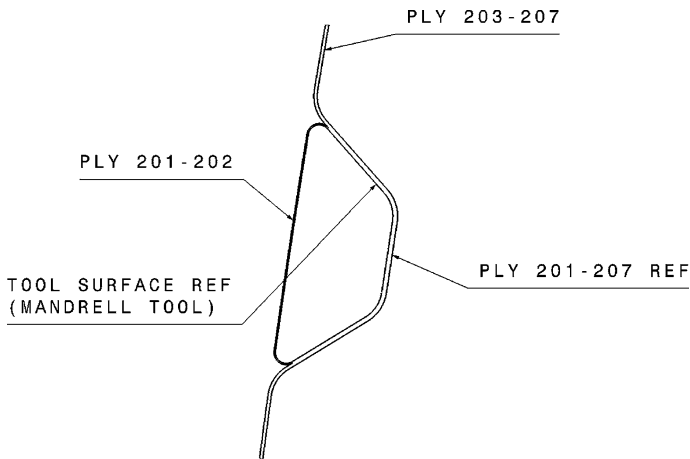


Fig. 12 Layup definition—stringer

- 2 plies wrapped around the stringer mandrel with the two butt joints staggered.
- Triangular filler in lengths of 500 mm applied along the stringer edges.
- The 5 final plies cover the stringers and acting as the stringer feet along its extension. These plies were allowed to be butt jointed. This creates an easier layup.

4 Skin and Stringer Tooling

A suitable in-house available female tool was identified for layup of the stiffened skin (see Fig. 13). The tool was in good condition and was accepted for use of the side panel manufacturing. The tool was cleaned and temporary stored. Prior to start of layup, the cleaning process was repeated followed by a pretreatment process with applicable release agent prior to start of prepreg layup.

Ancillary tooling needed to cocure the stringers was designed by Saab (Fig. 14). The mandrel tools, to shape and cure the stringers, were made out of aluminium. Aluminium was used due to its thermal properties and since only a few side panels were expected to be manufactured. Due to the fact that only the constant radius section of the skin tool was used, the 4 mandrels could be identical in terms of definition.

Fig. 13 Saab in-house skin tool



Fig. 14 Mandrels and guide tool



Each mandrel was secured in position by an attachment to the guide tool. Guide tool was then attached to each end of the mother tool. This secured the tolerance for the assembly process of the frame mouse hole.

5 Skin Panel Manufacturing

5.1 Material Preparation

All plies were prepared and nested directly from design CAD model using CATIA Composite Work Bench. All plies were cut in machine in advance of the manufacturing start. The prepreg material was delivered in rolls with 300 mm width causing some additional work (Fig. 15). To fix all 45-, 135- and 90-ply in continues plies, they had to be fixed by tape in advance of the layup step .

5.2 Prepreg Layup

The layup started with the ECF and the adhesive film (FM-300M). The width of the foil was less than the panel width. An overlap of approximately 1" was used to secure full connection. The following 9 CFRP skin plies were then added in sequence as stated in the design definition. Two vacuum operations were performed to secure high quality of the laminate.

Then followed the two wrap plies on each mandrel and after that mandrels installation on the main skin tool using the guide tool for correct position. The triangular fillers were then added, and finally, the 5 stringer cover plies were laid up (Fig. 16).

Fig. 15 Prepreg preparation

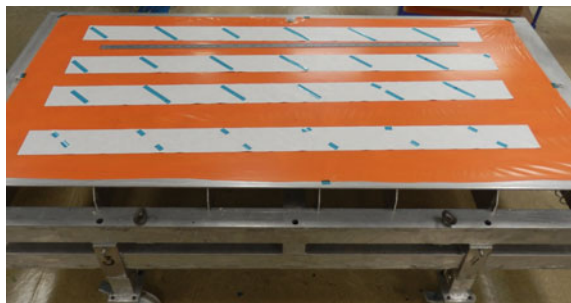
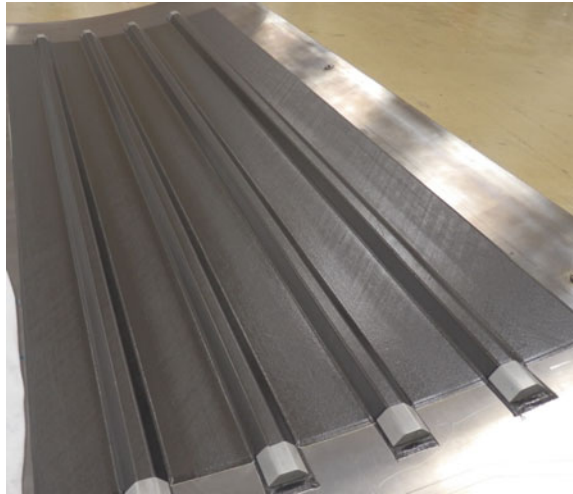
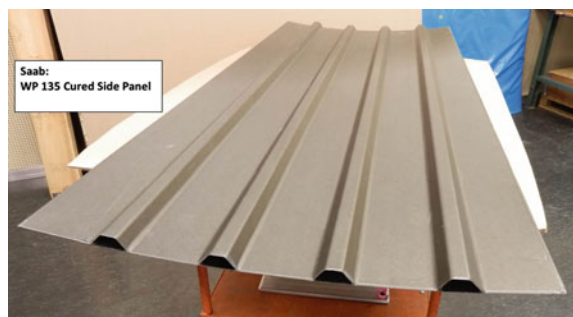


Fig. 16 Lay up of side panel

5.3 Curing, Machining and Inspection

The curing preparation took place with vacuum leader and bagging foil. Once all in place, the M21 standard curing process was used to cure the laminate. Debugging and demoulding after finalized autoclave stage was done, and the panel was then sent for machining of the edges.

Laminate quality inspection by NDI was performed with approved result, i.e. no defects above 6×6 mm were found. Geometrical control was performed on all edges of the circumference, and the reduced requirement to save cost—within 10 mm—was achieved. The shape of the panel was checked by using the form tool. No difference was found. Panel itself is very flexible from a global point of view (Fig. 17).

Fig. 17 Cured panel

6 Frame Design

The structural part of the composite fuselage side panel demonstrator includes a curved skin integrally stiffened in longitudinal direction which is additionally stiffened in circumferential direction by composite frames. For the design of these frames, a braided mousehole (BMH) C-Frame concept is chosen as already developed during the project MAAXIMUS. This means that the mouseholes needed to allow the omega-shaped stringers stiffening the fuselage skin along the aircraft longitudinal axis to run below the frames without machining cut-outs of the cured parts, but already incorporate them into the design and preforming process. This contributes to a lower amount of material scrap and machining effort.

The detailed frame design work is carried out in accordance with the general design rules defined for fuselage demonstrator parts within the scope of IS13 (frame height, radius, mousehole positions based on stringer pitch, minimum flange width, etc.) as well as assembly requirements (fastener positions, fastener edge distance, etc.) and braiding parameters (min./max. mousehole angle to ensure full braiding coverage). Due to the missing requirements for mechanical performance, a simplified layup is defined to reduce the amount of work and cost for the demonstrator parts. It consists of 4 braided layers including 2 layers of woven fabric as additional reinforcement in both flanges.

Additionally to the frame CFRP structure, a metallic strip (MS) is included at the inner flange for an integration of electrical systems into the load carrying structure as well as to provide a protection against damages resulting from internal impacts (e.g. dropped tooling during final assembly or maintenance). The aim of this damage protection is to reduce the total weight of the part since it has not to be sized for potential internal impacts. Thereby, the metallic strips made from an aluminium alloy are separated from the CFRP material by a rubber interface using a layer of a high-damping elastomer. This layer is supposed to provide damping in case of an impact as well as to prevent galvanic corrosion of the metal and also to compensate the differences in thermal expansion of the two different materials (Fig. 18).

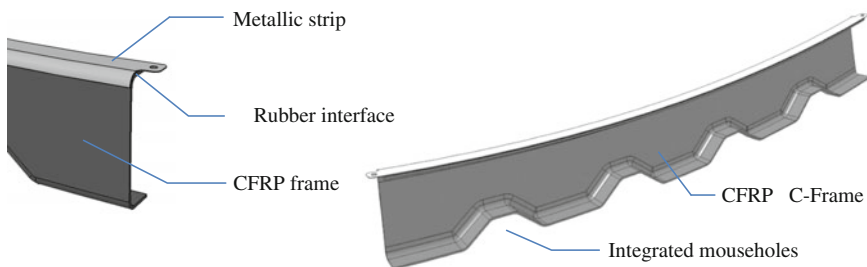


Fig. 18 Basic concept of metallic strip/rubber/CFRP composite and detailed frame design

7 Frame Manufacturing

The basic braiding principle for realizing the frame preforms is to overbraid a mandrel together with additional reinforcement layers for the flange areas, stabilize the fibre stacking with a binder and cut the braid to gain 2 C-shaped frame preforms. The demands for the braiding mandrel were a temperature resistance of 120 °C and a low CTE. These parameters combined with a low price could be realized with beech plywood. Figure 19 shows the braiding mandrel..

After definition of the correct braiding parameters, as there are the speed of the robot handling the mandrel and the speed of the braiding machine, the manufacturing of the preforms could start after several pretrials.

The following picture shows the four production steps necessary to gain the required stacking (Fig. 20).

The first layer applied on the braiding mandrel will be the inner layer on the later frame. This layer is defined as a $\pm 60^\circ$ braiding layer. To get a good fibre layup in the area of the mouse holes, a slight manual draping was necessary. Except of this, the braiding ran completely automatically. In case of a serial manufacturing of these kinds of frames, a simple pressing device could make the manual work obsolete (Fig. 21).

The additional reinforcement fabric layers were applied with a thermoplastic binder and activated with a hot iron after the first and third braiding layer. This

Fig. 19 Braiding mandrel for WP135 preforms



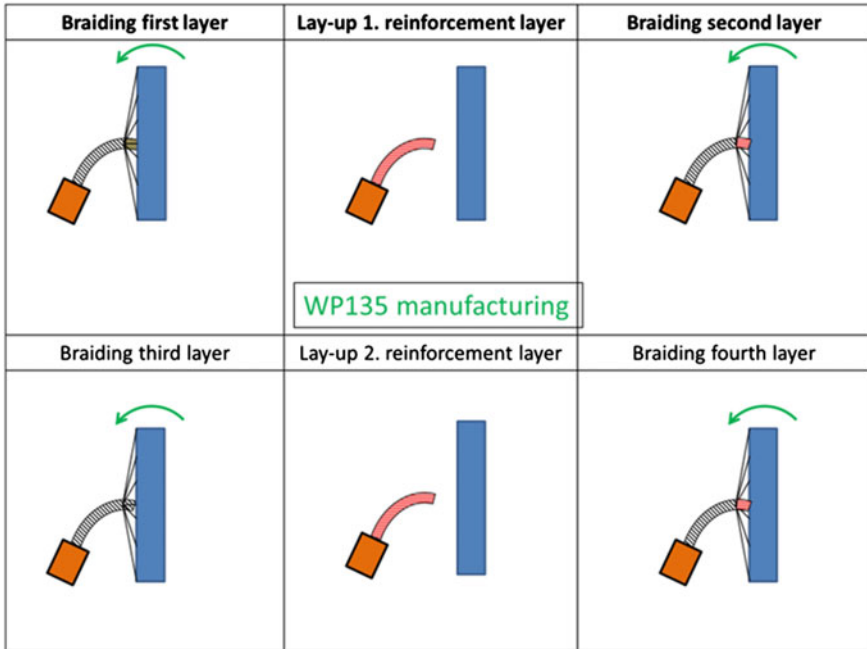


Fig. 20 Manufacturing principles WP135

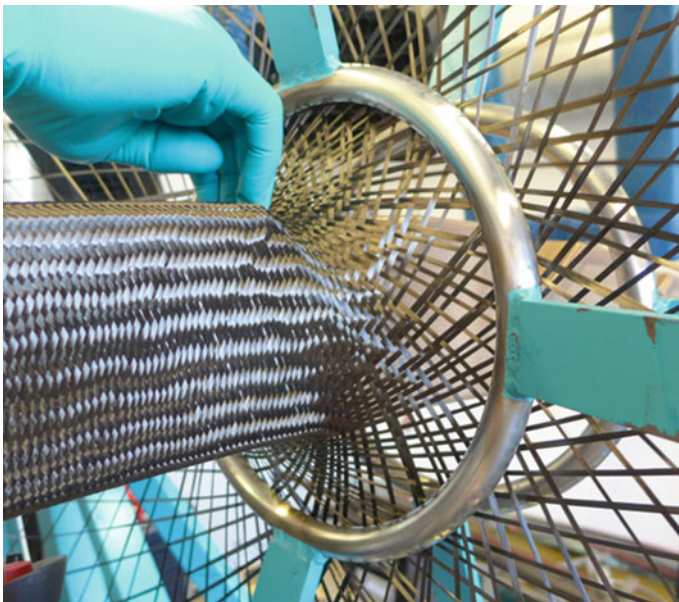


Fig. 21 Manual draping in mouse hole

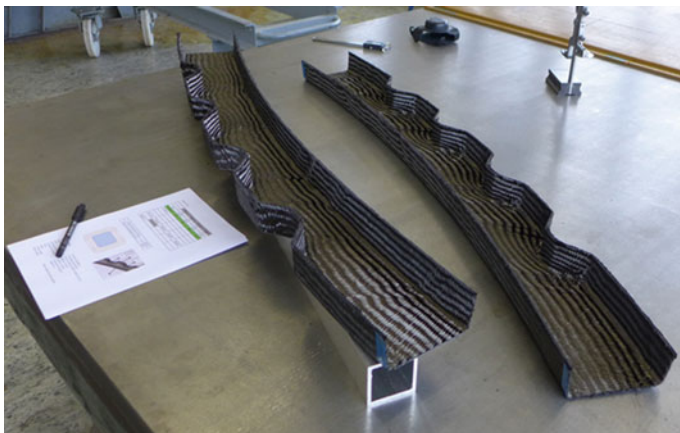


Fig. 22 Two frames preforms gained out of one preform

manual process could also be realized automatically relatively easy. After all layers have been applied, the preform was placed in a foil and the preform was stabilized with vacuum and temperature. After cooling, the preform was cut in the middle of the flange to get two C-frames (Fig. 22).

Since a state-of-the-art braiding is a dry fibre preforming process, a liquid resin infusion process afterwards is needed to impregnate the dry preform with the matrix material but also allows for curing in an out of autoclave process using an oven only. For this resin infusion process and also curing at 180 °C, a mould tool is needed to withstand the thermal loading and thereby providing sufficient dimensional stability. Taking the length of the frame, the mousehole geometry as well as the amount of mouseholes and thermal expansion of the tooling material into account steel is considered as the best material solution for manufacturing of a female mould tool.

For applying the rubber layer to the lower side of the metallic strip, a layer of adhesive film is used and cured at elevated temperature. Thereafter, the excess rubber is cut around the metallic strip edges and then the rubber/metal composite is placed into the mould tool together with the dry preform for preparation of the resin infusion process (Fig. 23).

The resin infusion process uses a flexible polymer vacuum bag foil at the inner side and the steel mould tool at the outer side. Thereby, the resin flow is assisted by the pressure differential between vacuum below the bagging foil and ambient pressure on the outside. For infusion, the tool is heated to 120 °C and then heated up to 180 °C for curing of the resin at a dwell time of 90 min. By that process, the CFRP part is cured, while at the same time also a bonded interface between the CFRP and the rubber layer is generated. In a last manufacturing step, the cured part is demoulded and all edges are machined to its final size to be used for assembly of the complete side panel (Fig. 24).

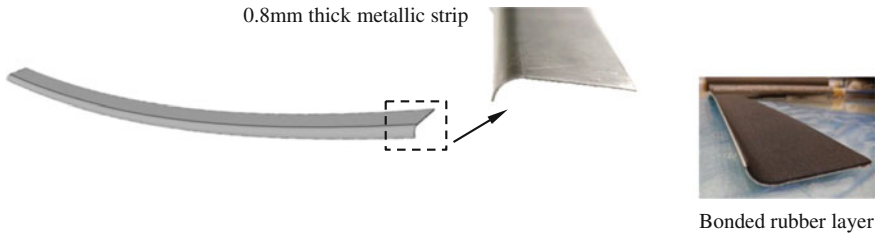
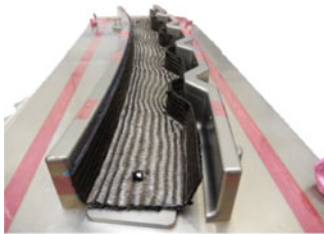


Fig. 23 Bonding of rubber layer onto metallic strip



Preparation of preform in mould tool for resin infusion



Resin infusion and curing process



Fig. 24 Resin infusion process and cured part after machining to final contour

8 Side Panel Assembly

Assembly took place without any additional jigs and fixing support structure. The premanufactured frames were used to shape the skin panel. The skin panel itself was extremely flexible and therefore very forgiving during the assembly process. Standard tools were used to fulfil the assembly step (Figs. 25 and 26).

All frames were undergoing a prefit verification. Gaps between panel and frame flanges were checked. Result showed a very good alignment, no gaps exceeded 0.2 mm.

Initial holes, 4 per frame, were drilled, and parts could then be “clamped” together using these holes. Some spring back effects on the frames were noticed. Mainly, it was the web of each frame that was not perpendicular to the skin when the flanges were used as the direction driver. This has on the other hand no effect on the testing campaign and was left without any further adjustments.

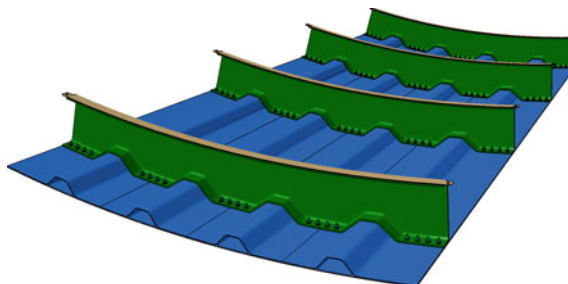


Fig. 25 CAD view of assembly

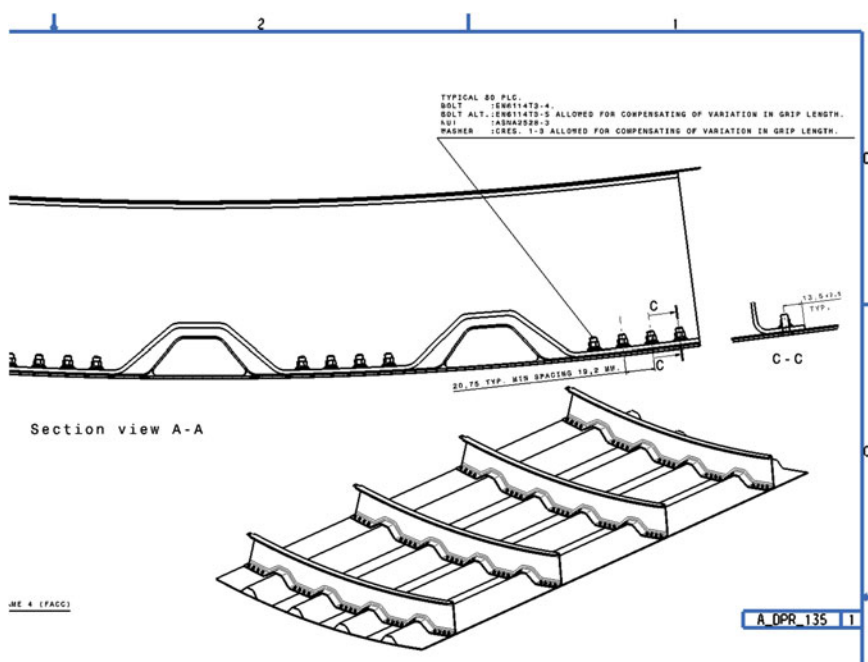


Fig. 26 Part of assembly drawing

Remaining holes were drilled, and during the installation, all frames were assembled with interfacial sealant.

All fasteners were measured and found to be 0.03–0.08 below the skin surface. This control should secure the contact between the fasteners and the ECF. With the result, the fact that the ECF applies around 0.1 mm below outer surface contact must exist with respect to these fasteners positions.

Electrical testing of the panel will be carried out by EADS F (Fig.27).



Fig. 27 Assembled side panel ready for delivery

Acknowledgments The research leading to these results has received funding from the European Union's Seventh Framework Programme for research, technological development and demonstration under Grant Agreement No 284562.